

# HEAT POWERED CYCLES 2018 Conference Proceedings



## Heat Powered Cycles Conference

University of Bayreuth, Germany  
16<sup>th</sup> -19<sup>th</sup> September 2018

Published by Heat Powered Cycles

This Conference Proceedings was prepared with the final versions of the manuscripts that were accepted by the Organizing Committee of the Eight Heat Powered Cycles Conference. This material aims to present the accepted and presented articles, including Keynote Lectures.

Art Work and information related to the Conference, Organizing Committee, Executive Committee and Advisory Board were taken from the conference's web site.

**Edited by:**

Prof. Dr. Roger R. Riehl - National Institute for Space Research - INPE/DMC - Brazil

Prof. (FH) Dr.-Ing. Markus Preißinger - Energy Research Center, University of Applied Sciences Vorarlberg, Austria

Prof. Dr. Ian W. Eames, University of Nottingham, UK

Prof. Dr. Mike Tierney, University of Bristol, UK

**HEAT POWERED CYCLES 2018**

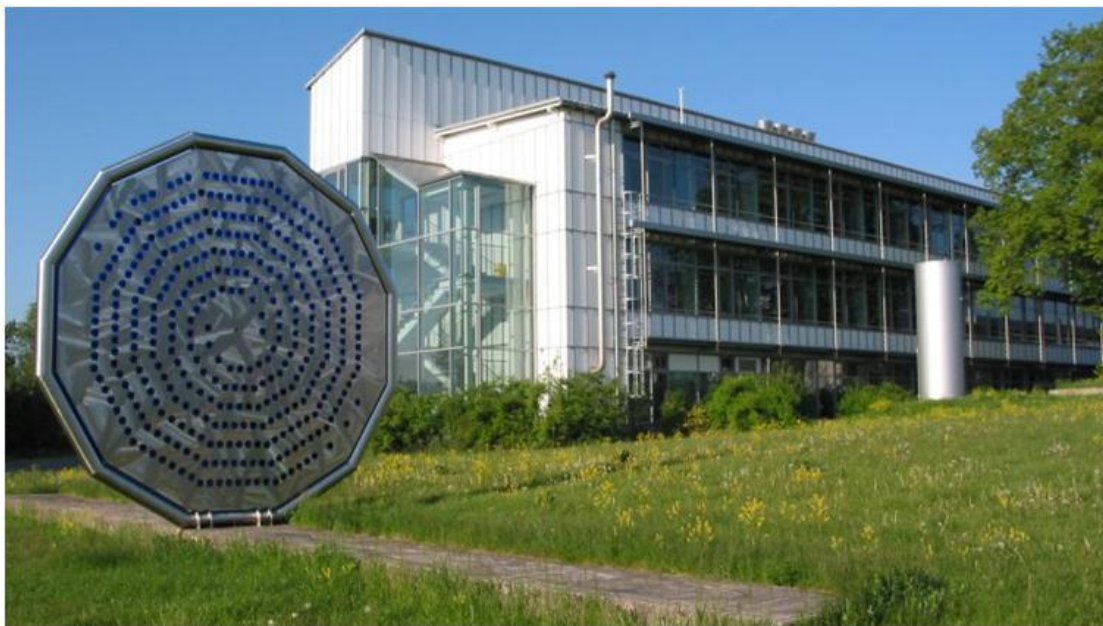
**Book of Abstracts**

Copyright©2018 is claimed by Heat Powered Cycles for the printed cover, layout and foreword of the publication, which must not be copied or distributed in any way without the permission of Heat Powered Cycles. Notwithstanding these claims and conditions, individual articles contained herein remain entirely the copyright© property of the authors and permission must be sought from them to reproduce or distribute any part in any way.

ISBN 978-0-9563329-6-7

## **Welcome to the Eight Heat Powered Cycles Conference**

This is the eighth Heat Powered Cycles Conference. The first was held at Nottingham in 1997. This time the event is being co-organised by the *University of Bayreuth*, (Germany), *The University of Applied Sciences, Vorarlberg*, (Austria), *The National Institute for Space Research*, (Brazil) and *The University of Bristol*, (UK). The conference is to be held at the University of Bayreuth and hosted by the Centre for Energy Technology at the University of Bayreuth by *Prof. Dieter Brüggemann*, as director of the Center, and *Prof. Markus Preißinger*, former executive manager of the Centre. In addition to formal presentations of technical papers, including invited Keynote papers, the event will include poster sessions and workshops. There will also be a full social programme for both delegates and accompanying partners. The conference is concerned with scientific and technological innovations relating to the efficient and economic use of heat, derived from all its sources, for the production of cooling, heating and mechanical power either independently or co-generatively.



*Center of Energy Technology at the Faculty of Engineering Science, University of Bayreuth*

Subject areas of particular interest include; hybrid cycles, ORCs, Stirling cycle machines, thermo-acoustic engines and coolers, sorption cycle refrigerators and heat pumps, jet-pump (ejector) machines, temperature amplifiers (heat transformers), chemical heat pumps, new working fluids, mass and heat transfer phenomena, desalination of brackish water and seawater, compact heat exchanger research (including foams and other micro-channel research), thermo-economics, process optimisation and modelling, process and cycle thermodynamics.

## History



2016: Nottingham

The seventh Heat Powered Cycles conference was co-organised by the Universities of Nottingham and Bristol. The conference was held at the University of Nottingham and was hosted by the HVASCR & Heat Transfer Group.



2012: Alkmaar

The sixth Heat Powered Cycles conference was hosted by Energy research Center of the Netherlands (ECN) in the Golden Tulip Hotel in Alkmaar.



2009: Berlin

The fifth Heat Powered Cycles conference was hosted by the Technical University of Berlin.



2006: Newcastle

The fourth Heat Powered Cycles conference was hosted by University upon Tyne Newcastle.

### Three special Issues after HPC 2018

The Organizing Committee of the Heat Powered Cycles Conference will select some presented manuscripts, after the conference is finished, to be invited for publication in a special issue of *Applied Thermal Engineering* (Elsevier), *Energy* (Elsevier) and *Energies* (MDPI). The selection of the manuscripts will be based on their quality and presentation. The selected manuscripts will undergo a the normal review process for those journals.

## **Organizing Committee**

### **Conference Chair**

Prof. Dr.-Ing. Dieter Brüggemann  
Center of Energy Technology, University of Bayreuth, Germany

### **Conference Co-Chair**

Prof. (FH) Dr.-Ing. Markus Preißinger  
illwerke vkw Endowed Professor for Energy Efficiency, Energy Research Center, University  
of Applied Sciences Vorarlberg, Austria

### **Review and Program Chair**

Prof. Dr. Roger R. Riehl  
Faculty of Thermal/Fluid Sciences and Thermal Control Specialist, National Institute for  
Space Research - INPE/DMC - Brazil

### **Executive Committee**

Prof. Dr. Ian W. Eames, University of Nottingham, UK  
Dr. Mike Tierney, University of Bristol, UK

### **Scientific Advisory Panel**

Adriano Milazzo, University of Florence, Italy  
Angelo Freni , CNR-ITAE, Italy  
Bob Critoph, University of Warwick, UK  
Brian Agnew , University of Newcastle, UK  
Christian Schweiger, Munich University of Applied Sciences, Germany  
Christos Markides, Imperial College, London UK  
David A. Reay, David Reay & Associates, UK  
David Hann, Nottingham University, UK  
Francis Meunier, CANAM, Paris, France  
Giovanni Restuccia, CNR-ITAE, Italy  
Giulio Santori, University of Edinburgh, UK  
Guangming Chen, Zhejiang University, China  
Hisham Sabir, QNRF, Qatar  
Ian Eames, University of Nottingham, UK  
Joan Carlos Bruno , Universitat Rovira i Virgili, Spain  
Larisa Gordeeva , Boreskov Institute of Catalysis  
Markus Preißinger, Vorarlberg University of Applied Sciences, Austria  
Michel van der Pal, ECN, Alkmar, Netherlands  
Mike Tierney, University of Bristol, UK  
Philip Davies, Aston University, UK  
Phillipe Blanc-Benon, École Centrale de Lyon , France  
Pierre Neveu, University of Perpignan, France  
Rayah Al-Dadah, University of Birmingham, UK  
Robert Keolian, Penn State University, USA  
Roger R. Riehl , National Institute for Space Research – INPE/DMC, Brazil  
Ruzhu Wang, SJTU, Shanghai, China  
Steven Garrett, Penn State University, USA  
Yann Bartosiewicz , University Catholique de Louvain UCL, Belgium  
Yukitaka Kato, Tokyo Institute of Technology, Japan  
Yuri Aristov, Boreskov Institute of Catalysis, Russia  
Zacharie Tamainot-Telto , University of Warwick, UK

# Summary

## Keynote Lectures

- HPC-2018-KEYNOTE-100: A Fission-Powered Thermoacoustic In-Core Sensor..... 13  
*Steven L. Garrett*
- HPC-2018-KEYNOTE-300: Honey, I Shrunk the Sorption Lab - Model-based Scale-up of Adsorption Systems - ..... 22  
*S. Graf, A. Gibelhaus, U. Bau, F. Lanzerath, A. Bardow*
- HPC-2018-KEYNOTE-400: Mining and Upgrading Low-Grade Heat: From Infinite Potential to Practical Reality ..... 25  
*Srinivas Garimella*
- HPC-2018-KEYNOTE-500: From cycle efficiency to physical properties - Comprehensive analyses of ORC working fluids by theoretical and experimental methods ..... 28  
*F. Heberle, T. Weith and D. Brüggemann*
- HPC-2018-KEYNOTE-600: Metal Organic Framework Materials for Adsorption Heat Pumps ..... 31  
*R.K. AL-Dadah, Saad Mahmoud, Eman Hussein, Peter Youssef, Fadhel Al-Mousawi*

## Full Manuscripts

- HPC-2018-102: Bubble Columns in Humidification Dehumidification Technology: From a Demonstration Unit to Fundamental Research in Optical Accessible Laboratory Bubble Columns..... 44  
*M. Preißinger*
- HPC-2018-103: Iron(III) Trimesate (MIL-100(Fe)) in Adsorption Desalination ..... 51  
*Eman Elsayed, Raya AL-Dadah, Saad Mahmoud, Paul Anderson, Ashraf Hassan*
- HPC-2018-201: The effects of graphite flake on specific cooling power of sorption chillers: An experimental study ..... 59  
*H. Bahrehmand, M. Khajehpour, W. Huttema, C. McCague and M. Bahrami*
- HPC-2018-204: The Influence of Heat Input Ratio on Electrical Power Output of a Dual-Core Travelling-Wave Thermoacoustic Engine ..... 67  
*Wigdan Kisha, Paul H. Riley, Jon McKechnie, David Hann*
- HPC-2018-205: Experimental and Numerical Study of the Thermal Performance of Water-Stainless Steel Heat Pipes Operating in Mid- Level Temperature ..... 75  
*Silva, Débora de O., Riehl, Roger R.*
- HPC-2018-207: CO selective methanation for PEMFC applications..... 83  
*P. Garbis, C. Kern and A. Jess*
- HPC-2018-209: On the Thermal Cyclic Precipitation of Aqueous Solutions for Osmotic Heat Powered Cycles..... 91

<i>Francisco J Arias, Salvador de las Heras</i>	
HPC-2018-210: Deliberate Salinization of Domestic Wastewater in Housing Estates for Energy .....	98
<i>Francisco J Arias, Salvador de las Heras</i>	
HPC-2018-211: A novel hybrid dew point cooling system for mobile applications.....	104
<i>Mark. Worall, Adam. Dicken, Mahmoud. Shatat, Sam. Gledhill, Saffa. Riffat</i>	
HPC-2018-300: Porous copper coated low pressure condenser/evaporator for sorption chillers.....	112
<i>P. Cheppudira Thimmaiah, A. Fradin, W. Huttema and M. Bahrami</i>	
HPC-2018-303: "LiCl/vermiculite – methanol" as the new working pair for adsorption cycle "HeCol" for upgrading the ambient heat .....	120
<i>A.D. Grekova, L.G. Gordeeva and Yu.I. Aristov</i>	
HPC-2018-304: Get your tubes wet: capillary-assisted thin-film evaporation of water for adsorption chillers .....	127
<i>J. Seiler, F. Lanzerath, C. Jansen and A. Bardow</i>	
HPC-2018-305: Analytical Investigation of Zeolite-NaY-Water for Sorption Heat and Cold Storage Utilizing High Temperature Heat .....	136
<i>K. Geilfuß and B. Dawoud</i>	
HPC-2018-306: Effect of Conductive Additives on Performance of CaCl <sub>2</sub> -Silica Gel Sorbent Materials .....	146
<i>M. Khajehpour, C. McCague, S. Shokoya and M. Bahrami</i>	
HPC-2018-307: An innovative solid-gas chemisorption heat transformer system with a large temperature lift for high-efficiency energy upgrade.....	153
<i>S. Wu, T.X. Li, T. Yan, R.Z. Wang</i>	
HPC-2018-308: Comparison of Storage Density and Efficiency for Cascading Adsorption Heat Storage and Sorption assisted Water Storage.....	161
<i>Matthias S. Treier, Aditya Desai and Ferdinand P. Schmidt</i>	
HPC-2018-309: Design and control of adsorption cooling systems based on dynamic optimization .....	169
<i>A. Gibelhaus, T. Tangkrachang, U. Bau, F. Lanzerath and A. Bardow</i>	
HPC-2018-310: Early Design of a Magnetic Mover for Adsorbents .....	177
<i>M. J. Tierney, J. Yon</i>	
HPC-2018-311: Squaring the circle in drying high-humidity air by a novel composite sorbent with high uptake and low pressure-drop.....	184
<i>Meltem Erdogan, Claire McCague, Stefan Graf, Majid Bahrami, and André Bardow</i>	
HPC-2018-312: Lab-scale sorption chiller comparison of FAM-Z02 coating and pellets....	190
<i>C. McCague, W. Huttema, A. Fradin, and M. Bahrami</i>	
HPC-2018-313: A new generation of hybrid adsorption washer dryers.....	196

<i>J. Cranston, A. Askalany, G. Santori</i>	
HPC-2018-314: Formulation influence on the preparation of silica nanoparticle-based ionogels .....	204
<i>Hongsheng Dong, Ahmed A. Askalany and Giulio Santori</i>	
HPC-2018-315: Heat rejection stage of an adsorption heat storage cycle: The useful heat and sorption dynamics .....	212
<i>V. Palomba, A. Sapienza and Y. Aristov</i>	
HPC-2018-317: Adsorptive heat transformation/storage: temperature-vs. pressure-initiated cycles.....	219
<i>Yu.I. Aristov</i>	
HPC-2018-319: Database of Sorption Materials Equilibrium Properties.....	227
<i>Zhiyao Yang, Kyle R. Gluesenkamp, and Andrea Frazzica</i>	
HPC-2018-320: Overview and step forward on SAPO-34 based zeolite coatings for adsorption heat pumps .....	236
<i>L. Calabrese, L. Bonaccorsi, A. Freni, P. Bruzzaniti, E. Proverbio</i>	
HPC-2018-321: Effects of storage period on the performance of salt composite sorption thermal energy storage .....	243
<i>M. Rouhani, W. Huttema, C. McCague, M. Khajepour and M. Bahrami</i>	
HPC-2018-323: Experimental investigation of a novel absorption heat pump with organic working pairs .....	249
<i>P. Chatzitakis, B. Dawoud, J. Safarov and F. Opferkuch</i>	
HPC-2018-324: Silica Gel microfibres by electrospinning for adsorption heat pumps. ....	257
<i>A. Freni, L. Calabrese, A. Malara, P. Frontera and L. Bonaccorsi</i>	
HPC-2018-325: Air-channel composite desiccant for northern climate humidity recovery ventilation system .....	263
<i>E. Cerrah, C. McCague, M. Bahrami</i>	
HPC-2018-326: Influence of the fluid dynamics on an air-cooled fixed-bed adsorber with connected water evaporator .....	271
<i>M. Jäger, K. Hurtig, R. Kühn and J. Römer</i>	
HPC-2018-328: Experimental proof of concept for a water/LiBr single stage absorption heat conversion system as a house connection station .....	280
<i>S. Hunt1, S. Petersen, F. Ziegler and C. Hennrich</i>	
HPC-2018-329: Temperature- vs. Pressure-Initiated Cycles for Upgrading Low Temperature Heat: Dynamic Comparison.....	287
<i>I. Girnik and Yu. Aristov</i>	
HPC-2018-330: Adsorption heat transformation: applicability for various climatic regions of the Russian Federation .....	295
<i>A.D. Grekova, L.G. Gordeeva, A. Sapienza and Yu.I. Aristov</i>	



HPC-2018-331: Design of a Gas-Fired Carbon-Ammonia Adsorption Heat Pump.....	304
<i>A. M. Rivero Pacho, S. J. Metcalf, R. E. Critoph, H. Ahmed</i>	
HPC-2018-334: High temperature heat and water recovery in steam injected gas turbines using an open absorption heat pump.....	312
<i>Annelies Vandersickel, Wolf G. Wedel, Hartmut Spliethoff</i>	
HPC-2018-335: Methanol and its Sorption Heat Pump and Refrigeration Potential .....	319
<i>S. Hinners, R.E. Critoph</i>	
HPC-2018-400: Optimal design and control of a low-temperature geothermally-fed parallel CHP plant.....	328
<i>Sarah Van Erdeweghe, Johan Van Bael, Ben Laenen and William D'haeseleer</i>	
HPC-2018-401: A Study on Optimum Discharge Pressure of Transcritical CO <sub>2</sub> Heat Pump System under Different Ambient Temperatures and Compressor Frequencies .....	336
<i>Xiang Qin, Xinli Wei, Dongwei Zhang and Xiangrui Meng</i>	
HPC-2018-402: Numerical analysis for dehydration and hydration of calcium hydroxide and calcium oxide in a packed bed reactor .....	344
<i>S. Funayama, M. Zamengo, H. Takasu, K. Fujioka, and Y. Kato</i>	
HPC-2018-403: Development of a low-cost, electricity-generating Rankine cycle, alcohol- fuelled cooking stove for rural communities .....	350
<i>Wigdan Kisha, Paul H.Riley and David Hann</i>	
HPC-2018-405: A Micro-Turbine-Generator-Construction-Kit (MTG-c-kit) for Small-Scale Waste Heat Recovery ORC-Plants .....	358
<i>A. P. Weiß, T. Popp, G. Zinn, M. Preißinger and D. Brüggemann</i>	
HPC-2018-407: Real-time operational optimization of a complex district heating and cooling plant.....	365
<i>L. Urbanucci, D. Testi and J. C. Bruno</i>	
HPC-2018-408: Thermodynamic analysis of S-CO <sub>2</sub> cycle for coal-fired plant .....	373
<i>Yawen Zheng, Jinliang Xu, Lei Lei</i>	
HPC-2018-409: Pumped Thermal Energy Storage (PTES) as Smart Sector-Coupling Technology for Heat and Electricity .....	381
<i>W.-D. Steinmann, H. Jockenhöfer and D. Bauer</i>	
HPC-2018-410: A theoretical approach to identify optimal replacement fluids for existing vapour compression refrigeration systems and heat pumps .....	389
<i>D. Roskosch, V. Venzik and B. Atakan</i>	
HPC-2018-412: Experimental Results of a 1 kW Heat Transformation Demonstrator based on a Gas-Solid Reaction.....	397
<i>J. Stengler, E. Fischer, J. Weiss and M. Linder</i>	
HPC-2018-413: A study on optimizing of pure working fluids in Organic Rankine Cycle (ORC) for different low grade heat recovery.....	404

<i>Rong He, Xinling Ma, Xinli Wei, Hui Li</i>	
HPC-2018-416: Numerical analysis of a heat pump based on combined thermodynamic cycles using ASPEN plus software.....	411
<i>Mohammed Ridha Jawad Al-Tameemi, Youcai Liang and Zhibin Yu</i>	
HPC-2018-417: Latent heat storage for direct integration in the refrigerant cycle of an air conditioning system .....	419
<i>T. Korth, F. Loistl, A. Storch, R. Schex, A. Krönauer and C. Schweigler</i>	
HPC-2018-418: Detailed exergetic analysis of a packed bed thermal energy storage unit in combination with an Organic Rankine Cycle .....	427
<i>A. König-Haagen and D. Brüggemann</i>	
HPC-2018-419: Novel High Temperature Steam Transfer Pipes.....	435
<i>M. J. Tierney, M. Pavier, P. Flewitt</i>	
HPC-2018-421: Technical and thermodynamic evaluation of hybrid binary cycles with geothermal energy and biomass.....	443
<i>D. Toselli, F. Heberle and D. Brüggemann</i>	
HPC-2018-422: Experimental Analysis of a Regenerative Organic Rankine Cycle using Zeotropic Working Fluid Blends .....	451
<i>Peter Collings, Andrew McKeown and Zhibin Yu</i>	
HPC-2018-423: Experimental Results from R245fa Ejector Chiller .....	459
<i>J. Mahmoudian, A. Milazzo, I. Murmanskii, A. Rocchetti</i>	
HPC-2018-424: Adapting the MgO-CO <sub>2</sub> working pair for thermochemical energy storage by doping with salts .....	467
<i>A. I. Shkatulov, S. T. Kim, Y. Kato, Yu. I. Aristov</i>	
HPC-2018-425: Effect of the apex gap size on the performance of a small scale Wankel expander.....	475
<i>G. Tozer, R. Al-Dadah, S. Mahmoud</i>	
HPC-2018-427: Water Mixtures as Working Fluids in Organic Rankine Cycles.....	483
<i>P. Bombarda, G. Di Marcoberardino, C. Invernizzi, P. Iora and G. Manzolini</i>	
HPC-2018-428: Constant power production with an organic Rankine cycle from a fluctuating waste heat source by using thermal storage .....	492
<i>K. Couvreur, J. Timmerman, W. Beyne, S. Gusev, M. De Paepe, W.D. Steinmann, and B. Vanslambrouck</i>	
HPC-2018-429: An Investigation of Nozzle Shape on the Performance of an Ejector.....	501
<i>Mehdi Falsafioon, Zine Aidoun</i>	
HPC-2018-431: Salt hydrate-silicone foam composite for heat storage application.....	509
<i>A. Frazzica, V. Palomba, V. Brancato, L. Calabrese, A.G. Fernández, M. Fullana-Puig, A. Solé, L. F. Cabeza</i>	

HPC-2018-432: Model based assessment of working pairs for gas driven thermochemical heat pumps .....	516
<i>E. Laurenz, G. Földner, J. Doell, C. Blackman, Lena Schnabel</i>	
HPC-2018-433: The Obtention of an Ejector Cooling System's Performance Map Through Different Graphical Representations.....	523
<i>Jorge I. Hernandez, Roberto Best, Ruben Dorantes, Humberto Gonzalez, Raul Roman, Jacobo Galindo and Pablo Aragon</i>	
HPC-2018-434: Thermodynamic and Thermo-economic Assessment of a PVT-ORC Combined Heating and Power System for Swimming Pools .....	530
<i>Kai Wang, Maria Herrando, Antonio Marco Pantaleao, and Christos N. Markides</i>	
HPC-2018-435: Application of Liquid-Air and Pumped-Thermal Electricity Storage Systems in Low-Carbon Electricity Systems .....	538
<i>S. Georgiou, M. Aunedi, G. Strbac and C. N. Markides</i>	
HPC-2018-436: Pumped Heat Electricity Storage at Intermediate Temperatures: Basics and Limits .....	547
<i>B. Atakan and D. Roskosch</i>	
HPC-2018-437: Performance analysis of a novel polygeneration plant for LNG cold recovery.....	554
<i>Antonio Atienza-Márquez, Joan Carles Bruno, Alberto Coronas</i>	
HPC-2018-438: Small-scale Pumped Heat Electricity Storage for decentralised combined Heat and Power Generation .....	560
<i>Annelies Vandersickel, J Loeff, Amir Aboueldahabb, Hartmut Spliethoff</i>	
HPC-2018-500: Experimental Investigation of the Effect of Magnetic Field on Vapour Absorption Rate of LiBr+H <sub>2</sub> O Nanofluid.....	567
<i>Shenyi Wu and Camilo Rincon Ortiz</i>	
HPC-2018-501: Thermal Performance of Nanofluids Applied to the Temperature Control of Electronic Components .....	575
<i>Roger R. Riehl</i>	
HPC-2018-600: Two-Phase Pressure Drop Correlation During the Convective Condensation in Microchannel Flows .....	586
<i>Roger R. Riehl</i>	
HPC-2018-601: Numerical Investigation of MOFs Adsorption Cooling System Using Microchannel Heat Exchangers .....	595
<i>Majdi M. Saleh, Raya AL-Dadah and Saad Mahmoud</i>	
HPC-2018-602: Natural graphite: Potential material for heat exchangers of waste heat recovery systems.....	603
<i>N. Mohammadaliha, W. Huttema and M. Bahrani</i>	
HPC-2018-701: Ultra-clean Biomass Gasification/Combustion Unit for Micro-CHP based on a Stirling Engine .....	609
<i>M. Steiner, S. Beer, D. Hummel</i>	

## **Keynote Lectures**

# A Fission-Powered Thermoacoustic In-Core Sensor

Steven L. Garrett

151 Sycamore Drive, State College, PA 16801

[sxg185@psu.edu](mailto:sxg185@psu.edu)

## Abstract

Motivated by the Fukushima nuclear reactor disaster in March 2011, a thermoacoustic engine was designed to have dimensions that are identical to a fuel rod to exploit the energy-rich conditions in the core of a nuclear reactor to acoustically measure and telemeter core condition information to reactor operators without a need for external electrical power. The standing-wave thermoacoustic heat engine is self-powered and can wirelessly transmit the temperature (encoded as a frequency) and reactor power level (proportional to sound amplitude) by generation of a pure tone that can be detected outside the reactor.

**Keywords:** Thermoacoustic engines, Wireless telemetry, Nuclear reactor sensing

## Introduction/Background

The generation of sound by heat has been documented as an “acoustical curiosity” since 1568 when a Buddhist monk reported the loud tone generated by a ceremonial rice-cooker in his diary [1]. In 1850, Karl Friedrich Julius Sondhauss investigated an observation made by glassblowers who noticed that when a hot glass bulb was attached to a cooler glass tubular stem, the stem tip sometimes emitted a pure tone [2]. The Sondhauss tube [3] is the earliest thermoacoustic engine that is a direct antecedent of this fission-powered in-core sensor.

The first qualitative explanation of the Sondhauss effect was provided by Lord Rayleigh: “If heat be given to the air at the moment of greatest condensation or be taken from it at the moment of greatest rarefaction, the vibration is encouraged” [4]. This new thermoacoustic sensor automatically does both. The standing sound wave transfers heat from a solid substrate to the gas (in our case a mixture of 75% helium and 25% argon rather than air) at the phase of the acoustic cycle during which the condensation (*i.e.*, density and pressure) is maximum and removes heat from the gas and deposits it on a solid substrate (at a different location) at the phase of the cycle when the condensation is a minimum [5].

In our case, the solid substrate, called the “stack” [2], is visible in Fig. 1 (Lower right). It consists of an extruded cordierite ceramic material with straight pores of square cross-section that has commercial application as a substrate in automotive catalytic converters [6] A previous publication provides a (qualitative) Lagrangian description of the cyclic heat transfer resulting in the production and maintenance of an acoustic standing-wave resonance [7].

It is worthwhile to point out that our thermoacoustic sensor is an extremely simple heat engine when compared to an automobile engine that requires pistons, valves, cams, rocker-arms, flywheel, etc. to ensure that the compressions and expansions are synchronized with the heat input and exhaust at the proper phases in the cycle. By contrast, this standing-wave thermoacoustic process is phased by thermal diffusion and requires no moving parts other than the oscillatory motion of the gas. The irreversibility of the diffusion process reduces efficiency from that achievable using a traveling-wave thermoacoustic-Stirling cycle [8], but in the energy-rich core of a nuclear reactor, efficiency is less important than simplicity.

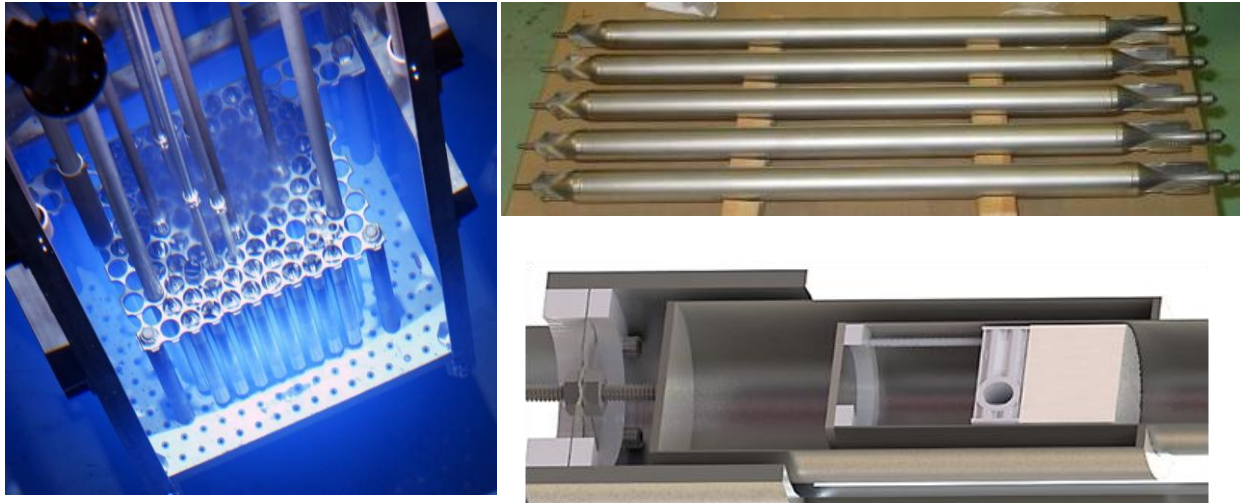


**Figure 1. Fuel rods used in the Breazeale Nuclear Reactor.** (Left) Photograph of the reactor's core. (Upper right) Several fuel rods. (Lower right) Cross-sectional rendering of the hot end of the thermoacoustic resonator showing one of two suspension springs that attach the resonator to the "slotted tube," the insulation space surrounding the hot end ( $\text{SiO}_2$  insulation floss not shown), and the hot heat exchanger that is in physical contact with the Celcor<sup>®</sup> ceramic stack that had 170 cells/cm<sup>2</sup>.



**Figure 2. "Fuel rod" thermoacoustic sensor.** (Above) The thermoacoustic resonator is shown at the center of the photograph. The resonator tube has an inside diameter of 2.2 cm and is 22 cm long. The insulated hot section of the resonator holds the hot heat exchanger that contains two enriched  $^{235}\text{U}$  fuel pellets that are each approximately 5 mm in diameter and 10 mm long, as well as the extruded ceramic "stack" shown in Fig. 1. The resonator tube contains the 2.0 MPa He/Ar gas mixture. The empty portion of the resonator, to the right of the insulated section, is in good thermal contact with the reactor's coolant. Two 4-40 threaded rods extend from either end of the resonator. The rods are attached to two circular stainless steel disks (200  $\mu\text{m}$  thick) that have six spokes acting as cantilever springs to allow the resonator to vibrate axially but constrain the resonator to remain coaxial within the surrounding "slotted tube." One of the thermocouples is silver-soldered (brazed) to the thin-walled section of the resonator next to the heat exchanger and the other is silver-soldered to the hot end of the resonator. Both thermocouples are located within the insulation space. (Below) The resonator and springs are contained within a "slotted tube" that has the same outer diameter as the fuel rods. The slots allow the reactor's coolant to remove the heat of

fission from the thermoacoustic sensor and facilitated testing of the resonator’s axial mobility before insertion in the reactor’s core.

## Discussion and Results

This thermoacoustic sensor converts the heat released by  $^{235}\text{U}$  fission to create a standing sound wave. It was designed to have a size and shape that is identical to the fuel rods in the Breazeale Nuclear Reactor on Penn State’s University Park campus, shown in Fig. 1. Those fuel rods have a maximum external diameter of 3.7 cm and an overall length of 72 cm. The acoustic resonator and the “slotted tube” that contains the resonator are shown in Fig. 2. A cut-away representation of the stack, heat exchanger, suspension spring, and insulation space is provided in Fig. 1. Based on our measurements of the vibro-acoustic spectra of the pump-dominated background noise in the coolant pool [9], a 2.0 MPa mixture of 75% helium and 25% argon was selected as the engine’s “working fluid” to place the resonance frequency at approximately 1,350 Hz, above most of that background noise, which was below 1.0 kHz. That inert gas mixture provides the largest possible polytropic coefficient (*i.e.*, ratio of specific heats) while also lowering the Prandtl number [10], thus improving the thermoacoustic energy conversion process [11].

The high-amplitude acoustic standing wave that is generated thermoacoustically causes the gas in the “empty” section of the resonator to be pumped by non-zero time-averaged nonlinear acoustic forces that create streaming cells [12]. This acoustically-induced flow forcibly convects heat from the ambient-temperature end of the stack to the walls of the resonator that are bathed in the reactor’s cooling water. Previous measurements in a similar electrically-heated “fuel rod resonator” have shown that this acoustically-driven streaming flow increases the thermal contact between the gas in the ambient-temperature end of the stack and the coolant by a factor-of-three [13]. This acoustically-enhanced heat transfer makes our thermoacoustic sensor even simpler than previous standing-wave thermoacoustic engines [14], since no separate cold heat exchanger is required.

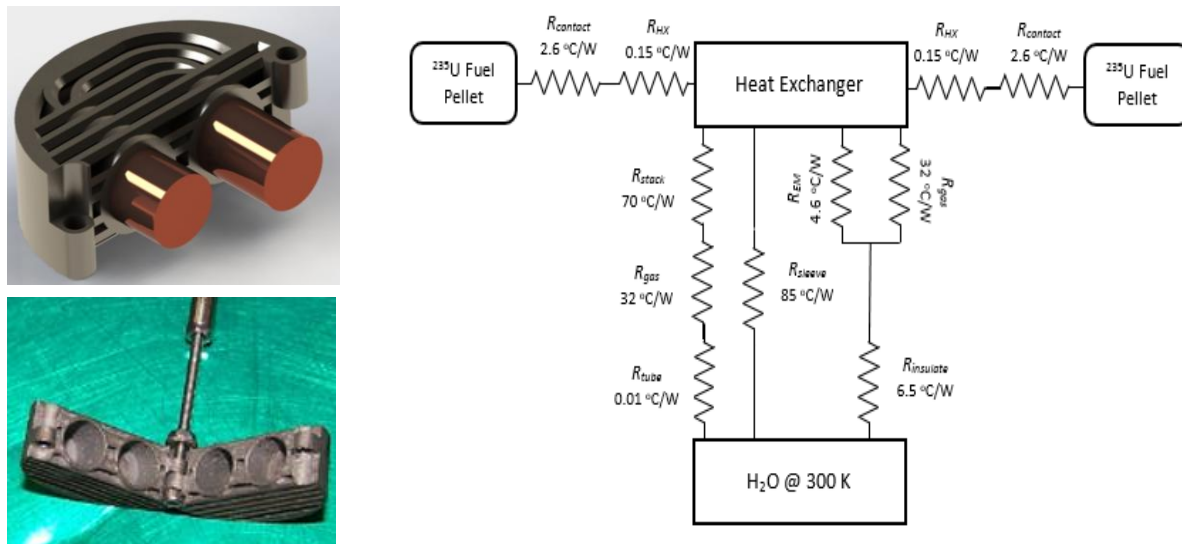


**Figure 3. Hot heat exchanger.** (Left) SolidWorks<sup>®</sup> rendering of one-half of the hot heat exchanger containing both enriched  $^{235}\text{U}$  pellets. The exchanger was fabricated by additive manufacturing in two halves that were joined by two 0-80 machine screws as shown in the photo below the rendering. (Right) The lumped-element static thermal conduction model includes the contact resistance from each pellet to the heat exchanger,  $R_{\text{contact}}$ , as well as the resistance of the stainless steel exchanger,  $R_{\text{HX}}$ . Heat from the pellets can reach the coolant along the resonator wall,  $R_{\text{sleeve}}$ , or can leak through the insulation’s thermal resistance,  $R_{\text{insulate}}$ , after either conduction through the gas or by electromagnetic radiation,  $R_{\text{EM}}$ . The

heat that passes through the stack will generate the thermoacoustic oscillations once the system reaches onset. Prior to onset, the heat diffuses through the ceramic stack material and the gas within the stack's pores,  $R_{stack}$ , then reaches the water through the static gas's thermal resistance,  $R_{gas}$ .

The hot heat exchanger is responsible for the transfer of the heat produced by the irradiated  $^{235}\text{U}$  pellets to the gas within the resonator. The left side of Fig. 3 shows the SolidWorks<sup>®</sup> model used to produce the two halves of the 3-D printed stainless steel heat exchanger that contained both pellets. The right side of Fig. 3 shows the static conduction model used to determine the temperature of the hot heat exchanger prior to thermoacoustic onset. Such a model is necessary to assure that no part of the stainless steel resonator reaches a temperature that would cause the material to weaken and possibly release either the compressed gas mixture or the enriched uranium prior to onset of the oscillations, which enhance the heat transfer and limit the temperature.

The detectability of the sound radiated by the thermoacoustic sensor depends upon the acoustics of the coolant pool and the vibroacoustic background noise level that was dominated by the pumps used to circulate the coolant. In the Breazeale Nuclear Reactor's coolant pool, the dominant noise was created by a diffusor pump that is used to circulate coolant (deionized light water) over the reactor core to prevent aggregation of short-lived radioactive  $^{16}\text{N}$  into bubbles that would rise before decaying, thus triggering radiation alarms.

The reactor pool is a reverberant acoustical environment. The standing-wave modal structure of the pool and the acoustic reverberation times were measured. The reactor's 70,000 gallon (265  $\text{m}^3$ ) coolant pool has equivalent rectangular dimensions that are 8.65 m long, 4.27 m wide, and 7.32 m deep. The lowest standing-wave modal frequency occurs at about 51 Hz. In a 3-dimensional enclosure, the number of modes below a given frequency increases with the cube of that frequency [15]. At some frequency, there will be three modes with resonance frequencies which overlap within the half-power bandwidth of the central mode. That "overlap" frequency is known within the architectural acoustics community as the Schroeder frequency,  $f_S$  [16]. Above that frequency, the sound field can be treated as being diffuse (*i.e.*, uniform energy density approximately independent of the location of the source and the sensors), so the sound field can be approximated as a "phonon gas" and the sound pressure can be estimated using statistical energy analysis. Based on our measurements of the reverberation time ( $T_{60} = 120 \pm 20$  ms),  $f_S \cong 230$  Hz  $\ll f \cong 1,350$  Hz. The sound pressure created by the fuel-rod thermoacoustic sensor will then be fairly homogeneous and isotropic at measurement distances from the source greater than the critical radius,  $r_d = c_{H_2O} / 5f_S \cong 1.3$  m [15]. The speed of sound in water is  $c_{H_2O} \cong 1,500$  m/s.

Our thermoacoustic sensor was tested during eight irradiation runs in the Breazeale Nuclear Reactor. Provisions of the reactor's license limit the accumulation of radioactive iodine isotopes produced by the fuel pellets to less than a total of 1.5 Ci. As a consequence, the sensor's irradiation dose restricted operations to a reactor time-integrated-power of approximately seven MW-minutes. Following each run, the experiment was idled while the unstable iodine isotopes were allowed to decay [5].

Figure 4 is a time record made during the 5<sup>th</sup> irradiation. It shows the temperature of the thermocouple that was brazed to the hot-end of the thermoacoustic resonator, contained within the insulation space, as well as the output of two hydrophones that were located far from the core in the reactor's coolant pool. Short Time Fast (essentially sliding-average) Fourier transforms of ten-second time records were produced every two seconds and the frequency of only the largest-amplitude spectral component is plotted in Fig. 4 for both hydrophones. The thermoacoustic



sensor achieved onset at about  $t = 810$  s, which is the time the largest amplitude spectral components for both hydrophones coalesced to the same frequency. It is also possible to detect a subtle indication of the onset of thermoacoustic oscillations suggested by the slight increase of the slope of the thermocouple's temperature vs. time after onset. This increased heating rate indicated a hydrodynamically-enhanced increase in the uniformity of the distribution of the heat from the hot heat exchanger to all other locations within the resonator.

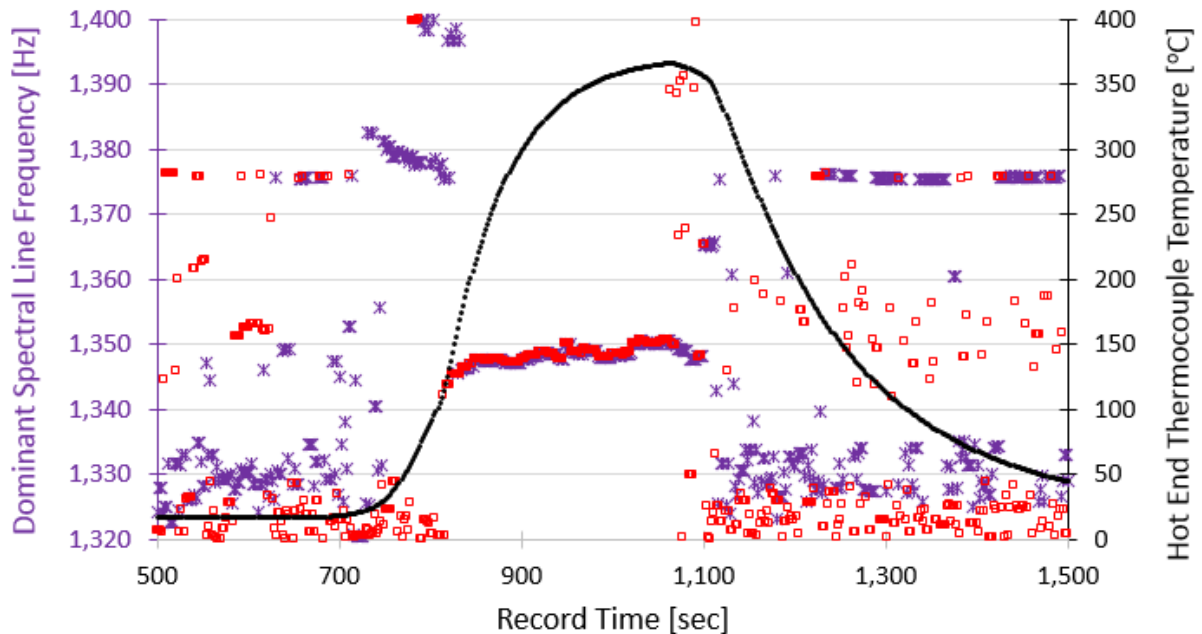


**Figure 4. Time record of the temperature and the frequency of the largest spectral component received by two hydrophones at different locations.** The temperature of a Type-K thermocouple brazed to the hot-end of the thermoacoustic resonator is plotted as the black circles. Those temperatures should be read from the black right-hand axis. The star symbols “\*” and hollow square symbols “□” are the frequencies of the largest spectral component within the frequency range between  $1,320 \text{ Hz} \leq f \leq 1,400 \text{ Hz}$ . Those frequencies should be read from the left-hand axis. All data points are plotted every two seconds. The time axis is labeled from the start of the recording. The reactor reached full power (1.0 MW) at  $t \cong 800$  s. The reactor power was reduced to 800 kW at  $t \cong 1,060$  s, then the reactor was shut down at  $t \cong 1,100$  s, since fission had produced the maximum allowable amount of radioactive iodine.

Before onset of thermoacoustic oscillations ( $t < 810$  s) and after their cessation ( $t > 1,100$  s), the frequencies of the dominant spectral components from both hydrophones' signals are fairly random and were different due to the proximity of the hydrophones to the sources of pump noises in those different locations. This is as would be expected when only the pump noises were received within the displayed bandwidth,  $\Delta f = \pm 40$  Hz.

Figure 5 shows one of several accelerometers that were attached to structures external to the reactor's coolant pool. The sonogram is taken from a 16-bit, 44.1 kilosamples/second digital audio recording of one accelerometer's output and displays the frequency of the detected vibration as a function of time with the amplitude of the signal coded as color from blue to yellow. Because the characteristic impedance of the water is close to the impedance of the solid structures that penetrate the reactor pool, the sound produced by the sensor couples well to those structures.

As demonstrated in Fig. 6, the frequency of the thermoacoustically generated sound provides an accurate determination of the reactor’s coolant temperature. We were able to reduce the reactor coolant temperature by running the reactor’s heat exchanger overnight.

The speed of sound in an ideal gas or gas mixture,  $c$ , is related to the acoustically-averaged absolute (Kelvin) temperature [7],  $T$ , the mean molecular mass of the gas mixture,  $M$ , the mixture’s polytropic coefficient,  $\gamma \equiv c_p/c_v = 5/3$ , and the Universal Gas Constant,  $\mathfrak{R}$ :  $c = (\gamma \mathfrak{R} T / M)^{1/2}$ .

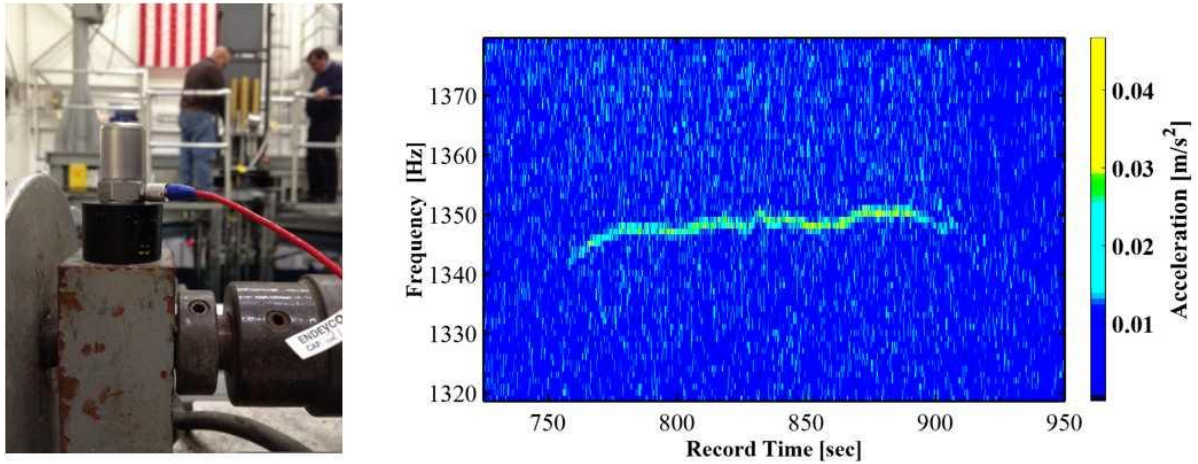


**Figure 5. Time record (spectrogram) of the vibration signal received by an accelerometer mounted on a structure outside the reactor pool.** (Left) Accelerometer with a magnetic base attached to the motor mount of an instrumentation tower that extends into the reactor pool. (Right) Spectrogram showing the accelerometer’s output frequency on the vertical axis as a function of time represented by the horizontal axis.

Ignoring the small localized changes in the resonator’s otherwise uniform cross-sectional area caused by the porous heat exchanger and the stack, the fundamental resonance frequency of the thermoacoustic sensor occurs when the wavelength of the sound in the gas mixture,  $\lambda = c/f$ , is approximately twice the resonator’s length,  $L \cong \lambda/2$ :  $f^2 = (c^2/4L^2) = (\gamma \mathfrak{R} T / 4 M L^2) \propto T$ .

The temperature of the gas mixture within the thermoacoustic resonator varies significantly from the high temperatures at the hot end (containing the heat exchanger) to about the temperature of the reactor coolant in the longest portion of the resonator between the ambient-temperature end of the stack and the ambient-temperature end of the resonator. A simple lumped-element model of the resonator as a “gas mass” at the center of the resonator surrounded by two “gas springs” suggests that the frequency is determined largely by the density of the lower temperature gas near the center of the resonator. The temperature of the central gas mass is controlled by the temperature of the reactor’s coolant. A more detailed model, treating the resonator as the concatenation of 31 lumped-elements, is able to provide a better estimate of the relationship between resonance frequency and coolant temperature [7].

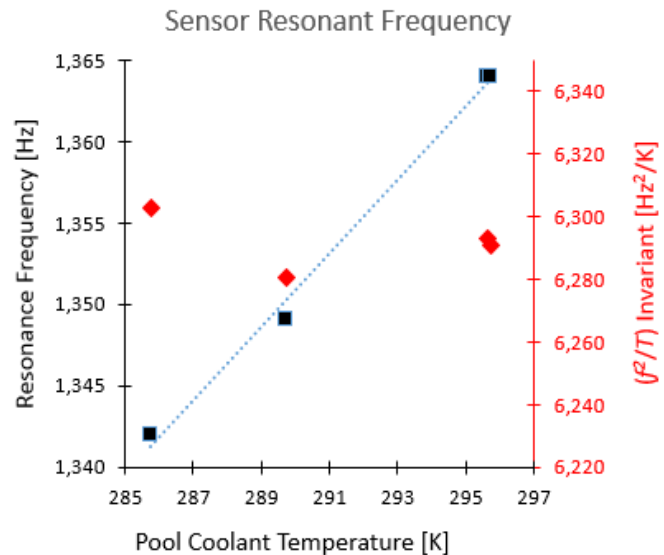
As is apparent from Fig. 6, just forming the ratio of the square of the measured resonance frequency,  $f^2$ , to the absolute (Kelvin) temperature of the reactor’s coolant,  $T$ , produces values of  $f^2/T$  that vary by only  $\pm 0.12\%$ , while the temperature changes by  $3.4\%$  [17].

### Summary/Conclusions

We have demonstrated the ability to acoustically telemeter temperature and power information beyond the core of a nuclear reactor without requiring external electrical power or wiring. Such

a sensor might have provided useful information in a reactor accident like the one which destroyed the Fukushima complex in March 2011. In a commercial reactor, the flux of gamma radiation could provide sufficient heating that tungsten or stainless steel could be used instead of fissionable fuel. This would avoid degradation in the sensor's sensitivity with time due to fuel depletion and remove the regulatory controls required for handling of enriched uranium. Multiple sensors in various core locations could also be used to optimize power distribution and improve a commercial reactor's operational efficiency.

**Figure 6. Resonance frequency of the thermoacoustic sensor's standing-wave for different coolant temperatures.** The sensor's resonance frequencies were measured at four different water temperatures between 12.6 °C and 22.6 °C in the reactor's pool. Frequencies corresponding to those temperatures are plotted as the black squares and their values are given by the left-hand axis that spans  $\pm 1.7\%$ . The right-hand axis has the same relative span, but the value of the  $f^2/T$  invariant, plotted as red diamonds, has a standard deviation of only  $\pm 0.12\%$  [17].



While this report has focused on in-pile nuclear reactor sensing, the thermoacoustic sensor is an utilitarian device that could be effectively adapted to other applications that involve large temperature gradients, hostile or corrosive environments, and hard to “wire” locations. Effective sensor adaptations can be configured to monitor melting glass or metal, hydrocarbon crackers, smoke stacks, and other processes or systems in which high temperatures are used that are difficult to measure. [18] Multiple sensors can be frequency multiplexed wirelessly using only a single detector (*e.g.*, microphone, hydrophone, or accelerometer). The sensors can be configured to be temperature sensors by monitoring the frequency of the acoustic standing wave, which depends upon the effective temperature of the gas in the resonant chamber. The thermoacoustic sensor can also be used to monitor the molecular mass of the gas mixture within the resonant chamber [19], thus the thermoacoustic sensor can also be used to monitor the progress of chemical reactions.

### Acknowledgements

The design and optimization of this sensor relied upon the Design Environment for Low-Amplitude Thermoacoustic Energy Conversion (DELTAEC), a software package developed and supported for over twenty-five years by G. W. Swift and W. W. Ward at the Los Alamos National Laboratory. The author is grateful for the support of Larry Bodendorf, Iain Wilson, James Lynch, and Brandon Rieck of IST Mirion for fabrication of the resonator and for its fueling. Support provided by Penn State's Radiation Science & Engineering Center for ensuring that the experiment could be operated safely and in full compliance with all NRC regulatory limits is appreciated. James A. Smith, James Lee, Vivek Agarwal, and Keith Jewell, from Idaho

National Laboratory, assembled and tested the data acquisition system and also provided assistance with the data analysis. The participation of Randall Ali, Joshua Hrisiko, and Andrew Bascom, three of the author's graduate students, each contributed to the success of these experiments. This research was supported by the U.S. Department of Energy's Idaho National Laboratory and by the Westinghouse Global Technology Development Department of the Westinghouse Electric Company.

### References:

- [1] Noda, D. and Ueda, Y., "A thermoacoustic oscillator powered by vaporized water and ethanol," *Am J. Phys.* **81**(2), 124-126 (2013).
- [2] Swift, G. W., "Thermoacoustic engines," *J. Acoust. Soc. Am.* **84**(4), 1145-1180 (1988).
- [3] Sondhauss, K. F. J., "Über die Schallschwingungen der Luft in erhitzten Glasröhren und in geteckten Pfeifen von ungleicher Weite," *Ann. Phys. (Leipzig)* **79**, 1 (1850).
- [4] Strutt, J. W. (Lord Rayleigh), "The explanation of certain acoustical phenomena," *Nature* **18**, 319-321 (1878).
- [5] Garrett, S. L., Smith, J. A., Smith, R. W. M., B. J. Heidrich, and M. D. Heibel, "Using the sound of nuclear energy," *Nuclear Technology* **195**(3), 353-362 (2016).
- [6] Liu, J., Garrett, S., Long, G., and Sen, A., "Separation of thermoviscous losses in Celcor™ ceramic," *J. Acoust. Soc. Am.* **119**(2), 857-862 (2006).
- [7] Ali, R. A., Garrett, S. L., Smith, J. A., and Kotter, D. K., "Thermoacoustic thermometry for nuclear reactor monitoring," *IEEE J. Instrumentation & Measurement* **16**(3), 18-25 (2013).
- [8] Backhaus, S. and Swift, G. W., "A thermoacoustic-Stirling engine," *Nature* **399**, 335-338 (1999).
- [9] Hrisiko, J., Garrett, S. L., Smith, R. W. M., Smith, J. A. and Agarwal, V., "The vibroacoustical environment in two nuclear reactors," *J. Acoust. Soc. Am.* **137** (2), 2198 (2015).
- [10] Giacobbe, F. W., "Estimation of Prandtl numbers in binary mixtures of helium and other noble gases," *J. Acoust. Soc. Am.* **96**(6), 3538-3580 (1994).
- [11] Swift, G. W., *Thermoacoustics: A unifying perspective for some engines and refrigerators*, 2<sup>nd</sup> ed., Springer-ASA Press 2017; ISBN 978-3-319-66932-8. See §8.1.
- [12] Strutt, J. W. (Lord Rayleigh), "On the circulation of air observed in Kundt's tubes, and on some allied acoustical problems," *Phil. Trans. Royal Soc. London* **175**, 1-21 (1883); *Scientific Papers*, Dover, 1964, Art. 108, Vol. II, pp. 239-257.
- [13] Ali, R. A. and Garrett, S. L., "Heat transfer enhancement through thermoacoustically-driven streaming," *Proc. of Meetings on Acoustics (POMA)* **19**, 030001 (2013); DOI: 10.1121/1.4799202.
- [14] Swift, G. W. "Analysis and performance of a large thermoacoustic engine," *J. Acoust. Soc. Am.* **92**(3), 1551-1563 (1992).
- [15] Garrett, S. L., *Understanding Acoustics: An experimentalist's view of sound and vibration*, Springer-ASA Press, 2017; ISBN 978-3-319-49976-5. See Ch. 13.
- [16] Schroeder, M. R., "The 'Schroeder frequency' revisited," *J. Acoust. Soc. Am.* **99**(5), 3240-3241 (1996).
- [17] Garrett, S. L., Smith, J. A., Smith, R. W. M., Heidrich, B. J. and Heibel, M. D., "Fission-powered in-core thermoacoustic sensor," *Appl. Phys. Lett.* **108**, 144102 (2016).

- [18] Garrett, S. L., Smith, J. A. and Kotter, D. K., "Thermoacoustic enhancements for nuclear fuel rods and other high temperature applications," US Pat. No. 9,646,723 (May 9, 2017).
- [19] Polturak, E., Garrett, S. L. and Lipson, S. G., "Precision acoustic gas analyzer for binary mixtures," Rev. Sci. Inst. **57**, 2837-2841 (1986).

# Honey, I Shrunk the Sorption Lab - Model-based Scale-up of Adsorption Systems -

S. Graf, A. Gibelhaus, U. Bau, F. Lanzerath, A. Bardow\*

Institute of Technical Thermodynamics, RWTH Aachen University, Schinkelstraße 8, 52062 Aachen, Germany

\*Corresponding author: andre.bardow@itt.rwth-aachen.de

## Abstract

Performance assessment and development of adsorption chillers typically requires large-scale experiments of whole adsorption chiller setups. In this work, we present a model-based approach to drastically reduce the required lab space and time. A workflow is illustrated that starts with a simple kinetic experiment with a small adsorbent sample to determine heat and mass transfer coefficients of a packed-bed adsorbent. These coefficients are used in a dynamic model to predict the SCP and COP of a full-size adsorption chiller. We show that the resulting model is able to predict the performance close to the measurement accuracy. With our approach, we thus can scale-up adsorption systems from milligram adsorbent samples to real machines with kilograms of adsorbent material. The underlying models for performance evaluation and development of adsorption machines are based on our freely available Modelica library SorpLib. The SorpLib library provides opportunities for the broad model-based development and optimization of adsorption systems and their control.

## Introduction

Dynamic models of adsorption chillers are widely used to study the influence of input conditions, component designs, cycle designs or control on performance. With the availability of object-oriented modeling languages such as Modelica, dynamic models are increasingly easy to setup. However, they not necessarily lead to a reliable prediction of the specific cooling power SCP and the coefficient of performance COP compared to experimental results [1].

For reliable performance prediction, the models need to be calibrated. In previous studies, high accuracies required experimental data from full-scale adsorption chiller setups [2, 3].

In this work, we exploit the predictive power of physical models to simplify the required experiments to the Infrared-Large-Temperature-Jump (IR-LTJ) experiment that uses only a small adsorbent sample ( $< 1$  g). A dynamic model is used to calibrate the heat and mass transfer coefficients. With the heat and mass transfer coefficients, we parametrize an adsorption chiller model. We show that the model is able to predict the SCP and COP of a complete adsorption chiller with high accuracy allowing for model-based optimization and control.

## Discussion and Results

To illustrate the suggested approach, we first determine heat and mass transfer coefficients for a packed bed of silica gel 123 with a mean particle size of 0.9 mm. For this purpose, we place 1 to 3 layers of adsorbent ( $< 1$  g) on a planar adsorbent carrier and conduct an IR-LTJ experiment [4]. The experimental data is used in a dynamic model for the adsorbent and the vapor phase. By fitting the measured pressure and temperature, we determine the heat and mass transfer coefficients  $\alpha$ ,  $\lambda$ , and  $D_{\text{eff}}$ , cf.

Table 1: Heat and mass transfer coefficients for packed bed of SG 123 from IR-LTJ-experiments.

	Adsorption	Desorption
$\alpha_{\text{eff}}$ in W/m <sup>2</sup> K	331	406
$\lambda_{\text{eff}}$ in W/mK	0.15	0.2
$D_{\text{eff}}$ in m/s <sup>2</sup>	$1.17 \times 10^{-9}$	$6.33 \times 10^{-10}$

table 1.

Second, we use the coefficients to parametrize a full-scale model of an adsorption chiller. The adsorber consists of aluminum tubes with an outer fin structure, which also holds the adsorbent. To account for the adsorber geometry, we discretize in 3 dimensions. The adsorber model is connected to models for the evaporator and condenser. We predict the heat flows of the adsorption chiller for the cycle temperatures 10/35/90°C, times for adsorption and desorption of 900s and compare them with measurements of a whole adsorption chiller setup (Figure 1).

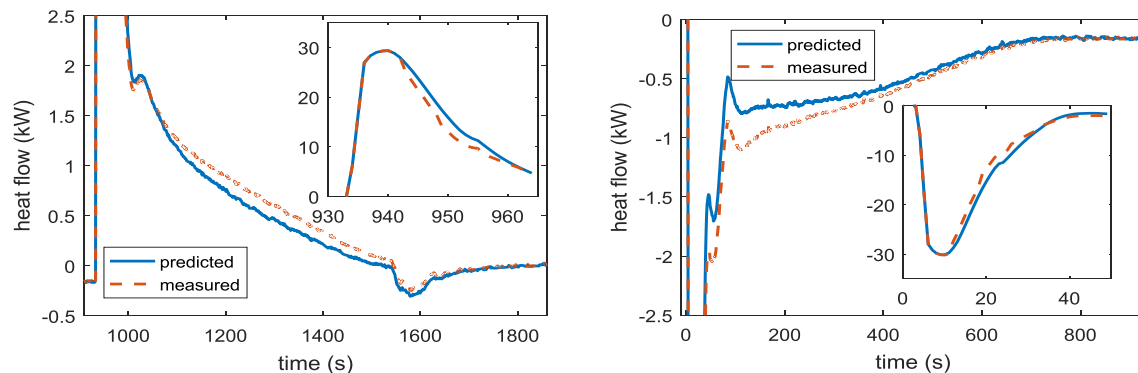


Figure 1: Predicted and measured heat flows in the adsorber for adsorption (left) and desorption (right).

From the predicted heat flows, the SCP and COP are determined to 81W/kg and 0.35. These values differ by 8.7% and 5.4% from the measured SCP of 88.7W/kg and COP of 0.37. Even the measured heat flows are well captured. Thus, the prediction has the same high accuracy as directly calibrated models in literature.

## Summary

For reliable adsorption chiller models, calibration with experimental data is necessary. Instead of conducting experiments with a full-size adsorption chiller, we require only a simple IR-LTJ experiment with a small adsorbent sample (<1g) to determine heat and mass transfer coefficients. With the coefficients, we parameterize a complex adsorption chiller model. The model predicts the SCP and the COP in the whole adsorption chiller with deviations of less than 9% compared to experiments. Thus, the accuracy is in the same range as for models calibrated to full-size adsorption chillers. Our approach allows for an easy and reliable performance prediction of full-scale adsorption chillers based on small-scale IR-LTJ experiments. The underlying models are freely available in our Modelica library SorpLib [5] and can be used for scaling up small-sized experiments and to develop and optimize adsorption systems.

## Acknowledgement

This work has been carried out within the project “TailorSorb – Tailored adsorbents for stationary adsorption thermal energy transformation” (03SF0515A). The project is funded by the German Federal Ministry of Education and Research (BMBF) within the funding priority “Materialforschung für die Energiewende”.

## References

- [1] Pesaran, A., Lee, H., Hwang, Y., Radermacher, R., Chun, H.-H., „Review article: Numerical simulation of adsorption heat pumps“, *Energy*, 2016, [doi:10.1016/j.energy.2016.01.103](https://doi.org/10.1016/j.energy.2016.01.103)
- [2] Schick Tanz, M., Núñez, T., „Modelling of an adsorption chiller for dynamic system simulation“, *International Journal of Refrigeration*, 2009, [doi:10.1016/j.ijrefrig.2009.02.011](https://doi.org/10.1016/j.ijrefrig.2009.02.011)
- [3] Lanzerath, F., Bau, U., Seiler, J. Bardow, A., Optimal design of adsorption chillers based on a validated dynamic object-oriented model”, *Science and Technology for the Built Environment*, 2015, [doi:10.1080/10789669.2014.990337](https://doi.org/10.1080/10789669.2014.990337)

- [4] Graf, S., Lanzerath, F., Bardow, A., “The IR-Large-Temperature-Jump method: Determining heat and mass transfer coefficients for adsorptive heat transformers”, Applied Thermal Engineering, 2017, [doi:10.1016/j.applthermaleng.2017.06.054](https://doi.org/10.1016/j.applthermaleng.2017.06.054)
- [5] Bau, U., Lanzerath, F., Gräber, M., Schreiber, H., Thielen, N., Bardow, A., Adsorption energy systems library - Modeling adsorption based chillers, heat pumps, thermal storages and desiccant systems. In: H. Tummescheit und K.-E. Arzen, Hg. Proceedings of the 10th International Modelica Conference. Linköping: Modelica Association, 2014, S. 875-883. ISBN 9789175193809. <http://www.ep.liu.se/ecp/096/091/ecp14096091.pdf>



# **Mining and Upgrading Low-Grade Heat: From Infinite Potential to Practical Reality**

**Srinivas Garimella<sup>1</sup>**

<sup>1</sup>George W. Woodruff School of Mechanical Engineering, Georgia Institute of Technology,  
Atlanta, GA 30332 USA

\*Corresponding author: sgarimella@gatech.edu

## **Abstract**

Much is made of the abundance of waste heat and its potential to offset primary energy needs. However, waste heat is waste heat for a reason! It is hard to eke out useful output from waste heat without potentially crippling capital costs, and without parasitic loads. Realistic opportunities, challenges, and innovations in the implementation of low-grade heat powered cycles are discussed. An overall framework for assessing the potential for waste heat without detailed design exercises, and the matching of different kinds of waste heat to a variety of applications are presented. In addition, examples of compact thermal systems that harvest low-grade heat and upgrade it to produce power, cooling, and other end uses are presented.

**Keywords:** Waste heat; sorption; work recovery; cooling; heat transformation.

## **Introduction/Background**

A Nobel prize-winning physicist interested in energy for the masses asks, “What is the Carnot limit for this technology?” and “Why are we not there?” The responsible engineer should respond, “It does not matter,” and “Irrelevant question.” Carnot limits are good expressions of the limits of achievability; however, they also need infinite heat transfer capabilities, infinite thermal capacities, and other “infinities and infinitesimals” to be converted to reality. Unfortunately, these infinities translate to infinite \$, and when addressing the issue of waste heat, one must recognize that to begin with, it is waste heat for some very good reasons. To achieve or even approach a small fraction of Carnot limits requires investments in capital cost that cannot be justified, especially in this mission, which is by definition, a scavenging task.

## **Waste Heat Availability and Constraints**

Waste heat is ubiquitous: at the national and global levels, as much as 2/3 of the primary energy utilization is rejected as waste heat [1]. Depending on the location and exergy of the available waste heat, applications such as power generation, residential air-conditioning, process heating, water heating, industrial and commercial and residential space heating can be found. However, this requires an appropriate distributed generation infrastructure, temporal and spatial matching between sources and applications, and/or thermal, chemical, mechanical or electrical storage, all of which need significant capital investment. Practical considerations such as working fluids with appropriate vapor-liquid-equilibrium characteristics, thermodynamic and transport properties, and compatibility with heat exchanger materials also present challenges.

## **Avenues for Utilization, Realistic Performance Expectations**

Options for outputs from a waste heat recovery system include recuperation and reuse, power generation, cooling, temperature boosting, and storage. An overall framework for assessing the potential for waste heat without detailed design exercises, and the matching of different kinds of waste heat to a variety of applications can be developed [2]. Source and sink temperatures, waste heat availability and coupling to gas or liquid streams, and heat source

scale (W – MW) are factors in choosing an appropriate cycle and output. For a representative gas source stream at 120°C with  $T_{\text{sink}} = 35^{\circ}\text{C}$ , a maximum efficiency of power production through an organic Rankine cycle would be ~0.11. While this low efficiency limits the applications in which it may be implemented, an even bigger challenge is the heat transfer surface requirement: this efficiency means that for every 11 W generated, ~100 W must be supplied across typically high gas-phase thermal resistances, and ~89 W must be rejected across similarly high thermal resistances, leading to large capital investment requirements. If on the other hand, the source was a hot liquid stream and heat rejection was also to a liquid, even with  $T_{\text{source}} = 60^{\circ}\text{C}$  and  $T_{\text{sink}} = 20^{\circ}\text{C}$  (representing an indoor condition), an efficiency of 0.08 can be achieved, with heat exchangers an order of magnitude smaller than those needed for gas-phase sources and sinks due to the high density, specific heat, and thermal conductivity of liquids. Even greater utility can be achieved if the end use is cooling instead of work or electricity production. Organic Rankine vapor compression cycles can provide cooling at 5°C with COPs of ~0.41 for the abovementioned gas-source case, and 0.68 for the liquid coupling case due to the heat pumping accomplished in a cooling scenario. Absorption heat pumps would yield even better results for these cases, COPs of ~0.70-0.80, respectively. For the very low grade heat sources, e.g., data-center waste heat at ~60°C, instead of cooling or work output, temperature boosting up to ~120°C can be achieved at a COP of ~0.47, providing upgraded heat as a commodity. Thus, useful outcomes are possible in these temperature constrained low-grade heat recovery applications, but only with proper selection of end uses, cycles, and protection of temperature lift against the penalties of caloric  $\Delta T$  of the source and sink, and driving  $\Delta T$  due to thermal resistances. Adsorption cycles provide more passive operation, and ejector-based refrigeration cycles offer lower complexity at the cost of efficiency.

### Representative Cases and Conclusions

Enhancement of phase-change heat and mass transfer in microchannels can also be exploited to enhance the performance potential and/or compactness of such waste heat recovery cycles. Applications range from systems that use waste heat to deliver 300 W [3] of cooling in modular, monolithic absorption heat pumps the size of a textbook, all the way up to MW of cooling [4] in cascaded cycles for aircraft carriers. Such systems have also been developed for thermally driven residential cooling and water heating systems, and systems that use exhaust heat from diesel engines to provide cooling at military bases at  $T_{\text{ambient}} \sim 52^{\circ}\text{C}$  [5]. It is emphasized, however, that implementation of real-world waste heat recovery systems presents challenges ignored in conceptual analyses, such as auxiliary high-grade electric loads of recirculation pumps and fans. Despite the potential of innovative cycles, these constraints determine the bounds for the utility and economic viability of waste heat.

### References

1. A. S. Rattner and S. Garimella (2011), “Energy Harvesting, Reuse and Upgrade to Reduce Primary Energy Usage in the USA,” *Energy*, Oct 2011, Vol. 36, Issue 10, pp. 6172-6183.
2. A. B. Little and S. Garimella (2011), "Comparative Assessment of Alternative Cycles for Waste Heat Recovery and Upgrade," *Energy*, Vol. 36, pp. 4492-4504.
3. M. D. Determan and S. Garimella (2012), Design, Fabrication, and Experimental Demonstration of a Microscale Monolithic Modular Absorption Heat Pump, *Applied Thermal Engineering*, vol. 47, p. 119-125.
4. S. Garimella, A. M. Brown and A. K. Nagavarapu (2011), “Waste Heat Driven Absorption/Vapor Compression Cascade Refrigeration System for Megawatt Scale, High-Flux, Low Temperature Cooling,” *Int. J. Refrig.*, Vol. 34, Issue 8, pp. 1776-1785.

5. M. J. Ponkala, A. Goyal, M. A. Staedter, S. Garimella, "A packaged waste-heat driven ammonia-water absorption chiller for severe ambient operation," *Int. Sorption Heat Pump Conf.* 2017, Aug. 7-10, Tokyo, Japan.

# **From cycle efficiency to physical properties - Comprehensive analyses of ORC working fluids by theoretical and experimental methods**

**F. Heberle<sup>\*</sup>, T. Weith and D. Brüggemann**

Chair of Engineering Thermodynamics and Transport Processes (LTTT),  
Center of Energy Technology (ZET), University of Bayreuth  
Universitätsstraße 30, 95447 Bayreuth, Germany

<sup>\*</sup>Corresponding author: florian.heberle@uni-bayreuth.de

## **Abstract**

The selection of a suitable working fluid is one of the key decisions regarding the design of an organic Rankine cycle (ORC) power system. The determination of the ORC fluid is crucial for the cycle efficiency, component design and costs. Depending on the characteristics of the heat source and the heat sink, different groups of substances like refrigerants, hydrocarbons or siloxanes are potential candidates. In case of applications for waste heat recovery within a temperature range of 250 °C and 500 °C, first and second law analysis show that hexamethyldisiloxane (MM) is a promising working fluid. The applied simulation models are validated by experimental data from an ORC test rig with a nominal electrical power output of 15 kW. In addition, extensive experimental investigations are conducted for MM in order to improve the existing heat transfer prediction methods and reduce uncertainties regarding fluid properties. Consequently, a more reliable heat exchanger sizing and an increase in cost efficiency can be realized.

**Keywords:** Organic Rankine Cycle, working fluid, fluid properties, heat transfer

## **Introduction/Background**

In general, organic Rankine cycle (ORC) power systems are applied for heat source temperatures in the range of 100 °C up to 500 °C. In this context, waste heat recovery from industrial processes as well as stationary or mobile combustion engines has high energy-saving potential. The wide range of heat source temperatures for these applications lead in principal to a large number of candidates for the ORC working fluid. A preselection can be achieved by considering non-thermodynamic aspects like toxicity, safety issues or climate relevance. However, a first reliable technical and energetic evaluation is realized by a thermodynamic analysis based on steady state or dynamic simulation models. In order to validate these models on cycle or component level, a 15 kW test rig is set up in operation at the Center of Energy Technology (University of Bayreuth). Figure 1 shows the experimental setup in the test hall. A special focus is led on the analysis of the turbine-generator-unit, in particular the turbine efficiency at part load condition is investigated. In addition, flow boiling measurements are conducted for pure siloxanes and their mixtures. A scheme of the corresponding test rig is presented in Figure 2. The experimental data lead to a fundamental understanding of the heat transfer process, pressure losses and evolving flow patterns. In this context, heat flux density, mass flux density and saturation pressure are systematically varied during measurements. Finally, the characteristic fluid properties like density, surface tension and dynamic viscosity of MM are measured in the temperature range from 283.15 K and 343.15 K using the IMETER®. The experimental data are compared to common prediction methods for fluid properties like Peng-Robinson equation-of-state or the REFPROP database in order to quantify the uncertainties of the applied models.



**Figure 1:** ORC test rig at the Center of Energy Technology with an electrical power of up to 15 kW

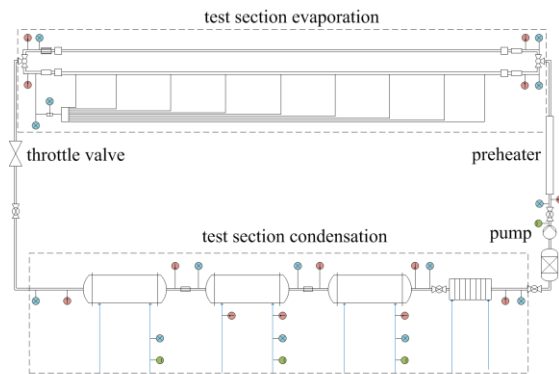


**Figure 2:** Scheme of test rig for the measurement of flow boiling heat transfer coefficients

## Discussion and Results

First and second law analyses of ORC systems for waste heat recovery show that MM is a promising working fluid for temperatures between 250 °C and 500 °C. A case study is conducted for a stationary biogas-engine as heat source [1]. For the ORC module, MM is considered as working fluid. In the case of a pure electricity generation, the determined second law efficiency of 26.2 % is significantly higher compared to the use of octamethyltrisiloxane (MDM) as working fluid. In general, the heat transfer measurements show that especially at constant saturation temperature, the present flow pattern has a considerable effect on the heat transfer characteristics. The observed effects at varying operational parameters are in accordance to literature. Exemplarily, high pressure and heat flux density lead to an increase in the heat transfer coefficient in the nucleate boiling dominated region. The model of Wojtan et al. and the correlation of Kandlikar can be recommended for the prediction of flow pattern and heat transfer coefficients. A further adaption of these models leads to a reduction of the mean deviation. Concerning the fluid properties of MM, a comparison between experimental data and predicted values lead to a maximum relative error below 7 %. This accuracy is sufficient for the experimental determination of heat transfer coefficients as well as for their theoretical prediction.

## Summary/Conclusions

Based on a comprehensive investigation consisting of thermodynamic modelling and experimental setups, a reliable ORC design procedure can be established for an ORC working fluid and its class of substance. In particular, the uncertainties of the simulation models and design methods can be significantly reduced by the fluid-specific adaption of existing approaches.

## Acknowledgments

The authors acknowledge the support of the co-workers and students of the research group “Energy Systems and Technologies”, which were involved in the ORC related research activities in the last decade. In particular, we would like to thank at this point Tim Eller, Markus Görl, Ivanka Milcheva, Markus Preißinger, Sebastian Kuboth, Sebastian Kutzner and Matthias Welzl.

## References:

- [1] T. Weith, F. Heberle, M. Preißinger, D. Brüggemann, *Performance of Siloxane Mixtures in a High-Temperature Organic Rankine Cycle Considering the Heat Transfer Characteristics during Evaporation*, *Energies* 2014, vol. 7, Issue 9, pp. 5548-5565, [doi:10.3390/en7095548](https://doi.org/10.3390/en7095548)

# Metal Organic Framework Materials for Adsorption Heat Pumps

R.K. AL-Dadah<sup>1</sup>, Saad Mahmoud<sup>1</sup>, Eman Hussein<sup>1</sup>, Peter Youssef<sup>1</sup>, Fadhel Al-Mousawi<sup>1</sup>

<sup>1</sup> School of Engineering, University of Birmingham, Birmingham, B15 2TT United Kingdom

\* [r.k.al-dadah@bham.ac.uk](mailto:r.k.al-dadah@bham.ac.uk)

## Abstract

There are huge amounts of low grade heat sources with temperatures below 150<sup>0</sup>C like solar thermal energy, geothermal and many industrial processes which are currently not exploited. Adsorption heat pumps offer a huge potential in a number of vital applications like energy storage, cooling and heating, and water desalination which can be driven by these low grade heat sources leading to significant reduction on fuel consumption and CO<sub>2</sub> emissions. The adsorbent material is the key element in adsorption heat pump systems which determine the performance, size and cost of such technology. Metal Organic Framework Materials (MOFs) are new class of adsorbent materials with superior water uptake, high pore volume and surface area. This abstract presents research work at the University of Birmingham, United Kingdom on the development of adsorption heat pumps using MOFs for various applications including heat storage, cooling, power generation and water desalination.

**Keywords:** Adsorption heat pumps, Metal Organic Framework materials (MOFs), Heat storage, Cooling, Water desalination, Power generation.

## Introduction/Background

Thermally-driven adsorption heat pumps and chillers have clear advantages over traditional heating/cooling and vapour compression heat pump systems due to their low environmental impact and their ability to efficiently use low grade heat sources, such as solar energy, industrial or automotive waste heat and geothermal resources. Adsorption systems utilise the affinity of a porous material to a certain working fluid such as water to generate the heat pumping mechanism. Figure 1 and Figure 2 illustrate schematically the operation of two bed adsorption system and the Duhring thermodynamic cycle diagram respectively. Using water as a refrigerant, the adsorption system can be used for water desalination where sea water is evaporated in the evaporator due to the adsorption effect. Thus water based adsorption systems can be applied for cooling and heating (heat pump) [1-3], energy storage [4] and water desalination [5-6].

Currently available adsorption heat pump systems utilise silica gel/ water, zeolite/water and activated carbon/ammonia working pairs which suffer from low water uptake or hazardous fluid in the case of ammonia. Metal Organic Frameworks (MOFs) are new micro-porous materials with exceptional high porosity, well-defined molecular adsorption sites and large surface area (up to 5500m<sup>2</sup>/g). The author and her co-workers have synthesised and tested a wide range of MOF materials that have shown superior water adsorption performance compared to that of the existing conventional porous materials like silica gel and zeolites. This abstract describes research work carried out at the School of Engineering, University of Birmingham, United Kingdom on MOF/water adsorption systems in terms of (i) MOF materials water adsorption characteristics and thermal properties; (ii) enhancement of MOF material thermal properties using Graphene Oxide and Calcium Chloride; (iii) experimentally testing MOF materials in single bed adsorption system for energy storage application and (iv) experimentally testing MOFs in two-bed adsorption system for water desalination and cooling.

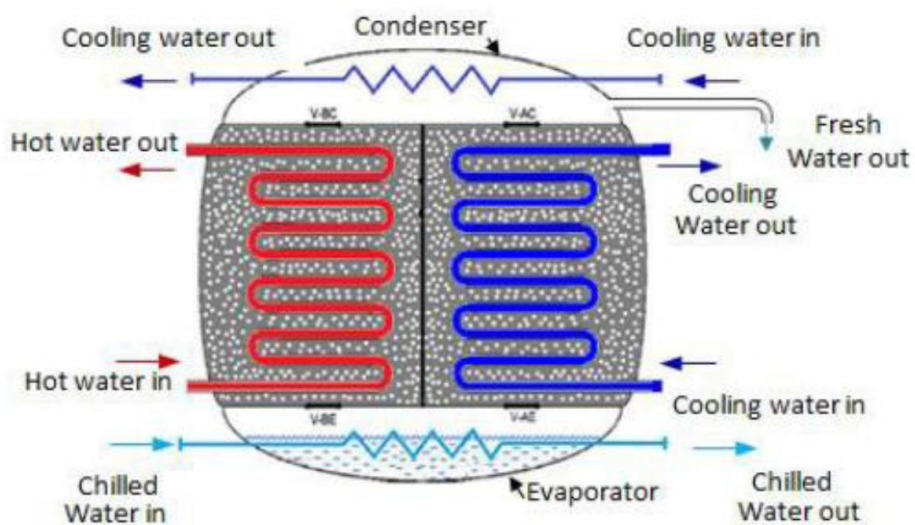


Figure 1, Schematic diagram of the 2-bed system [5]

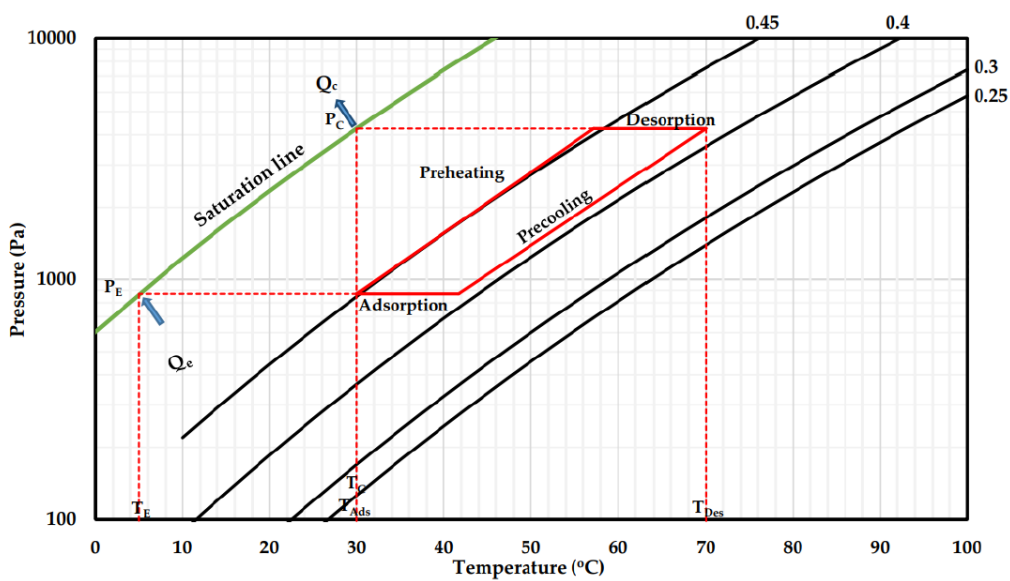


Figure 2, P-T-X diagram of Adsorption Cycle [2]



## Discussion and Results

### MOF Materials

Figure 3 shows the water adsorption isotherms of the MOF materials synthesised and characterised by the author's research group. It can be seen that MIL-101(Cr) shows the highest equilibrium water uptake followed by MIL-100(Fe), Aluminium Fumarate and CPO-27(Ni). However, MIL101(Cr) and MIL100(Fe) show isotherm shape of type IV with the adsorption of water occurring at high relative pressure of (0.5 and 0.3 respectively). Aluminium Fumarate shows the same isotherm type IV but the steep increase occurs at a partial pressure of 0.2. On the other hand, CPO-27(Ni) shows water adsorption isotherm of type I. Figure 4 shows the adsorption kinetics of the four MOF materials mentioned above. It can be seen that CPO-27(Ni) has the fastest adsorption kinetics followed by MIL-101(Cr) and MIL-100(Fe) then aluminium fumarate.

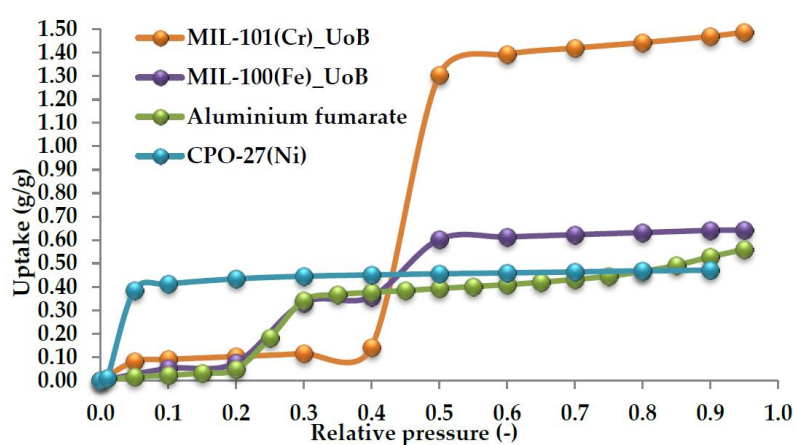


Figure 3, Water adsorption isotherm of metal-organic framework materials and silica gel at 25°C.

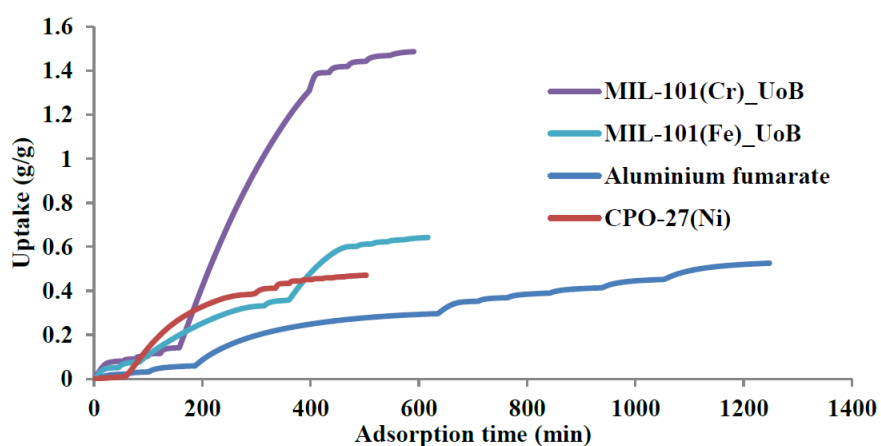


Figure 4, Water adsorption rate of metal-organic framework materials and silica gel at 25°C.

Figure 5 (a) and (b) show the effect of using Graphene Oxide and Calcium Chloride on the water adsorption isotherms of MIL101(Cr) respectively. It can be seen that introducing GrO and  $\text{CaCl}_2$  improved the water uptake on both the high and low relative pressure range.

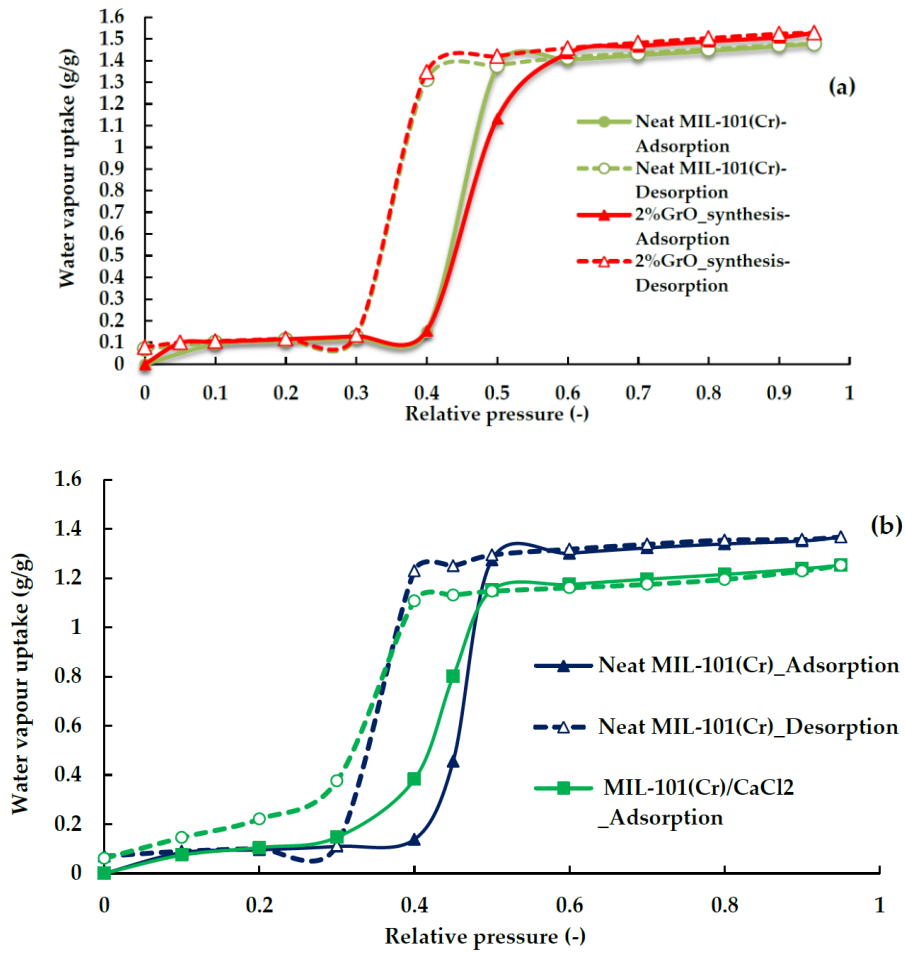


Figure 5, Water adsorption isotherm of  
 (a) MIL-101(Cr)/GrO and (b) MIL-101(Cr)/CaCl<sub>2</sub> at 25°C.

Also, Figure 6 shows the effect of incorporating MIL-100(Fe) with MIL-101(Cr) on the water adsorption isotherms of MIL100(Fe). It can be seen that it improved the water vapour capacity in the high relative pressure range.

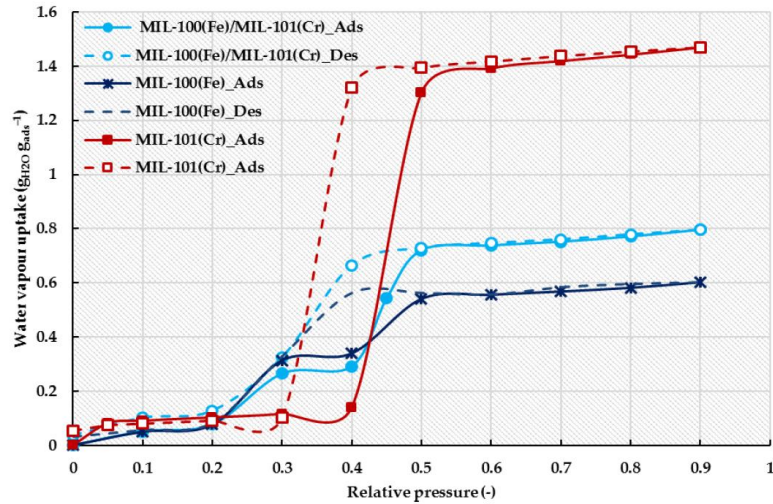


Figure 6, Water adsorption isotherms of MIL-100(Fe)/ MIL-101(Cr) composite at 25°C.

### MOF/Water Adsorption Systems

Thermodynamic simulation of these MOF materials in an industrial adsorption system manufactured by Weatherite Air Conditioning Ltd for water desalination and cooling illustrated the potential of such material. Figure 7 and Figure 8 show the specific daily water production and specific cooling of CPO-27Ni that can be obtained at 95 °C heat source temperature at a range of condenser cooling temperature of 5 to 30°C and evaporator temperatures of 10 to 40°C. It is clear that increasing the condenser water inlet temperature has the same effect as decreasing the evaporator inlet water temperature resulting in less water production and cooling. The reason for that is the difference between the system's two partial pressure ratios, which depend on the condenser and evaporator operating temperatures. It is found that by decreasing the evaporator temperature from 40 to 10°C, water production decreases by 202% from 20.6 to 6.8 m<sup>3</sup>.tonne adsorbent<sup>-1</sup>.day<sup>-1</sup> at condenser water inlet temperature of 10°C. Similarly, increasing the condenser water temperature from 5 to 30°C, decreases SDWP by 135% from 7.5 to 3.2 m<sup>3</sup>.tonne adsorbent<sup>-1</sup>.day<sup>-1</sup> at evaporator water inlet temperature of 10°C. The cooling effect produced by the cycle can be used for different applications depending on the evaporation temperature. For air conditioning applications where evaporation temperature of 10-20°C is required, the adsorption-desalination system can provide specific cooling capacity of 225 W.kg<sup>-1</sup>. For process cooling where evaporation temperature of 40°C can be used, the adsorption desalination system can provide specific cooling power of 750 W.kg<sup>-1</sup>.

Figure 9 shows the two-bed adsorption experimental facility developed to evaluate the performance of MOF materials for water desalination & cooling applications. Two commercially available MOF materials were used in these test facilities namely CPO-27(Ni) manufactured by Johnson Matthey Plc and Aluminium Fumarate manufactured by MOF Technology Ltd. Figure 10 and Figure 11 show the specific daily water production and specific cooling obtained at heat source temperature range of 65 to 95°C, condenser cooling temperature of 30°C and various evaporator temperatures. It can be seen that evaporator water inlet temperature significantly affects cycle outputs where SDWP increased by 366% from 5.4 to 25.2 m<sup>3</sup>.tonne<sup>-1</sup>.day<sup>-1</sup> and SCP increased by 464% from 140 to 790 W/kg when

evaporator inlet water temperature increased from 10 to 40°C. On the other hand, desorption temperature has a minimal effect on cycle outputs specially at low evaporator temperatures less than 20°C where water and cooling production rise by 17% and 13% respectively when desorption temperature increases from 65 to 95°C. This behaviour is attributed to the shape of Aluminium Fumarate isotherm type IV where the uptake value is almost constant at all pressure ratios <0.2, therefore changing desorption temperature (i.e. the lower pressure ratio) does not affect the system uptake and hence the system performance. It is found that 95°C desorption temperature and 40°C evaporator water inlet temperature achieve maximum SDWP and SCP of 25.3 m<sup>3</sup>.tonne<sup>-1</sup>.day<sup>-1</sup> and 789.4 W/kg, respectively.

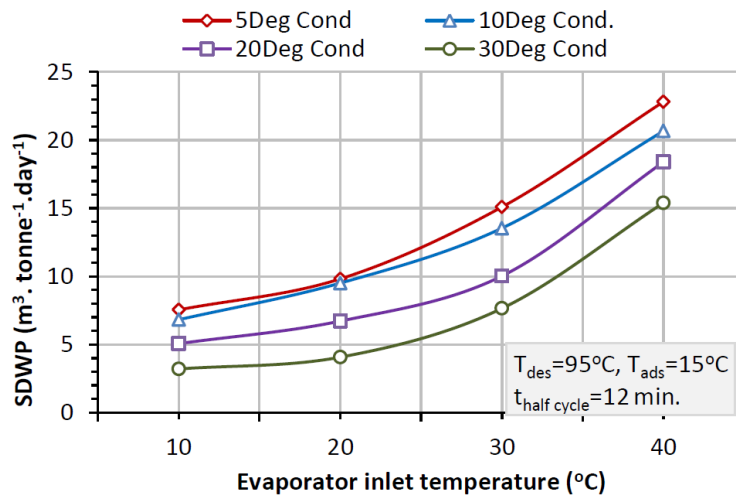


Figure 7, Specific daily water production at various evaporator and condenser water inlet temperatures using CPO-27Ni [6]

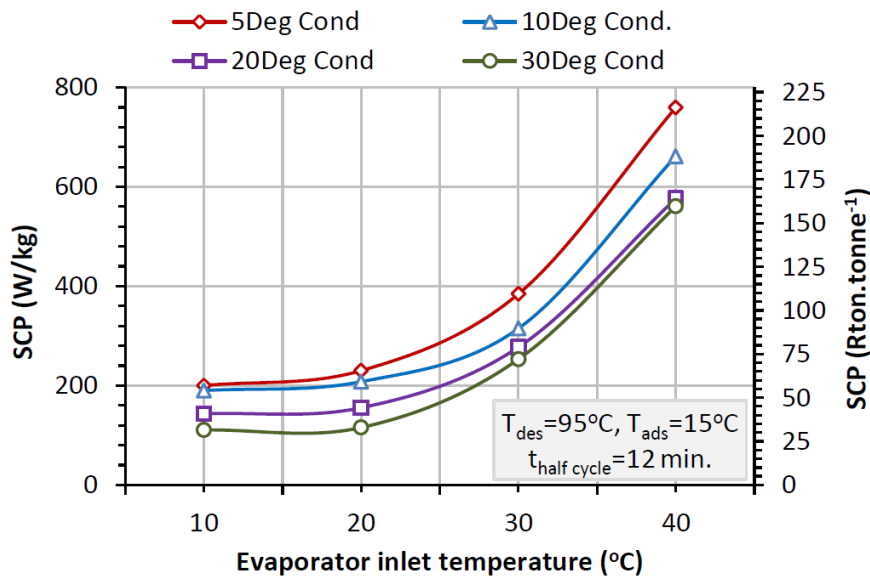


Figure 8, Specific cooling power for various evaporator and condenser water inlet temperatures using CPO-27Ni [6]



Figure 9, Testing facility of the double-bed adsorption system

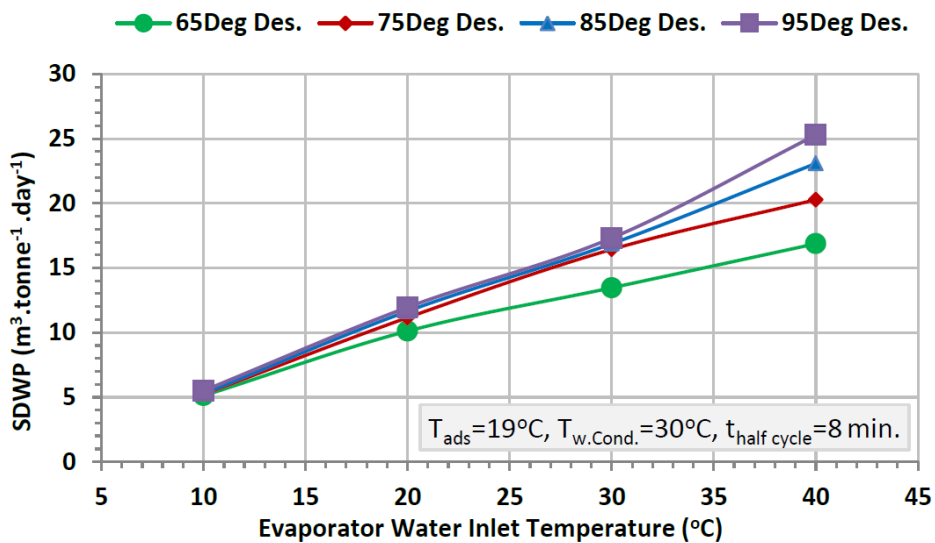


Figure 10, Specific daily water production at various desorption and evaporator water inlet temperatures using (Al-Fumarate)

For energy storage, a single bed adsorption was used to investigate the energy storage performance of CPO-27(Ni) as shown in Figure 12 where energy is stored during the desorption process and recovered during the adsorption process. Figure 13 shows the water uptake of the adsorbent material using various energy storage time of one day, 3 days and one week. It can be seen that the uptake of the adsorbent material was not affected by the length of storage time highlighting the potential of MOFs for both short and long term energy storage. The energy density achieved was found to be  $166\text{kW}\cdot\text{hr}\cdot\text{m}^{-3}$ .

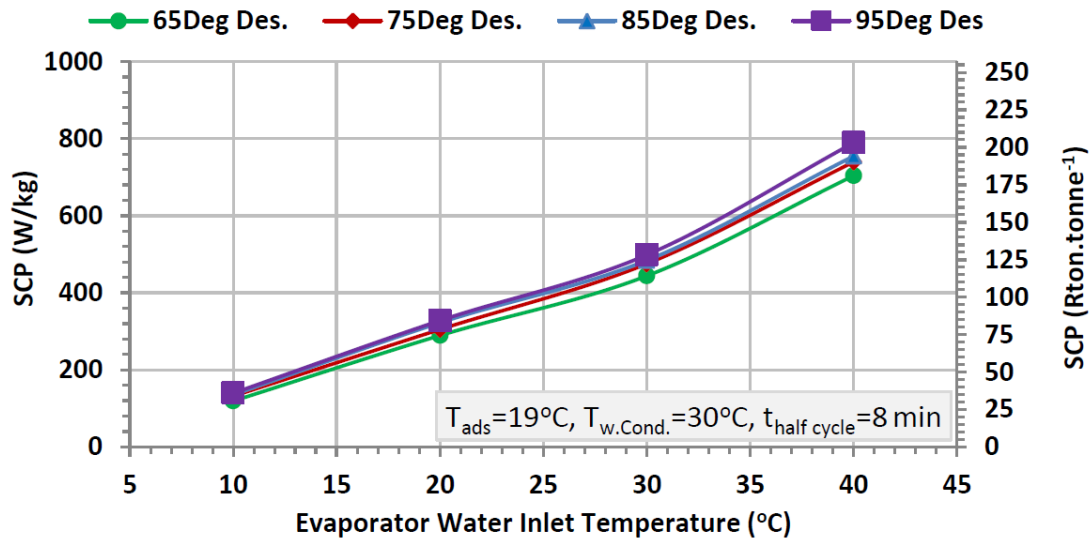


Figure 11, Specific cooling power at various desorption and evaporator water inlet temperatures using (Al-Fumarate)

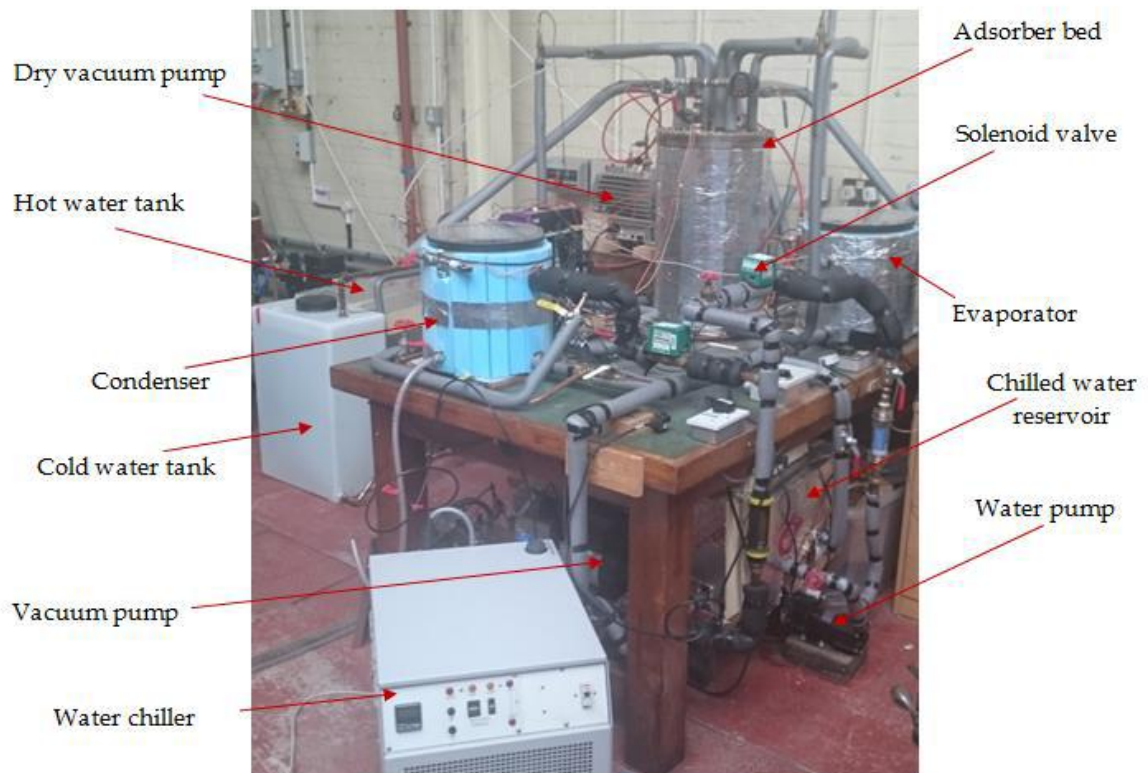


Figure 12, Pictorial view of the single bed test facility [6]

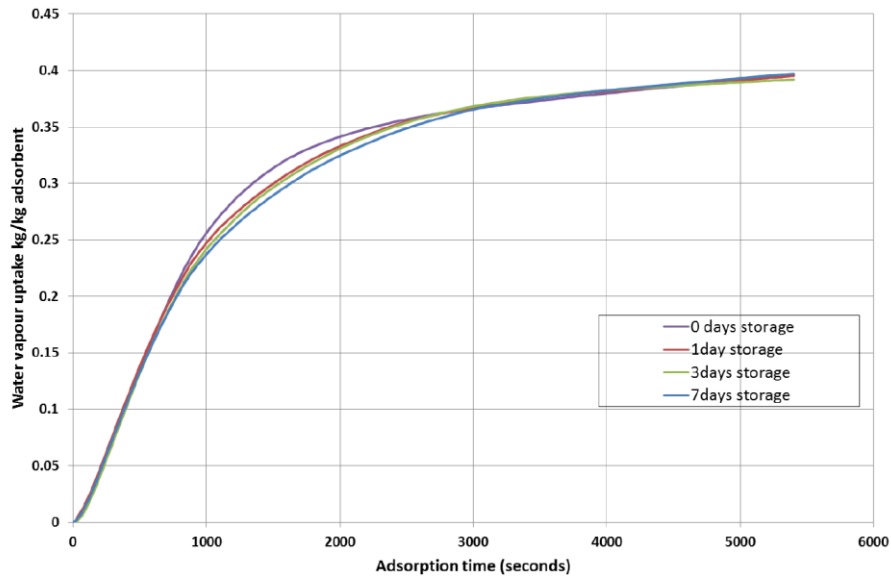


Figure 13. Water uptake of CPO-27(Ni) at various storage times.

Finally research work to investigate theoretically the potential of producing power in addition to cooling was carried out by integrating a turbine between the desorber bed and the condenser or by integrating the adsorption system with Organic Rankine Cycle as shown in Figure 15 which shows the modified adsorption system for cooling and electricity ASCE (to the right) and the basic adsorption cooling system BACS (to the left) or by integrating the adsorption system with Organic Rankine Cycle IAOSCE as shown in Figure 15. Figure 16 shows the effective Coefficient of Performance of the systems shown in Figure 14 and Figure 15 where IAOSCE shows the highest COPE. Experimentally, the two bed adsorption system was integrated with Organic Rankine Cycle consisting of evaporator, condenser pump and radial inflow turbine with R245fa as the refrigerant. Two operating scenarios were investigated where in scenario 1, the ORC was driven by the cooling fluid leaving the adsorber bed to recover the adsorption energy, scenario 2, the ORC was driven by the heating fluid after passing through the desorber bed. Figure 17 shows the experimental COP/COPE values IAOSCE (scenario 1) utilising CPO-27(Ni) and R245fa.

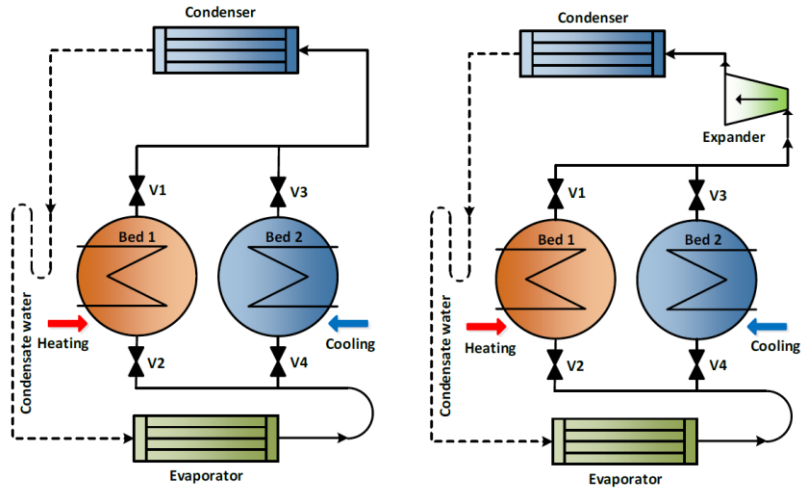


Figure 14, Schematic diagram of basic adsorption cooling system BACS (left), and adsorption system for cooling and electricity ASCE (right)

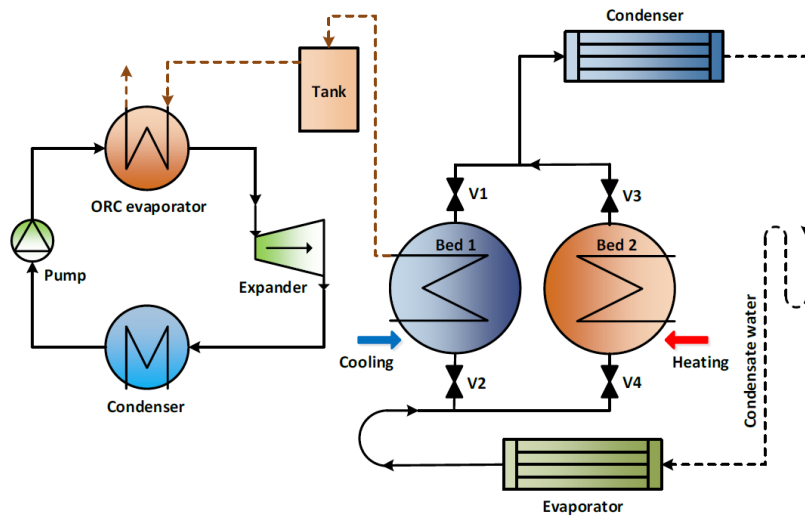


Figure 15, Schematic diagram of integrated adsorption-ORC system for cooling and electricity IAOSCE



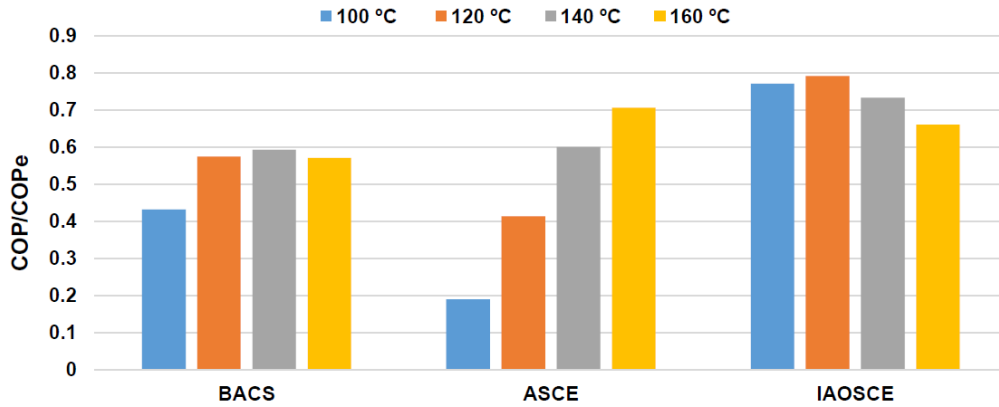


Figure 16, COP/COPE of different adsorption configurations used to generate cooling and electricity compared to that of BACS utilising CPO-27(Ni) with a range of heat source temperature

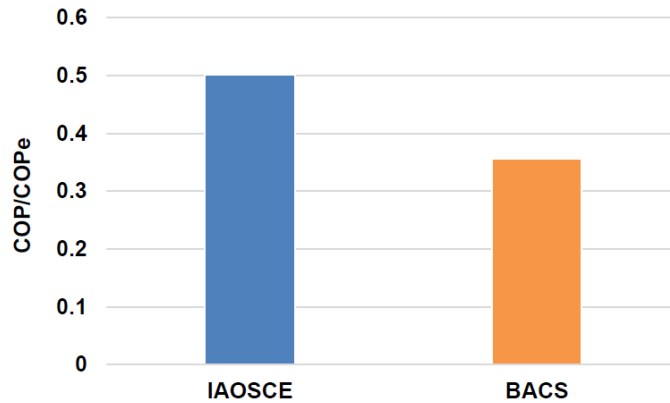


Figure 17, Experimental COP/COPE values for the integrated adsorption-ORC system for cooling and electricity IAOSCE (scenario 1) utilising CPO-27(Ni) and R245fa utilising heat source temperature of 95 °C

### Summary/Conclusions

MOF/Water adsorption heat pumps offer significant potential in various applications including energy storage, water desalination & cooling and power generation. For water desalination, Al-Fumarate can work at low desorption temperatures as low as 65°C while at 95°C maximum SDWP of 25.3 m<sup>3</sup>.tonne<sup>-1</sup>.day<sup>-1</sup> and SCP of 789.4 W/kg were obtained while according to literature, the maximum experimentally obtained specific daily water production (SDWP) using “Silica-gel” is 13.5 m<sup>3</sup> per tonne of adsorbent per day. For energy storage, CPO27(Ni) MOF material showed energy density of 166 kW.hr.m<sup>-3</sup> more than 3 times that of hot water tanks. For power generation, including a turbine in the adsorption system can produce power output and increase the effective Coefficient of Performance of the adsorption cooling system by 22%. Integrating the adsorption cooling system with Organic Rankine Cycle can produce an effective Coefficient of performance of 0.8.

## References:

- [1] Shi, B., Al-Dadah, R., Mahmoud, S., Elsayed, A., Elsayed, E., *CPO-27(Ni) metal-organic framework based adsorption system for automotive air conditioning*. Applied Thermal Engineering, 2016 <https://doi.org/10.1016/j.applthermaleng.2016.05.109>
- [2] Elsayed, E., Al-Dadah, R., Mahmoud, S., Elsayed, A., & Anderson, P. A. Aluminium fumarate and CPO-27(Ni) MOFs: *Characterization and Thermodynamic Analysis for Adsorption Heat Pump Applications*. Applied Thermal Engineering, 2016. [doi: 10.1016/j.applthermaleng.2016.01.129](https://doi.org/10.1016/j.applthermaleng.2016.01.129)
- [3] Elsayed, E., Wang, H., Anderson, P., Al-Dadah, R., Mahmoud, S., Navaro, H., Ding, Y., Bowen, J., *Development of MIL-101(Cr)/GrO composites for adsorption heat pump applications*, Microporous and Mesoporous Materials, 2017. <https://doi.org/10.1016/j.micromeso.2017.02.020>
- [4] Elsayed, A., Elsayed, E., Al-Dadah, R., Mahmoud, S., Elshaer, A., & Kaiyaly, W. *Thermal energy storage using metal-organic framework materials*. Applied Energy, 2016 <http://dx.doi.org/10.1016/j.apenergy.2016.03.113>
- [5] Youssef, P. G., Al-Dadah, R. K., Mahmoud, S. M., Dakkama, H. J., & Elsayed, A., *Effect of Evaporator and Condenser Temperatures on the Performance of Adsorption Desalination Cooling Cycle*. Energy Procedia, 2015, [doi: 10.1016/j.egypro.2015.07.263](https://doi.org/10.1016/j.egypro.2015.07.263)
- [6] Youssef, P. G., Dakkama, H., Mahmoud, S. M., & Al-Dadah, R. K., *Experimental investigation of adsorption water desalination/cooling system using CPO-27Ni MOF*. Desalination, 2017, [doi: http://dx.doi.org/10.1016/j.desal.2016.11.008](http://dx.doi.org/10.1016/j.desal.2016.11.008)

## **Full Manuscripts**

# Bubble Columns in Humidification Dehumidification Technology: From a Demonstration Unit to Fundamental Research in Optical Accessible Laboratory Bubble Columns

M.Preißinger<sup>1</sup>

<sup>1</sup>illwerke vkw Professorship for Energy Efficiency, University of Applied Sciences Vorarlberg, 6850 Dornbirn, Austria, [www.fhv.at/en/research/energy](http://www.fhv.at/en/research/energy)

\*Corresponding author: markus.preissinger@fhv.at

## Abstract

For many countries, water is the foundation for a liveable world in the future. Desalination is a crucial application in this context; however, also treatment technologies for brackish water and industrial wastewater are necessary. Hence, we present a demonstration unit based on humidification dehumidification technology, which is able to use low-grade heat. In the first part, the demonstration unit and some experimental results are analysed. In the second part, we report about the design of two new test-rigs, in which we are able to analyse the humidification of air in a bubble column in more detail. Hopefully, this will help the research community to increase the efficiency of HDH technology in the future.

**Keywords:** Humidification Dehumidification Technology, HDH, Desalination, Wastewater Treatment, Bubble Columns

## Introduction

Secure, affordable and resource efficient water supply systems will be as significant for future societies as the energy system, and both undergo similar changes. So far, desalination units in arid regions are coupled with large-scale centralized oil and gas power plants. However, especially in Southern Europe and Northern Africa a trend to small-scale and decentralized systems based on membrane processes has become apparent [1]. In industrialized countries, the importance of combined water and energy systems especially for the treatment of industrial wastewater is also emphasized in the last years [2]. Within this context, desalination based on solar energy as well as wastewater treatment based on industrial waste heat are highly important fields of research and development. One opportunity would be a combination of an Organic Rankine Cycle with an electrical driven Reverse Osmosis (RO) unit. However, ORC systems for heat source temperatures of less than 200 °C need a power output of more than 500 kW to become economically feasible [3]. Hence, thermal water treatment processes may be an alternative as it is possible to use energy sources with low exergy content like solar thermal energy or low-temperature industrial waste heat.

Humidification Dehumidification (HDH) technology is a promising process, which can be applied for solar desalination as well as for thermal treatment of industrial wastewater. Compared to conventional processes like multi-stage-flash distillation (MSF), multi-effect distillation (MED) and thermal vapour compression (TVC) several advantages occur [4]: the process is suitable for small-scale plants; the process is robust and has low maintenance; the process is operated at ambient pressure and it is independent of the Van't Hoff factors of the educts.

HDH adapts the natural water cycle of the earth (see Figure 1). In a first step, air is humidified and heated in direct contact with the educt (in case of Figure with seawater). The humidification is mostly realised in spraying towers with different assemblies to increase the wetting surface [5–7]. However, especially the group of Lienhard at MIT proposed bubble

column humidifiers [8]. After humidification, humid air is blown over a cold surface in the dehumidifier to condense drinking water. The educt seawater is preheated in the dehumidifier and further heated by an external heat source, which could be solar energy or industrial waste heat.

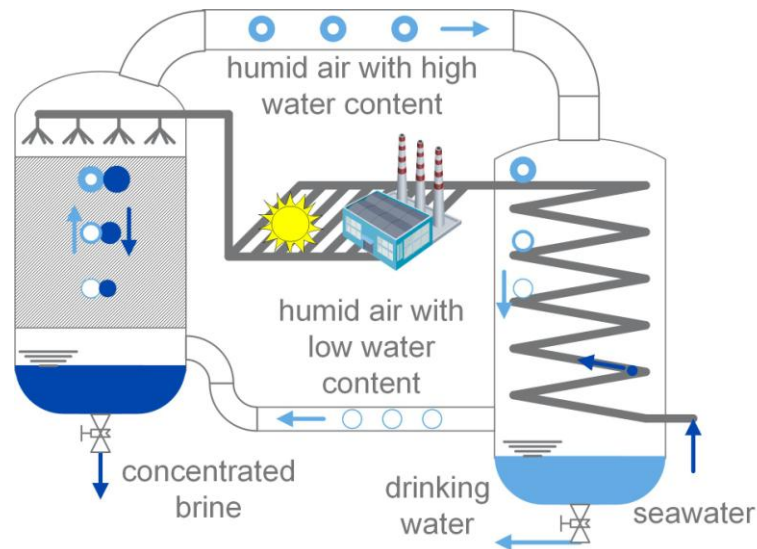


Figure 1: HDH process for the case of desalination (general operating principle)

HDH process has been widely discussed in the last years especially for solar-driven desalination and brackish water treatment [8–10]. However, it can also be applied to oil-containing educts due to its versatility [11]. The author used this versatility to set up a demonstration unit for bilge water treatment at its former institute, the Center of Energy Technology of the University of Bayreuth [12]. The demonstration unit was successfully operated, however, it was obvious that the process is energetically not yet competitive compared to conventional technologies, as contemporary technical design criteria for the process are scarce. This study is a first step towards a thorough understanding of the most crucial point: the humidification of air in a bubble column.

## Fundamentals

Several researchers in the field of HDH focus on the simulation and optimisation of the overall process [13–15]. For such studies, realistic boundary conditions are necessary. For the humidifier, full saturation with a relative humidity of 100 % at the end of the humidifier is chosen quite often [16]. However, this may be far too optimistic especially for humidifiers with assemblies inside. Therefore, enhancement in heat and mass transfer inside the humidifier has become a quite important research topic and bubble column humidifiers has been suggested. Compared to other types of humidifiers, bubble columns have several advantages:

- Heat and mass transfer can be increased by a factor of 100 with direct contact [17].
- As heat transfer takes place in direct contact and not on heated surfaces, fouling is reduced [8] and less heat transfer area is required [18].
- Even high-viscose media and high salt concentrations can be handled as cleaning of the unit is simplified and liquid spray nozzles are not required.

Research and development of bubble column humidifier is a comparably young branch of HDH-research. Important contributions in this field [19–24] show that the main parameters that influence the relative humidity at the end of the humidifier are

- the viscosity and surface tension of the fluid,
- the temperature of the fluid,
- the gas-holdup and gas velocity, as well as
- the height/diameter ratio of the bubble column.

As these parameters influence each other, a general mathematical description and, therefore, optimized values for the parameters are not available in literature. Especially the influence of the physico-chemical properties of the fluids occurring in the application on the behaviour of bubble columns complicates a general description. Therefore, in a first step we built a demonstration unit based on typical engineering principles.

### Discussion and Results of the demonstration unit

The demonstration unit for bilge water treatment is shown in Figure 2.



Figure 2: Demonstration unit of an HDH process for bilge water treatment

It consists of a cuboid humidifier with a base area of about 1 m<sup>2</sup> and a height of 1 m. The plant is operated with salt water as well as with bilge water. Salt water concentrations of up to 10 % are realised. Bilge water occurs in the shipping industry and is a mixture of machine oil, water, salt and other sediments. The composition is about 50 % water, 44 % oil and 6 % sediments. The demonstration unit is built to increase the oil content in bilge water to more than 98 % so that it can be used as recycling oil and gives a monetary value in the business case of such systems. Further details on bilge water and the demonstration unit itself can be found elsewhere [12]. Here, just several aspects concerning the humidifier are given.

In Figure 3, a scheme of the bubble column as well as a detail from the demonstration unit is given. The humidifier consists of five different nozzles (A1 to A5) through which air is bubbled through the medium. Furthermore, media inlet is realised via an inlet at the bottom of the humidifier and at the top of the humidifier (M1 and M2).

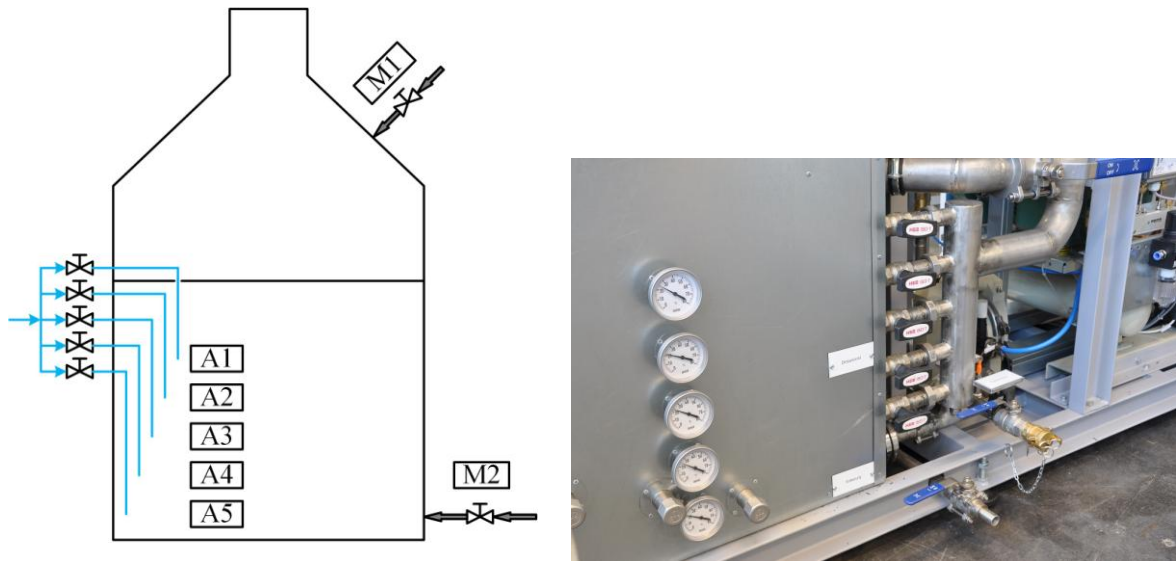


Figure 3: Scheme of the bubble column humidifier (left) and detail of air nozzles (right)

By increasing the contact time between air and medium (from nozzle A1 to A5), a higher productivity is expected due to an increase in relative humidity at the outlet of the humidifier. However, although the contact time between air bubbles and bilge water is about 2-3 times higher for nozzle A1 than for nozzle A5, Figure 4 shows an almost constant productivity.

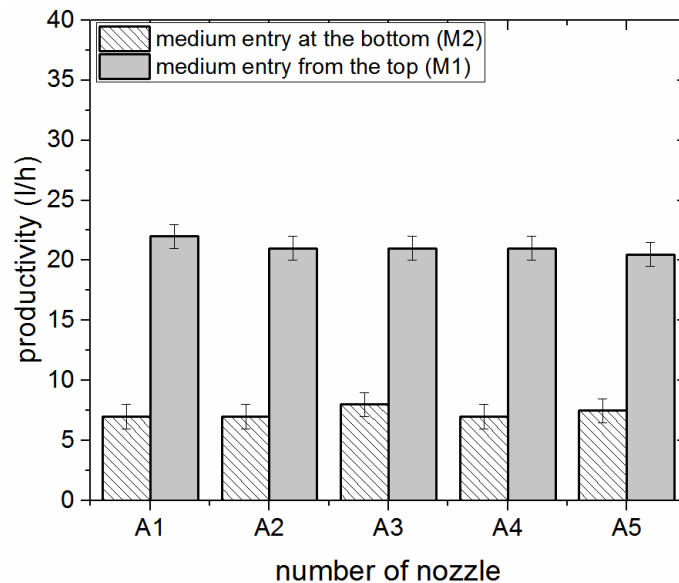


Figure 4: Productivity of bubble column humidifier for bilge water treatment (nozzles A1 to A5 are at different heights of the bubble column, hence, giving different contact times between air bubble and bilge water)

A possible explanation would be a fully saturated air bubble even for the shortest contact time (nozzle A1). However, if this were the case, spraying further medium from the top would not result in the higher productivity of Figure 4. Hence, the results are not in accordance with ideal thermodynamics. Obviously, it is necessary to intensify research towards a more sophisticated understanding on the mechanisms and parameters that influence humidification of air in a bubble column.

Based on the preliminary results of the demonstration unit with bilge water, the aim of a new project is to establish a fundamental understanding of the humidification of air in a bubble column. Within the project, we want to (1) develop a universally applicable optical measurement setup, (2) deduce semi-empirical correlations for the humidification of air in a bubble column based on an extensive experimental data set and (3) evaluate the time-dependency under varying boundary conditions. This is necessary to increase the accuracy of simulation studies of HDH processes and to show a clear path for the energetic optimisation of such systems. Therefore, in the second part of this publication two newly designed optical accessible laboratory humidifiers including different camera systems are presented.

### **Discussion of the new test-rigs**

As already mentioned, the main goal is to deduce semi-empirical correlations for the humidification of air in a bubble column and, therefore, correlations between the relative humidity at the outlet of the humidifier and different constructional aspects as well as thermodynamic boundary conditions:

$$\text{relative humidity} = f(\text{temperature, bubble diameter, gas velocity, ...})$$

Therefore, two bubble columns are set up in the lab, one cuboid and one cylindrical. The cuboid humidifier is advantageous from an optical point of view as analysis via a light source and a camera system is convenient due to the planar surface. The cylindrical humidifier, however, is closer to real systems. Therefore, the idea is to combine the results of both humidifier to get reliable data on the humidification of air in a bubble column. Furthermore, some methodological aspects are investigated with the two set-ups:

1. Is it possible to compare the results of a cuboid and a cylindrical humidifier? Do both test rigs give the same results or do they differ? Is it possible to combine the results of both test-rigs to increase the accuracy of semi-empirical correlations for the humidification of air in a bubble column?
2. Is it possible to increase the quality of the results by applying invasive and non-invasive measurement devices together or is it sufficient to apply just one measurement method?
3. Is it necessary to use a high-speed camera for optical measurements or are modern mirrorless cameras adequate to get reliable results?

At HPC 2018, these questions will be discussed based on the concept of the test-rigs of Figure 5. These test-rigs are set up in the lab at the moment and will be finished in the next months.

### **Conclusion**

Humidification Dehumidification technology is a promising way for desalination and wastewater treatment based on solar energy or industrial waste heat. A demonstration unit for salt water as well as for bilge water serves as prove of concept. However, we identified several necessary steps to optimize the process energetically with a special focus on a clear understanding of the applied bubble column humidifier. The semi-empirical correlations for the humidification of air in a bubble column, which we intend to deduce from the two test-rigs, will help to replace commonly applied assumptions with experimentally validated equations. This is necessary to reduce uncertainties during simulation and technology design, and to increase the efficiency of thermal water treatment systems based on HDH technology.

### **Acknowledgment**

The work is partly financed by the German Federal Ministry of Economic Affairs and Energy within the Central Innovation Programme for SMEs due to an enactment of the German Bundestag. The work is also partly financed by the Austrian Science Fund (FWF): Project



number P31103. The author want to thank the company “Hopf GmbH” in Bayreuth, Germany, for the construction of the demonstration unit. Special thanks goes to Sebastian Kutzner, B.Sc. from the Center of Energy Technology, University of Bayreuth for his effort in getting the demonstration unit running.

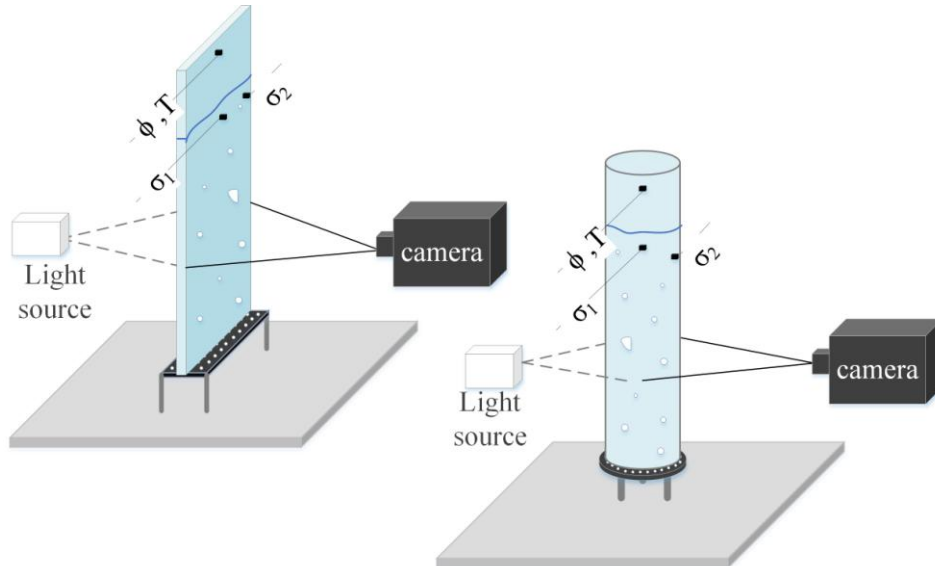


Figure 5: Planar humidifier and cylindrical humidifier for the investigation of humidification of air bubbles

### References:

- [1] Lattemann S. Development of an environmental impact assessment and decision support system for seawater desalination plants. Dissertation. Delft University of Technology, 2010.
- [2] Ante A, Behrendt J, Bennemann H, Blöcher C, Bolduan P, Geißen S-U, et al., editors. Trends und Perspektiven in der industriellen Wassertechnik. Frankfurt am Main; Hannover: DECHEMA e.V; 2014.
- [3] Preißinger M, Brüggemann D. Thermoeconomic Evaluation of Modular Organic Rankine Cycles for Waste Heat Recovery over a Broad Range of Heat Source Temperatures and Capacities. *Energies* 2017;10:269. doi:10.3390/en10030269.
- [4] Kucera J, editor. Desalination: water from water. Hoboken, New Jersey: John Wiley & Sons; 2014.
- [5] Soufari SM, Zamen M, Amidpour M. Experimental validation of an optimized solar humidification-dehumidification desalination unit. *Desalination Water Treat* 2012;6:244–51. doi:10.5004/dwt.2009.494.
- [6] Müller HC. Theoretische und praktische Untersuchung einer mehrstufigen solarthermischen Kleinanlage zur Meer- und Brackwasserentsalzung. Dissertation. RWTH Aachen, 2009.
- [7] Müller-Holst H. Mehrfacheffekt-Feuchtluftdestillation bei Umgebungsdruck. Dissertation. Technische Universität München, 2002.
- [8] Narayan GP, Sharqawy MH, Summers EK, Lienhard JH, Zubair SM, Antar MA. The potential of solar-driven humidification–dehumidification desalination for small-scale decentralized water production. *Renew Sustain Energy Rev* 2010;14:1187–201.

doi:10.1016/j.rser.2009.11.014.

- [9] Seifert B, Kroiss A, Spinnler M, Sattelmayer T. About the history of humidification-dehumidification desalination systems. In: The International Desalination Association, editor., Tianjin, China: 2013.
- [10] Abdelmoez W, Mahmoud MS, Farrag TE. Water desalination using humidification/dehumidification (HDH) technique powered by solar energy. *Desalination Water Treat* 2013;52:4622–40. doi:10.1080/19443994.2013.804457.
- [11] Thiel GP, Tow EW, Banchik LD, Chung HW, Lienhard JH. Energy consumption in desalinating produced water from shale oil and gas extraction. *Desalination* 2015;366:94–112. doi:10.1016/j.desal.2014.12.038.
- [12] Preißinger M. Experimental Analysis of a Demonstration Plant for Bilge Water Treatment and Desalination Based on Humidification Dehumidification Technology, Rhodes, Greece: 2018.
- [13] Sharshir SW, Peng G, Yang N, El-Samadony MOA, Kabeel AE. A continuous desalination system using humidification – dehumidification and a solar still with an evacuated solar water heater. *Appl Therm Eng* 2016;104:734–42. doi:10.1016/j.applthermaleng.2016.05.120.
- [14] Sharqawy MH, Antar MA, Zubair SM, Elbashir AM. Optimum thermal design of humidification dehumidification desalination systems. *Desalination* 2014;349:10–21. doi:10.1016/j.desal.2014.06.016.
- [15] Kabeel AE, El-Said EMS. A hybrid solar desalination system of air humidification–dehumidification and water flashing evaporation. *Desalination* 2013;320:56–72. doi:10.1016/j.desal.2013.04.016.
- [16] Ettouney H. Design and analysis of humidification dehumidification desalination process. *Desalination* 2005;183:341–52. doi:10.1016/j.desal.2005.03.039.
- [17] Deckwer W-D. On the mechanism of heat transfer in bubble column reactors. *Chem Eng Sci* 1980;35:1341–6. doi:10.1016/0009-2509(80)85127-X.
- [18] Tow EW, Lienhard JH. Experiments and modeling of bubble column dehumidifier performance. *Int J Therm Sci* 2014;80:65–75. doi:10.1016/j.ijthermalsci.2014.01.018.
- [19] Narayan GP. Thermal Design of Humidification Dehumidification Systems for Affordable and Small-Scale Desalination. Dissertation. Massachusetts Institute of Technology, n.d.
- [20] El-Agouz SA. A new process of desalination by air passing through seawater based on humidification–dehumidification process. *Energy* 2010;35:5108–14. doi:10.1016/j.energy.2010.08.005.
- [21] El-Agouz SA. Desalination based on humidification–dehumidification by air bubbles passing through brackish water. *Chem Eng J* 2010;165:413–9. doi:10.1016/j.cej.2010.09.008.
- [22] El-Agouz SA, Abugderah M. Experimental analysis of humidification process by air passing through seawater. *Energy Convers Manag* 2008;49:3698–703. doi:10.1016/j.enconman.2008.06.033.
- [23] Liu H, Sharqawy MH. Experimental performance of bubble column humidifier and dehumidifier under varying pressure. *Int J Heat Mass Transf* 2016;93:934–44. doi:10.1016/j.ijheatmasstransfer.2015.10.040.
- [24] Rajaseenivasan T, Shanmugam RK, Hareesh VM, Srithar K. Combined probation of bubble column humidification dehumidification desalination system using solar collectors. *Energy* 2016;116:459–69. doi:10.1016/j.energy.2016.09.127.

# Iron(III) Trimesate (MIL-100(Fe)) in Adsorption Desalination

Eman Elsayed<sup>1,2\*</sup>, Raya AL-Dadah<sup>1</sup>, Saad Mahmoud<sup>1</sup>, Paul Anderson<sup>2</sup>, Ashraf Hassan<sup>3</sup>

<sup>1</sup>School of Mechanical Engineering, University of Birmingham, Birmingham, B15 2TT, UK.

<sup>2</sup>School of Chemistry, University of Birmingham, Birmingham, B15 2TT, UK.

<sup>3</sup>Qatar Environment and Energy Research Institute (QEERI), Qatar Foundation, P.O. Box, 5825, Doha, Qatar.

\*Corresponding author: EXH496@student.bham.ac.uk

## Abstract

Iron(III) trimesate is a metal-organic framework (MOF) material that has a water vapour capacity of  $0.6 \text{ g}_{\text{H}_2\text{O}} \cdot \text{g}_{\text{ads}}^{-1}$  and high cyclic stability hence has the potential to be used in adsorption applications. One of the adsorption applications that have not been fully explored is adsorption desalination. Adsorption desalination has been identified with many advantages such as environmentally friendly, driven by low-grade heat sources, low capital cost, low evaporation temperature and hence reduced fouling (formation of scales causing the damage of the evaporation units) effect [1]. This study investigates the potential of MIL-100(Fe) (Materials Institute Lavoisier) in adsorption desalination application. The synthesized material is characterized in terms of its water adsorption uptake. The water adsorption isotherm showed a unique two step S shape isotherm which gave this material the advantage to work at a wider range of relative pressure compared to other MOF materials such as aluminium fumarate and MIL-101(Cr).

**Keywords:** Metal-organic framework, MIL-100(Fe), Adsorption, Desalination.

## 1. Introduction

Seven hundred million people around the world are suffering from water scarcity, while another 500 million are approaching this situation. Not only that, but the situation is expected to worsen by 2025 as 1.8 billion people will be living in regions with absolute water scarcity [2]. Seventy percent of the earth's surface is covered with water but only 1% of this percentage can be directly used in producing potable water. With 97% of the water body as salty water, an important approach to face the water scarcity problem is using seawater to produce fresh water using desalination processes. Conventional desalination methods such as Reverse Osmosis (RO), Multi-Stage Flash (MSF) and Multi-Effect Distillation (MED). Due to the high greenhouse gases (GHG) emissions of the conventional desalination methods and its effect on the global warming phenomenon, new technologies with lower energy consumption and CO<sub>2</sub> emissions are needed.

The adsorption technology has proven to be a sustainable system that has important advantages such as being driven by waste heat and low-grade heat sources such as solar energy and using environmentally friendly refrigerants such as water [3]. This technology can significantly participate in reducing the CO<sub>2</sub> emissions because it is operated on abundant renewable thermal energy sources. The system has no moving parts and hence low maintenance costs. Also, low evaporation temperature is used and hence the fouling effect is significantly reduced (formation of scales which may cause the damage of the evaporation units). Furthermore, adsorption desalination system can produce not only high-grade distilled water but also cooling effect using the same heat source [4]. The desalination adsorption system consists of an evaporator, a condenser and adsorption/regeneration beds. Each bed includes a finned tube heat exchanger with the adsorbent material packed between the fins. For a two-bed system, the first bed works as an adsorber while the other works as a desorber. After the half cycle time, the operation mode is reversed. For a desalination system and at the

beginning of the cycle, an evaporation–adsorption process takes place where the seawater is evaporated due to the affinity of the adsorbent resulting in the cooling effect from the evaporator. Heat of adsorption is released to cooling water in the adsorption bed. During the regeneration–condensation processes, the low-grade heat source is supplied to the regeneration bed to remove the adsorbed water vapour. As the regeneration bed and condenser are connected, the water vapour migrates to the condenser where the vapour is condensed and the desalinated water is collected [4].

Numerous studies of adsorption desalination have been conducted since its appearance in 2006 [5]. **Table 1** summarize some of the previously conducted research in adsorption desalination using conventional adsorbent materials such as silica gel and AQSOA-Z02.

**Table 1 Specific daily water production (SDWP) and specific cooling power (SCP) of some of previously developed adsorption desalination systems:**

Adsorbent	No. of beds	SDWP $\text{m}^3 (\text{ton day})^{-1}$	SCP $\text{Rton ton}^{-1}$	$T_{\text{eva}}$ (°C)	$T_{\text{reg}}$ (°C)	Half cycle time	Ref.
Silica gel	2	4.2	27.5	15	85	600	[6]
Silica gel	2 & 4	8.8 & 10	-	30	85	600-500	[7]
Silica gel	4	7.8	51	30	85	480	[8]
Silica gel	4	2.4	18	30	85	600	[9]
Silica gel	2	9.3	-	<32	70	570	[10]
Silica gel	4	26	-	<42	85	300	[11]
AQSOA-Z02	4	7.5	58	30	85	300	[12]

Further performance improvement can be accomplished by replacing the conventional adsorbent materials with advanced adsorbents that exhibit higher water capacity which produce higher distilled water production and cooling effect. Metal-organic frameworks (MOF) are highly crystalline materials, with high surface area and pore volume, that are moderately stable and can be synthesized in a very pure form and thus have the potential for various applications such as catalysis, gas separations and storage, sensors and heat pumps [13]. The adsorption performance of a number of MOFs including ISE-1, HKUST-1, MIL-100(Fe), MIL-53(Fe), Basolite 100A and Basolite F300 was investigated, showing high adsorption capabilities compared to silica gel and zeolite [13]. Other MOF materials such as CPO-27(Ni) and aluminium fumarate have been investigated in the adsorption desalination application showing a promising performance compared to conventional silica gel [1].

MIL-100(Fe) is a MOF material from the MIL family is which is also known as iron trimesate or iron-benzenetricarboxylate and commercially known as Basolite F300. An important advantage of such MOF is that its inorganic secondary building unit (SBU) is iron which is an environmentally benign and a non-toxic cheap component [14]. This means that this material can be safely used in treating and desalinating the seawater. The MOF material is built from trimesate as the organic moiety and iron (III) cluster as the inorganic SBU. The organic and inorganic linkers are connected together to form a super tetrahedra that is joined in a MTN topology to form two mesoporous cages. The cages diameters in the MIL-100(Fe) are 25 and 29 Å. The cages exhibit two types of pentagonal and hexagonal windows with

openings of 5.5 and 8.6 Å (**Fig. 1**). The MOF material exhibits a high Langmuir surface area of more than 2800 m<sup>2</sup> g<sup>-1</sup>, pore volume of 1.2 cm<sup>3</sup> g<sup>-1</sup> and a cell volume of 394,481 Å<sup>3</sup>[14].

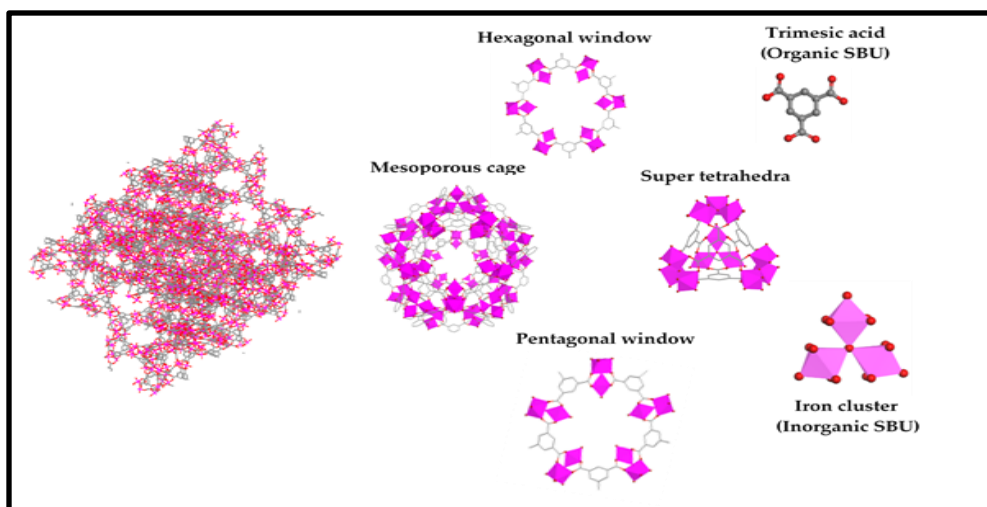


**Fig. 1** Crystal, mesoporous cage, pentagonal and hexagonal windows, super tetrahedra and secondary building units of MIL-100(Fe).

## 2. Experimental work

### a. Materials and methods

All chemicals were of reagent-grade quality obtained from commercial sources and used without further purification. Metallic iron (Fe<sup>0</sup>, Sigma-Aldrich), Trimesic acid (H<sub>3</sub>BTC, Sigma-Aldrich), and nitric acid (HNO<sub>3</sub>, Fisher scientific).

### b. Synthesis of MIL-100(Fe):

The material was synthesized at the University of Birmingham through low-temperature synthesis concept which was adopted from the work of *Shi et al.* [15].

The dynamic vapour sorption (DVS) test facility (Advantage DVS, Surface Measurement Systems, UK) was used to study the water adsorption characteristics at different temperatures.

## 3. Results and discussion

### a. Water adsorption characteristics

**Fig. 2** shows the water adsorption isotherms of MIL-100(Fe) at different adsorption temperatures. As it can be observed, the material exhibited a two-step type IV isotherm due to the presence of two types of cages. At low relative pressure ( $\leq 0.2$ ), the adsorption is mainly due to the presence of unsaturated metal centres (UMCs). These UMCs are metal binding sites formed after the removal of axial ligands from metal atoms attracting water molecules and offering extra binding sites to the guest molecules, especially at low pressure values. Nevertheless, the limited water uptake is related to the dominant effect of the hydrophobicity of the organic linker. At higher relative pressure (0.2-0.3), an increase in the water uptake took place due to the capillary condensation and water molecules starts filling the smaller cages. As the pressure increases (0.4-0.5), the water molecules start to fill the larger cages. At high relative pressure ( $\geq 0.5$ ), the pores are almost filled exhibiting a stable uptake.

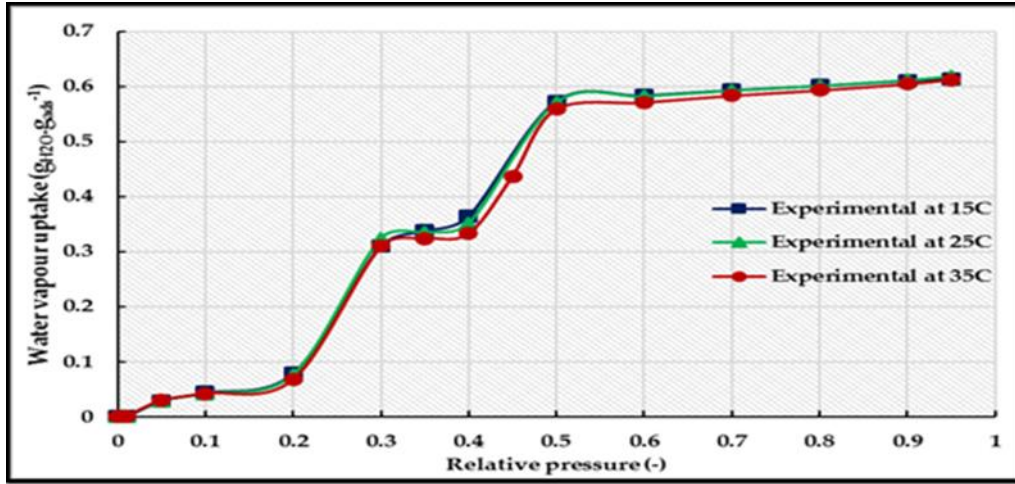


Fig. 2 Water adsorption isotherm of MIL-100(Fe) at different adsorption temperatures.

The previously shown measured data were fitted using a series of equations in terms of adsorption potential  $A$  (Eq. 1:3).

$$X = 1.59 \cdot \exp(-0.00064 \cdot A) \quad A > 3850 \quad (1)$$

$$X = 15.26 - 0.02 \cdot A + 0.00001 \cdot A^2 - 0.0000000023 \cdot A^3 + 1.86E - 13 \cdot A^4 \quad 2190 \leq A \leq 3950 \quad (2)$$

$$X = 0.64 - 0.0002 \cdot A + 0.00000024 \cdot A^2 - 0.000000000094 \cdot A^3 \quad A < 2190 \quad (3)$$

Where  $X$  is the Equilibrium uptake in  $\text{g}_{\text{H}_2\text{O}} \text{g}_{\text{ads}}^{-1}$  and  $A$  is the adsorption potential in  $\text{J mol}^{-1}$ . Fig. 3 shows good agreement between the MIL-100(Fe) experimental data and the proposed isotherm model.

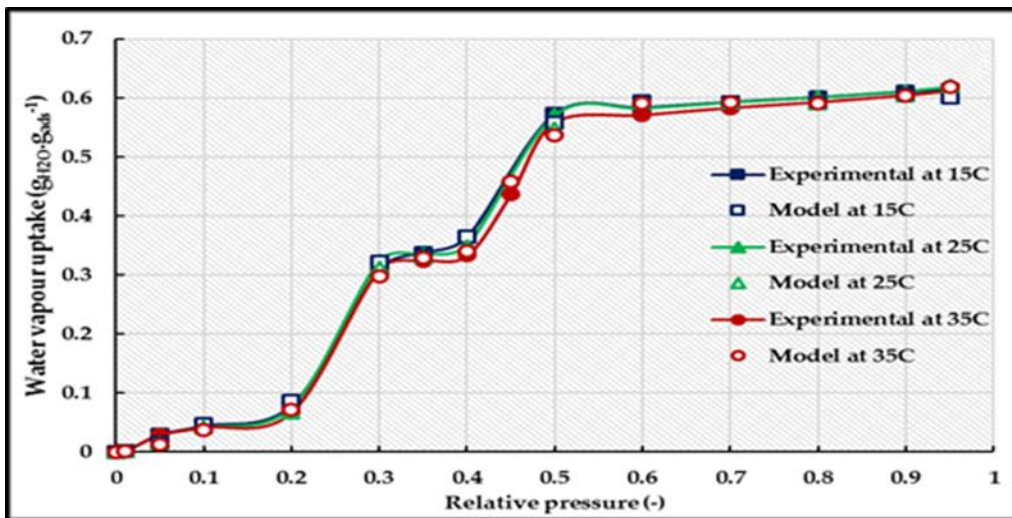


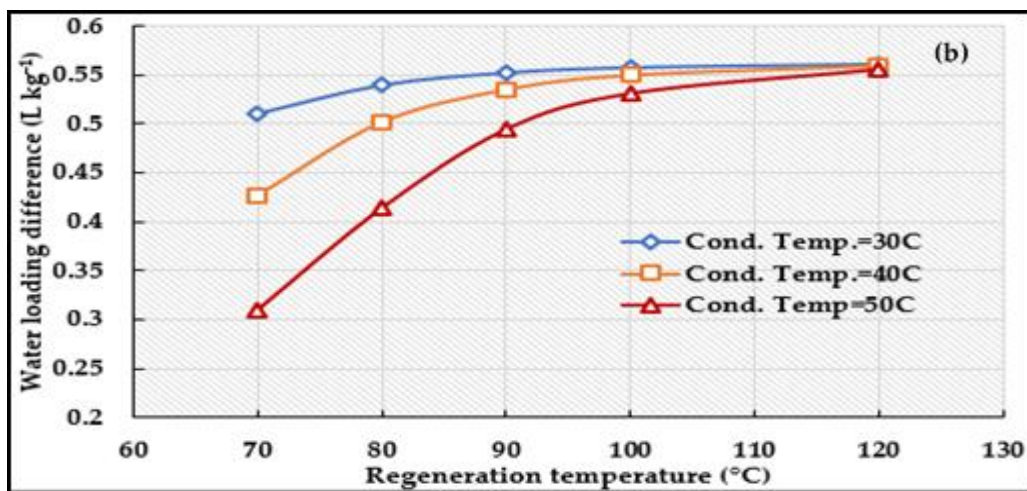
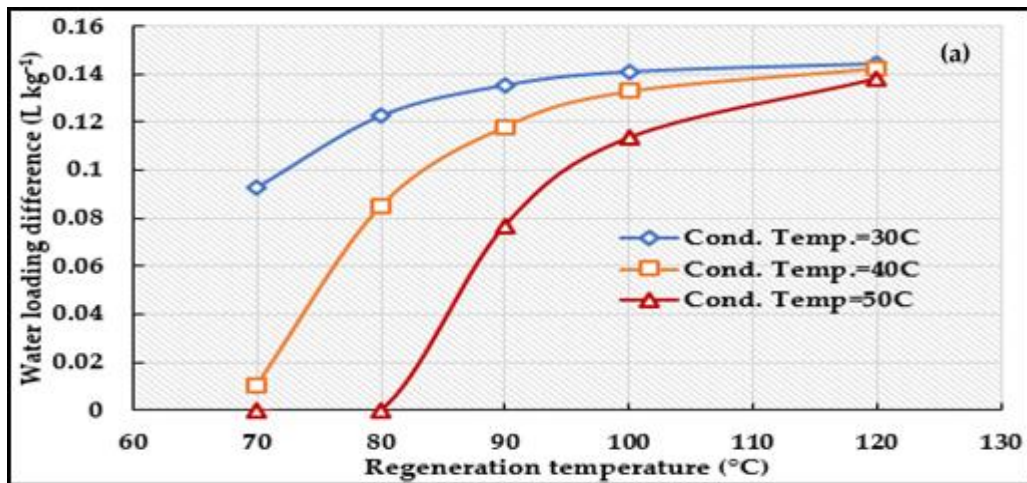
Fig. 3 Proposed isotherm model fitting of water adsorption on MIL-100(Fe) at different adsorption temperatures.

As desalination can produce both distilled water and cooling effect, the effect of evaporation, condensation and regeneration temperatures will be investigated at a fixed adsorption temperature of 30°C in the following section.

**b. Effect of operating conditions on the performance of MIL-100(Fe):**

**Fig. 4** shows the effect of regeneration and condensation temperature on the performance of MIL-100(Fe) at three evaporation temperature of 5°C, 20°C and 29°C. It can be well noticed that the evaporation temperature significantly affects the distilled water production specially in cases of the 5°C and 20°C as the produced water increased from only 0.09 to reach 0.5 L kg<sup>-1</sup> at a regeneration temperature of 70°C and a condensation temperature of 30°C. This is attributed to the isotherm shape which profoundly depends on the working relative pressure and evaporation temperature.

Regarding the effect of condensation temperature, it can be noticed that increasing the condensation temperature adversely affected the amount of distilled water when low regeneration temperature was used while it has almost no effect on the high regeneration temperature (i.e. 120°C) which may be attributed to that the regeneration temperature is high enough to effectively desorb the material. It is also evident that the increasing the regeneration temperature, increased the distilled water produced at all the evaporation temperature.



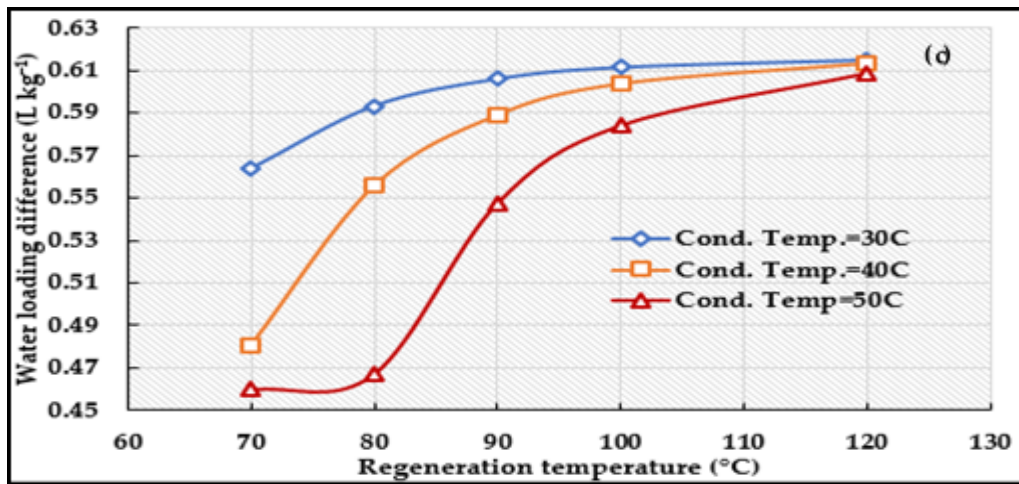


Fig.4 Effect of regeneration and condensation temperature on the performance of MIL-100(Fe) at an evaporation temperature of a. 5°C, b. 20°C and c. 29°C.

c. MIL-100(Fe), aluminium fumarate and CPO-27(Ni): A comparative study

The performance of MIL-100(Fe) was compared the performance of aluminium fumarate and CPO-27(Ni) [13] at an evaporation temperature of 5 and 20°C, adsorption temperature of 30°C and condensation temperature of 30°C. It can be noticed from Fig. 5 that at 5°C, MIL-100(Fe) outperformed aluminium fumarate at all the regeneration temperatures while it only outperformed CPO-27(Ni) at the low regeneration temperatures.

Increasing the evaporation temperature to 20°C, it can be noticed that MIL-100(Fe) outperformed both aluminium fumarate and CPO-27(Ni) at all the regeneration temperatures.

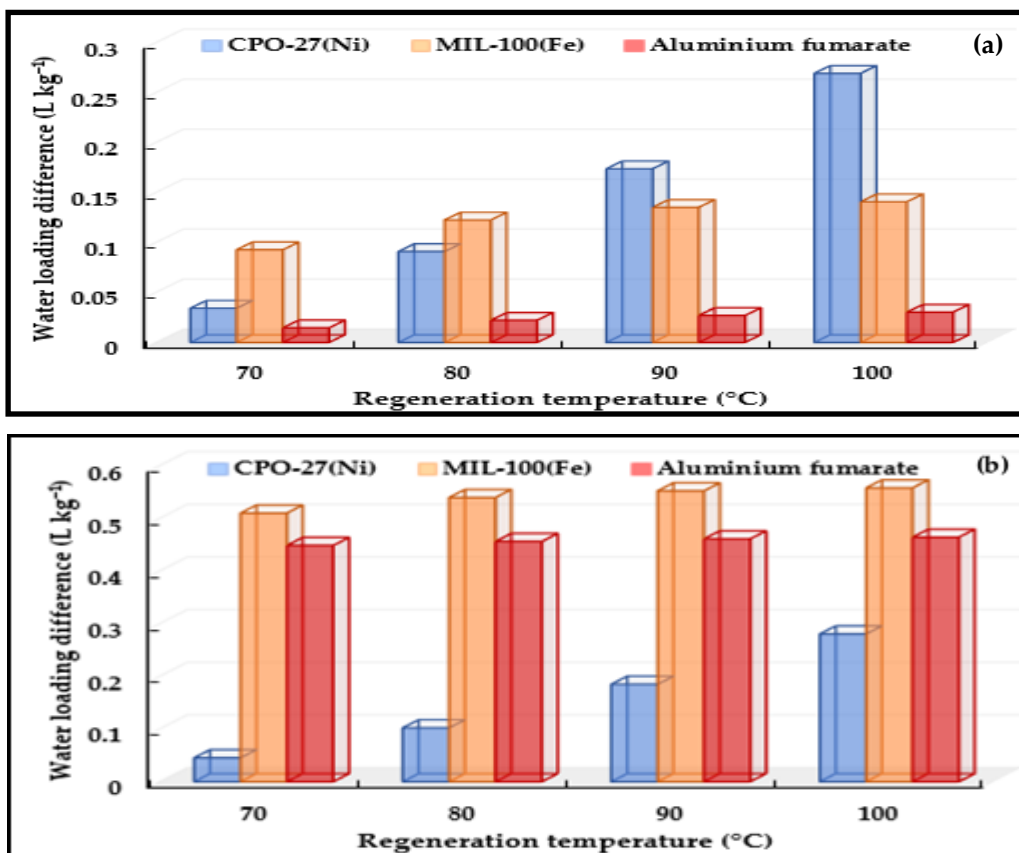


Fig.5 Comparative study between MIL-100(Fe), aluminium fumarate and CPO-27(Ni) at a. 5°C and b. 20°C.



## Conclusions

The potential of the MOF material, MIL-100(Fe), in adsorption desalination was investigated at different operating conditions. It was concluded that the performance of the material significantly depends on the evaporation temperature due to the IV isotherm shape. The effect of condensation and regeneration temperatures was also investigated showing the amount of distilled water increased with increasing the regeneration temperature while it decreased with increasing the condensation temperature.

When the performance of MIL-100(Fe) was compared to other MOF materials such as CPO-27(Ni) and aluminium fumarate, the material showed a higher performance compared to aluminium fumarate at different regeneration and evaporation temperature while in case of CPO-27(Ni), MIL-100(Fe) outperformed it at higher evaporation temperature of 20°C. This means that MIL-100(Fe) can be chosen over aluminium fumarate at the different operating conditions while CPO-27(Ni) is recommended for applications working at low evaporation temperatures and high regeneration temperatures. This highlights the potential of MIL-100(Fe) in the adsorption desalination application and the wide range of operating conditions that it can work at.

## References:

- [1] E. Elsayed, A.-D. Raya, S. Mahmoud, P. A. Anderson, A. Elsayed, and P. G. Youssef, "CPO-27 (Ni), aluminium fumarate and MIL-101 (Cr) MOF materials for adsorption water desalination," *Desalination*, vol. 406, pp. 25-36, 2017.
- [2] S. M. Salman, "United Nations General Assembly Resolution: International Decade for Action, Water for Life, 2005–2015: A Water Forum Contribution," *Water international*, vol. 30, no. 3, pp. 415-418, 2005.
- [3] K. Wang, "flsorpio," 2011.
- [4] A. S. Alsaman, A. A. Askalany, K. Harby, and M. S. Ahmed, "A state of the art of hybrid adsorption desalination–cooling systems," *Renewable and Sustainable Energy Reviews*, vol. 58, pp. 692-703, 2016.
- [5] K. C. Ng, X. WANG, L. Gao, A. Chakraborty, B. B. Saha, S. Koyama, A. Akisawa, and T. Kashiwagi, "Apparatus and method for desalination," Google Patents, 2006.
- [6] K. C. Ng, K. Thu, A. Chakraborty, B. B. Saha, and W. G. Chun, "Solar-assisted dual-effect adsorption cycle for the production of cooling effect and potable water," *International Journal of Low-Carbon Technologies*, vol. 4, no. 2, pp. 61-67, 2009.
- [7] K. Thu, K. C. Ng, B. B. Saha, A. Chakraborty, and S. Koyama, "Operational strategy of adsorption desalination systems," *International Journal of Heat and Mass Transfer*, vol. 52, no. 7, pp. 1811-1816, 2009.
- [8] K. C. Ng, K. Thu, B. B. Saha, and A. Chakraborty, "Study on a waste heat-driven adsorption cooling cum desalination cycle," *International Journal of refrigeration*, vol. 35, no. 3, pp. 685-693, 2012.
- [9] S. Mitra, K. Srinivasan, P. Kumar, S. Murthy, and P. Dutta, "Solar driven adsorption desalination system," *Energy Procedia*, vol. 49, pp. 2261-2269, 2014.
- [10] K. Thu, H. Yanagi, B. B. Saha, and K. C. Ng, "Performance analysis of a low-temperature waste heat-driven adsorption desalination prototype," *International Journal of Heat and Mass Transfer*, vol. 65, pp. 662-669, 2013.
- [11] K. Thu, A. Chakraborty, Y.-D. Kim, A. Myat, B. B. Saha, and K. C. Ng, "Numerical simulation and performance investigation of an advanced adsorption desalination cycle," *Desalination*, vol. 308, pp. 209-218, 2013.

- [12] P. G. Youssef, S. M. Mahmoud, and R. K. Al-Dadah, "Performance analysis of four bed adsorption water desalination/refrigeration system, comparison of AQSOA-Z02 to silica-gel," *Desalination*, vol. 375, pp. 100-107, 2015.
- [13] E. Elsayed, A.-D. Raya, S. Mahmoud, A. Elsayed, and P. A. Anderson, "Aluminium fumarate and CPO-27 (Ni) MOFs: characterization and thermodynamic analysis for adsorption heat pump applications," *Applied Thermal Engineering*, vol. 99, pp. 802-812, 2016.
- [14] P. Horcajada, S. Surblé, C. Serre, D.-Y. Hong, Y.-K. Seo, J.-S. Chang, J.-M. Greneche, I. Margiolaki, and G. Férey, "Synthesis and catalytic properties of MIL-100 (Fe), an iron (III) carboxylate with large pores," *Chemical Communications*, no. 27, pp. 2820-2822, 2007.
- [15] J. Shi, S. T. Hei, H. H. Liu, Y. H. Fu, F. M. Zhang, Y. J. Zhong, and W. D. Zhu, "Synthesis of MIL-100(Fe) at Low Temperature and Atmospheric Pressure," *Journal of Chemistry*, 2013.

# The effects of graphite flake on specific cooling power of sorption chillers: An experimental study

H. Bahrehmand, M. Khajepour, W. Huttema, C. McCague and M. Bahrami\*

Laboratory for Alternative Energy Conversion (LAEC), School of Mechatronic Systems Engineering, Simon Fraser University, Surrey, British Columbia, Canada

\*Corresponding Author: mbahrami@sfu.ca

## Abstract

Adding natural graphite flakes to sorbents of sorption cooling systems can enhance the total thermal diffusivity, while reducing the active material and increasing mass transfer resistance. To find the best compromise between these counteracting trends, the specific cooling power (SCP) of CaCl<sub>2</sub>-silica gel composite sorbents with 0-20 wt% graphite flake content was tested with a custom-built gravimetric large pressure jump (G-LPJ) test bed. It was observed that when the sorption rate is high, i.e. the first 20 min of sorption, graphite flake additive increases the SCP and COP due to the higher sorbent thermal diffusivity. Nevertheless, as the sorption rate reduces with time, the need for heat transfer enhancement, i.e. graphite flake additive, decreases. Furthermore, adding 20 wt.% graphite flakes to the composite sorbent has led to a 67% increase in SCP<sub>0.8</sub>.

**Keywords:** Sorption cooling system, graphite flakes, heat transfer enhancement, specific cooling power, thermal diffusivity

## Introduction/Background

Vapor compression refrigeration systems consume approximately 15% of global electrical energy and use environmentally harmful refrigerants [1]–[3]. Due to climate change and economic development, cooling demand is expected to increase [4]. Sorption cooling systems are an alternative clean technology in which an environmentally friendly refrigerant, such as water, is adsorbed by a sorbent material. Sorption cooling systems that utilize materials with low regeneration temperatures can be powered by low-grade heat sources (temperature sources around 80 °C), including solar thermal energy and industrial waste heat [5]. However, commercialization of sorption cooling systems is limited by fundamental challenges, including low specific cooling power (SCP) due to poor heat transfer between sorber bed heat exchanger (HEX) and the sorbent [6]–[8]. Sorber beds need to be cooled during the sorption process and heated during the desorption process. This oscillatory cooling and heating is performed with a heat transfer fluid flowing through the sorber bed HEX. As such, heat transfer characteristics of the sorbent and HEX are crucially important to the overall performance and SCP of the sorption systems. It was shown in our previous study [9] that the sorbent thermal diffusivity is the main limiting factor in the heat transfer from the sorbent to the heat transfer fluid through the heat exchanger.

Thermally conductive materials can be added to the sorbent to enhance the thermal diffusivity of the adsorbent bed [10], [11]. The addition of high thermal diffusivity material can form higher conductivity paths by filling up the pores in the microstructure of the adsorbent particles to increase the overall thermal diffusivity. However, in general, these additives decrease the active material fraction and increase the vapor transport resistance [12]. Moreover, many microporous adsorbents have open pore structures and high total pore volumes [13]; as a result, significant improvements in thermal diffusivity of microporous adsorbent materials have been limited to high additive fractions (>10 wt%), compromising the total adsorption capacity.

Graphite is by far the most selected additive when developing composite sorbents with the purpose of enhancing thermal conductivity [14]. When comparing different host matrices or/and additives, graphite presents the highest conductivity values [15]. For instance, Mauran et al. [16] reported thermal conductivities of about  $10\text{-}40 \text{ W}\cdot(\text{m}\cdot\text{K})^{-1}$  for  $\text{CaCl}_2$ -expanded natural graphite (ENG). Nonetheless, high concentrations of ENG are used and in some cases the sorbent is compressed to enhance thermal conductivity, which considerably reduces the sorption capacity.

Guilleminot et al. [17] reported that thermal conductivity of the expanded graphite/zeolite composite can be increased up to  $10 \text{ W}\cdot(\text{m}\cdot\text{K})^{-1}$  compared to  $0.09 \text{ W}\cdot(\text{m}\cdot\text{K})^{-1}$  for the packed bed of same adsorbent. However, they did not report the sorption capacity. Pino et al. [13] found that by increasing the graphite content in 4A-zeolite-based composites, the equivalent thermal conductivity increases and the equilibrium uptake decreases. Wang et al. [18] found that by adding expanded graphite to  $\text{CaCl}_2$  consolidating the composite, the thermal conductivity was enhanced up to  $9.2 \text{ W}\cdot(\text{m}\cdot\text{K})^{-1}$ . The uptake was not reported in their study.

Eun et al. [19] found that adding expanded graphite to silica gel, increases the thermal conductivity of the composite sorbent. They also observed that by increasing the graphite content, the water uptake increases because of the enhanced thermal conductivity. However, the graphite weight, which acts as dead weight, was not included in their calculations.

Zheng et al. [20] fabricated composite sorbents by combining silica gel with expanded natural graphite treated with sulfuric acid (ENG-TSA) as the host matrix. It was found that by increasing the graphite content, thermal conductivity, thermal diffusivity and water uptake increase. Nonetheless, their water uptake calculation did not include the graphite mass.

Fayazmanesh et al. [21] combined calcium chloride in a silica gel matrix with a binder and graphite flakes to produce water absorbent consolidated composites. The addition of 20 wt.% graphite flakes increased the thermal conductivity of the composite adsorbent from  $0.57$  to  $0.78 \text{ W}\cdot(\text{m}\cdot\text{K})^{-1}$ . The equilibrium uptake of samples at a 1.2 kPa vapor pressure decreased from  $0.32 \text{ g/g}$  for  $\text{CaCl}_2$ /silica gel to  $0.15 \text{ g/g}$  for silica gel/ $\text{CaCl}_2$  consolidated with 10 wt.% graphite flakes and 13 wt.% binder.

It is evident from the literature that the majority of the studies only reported the effect of additives on the equilibrium uptake. However, due to the transient behavior of adsorber beds, the sorbent does not become fully saturated/dried during sorption/desorption in sorption cooling systems. The studies that investigated the transient behaviour of the uptake, reported the sorption capacity per mass of “active material”, while the additive mass, as part of the composite sorbent, should be included in the calculations of water uptake. In this paper,  $\text{CaCl}_2$ -silica gel composite sorbents with 0-20 wt% graphite flake contents are prepared and tested in a custom-built gravimetric large pressure jump (G-LPJ) test bed to study the counteracting effect of graphite additive on the transient heat and mass transfer performance and SCP of sorption cooling systems.

### Sample preparation

Polyvinylpyrrolidone (PVP40) binder (40,000 MW, Amresco Inc.) was dissolved in water; subsequently,  $\text{CaCl}_2$  and silica gel (SiliaFlash<sup>®</sup> B150, Silicycle, Inc., Quebec, Canada) and graphite flakes (consisting of both  $150 \mu\text{m}$  fine particles and thin flakes up to 1.3 mm long, Sigma-Aldrich) were added to the aqueous solution. The composition and total mass of the sorbent composites prepared in this study are presented in Table 1. Sorbent mass was measured using an analytical balance (OHAUS AX124) with the accuracy of 0.0001 g and sorbent thickness was measured using a digital caliper (Mastercraft 58-6800-4) with the accuracy of 0.01 mm.

Thermal diffusivity of composite sorbents was measured with a transient plane source, hot disk thermal constants analyzer, as per ISO 22007-2 [22] (TPS 2500S, ThermTest Inc., Fredericton, Canada) for different graphite flake contents and presented in Table 1.

Table 1. Compositions, total mass, and measured thermal diffusivity of the sorbent composite samples

No.	Silica gel (wt.%)	CaCl <sub>2</sub> (wt.%)	PVP40 (wt.%)	Graphite flake (wt.%)	Mass (g)	Thickness (mm)	Thermal diffusivity (m <sup>2</sup> /s)
1	45.0	45.0	10	0	18.8068	5.15	0.23e-6
2	42.5	42.5	10	5	18.7018	5.12	0.34e-6
3	40.0	40.0	10	10	18.7841	5.08	0.41e-6
4	37.5	37.5	10	15	18.6930	5.09	0.98e-6
5	35.0	35.0	10	20	18.8815	5.06	1.38e-6

The solution of composite sorbent was coated on graphite sheets and oven dried at 70 °C and then 180 °C, each for 1 h. The composite sorbent with 20 wt% graphite flake content is shown in Fig. 1.

The solution of composite sorbent was coated on graphite sheets and oven dried at 70 °C and then 180 °C, each for 1 h. The composite sorbent with 20 wt% graphite flake content is shown in Fig. 1.

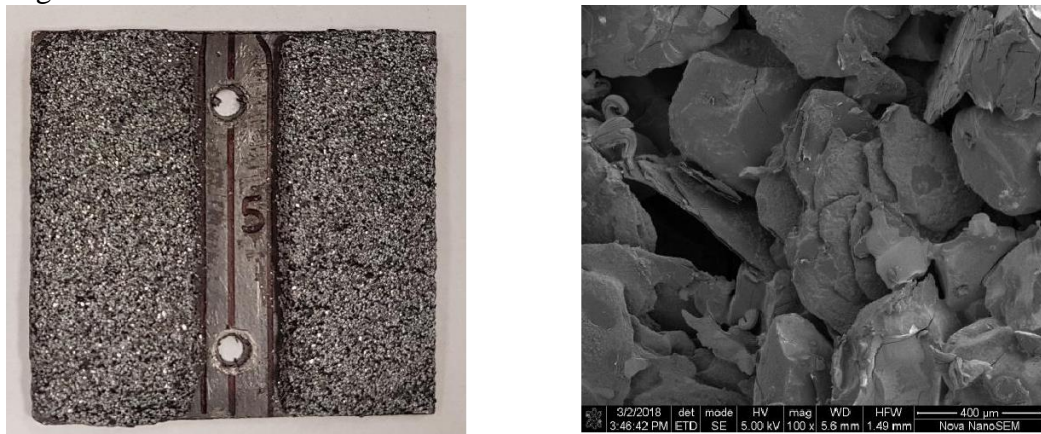


Fig. 1. The composite sorbent with 20 wt% graphite flake content coated on graphite sheets (left), SEM image (right)

### Experimental test-bed and measurements

A new gravimetric large pressure jump (G-LPJ) test bed was custom-built in our lab to investigate the heat and mass transfer performance of sorbent materials. The coated sorbent samples were bolted to a copper heat exchanger, see Fig. 2.



Fig. 2. Sorbent composite bolted to copper heat exchanger

A schematic diagram and a picture of the G-LPJ test bed is shown in Fig. 3. Heat transfer fluid flows through the copper heat exchanger and maintains its temperature constant at 39 °C. The sorber bed and the copper heat exchanger are placed inside a vacuum chamber which is connected to a capillary-assisted evaporator whose temperature is changed between 1 °C and 20 °C for desorption and adsorption, respectively. The whole test bed is vacuumed for 6 hours using a vacuum pump to dry the sorbent material. The vacuum chamber is placed on a precision balance (ML4002E, Mettler Toledo) with an accuracy of 0.01 g to measure the mass of the sorbate uptake. K-type thermocouples with an accuracy of 1.1 °C are passed via a feed-through in the vacuum chamber to measure the sorbent temperature. The pressure of the sorber bed and the evaporator is measured using 722B Baratron pressure transducer with the accuracy of 0.5%. The instruments are interfaced with a PC through a data acquisition system and software built in the LabVIEW environment.

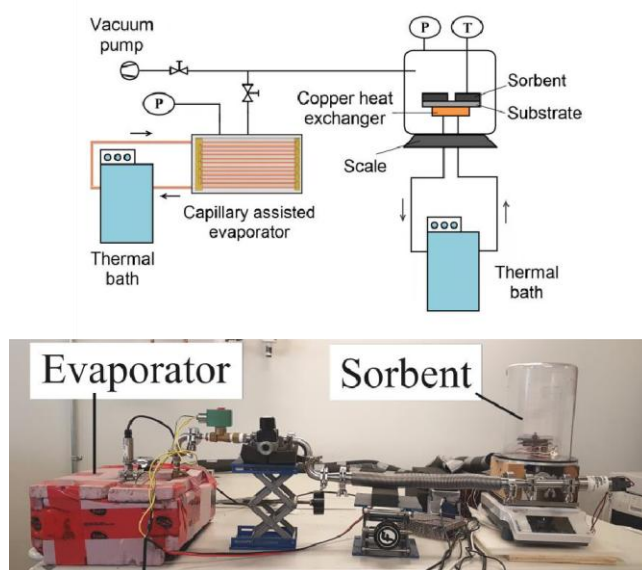


Fig. 3. Schematic (top) and picture (bottom) of the gravimetric large pressure jump test-bed

### Discussion and Results

Fig. 4 shows that the sorbent temperature decreases more rapidly for samples with greater graphite flake content. One reason is that by adding graphite flake, the sorbent thermal diffusivity increases, which enhances the heat transfer from the sorbent to the HEX, see Table 1.

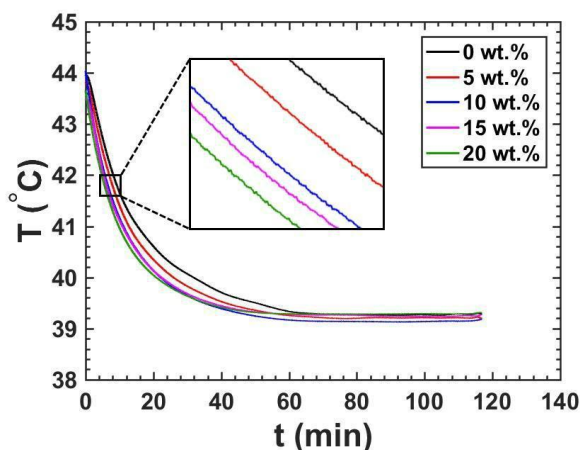


Fig. 4. Variation of sorbent temperature data collected in our G-LPJ testbed versus time for various graphite flake contents

Furthermore, the heat generation decreases for samples with larger graphite flake content as they have less active material.

The isotherm of the sorbent material was obtained using an IGA-002 thermogravimetric sorption analyzer (TGA) (Hiden Isochema). Sorbent material was placed on the sample cell, which is held by a microbalance to measure the mass changes of the sorbent, while the temperature and pressure are controlled. The mass changes of the sorbent are collected in the range of 0.04–2.84 kPa (our range for G-LPJ) with the pressure step of 0.2 kPa at 25°C. More details regarding the TGA measurements can be found elsewhere [21].

Fig. 5 shows the variation of water uptake with time for various graphite flake contents. As shown in Fig. 5, the equilibrium uptakes measured with the G-LPJ test bed are in good agreement with TGA equilibrium data. Moreover, as can be seen for the region that sorption rate ( $d\omega/dt$ ) is high, i.e. the first 20 min, the water uptake increases by increasing the graphite flake content, as expected. The reason is that during this time, the heat generation rate in the sorbent is high; hence, there is a high need for enhanced sorbent thermal diffusivity; thus, increasing the graphite flake enhances the overall performance. However, as the sorbent approach saturation, the trend starts to reverse, which means that the uptake increases with a decrease of graphite content. That is because as the sorbent approaches equilibrium, the heat generation rate reduces; as a result, the need for enhanced heat transfer decreases; consequently, the sorbent with higher active material can uptake more which leads to higher performance.

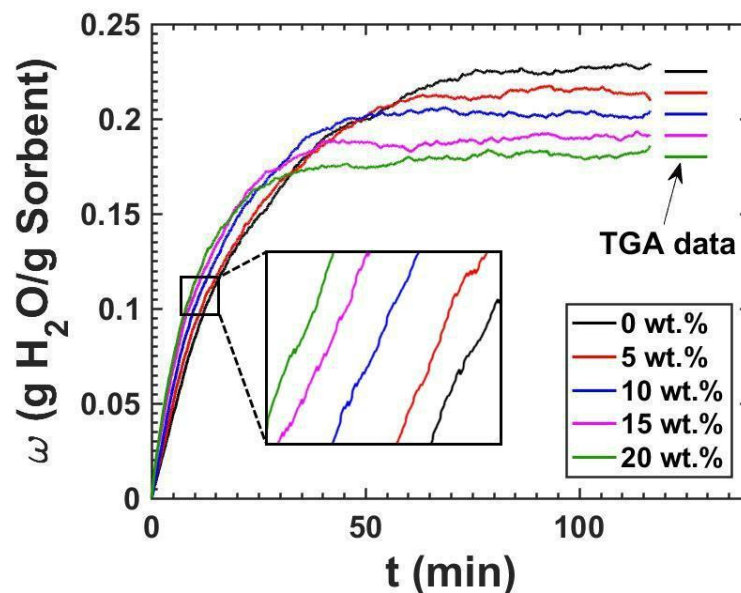


Fig. 5. Variation of water uptake data collected in our G-LPJ testbed versus time for various graphite flake content composites

Specific cooling power (SCP) is defined as the ratio of cooling energy to the product of sorbent mass and cycle time which represents the performance of sorber beds, as shown in Eq. (1).

$$SCP = \frac{Q_{evap}}{m_{sorb}\tau} = \frac{\Delta\omega h_{fg@T_{evap}}}{\tau} \quad (1)$$

$\omega$	Water uptake (g/g)
$h_{fg}$	Evaporation enthalpy (J/kg)
$\tau$	Cycle time (s)

Fig. 6. shows the experimental SCP data collected in our G-LPJ testbed for various sorption times and different graphite flake contents. It can be seen that adding graphite flake enhances the SCP because the sorbent thermal diffusivity increases. Furthermore, it can be observed that by reducing the sorption time, the SCP enhancement of adding graphite flake, increases because the heat generation rate increases. In addition, it is shown that adding 15 wt.% graphite flake or more, results in a significant increase in SCP for short sorption times. The reason can be attributed to the better connection between graphite flakes that can be established for composites with more than 10 wt.% additives.

A practical specific cooling power was proposed by Aristov et al. [23] to be calculated when the uptake reaches 80% of the equilibrium. Fig. 7 shows the effect of graphite flake on SCP<sub>0.8</sub>. It can be observed that SCP<sub>0.8</sub> increases with the increase of graphite flake content because the heat transfer rate increases; thereby reducing the time required for the sorbent to reach equilibrium. For example, composite sorbent containing 20 wt.% graphite flake has a 67% greater SCP<sub>0.8</sub> than the composite sorbent with no thermally conductive additive.

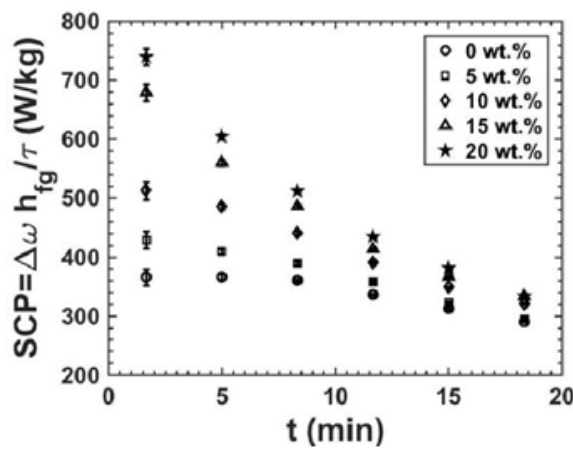


Fig. 6. Variation of specific cooling power versus sorption time for various graphite flake contents

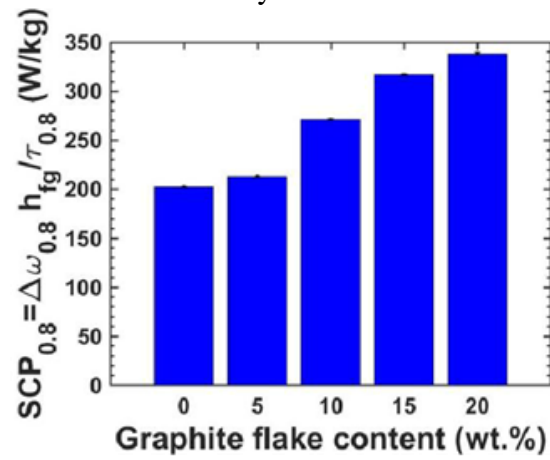


Fig. 7. Variation of SCP<sub>0.8</sub> versus graphite flake contents

Coefficient of performance (COP) is defined as the ratio of evaporative cooling energy to the input energy (Eq. (2)). Fig. 8 shows the variation of COP with time for different graphite flake contents. It can be seen that COP increases by increasing the graphite flake content as the sorbent thermal diffusivity and sorbate uptake increase; thus, evaporative cooling energy increases.

$$COP = \frac{Q_{evap}}{Q_{input}} = \frac{m_{sorb} \int_{ads} \frac{d\omega}{dt} h_{fg} dt}{\int_{des} \left( \left( m_{sorb} (c_{p,s} + \omega c_{p,w}) + m_{HEX} c_{p,HEX} \right) \frac{dT}{dt} - m_{sorb} \frac{d\omega}{dt} h_{ads} \right) dt} \quad (2)$$

$c_p$	Specific heat capacity (J/kg K)	T	Temperature (K)	t	Time (s)	
Subscripts	s, sorb	Sorbent	w	Water	HEX	Heat exchanger

## Summary/Conclusions

The effect of adding graphite flakes on the SCP and COP of sorption cooling systems was studied using a custom-built G-LPJ testbed. It was found that for high sorption rates, the sorber bed performance enhances by adding graphite flake due to the higher sorbent thermal diffusivity; however, as the sorbent approaches equilibrium, the performance deteriorates by adding graphite flake because of the less active material. Therefore, there exists an optimum



graphite flake content to achieve the highest SCP and COP, which will be investigated in our future study.

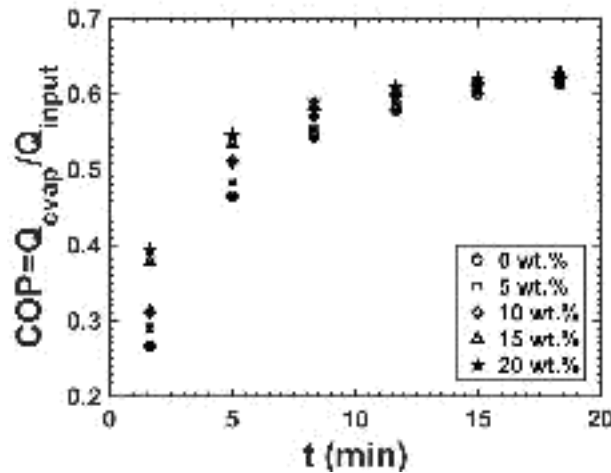


Fig. 8. Variation of COP versus sorption time for various graphite flake contents

### Acknowledgements

The authors gratefully acknowledge the financial support of the Natural Sciences and Engineering Research Council of Canada (NSERC) through the Automotive Partnership Canada Grant No. APCPJ 401826-10. The SEM studies were conducted in the Simon Fraser University 4D Labs facility with the assistance of the technical staff. 4D LABS shared facilities are supported by the Canada Foundation for Innovation (CFI), British Columbia Knowledge Development Fund (BCKDF), Western Economic Diversification Canada (WD), and Simon Fraser University (SFU).

### References

- [1] "Building Energy Data Book.," U.S. Department of Energy, 2012.
- [2] Askalany, A. A., Salem, M., Ismael, I. M., Ali, A. H. H., Morsy, M. G., and Saha, B. B., "An overview on adsorption pairs for cooling," *Renewable and Sustainable Energy Reviews*, vol. 19, pp. 565–572, 2013.
- [3] Pridasawas, W., "Solar-driven refrigeration systems with focus on the ejector cycle," 2006.
- [4] Sharafian, A., Nemati Mehr, S. M., Huttema, W., and Bahrami, M., "Effects of different adsorber bed designs on in-situ water uptake rate measurements of AQSOA FAM-Z02 for vehicle air conditioning applications," *Applied Thermal Engineering*, vol. 98, pp. 568–574, 2016.
- [5] Wang, R. and Oliveira, R., "Adsorption refrigeration—An efficient way to make good use of waste heat and solar energy," *Prog. Energy Combust. Sci.*, vol. 32, no. 4, pp. 424–458, 2006.
- [6] Wu, W., Zhang, H., and Sun, D., "Mathematical simulation and experimental study of a modified zeolite 13X–water adsorption refrigeration module," *Appl. Therm. Eng.*, vol. 29, pp. 645–651, 2009.
- [7] Zhao, Y., Hu, E., and Blazewicz, A., "Dynamic modelling of an activated carbon-methanol adsorption refrigeration tube with considerations of interfacial convection and transient pressure process," *Applied Energy*, vol. 95, pp. 276–284, 2012.

- [8] Sharafian, A., McCague, C., and Bahrami, M., "Impact of fin spacing on temperature distribution in adsorption cooling system for vehicle A/C applications," *International Journal of Refrigeration*, vol. 51, pp. 135–143, 2015.
- [9] Bahrehmand, H., Ahmadi, M., and Bahrami, M., "Analytical modeling of oscillatory heat transfer in coated sorption beds," *Int. J. Heat Mass Transfer*, vol. 121, pp. 1–9, 2018.
- [10] Chan, K. C. and Chao, C. Y. H., "A theoretical model on the effective stagnant thermal conductivity of an adsorbent embedded with a highly thermal conductive material," *International Journal of Heat and Mass Transfer*, vol. 65, pp. 863–872, 2013.
- [11] Rezk, A., Al-Dadah, R. K., Mahmoud, S., and Elsayed, A., "Effects of contact resistance and metal additives in finned-tube adsorbent beds on the performance of silica gel/water adsorption chiller," *Applied Thermal Engineering*, vol. 53, no. 2, pp. 278–284, 2013.
- [12] Yang, S., Kim, H., Narayanan, S., and McKay, I. S., "Dimensionality effects of carbon-based thermal additives for microporous adsorbents," *Materials and Design*, vol. 85, pp. 520–526, 2015.
- [13] Pino, L., Aristov, Y., Cacciola, G., and Restuccia, G., "Composite materials based on zeolite 4A for adsorption heat pumps," *Adsorption*, vol. 3, pp. 33–40, 1997.
- [14] Cabeza, L. F., Sole, A., and Barreneche, C., "Review on sorption materials and technologies for heat pumps and thermal energy storage," *Renewable Energy*, vol. 110, pp. 3–39, 2017.
- [15] Aydin, D., Casey, S. P., and Riffat, S., "The latest advancements on thermochemical heat storage systems," *Renew. Sustain. Energy Rev.*, vol. 41, pp. 356–367, 2015.
- [16] Mauran, S., Parades, P., and L'haridon, F., "Heat and mass transfer in consolidated reacting beds for thermochemical systems," *Heat. Recovery Syst.*, vol. 13, pp. 315–319, 1993.
- [17] Guilleminot, J. J., Chalfen, J. B., and Choisier, A., "Heat and mass transfer characteristics of composites for adsorption heat pumps," in *International Absorption Heat Pump Conference, AES 31, ASME, New York*, 1993.
- [18] Wang, K., Wu, J. Y., Wang, R. Z., and Wang, L. W., "Effective thermal conductivity of expanded graphite-CaCl<sub>2</sub> composite adsorbent for chemical adsorption chillers," *Energy Conversion and Management*, vol. 47, no. 13–14, pp. 1902–1912, 2006.
- [19] Eun, T., Song, H., Hun Han, J., Lee, K., and Kim, J., "Enhancement of heat and mass transfer in silica-expanded graphite composite blocks for adsorption heat pumps:: Part I. Characterization of the composite blocks: Amélioration du transfert de chaleur de blocs en matériaux composite graphite-silice expansé/d," *International journal of refrigeration*, vol. 23, no. 1, pp. 64–73, 2000.
- [20] Zheng, X., Wang, L. W., Wang, R. Z., Ge, T. S., and Ishugah, T. F., "Thermal conductivity, pore structure and adsorption performance of compact composite silica gel," *International Journal of Heat and Mass Transfer*, vol. 68, pp. 435–443, 2014.
- [21] Fayazmanesh, K., McCague, C., and Bahrami, M., "Consolidated adsorbent containing graphite flakes for heat-driven water sorption cooling systems," *Applied Thermal Engineering*, vol. 123, pp. 753–760, 2017.
- [22] ISO22007-2, "Plastics-determination of thermal conductivity and thermal diffusivity-part 2: transient plane heat source (hot disc) method." 2008.
- [23] Aristov, Y. I., Glaznev, I. S., and Girnuk, I. S., "Optimization of adsorption dynamics in adsorptive chillers: loose grains configuration," *Energy*, vol. 46, no. 1, pp. 484–492, 2012.

# The Influence of Heat Input Ratio on Electrical Power Output of a Dual-Core Travelling-Wave Thermoacoustic Engine

Wigdan Kisha<sup>1\*</sup>, Paul H. Riley<sup>2</sup>, Jon McKechnie<sup>3</sup>, David Hann<sup>4</sup>

<sup>1,3,4</sup> Faculty of Engineering, University of Nottingham, UK

<sup>2</sup> School of Mathematics, Computer Science & Engineering. City, University of London, UK

Corresponding author: \*Email address: wigdan.kisha@nottingham.ac.uk

## Abstract

This paper presents an analytical and experimental investigation of an electricity generator that employs a two-stage looped tube travelling-wave thermoacoustic prime-mover to deliver acoustic power from heat energy, a loudspeaker to extract electricity from sound energy and a tuning stub to compensate the changes in the acoustic field within the engine to enable close to travelling wave operation at the loudspeaker. Furthermore, the paper explains how to enhance the output power utilizing different heat input ratios through the engine cores. A well-known thermoacoustic design tool called DeltaEC is used to simulate the wave propagation through the different parts of the system. The electrical power predicted from the low-cost prototype was 24.4 W acoustic power which confirms the potential for developing low-cost thermoacoustic electricity generator for heat recovery from low-grade heat sources. The electrical power can be increased to 31.3 W using different heating power percentages through the two units. The verified experimental data shows good agreement with DeltaEC results.

**Keywords:** Regenerator, thermoacoustic, acoustic power, loudspeaker as a generator, DeltaEC

## Background

The development of new techniques utilizing low-temperature waste heat and renewable energy sources have drawn enormous attention worldwide in recent years. There are many sources of such low-grade heat that, if they could efficiently and economically be harvested, would decrease carbon footprint significantly. One application where it has the potential to make significant changes to the standard of life is in the generation of electricity in low-income rural areas of the world. Over three billion people in the developing world use open fires for cooking process and one billion do not have access to electricity. An estimated 4 million people die prematurely by the smoke from open fires, mostly women, and children, making this one of the serious health threats facing people in developing countries [1]. The target of this research is to provide healthy cooking and electric power for the households of Sudan and South - Sudan countries by means of thermoacoustic technology.

Thermoacoustics is a new promising technique that uses heat to produce high-intensity sound waves which can, in turn, produce electricity. A thermoacoustic engine (TAE) eliminates the majority of mechanical moving parts by its simple construction, which comprises an acoustic resonating tube and a section of porous media in between two heat exchangers [2]. The well-known torus configuration travelling-wave engine developed by Backhaus and Swift has demonstrated a high efficiency of 30% which corresponds to 41% Carnot efficiency using 30 bar pressurized helium at a high operating temperature of 725°C [3], which is comparable to the efficiencies from petrol and diesel engines, but at lower temperatures, although efficiency is much lower when a flame is used as heat [4]. At these high temperatures travelling wave thermoacoustic engine has to compete with other conventional devices such as Stirling engine. However, clearance sealing is an issue in conventional Stirling engine at high temperature.

Several variations of systems have been attempted to convert the acoustic power to useful electric power, utilizing different system configurations and transduction mechanisms [5, 6]. Thermoacoustic stoves have been shown to be a cheap option compared to others in situations where hydropower is not available, but since the technology is relatively new, and these low temperature systems are subject to non-linear effects that are not well understood, present work is concentrating on understanding the non-linear effects and minimising the losses.

The idea of thermoacoustic power has been proved over the last 20 years since the first working engines were produced. A number of designs have been developed that can achieve good efficiencies relative to Carnot for. An early thermoacoustic engine was designed for space application using a flexure-bearing linear alternator, the electrical power produced from this engine was 39 W with 18% thermal-to-electrical efficiency [7, 8]. A novel three-cylinder double-acting thermoacoustic Stirling electricity generator was developed and tested [9], using 3.12 KW heating power from each heater block and three alternators to extract the electric power. 5 MPa pressurized helium was adopted as the working gas and the system produced a maximum electrical power of 1570 W. The performance was highly degraded due to the significant difference in the performance of the engines and the alternators. Another investigation on generating electricity using multiple- stage travelling-wave thermoacoustic engines was undertaken by Kang et al.[10]. In this case, the total electric power output had a maximum value of 204 W using 1.8 MPa helium and 6 kW total heating power (with the same input through the two heaters). The parasitic heat loss in the experiments was very large and there was non-linear behavior in the system due to the high-pressure amplitude. Most recently, a three-stage travelling-wave thermoacoustic electricity generator was proposed by Bi et al. [11]. This prototype achieved a maximum electric power of 4.69 kW with thermal-to-electric efficiency of 15.6% using 6 MPa helium gas. The heat transfer was again poor and there were large flow losses and friction losses from the alternator which dropped the power rate.

The conversion of the acoustic field to electrical output is mostly carried out using linear alternators, although more recently bi-directional turbines have shown some potential in improving performance [12]. Linear alternators purpose-designed for thermoacoustic systems are expensive, which limit the advantages of the thermoacoustic heat engines for low-cost energy conversion applications and therefore, it is possible to consider low-cost commercial available loudspeakers to convert acoustic power gain into electricity. In these low cost applications the main driver is the cost of the system, not the transduction efficiency [13, 14]. In 2012, SCORE project ([www.score.uk.com](http://www.score.uk.com)) developed and tested two low-cost double-regenerator traveling-wave thermoacoustic electricity generators, to produce electricity using waste heat energy from cooking stoves. A propane-driven stove delivered approximately 15 W of electricity. While, a wood burning cooking stove was successfully demonstrated 22.7 W of electricity. The performance of the devices was low due to the high acoustic losses and the inefficient linear alternators being used [15], but also because, at these low temperatures, the system is very sensitive to losses. Understanding this and minimising losses is important if we want to reach the commercially needed target of producing at least 100 W of electrical power from a cook-stove that costs less than £200.

Many of the configurations that have been tested use multiple stages and it has been the practice to input the same amount of heat in each exchanger. In this paper, a new operational methodology using different percentages of thermal energy is employed for the optimization of the system for the first time. This paper will look at whether there is a strategic advantage in varying the heat power ratio.

### **Modeling of the system**

To further understand the behavior of the thermoacoustic system considered in this research and to predict the performance of the existing build engine, a design software code referred as

DeltaEC (Design Environment for Low-amplitude ThermoAcoustic Energy Conversion) is utilized [16]. DeltaEC integrates numerically the wave equation and other equations such as the energy equation throughout the whole system in one spatial dimension based on a low-amplitude “acoustic” approximation and sinusoidal time dependence of the variables [17]. The governing equations used in DeltaEC as follows:

$$\frac{dp_1}{dx} = -\frac{i\omega\rho_m}{A_g(1-f_v)}U_1 \quad (1)$$

$$\frac{dU_1}{dx} = -\frac{i\omega A_g}{\gamma P_m}(1+(\gamma-1)f_k)p_1 + \frac{(f_k-f_v)}{(1-f_v)(1-\sigma)}\frac{1}{T_m}\frac{dT_m}{dx}U_1 \quad (2)$$

Where:  $p_1$  pressure amplitude of oscillation (Pa),  $U_1$  volumetric velocity amplitude ( $\text{m}^3/\text{sec}$ ),  $\omega$  angular velocity which equals  $2\pi f$  (rad/sec),  $\rho_m$  mean density ( $\text{kg}/\text{m}^3$ ),  $P_m$  mean pressure of the working gas (Pa),  $T_m$  mean temperature of the working gas (K),  $\gamma$  is the ratio of the specific heats of the gas,  $f_k$  is the thermal spatially averaged diffusion function,  $f_v$  is the viscous spatially averaged diffusion function,  $\sigma$  is Prandtl number,  $A_g$  is the cross-sectional area available for the gas,  $A_s$  is the cross-sectional area of the solid. This model was validated against experimental results shown below to confirm the findings.

### Explanation of test-bed apparatus

The SCORE system comprises a two-stage thermoacoustic engine operating in mainly travelling wave mode, with two tuning stubs and a loudspeaker as shown in Figure 1. Which is based on the loop-tube configuration. This arrangement gives an advantage of using low-temperature heat source with a lower temperature gradient through each stage [18, 19]. Both stages comprise an ambient heat exchanger (AHX), regenerator, hot heat exchanger (HHX), thermal buffer tube (TBT) and a secondary ambient heat exchanger (SAHX) as in Figure 1(b). The AHX is made out of the core of a commercial low-cost car radiator, suitably modified to fit the thermoacoustic engine. A thermos-siphon water circulation method was applied to take heat from the system, so a pump isn't required in the system. To maintain a low cost for the engine core and to achieve a quick warm-up time, a low-mass convoluted stainless steel plate design has been adopted for the HHX. The HHX is  $233 \times 307 \text{ mm}$  and is made out of 3 mm thick Stainless steel plate. The plate was welded to a flange that designed to be directly bolted to the engine housing. The regenerator is sandwiched between the AHX and the HHX and was formed by stacking 50 pieces, 80-mesh Stainless-steel wire mesh machined to a required size of  $20 \times 20 \text{ mm}$ . The mesh wire has a diameter of  $95 \mu\text{m}$  and a pitch of  $250 \mu\text{m}$ . The AHX and the HHX are clamped between upper and lower housings [5]. The TBT is simply a section of stainless steel pipe and is located below the HHX to separate the SAHX from the hot gas and thus minimizing parasitic heat losses. A SAHX is introduced after the TBT to cool the air before it flows to the alternator. The stages are connected using 70 mm diameter standard PVC pipes and fittings. Two extra pipes perpendicular to the feedback loop “denoted as tuning stubs” are introduced in the loop to enhance the impedance matching between the acoustic wave and the linear alternator and to maintain the phase angle between the velocity and the pressure in a travelling-wave condition through the regenerators. To extract the electric power from the circulating acoustic power, a low-cost commercial loudspeaker (model JL 6W3v3-4) was used as a linear alternator and is connected in series in the loop. This arrangement allows suppressing the acoustic streaming which could cause heat dissipations from a HHX. To simulate more closely to the final application, two custom-made electrical heaters are used to supply the heat to the HHXs. For temperature measurements, eight thermocouples (Type-K) were placed in different locations to monitor the hot and the cold temperatures of each regenerator unit as well as the

temperatures the cooling water. Three absolute pressure transducers (model IMPRESS) were distributed along the feedback pipe and a differential pressure sensor (model ABPMJTT015PGAA5) was used to capture the volumetric flow rate across the loop. The readings of the thermocouples and the pressure transducers were collected by a Data Acquisition system (NI cDAQ 9172) which is connected to a data logger system. To harvest the electrical power from the system, a wide range variable resistor (model VISHAY®) was adjusted to the optimal electrical load for the loudspeaker. The voltage and the current from the alternator are measured using a power analyzer (model KintiQPPA2530).

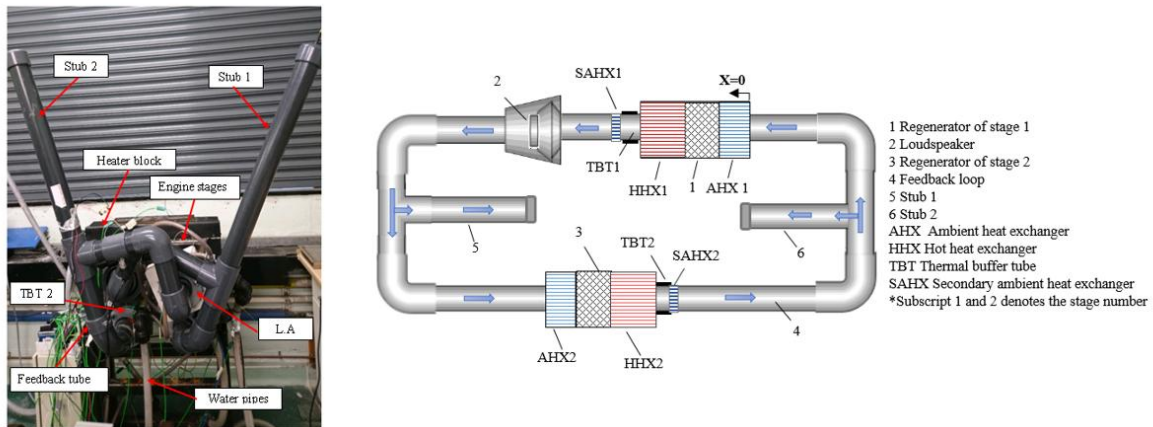


Figure 1. The two-stage thermoacoustic electricity generator. (a) Photo of the system. (b) Functional diagram

In order to address the performance of the system, it is important to estimate the flow of the acoustic power which is defined as a time-average energy flux accompanied by pressure oscillations and velocity of the working gas. The most common method to measure the acoustic power is the so-called two-microphone method [20]. Conceptually, this method employs two absolute pressure sensors to obtain the velocity of the oscillating gas. However, one of the drawbacks of this technique is obtaining the high accuracy of the phase angle between the pressure and the velocity. Therefore, to get a more durable way of measuring the acoustic power, an alternative method referred as “gradient method” is used in the current system. It employs one absolute pressure transducer and one differential pressure sensor to directly calculate the mass of the air between the two sensors, the acoustic velocity, and the acceleration. The distance between the two sensors is small compared to the two-microphone method. Therefore, no empirical correction for acoustic loss is required. The acoustic power propagation in the feedback loop can be given as [21]:

$$P_{Ac.} = A \cdot \hat{p}_1 \frac{\Delta p_1}{2\omega \rho_m \Delta x} \sin \phi \quad (3)$$

Here:  $A$  is the cross-sectional area of the feedback loop,  $p_1$  is the pressure amplitude (Pa) which is the signal from the absolute sensor,  $\Delta p_a$  is the output signal of the differential pressure sensor (Pa),  $\Delta x$  is the distance between the two probes of the differential sensor (m),  $\phi$  is the measured phase between  $p_1$  and  $\Delta p_1$ ,  $\omega$  is the angular velocity (rad/sec),  $\rho_m$  is the mean density ( $\text{kg/m}^3$ ),  $p_m$  is the mean pressure (Pa).

Since the application is for the developing world, air at atmospheric pressure is used as the working gas. The maximum hot and the cold temperatures were set to 650 °C and 90 °C, respectively and the total heat input power was varied between 2.1 - 3 kW. This was split at different ratios between the two stages. DeltaEC model had predicted that changing the heat ratio to each core could affect the performance, so in the experiment the heat was inputted as

40%-60%, 50%-50%, 55%-45%, 60%-40%. The system operates at working frequency of 73 Hz. To verify the numerical results with the lab data, the load resistance of the loudspeaker was adjusted to 35.5 Ohm. In most applications the heat input would be split between the two cores evenly, providing  $Q/2$  W to each core. In this paper we have investigated whether the results of the model which suggested that a 60% - 40% split would improve performance. These results are used to validate the numerical model.

## Results and discussion

The schematic diagram of the model used in DeltaEC simulation is presented in Figure 1 (b). The model was constructed using the same design parameters of the existing prototype and using some of DeltaEC segments [17]. The model starts at  $x = 0$  which is located at the hot end of the first AHX and goes anticlockwise until it returns. The pressure amplitude, the volumetric velocity amplitude, and their phases are adjusted so that they match at the start and the end of the model. The acoustic power flow is indicated by the blue arrows. Figure 2 demonstrates how the key acoustic parameters obtained from DeltaEC vary around the system. The 4 curves correspond to varying heat input into the two cores, with 40%, 50%, 55% and 60% of the heat being directed to core 1, which is just before the linear alternator, and the power in core 2 being adjusted so that the total energy input was a constant. No other variables were adjusted. It is clear that the curves have the same trend among the four heat supply percentages. In Figure 2(a), the Pressure amplitude drops at each of the two regenerators due to their flow resistance. It also decreases across the linear alternator due to its acoustic resistance. The two stubs don't influence the pressure amplitude. The standing wave ratio in the system is approximately around 2.97 due to the reflections where the feedback pipe area changes.

These numerical results demonstrate that using 60% of the heat in the first HHX resulted in higher pressure drop across the alternator diaphragm which indicates better extraction of the electric power. In other words, the electrical power output increased from X to Y when the balance of heat went from 50% to 60%, an X% increase. It can be seen that the pressure anti-nodes altered location slightly in the four heat supply ratios, particularly near the end of the feedback loop due to the slight change in the operating frequency. There is a high decrease in the flow at the location of the stub which indicates that the stub removes part of the volumetric flow from the loop. In contrast, the volumetric velocity increases significantly along the two regenerators due to the sharp temperature gradient across them. Between the alternator and the SAHX, there is a part of connecting pipe where the volumetric velocity increases due to the change in the area. The acoustic impedance Figure 2(c) has high values at the cold end of the two regenerators which led to  $[|Z| * A/a * \rho_m] \sim 7$  & 12 at regenerator 1 and regenerator 2, respectively. In travelling-wave thermoacoustic engines, a common practise is to set the absolute value of the regenerator impedance in the range of 10-20 times the gas characteristic impedance [19]. At the locations of the tuning stubs, the impedance decreased due to the constant pressure amplitude at the junction between the stub and the feedback tube. The acoustic loop power Figure 2(d) increases when adding higher heat in the first HHX. Again for all the cases, the curve has the same characteristics, but it is clear that there is higher acoustic power when the ratio of heat input is 60% / 40%. Considering the case where the total heat splits eventually between the two heaters, the results revealed that, around 58.4 W of the acoustic power from the resonance tube is introduced into unit 1 and only about 1 W is dissipated within its AHX, leading to an amplification of 57.4W. This is then fed into the cold side of the regenerator where the acoustic power is amplified to 77.5 W. Minor acoustic loss of 1.8 W occurred through the HHX, the TBT and the SAHX of the first unit. The alternator delivered 24.4 W electrical power with a thermal-to-acoustic efficiency of 2.3%, and thermal-to-electrical efficiency of 0.98%.

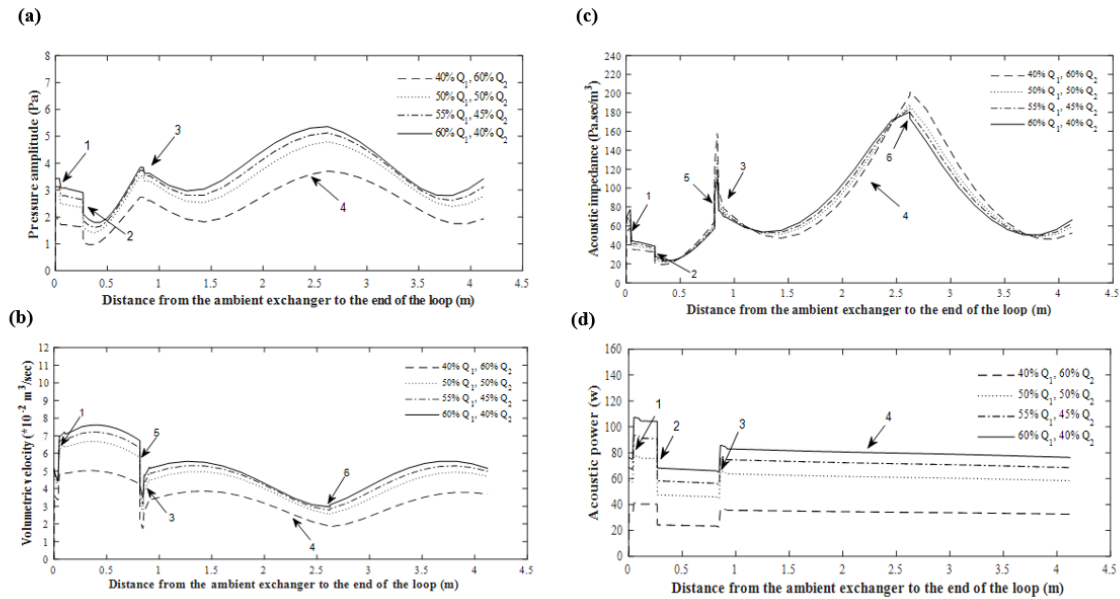


Figure 2. The variation of the key performance parameters through the loop using different percentages of the total heat input:  $Q_1$  in heater 1 and  $Q_2$  in heater 2 (a) Pressure amplitude (b) volumetric velocity (c) acoustic impedance (d) acoustic power. \* Numbers from 1 to 6 correspond to the defined ones in Figure 1

The results of the numerical modelling were surprising, thus the performance of the experimental rig was assessed using the same concept. Figure 3 compares the lab results of several percentage of the heat power (range 2.1 to 3 kW). Both the acoustic power and the electric output increase linearly with the total heat input. Extra power could be gained by simply supplying a higher heat percentage to the first HHX. This can be justified by the location of the loudspeaker which is immediately after the TBT of the first engine. Using 2.5 kW power with 50%  $Q_1$ , 50%  $Q_2$  generated 48.4W acoustic power. This power is raised to 68 W when using 60%  $Q_1$ , 40%  $Q_2$  which resulted in an extra 6.5 W electric power (10% increase). However, DeltaEC models predict loop power as high as 0.1- 2.8 percent, and electric power as high as 0.4 to 3.7 percent which indicates that the system isn't quite efficient in converting heat energy into acoustic power and the heat dissipation is potentially an issue. The alternator in this system is installed next to the SAHX of the first unit. At this location, the acoustic impedance has a low value. In fact, almost a maximum alternator stroke is reached at 3 kW thermal power. Therefore, if more electrical power is to be extracted, the alternator should be placed in a high-impedance zone to avoid the stroke limitation.

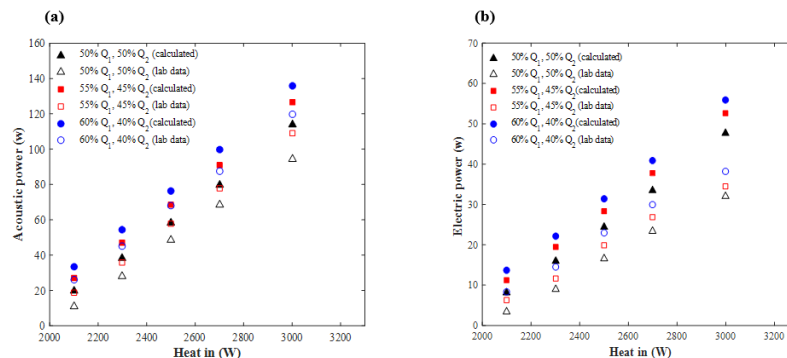


Figure 3. Performance of the engine under four heat input ratios. (a) Acoustic power (b) Electrical power

The thermal-to-electric efficiency reached a maximum value of 1.25% when using 60%  $Q_2$ , which is indeed much lower than that noted in Ref [8], where the linear alternator acted as a



mechanical resonator as well as a transduction mechanism. In the current design, two reasons are contributed to the poor efficiency. The first one, using a linear alternator instead of resonating tube minimizes the acoustic losses where the long resonator dissipated a considerable amount of the loop power. The second reason, the transduction efficiency of the loudspeaker is quite low (about 34%) compared to the linear alternator which was approximately around 90%. However, the linear alternator is expensive and this counteracts the affordability of the system. Therefore, the loudspeaker is a viable competitive candidate for developing a thermoacoustic generator.

The onset temperature is also important. Low onset temperatures can help improve efficiency. Therefore, the electric power against the temperature difference across the two regenerators is plotted in Figure 4 for several heat input percentages. Clearly, the amplification in the second core decreases when the heat input into the core decreases and the onset temperature increases. However, in the first core, the reverse happens. In fact, the onset temperature of the first core drops significantly and by much more than the increase in the second core. Reversing the heat ratio results in reduced performance. Further study is required to find out why this occurred. The onset temperature difference and the steepness of the power against temperature curve are indicators of the performance of a thermoacoustic system. A low onset temperature means low loss and adequate acoustic matching between the various components of the system. A steep temperature curve reflects good heat transfer of the ambient and the hot heat exchangers and also indicates low acoustic dissipation [19]

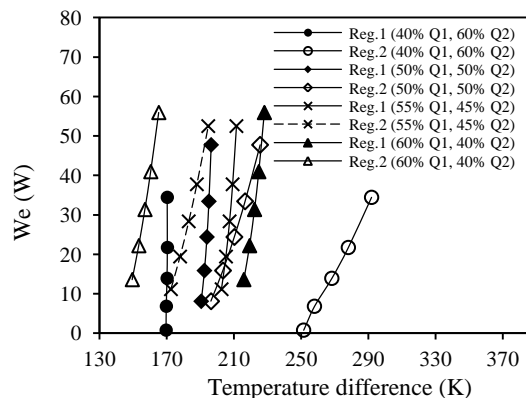


Figure 4. Electric power relation with the temperature difference across the regenerator

## Summary

In this paper, the influence of the heat input ratio into a looped-tube thermoacoustic engine was discussed. The engine converts acoustic power to electrical energy using a commercially available low-cost loudspeaker. DeltaEC is used to simulate the acoustic field within the system. DeltaEC results reflect that the electrical power output from the system equals 24.4 W from 2.5 kW heat input. An extra 7 W of electricity could be obtained by applying 60% of the heat into the first hot heat exchanger. DeltaEC models predict acoustic loop power as high as 0.1- 2.8 percent, and electric power as high as 0.4 to 3.7 from the lab data percent which indicates that the system isn't quite efficient in converting heat energy into acoustic power and the thermal dissipation is potentially an issue.

## References:

- [1] A. A. Cruz, *Global surveillance, prevention and control of chronic respiratory diseases: a comprehensive approach*: World Health Organization, 2007.
- [2] S. Backhaus and G. W. Swift, "A thermoacoustic-Stirling heat engine: Detailed study," *The Journal of the Acoustical Society of America*, vol. 107, pp. 3148-3166, 2000.

- [3] S. Backhaus and G. W. Swift, "A thermoacoustic Stirling heat engine," *Nature*, vol. 399, pp. 335-338, May 27 1999.
- [4] P. H. Riley, "The myth of the high-efficiency external-combustion Stirling engine," *Engineering*, vol. 7, pp. 789-795, 2015.
- [5] B. Chen, A. A. Yousif, P. H. Riley, and D. B. Hann, "Development and Assessment of Thermoacoustic Generators Operating by Waste Heat from Cooking Stove," *Engineering*, vol. Vol.04No.12, p. 4, 2012.
- [6] Z. Yu and A. J. Jaworski, "Demonstrator of a combustion driven thermoacoustic electricity generator for remote and rural areas of developing countries," in *19th International Congress on Sound and Vibration 2012, ICSV 2012*, Vilnius, 2012, pp. 1581-1588.
- [7] M. Petach, E. Tward, and S. Backhaus, "Design and testing of a thermal to electric power converter based on thermoacoustic technology," in *2nd International energy conversion engineering conference. The American Institute of Aeronautics and Astronautics, Providence, Rhode Island*, 2004.
- [8] S. Backhaus, E. Tward, and M. Petach, "Traveling-wave thermoacoustic electric generator," *Applied Physics Letters*, vol. 85, pp. 1085-1087, 2004.
- [9] Z. Wu, G. Yu, L. Zhang, W. Dai, and E. Luo, "Development of a 3 kW double-acting thermoacoustic Stirling electric generator," *Applied Energy*, vol. 136, pp. 866-872, 2014.
- [10] H. Kang, P. Cheng, Z. Yu, and H. Zheng, "A two-stage traveling-wave thermoacoustic electric generator with loudspeakers as alternators," *Applied Energy*, vol. 137, pp. 9-17, 2015.
- [11] T. Bi, Z. Wu, L. Zhang, G. Yu, E. Luo, and W. Dai, "Development of a 5 kW traveling-wave thermoacoustic electric generator," *Applied Energy*, vol. 185, pp. 1355-1361, 2017.
- [12] K. De Blok, P. Owczarek, and M. François, "Bi-directional turbines for converting acoustic wave power into electricity," in *Proceedings of 9th PAMIR International Conference on Fundamental and Applied MHD*, 2014.
- [13] P. H. Riley, C. Saha, and C. Johnson, "Designing a low-cost, electricity-generating cooking stove," *IEEE Technology and Society Magazine*, vol. 29, pp. 47-53, 2010.
- [14] C. R. Saha, P. H. Riley, J. Paul, Z. Yu, A. J. Jaworski, and C. M. Johnson, "Halbach array linear alternator for thermo-acoustic engine," *Sensors and Actuators, A: Physical*, vol. 178, pp. 179-187, 2012.
- [15] B. Chen, P. Riley, Y. Abakr, K. Pullen, D. Hann, and C. Johnson, "Design and development of a low-cost, electricity-generating cooking Score-Stove™," *Proceedings of the Institution of Mechanical Engineers, Part A: Journal of Power and Energy*, vol. 227, pp. 803-813, November 1, 2013 2013.
- [16] G. W. Swift and S. L. Garrett, "Thermoacoustics: A Unifying Perspective for Some Engines and Refrigerators," *The Journal of the Acoustical Society of America*, vol. 113, pp. 2379-2381, 2003.
- [17] W. C. Ward and G. W. Swift, "Design environment for low-amplitude thermoacoustic engines," *The Journal of the Acoustical Society of America*, vol. 95, pp. 3671-3672, 1994.
- [18] K. de Blok, "Novel 4-stage traveling wave thermoacoustic power generator," in *ASME 2010 3rd joint US-European fluids engineering summer meeting collocated with 8th international conference on nanochannels, microchannels, and minichannels*, 2010, pp. 73-79.
- [19] K. D. Blok, "Low operating temperature integral thermo acoustic devices for solar cooling and waste heat recovery," *The Journal of the Acoustical Society of America*, vol. 123, pp. 3541-3541, 2008.
- [20] A. M. Fusco, W. C. Ward, and G. W. Swift, "Two-sensor power measurements in lossy ducts," *The Journal of the Acoustical Society of America*, vol. 91, pp. 2229-2235, 1992.
- [21] K. de Blok, "Acoustic power measurements in thermoacoustic systems," *Aster Thermoacoustics*, 2013.

# Experimental and Numerical Study of the Thermal Performance of Water-Stainless Steel Heat Pipes Operating in Mid- Level Temperature

Silva. Débora de O.<sup>1</sup>, Riehl. Roger R.<sup>2\*</sup>

<sup>1</sup>PhD Student, Space Mechanics and Control Division - DMC

<sup>2</sup>Senior Research Engineer and Faculty, Space Mechanics and Control Division – DMC

National Institute for Space Research, São José dos Campos, 12227-010 SP Brazil,

\*E-mail: roger.riehl@inpe.br

## Abstract

Thermal performance of water-stainless steel screen mesh wick heat pipes was investigated in this study. Three screen mesh wick heat pipes were fabricated and tested all different inclinations, and their thermal conductance in different modes were compared (experimental, calculated and numerical). The different mesh numbers can bring different meanings in terms of both liquid flow resistance and capillary pumping. The aim was to analyze the thermal behavior in the permanent and transient regime for each power when operated with the power step in mid-level temperature, for use in several industrial and aerospace applications when those levels of temperature are required. The calculated thermal conductances based on the thermal resistance analysis were used to be compared with the obtained experimental thermal conductances. An adjustment factor was calculated with the objective of being used in the results of the calculated thermal conductances to bring them closer to the actual results that were obtained experimentally with the water-stainless heat pipes. The numerical approaches undertaken in analysing the transient thermal performance was used the multifluid model where two different fluid zone were created to represent vapour flow in the middle and liquid flow in the porous wick. The predicted surface temperatures with varying heat inputs (25 W - 125 W) from the numerical model and experimental tests were used for thermal conductance (numerical and experimental) were compared with calculated thermal conductance.

**Keywords:** heat pipe, experimental heat pipe, simulation, thermal performance.

## Introduction

Heat pipes are passive heat transfer devices that can successfully transfer large amounts of heat. The robust and simple tubular structure with no moving parts makes the heat pipe a perfect choice for different applications such as industrial or aerospace. The application of heat pipes have increased over the last 20 years and can be seen in many areas such as industrial and aerospace, due to their high capacity of heat transport. Heat Pipes have been successfully applied for space missions where the operational conditional are extremely severe; ground applications have found then to be very important devices to be considered for the heat dissipation issues faced by new projects [1-4]. Applications vary from satellites and spacecrafts to computer's cooling, but heat pipes have gained attention for other applications as well, especially those related to military and surveillance systems [4]. The continuous development of the heat pipe technology has given to this passive thermal control device a great interest for the new applications that were not considered before. Special attention should be given to heat pipes that operate at mid-level temperatures (up to 200° C), which have found several applications in both aerospace and industrial areas [4]. The thermal transient behaviour of the heat pipe is an important aspect in the evaluation of the heat pipe performance, particularly during the start-up period. The transient analysis would indicate whether the start-up is too fast, which could lead to evaporator section being overheated and consequently reducing the heat pipe efficiency. A number of experimental studies on the transient behaviour of heat pipes have been investigated, which further validated by numerical simulation [5]. Kempers et al. [6] realized an experimental study to determine the effect of the number of mesh layers and amount of working fluid on the heat transfer performance of water-copper heat pipes with screen mesh wicks. For the heat pipes with the smaller number of

mesh layers, the effective thermal resistance was non-linear, especially at low heat flux and the thermal resistance decreases significantly with the heat flux, and then approaches a constant value. In the nearly constant region, the thermal resistance increases with the number of mesh layers. However, a six fold increase in the number of mesh layers resulted in only a 40% increase in thermal resistance of the heat pipe [6]. Kempers et al. [7] investigated experimentally the heat transfer mechanisms in the condenser and evaporator section of a water-copper wicked heat pipe. The heat transfer was characterized by measuring the internal and wall temperature distributions under different operating conditions and as the heat transfer is dependent on the vapour pressure and heat flux, with boiling occurring even for very low heat fluxes, or superheat for operating temperatures above 50°C the onset of boiling in the evaporator could be reasonably predicted using a bubble nucleation criterion. Silva and Riehl [8] conducted an experimental investigation for copper-water heat pipes with different mesh number for heat pipes operating in different inclinations. In the series of tests, the heat input to the evaporator was increased in steps of 25 W until 125 W and presented start-ups without oscillations of temperatures, reaching the temperature of the evaporator, adiabatic and condenser near the isothermal condition. Therefore, the heat pipes confirmed good performances when analysed by their thermal conductances [9] and compared with experimental results between copper and stainless steel heat pipes. In this paper, heat pipes were designed and manufactured with the objective of investigating the potential application of heat pipes operating at mid-level temperature. The thermal conductance obtained from the experimental tests were used to correlate the thermal conductances obtained analytically, with results showing high accuracy based on the adjustment factor applied. A numerical model was made for analyzing the transient thermal performance of heat pipes with screen mesh wick and the results validated with the experimental results.

### Experimental Investigation

In order to investigate the potential application of heat pipes for industrial use, were designed and manufactured three heat pipes for experimental tests shown in Figure 1. The heat pipes are stainless steel 316-L by its wide acceptance and application in industry and the compatibility with water. The geometrical properties of the heat pipe used in this experimental work is shown in Table 1. The heat was applied to the evaporator by a controlled electric heater, being used the testing power step, the heat source was applied to each heat pipe to observe, at first, the start-up effect. Once the temperatures for the start-up power have reached stability, power was changed according to the testing profile, following the sequence to temperature stabilization.



Figure 1 - Heat Pipes Experimental Bench.

The experimental test rig comprises a test bench, a DC power controller (Agilent N5749A), and a National Instrument SCXI data acquisition system controlled by LabVIEW. Six Omega T-type thermocouples with accuracy of  $\pm 0.3^{\circ}\text{C}$  were used to measure the wall temperatures of each heat pipe in two locations of the evaporation, adiabatic and condenser sections. Another thermocouple was used for measuring the ambient temperature. All tests were performed under controlled room conditions, with the temperature set at  $22^{\circ}\text{C} \pm 2^{\circ}\text{C}$ . The condenser was open to the ambient air, exchanging heat by natural convection. Therefore, oscillations on the ambient temperature were expected due to the air conditioning on/off operation.

Table 1. Characteristics of heat pipes - HP1, HP2 and HP3.

Geometric Characteristics of the Experimental HP			
	HP 1	HP 2	HP 3
Evaporador/Adiabatic/Condenser/Total length (m)	0.25 / 0.9 / 0.35 / 1.5		
Working Fluid	Water		
Tube material	316L - SS		
Outside diameter (m)	0.01905		
Inside diameter (m)	0.0135		
Screen wick material	316L - SS		
Screen mesh number	100	200	400
N° of layers of wick	3		
Wick Porosity %	0.68	0.64	0.61
Wick Permeability (m <sup>2</sup> )	2.39x10 <sup>-10</sup>	5.16x10 <sup>-11</sup>	1.10x10 <sup>-11</sup>
Mean pore radius (m)	1.1827x10 <sup>-4</sup>	6.35x10 <sup>-5</sup>	3.18x10 <sup>-5</sup>
Operating temperature range (° C)	22 - 160		
Operating Power (W)	25 - 125		

The heat source was a silicone flexible electric heater, being insulated by rock wool with the thermal conductivity of 0.04 W/m\*K, which was wrapped around the adiabatic section to reduce the heat loss to the surroundings. Prior to charging the heat pipes, they were properly cleaned and evacuated at a vacuum level of 10<sup>-5</sup> mbar. Charging was only performed once the heat pipe was able to sustain such a vacuum level for at least 12 h. At this point in the test procedure, it was made a pressurized verification test to determine if the fittings, enclosures, and/ or seams of the heat pipe cases were appropriately sealed. This was best done by pressurizing the case using conventional leak testing equipment to check the case for leaks.

The laboratory tests were conducted with the following procedures:

- The heat was applied to the evaporator by a controlled electric heater, being used the power of 25W, 50W, 75W, 100W and 125W per heat pipe;
- Heat was applied to each heat pipe to observe, at first, the start-up effect. Once the temperatures for the start-up power have reached stability (presenting variation of ±1°C during the last 20 minutes), the power was changed according to the testing profile, following the sequence to temperature stabilization. Once all power levels were tested, the power was switched off and waited for temperature equalization with ambient.

### Thermal resistance analysis

The overall thermal resistance is comprised of nine different resistances arranged in series-parallel combination as shown by Fig. 2 [10,11]. In this model, the overall resistance of the cylindrical heat pipe is given by

$$R_T = R_{pe} + R_{we} + R_v + R_{pc} + R_{wc} \quad (1)$$

The thermal resistance due to the pipe wall in the evaporator ( $R_{pe}$ ), liquid-wick at evaporator ( $R_{we}$ ), liquid-wick at condenser ( $R_{wc}$ ) and pipe wall in the condenser ( $R_{pc}$ ) are

$$R_{pe} = \frac{\ln(d_o|d_i)}{2\pi L_e K_p}, R_{we} = \frac{\ln(d_i|d_v)}{2\pi L_e K_{eff}}, R_{wc} = \frac{\ln(d_i|d_v)}{2\pi L_c K_{eff}}, R_{pc} = \frac{\ln(d_o|d_i)}{2\pi L_c K_p} \quad (2)$$

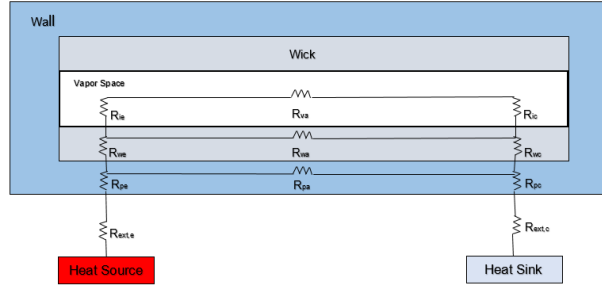


Figure 2. Overall thermal resistance of a heat pipe.

Where, the effective thermal conductivity of the wick structure is [10]

$$K_{eff} = \frac{k_l[(k_l+k_w)-(1-\epsilon)(k_l-k_w)]}{(k_l+k_w)(1-\epsilon)(k_l-k_w)} \quad (3)$$

The thermal resistance of the vapour flow,  $R_v$  is determined by [10]

$$R_v = \frac{\pi r_0^2 T_v F_v [(1/6)L_e + L_a + (1/6)L_e]}{\rho_v h_{f,g}} \quad (4)$$

Where  $F_v$  is the vapour frictional coefficient. Considering some simplifications, Chi [10] developed a simplified analytical equation to predict the approximate overall thermal resistance for a cylindrical heat pipe as follows

$$R_T = R_{pe} + R_{we} + R_v + R_{pc} + R_{wc} \quad (5)$$

Summing all individual resistances (Eq. 5) and the comparative magnitudes of the resistance of the axial resistance of the pipe wall and liquid-wick combinations may be treated as open circuits and neglected. The theoretical thermal conductance of the heat pipe is then estimated as

$$G = \frac{1}{R_T} \quad (6)$$

The experimental results may raise possible variations, which came from heat pipe manufacturing standpoint and it affects heat pipe operation. Considering that the heat pipes were manually manufactured, an adjustment factor was taken into consideration for the thermal conductance results in such a way that it could result in a more accurate analysis in a way to put into consideration these possible variations. The adjustment factor is defined as follows

$$Factor = \frac{G_E}{G_{global}} \quad (7)$$

$$G_{global} = \alpha \frac{Q}{T_e - T_a} \quad (8)$$

where  $0.8 \leq \alpha \leq 3.0$ . The calculated thermal conductance used in this study for each power applied to the heat pipe can be defined as

$$G_C = \frac{1}{R_T} * Factor \quad (9)$$

With the consideration of the thermal conductance, it was expected that the calculated thermal conductance (theoretical with adjustment factor) presented the same trends of the ones obtained experimentally. The calculated thermal conductances, by the analysis of thermal resistances, do not consider important characteristics of an experiment, such as mounting characteristics for each heat pipe, volume of fluid inserted in each heat pipe, differences in the mesh of the porous structure after

inserted into each heat pipe, or even in the folding of the mesh for closing each heat pipe and etc. Therefore, adjustment factors for the thermal conductance calculated were considered for a better comparison with the results of the calculated and experimental thermal conductances.

### Numerical Model

The working fluid is assumed to be liquid phase in the wick region (liquid zone) and vapour phase in the vapour region. When the evaporator is heated, the working fluid in the wick region is vaporized to the vapour space and the vapour flows to the condenser section. In the condenser section, after the vapour releases its latent heat to the environment through the outer surface of the condenser, it returns to the wick region as saturated liquid. For the mathematical formulation of this numerical unsteady simulation work, the following assumptions were made:

- Vapour and liquid flow are unsteady, 2-D, laminar and incompressible;
- Viscous dissipation and gravity effects are negligible;
- Heat generation or dissipation due to the phase change process in the heat pipe is ignored;
- The physical properties are constant;

With the above assumptions, the resulted governing equations in cartesian coordinates are as follows:

#### Vapour Flow Region

Continuity:

$$\frac{\partial u_v}{\partial x} + \frac{\partial v_v}{\partial y} = 0 \quad (10)$$

Momentum in the x-direction:

$$\rho_v \left( \frac{\partial u_v}{\partial t} + u_v \frac{\partial u_v}{\partial x} + v_v \frac{\partial v_v}{\partial y} \right) = \mu_v \left( \frac{\partial^2 u_v}{\partial x^2} + \frac{\partial^2 u_v}{\partial y^2} \right) - \frac{\partial P}{\partial x} \quad (11)$$

Momentum in y-direction:

$$\rho_v \left( \frac{\partial v_v}{\partial t} + u_v \frac{\partial v_v}{\partial x} + v_v \frac{\partial v_v}{\partial y} \right) = \mu_v \left( \frac{\partial^2 v_v}{\partial x^2} + \frac{\partial^2 v_v}{\partial y^2} \right) - \frac{\partial P}{\partial y} \quad (12)$$

Energy:

$$\rho_v C_{p,v} \left( \frac{\partial T_v}{\partial t} + u_v \frac{\partial T_v}{\partial x} + v_v \frac{\partial T_v}{\partial y} \right) = k_v \left( \frac{\partial^2 T_v}{\partial x^2} + \frac{\partial^2 T_v}{\partial y^2} \right) + \dot{q} \quad (13)$$

#### Liquid Flow Region

$$\frac{\partial u_l}{\partial x} + \frac{\partial v_l}{\partial y} = 0 \quad (14)$$

The Darcy's Law is employed in the momentum equation for the porous liquid-wick region. The resulted unsteady momentum equation are:

Momentum in the x-direction:

$$\rho_l \left( \frac{\partial u_l}{\partial t} + u_l \frac{\partial u_l}{\partial x} + v_l \frac{\partial u_l}{\partial y} \right) = \mu_l \left( \frac{\partial^2 u_l}{\partial x^2} + \frac{\partial^2 u_l}{\partial y^2} \right) - \frac{\partial P}{\partial x} - \frac{\mu_l u_l \epsilon}{K} \quad (15)$$

Momentum in y-direction:

$$\rho_l \left( \frac{\partial v_l}{\partial t} + u_l \frac{\partial v_l}{\partial x} + v_l \frac{\partial v_l}{\partial y} \right) = \mu_l \left( \frac{\partial^2 v_l}{\partial x^2} + \frac{\partial^2 v_l}{\partial y^2} \right) - \frac{\partial P}{\partial y} - \frac{\mu_l v_l \epsilon}{K} \quad (16)$$

Energy:

$$\rho_l C_{p,l} \left( \frac{\partial T_l}{\partial t} + u_l \frac{\partial T_l}{\partial x} + v_l \frac{\partial T_l}{\partial y} \right) = k_{eff} \left( \frac{\partial^2 T_l}{\partial x^2} + \frac{\partial^2 T_l}{\partial y^2} \right) + \dot{q} \quad (17)$$

#### Boundary Conditions

The imposed boundary conditions are illustrated in Figure 3. The heat transfer coefficient,  $h$  can be determined using the Churchill and Chu correlation for the Nusselt number given below.

$$\overline{Nu}_d = \left\{ 0.60 + \frac{0.387 Ra_d^{1/6}}{[1 + (0.559/Pr)^{9/16}]^{8/27}} \right\}^2 \quad (18)$$

where  $Pr$  is the Prandtl number and  $Ra_d$  is the Rayleigh number.

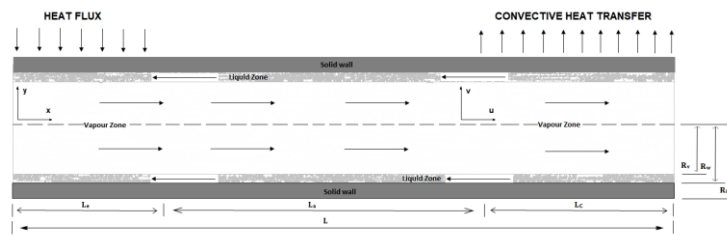


Figure 3 - Boundary conditions of heat pipe.

The detailed boundary conditions for evaporator, adiabatic and condenser region at the various radius and also at the ends of the heat pipe are given in Table 2 below.

Table 2 – Boundary Conditions

N <sup>o</sup>	Locations	Evaporator	Adiabatic	Condenser
1	Both ends of HP ( $x = 0, L$ )	$u = v = 0$ $\dot{m}_v = \frac{\dot{Q}}{h_{f,g}}$		$u = v = 0$
2	Centreline of HP ( $y = 0$ )	$v_v = 0, \frac{\partial v_v}{\partial y} = 0, \frac{\partial T_v}{\partial y} = 0$		
3	Liquid-vapour interface ( $y = R_v$ )	$\rho_v v_v = \rho_l v_l$		
4	Wick-wall interface ( $y = R_w$ )	$k_p \frac{\partial T_p}{\partial y} = k_{eff} \frac{\partial T_l}{\partial y}$ , $u_l = v_l = 0, \rho_v v_v = \rho_l v_l = 0$		
5	Outer pipe wall ( $y = R_o$ )	$\dot{q} = k_p \frac{\partial T_p}{\partial y}$	$\frac{\partial T_p}{\partial y} = 0, \frac{\partial T_p}{\partial x} = 0$	$\frac{\partial T_p}{\partial y} = h(T_p - T_\infty)$

#### Method of Solution

The governing equations are discretized using a finite volume approach and equations were solved using SIMPLE algorithm. The unsteady state incompressible flow has been solved in both vapour and liquid region, using ANSYS Fluent software. The physical domain of problem was separated into 2 regions as follows.

1. vapour region;
2. liquid region and pipe wall

The numerical analysis was performed in both separated regions. The solution procedure is as follows.

1. Continuity and momentum equation are solved in vapour region with mentioned boundary conditions to find the pressure distribution;
2. Clausius-Clapeyron equation has been used to find temperature boundary condition at the liquid-vapour interface;
3. All of the equations have been solved in vapour region;
4. The mentioned equations with related boundary condition have been solved in liquid region and pipe wall simultaneously;

#### Discussion and Results

The temperature profiles to evaluate their thermal performance for wall power levels are shown by Figure 4a. Typically, the temperature of the outer wall of heat pipe's adiabatic section is selected as the parameter to study the response time since it shows the status of the heat pipe. First, to verify the operation functionality of the heat pipes the power step test was realized. This test was carried out with the heat pipes to evaluate the temperatures reached at each power applied at the moment of the start-up and of temperature stabilization, to obtain an initial analysis regarding their heat pipe transport capacity, and the behaviour of the evaporator in the change of each power. As the heat flux increases in the evaporator wall and the liquid (porous structure) that is in contact with the evaporator wall can progressively overheat and form bubbles at the nucleation sites. These bubbles can carry energy to the surface by latent heat of vaporization. With increasing heat flux, a critical value can be reached and dry-out of the porous structure that will potentially interrupt the operation of heat pipes.

For a better analysis of the heat transfer capacity of the heat pipes, the temperature difference between the evaporator and the condenser for each applied power was calculated (Figure 4b). A small



temperature difference between the evaporator and the condenser ensures proper operation and steady heat transfer by the heat pipes.

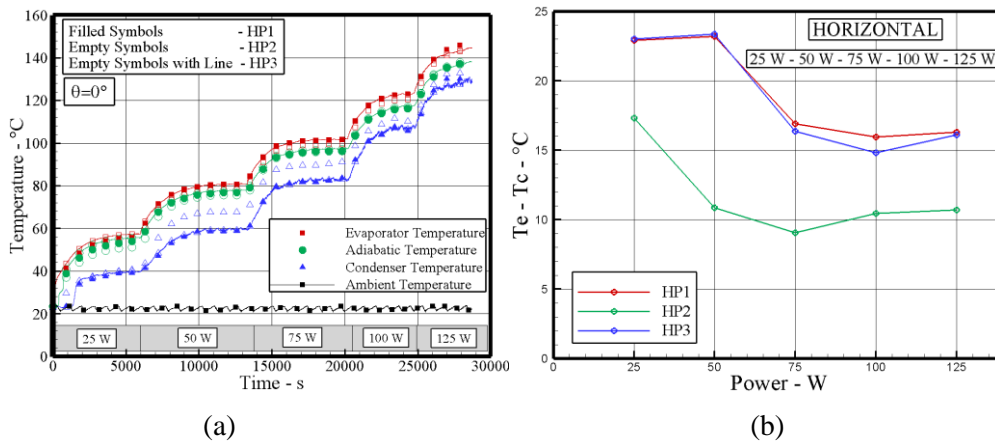


Figure 4 – (a) Temperature profiles of HP1, HP2 and HP3 and (b) Temperature difference of heat pipes at different power.

The largest temperature difference between the evaporator and the condenser of approximately 23.35 °C was presented for HP3 at 50 W and the lowest temperature difference was 6.75°C for the HP2 operating at 100W of applied power.

For the improved analysis, the experimental thermal conductance of the heat pipe was calculated and compared with the calculated thermal conductance (Eq. 12), which considers an adjustment given by the variable factor that involves uncontrolled variables that are innerherent to the manufacturing processes of the heat pipes and thermal conductance numerical. The calculated thermal conductance was introduced in the thermal resistance analysis (Eq. 6) along with the adjustment factor (Eq. 7) for each applied power, and the results of this comparison are presented by Figure 5.

The results show a good correlation between the experimental, calculated and numerical results. The proposed calculated thermal conductance and thermal conductance numerical, correctly predicted the increase in thermal conductance with the increase in the heat input and the same has been validated experimentally.

The highest experimental thermal conductance was obtained by HP2 of 12 W/°C and numerical thermal conductance the 12.7 W/°C. The heat pipe HP2 showed better thermal performance due to smaller pore size, lower porosity and permeability and higher capillary pressure. The theoretical thermal conductance presented results of approximately 9.6 W/°C for the HP1, 15.5 W/°C for the HP2 and 23 W/°C for the HP3.

## Conclusions

The development of the heat pipe technology for industrial applications presents to be very important to improve the heat recovery systems performance, since they can greatly contribute to increase heat exchangers performances without great increase on their final costs. The continuous development of this technology for industrial purposes is highly desirable in order to give more degrees of freedom to thermal engineers to face the increase of heat dissipation and new challenges on thermal management issues.

For better thermal performance and conditions evaluation: the thermal profiles before and after the start-up, transient behavior during the changes on applying power, thermal behavior under steady state conditions were analyzed. The following conclusions were drawn from this study.

- The heat pipes presented stable behavior, for both transient and steady state conditions, when operated using the power levels of 25-125W. During the experimental tests, heat pipes did not present dry-out tendencies or superheat in the evaporator.
- The main objective of this study is a development of a numerical model that allows to perform simulation of the evaporation and condensation phenomena in heat pipes. The numerical model results of this paper show that FLUENT with the VOF method can successfully model the complex phenomena inside the heat pipe.

- The numerical thermal conductance has been verified with experimental thermal results and has shown good agreement.

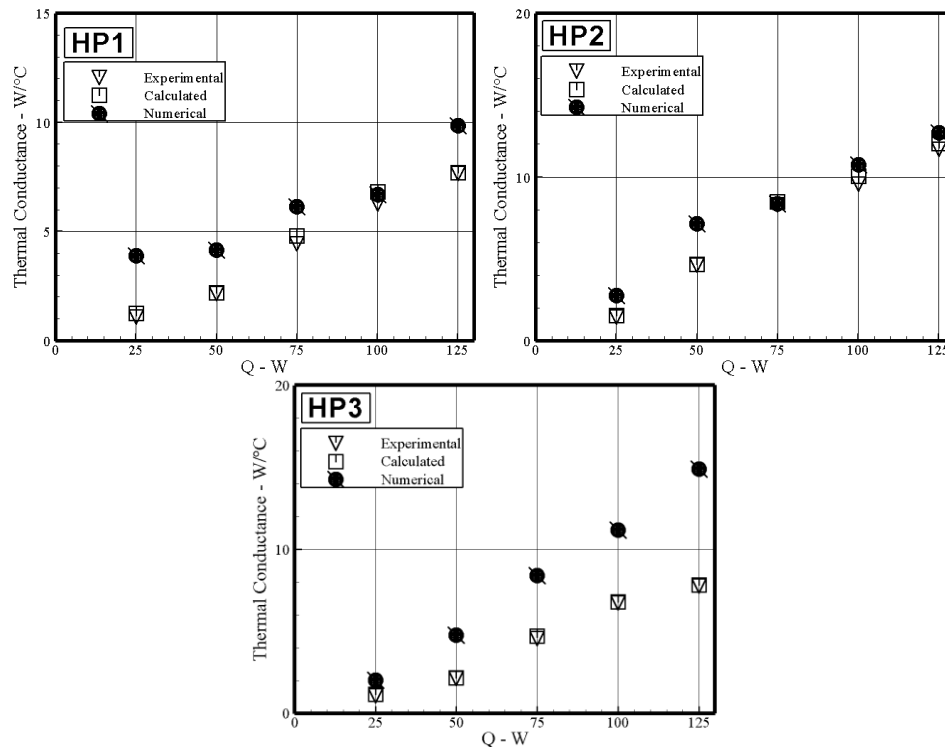


Figure 5 – Thermal conductance comparison between experimental, calculated and numerical for different heat inputs.

### References:

- [1] Riehl, R. R., Cachute, L., Thermal Control of Surveillance Systems Using Pulsating Heat Pipe and Heat Pipes, *Proceedings of the AIAA Propulsion and Energy Forum and Exposition 2013 - 11th Annual International Energy Conversion Engineering Conference (IECEC)*, July 15-17, San Jose, CA, 2013.
- [2] Riehl, R. R., Passive thermal management of surveillance systems using pulsating heat pipes. In: *9th Minsk International Seminar-Heat Pipes, Heat Pumps, Refrigerators, Power Sources*, 2015.
- [3] Riehl, R. R. Utilization of passive thermal control technologies in cooling electronics: A brief review. *Heat Pipe Science and Technology: An International Journal*, Begell House Inc., v. 7, n. 3-4, pp. 161–183, 2016.
- [4] Silva, D. de O., and Riehl R. R. Development of Heat Pipes Operating at Mid-Level Temperature Range Applied for Industry, Defense and Aerospace, *Proceedings of the AIAA Propulsion and Energy Forum 2014 - 12th International Energy Conversion Engineering Conference (IECEC)*, July 28-30, Cleveland, OH, 2014.
- [5] J. M. Tournier, M. El-Genk, A transient analysis of water heat pipe, in: ASME Winter Conf., 28 Nov 1993, ASME, New Orleans, L.A, USA, 1993.
- [6] Kempers, R., Ewing, D., and Ching, C. Y., Effect of number of mesh layers and fluid loading on the performance of screen mesh wicked heat pipes. *Applied Thermal Engineering*, 26(5), pp. 589-595, 2006.
- [7] Kempers, R., Robinson, A. J., Ewing, D., and Ching, C. Y., Characterization of evaporator and condenser thermal resistances of a screen mesh wicked heat pipe. *International Journal of Heat and Mass Transfer*, 51(25), pp. 6039-6046, 2008.
- [8] Silva, D. de O., Marcelino, E. W. and Riehl R. R. Thermal Performance Comparison Between Water-Copper and Water-Stainless Steel Heat Pipes. *13th International Energy Conversion Engineering Conference*, August 9-12, New York, USA, 2015.
- [9] Silva, D. de O., Marcelino, E. W. and Riehl R. R., Experimental investigation of copper water heat pipes operation at mid-level temperature range for aerospace and industrial applications, *13th International Energy Conversion Engineering Conference*, August 9-12, New York, 2015.
- [10] Chi, S.W., *Heat Pipe Theory and Practice*, Washington: Hemisphere Publishing Corporation, 1976.
- [11] Reay, D. A., Kew, P. A., *Heat Pipes-theory, design and applications*, 5a Ed., Oxford, UK: Elsevier's Science & Technology, 2006.

# CO selective methanation for PEMFC applications

P. Garbis, C. Kern and A. Jess

Chair of Chemical Engineering, University of Bayreuth, Universitätsstraße 40, 95440 Bayreuth  
Center of Energy Technology (ZET), Universitätsstraße 30, 95447 Bayreuth

panagiota.garbis@uni-bayreuth.de

## Abstract

The world's shift to alternative forms of energy production leads to the housing constructions which are independent from electricity prices and reduce CO<sub>2</sub> emission. In the recent years, the interest in the development of proton exchange membrane fuel cells (PEMFC) in stationary application is increased. PEMFCs could supply households with electrical power using natural gas or, as a perspective, biogas. As is well known, the compound CO is undesirable in the PEMFC operating gas, as CO degrades the PEMFC by poisoning the hydrogen oxidation reaction catalyst [1–3]. One of options to reduce the CO content to a value lower than 10 ppm is the selective methanation of CO [3–5]. For this purpose, supported noble metal catalysts were prepared by impregnation of  $\gamma$ -Al<sub>2</sub>O<sub>3</sub> spheres and screened for the selective CO methanation. A manufactured Ru/Al<sub>2</sub>O<sub>3</sub> catalyst was selected for further investigation. In this paper, the CO methanation with and without the presence of water is examined and a kinetic approach based on a Langmuir-Hinshelwood expression is suggested. Furthermore, the influence of CO<sub>2</sub> in the feed gas is presented.

**Keywords:** CO methanation, ruthenium, Fuel Cell, carbon monoxide, kinetic model

## Introduction

PEMFCs have potential for generating electrical power in household use (see Fig. 1) by utilizing the hydrogen-containing gas produced from natural gas or, as a perspective, from biogas via steam reforming. Since the hydrogen production is always accompanied with such a by-product as carbon monoxide, which represents a strong poison for PEMFC, its content in the operating gas has to be reduced below the threshold values as to prevent the fuel cell catalyst degradation.

CO methanation can be considered an attractive technique to reduce the carbon monoxide content to guarantee the long life of PEMFCs. Conventionally, in the course of carbon monoxide methanation of a reformat gas, three main reactions can take place. viz.: CO methanation itself (Eq. (1)), CO<sub>2</sub> methanation (Eq. (2)) and the Reverse-Water-Gas-Shift (RWGS) reaction (Eq. (3)) where CO is produced again.



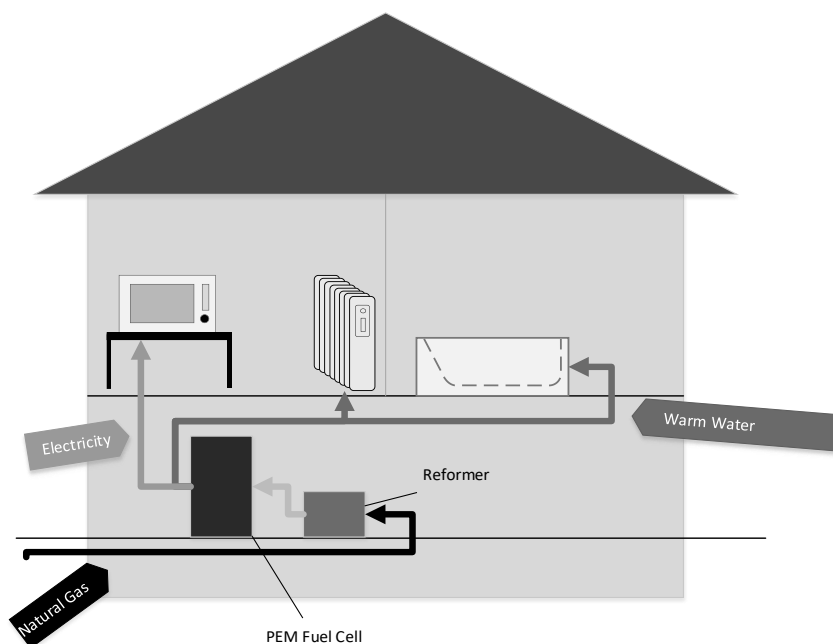


**Figure 1:** The idea of combined heat and power supply of households with natural gas.

For these purposes, different catalysts have been prepared to select the most appropriate one. The suitable catalyst should promote the CO methanation and at the same time suppress both the CO<sub>2</sub> methanation and the RWGS reaction. In the course of catalyst screening, a ruthenium based catalyst has indicated the highest activity and selectivity. A kinetic model for this catalyst including an inhibiting impact of water and carbon dioxide has been developed according to the Langmuir-Hinshelwood approach.

## Discussion and Results

### Experimental set-up and procedure

The experimental set-up (Fig. 2) consists of a fixed-bed reactor thermostated by an oil heating system. Two thermocouples in a guide tube are positioned in the catalyst bed to monitor the reaction temperature. The gas composition leaving the reactor is analysed with a gas analyser (X-STREAM Enhanced Process Gas Analyzer, Emerson) (CO, CO<sub>2</sub>, H<sub>2</sub> and CH<sub>4</sub>) and Gas Chromatography (long-chain hydrocarbons).

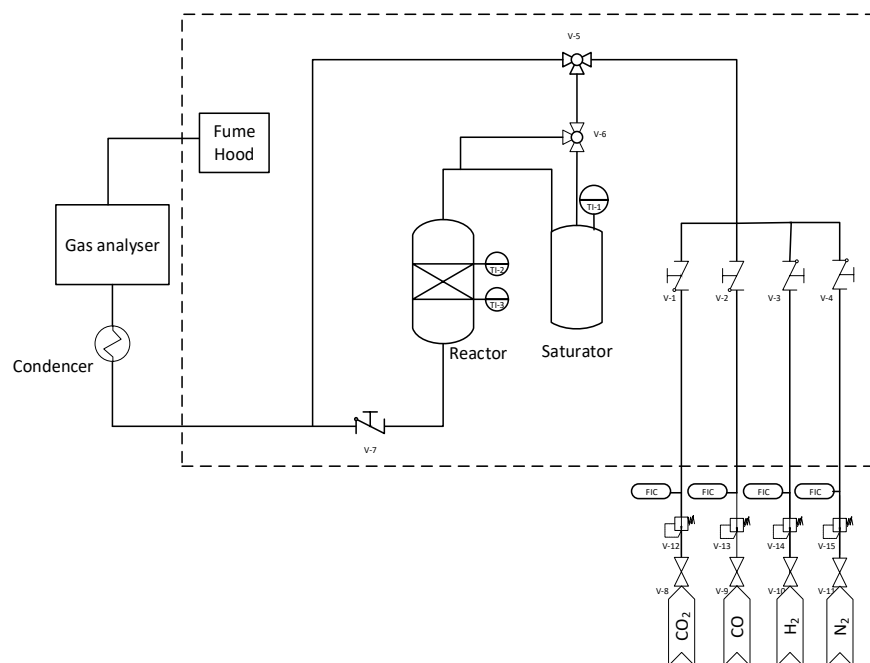


**Figure 2:** Experimental set-up.

The kinetics of CO methanation as well as the influence of H<sub>2</sub>O on the reaction system is obtained for a Ru/Al<sub>2</sub>O<sub>3</sub> catalyst. The reactor is charged with 2 g of catalyst particles diluted with 4 g of quartz sand, to keep the temperature of the catalyst bed stable. The reaction orders are defined in a temperature range from 160 to 185 °C by variation of the concentration of only one reactant (CO, H<sub>2</sub> or H<sub>2</sub>O). N<sub>2</sub> is used in order to maintain the volumetric flow rate constant in each measurement. The volume flows are given at standard temperature and pressure conditions (STP) (T = 0°C, p = 1 bar).

### Preparation and catalyst screening

Catalysts are prepared by wet impregnation of 2.5 mm Al<sub>2</sub>O<sub>3</sub> spheres with rutheniumnitrosylnitrate Ru(NO)(NO<sub>3</sub>)<sub>3</sub>, cobalt (II) nitrate hexahydrate and manganese (II) nitrate. A commercial catalyst (2 wt% Ru supported on Al<sub>2</sub>O<sub>3</sub>) is also tested. After reduction by 10 vol% H<sub>2</sub> in N<sub>2</sub> at 350 °C, the catalysts are utilized in the methanation of CO. The catalyst loaded with 2 wt% Ru is further impregnated with NH<sub>4</sub>Cl to improve selectivity of the CO methanation [2, 6].

Five catalysts are screened in order to find a suitable one for the selective CO methanation. Fig. 3 and Fig.4 show the conversion of CO and CO<sub>2</sub> over the examined catalysts. It is important to note that at temperatures over 230 °C, the RWGS reaction takes place producing CO which accounts for the negative CO conversion.

In comparison with the other catalysts, the Ru based catalysts indicate higher activity and selectivity. Although the catalyst loaded with 2 wt% Ru and 1.3 wt% Cl shows the highest selectivity, the catalyst is unsuitable for further applications. Since chloride is discharged from the catalyst bed during the run. Not only does not it guarantee the selectivity of the reaction, but could also affect the PEMFC. Therefore, the catalyst with 2 wt% Ru/Al<sub>2</sub>O<sub>3</sub> is more preferable for further investigations.

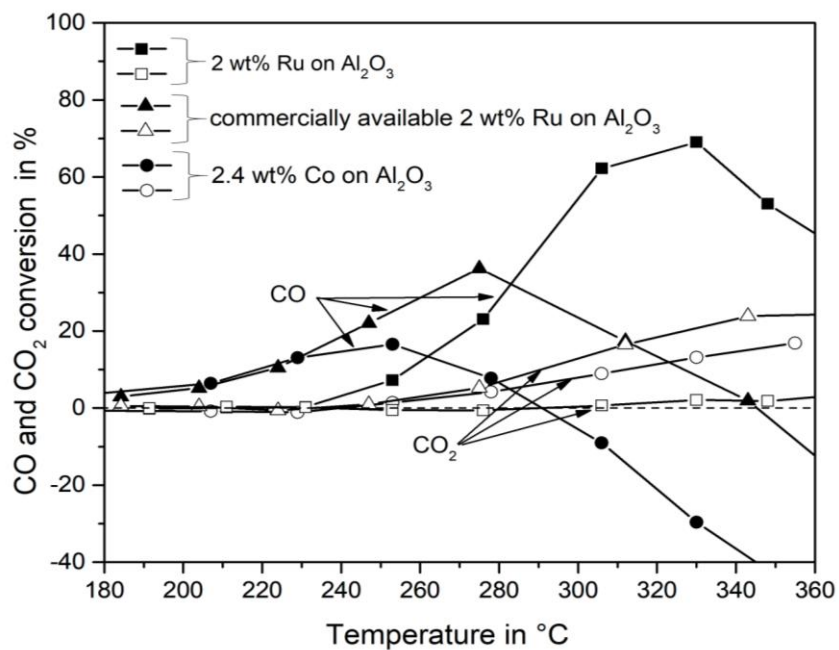


**Figure 3:** CO and CO<sub>2</sub> conversion as a function of reaction temperature;  $m_{\text{cat}} = 0.6 \text{ g}$ ;  $\dot{V}_{STP} = 68 \text{ l h}^{-1}$  (1 vol% CO, 14 vol% CO<sub>2</sub>, 30 vol% H<sub>2</sub>, 55 vol% N<sub>2</sub>).

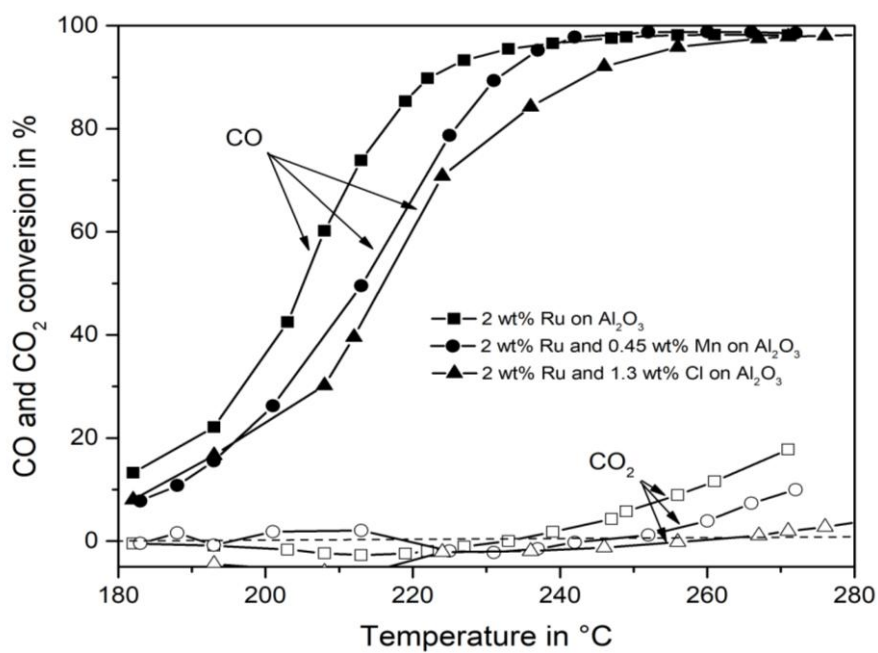


**Figure 4:** CO and CO<sub>2</sub> conversion as a function of reaction temperature;  $m_{\text{cat}} = 1.3 \text{ g}$ ;  $\dot{V}_{STP} = 10 \text{ l h}^{-1}$ , (1 vol% CO, 10 vol% CO<sub>2</sub>, 89 vol% H<sub>2</sub>).

## Kinetic of CO methanation

The reformat gas, which is the feed for the PEMFC, consist in particular of CO, H<sub>2</sub>, H<sub>2</sub>O and CO<sub>2</sub>. For this reason, it is important to evaluate the impact of each component on CO methanation.

A kinetic approach based on a Langmuir-Hinshelwood approach (Eq. (4)) is suggested as

$$r_{CO} = -k(T) \frac{C_{CO}C_{H_2}}{(1 + K_1C_{CO} + K_2C_{H_2O})^2}, \quad (4)$$

follows:

where C<sub>i</sub> (i = CO, H<sub>2</sub>, H<sub>2</sub>O) is the gas concentration, K<sub>1</sub> and K<sub>2</sub> are the adsorption equilibrium constants for CO and H<sub>2</sub>O, respectively and k(T) is the reaction rate constant according to the Arrhenius law (Eq. 5) :

$$k(T) = k_0 e^{\frac{-E_A}{RT}}, \quad (5)$$

here k<sub>0</sub> is the pre-exponential factor, E<sub>A</sub> is the activation energy and R is the universal gas constant.

The reaction rate dependence on the CO concentration is shown in Fig. 5. As is seen, the CO and H<sub>2</sub>O components demonstrate an inhibiting influence on the reaction rate. The defined parameters of the kinetic model are shown in Table 1.

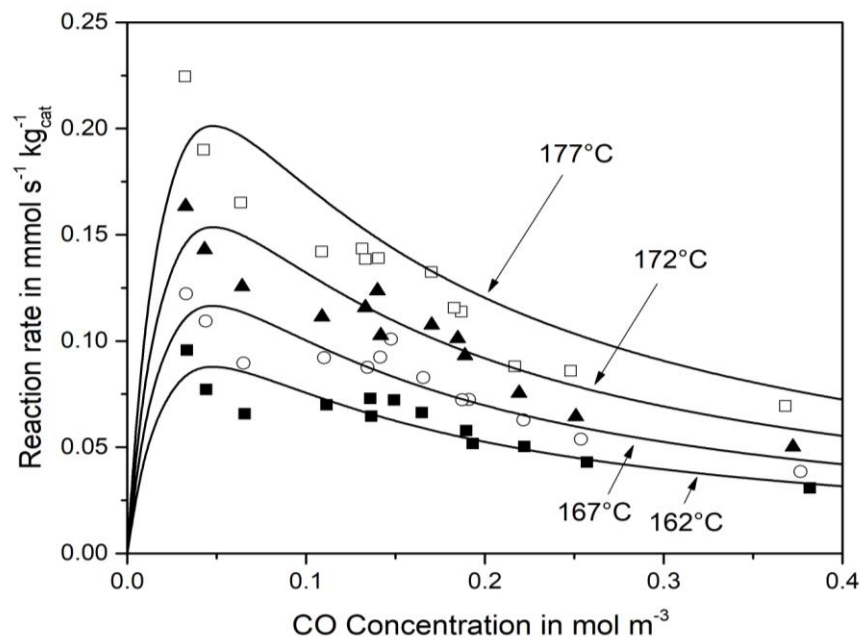


**Figure 5:** Reaction rate determined experimentally compared with calculated from Eq.(4) in the range from 162°C to 177°C. 0.4 - 1.4 vol% CO, 55 vol% H<sub>2</sub>, Rest N<sub>2</sub>, m<sub>cat</sub> = 2g;  $\dot{V}_{STP}$  = 15 l h<sup>-1</sup>.

**Table 1:** Parameters of the kinetic model

Parameter	
pre-exponential factor, $k_0$	$3.61 \cdot 10^7 \text{ m}^6 \text{ s}^{-1} \text{ kg}^{-1} \text{ mol}^{-1}$
Activation energy, $E_A$	$90.000 \text{ J mol}^{-1}$
adsorption equilibrium constant for CO, $K_1$	$23 \text{ m}^3 \text{ mol}^{-1}$
adsorption equilibrium constant for $\text{H}_2\text{O}$ , $K_2$	$0.3 \text{ m}^3 \text{ mol}^{-1}$

Through integration of Eq. 4, the CO conversion was calculated and compared to the experimental data (Fig. 6). As is seen, the kinetic model of the CO methanation very well corresponds to the experimental data.

Since  $\text{CO}_2$  has to be a content of the feed gas, the influence of  $\text{CO}_2$  in the CO methanation was examined. It turned out that  $\text{CO}_2$  had a small inhibiting effect on the CO conversion (Fig. 7) which could be neglected. Furthermore, no  $\text{CO}_2$  conversion was noticed for temperatures lower than  $220 \text{ }^\circ\text{C}$ .

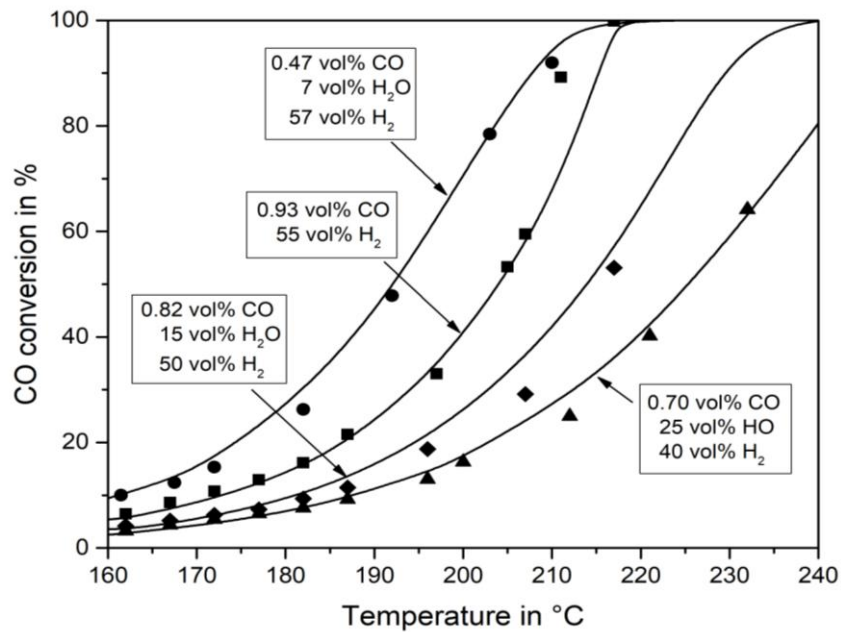


**Figure 6:** Comparison of experimental with modelled CO conversion for different inlet gas compositions in the feed gas.  $m_{\text{cat}} = 2\text{g}$ ;  $\dot{V}_{STP} = 17 \text{ l h}^{-1}$ .



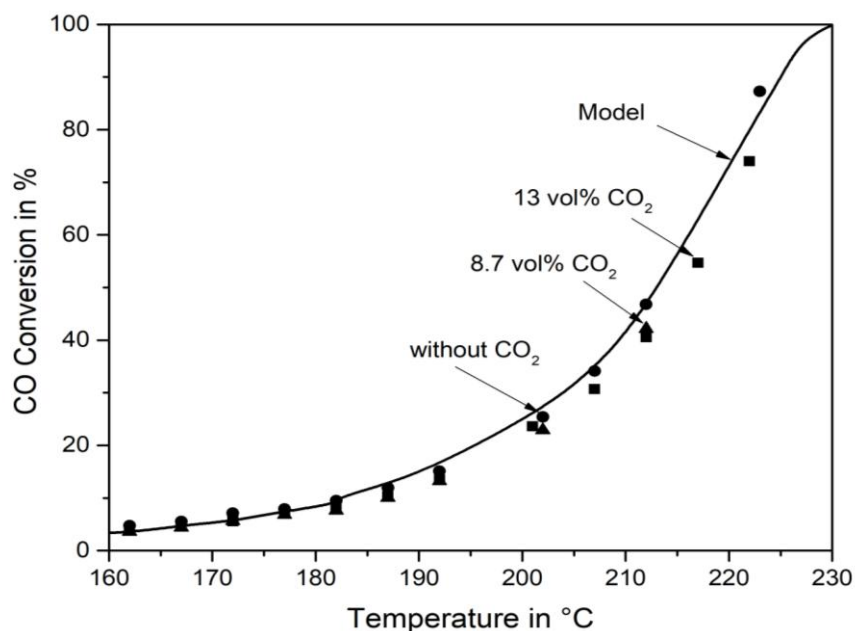


**Figure 7:** Impact of CO<sub>2</sub> on CO conversion. 1.15 vol% CO, 55 vol% H<sub>2</sub>, rest balanced with N<sub>2</sub>;  $m_{\text{cat}} = 2\text{g}$ ;  $\dot{V}_{STP} = 15\text{ l h}^{-1}$ .

The next aim is the expansion of the kinetic model in order to describe the selective CO methanation. For this purpose, further experiments have to take place by a varying of the CO<sub>2</sub> concentrations.

### Conclusions

After catalyst screening, the synthesized catalyst loaded with 2 wt% Ru on Al<sub>2</sub>O<sub>3</sub> represented the highest activity and selectivity for the selective CO methanation. A kinetic model, based on a Langmuir-Hinshelwood approach, was suggested for the CO methanation taking into consideration H<sub>2</sub>O in the feed gas. The influence of CO<sub>2</sub> in the CO methanation was investigated. CO<sub>2</sub> has an almost negligible inhibiting effect on the methanation of CO. Our first results are promising for the further efforts in developing a catalyst and model for the selective CO methanation.

### Acknowledgements

This work has been funded by the Bavarian State Ministry of Education, Science and the Arts within the framework “TechnologieAllianzOberfranken (TAO)”. The authors gratefully acknowledge this support.

### References

- [1] Baschuk, J. J. and Li, X., Carbon monoxide poisoning of proton exchange membrane fuel cells, *Int. J. Energy Res.*, 2001, [DOI:10.1002/er.713](https://doi.org/10.1002/er.713).
- [2] Djinovi, P., Galletti, C., Specchia, S., and Specchia, V., CO Methanation Over Ru, *Top Catal*, 2011, [DOI:10.1007/s11244-011-9724-8](https://doi.org/10.1007/s11244-011-9724-8).

- [3] Djinović, P., Galletti, C., Specchia, S., and Specchia, V., Ru-based catalysts for CO selective methanation reaction in H<sub>2</sub>-rich gases, *Catalysis Today*, 2011, [DOI:10.1016/j.cattod.2010.11.007](https://doi.org/10.1016/j.cattod.2010.11.007).
- [4] Eckle, S., Denkwitz, Y., and Behm, R. J., Activity, selectivity, and adsorbed reaction intermediates/reaction side products in the selective methanation of CO in reformat gases on supported Ru catalysts, *Journal of Catalysis*, 2010, [DOI:10.1016/j.jcat.2009.10.025](https://doi.org/10.1016/j.jcat.2009.10.025).
- [5] Jiménez, V., Sánchez, P., Panagiotopoulou, P., Valverde, J. L., and Romero, A., Methanation of CO, CO<sub>2</sub> and selective methanation of CO, in mixtures of CO and CO<sub>2</sub>, over ruthenium carbon nanofibers catalysts, *Applied Catalysis A: General*, 2010, [DOI:10.1016/j.apcata.2010.09.026](https://doi.org/10.1016/j.apcata.2010.09.026).
- [6] Miyao, T., Shen, W., Chen, A., Higashiyama, K., and Watanabe, M., Mechanistic study of the effect of chlorine on selective CO methanation over Ni alumina-based catalysts, *Applied Catalysis A: General*, 2014, [DOI:10.1016/j.apcata.2014.08.025](https://doi.org/10.1016/j.apcata.2014.08.025).

# On the Thermal Cyclic Precipitation of Aqueous Solutions for Osmotic Heat Powered Cycles.

Francisco J Arias<sup>1\*</sup>, Salvador de las Heras<sup>1</sup>

<sup>1</sup>Department of Fluid Mechanics, Universitat Politècnica de Catalunya (UPC),

ESEIAAT C/ Colom 11, 08222 Barcelona, Spain

\*Corresponding author: francisco.javier.arias@upc.edu

## Abstract

Consideration is given to an osmotic heat engine (OHE) driven by the cyclic precipitation of an aqueous solutions when an input of heat is applied or extracted from the solution. It is shown that owing to the dependence of the solubility with the temperature, the initial aqueous solution (after heated or cooled) can be physically separated into two streams with different salinities, namely, one enriched in solute and the other depleted in solute. Then, by mixing both streams using a semipermeable membrane it is possible to extract energy from the osmotic mixing. Utilizing a simplified physical model, calculation of the maximum extractable energy by this OHE was performed.

**Keywords:** Thermal solubility of aqueous solutions; Osmotic heat engines; Pressure-retarded osmosis, (PRO); Salinity power.

## Introduction

The object of this work was to analyze the possibility for an osmotic heat engine (OHE) based in the physical property of aqueous solutions to precipitate when an input of heat is applied or extracted, [1]. Today, osmotic heat engines operate with a poor efficiency limited by the high heat of vaporization of the working fluid required (vaporization is needed to re-concentrate the draw solution ) by vaporizing a portion of the water into steam, [2]).

In this manuscript, it will be demonstrated that by the proper choice of the concentration of a given aqueous solution an osmotic heat engine can be driven by the thermal dependence of the solubility of the solution -coefficient of thermal solubility, by alternating solute and solvent precipitation and mixing when heat is either applied (by heating the solution) or extracted (by cooling the solution) depending of the specific thermal dependence of the solubility of given solution.

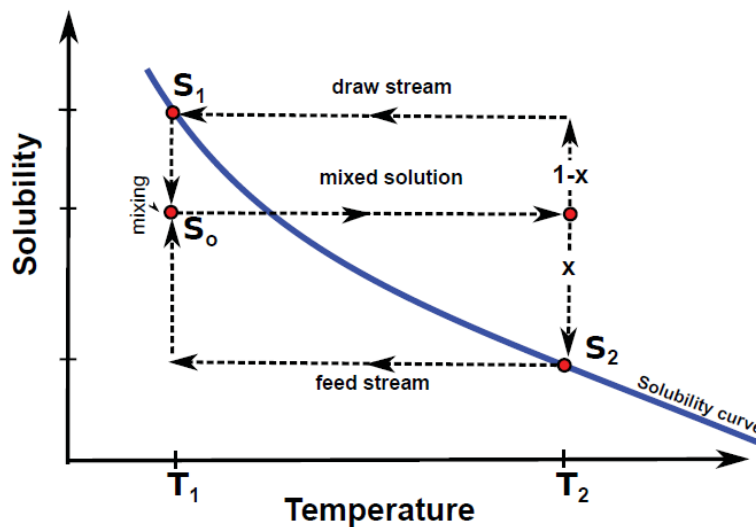


Fig. 1. Thermo-osmotic convection on aqueous solutions.

## Methods

To begin with, let us consider the thermal cycle depicted in Fig. 1. The meaning of the various terms in the Figure are defined in the Nomenclature. Let us fix a solution with an initial temperature  $T_1$  and concentration  $S_0$  -which is below of its saturation at that temperatures (i.e., below of  $S_1$ ) as depicted in Fig. 1., i.e, the solution is "*undersaturated*". Now, if this solution change its temperature from  $T_1$  to  $T_2$ , and if the initial solubility  $S_0$  is now higher than the saturation solubility  $S_2$  at  $T_2$ , then the initial unsaturated solution is now "*supersaturated*" and precipitation occurs. Therefore, one requirement for thermo-osmotic convection, is that the initial concentration of the aqueous solution be supersaturated at its initial temperature and supersaturated at the final temperature, i.e., satisfying

$$S_1 > S_0 > S_2 \quad (1)$$

Suffice is to say that because the solubility can increase or decrease with temperature, then thermo-osmotic convection is possible with  $T_1 > T_2$  or  $T_1 < T_2$ , as a manner of illustration in Fig. 2 is plotted the thermal dependecne of the solubility for some salts. Now, once supersaturation occurs, the excess of particles of solute precipitate and can be separated by using a proper filter. At this point, we have on one hand a solution which has been depleted of solute with a new concentration  $S_2$  equal to its saturation at temperature  $T_2$  and the the precipitated solute.

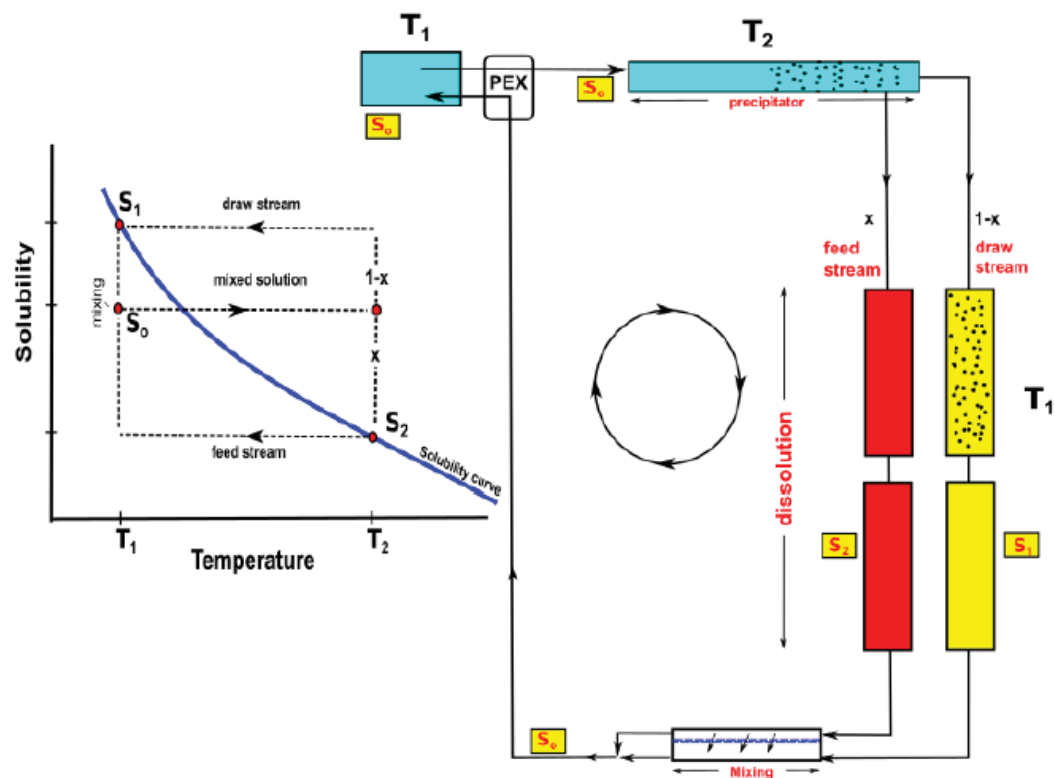


**Fig. 3.** Sketch for a heat osmotic engine driven by the thermal dependence of the solubility.

Referring to Fig. 1, let us separate the supersaturated solution into a volume fraction of the depleted solution, say, ( $x$ ) and the rest of volume. i.e., a fraction ( $1 - x$ ) containing the precipitated. After this, the solutions are recovering its initial temperature  $T_1$  and as a

result, their solubility increase. This makes that the solute in the fraction  $(1 - x)$  is totally dissolved. If the proper fraction  $x$  was chosen, then it is possible that the dissolved fraction  $(1 - x)$  get the maximum solubility at  $T_1$ , i.e.,  $S_1$ . In summary, from an initial solution with concentration  $S_o$  at  $T_1$ , and after a change in temperature to  $T_2$ , we are forming a low-salinity solution  $S_2$  and a high-salinity solution  $S_1$ . Now, if both solutions are brought together by using a permeate membrane, it is possible harnessing the osmotic pressure released generated to propel the fluid.

Fig. 3 shows a sketch what a osmotic heat engine would look. Referring to this figure, an initial solution with concentration  $S_o$  and temperature  $T_1$ , enters the precipitator-module where the temperature is  $T_2$  and then becomes supersaturated. The solution, after passing through the precipitator, is separated into two solutions: one volume fraction  $(1 - x)$  where is the precipitated solute, and the rest volume fraction  $x$  where is the depleted solution. This process is entirely driven by the motion of the fluid owing to the very small size of particles where the Stokes number,  $Stk \ll 1$  and then particles follow fluid streamlines closely. Then by interposing a simple microporous-filter, the solute can easily be separated from the main solvent. Now, the two solutions recover the initial temperature  $T_1$  in two separated containers. At this point, the fraction of volume  $(1 - x)$  which so far contained the precipitated solute redissolves (because at  $T_1$  the solubility increase) and form a homogenous solution with concentration  $S_1$ . Now, the draw solution (fraction  $(1 - x)$ ) and the feed solution (fraction  $x$ ) enter the membrane module. In this membrane-module, driven by the osmotic pressure differences across the membrane, water molecules permeate from the feed stream to the draw stream, increasing the flow rate and diluting the pressurized draw stream while decreasing the flow rate and concentrating the feed stream. Then, the diluted draw stream and the concentrate feed stream exit the membrane-module and are mixed. The exiting pressurized draw-feed mixture flows trough a pressure exchanger (PEX), which transfer pressure to the incoming mix solution to propel this through the precipitator.

With this simplified picture in mind, we will proceed to do some preliminary calculations and find the dependence with several parameters for a thermo-osmotic convection.

First of all, we need to calculate the required volume fraction  $x$  which allows the mentioned cycle. This calculation may be easily developed as follows.

Considering that the volume of the precipitated solute can be negligible in comparison with the solution, and also that the density is almost constant, then by a simple balance of mass in the initial content of salt in the mixed- initial solution with concentration  $S_o$  and the final two solutions with concentrations  $S_1$  and  $S_2$  we have:

$$S_o = S_2x + S_1(1 - x) \quad (2)$$

and then the volume fraction of the feed is given by

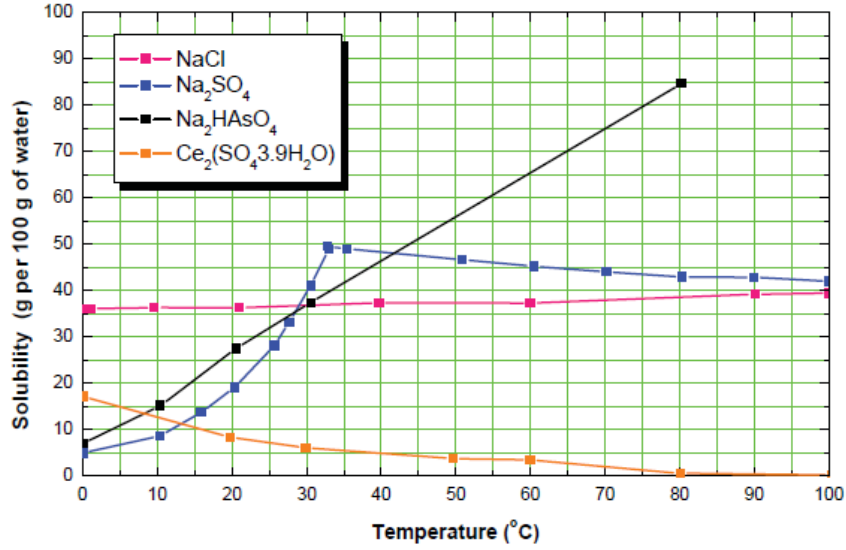


**Fig. 3.** Solubility vs. temperature for a variety of salts.

$$x = \frac{S_1 - S_o}{S_1 - S_2} \quad (3)$$

where the mixed solution  $S_o$  must satisfy Eq.(1), i.e.,  $S_1 > S_o > S_2$ .

On the other hand, salinity variations due to thermal solubility may be expressed as

$$S_2(T_2) = S_1(T_1) - S_1(T_1)\Sigma\Delta T \quad (4)$$

where for analogy with natural convection, a coefficient of thermal solubility  $\Sigma$  has been defined as

$$\Sigma = -\frac{1}{S} \frac{\partial S}{\partial T} \quad (5)$$

By using the above expression, the volume fraction  $x$  given by Eq.(3) may be rewritten as

$$x = \left[1 - \frac{S_o}{S_1}\right] \frac{1}{\Sigma\Delta T} \quad (6)$$

If we call the fraction of initial saturation as  $\Phi = \frac{S_o}{S_1}$ , then Eq.(6) becomes

$$x = \frac{1 - \Phi}{\Sigma\Delta T} \quad (7)$$

Therefore by knowing the initial unsaturation of a given solution  $\frac{S_o}{S_1}$  and the specific parameter  $\Sigma\Delta T$  we can find the optimized volume fraction  $x$  and with the solubility of the mixture  $S_o$ , the solubility of the feed  $S_2$ , and ) the solubility of the draw  $S_1$  we can obtain the osmotic energy released as follows.

### Extractable energy

It is known that the maximum energy available from an osmotic mixing is equal to the Gibbs free energy of mixing. Although a realistic system will result in and energy amount

less than this values, nevertheless, it provides a useful upper limit as first assessment. The Gibbs energy per volume for an infinite diluted solution is given by

$$\Delta G = \frac{\Pi(c)}{c} [c_M \ln(c_M) - x c_F \ln(c_F) - (1-x)c_D \ln(c_D)] \quad (8)$$

where  $\Pi(c)$  is a given reference osmotic pressure for a given concentration  $c$  (moles/ $m^3$ ); and  $c_M$ ,  $c_F$ ;  $c_D$  are the concentrations of the mixture, feed and draw, respectively. Taking into account that the concentration and solubility are related as

$$c = \frac{\rho}{\bar{m}} S \quad (9)$$

where  $\rho$  and  $\bar{m}$  are the density and the molecular weight of the solution, respectively. Thus we have

$$c_M = \frac{\rho}{\bar{m}} S_o \quad ;$$

$$c_F = \frac{\rho}{\bar{m}} S_2 \quad ;$$

$$c_D = \frac{\rho}{\bar{m}} S_1 \quad (10)$$

and  $x$  given by Eq.(7).

The maximum  $\Delta G$  occurs when the derivative with respect to  $c_M$  is zero:

$$\frac{\partial \Delta G}{\partial c_M} = 0 \quad (11)$$

Taking into account Eq.(8) and solving Eq.(11) leads to the concentration  $c_M$  with which the specific Gibbs free energy of mixing is maximized.

$$c_M^* = \exp \left[ \frac{c_D \ln c_D - c_F \ln c_F}{c_D \Sigma \Delta T} - 1 \right] \quad (12)$$

or by using Eq.(10)

$$S_o^* = \frac{\bar{m}}{\rho} \exp \left[ \frac{S_1 \ln S_1 - S_2 \ln S_2 + (S_1 - S_2) \ln \frac{\bar{m}}{\rho}}{S_1 \Sigma \Delta T} - 1 \right] \quad (13)$$

To obtain some idea of the extractable energy predicted by Eq.(8) for  $Na_2SO_4$  we assume some possible parameters:  $\Delta T = 30$  K;  $T = 273$  K;  $S_1$  and  $S_2$  calculated from Fig .3 and the fraction of volume  $x$  was calculated from Eq.(7).

From Fig. 4, it is seen that, up to 3.5 kWh per  $m^3$  of solution could be obtained. However, taking into account several uncertainties as well as the approximation of infinite dilute (ideal) solution which is not valid for highly saturated solutions as is pour case, we may assume a more conservative value around 1 kWh per  $m^3$  of solution or thereabouts.

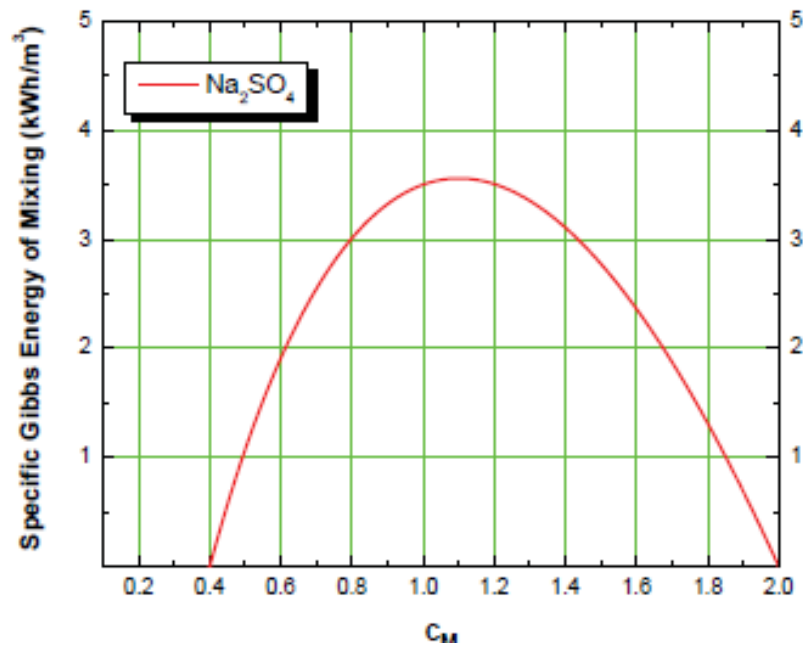


Fig. 4. Specific Gibbs free energy of mixing for  $\text{Na}_2\text{SO}_4$  solution with  $\Delta T = 30$  K;  $T = 273$  K;  $S_1$  and  $S_2$  from Fig. 3 and the fraction of volume  $x$  calculated from Eq.(7).

### Summary of results and conclusions

- It is possible an osmotic heat engine (OHE) driven by the thermal precipitation of saturated solutions and then increasing the poor efficiency of current OHEs limited by the high heat of vaporization of the working fluid required.
- Additional R&D is required to arrive at a reliable practical and optimized design.

### Nomenclature

$c$  = concentration  
 $c_p$  = heat capacity of fluid  
 $g$  = gravity  
 $\Delta G$  = free Gibbs energy per unit volume of solution  
 $R$  = ideal gas constant  
 $S$  = solubility  
 $\Delta T$  = difference temperature  
 $T$  = temperature  
 $V$  = volume  
 $V_p$  = volume of the particle  
 $x$  = volume fraction of the low-concentration solution



### **Greek symbols**

$\beta$  = coefficient of thermal expansion

$\Sigma$  = coefficient of thermal solubility

$\rho$  = density of the fluid

$\rho_p$  = density of the solute

$\kappa$  = Boltzmann constant

$\mu$  = dynamic viscosity of the fluid

$\eta$  = kinematic viscosity of the fluid

### **subscripts symbols**

$o$  = initial, reference

$1$  = supersaturation

$2$  = subsaturation

$D$  = high salinity concentration

$F$  = low salinity concentration

$M$  = mixture

$d$  = diffusion-governed growth

$f$  = fluid motion -governed growth

$t$  = total

$p$  = solute particle

### **Acknowledgements**

This research was supported by the Spanish Ministry of Economy and Competitiveness under fellowship grant Ramon y Cajal: RYC-2013-13459.

### **References**

[1] Arias F.J. 2018. On osmotic heat engines driven by thermal precipitation-dissolution of saturated aqueous solutions. *In Journal peer-review (submitted-December-2017)*

[2] McGinnis RL, McCutcheon JR, Elimelech M. A novel ammonia-carbon dioxide osmotic heat engine for power generation. *J. Membr. Sci* 2007; 305: 13-19.

# Deliberate Salinization of Domestic Wastewater in Housing Estates for Energy

Francisco J Arias<sup>1\*</sup>, Salvador de las Heras<sup>1</sup>

<sup>1</sup>Department of Fluid Mechanics, Universitat Politècnica de Catalunya (UPC),

ESEIAAT C/ Colom 11, 08222 Barcelona, Spain

\* Corresponding author: [francisco.javier.arias@upc.edu](mailto:francisco.javier.arias@upc.edu)

## Abstract

Consideration is given to the deliberate salinization of domestic wastewater before being drained to the sewer for harnessing energy by pressure retarded osmosis (PRO) process for the self-supply of communal electricity in housing states. The key point, at least from an engineering standpoint, of such a technique is the competition between the price of the salt in comparison with the price of the electricity from the grid. It is shown that with the current prices and trends of the salt in the market, the deliberate salinization of domestic wastewaters could be attractive by using a hypersaline draw solution cyclic loop with the highest possible volume fraction for the non-salinized solution. In some countries with high cost of electricity as Germany or USA, the break-even point is not far from the near future, if the current trend is maintained.

**Keywords:** Pressure retarded osmosis (PRO), Domestic wastewater, Sustainable use of water.

## Introduction

With the accelerated growth of global population and the subsequent increase in the demand for domestic water, there is an increase in the amount of domestic wastewater. In general, society aims at the disposal of wastewater with the minimum possible environmental impact, or at least the maximization of the use of this wastewater before being dumped into the sewers. To illustrate this problem, it suffices to say that approximately  $0.17 \text{ m}^3$  per day of domestic wastewater can be produced per person, (Pescod 1992), which, for an average family composed of 4 persons, could result in  $0.68 \text{ m}^3$  per day. If we consider a housing estate composed of around 50 families, this figure rises to  $30 \text{ m}^3$  per day.

The salinity gradient energy, also known as blue energy or osmotic energy, has been investigated since the 1970s as a method for extracting energy from wastewater. This blue energy can be obtained from the difference in salt concentration between two feed solutions, for example, seawater and river water or wastewater.

The object of this work was to assess the deliberate salinization of domestic wastewater before being drained to the sewer for harnessing osmotic energy for the self-supply of communal electricity in housing states

## Methods

At first, let us consider the Fig. 1 where is sketched the core idea of this work. As shown in this figure, an initial flow of domestic wastewater (1) is bifurcated (only physical separation) into two streams (2) and (3). Stream (3) is diverted into a chamber containing salt tablets, and stream (4), which leaves this chamber, has an increased salinity. Finally, both

streams (2) (low salinity) and (4) (enhanced salinity) are mixed together, to form stream (5). As there is a salinity gradient between streams (2) and (4), energy can be extracted using the PRO process.

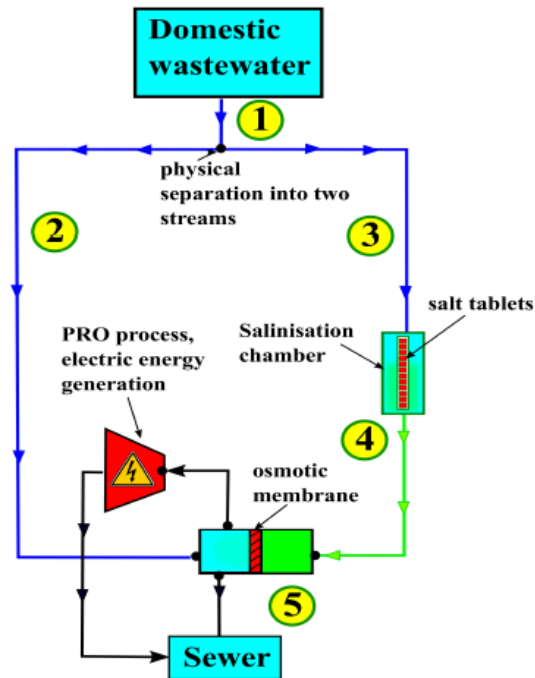


**Fig. 1.** Schematic for the *in situ* PRO process for energy extraction from domestic wastewater

The above scheme although simple, however, a simple analysis will show that is not economically feasible and modifications must be provided.

To begin with, let us consider the maximum theoretical energy that can be extracted using the PRO process. A rough approximation can be obtained by estimating the Gibbs free energy of mixing  $\Delta G$  for an ideal or diluted solution and is given by

$$\Delta G = \nu RT [c_M \ln(c_M) - \phi_F c_F \ln(c_F) - (1 - \phi) c_D \ln(c_d)] \quad (1)$$

where  $c_M$ ,  $c_F$ , and  $c_D$  are the mixed, feed, and draw solution concentrations, respectively. Here, feed and draw indicate the low and high salinity solutions, respectively. On the other hand, the feed fraction,  $\phi$ , is the initial volume of the feed solution divided by the total initial volume of the feed and draw solutions.  $\nu$  is the van't Hoff factor of strong electrolytes (e.g.,  $\nu = 2$  for NaCl),  $R$  is the ideal gas constant, and  $T$  is the absolute temperature. Fig. 2 shows the specific Gibbs free energy for the mixing of water from different sources as a function of the feed volume fraction,  $\phi$ .

## Discussion

From Fig. 2, we can deduce the following important insights. It can be seen that the maximum energy for the saturated solution of seawater mixed with wastewater effluent is around 2.7 kWh/m<sup>3</sup>. Considering the practical PRO constraints, which reduce the efficiency of energy extraction by at least 30% or thereabouts, we obtain energy of approximately 1.62

kWh/m<sup>3</sup>. This maximum energy occurs when the feed fraction is around  $\phi \approx 0.6$ , which is the same as a draw fraction of around  $(1 - \phi) \approx 0.4$ . This means that since each 0.4 m<sup>3</sup> of saturated feed solution with 6.0 M of NaCl (having a molecular weight of 58.44 g/mol) requires 140 kg of NaCl, we need 140 kg of NaCl for each 1.62 kWh obtained.

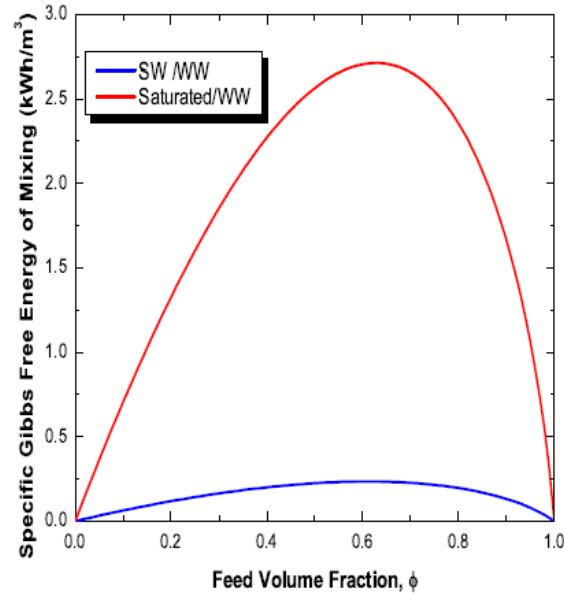


**Fig. 2.** Specific Gibbs free energy for the mixing of water from different sources as a function of the feed volume fraction,  $\phi$ , considering the following sources of water: seawater (SW, 0.6 M NaCl); wastewater effluent (WW, 0.015 M NaCl), and saturated (Saturated, 6.0 M NaCl).

The price of NaCl can be as low as 10 dollars per ton, which results in 1.15 dollars per kWh. However, the current price of electricity from the grid is almost ten times lower than that. It is easy to see that a simple scheme (as depicted in Fig. 1) that works with a fraction of the feed (or draw), which maximizes the energy (but does not minimize the cost), is not economically attractive.

#### In situ deliberate hypersaline cycle

It is possible to envisage an economically attractive solution as discussed below.

Let us now consider a modified scheme, as depicted in Fig. 3, instead of our previous scheme (shown in Fig. 1). This scheme is designed for reducing the amount of salt needed per kilowatt-hour produced.

As shown in Fig. 3, the initial flow of domestic wastewater (1) is mixed with a draw solution (hypersaline solution) (2). A portion of the mixed solution is directed to the sewer (4), and the remaining portion is recirculated to the salinization chamber (3), in which its salinity is recovered, and the process is repeated.

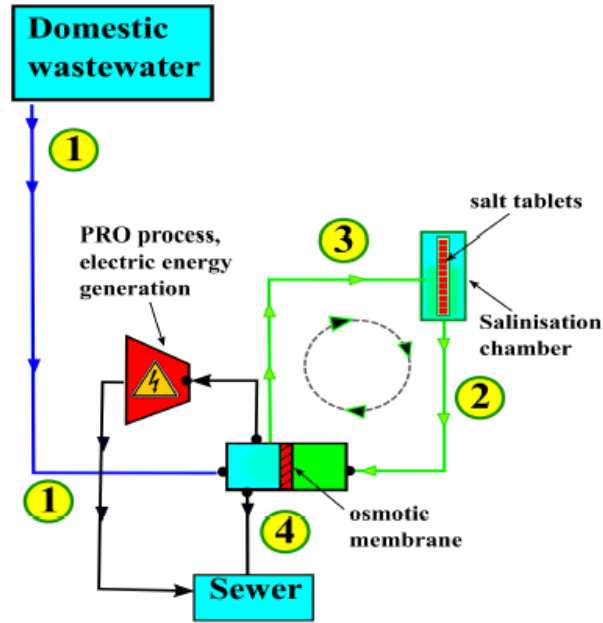


**Fig. 3** Schematic of an in situ deliberate hypersaline PRO cycle for extracting energy from domestic wastewater.

In comparison with the basic process depicted in Fig. 1, the amount of salt required per kilowatt-hour is considerably reduced.

### Calculations for the in situ deliberate hypersaline PRO cycle

The calculations for the in situ hypersaline PRO cycle are straightforward. The problem is stated as follows. Given, a volume fraction  $(1 - \phi)$  of wastewater, which was deliberately salinized (using salt tablets in a separate chamber, for example) and then mixed with the remaining volume fraction  $\phi$  of wastewater (low salinity) having a concentration of  $c_F$  resulting in a mixed concentration  $c_M$ . Then, what must be the amount of salt that has to be added to the fraction  $(1 - \phi)$  of the resulting mixture to recover the concentration  $c_D$  so that it can be used again in the next cycle?

The final concentration of the mixture,  $c_M$ , is given by

$$c_M = c_F\phi + c_D(1 - \phi) \quad (2)$$

If we take a volume  $V_d$ , which is equal to the volume of the draw (hypersaline) solution that was used previously, from this mixture with concentration  $c_M$ , and add  $X$  number of moles of salt, then the final concentration must be equal to that of the original draw solution. This can be expressed mathematically as

$$\frac{c_M V_d + X}{V_D} \approx c_D \quad (3)$$

where it is a valid approximation to consider that the volume of salt solute is negligible. Eq.(3) may be rewritten as

$$X = V_D(c_D - c_M) \quad (4)$$

The draw volume is given by

$$V_D \approx (1 - \phi)V_T \quad (5)$$

where  $V_T$  is the total volume of the mixture.

Then, from Eq.(5), we obtain the number of moles of salt needed per volume of mixture  $X^* = \frac{X}{V_T}$  as

$$X^* = (1 - \phi)(c_D - c_M) \quad (6)$$

Inserting Eq.(2) into Eq.(6) yields

$$X^* = \phi(1 - \phi)(c_D - c_F) \quad (7)$$

and the mass of salt per unit of mixed volume as

$$X^* = \phi(1 - \phi)(c_D - c_F)\bar{M} \quad (8)$$

where  $\bar{M}$  is the molecular mass of the salt.

Finally, the energy obtained per mass of salt is given by dividing Eq.(1) with Eq.(8).

$$\frac{\Delta G}{\text{mass salt}} = \left[ \frac{\nu RT}{\bar{M}} \right] \left[ \frac{[c_M \ln(c_M) - \phi_F c_F \ln(c_F) - (1 - \phi) c_D \ln(c_d)]}{\phi(1 - \phi)(c_D - c_F)} \right] \quad (9)$$

If the cost per unit mass of salt is \$, then the energy cost is given by

$$\frac{\Delta G}{\text{cost salt}} = \left[ \frac{\nu RT}{\bar{M}} \right] \left[ \frac{[c_M \ln(c_M) - \phi_F c_F \ln(c_F) - (1 - \phi) c_D \ln(c_d)]}{\phi(1 - \phi)(c_D - c_F)} \right] \frac{1}{\$} \quad (10)$$

Eq.(10) is the expression that should be used to compare the costs of energy from the electrical grid and that obtained using the proposed method, in order to assess the attractiveness of the in situ deliberate hypersaline cycle for PRO energy extraction.

## Discussion

Fig. 4 shows the curves predicted by Eq.(10) (left axis) and the associated energy given by Eq.(1) (right axis) as a function of the volume fraction of feed. The cost of NaCl salt was taken as 10\$ per ton, which was the lowest value recorded in the stock market in 2016 (Matthew, 2016).

It is seen that with a feed fraction of around  $\phi = 0.98$ , it is possible to obtain around 8 kW-h per dollar and an extractable energy of around 1 kW-h/m<sup>3</sup>. If we consider the typical prices in the electrical market in countries such as Germany (which is around 3.36 kW-h per dollar) (Electricity statistic Eurostat, 2016), we can conclude that the proposed in situ deliberate hypersaline PRO cycle could be a very attractive option.

From our previous discussion (in the introduction), a housing estate producing around 30 m<sup>3</sup> of wastewater per day will be able to generate around 50 kW-h per day. Even when considering an efficiency of around 30%, we will have a non-depreciable generation of 15 KW-h per day, which can help the community become self-sufficient with regard to its electricity needs.

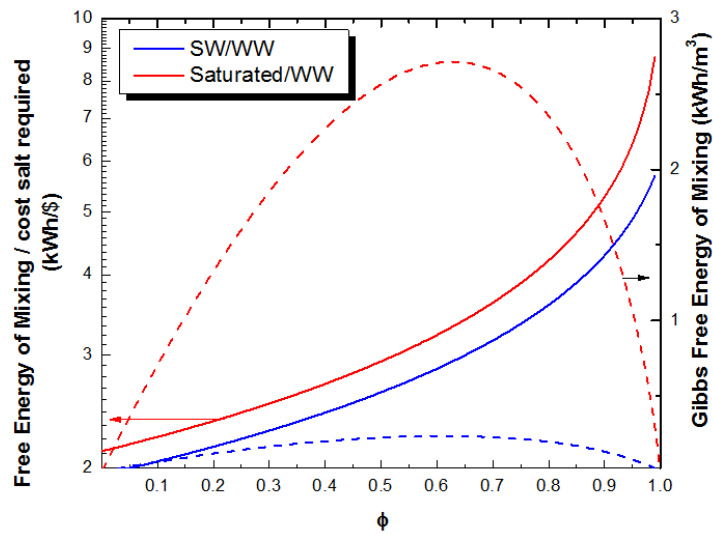


**Fig. 4.** *Left axis:* Specific Gibbs free energy per dollar required for the mixing of water from different sources as a function of the feed volume fraction,  $\phi$ , considering the following sources of water: seawater (SW, 0.6 M NaCl); wastewater effluent (WW, 0.015 M NaCl), and saturated (Saturated, 6.0 M NaCl). *Right axis:* their specific Gibbs free energy for mixing.

### Summary of results and conclusions

An assessment of the feasibility of using in situ pressure-retarded osmosis (PRO) at homes or housing estates was proposed/discussed for the first time in this work. Unlike previous studies, seawater is not used in this study. Instead, a fraction of the domestic wastewater is deliberately salinized (for example, by using salt tablets in a dedicated chamber) and then mixed with the remaining fraction for the PRO process. It was demonstrated that in order to attain an economically attractive process, considering the cost of salt, it is necessary that the draw (salinized) solution is cyclic and that the feed (not salinized) solution has a high fraction. The energy obtained from this process is around 10 to 50 kW-h per day for housing estates, and the price can be half that of the electricity from the local electrical grid.

The result of this preliminary assessment is encouraging, and additional R&D for exploring the full potential of the in situ PRO process is viable.

### Acknowledgements

This research was supported by the Spanish Ministry of Economy and Competitiveness under fellowship grant Ramon y Cajal: RYC-2013-13459.

### References

- [1] Arias F.J., 2017, Deliberate Salinization of Seawater for Desalination of Seawater. *Journal of Energy Resources Technology*.
- [2] Electricity price statics. Eurostat. Statics Explained. Data extracted in November 2016.

# A novel hybrid dew point cooling system for mobile applications

Mark. Worall<sup>1\*</sup>, Adam. Dicken<sup>2</sup>, Mahmoud. Shatat<sup>1</sup>, Sam. Gledhill<sup>2</sup>, Saffa. Riffat<sup>1</sup>

<sup>1</sup>Buildings, Energy and Environment Research Group, Faculty of Engineering, The University of Nottingham, University Park, Nottingham, NG7 2RD, UK

<sup>2</sup> Environmental Process Systems, Unit 32 Mere View Industrial Estate, Yaxley, PE3 7HS, UK

\*Corresponding author: mark.worall@nottingham.ac.uk

## Abstract

A novel dew point cooling system for truck cabin cooling has been designed and tested, which shows excellent performance in environments of low to medium relative humidity. Experimental results showed that cooling capacity of over 1kW could be achieved with up to 12K of sensible cooling of the supply air and a COP of up to 7. The DPC unit can provide comfort cooling to a vehicle using a rooftop unit whose DPC core is no larger than 0.5m x 0.5m x 0.25m.

**Keywords:** indirect evaporative cooler, dew point cooler, mobile air conditioning, natural refrigerants

## Introduction

In 2010, the global transport sector consumed over 2,000 million tons oil equivalent, representing about 20% of global energy supplies WEC[1], whilst more than 60% of oil consumed was for the transport sector. Of this, around 75% was consumed by road transport. Transport energy consumption is largely based on oil, so contributes to pollution and carbon emissions. Mobile air conditioning (MAC) is now a standard facility in road vehicles such as automobiles, trucks and buses, but can consume over a quarter of all the power available from the engine. Most MAC systems utilise vapour compression cycles whose working fluids are high global warming potential refrigerants, such as HFC134a (GWP~3500 (Forster *et al* [2])). MAC systems contribute to global warming both directly due to leakage of refrigerant into the atmosphere and indirectly due to the carbon dioxide released in combusting fossil fuels (Grof, [3]). The significant leakage associated with MAC systems has led to many authorities prohibiting the use of HFC refrigerants such as HFC134a, and so alternatives are being developed. However this does not address the power consumption and associated global warming effects of operating a MAC system. If natural or low carbon cooling systems could be integrated into MAC systems, then carbon emissions and engine power consumption could be reduced. In many climates around the world where cooling is required, evaporative cooling is an effective way of providing comfort cooling if the relative humidity is medium to low and water is available.

Surveys were carried out to investigate whether evaporative cooling would be suitable for MAC systems, and it was found that the most appropriate application would be truck cabin parking coolers. Many of these products are mounted on roofs and provide cooling to occupants when the truck is not being driven. These are mainly based on MAC vapour compression technology, but some use direct evaporative cooling. There are two main disadvantages to these systems; MAC systems consume battery power that is ultimately derived from the truck engine, whilst direct evaporative coolers increase the moisture in the air that is being conditioned and therefore can reduce comfort. An alternative is indirect evaporative cooling based on the Maisotsenko cycle (M-cycle) (Muhammad *et al* [4]), which we also term the dew point cooler, because it can potentially cool to the dew point temperature.



## Dew point cooler

Figure 1a shows a simple schematic diagram to illustrate the cooling process and Figure 1b shows the process on a psychrometric chart. The dew point cooler consists of a number of paired channels separated by an impermeable wall. One channel is termed the dry channel (product channel in Fig 1a) and the other is termed the wet channel (working channel in Fig 1a). A number of openings are provided in the wall to allow the flow of air from one side to the other. The wall is usually provided with a wick type structure to draw water into the channel and provide a wetted surface for the wet channel.

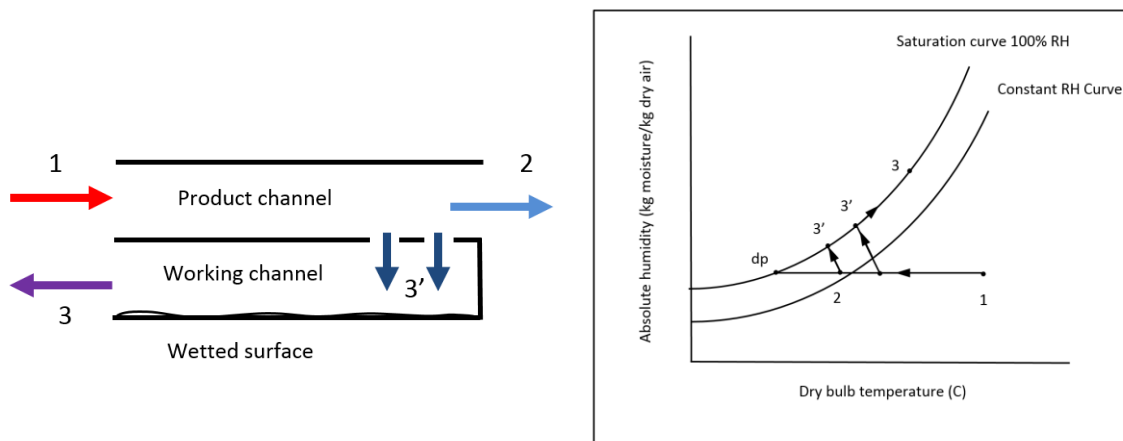


Figure 1. (a) Diagram of dew point cooler (b) indirect evaporative cooling process illustrated on psychrometric chart

In figure 1b, the x-axis represents the dry bulb temperature and the y-axis represents humidity ratio (ratio of the mass of water vapour to the mass of dry air). Air is introduced into the exchanger at (1) at a particular temperature and humidity. As the air flows through the dry channel, some of the flow is directed to the wet channel (3') through the openings. The air in the wet channel flows counter to the flow in the dry channel. The difference in vapour pressure between the water vapour in air and water at the wetted surface drives evaporation from the water to the air. The latent heat transferred cools the dry channel and therefore provides sensible cooling of the product air. The process continues along the exchanger until the product air leaves the dry channel at (2), and the working air leaves the wet channel at (3). In theory, the dry air could be cooled to its dew point temperature from 1 to dp.

This paper reports on a novel vehicle cooling system that uses natural refrigerants to provide cooling for a truck cabin. A compact and lightweight dew point cooling system is being developed that will either reduce the need for conventional vapour compression systems or replace them altogether.

The smallest standard core available to us was approximately 0.5m x 0.5m x 0.25m (L x W x H), so we obtained a core and designed a system around it that would minimise the weight and envelope whilst maximising its cooling performance.

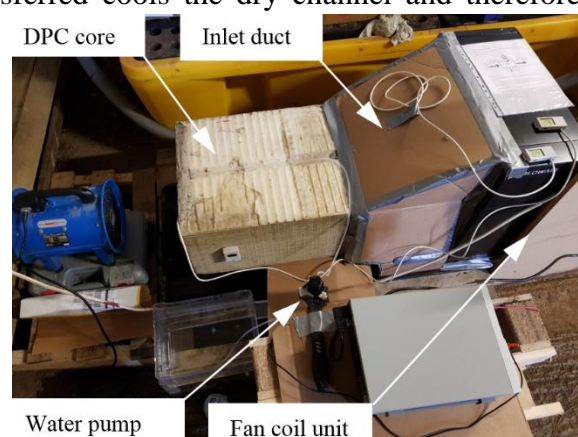


Figure 2. Image of DPC core preliminary test rig@ EPS Ltd.

Our consortium partners EPS Ltd carried out some preliminary testing of a single dew point cooler core to assess its potential for cooling prior to integration into the dew point cooling air conditioning system. Figure 2 shows an image of the test rig. The rig consists of a heat pump and fan coil unit that controls inlet temperature and air flow with 5 speed variability, a sealed ducting system that directs the inlet flow to the DPC core, a 12VDC peristaltic pump that can supply water flows of up to 5kg/min, temperature and humidity sensors for the inlet, supply and outlet streams, rotary vane type anemometer to measure velocities, weighing machine to determine mass flow of water pumped, and fan coil power measurement devices.

Table 1 shows average flows and fan power consumption for three fan speed settings. It can be seen that AR decreases slightly from 3.75 at speed 1 to 2.75 at speed 3. Figure 3 shows the variation in a) cooling capacity and b) dew point effectiveness with inlet temperature. Inlet relative humidity was approximately constant at 20% during the tests. Cooling capacity increases from approximately 300W at 20°C to 1200W at 40°C. Dew point effectiveness increased from about 70% at 20°C to approaching 100% around 35-40°C.

**Table 1. Air flows and power consumption for DPC core testing**

Speed	Inlet (m <sup>3</sup> /hr)	Product (m <sup>3</sup> /hr)	Working (m <sup>3</sup> /hr)	AR	Fan Power (W)
1	721	152	570	3.75	40
2	941	231	711	3.08	57
3	1390	371	1019	2.75	83

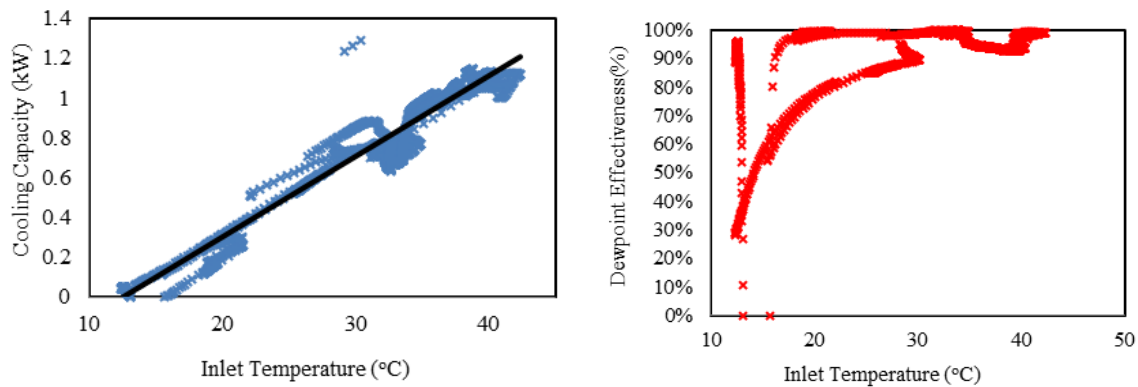


Figure 3. Variation in a) cooling capacity and b) dew point effectiveness with inlet temperature

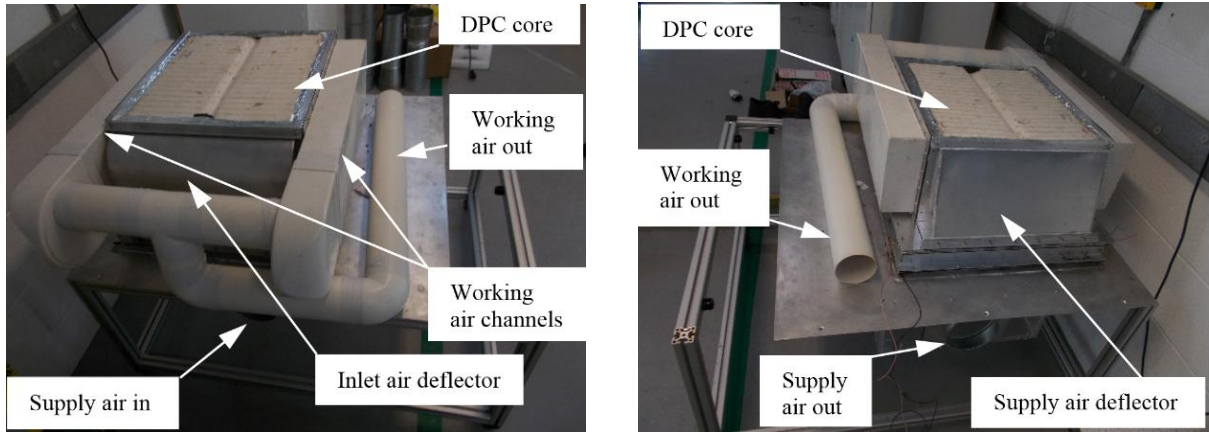


Figure 4 (a) front view of dew point cooler system, (b) rear view of dew point cooler system.

The working air is collected on both sides and leaves in a single duct. Figure 3b) shows that we almost reached saturation conditions in the supply air stream. The working air is collected on both sides and leaves in a single duct. meaning that almost all of the potential for evaporation was realised. This was partly due to the low RH, thus providing a large driving mechanism for evaporation in the wet channels, and low inlet temperatures prior to processing by the fan coil (tests were carried out during winter UK conditions in an outbuilding). The results gave us confidence that the process could work successfully and effectively, so in the next section we report results from controlled experiments on an integrated dew point cooler air conditioner.

### Dew point cooler rooftop cabin cooler

In order to draw air from the cabin (air inlet), direct it through the core and back to the cabin, whilst discharging the working air, we needed to design a compact air distribution system. In comparable rooftop air conditioning systems, the air being drawn from the cabin and delivered back to the cabin is usually located within the roof hatch. In a conventional rooftop A/C unit, the air is drawn from the cabin by a blower and directed a short distance across the

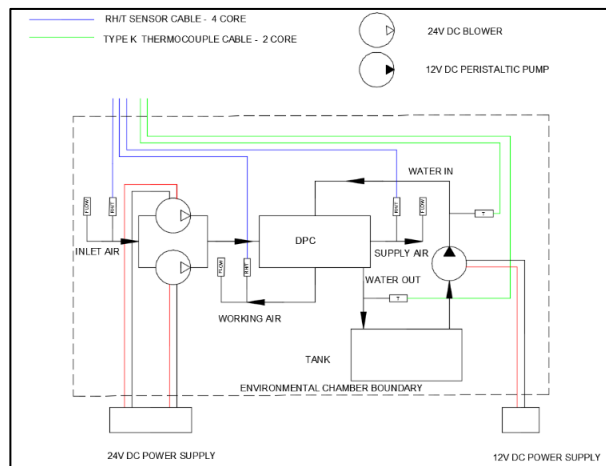


Figure 5. Dew point cooler schematic diagram

evaporator of the A/C unit. In most cases these consist of narrow double row heat exchangers, and so the width (in the direction of air flow) can be as low as 50mm. Unfortunately, the width of the dew point core is around 500mm, and so we needed to design a distribution system that could draw in the air, direct it to the inlet to the dew point core, channel the supply air back to the cabin whilst distributing the working air away. We decided to site the blowers directly above the air inlet, direct the air in channels formed from aluminium channel section underneath the core, deflect the air 180° using an inlet air deflector, so that it flowed in line with the product channels, directed the supply air back to the cabin through a supply air deflector, whilst also directing

working air using two 90mm x 200mm working air channels and various transition pieces, elbows, etc. Figures 4a and 4b show front and rear views of the dew point cooler with labels showing various features.

A simple schematic diagram of the system is shown in figure 5. Two 24V DC compact blowers 220 x 220 x 56 were provided to give the required volume flow. Vaisala HMP110 humidity/temperature sensors were used at the inlet, supply and working air outlets. K Type thermocouples were used to measure temperatures at various locations. Air flows were determined by measuring air velocity at various locations using a Testo 416 vane type anemometer. Descriptions of the measuring instruments used, their range and accuracy can be found in Table 2. DC power was supplied

Table 2. Instrumentation

Sensor description	Parameter	Range	Accuracy
K Type Thermocouple	Temperature	0-1100°C	±1.5°C
Vaisala HMP110 humidity/temperature probe	Relative humidity	0-90%RH	±1.5%RH
	Temperature	0-40°C	±0.2°C
	Temperature	40-80°C	±0.4°C
Testo 416 Vane Anemometer	Air speed	0-40m/s	±0.2m/s (0-60°C)
CPS 66220 weighing platform	mass	0-100kg	±5g

to the 24V DC blowers by a TTI CPX200 dual channel power supply unit and DC power was supplied to the 12V DC peristaltic pump by a Extech 37220 Quad power supply unit. A 10 litre water tank was provided to supply the system with water. Water flow was determined by placing the water tank on a digital weighing platform (CPS 66220) and recording the difference in mass over a given time period. Testing was carried out in a climate chamber which allowed us to set and control temperature and relative humidity.

### Test procedure

Tests were carried out over a range of temperatures and relative humidities from 25°C to 45°C and from 40% to 80%RH. During individual tests, monitoring and logging was carried out for at least 60 minutes at steady state for each test point. At various intervals, but for only short periods of time to minimise changes to the conditions, the chamber was accessed to record the mass of the water tank and air speeds, so that the mass flow of water and the air volume flow rates could be determined.

The experimental results were used to determine the change in temperature between inlet and supply  $\Delta T$ , cooling capacity  $Q_{supply}$ , dew point effectiveness  $\epsilon_{dp}$ , and coefficient of performance  $COP$ .

$$\Delta T = T_{in} - T_{supply} \quad [1]$$

$$Q_{supply} = V_{supply} \cdot c_{p_{supply}} \cdot \rho_{supply} \cdot \Delta T \quad [2]$$

$$\epsilon_{dp} = \frac{T_{in} - T_{supply}}{T_{in} - T_{dp}} \quad [3]$$

$$COP = \frac{Q_{supply}}{W} \quad [4]$$

$$W = W_{fans} + W_{pump} \quad [5]$$

Where  $T_{in}$  (°C) is inlet temperature,  $T_{supply}$  (°C) is supply air temperature,  $V_{supply}$  (m<sup>3</sup>/s) is supply volume flow,  $c_{p_{supply}}$  (J/kg/K) is specific heat capacity,  $\rho_{supply}$  (kg/m<sup>3</sup>) is density of

supply air,  $T_{dp}$  ( $^{\circ}\text{C}$ ) is the dew point temperature,  $W$  (W) is the total work input to the system,  $W_{fans}$  (W) is the fan work input and  $W_{pump}$  (W) is the pump work input.

## Results

Figures 6a, 6b and 6c show the variation in temperature difference from inlet to supply with inlet temperature and relative humidity. They represent results at approximately 40%, 60% and 80% RH, respectively. The data were reduced by filtering temperature and RH readings within  $\pm 1^{\circ}\text{C}$  and  $\pm 1\%$  RH of the values of interest. The results were then statistically analysed by obtaining the sample mean and sample standard deviation for values  $25^{\circ}\text{C}$ ,  $30^{\circ}\text{C}$ ,  $35^{\circ}\text{C}$ ,  $40^{\circ}\text{C}$  and  $45^{\circ}\text{C}$ , and RH values of 40%, 60% and 80%.

The sample mean  $\bar{X}$  and the sample standard  $s$  deviation of a given variable  $X$  for a sample size  $n$  are determined in the usual way (Evans and Rosenthal [4]).

Table 3 shows the results of reducing the data and applying the statistical analysis. It should be noted that there were not enough data points at  $25^{\circ}\text{C}/80\%$  RH and  $45^{\circ}\text{C}/40\%$  RH, so we propose to interpolate from the data obtained.

Figure 6d shows the variation of temperature difference with inlet temperature and for RH at 40%, 60% and 80%, figure 7a shows the variation of cooling capacity with inlet temperature and for RH at 40%, 60% and 80% and figure 7b shows the variation of COP with inlet temperature and for RH at 40%, 60% and 80%.

$T_{in}$ ( $^{\circ}\text{C}$ )	$\text{RH}_{in}$ (%)	$\bar{\Delta T}$ (K)	$n$	$s$ (K)
25	40	5.18	29	0.23
25	60	3.16	34	0.44
25	80	-	-	-
30	40	7.34	22	0.09
30	60	3.55	7	0.41
30	80	2.17	23	0.34
35	40	8.36	104	0.29
35	60	4.86	23	0.49
35	80	2.33	59	0.23
40	40	9.44	119	0.23
40	60	5.31	16	0.63
40	80	2.67	87	0.25
45	40	-	-	-
45	60	6.41	17	0.51
45	80	3.37	84	0.25

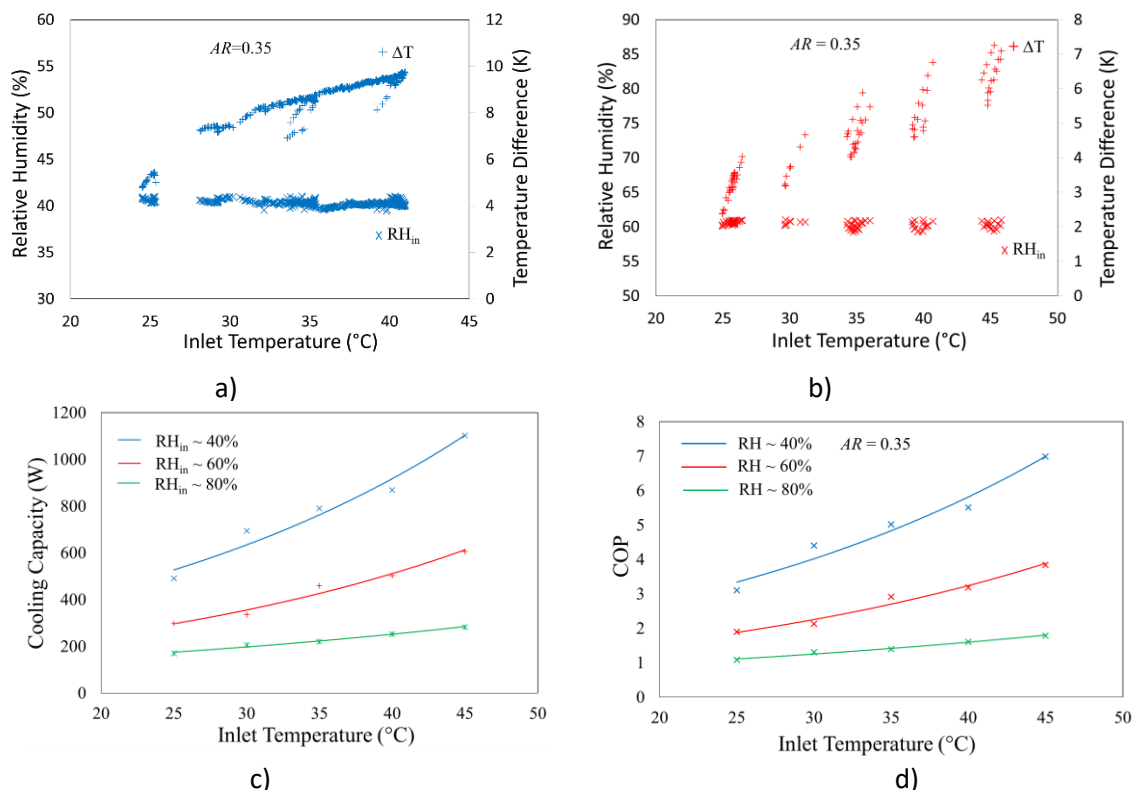


Figure 6 a)  $\Delta T$  data at 40% RH, b)  $\Delta T$  data at 60% RH, c)  $\Delta T$  data at 80% RH, and d) variation in  $\Delta T$  with  $T_{in}$  and constant RH.

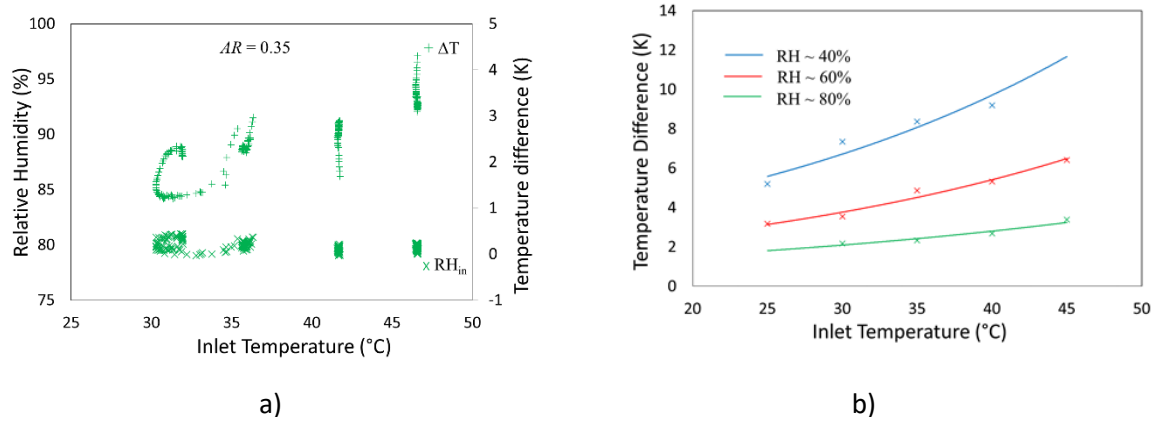


Figure 7. Variation in a) cooling capacity with  $T_{in}$  and constant RH, f) and b) COP with  $T_{in}$  and constant RH.

In figure 6d, temperature difference increases with inlet temperature and RH. For instance, at 25°C and 40% RH, the temperature difference is 5.5K and increases to 11.5K at 45°C. The system can therefore deliver a supply air temperature of approximately 20°C for an inlet temperature of 25°C and just under 33.5°C for an inlet temperature of 45°C. At 60% RH, temperature difference increases from approximately 3K at 25°C to 6.5K at 45°C, delivering processed air at 22°C and 38.5°C respectively. At 80% RH, temperature difference increases from just under 2K at 25°C to just over 3K at 45°C. This is to be expected as the driving mechanism for evaporative cooling is low.

Cooling capacity was determined based on the temperature difference and the average volume flow measured during the experiments. From a sample of  $n = 12$  air speed measurements, the average volume flow for the supply and working air were determined and the working to supply air volume flow ratio ( $AR$ ). Table 4 shows the results.

Figure 7a shows that the maximum cooling capacity was just over 1100W at an inlet temperature of 45°C and an RH of 40%, and the minimum was just over 130W at an inlet temperature of 25°C and an RH of 80%. These results show that substantial cooling can be achieved together with a decent sensible cooling effect.

The high temperature, low RH environment gives maximum performance because of the large driving mechanism, but it is applicable in only a few locations around the world, such as arid and dry regions, for example Houston, Arizona and Dubai, UAE. The largest potential market for such a system would be temperate, but hot climates around North America and the Mediterranean.

These climates experience moderate and high cooling demands ranging from 25°C and 40% to 60%RH to 35°C and 40% to 60%RH, so we can see from the results that the system could provide a supply air temperature of 19°C and 22°C, with cooling capacities of 500W and 300W at an inlet temperature of 25°C and 27°C

Table 4. Air speed and volume flows  $n = 12$

	Air speed $\bar{U}$ (m/s)	Duct diameter (mm)	Volume flow $\bar{V}$ (m <sup>3</sup> /h)
Supply air	6.39±0.18	125	282.42±8.07
Working air	3.51±0.51	100	99.22±4.09
Working to supply air ratio $AR$			0.35±0.02

Table 5. Electrical power consumption  $n = 15$

	Voltage $\bar{E}$ (V)	Current $\bar{I}$ (A)	Power $\bar{W}$ (W)
Blower 1	24.00	3.41	81.91±1.48
Blower 2	23.99	3.07	73.66±1.03
Pump	9.00	1.48	2.21±0.21
Total			157.78±2.13

and 30°C with cooling capacities of 750W and 600W, respectively at an inlet temperature of 35°C. The voltage and current consumed by the blowers and the pump were recorded during testing and Table 5 shows the mean of the voltages and currents from the individual components and the average overall power consumption. The power consumed by the system was on average approximately 158W. This was used to determine the COP of the system. Figure 7b shows how COP varies with inlet temperature and relative humidity. At 40%RH, COP increases from 3.28 at 25°C to 6.85 at 45°C. As RH increases, COP decreases. At 60%RH, COP increases from 1.87 at 25°C to 3.78 at 45°C and at 80%RH, COP increases from 0.84 at 25°C to just under 2 at 45°C. At low to medium conditions the system provides cooling with a COP from 2 to 5, and can achieve a COP up to 7.

### **Discussion and conclusions**

Preliminary testing showed great potential for the dew point cooler to provide cooling at high effectiveness. The product and working air flows discharged directly to the surroundings and so the pressure losses were low, resulting in an *AR* of around 4. When the core was integrated into a unit designed to provide cooling to a truck cabin and exhaust the working air, losses due to friction were introduced thus reducing flows. The working air flows were collected in side channels and ducted into one outlet and so there were large restrictions on that side, resulting in an *AR* of around 0.3. The restriction on working air flow meant that the system could not achieve high dew point effectiveness. However, we were able to achieve over 1kW of cooling and over 12K in temperature reduction in favourable operating conditions (low to medium RH and high ambient temperatures). The initial design utilised aluminium sections and plates to assist easy assembly and dismantling, but updates in its design will develop a one piece moulded plastic housing with a minimum of sharp turns, and restrictions. By improving the design, it is predicted that we can improve dew point effectiveness toward 80%, increase temperature reductions to 15K, cooling capacities of 1.5kW whilst reducing power consumption and thus increasing COP approaching 10.

### **Acknowledgements**

The research leading to these results has received funding from Innovate, UK, grant agreement No: 85311-533176.

### **References**

- [1] WEC, *Global Transport Senarios 2050*, World Energy Council, London, UK, p.76, 2010.
- [2] Forster, P. *et al*, *Changes in Atmospheric Constituents and in Radiative Forcing*, In: *Climate Change 2007: The Physical Science Basis. Contribution of Working Group I to the Fourth Assessment Report of the Intergovernmental Panel on Climate Change*, Cambridge University Press, UK, 2007.
- [3] Grof, T, *Greening of Industry under the Montreal Protocol*, United Nations Industrial Development Organization (UNIDO), p.30, 2009.
- [4] Mahmood, M, H, Sultan, M, Miyazaki, T, Koyama, S, Maisotsenko, V, S, “Overview of the Maisotsenko cycle,- a way towards dew point evaporative cooling”, *Renewable and Sustainable Enrgy Reviews*, V66, pp.537-555, 2016.
- [5] Evans, M, Rosenthal, J, S, *Probability and statistics: the science of uncertainty*, 2<sup>nd</sup> Ed, W. H. Freeman and Company, USA, p.638, 2009.

# Porous copper coated low pressure condenser/evaporator for sorption chillers

P. Cheppudira Thimmaiah<sup>1</sup>, A. Fradin<sup>1</sup>, W. Huttema<sup>1</sup> and M. Bahrami<sup>1\*</sup>

<sup>1</sup>Simon Fraser University, Laboratory for Alternative Energy Conversion (LAEC), School of Mechatronic Systems Engineering, Surrey, British Columbia, Canada

\*Corresponding author: mbahrami@sfu.ca

## Abstract

In sorption chillers, a vapor passage constriction between the evaporator or condenser and the sorber beds can significantly reduce the specific cooling power (SCP). Therefore, developing an efficient low pressure (LP) integrated evaporator/condenser unit (ECU) is key for enhancing the performance, reducing footprint, and costs. At low pressure (~1 kPa), the performance of a flooded evaporator is negatively affected by the hydrostatic pressure of the water column. To overcome this issue, it is necessary to exploit thin-film evaporation. However, for efficient condensation, dropwise condensation corresponds to a high heat transfer coefficient. Therefore, an integrated ECU should perform as both evaporator and condenser. In this study, we built a porous copper coated evaporator/condenser unit (ECU) and performed comprehensive experiments to investigate its performance. The primary objective of this study was to examine the performance of the coated ECU during condensation mode. Therefore, the performance of the coated ECU was compared with the performance of a commercial condenser (coil-in-shell coil, see Fig.1). The results showed that for the same chilled water inlet temperature, the condensing power of the ECU was, on average, 40% higher than the commercial condenser.

**Keywords:** Low-pressure, Heat Exchangers, Adsorption chillers, Integrated evaporator/condenser unit, open foam coating, Thermal spray.

## Introduction/Background

The sales of air conditioners are poised to intensely increase over the next several years as incomes and global temperatures rise around the world. The growth is not only driven by developed countries like the US, where almost 90% of homes have air conditioning systems but also driven by developing countries [1]. The leading example is China, where sales of air conditioners have nearly doubled over the last five years [2]. A surge in use of air conditioning systems may put an unparalleled demand on the global energy supply. Conventional air conditioning systems use vapor-compression refrigeration (VCR) technology that has been the dominant technology for close to a century, but their high energy consumption, around 36% of the consumption in the US building sector [3], and environmental impact are contrary to sustainable development. In addition to the residential sector, VCR systems for vehicle air conditioning (A/C) applications can cause a 20% increase in fuel consumption [4]. The automotive industry is coming to widespread agreement on the need to reduce emissions, and it is evident that in an internal combustion engine of a light-duty vehicle 65-70% of the total fuel energy released is dissipated as waste heat [5]. Moreover, while the commonly used refrigerants in VCR systems, hydrofluorocarbons (HFCs), are ozone-friendly, they still contribute to global warming. Therefore, using natural refrigerant such as water as an alternative refrigerant provides substantial environmental benefits over HFCs, including no toxicity and significantly lower global warming potential. Furthermore, water is an ideal refrigerant for systems driven by low-grade thermal energy (LGTE). LGTE, with a temperature less than 100°C, is available from many sources such as



solar-thermal, geothermal, and waste-heat from industrial facilities and data centers. LGTE can be used to run adsorption chillers for air conditioning of vehicle cabins, trains, ships and residential units. Due to the environmental benefits and energy savings, an LGTE-driven adsorption chiller is a promising technology. However, low specific cooling power (SCP) and low coefficient of performance (COP) are the main technical challenges facing commercialization of adsorption chillers and lead to its large size and mass compared to a VCR system. Furthermore, a vapor passage constriction between the evaporator or condenser and the sorber beds can significantly reduce the SCP. To this end, designing an efficient evaporator/condenser unit (ECU) plays a significant role in reducing the mass and size of a sorption chiller.

In a low pressure evaporator, the operating pressure of the refrigerant (water) is quite low (~1 kPa), and the cooling power generation in a flooded evaporator is negatively affected by the hydrostatic pressure along the height of the water column. This is particularly the case in a system that operates below atmospheric pressure, such as an adsorption chiller. Under such low evaporation pressures (~1 kPa), the height of the water column in the evaporator affects the water saturation pressure and, thus, its saturation temperature. For example, as shown in Figure 1, having a liquid water column of 5 cm in an evaporator creates a hydrostatic pressure of 0.49 kPa. For an evaporator operating at 1.0 kPa, this additional hydrostatic pressure increases the saturation temperature of water from 6.9°C at the surface to 13.0°C at a depth of 5 cm, where the pressure is 1.49 kPa (1.0 + 0.49 kPa). This temperature gradient inside the evaporator severely reduces the performance of an adsorption chiller. Despite this limitation, water is still an attractive choice of refrigerant due to its non-toxicity and high enthalpy of evaporation. This has motivated researchers to develop LP evaporators that optimize heat transfer by exploiting the evaporation of water in a thin film. Therefore, falling film evaporators that utilize pumps to spray a thin film of water on the external surface of the evaporator tubes are used. The benefit of falling film evaporators is a high overall heat transfer coefficient. However, there are drawbacks due to system complexity and added power consumption, weight, cost, and maintenance for the internal pumps.

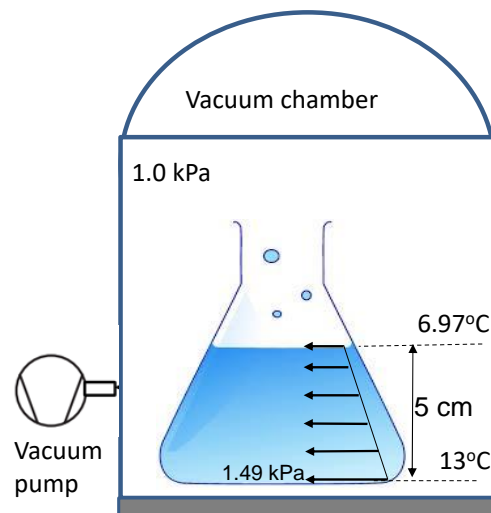


Figure 1. Schematic of the effect of hydrostatic pressure

To resolve this issue, we designed a new capillary assisted low pressure evaporator (CALPE). A CALPE draws water from a pool into the grooves between fins and covers the external surface of the evaporator tube using capillary forces, which draw the water along the grooves without the use of external power and uniformly distribute the water along the tubes, leading to thin film evaporation. We performed comprehensive experimental studies to investigate the performance of our CALPE. The test results showed that the external thermal resistance on

the outside of the evaporator tubes accounts for up to 60% of the overall thermal resistance in the LP evaporator [6]. To reduce the external thermal resistance, the outside surface of the evaporator tubes was coated with highly-porous open-cell copper metal foam. The overall heat transfer coefficient of the coated CALPE increased by a factor of 1.4, and the cooling power by a factor of two [9]. However, for efficient condensation, dropwise condensation corresponds to a higher heat transfer coefficient. Therefore, an integrated ECU should perform as both evaporator and condenser. In this study, we built a porous copper coated evaporator/condenser unit (ECU) and performed a comprehensive experimental study to investigate its performance. The primary objective of this study was to examine the performance of the coated ECU and analyze the impacts of geometry and porous coatings on the condensation performance of an ECU.

### Discussion and Results

Figure 2 shows our custom-made porous coated ECU and a commercial condenser (CC). A metal foam coating is applied by a thermal spray process using a Metco 12 E wire flame spray gun with 1/8" diameter copper wire. The spray gun was positioned 10" from the tubes, and burned acetylene and oxygen to heat the wire and deposit the atomized copper particles, more details can be found in Ref. [7]. The coating increases the external surface area and reduces the effective fin spacing. In Table 1, geometrical details of the tested ECU, CC and a vapor generator (VG) are listed.

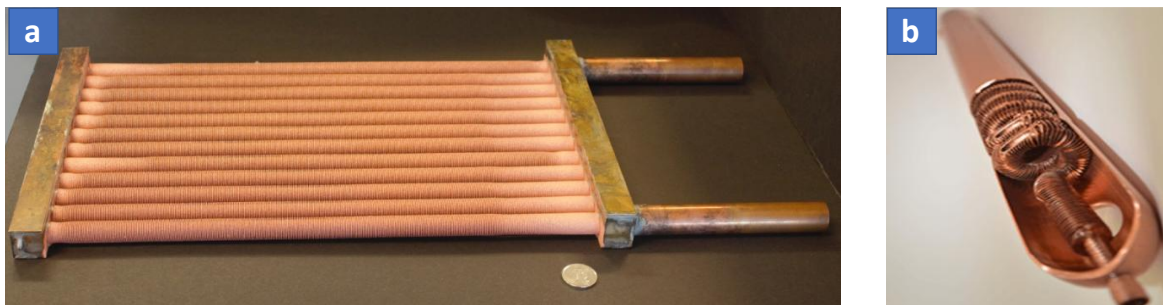


Figure 2: (a) our coated evaporator/condenser unit (ECU); b) commercial condenser unit.

Table 1: Comparison of porous coated condenser, commercial condenser and the vapor generator used in this study.

	<b>Porous coated condenser</b>	<b>Commercial condenser (CC)</b>	<b>Vapor Generator (VG)</b>
<b>Tubes</b>	GEWA®-K-2615 (Wieland Thermal Solutions)	King B Coil, (Wolverine Tube Inc.)	Turbo Chil-40 FPI (Wolverine Tube Inc.)
<b>Outside Diameter:</b>	1/2" (12.7 mm)	1/2" (12.7 mm)	3/4" (19.05 mm)
<b>Number of Fins</b>	26 fins per inch	9 fins per inch	40 fins per inch
<b>Inside surface area:</b>	0.024 m <sup>2</sup> /m	0.024 m <sup>2</sup> /m	0.051 m <sup>2</sup> /m
<b>Outside surface area:</b>	0.024 m <sup>2</sup> /m	0.33 m <sup>2</sup> /m	0.263 m <sup>2</sup> /m

The coating consists of open cell porous structures applied uniformly on all external faces of the tubes. In Figure 3a SEM imagery of the porous copper coating is shown from a top view at a scale range of 200  $\mu\text{m}$ . Zooming in to the 50  $\mu\text{m}$  scale range shows the open cell pores (Figure 3b). Zooming in further shows a pore opening at 12.1  $\mu\text{m}$  wide (Figure 3c). The thickness of the coated layer is approximately 250  $\mu\text{m}$ . The side view shows the small channels that are formed through connections between pores that allow the flow of water and vapor (Figure 3d).

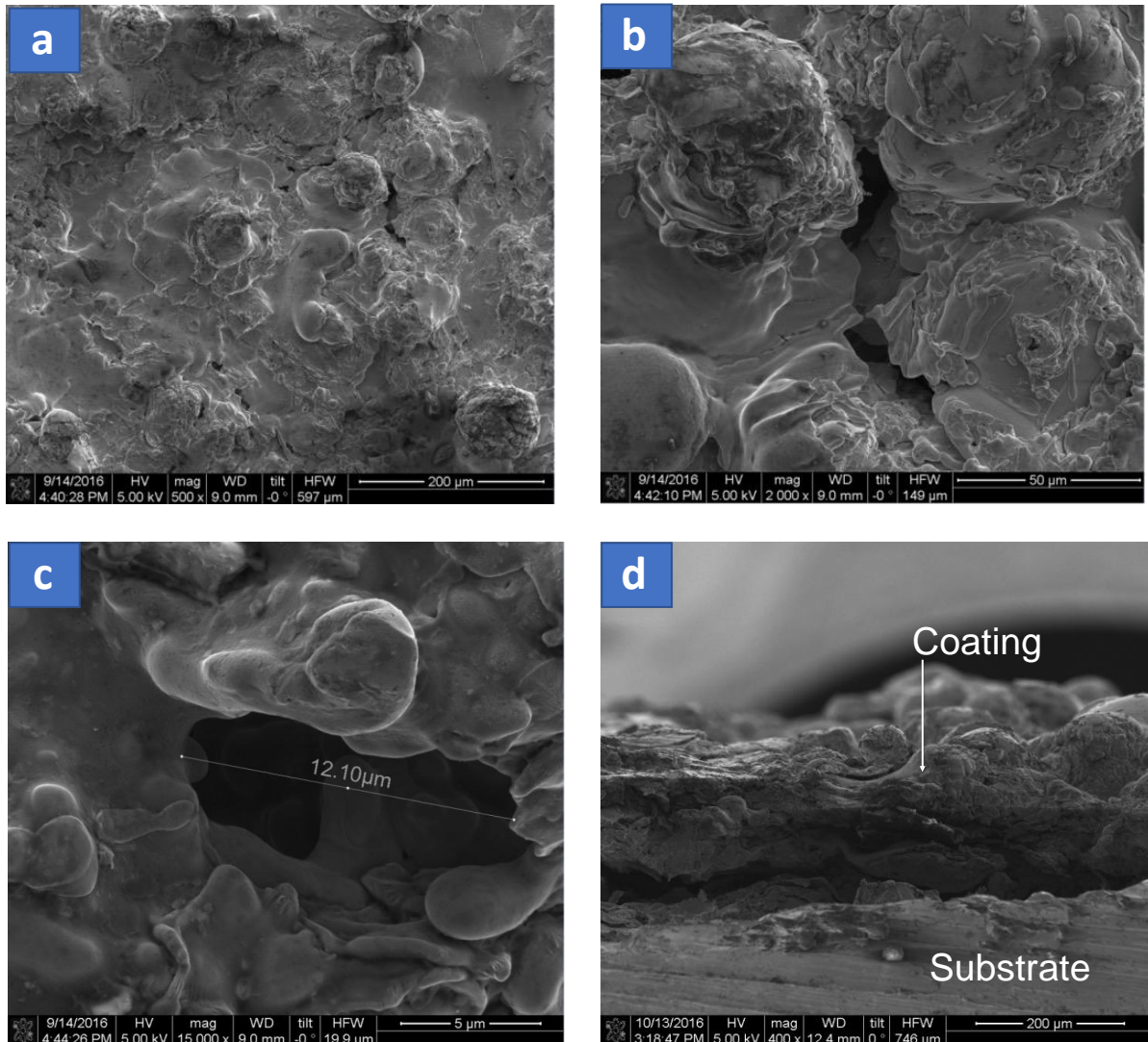


Figure 3 (a), (b), (c) and (d) SEM images of porous copper coatings.

The experimental setup, as shown in Figure 4, consisted of two vacuum chambers which were evacuated before the measurement using a vacuum pump. The condenser to be tested was mounted inside the measurement chamber (MG) while the secondary chamber (SG) contained a permanently installed large evaporator which was partially flooded by water and serves as a vapor generator (VG). The condenser and the vapor generator were connected to temperature control systems (TCS) to provide a constant temperature thermal fluid (chilled water) at different mass flow rates. Experiments began with the VG tubes submerged in a pool of water and continued as continuous evaporation decreased the height of the water and the water vapor was condensed on the surface of the coated tubes in the MG. The experiment was ended when the secondary chamber was dry. Our previous paper [8] contains the uncertainty analysis and detailed procedure of the test, along with the types of thermocouples,

pressure transducers, and flowmeters used and the details of the vacuum pump, cold trap and other components.

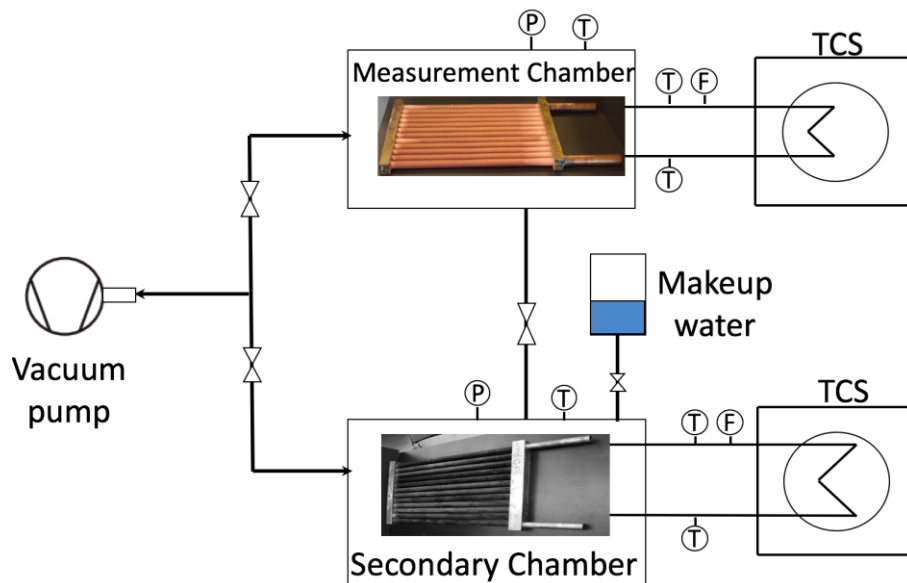


Figure 4 Schematic of the experimental setup.

The chilled water inlet and outlet temperatures,  $T_{in}$  and  $T_{out}$ , and mass flow rate as given in Table 1, are used to calculate the heat flow rate [20] as follows:

$$\dot{q} = \dot{m}_{in}(T_{out} - T_{in}) \quad (1)$$

The total condensation rate is calculated by time averaging the heat flow rate given in Eq. (1):

$$\dot{Q} = \frac{\int_{t_1}^{t_2} \dot{q} dt}{t_2 - t_1} \quad (2)$$

where  $t_1$  and  $t_2$  are the beginning and end of the time when the temperatures in the condenser are constant.

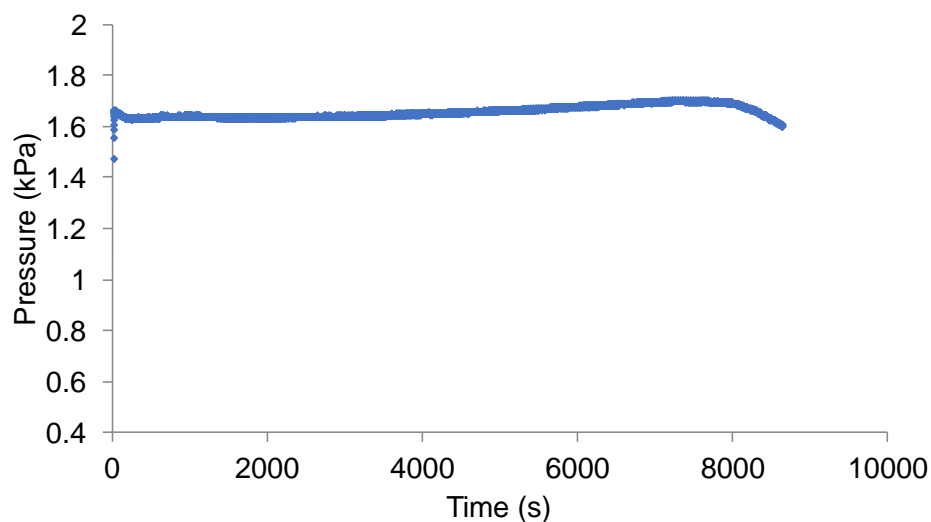


Figure 5: Operating pressure of condenser with coated ECU at the thermal fluid (chilled water) inlet temperature of 10°C over time. Data collection period is marked.

Figure 5 shows the operating pressure of the MG for a constant 10°C thermal fluid inlet temperature. As shown in Figure , when the control valve between the MG and the VG is opened, the condenser pressure slightly increases and then remains constant until the VG runs

out of water. The total heat transfer rate calculated from the steady state data from the region demarcated in grey in Figure .

In Figure 6, the total heat transfer rates are shown for the ECU custom-built from porous coated tubes and the evaporator (VG) built from Turbo Chil-40 FPI tubes. ECU has an average heat transfer rate of 260 W when operated at an inlet chilled water mass flow rate of 2.5 kg/m and 10°C. It should be noticed from Figure 6, when the control valve between the MG and the VG is opened, the condensing power of ECU starts to increase. This is because the entire porous coated surface area is available for condensation. It can also be attributed to dropwise condensation. However, this mechanism was not visually confirmed.

Also as the height of the liquid water increases over time due to condensation, it covers the available surface area of the porous copper coated tubes. Subsequently, the condensing power decreases over time. This behavior could be attributed to filmwise condensation taking over the initial dropwise condensation. However, visual confirmation is required to substantiate this claim.

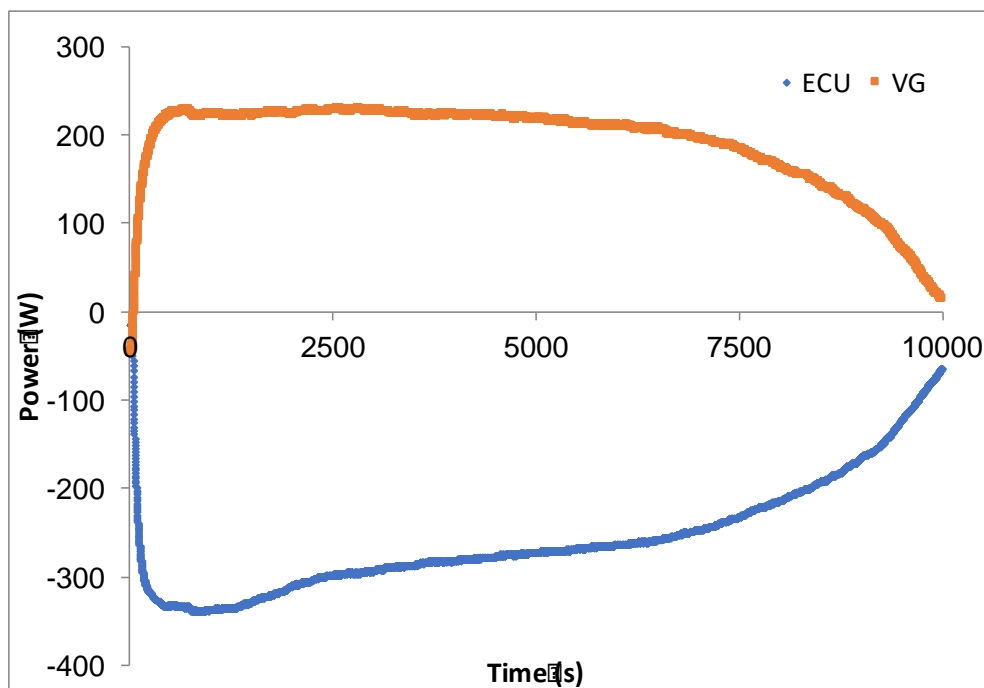


Figure 6 The behaviour of condensing power of ECU and cooling power of VG

Figure 6, also shows the cooling power of the VG. The VG is operated at an inlet chilled water mass flow rate of 2.5 kg/m and 15°C. As shown in Figure 6, the capillary phenomenon on the Turbo Chil-40 FPI finned tubes results in almost constant behavior starts to decreases when the water in the VG runs out of water. As the height of the liquid water decreases, the capillary action continues to cover the entire outside surface of the tube and maintains constant evaporation.

An off-the-shelf commercial condenser (CC) called King B Coil from Wolverine Tube Inc., featuring a larger surface area (0.33 m<sup>2</sup>/m) comparable to the surface area of VG was also tested; also see Table 1 for geometrical specs. The condensing power of the ECU and commercial condenser (CC) are compared in Figure 7. By increasing the chilled water inlet temperature difference ( $\Delta T$ ) between VG and ECU from 5°C to 15°C, the condensing power ( $\dot{Q}$ ) of the ECU increases from 260 to 1,000 W. The average  $\dot{Q}$  of our coated ECU is 40% higher than that of the CC.

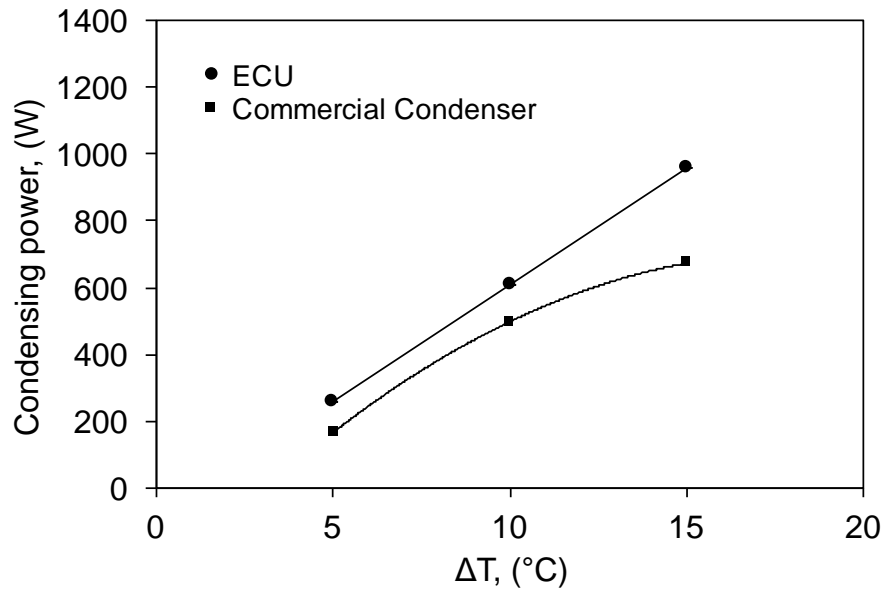


Figure 7: Comparison between custom-made evaporator-condenser unit and commercially available condenser

### Conclusions

Suitability of a porous copper coated evaporator/condenser unit (ECU) was tested for adsorption chillers with applications in vehicle air conditioning. In this study, we custom-built a porous copper coated evaporator/condenser unit (ECU) and performed a comprehensive experimental study to investigate its performance in our adsorption chiller testbed in the lab. The primary objective was to examine the performance of the coated ECU during condensation mode and compare it with a commercially available condenser. The ECU consisted of horizontal finned porous copper coated tubes. The vapor was generated using a commercial Turbo-Chil 40 FPI tubes. The condensing power of ECU was compared to an off the shelf commercial condenser (CC). The test results were promising and showed that the condensing power of the ECU was on average x% higher than that of the commercial condenser.

### Acknowledgements

The authors gratefully acknowledge the financial support of the Natural Sciences and Engineering Research Council of Canada (NSERC) through the Automotive Partnership Canada Grant No. APCPJ 401826-10. Authors are thankful to Wolverine Tube Inc. and Wieland Thermal Solutions for assisting our research by providing tube samples. Authors are also thankful to Dr. Claire McCague and Mr. Raaj Chatterjee for their kind support in conducting the experiments in the laboratory.

### References:

- [1] U.S. Department of Energy., *An Assessment of Energy Technologies and Research Opportunities*. Quadrennial Technology Review, 2015:1–505.
- [2] Lucas Davis., *The global impact of air conditioning: big and getting bigger*, The Conversation, 2016, <http://theconversation.com/the-global-impact-of-air-conditioning-big-and-getting-bigger-62882>.
- [3] William Goetzler, Robert Zogg, Jim Young CJ., *Energy Savings Potential and RD & D Opportunities for Non- Vapor-Compression HVAC*, Energy Effic Renew Energy 2014:3673. doi:10.2172/1220817.
- [4] Government of Canada., *Learn the facts Air conditioning and its effect on fuel consumption*, Natural Resources Canada, 2016.

- [5] Suzuki, M., *Application of adsorption cooling systems to automobiles*, Heat Recover Syst CHP,13:335–40.
- [6] Cheppudira Thimmaiah P, Sharafian A, Rouhani M, Huttema W, Bahrami M., *Evaluation of low-pressure flooded evaporator performance for adsorption chillers*, Energy 2017;122:144–58.
- [7] Menard E., *Thermal spray coatings*, Pyro Spray Inc., 2016.
- [8] Cheppudira Thimmaiah P, Sharafian A, Huttema W, McCague C, Bahrami M., *Effects of capillary-assisted tubes with different fin geometries on the performance of a low-operating pressure evaporator for adsorption cooling system applications*, Appl Energy 2016;171:256–65. doi:10.1016/j.apenergy.2016.03.070.
- [9] Poovanna, C.T., *Impact of Porous Copper Coating on Capillary-Assisted Low Pressure Evaporator for an Adsorption Chiller*, International Sorption Heat Pumps Conference, 2017

# "LiCl/vermiculite – methanol" as the new working pair for adsorption cycle “HeCol” for upgrading the ambient heat

A.D. Grekova<sup>1,2</sup>, L.G. Gordeeva<sup>1,2\*</sup> and Yu.I. Aristov<sup>1,2</sup>

<sup>1</sup>Boreshkov Institute of Catalysis, Ac. Lavrentiev av. 5, Novosibirsk 630090, Russia

<sup>2</sup>Novosibirsk State University, Pirogova st. 2, Novosibirsk 630090, Russia

\*Corresponding author: gordeeva@catalysis.ru

## Abstract

Adsorption heat transformation is an environment and energy saving technology for effective utilization of low-temperature heat sources. Recently, a novel adsorption cycle, so-called “Heat from Cold” (HeCol), has been suggested for upgrading the temperature of the ambient heat in cold regions up to higher level suitable for heating. This paper addresses the new composite sorbent of methanol LiCl/Verm, based on LiCl confined to pores of expanded vermiculite, specialized for the HeCol cycle. The equilibrium and dynamics of methanol sorption on the LiCl/Verm was studied under conditions of the HeCol cycle, and potential of this sorbent for utilization in the HeCol cycle was evaluated in terms of the heating capacity. The main findings are as follows: 1) the amount of methanol cycled at the HeCol cycle reaches 1.2 -1.5 g/g that far exceeds that for other adsorbents; 2) the heating capacity of the LiCl/Verm varies from 1.4 to 2.0 kJ/g under conditions of tested HeCol cycles that is of high practical interest.

**Keywords:** Adsorption heat amplification, Composite sorbent LiCl/vermiculite, Methanol, Equilibrium, Dynamics.

## Introduction/Background

Owing to growing living standards cooling and heating (C/H) have become one of the biggest energy sectors, and it is forecasted to remain so [1]. Nowadays growing C/H demands are still mainly being complied by utilizing fossil fuels as a primary energy source. However, renewable energy sources are expected to meet 40% of the increase in primary demand by 2040 [2]. Renewable C/H technologies have been recently compared to “sleeping giants”, since demand for such services is substantial, however historically renewable energy policies is focused primarily on renewable electricity or transport, missing an opportunity to target the largest energy demand sector. Thus, renewable cooling/heating represents low-hanging fruits that have often been overlooked [3]. The main barriers for the use of renewable heat sources for heating is a low temperature potential of the available heat, which is not sufficient for direct heating of dwellings. In this vein, sorption methods of heat amplification, or upgrading the temperature potential of the heat sources is gaining an increasing attention of the scientific community as an emerging technology, which makes it possible to overcome this barriers and to utilize the renewable heat sources for heating. To date, the major share of the researches on heat amplification relates to thermo-chemical heat amplification, or chemical heat pumps [4, 5, 6, 7, 8]. Different systems, namely “salt – ammonia” [4, 5], “salt – water” [6, 7], “metal oxide – water” [8], etc. have been suggested and studied as working pairs for heat amplification. The chemical heat pumps are mainly aimed to utilization of industry waste heat at temperature  $T = 80-150^{\circ}\text{C}$  as heat source to produce useful heat at  $T \approx 150 - 250^{\circ}\text{C}$ , which can be returned to the industry process that enhances its efficiency.



The working principle of the adsorption heat amplification (AHA) is based on the reversible processes of exothermal adsorption (heat generation) and endothermic desorption (heat consumption) [9]. AHA is still being at the initial research level, which is pointed out by the scarcity of reports on this subject [9, 10, 11]. Thus, 1-4 beds AHA system employing “zeolite– water” working pair was suggested in [9]. The temperature lift of 50 °C was shown can be reached; the 2-4 beds system allows enhancement of COP. Frazzica et al. have analysed the potential of two working pairs, namely “AQSOA FAM-Z02 – water” and “activated carbon AC208c – ammonia” for AHA. They demonstrated that the first pair can be employed for the cycles with the temperature of the heat source (65-85°C) and heat sink of 5°C with the temperature lift of 35-60°C and COP of 0.35-0.45. That makes it more interesting for upgrading the industrial waste heat [10].

Recently, a novel adsorption cycle, the so called “Heat from Cold” (HeCol), has been suggested for amplification of the ambient heat with ultra-low temperature potential [12]. It uses two natural heat reservoirs, both being at low temperature (about 0°C and below), to produce the heat at higher temperature. The ambient air at low temperature  $T_L$  is the heat sink, while a natural non-freezing water basin (ocean, sea, river, lake, underground water, etc.) at medium temperature  $T_M$  is the heat source. In cold countries during winter time, the temperature difference between them can reach 30°C and more, thus having a potential to produce a work, which then can be used for upgrading the temperature of the heat source up to a higher level  $T_H$  sufficient for heating. In the isothermal HeCol cycle (Fig. 1) the useful heat  $Q_{ad}$  is produced during the isothermal adsorption (2-3) and transferred to a consumer at temperature  $T_H$  [12]. The heat for evaporation  $Q_{ev}$  is consumed from the water basin at  $T_M$ . The regeneration of the adsorbent is carried out by a drop of the methanol pressure over the adsorbent. The desorption heat  $Q_{des}$  is consumed from the same water basin at temperature  $T_M$ ; the condensation heat  $Q_{con}$  is dissipated to the ambient at  $T_L$ . Thus, the heat of natural source at temperature  $T_M = 0-20^\circ\text{C}$  is transferred partially to the useful heat at higher temperature by means of rejection of the rest to the ambient at lower temperature. The HeCol cycle can be interesting for countries with cold climate: North Siberia, Canada, and especially for the Arctic.

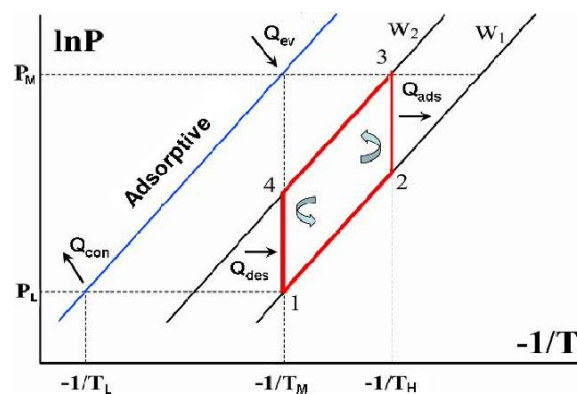


**Figure 1.** The isothermal 3-T HeCol cycle.

The adsorbent is a key component of the HeCol unit [13]. On the one hand, its affinity to working fluid (e.g. methanol) has to be large enough to adsorb methanol at high temperature  $T_H$  sufficient for heating. On the other hand, it has not to be too high to ensure the adsorbent be easily regenerated at the low temperature  $T_M$  of the available heat source.

Here we analyse the properties of the adsorbent optimal for the HeCol cycle and present the composite methanol sorbent, based on LiCl confined to the pores of expanded vermiculite, specialized for the HeCol cycle. The methanol sorption equilibrium is studied under typical

conditions of the HeCol cycle to evaluate the potential of the LiCl/Verm composite for selected HeCol cycles.

### 1. ADSORBENTS FOR HECOL CYCLE

For the adsorbents, whose equilibrium “adsorbent – methanol” obeys the Polanyi principle of temperature invariance [14] the uptake is a function of the only parameter – the Polanyi adsorption potential,  $w = f(\Delta F) = f(-RT \ln(P/P_0(T)))$  (Fig. 2 a). Consequently, the adsorbent optimal for the HeCol cycle has to exchange a large amount of methanol ( $\Delta w > 0.2-0.4$  g/g) under conditions of the HeCol cycle, means, between the values ( $\Delta F_2$  and ( $\Delta F_1$ ) corresponding to stages (1-2) and (3-4) in Fig. 1

$$\Delta w = w_2 - w_1 = w(\Delta F_2) - w(\Delta F_1) = w(-RT_H \ln(P_M/P_H)) - w(RT_M \ln(P_L/P_M)). \quad (1)$$

If two temperatures of the HeCol cycle, namely  $T_M$ , which is determined by the available heat source (natural water basin), and  $T_H$ , which depends on the consumer demands, are fixed, the pressure  $P_L^*$  necessary for the adsorbent to be regenerated can be estimated from the isotherms  $w = f(\Delta F)$ . Let's consider two adsorbents A1 and A2, whose adsorption equilibrium with methanol vapour is represented by isotherms A1 and A2, respectively (Fig. 2). At point 3 ( $T_H, P_M$ , Fig. 1), the methanol uptake equals  $w_2 = w(\Delta F_2) = w[-RT_H \ln(P_M/P_H)]$ . During desorption stage at ( $T_M, P_L$ ), the adsorbent can be regenerated if the value of  $\Delta F_1 = -RT_M \ln(P_L/P_M) \geq \Delta F^* = -RT_M \ln(P_L^*/P_M)$ , at which the methanol uptake falls down to minimum  $w^*$ . Then, the methanol pressure  $P_L^*$ , necessary for adsorbent to be regenerated, can be evaluated from the expression

$$P_L^* = P_M \exp(-\Delta F^*/RT_M). \quad (2)$$

Evidently, that adsorbent A2 with step-wise adsorption isotherm can be regenerated at higher pressure  $P_L^* = P_0(T_L^*)$ , means, under “milder” conditions of the HeCol cycle.

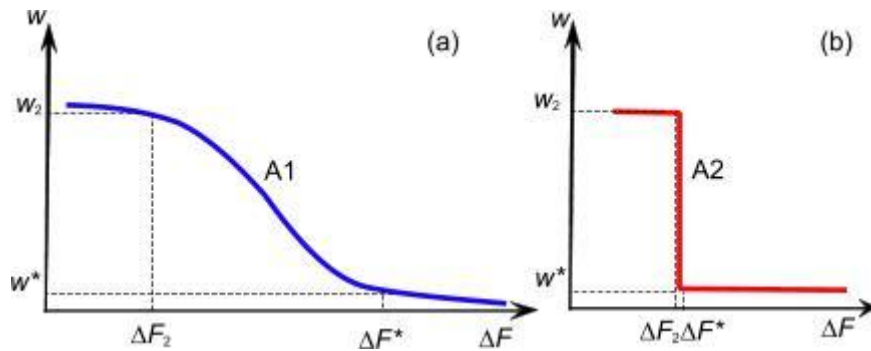


**Figure 2.** The common (A1) and step-wise (A2) methanol adsorption isotherms of the adsorbent optimal for the HeCol cycle.

Thus, the ideal adsorbent for the HeCol cycle is characterized by the step-wise (or more realistic S-shaped) adsorption isotherm with large uptake  $w_2 = w(\Delta F_2) = w(-RT_H \ln(P_M/P_H))$  and the step at  $\Delta F^*$  equal to (or somewhat higher)  $\Delta F_2$ .

## Experimental

Expanded vermiculite (specific surface area  $S_{sp} = 5.9 \text{ m}^2/\text{g}$ , pore volume  $V_p = 2.7 \text{ cm}^3/\text{g}$ , pore size  $d_{av} = 6.5 \text{ }\mu\text{m}$ ) was used as a host matrix for preparation of the composite sorbent. LiCl was purchased from Aldrich and used as delivered. The composite was synthesized by a dry impregnation method as follows. The vermiculite was dried at  $160^\circ\text{C}$  for two hours, impregnated with appropriate amount of the aqueous salt solution and dried again at  $160^\circ\text{C}$  until the sample weight remained constant. The composite LiCl/Ver was synthesized with the LiCl content 35 wt.%.

Sorption equilibrium of the LiCl/Verm composite with methanol vapour was studied by thermogravimetric method using a Rubotherm thermal balance (the accuracy  $\pm 0.00002\text{g}$ ). Sorption isobars and isotherms were measured in the temperature range  $28\text{--}150^\circ\text{C}$  at the vapour pressure of methanol  $P = 73, 96, 165, \text{ and } 213 \text{ mbar}$ . The equilibrium sorption was expressed as the mass  $m$  of sorbed methanol related to the dry sorbent mass  $m_0$

$$w = m(P,T)/m_0, \quad (3)$$

or by the number of methanol molecules per one molecule of LiCl

$$n = (w \cdot M_{\text{LiCl}}) / (M_{\text{CH}_3\text{OH}} \cdot C) \cdot 100, \quad (4)$$

where  $M_{\text{LiCl}}$  and  $M_{\text{CH}_3\text{OH}}$  are the molar masses of LiCl and methanol, respectively.

## Results and Discussion

### *Methanol adsorption equilibrium*

Isobars of methanol sorption on the LiCl/Verm composite are step-wise curves (Fig. 3a), which can be advantageous for the HeCol cycles. At high temperature, only minor amount of methanol ( $n = 0.2 \text{ mole/mole}$ ) adsorbs on the active centres of the surface. At decreasing temperature, LiCl starts to react with methanol according to the reaction [15],



that results in the sharp rise of the methanol uptake up to  $n \approx 3.0 \text{ mole/mole}$  with a mono-variant sorption equilibrium. At further decrease in temperature, the crystalline complex  $\text{LiCl} \cdot 3\text{CH}_3\text{OH}$  dissolves in the sorbed methanol forming a LiCl-methanol solution inside the pore space, which further absorbs methanol vapour. The uptake rises gradually; so that the equilibrium becomes di-variant. The methanol sorption capacity of LiCl/Verm composite reaches  $1.3 \text{ g/g}$  (Fig. 3a).

One can see from Fig. 3a that sorption and desorption branches of the isobars coincide with each other; no sorption-desorption hysteresis typical of bulk salts [16] is observed. That gives the indirect indication that dispersion of the salt inside the vermiculite pores is high enough to avoid the hysteresis. This is profitable for heat transformation, because allows the adsorbent to be regenerated at higher temperature  $T_L$  (or lower  $T_M$ ).

Based on the equilibrium data the isosteric heat of methanol sorption was calculated according to the equation

$$\ln P = \Delta H_{\text{ads}} / (R T) + C. \quad (6)$$

In the range of  $n$  from 0.1 to 3 mole/mole the isosteric heat of methanol sorption  $\Delta H_{\text{ads}} = (42 \pm 2)$  kJ/mol that is larger than the heat of methanol condensation  $\Delta L = 37.4$  kJ/mol [17]. This indicates a strong binding between the methanol molecules and LiCl in the structure of the crystalline complex  $\text{LiCl} \cdot 3\text{CH}_3\text{OH}$ .

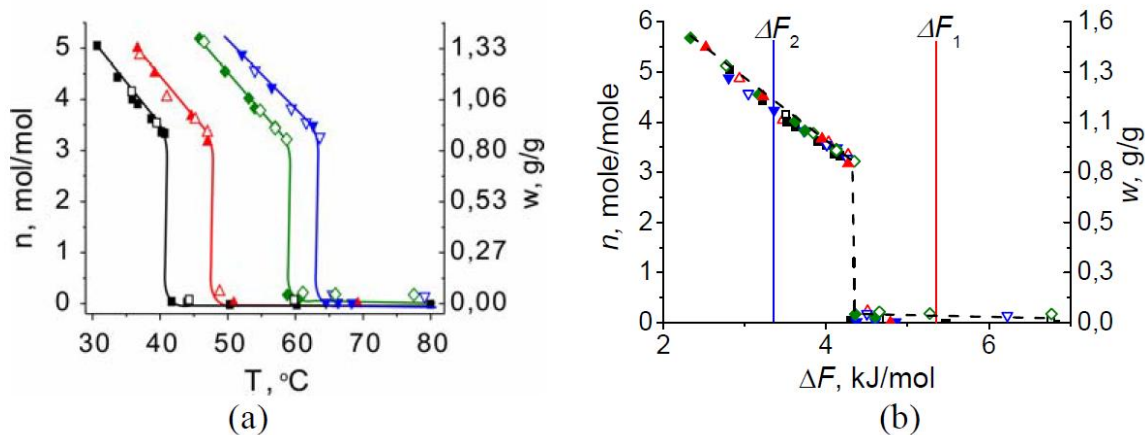


**Figure 3.** The isobars (a) and characteristic curve (b) of methanol sorption on the LiCl/Verm composite at  $P = 73$  (■, □),  $96$  (▲, △),  $165$  (◆, ◇) and  $213$  (▼, ▽) mbar. Solid symbols – sorption, open symbols – desorption.  $F_2$  and  $F_1$  – the values of the Polanyi potential corresponding to the adsorption and regeneration stages, respectively.

The methanol sorption isobars, presented as function of the Polanyi potential  $\Delta F$  coincide with each other (Fig. 3b) giving the characteristic curve of methanol sorption on the LiCl/Verm. The step-wise character of this curve with the abrupt uptake at  $F^* = 4.35$  kJ/mol is advantageous for the HeCol cycles.

Taking into account the dynamic aspects, some driving force is necessary during both adsorption and desorption stages to provide a reasonable reaction rate and consequently, a sufficient specific power of the heat release/consumption. The driving force for reaction (5) between LiCl and methanol is the difference  $\Delta(\Delta F)$  of the current adsorption potential  $F(P, T)$  during adsorption/desorption and the equilibrium potential of reaction (5)  $F^* = 4.35$  kJ/mol. It has been shown previously [18] that when  $\Delta(\Delta F) \approx 1.0$  kJ/mol reaction (5) did not limit the adsorption rate. In real cycles, the value of  $\Delta F_1$  during regeneration stage has to be higher than  $\Delta F^*$ , and  $\Delta F_2$  during adsorption stage has to be lower than  $\Delta F^*$  by  $\Delta(\Delta F) \approx 1.0$  kJ/mol. Consequently, the LiCl/Ver composite can be considered promising for the HeCol cycles with the operating conditions, satisfying the relationships  $\Delta F_2 \approx 3.35$  kJ/mol and  $\Delta F_1 \approx 5.35$  kJ/mol (Fig. 3 b). Several HeCol cycles that meet these requirements are presented in Table 2. The amount of methanol  $\Delta w$  exchanged under conditions of different HeCol cycles was evaluated according to eq. 1.

Under the tested operating conditions,  $\Delta w$  reaches 1.2-1.5 g/g (Table 2) that far exceeds the appropriate values for active carbons, LiCl/silica and CaClBr/silica composites [13, 19, 20].

#### **Evaluation of the heating capacity of LiCl/Verm**

The heating capacity of the LiCl/Verm was estimated as

$$Q_{\text{use}} = \Delta H_{\text{ads}} \Delta w - c_p (T_H - T_M) \quad (7),$$

where  $c_p$  is the specific heat of the composite. The  $Q_{use}$  varies from 1.4 to 2.0 kJ/g (Table 2) for different HeCol cycles that is superior to the appropriate values for activated carbons, LiCl/silica and CaClBr/silica composites [13, 19, 20]. Due to the high heating capacity of the LiCl/Verm it could be considered the promising adsorbent for the HeCol cycle.

**Table 2.** The amount  $\Delta w$  of methanol exchanged and the heating capacity of the LiCl/Verm at various HeCol cycles.

TL/TM/TH, °C	F2, kJ/mol	F1, kJ/mol	$\Delta w$ , g/g	$Q_{use}$ , kJ/g
-30/3/27	3.35	5.35	1.2	1.4
-25/10/35	3.40	5.61	1.2	1.4
-25/10/30	2.72	5.61	1.3	1.6
-20/20/45	3.2	6.20	1.2	1.4
-20/20/35	1.96	6.20	1.5	2.0

### Summary/Conclusions

The novel composite sorbent LiCl/Verm is intently prepared for the adsorption cycle HeCol recently suggested for upgrading the ambient heat temperature. The equilibrium of methanol sorption on the LiCl/Verm is studied under conditions of the HeCol cycles. It is shown that the amount of methanol exchanged reaches 1.0-1.5 g/g under the operating conditions of various HeCol cycles. The heating capacity of the LiCl/Verm varies from 1.4 to 2.0 kJ/g, which exceeds the appropriate values for other adsorbents.

### Acknowledgements

This work is supported by the Russian Science Foundation (grant 16-19-10259).

### References:

- [1] *Communication from the commission to the European parliament, the council, the European economic and social committee and the committee of the regions*, Brussel-2016, [https://ec.europa.eu/energy/sites/ener/files/documents/1\\_EN\\_ACT\\_part1\\_v14.pdf](https://ec.europa.eu/energy/sites/ener/files/documents/1_EN_ACT_part1_v14.pdf)
- [2] *World Energy Outlook-2017 (WEO-2017)*: International Energy Agency <http://www.iea.org/weo2017/>
- [3] de Vos, R., Sawin, J., *Heating and Cooling Policies, in: Renewable Energy Action on Deployment*, Elsevier Inc., 2012, pp. 115–135, [doi:10.1016/B978-0-12-405519-3.00007-4](https://doi.org/10.1016/B978-0-12-405519-3.00007-4)
- [4] Pal, M.V.D., de Boer, R., Veldhuis, J., “Thermally driven ammonia-salt type heat pump: development and test of a prototype”, *Proceedings of the Heat Powered Cycles Conference*, 2009, 7-9 September, Berlin.
- [5] Wu, S., Li, T.X., Yan, T., Wang, R.Z., “Experimental investigation on a novel solid-gas thermochemical sorption heat transformer for energy upgrade with a large temperature lift”, *Energy Conversion Management*, 2017,148, 330–338, [doi:10.1016/j.enconman.2017.05.041](https://doi.org/10.1016/j.enconman.2017.05.041)
- [6] Richter, M., Habermann, E.-M., Siebecke, E., Linder, M., “A systematic screening of salt hydrates as materials for a thermochemical heat transformer”, *Thermochimica Acta*, 2018, 659, 136–150. [doi:10.1016/j.rser.2010.10.007](https://doi.org/10.1016/j.rser.2010.10.007)
- [7] Esaki, T., Yasuda, M., Kobayashi, N., “Experimental evaluation of the heat output/input and coefficient of performance characteristics of a chemical heat pump in the heat

- upgrading cycle of CaCl<sub>2</sub> hydration”, *Energy Conversion and Management*, 2017, 150, 365–374, [doi:10.1016/j.enconman.2017.08.013](https://doi.org/10.1016/j.enconman.2017.08.013)
- [8] Odukoya, A., Naterer, G.F., “Calcium oxide/steam chemical heat pump for upgrading waste heat in thermochemical hydrogen production” *International Journal of Refrigeration*, 2015, 40, 11392-11398, [doi:10.1016/j.ijhydene.2015.03.086](https://doi.org/10.1016/j.ijhydene.2015.03.086)
- [9] Chandra, I., Patwardhan, V. S., “Theoretical studies on adsorption heat transformer using zeolite-water vapour pair.”, *Heat Recovery Systems and CHP*, 1990, 10, 527–537.
- [10] Frazzica, A., Dawoud, B., Critoph, R., “Theoretical analysis of several working pairs for adsorption heat transformer application” *Proceedings of HPC-2016*, 2016, 27-29 June, Nottingham, UK, paper n. 510.
- [11] Oktariani, E., Noda, A., Nakashima, K., Tahara, K., Xue, B., Nakaso, K., Fukai, J., “Potential of a direct contact adsorption heat pump system for generating steam from waste water”, *International Journal Energy Research*, 2012, 36, 1077–1087, [doi:10.1002/er.1855](https://doi.org/10.1002/er.1855)
- [12] Aristov, Yu. I., “Adsorptive transformation of ambient heat: a new cycle”, *Applied Thermal Engineering*, 2017, 124, 521–524, [doi:10.1016/j.applthermaleng.2017.06.051](https://doi.org/10.1016/j.applthermaleng.2017.06.051)
- [13] Gordeeva, L.G., Tokarev, M.M., Aristov, Yu.I., “New adsorption cycle for upgrading the ambient heat”, *Russian Theoretical Fundamentals Chemical Engineering*, 2018, 52, 195-205, [doi:10.1134/S0040579518020069](https://doi.org/10.1134/S0040579518020069)
- [14] Polanyi, M., “Theories of the adsorption of gas”, *Trans. Faraday Soc.*, 1932, 28, 316-333
- [15] Gmelin Data: 2000–2005 Gesellschaft Deutscher Chemiker licensed to MDL Information Systems GmbH; 1988–1999: Gmelin Institut fuer Anorganische Chemie und Grenzgebiete der Max-Planck- Gesellschaft zur Foerderung der Wissenschaften, vol. Li: SVol., pp. 395–440.
- [16] Gordeeva, L., Freni, A., Krieger, T., Restuccia, G., Aristov, Yu., “Composites “Lithium Halides in Silica Gel Pores”: Methanol Sorption Equilibrium”, *Microporous Mesoporous Materials*, 2008, [doi:10.1016/j.micromeso.2007.09.040](https://doi.org/10.1016/j.micromeso.2007.09.040)
- [17] CRC Handbook of Chemistry and Physics, 95th Edition Edited by William M. Haynes CRC Press New York; 2015, p 6-5, 6-140.
- [18] Gordeeva, L.G., Aristov, Yu.I., “Novel adsorbent of methanol “LiCl inside silica pores” for adsorption cooling: dynamic optimization”, *Energy*, 2011, [doi:10.1016/j.energy.2010.11.016](https://doi.org/10.1016/j.energy.2010.11.016)
- [19] Tokarev, M. M., Gordeeva, L.G., Aristov, Yu. I., “Testing the lab-scale “heat from cold” prototype with the “LiCl/silica – methanol” working pair”, *Energy Conversion and Management*, 2018, 159, 213-220, [doi:10.1016/j.enconman.2017.12.099](https://doi.org/10.1016/j.enconman.2017.12.099)
- [20] Tokarev, M. M., Gordeeva, L. G., Grekova, A. D., Aristov Yu. I., “A new cycle “Heat from Cold” for upgrading the ambient heat: the testing a lab-scale prototype with the composite sorbent CaClBr/silica”, *Applied Energy*, 2018, 211, 136-145, [doi:10.1016/j.apenergy.2017.11.015](https://doi.org/10.1016/j.apenergy.2017.11.015)

# Get your tubes wet: capillary-assisted thin-film evaporation of water for adsorption chillers

J. Seiler<sup>1</sup>, F. Lanzerath<sup>1</sup>, C. Jansen<sup>2</sup> and A. Bardow<sup>1\*</sup>

<sup>1</sup>Institute of Technical Thermodynamics, RWTH Aachen University, Schinkelstraße 8, 52062 Aachen

<sup>2</sup>Pallas Oberflächentechnik GmbH & Co. KG, Adenauerstraße 17, 52146 Würselen

\*Corresponding author: Andre.Bardow@ltt.rwth-aachen.de

## Abstract

The power density of water based adsorption chillers can be increased by thin-film evaporators. Thin-film evaporation is efficient, as it requires only low superheats. Here, the thin film is maintained by capillary action on copper tubes. We experimentally determine the overall heat transfer at evaporator temperatures of 10, 15 and 20°C with varied driving force at all filling levels. Our experiments show that good tubes remain fully wetted even at high driving force. Furthermore, we show that high porosity, surface extension and roughness promote the creation of a thin film and increase the heat transfer  $UA$ -value of the investigated tubes up to a factor of 10.

**Keywords:** capillary action, copper coating, overall heat transfer coefficient, tube.

## Introduction

Adsorption-based heat transformation devices can utilize low grade heat to provide environmentally benign heat and cold. Yet, these devices suffer from poor power density [1]: besides the adsorber, the evaporator design is crucial for higher power densities [2], [3]. Key for higher power densities in the evaporator is an increased heat transfer coefficient.

Efficient heat transfer is difficult for adsorption processes, since they often use the natural refrigerant water which is environmentally safe and offers high enthalpy of vaporization [4]. Efficient evaporation of water is challenging due to its low saturation pressure at typical operating conditions of adsorption devices that prevents high heat transfer rates through nucleate boiling. Nucleate boiling would start at the heated surface. Here, the actual saturation temperature is higher than at the water surface since the static head of the liquid above the heat exchanger surface increases the pressure. For water at typical operating conditions of adsorption devices, this pressure increase is of the same order as the saturation pressure. As a result, nucleate boiling of water at sub-atmospheric pressure occurs with strong wall temperature fluctuations and mainly at high superheat [5]. However, heat transfer involving high superheat is inefficient and leads to higher evaporator temperatures. Therefore, using nucleate boiling is not feasible for efficient sub-atmospheric evaporation of water.

Efficient sub-atmospheric evaporation of water with small superheats is possible when the static head of the liquid is reduced by employing thin-film evaporation. A thin film can be created on the surface of the heat exchanger by capillary action [6]. To create the necessary capillary action different structures have been proposed:

- (1) Macroscopic structures, e.g. finned tubes [6–8], tube-fin [9] and metallic short fiber structures [10]
- (2) Microscopic structures, e.g. coatings [7, 11, 12]
- (3) Combination of macroscopic and microscopic structures [7]

Today, these structures need to be characterized experimentally as commonly accepted design and sizing guidelines are lacking. Besides structure, previous studies investigated the influences of many parameters on capillary-assisted-thin-film evaporation: all experiments show that the heat transfer increases with rising evaporator temperature [6, 7, 11].

Furthermore, the filling level, which describes the degree to which the heat exchangers are submerged in the refrigerant, is an important parameter. Lanzerath et al. [7] and Xia et al. [6] found increasing heat transfer with lower filling levels. In contrast, Thimmaiah et al. [11] observed a maximum heat transfer coefficient at a filling level of about 0.8, whereas Volmer et al. [9] reported that the combination of filling level and heat exchanger geometry affects the heat transfer. The different findings show that the filling level is important for evaluation, however its impact is not yet fully understood. The influence of the driving force for heat transfer has also been investigated: In common pool boiling with natural convection (stagnant boiling), the heat transfer coefficient increases with increasing driving force [13]. For thin-film evaporation, however, Xia et al. [6] reported a decrease of the heat transfer coefficient with increasing driving force. In contrast, Lanzerath et al. [7] found no influence of the driving force. Volmer et al. [9] also stated that pretests to their study showed no significant impact of the driving force. Hence, the effect of driving force is also inconclusive in the published studies and requires further investigation.

In this study, we investigate the influence of filling level, driving force, and temperatures on the heat transfer. We show that previous different findings can be understood by the role of wetting. Wetting of the tube is crucial for thin-film evaporation and is enabled by capillary action on the tube's surface. To analyze the impact of the microscopic structural properties on wetting, we vary and experimentally examine the tubes' surfaces. We characterize the evaporation performance at different temperatures and driving forces. Finally, we correlate the tube surface properties with the measured evaporation performance of the tubes to provide a guideline for future thin-film evaporation evaporator design.

### Experimental setup

An experimental setup was designed to determine the evaporation performance of the investigated tubes at different evaporator temperature, driving force and filling level. The setup consisted of two main components: evaporator and condenser. Both components were connected via a steam valve and a valve for liquid reflux. All components and tubes were thermally insulated to minimize heat flows to and from the surroundings. The evaporator was a vacuum-tight, cylindrical steel vessel that holds four identical tubes, which were connected in series. The investigated coated-copper tubes (inner diameter 13 mm, outer diameter 15 mm) were coated for a length of 500 mm each.

Thermal energy for the evaporation process was provided by a thermostat with water as heat transfer fluid. The driving force of the evaporation process was set by the condenser via its saturation pressure. The condenser consisted of a vacuum-tight, cylindrical steel vessel that contained a double helix made from copper tube as heat exchanger. The heat exchanger was connected to a thermostat, again with water as heat transfer fluid. The inlet temperature of the water was kept constant by a thermostat.

In- and outlet temperatures  $T_{\text{in}}$  and  $T_{\text{out}}$  in the evaporator were measured with calibrated PT100 resistance thermometers (class A, four-wire connection,  $u_{T_{\text{in}}-T_{\text{out}}} < 0.01$  K). The volume flow  $\dot{V}$  through the investigated tubes was determined by a volume flow sensor (Huba Control, type 210,  $u_{\dot{V}} = 0.32$  lmin<sup>-1</sup>). The evaporation pressure was determined by two separate pressure transducers (ABB, 266AST,  $u_p = 0.04$  mbar); both showed the same readings within the measurement uncertainty in all experiments.

### Experimental procedure

The tubes were fully immersed in the refrigerant, since the dry tubes are hydrophobic and not able to wet themselves by capillary action only. However, once the tubes are fully wetted, they show hydrophilic behavior. The driving force of the evaporation process is adjusted by the temperature difference between evaporator and condenser. The water was evaporated and



the filling level decreased continuously, since no water was refilled into the evaporator. The experiment ended when the refrigerant lost contact to the tubes. This experimental procedure allows to include all possible filling levels in one single experiment [7]. Technically, we did not measure steady-state values. However, all measured sensor values were in quasi-steady state condition. Experiments were conducted according to common operation conditions of evaporators in adsorption systems. Each experiment was repeated at least three times. The standard deviations of the repeated experiments amplified by the corresponding value from the t-distribution from GUM [14] are mostly below the size of the symbols used in Figs. 4-6. Therefore, we did not include error bars in the figures.

### Data reduction

To characterize the heat transfer, we used the overall heat transfer coefficient  $U$  multiplied by the effective surface area  $A_{\text{eff}}$  where the heat transfer takes place.  $UA_{\text{eff}}$  is calculated by

$$UA_{\text{eff}} = \frac{\dot{Q}}{\Delta T_{\text{ln}}}, \quad (1)$$

with the heat flow  $\dot{Q}$  from the heat transfer fluid into the evaporator and the logarithmic temperature difference  $\Delta T_{\text{ln}}$ . The heat flow  $\dot{Q}$  was calculated from a steady-state energy balance of the tubes by

$$\dot{Q} = \dot{V} \rho_{\text{in}} (h_{\text{in}}(T_{\text{in}}) - h_{\text{out}}(T_{\text{out}})), \quad (2)$$

where  $\dot{V}$  is the volume flow of the heat transfer fluid in the inside of the tubes,  $\rho_{\text{in}}$  the density,  $h_{\text{in}}(T_{\text{in}})$  and  $h_{\text{out}}(T_{\text{out}})$  the enthalpies of the heat transfer fluid at the in- and outlet of the evaporator. The steady-state assumption for this energy balance is reasonable as shown by Lanzerath et al. [7]. The logarithmic temperature difference between the heat transfer fluid and the refrigerant is the driving force for the heat flow from the heat transfer fluid into the refrigerant. The logarithmic temperature difference  $\Delta T_{\text{ln}}$  is calculated from

$$\Delta T_{\text{ln}} = \frac{T_{\text{in}} - T_{\text{out}}}{\ln \left( \frac{T_{\text{in}} - T_{\text{s}}}{T_{\text{out}} - T_{\text{s}}} \right)}, \quad (3)$$

where  $T_{\text{in}}$  and  $T_{\text{out}}$  are the measured temperatures at the evaporator in- and outlet. The steam temperature  $T_{\text{s}}$  is the saturation temperature of water corresponding to the measured pressure  $p$  in the evaporator:

$$T_{\text{s}} = T_{\text{sat}}(p). \quad (4)$$

All needed fluid properties were calculated with TILMedia [15] based on RefProp [16] with data from [17] and [18].

### Investigated tubes

We investigated 7 sets of tubes with coatings A-G and one set of plain uncoated tubes H as benchmark. The coatings were characterized by microscopic metallographic analysis of cross-section polishes to obtain surface properties. Properties were analyzed which are influenced by the coating process and may have an impact on the evaporation performance.

Measured surface properties were: surface extension, layer thickness, surface roughness ( $R_z$ ) and porosity (Table 1). Surface extension is the ratio of the available heat transfer area and a perfect cylinder with the same diameter. The plain tube (H) also has a surface extension slightly larger than 1 indicating that the raw material for the coated tubes is not a perfect cylinder. Layer thickness of the coating is a key parameter of the coating process as it reflects the amount of coating material on the tube and thus also affects its production cost. Profile roughness and porosity are two important properties for wetting and capillary action on the surface [19, 20]. The profile roughness  $R_z$  used here is determined by averaging the maximum valley-to-peak distances of five consecutive sampling lengths of 100  $\mu\text{m}$ . The porosity is the ratio of the available pore volume to the total volume in the coating determined by graphical analysis of the cross-section polishes.

Table 1: Surface properties measured for tubes A-H in descending order of surface roughness.

tube	unit	A	B	C	D	E	F	G	H
surface roughness $R_z$	$\mu\text{m}$	72	71	61	56	47	38	37	5
surface extension	-	1.71	1.53	1.69	1.53	1.48	1.47	1.27	1.08
layer thickness	$\mu\text{m}$	218	282	105	189	49	89	322	0
porosity	%	18.3	4.1	13.8	11.5	14.1	8.6	1.2	0
Symbol in Fig. 2		×	△	□	◇	+	○	*	▽

## Discussion and Results

The conducted experiments vary in 4 dimensions: 1) evaporator temperature  $T_{\text{in}}$ , 2) driving temperature difference  $T_{\text{in}} - T_{\text{in,cond}}$ , 3) filling level  $f$  and 4) tube coating A to H. In order to present the results of all conducted experiments, further data reduction is necessary. The  $UA_{\text{eff}}$ -value is determined as a function of the filling level  $f$ . Since the objective of this work is to increase the  $UA_{\text{eff}}$ -value, we characterize each tube by the maximum  $UA_{\text{eff}}$ -value,  $UA_{\text{eff,max}}$ , at the corresponding filling level  $f(UA_{\text{eff,max}})$ . For tube A and B, these characteristic numbers are shown as function of the measured driving force  $\Delta T_{\text{in}}$  for different evaporator temperatures in Fig. 1.

For both tubes A and B,  $UA_{\text{eff,max}}$  increases with higher evaporator temperature  $T_{\text{in}}$ . This finding holds in fact for all tubes and is in agreement with other published studies. The increase in  $UA_{\text{eff,max}}$  has most likely two main causes [6, 7, 11]: (1) The heat transfer on the inner side of the tube is part of the overall heat transfer  $U$  and increases with temperature [6, 7]. (2) Properties of water such as density and viscosity are also temperature-dependent: the steam density generally increases with increasing temperature also resulting in a better heat transfer [13]. The viscosity decreases with increasing temperature possibly leading to a lower resistance for the mass transfer through capillary action.

Another important characteristic is the filling level  $f(UA_{\text{eff,max}})$  at which  $UA_{\text{eff,max}}$  was detected: if  $UA_{\text{eff,max}}$  does not occur at the lowest possible filling level, not all of the available heat transfer area on the tube is used and dry-out of the tube has most likely started. Although, theoretically, the available heat transfer area should not further increase below a filling level of zero, the area occupied by the meniscus connecting the water to the tube continues to decrease for filling levels below zero. Thus, the available area for thin-film evaporation increases even further for filling levels below zero. The measured filling levels  $f(UA_{\text{eff,max}})$  in Fig. show that  $UA_{\text{eff,max}}$  starts decreasing strongly when the corresponding filling level  $f(UA_{\text{eff,max}})$  increases. For tube A, only a minor increase in  $f(UA_{\text{eff,max}})$  is present at logarithmic temperature differences  $\Delta T_{\text{in}} > 3 \text{ K}$ . Tube A showed the best evaporation performance of all investigated tubes: good tubes thus work at high driving

forces (heat flows) without dry-out. Therefore, in order to assess the performance limits of tubes, maximum  $UA_{eff}$ -values at high driving forces need to be evaluated.

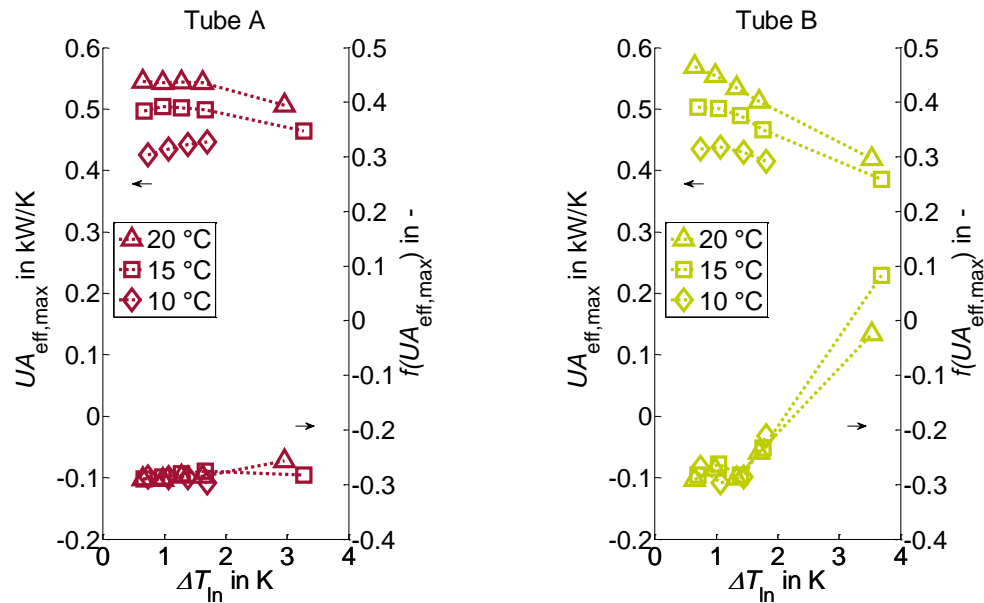


Fig. 1: Maximum overall heat transfer coefficient multiplied with effective heat transfer area  $UA_{eff,max}$  (left axis of the graphs) with corresponding filling level  $f(UA_{eff,max})$  (right axis of the graphs) for evaporator temperatures of 10, 15 and 20°C as function of driving force ( $\Delta T_{in}$ ) for coated tubes A (left) and B (right). Each experiment was repeated at least three times. Error bars are mostly below the symbols' size (see Experiments).

The experiments suggest that the impact of driving force  $\Delta T_{in}$  on the heat transfer coefficient in the investigated range ( $\Delta T_{in} < 4\text{K}$ ) is negligible as long as the thin film is present on the whole tube and dry-out does not occur. In this case, the lowest possible filling level is optimal in terms of heat transfer. However, for reliable operation, it is important to ensure that the contact between the water and the tube is not lost. Therefore, a higher filling level might be chosen as a tradeoff between reliability and performance in practice.

Direct comparison of the findings with previous studies is difficult, since not all previous studies state whether dry-out occurred during the experiments. Xia et al. [6], for example, measured lower  $U$ -values for higher driving forces for macroscopic structures. However, they did not mention whether dry-out occurred. Lanzerath et al. [7] found no impact of the driving force on the  $U$ -value. The authors observe the maximum  $U$ -value at the lowest possible filling level indicating that dry-out did not occur. Thimmaiah et al. [11] determined the optimal filling level to be at 0.8. They report that the tube did not provide sufficient capillary action to fully wet the tubes at lower filling levels, thus parts of the tubes were dry in their experiments. Thus, as mentioned before, the impact of the driving force is inconclusive in literature but possible dry-out in the experiments by Xia et al. [6] could, however, explain the different results: dry-out of the tubes could be responsible for the decrease in  $U$ -values for higher driving forces reported by Xia et al. [6] as we observe the same effect.

Generally, previous studies agree that lower filling levels lead to higher  $U$ -values [6, 7], which is in agreement with our findings reported here. Our work now shows that this behavior is found as long as the tube is fully wetted.

As long as a thin water film is present on the tube, our results show that the  $UA$ -value for evaporation is independent of the driving force. The larger the available surface area for thin-film evaporation is, the larger the  $UA$ -value becomes. Therefore, it is important to create and

maintain a thin-film on the entire surface of the tube. The thin film is maintained by capillary action, which is governed by the characteristics of the surface. Therefore, we correlate the tubes surface characteristics to the maximum  $UA$ -value. For each tube, we correlate the evaporation performance measured by the  $UA_{\text{eff,max}}$ -value to the surface properties given in Table 1. Since measured  $UA_{\text{eff,max}}$ -values depend on the evaporator temperature  $T_{\text{in}}$  and the driving force  $\Delta T_{\text{ln}}$ , further data reduction is necessary to obtain a single evaluation parameter for each investigated tube. As the influence of evaporator temperature is similar for all tubes, we choose the medium temperature  $T_{\text{in}}$  of  $15^\circ\text{C}$  for further data reduction. To merge the measurements with different driving forces  $\Delta T_{\text{ln}}$  into one single value, we use a weighted average value. We select the logarithmic temperature differences  $\Delta T_{\text{ln}}$  as weights, to reflect the difficulty to keep the tubes wetted at higher driving forces:

$$\overline{UA_{\text{eff,max}}} = \frac{\sum_i UA_{\text{eff,max}}(\Delta T_{\text{ln},i}) \Delta T_{\text{ln},i}}{\sum_i \Delta T_{\text{ln},i}} \quad (5)$$

The calculated average maximum  $UA$ -values  $\overline{UA_{\text{eff,max}}}$  are correlated to the 4 surface properties of the tubes A-H characterized in Table 1 (Fig. 2). Tube A has the highest  $(\overline{UA_{\text{eff,max}}})$ -value of almost 0.5 kW/K. Tubes B, C, E and D have similar high  $(\overline{UA_{\text{eff,max}}})$ -values, tubes F and G show comparably low  $(\overline{UA_{\text{eff,max}}})$ -values. The plain tube H offers the lowest  $(\overline{UA_{\text{eff,max}}})$ -value of about 0.05 kW/K. Thus, the coating improves the  $(\overline{UA_{\text{eff,max}}})$ -value by up to a factor 10.

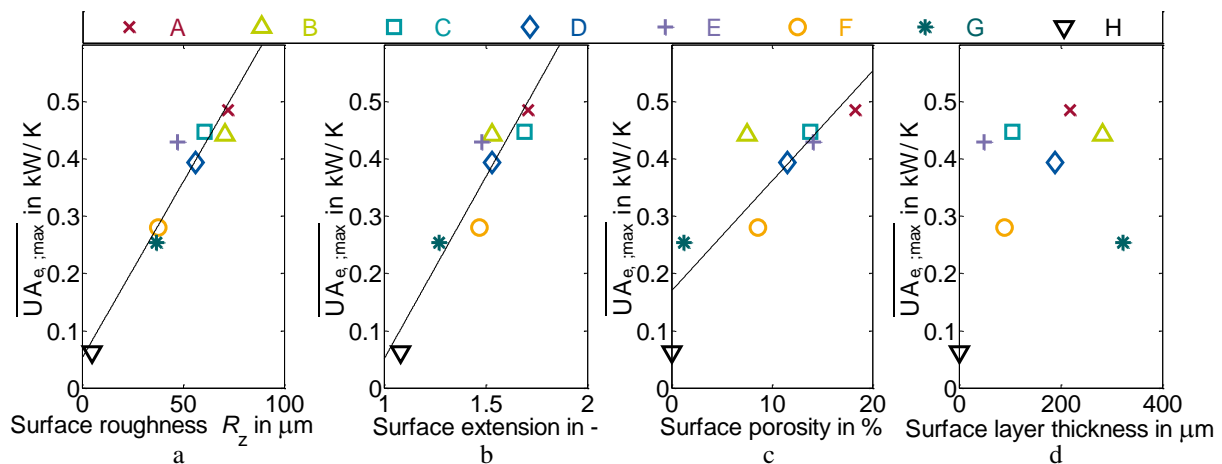


Fig. 2: Average maximum overall heat transfer coefficient multiplied with effective heat transfer area -  $\overline{UA_{\text{eff,max}}}$  as function of roughness, surface extension, porosity and layer thickness (left to right) for different tubes A-H. Linear correlations are given as black lines.

Fig. 2 (a) and b) demonstrates a positive correlation between surface roughness and  $(\overline{UA_{\text{eff,max}}})$ -value and between surface extension and  $(\overline{UA_{\text{eff,max}}})$ -value. Surface extension directly affects the available surface area for the heat transfer process. Thus, a positive correlation between surface extension and  $(\overline{UA_{\text{eff,max}}})$ -value is probably causal. However, the increase in the  $(\overline{UA_{\text{eff,max}}})$ -value is larger than the proportional relationship of  $U$  multiplied by  $A$  suggests. Therefore, other effects should also be of significance. Surface roughness has been shown to amplify capillary forces [21]. Therefore, the positive trend in the correlation between surface roughness and  $(\overline{UA_{\text{eff,max}}})$ -value might also be based on a causal connection.

Fig. 2 (c) suggests that surface porosity also seems to be correlated to the  $(\overline{UA_{\text{eff,max}}})$ -value. In general, porosity might enhance mass transfer through the coating as porosity could create

capillary action and increase the cross section available for mass transfer. However, more experiments are necessary to fully understand the effect of porosity on the evaporation performance.

The layer thickness of the coating seems not to be correlated to the  $(\overline{UA_{\text{eff,max}}})$ -value (Fig.2, d). It is possible that lower layers of the coating are not accessible for the refrigerant. Therefore, thin coatings are favorable, as layer thickness does not have a significant impact on performance and costs can generally be reduced with thinner coatings.

It is to be noted that the best evaporation performance was measured at the highest value of all three correlated surface characteristics: surface roughness, extension and porosity. Therefore, it seems likely that further improvements are possible which should be experimentally evaluated.

## Conclusions

To improve the understanding of thin-film evaporation phenomena, we experimentally investigated the evaporation performance of 7 coatings and a plain tube for all filling levels at different temperatures and driving forces. Evaporation performance was then correlated with surface characteristics of the tubes. The conducted experiments contribute the following key results:

- (1) The investigated coatings increase the  $UA$ -value compared to plain tubes by a factor of up to 10.
- (2) Increasing evaporator temperatures lead to higher  $UA$ -values.
- (3) The optimal filling level should be as low as possible to exploit the maximal available heat transfer area for thin-film evaporation. For reliable operation, however, higher filling levels can be reasonable to ensure continuous contact between tube and refrigerant.
- (4) The impact of the driving force on the  $U$ -value is not detectable as long as the tubes are kept fully wetted by sufficient capillary action. At high driving forces, dry-out of the tubes decreases the  $U$ -value.
- (5) Good coatings are able to maintain a thin film on the tubes' surfaces by capillary action even at higher driving forces. The investigated coatings vary considerably in their ability to maintain a thin film.
- (6) Higher porosity, surface extension and roughness improve the evaporation performance. Coating layer thickness can be thin as no impact on evaporation performance was found.

Thin-film evaporation increases the overall heat transfer coefficient for sub-atmospheric evaporation about one magnitude compared to pool boiling with a plain tube. Hence, more efficient evaporators for adsorption heat pumps are rendered possible. To tap this potential, creation of a thin film on the heat exchanger is crucial. Our results show that the way is: get your tubes wet!

## Acknowledgements

We thank Pallas Oberflächentechnik GmbH & Co. KG for providing the coated heat exchanger tubes and gratefully acknowledge the financial support from the German Federal Ministry for Economic Affairs and Energy in the Central Innovation Programme for SMEs (ZIM).

## References

- [1] Li, X. H., Hou, X. H., Zhang, X., Yuan, Z. X., "A review on development of adsorption cooling— Novel beds and advanced cycles", *Energy Conversion and Management*, 2015, doi:10.1016/j.enconman.2015.01.076.

- [2] San, J.-Y., Tsai, F.-K., "Testing of a lab-scale four-bed adsorption heat pump", *Applied Thermal Engineering*, 2014, doi:10.1016/j.applthermaleng.2014.05.014.
- [3] Lanzerath, F., Bau, U., Seiler, J., Bardow, A., "Optimal design of adsorption chillers based on a validated dynamic object-oriented model", *Science and Technology for the Built Environment*, 2015, doi:10.1080/10789669.2014.990337.
- [4] Wang, L. W., Wang, R. Z., Oliveira, R. G., "A review on adsorption working pairs for refrigeration", *Renewable and Sustainable Energy Reviews*, 2009, doi:10.1016/j.rser.2007.12.002.
- [5] Giraud, F., Rullière, R., Toublanc, C., Clause, M., Bonjour, J., "Experimental evidence of a new regime for boiling of water at subatmospheric pressure", *Experimental Thermal and Fluid Science*, 2015, doi:10.1016/j.expthermflusci.2014.07.011.
- [6] Xia, Z. Z., Yang, G. Z., Wang, R. Z., "Experimental investigation of capillary-assisted evaporation on the outside surface of horizontal tubes", *International Journal of Heat and Mass Transfer*, 2008, doi:10.1016/j.ijheatmasstransfer.2007.11.042.
- [7] Lanzerath, F., Seiler, J., Erdogan, M., Schreiber, H., Steinhilber, M., Bardow, A., "The impact of filling level resolved", *Applied Thermal Engineering*, 2016, doi:10.1016/j.applthermaleng.2016.03.052.
- [8] Thimmaiah, P. C., Sharafian, A., Huttema, W., Osterman, C., Ismail, A., Dhillon, A., Bahrami, M., "Performance of finned tubes used in low-pressure capillary-assisted evaporator of adsorption cooling system", *Applied Thermal Engineering*, 2016, doi:10.1016/j.applthermaleng.2016.06.038.
- [9] Volmer, R., Eckert, J., Fuldner, G., Schnabel, L., "Evaporator development for adsorption heat transformation devices – Influencing factors on non-stationary evaporation with tube-fin heat exchangers at sub-atmospheric pressure", *Renewable Energy*, 2017, doi:10.1016/j.renene.2016.08.030.
- [10] Witte, K., *Experimentelle Untersuchungen zum Sieden in Metallfaserstrukturen im Bereich niedriger Drücke* [PhD thesis]. Darmstadt, Technische Universität Darmstadt, 2016.
- [11] Thimmaiah, P. C., Sharafian, A., Rouhani, M., Huttema, W., Bahrami, M., "Evaluation of low-pressure flooded evaporator performance for adsorption chillers", *Energy*, 2017, doi:10.1016/j.energy.2017.01.085.
- [12] Sabir, H. M., Bwalya, A. C., "Experimental study of capillary-assisted water evaporators for vapour-absorption systems", *Applied Energy*, 2002, doi:10.1016/S0306-2619(01)00042-3.
- [13] Baehr, H. D., Stephan, K., *Heat and Mass Transfer*, 3rd ed., Springer Berlin, 2014.
- [14] Joint Committee for Guides in Metrology (JCGM), "Evaluation of measurement data - Guide to the expression of uncertainty in measurement", 2008, [http://www.bipm.org/en/publications/guides/gum\\_print.html](http://www.bipm.org/en/publications/guides/gum_print.html).
- [15] Schulze, C., *A Contribution to Numerically Efficient Modelling of Thermodynamic Systems* [PhD thesis]. Braunschweig, Technische Universität Braunschweig, 2013.
- [16] Lemmon, E. W., McLinden, M. O., Friend, D. G., "Thermophysical properties of fluid systems", In: Lindstrom, P. J., Mallard, W. G. (Eds.), *NIST Standard Reference Database*, 2013.
- [17] Cox, J. D., Wagman, D. D., Medvedev, V. A., *CODATA Key Values for Thermodynamics*, Hemisphere Publishing Corp, 1989.
- [18] Chase, M. W., Jr., *NIST-JANAF Thermochemical Tables*, 4. Edition, J. Phys. Chem. Ref. Data Monograph, 1998.
- [19] Faghri, A., *Heat pipe science and technology*, Taylor & Francis, 1995.
- [20] Cho, H. J., Preston, D. J., Zhu, Y., Wang, E. N., "Nanoengineered materials for liquid–vapour phase-change heat transfer", *Nature Reviews Materials*, 2016, doi:10.1038/natrevmats.2016.92.

[21] Chu, K.-H., Enright, R., Wang, E. N., "Structured surfaces for enhanced pool boiling heat transfer", Applied Physics Letters, 2012, [doi:10.1063/1.4724190](https://doi.org/10.1063/1.4724190).

# Analytical Investigation of Zeolite-NaY-Water for Sorption Heat and Cold Storage Utilizing High Temperature Heat

K. Geilfuß<sup>1</sup> and B. Dawoud<sup>2\*</sup>

<sup>1</sup>OTH Regensburg Technical University of Applied Sciences, Faculty of Engineering, Galgenberg Str. 30, 93053 Regensburg, Germany, Tel.: +49-941-943-9418 (Laboratory for sorption processes), Email: [kristina.geilfuss@st.oth-regensburg.de](mailto:kristina.geilfuss@st.oth-regensburg.de)

<sup>2</sup> OTH Regensburg Technical University of Applied Sciences, Faculty of Engineering, Galgenberg Str. 30, 93053 Regensburg, Germany, Tel.: +49-941-943-9892, Email: [belal.dawoud@oth-regensburg.de](mailto:belal.dawoud@oth-regensburg.de)  
Corresponding author: email address ([belal.dawoud@oth-regensburg.de](mailto:belal.dawoud@oth-regensburg.de))

## Abstract

Storage technologies play an essential role in compensating the discrepancy between surplus energy and peak times. Sorption processes, in particular, offer an environment friendly way for almost loss-free heat (of adsorption or absorption) and cold storage. This work is dedicated to analytically investigate the potential of applying NaY-Water/Zeolite as a working pair for heat and cold storage upon utilizing high temperature heat. It turned out that the mass of the adsorber heat exchanger increases the useful specific heat stored from 229 kWh/t<sub>zeolite</sub> for the ideal storage to 538 kWh/t<sub>zeolite</sub> or even higher depending on the thermal capacity of the adsorber heat exchanger (AdsHX). Contrary to that trend, COP will decrease with increasing the thermal capacity of the AdsHX. Sensible heat losses between charging and discharging phases do have a **negative** effect on both stored heating capacity and COP.

**Keywords:** Adsorption, heat storage, cold storage, zeolite NaY-Water

## Introduction

Increasing emissions of greenhouse gases and other climate-damaging gases accelerate global warming. The energy sector, especially the generation of heat, cold and electricity, contributes significantly to the climate change. Therefore, more efficient and environment friendly technologies are indispensable. Over the last decades, the interest in storage techniques has been increasing in order to find a solution for the discrepancy between periods of surplus energy and peak times. Sorption processes offer a very promising technology for heat and cold storage. One of the main advantages encountered herewith, is that most of the working pairs are entirely environment friendly, have neither ozone-depletion nor global-warming potential. In the last decades, sorption technologies have been considered mainly for solar cooling or heat pumping [1]. Research in sorption technologies is still focusing on decreasing the unit cost and increasing both durability and efficiency in order to increase the market penetration rates [2-4].

The two main sorption principles are absorption (liquid-gas) and adsorption (solid-gas). Adsorption can be further divided into physisorption, attributed to Van der Waals forces, and chemisorption, attributed to the reaction between the adsorbate and the surface molecules of the adsorbent [3]. Common adsorbents for physisorption are activated carbon, silica gel and zeolite. For chemisorption, metal chlorides, metal hybrids and metal oxides are used as adsorbents. The monovariant characteristic of chemisorption leads to stable working temperatures in contrast to the unstable working temperature of physisorption due to its



bivariant characteristic [5]. Chemisorption has shown some critical shortcomings: after desorption, complexation can occur between chlorides and ammonia leading to salt swelling and agglomeration that reduces heat and mass transfer performance [3, 6]. Zondag et al. [7] found that HCl was formed during the dehydration of  $\text{MgCl}_2 \cdot 6\text{H}_2\text{O}$  at temperatures above 135 °C and has degraded the storage material and the metal parts due to its strong corrosive nature. In order to improve the heat and mass transfer performance of the original chemical adsorbents, composite adsorbents combine chemical adsorbents with porous mediums, such as activated carbon or expanded graphite [3, 5, 8-10]. Another group of adsorbent material are the so-called metal-organic frameworks (MOFs) that offer a huge surface area, large pore volume and flexible chemical and physical properties, but suffer from weak thermal and hydrothermal stability [11].

First storage prototypes have been tested or designed with different or innovative storage materials and new reactor concepts [3, 12]. In view of exergy analysis, sorption systems may be as efficient as and more compact than other thermal energy storage systems [13]. Thereby, the working performance of sorption energy storage does not only depend on stored materials and the design of heat exchangers, but also on the thermodynamic cycle within the specified operating conditions [12, 14].

The heat of adsorption can be stored almost loss-free whereas sensible heat may be lost during the storage time [15, 16]. The experimental analysis of Schreiber et al. [15] shows that the energy recovery ratio is reduced upon increasing the charging temperature from 170 °C to 250 °C from 91 % to 85 % for continuous cycling and from 74 % to 69 % for cyclic operation with 2 h storage time. At a charging temperature of 250 °C, the maximum energy storage density of 22 kWh/m<sup>3</sup> for the ideal operation without heat losses (energy recovery ratio of 100 %) is diminished to 20 kWh/m<sup>3</sup> for the continuous cycling and to 17 kWh/m<sup>3</sup> for the cyclic operation with 2 h storage time. These results show indeed quite high sensible losses and define the construction target for design reviewing the storage concept to minimize such storage losses.

Li et al. [17] analyzed the performance of an integrated energy storage and energy upgrade thermochemical gas-solid sorption system for seasonal storage of solar thermal energy. Two operation modes depending on the ambient temperature (-30 °C to 15 °C) are encountered in winter; at ambient temperatures above 0 °C, the released heat is used directly for heating the building, whereas at lower temperatures, the stored thermal energy must be upgraded first using a solid-gas thermochemical sorption heat transformer cycle. In this work, the effect of reactor thermal capacity and global conversion on the working performance was considered. A reactor mass ratio  $R$  is defined as the mass of metallic parts of the reactor heat exchanger divided by the mass of the reactive salt in a solid-gas reactor. The global conversion  $X$  represents the percentage of the salt that reacted with the refrigerant during a reaction process. Thermodynamic analysis shows that at  $R$  of 5,  $X$  of 0.85 and heat output temperature of 62 °C, a useful heat of 1043 kJ/kg<sub>salt</sub> at a COP of 0.60 is obtained when the ambient temperature is 0 °C. At an ambient temperature of -20 °C, heat of 579 kJ/kg<sub>salt</sub> with a COP of 0.34 is obtained by first upgrading the ambient heat using the thermochemical heat transformer cycle. An experimental study carried out by Li et al. [18] showed, that  $X$  must be increased, which requires a considerably long reaction time or high heat and mass transfer rates, whereas heat losses and  $R$  must be reduced.

Schreiber et al. [19] considered the adsorption thermal energy storage for cogeneration in industrial batch processes such as beer brewing. Once in every 6 hours, a large amount of process heat is needed at a temperature level of 120 °C for 1h. Cogeneration charges an adsorption thermal energy storage unit with heat up to 250 °C for 5 h. During the discharge of the storage, the combined heat outputs of the storage and cogeneration satisfy the high process heat demand. In order to reduce heat losses, a performant insulation is recommended. It has been proposed that, in order to reach the highest system performance, the heat needed for the evaporator should be supplied from waste, excess or ambient heat, and the heat of condensation should be used.

In combination with water as refrigerant, zeolites offer an environment friendly, effective and easy-to handle alternative to the above-mentioned materials. Zeolite NaY is one of the most stable zeolites against hydro-thermal cycling [20] and its application becomes more promising at temperatures above 150 °C. This work introduces an analytic study to investigate the effect of the most important design and operating conditions on the performance of high temperature heat ( $\geq 200$  °C) storage for day/night heat and cold storage applications. Following the procedure of Freni et al. [20], the coefficient of performance *COP*, defined as the ratio between the mass-specific useful heat as well as the mass-specific cooling effect and the mass specific heat of desorption will be represented by a set of dimensionless parameters and their effect on *COP* shall be **investigated** and thoroughly discussed.

### Thermochemical storage cycle

Figure 1 depicts a schematic of the investigated zeolite water sorption storage module. The hermetically sealed module composes three heat exchangers. The adsorber/desorber heat exchanger (AdsHX) is located between an evaporator at the lower part and a condenser at the upper part. The evaporator is connected to the AdsHX by an actuated valve, while the AdsHX to the condenser by a non-return valve. Additionally, the condenser and evaporator are connected by a pipe and an actuated valve. The adsorption cycle is illustrated schematically in Figure 2 in a Clapeyron diagram of the working pair zeolite NaY-water (Clariant). An ideal periodical cycle is represented by the state points 1 to 6. Temperature gradients encountered in the heat exchangers are represented by  $\Delta T_{Ads}$ ,  $\Delta T_{Ev}$ ,  $\Delta T_{Con}$  and  $\Delta T_{Des}$ , shifting the state points 1 to 6 to I to VI.

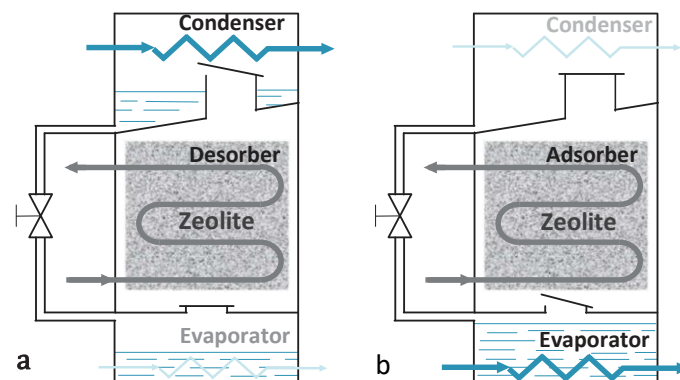


Figure 1: Schematic of a sorption storage with three heat exchangers; a) during charging: desorption and condensation and b) during discharging: adsorption and evaporation

Figure 1a illustrates the storage in the charging phase, during which the adsorber/desorber heat exchanger is connected to the heat source at high temperature. During the first part of this operation phase; namely, the preheating of the adsorbent (from state point I to II), the pressure of the gas phase increases from the evaporator (VI) to the condenser level (V). As soon as the water vapor pressure exceeds the saturation pressure corresponding to the cooling water inlet temperature into the condenser, the condenser non-return valve opens. From this point on, water vapor is condensed and collected in the condenser. This desorption and condensation phase proceeds almost isobaric until the maximum temperature and, consequently, the corresponding minimum refrigerant uptake is reached (III). The storage time begins and the adsorbent may be cooled due to stand-by thermal losses down to state (III'). The pressure in the adsorber/desorber compartment decreases leading to closing the condenser non-return valve. During the storage time, the actuated valve connecting the evaporator and adsorber is kept closed.

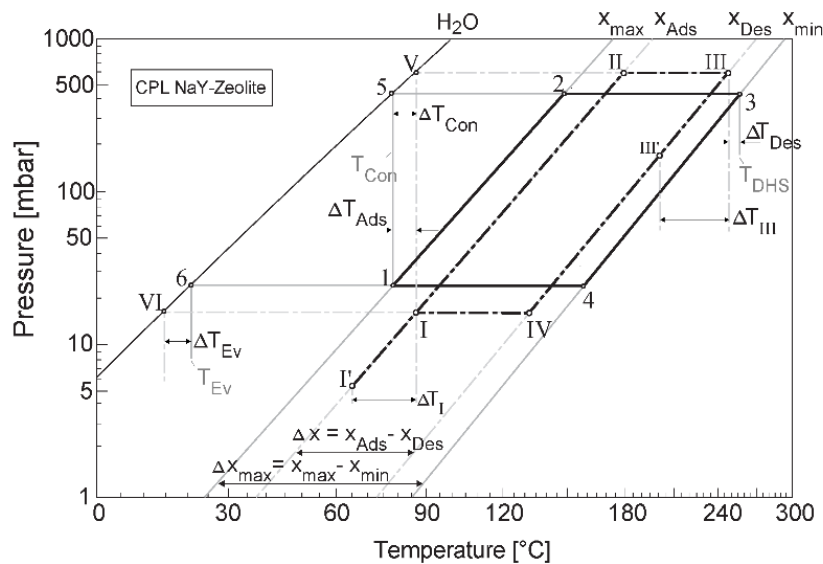


Figure 2: Clapeyron diagram of the working pair zeolite NaY-water (Clariant)

The discharge phase (Figure 1b) begins first by opening the water discharge valve in the pipe connecting the condenser and the evaporator, in order to let the desorbed and condensed water to flow into the evaporator. The adsorber heat exchanger is then connected to the heating network. The adsorbent cools down (precooling) until the pressure decreases to the corresponding saturation pressure of the inlet temperature of the evaporator (IV). The valve is then opened and the adsorbent starts to adsorb water vapor from the evaporator and the heat of adsorption is released, which is transferred to the heating network as useful heat. The adsorption phase continues until the zeolite is saturated at the evaporator pressure and heating network temperature (I). Due to standby thermal losses  $T_I$  may decrease to  $T_I'$ .

### Energy balance

The complete energy balance, neglecting heat losses to the surroundings and the electrical work for pumps and valves, is described by

$$Q_{PC} + Q_{Ads} + Q_{Con} = Q_{Ev} + Q_{PH} + Q_{Des} \quad (1)$$

A thermochemical storage stores mainly the heat of adsorption ( $Q_{Ads}$ ). For short term storage applications, both heat of precooling ( $Q_{PC}$ ) and heat of condensation ( $Q_{Con}$ ) can be utilized. The sum of those three types of heat represent the useful heat ( $Q_h$ ). If the cooling effect of the evaporator ( $Q_{Ev}$ ) upon discharging is also utilized, the maximum performance ( $COP_{h\&c}$ ) can be obtained.

$$COP_{h\&c} = \frac{Q_{PC} + Q_{Ads} + Q_{Con} + Q_{Ev}}{Q_{PH} + Q_{Des}} \quad (2)$$

The heat of precooling considers the cooling of the adsorbent mass (zeolite) and of the adsorber/desorber heat exchanger including its heat transfer medium (AdsHX) from  $T_{III'}$  to  $T_{IV}$ . The average heat capacity of the wetted zeolite  $\bar{c}_{p,III'-IV}$  is estimated at the average temperature per kg of dry zeolite.

$$Q_{PC} = [m_{Ads} \cdot \bar{c}_{p,III'-IV} + (m \cdot c)_{AdsHX}] \cdot (T_{III'} - T_{IV}) \quad (3)$$

During the adsorption phase, the adsorbent and the AdsHX, including its heat transfer medium, are cooled down from  $T_{IV}$  to  $T_I$  and heat of adsorption is released upon adsorbing (= condensing and binding) the refrigerant (water) in the adsorbent.

$$Q_{Ads} = [m_{Ads} \cdot \bar{c}_{p,IV-I} + (m \cdot c)_{AdsHX}] \cdot (T_{IV} - T_I) + m_{ref} \cdot \bar{q}_{Ads} \quad (4)$$

The heat of adsorption  $\bar{q}_{Ads}$  includes the binding energy  $q_B$  applied by the adsorbent on the adsorbed refrigerant and the evaporation enthalpy  $h_{fg,ref}$ .

$$\bar{q}_{Ads} = q_B + h_{fg,ref} \quad (5)$$

The heat of preheating includes the preheating of the adsorbent mass and of the AdsHX, including its heat transfer medium, from  $T_{I'}$  to  $T_{II}$ .

$$Q_{PH} = [m_{Ads} \cdot \bar{c}_{p,I'-II} + (m \cdot c)_{AdsHX}] \cdot (T_{II} - T_{I'}) \quad (6)$$

The heat required for the desorption includes the heating up of the adsorbent and of the AdsHX, including its heat transfer medium, from  $T_{II}$  to  $T_{III}$  and the release of the refrigerant in its vapor phase ( $\bar{q}_{Ads}$ ).

$$Q_{Des} = [m_{Ads} \cdot \bar{c}_{p,II-III} + (m \cdot c)_{AdsHX}] \cdot (T_{III} - T_{II}) + m_{ref} \cdot \bar{q}_{Ads} \quad (7)$$

During desorption, the desorbed refrigerant vapor is first de-superheated from the average temperature between state points II and III down to the saturation temperature  $T_V$  and condenses then at the same temperature

$$Q_{Con} = m_{ref} \cdot (\bar{h}_{II-III} - h_{f,V}) \quad (8)$$

The heat of evaporation is estimated as the heat of evaporation of the refrigerant at  $T_{VI}$ .

$$Q_{Ev} = m_{ref} \cdot h_{fg,ref,VI} \quad (9)$$

The mass of refrigerant exchanged in one charging/discharging phase is calculated according to eq.(10).

$$m_{ref} = m_{Ads} \cdot \Delta x \quad (10)$$

The differential water uptake ( $\Delta x$ ) is defined by eq. (11), as the difference between the water uptakes at state points I and III, where the refrigerant uptake  $x$  describes the ratio between the adsorbed refrigerant mass to the dry absorbent mass.

$$\Delta x = x_{Des} - x_{Ads} \quad (11)$$

#### Dimensionless parameters

The coefficient of performance ( $COP_{h\&c}$ ) for heat and cold storage illustrated in Figure 1 will be represented by a set of dimensionless parameters based on the approach described by Freni et. al. [20] for intermittent adsorption heat pumps. In addition, the heat of precooling and the heat of adsorption are summed up to  $Q_{PC,Ads}$  and the heat of preheating and the heat of desorption are summed up to  $Q_{PH,Des}$  in order to simplify the derivation of dimensionless parameters.

$$COP_{h\&c} = \frac{Q_{PC,Ads} + Q_{Con} + Q_{Ev}}{Q_{PH,Des}} \quad (12)$$

The specific heat capacity  $\bar{c}_{Ads}$  per kg of dry adsorbent is averaged from state point I to state point III'.

$$Q_{PC,Ads} = [m_{Ads} \cdot \bar{c}_{Ads} + (m \cdot c)_{AdHX}] \cdot (T_{III'} - T_I) + m_{Ads} \cdot \Delta x \cdot \bar{q}_{Ads} \quad (13)$$

The total useful heat  $Q_h$  and cold  $Q_c$  are expressed by Eq. (14).

$$Q_{PC,Ads} + Q_{Con} + Q_{Ev} = [m_{Ads} \cdot \bar{c}_{Ads} + (m \cdot c)_{AdHX}] \cdot (T_{III'} - T_I) + m_{Ads} \cdot \Delta x \cdot \bar{q}_{Ads} + m_{Ads} \cdot \Delta x \cdot (\bar{h}_{II-III} - h_{f,v}) + m_{Ads} \cdot \Delta x \cdot \bar{h}_{fg,ref} \quad (14)$$

By analogy to Eq.(13), the temperature difference of  $(T_{III} - T_I')$  takes the additional heat of preheating into account, due to sensible heat losses during the storage (standby) time.

$$Q_{PH,Des} = [m_{Ads} \cdot \bar{c}_{Ads} + (m \cdot c)_{AdHX}] \cdot (T_{III} - T_I') + m_{Ads} \cdot \Delta x \cdot \bar{q}_{Ads} \quad (15)$$

The temperature loss after the desorption phase (during the storage time) can be specified using  $\Delta T_{III}$ .

$$T_{III'} - T_I = (T_{III} - T_I) + (T_{III'} - T_{III}) = (T_{III} - T_I) - \Delta T_{III} \quad (16)$$

By analogy, the temperature loss after the adsorption phase (before the next charging phase) can be represented using  $\Delta T_I$ .

$$T_{III} - T_I' = (T_{III} - T_I) + (T_I - T_I') = (T_{III} - T_I) - \Delta T_I \quad (17)$$

$COP_{h\&c}$  can be obtained by dividing eq. (14) by eq. (15). The temperature differences are then replaced by eq. (18) and (19), the counter and denominator are divided by  $m_{Ads} \cdot \Delta x \cdot \bar{h}_{fg,ref}$  and the dimensionless parameters are introduced (cf. eq. (22)).

$$COP_{h\&c} = \frac{2 + K_{2-ads-ref} \cdot \left(1 - \frac{\Delta T_{III}}{T_{III} - T_I}\right) \cdot (1 + K_{AdsHX}) + K_{1-ads-ref} + K_{ref}}{1 + K_{2-ads-ref} \cdot \left(1 + \frac{\Delta T_I}{T_{III} - T_I}\right) \cdot (1 + K_{AdsHX}) + K_{1-ads-ref}} \quad (18)$$

The dimensionless factor  $K_{AdsHX}$  describes the ratio of the heat capacity of the adsorber/desorber heat exchanger and its heat transfer medium to the heat capacity of the incorporated adsorbent. Reducing this factor does not only increase  $COP$  but also the dynamics of the storage process [13].

$$K_{AdsHX} = \frac{(m \cdot c)_{AdsHX}}{(m \cdot c)_{Ads}} \quad (19)$$

The first dimensionless adsorbent-refrigerant parameter  $K_{1-ads-ref}$  compares the binding energy exerted by the adsorbent on the refrigerant with the latent heat of vaporization of pure refrigerant. This factor depends consequently on the chosen working-pair and on the refrigerant uptake range.

$$K_{1-ads-ref} = \frac{\bar{q}_B}{\bar{h}_{fg,ref}} = \frac{\bar{q}_{Ads}}{\bar{h}_{fg,ref}} - 1 \quad (20)$$

$K_{2-ads-ref}$  is the second dimensionless adsorbent-refrigerant parameter, which describes the ratio of the sensible heat required for achieving the temperature lift ( $T_{III} - T_I$ ) of the adsorbent to the cooling effect of the evaporator.

$$K_{2-ads-ref} = \frac{\bar{c}_{Ads} \cdot (T_{III} - T_I)}{\Delta x \cdot \bar{h}_{fg,ref}} \quad (21)$$

The adsorbent structure determines the energetic interaction of adsorbent and refrigerant and thereby the derivative  $(T_{III} - T_I)/\Delta x$  (cf. eq.(21)).  $K_{ref}$  compares the heat released during de-superheating and condensation the refrigerant vapor to the latent heat of vaporization of the refrigerant, which lies in the order of magnitude of one.

$$K_{ref} = \frac{\bar{h}_{II-III} - h_{f,V}}{\bar{h}_{fg,ref}} \quad (22)$$

## Results and discussion

The influence of the dimensionless parameter  $K_{AdsHX}$  (cf. eq.(19)),  $\Delta T_I$  and  $\Delta T_{III}$  on  $q_h$ ,  $q_c$  and  $COP_{h\&c}$  (cf. eq.(12), eq.(18)) have been studied under different operating conditions for the investigated thermochemical heat storage depicted in Figure 1. Figure 3 presents the obtained results for the evaporator, condenser-adsorption and desorption temperatures of 20, 60 and 200 °C, respectively. A temperature gradient of 5 K is considered for all heat exchangers.

Figure 7: Influence of the dimensionless parameter  $K_{AdsHX}$  and  $\Delta T_I$  on the useful mass-specific heat  $q_h$  and on the useful specific cold  $q_c$  as well as on the coefficient of performance  $COP$  with a temperature gradient of  $\Delta T_{HX} = 5$  K for heat transfer inside all components at  $T_{Ev} = 20$  °C,  $T_{Con} = 60$  °C,  $T_{DHS} = 200$  °C and a)  $\Delta T_{III} = 0$  K and b)  $\Delta T_I = 0$  K

The temperature gradient  $\Delta T_I$  shall be understood as the temperature reduction of the adsorber heat exchanger after the discharging phase and before the next charging phase;  $\Delta T_{III}$  as the temperature reduction after the charging phase (during the storage time). The effect of different values of  $\Delta T_I$  and  $\Delta T_{III}$  have been investigated:  $\Delta T_I = \Delta T_{III} = 0$  K for an ideal (loss-free) storage as well as 20 K and 40 K or rather 60 K for real storage. The influence of  $K_{AdsHX} = 0$  for the ideal storage (neglecting the heat capacity of the AdsHX and its heat transfer medium content) up to 7 for real storages has been investigated as well.

The ideal process ( $\Delta T_I = \Delta T_{III} = 0$ ,  $K_{AdsHX} = 0$ ) shows a  $COP_{h\&c}$  of 2.01 (cf. Figure 3a). Temperature drops  $\Delta T_I$  of 20 K and 40 K reduce the  $COP_{h\&c}$  of the ideal storage by 5.9 % and 11.1 %, respectively, as such sensible heat losses increase the energy needed for charging the

storage. For a storage with  $K_{AdSHX} = 5$  ( $\Delta T_I = \Delta T_{III} = 0$ ), a  $COP_{h\&c}$  of 1.33 is obtained, which is reduced at  $\Delta T_I$  of 20 K and 40K by 11.0 % and 19.8 %, respectively.

Increasing  $K_{AdSHX}$  from 0 to 7 ( $\Delta T_{III} = 0$ ) results in enhancing  $q_h$  from 229 to 661 kWh/t<sub>zeolite</sub>. Typical values of  $K_{AdSHX}$  for so far realized adsorber heat exchangers lie between 4 and 7. This is advantageous for enhancing the stored heat  $q_h$ , but it clearly diminishes  $COP_{h\&c}$ . An adsorber heat exchanger characterized with  $K_{AdSHX}$  of 5 is accompanied with a reduction of  $COP_{h\&c}$  by 33.6 % (from 2.01 to 1.33) compared to the ideal COP ( $K_{AdSHX} = 0$ ). Heat losses between charging and discharging phases, leading to  $\Delta T_{III}$  of 20 K, 40 K and 60 K, result in a reducing of  $COP_{h\&c}$  by further 9.3 %, 18.6 % and 27.9 % (from 1.33 to 1.21, 1.09 and 0.96), respectively. Heat losses  $\Delta T_I$  between discharging and charging influence the  $COP_{h\&c}$  in almost the same extent. Thereby, the effect of both  $\Delta T_I$  and  $\Delta T_{III}$  becomes more dominant with increasing  $K_{AdSHX}$ . Additionally,  $\Delta T_{III}$  of 20 K, 40 K and 60 K diminish the useful specific heat  $q_h$  from 578 kWh/t<sub>zeolite</sub> ( $\Delta T_{III} = 0$  K) to 481 kWh/t<sub>zeolite</sub>, 424 kWh/t<sub>zeolite</sub> and 347 kWh/t<sub>zeolite</sub> by 10.6 %, 21.2 % and 31.8 %, respectively.

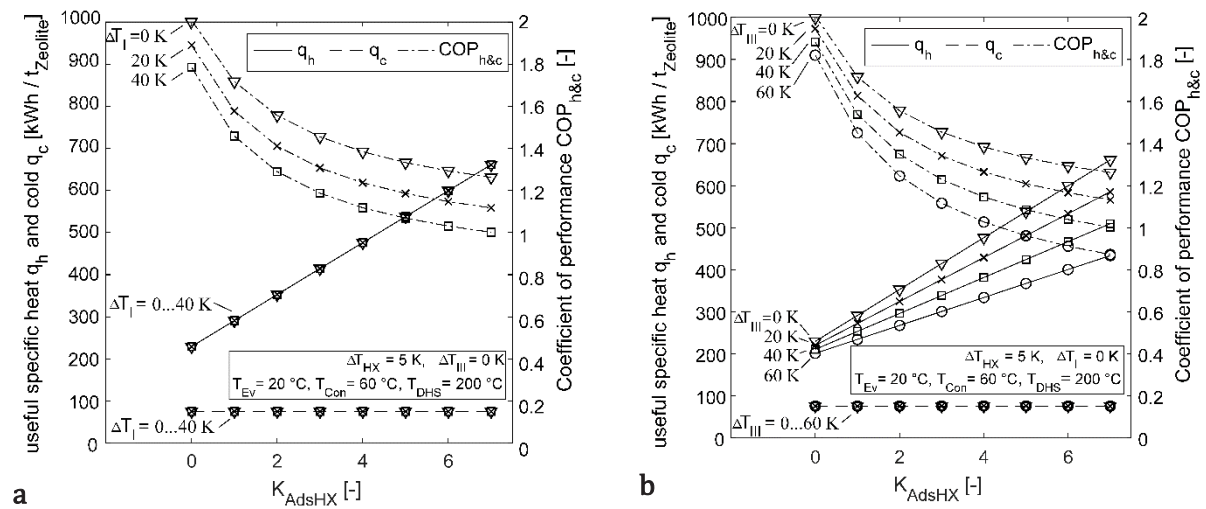


Figure 3b presents the results obtained at the same operating conditions of Figure 3a but at different values for  $\Delta T_{III}$ ; namely, 0, 20, 40 and 60 K while keeping  $\Delta T_I = 0$ K. Temperature drops  $\Delta T_{III}$  of 20 K, 40 K and 60 K reduce the  $COP_{h\&c}$  of the ideal storage (2.01) by 3.1 %, 6.2 % and 9.3 %, respectively.

The specific cooling effect  $q_c$  is only dependent on the differential water uptake, which is not altered by  $\Delta T_I$ ,  $\Delta T_{III}$  or  $K_{AdSHX}$ . This is why, it remains constant at the level of 76 kWh/t<sub>zeolite</sub>. From the results obtained so far, it can be recommended that  $K_{AdSHX}$  shall be reduced below 5, in order to maximize the coefficient of performance of adsorption storages. A highly efficient adsorber heat exchanger can be represented by  $K_{AdSHX} = 3$ , which is the target of our recent developments.

## Conclusion

The dimensionless parameter  $K_{AdSHX}$  describes the ratio of the heat capacity of the adsorber/desorber heat exchanger including its heat transfer medium to the heat capacity of the incorporated adsorbent. An increase of this factor from 0 (ideal) to 5 (realistic) increases the mass-specific useful stored heat  $q_h$  of a high temperature thermochemical storage ( $T_{Ev} =$

20 °C,  $T_{Con}= 60$  °C,  $T_{DHS}= 200$  °C) from 229 kWh/t<sub>zeolite</sub> to 538 kWh/t<sub>zeolite</sub> on the one side, but on the other side it reduces the coefficient of performance  $COP_{h\&c}$  from 2.01 to 1.33. Sensible heat losses between the discharging and the charging phase are represented by the temperature drop  $\Delta T_I$  and between the charging and discharging phase by  $\Delta T_{III}$ . Both diminish  $COP_{h\&c}$ , however  $q_h$  is only reduced by  $\Delta T_{III}$ . For an adsorber heat exchanger having a  $K_{AdHX}$  of 5, a temperature drop  $\Delta T_{III}$  of 60 K reduces  $COP_{h\&c}$  by further 27.9 % and  $q_h$  by 31.8 %. The specific cooling effect  $q_c$ , on the other hand, is only dependent on the differential water uptake, which is not altered by  $\Delta T_I$ ,  $\Delta T_{III}$  or  $K_{AdHX}$  so that it remains constant at 76 kWh/t<sub>zeolite</sub>.

It can be concluded that adsorber heat exchangers of  $K_{AdHX} < 4$  are quite necessary to enhance the heat utilization efficiency ( $COP_{h\&c}$ ) of thermochemical heat and cold storages. Constructive measures to reduce the thermal losses deem also of the same importance to enhance  $COP_{h\&c}$  and the dischargeable heat of thermochemical heat storage systems.

### Appendix. Nomenclature

c	specific heat capacity [kJ/(kg·K)]	<b>Subscripts</b>	
COP	coefficient of performance [-]	AdHX	adsorber heat exchanger
$h_f$	enthalpy of fluid [kJ/kg]	Ads	adsorber/adsorption
$h_{fg}$	latent heat of vaporization [kJ/kg]	c	cold
K	dimensionless parameter [-]	Con	condensation
m	mass in [kg]	Des	desorption
Q	heat amount in [kJ]	DHS	driving heat source
$q_{Ads}$	specific heat of adsorption [kJ/kg]	Ev	evaporation
$q_B$	specific binding energy [kJ/kg]	h	heat
t	temperature [°C]	h&c	heat and cold
x	water loading [g/g]	HX	heat exchanger
		PC	precooling
		PH	preheating
<b>Greek symbols</b>			
$\Delta$	differential operator	ref	refrigerant

### References

- [1] N. Yu, R. Z. Wang, and L. W. Wang, "Sorptions thermal storage for solar energy," *Prog. Energy Combust. Sci.*, vol. 39, no. 5, pp. 489–514, 2013.
- [2] K. Bataineh and Y. Taamneh, "Review and recent improvements of solar sorption cooling systems," *Energy Build.*, vol. 128, pp. 22–37, Sep. 2016.
- [3] L. F. Cabeza, A. Solé, and C. Barreneche, "Review on sorption materials and technologies for heat pumps and thermal energy storage," *Renew. Energy*, vol. 110, pp. 3–39, Sep. 2017.
- [4] L. A. Chidambaram, A. S. Ramana, G. Kamaraj, and R. Velraj, "Review of solar cooling methods and thermal storage options," *Renew. Sustain. Energy Rev.*, vol. 15, no. 6, pp. 3220–3228, Aug. 2011.
- [5] T. X. Li, J. X. Xu, T. Yan, and R. Z. Wang, "Development of sorption thermal battery for



- low-grade waste heat recovery and combined cold and heat energy storage,” *Energy*, vol. 107, pp. 347–359, 2016.
- [6] R. Z. Wang et al., “Heat transfer design in adsorption refrigeration systems for efficient use of low-grade thermal energy,” 2011.
- [7] H. A. Zondag, V. M. Van Essen, L. P. J. Bleijendaal, B. W. J. Kikkert, and M. Bakker, “Application of  $\text{MgCl}_2 \cdot 6\text{H}_2\text{O}$  for thermochemical seasonal solar heat storage,” 5th Int. Renew. Energy Storage Conf. IRES 2010, 2010.
- [8] S. Wu, T. X. Li, T. Yan, and R. Z. Wang, “Experimental investigation on a novel solid-gas thermochemical sorption heat transformer for energy upgrade with a large temperature lift,” *Energy Conversion and Management*, vol. 148, pp. 330–338, 2017.
- [9] D. Aydin, S. P. Casey, and S. Riffat, “The latest advancements on thermochemical heat storage systems,” *Renew. Sustain. Energy Rev.*, vol. 41, pp. 356–367, Jan. 2015.
- [10] L. G. Gordeeva and Y. I. Aristov, “Composites ‘salt inside porous matrix’ for adsorption heat transformation: a current state-of-the-art and new trends,” *Int. J. Low-Carbon Technol.*, vol. 7, no. 4, pp. 288–302, Dec. 2012.
- [11] S. K. Henninger, F. Jeremias, H. Kummer, and C. Janiak, “MOFs for Use in Adsorption Heat Pump Processes,” *Eur. J. Inorg. Chem.*, vol. 2012, no. 16, pp. 2625–2634, Jun. 2012.
- [12] T. X. Li, R. Z. Wang, and T. Yan, “Solid-gas thermochemical sorption thermal battery for solar cooling and heating energy storage and heat transformer,” *Energy*, vol. 84, pp. 745–758, 2015.
- [13] A. H. Abedin and M. A. Rosen, “Closed and open thermochemical energy storage: Energy- and exergy-based comparisons,” *Energy*, vol. 41, pp. 83–92, 2012.
- [14] Y. I. Aristov, “Challenging offers of material science for adsorption heat transformation: A review,” *Appl. Therm. Eng.*, vol. 50, no. 2, pp. 1610–1618, 2013.
- [15] H. Schreiber, F. Lanzerath, C. Reinert, C. Grüntgens, and A. Bardow, “Heat lost or stored: Experimental analysis of adsorption thermal energy storage,” *Appl. Therm. Eng.*, vol. 106, pp. 981–991, Aug. 2016.
- [16] D. M. Dawoud, B., Amer, E.H., Gross, “Experimental investigation of an adsorptive thermal energy storage B.,” *Int. J. Energy Res.* 31, pp. 135–147, 2007.
- [17] T. Li, R. Wang, J. K. Kiplagat, and Y. Kang, “Performance analysis of an integrated energy storage and energy upgrade thermochemical solid–gas sorption system for seasonal storage of solar thermal energy,” *Energy*, vol. 50, pp. 454–467, Feb. 2013.
- [18] T. X. Li, S. Wu, T. Yan, R. Z. Wang, and J. Zhu, “Experimental investigation on a dual-mode thermochemical sorption energy storage system,” *Energy*, vol. 140, pp. 383–394, 2017.
- [19] H. Schreiber, S. Graf, F. Lanzerath, and A. Bardow, “Adsorption thermal energy storage for cogeneration in industrial batch processes: Experiment, dynamic modeling and system analysis,” *Appl. Therm. Eng.*, vol. 89, pp. 485–493, Oct. 2015.
- [20] A. Freni et al., *Characterization of Zeolite-Based Coatings for Adsorption Heat Pumps*. Springer International Publishing, 2015..

# Effect of Conductive Additives on Performance of CaCl<sub>2</sub>-Silica Gel Sorbent Materials

M. Khajepour, C. McCague, S. Shokoya and M. Bahrami\*

Laboratory for Alternative Energy Conversion (LAEC), School of Mechatronic Systems Engineering, Simon Fraser University, BC, V3T 0A3 Canada

\*Corresponding author: [mbahrami@sfu.ca](mailto:mbahrami@sfu.ca)

## Abstract

Several CaCl<sub>2</sub>-silica gel composite samples were prepared with a range of added carbon nanotubes (CNT) and graphite flakes (GF). Water uptake, thermal conductivity, and thermal diffusivity of the samples were tested to establish an optimum composition for the consolidated composites. Results indicate that: i) GF and CNTs have various structural effects and different optimum loadings to improve the performance of the composites, ii) thermal conductivity and diffusivity of the composites increases up to 376% and 483% by addition of conductive additives; iii) thermal property improvement associated with CNT addition is limited due to possible agglomeration of CNTs within a specific binder volume in the composite matrix while the increase in thermal properties with GF shows linear relationship; iv) water uptake reduces by increasing additives. The results show potential for optimization of sorption composite using conductive additives for various applications ranging from thermal storage to chillers.

**Keywords:** Sorbent material, Adsorption, Silica gel, Graphite flakes, Carbon nanotube

## Introduction

Adsorption cooling systems (ACS), in which low-grade waste heat or renewable energy sources are used, are environmentally benign systems that are being considered as viable alternatives to compression refrigeration systems [1-5]. However, there are significant challenges and operational complexities facing widespread application of ACS including low specific cooling power (SCP) and relatively large specific mass and volume [6]. The main limitations are heat and mass transfer which originate from low thermal transport and uptake capacity of active sorbent materials under the operating conditions [7-10]. Therefore, the performance of ACS systems significantly relies on properties and effectiveness of the adsorbent-adsorbate working pairs [11].

To overcome the limitations of the current sorbents, synthesis of new composites - featuring additives to improve heat transfer properties, operational cycles and/or overall power densities - have received great attention [8, 12]. In previous studies in our lab, we established that thermal diffusivity ( $\alpha = k/\rho C_p$ ), which is a combination of thermal conductivity ( $k$ ), specific heat ( $C_p$ ) and density ( $\rho$ ) is the key parameter for improving SCP [13]. Demir et al. studied the effect of different metal particle additives to improve thermal conductivity of unconsolidated silica gel bed [14]. In another work, Saha et al. reported that addition of metallic fillers up to 30 wt.% could enhance thermal conductivity and SCP [6]. Fayazmanesh et al. evaluated the effect of graphite flakes (GF) as thermal conductive additives to CaCl<sub>2</sub>-silica gel composites [15]. Chan et al. studied the effect of adding carbon nanotube (CNT) to CaCl<sub>2</sub>-zeolite. They concluded that addition of CNTs can enhance the thermal conductivity while it doesn't have noticeable effect on uptake capacity of the composites [16].

The present study investigates the effect of GF and CNTs as combined conductive additives on thermal conductivity and thermal diffusivity of CaCl<sub>2</sub>-silica gel sorption composite materials. Moreover, the uptake capacity is evaluated through water adsorption/desorption isotherms for two set of composites. To this end, our goal is to establish an optimum composition of CaCl<sub>2</sub>-silica gel-conductive additives composites to improve SCP in ACS. The SCP of the targeted composite sorbents are discussed elsewhere [17].

## Results and Discussion

### *Sorbent material preparation*

Among sorbent materials suggested for water sorption cooling systems, CaCl<sub>2</sub> in mesoporous silica gel has been reported as one of the most promising solid sorbent composites [3]. The focus of this study is modification of consolidated CaCl<sub>2</sub>-silica gel composites by addition of varying concentrations of GF and CNT and compare their effectiveness. The silica gel is SiliaFlash B150 with 250-500 μm irregular shaped grains and average pore diameter of 15 nm, purchased from Silicycle, Inc., Quebec, Canada. CaCl<sub>2</sub> was added to silica gel in 1:1 weight ratio. Then the thermally conductive additive which is either GF or CNT were added in weight percentages between 0 and 20 wt.%. Graphite flakes (150 lm, 332461 Sigma-Aldrich), has a thickness of ≥150 μm with width of graphene sheets between 50-800 μm. The CNT is an industrial grade of multiwall carbon nanotube from Nanolab, USA with 5-20 μm nominal length and 10-30 nm diameter. Polyvinylpyrrolidone, 40,000MW (PVP-40), purchased from Amresco Inc., US, was used as binder. For the consolidated composite preparation, a total amount of 10 wt.% of the binder was dissolved in water. Then the aqueous solution of PVP-40 was added to the powder mixture of silica gel, CaCl<sub>2</sub> and either GF or CNT. The slurry composites were dried at the oven at 80 °C for 5 hours, and then baked at 120 °C for another 5 hours to produce the consolidated material.

### *Analyses and characterization*

To compare the performances of the targeted additives, thermal transport and uptake characteristics are measured for the composites. The composites with 5 wt.% concentration of CNT and GF were chosen as representatives of the composites to study the effect of different additives on pore volume, surface area, and the morphology of the composites. Then, composites with various amount (0 to 20 wt.%) of conductive additives are considered in the next section to evaluate the thermal transport properties. Total pore volume and specific surface area of the composites, as listed in Table 1, were calculated based on nitrogen sorption isotherms of the samples collected with a volumetric physisorption analyser (ASAP 2020, Micromeritics Instruments). The samples were dried prior to the tests under vacuum at 150 °C for 1 hour followed by 2 hours at 200 °C. The specific surface area ( $S_{BET}$ ) was calculated using the Brunauer, Emmett and Teller (BET) model while the pore volume was calculated from the adsorption curves at highest relative pressures (~ 0.98) using the Barrett, Joyner and Halenda (BJH) model [18, 19]. According to the porosity characterization results, both surface area and pore volume were slightly higher for the CNT sample compared to that of the GF sample. This could be attributed to the geometry and size of the additive particles and their interaction with the host matrix. The combination of higher surface area and smaller particle size of CNTs, (0.01-0.03) x (5-20) μm versus (50-800) x (≥150) μm for GFs, leads to more available surface and less possible pore-plugging with CNTs compared to GFs.

Scanning electron microscope (FEI/Aspex-Explorer) images (Figure 1) show the dispersion of 5 wt.% of GF and CNT inside the silica gel-CaCl<sub>2</sub>-binder composites. SEM images indicate notable changes in the morphology and binder structure as a result of GF and CNT addition. It seems that the CNTs are more engaged with the polymer binder and are

concentrated within the polymer matrix while GFs are most likely exist as stacks and are distributed throughout the composite. Therefore, it is expected that mechanical and thermal transport properties of the composites with the mentioned additives would be different due to different interactions and morphologies of the components.

Table 1- Surface area and pore volume of composites

Sample	Composition (wt.%)					$S_{BET}$ (m <sup>2</sup> /g)	Total pore volume (cm <sup>3</sup> /g) at P/P <sub>0</sub> = 0.98
	PVP	Silica Gel	CaCl <sub>2</sub>	Graphite flakes	CNT		
PVP-SG-CaCl <sub>2</sub> -GF 5%	10	42.5	42.5	5	0	60	0.20
PVP-SG-CaCl <sub>2</sub> -CNT 5%	10	42.5	42.5	0	5	66	0.23
PVP-SG-CaCl <sub>2</sub>	10	45	45	0	0	270	1.13
Silica Gel (B150)	0	100	0	0	0	112	0.48

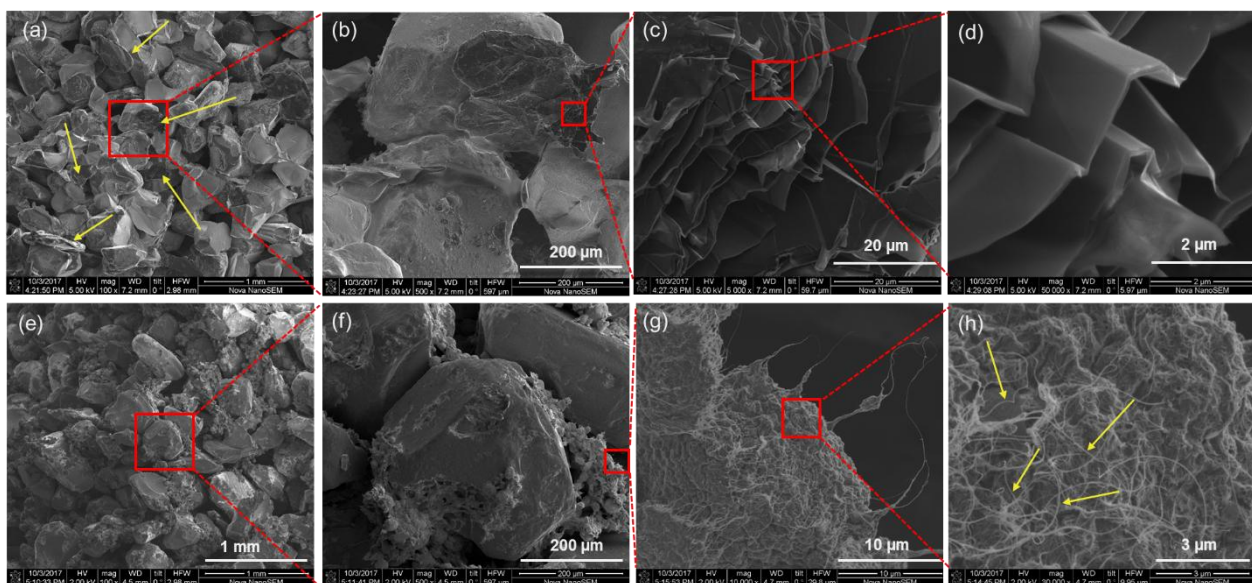


Figure 1. SEM images (a), (b), (c) and (d) PVP-SG-CaCl<sub>2</sub>-5 wt.% GF, (e), (f), (g) and (h) PVP-SG-CaCl<sub>2</sub>-5 wt.% CNT. Yellow arrows point at (a) graphite flakes and (h) CNTs dispersed in the composites

It is well known that thermal conductivity in a porous medium is a function of several factors including pore space, solid matrix properties, shape of components, and a percolation threshold [20]. Percolation threshold is a concept which determines the probability that fillers within a medium are sufficiently connected to form a conductive network [21]. Hence, it is important to consider the amount of the conductive additive relative to the available volume for their dispersion in the composite. While the amount of conductive additives should be enough for building a “conductive network” within the composite, the volume should be large enough to give the conductive additives sufficient space to form the conductive network structure. When certain free volume is available within the composite, conductive additives should be added up to a percolation threshold to make the material thermal conductive. Since this threshold depends on the size and shape of the conductive additive, it would be different for CNT versus GF particles. We would see the effect on conductivity performance of the samples in the following section.

To evaluate the effect of addition of the targeted conductive additives (CNT and GF) on the thermal conductivity and diffusivity of the composite samples, these properties were measured using a transient plane source (TPS) “hot disk” thermal constants analyzer (TPS

2500S, ThermTest Inc., Fredericton, Canada) as per ISO 22007-2 [22]. A Kapton encapsulated double spiral nickel wire sensor (design #5465) with a 2 mm radius, was used for both transient heating of the sample and as precise resistance thermometer for simultaneous temperature measurements. The sensor was placed between a pair of identical samples. During TPS measurements, constant temperature difference develops at the sample-sensor interfaces as a result of contact resistance between the sensor and sample surface. The effect of this constant temperature difference on the measured sample properties was deconvoluted in the calculations [15].

In Figure 2, thermal conductivity and diffusivity results reveal that addition of conductive additives improves thermal transport; e.g. up to 376% higher conductivity and 483% higher diffusivity for sample with 20 wt.% of GF, and up to 90% higher conductivity and 95% higher diffusivity with 15 wt.% of CNT. Figure 2a shows that both thermal conductivity and thermal diffusivity change linearly with the GF content. New correlations are proposed for thermal diffusivity ( $\alpha$ ) and thermal conductivity ( $k$ ) as a function of GF wt.% below:

$$k = 0.1267 + 0.0176 \times GF\% \quad (1)$$

$$\alpha = 0.1133 + 0.0572 \times GF\% \quad (2)$$

One can conclude that addition of GF would linearly increase thermal transport properties as the GF particles are dispersing and forming conductive networks within the composites without agglomerating in a specific part. We can see a thermal percolation threshold at ~ 10 wt.% of GF at which the increase in thermal diffusivity is more pronounced. However, as Figure 2b shows, there is not such a linear trend for increasing thermal diffusivity and conductivity by CNT addition at concentrations above 5 wt.%. Although there is a kind of percolation threshold at ~ 5 wt.% for CNTs, this is an optimum concentration for CNTs and no significant improvement is achieved by adding more CNT content beyond this concentration. The reason is that CNTs are more likely agglomerate in the binder matrix, as shown in SEM images (Figure 1, e-h). Therefore, extra CNTs within the same amount of binder wouldn't have enough space to form a network to conduct heat in the composite. Consequently, the excessive amount of CNTs might interfere with the network formation and negatively impact the heat conduction. In conclusion, the difference in the effect of conductive additives and their percolation loading is attributed to their different interaction with the other components in the composite specifically the binder.

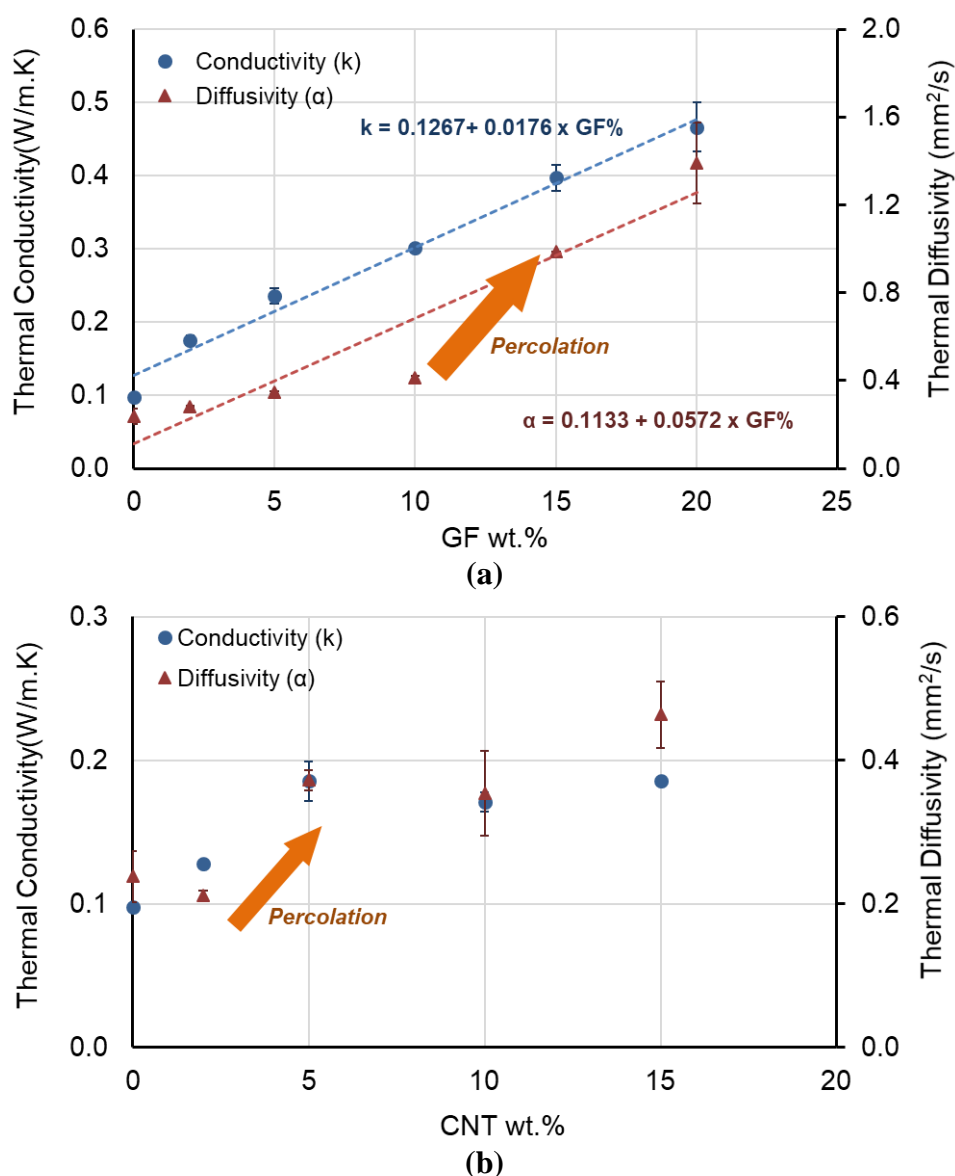


Figure 2. Thermal conductivity and thermal diffusivity of composites with (a) GF and (b) CNT

The other key factor for the choice of sorbent material is the uptake capacity. According to literature, further studies are still required to find optimal compromise(s) between heat and mass transfer properties of the solid sorbent material [3]. As such, water sorption isotherms were evaluated using a thermogravimetric vapor sorption analyzer (IGA-002, Hiden Isochema) available in our lab at 0.04–2.84 kPa with the pressure step of 0.2 kPa at 25°C. Confirmed with water uptake isotherms in Figure 3, there is no significant change in the uptake capacity of the composites at 5 wt.% concentration of either GF or CNT in comparison with the sample without conductive additives. This can be used to develop new composites with increased thermal conductivity (up to 140%) and thermal diffusivity (up to 56%) with negligible impact on uptake capacity. However, the composites with larger amount of conductive additives would have less water uptake due to less active sorbent material content, as expected. Therefore, optimal compromise for water sorption capacity and thermal transport properties should be found according to the specific operation conditions.

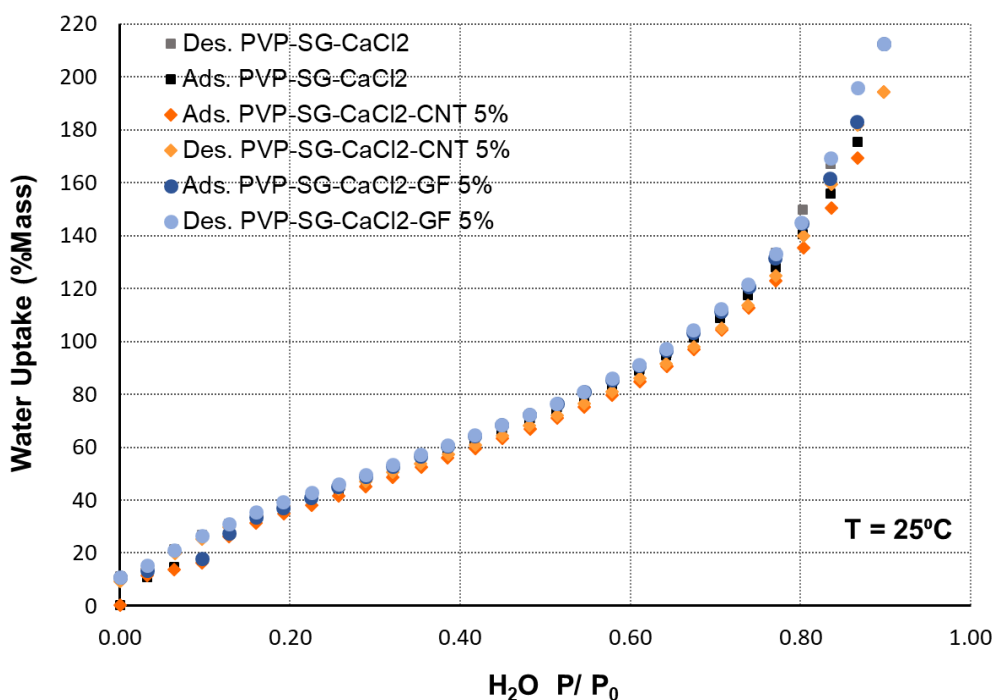


Fig 3. Water uptake isotherms of composites with 0 and 5 wt.% of GF and CNT.

### Summary and Conclusion

Two sets of consolidated composites with various loadings of GF and CNT were prepared to evaluate the effect of different conductive additives on the performances of sorbent materials. Results confirm that there are differences in the effect of CNT and GF on the structure, thermal transport and uptake characteristics of the composites due to their different geometry, morphology, and interaction within the composites. In this study, dependence of percolation threshold and effectiveness of the thermally conductive additives on shape and dispersion of the particles within the consolidated sorbent composites has been discussed. In addition, minimal negative effect on water uptake capacity was observed when 5% CNT or GF were added to  $\text{CaCl}_2$ -silica gel composites, while 90 to 140% and 56 to 45% improvement on thermal conductivity and diffusivity were measured, respectively. Further studies for optimal type, shape and amount of conductive additives is required.

### References

- [1] Gordeeva, L., Frazzica, A., Sapienza, A., Aristove, Y., Freni, A., "Adsorption cooling utilizing the LiBr/silica-ethanol working pair: Dynamic optimization of the adsorber/heat exchanger unit", *Energy*, 2014.
- [2] Askalany, A.A., Salem, M., Ismael, I. M., Ali, A. H. H., Morsy, M. G., Saha, B.B., "An overview on adsorption pairs for cooling", *Renewable & Sustainable Energy Reviews.*, 2013.
- [3]: Freni, A., Russo, R., Vasta, S., Tokarev M., Aristov, Y.I., Restuccia, G., "An advanced solid sorption chiller using SWS-1L", *Applied Thermal Engineering*, 2007.
- [4] Aristov, Y., "Concept of adsorbent optimal for adsorptive cooling/heating", *Applied Thermal Engineering*, 2014.
- [5] Younes, M.M., El-Sharkawy, I. Kabeel A.E., Saha, B.B., "A review on adsorbent-adsorbate pairs for cooling applications", *Applied Thermal Engineering*, 2017.

- [6] Askalany, A.A., Henninger S.K., Ghazy, M., Saha, B.B., “Effect of improving thermal conductivity of the adsorbent on performance of adsorption cooling system”, *Applied Thermal Engineering*, 2017.
- [7] Sharafian, A., NematiMehr, M., Huttema, W., Bahrami, M., “Effects of different adsorber bed designs on in-situ water uptake rate measurements of AQSOA FAM-Z02 for vehicle air conditioning applications”, *Applied Thermal Engineering*, 2016.
- [8] Narayanan, S., Kim, H., Umans, A., Yang, S., Li, X., Schiffres S. N., Rao S. R., McKay, I. S., Perez, C. A. R., Hidrovo, C. H., Wang, E. N., “A thermophysical battery for storage-based climate control”, *Applied Energy*, 2017.
- [9] Rieth, A. J., Yang, S., Wang, E. N., Dinca, M., “Record Atmospheric Fresh Water Capture and Heat Transfer with a Material Operating at the Water Uptake Reversibility Limit”, *ACS Central Science*, 2017.
- [10] Cabeza, L.F., Sole, A., Barreneche, C., “Review on sorption materials and technologies for heat pumps and thermal energy storage”, *Renewable Energy*, 2017.
- [11] Sapienza, A., Velte, A., Girnik I., Frazzica, A., Földner, G., Schnabel, L., Aristov, Y., “Water - Silica Siogel working pair for adsorption chillers: Adsorption equilibrium and dynamics”, *Renewable Energy*, 2017.
- [12] Graf, S., Lanzerath, F., Sapienza, A., Frazzica, A., Freni, A., Bardow, A., “Prediction of SCP and COP for adsorption heat pumps and chillers by combining the large-temperature-jump method and dynamic modeling”, *Applied Thermal Engineering*, 2016.
- [13] Bahrehmand, H., Ahmadi, M., and Bahrami, M., “Analytical modeling of oscillatory heat transfer in coated sorption beds”, *International Journal of Heat and Mass Transfer*, 2018.
- [14] Demir, H., Mobedi, M., Ulku, S., “The use of metal piece additives to enhance heat transfer rate through an unconsolidated adsorbent bed”, *International Journal of Refrigeration*, 2010.
- [15] Fayazmanesh, Kh., McCague, C., Bahrami, M., “Consolidated adsorbent containing graphite flakes for heat-driven water sorption cooling systems”, *Applied Thermal Engineering*, 2017.
- [16] Chan, C., Chao, C.Y.H., Wu, C.L., “Measurement of properties and performance prediction of the new MWCNT-embedded zeolite 13X/CaCl<sub>2</sub> composite adsorbents”, *International Journal of Heat and Mass Transfer*, 2015.
- [17] Bahrehmand, H., Khajehpour, M., Huttema, W., McCague, C., Bahrami, M., “The effects of graphite flake on specific cooling power of sorption chillers: An experimental study”, *Heat Power Cycles conference*, 2018.
- [18] Barrett, P.P., Joyner, E.P., Halenda, L.G., “The determination of pore volume and area distributions in porous substances, computations from nitrogen isotherms”, *Journal of the American Chemical Society*, 1951.
- [19] Bauer, W., Herrmann, J., Mittelbach, R., Schwieger, W., “Zeolite/aluminum composite adsorbents for application in adsorption refrigeration”, *International Journal of Energy Research*, 2009.
- [20] Ghanbarian, B. and Daigle, H., “Thermal conductivity in porous media: Percolation-based effective-medium approximation”, *Water Resources Research*, 2016.
- [21] Kirkpatrick, S., “Percolation and Conduction”, *Review of Modern Physics*, 1973.
- [22] ISO22007-2, “Plastics-determination of thermal conductivity and thermal diffusivity-part 2: transient plane heat source (hot disc) method”, 2008.



# An innovative solid-gas chemisorption heat transformer system with a large temperature lift for high-efficiency energy upgrade

S. Wu<sup>1</sup>, T.X. Li<sup>\*1</sup>, T. Yan<sup>2</sup>, R.Z. Wang<sup>1</sup>

<sup>1</sup>Institute of Refrigeration and Cryogenics, Shanghai Jiao Tong University, Shanghai 200240, China

<sup>2</sup>College of Energy and Mechanical Engineering, Shanghai University of Electric Power, Shanghai 200090, China

\*Corresponding author: Litx@sjtu.edu.cn

## Abstract

Heat transformer can reutilize the low-grade heat by upgrading its temperature to meet the energy demand. Conventional heat transformers based on sorption process suffer from the common drawback of low temperature-lift capacity. In this paper, we propose an innovative solid-gas chemisorption heat transformer system based on the pressure-reducing desorption and temperature-lifting adsorption techniques for the energy upgrade of low-grade heat with a high temperature lift and high energy efficiency. The sorption working pairs of  $\text{MnCl}_2\text{-SrCl}_2\text{-NH}_3$  were employed to analyse its working performance. The innovative four-component system has shorter cycle time compared to the previous one owing to the simultaneous regeneration of high temperature reactive salt and low temperature reactive salt. The system can upgrade low-grade heat from 60~100°C to 180~220 °C at ambient temperature of -10~30°C, and the energy efficiency can reach about 0.3. Two main impact factors of energy efficiency including global conversion of reactive salts and mass ratio of metallic reactor and reactive salt were analysed and discussed.

**Keywords:** energy upgrade, chemisorption; heat transformer; energy efficiency; large temperature lift.

## Introduction

There exists an enormous amount of low-grade energy resources such as the industrial waste heat, renewable energy, and exhaust gases from engines, which are usually directly released to the atmosphere or surface water without utilization due to the limitation of their relatively low temperature. The rational utilization of low-grade thermal energy is an essential solution to compensate for the inconsistency between the insufficient energy supply and growing energy consumption [1-2]. Upgrading these low-grade waste heats by advanced heat transformer technologies to make them become useful is a promising approach to high-efficiently utilize energy resources. Electrical-powered vapor compression heat pump and thermal-driven chemical heat transformer are two common methods to realize the temperature lift of low-grade heat. The former usually has higher system efficiency than the latter, but it still consumes high-grade electricity as main energy. Thermal-driven heat transformers have the remarkable advantage of energy-saving due to the fact that it can be driven by the low-grade/middle-grade heat [3].

Solid-gas chemisorption heat transformer has advantages of high energy density, stable working temperature, wide operating temperature range, etc. Among various kinds of working pairs, metal halide-ammonia (water, methanol) and metal hydride-hydrogen, metal chloride-ammonia working pairs have great potential to energy upgrade of different low-grade/middle-grade heat sources due to its wide candidates of sorption working pairs with different operating temperature, which make it adapt to different occasions [4-5].

The basic solid-gas chemisorption heat transformers include the single-salt system and double-salt system. The single-salt system is made of a reactor and a condenser/evaporator, which is called the basic chemisorption heat transformer. The double-salt system composes of two reactors with different reactive salts, which is called the basic chemical resorption heat transformer. Generally, for the single-salt system, a high system pressure is necessary to realize a large temperature lift. However, high system pressure would cause safety problem and high thermal capacity of reactor which consumes the chemical synthesis heat and decreases the effective upgraded heat output. Thus it is very important to control the system pressure within a reasonable range by setting a suitable evaporation temperature. Consequently, the single-salt system usually has relatively low temperature-lift range. [6] Two-salt system using the resorption process between two different reactive salts has lower system pressure when operated in the same working temperature range with the single-salt system [7]. Haije et al. [8] investigated the feasibility of a chemical resorption heat transformer with temperature lift from 155 to 200°C based on working pairs of LiCl-MgCl<sub>2</sub>-NH<sub>3</sub> at ambient temperature of 20°C. However, the system COP was as low as 0.11 and only 40% of the expected theoretical value. In order to further lift the low-grade/middle-grade heat and improve the system efficiency, a series of advanced solid-gas chemisorption cycles were introduced, namely, two-stage three-salt cycle [9], double-effect three-salt cycle [10], two-stage two-salt cycle [11], two-stage three-salt cycle with internal heat recovery [12], and four-salt cycle with internal heat recovery [13]. Yu et al. [14] compared different chemisorption heat transformer cycles based on metal chloride-ammonia working pairs, and found that only the two-stage three-salt cycle and the two-stage four-salt cycle with internal heat recovery could realize the temperature lift more than 50°C with energy efficiency about 0.28 and exergy efficiency about 0.42 when heat source temperature was about 100°C. However, these heat transformation cycles would be very complicated and have less potential for practical application. Moreover, for heat transformation cycles based on chemisorption resorption process the fluctuation and decrease of heat output temperature is a key issue due to the oscillation of system operating pressure, which is caused by the mismatch of chemical reaction rates in different reactors.

To overcome the above-mentioned drawbacks, Li et al. [15] proposed a novel solid-gas chemisorption heat transformation cycle for the integrated energy storage and energy upgrade of low-grade thermal energy. It can realize the stable heat output temperature and relatively large temperature lift by combining the merits of conventional chemisorption and resorption heat transformation cycles. A pressure-reducing desorption method was adopted to lower heat input temperature by employing a thermochemical resorption process during energy storage phase, and a temperature-lift adsorption technique was used to enhance energy upgrade capacity and avoid the fluctuation of heat output temperature by employing a thermochemical adsorption process during energy release phase. We has verified its feasibility by constructing an experimental system and realized a temperature lift of low-grade heat from 96 °C to 161°C at ambient temperature of 25°C [16].

In this paper, we further investigate the performance of novel solid-gas chemisorption heat transformation cycle using working pairs of MnCl<sub>2</sub>-SrCl<sub>2</sub>-NH<sub>3</sub>. The equilibrium characteristics of ammonia sorption on MnCl<sub>2</sub> and SrCl<sub>2</sub> were firstly obtained by high-precise thermo-gravimetry apparatus Rubotherm. Then the equilibrium sorption characteristics were used to theoretically analyse the working performance of the novel heat transformation cycle with consideration of adsorption/desorption hysteresis. Subsequently, an innovative chemisorption heat transformer system was proposed to shorten the system cycle time and its performance was analysed in view of the recovery of sensible heat. Lastly, two main impact

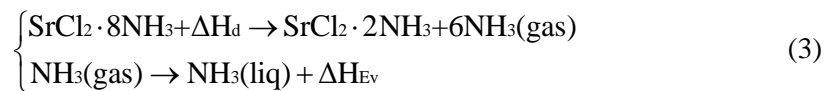
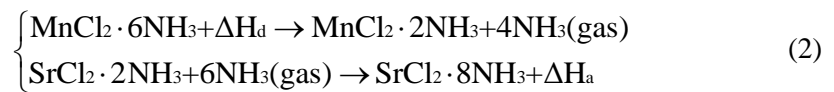
factors of energy efficiency including global conversion of reactive salts and mass ratio of metallic reactor and reactive salt were analysed and discussed.

## Discussion and Results

Fig.1 shows the schematic diagram of novel solid-gas chemisorption heat transformation cycle for energy upgrade with a large temperature lift. The sorption equilibrium lines (solid lines represent the desorption lines and dot lines represent the adsorption lines) of SrCl<sub>2</sub> and MnCl<sub>2</sub> are drawn based on the obtained equilibrium characteristics of ammonia sorption on SrCl<sub>2</sub> and MnCl<sub>2</sub>. We used the Rubotherm magnetic suspension balance to perform the thermo-gravimetric measurement so as to achieve the adsorption and desorption characteristic of ammonia on SrCl<sub>2</sub> and MnCl<sub>2</sub>. The reaction enthalpy ( $\Delta H$ ) and reaction entropy ( $\Delta S$ ) of working pairs of SrCl<sub>2</sub>/NH<sub>3</sub> and MnCl<sub>2</sub>/NH<sub>3</sub> are demonstrated in Table 1. The sorption equilibrium lines of SrCl<sub>2</sub> and MnCl<sub>2</sub> are drawn depending on the Clapeyron-Clausius equation:

$$\ln P = \frac{\Delta H}{RT} - \frac{\Delta S}{R} \quad (1)$$

The novel heat transformation cycle involves three temperatures, ambient temperature ( $T_0$ ), input temperature ( $T_{in}$ , or heat source temperature) and output temperature ( $T_{out}$ , or the target temperature). The whole cycle mainly includes two storage phases of low-grade thermal energy (① and ② in Fig. 1) and one release phase of upgraded thermal energy (③ in Fig. 1). Two energy storage phases involve the chemical and physical changes:



During energy release phase of upgraded thermal energy, the chemisorption process involves the chemical and physical changes:

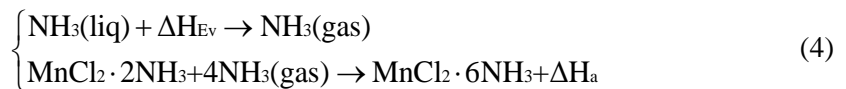


**Table 1** The reaction enthalpy and reaction entropy of sorption working pairs SrCl<sub>2</sub>/NH<sub>3</sub> and MnCl<sub>2</sub>/NH<sub>3</sub>.

Conversions	$\Delta H$ (kJ/mol)		$\Delta S$ [kJ/(molK)]	
	Desorption	Adsorption	Desorption	Adsorption
SrCl <sub>2</sub> ·(8↔2)NH <sub>3</sub>	43.82	43.24	0.2378	0.2367
MnCl <sub>2</sub> ·(6↔2)NH <sub>3</sub>	52.46	41.41	0.2393	0.2152

Due to the monovariant characteristic of chemisorption between ammonia and metal halides, the minimum heat source temperature and maximum output temperature would be a determined value in theory once the ambient temperature is determined. Fig. 2 shows the route to acquiring the heat source temperature ( $T_{in}$ ) and maximum heat output temperature

( $T_{out}$ ) according to a given ambient temperature ( $T_0$ ). Table 2 demonstrates the theoretical  $T_{in}$ ,  $T_{out}$ , temperature lift  $\Delta T$  ( $\Delta T = T_{out} - T_{in}$ ), and maximum working pressure ( $P_H$ ) at different ambient temperatures. It is found that  $\Delta T$  decreases a little while  $P_H$  rapidly increases with increasing  $T_0$ .

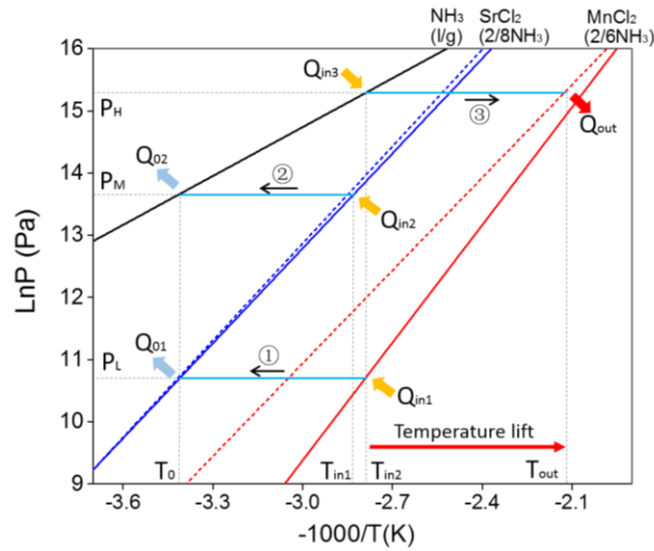


**Fig.1.** Schematic illustration of the novel solid-gas thermochemical sorption heat transformation cycle for energy upgrade with a large temperature lift.

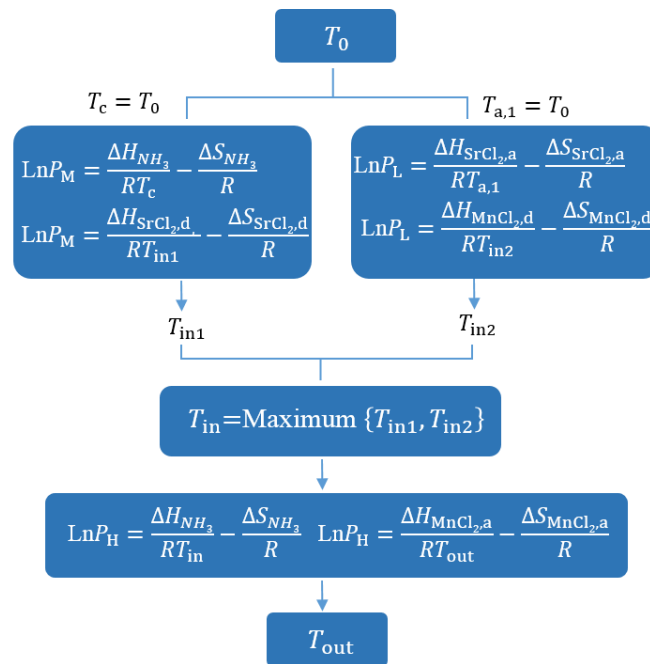


**Fig. 2.** Flow diagram of calculating the heat source temperature ( $T_{in}$ ) and maximum heat output temperature ( $T_{out}$ ) according to a given ambient temperature ( $T_0$ ).

Based on the novel chemisorption heat transformation cycle, two kinds of thermochemical sorption system can be constructed including three-component system and four-component system. The three-component system mainly includes high temperature reactor (HTR) filled with high temperature salt (HTS), low temperature reactor (LTR) filled with low temperature salt (LTS) and condenser/evaporator (Con/Ev), which has been demonstrated in our previous

report [16]. The system operational cycle goes through three processes and only one process releases the upgraded thermal energy. Consequently, the mean power of system in the whole cycle will be very low. In addition, it is difficult to recover the sensible heat of every component and improve its energy efficiency unless an extra thermal accumulator is used as affiliated device.

**Table 2** Theoretical values of  $T_{in}$ ,  $T_{out}$ ,  $\Delta T$ , and  $P_H$  at different ambient temperatures  $T_0$ .

$T_0$ (°C)	$T_{in1}$ (°C)	$T_{in2}$ (°C)	$T_{in}$ (°C)	$T_{out}$ (°C)	$\Delta T$ (°C)	$P_H$ (MPa)
-10	55.4	48.9	55.4	188.0	132.6	2.31
0	63.2	61.0	63.2	194.2	131.1	2.81
10	70.7	73.1	70.7	200.2	129.5	3.39
20	78.0	85.1	85.1	211.4	126.3	4.61
30	85.2	97.2	97.2	220.4	123.2	5.90

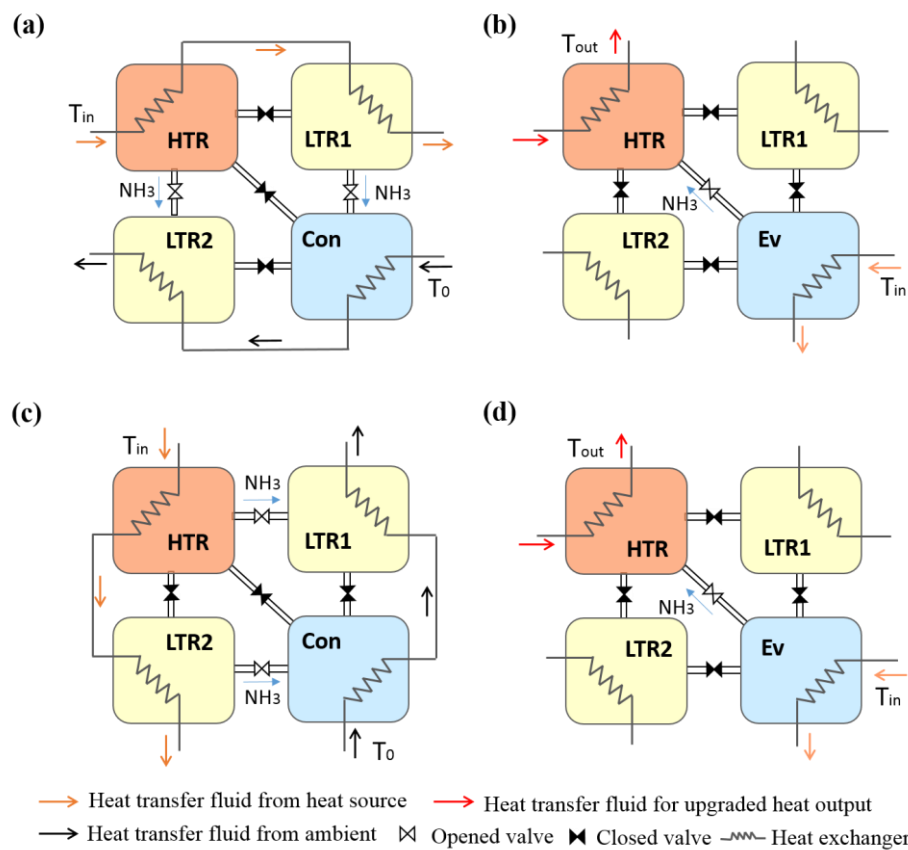


**Fig. 3.** Schematic diagram of innovative chemisorption heat transformation system. (a) Desorption of HTR and resorption of LTS2; Desorption of LTS1 and condensation of gaseous ammonia. (b) Evaporation of liquid ammonia and adsorption of HTR. (c) Desorption of HTR and resorption of LTS1; Desorption of LTS2 and condensation of gaseous ammonia. (d) Evaporation of liquid ammonia and adsorption of HTR.

In order to improve the mean power and energy efficiency of system, an innovative chemisorption heat transformation system with four components is proposed as shown in Fig. 3. The HTR is filled with  $MnCl_2$ , LTR1 and LTR2 are both filled with  $SrCl_2$ , and Con/Ev is used to store liquid ammonia. The whole cycle includes four phases (Fig. 3a-d), among which

two phases (Fig. 3b and d) involve the release of upgraded thermal energy. Thus the mean power of system can be enhanced when compared to previous one [16]. In addition, the sensible heat of LTR1 and LTR2 can also recovered between  $T_0$  and  $T_{in}$  in Fig. 3b and d, which would improve the energy efficiency.

We evaluate the energy efficiency of the innovative thermochemical sorption system by energy conservation law. Considering the half system cycle as illustrated in Fig. 3a and b. The input heat includes evaporation heat of liquid ammonia ( $Q_{Ev}$ ), sensible heat of evaporator and liquid ammonia from  $T_0$  to  $T_{in}$  ( $Q_{Ev,s}$ ), desorption heat of HTS in HTR at  $T_{in}$  ( $Q_{HTR,d}$ ), desorption heat of LTS in LTR1 at  $T_{in}$  ( $Q_{LTR1,d}$ ), and sensible heat of LTR1 and LTS from  $T_0$  to  $T_{in}$  ( $Q_{LTR1,s}$ ). They can be calculated as follows:

$$Q_{Ev} = m \cdot \Delta H \quad (5)$$

$$Q_{Ev,s} = (CM)_{Ev} \cdot (T_{in} - T_0) \quad (6)$$

$$Q_{HTR,d} = m_{MnCl_2} \cdot \Delta H_{MnCl_2,d} \quad (7)$$

$$Q_{LTR1,d} = m_{SrCl_2} \cdot \Delta H_{SrCl_2,d} \quad (8)$$

$$Q_{LTR1,s} = (CM)_{LTR1} \cdot (T_{in} - T_0) \quad (9)$$

$$Q_{in} = Q_{Ev} + Q_{Ev,s} + Q_{HTR,d} + Q_{LTR1,d} + Q_{LTR1,s} \quad (10)$$

where  $CM$  is the overall thermal capacity of vessel and its inclusion.

The effective output heat is equal to the adsorption heat of HTS in HTR at  $T_{out}$  ( $Q_{HTR,a}$ ) subtracted the sensible heat consumption of HTR and HTS from  $T_{in}$  to  $T_{out}$  ( $Q_{HTR,s}$ ).

$$Q_{HTR,a} = m_{MnCl_2} \cdot \Delta H_{MnCl_2,a} \quad (11)$$

$$Q_{HTR,s} = (CM)_{HTR} \cdot (T_{out} - T_{in}) \quad (12)$$

$$Q_{out} = Q_{HTR,a} - Q_{HTR,s} \quad (13)$$

The consumed sensible heat of HTR and HTS during the release phase of upgraded thermal energy can be recovered to provide desorption heat for itself (Fig. 3a and c). Besides, the sensible heat of LTR1/LTR2 can also recovered to preheat LTR2/LTR1 (Fig. 3b and d). Considering the complete sensible heat recovery, the total recovered heat can be calculated.

$$Q_{recovery} = Q_{HTR,s} + Q_{LTR,recovery} \quad (14)$$

$$Q_{LTR,recovery} = (CM)_{LTR} \cdot (T_{in} - \frac{T_{in} + T_0}{2}) \quad (15)$$

Here, the recovered sensible heat of LTR1/LTR2 is calculated based on the same parameters of LTR1 and LTR2. Thus the energy efficiency ( $\eta$ ) can be obtained.

$$\eta = \frac{Q_{out}}{Q_{in} - Q_{recovery}} = \frac{Q_{HTR,a,d} - Q_{HTR,s}}{Q_{HTR,d,e} + Q_{LTR1,d,e} + Q_{Ev} + Q_{Ev,s} + \frac{Q_{LTR1,s}}{2} - Q_{HTR,s}} \quad (16)$$

To simplify the calculation, some parameters are given to evaluate the effect of global conversion of reactive salt ( $X$ ) and mass ratio of reactor metal and reactive salt ( $R$ ) on the energy efficiency. Table 3 shows the given parameter. Considering the heat transformer for practical application, the composite sorbent expanded graphite/reactive salt is used in the reactor. The mass fraction of expanded graphite in the composite sorbent is 15% [16]. Then the relationship among  $\eta$ ,  $X$ , and  $R$  can be expressed:

$$\eta = \frac{1257X - 51.7R}{3191X - 7R} \quad (17)$$

**Table 3** The related parameters for calculating the energy efficiency of system.

Specific thermal capacity (kJ/kgK)	Temperature (°C)	Mass (kg)	Enthalpy (kJ/kg)
$C_{\text{metal}}$ : 0.47	$T_{\text{in}}$ : 90	$M_{\text{NH}_3} = 0.54XM_{\text{MnCl}_2}$ ;	$\Delta H_{\text{NH}_3}$ : 874
$C_{\text{ammonia}}$ : 2.05	$T_{\text{Ev}}$ : 80	$M_{\text{SrCl}_2} = 0.62XM_{\text{MnCl}_2}$ ;	$\Delta H_{\text{SrCl}_2, \text{d}}$ : 1657.7
$C_{\text{composite sorbent}}$ : 0.53	$T_0$ : 20	$R = M_{\text{metal}}/M_{\text{MnCl}_2}$	$\Delta H_{\text{SrCl}_2, \text{a}}$ : 1635.8
	$T_{\text{out}}$ : 200		$\Delta H_{\text{MnCl}_2, \text{d}}$ : 1678.7
			$\Delta H_{\text{MnCl}_2, \text{a}}$ : 1325.0

Fig. 4 shows  $\eta$  as a function of mass ratio  $R$  at different global conversions  $X$ . Generally, the mass ratio of about 5 can be reached for the practical heat transformer with optimization design, so the energy efficiency can reach 0.27-0.32 when the global conversion varies from 0.6 to 0.9..

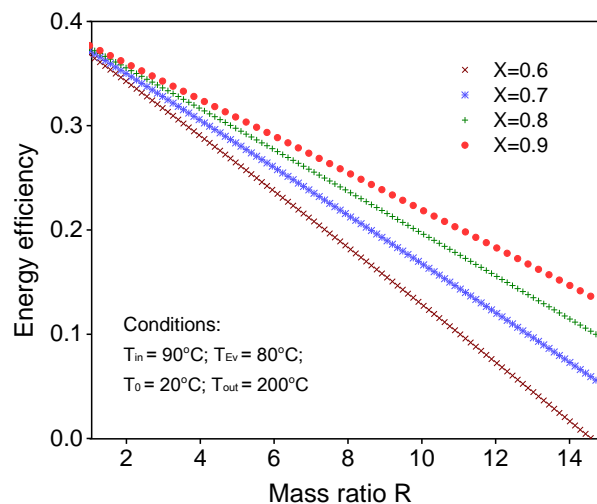


**Fig. 4.** Variation of  $\eta$  with the mass ratio  $R$  at different global conversions  $X$ .

## Conclusion

We propose an innovative solid-gas chemisorption heat transformer system with four components for high-efficiency energy upgrade. Sorption working pairs of  $\text{MnCl}_2$ - $\text{SrCl}_2$ - $\text{NH}_3$  were employed to theoretically analyse the working performance of system. The system can upgrade low-grade heat from 60~100°C to 180~220 °C at ambient temperature of -10~30°C in

theory. The temperature lift range is more than 120°C at working pressure of blow 6MPa. The system cycle time is largely shorten compared to previous reported chemisorption heat transformer. The sensible heat during the operation process can be easily recovered. The system energy efficiency can reach about 0.3 within feasible technical scope.

### Acknowledgement

This work was supported by the National Natural Science Funds for Excellent Young Scholar of China under the contract No. 51522604.

### References:

- [1] Chidambaram, L. A., Ramana, A. S., Kamaraj, G., Velraj, R., “Review of solar cooling methods and thermal storage options”, *Renew and Sustain Energy Rev*, 2011; 15: 3220-8.
- [2] Miró, L., Gasia, J., Cabeza, L. F., “Thermal energy storage (TES) for industrial waste heat (IWH) recovery: A review”, *Appl Energ*, 2016; 179: 284-301.
- [3] Cabeza, L. F., Solé, A., Barreneche, C., “Review on sorption materials and technologies for heat pumps and thermal energy storage”, *Renew Energ*, 2016; 110: 3-39.
- [4] Bougard, J., Jadot, R., Poulain, V., “Solid-gas reactions applied to thermotransformer design”, *Int Absorpt Heat Pump Conf*, 1993; 31: 413-8.
- [5] Meunier, F., “Solid sorption heat powered cycles for cooling and heat pumping applications”, *Appl Therm Eng*, 1998; 18: 715-729.
- [6] Neveu, P., Castaing, J., “Development of a numerical sizing tool for a solid-gas thermochemical transformer-impact of the microscopic process on the dynamic behaviour of a solid-gas reactor”, *Appl Therm Eng*, 1997; 17: 501-518.
- [7] Goetz, V., Elie, F., Spinner, B., “The structure and performance of single effect solid/gas chemical heat pumps”, *Heat Recovery Syst CHP*, 1993; 13(1):79-96.
- [8] Haije, W. G., Veldhuis, J. B. J., Smeding S. F., “Grisel RJH. Solid/vapour sorption heat transformer: Design and performance”, *Appl Therm Eng*, 2007; 27(8-9):1371-6.
- [9] Suda, S., Komazaki, Y., Narasaki, H., Uchida M. “Development of double stage heat pump: experimental and analytical surveys”, *J Less-Common Met*, 1991; 172: 1092-110.
- [10] Sun, D.W., “Thermodynamic analysis of the operation of two-stage metal-hydride heat pumps”, *Appl Energ*, 1996; 54(1): 29-47.
- [11] Neveu, P., Castaiang, J., “Solid-gas chemical heat pumps: field of application and performance of the internal heat recovery process”, *Heat Recovery Syst CHP*, 1993; 13(3):233-51.
- [12] Spinner, B., “Ammonia-based thermochemical transformers”, *Heat Recovery Syst CHP*, 1993; 13(4):301-7.
- [13] Spinner, B., Sorin, M., Berthiaud. J., Mazet. N., Rheault, F., “New cascades for thermochemical refrigeration”, *Int J Therm Sci*, 2005; 44:1110-4.
- [14] Yu, Y. Q., Zhang, P., Wu, J. Y., Wang, R. Z., “Energy upgrading by solid-gas reaction heat transformer: A critical review”, *Renew and Sustain Energy Rev*, 2008; 12(5):1302-24.
- [15] Li, T. X., Wang, R. Z., Kiplagat, J. K., “A target-oriented solid-gas thermochemical sorption heat transformer for integrated energy storage and energy upgrade”, *AICHE J*, 2013; 59(4):1334-47.
- [16] Wu, S., Li, T.X., Yan, T. & Wang, R.Z., “Experimental investigation on a novel solid-gas thermochemical sorption heat transformer for energy upgrade with a large temperature lift”, *Energy Conversion and Management*, 2017; 148, 330-338.



# Comparison of Storage Density and Efficiency for Cascading Adsorption Heat Storage and Sorption assisted Water Storage

Matthias S. Treier<sup>1\*</sup>, Aditya Desai<sup>1</sup> and Ferdinand P. Schmidt<sup>1</sup>

<sup>1</sup>Karlsruhe Institute of Technology, Institute of Fluid Machinery, Karlsruhe, Germany

\*Corresponding author: Matthias.Treier@kit.edu

## Abstract

Storage of thermal energy can be important for compensating the mismatch between demand and supply of energy, especially due to fluctuating renewable energy sources. Within this study, two different systems are analysed with the aim of increasing storage efficiency and storage density compared to known systems. Both systems indicate a possible benefit in energy density and storage efficiency but it is also shown, that system and temperature boundaries play an important role in the outcome of the simulations.

**Keywords:** Sorption, Cascading Adsorption, Heat Storage

## Introduction/Background

For heat storage systems, the storage density and efficiency are the two key figures of merit. These two figures have to be defined carefully for every case of use in adsorption based systems because both adsorption and desorption half cycle involve a heat transformation step with an additional heat source or sink [1,2].

For this simulation study it is important to assume system boundaries and operating conditions (e.g. minimal usable temperature lift) since they influence the achievable storage densities and efficiencies. Initial work on standardizing the evaluation of thermo-chemical heat storages has been performed in the framework of a joint IEA task/Annex [3]. A comparison to literature is nevertheless difficult, since often important system or temperature boundaries are not mentioned or vary in different literature sources.

Here, a cascading adsorption heat storage and a sorption assisted water storage (SAWS) are discussed and compared with regard to storage density and storage efficiency for short time storage. The storage time could be for example a day/night cycle.

In earlier projects, storage densities of 130 kWh/m<sup>3</sup> have been reached. A main difference to literature is that here, the adsorber can be operated with low diving temperature differences and has a smaller effective adsorbent density of only 400 kg/m<sup>3</sup>.

## Definition of figures of merit

In an adsorption storage heat can be stored by desorbing the storage (charging of the storage). For using the stored heat, the adsorption half cycle is started (storage discharge) and the heat of adsorption can be extracted from the storage. During adsorption, the adsorption storage gradually cools down and thus, the heat released is at different temperature levels.

According to equation 1, the volumetric storage density  $w$  is the ratio of the usable heat out of the storage in discharge phase  $Q_{discharge}$  to the volume of the storage  $V$ .

$$w = \frac{Q_{discharge}}{V} \quad (1)$$

There are multiple ways to set the system boundaries which have a direct influence on the storage volume. In this study, the system boundary for the determination of the storage volume is chosen such as to include the storage vessels as well as the required auxiliary components (e.g. pipes and insulation) for each type of storage. The same boundary is employed for the determination of the usable heat that is delivered by the storage system. Storage efficiency  $\eta$  is the other value that is examined within this work (see equation 2).

$$\eta = \frac{Q_{discharge}}{Q_{charge}} \quad (2)$$

It is a ratio of two amounts of heat, the heat than can be extracted from the storage after storage time divided by the heat that is needed to desorb the storage  $Q_{charge}$  [kWh]. During the desorption half cycle, heat of condensation is also released. This heat may in some cases be considered as useful heat with respect to storage efficiency. Within this work, the storage efficiency is calculated without the condensation heat.

During the storage time, sensible heat losses can occur and have to be taken into account for both of the storages. The effects of the losses on sorption and sensible storage components are different.

### Description of the different systems

For the examined cascading adsorption heat storage the part of the heat of adsorption at a high temperature is used to drive a sorption heat pump cycle. This heat pumping effect may increase the effective volumetric density of the storage. Once the temperature of the heat is too low to drive the sorption heat pump, the heat is used directly. The scheme of the cascading adsorption heat storage is shown in Figure 1.

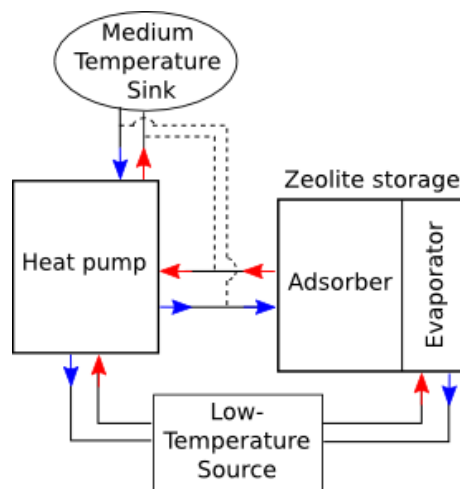


Figure 1: Cascading adsorption heat storage during storage discharge; continuous lines for cascading use, dotted lines for direct use

A requirement for the cascading adsorption heat storage is an adsorber that can be operated at nominal power with low driving temperature differences between adsorber and heat transfer fluid and a high-temperature heat source for the direct desorption. Possible materials for this cycle are classical hydrophilic zeolites of faujasite and LTA (Linde type A) types [1].

For the calculations of the cascading cycle, the heat of adsorption that is used  $Q_{discharge,CAS}$  is determined according to equation 3.

$$Q_{discharge,CAS} = Q_{discharge,direct} + Q_{discharge,casc} * COP_{AHP} \quad (3)$$

It is a sum of the cascading part of the heat  $Q_{discharge,casc}$  multiplied by the COP of the used heat pump  $COP_{HP}$  and the direct part  $Q_{discharge,direct}$ .

The adsorption heat pump (AHP) that was considered for the cascading system is an advanced adsorbent/fiber composite module [4] recently developed by SorTech /Fahrenheit. It is based on two adsorbers which are operated such that a heat recovery between the hot and cold adsorber is achieved through a delayed switching of return flows at every switching of the half cycles.

In a SAWS, the heat is stored in a stratified water storage. In order to achieve higher storage densities, a large change in the temperature of the water is desirable. The direct unloading of such a storage does not fully utilize the exergy of the hot water. This can be achieved by using hot water from the top of the storage tank to drive an adsorption heat pump (AHP)[5]. The performance of the SAWS is improved by using the stratified storage for internal heat recovery between the half-cycles of the AHP, according to the Stratisorp concept [6,7]. The heat released in the adsorber of the AHP during the adsorption cycle can be stored in the stratified storage and used to heat the adsorber during the desorption half-cycle. As soon as the temperature of the water in the tank is insufficient for desorbing the AHP, the heat is used directly. Thus, the cascading sorption storage and the SAWS have in common that they both make use of an adsorption heat pump to increase efficiency and effective storage density.

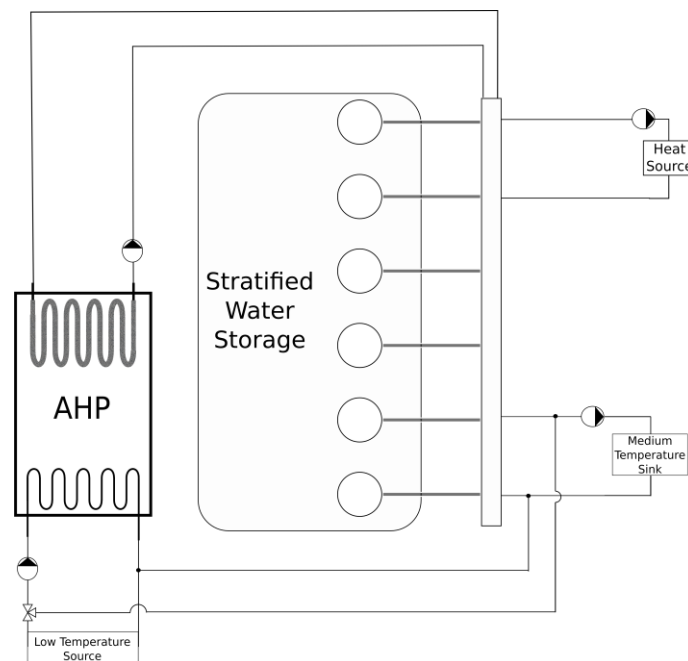


Figure 2: System Schematic for the sorption-assisted water storage

The components of this system are depicted in Figure 2. The AHP is connected to the water storage through a valve bank, which allows water to be extracted from/inserted into the storage at different heights, according to its temperature. The storage can be charged from the heat source which is connected to the top of the tank. Useful heat is extracted from the bottom of the tank and released to the medium temperature sink. The heat sink, thus, acts as a cooler

for the tank. During the desorption half-cycle of the AHP, useful heat is also released in the condenser of the AHP. A commercially available eZea-module from Fahrenheit GmbH is used as the AHP in the SAWS system since heat and mass transfer parameters required for dynamic simulation have been determined earlier for this module type.

Models for the components of the SAWS system have been prepared earlier in MATLAB® [8]. The AHP simulation is started with the temperature distribution inside the storage, assumed to be as shown in Figure 3. The temperature profile shows a plateau region, where the temperature is uniform and equal to the maximum temperature in the storage, and a linear region where the temperature drops linearly from the maximum temperature to the minimum adsorber inlet temperature. As the adsorber of the AHP is connected to the storage during both half-cycles, the linear region is necessary in order to provide enough cooling water for the adsorber. If the storage is charged completely to the maximum temperature, it can be directly discharged initially until this profile is reached - after which the AHP is operated.

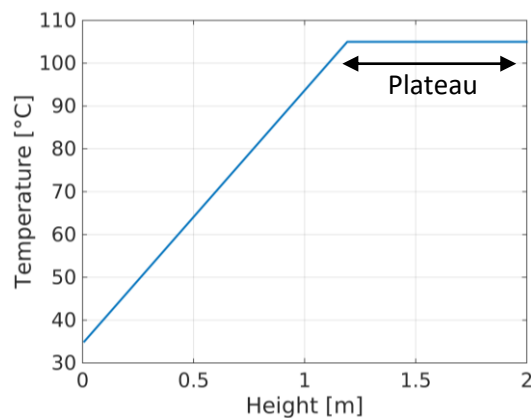


Figure 3: Temperature profile in the water storage at the beginning of the discharge phase

### Boundary conditions and assumptions for the simulations

The boundary conditions vary for both examined systems, as shown in Tables 1 and 2. A common required temperature lift of 30K is assumed for both systems.

Table 1: Boundary conditions for cascading system

Parameter	Value
<i>Working Fluid</i>	Water
Desorption temperature	200 °C
Condensation temperature	35 °C
Adsorption temperature	35 °C
Evaporation temperature	5 °C
<i>Desorption configuration</i>	Parallel
Adsorbent packing density in adsorber vessel	400 kg/m <sup>3</sup>
Material	NaY, Z13X
Loss of sensible heat	20 %
Mean COP of AHP over storage discharge	1.2
System volume including AHP	1.16 m <sup>3</sup>

Table 2: Boundary conditions for SAWS

Parameter	Value
Working Pair - AHP	Water/SAPO-34
Heat Storage Medium	Water
Max. Temperature in Storage	105 °C
Cooler/Condenser inlet temperature	35 °C
Evaporator inlet temperature	5 °C
Volume of Water Storage	1 m <sup>3</sup>
Height of Water Storage	2 m
Volume of AHP	0.1 m <sup>3</sup>
System Volume with pipes & insulation	1.3 m <sup>3</sup>

## Discussion and Results

The storage density and efficiency of the cascading adsorption system for the materials Z13X and NaY are pictured in Figure 4. As already described earlier, the boundary for the calculations is set as to include all components of the system in the volume of the storage. To depict the importance of the chosen system boundary, a comparison to the values that were produced only on a material level is drawn.

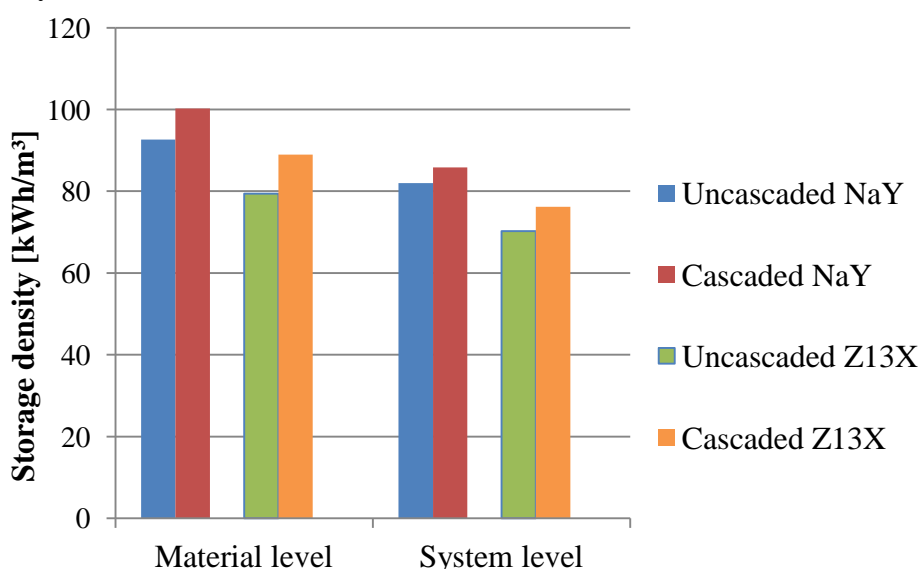


Figure 4: Comparison of energy densities with different materials for uncascaded/cascaded system on material and system level

In the graph it can be seen, that the storage density for NaY is higher than the storage density of Z13X. For both materials, the storage density can be increased through the use of the cascading system.

The absolute numbers are smaller compared to values in literature [9,10] for two main reasons. One reason is that a temperature lift of 30 K between evaporator and adsorber as a realistic value for heating applications was assumed. The other reason is the adsorber type. A coated adsorber was assumed here, that can be operated with low driving temperature differences, hence the effective adsorbent density of only 400 kg/m<sup>3</sup>.

Comparing the numbers for NaY between material and system level, the storage density is smaller on system level due to a larger volume that was considered. The cascading only brings a small benefit on system level but the system is more complicated than only using an uncascaded

system. For Z13X the same tendency can be seen. Therefore a future use of the cascading system is questionable according to these results alone.

The storage efficiency is the second value that is presented in the following. Table 3 shows the storage efficiencies that were calculated for the same materials for both the uncascaded and the cascading adsorption system.

Table 3: Storage efficiencies for different materials for uncascaded/cascaded system

Material	$\eta$ uncascaded	$\eta$ cascaded
NaY	0.94	1.02
Z13X	0.94	1.05

An increase in storage efficiency can be seen for both materials with the cascading adsorption system compared to the uncascaded system. The storage efficiency in the uncascaded system is equal for both materials, the difference to 1 mainly results from the loss of sensible heat. Z13X benefits more from the cascading system than NaY, thus the storage efficiency for Z13X is slightly higher than for NaY.

For the SAWS, a sensitivity analysis of the charging state of the storage at the beginning of the AHP operation is performed. This is achieved by varying the plateau height ratio (PHR) i.e. the ratio of height of the plateau region in the initial tank temperature profile to the total tank height. The effect of varying the PHR on the storage density and efficiency is shown in Figure 5. Two different modes of operation were considered here, namely continuous and intermittent supply of useful heat during the discharging phase. During the continuous operation, heat is continuously extracted from the storage tank with additional heat supplied by the condenser during the desorption half-cycle. During the intermittent operation, useful heat is extracted directly from the adsorber near the end of the adsorption half-cycle and from the condenser during the desorption half-cycle. The heat from the storage is, thus, used exclusively for desorbing the AHP. The direct discharge phase is the same for both modes of operation and is accounted for by calculating the energy content in the storage at the end of the AHP operation.

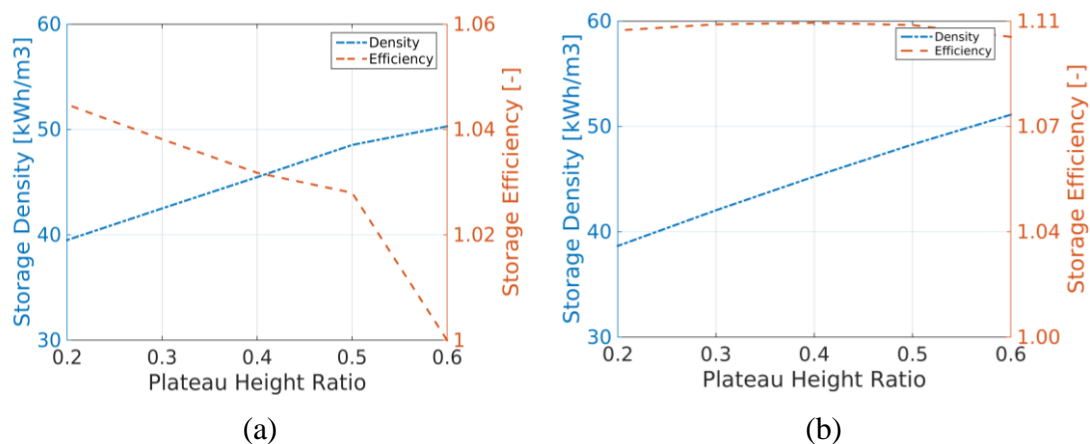


Figure 5: Variation of storage density and efficiency with the plateau height ratio in the initial storage temperature profile for (a) continuous and (b) intermittent supply of useful heat

The storage density increases with an increase in the PHR for both modes. A larger PHR indicates a larger amount of heat stored during the charging phase which leads to an increase in the storage density. This increased density comes at the cost of decreased efficiency during

continuous operation, as there is lesser cool water available for the adsorption half-cycle leading to nearly direct discharge of the tank initially. The large temperature lift of 30 K that the AHP needs to achieve lead to a low COP\_AHP and thus, a storage efficiency only slightly greater than 1. The large temperature lift also requires a high desorption temperature for the AHP to function, leading to a decrease in the time when the heat pumping effect can be used in the SAWS and a correspondingly larger share of direct discharge.

The intermittent operation, on the other hand, results in a greater storage efficiency because direct discharge of the tank is reduced. Further, this also does away with the trade-off between density and efficiency for higher PHRs as the adsorber is also connected directly to the heat sink. The intermittent operation, however, has low powers (2-3 kW) during the AHP operation which would require a direct discharge power of about 12 kW for a complete discharge time of 12 hours.

It must be noted here that the temperature at the top of the tank is relatively high for the intermittent operation, after the same number of AHP cycles as the continuous operation, as can be seen from the curve labelled 'AHP End' in Figure 6. This represents a potential for optimising the SAWS by decreasing the time during which the storage is discharged directly and requires further investigation.

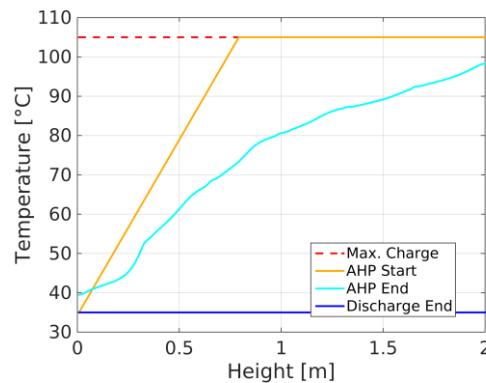


Figure 6: Temperature profile in the water storage at the beginning of the discharge phase

The storage density can be increased further by charging the storage to the 'Maximum Charge' state and using the energy content until the initial temperature profile described as 'AHP Start' (same as that in Figure 3) directly i.e. without the AHP. For the case of intermittent operation with  $PHR = 0.6$ , this leads to an increase in the storage density from  $51 \text{ kWh/m}^3$  to  $63 \text{ kWh/m}^3$ , but a decrease in the efficiency from 1.11 to 1.08.

### Summary/Conclusions

Two concepts for heat storage involving adsorption, namely a cascading adsorption storage and a sorption-assisted water storage have been investigated in this work in terms of storage density and efficiency. In order to compare, different storage media and concepts, it is important to consider the volume of the system and not just the materials themselves. Further, for heat storage concepts involving heat pumping effects a realistic temperature lifts needs to be considered. In this work, a lift of 30 K was studied.

It is shown that cascading can lead to a moderate increase in the storage density for an adsorption heat storage. Amongst the materials considered here, a maximum storage density of  $86 \text{ kWh/m}^3$  at an efficiency of 1.02 for the working pair NaY-Water was reached.

Where a water storage is available and an adsorption storage is not feasible or desired, a SAWS can be considered. For a system volume similar to the cascading sorption storage, a storage density of 51 kWh/m<sup>3</sup> at an efficiency of 1.11 during intermittent operation was reached. Using smart control strategies, like direct discharge both before and after the 'sorption-assisted' phase, the difference between the storage density of the SAWS and cascading adsorption storage can be further reduced. The AHP in the SAWS system is small as compared to the adsorption storage module and has less demands on the peripheral components due to the relatively moderate temperatures. Thus, the SAWS represents a lower cost system to boost storage density and efficiency.

The 30K temperature lift that the AHP has to provide in the cases considered here reduces the advantage gained in the cascading adsorption storage and the SAWS as compared to the uncascaded adsorption storage and a water storage, respectively. In case of the SAWS, the storage density could be further increased by cooling the lower part of the stratified storage below the assumed supply temperature (35°C) by heating the AHP evaporator from the storage during part of the adsorption phases. It seems promising to develop an adapted adsorption cycle for this mode of operation of the SAWS.

### Acknowledgements

Funding by the German Federal Ministry of Education and Research (BMBF) through the cooperative project MAKSOE (grant no. 03SF0441A) is gratefully acknowledged.

### References

- [1] Hauer, A., *Thermal Energy Storage with Zeolite for Heating and Cooling*, Proceedings of the 7th International Sorption Heat Pump Conference ISHPC, 385-390, 2002.
- [2] N'Tsoukpoe, K.E., Liu H, Le Pierres, N. & Luo, L., *A review on long-term sorption solar energy storage*, Renewable and Sustainable Energy Reviews 13, 2385-2396, 2009.
- [3] Rommel M., Hauer A., van Helden, W., *IEA SHC Task 42 / ECES Annex 29 Compact Thermal Energy Storage*, Proceedings of the 4th International Conference on Solar Heating and Cooling for Buildings and Industry, 226-230, 2015
- [4] Wittstadt, U., Fueldner, G., Laurenz, E., Warlo, A., Große, A., Herrmann, R., Schnabel, L., Mittelbach, W., *A novel adsorption module with fiber heat exchangers: Performance analysis based on driving temperature differences*, Renewable Energy 110 (Supplement C), 154-161, 2017
- [5] Schwamberger, V., Schmidt, F. P., *Smart use of a stratified hot water storage through the coupling to an adsorption heat pump cycle*, Proceedings of 8th International Renewable Energy Storage Conference and Exhibition (IRES), 2013
- [6] Munz, G., Schmidt, F.P., Nunez, T., & Schnabel, L., Patent No. US 20090282846 A1, United States of America, 2009
- [7] Schwamberger, V., Joshi, C., & Schmidt F.P., Second law analysis of a novel cycle concept for adsorption heat pumps, *Proceedings of the International Sorption Heat Pump Conference ISHPC11*, 991-998, 2011.
- [8] Schwamberger, V., *Thermodynamische und numerische Untersuchung eines neuartigen Sorptionszyklus zur Anwendung in Adsorptionswärmepumpen und -kältemaschinen*, Karlsruhe Institute of Technology, 2016
- [9] Cabeza, L. F., Solé, A., Barreneche, C., *Review on sorption materials and technologies for heat pumps and thermal energy storage*, Renewable Energy 110, 3-39, 2017
- [10] Aydin, D., Casey, S. P., Riffat, S., *The latest advancements on thermochemical heat storage systems*, Renewable and Sustainable Energy Reviews, 356-367, 2015.



# Design and control of adsorption cooling systems based on dynamic optimization

A. Gibelhaus, T. Tangkrachang, U. Bau, F. Lanzerath and A. Bardow\*

RWTH Aachen University, Chair of Technical Thermodynamics, Aachen, Germany

\*Corresponding author: [andre.bardow@itt.rwth-aachen.de](mailto:andre.bardow@itt.rwth-aachen.de)

## Abstract

Thermally driven adsorption chillers offer a sustainable alternative to compression chillers. However, the expected sustainability of adsorption chillers is often not realized in practice due to high electrical energy consumption of peripheral devices, such as pumps and fans. To minimize the consumption of electrical energy, we propose a method for simultaneous optimisation of control and design. For this purpose, first, we set up a holistic system model of a solar-driven adsorption cooling system, including peripheral devices (circulating pumps, dry cooler and solar collector). Then, we use an efficient dynamic optimisation algorithm to simultaneously optimise control and system design aiming at minimum consumption of electrical energy. The proposed method is shown to increase the electrical efficiency by almost one order of magnitude, compared to a system optimized for power density.

**Keywords:** thermal cooling, adsorption chiller, system simulation, electrical efficiency

## Introduction/Background

Thermally driven adsorption chillers allow for an efficient use of solar or waste heat to meet cooling demands and, thus, offer a promising alternative to conventional compression chillers [1]. Although adsorption chillers are primarily driven by thermal energy, they often still suffer from low electrical efficiency due to peripheral devices, such as circulating pumps and heat rejection fans [2]. In some cases, the electrical efficiency of adsorption cooling systems over an entire cooling season is only marginally higher than that of conventional compression cooling systems [3, 4]. Poor electrical efficiency of adsorption cooling systems has two main sources: Poor control and poor system design. Poor control is due to non-optimal choice of control parameters, such as adsorption chiller phase times, pump speeds, or fan speeds, particularly at part load conditions. Poor system design is due to under- or oversizing of components, such as dry cooler or solar collector, leading to an unbalanced system design with bottlenecks.

To overcome poor control, Nienborg et al. [5] recently proposed a generic control algorithm to optimise the operation of the dry cooler and the cooling water pump as the main electrical energy consumers. With this control algorithm, these authors save up to 25% of electrical energy. As an existing system was investigated, the system design was kept constant. However, control and system design influence each other, since an unbalanced system design leads to inefficient operation: e.g. an undersized dry cooler forces inefficient operation of pumps and fans to release the required heat and increases the recooling temperature of the adsorption chiller, both leading to low electrical efficiency. Thus, to achieve maximum electrical efficiency, control and system design have to be considered simultaneously.

In this study, we propose an efficient method to simultaneously optimise control and system design of a thermally driven adsorption cooling system. For this purpose, we set up a holistic dynamic model consisting of adsorption chiller and peripheral devices (circulating pumps, dry cooler and solar collector), which is described in Section 2. In Section 3, we formulate an optimisation problem, which is solved by the efficient multiple-shooting optimisation algorithm MUSCOD-II [6]. In Section 4, we show the results of control and design

optimisation for exemplarily ambient conditions. The results show great potential to increase the electrical efficiency of the adsorption cooling system by almost one order of magnitude, compared to a system optimized for power density.

### Modelling of the solar-thermally driven adsorption cooling system

The solar-thermally driven adsorption cooling system is modelled in the object-oriented language Modelica, using the adsorption energy systems library SorpLib developed at RWTH Aachen University [7]. The modelled system is shown in Figure 1 and consists of following main components: 1) adsorption chiller, 2) solar collector, 3) dry cooler and 4) circulating pumps. The cooling load is modelled as ideal heat source with constant cooling demand. The components are connected by the heat transfer fluid water. Fluid properties of water are calculated with TILMedia [8] based on RefProp [9] with data from Chase [10] and Cox et al. [11].

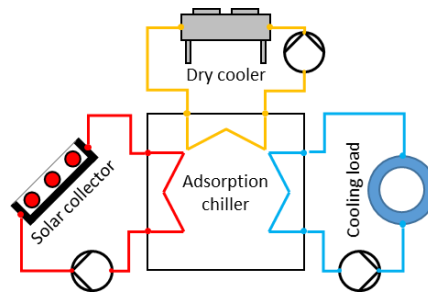


**Figure 1:** Scheme of solar-thermally driven adsorption cooling system: The main components of the system are adsorption chiller, solar collector, dry cooler, and circulating pumps.

#### 1) Adsorption chiller

For the adsorption chiller, we use an experimentally validated dynamic model with the working pair silica gel / water [12]. We extend the model to a 2-bed chiller by adding a second identical adsorber. The dynamic adsorption chiller model consists of 1-D discretized models for the heat exchangers and lumped-parameter models for the adsorbent and the refrigerant with transient energy and mass balances, described by differential equations. Besides, the model includes algebraic equations for equilibrium data of the working pair and heat and mass transfer resistances limiting the adsorption process. For detailed information and full equations, the reader is referred to Lanzerath et al. [12].

#### 2) Solar collector

For the solar collector, a simplified model is derived from a TRNSYS model [13]. The collector outlet temperature  $T_{col}$  is calculated from the energy balance

$$\dot{m}_{coll} [h_{out}(T_{col}) - h_{in}] = \dot{Q}_{solar} - \dot{Q}_{loss}, \quad (6)$$

where  $\dot{m}_{coll}$  is the mass flow rate of the heat transfer fluid,  $h_{out}$  and  $h_{in}$  are the outflowing and the incoming specific enthalpy of the heat transfer fluid, respectively,  $\dot{Q}_{solar}$  is the solar heat flow and  $\dot{Q}_{loss}$  is the heat loss of the collector.

The solar heat flow  $\dot{Q}_{solar}$  is calculated by

$$\dot{Q}_{solar} = (I_b + I_d) A \eta_0, \quad (7)$$

where  $I_b$  is the beam radiation,  $I_d$  is the diffuse radiation,  $A$  is the collector area and  $\eta_0$  is the zero-loss efficiency of the collector. The heat loss of the collector  $\dot{Q}_{\text{loss}}$  is calculated by

$$\dot{Q}_{\text{loss}} = a_1 A (T_{\text{col}} - T_{\text{amb}}) + a_2 A (T_{\text{col}} - T_{\text{amb}})^2, \quad (8)$$

where  $a_1$  and  $a_2$  are first and second order loss coefficients, respectively, and  $T_{\text{amb}}$  is the ambient temperature. For the parameters  $\eta_0$ ,  $a_1$  and  $a_2$  values 0.717,  $1.52 \frac{\text{W}}{\text{m}^2\text{K}}$  and  $0.0085 \frac{\text{W}}{\text{m}^2\text{K}^2}$  are used according to the specifications of commercially available solar collectors [14]. The area of one of these collectors is  $1.6 \text{ m}^2$  and the total area is determined by the number of thermal collectors  $n_{\text{col}}$ .

### 3) Dry cooler

The dry cooler model is derived from a TRNSYS model employing the effectiveness-NTU (Number of Transfer Units) method [15]. The model introduces 2 parameters to describe the dry cooler: 1. the internal heat transfer  $F_{\text{int}}\delta$  and 2. the external heat transfer  $F_{\text{ext}}\gamma$ . These 2 parameters can be obtained for a specific dry cooler from measurement data or manufacturers' catalogues. In this study, the parameters are determined for the dry cooler Guntner GFHC WD 035 from Guntner Product Calculator ( $F_{\text{int}}\delta = 1086$  and  $F_{\text{ext}}\gamma = 1.868$ ) [16]. The electrical power of the dry cooler  $P_{\text{dry}}$  depends on the air flow rate  $\dot{V}_{\text{air}}$  via the affinity law [15]:

$$P_{\text{dry}} = P_{\text{dry,max}} \left( \frac{\dot{V}_{\text{air}}}{\dot{V}_{\text{air,max}}} \right)^3. \quad (9)$$

The maximal air flow rate  $\dot{V}_{\text{air,max}}$  is  $1734 \frac{\text{m}^3}{\text{h}}$  and the corresponding electrical power  $P_{\text{dry,max}}$  is 70 W for the Guntner GFHC WD 035 [16]. The total recoler capacity can be adjusted by the number of identical dry coolers  $n_{\text{dry}}$ .

### 4) Circulating pumps

For the circulating pumps, an efficiency-based model is used. The electrical power of a pump  $P_p$  is calculated by

$$P_p = \frac{1}{\eta_p} \dot{V} \Delta p, \quad (10)$$

where  $\eta_p$  is the total pump efficiency,  $\dot{V}$  is the volume flow rate and  $\Delta p$  is the pressure drop in a component. The efficiency of all pumps is assumed to 0.4, which is a typical average value of circulating pumps in heating and cooling applications [17]. The pressure drops in the heat exchangers of the adsorption chiller are calculated with the pressure drop correlation for tubes from the VDI Heat Atlas [18] with the equation of Konakov [19] for the turbulent regime. For the solar collector and the dry cooler, a simple quadratic pressure drop correlation is used:

$$\Delta p = \Delta p_{\text{nom}} \left( \frac{\dot{V}}{\dot{V}_{\text{nom}}} \right)^2 \quad (11)$$

The nominal pressure drops  $\Delta p_{\text{nom}}$  and the nominal volume flow rates  $\dot{V}_{\text{nom}}$  are derived from manufacturer data [14, 16].

## Optimisation method for control and system design

The combination of all models leads to a differential-algebraic equation (DAE) process model. The process model has 6 control parameters:

- 4 volume flow rates  $\dot{V}$  in the heat exchangers of the adsorption chiller, i.e., for the processes of adsorption, desorption, evaporation, and condensation,
- air flow rate of the dry cooler  $\dot{V}_{\text{air}}$ , and
- cycle time of the adsorption chiller  $t_{\text{cycle}}$

and 2 design parameters:

- number of solar collectors  $n_{\text{col}}$  and
- number of dry coolers  $n_{\text{dry}}$ .

The control parameters influence the thermal performance as well as the electrical performance of the system: For a high thermal performance, high volume flow rates are preferable, since convective heat transfer coefficients increase and higher heat flow rates can be transferred. At the same time, higher volume flow rates increase the pressure drops quadratically and the electrical efficiency decreases. Furthermore, control parameters influence each other, e.g. a higher air flow rate in the dry cooler can compensate a lower volume flow rate of the circulating pump and vice versa. Thus, there are many possible combinations of control parameters. Additionally, the choice of control parameters also depends on system design, since e.g. a higher number of solar collectors allows for a lower volume flow rate for desorption.

The objective is to provide the required thermal performance (cooling power) with the optimal electrical performance (maximal electrical efficiency). To characterise the electrical efficiency, we define the Energy Efficiency Ratio (EER) as ratio between cooling power  $\dot{Q}_{\text{cool}}$  over one cycle and electrical power of dry cooler and pumps over one cycle:

$$\text{EER} = \frac{\int_0^{t_{\text{cycle}}} \dot{Q}_{\text{cool}} dt}{\int_0^{t_{\text{cycle}}} P_{\text{dry}} + \sum P_p dt} \quad (12)$$

The resulting optimisation problem reads:

$$\begin{aligned} \min_{x(\cdot), z(\cdot), p_c, p_d, t_{\text{cycle}}} \quad & -\text{EER}(x(t_{\text{cycle}}), z(t_{\text{cycle}}), p_c, p_d) && \text{(Objective function)} \\ \text{s.t.} \quad & \dot{x} = f(x(t), z(t), p_c, p_d) && \text{(Dynamic model)} \\ & 0 = g(x(t), z(t), p_c, p_d) && \\ & x(t = 0) = x(t = t_{\text{cycle}}) && \text{(Cyclic steady state)} \\ & \frac{Q_{\text{cool}}(t_{\text{cycle}})}{t_{\text{cycle}}} \geq \dot{Q}_{\text{cool, set}} && \text{(Set cooling power)} \\ & 0.3 p_{c, \text{nom}} < p_c < p_{c, \text{nom}} && \text{(Part load of pumps and fan)} \\ & p_d = p_{d, i} && \text{(Fixed design parameters)} \end{aligned}$$

where  $x$  summarises the differential states,  $z$  summarizes the algebraic states,  $p_c$  summarizes the control parameters and  $p_d$  summarizes the design parameters. This optimisation problem has to be solved for each system design and for each set cooling power, since optimal control parameters depend on system design and on required cooling power. The resulting multiple optimisation problems are solved using the efficient multiple-shooting algorithm MUSCOD-II [6].

## Results and Discussion

In this section, we determine the optimal control and design parameters of a solar-thermally driven adsorption cooling system. First, we consider a fixed system design. For this design, we optimise the control parameters for different load points to quantify the influence of control on the electrical efficiency. Second, we investigate the influence of the design parameters on the electrical efficiency under optimal control to isolate and quantify the effect of design. For the investigations, we exemplarily use ambient conditions for a summer day in southern Europe: Beam radiation is  $I_b = 800 \frac{W}{m^2}$ , diffuse radiation is  $I_d = 160 \frac{W}{m^2}$  and ambient temperature is  $T_{amb} = 30 \text{ }^\circ\text{C}$ .

### Control optimisation

For the investigation of control parameters, we use an exemplary random design as reference case: the number of solar collectors  $n_{col}$  is 4 and the number of dry coolers  $n_{dry}$  is 1. Figure 2 (a) shows the energy efficiency ratio EER of the system with optimal control parameters as function of the load point  $\dot{Q}_{cool,set}$ . Figure 2 (b) shows the corresponding optimal volume flow rates and the optimal cycle time as function of the load point  $\dot{Q}_{cool,set}$ . For the full load of  $\dot{Q}_{cool,set} = 1.05 \text{ kW}$ , the optimal cycle time is short to achieve a high cooling power. At the same time, the EER is very low, with a value of 11, due to high volume flow rates required to provide sufficient power for recooling and heating. Decreasing set cooling power  $\dot{Q}_{cool,set}$  down to 0.6 kW allows for longer cycle times and the optimised volume flow rates of the pumps and the fan decrease down to minimum part-load, which we define as 30 % of the full load values. The EER increases up to 227. For a cooling power of 0.6 kW, the minimum part-load for the pumps and the fan is reached and thus, the highest achievable EER is also reached. Below this set cooling power  $\dot{Q}_{cool,set}$ , the EER would decrease, if the consumption of electrical energy remains constant and the actual cooling power  $\dot{Q}_{cool}$  decreases. This effect is not shown in Figure 2 since the actual cooling power  $\dot{Q}_{cool}$  also remains constant due to the constraint  $\dot{Q}_{cool} \geq \dot{Q}_{cool,set}$  in the optimisation problem.

These results show the importance of control parameter adaption in part-load for adsorption cooling systems: With constant control parameters, the low EER of full load would even decrease in part-load, since the consumption of electrical energy remains constant and the cooling power decreases. With control parameter optimisation, the EER can be increased by up to factor 20 in part-load. The higher EER of adsorption cooling systems in part-load has to be considered for the design. An over-sized system could increase the electrical efficiency significantly.

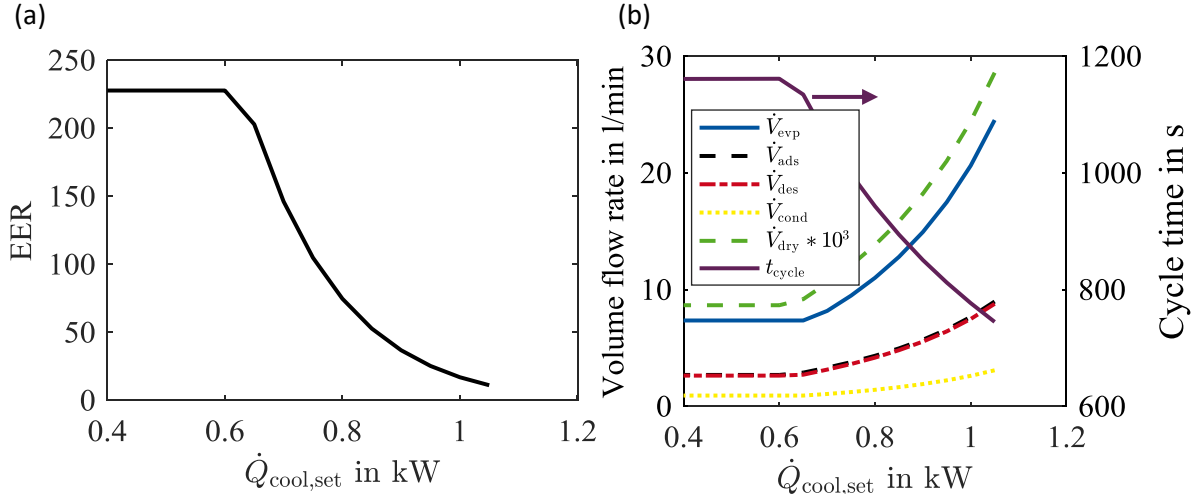


**Figure 2:** (a): Energy efficiency ratio EER (Equation (12)) with optimal control parameters as function of the load point  $\dot{Q}_{cool,set}$ . (b): Optimal volume flow rates in evaporator  $\dot{V}_{evp}$ , adsorber in adsorption phase  $\dot{V}_{ads}$  and in desorption phase  $\dot{V}_{des}$ , condenser  $\dot{V}_{cond}$ , dry cooler  $\dot{V}_{dry}$ , and optimal cycle time as function of the load point  $\dot{Q}_{cool,set}$ . The diagrams correspond to the exemplary reference design: number of solar collectors  $n_{col} = 4$  and number of dry coolers  $n_{dry} = 1$ .

### Design optimisation

Figure 3 (a) shows the energy efficiency ratio EER of the reference case (cf. Figure 2) and of 2 larger systems with a higher number of collectors and dry coolers ( $n_{col} = 7, n_{dry} = 3$  and  $n_{col} = 10, n_{dry} = 5$ ). For all 3 cases, the control parameters are optimised. Thus, the results capture the influence of the system design. For larger systems, the maximum cooling power increases up to 1.5 kW for the design with 10 collectors and 5 dry coolers because of higher available power for heating and recooling. A larger system can also provide a lower cooling power more efficiently than a smaller system in full load due to higher efficiency in part-load. For example, a cooling power of 1.35 kW can be provided by the system with 7 collectors and 3 dry coolers with an EER of 8. The larger system with 10 collectors and 5 dry coolers can provide the same cooling power with an EER of 29 which is 3.6 times higher than for the smaller system. The maximum EER for each design is limited by the minimum possible part-load for the control parameters which is given by the constraint  $0.3 p_{c,nom} < p_c < p_{c,nom}$  in the optimisation problem.

To illustrate the effect of system design on EER, Figure 3(b) shows the EER for a constant cooling power of 1.35 kW as function of the number of solar collectors  $n_{col}$  and the number of dry coolers  $n_{dry}$ . Each configuration is evaluated at optimal control parameters. A system optimised for power density, which can still provide a cooling power of 1.35 kW ( $n_{col}=7$  and  $n_{dry}=3$ ) reaches an EER of 8. For larger systems, the EER increases above 70 ( $n_{col}=25$  and  $n_{dry}=6$ ), which is almost one order of magnitude higher than for the system with optimal power density. For the number of dry coolers, an optimum regarding EER exists due to the minimal part-load of 30 % for each dry cooler. Therefore, a higher number of dry coolers also increases the minimum electrical energy demand in part-load. Thus, an oversized as well as an undersized dry cooler reduces the electrical efficiency of the system. For the number of solar collectors, no optimum exists: For a higher number of solar collectors, the heat flow rate increases and allows for lower volume flow rates in desorption phase and shorter cycle times

leading to a lower electrical energy demand. The choice of the system design is a trade-off between investment costs and operating costs: E.g. a low number of collectors and dry coolers lead to high operating costs due to low EER, but the investment costs are low and vice versa for a high number of collectors and dry coolers. If investment costs are available the presented method allows to identify the optimal system design for a specific case.

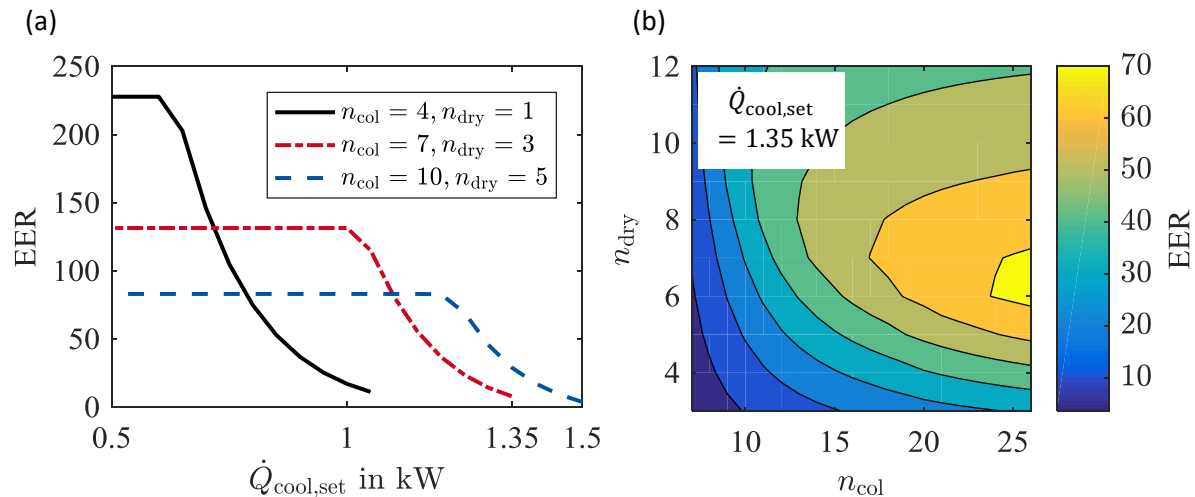


**Figure 3:** (a): Energy efficiency ratio EER at optimal control parameters as function of the set cooling power  $\dot{Q}_{cool,set}$  for 3 system designs. (b): EER at optimal control parameters as function of the number of solar collectors  $n_{col}$  and the number of dry coolers  $n_{dry}$  for a set cooling power of 1.35 kW.

## Conclusions

Control and system design of thermally driven adsorption cooling systems are key to achieve high electrical efficiencies (EER) required to compete with conventional compression cooling systems. In this study, we propose an efficient method to optimise both control and system design. The results show that control optimisation can increase the EER by about factor 20 in part-load. The higher efficiency in part-load can be systematically exploited even further in system design. With an oversized system, the EER to provide a cooling power of 1.35 kW increases by almost one order of magnitude compared to a system optimised for power density. Thus, the resulting system design is a trade-off between investment costs and operating costs and can be determined by the proposed method.

## References

- [1] Choudhury, B., Saha, B. B., Chatterjee, P. K., Sarkar, J. P., "An overview of developments in adsorption refrigeration systems towards a sustainable way of cooling", *Applied Energy*, 2013, [doi:10.1016/j.apenergy.2012.11.042](https://doi.org/10.1016/j.apenergy.2012.11.042).
- [2] Speerforck, A., Schmitz, G., "Integration of an adsorption chiller in an open-cycle desiccant-assisted air-conditioning system", *Science and Technology for the Built Environment*, 2015, [doi:10.1080/23744731.2015.1015382](https://doi.org/10.1080/23744731.2015.1015382).
- [3] Weber, C., Mehling, F., Fregin, A., Daßler, I., Schossig, P., "On Standardizing Solar Cooling – Field Test in the Small Capacity Range", *Energy Procedia*, 2014, [doi:10.1016/j.egypro.2014.02.117](https://doi.org/10.1016/j.egypro.2014.02.117).

- [4] Jaehnig, D., Thueer, A., "Task 38 - Solar Air-Conditioning and Refrigeration - Monitoring Results", IEA SHC, 2011.
- [5] Nienborg, B., Dalibard, A., Schnabel, L., Eicker, U., "Approaches for the optimized control of solar thermally driven cooling systems", *Applied Energy*, 2017, doi:10.1016/j.apenergy.2016.10.106.
- [6] Leineweber, D. B., Bauer, I., Bock, H. G., Schlöder, J. P., "An efficient multiple shooting based reduced SQP strategy for large-scale dynamic process optimization. (Parts I and II)", *Computers & Chemical Engineering*, 2003, doi:10.1016/S0098-1354(02)00158-8.
- [7] Bau, U., Lanzerath, F., Gräber, M., Graf, S., Schreiber, H., Thielen, N., Bardow, A., "Adsorption energy systems library - Modeling adsorption based chillers, heat pumps, thermal storages and desiccant systems", *Proceedings of the 10th International Modelica Conference*, Lund, Sweden, 2014, doi:10.3384/ecp14096875.
- [8] Schulze, C. W., "A Contribution to Numerically Efficient Modelling of Thermodynamic Systems", TU Braunschweig, 2013.
- [9] Lemmon, E. W., McLinden, M. O., Friend, D. G., "Thermophysical properties of fluid systems", In: Lindstrom, P. J., Mallard, W. G. (Eds.): *NIST Standard Reference Database*, 2013,
- [10] Chase, M. W. J., *NIST-JANAF Thermochemical Tables*, American Inst. of Physics, 1998.
- [11] Cox, J. D., Wagman, D. D., Medvedev, V. A., *CODATA key values for thermodynamics*, Hemisphere Pub. Corp., 1989.
- [12] Lanzerath, F., Bau, U., Seiler, J., Bardow, A., "Optimal design of adsorption chillers based on a validated dynamic object-oriented model", *Science and Technology for the Built Environment*, 2015, doi:10.1080/10789669.2014.990337.
- [13] Haller, M., "TRNSYS Type 832 v5.01 "Dynamic Collector Model by Bengt Perers"", Hochschule für Technik, Rapperswill, 2013.
- [14] Apricus, "Apricus AP Solar Collector Specifications ", 2018, <https://www.energymatters.com.au/images/apricus/Brochure.pdf> [cited 21.03.2018].
- [15] Dalibard, A., "TRNSYS Type 821 - Closed wet cooling tower model for TRNSYS, Model Description", Research Center for Sustainable Energy Technology (zafh.net), Stuttgart, 2013.
- [16] Güntner Group Europe, "Güntner Product Calculator", 2018, <https://www.guentner.de/know-how/product-calculator-gpc/gpc-software/> [cited 21.03.2018].
- [17] Helm, M., "Task 48 - Pump Efficiency and Adaptability", IEA SHC, 2015.
- [18] Kast, W., Nirschl, H., Gaddis, E. S., Wirth, K.-E., Stichlmair, J., "L1 Einphasige Strömungen", In: *VDI-Wärmeatlas*, 2013, pp. 1221-1284.
- [19] Konakov, P. K., "A new correlation for the friction coefficient in smooth tubes", Report of the Academy of Science USSR, 1946.



# Early Design of a Magnetic Mover for Adsorbents

M. J. Tierney<sup>1</sup>, J. Yon<sup>1</sup>

<sup>1</sup>Department of Mechanical Engineering, University of Bristol, BS8 1TR, UK

<sup>2</sup>Affiliation and full institutional address

\*Corresponding author: mike.tierney@bristol.ac.uk

## Abstract

The use of magnetic fields to move adsorbent within an adsorption heat pump (AHP) is proposed. (It is envisaged that a zeolite or silica gel pellet could be bonded around an iron core.) The AHP would then possess the advantages of a continuous flow absorption heat pump, without resorting to corrosive and toxic working fluids. The simplest “magnetic mover” comprises a single coil switched on for a specified duration directing pellets up a vertically oriented tube. A mathematical model demonstrated an electrical COP (ratio of cooling power to electrical power) in the region from 33 to 49 and the cooling power for a 3-mm diameter guide tube was 47-to-115 watts. The calculated thermal COP was 0.77 versus 0.50 for a fixed bed and 0.78 for absorption chillers. To obtain a sufficiently low exit velocity of pellets, the “magnetic mover” should be controlled by means of sensing pellet location (rather than by adjusting a cut-off time). A prototype provided helpful observations.

**Keywords:** Adsorption, heat pump (AHP), magnetic field

## Introduction

Absorption heat pumps convert medium grade heat to refrigeration and/ or heat amplification by replacing the usual vapour compressor with a refrigerant solution, circulated between a vapour absorber and a vapour generator. In the absorber ( at ~20°C) the solution absorbs exothermically refrigerant vapour originating in the evaporator whereas in the generator (at ~80°C to ~100°C) refrigerant vapour desorbs endothermically from solution and passes to the condenser. The ratio of cooling power to rate of supply of thermal energy (coefficient of performance, COP) is 0.78 for a typical single-effect machine [1]. The absorbent liquids are corrosive and in the case of ammonia-water trace quantities of water must be removed from the nominal ammonia vapour; an additional rectifier is needed. The use of solid adsorbents, employed in adsorption heat pumps, offers more straightforward mechanical construction and the use of low cost materials [2]. The usual confinement of the adsorbent pellets to fixed, packed beds of adsorbent necessitates thermal cycling of the bed itself plus containment walls and extended surfaces. There is then an uneven load on the evaporator and dynamic heat losses reduce COP. Circulating the solid adsorbent – notwithstanding obvious practical difficulties – has attractions. The proposed AHP (Figure 1) would comprise sequences of holding chambers, adsorption chamber and desorption chamber (items 1 to 4) plus a "magnetic mover" (item 5). Note zones #1 and #3 act to allow the necessary pressure differential between the adsorber (#2) and the generator (#4). Adsorbent pellets would be impregnated with iron; item #5 is therefore a modified "coil gun" [3].

The demanding construction of such a moving bed AHP would require (1) packed beds fitted with effective internal heat transfer surfaces that permit pellet flow (2) special valves that

could halt the pellet flow and seal against a net gas pressure (3) a means of moving pellets. Assuming magnetic movement, one then is faced with finding a binder that adheres adsorbent particles to an iron core, resists mechanical forces, and yet minimises any deterioration in adsorption capacity. In this paper these problems will be set to one side; our aim is simply to assess whether or not a “magnetic mover” would operate with satisfactory energy efficiency.

Our objectives were (1) to model the pump mathematically (2) to derive the likely improvement in thermal coefficient of performance (3) to derive the likely electrical coefficient of performance. Observations from a prototype led to objective (4), to specify a satisfactory control strategy.

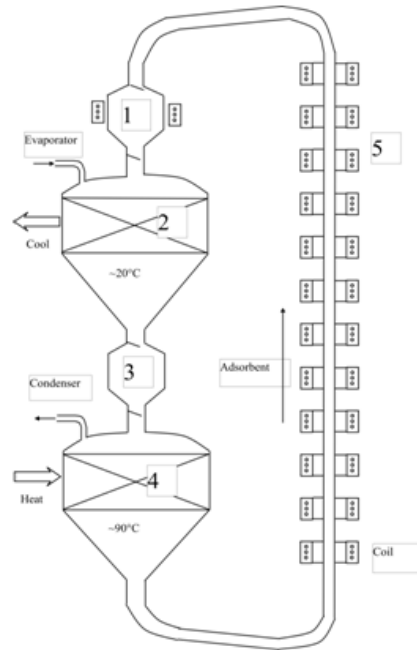


**Figure 1 AHP with Magnetic Mover (#1- air lock, #2- generator, #3- air lock, #4- adsorber, #5- magnetic mover)**

## Theory

The magnetic field along the centre-line of a coil with air-core (item #5 on Figure 1),  $H(z)$ , is found from an analytical expression. The force on a very small particle is then in proportion to  $H \cdot \nabla H$  and particle acceleration can be integrated to give height versus time. If the particle carries a certain payload of adsorbent, then from the residence time in the magnetic field the rate of refrigerant transport and hence refrigeration effect can be found.

The magnetic field and magnetic force on a small particle [4] are respectively

$$H(t, z) = \frac{N I(t)}{2 b} \left( \frac{z}{\sqrt{z^2 + a^2}} - \frac{z + b}{\sqrt{(z + b)^2 + a^2}} \right) \quad 1$$

$$F_z(t, z) = \frac{m_{fe} \mu_0 X_v H(t, z) \nabla H(t, z)}{\rho_{fe}} - m_p g - f = m_p \frac{d^2 z}{dt^2} \quad 2$$

where  $I$  is electrical current,  $a=0.0254\text{m}$  is the average radius of a coil,  $b=0.0508\text{m}$  is the length of the solenoid,  $f$  is an allowance for friction,  $F_z$  is the vertical component of net force,  $m$  is mass of either a complete particle ( $m_p$ ) or the ferrous part ( $m_{fe}$ ),  $N$  is the number of coils,  $z$  is the distance below the leading edge of the solenoid,  $X_v$  is the magnetic susceptibility of the iron ( $=5000$ ),  $\rho_{fe}$  is density of the iron,  $\mu_0$  is magnetic permittivity in vacuum. (The many turns  $N$  make for a comparatively thick solenoid and a range of coil radii,  $a$ , necessitating finite element methods for precise calculations.) The current  $I(t)$  was “cut-off” after time  $t_{cut}$  ( $I(t) = 0$  if  $t > t_{cut}$ ) to avoid excessive deceleration. The time interval between the passing of each particle was taken as  $3 \times t_{cut}$  to allow sufficient time for a particle to move clear of a re-energised magnetic field.

The electrical power requirement accounted for electrical resistance and self-inductance of the coil.

$$P_{elec} = \frac{I^2}{3} \left( \frac{l}{\sigma A_{wire}} + \mu_0 \frac{\pi N^2 a^2}{l t_{cut}} \right) \quad 3$$

where  $A_{wire}$  is the cross-sectional area of the wire,  $l$  its length and  $\sigma$  its electrical conductivity. The self-inductance term was very small, about 2% of total. (Also, the self-inductance was so low that it was reasonable (and simpler) to treat  $I(t)$  as a step function rather than an exponential recovery.) The cooling power was in proportion to the rate of mass transport of refrigerant,

$$P_{cool} = \frac{m_{ads}}{3 t_{cut}} \Delta X^* (h_e - h_c) \quad 4$$

where  $m_{ads} = (m_p - m_{fe})$  is the mass of adsorbent per particle,  $\Delta X^*$  is the change in pellet adsorption capacity (grams of moisture per gram of dry adsorbent) brought about by moving pellets from generator to adsorber,  $h_c$  is the specific enthalpy of condensate and  $h_e$  is the specific enthalpy of refrigerant vapour exiting the evaporator. Thus the ratio  $COP_e = P_{cool}/P_{elec}$  is the electrical coefficient of performance.

Heating regenerates the adsorbent, reducing the adsorbent loading by  $\Delta X^*$  (approximately). The required heating power in a “usual” adsorption cycle is calculated in full by Meunier [5] and for current purposes presented in simplified form as

$$P_{heat} = \frac{m_{ads}}{3 t_{cut}} \left( \Delta X^* h_{ads} + \Delta T_x \left( \beta X_{max} c_{ate} + c_{ads} \left( 1 + \sum \gamma_i \right) \right) \right) \quad 5$$

where  $h_{ads}$  is the specific enthalpy of adsorption,  $X_{max}$  is the maximum loading of the adsorbent (after the adsorption phase),  $c_{ads}$  is the specific heat capacity of the dry adsorbent,  $c_{ate}$  is the specific heat capacity of the adsorbate,  $\gamma_i$  is a series of heat capacity ratios relating to that of the adsorbent the extensive heat capacity of the ferrous carrier (moving bed only), the containment vessel (fixed bed only) and heat transfer surfaces (fixed bed only). Term  $\Delta T_x$  is the temperature change (from low to high) experienced by adsorbents and  $\beta$  corrects for the change in loading throughout the desorption phase. The ratio  $COP_{th} = P_{cool}/P_{heat}$  is the thermal coefficient of performance. For the silica-gel/ water pair,  $X^*$ , has (for practical purposes) been approximated as directly proportional to refrigerant pressure [6].

$$X^* = 1.92 \times 10^{-12} e^{\left(\frac{2.495 \times 10^6}{R_{gas} T_{ads}}\right)} \left[\frac{p_v(T_{ec})}{Pa}\right]$$

where  $p_{ve}$  is the saturation vapour pressure at evaporator or condenser temperature,  $T_{ec}$ , and  $R_{gas}$  is the specific gas constant for water vapour.

## Results and discussion

We considered a single coil, raising 3-mm diameter particles 1 metre and with sufficient coil turns (N) for an exit velocity of 0.5 m/s at an apogee of 1m. (Also  $I = 1$  amp,  $a = 0.0254$  m,  $b = 0.0508$ m.) The time to “cut-off” coincided with specified location  $\zeta=z/b$ ,  $\zeta = 0.0$  being the leading edge of the coil and  $\zeta=1.0$  the trailing edge. Figure 2 shows the impact of  $\zeta$  on electrical COP, N, and cooling power ( $\times 10$  for clarity). If  $\zeta > 0.5$  particles experienced some deceleration to the detriment of an increased N. However, a faster mean velocity under magnetic force, and concomitant reduced time to cut-off, enabled greater cooling power (Equation 4).

Table 1 shows the thermal COP for different mass ratio (mass of metal divided by mass of adsorbent), assuming the adsorbent achieves loading close to its equilibrium value (data [6] apply to silica gel 4A as adsorbent and water as refrigerant). The lower ratio of 0.25 characterises “magnetic moving”, whereas 6 might be more representative of a basic cycle. The corresponding specific cooling power was 53 W/ kg (adsorbent) assuming the residence time in the generator and adsorber vessels to be four times the reported characteristic times

Exit velocity should be minimised to reduce damage to pellets. Adjusting  $t_{cut}$  to account for changes in susceptibility is impractical owing to the non-linear trends (Figure 3); a proportionality constant could not be set in a conventional PID controller. An alternative strategy concerned sensors (1) in the centre of coil#1 ( $\zeta_1=0.5$ ), (2) near the leading edge of coil #2 at  $z = 0.3$ m, and (3) in the centre of coil#2 ( $\zeta_2=0.5$ ). The time delay from sensor 1 to sensor 2 yielded the exit velocity in coil 1,  $v_1$ , and the current for coil 2 was set to  $I_2 = I_1 (1 - (g z_1 + v_1^2/2)/g H)^{0.5}$ . A 3-mm separation in the solenoid (to accommodate the sensor) resulted in a small point of inflection in the magnetic force (point P on part (a) on Figure 4, showing force from coil 2 for a constant 1 amp current). The current demand and velocity profile are illustrated on the rest of Figure 4. Adjusting current in coil 1 and susceptibility by  $\pm 20\%$  retained exit velocities in the range from 0.27 to 0.52 m/s.

A small prototype has been constructed, using manually adjusted cut-off times. It was observed that (1) iron particles were projected at speed up a 0.3 m-high tube (2) the exit velocity (judged by particle apogee) was consistent from test-to-test with the same particle (3) exit velocities were inconsistent from particle-to-particle, possibly owing to variations in particle shape and susceptibility (4) a particle could lift 37x3-mm diameter silica- gel particles. Owing to excessive velocities, many particles broke. (This emphasises the requirement to control exit velocity.) (5) the “magnetic mover” worked moderately well with mild steel particles (rather than iron).

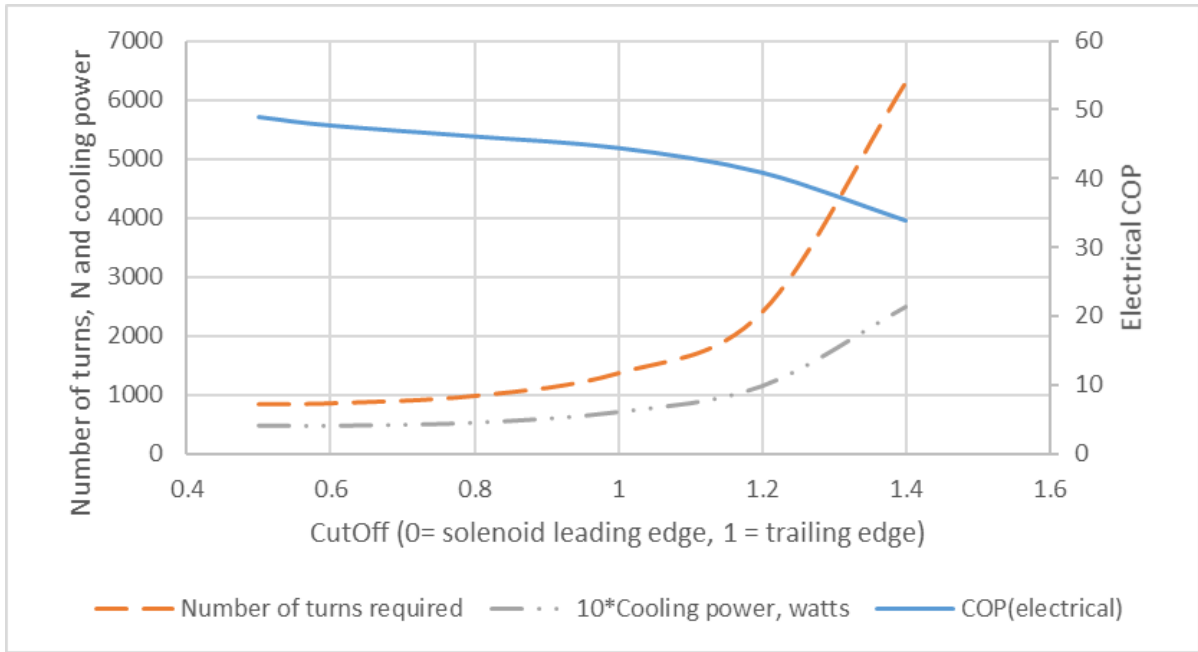


**Figure 2 Influence of coil design and machine performance to cut-off ( $I= 1$  amp,  $a = 0.0254$  m,  $b = 0.0508$  m,  $X_v=5000$ , pellet diameter = 3mm, iron comprises 20% of pellet mass )**

**Table 1 Mass Ratio versus Thermal Coefficient of Performance (Condenser and adsorber at 20°C, evaporator at 5°C, desorber at 90°C.**

Mass Ratio	0.25	1	3	6
COP (thermal)	0.771	0.732	0.646	0.550
SCP, watts/kg	53	53	53	53

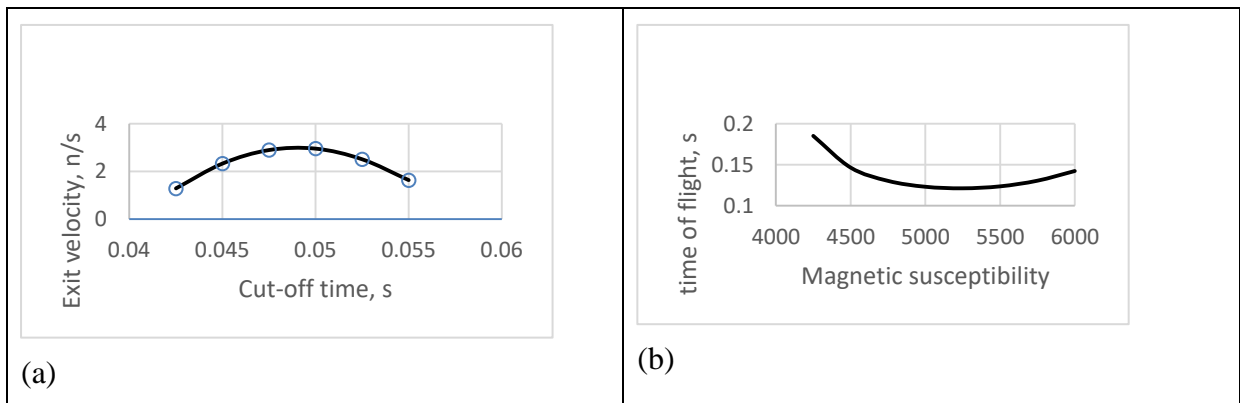
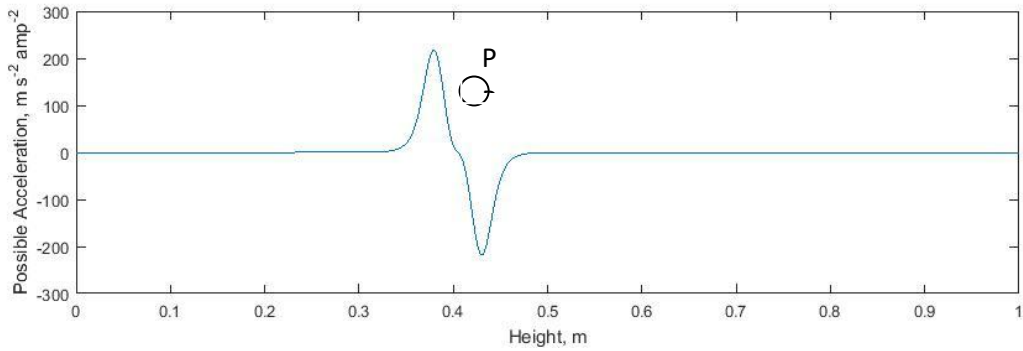
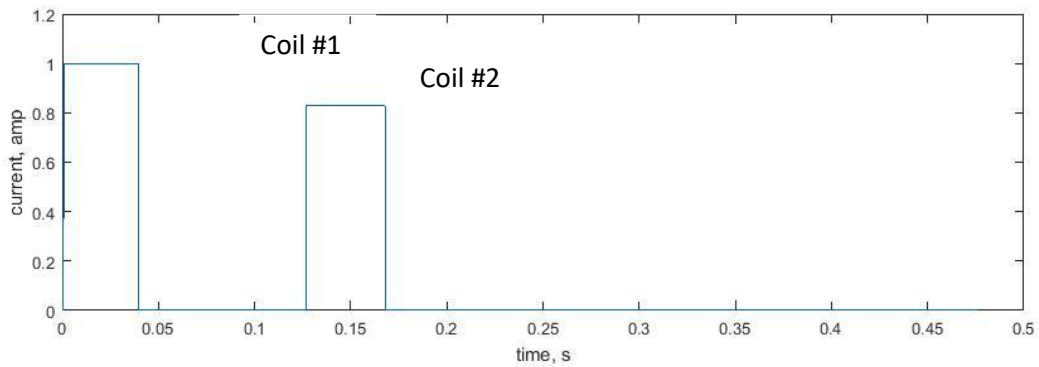


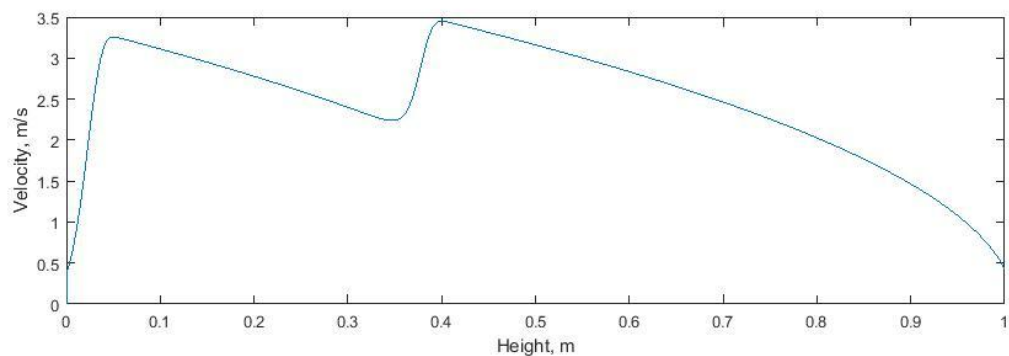
**Figure (3) Non-linearity effects (a) cut-off time ( $X_v=5000$ ) (b) magnetic susceptibility ( $t_{cut} = 0.049$  s,  $I = 1$  amp,  $a = 0.0254$  m,  $b = 0.0508$  m)**



(a)



(b)



(c)

**Figure 4 Attempts to control particle velocity at tube exit (a) magnetic component of force from coil #2 (b) current supplied (c) particle velocity – peaks correspond to coil locations**

### Conclusions

A mathematical model has been formulated for a "magnetic mover". In principle, such a device could operate with a satisfactory electrical COP (>30) and with a thermal COP approaching that of an absorption machine (~0.78). Cooling power for a single guide tube is modest (48 to 248 watts) and higher cooling powers are achieved at the cost of lower electrical COP (reduced from 49 to 34). Particle trajectories would require thoughtful control and

sensing of particle location. A prototype tentatively demonstrates capability to move iron particles and the requirement for control with multiple sensors.

## References

- [1] Stoecker, W. F., and J. W. Jones. "Refrigeration and air conditioning", 1982. McGrawHill Book Co, New York.
- [2] K. C. Ng, "Recent developments in heat-driven silica gel-water adsorption chillers," Heat Transfer Engineering, vol. 24, no. 3, pp. 1-3, 2003.
- [3] Cole A. A., "Electric gun." U.S. Patent 2,235,201, issued March 18, 1941.
- [4] S.J. Gill and C.P Malone (1963) "Force on a small particle in the vicinity of a cylinder in a homogenous magnetic field", Review of Scientific Instruments, 34, 788-790
- [5] F. Meunier, "Solid sorption heat powered cycles for cooling and heat pumping applications," Applied Thermal Engineering, pp. 715-729, 1998.
- [6] Ahamat, M.A. and Tierney, M.J., 2012." Calorimetric assessment of adsorbents bonded to metal surfaces: Application to type A silica gel bonded to aluminium". Applied Thermal Engineering, 40, 2012, doi.org/10.1016/j.applthermaleng.2012.02.021.77F. Meunier, "Solid sorption heat powered cycles for cooling and heat pumping applications," Applied Thermal Engineering, pp. 715-729, 1998..

# Squaring the circle in drying high-humidity air by a novel composite sorbent with high uptake and low pressure-drop

Meltem Erdogan<sup>1</sup>, Claire McCague<sup>2</sup>, Stefan Graf<sup>1</sup>, Majid Bahrami<sup>2</sup>,  
and André Bardow<sup>1\*</sup>

<sup>1</sup> Institute of Technical Thermodynamics, RWTH Aachen University,  
Schinkelstraße 8, 52062 Aachen, Germany,

<sup>2</sup>Laboratory for Alternative Energy Conversion, Simon Fraser University, Surrey, BC, Canada V3T 0A3

\*Corresponding author: [andre.bardow@itt.rwth-aachen.de](mailto:andre.bardow@itt.rwth-aachen.de)

## Abstract

A novel sponge-structured composite sorbent was prepared for drying of air with relative humidity higher than 60 % RH. The composite consisted of CaCl<sub>2</sub> in a mesoporous silicagel host matrix consolidated with poly(vinyl alcohol) binder. The uptake capacity was determined by thermogravimetric vapor sorption analysis. Air drying performance was tested in an open sorption bed that also allowed pressure drop measurements. The bulk density of the composite sorbent is about 3 times lower than a benchmark microporous silicagel. Thus, the water removal for fixed volumes of the composite sorbent is lower than the water removal for fixed volumes of silicagel. However, the composite sorbent increased mass-specific uptake by a factor of 2.6 and reduced pressure drop by a factor of 8 to 10 compared to silicagel. The higher mass-specific uptake and the lower pressure drop enable the proposed novel composite sorbent to reduce adsorber weight and fan power in adsorption drying.

**Keywords:** adsorptive drying, calcium chloride, silicagel

## Introduction

In desiccant dehumidification, water vapor is adsorbed or absorbed from humid air flowing through the desiccant. The desiccant is then regenerated by heating to desorb the water. The key to efficient desiccant dehumidification are sorbents with high dehumidification rate, high water uptake and low pressure drop [1–3]. High water uptake has been reported for composite sorbents of hygroscopic salts in mesoporous host matrices [4–7]. However, since these sorbents are used in packed beds, they lead to large pressure drops which increases the required fan power [8]. Thus, composite desiccants have been designed with air flow channels. For example, silicagel/polymer or salt composites have been molded into beds with radial flow designs (e.g. hollow cylinders or sorbent disks with multiple flow channels) and have theoretically and experimentally been shown to maintain high dehumidification rates while reducing the pressure drop compared to packed beds [9–12]. However, such adsorber designs have lower sorbent masses compared to packed bed adsorbers tending to lower water uptake.

Therefore, in this study, a promising composite sorbent is presented that is easy to produce as sponge structure which reduces the pressure drop while retaining high uptake. Open sorption system testing indicates that the novel composite is highly suitable for drying high humidity air (> 60 % RH).

The following experimental part describes the preparation of the composite sorbent and the test bed for performance assessment. Pressure drop, uptake and dehumidification rate are determined for a benchmark silicagel and the novel composite sorbent. Results are compared for a fixed packed bed volume to mass-specific results. Finally, the results are summarized.



## Experimental

The composite sorbent was prepared in batches of 400 g with a ratio of 55 wt.% silicagel (SiliaFlash® B150, Silicycle Inc.), 30 wt.%  $\text{CaCl}_2$  and 15 wt.% polyvinyl alcohol (PVA, MW 85,000-124,000, 99+% hydrolyzed, Sigma Aldrich). PVA binder was combined with anhydrous calcium chloride (ACP Chemicals) and dissolved in 600 mL of distilled water. The solution was combined with a mesoporous silicagel (250-500  $\mu\text{m}$  irregular grains) to create a slurry. The composite was spread in a layer less than 5 mm thick, guided by glass rods, on Pyrex baking dishes that were lined with aluminum foil. The composite was oven dried at 80 °C and cured at 150 °C. The PVA adhered to the aluminum foil, requiring the foil be peeled and scraped away, to produce 3-5 mm thick pieces of solid sorbent. The sorbent was further baked at 250 °C for 24 h, during which it darkened (Figure 1) due to the partial pyrolysis (charring) of the PVA binder [13].

The sorbent was broken into irregularly shaped pieces (1-3 mm) and packed into the fixed bed volume (0.393 L with a diameter of 100 mm and a length of 50 mm). The regeneration temperatures,  $T_{\text{Desorption}}$  of 150 °C, were above the softening point of the polymer binder, resulting in the loosely packed bed fusing into a solid “sponge-like” piece with significant open pore volume between the sorbent pieces.

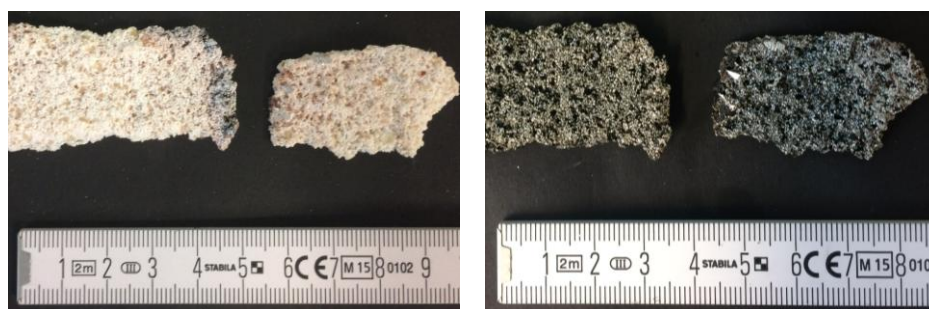


**Figure 1:** Composite after oven drying and curing at 80 °C and 150°C (left image) and composite after additional baking at 250 °C for 24 h (right image).

The composite sorbent was compared to microporous silicagel in 3.2 mm diameter beads (Sylobead® B 125, Grace Materials Technologies). A thermogravimetric analyzer (IGA-002, Hiden Isochema) was used to collect vapor sorption isotherms at 25 °C and to run 150 pressure swing cycles to assess the uptake capacity and durability of the composite sorbent. The practical performance of the sorbents was then evaluated in a fixed packed bed for 40 °C air flow of 40  $\text{m}^3/\text{h}$  with 60, 70 and 80 % RH, and regeneration temperatures of 100 °C and 150 °C. A schematic of the custom test-bed is shown in Figure .

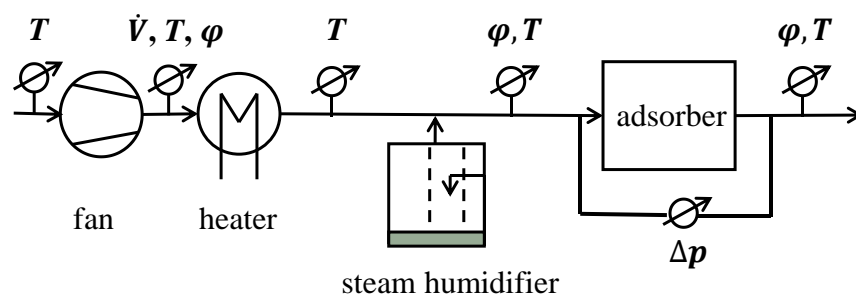


**Figure 2:** Schematic of custom test-bed for drying high humidity air. Measured values are temperatures  $T$ , volume flow  $\dot{V}$ , pressure drop  $\Delta p$  across the bed and relative humidities  $\phi$ .

The sorbent was exposed to ambient air conditioned with a heater and steam humidifier. Temperature and relative humidity were measured before and after the packed bed. Temperature was measured using Pt100-temperature-sensors ( $\pm 0.15$  [K] +  $0.002T$  [K]) and humidity was measured by capacitive humidity sensors ( $\pm 2$  % for  $0 < T < 30^\circ\text{C}$ ,  $\pm 2.3$  % for  $30 < T < 50^\circ\text{C}$ ,  $\pm 3.4$  % for  $50 < T < 70^\circ\text{C}$ ,  $\pm 4.4$  % for  $T > 70^\circ\text{C}$ ). The volumetric flow after the fan and the pressure drop across the bed were measured. The volumetric flow was measured by a thermal flow sensor ( $\pm 0.15\dot{V}$  [m<sup>3</sup>/h] +  $0.085$  [m<sup>3</sup>/h]) and the pressure drop by a differential pressure sensor ( $\pm 0.5$  [Pa] +  $0.05T$  [Pa/K]). The mass of the sorbent was measured when each equilibrium was reached ( $T_{\text{in}} - T_{\text{out}} < 1^\circ\text{C}$ ).

## Discussion and Results

Water sorption isotherms are shown for the composite sorbent and the silicagel in Figure 3. The composite sorbent takes up more than twice the water as silicagel. For high humidity air ( $> 80$  % RH), the composite sorbent reaches a maximum uptake of more than 1 kg/kg.

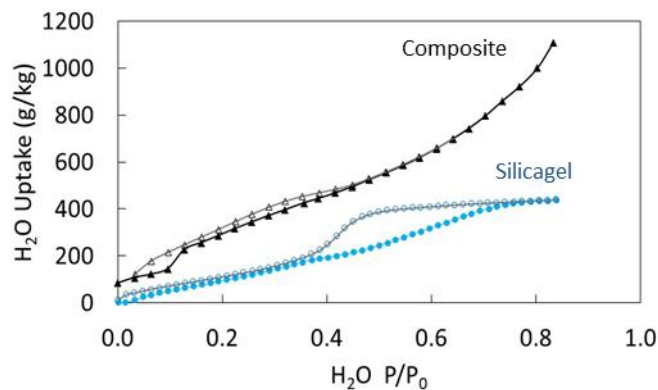


**Figure 3:** Water vapor sorption isotherms of silicagel and CaCl<sub>2</sub> composite at a temperature of 25 °C. Closed symbols for adsorption and open symbols for desorption.

To determine the hydrothermal stability, in the thermogravimetric analysis, a sample of composite sorbent was subjected 0 to 1.2 kPa swings in water vapor pressure in 40-minute cycles at 35 °C. The average change in water content per cycle was  $0.1662 \pm 0.0006$ , with no measurable loss in uptake capacity across 150 cycles.

Water removal in the test-bed experiments are shown in Figure 4 for 60 - 80 % RH and desorption at 100 °C and 150 °C both for a) a fixed bed volume of 0.393 L and b) mass-specific uptake. The water removal of the fixed bed volume filled with composite sorbent is about 37 % lower than silicagel for low relative humidity ( $> 60$  % RH) and up to 20 % lower than the silicagel for high relative humidity ( $> 80$  % RH). The water removal of silicagel is higher for a given fixed bed volume because bulk density is about 3 times higher than for the composite sorbent.

For applications where weight is a crucial issue, e.g. in the automotive industry, the mass-specific uptake (removed water per kg sorbent) is important [14, 15]. The mass-specific uptake of the composite sorbent is more than twice as high as for the silicagel (Figure 4(b)). For high humidity air ( $> 80$  % RH), the composite sorbent had a maximum uptake of about 0.78 kg/kg and absorbs 2.6 times more than silicagel.

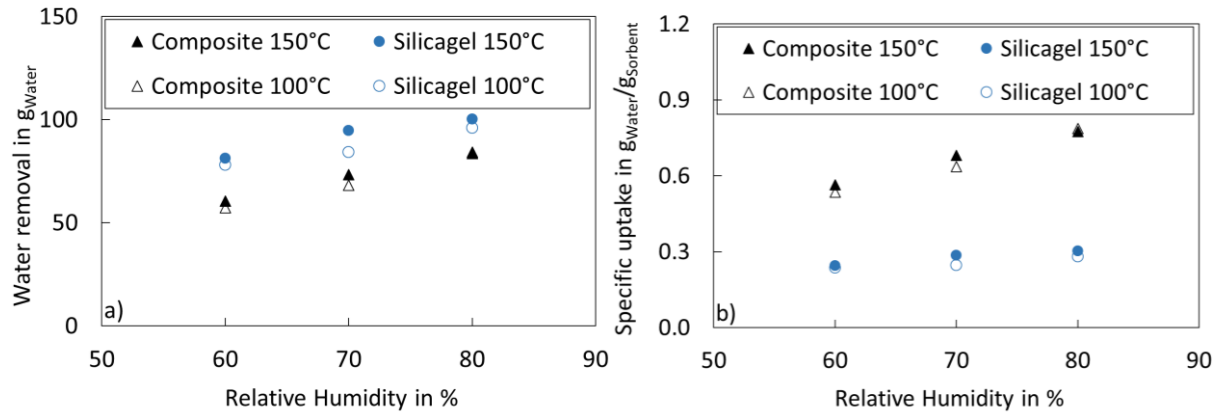


**Figure 4:** a) Water removal over relative humidity for composite sorbent and silicagel dried at 100 °C (open symbols) and 150 °C (filled symbols) in the open sorption test bed for a constant volume. b) Mass-specific uptake over relative humidity for composite sorbent and silicagel dried at 100 °C (open symbols) and 150 °C (filled symbols) in the open sorption test bed.

At the same time, the composite sorbent had a 8-10 times lower pressure drop than silicagel (Figure 5). The silicagel bed was packed with spherical beads of approximately 2 mm in diameter, while the composite sorbent formed an open porous sponge structure inside the adsorber during drying to determine the dry weight. The sponge structure reduces the pressure drop across the adsorber for all regeneration temperatures and relative humidities studied.

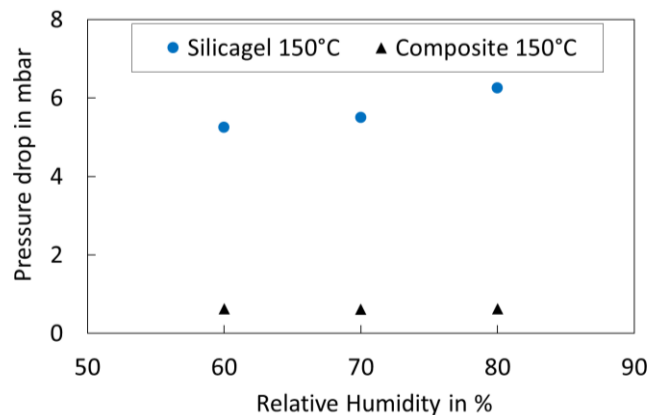


**Figure 5:** Pressure drop across the sorbent beds for composite and silicagel at 60 - 80 % RH.

The trade-off between dehumidification rate and pressure drop is shown for the fixed packed bed volume in Figure 6 a) for the composite sorbent and in Figure 6 b) for silicagel, for 60 - 80 % RH and desorption at 100 °C and 150 °C. Both, the dehumidification rate and the pressure drop are favorable for the lower regeneration temperature of 100 °C. The dehumidification rate is lower for a regeneration temperature of 150 °C due to a longer cooling period.

For silicagel, the dehumidification rate is shown over pressure drop in Figure 6 b) for 60 - 80 % RH and desorption at 100 °C and 150 °C. The dehumidification rate of the fixed packed bed volume is in the range of 69 g<sub>water</sub>/h to 103 g<sub>water</sub>/h and the pressure drop in the range of 5 to 6.5 mbar. Similar to the results of composite sorbent, the silicagel has the highest dehumidification rate for the lower regeneration temperature of 100 °C and 70 % RH. Compared to the composite sorbent, the dehumidification rate of silicagel for a fixed packed bed volume is about 24 % higher for the best case.

The dehumidification rate decreases for 80 % RH for both regeneration temperatures, since time to reach equilibrium state during adsorption increases. The pressure drop of the composite sorbent is similarly low for all measurements irrespective of the regeneration temperature (Figure 6 a).

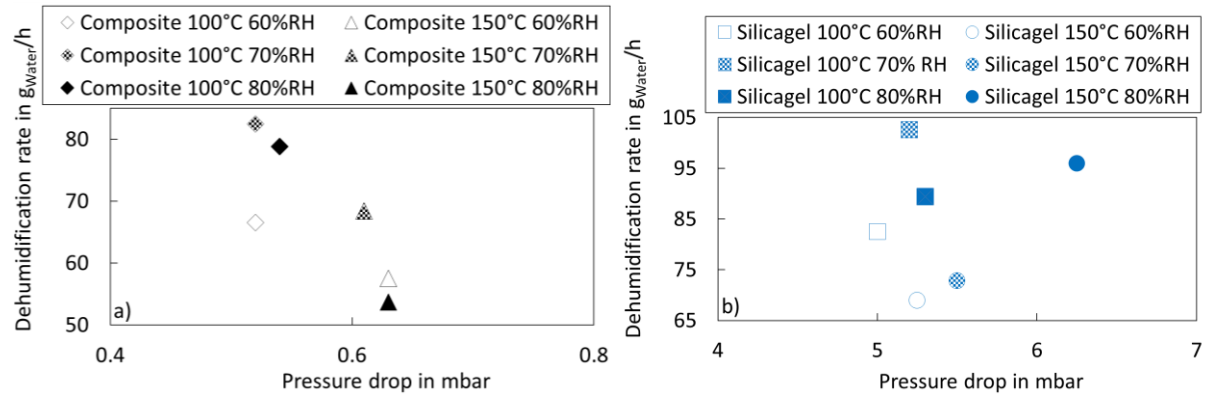


**Figure 6:** Dehumidification rate over pressure drop for a) composite sorbent dried at 100 °C and 150 °C in the open sorption test bed and for b) silicagel dried at 100 °C and 150 °C in the open sorption test bed.

The mass-specific dehumidification rate is shown over pressure drop in Figure 7. For the composite sorbent, the mass-specific dehumidification rate is in a range of about  $0.5 g_{water}/g_{sorbent}h - 0.77 g_{water}/g_{sorbent}h$  (in Figure 7 a). For silicagel, the mass-specific dehumidification rate is in a range of about  $0.2 g_{water}/g_{sorbent}h - 0.3 g_{water}/g_{sorbent}h$  and thus, up to 2-3 times lower than the mass-specific dehumidification rate of the composite sorbent. Thus, applying the composite sorbent would reduce the sorbent mass up to 2-3 times and still reach higher specific dehumidification rates as silicagel.

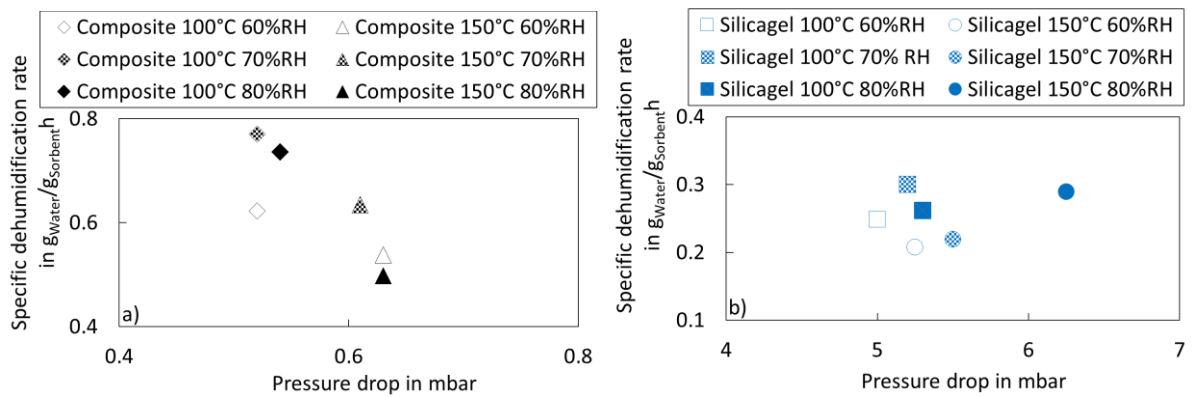


**Figure 7:** Specific dehumidification rate over pressure drop for a) composite sorbent dried at 100 °C and 150 °C in the open sorption test bed and for b) silicagel dried at 100 °C and 150 °C in the open sorption test bed.

## Conclusions

A composite sorbent allowing for simple synthesis was prepared and examined to quantify its suitability for drying high humidity air. The composite sorbent has a lower bulk density than silicagel and thus, less sorbent mass inside the adsorber. As a result, the water removal of the

composite sorbent is lower than the water removal of silicagel. However, due to its high mass-specific uptake and low pressure drop, the composite sorbent allows lower adsorber weight and requires low fan power.

## References

- [1] Sultan, M., El-Sharkawy, I. I., Miyazaki, T., Saha, B. B., Koyama, S., "An overview of solid desiccant dehumidification and air conditioning systems", *Renewable and Sustainable Energy Reviews*, 2015, [doi:10.1016/j.rser.2015.02.038](https://doi.org/10.1016/j.rser.2015.02.038).
- [2] Yadav, L., Yadav, A., Dabra, V., Yadav, A., "Effect of desiccant isotherm on the design parameters of desiccant wheel", *Heat and Mass Transfer*, 2014, [doi:10.1007/s00231-013-1219-7](https://doi.org/10.1007/s00231-013-1219-7).
- [3] Zheng, X., Ge, T. S., Wang, R. Z., "Recent progress on desiccant materials for solid desiccant cooling systems", *Energy*, 2014, [doi:10.1016/j.energy.2014.07.027](https://doi.org/10.1016/j.energy.2014.07.027).
- [4] Aristov, Y. I., " Selective Water Sorbents, A new family of materials for adsorption cooling/heating: state-of-the art", *Proc. V Minsk International Seminar "Heat Pipes, Heat Pumps, Refrigerators"*, Minsk, Belarus.2003. Pp. 379-390.
- [5] Liu, H., Nagano, K., Togawa, J., "A composite material made of mesoporous siliceous shale impregnated with lithium chloride for an open sorption thermal energy storage system", *Solar Energy*, 2015, [doi:10.1016/j.solener.2014.10.044](https://doi.org/10.1016/j.solener.2014.10.044).
- [6] Ponomarenko, I. V., Glaznev, I. S., Gubar, A. V., Aristov, Y., Kirik, S. D., "Synthesis and water sorption properties of a new composite "CaCl<sub>2</sub> confined into SBA-15 pores"", *Microporous and Mesoporous Materials*, 2010, [doi:10.1016/j.micromeso.2009.09.023](https://doi.org/10.1016/j.micromeso.2009.09.023).
- [7] Wu, H., Wang, S., Zhu, D., "Effects of impregnating variables on dynamic sorption characteristics and storage properties of composite sorbent for solar heat storage", *Solar Energy*, 2007, [doi:10.1016/j.solener.2006.11.013](https://doi.org/10.1016/j.solener.2006.11.013).
- [8] Tretiak, C. S., Abdallah, N. B., "Sorption and desorption characteristics of a packed bed of clay–CaCl<sub>2</sub> desiccant particles", *Solar Energy*, 2009, [doi:10.1016/j.solener.2009.06.017](https://doi.org/10.1016/j.solener.2009.06.017).
- [9] Awad, M. M., Ramzy K, A., Hamed, A. M., Bekheit, M. M., "Theoretical and experimental investigation on the radial flow desiccant dehumidification bed", *Applied Thermal Engineering*, 2008, [doi:10.1016/j.applthermaleng.2006.12.018](https://doi.org/10.1016/j.applthermaleng.2006.12.018).
- [10] Chen, C.-H., Hsu, C.-Y., Chen, C.-C., Chiang, Y.-C., Chen, S.-L., "Silica gel/polymer composite desiccant wheel combined with heat pump for air-conditioning systems", *Energy*, 2016, [doi:10.1016/j.energy.2015.10.139](https://doi.org/10.1016/j.energy.2015.10.139).
- [11] Girnik, I. S., Grekova, A. D., Gordeeva, L. G., Aristov, Y., "Dynamic optimization of adsorptive chillers", *Applied Thermal Engineering*, 2017, [doi:10.1016/j.applthermaleng.2017.06.141](https://doi.org/10.1016/j.applthermaleng.2017.06.141).
- [12] Kumar, A., Yadav, A., "Experimental investigation of solar-powered desiccant cooling system by using composite desiccant "CaCl<sub>2</sub>/jute"", *Environment, Development and Sustainability*, 2017, [doi:10.1007/s10668-016-9796-5](https://doi.org/10.1007/s10668-016-9796-5).
- [13] Gilman, J. W., VanderHart, D. L., Kashiwagi, T., "Thermal Decomposition Chemistry of Poly(vinyl alcohol)", In: *Fire and Polymers II*, American Chemical Society, 1995, pp. 161–185.
- [14] Christopher Y.H. Chao and Chili Wu and Chi Yan Tso and Ka Chung Chan, "Enhancement of the Performance of Adsorption Cooling System by Improving Adsorber Design and Operation Sequence", *9th International Conference of Indoor Air Quality Ventilation & Energy Conservation in Buildings (IAQVEC2016)*, 2016.
- [15] Hamdy, M., Askalany, A. A., Harby, K., Kora, N., "An overview on adsorption cooling systems powered by waste heat from internal combustion engine", *Renewable and Sustainable Energy Reviews*, 2015, [doi:10.1016/j.rser.2015.07.056](https://doi.org/10.1016/j.rser.2015.07.056).

# Lab-scale sorption chiller comparison of FAM-ZO2 coating and pellets

C. McCague, W. Huttema, A. Fradin, and M. Bahrami\*

Laboratory for Alternative Energy Conversion (LAEC), School of Mechatronic Systems Engineering,  
Simon Fraser University, 250-13450 102 Avenue, Surrey, BC, Canada, V3T 0A3

\*Corresponding author: mbahrami@sfu.ca

## Abstract

Water adsorbent AQSOA™ FAM-ZO2 (ZO2) coatings and pellets were evaluated in our custom-built lab-scale sorption chiller with two adsorber beds. Two finned-tube heat exchangers (HEX) (4.08 dm<sup>3</sup>) were coated with ZO2 by Mitsubishi Plastics and compared with two equivalent HEX packed with ZO2 pellets. When tested with 15, 30, 30 and 90 °C operating temperatures for the evaporator, condenser, adsorption and desorption, and 5 to 30 min cycle times, the sorption chiller had a peak volumetric specific cooling power of  $90 \pm 5$  kW/m<sup>3</sup> with ZO2 coated HEX compared to  $59 \pm 2$  kW/m<sup>3</sup> for HEX packed with ZO2 pellets. The specific cooling power (SCP) and coefficient of performance (COP) were determined for a range of operating conditions and were greater for ZO2 coatings compared to pellets.

**Keywords:** Sorption chiller, ASQOA FAM-ZO2, specific cooling power, coefficient of performance.

## Introduction

Silicoaluminophosphate adsorbent material AQSOA™ FAM-ZO2 was developed and commercialized by Mitsubishi Plastics Inc. for desiccant wheels and adsorption chillers operating with low regeneration temperatures [1]. ZO2 has an S-shaped isotherm and a  $\Delta w \sim 0.21$  g/g (H<sub>2</sub>O/sorbent) under 15/30/90 °C sorption chiller operation cycle temperatures. Freni et al. used a mathematical model to evaluate the sorption cycle performance of numerous adsorbent/adsorbate working pairs and concluded that, amongst water sorbents for air conditioning cycles, ZO2 and salt-silica gel composites had the highest potential coefficient of performance (COP) and specific cooling power (SCP) [2].

Girnik and Aristov studied dynamics of water ad-/desorption by ZO2 loose grains in detail through volumetric large temperature jump (V-LTJ) on monolayers and multilayers of pellets of various sizes of ZO2 pellets and found that the kinetic curves were exponential and could be described by a single characteristic time,  $\tau$ , and that in monolayer configurations ZO2 could deliver reasonable specific cooling power for compact AC systems, even for ~2 mm grains [3]. Temperature step adsorption and desorption dynamics tests on small heat exchangers (~0.2 m<sup>2</sup>, three designs) packed with 70-90 g of ZO2 with four different grain sizes were studied by Santamaria et al. with reported cooling powers up to 2.3 kW/kg, 6-8 times greater than the cooling powers achieved in tests of larger prototypes [4].

Freni et al. performed accelerated aging tests and determined that ZO2 coated by Mitsubishi Plastics Inc. and a coating of a similar silicoaluminophosphate zeolite, SAPO-34, were hydrothermally stable [5]. Further experiments by Freni et al. compared aluminium finned flat tube heat exchangers (HEX) (510 g) that were coated with SAPO-34 (0.1 mm thick, 84 g) and filled with granular SAPO-34 (0.6-0.7 mm grains, 260 g) using a single bed lab-scale sorption chiller comparing them for 5 min cycles under 15 °C/28 °C/90 °C operating temperatures [6]. The coated HEX had a SCP of 675 W/kg and volumetric SCP of 93 W/dm<sup>3</sup>, compared to the granular HEX performance of 498 W/kg and 212 W/dm<sup>3</sup>. The cooling COP

was 0.24 for the coated HEx compared to 0.4 for the granular HEx with its substantially higher sorbent/HEx ratio.

Dawoud tested ZO<sub>2</sub> coatings deposited by Mitsubishi Plastics on small substrates and HEx. For small samples, the adsorption rate decreased by 47% as the coating thickness was increased from 0.2 to 0.5 mm, however the adsorption kinetics for ZO<sub>2</sub> coatings on extruded finned-tube and finned-plate heat exchangers were substantially lower [7].

During initial tests of our sorption chiller with finned-tube heat exchangers packed with 2 mm diameter ZO<sub>2</sub> grains were performed by Sharafian et al., the highest SCP (W per kg adsorbent) was observed when the adsorbent loaded into each of the two HEx was reduced from 1.9 to 0.5 kg because the system performance was limited by the heat transfer rate in the evaporator and pressure drops in the piping and valves between the evaporator and the sorber beds in our testbed [8]. Here, an improved sorption chiller testbed is used to compare the performance of ZO<sub>2</sub> pellets and coatings. Upgrades made to the sorption chiller testbed include: i) installation of four-way valves for faster adsorption to desorption temperature switches between the two sorber beds, ii) larger diameter pipes and gate valves between the evaporator and sorber beds, and iii) a more powerful capillary-assisted low-pressure evaporator. The improvements result in higher system SCP and greater ability to compare sorbent and sorber bed performance.

## Experimental

Isotherms and isobars of ZO<sub>2</sub> powder, spherical pellets with dia.=1.8 mm, and coating were collected using a thermogravimetric vapor sorption analyser (TGA) with active pressure control (IGA-002, Hiden Isochema). Water uptake,  $w$ , is reported as

$$w = \frac{\text{mass } H_2O}{\text{mass dry sorbent}} \quad (4)$$

The lab-scale sorption chiller is shown in Fig. 1. The two sorber beds (Fig. 2) were connected to two heating/cooling (H/C) circulators using two four-way valves for automated cycling

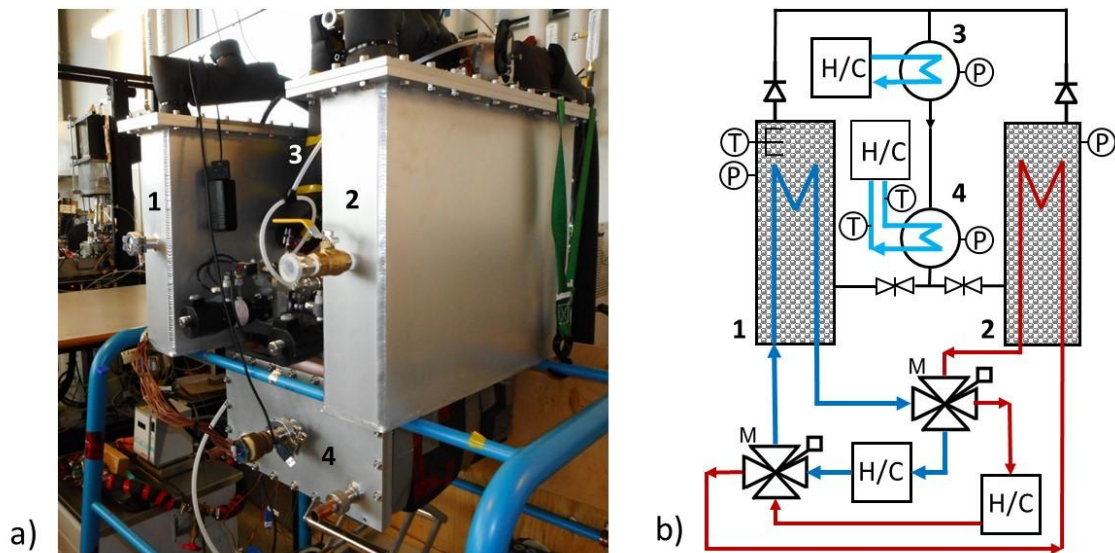


**Fig. 1.** a) Photo and b) schematic of the lab-scale sorption chiller with two sorber beds (1,2), condenser (3), *capillary-assisted low-pressure evaporator* (CALPE) evaporator (4), valves, sensors and heating/cooling (H/C) circulators.

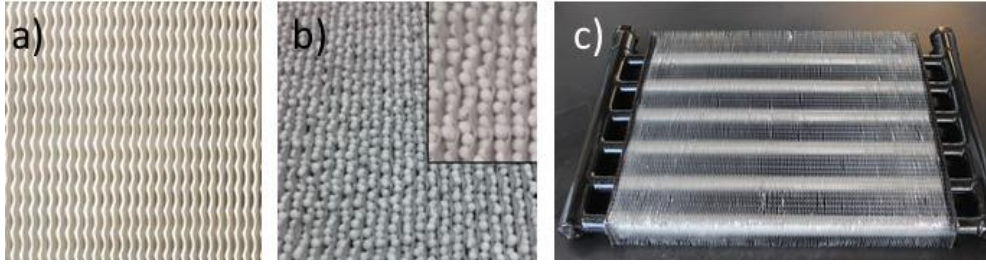


**Fig. 2.** a) Heat exchanger (HEX) coated with ZrO<sub>2</sub>, b) HEX packed with ZrO<sub>2</sub> pellets, c) empty sorber bed HEX

from adsorption to desorption temperatures. The sorber bed specifications and operating conditions are given in Table 1. Two additional heating/cooling circulators controlled the temperature of the condenser and the custom-built capillary-assisted low-pressure evaporator (CALPE). The evaporator features a serpentine HEX with  $12 \times 35.5$  cm tubes with 1.9 cm diameter, 1.47 mm fin height, 0.64 mm fin spacing and an inner spiral groove (Turbo Chil-40 FPI, Wolverine Tube Inc.). The inner and outer surface areas of the evaporator were  $0.051 \text{ m}^2/\text{m}$  and  $0.263 \text{ m}^2/\text{m}$  and the overall heat transfer rate measured by our custom-built apparatus for evaluating cooling power [9, 10] was  $1,762 \text{ W}/(\text{m}^2 \cdot \text{K})$ , such that the evaporator can provide 960 W cooling power when operated with a 2.5 L/min flow rate.

Vapor flow was controlled by a check valve (cracking pressure  $< 0.25$  kPa) between each sorber bed and the condenser, and by a 50 mm gate valve between each sorber bed and the evaporator. Three flowmeters, four pressure sensors, and twelve thermocouples were used for detailed monitoring of the cycle. The sorber bed specifications and operating conditions are listed in Table 1.

The total heat transfer measured at the evaporator per cycle,  $Q_{\text{evap}}$  (J), is calculated as

$$Q_{\text{evap}} = \int_0^{\tau} \dot{m} c_p (T_{\text{in}} - T_{\text{out}}) dt \quad (2)$$

where the mass flow rate of cold water,  $\dot{m}$ , is 2.5 L/min, and the specific heat for water,  $c_p$ , is 4.18 kJ/kg. The coefficient of performance (COP), specific cooling power (SCP) and volumetric specific cooling power (VSCP) are calculated as follows

$$\text{COP} = Q_{\text{evap}}/Q_{\text{heat}} \quad (3)$$

$$\text{SCP} = Q_{\text{evap}}/(m_{\text{ads}} \cdot t_{\text{cycle}}) \quad (4)$$

$$\text{VSCP} = Q_{\text{evap}}/(V_{\text{ads}} \cdot t_{\text{cycle}}) \quad (5)$$

The water uptake of the adsorbent as a function of time can be calculated from the heat transfer at the evaporator. Dimensionless uptake,  $X(t)$ , as a function of time can be described by following equation, yielding a characteristic time,  $\tau$ , for the process.

$$X(t) = 1 - \exp(-t/\tau) \quad (6)$$

where  $X(t)$  is the water uptake divided by equilibrium water uptake ( $\Delta w(t)/\Delta w_{\text{final}}$ ).



**Table 1.** Adsorber bed specifications and operating conditions

HEX (L,W,H)	35.2cm×3.8cm×30.5cm	Cycle times	5, 10, 20, 30 min
Fin spacing	2.54 mm (10 fpi)	$T_{\text{desorption}}$	75, 80, 90 °C
Surface area	2.8 m <sup>2</sup>	$T_{\text{adsorption}}$	20, 30, 40 °C
HEX weight	2.51 ± 0.03 kg	$T_{\text{condenser}}$	20, 30, 40 °C
ZO2 coating	0.80 kg per Hex	$T_{\text{evaporator}}$	5, 10, 15 °C
ZO2 pellets	1.97 kg per Hex		

## Discussion and Results

Isobars and isotherms for ZO2 powder, pellets, and coating samples are shown in Fig. 3 (a) and (b). The ZO2 equilibrium water uptake for the pellets and coating samples was 9% and 13% lower than that of the ZO2 powder, respectively, due to the addition of silicon dioxide-based binder by Mitsubishi Plastics' proprietary methods. The 285 data points from the adsorption branches of eight ZO2 pellet isotherms (5 to 80 °C) were used to generate the isosters that were fitted to determine the heat of adsorption as a function of water content plotted in Fig. 3 (c).

As shown in Fig. 3, in lab-scale sorption chiller tests the ZO2 coated HEX had greater volumetric and mass specific cooling powers than the ZO2 pellet filled HEX. This was in part due to the thermal contact resistance at the interface between the pellets and the HEX, which impedes heat transfer. Rouhani et al. measured the thermal conductivity of a packed bed of the ZO2 pellets as  $0.2 \text{ W}\cdot\text{m}^{-1}\cdot\text{K}^{-1}$ , and the thermal contact resistance of a monolayer of pellets pressed between metal plates under contact pressure of 0.7 kPa was determined to be 67% of the overall thermal resistance [11].

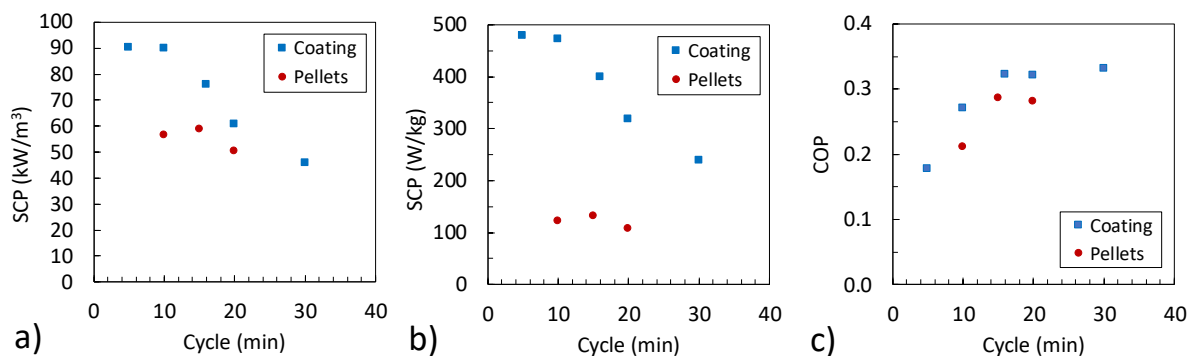


**Fig. 3.** Performance of sorption chiller for ZO2 coating and pellet; a) SCP by HEX volume, b) SCP by sorbent weight, and c) COP. Operating conditions:  $T_{\text{evap}}= 15 \text{ }^\circ\text{C}$ ,  $T_{\text{cond}}=T_{\text{ads}}= 30 \text{ }^\circ\text{C}$ , and  $T_{\text{des}}= 90 \text{ }^\circ\text{C}$

For 10 min cycles, an SCP of 456 W/kg (90 kW/m<sup>3</sup>) and a COP 0.27 was achieved with the ZO2 coated HEX. Sorption chiller tests on a small coated HEX (0.08 kg sorbent) by Freni et al. achieved 93 kW/m<sup>3</sup> and 675 W/kg [6]. Dawoud reported a sorption rate of 0.06 g/100 g·s for small samples of 0.3 mm ZO2 coatings, and much slower uptake rates for HEX coated with 1.5 kg of sorbent (57% uptake capacity in 10 min) [7]. For 30 min cycles with the ZO2 coated

HEX, the uptake rate was 0.04-0.05 g/100 g-s during with first 4 min of sorption and 96% of sorption capacity was achieved in 10 min.

The evaporator inlet and outlet temperatures were used to determine the total heat transfer measured at the evaporator per cycle,  $Q_{\text{evap}}$  (J), and system performance (SCP and COP) are shown in Fig. 4 (a) for Z02 coated beds operated with 5, 16 and 30 min cycles and evaporator, condenser, adsorption and desorption temperatures of 15, 30, 30 and 90 °C, respectively. The cooling power can be used to calculate the evaporation rate and, consequently, the uptake rate of the active adsorber bed. Fig. 4 (b) shows the cumulative uptake as a function of time for a 15 min half cycle including the initial brief transition period during which the temperature of the bed decreases from the desorption temperature (the outlet temperature of the 30 °C bed cooling loop is shown in red). No evaporation occurs until after the vapor pressure in the adsorber decreases triggering the opening of the valve between the adsorber and evaporator (~20 s for the cycle shown). For the equilibrium cycle data, the uptake rate calculated from delivered cooling power was underestimated in the initial minutes of the cycle as it did not include the evaporation required to rapidly cool the evaporator (~ 4.5 kg of copper) from 15 °C to 9 °C. As shown, the temperature fluctuation of the evaporator was much lower for shorter cycles, and the impact of the thermal inertia of the evaporator on the adsorbent water uptake calculation was less significant, Fig. 4 (a) and (c). Neglecting the initial 150 s of the half cycle, correlations of the dimensionless uptake as a function of time, as per Eq. (6), of six half cycles yielded a characteristic time of  $194 \pm 2$  s for the system operating with Z02 coating (800 g per HEX).

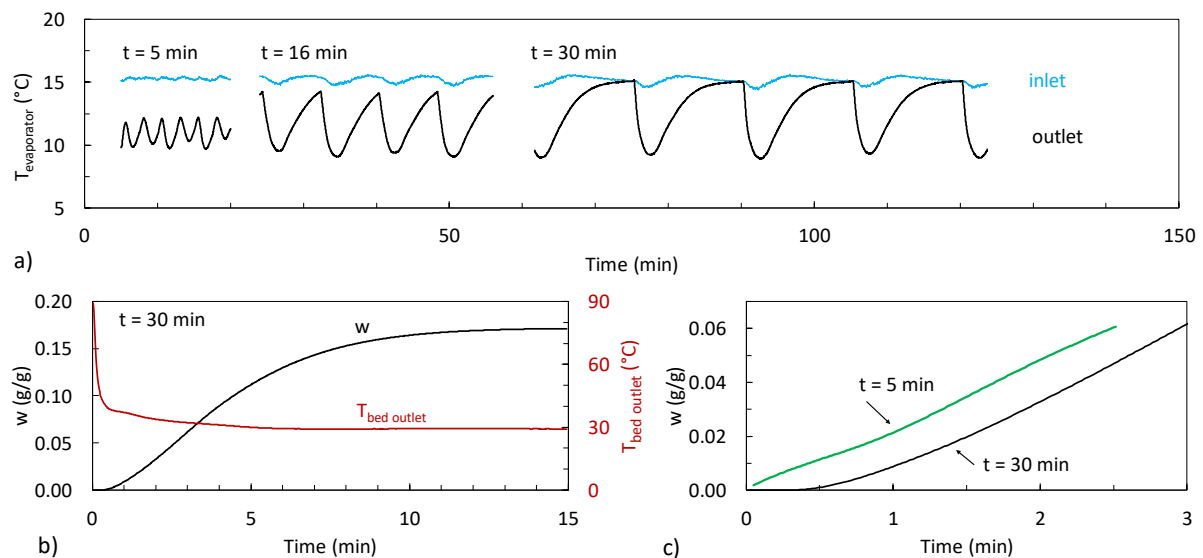


**Fig. 4.** a) The inlet and outlet temperatures of the evaporator for different cycle times, and the sorption as a function of time calculated from the cooling power delivered by the evaporator for b) the 30-minute cycles, and c) the first minutes of sorption for short and long cycles. Note: The initial uptake rate is under represented for the equilibrium (30 min) cycles as the thermal inertia of the evaporator was not included in the calculation.

## Summary

The performance of the lab-scale sorption chiller was comparable to the expected potential of Z02 coatings based on previous kinetic studies of small samples and small coated heat exchangers. For the operating conditions tested, Z02 coated sorber beds the highest cooling

power observed was 456 W/kg (90 kW/m<sup>3</sup>) for 10 min cycles for which system the COP was 0.27. Correlations of water uptake rates from tests with longer cycle times yielded a characteristic time,  $\tau$ , of  $194 \pm 2$  s.

## Acknowledgements

The authors gratefully acknowledge the financial support of the Natural Sciences and Engineering Research Council of Canada (NSERC) through the Automotive Partnership Canada Grant No. APCPJ 401826-10.

## References

- [1] Kakiuchi, H., Iwade, M., Shimooka, S., Ooshima, K., Yamazaki, M., Takewaki, T., “Novel Zeolite Adsorbents and Their Application for AHP and Desiccant System”, Proc. IEA Annex-17 Meeting, 2005, Beijing, China
- [2] Freni, A., Maggio, G., Sapienza, A., Frazzica, A., Restuccia, G., Vasta, S., “Comparative analysis of promising adsorbent/adsorbate pairs for adsorptive heat pumping, air conditioning and refrigeration”, *Applied Thermal Engineering*, 2016, doi.org/10.1016/j.applthermaleng.2016.05.036
- [3] Girnuk, I. S., Aristov, Yu. I., “Dynamics of water vapour adsorption by a monolayer of loose AQSOA™-FAM-Z02 grains: Indication of inseparably coupled heat and mass transfer”, *Energy*, 2016, doi.org/10.1016/j.energy.2016.08.056
- [4] Santamaria, S., Sapienza, A., Frazzica, A., Freni, A., Girnuk, I.S., Aristov, Yu. I., “Water adsorption dynamics on representative pieces of real adsorbents for adsorptive chillers”, *Applied Energy*, 2014, doi.org/10.1016/j.apenergy.2014.07.053
- [5] Freni, A., Frazzica, A., Dawoud, B., Chmielewski, S., Calabrese, L., Bonaccorsi, L., “Adsorbent coatings for heat pumping applications: Verification of hydrothermal and mechanical stabilities”, *Applied Thermal Engineering*, 2013, https://doi.org/10.1016/j.applthermaleng.2011.07.010
- [6] Freni, A., Bonaccorsi, L., Calabrese, L., Capri, A., Frazzica, A., Sapienza, A., “SAPO-34 coated adsorbent heat exchanger for adsorption chillers”, *Applied Thermal Engineering*, 2015, doi.org/10.1016/j.applthermaleng.2015.02.052
- [7] Dawoud, B., “Water vapor adsorption kinetics on small and full scale zeolite coated adsorbents; A comparison”, *Applied Thermal Engineering*, 50, 2013, doi.org/10.1016/j.applthermaleng.2011.07.013
- [8] Sharafian, A., Nemati Mehr, S. M., Thimmaiah, P., Huttema, W., Bahrami, M., “Effects of adsorbent mass and number of adsorbent beds on the performance of a waste heat-driven adsorption cooling system for vehicle air conditioning applications”, *Energy*, 2016, doi.org/10.1016/j.energy.2016.06.099
- [9] Thimmaiah, P. C., Sharafian, A., Huttema, W., McCague, C., Bahrami, M. "Effects of capillary-assisted tubes with different fin geometries on the performance of a low-operating pressure evaporator for adsorption cooling systems", *Applied Energy*, 2016, doi.org/10.1016/j.energy.2016.06.099
- [10] Thimmaiah, P. C., Sharafian, A., Rouhani, M., Huttema, W., Bahrami, M., “Evaluation of low-pressure flooded evaporator performance for adsorption chillers”, *Energy*, 2017, doi.org/10.1016/j.energy.2017.01.085
- [11] Rouhani, M., Huttema, W., Bahrami, M. "Effective thermal conductivity of packed bed adsorbents: Part 1 – Experimental study" *International Journal of Heat and Mass Transfer*, 2018, doi.org/10.1016/j.ijheatmasstransfer.2018.01.142

# A new generation of hybrid adsorption washer dryers

J. Cranston<sup>1</sup>, A. Askalany<sup>1,2\*</sup>, G. Santori<sup>1</sup>

<sup>1</sup>The University of Edinburgh, School of Engineering, Institute for Materials and Processes, Mayfield Road, The King's Buildings, EH9 3JL, Edinburgh, UK

<sup>2</sup>Mechanical Engineering Department, Faculty of Industrial Education, Sohag University, Sohag, 82524, Egypt

\*Corresponding author: ahmed\_askalany3@yahoo.com

## Abstract

Wet appliances are an energy intensive class of household devices which play an important role in energy demand management. This paper focuses on washer-dryers and investigates a novel concept that uses adsorption alongside a classical heat-pump for drying. The experimental characterization of a commercial heat-pump washer-dryer demonstrates that the inclusion of an adsorption unit for drying can enable further energy savings, especially when relative humidity is >90% and temperatures <30°C. Different options for the integration of an adsorption bed in the process are assessed showing that the most appropriate is before the heat-pump evaporator. Different adsorption materials, such as Zeolite 13X, Silica gel, SWS-1L and silica supported ionic liquid are compared on the working capacity to identify the best adsorbent and to infer general requirements. Materials with Type 3 isotherms, such as silica supported ionic liquid, are best suited for drying applications at very high relative humidity.

**Keywords:** Adsorption, Drying, Energy efficiency, heat-pump

## Introduction

The Paris Agreement in 2016 resulted in a global pledge to combat climate change [1]. With the current energy demands, the agreement's goal of maintaining the global temperature change below 2°C is challenging. However, with ever increasing world population and prosperity, the global energy demand is only expected to increase [2, 3]. As a result, the most important and effective way to meet the climate goals is through significant improvements in energy efficiency [4]. This requirement is reflected in governmental policy. In the UK, the department for Business, Energy and Industrial Strategy (BEIS) implemented the Low Carbon Transition Plan, which stated that a reduction in UK energy consumption of 43% is required to achieve an 80% reduction in carbon emissions by 2050 [5]. Initial steps to achieve such targets should be focused on the most energy intensive technologies.

In 2016 the UK's domestic sector accounted for 26% of total energy consumption, with wet appliances categorised as the second most energy intensive class of household devices [6]. The category wet appliances includes dishwashers, washing machines, dryers and washer-dryer combination units. Santori et al. [7] and Hauer et al. [8] have created adsorption based dishwashers, demonstrating energy savings of 25-41% compared with standard A class technology. Adsorptive porous material is used during the drying phase, removing the need of electric heating during this most energy intensive stage. This follows the global trend of using adsorption materials within thermodynamic cycles due to their improved energy efficiency compared with traditional technologies [9]. Despite the developments of integrating adsorption materials in dishwashers, there is yet to be the same breakthrough with the other wet appliances such as washer-dryers.

Currently the most advanced washer-dryers on the market are heat-pump washer-dryers. They have marked a dramatic improvement in energy efficiency from the traditional vented and ventless designs. In these systems the traditional method of heating air with an electrical resistor is replaced by a heat-pump. This creates a closed-loop system where thermal energy is transferred to and from a refrigerant, resulting in minimal heat losses to the environment [10].

Furthermore, heat-pumps have an efficiency higher than conventional electrical resistors, creating energy savings in washer-dryers of 40% compared with the traditional designs [11, 12]. However, this technology is mature and refinements only lead to small incremental changes in energy efficiency. Although 40% energy saving is significant, in theory further enhancements can be expected by adding an adsorption unit, similar to dishwashers

Nonetheless, the washer-dryer presents different challenges from the dishwasher. In a dishwasher the minimal amount of water to be removed is in the order 120 g, whereas for a washer-dryer this amount can be as high as 1 kg<sub>water</sub> per kg<sub>dry load</sub>. An adsorption bed capable of capturing this amount of water would be too large to fit within the machine, therefore a combined hybrid process is required. This leads to a new concept of hybrid adsorption heat-pump washer-dryer.

### Standard Heat-Pump Washer-Dryer

The design of a standard heat-pump washer-dryer is illustrated in Figure 1. The fan pulls air through the system during the drying cycle. Warm wet air exits the drum, which is cooled using the heat pump evaporator to remove water. The dry and cold air is heated through the condenser and feeds the drum. This cycle continues until a prescribed humidity in the drum is achieved or a set time is reached. The knowledge of relative humidity (RH) and temperature throughout the process is crucial to determine the possibility of integration of an adsorption bed.

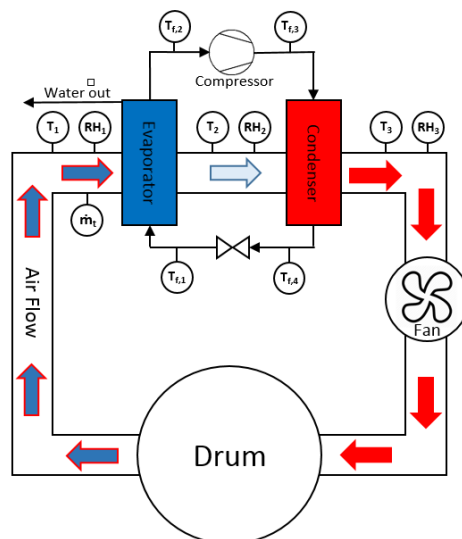


Figure 1: Schematic of a heat-pump washer-dryer. Air cycle: temperatures - before the evaporator ( $T_1$ ), after the evaporator ( $T_2$ ) and after the condenser ( $T_3$ ); relative humidities - before the evaporator ( $RH_1$ ), after the evaporator ( $RH_2$ ) and after the condenser ( $RH_3$ ); and mass flow rate – before evaporator ( $\dot{m}_1$ ). Refrigerant cycle: temperatures – before the evaporator ( $T_{f,1} = 14 \text{ }^\circ\text{C}$ ), after the evaporator ( $T_{f,2} = 23 \text{ }^\circ\text{C}$ ), after the compressor ( $T_{f,3} = 70 \text{ }^\circ\text{C}$ ) and after the condenser ( $T_{f,4} = 40 \text{ }^\circ\text{C}$ )

The Electrolux AEG L 99695 HWD is the only heat-pump washer-dryer currently commercialised. This was fitted with Omega type T thermocouples ( $\pm 1\text{ }^{\circ}\text{C}$ ) and Honeywell HIH-4000 relative humidity sensors in the positions illustrated in Figure 2 ( $\pm 3.5\%$  RH ). At steady state, an air mass flow rate of 0.02 kg/s is measured before the evaporator using a Pitot tube. An inhomogeneous mix of clothes of 2.78 kg dry weight is used as test materials.

The temperature and relative humidity of the air cycle are recorded as a function of time during the drying phase. The experimental results are displayed in Figure 2, with the drying phase consisting of 3 phases: (1) start-up, (2) bulk-drying and (3) further-drying.

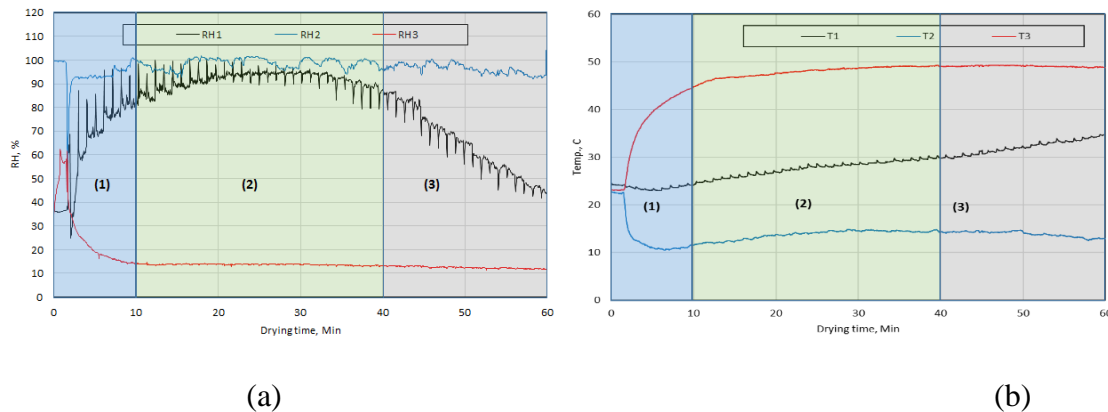


Figure 2: a) Relative humidity - before the evaporator ( $\text{RH}_1$ ), after the evaporator ( $\text{RH}_2$ ) and after the condenser ( $\text{RH}_3$ ) - and b) Temperatures - before the evaporator ( $\text{T}_1$ ), after the evaporator ( $\text{T}_2$ ) and after the condenser ( $\text{T}_3$ ) - during the drying cycle of the heat-pump washer-dryer experiments.

During start-up the heat-pump and fan begin circulation. The temperatures  $\text{T}_3$  and  $\text{T}_2$  increase and decrease respectively to their steady state values, while  $\text{RH}_3$  and  $\text{RH}_2$  begin to reach steady state. These two process positions remain at steady state for the rest of the drying cycle. The conditions of the air exiting the drum ( $\text{T}_1$  and  $\text{RH}_1$ ) continue to change throughout the drying process.  $\text{T}_1$  increases steadily throughout the drying cycle as moisture is removed from the drum. During the start-up phase,  $\text{RH}_1$  increases as the increased temperature causes more water to evaporate. In the bulk-drying,  $\text{RH}_1$  reaches its maximum value and remains there while the bulk of the water is removed. In the further-drying stage,  $\text{RH}_1$  reduces steadily as the clothes in the drum become dryer.

The drying process cycle during the continuous bulk-drying phase is illustrated in the psychrometric chart of Figure 3.

In the drum the hot dry air which entered heats up the clothes, causing the temperature of the air to decrease and humidification to occur. In the evaporator the temperature drops while RH increases to 100%. The condenser provides sensible heat, increasing the air temperature while reducing the RH.

### Hybrid Heat-Pump Washer-Dryer

In drying applications water moisture within wet air is adsorbed onto the surface of the adsorbent material. The adsorbent removes the water drying the air, while simultaneously heating the air due to the heat of adsorption. The performance of an adsorbent is dependent on the process conditions, with high relative humidity and low temperature, in general, promoting adsorption [13]. The three possible configurations for the integration of an adsorption bed in a heat-pump washer-dryer are presented in Figure 4.

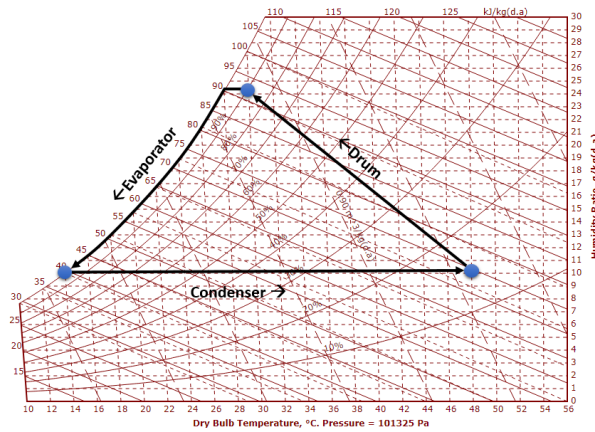


Figure 3: Drying cycle during bulk-drying phase of heat-pump washer-dryer

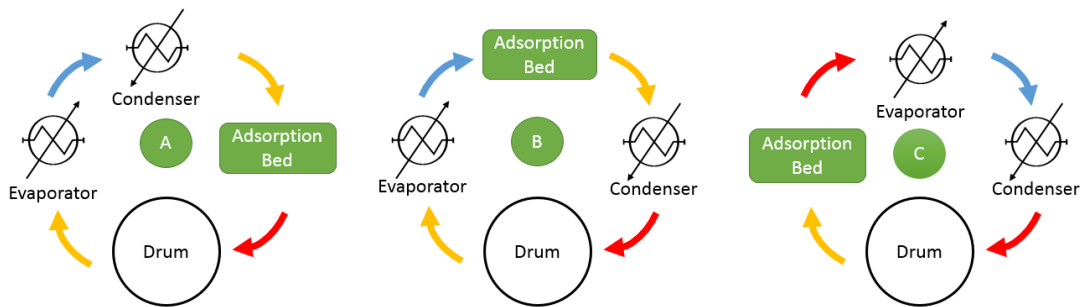


Figure 4: Possible configurations of adsorption bed in a hybrid heat-pump washer-dryer. Position A – After the condenser, Position B – Between evaporator and condenser, Position C – Before the evaporator.

In position A the process conditions are unfavourable as the high temperature and low RH reduces the adsorption capacity.

Position B is ideal for adsorption owing to low temperatures and high RH, resulting in a high water adsorption capacity. The inclusion of an adsorption bed in this position is qualitatively illustrated in Figure 5a).

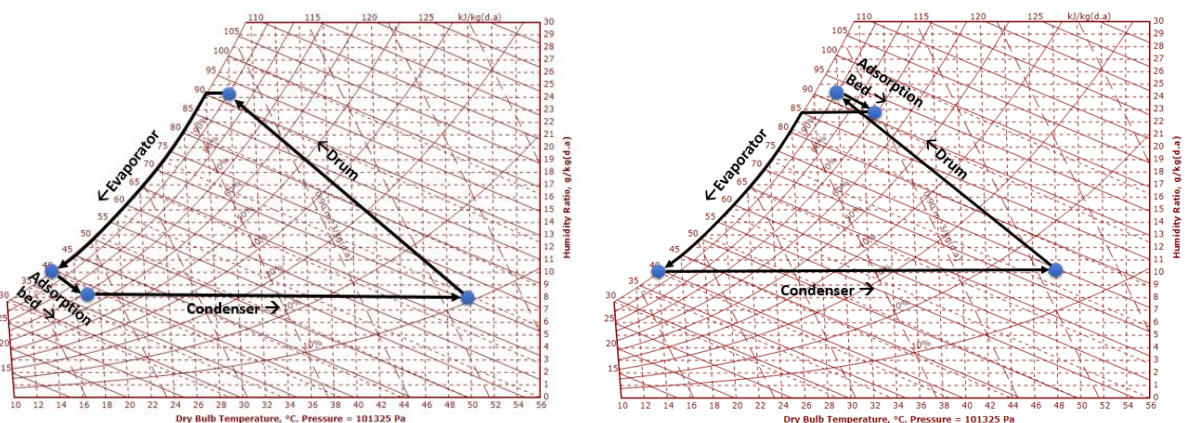


Figure 5: a) (left) Effect of the adsorption bed after the evaporator (Position B in Figure 4) on the drying cycle of a hybrid heat-pump washer-dryer; b) (right) Effect of the adsorption bed before the evaporator (Position C in Figure 4) on the drying cycle of a hybrid heat-pump washer-dryer

However, at 100% RH, condensation of water in the adsorption materials can occur [14] and, after many cycles, issues such as limited hydrothermal stability or even leakages in case of composite sorbents appear. [15].

In order to overcome these material limitations, position C is the most favourable, with average bulk-drying conditions of 90% RH and 30°C. These conditions are still acceptable for adsorption while preventing condensation. The process conditions with the adsorption bed in position C is qualitatively illustrated in Figure 5b).

### Regeneration

After drying, regeneration of the adsorption bed is required in order to restore the initial bed conditions. Regeneration is an energy penalty in the system. However, since the process of adsorption is theoretically reversible, the energy spent for regeneration equals the energy developed during adsorption. Locating the adsorption bed before the evaporator allows the utilisation of the heat-pump for regeneration without major design changes to the system. This is an energetic advantage as the alternative regeneration method with joule effect is less energy efficient. However, the main energy benefit of the hybrid heat-pump washer-dryer can be considered in terms of the drying time.

Eq. (1) to (3) represent the main energy contributions to the heat-pump washer-dryer process. The energy added to the heat-pump from the condensation of water,  $Q_{ev}$  (kJ s<sup>-1</sup>):

$$Q_{ev} = \int_0^{t_{cycle}} [\dot{m}_w LH + (\dot{m}_{wv} c_{p,wv} + \dot{m}_a c_{p,a}) dT] dt \quad (1)$$

Where  $\dot{m}_w$  is the condensed water rate (kg/s),  $LH$  is the latent heat of water (kJ kg<sup>-1</sup>),  $\dot{m}_{wv}$  is the water vapour flow rate (kg s<sup>-1</sup>),  $C_{p,wv}$  is the specific heat capacity of water vapour (kJ kg<sup>-1</sup> °C<sup>-1</sup>),  $\dot{m}_a$  is the air flow rate (kg s<sup>-1</sup>) and  $C_{p,a}$  is the specific heat capacity of air (kJ kg<sup>-1</sup> °C<sup>-1</sup>). The compressor adds more energy to the system,  $Q_{comp}$  (kJ s<sup>-1</sup>):

$$Q_{comp} = \int_0^{t_{cycle}} P_{comp} dt \quad (2)$$

Where  $P_{comp}$  is the power of the compressor (kW). The combined sum of these energies,  $Q_{cond}$  (kJ s<sup>-1</sup>), is discharged by the condenser:

$$Q_{cond} = \int_0^{t_{cycle}} [\dot{m}_w LH + (\dot{m}_{wv} c_{p,wv} + \dot{m}_a c_{p,a}) dT] dt + \int_0^{t_{cycle}} P_{comp} dt \quad (3)$$

All of these equations are integrated over cycle time,  $t_{cycle,heat-pump}$  (s), which depends on the mass of water inside the drum,  $m_{w,inside\ drum}$  (kg), and the flow rate of condensed water:

$$t_{cycle,heat-pump} = \frac{m_{w,inside\ drum}}{\dot{m}_w} \quad (4)$$

When the adsorption bed is integrated into the process, the heat of adsorption,  $Q_{ads}$  (kJ s<sup>-1</sup>), is also released to the air. The heat of desorption  $Q_{ads}$  (kJ s<sup>-1</sup>):

$$Q_{ads} = \int_0^{t_{ads}} m_{ads} \frac{dw}{dt} H_{st} dt \quad (5)$$

Where  $w$  is the adsorbed/desorbed water (kg<sub>water</sub> kg<sub>sorbent</sub><sup>-1</sup>),  $m_{ads}$  is the amount of adsorption material in the process (kg),  $H_{st}$  is the isosteric heat of adsorption (kJ kg<sup>-1</sup>) and is integrated over the time for the adsorption step,  $t_{ads}$  (s).

The inclusion of  $Q_{ads}$ , reduces the total cycle time,  $t_{cycle,adsorption}$  (s):

$$t_{cycle,adsorption} = \frac{m_{w,inside\ drum} - m_{ads} \Delta w}{\dot{m}_w} \quad (6)$$



Where  $\Delta w$  is the working capacity of the adsorption material ( $\text{kg}_{\text{water}} \text{kg}_{\text{sorbent}}^{-1}$ ) at given adsorption and desorption conditions.

Table 1 reports the performance of the heat-pump washer-dryer at steady state. The performance of the hybrid heat-pump washer dryer are now dependent on the adsorption material used.

Table 1: Performance of heat-pump washer-dryer and hybrid adsorption washer-dryer. Characteristic data from experimental results, with performance based on a theoretical steady state.

Symbol	Description	Unit	Value
<b>Heat-pump washer-dryer</b>			
$Q_{\text{ev}}$	Heat added to evaporator	$\text{kJ s}^{-1}$	1.457
$Q_{\text{con}}$	Heat discharged by compressor	$\text{kJ s}^{-1}$	1.797
$P_{\text{comp}}$	Power of compressor	$\text{kJ s}^{-1}$	0.340
COP	Heat-pump coefficient of performance		4.28
$\dot{m}_{\text{f}}$	Mass flow of refrigerant r134a	$\text{kg s}^{-1}$	0.01025
$T_{\text{f},1}$	Temperature of r134a before evaporator	$^{\circ}\text{C}$	14
$T_{\text{f},2}$	Temperature of r134a after evaporator	$^{\circ}\text{C}$	23
$T_{\text{f},3}$	Temperature of r134a before condenser	$^{\circ}\text{C}$	70
$T_{\text{f},4}$	Temperature of r134a after condenser	$^{\circ}\text{C}$	40
$P_{\text{f},1}$	Pressure of r134a before evaporator	bar	4.72
$P_{\text{f},2}$	Pressure of r134a after evaporator	bar	4.72
$P_{\text{f},3}$	Pressure of r134a before condenser	bar	10.14
$P_{\text{f},4}$	Pressure of r134a after condenser	bar	10.14
H	Isentropic efficiency of compression	%	45
$T_1$	Temperature of air before evaporator	$^{\circ}\text{C}$	30
$T_2$	Temperature of air between evaporator and condenser	$^{\circ}\text{C}$	14
$T_3$	Temperature of air after condenser	$^{\circ}\text{C}$	48
$\text{RH}_1$	Relative humidity of air before evaporator	%	90
$\text{RH}_2$	Relative humidity of air between evaporator and condenser	%	100
$\text{RH}_3$	Relative humidity of air after condenser	%	15
$\dot{m}_{\text{w}}$	Mass flow of condensed water	$\text{kg s}^{-1}$	0.0002
$m_{\text{w,inside drum}}$	Mass of water inside the drum	kg	1000 <sup>1</sup>
$t_{\text{cycle,heat-pump}}$	Time of drying for heat-pump washer-dryer	s	5000
$E_{\text{cycle,heat-pump}}$	Energy consumed by heat-pump during drying cycle	kW	1700
<b>Hybrid Adsorption heat-pump washer-dryer</b>			
$m_{\text{ads}}$	Mass of adsorbent	kg	0.5 <sup>2</sup>
$\Delta w$	Working capacity of adsorbent	$\text{kg}_{\text{water}} \text{kg}_{\text{sorbent}}^{-1}$	0.82 <sup>2</sup>
$H_{\text{st}}$	Isosteric heat of adsorption	$\text{kJ kg}^{-1}$	2558 <sup>2,3</sup>
$t_{\text{cycle,adsorption}}$	Time of drying for hybrid adsorption washer-dyer	s	2950
$E_{\text{cycle,adsorption}}$	Energy consumed by heat-pump during drying cycle with adsorption bed integrated	kW	1003

<sup>1</sup>Assumed value

<sup>2</sup>Adsorbent is silica gel supported ionic liquid with assumed adsorption and desorption conditions of  $\text{RH}_1$ ,  $T_1$  and  $\text{RH}_2$ ,  $T_2$  respectively.

<sup>3</sup>Assumed constant in working range of hybrid adsorption washer-dryer

### Adsorption material comparison

Conventional materials for water adsorption are zeolite 13X and silica gels. However, composite materials consisting of hygroscopic salts impregnated in silica gel have been

developed displaying improved properties [16]. These materials include calcium-chloride impregnated silica gel (SWS-1L) [17] and silica supported ionic liquid (1-ethyl-3-methylimidazolium) (Si-IL) developed at the University of Edinburgh.

These materials water adsorption isotherms are compared in Figure 6. Zeolite 13X displays a Type 1 adsorption isotherm with the highest loadings at low partial pressure. Silica gel (Type A) also displays a Type 1 isotherm there is less water loading at low relative humidity.

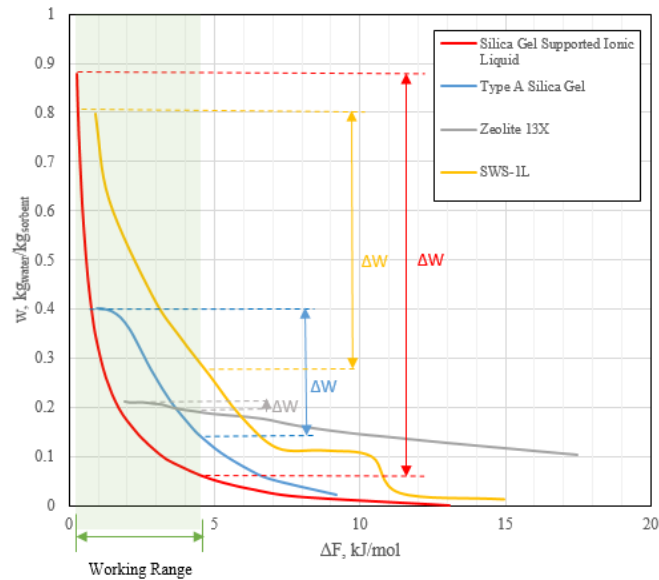


Figure 6: Water adsorption isotherms of various materials. Working range of washer-dryer illustrated in green and working-capacities within this range illustrated. [17-20]

Nonetheless, silica gel has a higher pore volume than zeolite 13X [21] which results in a higher loading capacity. SWS-1L displays a Type 4 isotherm illustrative of the composite nature of the material. The initial step in the isotherm is because of the silica gel water interactions and the later increased loading due to the calcium-chloride interactions. Finally, Si-IL adsorption isotherm is of Type 3. This type of isotherm usually occurs when the water-water interaction is significantly stronger than the water-adsorbent interactions [22].

The working range of the washer-dryer between 15-90 % RH is illustrated in Figure 6, where the Si-IL demonstrates the highest working capacity among the adsorbents. The benefit of integrating an adsorption bed with this material is demonstrated in Table 1, where an energy or time saving of 41% is observed.

## Conclusions

The concept of a hybrid adsorption heat-pump washer dryer is introduced. The inclusion of the adsorption bed is expected to reduce the energy consumption of the heat-pump washer-dryer through reduction of drying time that has been proved theoretically. The experimental characterisation of the heat-pump washer-dryer has shown that the optimal position of the adsorption bed is before the evaporator. Relative humidity of 90% and temperatures of 25-35°C provide favourable conditions for adsorption while preventing hydrothermal stability issues common to many adsorbents. This position uses the heat-pump for regeneration without further complicating the process design, allowing the system to benefit from the heat-pump's coefficient of performance. Silica supported ionic-liquid composite displays a very promising working-capacity of  $0.82 \text{ kg}_{\text{water}} \text{ kg}_{\text{sorbent}}^{-1}$ , well above other available materials. This material is able to process significant amounts of water, leading to a reduction in drying time and energy consumption of the device.

## Acknowledgements

This research is supported by EPSRC within the “Micro-scale energy storage for super-efficient wet appliances” project EP/P010954/1.

## References

1. UN, *Paris Agreement*. 2016, United Nations: United Nations Treaty Collection.
2. BP. *BP Energy Outlook*. 2018 01/06/2018]; Available from: <https://www.bp.com/en/global/corporate/energy-economics/energy-outlook.html>.
3. IEA. *WEO 2017 : Key Findings*. 2018 01/06/2018]; Available from: <http://www.iea.org/weo2017/#section-1-1>.
4. IEA. *Energy and Climate Change*. 2015 01/06/2018]; Available from: <https://www.iea.org/publications/freepublications/publication/WEO2015SpecialReportonEnergyandClimateChange.pdf>.
5. BEIS. *The Carbon Plan: Delivering our low carbon future* 2011 01/06/2018]; Available from: [https://assets.publishing.service.gov.uk/government/uploads/system/uploads/attachment\\_data/file/47613/3702-the-carbon-plan-delivering-our-low-carbon-future.pdf](https://assets.publishing.service.gov.uk/government/uploads/system/uploads/attachment_data/file/47613/3702-the-carbon-plan-delivering-our-low-carbon-future.pdf).
6. BEIS, *Energy Consumption in the UK*. 2017.
7. Santori, G., Frazzica, A., Freni, A., Galieni, M., Bonaccorsi, L., Polonara, F. and Restuccia, G. *Optimization and testing on an adsorption dishwasher*. *Energy*, 2013. 50: p. 170-176
8. Hauer, A. and F. Fischer, *Open Adsorption System for an Energy Efficient Dishwasher*. *Chemie Ingenieur Technik*, 2011. 83(1-2): p. 61-66.
9. Santori, G. and M. Luberti, *Thermodynamics of thermally-driven adsorption compression*. *Sustainable Materials and Technologies*, 2016. 10: p. 1-9.
10. Alves-Filho, O., *Heat Pump Dryers: Theory, Design and Industrial Applications*. 2015: CRC Press.
11. Pillot, S., *Washer-dryer machine with a heat pump*. 2013, Google Patents.
12. Bansal, P., J. Braun, and E. Groll, *Improving the energy efficiency of conventional tumbler clothes drying systems*. *International Journal of Energy Research*, 2001. 25(15): p. 1315-1332.
13. Ruthven, D.M., *Principles of adsorption and adsorption processes*. 1984, New York Chichester: New York Chichester : Wiley.
14. Liu, Y. and R. Wang, *Pore structure of new composite adsorbent  $\text{SiO}_2 \cdot x\text{H}_2\text{O} \cdot y\text{CaCl}_2$  with high uptake of water from air*. *Science in China Series E: Technological Sciences*, 2003. 46(5): p. 551-559.
15. Gordeeva, L.G. and Y.I. Aristov, *Composites 'salt inside porous matrix' for adsorption heat transformation: a current state-of-the-art and new trends*. *International Journal of Low-Carbon Technologies*, 2012. 7(4): p. 288-302.
16. Aristov, Y., *New family of solid sorbents for adsorptive cooling: Material scientist approach*. *Journal of Engineering Thermophysics*, 2007. 16(2): p. 63-72.
17. Aristov, Y., Tokarev, M.M., Cacciola, G. and Restuccia, G. *Selective water sorbents for multiple applications, 1.  $\text{CaCl}_2$  confined in mesopores of silica gel: Sorption properties*. *Reaction Kinetics and Catalysis Letters*, 1996. 59(2): p. 325-333.
18. Aristov, Y.I., *Novel materials for adsorptive heat pumping and storage: screening and nanotailoring of sorption properties*. *Journal of Chemical Engineering of Japan*, 2007. 40(13): p. 1242-1251.
19. Chua, H.T., Ng, K.C., Chakraborty, A., Oo, N.M. and Othman, M., *Adsorption Characteristics of Silica Gel + Water Systems*. *Journal of Chemical & Engineering Data*, 2002. 47(5): p. 1177-1181.
20. Askalany, A., Freni, A. and Santori, G., *Supported ionic liquid water sorbent for high throughput desalination and drying*, Submitted to *Desalination*. 2018
21. Green, D.W. and R.H. Perry, *Perry's Chemical Engineers' Handbook, Eighth Edition*. 2007: McGraw-Hill Professional.
22. Keller, J.U. and R. Staudt, *Gas Adsorption Equilibria: Experimental Methods and Adsorptive Isotherms*. 2006: Springer US.

# Formulation influence on the preparation of silica nanoparticle-based ionogels

Hongsheng Dong<sup>1,2</sup>, Ahmed A. Askalany<sup>2,3</sup> and Giulio Santori<sup>2\*</sup>

<sup>1</sup> Key Laboratory of Ocean Energy Utilization and Energy Conservation of Ministry of Education, School of Energy & Power Engineering, Dalian University of Technology, Dalian 116024, China

<sup>2</sup> The University of Edinburgh, School of Engineering, Institute for Materials and Processes, Sanderson Building, The King's Buildings, Mayfield Road, EH9 3BF Edinburgh, Scotland, UK

<sup>3</sup> Mechanical Engineering Department, Faculty of Industrial Education, Sohag University, Sohag, 82524, Egypt

\*Corresponding author: G.Santori@ed.ac.uk

## Abstract

Adsorption desalination is an emerging and potential technology to save energy. Adsorbent with high adsorption working capacity holds the keys to efficient adsorption desalination system. In this study, we synthesized high performance ionogels adsorbents. Silica supported ionic liquid tablets with different formulations were prepared and their hydrothermal stability and adsorption capacity were studied. The results indicated that: 1) the tablets with Syloid 72FP are water-stable and thermally stable; 2) the tablets with no less than 50% (wt) silica can confine EMIM Ac ionic liquid (IL) tightly at low and high humidity; 3) sorption rate is controlled jointly by IL amount and porosity of ionogel. About 60% of water uptake can be achieved using the tablet with 50% (wt) IL and 50% Syloid 72FP. These results suggested that the synthesized ionogel can be applied on adsorption desalination applications.

**Keywords:** ionic liquid, silica, ionogel

## Introduction

Salts (generally salts of organic cations: ammoniums, phosphoniums, imidazoliums, pyridiniums, etc.) which have melting points lower than 373.15 K are called ionic liquids (ILs). A large number of them are air and water stable, as well as thermally stable at temperatures higher than 570 K[1]. Interestingly, most ILs, due to their ionic character, readily absorb water from the environment[2, 3], even hydrophobic ILs absorb traces of water rapidly[4]. Also, ILs have an extremely low vapor pressure which, for example, makes them attractive for evaporative separation processes, thus, impurities in product streams are avoided[5]. These interesting properties show good potential for use in adsorption desalination.

Adsorption desalination (AD) is an emerging thermally-driven method that is proven to be energy efficient and environment-friendly[6]. The basic working principles of an AD cycle focuses on the efficient water vapor uptake by the chemical potential of an unsaturated adsorbent in one half-cycle period, where the same adsorbent could later be regenerated in the next half-cycle by heating it with a low temperature heat source in the range of 50–85°C which is essentially “free” if unused[7, 8].

Taking advantage of IL properties in solid-state materials remains a major challenge. The immobilization of ionic liquids within organic or inorganic matrices, which are called ionogels, makes it possible to retain or enhance its liquid dynamics in the solid state, thus circumventing has some drawbacks related to shaping and risk of leakage[1, 9].

Synthetic routes to ionogels fall into three categories depending on the nature of the solid-like network, which may be organic (using low molecular weight gelators or polymers) [10], inorganic (typically using oxide nanoparticles, carbon nanotubes or oxide networks arising from sol–gel) [11], or hybrid organic–inorganic (typically polymers reinforced with inorganic fillers) [12]. Usually, the dispersion of nanoparticles into ILs offers a simple route to the fabrication of IL-based solid materials and the final ionogel properties are easy to tune by changing the amount of ILs. Therefore, the formulation of ionogel has a significant influence on the properties of ILs, especially the confinement stability and adsorption performance. It is worth underlining that the intrinsic hybrid character of ionogels relies on the intimate combination of an IL and a solid-like network. Actually, the properties and behavior of confined ILs may be significantly modified by the confinement. This change influences the properties and performance of the respective component in the device and must thus be quantified and understood.

In this study, a simple and inexpensive physical immobilization method is chosen, two kinds of silica nanoparticles and EMIM Ac are used to prepare ionogel. Ionogels are pressed into tablets to check their confinement stability, water stability, thermal stability, and adsorption performance.

### Materials and method

Materials and devices specifications are shown in Table 1. Specifications of experimental materials and devices..

Table 1. Specifications of experimental materials and devices.

Name	Supplier	Purity/Precision
Syloid 63FP	Grace	
Syloid 72FP	Grace	
EMIM Ac	Sigma Aldrich	95.0%
Deionized water	Self-produce	
Balance:	Sartorius, ED224S	0.1 mg
Oven	Thermo Fisher Scientific, Heraeus vacutherm	0.1°C
DVS	Surface Measurement Systems, Advantage	
Handheld press	LFA	












The silica nanoparticles used in this study have hydrophilic silanol (Si-OH) groups on their surface. The silica particles and IL were dried for 24 h in a vacuum oven at 80 °C before use. In general, a measured amount of Syloid was loaded into a vial. Samples are briefly shaken to ensure mixing of all components. EMIM Ac is added last in order to prevent premature initiation of the sol-gel reaction. Samples are shaken and agitated to be homogeneous. The obtained samples are again dried for 24 h under vacuum with heating at 80 °C prior to use for each measurement. All ionogels are prepared under ambient laboratory conditions. A hand-held tablet making device is used to press the ionogel powder into regular tablets. The diameter and height of the tablet is 6 mm and 2.5-4 mm respectively. To check the confinement stability, tablets are initially exposed to air at 60% relative humidity, and in a confined space where the relative humidity is increased at 80%. The mass change was recorded at a regular period. Finally, the samples are analyzed in a DVS Adventure automated vapor sorption instrument at 25°C. The samples are initially dried for 6 hours under a continuous flow of nitrogen to establish the dry mass. The relative humidity is then increased from 0% to 90% relative humidity.

## Results & discussion

### IL confinement stability

Six tablets with different EMIM Ac/Syloid mass ratio are made to examine IL confinement stability. *Table* shows the appearances of the silica dispersions in EMIM Ac. After EMIM Ac immobilization, the silica particles maintained white color. The tablet with formulation 1 is very viscous and cannot maintain regular shape. A further addition of Syloid increases the hardness of the nanocomposite ion gels, the colors of tablets changed from transparent white to opaque white with the increase of Syloid. For Syloid 63FP, when the proportion of EMIM Ac decreased to 50%, the tablet is very compliant. For Syloid 72FP, when the ionogel has 70% EMIM Ac, tablet is too soft, some IL leaks out of the tablet and tablet appears to wet on the surface. Some amount of IL leaks out on the surface of the tablet, and IL cannot be confined very well. The tablets with a Syloid/IL ratio equal to or higher than 66% appeared to be dry. It showed an excellent confinement. It can be concluded that the self-standing ionogel can be obtained by five formulations except formulation 1.

Table 2. IL confinement stability comparison of tablets with different formulations at 60% relative humidity.

ID	Formulation	Initial photo	Exposed in air for 15 hours
1	45% Syloid 63FP, 55% EMIM Ac		
2	50% Syloid 63FP, 50% EMIM Ac		
3	55% Syloid 63FP, 45% EMIM Ac		
4	30% Syloid 72FP, 70% EMIM Ac		
5	40% Syloid 72FP, 60% EMIM Ac		
6	50% Syloid 72FP, 50% EMIM Ac		







For further examining the tablets stability, other five tablets are exposed in air for 15 hours. Obviously, the color of the tablet of formulation 4 changed from opaque white to transparency, and there is a small amount of IL leakage. Tablets with formulation 2, 3, 5, and 6 show good confinement stability at 60% relative humidity. Nevertheless, in order to obtain high adsorption performance, more IL is required in the silica network. According to this requirement, formulation 2 and 5 are suitable. When ionogel was used in adsorption

desalination, it is exposed at relative humidity >70%. Therefore, it is necessary to check the confinement stability in a high humidity environment. As shown in Table 3, after exposure at 80% relative humidity for 5 hours, a large amount of liquid formed around tablets with formulations 2 and 5. To verify what the liquid is, the liquid was removed and the tablets dried and weighted. The mass of tablet with formulation 5 reduced from 0.0884 g to 0.0728g. Since the IL held within the gel framework is hydrophilic and is miscible with water, absorption of water into the gel must, necessarily, result in the formation of both hydrophilic and hydrophobic phase domains within the gel. This induces the leakage of some IL out from ionogel particle through dissolution in the bulk aqueous phase on hydration. As a result, the tablets with Syloid 63FP or 72FP both leaked.

### Hydrothermal stability

An important question with respect to many applications is whether ionogels can be used in the presence of water or not. As shown in Table 3, tablets with formulation 2 and 5 were exposed at 80% relative humidity for 5 hours, and then dried for 1 hour at 80°C. Tablets fragmented, losing mechanical stability. To solve this problem, binder addition is an option but the presence of binder increases the vapor transfer resistance and reduces the amount of IL. In contrast, tablet with formulation 5 is still intact after adsorption and drying although IL leakage is still a significant problem.

Table 3. Tablet stability toward water and IL confinement stability at 80% relative humidity.

Formulation	Initial photo	Exposed in 80% relative humidity for 5 hours	Drying for 1 h at 80 °C
50% Syloid 63FP, 50% EMIM Ac			
40% Syloid 72FP, 60% EMIM Ac			

One way to solve this problem consists of removing the leaked liquid in repeated cycles until it does not have any leakage (aging). Therefore, formulation 5 was placed in 80% relative humidity to adsorb moisture for 5 hours, and then the leaked liquid was removed, finally, the tablet was dried in oven for 1 hour at 80°C and cycle in this way a number of times. It is found that the tablet does not show any leakage after two cycles (Figure 1). The proportion of water firstly increased and then kept steady at a certain value with the increase of adsorption time for every cycle, the final proportion of water decreased from 76.58% to 61.79 % between cycle 1 and cycle 3. The sharp decrease of water uptakes between different cycles further demonstrated that the leaked liquid around tablets was partly IL, where the IL played the major role in vapor adsorption comparing with silica nanoparticle. Indeed, the IL amount decreased by 11.4% and only 48.60% of EMIM Ac was retained in the tablet after 3 cycles (Figure 2). The IL leaked amount decreased over the cycles. These results indicated this way can solve leakage, but it is a little complicated operationally.

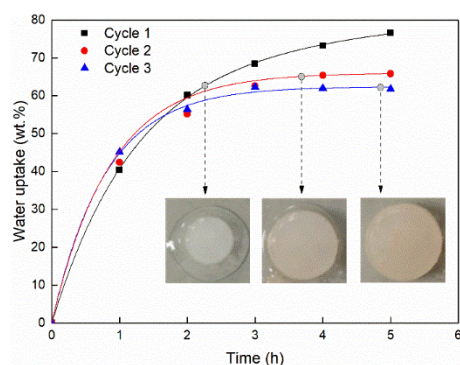


Figure 1. Adsorption capacity of tablet with formulation 5 through three adsorption-drying cycles at 80% relative humidity.

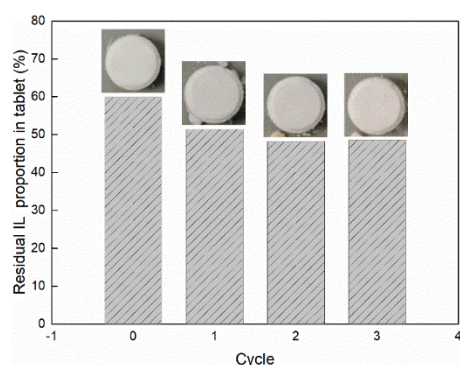




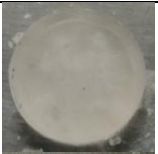








Figure 2. Residual IL proportion of tablet with formulation 5 through three adsorption-drying cycles at 80% relative humidity.

Another way to solve leakage is to decrease the proportion of IL in the ionogel, but higher silica contents can lead to brittle tablets. To settle this issue, a small amount of water has been added to ionogel to bind tablet before drying it. From the cycle test, it can be concluded that tablet of 50% EMIM Ac/Syloid 72FP does not leak. Thus, tablet with this formulation is used to test confinement stability and stability toward water adsorption. As shown in Figure 3, no leakage and fragmentation are found after exposing the material at 80% relative humidity for 6 hours and drying for 1 hour at 80°C. The tablet color changed over the cycles from white to transparent and turned back to original white after drying for 1 hour. This tablet with formulation 6 showed good confinement and water stability.

To examine the reversibility of the hydration process, the behavior of the ionogel is observed when the gels are subjected to a range of dehydrating conditions. The tablet with formulation 5 is tested for 5 cycles, as shown in Table 4. During every cycle, the tablet is placed in a humid air for 15 hours to adsorb moisture, and then dried in oven for 2 hours. When the hydrated ionogel is removed from air under ambient conditions and dried in oven at 80°C, the ionogel underwent dehydration, and the ionogel appearance changed back from transparent white to the opaque white, non-hydrated form. This demonstrated tablets with formulation 5 has good thermal stability at 60% relative humidity. Similarly, as the images in *Figure* showed, the tablet with formulation 5 does not have any breakage after adsorption and drying of 3 cycles at 80% relative humidity. These results suggested that Syloid 72FP boosted consistency during the tableting process and provided improvement in reducing friability, improved hardness and structural stability. Compliant tablet can be obtained by pressing ionogel with EMIM Ac and Syloid 72FP.



Table 4. Thermal stability test using tablet with formulation 5 at 60% relative humidity.

Cycle	0	1	2	3	4	5
Wet						
Dry						

### Adsorption capacity

Adsorption capacity is the most important property for ionogel-based adsorption desalination. The adsorption capacities of two promising tablets are studied. Figure 3 shows the trends of water content in the tablet with formulation 6. The proportion of water increased and then leveled at 60.03% while sorption rate had opposite trend. A comparison between the sorption rates of formulation 5 and 6 after two cycles shows that despite they have almost same 61.78% of water uptake is achieved, this value is very close to the water uptake (60.03%) of the tablet with formulation 6. But at the first hour, their sorption rates show obvious difference, this is because that the tablet with formulation 5 after two cycles has more pores caused by IL loss for water vapor dispersion into IL. So tablet with formulation 5 after two cycles can arrive to adsorption equilibrium at less time. These suggested that the amount of adsorbed water is determined by the IL amount in IL and sorption rate is bigger if there were more pores in ionogel.

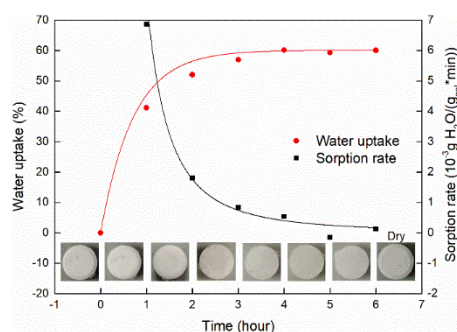


Figure 3. Adsorption performance of tablet with formulation 6 at 60% relative humidity.

The sorption rates of three cycles for tablet with formulation 5 are also calculated to illustrate the influence of IL amount on sorption rate. It can be seen from Figure 4 that the tablet with less IL show fast adsorption at the beginning and slow adsorption in the end. Syloid 72FP has a highly developed network of mesopores that provide access to the large surface area. When ionogel formed, IL fills most of the pores. However, it is very crucial to maintain a certain porosity which helps the water vapor mass transfer into the material. The ionogel with less IL has larger pore volume, thus water vapor can disperse into IL very fast, but in the end of the adsorption, the tablet with more IL can perform more layers hence it can adsorb water vapor faster.

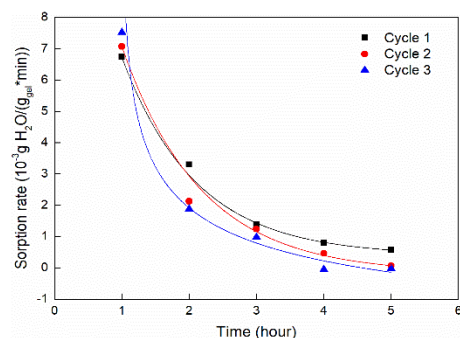


Figure 4. Sorption rate of tablet with formulation 5 through three adsorption-drying cycles.

In order to clarify the effect of leakage on adsorption capacity, tablet with formulation 5 and 6, and tablet with formulation 5 after 3 cycle leakage, are tested in the DVS Adventure. Figure 5 shows the isotherms of three types of ionogels. The amount of water adsorbed is linearly related to the relative humidity at lower relative humidity, so the isotherm of ionogel should be Henry law isotherm. However, isotherms for all three ionogels exhibit nonlinear increases as the amount of water absorbed in the sample increases at higher relative humidity. This phenomenon suggests that water is sufficiently soluble in the IL that liquid-liquid interactions are important, as well as water-ion interactions; i.e., the concentrations are well above what could be considered infinite dilution. Considering these two points, the isotherm of silica nanoparticle-based ionogel should be type III isotherm. Tablet with 60% EMIM Ac took up water at any relative humidity higher than other two tablets with less IL. The water uptake of tablets with 60.0% EMIM Ac, 48.60% EMIM Ac and 50.0% EMIM Ac are 132.20%, 72.89%, and 71.83% at 90% relative humidity, respectively. The adsorption capacity of tablet obtained by complete leakage is always higher than the tablet with 50.0% EMIM Ac, but their equilibrium absorption capacities at 90% relative humidity are very close, the gap between their adsorption capacities increased first and then decreased with the increase of relative humidity. This suggested further that adsorption capacity is controlled by the amount of IL.

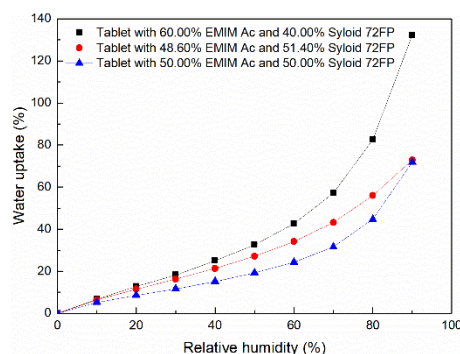


Figure 5. Adsorption capacity comparison of tablets with 60.00% EMIM Ac and 40.00% Syloid 72FP before and after IL loss, and with 50.00% EMIM Ac and 50.00% Syloid 72FP.

## Conclusion

In this study, we analyzed the influence of formulation on the preparation of silica nanoparticle-based ionogels, including their confinement stability, thermal stability, water stability, and adsorption capacity. Four conclusions could be obtained: 1) 50% EMIM Ac and 50% Syloid 72FP was identified as the most suitable formulation for making non-leaked, thermally stable, hydro-table ionogel; 2) sorption rate and adsorption capacity increased with the increase of relative humidity; 3) adsorption capacity is determined by the amount of IL,

and sorption rate is controlled jointly by IL amount and porosity of ionogel. These results suggested the synthesized ionogel can be applied on adsorption desalination. More work need to be done for the more detailed adsorption-desorption measurements and actual application on adsorption desalination.

## Reference.

- [1] Vioux A, Viau L, Volland S, Le Bideau J. Use of ionic liquids in sol-gel; ionogels and applications. *Comptes Rendus Chimie*. 2010;13:242-55.
- [2] Arellano IHJ, Guarino JG, Paredes FU, Arco SD. Thermal stability and moisture uptake of 1-alkyl-3-methylimidazolium bromide. *Journal of thermal analysis and calorimetry*. 2011;103:725-30.
- [3] Di Francesco F, Calisi N, Creatini M, Melai B, Salvo P, Chiappe C. Water sorption by anhydrous ionic liquids. *Green Chemistry*. 2011;13:1712-7.
- [4] Cao Y, Chen Y, Sun X, Zhang Z, Mu T. Water sorption in ionic liquids: kinetics, mechanisms and hydrophilicity. *Physical Chemistry Chemical Physics*. 2012;14:12252-62.
- [5] Heym F, Haber J, Korth W, Etzold BJ, Jess A. Vapor Pressure of Water in Mixtures with Hydrophilic Ionic Liquids—A Contribution to the Design of Processes for Drying of Gases by Absorption in Ionic Liquids. *Chemical Engineering & Technology*. 2010;33:1625-34.
- [6] Chakraborty A, Thu K, Saha BB, Ng KC. *Adsorption-Desalination Cycle*: John Wiley & Sons, Inc.; 2012.
- [7] Ng KC, Thu K, Kim Y, Chakraborty A, Amy G. Adsorption desalination: An emerging low-cost thermal desalination method. *Desalination*. 2013;308:161-79.
- [8] Ng KC, El-Sharkawy II, Saha BB, Chakraborty A. Adsorption desalination: A novel method. *Membrane and Desalination Technologies*: Springer; 2011. p. 391-431.
- [9] Buchtová N, Guyomard-Lack A, Le Bideau J. Biopolymer based nanocomposite ionogels: high performance, sustainable and solid electrolytes. *Green Chemistry*. 2014;16:1149-52.
- [10] Néouze M-A, Le Bideau J, Gaveau P, Bellayer S, Vioux A. Ionogels, new materials arising from the confinement of ionic liquids within silica-derived networks. *Chemistry of materials*. 2006;18:3931-6.
- [11] Xie Z-L, Jeličić A, Wang F-P, Rabu P, Friedrich A, Beuermann S, et al. Transparent, flexible, and paramagnetic ionogels based on PMMA and the iron-based ionic liquid 1-butyl-3-methylimidazolium tetrachloroferrate (III)[Bmim][FeCl<sub>4</sub>]. *Journal of Materials Chemistry*. 2010;20:9543-9.
- [12] Le Bideau J, Viau L, Vioux A. Ionogels, ionic liquid based hybrid materials. *Chemical Society Reviews*. 2011;40:907-25.

# Heat rejection stage of an adsorption heat storage cycle: The useful heat and sorption dynamics

V. Palomba<sup>1\*</sup>, A. Sapienza<sup>1</sup> and Y. Aristov<sup>2,3</sup>

<sup>1</sup>CNR ITAE Institute for Advanced Energy Technologies, Salita S. Lucia sopra Contesse 5, 98126 Messina, Italy

<sup>2</sup>Boreskov Institute of Catalysis, Lavrentiev Av. 5, Novosibirsk, Russia

<sup>3</sup>Novosibirsk State University, Pirogova Str. 2, Novosibirsk, Russia

\*Corresponding author: valeria.palomba@itae.cnr.it

## Abstract

In this work, a performance of the adsorption stage of a seasonal heat storage cycle was experimentally investigated under realistic boundary conditions. The tests were performed by a lab scale testing bench developed in ITAE-CNR. The studied adsorber is based on a compact aluminium heat exchanger of a flat tube type. Three water sorbents were tested: two commercial materials (microporous silica Siogel and AQSOA FAM Z02) and a composite "LiCl in mesoporous silica KSK".

**Keywords:** adsorption heat storage, pressure initiated process, sorption dynamics

## Introduction/Background

Thermal energy storage (TES) is a key component in HVAC systems, especially those driven by renewable energy sources or when waste heat is to be recovered. The TES technologies available are sensible, latent and thermochemical heat storage. Among these opportunities, thermochemical systems represent a promising alternative, thanks to the higher energy density and virtually infinite storage time [1]. Within the class of thermochemical storage, one interesting opportunity is offered by adsorption heat storage (AHS), which allows exploiting low-temperature (i.e. < 100°C) heat sources. Intense research activity is currently focused on these systems, but it is mainly centred on development of materials with a high heat density [2–4]. On the contrary, the study of AHS cycle dynamics is still an unexplored topic although it can strongly affect the operation of both charge and discharge steps of an AHS system.

In the past years, the dynamic study of adsorption heat pumps/chillers was extensively performed by means of a Large Temperature Jump (LTJ) method. It was firstly suggested in a volumetric version, and then extended to gravimetric, calorimetric [5], and thermal [6] versions. The LTJ method has been proven useful for the assessment of various adsorbents or/and adsorber configurations, including FAM Z02 [7], silica gel and more recently, MOFs [8] and composite sorbents [9].

However, all these studies were focused on the ad/desorption dynamics of an adsorptive cooling cycle driven by a fast change of temperature (Temperature Initiated (TI) cycle) while for AHS cycles only the charge (desorption) step is a TI process. On the contrary, the discharge (adsorption) step is initiated by a pressure jump, thus being Pressure Initiated (PI) process as detailed in the next section.

The dynamics of PI processes can differ from that of TI ones[10], therefore more attention should be paid on this subject. Hence, the aim of the present paper is to study, for the first time, the dynamics of PI heat rejection stage of AHS cycle. The experimental investigation is carried out on a lab-scale adsorption heat transformer test bench developed in ITEA/CNR. Three adsorbents were tested, either commercial or at lab-scale development. The useful heat and power achievable under different boundary conditions were investigated and the effect of the flow rate of a heat transfer fluid (HTF) in the discharge loop, is analysed.

## The adsorption heat storage cycle

A typical adsorption cycle for long-term heat storage (1-2-3-5-4'-1) is presented in Figure 1. It consists of the heat storage (desorption, 2-3) and heat rejection (adsorption, 5-4'-1) stages and is completed by isosteric heating and cooling along weak (3-5) and rich (1-2) isosteres. It differs from the common chilling cycle (1-2-3-4-1) consisting of two isobars (2-3) and (4-1) between the same isosteres. Thus, the heat storage stage is identical for the two cases, while the heat release stage differs substantially, being a PI process as opposed to a TI process for the storage stage.

At the end of the heat storage stage (point 3), the adsorbent is cooled down to the ambient temperature  $T_{am}$  (point 5 in Figure 1) that leads to a quite low pressure  $P_5$  over the adsorbent. Under these conditions ( $P_5$ ,  $T_{am}$ ), the heat is store for a long time, e.g. for several months. To release the heat back, the adsorber is connected to an evaporator at the ambient temperature that generates vapour pressure  $P_e = P_{4'} = P_o(T_{am})$ . Once the connection is opened, the large pressure jump  $P_5 \rightarrow P_{4'}$  causes the adsorption process and release of the adsorption (useful) heat  $Q_{ads}$ . The adsorbent temperature increases to the maximal temperature (point 4' in Figure 1a) and then gradually decreases until it reaches the minimal temperature  $T_{min}$  acceptable for heating (point 1). To stop the heat released process, the adsorber and the evaporator are disconnected. The adsorbent is discharged and should be charged again by heating (1-2-3) to the desorption temperature  $T_d$ .

If the ambient temperature  $T_{am}$  is too low and, hence, the pressure  $P_{4'}$  is not sufficient to cause essential adsorption and heat release, another cycle should be realized (Figure 1b). It needs one more external heat source (e.g. solar thermal collector or heat storage tank) to maintain the evaporator at a sufficiently high  $T_{ev}$  to ensure the heat release at the temperature suitable for heating. To get back the stored heat, the connection between the adsorber and the evaporator is opened to cause the pressure jump  $P_5 \rightarrow P_{4'}$  initiated the vapour adsorption and release of the useful heat at  $T \geq T_{min}$ .

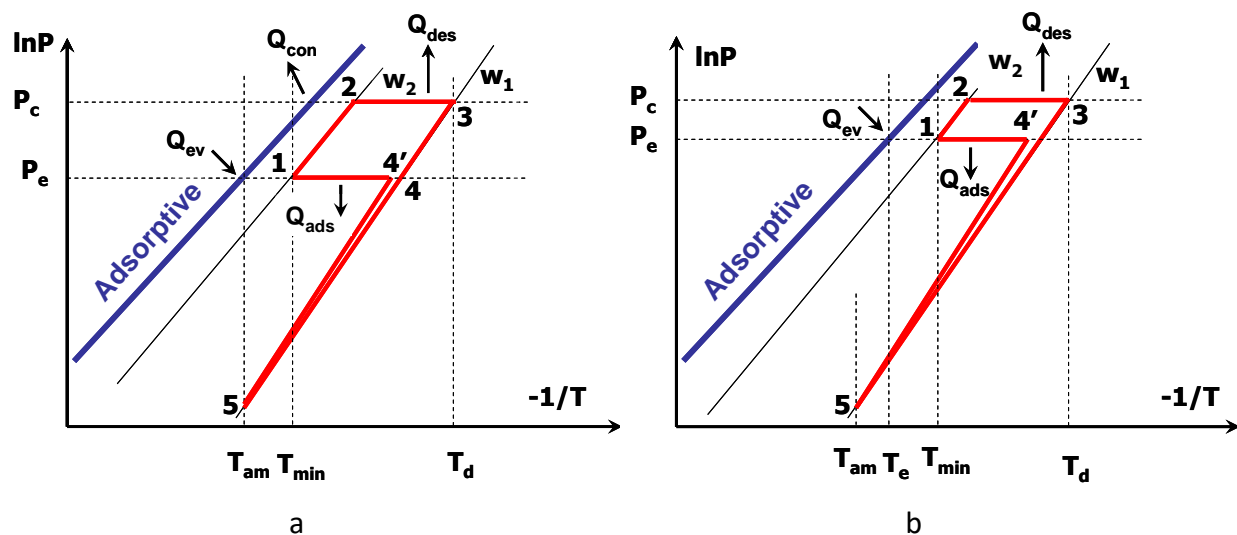


Figure 1: P-T diagram of an adsorptive cycle for long term heat storage: moderate (a) and cold (b) climates.

## Testing facilities and materials

The experimental campaign was carried out in a lab-scale adsorption transformer test bench available at CNR-ITAE and described in [11]. The lab-scale setup consists of a vacuum chamber, for the adsorber allocation, connected to a single evaporator and a single condenser.

Evaporator and condenser consist of finned copper coils. Connection between the bench components is obtained through pneumatic vacuum valves.

The external thermal source and sink for adsorber heating and cooling are an electric diathermic oil boiler (nominal heating power 24 kW) and an electric water chiller (nominal cooling power 14 kW). Two thermocryostats are used for keeping the desired temperature level in the evaporator and condenser. A picture of the test bench is shown in Figure 2.

All the components are thermally insulated and the rig is equipped with high accuracy sensors: Pt100 1/3 DIN to measure the HTF temperature, Class A T-thermocouples to measure the temperature of the adsorbent, piezoresistive pressure sensors in the vacuum chambers and magnetic inductive flow meters to measure the HTF flow rate in all the circuits. The approach followed in materials selection was to focus on sorbents that can be effectively regenerated at low temperatures, suitable for residential applications (i.e. < 100°C). The reference sorbent chosen was an RD silica gel Siogel produced by Oker Chemie [12], the advanced sorbent selected is AQSOA FAM Z02, specifically developed by Mitsubishi Chemicals for adsorption heat pumping applications [13]. Finally, an innovative adsorbent was evaluated, i.e. (17% wt LiCl/SG) belonging to the class of Composite Sorbents “salt in Porous Matrix (CSPM) [14], realised by wet impregnation of a mesoporous silica gel KSK (Russia) with the salt.

All materials were embedded in a flat-tube finned heat exchanger, closed by means of a metallic mesh and installed inside the vacuum chamber of the lab-scale unit, as shown in Figure 3.

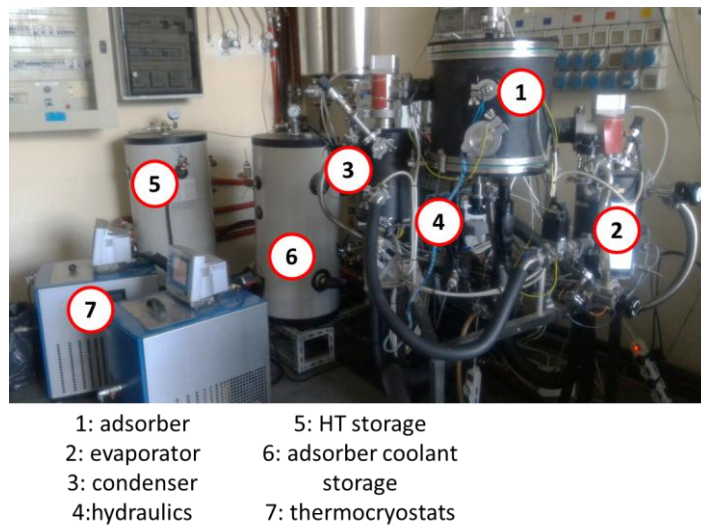


Figure 2: the testing bench at CNR-ITAE.



Figure 3: the heat exchanger filled with the composite material

## Testing procedure and conditions

Since the main aim of the experimental campaign was the dynamic study of the *adsorption* stage of the AHS cycle, the unified conditions were considered for the *desorption* stage:  $T_{des} = 85^{\circ}\text{C}$  (for silica gel) and  $95^{\circ}\text{C}$  (for AQSOA FAM Z02 and the composite sorbent) and  $T_{cond} = 30^{\circ}\text{C}$ . Prior to starting the test, the adsorbent was equilibrated at point 3 (Figure 1) and then cooled down to the initial adsorption temperature  $T_{am}$ . At the same time, the evaporation temperature  $T_e$  was set to a needed value. Once steady-state conditions in both components were reached, the vacuum valve connecting them was opened and the recording was started. The test was considered finished when  $\Delta T$  between the inlet and outlet of the adsorber was lower than 4 K, which was considered the minimum value suitable for practical applications. The variable parameters were the adsorber and evaporator temperatures and the flow rate in the adsorber (Table 1). The figures calculated and used in the analysis are the adsorption power  $\dot{Q}_{ads}$  and the specific useful heat released SUH:

$$\dot{Q}_{ads} = \frac{\sum_{t=1}^{t_{ads}} \dot{m}_{ads} c_p (T_{ads\_out} - T_{ads\_in}) \Delta t_{step}}{t_{ads}} \quad (1)$$

$$SUH = \frac{\sum_{t=1}^{t_{ads}} \dot{m}_{ads} c_p (T_{ads\_out} - T_{ads\_in}) \Delta t_{step}}{m_{sor}} \quad (2)$$

where  $\dot{m}_{ads}$  is the HTF flow rate in the adsorber,  $T_{ads,out}$  and  $T_{ads,in}$  are the HTF outlet and inlet temperatures,  $t_{ads}$  is the duration of adsorption stage,  $\Delta t_{step}$  is the acquisition time of data logging system and  $m_{sor}$  is the adsorbent mass.

Table 1: experimental conditions.

Adsorbent	$T_{ads}$	$T_{ev}$	Flow rate adsorber
	$^{\circ}\text{C}$	$^{\circ}\text{C}$	$\text{kg min}^{-1}$
Silica gel	20,30	5,10,15,20	1.2, 2.5, 3.2
FAM Z02	20,30	5,10,15,20	1.2, 2.5, 3.3
LiCl/KSK 17%	20,30	5,10,15	1.2, 2.5

## Results

Firstly, the trends obtained during a reference cycle will be reported, with the aim of giving an overview of the experimental data collected and analysed. Subsequently, the data for the three adsorbents tested will be further compared, presenting the energy and dynamic studies.

Figure 4a shows evolution of the adsorbent and the HTF outlet temperatures in a typical dynamic test. At the beginning of adsorption stage, when the connection to the evaporator is opened, there is an increase in the adsorbent temperature  $T_{ads}$  from 20 up to  $32^{\circ}\text{C}$ . The temperature then gradually decreases. The evolution of the HTF temperature is similar: it passes a maximum and gradually reduces. However, the maximum corresponds to a lower temperature ( $25^{\circ}\text{C}$ ) and is shifted in time, due to heating of inert metal masses in the unit. At  $t = 0$ , the difference  $\Delta T_{dr} = (T_{adsorbent} - T_{HTF\_out}) = 0$ , so that a driving force for heat transfer is zero which is typical for PI processes [15]. Subsequently, the difference increases due to release of the adsorption heat and reaches a maximum of  $13^{\circ}\text{C}$  at  $t = 10$  s (Figure 4a).

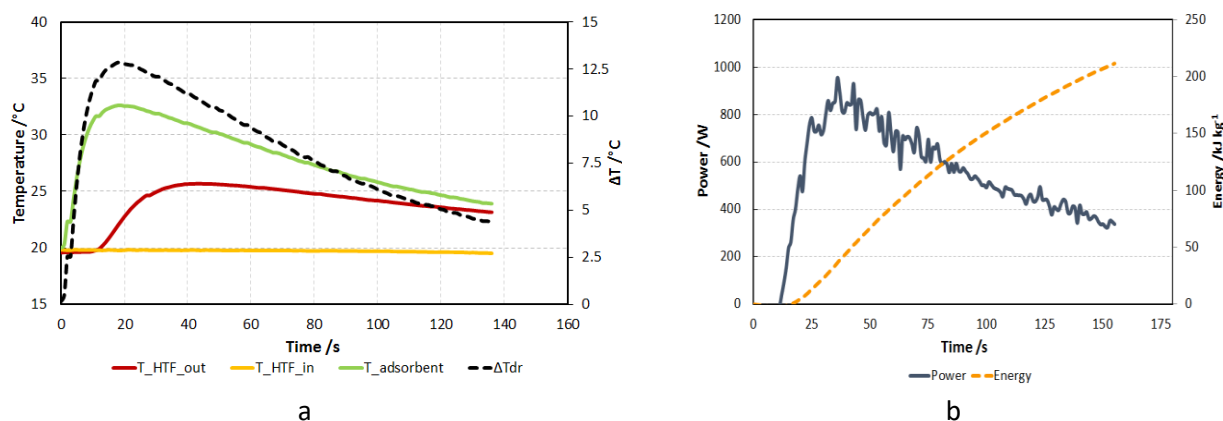


Figure 4: a, evolution of temperatures in the adsorber; b, the power and the specific useful heat for the typical test with FAM Z02. The test conditions:  $T_{ads} = 20^{\circ}\text{C}$ ,  $T_e = 10^{\circ}\text{C}$ , the HTF flow rate  $1.2 \text{ kg min}^{-1}$ .

Figure 4b shows the power and the specific useful heat calculated for the typical test with FAM-Z02. For the first 15-20 s, both values are equal to zero, that is in line with the delay in heating the HTF. Subsequently, the useful power rapidly increases up to a maximum of around 850 W (2.3 kW/kg) at 30-50 s and slowly reduces in time. Integration of the power (eq. (2)) gives the specific useful heat which gradually increases in time up to 200 kJ/kg.

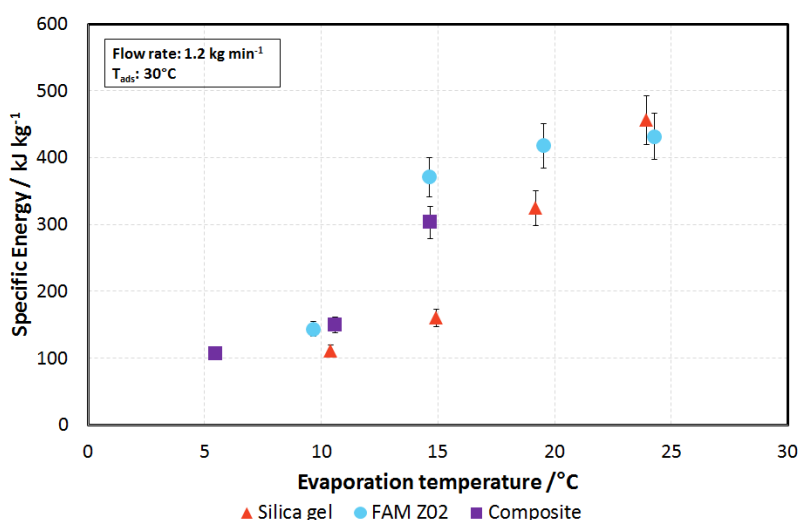


Figure 5: comparison of energy released by the tested adsorbents at variable evaporation temperature.

The evaluation and comparison of the adsorbents were then carried out by analyzing the specific useful heat released during the adsorption stage. Figure 5 presents this value for the tested materials as a function of the evaporation temperature for a fixed HTF flow rate and its initial temperature  $30^{\circ}\text{C}$ . The trend is the same for the various adsorbents: the higher the evaporation temperature, the larger the storage capacity of the adsorbent. For the silica gel, passing from  $T_e = 10^{\circ}\text{C}$  to  $25^{\circ}\text{C}$ , the storage capacity increases from 100 kJ/kg to 450 kJ/kg. For FAM Z02, passing from  $6$  to  $25^{\circ}\text{C}$ , the storage capacity increases from 130 kJ/kg to 430 kJ/kg. Interestingly, the storage capacity of FAM Z02 is larger than that for the silica under all the investigated conditions by 30% to 50%, with the exception of the highest evaporation temperature ( $25^{\circ}\text{C}$ ). This indicates that, when the ambient conditions are favourable, it is possible to use the silica gel instead of the much more expensive FAM Z02. For the composite material, tests were done also at lower evaporation temperatures, i.e.  $5^{\circ}\text{C}$ , since a



useful effect ( $\Delta T > 4\text{K}$ ) was measured even under these unfavourable conditions. On the contrary, evaporation temperatures of  $20^\circ\text{C}$  and  $25^\circ\text{C}$  were not investigated, in order to avoid oversaturation of the material. For this sorbent, the heat storage capacity is in the range  $100\text{--}300\text{ kJ/kg}$ .

Finally, a comparison of the adsorbents was realized regarding the adsorption dynamics. Figure 6 shows the effect of the HTF flow rate on the dynamics of the discharge stage, in terms of the average heat release power during the entire adsorption stage. Under the selected conditions, i.e.  $T_{\text{ads}} = 30^\circ\text{C}$  and  $T_{\text{e}} = 15^\circ\text{C}$ , with FAM Z02, the power increases from  $2.6\text{ kW kg}^{-1}$  to  $4.2\text{ kW kg}^{-1}$  when a flow rate of  $3.3\text{ kg min}^{-1}$  is chosen. On the contrary, for the composite, the effect of HTF flow rate increases from  $1.5\text{ kW kg}^{-1}$  to  $2.6\text{ kW kg}^{-1}$ . For the silica gel, the average power measured was almost independent on the flow rate, but it was the lowest among the investigated materials, around  $1\text{ kW kg}^{-1}$ . The results indicate that the flow rate affects mostly FAM Z02 and the composite. Indeed, increasing the HTF flow rate, the heat transfer in the heat exchanger of the adsorber increases and heat is transferred to the HTF more efficiently.

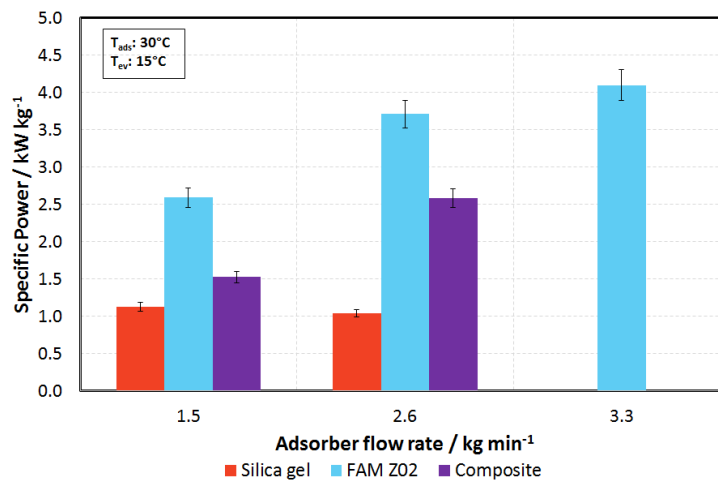


Figure 6: comparison of heat release power of the different materials as a function of adsorber flow rate.

## Conclusions

A dynamic investigation on the adsorption stage of a seasonable adsorption heat storage cycle was presented. The main peculiarity of the investigated process is that it is pressure-initiated. To cover the gap in the study and evaluation of such a cycle, the useful heat released as well as the adsorption dynamics were studied for three adsorbents: a reference adsorbent (silica gel), an advanced adsorbent (FAM Z02) and an innovative sorbent (17% wt LiCl/KSK silica gel). The results indicated that with the silica gel, the useful heat released is in a range of  $100\text{ kJ/kg}$  to  $450\text{ kJ/kg}$  depending on the evaporation (or ambient) temperature. For FAM Z02, the useful heat released goes from  $130\text{ kJ/kg}$  to  $430\text{ kJ/kg}$  and for the composite it is in the range  $100\text{--}300\text{ kJ/kg}$ . Regarding sorption dynamics, the HTF flow rate proved to be a key parameter. Specific power measured is in the range of  $2.6\text{ kW kg}^{-1}$  to  $4.2\text{ kW kg}^{-1}$  for FAM Z02,  $1.5\text{ kW kg}^{-1}$  to  $2.6\text{ kW kg}^{-1}$  for the composite and  $1\text{ kW kg}^{-1}$  for the silica gel.

## Acknowledgments

Y.I.Aristov thanks the RFBR (grant n. 18-58-7809) for partially financial support of this work.

## References

- [1] G. Alva, L. Liu, X. Huang, G. Fang, Thermal energy storage materials and systems for solar energy applications, *Renew. Sustain. Energy Rev.* 68 (2016) 693–706. doi:10.1016/j.rser.2016.10.021.
- [2] L. Scapino, H.A. Zondag, J. Van Bael, J. Diriken, C.C.M. Rindt, Sorption heat storage for long-term low-temperature applications: A review on the advancements at material and prototype scale, *Appl. Energy*. 190 (2017) 920–948. doi:10.1016/j.apenergy.2016.12.148.
- [3] L.F. Cabeza, A. Solé, C. Barreneche, Review on sorption materials and technologies for heat pumps and thermal energy storage, *Renew. Energy*. 110 (2017) 3–39. doi:10.1016/j.renene.2016.09.059.
- [4] N. Yu, R.Z. Wang, L.W. Wang, Sorption thermal storage for solar energy, *Prog. Energy Combust. Sci.* 39 (2013) 489–514. doi:10.1016/j.pecs.2013.05.004.
- [5] M. Tierney, L. Ketteringham, R. Selwyn, H. Saidani, Calorimetric measurements of the dynamics of a finned adsorbent: early assessment of the activated carbon cloth–ethanol pair with prismatic aluminium fins, *Appl. Therm. Eng.* 93 (2016) 1264–1272. doi:10.1016/J.APPLTHERMALENG.2015.10.009.
- [6] M.M. Tokarev, Y.I. Aristov, A new version of the Large Temperature Jump method: The thermal response (T–LTJ), *Energy*. 140 (2017) 481–487. doi:10.1016/J.ENERGY.2017.08.093.
- [7] S. Santamaria, A. Sapienza, A. Frazzica, A. Freni, I.S. Girmik, Y.I. Aristov, Water adsorption dynamics on representative pieces of real adsorbents for adsorptive chillers, *Appl. Energy*. 134 (2014) 11–19. doi:10.1016/J.APENERGY.2014.07.053.
- [8] L.G. Gordeeva, M. V. Solovyeva, Y.I. Aristov, NH<sub>2</sub>-MIL-125 as a promising material for adsorptive heat transformation and storage, *Energy*. 100 (2016) 18–24. doi:10.1016/J.ENERGY.2016.01.034.
- [9] A.D. Grekova, L.G. Gordeeva, Z. Lu, R. Wang, Y.I. Aristov, Composite “LiCl/MWCNT” as advanced water sorbent for thermal energy storage: Sorption dynamics, *Sol. Energy Mater. Sol. Cells*. 176 (2017) 273–279. doi:10.1016/j.solmat.2017.12.011.
- [10] Y.I. Aristov, Adsorptive transformation and storage of renewable heat: Review of current trends in adsorption dynamics, *Renew. Energy*. 110 (2017) 105–114. doi:10.1016/J.RENENE.2016.06.055.
- [11] Y.I. Aristov, A. Sapienza, D.S. Ovoshchnikov, A. Freni, G. Restuccia, Reallocation of adsorption and desorption times for optimisation of cooling cycles Optimisation des cycles de refroidissement par modification des durées d’adsorption et de désorption, *Int. J. Refrig.* 35 (2012) 525–531. doi:10.1016/j.ijrefrig.2010.07.019.
- [12] Siogel datasheet, (n.d.). [http://www.oker-chemie.de/downloads/SIOGEL/Datenblaetter/EN/PI\\_SIO-01-SW-engporig-engl.pdf](http://www.oker-chemie.de/downloads/SIOGEL/Datenblaetter/EN/PI_SIO-01-SW-engporig-engl.pdf).
- [13] AQSOA FAM Z02 datasheet, (n.d.). [http://www.aaasaveenergy.com/products/001/pdf/AQSOA\\_1210E.pdf](http://www.aaasaveenergy.com/products/001/pdf/AQSOA_1210E.pdf).
- [14] L.G. Gordeeva, Y.I. Aristov, Composites “salt inside porous matrix” for adsorption heat transformation: a current state-of-the-art and new trends, *Int. J. Low-Carbon Technol.* 7 (2012) 288–302. doi:10.1093/ijlct/cts050.
- [15] Y.I. Aristov, “Heat from Cold” – A new cycle for upgrading the ambient heat: Adsorbent optimal from the dynamic point of view, *Appl. Therm. Eng.* 124 (2017) 1189–1193. doi:10.1016/J.APPLTHERMALENG.2017.06.107.

# Adsorptive heat transformation/storage: temperature- vs. pressure-initiated cycles

Yu.I. Aristov<sup>1,2</sup>

<sup>1</sup>Boreshkov Institute of Catalysis, Ac. Lavrentiev av. 5, Novosibirsk 630090, Russia

<sup>2</sup>Novosibirsk State University, Pirogova st. 2, Novosibirsk 630090, Russia

\*Corresponding author: aristov@catalysis.ru

## Abstract

Adsorption heat transformation/storage is an environmentally benign and energy saving technology for effective utilization of low-temperature heat from various sources (renewable heat, thermal wastes, geothermal heat, etc). Two types of the adsorptive cycles have been suggested, which essentially differ by the way of adsorbent regeneration: either adsorbent heating (*temperature-initiated* cycles) or reducing the adsorptive pressure over adsorbent (*pressure-initiated* cycles). This communication addresses a preliminary comparison of these cycles from both thermodynamic and dynamic points of view.

**Keywords:** Adsorption cooling/heating/storage, Adsorbent regeneration, Entropy generation, Cycle dynamics

## Introduction

The adsorptive heat transformation/storage (AHTS) is an emerging technology gaining more and more attention for the past decades. A simplest three temperature (3T) AHTS unit exchanges heat between three thermostats at high ( $T_H$ ), middle ( $T_M$ ) and low ( $T_L$ ) temperatures and transforms heat at three modes: (1) cooling, (2) heating, and (3) upgrading the temperature potential. Two types of the suggested AHTS cycles essentially differ by the way of adsorbent regeneration: (i) adsorbent heating up to the temperature sufficient for the adsorbate removal (*temperature-initiated*, TI cycles, Fig. 1a), (ii) reducing the adsorptive pressure over the adsorbent (*pressure-initiated*, PI cycles, Fig. 1b). In a more wide sense, a single adsorption stage can also be either TI (cycle **a** in Figs. 1 and 2) or PI (cycle **b** in Figs. 1 and 2).

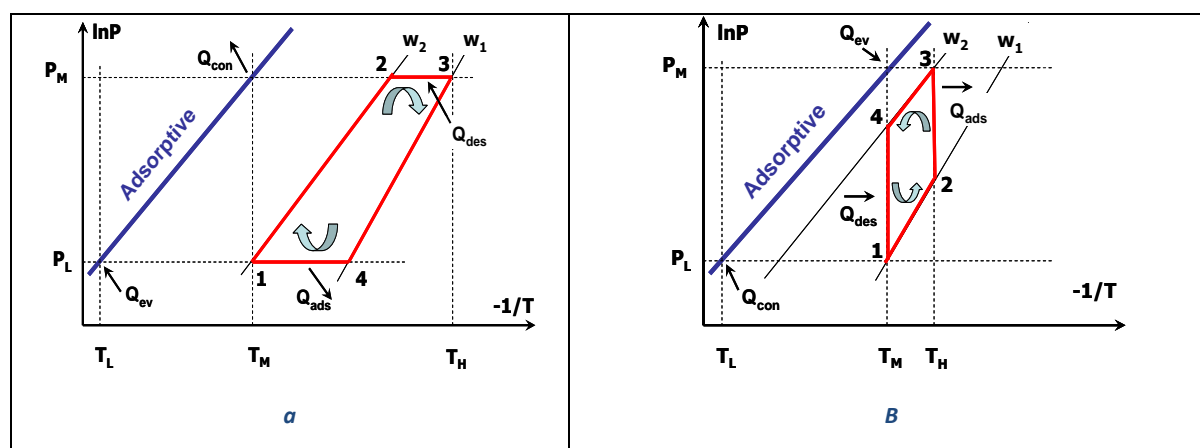


Fig. 1. P-T diagrams of various 3T AHTS cycles: a – TI cycle (cooling/heating), b – PI cycle (heat amplification).

The TI cycles are very common and widely used to realize cooling and heating modes [1,2]. The PI cycles are much less spread and suggested so far mainly for temperature upgrading mode [3,4]. In this work, we endeavour to make a preliminary comparison of the TI and PI

cycles from both thermodynamic and dynamic points of view. We take into account literature data which are plentifully available for TI cycles and rarely accessible for PI cycles as well as our own experimental data on a new “Heat from Cold” (HeCol) cycle recently suggested for upgrading the ambient heat in [4] and studied in [5-8]. Moreover, combined TI/PI cycles which have both TI and PI stages (Fig. 2) are also briefly considered. For instance, cycle **a** (route 1→2→3→4→1 in Fig. 2) represents a non-isothermal HeCol cycle for heat amplification [4,5-7]. It can also operate as an adsorptive cycle for short-term heat storage (route 1→4→3→2→1), whereas cycle **b** can be applied for long-term heat storage [9].

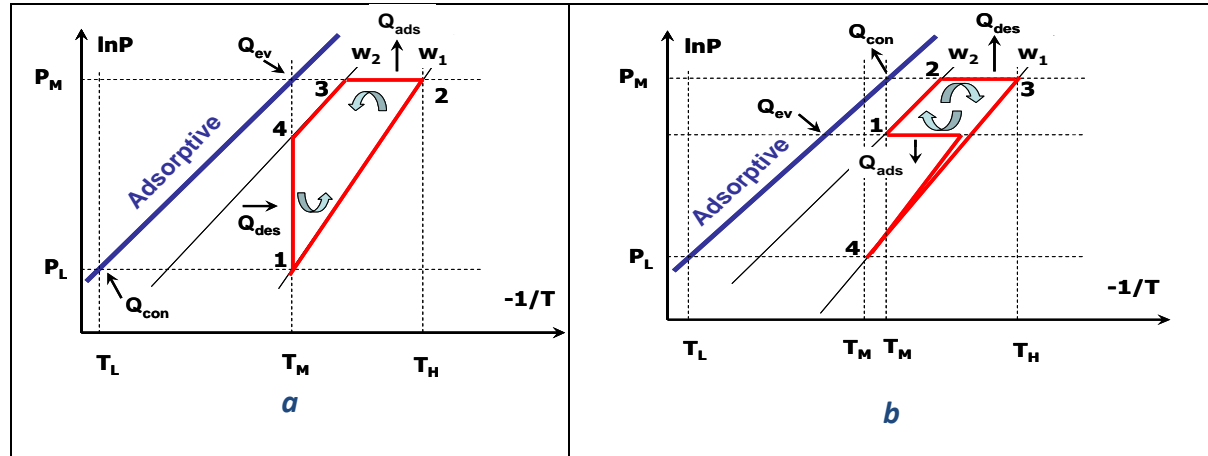


Fig. 2. *P-T* diagrams of combined TI/PI AHTS cycles.

## Discussion and Results

### *Thermodynamic considerations.*

*The first law efficiency.* The first law efficiency of the two basic TI and PI cycles (**a** and **b** in Fig. 1) depends only on the ratio of heats [1]. If neglect inert masses in the system, for cycle **a**, the cooling and heating efficiencies are  $COP_c = Q_{ev}/Q_{des} < 1$  and  $COP_h = (Q_{con} + Q_{ads})/Q_{des} > 1$ , respectively. The efficiency of heat amplification for cycle **b** is  $COP_a = Q_{ads}/(Q_{ev} + Q_{des}) \approx 0.5$ . For the HeCol cycle, the latter value, however, has no practical meaning because the heats  $Q_{des}$  and  $Q_{ev}$  are taken for free from an inexhaustible natural heat reservoir, such as river, lake, sea, at low temperature  $T_M = 0-20$  °C [4]. On the contrary, the useful heat  $Q_{ads}$  may have a commercial value and be used for heating.

For basic 3T cycles **a** and **b**, accounting for the heat capacity of inert masses reduces the above ultimate COPs. In this case, the first law efficiency also depends on the adsorbate mass  $\Delta w$  exchanged in the cycle

$$COP_c(\Delta w) = Q_{ev} \Delta w / [Q_{des} \Delta w + C(T_H - T_M)] = COP_c^{id} [\Delta w / (\Delta w + B)], \quad (1)$$

where  $B = C(T_H - T_M)/Q_{des}$  is the ratio of the sensible heat of all inert masses to the latent heat necessary for desorption. Therefore, to increase the first law efficiency, the exchanged mass  $\Delta w = w_{max} - w_{min}$  has to be maximized [10], whereas the inert masses should be minimized [11]. However, for well-designed AHTS units, the cooling COP approaches its maximum value ( $Q_{ev}/Q_{des}$ ) already at  $\Delta w \geq (0.1-0.15)$  g/g and  $(0.2-0.3)$  g/g for the exchange of water and methanol (ammonia), respectively [10].

Much more important is the effect of inert masses on the efficiency of adsorptive cycles for heat storage (Fig. 2). For instance, for short-term (daily) storage by using the working pair "AQSOA FAM-Z01 – water" studied in [12], the sensible heat of the AdHEX unit (including HTF, tubes, fins and adsorbent) gives ca. 40% contribution to the useful heat transferred by the HTF to a Consumer. This heat has been accumulated in the inert masses during the heat

storage phase (1→2→3 in Fig. 2b or 4→3→2 in Fig. 2a). The major thermal masses are the HTF (water) (40%) and the adsorbent itself (27%). The heat released directly in the adsorption process contributes only 60%. For long-term (seasonal) heat storage, this sensible contribution is completely lost as the AHTS unit is cooled down to ambient temperature (isostere 2→1 in Fig. 2a or 3→4 in Fig. 2b). Moreover, in this case, a part of the potentially useful adsorption heat is spent for sensible heating of inert masses from ambient temperature  $T_{\text{am}}$  to  $T_M$ , thus additionally reducing the net useful heat. This part depends on the particular design of the AdHEX heat storage unit, the cycle boundary conditions and the HTF flow rate. Therefore, more attention should be paid to all these issues for optimization of heat storage performance.

*The second law efficiency.* The second law analysis of a 3T adsorptive cycle (Fig. 1) is well known and presented e.g. in [13,14]. The Carnot efficiency  $\text{COP}^C$  was calculated for cooling, heating and temperature amplification modes as

$$\text{COP}_c^C = (1/T_M - 1/T_H) / (1/T_L - 1/T_M), \quad (2)$$

$$\text{COP}_h^C = (1/T_L - 1/T_H) / (1/T_L - 1/T_M), \quad (3)$$

$$\text{COP}_{\text{amp}}^C = (1/T_L - 1/T_M) / (1/T_L - 1/T_H). \quad (4)$$

In fact, eqs. (2-4) give the limiting efficiencies which are fully determined by the three cycle temperature and do not take into account the particular way of the cycle initiation (TI or PI).

It is well known from the previous broad experience, that the maximum  $\text{COP}_c$  for real adsorptive cycles initiated by a T-change is significantly lower than predicted for a reversible Carnot cycle (eqs. (2-4)) with the same boundary temperatures [14,15]. The main reason of this distinction is the thermal entropy production caused by the external thermal coupling  $\Delta T = T_H - T_2$  (for desorption) and  $\Delta T = T_4 - T_M$  (for adsorption), which is responsible for about 95% of the total entropy production [14]. Here  $T_2$  and  $T_4$  are the initial desorption and adsorption temperatures (Fig. 1a). Indeed, the process of heat transfer during the adsorber heating (stages 1-2 and 2-3) and cooling (3-4 and 4-1) is highly irreversible. The thermal entropy generated due to the thermal coupling at desorption stage (2-3) can be calculated as  $S_{\text{des}} = \int (\frac{1}{T} - \frac{1}{T_H})dq$ , where  $T$  is the internal temperature at which the heat  $dq$  is effectively transferred during the desorption stage. If the whole desorption heat is transferred at  $T = T_H$ , no entropy is generated [10]. If the whole heat is transferred at  $T = T_2$ , the maximal entropy is generated  $S_{\text{max}} = Q_{\text{des}} (\frac{1}{T_2} - \frac{1}{T_H})$ . The latter value can be estimated for the typical TI cooling cycle ( $T_{\text{ev}} = 10$  °C,  $T_{\text{con}} = 30$  °C,  $T_H = 90$  °C) with the working pair "AQSOA FAM-Z02 – water" for which  $T_2 = 46$  °C and  $Q_{\text{des}} = \Delta H_{\text{des}} \Delta w = (3.6 \text{ kJ/g H}_2\text{O}) [0.22 \text{ (g H}_2\text{O)/(g ads)}] = 790 \text{ J/(g ads)}$  [16], thus, giving  $S_{\text{max}} = 0.3 \text{ J/[K (g ads)]}$ . Similar entropy is generated in the adsorber during the adsorption phase of the cycle. Much less entropy is generated during the isosteric stages of the TI cycle (1-3 and 3-4 in Fig. 1a).

In ref. [8], the entropy balance was calculated at each stage of the *pressure-initiated* HeCol cycle and in each converter element under conditions of an ideal heat transfer. The entropy is generated in

- a) the condenser, because the vapour temperature  $T_M$  differs from the condenser temperature  $T_L$ ;
- b) the evaporator, because the liquid adsorptive is moved from the condenser at  $T_L$  and heated irreversibly to  $T_M$ ;
- b) the adsorber, because the vapour temperature  $T_M$  differs from the adsorber temperature  $T_H$  as well as due to isosteric heating (1-2) and cooling (3-4) of the adsorbent;
- d) the adsorber, due to vapour drop from  $P_4$  to  $P_1$  at desorption stage (4-1) and to vapour jump from  $P_2$  to  $P_3$  at adsorption stage (2-3).

All these processes of entropy generation are inevitable due to the intrinsic irreversibility of the system. Processes (a)-(c) that involve sensible heat are similar to those in a common 3T TI cycle and lead to a similar entropy generation. Process (d) concerns the entropy produced in the adsorber during ad-/desorption stages. This entropy is lower than for TI ad-/desorption, because both these PI stages are isothermal, so that there is a zero thermal coupling. The isothermal vapour drop/jump is irreversible, however, results in a small entropy generation in the adsorber, because the mass  $\Delta w_g$  of gaseous adsorptive compressed/expanded during the pressure equalization is very low as compared to the difference of adsorbate mass  $\Delta w$  exchanged between isosteres (1-2) and (3-4) of the cycle [8]. The  $\Delta w_g$ -value depends on the "dead" volume of AHTS unit, but never exceeds 0.01 g/g for well-designed units, so that  $\Delta w_g \ll \Delta w \approx 0.2-0.5$  g/g.

As a result, the second law efficiency of HeCol cycles is expected to be higher as compared to the common TI AHTS cycle and even close to the Carnot efficiency, if consider only processes in the adsorber. For the common TI cycle, the Carnot efficiency in the adsorber can be reached only, if the weak and rich isosteres of the cycle coincide, i.e. for a mono-variant adsorption equilibrium [17]. This encouraging thermodynamic finding may be extended to *any* AHTS cycle initiated by a drop of the adsorptive pressure.

### ***Dynamic considerations.***

*The effect of non-zero power.* Strictly speaking, the above statement is true for *quasi-equilibrium* PI cycles that are usually not a case in actual practice. Indeed, apart from the efficiency, a high specific power is another target parameter which is important to develop compact AHTS units. Since this power is exchanged between an adsorbent bed and a heat transfer fluid (HTF), a certain temperature difference  $\Delta T$  between them is necessary to reach a reasonable specific power  $W_{sp}$  (in kW/(kg adsorbent)), according to the following heat balance equation

$$W_{sp} = U (S/m) \Delta T, \quad (5)$$

where  $U$  is the heat transfer coefficient,  $S$  is the heat transfer surface area, and  $m$  is the adsorbent mass. The minimal "obligatory" temperature difference can be briefly estimated as  $\Delta T = 10\text{K}$ , if assume the typical values of  $W_{sp} = 1$  kW/(kg ads),  $U = 100$  W/(m<sup>2</sup> K), and  $(S/m) = 1$  m<sup>2</sup>/(kg ads) [16]. This thermal coupling appears in real PI AHTS units and leads to appropriate entropy generation and reduction of the actual second law efficiency below the high theoretical value predicted above. However, the estimated coupling (10K) is still much smaller than the typical external thermal coupling in TI cycles (30-50K). Moreover, the "obligatory" coupling for PI cycles can be further reduced if utilize advanced heat exchangers with  $(S/m) = 2-4$  m<sup>2</sup>/kg [18-23]. Thus, the above conclusion about the higher second law efficiency of PI cycles still remains valid even for real non-equilibrium PI cycles with the average power of about 1 kW/kg that can be promising for practical use.

For PI stages (4-1) and (2-3), which are theoretically isothermal (Fig. 1b), the mentioned "obligatory" coupling  $\Delta T$  is caused by cooling/heating of the adsorbent bed due to the heat of desorption/adsorption. Indeed, the desorption process starts at point 4 and is initiated by the pressure drop from the initial desorption pressure  $P_4$  to the final pressure  $P_1 = P_0(T_L)$  at constant temperature  $T_M$ . At  $t = 0$ , right after this pressure drop, the driving force for heat transfer *equals zero* because the system is isothermal and there is no temperature gradient. At the same time, the driving force for mass transfer *is maximal* because the pressure difference  $\Delta P(t) = [P_{gr}(t) - P_L]$  between the vapour pressure inside and outside the grain/bed is maximal and equals  $\Delta P(0) = P_4 - P_1$ . This pressure gradient causes the diffusion of adsorptive, occupied the pores, out of the grain. The pressure  $P$  inside the grain reduces that, in its turn, initiates desorption of the adsorbate from the grain surface.

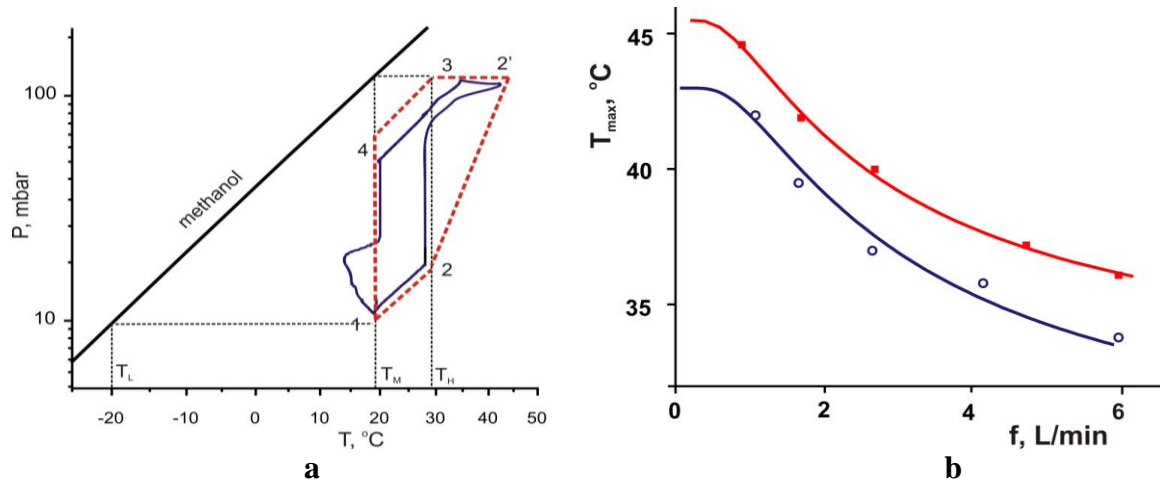


Fig. 3. a - The experimental (—) and theoretical (----)  $\ln P - (-1/T)$  diagrams of real HeCol cycle as reported in [5]. Boundary temperatures  $T_L/T_M/T_H = -20/20/28^\circ\text{C}$ , the HTF flux  $f = 1.1$  L/min. The CaClBr/SiO<sub>2</sub> sorbent. b - the maximum outlet HTF temperature  $T_{\max}$  vs the HTF rate  $f$ .  $T_L/T_M/T_H = -20/20/28^\circ\text{C}$ . ■ - LiCl/silica, ○ - CaClBr/silica [6].

This process needs a heat consumption that leads to the grain *cooling* which creates a temperature difference  $\Delta T$  between the grain/bed and the external heat source (HTF) at  $T_M$ . As a result, the driving force for heat transfer appears so that the intensive vapour flux causes appropriate heat flux [24] to generate the significant power  $W_{sp}$  (see eq. (5)). This increases the first law efficiency. On the other hand, this induced thermal coupling can somewhat reduce the second law efficiency as discussed above.

The predicted cooling of adsorbent bed during PI desorption was experimentally revealed in [5] where a first lab-scale HeCol prototype loaded with the CaClBr/SiO<sub>2</sub> composite sorbent was tested. A thermocouple located at the adsorber outlet detected the HTF cooling by  $\Delta T \approx 6^\circ\text{C}$  (Fig. 3a). One can guess much stronger cooling of the granulated adsorbent bed. Hence, the real process of PI methanol desorption occurs in the non-isothermal mode, different from the theoretically assumed for the ideal HeCol cycle. The deviation of the real cycle from the ideal one strongly depends on the HTF flux  $f$  [5-7]: the cycles approach each other at  $f \rightarrow \infty$  (see Fig. 3b and the explanation right below).

The same was found for the methanol adsorption stage: a significant HTF heating (by 15-20 °C) was detected ((2-2') in Fig. 3a). For the HeCol cycle, it is the useful effect as the released heat has the temperature potential sufficient for heating (e.g. in warm floor systems) and, hence, gains the commercial value [4,5]. Fig. 3b shows that the maximum outlet HTF temperature gradually approaches the set (equilibrium) temperature  $T_2 = 28^\circ\text{C}$  when the HTF flux increases [6].

*Adsorbent optimal for TI and PI cycles from the dynamic point of view.* Here we only briefly survey the results of our previous analysis of adsorbents dynamically optimal for TI [25] and PI [26] cycles. The main findings can be generalized as follows:

- (i) the dynamically optimal (*ideal*) adsorbent should have a *step-like* adsorption isotherm (for PI process)/isobar (for TI process) with the step positioned at the initial pressure (PI)/temperature (TI) of appropriate isothermal (PI)/isobaric (TI) stage. For instance, for PI cycle in Fig. 1b, the step should be at  $P_4$  for desorption and at  $P_2$  for adsorption [26];
- (ii) the adsorbent, which is the best for desorption stage, is the worst for adsorption stage and vice versa. To compromise between reasonable rates of both adsorption and desorption, the step should be at an intermediate point between the rich and weak isosteres. The position of this point provides an efficient tool to manage rates of the HeCol stages;

(iii) the *real* adsorbent optimal for desorption/adsorption stages of both TI and PI cycles should have concave/convex segment of the adsorption isobar (TI)/isotherm (PI) between the boundary pressures/temperatures of the cycle.

We believe that these general findings can be a lodestar for reliable selection of adsorbents, proper for particular TI and PI cycles, among those already known or for tailoring new adsorbents specialized for the given cycles.

*Direct comparison of TI and PI dynamics.* Even if the adsorptive is exchanged between the same weak and rich isosteres, the initial driving forces for TI and PI processes are different. At the beginning of TI processes ( $t = 0$ ), the driving force is the temperature drop/jump so that the *heat* transfer rate is maximum, whereas the mass transfer rate is zero [25]. On the contrary, for PI processes, at  $t = 0$  the driving force is the pressure drop/jump so that the *mass* transfer rate is maximum, whereas the heat transfer rate is zero [26]. Hence, one can expect different dynamics of the TI and PI processes [24].

The first direct comparison of the TI and PI dynamics has recently been performed in [27] in the frame of studying the new HeCol cycle. The aim was to investigate the methanol desorption dynamics initiated by the pressure drop (4-1) as well as by the temperature jump (4\*-1) between the same isosteres of the tested cycle (Fig. 4a). For the two versions of the adsorbent regeneration stage, the heat for methanol desorption was taken at a quite low temperature  $T_M = 2^\circ\text{C}$ , so that both versions can be used for upgrading the ambient heat in cold countries [4]. A commercial activated carbon ACM-35.4 was used as methanol adsorbent according to [28]. The boundary conditions for the regeneration were as follows: for the PI stage (4-1) -  $T_M = 2^\circ\text{C}$ ,  $P_4 = 8.2$  mbar and  $P_L = 4.7$  mbar; for the TI stage (4\*-1) -  $P_L = 4.7$  mbar,  $T_{M^*} = -6^\circ\text{C}$  and  $T_M = 2^\circ\text{C}$ .

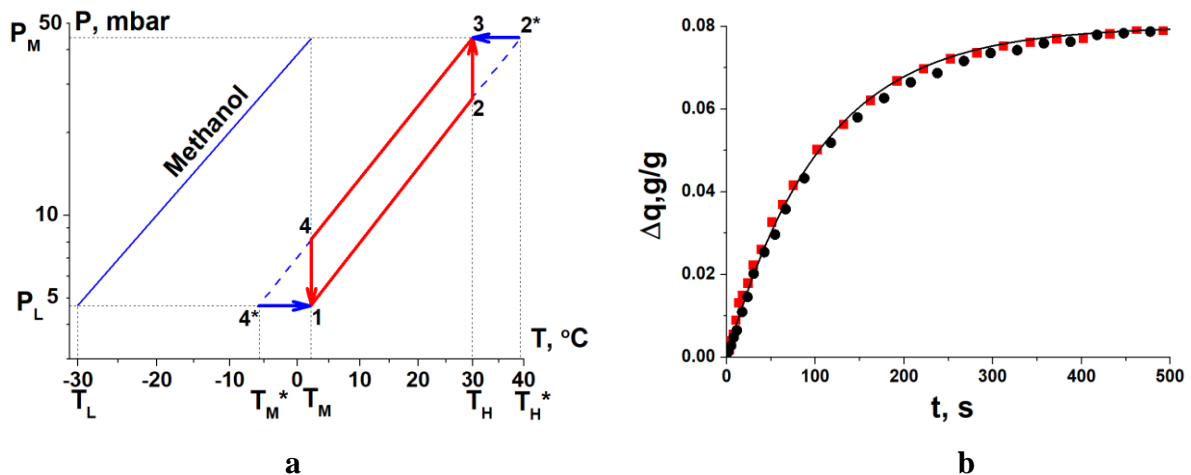


Fig. 4. a - P-T diagram of the studied cycles with isothermal (4-1 and 2-3) and isobaric (4\*-1 and 2\*-3) transitions between rich (3-4) and weak (1-2) isosteres of the HeCol cycle; and b - Methanol release curves as a function of time for PI (4-1) (●) and TI (4\*-1) (■) stages. Solid line – exponential approximation.

The main finding of this study is that the kinetic curves for both PI and TI desorption stages are identical (Fig. 4b). Hence, the regeneration dynamics does not depend on the regeneration path, either isothermal (4-1) or isobaric (4\*-1). The release curves can be well approximated by the exponential function

$$\Delta q = (0.08 \cdot g / g) \cdot (1 - e^{-t/\tau}) \quad (6)$$

with a single characteristic time  $\tau = 104 \pm 6$  s regardless the way of the desorption initiation. The same trend is found for the adsorption dynamics which does not depend on whether the



path is isobaric (2\*-3) or isothermal (2-3) (not presented) [27]. Again, both uptake curves are exponential with  $\tau = 78 \pm 4$  s that is shorter than for the desorption run. The adsorption boundary conditions were: for the PI stage (2-3) –  $T_H = 30^\circ\text{C}$ ,  $P_2 = 26.2$  mbar and  $P_M = 45.1$  mbar; for the TI stage (2\*-3) –  $P_L = 45.1$  mbar,  $T_H^* = 39^\circ\text{C}$  and  $T_H = 30^\circ\text{C}$  (Fig. 4a).

The revealed invariance of ad-/desorption dynamics is somewhat unexpected because isothermal and isobaric processes are initiated by quite different driving forces as considered above. The invariance is likely to indicate that heat and mass transfer processes are strongly coupled so that after a short transient period a steady state regime is established in the adsorbent bed, and this regime is similar, regardless the initial driving force ( $\Delta P$  or  $\Delta T$ ) applied. The formation of this steady-state regime for TI adsorption cycle was numerically studied in [29], and the time interval for setting the stationary mode was found to be ca. 5 s. No similar study has been done yet for PI adsorption cycles.

### Summary/Conclusions

Both *temperature- and pressure-initiated* adsorptive cycles for heat transformation/storage allow an efficient heat conversion process to be realized. The PI cycles can ensure the higher second law efficiency due to smaller (or zero) temperature coupling of the adsorber and external heat source/sink. This is true for *quasi-equilibrium* PI cycles, however, the *real* PI process can occur in the non-isothermal mode due to significant adsorbent cooling/heating during the desorption/adsorption modes. The preliminary direct comparison of the TI and PI dynamics for particular HeCol cycle revealed that the kinetic curves do not depend on the process path, either isothermal or isobaric. Further experimental and numerical study of the TI and PI dynamics is necessary to answer a question what is the true driving for AHTS cycles – pressure drop  $\Delta P$ , temperature jump  $\Delta T$ , variation of the uptake  $\Delta w$  or of the adsorption potential  $\Delta F$ . More attention should be also paid to dynamic studying PI cycles for heat amplification as well as combined TI/PI cycles for heat storage.

### Acknowledgements

This work is supported by the Russian Science Foundation (grant 16-19-10259). The author thanks Drs. L.G. Gordeeva, M.M. Tokarev, A.D. Grekova, B.N. Okunev and I.S. Girnik for their experimental contributions and useful discussions.

### References:

- [1] Li, T., Wang, R. Z., Li, H., Progress in the development of solid-gas sorption refrigeration thermodynamic cycle driven by low-grade thermal energy, Progress in Energy Combustion Science, 2013, doi:[10.1016/j.pecs.2013.09.002](https://doi.org/10.1016/j.pecs.2013.09.002)
- [2] F. Meunier, Adsorptive cooling: a clean technology, Clean Prod. Processes, 2001, v. 3, pp. 8-20.
- [3] Chandra, I., Patwardhan, V. S., Theoretical studies on adsorption heat transformer using zeolite-water vapour pair, Heat Recovery Systems and CHP, 1998, doi:[10.1016/0890-4332\(90\)90203-V](https://doi.org/10.1016/0890-4332(90)90203-V)
- [4] Aristov, Yu., Adsorptive transformation of ambient heat: a new cycle, Appl. Therm. Eng. 2017, doi:[10.1016/j.applthermaleng.2017.06.051](https://doi.org/10.1016/j.applthermaleng.2017.06.051)
- [5] Tokarev, M. M., Grekova, A. D., Gordeeva, L. G., Aristov, Yu., A new cycle "Heat from Cold" for upgrading the ambient heat: the testing a lab-scale prototype with the composite sorbent CaClBr/silica, Applied Energy, 2018, doi:[10.1016/j.apenergy.2017.11.015](https://doi.org/10.1016/j.apenergy.2017.11.015)
- [6] L.G. Gordeeva, M.M. Tokarev, A. Shkatulov, Yu.I. Aristov, Testing the lab-scale "Heat from Cold" prototype with the "LiCl/silica –methanol" working pair, Energy Conv. Manag., 2018, doi:[10.1016/j.enconman.2017.12.099](https://doi.org/10.1016/j.enconman.2017.12.099)
- [7] L.G. Gordeeva, M.M. Tokarev, Yu.I. Aristov, New adsorption cycle for upgrading the ambient heat, Rus. Theor. Found. Chem. Engn., 2018, doi: [10.1134/S0040579518020069](https://doi.org/10.1134/S0040579518020069)
- [8] B.N. Okunev, N.M. Voskresensky, I.S. Girnik, Yu.I. Aristov, Thermodynamic analysis of a new adsorption cycle for ambient heat upgrading: Ideal heat transfer, J. Eng. Thermophysics, 2018, v. 27, N 3 (in press).

- [9] Palomba, V., A. Sapienza, A., Aristov, Yu. I., Heat rejection stage of an adsorption heat storage cycle: the useful heat and sorption dynamics, Abstract HPC2018.
- [10] Aristov, Yu. I., Concept of adsorbent optimal for adsorptive cooling/heating, Applied Thermal Engineering, 2014, doi: 10.1016/j.applthermaleng.2014.04.077
- [11] Freni, A., Maggio, G., Sapienza, A., Frazzica, A., Restuccia, G., Vasta, S., Comparative analysis of promising adsorbent/adsorbate pairs for adsorptive heat pumping, air conditioning and refrigeration, Applied Thermal Engineering, 2016, doi: 10.1016/j.applthermaleng.2016.05.036.
- [12] Li G, Qian S, Lee H, Hwang Y, Radermacher R. Experimental investigation of energy and exergy performance of short term adsorption heat storage for residential application. Energy 2014;65:675-691.
- [13] W.M. Raldow, W.E. Wentworth, Chemical heat pumps - a basic thermodynamic analysis, Sol. Energ. 23 (1979) 75-79.
- [14] F. Meunier, F. Poyelle, M.D. LeVan, Second-law analysis of adsorptive refrigeration cycles: the role of thermal coupling entropy production, Appl. Therm. Eng. 17 (1997) 43-55.
- [15] Henning, H.-M., Solar assisted air conditioning in buildings – an overview, Appl. Therm. Engn., 2007, v. 27, pp. 1734-1749.
- [16] Santamaria S, Sapienza A, Frazzica A, Freni A, Girknik IS, Aristov YI. Water adsorption dynamics on representative pieces of real adsorbents for adsorptive chillers. Appl Energy 2014;134:11-9.
- [17] Sharonov, V.E., Aristov, Yu.I., Chemical and adsorption heat pumps: comments on the second law efficiency, Chem. Engn. J, 2008, v. 136, N 2-3, pp. 419-424.
- [18]. L.X. Gong, R.Z. Wang, Z.Z. Xia, C.J. Chen, Design and performance prediction of a new generation adsorption chiller using composite adsorbent, Energy Conv. Manag. 52 (2011) 2345–2350. doi: 10.1016/j.enconman.2010.12.036.
- [19] R.J.H. Grisel, S.F. Smeding, R. de Boer, Waste heat driven silica gel/water adsorption cooling in trigeneration, Appl. Therm. Eng. 30 (2010) 1039-1046. doi: 10.1016/j.applthermaleng.2010.01.020.
- [20] A. Sharafian, S.M.N. Mehr, W. Huttema, M. Bahrami, Effects of different adsorbent bed designs on in-situ water uptake rate measurements of AQSOA FAM-Z02 for vehicle air conditioning applications, Appl. Therm. Eng. 98 (2016) 568-574. doi: 10.1016/j.applthermaleng.2015.12.060.
- [21]. J. Bauer, R. Herrmann, W. Mittelbach, W. Schwieger, Zeolite/aluminum composite adsorbents for application in adsorption refrigeration, Int. J Energy Res. 33 (2009)1233–49. doi: 10.1002/er.1611
- [22]. R.Z. Wang, Z.Z. Xia, L.W. Wang, Z.S. Lu, S.L. Li, T.X. Li, et al., Heat transfer design in adsorption refrigeration systems for efficient use of low-grade thermal energy. Energy 36 (2011) 5425–39. doi: 10.1016/j.energy.2011.07.008.
- [23]. W.S. Chang, C.C. Wang, C.C. Shieh, Experimental study of a solid adsorption cooling system using flat-tube heat exchanger as adsorption bed, Appl. Therm. Eng. 27 (2007) 2195-2199. doi: 10.1016/j.applthermaleng.2005.07.022.
- [24] Aristov, Yu., Adsorptive transformation and storage of renewable heat: review of current trends in adsorption dynamics, Renewable Energy, 2017, doi:10.1016/j.renene.2016.06.055
- [25] I.S. Glaznev, D.S. Ovoshchnikov, Yu.I. Aristov, Kinetics of water adsorption/desorption under isobaric stages of adsorption heat transformers: the effect of isobar shape, Int. J. Heat Mass Transfer, 52 (2009) 1774-1777.
- [26] Yu.I. Aristov, "Heat from cold" – a new cycle for upgrading the ambient heat: adsorbent optimal from the dynamic point of view, Appl. Therm. Engn., 2017, v. 124, pp. 1189–1193.
- [27] I.S. Girknik, Yu.I. Aristov, Temperature- vs. Pressure-Initiated Cycles for Upgrading Low Temperature Heat: Dynamic Comparison, Abstract HPC2018.
- [28] Gordeeva, L., Aristov, Yu., Dynamic study of methanol adsorption on activated carbon ACM-35.4 for enhancing the specific cooling power of adsorptive chillers, Applied Energy, 2014. doi:10.1016/j.apenergy.2013.11.073
- [29] Okunev, B.N., Aristov, Yu.I. Modeling of isobaric stages of adsorption cooling cycle: Transient and quasi-stationary mode, Applied Thermal Engineering, 2013. doi: 10.1016/j.applthermaleng.2013.01.018.

# Database of Sorption Materials Equilibrium Properties

Zhiyao Yang<sup>1,2</sup>, Kyle R. Gluesenkamp<sup>2\*</sup>, and Andrea Frazzica<sup>3</sup>

<sup>1</sup>Lyle School of Civil Engineering, Purdue University  
550 W Stadium Ave  
West Lafayette, IN 47907 USA

<sup>2</sup>Oak Ridge National Laboratory  
1 Bethel Valley Rd  
Oak Ridge TN 37831 USA

<sup>3</sup>Istituto di Tecnologie Avanzate per l'Energia "Nicola Giordano"  
Consiglio Nazionale delle Ricerche  
Salita Santa Lucia Sopra Contesse, 5  
Messina, Italy

\*Corresponding author: [gluesenkampk@ornl.gov](mailto:gluesenkampk@ornl.gov)

## Abstract

Thermally-driven sorption systems can utilize a wide range of heat source to provide heating, cooling, heat transforming, and energy storage. The performance of a sorption system strongly depends on the equilibrium vapor pressure of the sorbate, which can be calculated using an equilibrium equation of state for the working pair. Numerous studies have been published formulating the vapor equilibrium from experimental measurements for various sorption working pairs. However, each study typically includes only a few working pairs, and information is scattered across a large number of sources. Therefore, it takes considerable effort to pinpoint the correlation for a desired working pair. Moreover, variations of functional forms, terminologies, and conventions were found across different literatures, adding to the difficulty of implementing multiple correlations for computer simulation and comparison. To overcome these challenges, this study created a readily usable database of vapor equilibrium for both absorption and adsorption working pairs with easy indexing and convenient implementation for computer simulation. The database was constructed by generalizing the equilibrium equations of state to provide compatibility with data from various published sources, unifying terminologies and unit bases across coefficient constants were unified, and compiling the data into a system of tables providing convenient indexing. As a result, 402 readily usable correlations for 352 sorption working pairs have been compiled, covering a wide range of sorbates including water, ammonia, methanol, ethanol, HFCs, HFOs, and hydrocarbons. The compiled database was also implemented into an open-source library named SorpPropLib, which can be directly used for calculating equilibrium vapor pressure of working pairs as well as supporting sorption systems simulation in various software.

**Keywords:** Sorption, equation of state, isotherms, PTX, materials properties, database

## INTRODUCTION

Sorption heat pumping and cooling technologies are important tools for the development of sustainable energy systems as they can be driven by diverse energy sources, including combustion, waste heat, and renewable heat. These thermally-driven sorption systems can be used for various application including heating and cooling as heat pumps, boosting waste heat temperatures as heat transformers, and providing high-density thermal storage. The performance of a sorption systems is dependent on the equilibrium vapor pressure of the

sorbate at the given operating temperatures and composition, which can be calculated using equilibrium equation of state.

Various types of equilibrium equations of state have been formulated to describe vapor equilibria of different sorption processes. Coefficient constants in equilibrium equations of state were fitted from experimental measurement for a large number of liquid absorption and solid adsorption working pairs. However, most published vapor equilibrium data are scattered in numerous sources such as [1-3] where only a few particular working pairs are investigated and presented in each source. Therefore, it takes considerable effort to identify a desired correlation, then to find or convert it into a specific functional form. Moreover, the same equilibrium equation of state of in two different sources literatures often takes various functional forms, uses diverse terminologies, and uses different unit bases, making it difficult to directly implement literature sources into a computer simulation.

A few previous studies summarized the vapor equilibrium data for multiple working pairs. Hassan et al [4] collected the coefficients for 87 solid-gas adsorption working pairs using correlations including Toth equations and various forms of Dubinin-Astakov and Dubinin-Radushkevich equations. Tamainot-Telto et al. [5] summarized the coefficients of 26 adsorption working pairs using ammonia as the refrigerant and various carbon adsorbents. A modified Dubinin-Radushkevich equation form was used to describe the isotherm correlation for all working pairs.

This study aims to build a comprehensive database of vapor equilibrium data from published literature. The database covers the equilibrium data from existing summaries and other literature as well as the relevant equation forms to be ready for implementation for computer simulation. To build such a database, each equation of state from literature was adapted to the most generic functional form of its type to be compatible with all available data and ready for implementation; the values of coefficients in the adapted equations were adjusted and their units converted according to the particular functional form; finally, the equilibrium equations of state compiled in this study were implemented in a database program named SorpPropLib to provide convenient equilibrium vapor calculation for a wide range of sorption working pairs.

## METHODOLOGY

To build a database of sorption vapor equilibrium data, the functional forms of the commonly used equilibrium equations of state were first generalized to allow coefficient constants from different sources to be summarized and compiled. After generalization of functional forms, the base parameters and unit systems of variables were unified for consistency across the summarized data.

Variations of equation forms of many commonly used functional forms such as Dubinin-Astakov and Toth equations can be found in literature formulating the vapor equilibrium of sorption working pairs. These different functional forms of the same type of equations employ different number of coefficient constants. Therefore, a generalized functional form for each type of equilibrium equation of state is needed to provide compatibility to various coefficient constants from different sources. For example, the Toth equation used in [3] is in the form of equation (1):

$$Y = \frac{a * P}{[1 + (b * P)^n]^{\frac{1}{n}}} \quad (1)$$

And the Toth equation used in [4] is as shown in equation (2):

$$Y = \frac{q * b^m * P}{[1 + b * P^n]^{\frac{1}{n}}} \quad (2)$$

The most generic functional form for Toth equations used in the data is as shown in equation (3):

$$Y = \frac{q_s * b^m * P}{(1 + b^r * P^n)^{\frac{1}{n}}} \quad (3)$$

With the generic functional form, the coefficient constants originally corresponding to other functional forms need to be adjusted accordingly. In the above example, the coefficient constants from [3] (equation 1) were adjusted to the generic functional form by substituting coefficient  $a$  with  $q_s * b^m$  while also adding two coefficients:  $m = 1$  and  $r = n$ . For coefficient constants from [4] (equation 2), the only change necessary was to add one coefficient  $r = 1$ .

Six equilibrium equations of state were compiled along with coefficient constants for adsorption working pairs. The equilibrium equations of state for physical adsorption include Toth, Dubinin-Astakhov (D-A), Dubinin-Radushkevich (D-R), dual site Sips (DSS), and Langmuir. The van't Hoff equation was included for chemical adsorption working pairs. Coefficient constants of liquid absorption working pairs were compiled for Antoine, Dühring, and several vapor-liquid equilibrium equations for state based on activity coefficient such as Wilson, NRTL, Heil, and UNIQUAC equations. Apart from commonly used equations, custom-fitted correlations and coefficient constants were included for several working pairs (including LiBr/H<sub>2</sub>O and LiCl/H<sub>2</sub>O).

Table 1 lists the functional forms of commonly used equilibrium equations of state included in this study. Since the D-R equation can be expressed as a special form of the D-A equation with a constant coefficient of  $n = 2$ , the coefficient constants for D-R equations in literature were compiled under the general D-A equation category. The vapor-liquid equilibrium equations of states for some absorption working pairs are not listed here. Although the functional forms for these mixing-rule or activity-coefficient based equations are often more complex compared to those listed in the table, they are more standardized with rare variation across literatures. In equations such as D-A and Wilson, the saturated temperature or pressure of the pure refrigerant at the given condition is also involved in the calculation. Therefore, additional correlations to calculate pure refrigerant saturation state were also included to support such types of equations.

Table 1 Functional forms of equilibrium equations of state

<i>Equation</i>	<i>Functional form</i>
<b>Langmuir</b>	$Y = Y_0 * K * P * \left(1 - \frac{Y}{Y_0}\right)^a$ $K = K^0 * \exp\left(-\frac{\Delta H}{RT}\right)$
<b>Toth</b>	$Y = \frac{q_s * b^m * P}{(1 + b^r * P^n)^{\frac{1}{n}}}$
<b>Dubinin-Astakov (D-A)</b>	$Y = Y_0 * \exp\left[-\left(\frac{A}{E}\right)^n\right]$ $W = W_0 * \exp\left[-\left(\frac{A}{E}\right)^n\right]$ $A = R * T * \ln\left(\frac{P_s}{P}\right)$

	$Y = Y_0 * \exp \left[ -k \left( \frac{T}{T_s} - 1 \right)^n \right]$
<b>Freundlich</b>	$Y = \left( \sum A_i T^i \right) * \left( \frac{P}{P_s(T)} \right)^{\sum B_i T^i}$
<b>Dual Site Dips (DSS)</b>	$Y = Y_A * \frac{(b_{AP})^{\frac{1}{n_A}}}{1 + (b_{AP})^{\frac{1}{n_A}}} + Y_B * \frac{(b_{BP})^{\frac{1}{n_B}}}{1 + (b_{BP})^{\frac{1}{n_B}}},$ $b_i = b_{0,i} * \exp \left[ \frac{\Delta H}{RT} * \left( 1 - \frac{T}{T_0} \right) \right]$
<b>Van't Hoff</b>	$\log P_{eq} = -\frac{\Delta H}{RT} + \frac{\Delta S}{R}$
<b>Antoine</b>	$\log_{10} P = \sum_{i=0}^k \left[ A_i + \left\{ \frac{1000 * B_i}{T - 43.15} \right\} \right] * (100 * X_S)^i$
<b>Duhring</b>	$P = r * \exp \left( C + \frac{D}{T} + \frac{E}{T^2} \right)$ $T = \frac{\frac{n * t + m - B}{A} - m}{n} + 273.15$ $A = a_0 + a_1 X_S + a_2 X_S^2 + a_3 X_S^3$ $B = b_0 + b_1 X_S + b_2 X_S^2 + b_3 X_S^3$
<b>Peng-Robinson (PR) and Soave-Redlich-Kwong (SRK)</b>	$P = \frac{R \cdot T}{V_m - b} - \frac{a(T)}{V_m^2 + m \cdot b \cdot V_m + n \cdot b^2}$ $a(T) = a_c \cdot \frac{R^2 \cdot T_c^2}{P_c} \cdot \alpha(T)$ $b = b_c \cdot \frac{R \cdot T_c}{P_c}$ $\alpha(T_r, \omega) = [1 + \kappa_0 (1 - T_r^{0.5})]^2$ $\kappa_0 = \sum_{i=0}^3 c_i * \omega^i$
<b>1 parameter van der Waals (1PVDW) mixing rule</b>	$a = \sum_i \sum_j x_i x_j a_{ij}$ $a_{ij} = \sqrt{a_i a_j} (1 - k_{ij})$ $b = \sum_i x_i b_i$
<b>2 parameter conventional mixing rule (2PCMR)</b>	$a = \sum_i \sum_j x_i x_j a_{ij}$ $a_{ij} = \sqrt{a_i a_j} (1 - k_{ij})$

	$b = \sum_i \sum_j x_i x_j b_{ij}$ $b_{ij} = \frac{b_i + b_j}{2} (1 - l_{ij})$
<b>Wilson</b>	$P = y_R * P_{tot} = P_s * x_R * \gamma_R$ $\ln \gamma_1 = -\ln(x_1 + \Lambda_{12}x_2) + x_2 \left[ \frac{\Lambda_{12}}{x_1 + \Lambda_{12}x_2} - \frac{\Lambda_{21}}{x_2 + \Lambda_{21}x_1} \right]$ $\Lambda_{12} = \frac{V_{m,2}}{V_{m,1}} \exp\left(-\frac{\lambda_{12} - \lambda_{22}}{RT}\right)$ $\Lambda_{21} = \frac{V_{m,1}}{V_{m,2}} \exp\left(-\frac{\lambda_{21} - \lambda_{11}}{RT}\right)$
<b>Non-random two liquid (NRTL)</b>	$P = y_R * P_{tot} = P_s * x_R * \gamma_R$ $\ln \gamma_1 = (1 - x_1)^2 \left( \tau_{21} \left( \frac{\exp(-2\alpha_{12}\tau_{21})}{x_1 + (1 - x_1)\exp(-\alpha_{12}\tau_{21})} \right)^2 \right. \\ \left. + \tau_{12} \frac{\exp(-2\alpha_{12}\tau_{12})}{[(1 - x_1) + x_1\exp(-\alpha_{12}\tau_{12})]^2} \right)$ $\tau_{ij} = \frac{\Delta g_{ij}}{RT} \quad (i, j = 1, 2)$
<b>Universal (UNIQUAC)</b> <b>quasi-chemical</b>	$P = y_R * P_{tot} = P_s * x_R * \gamma_R$ $\ln \gamma_1 = \ln \frac{\phi_1}{x_1} + \left(\frac{Z}{2}\right) q_1 \ln \frac{\theta_1}{\phi_1} + l_1 - \frac{\phi_1}{x_1} \sum_j x_j l_j$ $- q_1 \ln \left( \sum_j \theta_j \tau_{ji} \right) + q_1 - q_1 \sum_j \frac{\theta_j \tau_{ij}}{\sum_k \theta_k \tau_{kj}}$ $\tau_{ij} = \exp\left(-\frac{\Delta u_{ij}}{RT}\right)$ $l_j = \left(\frac{Z}{2}\right) (r_j - q_j) - (r_j - 1)$
<b>Heil</b>	$P = y_R * P_{tot} = P_s * x_R * \gamma_R$ $\ln \gamma_1 = -\ln(x_1 + x_2 \Lambda_{21}) + x_2 \left[ \frac{\Lambda_{21}}{x_1 + x_2 \Lambda_{21}} - \frac{\Lambda_{12}}{x_1 \Lambda_{12} + x_2} \right]$ $+ x_2^2 \left[ \tau_{12} \left( \frac{\Lambda_{21}}{x_1 + x_2 \Lambda_{21}} \right)^2 + \frac{\tau_{12} \Lambda_{12}}{(x_2 + x_1 \Lambda_{12})^2} \right]$ $\Lambda_{ij} = \frac{V_{m,j}}{V_{m,i}} * \exp\left(-\frac{\Delta \lambda_{ij}}{RT}\right)$ $\tau_{ij} = \frac{\Delta \lambda_{ij}}{RT}$
<b>Flory-Huggins</b>	$P = y_R * P_{tot} = P_s * x_R * \gamma_R$

$$\ln \gamma_1 = \ln \left( 1 - \left( 1 - \frac{1}{r} \right) \phi_2^* \right) + \left( 1 - \frac{1}{r} \right) * \phi_2^* + \chi * \phi_2^{*2}$$

$$\phi_2^* = \frac{rx_2}{x_1 + rx_2}$$

$$\chi = \frac{w^0}{RT} \left( 1 + \frac{w^1}{T} \right)$$

All equilibrium equations for adsorption working pairs take equilibrium vapor pressure as the input and calculate the corresponding composition of the sorbent with given temperature; on the other hand, the equilibrium equations of absorption working pairs take the composition as the input and calculate the corresponding equilibrium vapor pressure under the given temperature. Such conventions for both adsorption and absorption working pairs were preserved in this database.

In contrast to the conventionally unified input/output of equations, a variety of definitions for composition were used by researchers of different fields to denote the composition of absorption and adsorption working pairs. For example, the use of mole fraction as the mole of sorbate over the total mole of the sorbent and sorbate is a convention for expressing composition of solutions by the chemical engineering community. As a result, mole-fraction based composition terms were used in equations such as the Wilson and NRTL equations from chemical engineering publications [6]. Since most vapor-liquid equilibrium equations of state based on mixing rule and activity coefficient apply such convention, it is preserved in the database. Meanwhile, the convention for the Antoine and Dühring equations is to express composition as mass fraction of sorbate over the solution mixture [7].

Similarly, for many adsorption working pairs, the conventional term for composition is “loading” or “uptake”: the mass ratio of sorbate over sorbent. Therefore, for those adsorption equilibrium equations that use mole sorbate over sorbent as composition, the coefficient constants were adjusted to convert to a mass-based expression of composition [1]. Meanwhile, some adsorption working pair correlations (such as D-A) used the volume of sorbate vapor per mass of sorbent to express the composition [2, 5, 8, 9]. Since insufficient data of the vapor specific volume was provided by the original literature, the coefficient constants for these working pairs along with their composition expressions were not converted to mass-based to avoid unnecessary error.

The SI unit system is used for all data summarized in this study. Therefore, for the few studies that used the IP unit systems in calculation, their coefficient constants were adjusted to SI. The terminologies of parameters were unified in this summary as well. Table 2 lists the composition expressions used in this study and the corresponding equations that apply them.

Table 2 expression for compositions used in this study

<i>Composition Expression</i>	<i>Denoted in this work as</i>	<i>Definition</i>	<i>Applied Equations</i>
<b>Concentration</b>	$X_S$	$\frac{m_{Sorbent}}{m_{Sorbent} + m_{Refrigerant}}$	Antoine, Duhring
<b>Mole fraction</b>	$n$	$\frac{n_{refrigerant}}{n_{refrigerant} + n_{sorbent}}$	Mixing rule, Wilson, NRTL, UNIQUAC, Heil, Florry-Huggins
<b>Loading</b>	$Y$	$\frac{m_{Refrigerant}}{m_{Sorbent}}$	Langmuir, DSS, D-A, Toth, Freundlich
<b>Volumetric uptake</b>	$W$	$\frac{V_R}{m_S}$	D-A



## RESULTS

Table 3 shows a summary of refrigerants and corresponding sorbent count for the total 352 working pairs included in this work. For some working pairs, multiple correlations were provided by different sources, therefore the total count of correlations adds up to 402.

Table 3 Summary of refrigerants and number of working pairs

<i>Category</i>	<i>Refrigerant</i>	<i>Sorbent count</i>	<i>Category</i>	<i>Refrigerant</i>	<i>Sorbent count</i>
<i>Inorganic</i>	Water	36	<i>Fluorocarbons</i>	R12	3
	Ammonia	110		R13B1	1
	CO <sub>2</sub>	12		R22	4
<i>Hydrocarbon</i>	Propane	12		R23	1
	Methane	8		R32	13
	Propylene	11		R123	1
	Isobutane	2		R124	1
	Butane	4		R125	11
	Hexane	1		R134a	17
	Benzene	5		R143a	8
	Toluene	1		R152a	5
	Cyclohexane	4		R507C	1
	Cyclohexene	1		R507A	2
	Acetone	4		R407C	1
	TFE	3		R404A	1
	THF	1		R1234ze(E)	2
	<i>Alcohol</i>	Ethanol		19	R134a/R227ca
Methanol		37		R125/R143a	1
2-propanol		6		R22/R142b	1

Due to the large amount of correlations in the compiled database, it is inefficient to directly search for the coefficient constant and equilibrium equation by the working pair. Instead, a system of tables was built to provide two-step quick indexing to pinpoint data for the desired working pair: based on the summarized data, tables of each refrigerant were first built to list the sorbent and point to the equilibrium equation of state available for the refrigerant-sorbent working pair; with a much narrowed range of available working pairs under a specific type of equation, the table for the equilibrium equation of state can now be directly indexed with the working pair, and the coefficient constant along with the original literature can be retrieved. This process is illustrated with an example of locating the data for ammonia-activated carbon working pair in Figure 1.

In addition to the generalized equations and the system of tables of available coefficient constants for sorption working pairs, the summarized data has been implemented into an open-source database program named SorpPropLib. The SorpPropLib takes the form of a dynamic linked library with both equation correlations and coefficients for all working pairs summarized in the database tables. The structure and calculation flow of SorpPropLib is illustrated in Figure 2. The program follows the same process of pinpointing the appropriate equilibrium equation and corresponding coefficient constants of a given working pair as using the system of tables. Once the type of equilibrium equation is identified and coefficient constants located, the program carries out the calculation and feeds result back to the user.

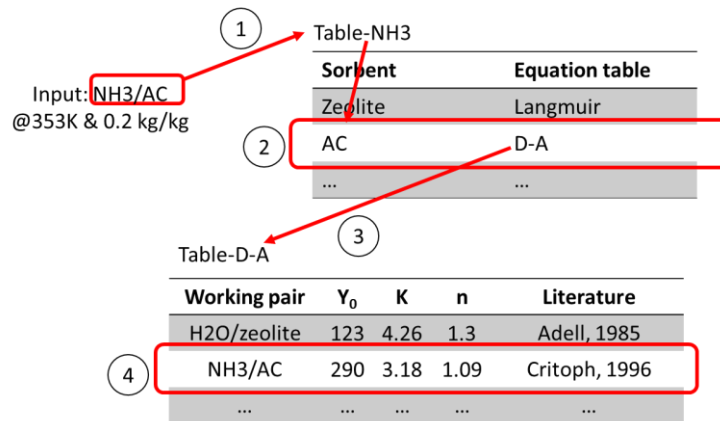


Figure 1 Example illustrating the indexing by working pair to locate vapor equilibrium data

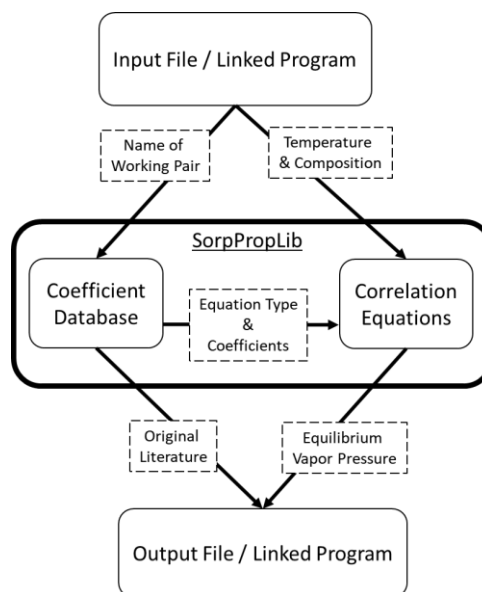


Figure 2 structure and calculation flow of SorpPropLib

Based on the basic function of convenient inquiry of equilibrium vapor given the operating conditions and the sorption working pair, SorpPropLib provides several convenient utilities that could facilitate research and development of sorption systems. The single-point inquiry function is handy for instant reference of vapor equilibrium. The program also provides batch inquiry capability for a series of varying operating conditions by using formatted text files for data input and output. Such text-file-based data communication allows SorpPropLib to be called by commercial software such as Engineering Equation Solver (EES) and MATLAB. Furthermore, SorpPropLib can be dynamically linked to open-source simulation software such as the Sorption system Simulation program (SorpSim) [10] and be incorporated in sorption system simulation and analysis.

As an open-source database program, SorpPropLib can be accessed, utilized, and continuously expanded with data for new working pairs by the sorption research community. Therefore, the goal of the current study as to facilitate research and development of sorption technologies can be further promoted with the open access of SorpPropLib.

## CONCLUSION

In this study the vapor equilibrium of 352 sorption working pairs were compiled and built into a comprehensive and readily usable database. The compiled data can be easily

implemented for computer simulation with generalized functional forms of equilibrium equation of state, unified terminologies and base parameters, and a system of tables for quick indexing. The compiled data has been implemented into a computer database library named SorpPropLib, which can be used alone as well as incorporated with modelling programs to provide material property support to sorption system simulation. The open-source and open-access nature of SorpPropLib allows collaboration in the sorption research community to provide a continuously expanding database with latest working pair properties for sorption system design and analysis.

### ACKNOWLEDGEMENT

This work was sponsored by the U. S. Department of Energy's Building Technologies Office under Contract No. DE-AC05-00OR22725 with UT-Battelle, LLC. The authors would also like to acknowledge Mr. Antonio Bouza, Technology Manager for HVAC&R, Water Heating, and Appliance, U.S. Department of Energy Building Technologies Office.

### REFERENCES

1. Wang, Y. and M.D. LeVan, *Adsorption equilibrium of carbon dioxide and water vapor on zeolites 5A and 13X and silica gel: pure components*. Journal of Chemical & Engineering Data, 2009. **54**(10): p. 2839-2844.
2. Henninger, S., et al., *Evaluation of methanol adsorption on activated carbons for thermally driven chillers part I: Thermophysical characterisation*. international journal of refrigeration, 2012. **35**(3): p. 543-553.
3. Huang, W., et al., *Vapor-Liquid Equilibrium Measurements of NH<sub>3</sub>+ H<sub>2</sub>O+ Ionic Liquid ([Dmim] Cl, [Dmim] BF<sub>4</sub>, and [Dmim] DMP) Systems*. Journal of Chemical & Engineering Data, 2013. **58**(5): p. 1354-1360.
4. Hassan, H., et al., *A review on the equations of state for the working pairs used in adsorption cooling systems*. Renewable and Sustainable Energy Reviews, 2015. **45**: p. 600-609.
5. Tamainot-Telto, Z., et al., *Carbon-ammonia pairs for adsorption refrigeration applications: ice making, air conditioning and heat pumping*. international journal of refrigeration, 2009. **32**(6): p. 1212-1229.
6. Döker, M. and J. Gmehling, *Measurement and prediction of vapor-liquid equilibria of ternary systems containing ionic liquids*. Fluid phase equilibria, 2005. **227**(2): p. 255-266.
7. de Lucas, A., M. Donate, and J.F. Rodríguez, *Vapour pressures, densities, and viscosities of the (water+ lithium bromide+ potassium acetate) system and (water+ lithium bromide+ sodium lactate) system*. The Journal of Chemical Thermodynamics, 2006. **38**(2): p. 123-129.
8. Passos, E., F. Meunier, and J.C. Gianola, *Thermodynamic performance improvement of an intermittent solar-powered refrigeration cycle using adsorption of methanol on activated carbon*. Journal of Heat Recovery Systems, 1986. **6**(3): p. 259-264.
9. Brancato, V., et al., *Ethanol adsorption onto carbonaceous and composite adsorbents for adsorptive cooling system*. Energy, 2015. **84**: p. 177-185.
10. Yang, Z., et al., *Liquid Desiccant System Component Models in the Sorption System Simulation Program (SorpSim)*. 2017.

# Overview and step forward on SAPO-34 based zeolite coatings for adsorption heat pumps

L. Calabrese<sup>1,3\*</sup>, L. Bonaccorsi<sup>2</sup>, A. Freni<sup>3</sup>, P. Bruzzaniti<sup>1</sup>, E. Proverbio<sup>1</sup>

<sup>1</sup>Department of Engineering, University of Messina, Contrada di Dio Sant'Agata, 98166 Messina, Italy

<sup>2</sup>Department of Civil Engineering, Energy, Environment and Materials, University Mediterranea of Reggio Calabria, Salita Melissari, 89124 Reggio Calabria, Italy

<sup>3</sup>CNR-ICCOM, Via G. Moruzzi 1, I-56124 Pisa, Italy

\* Corresponding author: lcalabrese@unime.it

## Abstract

In this work, at first, an overview on SAPO-34 zeolite coating for adsorption heat pumps was presented, highlighting current quality standard and open technological issues (i.e. the need for good mechanical and hydrothermal stability, high aging stability, etc.). Afterwards, we present an improved formulation of adsorbent composite coatings on aluminum support, having improved thermal and mechanical properties, especially when subjected to an impulsive stress. Specifically, the coated samples were prepared by dip-coating method starting from a water suspension of SAPO-34 zeolite and a hybrid polymer binder. Adhesive and mechanical properties were evaluated by pull-off test confirming the good interaction between metal substrate, filler and matrix. Adsorption equilibrium of water vapor on the adsorbent coating was measured in the range  $T=30\text{--}150^\circ\text{C}$  and  $p_{\text{H}_2\text{O}}=11\text{ mbar}$ . It was found that binder does not affect the water adsorption capacity and adsorption rate of the original SAPO-34 zeolite.

**Keywords:** SAPO-34, zeolite, coating, direct synthesis, composites.

## Introduction/Overview

Several research activities on adsorption heat pumps development are focused on the optimization of the integration between heat exchanger and adsorbent material, to create the so called adsorber. Two different approaches are currently evaluated: embedding of granular adsorbent inside an efficient heat exchanger [1] or coating the heat exchanger with the adsorbent material [2] [3]. Zeolites are the adsorbent materials most commonly employed, being structured by linked silica and alumina tetrahedra rearranged in a 3D structure. Their crystalline aluminosilicates architectures are characterized by channels and cavities with well-defined size, making zeolites very useful in several industrial fields as “molecular sieves”, catalysts and ion exchangers in solution [4]. Granular zeolite adsorbent inside the heat exchanger induces a low vapor transfer resistance and low manufacturing costs. However, a significant limit that avoid its use in high efficiency systems is the very low heat transfer efficiency due to a punctual contact between the grains and the surface of heat exchanger [5]. In this concern, coated exchanger choice is related mainly to its good thermal contact at the coating/metal interface and to the cycle times reduction.

The most promising coating methods are in-situ zeolite growth [6] [7] and binder-based coating processes [8] [9]. Direct accretion of zeolite crystals on the metal surface allows very good adhesion. However, multiple depositions are required to reach an acceptable zeolite layer thickness ( $<0.1\text{ mm}$ ). The binder-based coating method is an alternate way to deposit a thin layer of adsorbent on the heat exchanger surface. The binder-based coating method offers the possibility to vary coating thickness in the range  $0.1\text{--}1\text{ mm}$  by, e.g., controlling the viscosity of the liquid suspension and the dipping velocity. Earlier studies on the subject focused on the preparation of silica gel or zeolite-based coatings employing different inorganic or organic binders [10] [11] [12]. However, the resulting thermo-physical properties were not optimized and cycling stability was not proven.

Looking at the recent developments in field, Okamoto et al. [13] presented a relevant study on a SAPO-34 (coded AQSOA Z02) based composite coating produced by Mitsubishi Plastics Inc., by using an organic binder. The deposition procedure allowed obtaining coating thickness of 0.3 mm in aluminum lamellas usually used for heat exchanger. Their results evidenced an effective increase of thermal conductivity of the coating set-up (0.36 W/m K) compared to zeolite powders one (0.113 W/m K). Recently, silane based coating was evaluated to obtain effective and adsorptive coatings with good mechanical performances and long durability in severe environmental conditions [14] [15].

Full scale dip-coated adsorbers were experimentally tested in [16], showing encouraging results in terms of reduced adsorption cycle time and elevated specific power. Analogously, Bendix et al. [3] optimized power output and metal to adsorbent weight ratio on small scale and full scale adsorbers coated with increasing amounts of adsorbent. Freni et al. introduced a new coating composition, employing SAPO 34 powder as adsorbent and silane as binder [2] to obtain a coated adsorbent heat exchanger for adsorption chiller, evidencing the promising results of this technology. Utilization of a silane matrix in combination with zeolites as a coupling agent generates an interlayer with a good adhesion and homogeneity, able to provide a further barrier action, as protective layer. Indeed, the zeolite surface is covered by a large amount of silanol groups which guarantees a relatively high chemical reactivity and superficial interaction with several chemical compounds, including silanes [17]. It is expected that, the realization of a zeolite-based composite coating maintains the same adsorbent properties of the zeolite itself (thereby ensure the industrialization potential for the adsorption heat pumps), but at the same time create a coating with the typical mechanical resistance and durability characteristic of silane coatings [18] [19].

Nevertheless, still some issues are present. The coating is usually characterized by poor mechanical strength and brittle behavior that favors easy loss of zeolite particles from the supports upon repeated temperature swings, due to the difference in their thermal expansion coefficients. A drawback of this route is the low zeolite amount in the adsorber, due to the limited coating thickness, that induces low adsorbent density (typically 150-300 g/dm<sup>3</sup>). To overcome the previous issues, a new formulation based on a mixture of hybrid polymer binder with proper catalyst was employed to form an elasto-plastic composite coating. During the raw components mixing, the SAPO-34 powder (2 μm crystal dimension) was dispersed at different percentages (from 70 wt.% up to 90 wt.%). The experimental characterization of the new composite coating was carried out by pull-off, impact and adsorption tests.

## **Experimental Part**

### *Sample preparation*

Commercial aluminum 6061 rectangular strips, size 20 mm × 50 mm, were cut from a large aluminum sheet (thickness 0.5 mm). All samples were degreased in a diluted alkaline solution (0.1 N NaOH) for 60 s, washed in distilled water and finally treated with acetone. Afterwards, the composite hybrid zeolite coating was applied. In particular, the coating's preparation procedure involves the following steps:

- i) preparation of the composite slurry, mixing a specific ratios zeolite-hybrid polymer constituents in a water/ethanol solution. The slurry homogenization was carried out at first in an ultrasonic bath for 15 min followed by magnetically stirring for 15 min before the dip coating procedure;
- ii) pre-treatment of the aluminum substrate. Aluminum surface was degreased in a diluted alkaline solution (0.1 N NaOH) for 60s, washed in distilled water and finally with acetone;
- iii) the coating deposition was obtained by dipping coating procedure (dipping speed 4 cm/min) after that the substrate was maintained into the composite slurry for 60 s.
- iv) final drying (open to air for 5 min) and curing (12h at 80°C).

The studied zeolite coatings are categorized in the paper with the code “SZ” followed by a number, which identifies the percentage of the zeolite added to the polymer matrix. For instance, the code “SZ-80” indicates the sample made with 80 wt.% of SAPO-34 zeolite filler.

#### *Mechanical tests*

Impact and pull-off tests were used to evaluate mechanical stability and adhesive properties of the coating/support composite. The flexibility of coatings was roughly estimated by the drop-weight impact test in accordance to the experimental procedures defined in [9] [20]. Pull-off tests were carried out by using a DeFelsko PosiTest AT-M pull-off tester according to the experimental procedure reported in [20] [15].

#### *Adsorption tests*

The water vapor adsorption isobars of coated samples were measured by a thermogravimetric dynamic vapor system. First of all, the sample (about 0.5 cm<sup>3</sup>) was slowly heated up to 150 °C (heating rate 1°C/min) and kept at this temperature for about 6 hours under continuous evacuation (vacuum level: 10<sup>-4</sup> Pa), in order to degas the sample and determine its dry weight. Subsequently, a valve connecting the evaporator containing liquid water (maintained at T =23 °C) and the sample chamber was opened. The vapor flows through the system and the vapor (absolute) pressure is kept constant at the set value (P=11 mbar) by a butterfly valve automatically controlled and by the downstream vacuum pump. The system is controlled by a computer, which also regulates the sample temperature, following the defined temperatures steps (from 23 °C to 150 °C). At each temperature step, the pressure was kept constant until the sample weight equilibrium was reached.

The water uptake was calculated as

$$w\left(\frac{g}{g}\right) = \frac{m(p_{H_2O}, T_s) - m_0}{m_0} \quad (1)$$

where  $m(p_{H_2O}, T_s)$  [g], represents the weight of the sample at given water vapor pressure and sample temperature, while  $m_0$  [g] is the dry mass of the sample.

## **Discussion and Results**

#### *Mechanical properties*

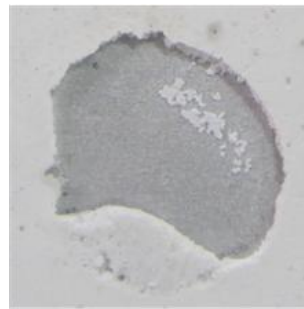
In Table 1, pull-off adhesion strength and drop weight impact energy (defined according to [20]) results are summarized for the composite coatings at varying zeolite content. For comparison, results from [9] [20] are also reported. The pull-off test results evidence that the SZ composite coatings exhibit good adhesion with aluminum substrate. Best results were observed for composite coating with lowest zeolite content (SZ-70). Although, quite good adhesion strength can be observed for other composite compositions, showing also properties compatible to literature reference coatings. The filler content in the coating adversely affects the adhesion strength of the coating with the substrate, favoring premature fracture of the joint. As proposed by Kahraman et al. [21], this behavior can be explained considering that high filler content favors high stress level at the adhesive-metal substrate interface.

Analyzing fracture surface a progressive transition from cohesive to adhesive fracture mechanism can be observed from SZ-70 to SZ-90 samples. Increasing the content of zeolite, the adhesive resistance of the composite layer decreases. For ZEO90 samples (Figure 1) inter-laminar crack starts and progressively evolves in the complete debonding areas at the layers interface. In this case, the energy necessary to start the crack within the coating is higher than at the layers interface, consequently the sample evidenced an adhesive failure mechanism.

Table 1: Pull-off strength and drop weight damage energy for SZ composite coatings at varying zeolite content. Comparison with literature composite coatings ([9], [20])

	<i>SZ Coating</i>			<i>Reference Composite coatings</i>			
	<i>SZ-70</i>	<i>SZ-80</i>	<i>SZ-90</i>	<i>ZS3-80 [20]</i>	<i>ZS2S3-80 [20]</i>	<i>ZS8-80 [20]</i>	<i>MPI [9]</i>
Pull-off strength [MPa]	1.30	1.09	0.89	1.12	1.41	1.35	0.85
Damage energy [mJ]	335	318	297	225	270	222	220

At lower content of zeolite the failure mechanism is related with the combination of crack formation and propagation within the coating bulk or at the polymer layer interface. Locally, the failure propagation occurs within the coating indicating that the strength of adhesion to the metal substrate surface is stronger than the strength in the coating bulk. The metal surface can promote both physical and chemical bond and consequently the necessary energy to induce a crack at the coating/adherent substrate is higher than the adhesive bulk; then the failure could occur by a cohesive mode.



**SZ-90**

Figure 1: Pull-off failure surface for SZ-90 coating

Further information can be argued analyzing drop-weight impact damage energy results. Concerning reference literature results good impact performances were observed for ZS2S3 samples. With regard to SZ coatings, further discussion is required in order to better interpret the results. Such coatings evidenced a significant impact performance improvement. The damaged area is always lower than other coating formulations. This behavior can be ascribed to the intrinsically elasto-plastic mechanical behavior of the polymer structure used as matrix. This implies that at low energy levels all impact energy is absorbed by surface deformation without giving fracture or indentation phenomena.

With the purpose to better clarify the impact behavior of the composite coatings, the damaged area at increasing impact energy for SZ-80 coating compared to literature reference was plotted in Figure 2. The damage diameter increased by increasing impact energy. For reference samples for impact energy under 40 mJ no damage effects on the coated surfaces were observed. For SZ-80 sample a threshold impact energy at about 150mJ can be identified. However, only above 200mJ impact energy there is a clear local surface damage due to the drop weight impact (damaged area about 0.85 mm<sup>2</sup>).

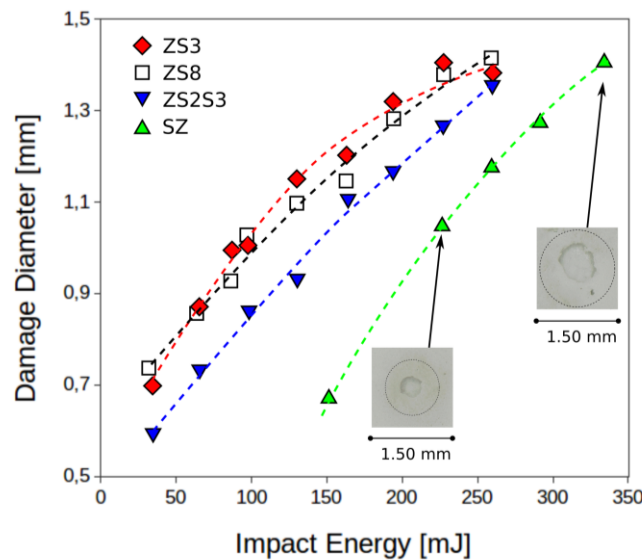


Figure 2: Damage diameter at increasing impact energy for the composite coatings

As the impact energy increases, however, there is a progressive increase in the damaged area dimension which anyway remains relatively low. This behavior is related to the improved mechanical properties under impulsive stress of the SZ composite coatings formulation, which involves a localized wrinkling phenomenon in the contact area between the coating and the drop-weight tool. This deformation state localizes the damage only in the impact region without causing the formation of delamination cracks, which are usually found in the thick coatings with brittle behavior.

#### *Adsorption properties*

Figure 3 shows the adsorption isobar at  $P_{H_2O}=11$  mbar in the temperature range 23-150°C for all coating formulations. For comparison purpose, the isobar measured for the pure SAPO-34 powder at the same water vapor pressure level was presented. The water pressure of 11 mbar was specifically selected as it corresponds to evaporation temperature  $T_{ev}$  of 7 °C, which represents the typical temperature level for adsorption chiller application, to provide cooling effect. Water uptake curves are characterized by the typical S-shape adsorption trend.

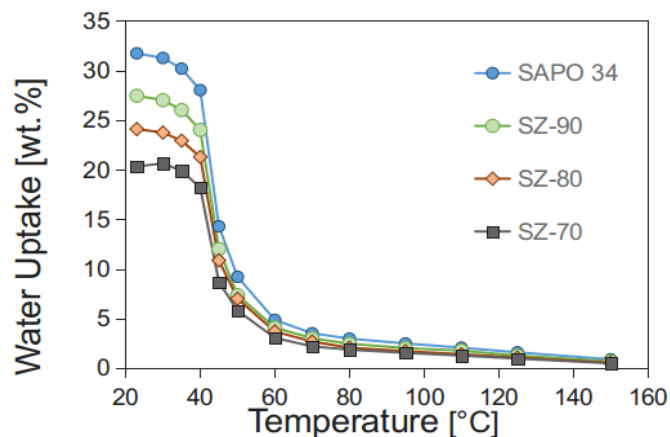


Figure 3: Water adsorption isobars at 11 mbar for zeolite composite coatings and pure zeolite powder (SAPO-34)

An abrupt increase of water uptake can be observed, at about 45°C, according with the typical SAPO-34 silico-alumino-phosphates behavior. Equilibrium isobars have been measured also in



desorption mode (not reported here), increasing the temperature from room temperature up to 150°C, without evidence of significant hysteresis phenomenon. This aspect is relevant for adsorption cycles energy performances. Adsorption capacity of the zeolite coating is lower than pure SAPO-34 powder. The adsorption behavior is consistent with the consideration that the filled zeolite coatings are characterized by specific amount of adsorbent material (different quantities of SAPO-34 filler into the composite coating) and complementary content of inert polymer matrix, which acts as binder between zeolite grains. However, the maximum adsorption value for the composite coating was observed for SZ-90 batch, where a water uptake above 27.4 wt.% is reached. Considering that the SAPO-34 evidenced a maximum water adsorption of 31.7 wt.%, this confirms that almost all the zeolite filler loaded inside the composite coating has an active action on the adsorption performances of the coating. This is a further validation of the permeability of the composite coating structure towards the water vapor flux. The presence of polymer matrix does not influence the adsorption capacity of the SAPO-34 filler. Indeed, for instance, for all composite coating about 95% of the zeolite loaded in the coating is actively able to participate to sorption and desorption process. An important aspect that will be investigated in future activities is to evaluate the performance stability in operating conditions. Durability of the composite coatings is an important issue in order to evaluate its potential applicability in AHP applications. Although, these preliminary results indicate that these composite adsorbent coatings could have good prospects in the optimization process of adsorbent beds for heat pump system.

### Summary/Conclusions

The advantages related to the use of coating technologies are:

- possibility of easily coat complex heat exchanger geometries with an adsorbent layer, maintaining a uniform thickness,
- tunable coating thickness changing the formulation parameters, typically between 0.1-0.5 mm,
- reduction of heat and mass transfer resistances, thanks to the good contact between adsorbent layer and heat exchanger surface and to the low adsorbent thickness

The new composite coating characteristic by hybrid polymer binder evidenced promising results concerning mechanical (especially when subjected to an impulsive stress) and adsorption performances thus indicating as potential alternative of conventional adsorbent materials and coatings.

### References:

- [1] Girkov IS, Aristov YI, "Making adsorptive chillers more fast and efficient: The effect of bi-dispersed adsorbent bed", *Applied Thermal Engineering* 2016,106:254–256, doi:10.1016/j.applthermaleng.2016.06.016
- [2] Freni A, Bonaccorsi L, Calabrese L, Caprì A, Frazzica A, Sapienza A, "SAPO-34 coated adsorbent heat exchanger for adsorption chillers", *Applied Thermal Engineering* 2015,82:1–7, doi:10.1016/j.applthermaleng.2015.02.052
- [3] Bendix P, Földner G, Möllers M, et al., "Optimization of power density and metal-to-adsorbent weight ratio in coated adsorbent for adsorptive heat transformation applications", *Applied Thermal Engineering* 2017,124:83–90, doi:10.1016/j.applthermaleng.2017.05.165
- [4] Fedosov DA, Smirnov A V., Knyazeva EE, Ivanova II, "Zeolite membranes: Synthesis, properties, and application", *Petroleum Chemistry* 2011,51:657–667, doi:10.1134/S0965544111080032
- [5] Aristov YI, "Challenging offers of material science for adsorption heat transformation: A review", *Applied Thermal Engineering* 2013,50:1610–1618, doi:10.1016/j.applthermaleng.2011.09.003

- [6] Bonaccorsi L, Calabrese L, Freni A, Proverbio E, Restuccia G, "Zeolites direct synthesis on heat exchangers for adsorption heat pumps", *Applied Thermal Engineering* 2013,50:1590–1595, doi:10.1016/j.applthermaleng.2011.10.028
- [7] Bauer J, Herrmann R, Mittelbach W, Schwieger W, "Zeolite/aluminum composite adsorbents for application in adsorption refrigeration", *International Journal of Energy Research* 2009,33:1233–1249, doi:10.1002/er.1611
- [8] Freni A, Bonaccorsi L, Calabrese L, Caprì A, Frazzica A, Sapienza A, "SAPO-34 coated adsorbent heat exchanger for adsorption chillers", *Applied Thermal Engineering* 2015,82:1–7, doi:10.1016/j.applthermaleng.2015.02.052
- [9] Freni A, Frazzica A, Dawoud B, Chmielewski S, Calabrese L, Bonaccorsi L, "Adsorbent coatings for heat pumping applications: Verification of hydrothermal and mechanical stabilities", *Applied Thermal Engineering* 2013,50:1658–1663, doi:10.1016/j.applthermaleng.2011.07.010
- [10] Dunne R, Taqvi SM, "Adsorption cooling using adsorbent coated surfaces", In: Elsevier Science (ed) *Proc. Int. Conf. Fundam. Adsorpt.* 1998. Amsterdam, pp 1101–1106
- [11] Freni A, Russo F, Vasta S, Tokarev M, Aristov YI, Restuccia G, "An advanced solid sorption chiller using SWS-1L", *Applied Thermal Engineering* 2007,27:2200–2204, doi:10.1016/j.applthermaleng.2005.07.023
- [12] Restuccia G, Freni A, Maggio G, "A zeolite-coated bed for air conditioning adsorption systems: Parametric study of heat and mass transfer by dynamic simulation", *Appl. Therm. Eng.* 2002. pp 619–630, doi:10.1016/S1359-4311(01)00114-4
- [13] Okamoto K, Teduka M, Nakano T, Kubokawa S, Kakiuchi H, "The Development of Aqsoa Water Vapor Adsorbent and Aqsoa Coated Heat Exchanger", *IMPRES Conf.* 2010. Research Publishing Services, pp 27–32
- [14] Calabrese L, Bonaccorsi L, Proverbio E, "Corrosion protection of aluminum 6061 in NaCl solution by silane–zeolite composite coatings", *Journal of Coatings Technology and Research* 2012,9:597–607, doi:10.1007/s11998-011-9391-5
- [15] Calabrese L, Bonaccorsi L, Caprì A, Proverbio E, "Adhesion aspects of hydrophobic silane zeolite coatings for corrosion protection of aluminium substrate", *Progress in Organic Coatings* 2014,77:1341–1350, doi:10.1016/j.porgcoat.2014.04.025
- [16] Dawoud B, "Water vapor adsorption kinetics on small and full scale zeolite coated adsorbents; A comparison", *Applied Thermal Engineering* 2013,50:1645–1651, doi:10.1016/j.applthermaleng.2011.07.013
- [17] Kawai T, Tsutsumi K, "Reactivity of silanol groups on zeolite surfaces", *Colloid and Polymer Science* 1998,276:992–998, doi:10.1007/s003960050338
- [18] Calabrese L, Bonaccorsi L, Caprì A, Proverbio E, "Electrochemical behavior of hydrophobic silane–zeolite coatings for corrosion protection of aluminum substrate", *Journal of Coatings Technology and Research* 2014,11:883–898, doi:10.1007/s11998-014-9597-4
- [19] Calabrese L, Bonaccorsi L, Caprì A, Proverbio E, "Enhancement of the hydrophobic and anti-corrosion properties of a composite zeolite coating on Al6061 substrate by modification of silane matrix", *Corrosion Engineering, Science and Technology* 2017,52:61–72, doi:10.1080/1478422X.2016.1209354
- [20] Calabrese L, Bonaccorsi L, Caprì A, Proverbio E, "Enhancement of the Mechanical Properties of a Zeolite Based Composite Coating on an Aluminum Substrate by Silane Matrix Modification", *Industrial and Engineering Chemistry Research* 2016,55:6952–6960, doi:10.1021/acs.iecr.6b00844
- [21] Kahraman R, Sunar M, Yilbas B, "Influence of adhesive thickness and filler content on the mechanical performance of aluminum single-lap joints bonded with aluminum powder filled epoxy adhesive", *Journal of Materials Processing Technology* 2008,205:183–189, doi:10.1016/j.jmatprotec.2007.11.121

# Effects of storage period on the performance of salt composite sorption thermal energy storage

M. Rouhani, W. Huttema, C. McCague, M. Khajepour and M. Bahrami\*

Laboratory for Alternative Energy Conversion (LAEC), School of Mechatronic Systems Engineering,  
Simon Fraser University, 250-13450 102 Avenue, Surrey, BC, Canada, V3T 0A3

\*Corresponding author: mbahrami@sfu.ca

## Abstract

Effects of storage duration, high-conductivity additives and non-condensable gases on the storage performance of salt composite sorption thermal energy storage are experimentally investigated. We observed that sorption hot storage is more suitable for short-term storage, since there is a 58% decrease in energy storage density (ESD) from 1.03 (no storage-time) to 0.43 MJ·kg<sup>-1</sup> (seasonal applications). The hot storage ESD is almost the same for silica gel-CaCl<sub>2</sub> and silica gel-CaCl<sub>2</sub>-graphite flake (1.04 MJ·kg<sup>-1</sup>), while the averaged specific discharge power of the composite with graphite flake is higher. A 25% decrease in the ESD of seasonal cold storage is observed, compared to the cyclic operation, when 1.7 kPa pressure build-up in condenser occurred. This indicates the importance of occasional degassing for long-term applications. For desorption temperature of 90 °C, proper heat insulation can increase the specific power up to 60 W·kg<sup>-1</sup>.

**Keywords:** sorption thermal energy storage, residual gas, storage period, salt composites, heat loss

## Introduction/Background

Thermal energy storage (TES) is essential for efficient use of intermittent renewables. Among TES systems, sorption thermal energy storage (sorp-TES) shows great potential for short- and long-term storage, because of high energy storage density (ESD) and negligible heat loss [1]. However, Schreiber et al. [2] showed that long-term storage dramatically decreased the ESD of a high-temperature (i.e. 250 °C) Zeolite-based hot storage sorp-TES. Composite sorbents, salts in porous matrix, provide the highest ESD [3], although salt composites are corrosive to most heat exchanger materials and corrosion reactions release non-condensable gasses, causing pressure build-up in the sorber bed and evaporator/condenser. Glaznev et al. [4] showed that presence of even small amount of residual gas can dramatically decrease the adsorption rate and the cooling power.

In this study, the effect of storage duration, from no storage to few minute-storage and seasonal application, is examined using a custom-built low-temperature driven sorp-TES with silica gel-CaCl<sub>2</sub> and silica gel-CaCl<sub>2</sub>-graphite flake. Similar to the study which is performed by Osterman et al. [5] for a paraffin latent thermal energy storage, steady-state heat loss of the sorber bed is assessed. Moreover, effects of residual gas build-up inside the sorber bed on ESD, for both cold and hot storage, are investigated. Moreover, the effects of adding high-conductive additives, graphite flake, to the salt composite on the ESD and discharge power are studied.

## Experimental study

Our custom-made closed sorption prototype is shown in Figure 1 and consists of: i) two sorber beds, fin-tube heat exchanger; ii) a condenser, shell-and-tube heat exchanger; and iii) an evaporator, custom-built capillary-assisted low-pressure evaporator. One of the sorber beds was filled with 1.302 kg silica gel-CaCl<sub>2</sub> (SG-CC: 55 wt% B150 silica gel, 30 wt% CaCl<sub>2</sub> and 15 wt% PVA), while the second one was filled with 1.513 kg silica gel-CaCl<sub>2</sub>-graphite flake (SG-CC-G: 42 wt% B150 silica gel, 23 wt% CaCl<sub>2</sub>, 20 wt% graphite flakes and 15 wt% PVA). Table 1 lists specifications of the sorbent composites with and without graphite flakes. Each bed was examined separately. Prior to the experiments, the entire sorption system was evacuated at 90 °C

for several hours to remove the residual gas. During the charging process, each sorber bed was heated by an external water loop and the desorbed water vapour was transferred to the condenser through a one-way valve. Any non-condensable gas in the sorber bed also flowed to the condenser. During the storage process, the sorber bed was isolated from the evaporator and condenser. To study the effect of storage duration on the performance, the sorp-TES was discharged in a cyclic mode (no storage time), and afterwards, for various storage durations. In cyclic operation (considered as a baseline test), periodically a quick degassing (few seconds) was performed between the half-cycles, to maintain a constant condenser pressure. For other storage durations, the degassing was not performed, to study the effect of the presence of residual (non-condensable) gases on the storage performance. For seasonal application, the system was turned off and reached the ambient temperature, which took 1 day for this testbed. In the discharging process, the valve between the evaporator and the sorber bed was opened and water vapour went to the sorber bed, at a lower pressure than that of the evaporator. For cold storage, the cooling energy provided by evaporator and for hot storage the heat (adsorption and sensible) produced in sorber bed were used.

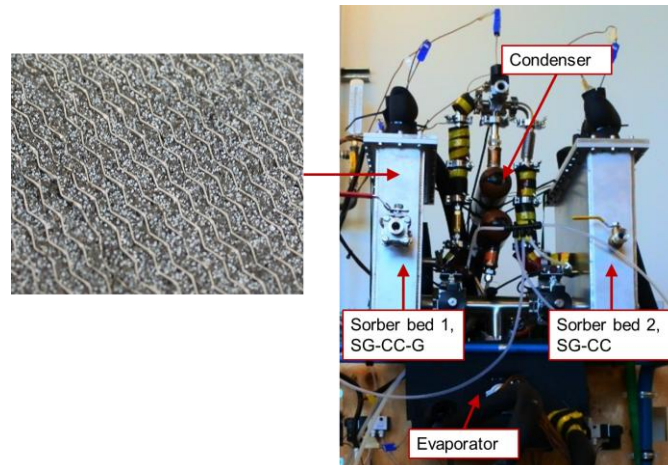


Figure 1. Sorption thermal energy storage prototype, including: i) 2 sorber beds, ii) condenser, and iii) evaporator.

Table 1. Specification of the sorbent composite of the sorption samples: Silica gel + CaCl<sub>2</sub> + graphite flakes (20%) and Silica gel + CaCl<sub>2</sub>.

	<b>Silica gel + CaCl<sub>2</sub> + graphite flakes (20%)</b>	<b>Silica gel + CaCl<sub>2</sub></b>
<b>Composition</b>	42% B150 silica gel 23% CaCl <sub>2</sub> 15% PVA 20% graphite flakes	55% B150 silica gel 30% CaCl <sub>2</sub> 15% PVA
<b>m<sub>ads</sub> (kg)</b>	1.513	1.302
<b>k<sub>ads</sub> (W·m<sup>-1</sup>·K<sup>-1</sup>)</b>	0.231 +/- 0.006	0.098 +/- 0.002
<b>c<sub>p,ads</sub> (MJ·m<sup>-3</sup>·K<sup>-1</sup>)</b>	0.45 +/- 0.03	0.42 +/- 0.06

## Discussion and Results

Inlet and outlet temperatures of the sorber bed heat transfer fluid and inlet and outlet temperatures of the evaporator chilled water are shown in Figure a and Figure b. As depicted in Figure 2, after five cyclic charging-discharging, storage times of 35, 70 and 105 min are considered. Figure 3a shows the ESD and specific discharge power of the SG-CC and SG-CC-G sorber beds, for cold and hot storages. As shown in Figure 3a, ESD of cold storage of SG-CC bed is higher than SGCC-G bed (0.57 compared to 0.39 MJ·kg<sup>-1</sup>), due to the more

active sorbent and more evaporation in the evaporator. ESD of hot storage for SG-CC-G (thermal conductivity of  $0.231 \pm 0.006 \text{ W}\cdot\text{m}^{-1}\cdot\text{K}^{-1}$ ) and SG-CC (thermal conductivity of  $0.098 \pm 0.002 \text{ W}\cdot\text{m}^{-1}\cdot\text{K}^{-1}$ ) are almost the same ( $1.04 \text{ MJ}\cdot\text{kg}^{-1}$ ). Similar to the cold storage ESD, the specific discharge power for cold storage is also higher for the SG-CC bed compared to SG-CC-G one. The discharge power for the first 10 min of discharge process for the hot storage is higher for the bed with graphite flake ( $1.30 \text{ kW}\cdot\text{kg}^{-1}$ ) compared to the bed without graphite flake ( $1.25 \text{ kW}\cdot\text{kg}^{-1}$ ), because of the higher thermal diffusivity of graphite flake, which expedites the discharging process and makes it more suitable for fast-heat delivery applications. However, the overall specific discharge power, similar to the ESD, is slightly higher for the SG-CC bed ( $487 \text{ W}\cdot\text{kg}^{-1}$ ) compared to the SG-CC-G bed ( $476 \text{ W}\cdot\text{kg}^{-1}$ ). Figure 3b shows the effect of storage duration on the cold and hot storage ESD. Cold ESD slightly decreases from the cyclic mode to a few minutes of storage and seasonal application. Sorp-TES systems are known for having no cold energy loss [6] and this drop in the cold ESD is due to the pressure build-up inside the condenser, as a result of existence of non-condensable gases by the corrosion reactions in the salt composite sorber bed. The residual gases add to the mass transfer resistance inside the sorber bed and, other than using corrosion-resistant materials and corrosion-protection layer, as stated in ref. [7], occasional degassing is necessary for long-term use of a closed sorption system, due to the residual gases and leakage. As shown in Figure 3b, the pressure difference between the sorber bed and the condenser is decreased during the time, falling by 38 Pa from the cyclic mode to seasonal mode, which causes a 25% decrease in the cold ESD. A significant decrease is observed in the hot ESD from the cyclic operation mode ( $1.03 \text{ MJ}\cdot\text{kg}^{-1}$ ) to seasonal application ( $0.43 \text{ MJ}\cdot\text{kg}^{-1}$ ), due to the (non-condensable gases) pressure increase in the condenser and sensible heat loss in the sorber bed. The latter highlighted that, for hot storage, the sorp-TES systems are suitable for short-term storage rather than seasonal applications, where a part of the input sensible heat can be discharged as well.

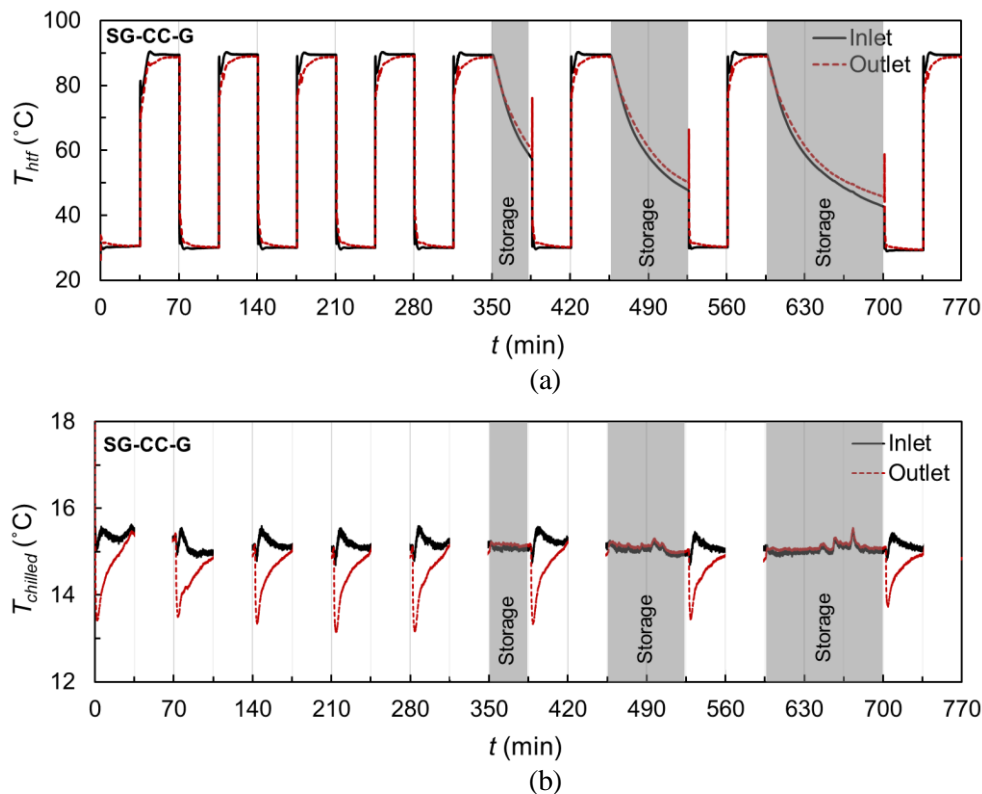


Figure 2. (a) Temperature of heat transfer fluid of the sorber bed with Silica gel +  $\text{CaCl}_2$  + graphite flake versus time and (b) temperature of evaporator chilled water versus time.

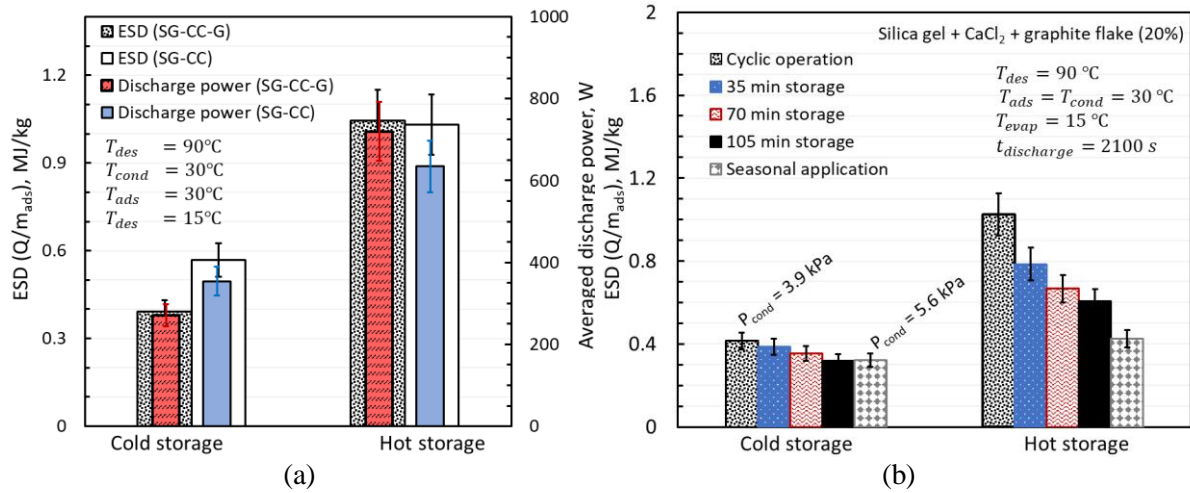


Figure 3. (a) Effect of high-conductive additives on ESD and discharge power and (b) effects of storage duration and residual gas on ESD.

Moreover, the steady-state heat loss during the charging process is studied here. After the sorber bed is fully desorbed, it is isolated from the evaporator/condenser and vacuumed by a vacuum pump. Afterwards, the sorber bed is heated up in three steps to the desorption temperatures of 70, 80 and 90 °C. As shown in Figure 4a, for each step, the heating at constant heat source temperature is continued to achieve a steady-state condition (i.e.  $\Delta T_{htf}$  is constant). Under steady-state condition, thermal losses can be determined from the steady-state constant temperature difference of the heat transfer fluid, using the following equation:

$$\frac{dQ}{dt} = \dot{m}_{htf} c_{p,htf} (T_{out,htf} - T_{in,htf}) + (UA)_{loss} (T_{casing} - T_{sorbent}) = 0 \quad (1)$$

where  $Q$ ,  $\dot{m}_{htf}$ ,  $c_{p,htf}$ ,  $T_{in,htf}$ ,  $T_{out,htf}$ ,  $(UA)_{loss}$ ,  $T_{casing}$  and  $T_{sorbent}$  are the total heat transfer rate, mass flowrate, specific heat capacity, inlet and outlet temperatures of the heat transfer fluid, overall heat transfer coefficient of heat loss, outside temperature of casing and the sorbent temperature inside the sorber bed, respectively. Figure 4b shows the heat transfer coefficient of thermal loss between the sorber bed and the casing outside temperature. The averaged  $UA_{loss}$  is  $1.79\text{ W}\cdot\text{K}^{-1}$ , which can, in part, as a result of not insulating the sorber casing. As shown in Figure 4c, the specific heat loss power shows a linear trend versus the desorption temperature. At desorption temperature of 90 °C, using proper thermal insulation, can add up to  $60\text{ W}\cdot\text{kg}^{-1}$  to the specific power of the storage system. The obtained heat loss as a function of desorption temperature, should be fed to the sorp-TES models for more accurate of the storage system.

## Conclusions

An experimental study was conducted to investigate the effects of storage time, noncondensable gases, high-conductivity additives and steady-state heat loss on the overall performance of a salt composite sorption thermal energy storage system (sorp-TES). For hot storage, the sorp-TES was preferable for short-term storage, due to a 58% decrease in ESD, from 1.03 (no storage-time) to  $0.43\text{ MJ}\cdot\text{kg}^{-1}$  (seasonal applications). There was no significant difference between the hot storage ESD of the silica gel- $\text{CaCl}_2$  and silica gel- $\text{CaCl}_2$ -graphite flakes. However, the averaged specific discharge power of the graphite flake composite, for the first 10 min of discharge process, was higher ( $1.30\text{ kW}\cdot\text{kg}^{-1}$  compared to  $1.25\text{ kW}\cdot\text{kg}^{-1}$ ). The measured ESD of seasonal cold storage was 25% less than that of the cyclic operation when a 1.7 kPa pressure built-up in the condenser due to the corrosion reactions with the heat exchangers, which indicated the importance of using of corrosion-protective layers as well as occasional degassing for long-term applications. Study of steady-state heat loss between the

inside of the sorber bed and the outside of the casing in the charging process showed that the averaged heat loss coefficient was  $1.79 \text{ W}\cdot\text{K}^{-1}$ . Specific power, at desorption temperature of  $90 \text{ }^\circ\text{C}$ , could be increased up to  $60 \text{ W}\cdot\text{kg}^{-1}$  with using proper thermal insulation.

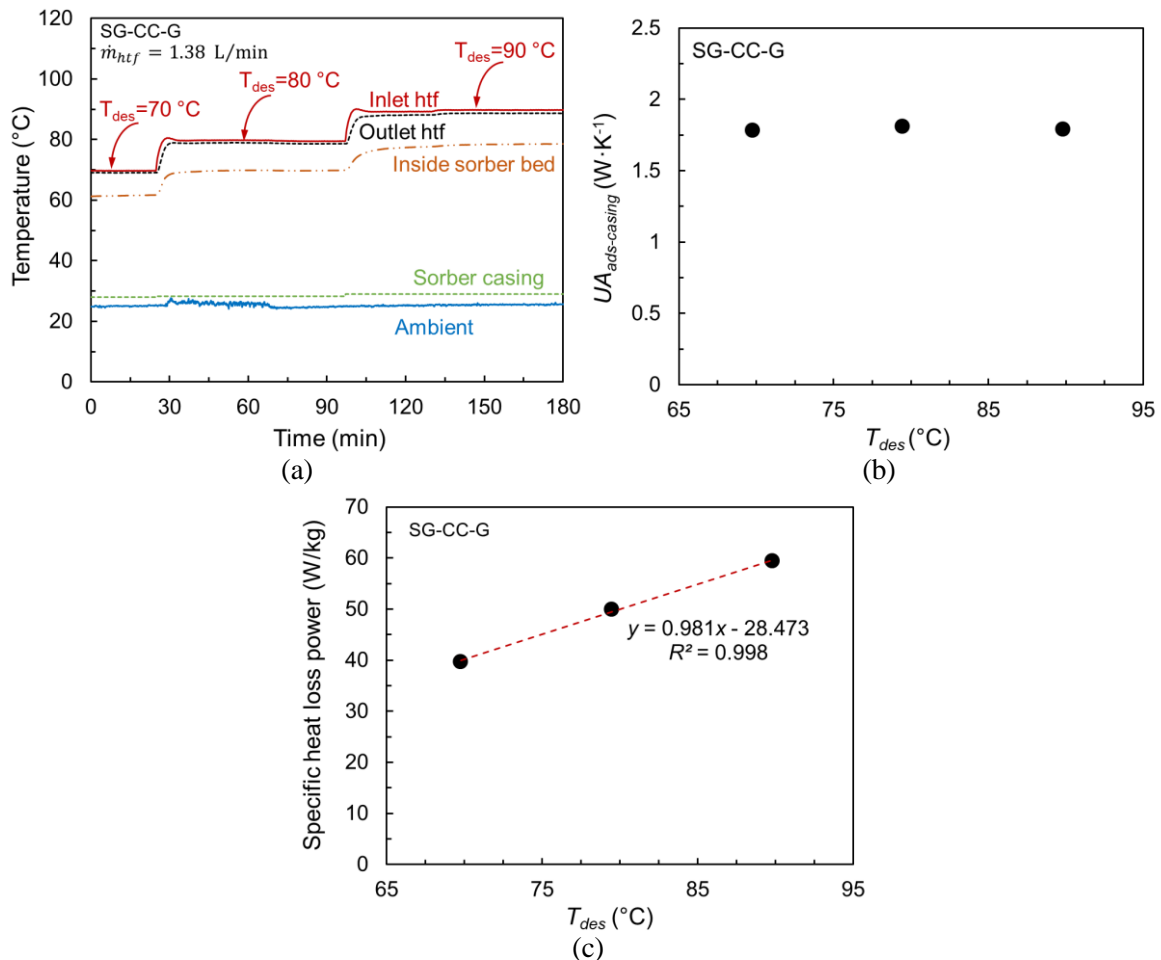


Figure 4. (a) Temperature versus time for inlet and outlet of heat transfer fluid, inside the sorber bed, sorber casing and ambient, (b) heat loss coefficient  $UA_{ads-casing}$  from the adsorber bed to the outside of the sorber bed casing versus desorption temperature and (c) specific heat loss power versus desorption temperature.

### Acknowledgements

The authors gratefully acknowledge the financial support of the Natural Sciences and Engineering Research Council of Canada (NSERC) through the Automotive Partnership Canada Grant No. APCPJ 401826-10.

### References:

- [1] L. F. Cabeza, *Advances in Thermal Energy Storage Systems: Methods and Applications*. Woodhead Publishing, 2014.
- [2] H. Schreiber, F. Lanzerath, C. Reinert, C. Grüntgens, and A. Bardow, "Heat lost or stored: Experimental analysis of adsorption thermal energy storage," *Appl. Therm. Eng.*, vol. 106, pp. 981–991, 2016.
- [3] Y. I. Aristov, "Current progress in adsorption technologies for low-energy buildings," *Futur. Cities Environ.*, vol. 1, no. 1, p. 10, 2015.
- [4] I. Glaznev, D. Ovoshchnikov, and Y. I. Aristov, "Effect of residual gas on water adsorption dynamics under typical conditions of an adsorption chiller," *Heat Transf.*

- Eng.*, vol. 31, no. 11, pp. 924–930, 2010.
- [5] E. Osterman, K. Hagel, C. Rathgeber, V. Butala, and U. Stritih, “Parametrical analysis of latent heat and cold storage for heating and cooling of rooms,” *Appl. Therm. Eng.*, vol. 84, pp. 138–149, 2015.
- [6] X.-R. Zhang and I. Dincer, *Energy Solutions to Combat Global Warming*. 2017.
- [7] A. Sapienza, A. Frazzica, A. Freni, and Y. Aristov, “Dramatic effect of residual gas on dynamics of isobaric adsorption stage of an adsorptive chiller,” *Appl. Therm. Eng.*, vol. 96, pp. 385–390, 2016.



# Experimental investigation of a novel absorption heat pump with organic working pairs

P. Chatzitakis<sup>1\*</sup>, B. Dawoud<sup>2</sup>, J. Safarov<sup>3</sup> and F. Opferkuch<sup>1</sup>

<sup>1</sup>Technische Hochschule Nuernberg Georg Simon Ohm, Nuremberg Campus of Technology,  
Fuerther Str. 246b, 90429 Nuernberg, Germany

<sup>2</sup>Ostbayerische Technische Hochschule Regensburg, Laboratory of Sorption Processes,  
Faculty of Mechanical Engineering, Galgenberg Str. 30, 93053 Regensburg, Germany

<sup>3</sup>University of Rostock, Institute of Technical Thermodynamics,  
Albert-Einstein-Str. 2, 18059, Rostock, Germany

\*Corresponding author: paris.chatzitakis@th-nuernberg.de

## Abstract

As part of a systematic approach towards the search for alternative absorption heat pump (AHP) working pairs that could potentially provide comparable performance to conventional ones, a previous work performed a detailed theoretical cycle analysis and simulation that revealed concrete correlations between key working fluid thermophysical properties and AHP performance indicators [1]. Following this work, targeted combinations of two organic refrigerants, 2,2,2-trifluoroethanol (TFE) and 2,2,3,3,3-pentafluoropropanol (5FP) and two organic absorbents, 1,3-dimethyl-2-imidazolidinone (DMI) and 2-pyrrolidone (PYR) were tested in a prototype 5 kW AHP, based on the highly compact plate heat exchanger design, which has been introduced in [2]. The purpose of this effort was to validate the findings of the previous work, through correlations based on experimental measurements and at the same time to test the performance of the new AHP system design. The working pair combinations were also subjected to vapor liquid equilibrium (VLE) and viscosity measurements, in order to determine reliable activity coefficient and improve the accuracy of the simulations. The experimental performance results agree well with the simulations and show to be consistent with the conclusions derived from the previous theoretical work.

**Keywords:** absorption heat pump, coefficient of performance, organic working pairs, specific solution circulation

## Introduction/Background

Commercially available absorption systems have traditionally been dominated by ammonia/water and water/lithium bromide (LiBr) working pairs. Although very efficient systems in terms of thermodynamic performance, significant disadvantages or flaws have slowed their adoption and commercialization. More specifically, ammonia/water heat pumps present considerable hazards due to ammonia's toxicity, corrosiveness and high system pressure whereas water/LiBr systems are considered safer but also plagued by severe temperature limitations and even higher corrosion problems.

Alternative absorption heat pump working pairs have been extensively researched and reviewed by many researchers [3-12] with main focus on absorbent replacements, water in the case of ammonia, and LiBr in the case of water. They have worked on pinpointing the fundamental working pair criteria that influence thermodynamic efficiency in order to facilitate the identification of alternative working pairs. A smaller part of the studies concerns refrigerant replacement with organic substances like alcohols, amines and hydrocarbons. Nevertheless, despite all efforts there is still no recognized alternative working pair with the potential to exceed the impact of the two conventional pairs [13].

<b>Nomenclature</b>	
COP	Coefficient of performance
CR	Circulation ratio
$c_p$	Average mass specific heat capacity
$H_{x_{sdes}}$	Excess enthalpy of desorption
$M_i$	Molecular weight of component i
$\dot{m}_j$	Mass flow of stream j
p	Vapor pressure
SSC	Specific solution circulation
T	Temperature
$X_{i,j}$	Liquid molar fraction of component i in stream j
Greek letters	
$\gamma_{i,j}$	Activity coefficient of component i in stream j
$\zeta_{i,j}$	Vapor mass fraction of component i in stream j
$\xi_{i,j}$	Liquid mass fraction of component i in stream j
$\rho$	Mass density
Subscripts	
1	Component 1, refrigerant
2	Component 2, absorbent
abs	Absorber conditions
ce	Condenser-evaporator
cond.	average
cool	Cooling
con	Condenser conditions
des	Desorber conditions
desin	Desorber inlet conditions
eva	Evaporator conditions
HP	Heat pump
sol	Solution
v	Vaporization
x <sub>sdes</sub>	Excess desorption

The lack of success of these partially qualitative screening processes signified the need for an alternative quantitative approach. Our previous work focused towards improving the quantitative understanding of the multitude of parameters that influence the performance of absorption heat pumps chillers by developing correlations between the coefficient of performance (COP) and the specific solution circulation (SSC), and readily available basic substance properties, like molecular mass and critical point properties. The current work aims to validate those findings with experimental property and heat pump performance measurements amongst 4 candidate working pairs, as an initial comparison. More specifically, two refrigerants, 2,2,2-trifluoroethanol (TFE) and 2,2,3,3,3-pentafluoropropanol (5FP), were paired with two absorbents, 1,3-dimethyl-2-imidazolidinone (DMI) and 2-pyrrolidone (PYR), each with similar chemical structure but significant differences in key properties, like molecular weight, vaporization enthalpy and vapor pressure. As absorption heat pump working pair candidates, all are more or less well known to the scientific community [2, 14].

TFE and DMI are well-known and documented and were chosen as a basis for the development effort. All of them are organic compounds and can be considered to represent a middle ground between the traditional working pairs' pitfalls. Maximum pressures are well within the vacuum region, the operational heat pump temperature lift is comparable to ammonia and corrosion reactions are negligible for stainless steel and copper. A few drawbacks are, TFE's toxicity and flammability, TFE and DMI are classified as damaging fertility or the unborn child [15,16]. On the other hand, 5FP is significantly less toxic and PYR is classified only as an irritant [17,18].

5FP (>99 mass %) was supplied by Daikin Industries Ltd., TFE (>99.5 mass %) by Solvay GmbH, DMI (>99 mass %) by Mitsui Chemicals Inc. and PYR (>99.5 mass %) by BASF Corporation. The working pair VLE vapor pressures were measured using two high precision static method apparatuses, whereas the viscosity measurements were performed with a stress-controlled rheometer equipped with a cone-and-plate geometry, both at the University of

Rostock [19, 20]. Using the available VLE data, the working pairs' activity coefficients were regressed and modelled using the NRTL method and were applied within the simulation models developed in the previous work [1]. The simulation calculations were programmed and executed in Microsoft Excel's® Visual Basic for Applications (VBA) environment. The actual system performance was determined following the VDI 4650-2 standard [21] on a single effect AHP-prototype having a rated heating power of 5kW and based on the highly compact plate heat exchanger design, which has been introduced in [2]. A simplified sketch can be seen in Fig.1. The system comprises six heat exchangers, the evaporator, absorber, solution heat exchanger, desorber, condenser, exhaust heat exchanger, one rectification column, four pumps (the two not shown are recirculation pumps, for the evaporator and absorber) and two expansion valves

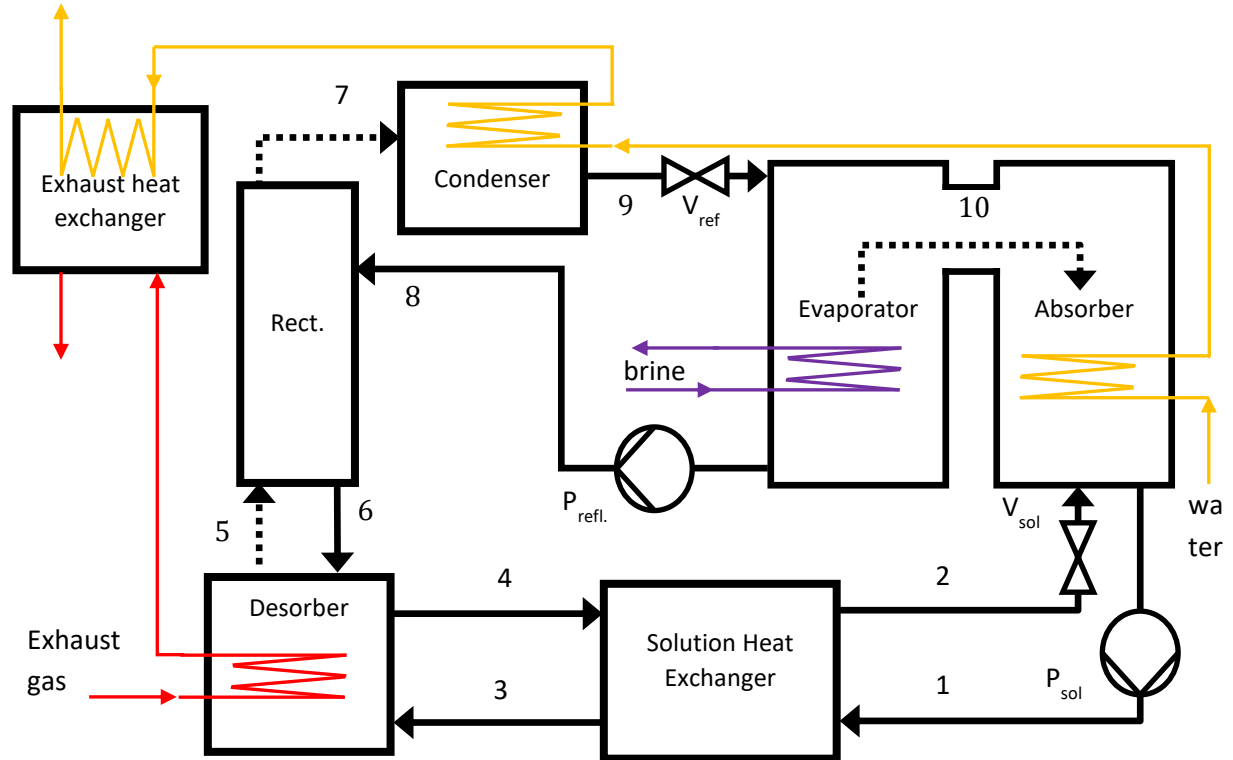


Figure 1: Absorption heat pump prototype main components.

The prototype was connected to a test stand able to satisfy variable heating and cooling loads, for the water and brine circuits respectively, and a broad temperature range.

## Results and discussion

The coefficient of performance (COP) general equation has been analyzed in the previous paper for an ideal system:

$$COP_{cool,ideal} = \frac{1 - \frac{c_{p,1,ce}}{H_{v,1,eva}}(T_{con} - T_{eva})}{CR \frac{(\xi_{1,3}c_{p,1,gen} + \xi_{2,3}c_{p,2,des})}{H_{v,1,eva}}(T_{des} - T_{desin}) + \frac{\xi_{1,5}\xi_{2,4}}{\xi_{1,5} - \xi_{1,4}} \frac{H_{v,1,des}}{H_{v,1,eva}} + \frac{\xi_{2,5}\xi_{2,4}}{\xi_{1,5} - \xi_{1,4}} \frac{H_{v,2,des}}{H_{v,1,eva}} + \frac{\xi_{2,4}}{\xi_{1,5} - \xi_{1,4}} \frac{H_{xsdes}}{H_{v,1,eva}}} \quad (1)$$

$$COP_{HP} = 1 + COP_{cool} \quad (2)$$

$$CR = \frac{\dot{m}_1}{\dot{m}_{10}} = \frac{1 - \xi_{14}}{\xi_{1,1} - \xi_{1,4}} = \frac{1 - X_{1,4}}{X_{1,1} - X_{1,4}} \left( X_{1,1} + X_{2,1} \frac{M_2}{M_1} \right) \quad (3)$$

Where

$$X_{1,1} \approx \frac{p_{1,eva}}{p_{1,abs} \gamma_{1,1}} \quad (4)$$

$$X_{2,1} = 1 - X_{1,1} \quad (5)$$

are the refrigerant and the absorbent rich solution molar fractions, respectively.

$$X_{1,4} \approx \frac{p_{1,con}}{p_{1,des} \gamma_{1,4}} \quad (6)$$

is the refrigerant poor solution molar fraction. Under equilibrium conditions, refrigerant concentrations are determined by the refrigerant vapor pressure ratios between the evaporator and absorber, for the rich solution, and between the desorber and condenser for the poor solution. This signifies that the CR is correlated to temperature differences between absorber-evaporator and desorber-condenser.

However, the prototype in question is a real system with components of finite size, rendering certain assumptions invalid. Eq. 7 below is a slightly modified relation, making accommodations for a realistic rectification column.

$$COP_{cool,real} = \frac{1 - \frac{\xi_{2,8}}{\zeta_{1,7} - \xi_{1,8}} \frac{c_{p,1,ce}}{H_{v,1,eva}} (T_{con} - T_{eva})}{CR \frac{(\xi_{1,3} c_{p,1,gen} + \xi_{2,3} c_{p,2,des}) (T_{des} - T_{desin})}{H_{v,1,eva}} + \frac{\zeta_{1,5} \xi_{2,6}}{\zeta_{1,5} - \xi_{1,6}} \frac{H_{v,1,des}}{H_{v,1,eva}} + \frac{\zeta_{2,5} \xi_{2,6}}{\zeta_{1,5} - \xi_{1,6}} \frac{H_{v,2,des}}{H_{v,1,eva}} + \frac{\xi_{2,6}}{\zeta_{1,5} - \xi_{1,6}} \frac{H_{xsdes}}{H_{v,1,eva}}} \quad (7)$$

In both cases, a correlation between the  $COP_{HP}$  and the heat pump temperature lift,  $T_{con} - T_{eva}$ , can be established from the equations above. Heat pump temperature lift is hereby defined as the temperature difference between the condenser and the evaporator.

The specific solution circulation (SSC) has also been modeled in the same paper, correlating with the circulation ratio (CR).

$$SSC_{ideal} = \frac{CR}{\left( \rho_{sol,abs} \left( H_{v,1,eva} - c_{p,1,ce} (T_{con} - T_{eva}) \right) \right)} \quad (8)$$

$$SSC_{real} = \frac{CR}{\left( \rho_{sol,abs} \left( H_{v,1,eva} - \frac{\xi_{2,8}}{\zeta_{1,7} - \xi_{1,8}} c_{p1,ce} (T_{con} - T_{eva}) \right) \right)} \quad (9)$$

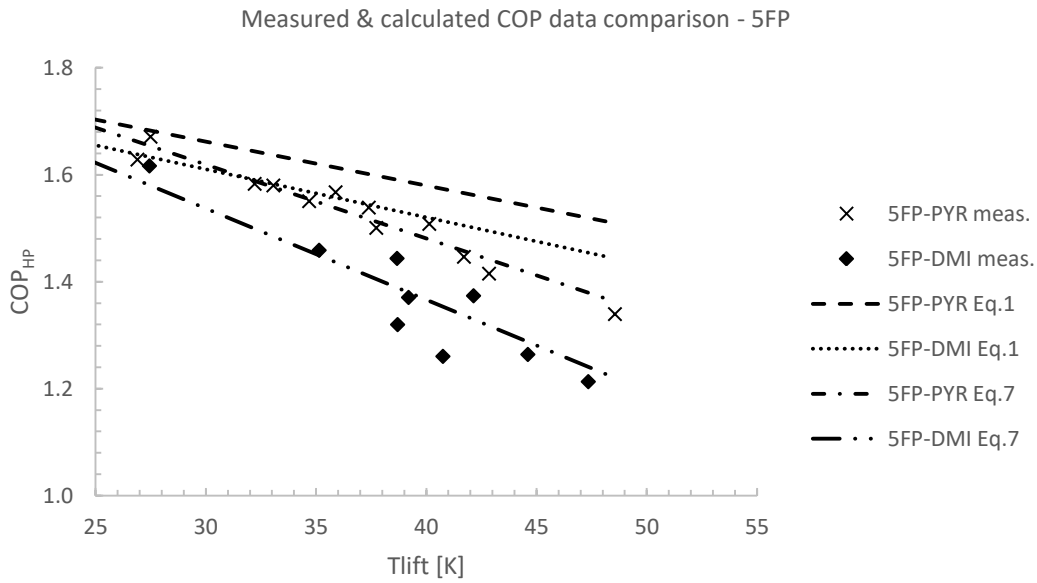


Figure 2: Comparison between measured 5FP COP data and calculation results from Eq.1 and Eq.7

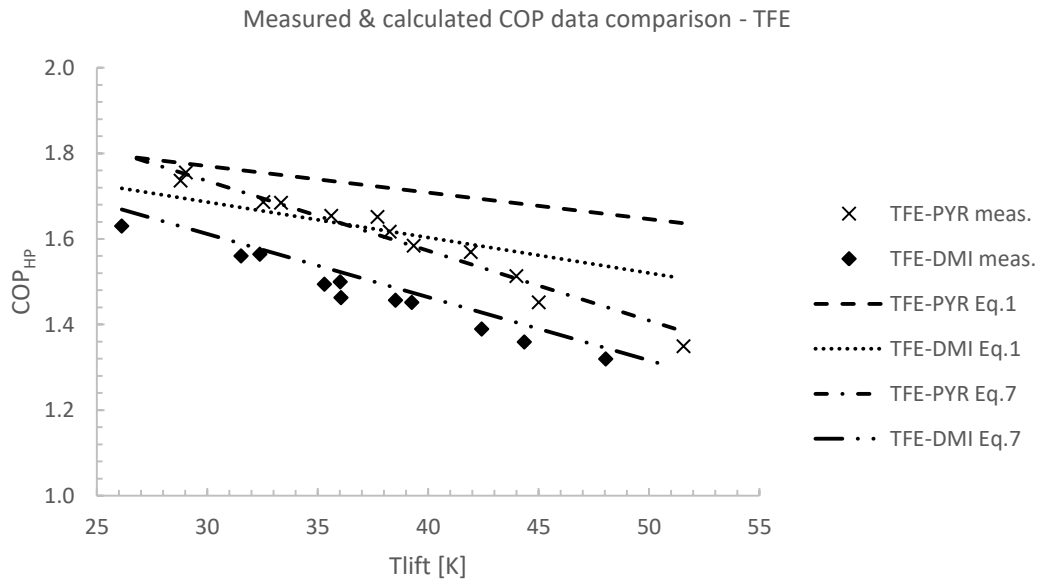


Figure 3: Comparison between measured TFE COP data and calculation results from Eq.1 and Eq.7

As with the COP, Eq. 9 provides the SSC of a real machine. The SSC is also directly correlated to the heat pump temperature lift.

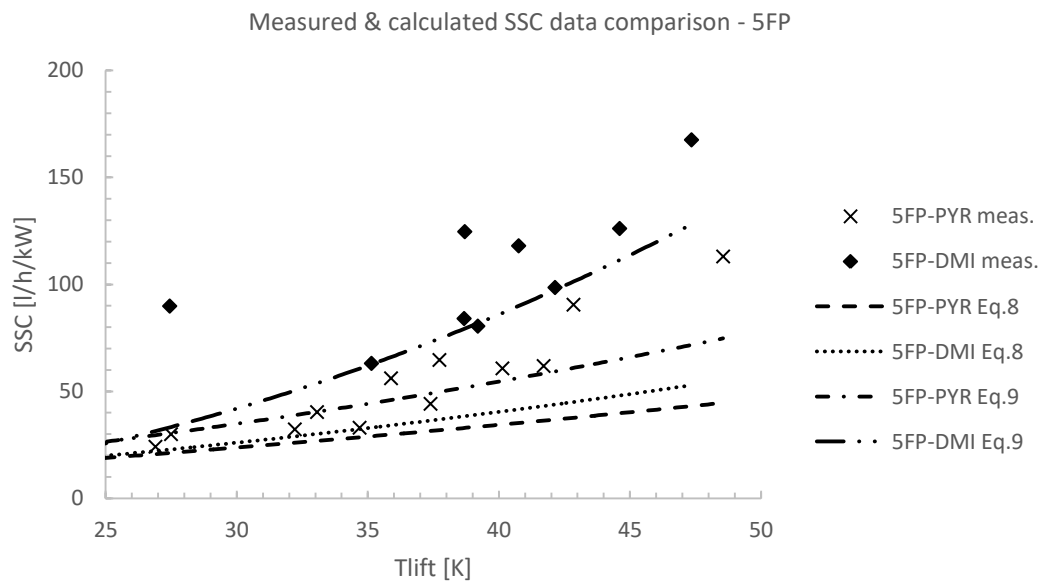


Figure 4: Comparison between measured 5FP SSC data and calculation results from Eq.8 and Eq.9

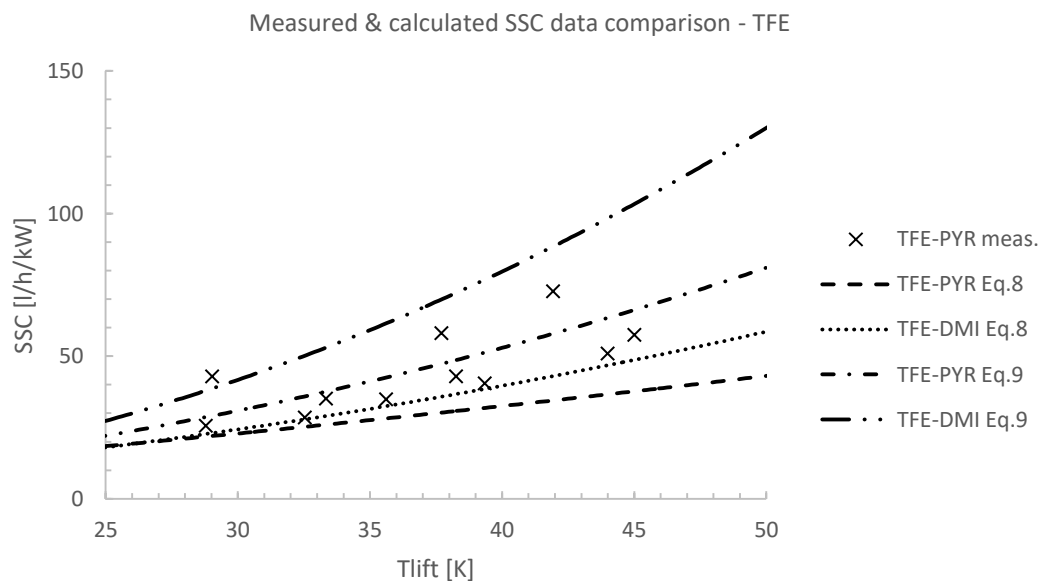


Figure 5: Comparison between measured TFE SSC data and calculation results from Eq.8 and Eq.9

Unfortunately, due to a volume flow sensor malfunction, the relevant data for the TFE-DMI measurements were not available.

### Summary/Conclusions

The experimental AHP performance measurements show that 2-Pyrrolidone performs significantly better in terms of both COP and SSC. The data also support the direct

correlations with the temperature lift. The ideal system calculations, based on Eqs. 1 and 8, are tendentially correct but show significant deviations at higher temperature lifts, where rectification losses play a dominant role. The modified equations (7 & 9) however, accounting for the rectification losses, provide results much closer to the experimental measurements.

Even though 2-Pyrrolidone in general exhibits higher activity coefficients and viscosity with the two refrigerants than DMI, the combination of lower molecular weight and relative volatility overcompensates and results in higher COPs and lower SSCs. Trifluoroethanol, without surprise, shows superior performance compared to 5FP, mainly due to its higher vaporization enthalpy values.

### Acknowledgements

Part of this work was sponsored by the European Union's "European Regional Development Fund".

### References

- [1] Chatzitakis, P., Dawoud, B., "An alternative approach towards absorption heat pump working pair screening", *Renewable Energy*, 2017, [doi.org/10.1016/j.renene.2016.08.014](https://doi.org/10.1016/j.renene.2016.08.014).
- [2] Ishikawa, M., Kayanuma, H., Isshiki, N., "Absorption heat pump using new organic working fluids", *Proceedings of the International Sorption Heat Pump Conference*, 1999.
- [3] Donellan, P., Cronin, K., Byrne, E., Recycling waste heat energy using vapour absorption heat transformers: a review, *Renewable and Sustainable Energy Reviews*, 2015, [doi.org/10.1016/j.rser.2014.11.002](https://doi.org/10.1016/j.rser.2014.11.002).
- [4] Shrikirin, P., Aphornratana, S., Chungpaibulpatana, S., A review of absorption refrigeration technologies, *Renewable and Sustainable Energy Reviews*, 2001, [doi.org/10.1016/S1364-0321\(01\)00003-X](https://doi.org/10.1016/S1364-0321(01)00003-X).
- [5] Sun, J., Fu, L., Zhang, S., A review of working fluids of absorption cycles, *Renewable and Sustainable Energy Reviews*, 2012, [doi.org/10.1016/j.rser.2012.01.011](https://doi.org/10.1016/j.rser.2012.01.011).
- [6] Alefeld, G., Radermacher, R., Hwang, Y., *Heat Conversion Systems*, CRC Press, 1994.
- [7] Eisa, M. A., Holland, F. A., A study of the optimum interaction between the working fluid and the absorbent in absorption heat pump systems, *Heat Recovery Systems*, 1987, [doi.org/10.1016/0890-4332\(87\)90075-5](https://doi.org/10.1016/0890-4332(87)90075-5).
- [8] Hodgett, D. L., "Absorption heat pumps and working pair developments in Europe since 1974", *Proceedings of New Working Pairs for Absorption Processes Workshop*, 1982.
- [9] Iedema, P.D., Mixtures for the absorption heat pump, *International Journal of Refrigeration*, 1982, [doi.org/10.1016/0140-7007\(82\)90065-2](https://doi.org/10.1016/0140-7007(82)90065-2).
- [10] Narodoslowsky, M., Otter, G., Moser, F., Thermodynamic criteria for optimal absorption heat pump media, *Heat Recovery Systems & CHP*, 1988, [doi.org/10.1016/0890-4332\(88\)90058-0](https://doi.org/10.1016/0890-4332(88)90058-0).
- [11] Nowaczyk, U., *Kriterien zur Auswahl von Arbeitsstoffgemischen für Absorptionsprozesse und Erste Auswahlmessungen*, DKV, 1991.
- [12] Perez-Blanco, H., Absorption heat pump performance for different types of solutions, *International Journal of Refrigeration*, 1984, [doi.org/10.1016/0140-7007\(84\)90024-0](https://doi.org/10.1016/0140-7007(84)90024-0).
- [13] Herold, K.E., Radermacher, R., Klein, S.A., *Absorption Chillers and Heat Pumps*, 2<sup>nd</sup> Ed., CRC Press, 2016.
- [14] Yin, J., Shi, L., Zhu, M. S., Han, L. Z., Performance analysis of an absorption heat transformer with different working fluid combinations, *Applied Energy*, 2000, [doi.org/10.1016/S0306-2619\(00\)00024-6](https://doi.org/10.1016/S0306-2619(00)00024-6).
- [15] 2,2,2-trifluoroethanol registration dossier, European Chemicals Agency, 2018, <https://echa.europa.eu/registration-dossier/-/registered-dossier/13741/2/1>.

- [16] 1,3-dimethyl-2-imidazolidinone registration dossier, European Chemicals Agency, 2018, <https://echa.europa.eu/registration-dossier/-/registered-dossier/11777/2/1>.
- [17] 2,2,3,3,3-pentafluoropropanol registration dossier, European Chemicals Agency, 2018, <https://echa.europa.eu/information-on-chemicals/cl-inventory-database/-/discli/details/130567>.
- [18] 2-pyrrolidone registration dossier, European Chemicals Agency, 2018, <https://echa.europa.eu/registration-dossier/-/registered-dossier/14900/2/1>.
- [19] Safarov, J., Kul, I., Talibov, M.A., Shahverdiyev, A., Hassel, E. Vapor pressures and activity coefficients of methanol in binary mixtures with 1-Hexyl-3-methylimidazolium bis(trifluoromethylsulfonyl)imide, *Journal of Chemical and Engineering Data*, 2015, [doi.org/10.1021/je501033z](https://doi.org/10.1021/je501033z).
- [20] Safarov, J., Lesch, F., Suleymanli, K., Aliyev, A., Shahverdiyev, A., Hassel E., Abdulagatov, I., Viscosity, density, heat capacity, speed of sound and other derived properties of 1-butyl-3methylimidazolium tris(pentafluoroethyl) trifluorophosphate over a wide range of temperature and at atmospheric pressure, *Journal of Chemical Engineering Data*, 2017, [doi.org/10.1021/acs.jced.7b00618](https://doi.org/10.1021/acs.jced.7b00618).
- [21] VDI 4650 Part 2, *Simplified method for the calculation of the annual heating energy ratio and the annual gas utilisation efficiency of sorption heat pumps. Gas heat pumps for space heating and domestic hot water*, Beuth Verlag GmbH, 2013.



# Silica Gel microfibres by electrospinning for adsorption heat pumps.

A. Freni<sup>1</sup>, L. Calabrese<sup>2</sup>, A. Malara<sup>3</sup>, P. Frontera<sup>3</sup> and L. Bonaccorsi<sup>3\*</sup>

<sup>1</sup>Affiliation and full institutional address (10-pt. Times New Roman)

<sup>2</sup>Dipartimento di Ingegneria, Università di Messina, C.da Di Dio, I-98166 Messina

<sup>3</sup>DICEAM, Università Mediterranea, Loc. Feo di Vito, I-89060 Reggio Cal.

\*Corresponding author: lucio.bonaccorsi@unirc.it

## Abstract

Silica gel is one of the most used porous material in commercial water adsorption heat pumps and chillers for the inexpensive cost and large market availability. In most applications, silica gel is used as granules with limitation in heat transfer and material hydrothermal stability. In this work, preliminary results of a new hybrid material made of microfibres obtained by the electrospinning of silica gel/polymer solutions are presented. The microfibres coating shows high surface area, high permeability and thermal stability combined with mechanical stability. Measurements of water adsorption properties of silica gel microfibres show that the original porosity and water uptake capability of the adsorbing component is largely preserved.

**Keywords:** Water adsorption, Silica gel, Heat pumps, Microfibres.

## Introduction

Silica gel is one of the most used porous material in adsorption heat pumps and chillers for its low cost and large availability on the market [1-4]. Competing as adsorbent with more performing materials like zeolites, silica gel is particularly appropriate in all adsorption applications where a low regeneration temperature is available. Compared to crystalline zeolites, silica gel has an amorphous structure and lower hydrothermal stability, lower adsorption enthalpy, lower maximum water capacity. Although the mentioned disadvantages, the availability of silica gel in large quantities at reduced costs compensates for the worst performances in adsorption cycles and it makes this material the preferred choice in commercial heat pumps and chillers [5]. Silica gel is offered on the market in a variety of granules and powders and is normally used in granular form in adsorption systems, added as filler among fins of the heat exchanger of the adsorber bed [6]. This configuration, however, shows important restrictions due to the high heat transfer resistance at the granules/metal interface and the intrinsic limited hydrothermal stability of silica gel. During the years, several solutions have been proposed for the realization of improved zeolite adsorbers, for example by synthesizing the material directly on the heat exchanger surfaces or by the realization of advanced zeolite coatings [7], while a similar development for silica gel has not been carried out. In this study, we propose an innovative material for adsorption applications made of hybrid microfibres of silica gel obtained by the electrospinning technique. The prepared electrospun fibres have been characterized by TGA/DSC, SEM-EDX and measurements of water adsorption properties in a vacuum microbalance.

## Experimental

### Silica gel microfibres synthesis

Two different commercial silica gel powders have been used for the synthesis of microfibres by electrospinning. A silica gel powder of size 70-230 mesh (high purity grade, Sigma-Aldrich), labeled from now SGA, and a silica gel in granules 1-3 mm (EMD Millipore, high

purity grade, Sigma-Aldrich), from now SGB. Both silica gels were pre-treated before electrospinning: part of the SGA was passed through a 140 mesh sieve (SGAs) and the remaining was ground in a planetary mill (Planetary Mono Mill Pulverisette 6 Fritsch) and successively sieved at 140 mesh (SGAm), all SGB was ground and sieved at 140 mesh (SGBms).

The typical precursor solution used in the electrospinning process was prepared as follow. A 4.5 %wt solution of polyacrylonitrile precursor, PAN (mol wt 150,000 Sigma-Aldrich) in N,N-dimethylformamide solvent, DMF (99%, Sigma-Aldrich) was prepared and stirred for 1 h at room temperature. The silica gel powder was then mixed (80 %wt) with 20 %wt of PAN/DMF solution and stirred for 1 h at room temperature. The prepared silica gel/PAN/DMF solution was loaded in 10 ml syringe fitted with 1 mm steel needle and electrospun at a flow rate of 1.1 mL/h with an applied voltage of 13.5 kV (kdScientific Model 100, Electro-spinner 2.0, Linari Engineering s.r.l.).

### Microfibrs characterization

The silica gel fibres have been morphologically characterized by electron microscopy SEM (Phenom ProX). The thermal stability of samples was analysed by TGA-DSC measurements (STA 409 PC Netzsch) from 25 to 300 °C in nitrogen flow with a heating rate of 10 °C/min. The adsorption properties of microfibrs were measured in a vacuum microbalance (Surface Measurements Systems DVS Vacuum) at P = 11 mbar and temperature range 30 – 120 °C.

### Discussion and Results

The advantage to produce microfibrs by electrospinning is the relative easy achievement of a woven fabric of silica microfibrs that can be directly deposited on a metal surface or used as auto-supporting foil. In figure 1 is shown a schematic diagram of the electrospinning process, based on the application of a high-voltage electrical field between the syringe needle tip and a collector plate. The polymeric/silica gel solution is forced at a constant rate through the syringe needle by an infusion pump.

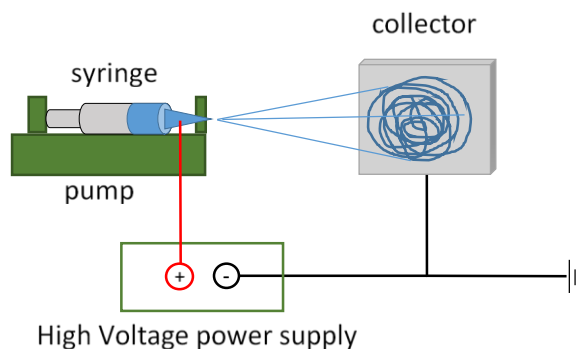


Figure 1. Schematic of a typical electrospinning setup.

The electrospinning process generated a fabric (figure 2) looking like a compact multilayer where silica gel particles are embedded in a polymeric network of microfibrs that keeps the whole granules interconnected, as shown in figure 3 for the three silica gel powders used. Comparing the SEM images of samples, it is evident the effect of the particle size of the silica gel powder added. In the SGAs sample (figure 3-a), the sieving was able to remove granules bigger than 100 µm, however, the granulometric distribution was shifted mainly to large particles that appeared only partially embedded in a matrix of polymeric fibres. The deposited multilayer coating was rather brittle. Because of the preliminary milling, fibres deposition of sample SGAm was improved, as shown in figure 3-b. The SGAm size distribution appeared

uniform and made of granules of sizes between 10 and 80  $\mu\text{m}$  with a consequent improved dispersion and better mechanical properties of the woven fabric. In sample SGBms, the preliminary grounding generated a powder with a wide size distribution and irregular shape particles so that the mixing with the polymeric precursor was more difficult and the final coating showed a low silica gel particles density (figure 3-c).



Figure 2. Fabric of silica gel microfibres deposited by electrospinning.

The SEM image of sample SGAMs at higher magnification, in figure 4, shows that the polymeric microfibres form a network trapping the larger silica gel particles with the smaller granules that are directly embedded in the PAN fibres. In such a configuration, it is evident how the polymeric phase is not allowed to hinder the vapor permeation due to the high porosity of the multilayer structured coating or to obstruct the silica gel mesoporosity.

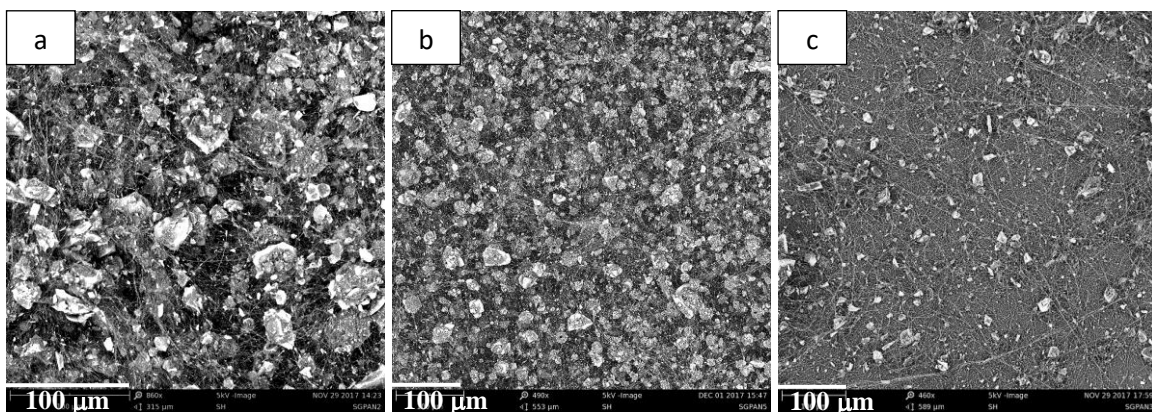


Figure 3. SEM images of SGAs (a), SGAMs (b), SGBms (c) microfiber coatings.

The behaviour on heating of the hybrid coatings has been evaluated by TGA-DSC analysis for a maximum temperature of 300  $^{\circ}\text{C}$ , considering this value satisfactory for most of applications. Silica gel, indeed, is typically used in adsorption cycles when regeneration temperatures are in the range of 120 – 180  $^{\circ}\text{C}$  [1,3].

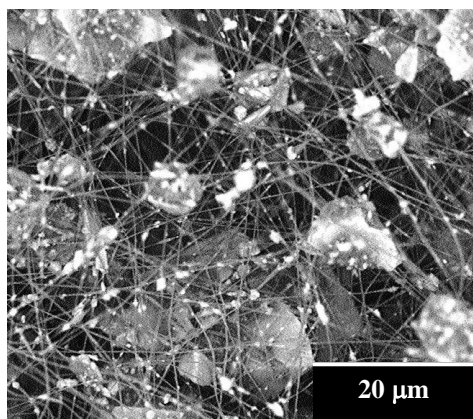


Figure 4. SEM magnification of the SGAMs coating.

In Figure 5, a comparison between TGA curves of pure SGAMs powder and SGAMs microfibres is shown. For pure silica gel the mass decrease was 10% while the total mass loss of the electrospun fibres was ~ 8%. The polymeric component of the SGAMs coating was stable even at 300 °C and the final mass loss due to water desorption, with a small difference compared to the pure adsorbent owing to PAN constituent weight.

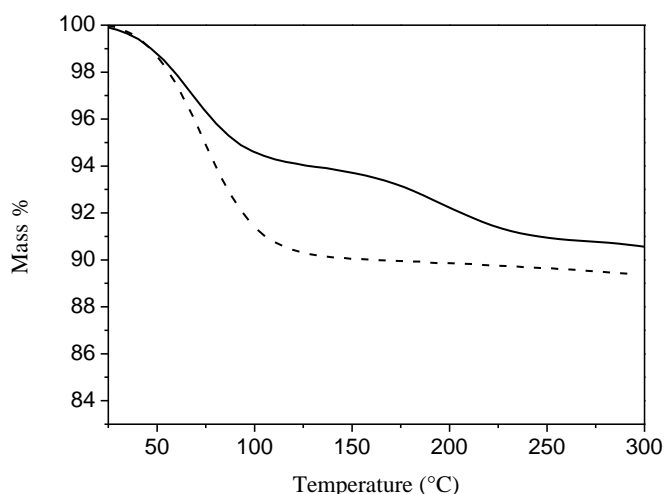


Figure 5. TGA of SGAMs powder (dashed line) and SGAMs microfibres (solid line).

The water adsorption properties of the electrospun fibres were measured at  $P = 11$  mbar, from room temperature to 120 °C. A comparison of the measured isobars for the most interesting sample, obtained with silica gel SGAMs, is shown in figure 6. According to TGA results, the polymeric phase of the fibres coating did not avoid the silica gel to adsorb the water vapor by obstructing the material porosity and the lower final adsorption capacity (figure 6) of microfibres is actually due to PAN, which has no adsorbing properties.

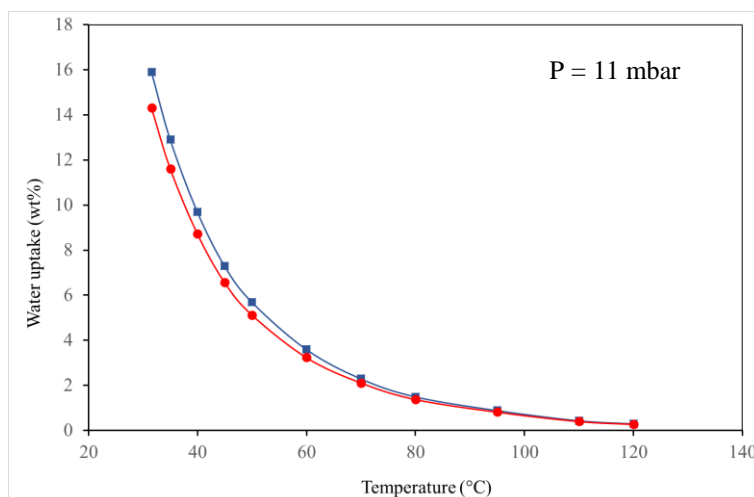


Figure 6. Isobar curves of pure SGAs (■) and SGAs microfibrils coating (●).

The electrospinning process allows to directly coat the metallic surfaces of the heat pump adsorber with silica gel hybrid microfibrils or to preliminary obtain a woven fabric which can be wrapped up on the heat exchanger pipes surface later. Such a flexibility, from the material side, could open to a re-engineering of the whole adsorber.

### Conclusions

A new silica gel coating made of a multilayer of hybrid microfibrils obtained by electrospinning was proposed. As preliminary characterization, the thermal stability and the water adsorption capability of the polymeric/silica gel fibres were tested. Results showed that the electrospinning process had no negative impact on the water adsorption/desorption of silica gel and fibres were stable to 300 °C (in nitrogen). The hydrothermal stability at adsorption/desorption cycles will be tested soon. Having structured the silica gel in a microfibrils multilayer coating has shown some advantages such as blocking the powder granules in a high porous and high surface area composite with intrinsic mechanical resistance. The electrospinning process, finally, is versatile and easily scalable.

### References:

- [1] Demir, H., Mobedi, M., Ülkü, S., “A review on adsorption heat pump: Problems and solutions”, *Renewable and Sustainable Energy Reviews*, 2008, 12, 2381.  
[doi:10.1016/j.rser.2007.06.005](https://doi.org/10.1016/j.rser.2007.06.005)
- [2] Meunier, F., “Adsorption heat powered heat pumps”, *Applied Thermal Engineering*, 2013, 61, 830.  
[doi: 10.1016/j.applthermaleng.2013.04.050](https://doi.org/10.1016/j.applthermaleng.2013.04.050)
- [3] Pan, Q.W., Wang, R.Z., “Study on boundary conditions of adsorption heat pump systems using different working pairs for heating application”, *Energy Conversion and Management*, 2017, 154, 322.  
[doi: 10.1016/j.enconman.2017.11.023](https://doi.org/10.1016/j.enconman.2017.11.023)
- [4] Núñez T, Mittelbach W, Henning HM., “Development of a small-capacity adsorption system for heating and cooling applications”, *HVAC&R Research*, 2006, 12, 749.  
[doi: 10.1080/10789669.2006.10391205](https://doi.org/10.1080/10789669.2006.10391205)
- [5] Chakraborty, A., Leong, K. C., Thu, K., Saha, B. B., Ng, K. C., “Theoretical insight of adsorption cooling”, *Applied Physics Letters*, 2011, 98, 221910.  
[doi: 10.1063/1.3592260](https://doi.org/10.1063/1.3592260)

- [6] Graf S, Lanzerath F, Sapienza A, Frazzica A, Freni A, Bardow A., “Prediction of SCP and COP for adsorption heat pumps and chillers by combining the large-temperature-jump method and dynamic modeling”, *Applied Thermal Engineering*, 2016, 98, 900.  
doi: 10.1016/j.applthermaleng.2015.12.002.
- [7] Freni, A., Dawoud, B., Bonaccorsi, L., Chmielewski, S., Frazzica, A., Calabrese L., Restuccia, G., *Characterization of Zeolite-Based Coatings for Adsorption Heat Pumps*, SpringerBriefs in Applied Sciences and Technology, Springer 2015.

# Air-channel composite desiccant for northern climate humidity recovery ventilation system

E. Cerrah<sup>1</sup>, C. McCague<sup>1</sup>, M. Bahrami<sup>1\*</sup>

<sup>1</sup>Laboratory for Alternative Energy Conversion, School of Mechatronic Systems Engineering, Simon Fraser University, Surrey, British Columbia, Canada

\*Corresponding author: mbahrami@sfu.ca

## Abstract

A composite sorbent of CaCl<sub>2</sub> in mesoporous silica gel consolidated with poly (vinyl alcohol) binder was prepared and tested for humidity recovery for building ventilation in northern climates. The composite was molded into 14 cm diameter disks that were 1.5 cm thick and had seventeen 5 mm diameter air flow channel. Stacks of seven composite disks were tested. The pressure drop was 22 to 58.5 Pa for flow rates of 7.6 to 14.8 m<sup>3</sup>/h. For ambient air with 5 g/kg specific humidity (water content/mass of air) flowing at 7.6 m<sup>3</sup>/h, the composite disks absorbed up to 2.5 g water / kg air. When cyclically regenerating the desiccant with cool, dry air, up to 78% of the ambient air stream humidity was recovered. The performance is comparable with the values presented in literature for a similar system [1,2].

**Keywords:** Desiccant, heat and mass transfer, ventilation, humidity swing adsorption

## Introduction

The residential sector is responsible from 23% of the annual energy use in USA and 50% of it is due to winter and summer air conditioning [3]. Infiltration and the costs associated with that is reduced by effective residential envelope air sealing, however it creates a need for mechanical ventilation to maintain indoor air quality. The minimum ventilation rate of a living space is determined by ASHRAE, e.g. 115 m<sup>3</sup>/h fresh air is required for a 110 m<sup>2</sup> typical two-bedroom apartment [4]. The annual total energy delivered for space conditioning in 13 developed countries, is estimated to 19 EJ and 48 % of it is lost due to air change [5].

At low ambient temperatures, e.g. -15 to -30°C, the moisture content in the air is low, i.e. in the range of 1 to 2 g/kg. Therefore, the fresh air drawn into buildings must be heated and humidified. Aristov et al. developed a cyclic adsorption/desorption and heat storage system, called VENTIREG, driven by the humidity difference between indoor and outdoor air. Laboratory and field tests of the system demonstrated 70-90% moisture recovery and 60-96% heat recovery from outlet to inlet air streams [1,2]. Packed beds of sorbent (silica gel, Al<sub>2</sub>O<sub>3</sub> and Al<sub>2</sub>O<sub>3</sub>/CaCl<sub>2</sub>) and glass pellets were used for humidity and heat recovery, respectively, and the only operating cost was the fan electric power, reported to be 20-40 W for a prototype supplying 135 m<sup>3</sup>/h fresh air.

The degree of humidification:

$$\beta = \frac{\int_0^{t_{cycle}} (\omega_{inflow} - \omega_{outdoor}) dt}{\int_0^{t_{halfcycle}} \omega_{inflow} dt} \quad (1)$$

is calculated by the ratio of water released from the sorbent to the total amount of water leaving the system during the inhale period as given in Eq. 1 where  $\omega$  is the specific humidity (g<sub>water</sub>/kg<sub>air</sub>),  $t_{halfcycle}$  is the sorption time.  $\beta$  was reported to range between 0.79 to 0.98, depending on the sorbent type and air flow rate [2]. The highest  $\beta$  was achieved with small pellet (1.88 mm in diameter, 6 mm in length) Al<sub>2</sub>O<sub>3</sub>/CaCl<sub>2</sub> (IK-011-1), i.e.,  $\beta = 0.96$  for an air flow of 14.6 m<sup>3</sup>/h,

however this had the highest pressure drop, ~90 Pa compared to other sorbents studied under the same operating conditions.

For moisture recovery ventilation systems latent effectiveness( $\varepsilon_L$ ) is a commonly used parameter as well. When the inhale and exhale air flow rates are equal  $\varepsilon_L$  is calculated as following:

$$\varepsilon_L = \frac{\omega_{inflow} - \omega_{outdoor}}{\omega_{indoor} - \omega_{outdoor}} \quad (1)$$

Latent effectiveness is the ratio of actual moisture recovery to the maximum possible moisture recovery which is basically calculated by the indoor and outdoor specific humidity difference. The maximum value of  $\varepsilon_L$  is 1 when the inflow specific humidity is equal to the indoor specific humidity.

The efficiency of the moisture recovery bed can be improved by increasing the amount of water released from air during the exhale period and accordingly increasing the amount of water released from the sorbent to the air during inhale period. Improvement in the moisture exchange was shown by using smaller size of adsorbent pellets and addition of  $\text{CaCl}_2$  [2]. The only operating cost of the system is the fan power therefore, decreasing the pressure drop has an important effect on the efficiency as well.

To improve the efficiency of this system we are proposing a new consolidated silica gel- $\text{CaCl}_2$  composite design. The de/sorption performance is improved due to improved uptake properties of the silica gel- $\text{CaCl}_2$  due to the higher surface area of small size pellets and high uptake properties of the  $\text{CaCl}_2$ . An increase in the pressure drop is expected due to smaller pellet size and the binder which is keeping the composite sorbent together. Air channels are included in the design of the composite sorbent to alleviate the increase in the pressure drop. A similar composite with air channels was previously tested by Chen et al. [6] in a desiccant air conditioning system and operated with lower pressure drop compared to a silica gel packed bed.

### Experimental set-up

A custom-designed test bed, shown in Fig. 1a, was loaded with seven consolidated sorbent pieces, ~1 kg in total. Each composite sample, shown in Fig. 2, was prepared with small size (0.25-0.5 mm) silica gel pellets, 27%  $\text{CaCl}_2$  bound by PVA and had 5 mm diameter air channels formed by glass rods. The consolidated sorbents were placed in a duct with ~1 cm spacing in between. Room air (~22 °C, 24-32% RH) passed through the bed during sorption. The desorption process was performed by flowing dry air (22-24°C, 4-5% RH) with 7.6, 10.5 and 14.8 m<sup>3</sup>/h flow rates from the opposite end of the test bed. Sorption and desorption processes were performed with 10 minute half cycles until cycle-to-cycle performance was consistent, typically after six cycles oscillatory steady-state condition was established.

The specific humidity at the indoor and outdoor ends of the test bed was determined from the temperature and RH measurements. The uncertainty for the specific humidity, which is a function of measured temperature and RH values, was calculated using the root sum square method [7] as follows.

$$s_\omega = \left[ \left( \frac{\partial \omega}{\partial T} \right)^2 (s_T)^2 + \left( \frac{\partial \omega}{\partial RH} \right)^2 (s_{RH})^2 \right]^{1/2} \quad (1)$$

The uncertainty of the specific humidity reaches up to 30% at the inlet of the bed due to very low RH condition. However, the actual value of the error is under 0.2 g/kg<sub>air</sub>.



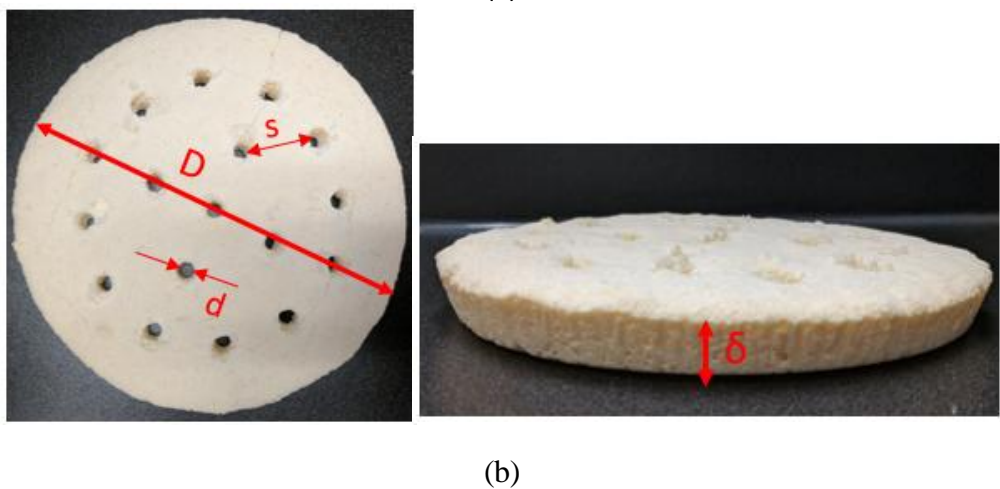
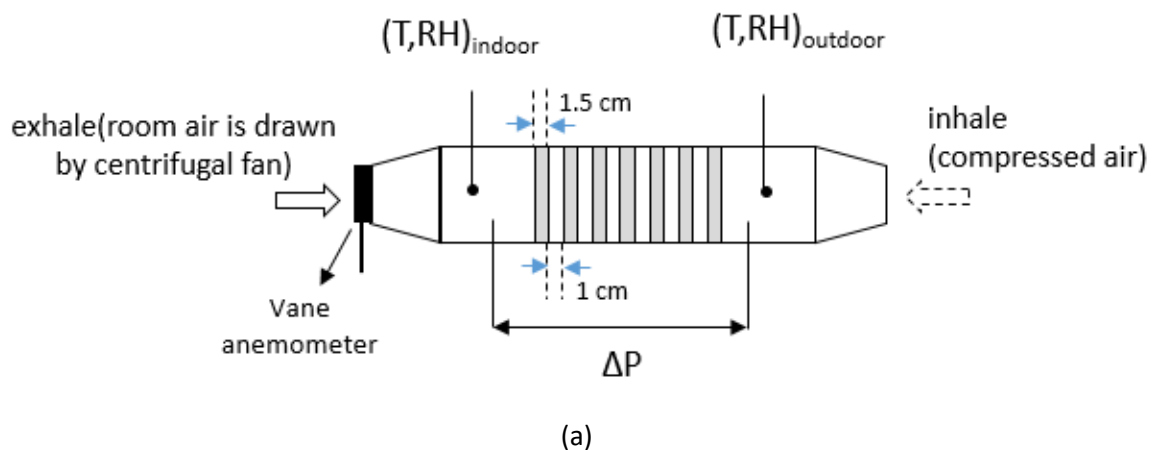


**Fig. 1** (a) Sorbents placed in a testbed where dry air is passed during inhale and room air is drawn in exhale period, (b) consolidated sorbent piece with 17 air channels  
 $D \cong 140$  mm,  $d \cong 5$  mm,  $s \cong 20$ -30 mm,  $\delta \cong 15$  mm

Table 1 shows the sensors' type and accuracies. The response time of the two T-RH sensors was relatively slow (up to 10 s), therefore, additional thermocouples were used to measure the temperature at the inlet and outlet of the testbed.

**Table 1** Specifications of sensors used in the present test set-up

Parameter	Instrument model, maker	Accuracy reported by supplier
RH	TH 210-R, capacitive sensor Kimo Instruments	$\pm 1.5\%RH$ , $15^\circ\text{C} \leq T \leq 25^\circ\text{C}$ $\pm 0.04(T - 20)\%RH$ , $T < 15^\circ\text{C}$ or $T > 25^\circ\text{C}$
Temperature	TH 210-R, Kimo Instruments	$\pm 0.3\%$ of reading $\pm 0.25^\circ\text{C}$
	T-type thermocouple, Omega	$\pm 0.5^\circ\text{C}$
Air velocity	Rotating vane anemometer, VelociCalc <sup>®</sup> , TSI Inc.	$\pm 1\%$ of reading $\pm 0.02$ m/s
Pressure difference	Very low differential pressure transducer, model 267, Setra Systems	$\pm 1\%$ of reading

## Discussion and Results

All the analyses were performed based on the data when cycle to cycle performance was consistent, i.e., when oscillatory steady-state conditions are established, typically after six cycles. Figure 2 shows an example of steady-state specific humidity data from the inlet and outlet of the testbed. Temperature and RH measurements at inlet and outlet of the testbed as dry air is humidified (inhale period) are reported in Table 2. The degree of humidification  $\beta$ , was calculated using the measurements.

**Table 2** Inlet and outlet specific humidity,  $\beta$  and  $\varepsilon_L$  for inhale (humidification) period

Air flow rate (m <sup>3</sup> /h)	Inlet			Outlet			Performance	
	T (°C)	%RH	$\omega$ (g/kg)	T(°C) max,min	%RH max,min	$\omega$ (g/kg) max, min	$\beta$	$\varepsilon_L$
7.6	22.7	4.2	0.7	23.2, 20.6	24, 19	4.2, 2.8	0.78	0.57
10.5	22.9	4.3	0.7	23.1, 20.7	28, 16	4.9, 2.4	0.76	0.49
14.8	23.4	4.7	0.8	23.1, 21.2	18, 15	3.1, 2.3	0.53	0.55

For dry air (specific humidity of 0.7 g/kg) flowed through the sorbent at 7.6 m<sup>3</sup>/h, at the outlet the specific humidity was 4.8 g/kg initially and gradually decreased to 2.8 g/kg during the 10 min half cycle, as shown in Fig. 2 (b). Degree of humidification  $\beta$ , was calculated by the ratio of the specific humidity difference between inlet and outlet to the specific humidity at the outlet.  $\beta$  was lower at higher flow rates. For tests with higher air flow rates, degree of dehumidification decreases however performance can be recovered by adjusting the cycle time as shown in Table 2.

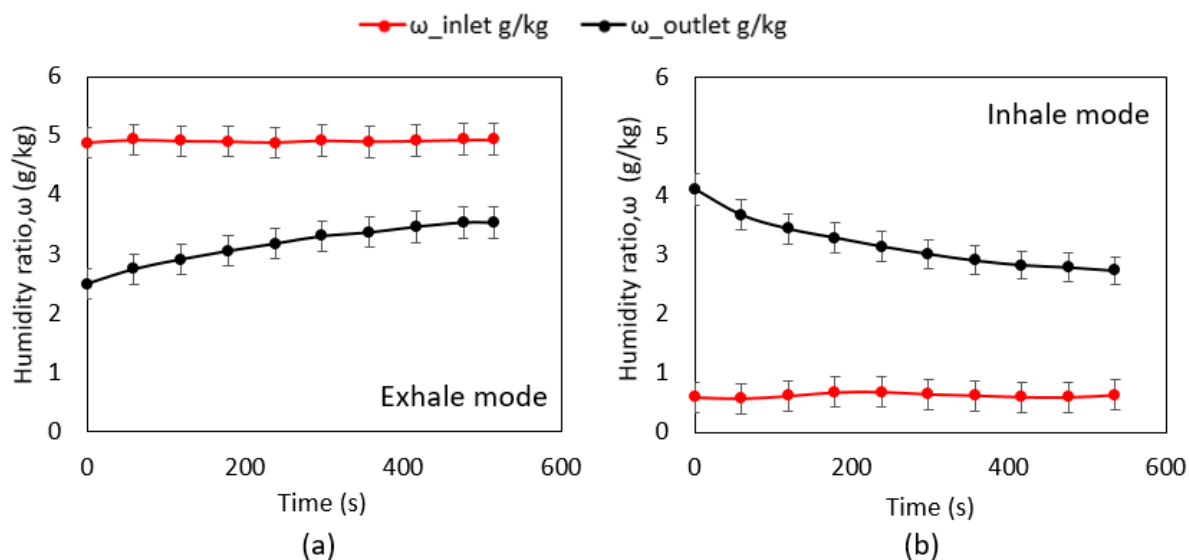


**Fig. 2** a) Humidity of room air is capture as it flows through the stack of sorbent disks (red = inlet, black = outlet). b) Dry air is humidified as it flows through the stack of sorbent disks during the regeneration step of the cycle (red = inlet. black = outlet). Air flow rate = 7.6 m<sup>3</sup>/h

Similar trends were observed in a study performed by Aristov et al. [2] for 3 kg (~5.5 L) samples of packed sorbents, including silica gel, Al<sub>2</sub>O<sub>3</sub> and Al<sub>2</sub>O<sub>3</sub>/CaCl<sub>2</sub> with different pellet sizes. Inlet air condition was in the range of 1-3% RH, 15-20.5 °C for inhale period and 27-31%

RH, 19-23 °C for exhale period. Al<sub>2</sub>O<sub>3</sub>/CaCl<sub>2</sub>(IK-011-1) with cylindrical pellets, 1.8 mm in diameter and 6 mm in length, had the highest β, between 0.98 to 0.91 for the air flow rate ranging from 5 m<sup>3</sup>/h to 31 m<sup>3</sup>/h.

Outlet air conditions and β are highly dependent on the inlet air conditions and the amount of sorption material. The performance of sorbents can also be evaluated based on the water uptake as a function of mass or volume of sorbent for the inlet air conditions of interest. The half cycle water uptake,  $W_{half\ cycle}$ , is calculated as

$$W_{half\ cycle} = \int_0^{t_{half\ cycle}} \dot{m}_{air}(\omega_{out} - \omega_{in})dt / M_{sor} \quad (1)$$

where  $\dot{m}_{air}$  is air mass flow rate,  $\omega_{out}$ ,  $\omega_{in}$  are specific humidity ratio of the air at the outlet (inflow) and inlet (outdoor) of the sorbent bed. To compare the composite sorbent to the published data for the IK-011-1 packed bed [2], the data for 10 min half cycles and 7.6 and 10.5 m<sup>3</sup>/h, and for two half cycles at 14.8 m<sup>3</sup>/h flow rate were used.

In Fig. 3,  $W_{half\ cycle}$  for the present study is plotted in comparison to the values calculated for IK-011-1 from the published β and specific humidities (inlet and outlet) for similar air flow rates [2]. Although the degree of de/humidification of the present composite sorbent was lower, its water uptake per kg of sorbent was higher at all tested air flow rates, with up to 30% difference.

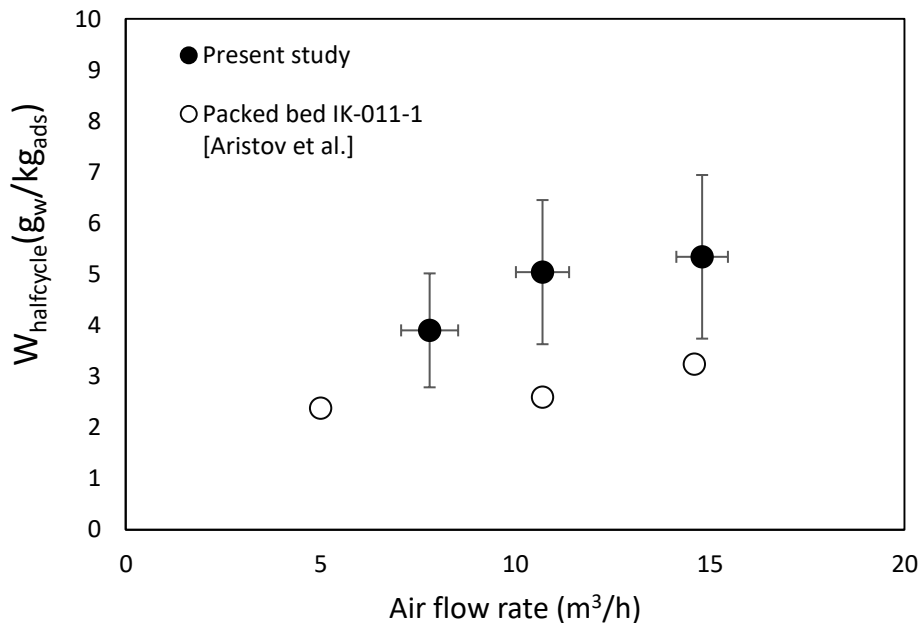


**Fig. 3** Comparison of the water uptake per kg of sorbent in 10 min half-cycle time calculated from the experimental data for ~1 kg of composite sorbent in the present study and for ~3 kg of IK-011-1[2]

For the half cycles shown in Fig. 3, the half cycle water uptake of the composite sorbent is 5.5 g/kg. The equilibrium uptake of the sorbent from TGA data is 400 g/kg at 35% RH, suggesting that there is significant potential for optimizing the sorbent geometry. The low uptake can be explained as the relatively wide air channels are providing a low-resistance path for the airflow. Thus air can only interact with a limited area of sorbent material within a specific diameter of area surrounding the channels. The sorbent material outside these areas are not fully utilized.

Decreasing the size sorbent pellets can enhance total water removal, however, it also increases the hydrodynamic resistance of the bed [2]. The amount of binder used to keep the sorbent together can also contribute to the pressure drop. Therefore, air channels were built through the sorbents to keep the pressure drop in a reasonable range. Establishing an optimal geometry to enable full potential of the sorbent requires a comprehensive modelling exercise that will be performed in our future work.

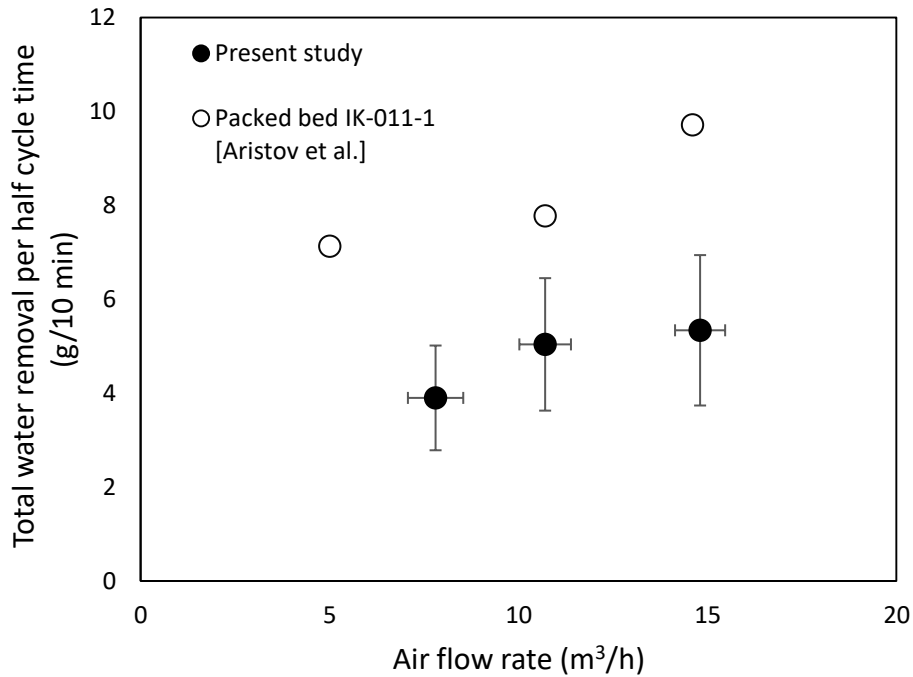


**Fig. 4** Comparison of total water uptake in 10 min half-cycle time calculated from the experimental data for ~1 kg of composite sorbent in the present study and for ~3 kg of IK-011-1 [2]

As shown in Fig. 4, when the total water removal is considered, the 3 kg IK-011-1 sorbent bed removes 20-29% more vapour from the air flowing through it, resulting a higher  $\beta$  compared to 1 kg of present composite sorbent. If the amount of composite sorbent is increased, its de/humidification performance can be increased, however pressure drop is also an important parameter.

The pressure drop per volume of sorbent is plotted for present study and the packed bed of IK-011-1 sorbent is shown in Figure 5. Measured pressure drop values were divided in the volume of the sorbent bed to make the different designs comparable. Volume of the present bed was about 2.5 L, consisting of seven disks of composite sorbents (0.2 L each) and about 1 cm space in between the disks. The packed bed of IK-011-1 was 5.5 L [2].

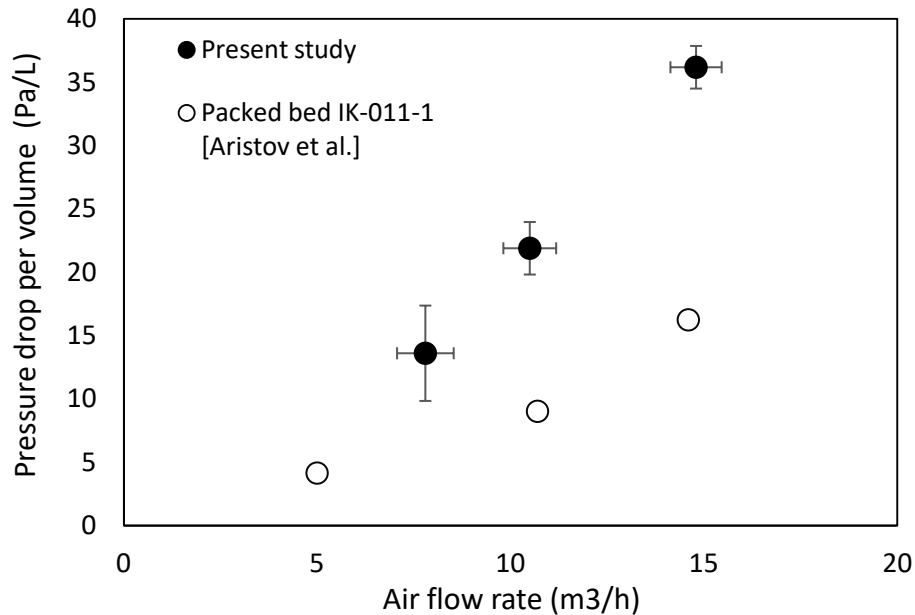


**Fig. 5** Pressure drop per 5.5 L of IK-011-1 [2] compared with the composite sorbent in the current study with 2.5 L of total volume (seven disks, ~0.2 L each, and 1 cm space between each disk)

The plot shows that the present composite sorbent bed causes 35% to 53% higher pressure drop per volume of sorbent compared to IK-011-1 packed bed. Also, it has a steeper increasing trend with the increasing air flow rate. It will be an issue for scaling up the system to perform at higher air flow rates with higher amount of sorbent. Therefore, reducing the pressure drop will be important in future optimization studies of the composite sorbent geometry.

### Conclusions

Composite  $\text{CaCl}_2$  in silica gel sorbent consolidated into disks with air flow channels using poly (vinyl alcohol) binder were prepared and tested for a humidity recovery ventilation system. A humidification degree of ranging between 0.68-0.78 was achieved for 7.6-14.8  $\text{m}^3/\text{h}$  air flow rate, which is in a comparable range of performance and higher water uptake compared with other sorbents presented in literature for this application in this range of air flow rate [2]. In order to scale up the system, an optimization study for the sorbent/air channel geometry should be performed with the objective of low pressure drop, high  $\beta$  and high water uptake.

### References

- [1] Aristov, Y. I., Mezentsev I. V., Mukhin V. A., "A new approach to regenerating heat and moisture in ventilation systems." *Energy and Buildings*, 2008. [doi.org/10.1016/j.enbuild.2007.02.029](https://doi.org/10.1016/j.enbuild.2007.02.029)
- [2] Aristov, Y. I., Mezentsev, I. V., & Mukhin, V. A., "Investigation of the moisture exchange in a stationary adsorbent layer through which air is passed" *Journal of Engineering Physics and Thermophysics*, 2005; 78(2), 248-255. [doi.org/10.1007/s10891-005-0055-0](https://doi.org/10.1007/s10891-005-0055-0)
- [3] Logue, J. M., Sherman, M. H., Walker, I. S., & Singer, B. C., "Energy impacts of envelope tightening and mechanical ventilation for the US residential sector", *Energy and Buildings*. 2013;65, 281-291. [doi.org/10.1016/j.enbuild.2013.06.008](https://doi.org/10.1016/j.enbuild.2013.06.008)
- [4] Standard, A. S. H. R. A. E. (2013). Standard 62.2-2013, "Ventilation for Acceptable Indoor Air Quality in Low-Rise Residential Buildings, ASHRAE, Atlanta, GA.

- [5] Orme, M., “Estimates of the energy impact of ventilation and associated financial expenditures”, *Energy and Buildings*. 2001; 33(3), 199-205.  
[doi.org/10.1016/S0378-7788\(00\)00082-7](https://doi.org/10.1016/S0378-7788(00)00082-7)
- [6] Chen, C. H., Hsu, C. Y., Chen, C. C., Chen, S. L., “Silica gel polymer composite desiccants for air conditioning systems.” *Energy and Buildings*, 2015.  
[doi.org/10.1016/j.enbuild.2015.05.009](https://doi.org/10.1016/j.enbuild.2015.05.009)
- [7] Angrisani, G., Minichiello, F., Roselli, C., & Sasso, M., “Experimental analysis on the dehumidification and thermal performance of a desiccant wheel.” *Applied Energy*, 2012.  
[doi.org/10.1016/j.apenergy.2011.11.071](https://doi.org/10.1016/j.apenergy.2011.11.071)

# Influence of the fluid dynamics on an air-cooled fixed-bed adsorber with connected water evaporator

M. Jäger<sup>1\*</sup>, K. Hurtig<sup>2</sup>, R. Kühn<sup>1</sup> and J. Römer<sup>2</sup>

<sup>1</sup>Dipl.-Ing., <sup>2</sup>M.-Sc., Researcher at Department of Mechanical and Systems Engineering, TU Berlin, Marchstr. 18, 10587 Berlin, Germany

\*Corresponding author: mike.jaeger@tu-berlin.de

## Abstract

In this publication two different levels of detail for a simulation model for fixed-bed adsorbers connected to an evaporator are introduced. Both approaches are compared to each other on basis of various design parameters. The considered adsorber is a cuboid chamber filled with spheres of silica gel to be used with water as refrigerant that is provided by an evaporator. The coupling of adsorber and evaporator induces increased computing time.

The first approach with the highest level of detail includes the thermal and fluidic bed dynamics by characterising every transport process: the heat transfer within the bed, the mass transfer inside the adsorbent, the mass transfer in the gaps of the fixed-bed and the momentum transfer of the adsorptive. The second approach does not include the fluid dynamics of the adsorptive in the gaps of the fixed-bed. The two approaches are compared concerning specific cooling power (SCP) and efficiency (COP). The mass and momentum transfer of the adsorptive influences the results most at the beginning of the adsorption process and its influence decreases with proceeded adsorption time. However, neglecting the fluid dynamics will lead to a noticeable offset on the specific cooling power.

**Keywords:** adsorber fluid dynamics, dynamic simulation, adsorption, air-cooled adsorber

## Introduction and background

Until 2030 the world-wide demand of energy will increase by 60% [1]. Adsorption cooling could be a promising alternative to conventional cooling methods by using waste heat, i.e. from district heating grids in summer [1]. According to cost-efficiency it is appropriate to use air-cooled fixed-bed adsorbers, thus expenses for an additional cooler and piping are saved. To achieve high energy efficiency, it is beneficial to describe the processes in an adsorber mathematically to improve design or operating parameters.

There are some publications considering fluid dynamics in an adsorber itself [2] [3], but without coupling it to an evaporator. The pressure drop of the adsorptive within the fixed-bed is a crucial effect influencing the specific cooling power (SCP) and efficiency (COP) of an air-cooled adsorber. To evaluate this effect, the mass and momentum transfer of the adsorptive must be considered. In this article an evaporator is connected to the adsorber mathematically by the boundary condition that the water evaporating in the evaporator must be adsorbed by the adsorber instantly. Due to this assumption the differential equations for the fluid dynamics of the adsorptive cannot be solved directly and therefore iteration is necessary. Thus, the evaporator can be simulated as a transient operating component.

## The simulation models

Figure 1 shows a schematic of the coupled simulation model of the considered system with refrigeration room, evaporator and adsorber.

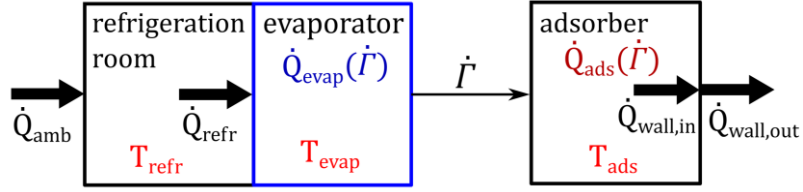


**Figure 1:** Coupled system of refrigeration room, evaporator and adsorber

$\dot{\Gamma}$  is the specific adsorption mass flow of water vapor which is provided by the evaporator and instantly adsorbed in the adsorber.

To evaluate the influence of the momentum and mass transfer of the adsorptive within the fixed-bed two different levels of detail for a simulation model are examined. The high level of detail (model B) includes the fluid dynamics of the water vapor whereas the other approach (model A) is neglecting it. The objective is to find out when it is appropriate to skip considering the fluid dynamics of the adsorptive in a fixed-bed adsorber to reduce computing time significantly.

Figure 2 shows the symmetric physical model of the cuboid fixed-bed adsorber. The working pair is spheres of silica gel as adsorbent and water as refrigerant and adsorptive.

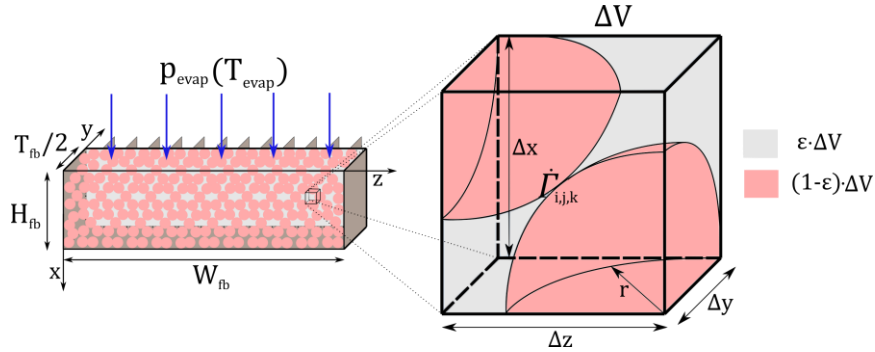


**Figure 2:** Sectional view of the fixed-bed adsorber and subdivision in discrete volumes  $\Delta V$

The height  $H_{fb}$ , width  $W_{fb}$  and thickness  $T_{fb}$  of the adsorber are the setting parameters. At the inlet on top of the chamber prevails the pressure  $p_{evap}$ , resulting from the boiling temperature  $T_{evap}$  in the evaporator. To extract the influence of flow length (x-direction) on the adsorber bed dynamics and to eliminate other effects, resulting from the coupling of the evaporator, the mass of adsorbent is always hold constant by changing the amount of identical operating fixed-beds shown in Figure 2. Otherwise a higher flow length would lead to a scaling effect so that an increasing mass of adsorbent would occur which means a higher potential of generated cooling power.

Subsequently, the governing mass, energy and momentum equations for both simulation models A and B are introduced. The major direction for heat transfer is along the y-axis and for mass and momentum transfer along the x-axis. Because there is no significant thermodynamic or fluid dynamic process in z-direction, the following differential equations for the adsorber only depend on the coordinates x or y. To solve the equations by the method of finite differences the adsorber is subdivided in discrete volumes  $\Delta V$  in which a specific adsorption mass flow  $\dot{\Gamma}_{i,j,k}$  is induced (see fig. 2).

#### Adsorber: mass transfer adsorbent model A and B

The specific adsorption mass flow  $\dot{\Gamma}$  in every discrete volume  $\Delta V$  is described by a Linear-Driving-Force (LDF) equation [4]:



$$\frac{\partial X}{\partial t} = \frac{15D_{\text{eff}}}{r^2} \left( X_{\text{eq}} \left( p_{w,v}(x, y, t), T(x, y, t) \right) - X(x, y, t) \right) \quad (1)$$

$$\dot{\Gamma}(x, y, t) = \rho_{\text{Ad,S}} \frac{\partial X}{\partial t} \quad (2)$$

$\rho_{\text{Ad,S}}$  is the apparent density of the adsorbent,  $D_{\text{eff}}$  a summarized diffusion coefficient containing all mass transfer constraints [4],  $r$  the radius of the spheres and  $X$  is the current uptake of the adsorbent. The equilibrium uptake  $X_{\text{eq}}$  depends on the local pressure of the adsorptive  $p_{w,v}$  and temperature  $T$ . A previous desorption phase at a constant desorption temperature  $T_{\text{des}}$  and condensing pressure  $p_{\text{cond}}$  provides the equilibrium uptake  $X_{\text{des}}$  of the adsorbent which is the initial condition for the chamber before starting adsorption phase. The used material data for  $X_{\text{eq}}$  of silica gel Grace 123 and water is taken from Schawe [5].

$$X(t = 0) = X_{\text{des}} = f(T_{\text{des}}, p_{\text{cond}}) \quad (3)$$

#### Adsorber: heat transfer fixed-bed model A

For the heat transfer equation, the fixed-bed is summarized as one homogenous mass with a constant voids fraction  $\varepsilon$ . Previous calculations provided that this assumption can be made due to the density of the adsorptive  $\rho_{w,v}$  being much less than that of the adsorbent  $\rho_{\text{Ad,S}}$  ( $\rho_{w,v} \ll \rho_{\text{Ad,S}}$ ).

$$\frac{\partial T_A}{\partial t} \left[ (1 - \varepsilon) \rho_{\text{Ad,S}} (c_{p,\text{Ad}} + c_{p,w,l} X) \right] = \lambda_{\text{eff}} \frac{\partial^2 T_A}{\partial y^2} + \dot{\Gamma} \Delta h_{\text{Ad}}(X) \quad (4)$$

The governing heat transfer process, the heat conduction within the fixed-bed, occurs in  $y$ -direction with an effective thermal conductivity  $\lambda_{\text{eff}}$ . The second term on the right side in equation (4), including the adsorption enthalpy  $\Delta h_{\text{Ad}}$  depending on the current uptake  $X$ , describes the heat source due to adsorption.  $c_{p,\text{Ad}}$  and  $c_{p,w,l}$  are the specific heat capacities of the adsorbent and the adsorbate water. The initial adsorber temperature is set by the equilibrium material data of the adsorbent at the initial uptake  $X_{\text{des}}$  (eq. (3)) and the evaporator pressure  $p_{\text{evap}}$ , assuming that the adsorption phase starts if a certain pressure difference  $\Delta p_i$  is needed between adsorption chamber and evaporator.  $p_{\text{evap}}$  is a direct function of  $T_{\text{evap}}$  because of the specification that there is only saturated vapor in the evaporator.

$$T_A(y, t = 0) = f(X_{\text{des}}, p_{\text{evap}}(T_{\text{evap}}) - \Delta p_i) \quad (5)$$

There is a symmetry condition in the middle of the fixed-bed (6). At the wall of the chamber ( $y = T_{\text{fb}}/2 = y_{\text{wall}}$ ) a transient equation as boundary condition is defined (6b), considering the heat capacity of the wall (see Fig. 1).

$$\left( \frac{\partial T_A}{\partial y} \right)_{y=0} = 0 \quad (6)$$

$$c_{p,\text{wall}} \frac{dT_A(y = y_{\text{wall}})}{dt} = \dot{Q}_{\text{wall,in}} - \dot{Q}_{\text{wall,out}} \quad (6b)$$

$$\text{with } \dot{Q}_{\text{wall,in}} = \lambda_{\text{eff}} W_{\text{fb}} H_{\text{fb}} \left( \frac{\partial T_A}{\partial y} \right)_{y=y_{\text{wall}}} \quad (6c)$$

$$\text{and } \dot{Q}_{\text{wall,out}} = \frac{1}{\frac{1}{\alpha_{\text{fb,wall}}} + \frac{\lambda_{\text{wall}}}{s_{\text{wall}}} + \frac{1}{\alpha_{\text{wall,amb}}}} W_{\text{fb}} H_{\text{fb}} (T_A(y = y_{\text{wall}}) - T_{\text{amb}}) \quad (6d)$$

All required coefficients for equation (6c) and (6d) are tabulated in Table 1.

**Table 1:** Conditions for the simulations

parameter	symbol	value	unit
mass of adsorbent	$m_{\text{ads}}$	3	kg
thickness fixed-bed	$T_{\text{fb}}$	0.015	m
width fixed-bed	$W_{\text{fb}}$	0.5	m
height fixed-bed	$H_{\text{fb}}$	variable	m
discrete local step size	$\Delta x$	0.005	m
discrete local step size	$\Delta y$	0.005	m
discrete local step size	$\Delta z$	0.5	m
discrete time step size	$\Delta t$	0.5	s
radius of spheres of adsorbent	$r$	0.0005	m
voids fraction fixed-bed	$\varepsilon$	0.4	-
diffusion coefficient adsorbent	$D_{\text{eff}}$	$10^{-10}$	$\text{m}^2 \text{s}^{-1}$
apparent density adsorbent	$\rho_{\text{Ad,S}}$	1250	$\text{kg m}^{-3}$
specific heat capacity adsorbent	$c_{\text{p,Ad}}$	1000	$\text{J kg}^{-1} \text{K}^{-1}$
specific heat capacity water liquid	$c_{\text{p,w,l}}$	4218	$\text{J kg}^{-1} \text{K}^{-1}$
specific heat capacity water vapor	$c_{\text{p,w,v}}$	1889	$\text{J kg}^{-1} \text{K}^{-1}$
heat capacity wall of chamber	$C_{\text{p,wall}}$	5770	$\text{J K}^{-1}$
heat capacity evaporator	$C_{\text{p,evap}}$	5000	$\text{J K}^{-1}$
uptake adsorbent after desorption	$X_{\text{des}}$	0.053	$\text{g g}^{-1}$
desorption temperature	$T_{\text{des}}$	353.15	K
initial temperature evaporator	$T_{\text{evap,initial}}$	275.15	K
condensing pressure while desorption	$p_{\text{cond}}$	42.6	mbar
pressure difference adsorber-evaporator	$\Delta p_i$	1	mbar
effective heat conductivity fixed-bed	$\lambda_{\text{eff}}$	0.048	$\text{W m}^{-1} \text{K}^{-1}$
ideal gas constant water vapor	$R$	461.4	$\text{J kg}^{-1} \text{K}^{-1}$
heat transfer coefficient fixed-bed-wall	$\alpha_{\text{fb,wall}}$	50	$\text{W m}^{-2} \text{K}^{-1}$
heat transfer coefficient wall-ambience	$\alpha_{\text{wall,amb}}$	10	$\text{W m}^{-2} \text{K}^{-1}$
heat conductivity wall	$\lambda_{\text{wall}}$	15	$\text{W m}^{-1} \text{K}^{-1}$
thickness wall	$s_{\text{wall}}$	0.001	m
temperature refrigeration room	$T_{\text{refr}}$	279.15	K
thermal resistance refrigeration room	$u_{\text{refr}} A_{\text{refr}}$	10	$\text{W K}^{-1}$

### Adsorber: heat transfer fixed-bed model B

In comparison to the heat transfer equation of model A, an extra term in model B is added due to the consideration of the momentum transfer of the adsorptive.

$$\frac{\partial T_B}{\partial t} [(1 - \varepsilon)\rho_{Ad,S}(c_{p,Ad} + c_{p,w,l}X)] = \varepsilon c_{p,w,v}\rho_{w,v} \left( \frac{\partial(uT_B)}{\partial x} \right) + \lambda_{\text{eff}} \frac{\partial^2 T_B}{\partial y^2} + \dot{\Gamma} \Delta h_{Ad}(X) \quad (7)$$

Because of the major flow direction along the x-axis a convective heat transfer term is added with the flow velocity  $u$ , the void fraction  $\varepsilon$  of the fixed-bed and the density  $\rho_{w,v}$  and heat capacity  $c_{p,w,v}$  of the adsorptive. The initial and boundary conditions are the same as in the fixed-bed heat transfer model A (eq. (5), (6) and (6b)) except of adding the x-direction. For model B an extra boundary condition must be added (eq. (9c)) because of the convective term.

$$T_B(x, y, t = 0) = f(X_{\text{des}}, p_{\text{evap}}(T_{\text{evap}}) - \Delta p_i) \quad (8)$$

$$\left( \frac{\partial T_B}{\partial y} \right)_{x,y=0} = 0 \quad (9)$$

$$dC_{p,\text{wall}} \frac{dT_B(x, y = y_{\text{wall}})}{dt} = d\dot{Q}_{\text{wall,in}}(x) - d\dot{Q}_{\text{wall,out}}(x) \quad (9b)$$

$$\left( \frac{\partial T_B}{\partial x} \right)_{x=0,y} = 0 \quad (9c)$$

### Adsorber: mass transfer adsorptive model B

Along the major flow direction (x-axis) the mass transfer of the adsorptive is solved by equation (10).

$$\varepsilon \frac{\partial(u\rho_{w,v})}{\partial x} = -\dot{\Gamma} \quad (10)$$

The mass transfer of the adsorptive can be simplified to a steady state equation which is solved every time step. This is done because the temporal change of the density of the adsorptive is much less than the convective term including the flow velocity  $u$  ( $\partial\rho_{w,v}/\partial t \ll \partial(u\rho_{w,v})/\partial x$ ). The specific adsorption mass flow  $\dot{\Gamma}$  is a function of the time  $t$  (eq. (2)), thus the mass transfer equation (10) has a different solution for each time step. The initial condition results from the equilibrium material data of the adsorbent at the uptake  $X_{\text{des}}$  and the temperature of the sorbent  $T_B(x, y, t = 0)$ . At the inlet of the adsorption chamber ( $x = 0$ ) a dynamic boundary condition is defined including the law of ideal gases (eq. (12)).

$$\rho_{w,v}(x, y, t = 0) = f(X_{\text{des}}, T_B(x, y, t = 0)) \quad (11)$$

$$\rho_{w,v}(x = 0, y, t) = \frac{p_{w,v}(x = 0, y, t)}{R T_B(x = 0, y, t)} \quad (12)$$

### Adsorber: momentum transfer adsorptive model B

Because of the very low density of the water vapor  $\rho_{w,v}$ , the momentum transfer model can be simplified to one pressure and one friction term [6]. A common equation to describe the pressure drop in a fixed-bed is the equation of Molerus [7] which is used for modelling the momentum transfer of the adsorptive in model B.

$$\frac{\partial p_{w,v}}{\partial x} = \frac{3Eu\rho_{w,v}u^2(1 - \varepsilon)}{8r\varepsilon^2} \quad (13)$$

$Eu$  is a parameter describing the flow in the fixed-bed by dint of the Reynolds number. The initial condition of the pressure (eq. (14)) results from the initial uptake  $X_{des}$  (eq. (3)) and the initial temperature  $T_B(x, y, t = 0)$ . For the pressure two boundary conditions exist. At the inlet of the fixed-bed prevails the pressure of the evaporator  $p_{evap}$  (eq. (15)). Within the fixed-bed the pressure at every time  $t$  must not be lower than a minimum pressure  $p_{min}$  which depends on the local uptake  $X$  and local temperature  $T_B$  (eq. (15b)). For the flow velocity  $u$  one direct and one iterative determinable boundary condition can be defined. At the end of the fixed-bed the flow velocity equals always zero (eq. (16)). At the inlet a boundary condition coupled with the mass transfer of the adsorbent (eq. (2)) has to be solved (eq. (16b)). Due to the fulfillment of equation (15b) and the high dependence on  $p_{w,v}$  in equation (2) an iterative solving process of the momentum transfer equation is necessary.

$$p_{w,v}(x, y, t = 0) = f(X_{des}, T_B(x, y, t = 0)) \quad (14)$$

$$p_{w,v}(x = 0, y, t) = p_{evap}(T_{evap}) \quad (15)$$

$$p_{w,v}(x, y, t) \leq p_{min} = f(X(x, y, t), T_B(x, y, t)) \quad (15b)$$

$$u(x = H_{fb}, y, t) = 0 \quad (16)$$

$$u(x = 0, y, t) = \frac{(\sum_{x=0}^{x=H_{fb}} \dot{r}(x, y, t)) \varepsilon \Delta V}{\rho_{w,v}(x = 0, y, t) \varepsilon \Delta y \Delta z} \quad (16b)$$

#### Evaporator: energy equation model

An integral energy equation for the evaporator is defined.

$$C_{p,evap} \frac{dT_{evap}}{dt} = \dot{Q}_{refr} - \dot{Q}_{evap}(\dot{r}) \quad (17)$$

$$\text{with } \dot{Q}_{refr} = u_{refr} A_{refr} (T_{refr} - T_{evap}) \quad (17b)$$

$$\text{and } \dot{Q}_{evap} = \left( \sum \dot{r}(x, y, t) \right) (1 - \varepsilon) \Delta V \Delta h_{lv}(T_{evap}) \quad (17c)$$

$C_{p,evap}$  is a summarized heat capacity considering all thermal masses of the evaporator. The boundary condition of the evaporator model is that the water which is adsorbed in the adsorber  $\dot{r}$  is provided by the evaporator instantly. All required temperatures and coefficients in equation (17b) and (17c) are listed in table 1.  $T_{evap,initial}$  is set for the initial condition.

$$T_{evap}(t = 0) = T_{evap,initial} \quad (18)$$

#### Specific cooling power (SCP) and coefficient of performance (COP):

The essential parameters to categorize an adsorption system is the specific cooling power (SCP) and the coefficient of performance (COP) which are calculated by equation (19) and (20).

$$SCP(t_{ads}) = \frac{1}{t_{ads} m_{ads}} \int_{t=0}^{t=t_{ads}} \dot{Q}_{evap}(\dot{r}(t)) dt \quad (19)$$

$$COP(t_{ads}) = SCP t_{ads} m_{ads} \left[ \int_{t=0}^{t=t_{ads}} \dot{Q}_{ads}(\dot{r}(t)) dt + F(T_{des} - T_{ads}(t_{ads})) \right]^{-1} \quad (20)$$

$$\text{with } F = m_{ads} [c_{p,Ad} + c_{p,w,l}(X_{ads}(t_{ads}) - X_{des})] \quad (20b)$$

$X_{ads}$  is the average uptake of the adsorbent and  $T_{ads}$  the average temperature of the adsorption chamber depending on the current adsorption time  $t_{ads}$ .

### Discussion and Results

Figure 3 shows the specific cooling power (SCP) depending on the flow length of the adsorptive at three different adsorption cycle times  $t_{ads}$  of simulation model A and B.

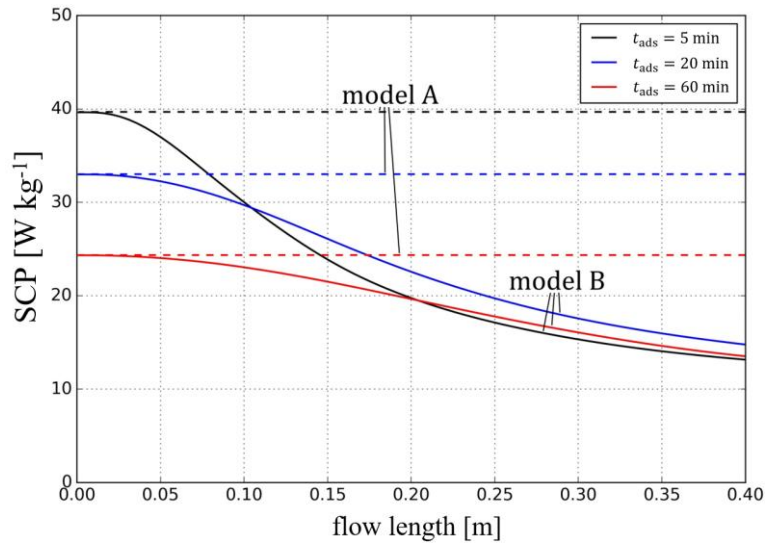


**Figure 3:** SCP depending on the flow length of the adsorptive for model A and B at three different adsorption cycle times  $t_{ads}$

The dotted lines represent model A in which the mass and momentum transfer of the adsorptive water vapor is not considered. Because of this negligence the constant mass of adsorbent adsorbs at any place and time water with evaporator pressure  $p_{evap}$ . This leads to a constant SCP for any flow length. The continuous lines belong to model B including mass and momentum transfer of the adsorptive. For each adsorption cycle time  $t_{ads}$  the trend begins to decrease progressively until reaching a turning point. Behind that the decrease of the SCP declines. This can be described by two effects. An increasing flow length leads to a non-proportional increasing pressure drop within the fixed-bed which has a negative effect on the SCP. The second phenomenon occurs inside the fixed-bed where the pressure of the surrounding water vapor converges to the minimum system pressure given by the silica gel properties. Thus, no further pressure drop can occur and the influence on the SCP decreases. The specific cooling power SCP decreases with increasing adsorption cycle time  $t_{ads}$  for constant flow length because of the decreasing adsorptive capacity of the silica gel over time. The pressure drop within the fixed-bed decreases with proceeded time which leads to a shift of the turning point to higher flow length of the curves for simulation model B. Additionally, this fact flattens the progressive and declining decrease of the curves with longer adsorption cycle time  $t_{ads}$ , being beneficial for long flow lengths and longer adsorption cycle times as can be seen for  $t_{ads} = 60$  min in figure 3.

Figure 4 shows the coefficient of performance (COP) depending on the flow length of the adsorptive at three different adsorption cycle times  $t_{ads}$  for simulation model A and B.

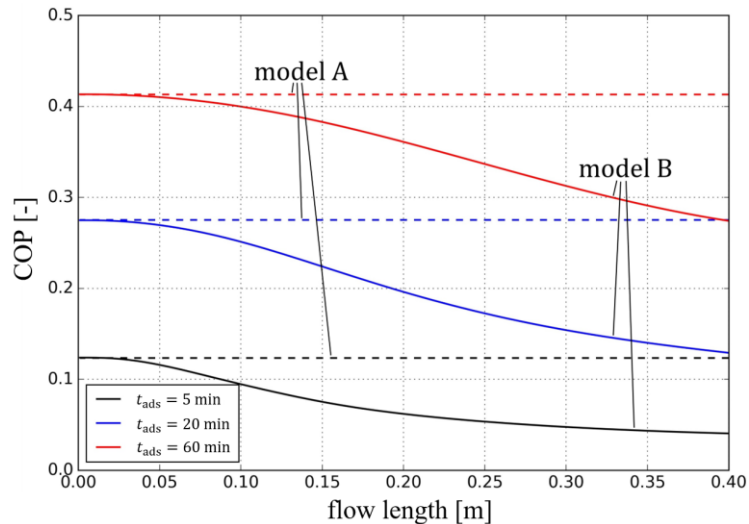


**Figure 4:** COP depending on the flow length of the adsorptive for model A and B at three different adsorption cycle times  $t_{ads}$

In opposition to the specific cooling power, the COP is increasing with longer adsorption cycle time. This fact is based on the increasing amount of water being adsorbed over time and thus, more of the adsorption capacity of the silica gel is used. Because of the constant SCP for model A (see fig. 3) also the coefficient of performance does not depend on flow length for simulation model A. For model B the curves of the COP have a similar but mirrored trend as to the curves of the SCP. The two effects explained for the SCP influence the coefficient of performance, too. The location of the turning points of the curves in figure 4 correspond with those in the SCP plot figure 3. The turning points of the COP become less apparent with increasing adsorption cycle time due to the decreasing of the pressure drop within in the fixed-bed.

Figure 3 and figure 4 shows the trends of the COP and SCP for a particle diameter of 0.001 m. With increasing particle diameter, the influence of the pressure drop decreases. Because of that the heat conductivity within the fixed-bed is an essential factor which limits the SCP, the adsorber bed design must be as thin as possible. Due to this design parameter  $T_{fb}$  the considered particle diameter in this paper represents an optimal value for such adsorber designs.

The following figure 5 shows the percentage deviation of the SCP and COP between the model A and B in dependence of the flow length at three different adsorption cycle times  $t_{ads}$ .

Generally, the percentage deviation decreases with longer adsorption cycle time  $t_{ads}$  which is due to the decrease of the influence of the pressure drop within the fixed-bed. The locations of the turning points of each curve in figure 5 correspond with those in the SCP and COP. It is shown that for almost every flow length the percentage deviation of the SCP is higher than that of the COP. This fact means that the negligence of the mass and momentum transfer of the adsorptive has a higher influence on the results of the specific cooling power than on the efficiency.

Regarding to the results in figure 5 the percentage deviation of the specific cooling power and efficiency show a strong dependency on the adsorption cycle time  $t_{ads}$ . The COP and SCP are similarly imprecise (for simulation model B) only for short adsorption cycle times.

## Summary and conclusions

SCP and COP are both decreasing with increasing flow length in the fixed-bed of an adsorber. Thus, a minimal flow length in the fixed-bed is beneficial. For practical reasons the flow length cannot be chosen arbitrary short, so that a significant deviation from reality can occur by using the simple simulation model A.

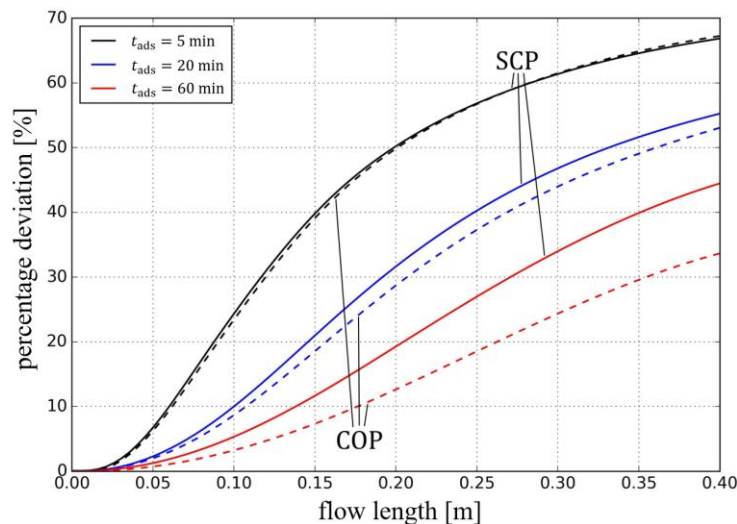


**Figure 5:** Percentage deviation of the SCP and COP between model A and B depending on the flow length of the adsorptive at three different adsorption cycle times  $t_{ads}$

In order to reach a good efficiency (e.g.  $COP > 0.4$ , fig. 4) for adsorption chillers with air-cooled fixed-bed adsorbers, long cycle times  $t_{ads} \geq 60$  min are necessary. In that case the deviation between simulation model A and B is reduced significantly in comparison to short cycle times. Nevertheless, there might remain a remarkable deviation from reality for realizable geometries while neglecting the fluid dynamics of the adsorptive.

Considering the fluid dynamics of the adsorptive (simulation model B) implicates an enormous increase in calculation time because of the necessary iterative approach and might be obstructive for wide range optimization. Here the simple simulation model A is applicable, but the user must be aware of the strong deviation from reality, especially for long flow length of the adsorptive within the fixed-bed.

## References

- [1] Rouhani, M., Sharafian, A., Cheppudira, P., Mehr, S. M. N., Dhillon, A., Huttema, W., Bahrami, M., *Performance enhancement of an adsorption cooling system with AQSOA FAM-Z02 and low-finned tube evaporator*, IMPRES Conference, Sicily, 2016.
- [2] Kwapinski, W., Salem, K., Mewes, D., Tsotsas, E., *Thermal and flow effects during adsorption in conventional, diluted and annular packed beds*, Chem. Eng. Sc. 65, pp. 4250-4260, 2010.
- [3] Otten, W., Kast, W., *Der Durchbruch in Adsorptions-Festbetten: Methoden der Berechnung und Einfluß der Verfahrensparameter*, Chem. Ing. Tech. 59, pp. 1-12, 1987.
- [4] Schönbacher, A., *Thermische Verfahrenstechnik Grundlagen und Berechnungsmethoden für Ausrüstungen und Prozesse*, Springer-Verlag, pp. 884, Berlin Heidelberg New York 2002, ISBN 3-540-42005-3.
- [5] Schawe, D., *Theoretical and Experimental Investigations of an Adsorption Heat Pump with Heat Transfer between two Adsorbers*, Dissertation, TU Stuttgart, 1999.
- [6] Gersten, K. et al., *Strömungsmechanik Grundlagen der Impuls-, Wärme- und Stoffübertragung aus asymptotischer Sicht*, Verlag Vieweg, pp. 233, Braunschweig Wiesbaden 1992, ISBN 3-528-06472-2.
- [7] Molerus, O., *A coherent representation of pressure drop in fixed bed and of bed expansion for particulate fluidized beds*, Chem. Ing. Tech. 35, pp. 1331-1340, 1980.

# Experimental proof of concept for a water/LiBr single stage absorption heat conversion system as a house connection station

S. Hunt<sup>1\*</sup>, S. Petersen<sup>1</sup>, F. Ziegler<sup>1</sup> and C. Hennrich<sup>1</sup>

<sup>1</sup>Technische Universität Berlin, Institute of Energy Engineering, KT2, Marchstr. 18,  
10587 Berlin, Germany

\*Corresponding author: sarah.hunt@tu-berlin.de

## Abstract

An installation of a single stage LiBr/Water absorption chiller was modified to enable operation in heat pumping mode within a house connection station of a district heating system. In this special case, the desorber is fired by a split stream of the district heat supply line and the evaporator further cools down this split stream before the latter is fed into the district heat return line. The reject heat of the absorption unit is given as supply heat to the building distribution system. This absorption heat conversion system has the aim to lower the district heating return temperature, thus increasing local grid capacity, and, possibly, the efficiency of the supply cogeneration plant. Moreover, the district heat supply line temperature could be decreased and the consecutive reduction in capacity can be compensated by the absorption heat conversion system. The concept is explained using preliminary operational results, showing potential savings of up to 30% of primary district heat volumetric flow. Results of the first heating season are presented.

**Keywords:** Absorption heat conversion system, absorption chiller, district heating system, district heat return line temperature

## Introduction

At Technische Universität Berlin, single stage LiBr/water absorption chillers with a nominal cooling capacity of 50 kW (Bee) and 160 kW (Bumble Bee) have been developed and are marketed by the company WBS. In 16 installations 25 absorption chillers are currently monitored within an extensive field test called “Absorption chillers for CHCP Systems” (Feldtest Absorptionskälteanlagen für KWKK Systeme, **FAkS**). Recent publications proof the energy efficiency of the new chillers [1, 2].

One of the systems, located in Berlin/Germany has been operated in cooling mode several years since. In September 2017 adaptations of the system to enable operation in heat pump mode started. Final changes were made in December 2017.

This paper is dedicated to introduce the background and the concept of the installation, and to present first results.

## Concept of the heat conversion system

*Figure* Figure shows the flow scheme of the installation and table 1 gives an overview for different standard operation situations and operation regimes. The conventional house connection station (HCS) consists mainly of a plate heat exchanger.

The entire absorption heat conversion (AHCS) system consists of the absorption unit AU and two optional plate heat exchangers HE1 and HE2. The desorber of the AU is driven by the district heating supply line, SL. Unlike in conventional heat pumps, the heat input into the evaporator of the absorption unit (AU) is also taken from the district heating return line, RL. HE1 just separates the district heating grid from the external evaporator circuit because the pressures in the lines are different and the evaporator is used in cooling operation, also. In the measurements which are described below HE1 always in operation.



The reject heat from condenser and absorber is supplied to the building as useful supply heat. HE2 increases the temperature of the supply heat and the system efficiency as the district heating split stream at the desorber outlet is still at least 10K hotter than the heat transfer fluid at the condenser outlet. Assuming a coefficient of performance ( $COP_{AC}$ , heat flow of evaporator divided by heat flow of desorber) of 70% for the AU and a heat exchanger effectiveness  $\varepsilon$  of 93% for HE2, Table shows the expected temperatures and local grid capacity increase. Operation of the full system including HE2 under full load will reduce the district heat volumetric flow rate by 35%, still covering the same heating load at the same temperatures.

### **State of the art of heat pumps and absorption heat pumping systems**

Heat pumps are considered to be environmentally friendly, which has led to an annual growth rate of 8% for the number of heat pumps sold for European heating installation with water circuits in the years from 2006-2016 [3]. In this paper, however, the focus is on heat pumps for application in industry and district heating grids rather than in domestic use. Oluleye et al [4] have screened several heat pump options for reevaluating low grade waste heat including mechanical heat pumps, absorption heat pumps, and absorption heat transformers. They found market penetration for interconnected systems as they are common in industry to be slow. They argue that a system-oriented approach based on a primary fuel recovery ratio would provide more insight into the energy savings compared to using the COP of the heat revaluation process as a measure. Sayegh et al [5] performed a review of heat pump placement, connection options, and operational modes for European district heating and cooling grids, including options similar to the placement of the heat pump presented here. Both papers include a literature review regarding the development of thermally heat revaluation systems.

The concept discussed in this paper has first been presented by Petersen et al. (2014) [6]. As explained above, it is different from conventional heat pump systems in that reevaluating heat from low grade sources such as the district heating return line is only part of the use. The main achievement of this concept is the larger glide in the split stream of the water from the district heat supply line or, with other words, the lower return temperature in the district heat return line. This improves the energy efficiency of the local grid and potentially also the fuel use in the power plants, especially if back pressure steam turbines supply the heat to the network. In addition, since the driving temperature difference at the HCS is increased, the primary volumetric flow rate at the HCS is reduced, if the same heat flow is to be supplied to the building. Thus, the flow can be used elsewhere within the local grid, thus increasing the local capacity of the grid.

A similar concept has been installed and monitored in northern China [7, 8]. However, the latter concept includes one or more absorption heat pumps at the site of the power plant. Moreover, the integration of the absorption heat pump at the customer site as proposed in the referred paper is less sophisticated, since control valves for adjusting the volumetric flow rate distribution to the different heat exchangers are missing. However, the control of volumetric flow rate is important to take full advantage of the AHCS and to avoid mixing of streams at different temperatures. Another advantage of the system presented in the paper at hand is the possibility to be also used as an absorption chiller in the summer to supply the building with cooling (see Fig.1).

Operation in both modes of operation is controlled by an advanced control system, which allows for meeting more than one control objective, e.g., the chilled water temperature and load, and the district heating return line temperature below or at a fixed temperature, simultaneously [9]. However, the possibility of switching between heating and cooling mode

evokes some challenges for controlling the absorption process. These will be discussed briefly within the following section.

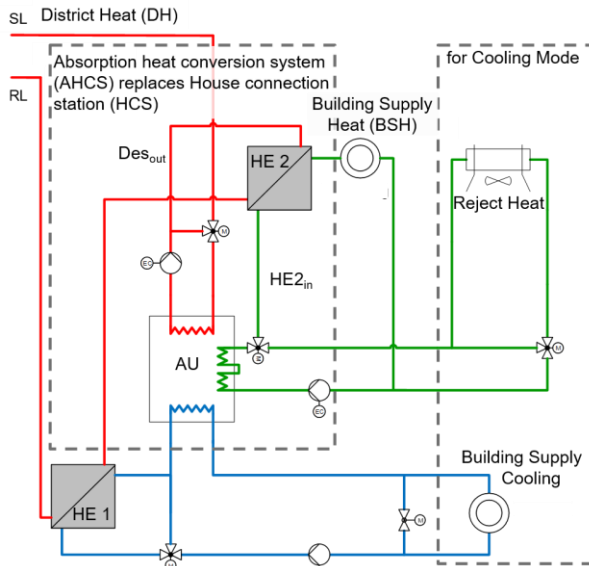


Figure 1: Flow scheme of Installation

Table 1: Temperatures and grid capacity increase for different load conditions (COP AC = 0.7,  $\epsilon=0.93$ )

Load		20%	50%	100%
Building Supply Heat Supply Line (BSH-SL)	[°C]	50	55	65
Building Supply Heat Return Line (BSH-RL)	[°C]	40	42	45
District Heat Supply Line (DH-SL)	[°C]	85	110	135
<b>Case 1: standard House Connection Station (HCS) only</b>				
District Heat Return Line (DH-RL)	[°C]	43	47	51
<b>Case 2: Absorption Unit (AU) without HE 2</b>				
Desorber Outlet (Des-out)	[°C]	60	65	75
District Heat Return Line (DH-RL)	[°C]	42.5	33.5	33
<b>Case 3: Absorption Heat Conversion System including HE 2</b>				
Desorber Outlet (Des-out)	[°C]	60	65	75
Heat Exchanger Hot Stream Outlet (HE2_out)	[°C]	48.8	54.2	63.9
District Heat Return Line (DH-RL)	[°C]	31.3	22.7	21.9
Heat Exchanger Cold Stream Inlet (HE2_in)	[°C]	47.9	53.4	63.0
<b>Increase of local grid capacity</b>				
Case 2: AU only	[%]	1%	21%	21%
Case 3: AU + HE2	[%]	28%	39%	35%

### Difference in process parameters between absorption heat pump and cooling mode

The external temperatures at the evaporator, absorber and condenser inlet of the absorption unit have to be significantly higher as compared to the operation as a chiller. This results in much higher pressures and especially pressure differences between the two vessels of the heat pump. Figure 2 shows a Dühring diagram containing pressures (dew points) and compositions of two typical process conditions for both modes of operation. When moving from chiller operation to heat pump mode as described, there are no critical limits due to process and operational fluid characteristics. Even when increasing the upper driving source temperature (see Figure 2) the process will shift to a lower salt mass fraction and increase the distance to both crystallization limit for the solution and freezing point for the refrigerant as the low temperature heat source is a lot higher than in cooling mode.

However, pressure levels of both evaporator and condenser will increase. Due to the logarithmic relation between temperature and saturation pressure, the pressure difference between high pressure vessel and low pressure vessel will increase significantly with non-trivial consequences for the components. Throttles and pumps within the process need to be adjusted as the operation conditions in cooling mode are limited to a pressure difference below 100 mbar (condenser pressure minus evaporator pressure), while to provide temperatures up to 70°C for heating in heat pump mode the required static pressure difference reaches values above 200 mbar. Pressure probes etc. have to be adjusted to keep process control and monitoring in proper operation. Moreover, the variability in pressure difference in heat pump mode is greater than in cooling mode since the supply temperature to the heating system of the building is adjusted to the ambient temperature over a wider range than the chilled and reject heat water temperatures during cooling mode. The throttling devices have to accommodate this and may need to be controlled accordingly.

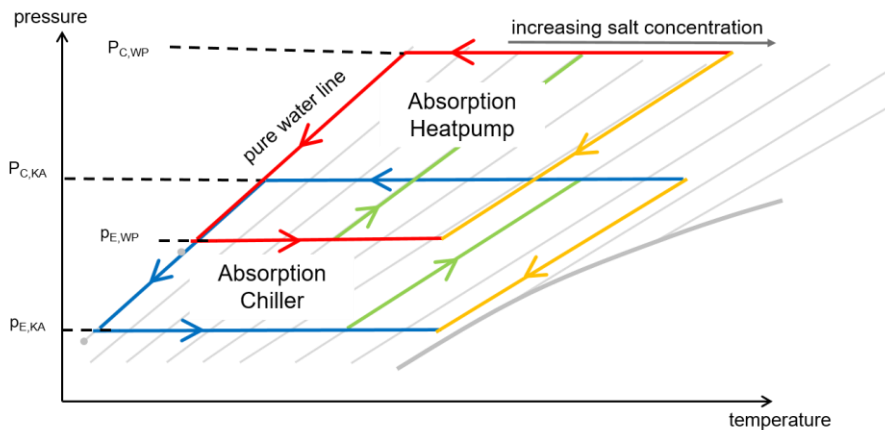


Figure 2: Process scheme AC and AHP

Moreover, changes in composition must be accounted for. As seen in Fig. 2 the process works with a significantly more diluted solution in heat pump mode. Consequently, with the salt content being constant, there will be more solution and the level of solution in the absorber sump (where the larger part of it is stored) will be higher in heat pump mode as compared to chiller mode. Conversely, the level of refrigerant in the evaporator sump (where refrigerant is stored) will be much lower - under some conditions even critically low. At low sump levels the pumps are prone to cavitate, which restricts the volumetric flow the pump is able to transfer. If, therefore, more water is introduced into the AU, raising filling levels, on the other hand, there is a larger chance of water spilling into the solution or vice versa, causing deterioration of performance of the system.

Moreover, the vacuum retention (purge) system is also affected. The units are equipped with a purge system, which is mainly driven by solution circulation. The functionality is strongly conditioned by the thermodynamic properties of the solution. These are, as mentioned above, affected by the higher evaporation pressure and more diluted solution. Operation has to be adjusted.

### Discussion and Results of operation

Results for one week in November 2017 from initial operation of the AHC without HE2 are shown in figure 3. The temperatures of the district heating grid (DH, supply line index SL, in red, return line RL dark orange) and building supply heat temperatures (BSH, SL in purple, RL in pink). The ambient temperature (index Amb in black) included for reference.

The district heating return temperature was up to 15 K below the building return temperature from Nov.16 on. This proves the concept and confirms the data from table 1. –During this time of operation, the heat exchanger HE1 was operated in parallel flow. A change of the installation of the heat exchanger to counter current operation and including heat exchanger HE2 should allow for even lower district heating return temperatures by about 10K.

In figure 4 the trends of district heating (DH, supply line index SL, in red, return line RL (dark orange) and building supply heat temperatures (BSH, SL in purple, RL in pink) are shown for one week at the end of February/ beginning of March of 2018, when ambient temperatures were the lowest in this winter and caused a reasonable heating load of about 50 kW with peaks of up to 65 kW. Ambient temperature (index Amb in black) is also depicted.

The district heat return line temperature ( $t_{DH,RL,is}$ ) was usually 2 to 5K below the building return line temperature, which would, of course, not be possible without the heat pump. For a comparison between operation with and without AHCS a theoretical district heating return line temperature (index DH,RL,th in orange) was calculated for heating directly from the grid by means of a heat exchanger at the same load and an efficiency of the heat exchangers (HE1, HE2

and HCS) of 0.93 The difference between the real return line temperature and this theoretical one was in the range of 4 to 15K.

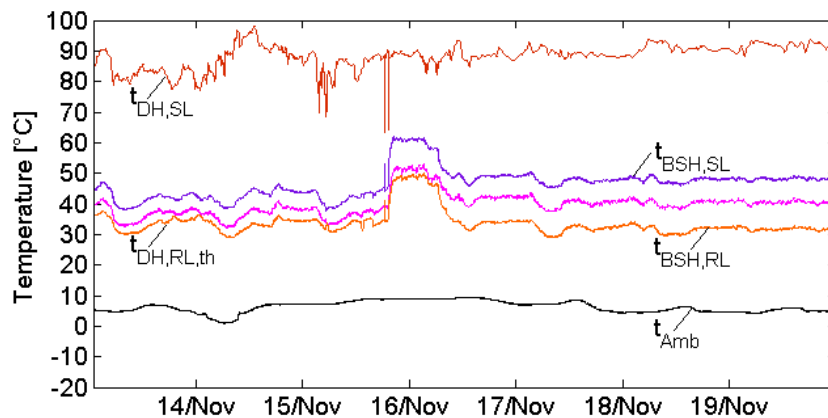


Figure 3: Operation HCS without HE2

Therefore, it can be concluded, that the absorption heat conversion system is generally working as intended. However, there are also four instances included in Figure during which the system was out of operation for about one hour. Reasons for system shut downs included an error of the external evaporator pump due to a defect of the circuit board, false triggering of a temperature limiter, and ill-adjusted control parameters. Other reasons for mal-functioning were low sump levels especially in the evaporator, as all refrigerant was absorbed by the solution as discussed above or was stored in the condenser sump. An adjustment of the throttle valve in the refrigeration circuit to avoid collection of refrigerant in the condenser has been required.

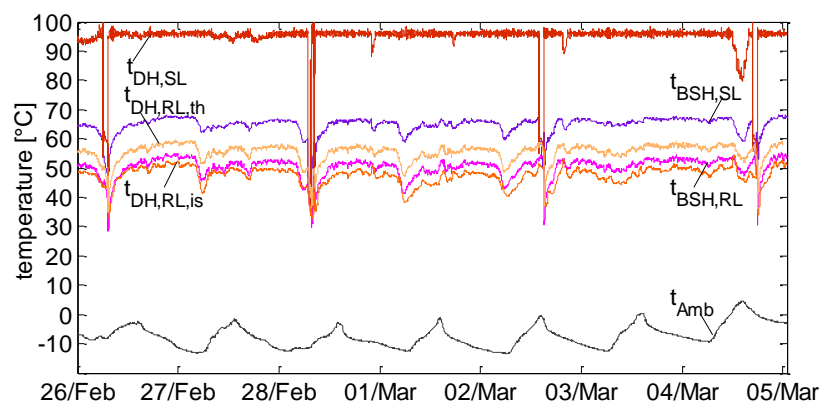


Figure 4: Temperatures for one week in March 2018

For further analysis figure 5 shows steady state values for the DH supply line temperature, the building return temperature and the temperature at the outlet of the HCS against the ambient temperature. Additionally, the theoretical value for the district heating return line temperature at the same load without AHCS and the difference between this theoretical value and the real, reduced return line temperature are plotted. All values for the temperature at the outlet of the AHCS are again lower than the building heating return line. When compared to the theoretical temperatures in the district heat return line the AHCS produces a decrease by 7K to 9K. This seems to be good, but especially at lower ambient temperatures and thus presumably higher loads, a greater advantage of the AHCS was expected (compare Table . There are two main reasons for not meeting the expectations. On the one hand, the minimum district heating volumetric flow in autonomous operation had to be adjusted manually as the control valve was designed for higher volumetric flows (for operation in cooling mode). Consequently, the

minimum volumetric flow during the monitoring period was set too high, causing a lower temperature glide between supply and return.

On the other hand, the expected heat demand according to the heat demand line should be compared to the measured values as provided in figure 6. At higher ambient temperatures and correspondingly lower building heating loads, the expected and measured values agree fairly well. At low ambient temperatures, however, the building load was much lower than previously expected. Ambient temperatures in the reported period were lowest during the night and on weekends, while they were significantly higher during the working days. Since the building is mainly used for office spaces, the convectors for distributing the heat to the individual rooms receive a lower set temperature during the night and on the weekends, thus causing a reduced load compared to low ambient temperatures during business hours.

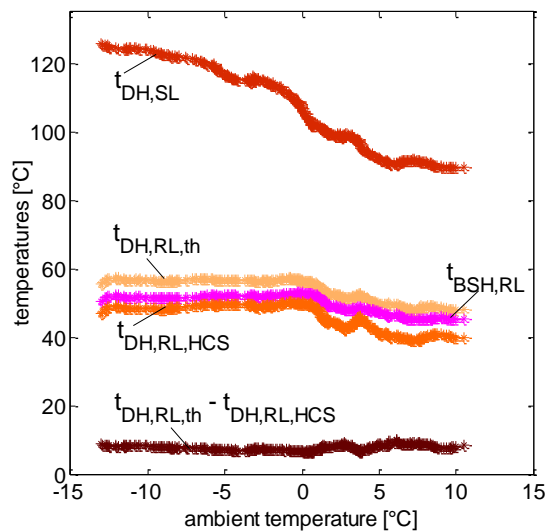


Figure 5: Temperatures in DH, heating of building and temperature difference for DH return line

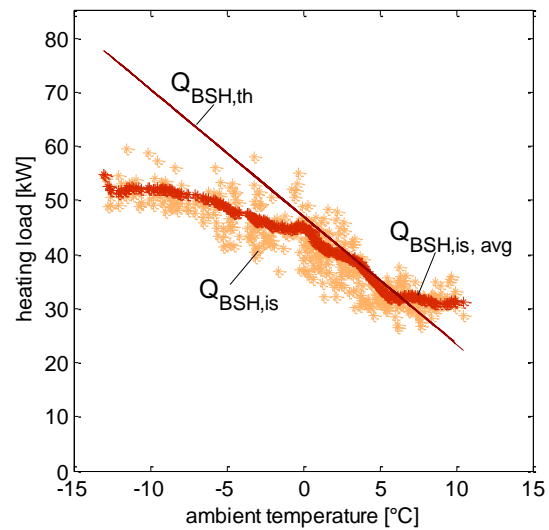


Figure 6: Theoretical, steady state and average of 40 steady states for building heating load

Figure 7 displays the volumetric flow rate  $V_{DH,AHCS}$ , which the AHCS draws from the district heating network. The figure also shows the theoretical value for conventional HCS use only ( $V_{DH,th}$ ). The difference between the flow rate of the AHCS to the standard HCS- flowrate ranges from savings of 16% to 28% - confirming that a significant increase in local grid capacity is feasible.

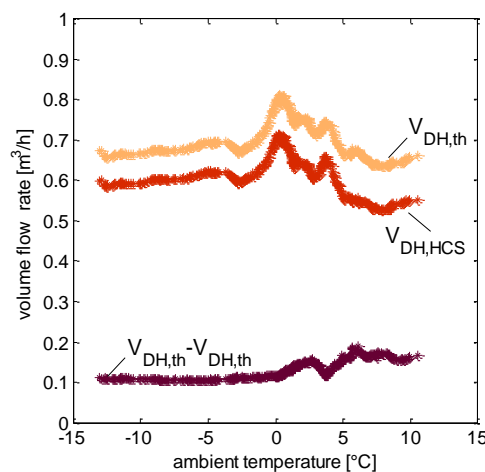


Figure 7: Volumetric flow rate for HCS only, AHCS and reduction of volumetric flow rate by employing the AHCS

## Conclusions

The results of the reported field test proofed the feasibility and usefulness of operating an absorption chiller in absorption heat pump mode, enabling a district heat return temperature 7-9K below the building return temperature while increasing local grid capacity up to 35% at full load. Since in the monitoring period very low ambient temperatures occurred only at times with low occupancy of buildings, performance at high heating loads could not be observed. At lower loads, however, the AHCS not only proved the concept but expectations were exceeded. Further monitoring of the system during the following years will be carried out in order to enlarge the data set.

For the future, the implementation of an automatically adjusting refrigerant valve is considered in order to choose the appropriate position depending on the load condition and associated pressure difference between condenser and evaporator. This has been observed to be of crucial importance for steady and efficient operation. Winter 2018/2019 is foreseen to reproduce the findings, and to overcome restrictions which have been encountered in the monitoring period so far, including full automatic control and operation.

TU Berlin is looking forward to accompany the installation within a follow up project, funding for which was applied for by the German Federal Ministry for Economic Affairs and Energy.

## Acknowledgement

We would like to acknowledge all our colleagues, scientific and field test partners within the discussed project, as well as funding by the German Federal Ministry for Economic Affairs and Energy and the administration by PTJ. The project funding is based on an energy efficiency action program, project number 03ET1171A.

Supported by:



on the basis of a decision  
by the German Bundestag

## References:

- [1] Paitazoglou, C., Petersen, S and Ziegler, F. „Primary energy analysis of the cold production for centralized and decentralized trigeneration systems” In Proc. of 14th International Symposium on District Heating and Cooling, pages 358-365, DHC, Stockholm, 09-2014
- [2] Hüls, W, Lanser, W, Petersen, S., and Ziegler, F. Performance of absorption chillers in field tests. ATE Elsevier. 1359-4311. 5. Feb.2018.
- [3] IEA HPT Magazine Vol. 35, No.2, 2017.
- [4] Oluleye G, et al, “Modelling and screening heat pump options for the exploitation of low grade waste heat in process sites”, Applied Energy, Elsevier, 2016
- [5] Sayegh, M.A., “Heat pump placement, connection and operational modes in European district heating”, Energy & Buildings, 2018
- [6] Petersen, S and Lanser, W, Poster, En+Eff 2014: 21. Fachmesse Energieeffizienz, Cologne, organized by AGFW
- [7] Fang, H, et al, “Key issues and solutions in a district heating system using low-grade industrial waste heat “, Energy, Elsevier, 2015
- [8] Li, Y, et al, “Technology application of district heating system with Co-generation based on absorption heat exchange”, Energy, Elsevier, 2015
- [9] Albers, J. and Ziegler, F. Control Strategies for Absorption chillers in CHPC-plants ensuring low hot water return temperatures. Proc. of Heat powered cycles conference. 2016.

# Temperature- vs. Pressure-Initiated Cycles for Upgrading Low Temperature Heat: Dynamic Comparison

I. Girnuk<sup>1,2\*</sup> and Yu. Aristov<sup>1,2</sup>

<sup>1</sup>Boreskov Institute of Catalysis, Lavrentiev ave., 5, Novosibirsk, 630090, Russia

<sup>2</sup>Novosibirsk State University, Pirogova str., 2, Novosibirsk, 630090, Russia

\*Corresponding author: girnik@catalysis.ru

## Abstract

This work addresses the study of methanol ad-/desorption dynamics for two adsorptive cycles aimed at upgrading low temperature heat. The first one is the common heat amplification cycle driven by a temperature jump. The second one is a novel “Heat from Cold” (HeCol) cycle recently proposed for upgrading the ambient heat in cold countries [1]. In the latter cycle, the adsorbent is deemed to be regenerated by a drop of the adsorptive pressure, whereas the heat needed for desorption is supplied from a natural heat reservoir at a quite low temperature close to 0°C (non-freezing water basins, such as river, lake, sea, etc). The aim of this study is to compare the methanol sorption dynamics initiated by the pressure drop as well as by the temperature jump between the same isosters of the tested cycles. A commercial activated carbon ACM-35.4 was used as an adsorbent. It has been shown that the dynamics for these two, quite different, ways of the process initiation are almost identical. The release/uptake curves can be described by exponential function with the characteristic time 104 and 78 s, respectively. This corresponds to the specific power 0.9-1.2 kW/kg which is acceptable for practical realization of AHT cycles for upgrading low temperature heat.

**Keywords:** Adsorptive heat transformation, activated carbon, methanol, driving force, HeCol cycle

## Introduction/Background

Adsorption heat transformation (AHT) is attracting increasing attention because of its ability of effective conversion/storage of waste and renewable heat [2,3]. At the moment, the AHT has made a significant progress and several adsorptive chillers/heat pumps have already appeared in the market [4]. These units are commonly driven by a temperature difference between the ambient (290–310 K) and an external heat source (330–400 K) which is used for adsorbent heating and regeneration. Recently, a novel AHT cycle “Heat from Cold” (or HeCol) has been suggested for amplification of the temperature potential of the ambient heat in cold countries [1].

The common HeCol cycle (1-2-3-4) suggested in [1] operates between three thermostats with constant temperatures  $T_L$ ,  $T_M$  and  $T_H$ , and consists of two isosters and two isotherms (Fig. 1a). The main feature of this cycle is that regeneration of adsorbent is performed at constant temperature  $T_M$  by dropping the vapour pressure over the adsorbent (stage 4-1). This pressure drop is ensured exclusively by low ambient temperature. Therefore, the regeneration does not need any supply of heat that has commercial value. The initial adsorbent state (point 1 on Fig. 1a) corresponds to temperature  $T_M$  and pressure of the adsorptive vapour  $P_L = P_0(T_L)$ , where  $P_0(T_L)$  is the saturation vapour pressure at low temperature  $T_L$  of the ambient air. Due to the low pressure  $P_L$ , the equilibrium adsorbate uptake  $w_1 = w(T_M, P_L)$  is small. Then, the adsorbent is heated up to temperature  $T_H$  (isoster 1-2). At point 2, the adsorber is connected to an evaporator maintained at  $T_M$  which generates the constant vapour pressure  $P_M = P_0(T_M)$ . This pressure jump causes the vapour adsorption that leads to an increase in the equilibrium uptake up to  $w_2 = w(T_H, P_M)$  (point 3 on Fig. 1a). The evaporation heat  $Q_{ev}$  is absorbed in the evaporator at  $T_M$  and the useful adsorption heat  $Q_{ads}$  is released at constant temperature  $T_H$

(isotherm 2-3) in the adsorber and supplied to the heating circuit of a Consumer. Then, the adsorber is disconnected from the evaporator and cooled down to temperature  $T_M$  (isoster 3-4). At point 4, the adsorber is connected to the condenser maintained at the low temperature  $T_L$  and pressure  $P_L = P_0(T_L)$ . This pressure drop results in the adsorbate removal to restore the initial uptake  $w_1 = w(T_M, P_L)$  (point 1). The heat  $Q_{des}$  needed for adsorbate desorption is supplied to the adsorbent from the water basin at temperature  $T_M$  (isotherm 4-1). The desorbed vapour is collected in the condenser releasing the heat  $Q_{con}$  to the ambient, and the cycle is closed.

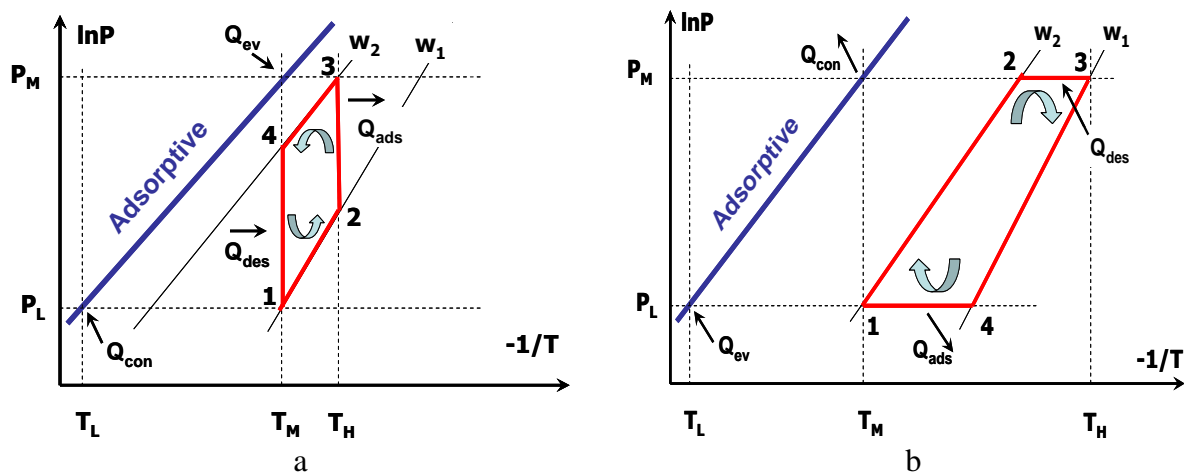


Fig. 1. P-T diagram of pressure-driven (a) and temperature-driven (b) 3T adsorptive cycles.

The suggested HeCol cycle is pressure-initiated (PI) and significantly differs from a classical adsorptive cycle (Fig. 1b) in which the adsorbate is exchanged along isobars (4-1) and (2-3). The adsorbent is regenerated due to the temperature jump from  $T_4$  to  $T_1$  at constant pressure  $P_M$ , thus being temperature-initiated (TI). Adsorption is initiated by a temperature drop from  $T_4$  to  $T_1$  (Fig. 1b) and takes place at constant pressure  $P_L$ . The first law efficiency and the useful heat are close for both cycles.

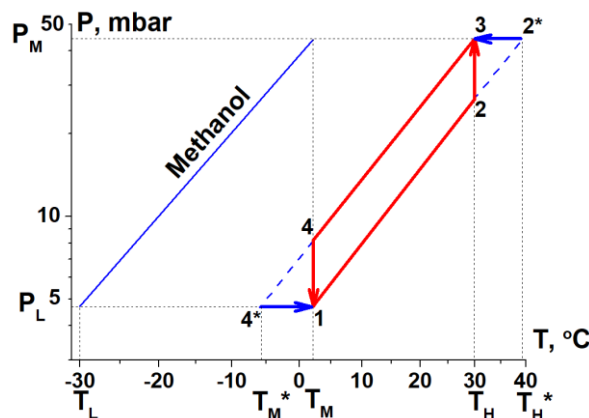


Fig. 2. P-T diagram of the studied cycles with isothermal (4-1 and 2-3) and isobaric (4\*-1 and 2\*-3) transitions between rich (3-4) and weak (1-2) isosters.

To find out which type of the desorption initiation (adsorbent regeneration) is preferable from the dynamic point of view, appropriate comparison of the both cycles is needed. The aim of this work has been to compare the dynamics of desorption (4-1 and 4\*-1) and adsorption (2-3 and 2\*-3) stages for two AHT cycles driven by pressure and temperature variations (Fig. 2).



For both cycles, the heat for methanol desorption is taken at a quite low temperature  $T_M = 2^\circ\text{C}$ , so that they can be used for upgrading the ambient heat in cold countries. A commercial activated carbon ACM-35.4 was used as methanol adsorbent according to [5,6].

### Experimental

Activated carbon ACM-35.4 (CECA Arkema group) has the average pore size  $d = 2.3$  nm, the specific surface area  $S = 1200$   $\text{m}^2\text{g}^{-1}$ , and the specific pore volume  $V = 0.69$   $\text{cm}^3\text{g}^{-1}$ . The tested cycles were plotted on the isosteric chart of the working pair "ACM-35.4 – methanol" taken from [7]. The three temperatures which uniquely define the tested AHT cycles were fixed at  $T_L = -30^\circ\text{C}$ ,  $T_M = 2^\circ\text{C}$ , and  $T_H = 30^\circ\text{C}$  or  $T_{H^*} = 39^\circ\text{C}$  (Fig. 2) that are typical for HeCol cycles [1]. The specific mass  $\Delta q_{eq}$  of methanol exchanged in this cycle was 0.08 g/(g-carbon). The boundary conditions for the regeneration were as follows: for the PI stage (4-1) -  $T_M = 2^\circ\text{C}$ ,  $P_4 = 8.2$  mbar and  $P_L = 4.7$  mbar; for the TI stage (4\*-1) -  $P_L = 4.7$  mbar,  $T_{M^*} = -6^\circ\text{C}$  and  $T_M = 2^\circ\text{C}$ . The boundary conditions for the adsorption stages were: for the PI stage (2-3) -  $T_H = 30^\circ\text{C}$ ,  $P_2 = 26.2$  mbar and  $P_M = 45.1$  mbar; for the TI stage (2\*-3) -  $P_L = 45.1$  mbar,  $T_{H^*} = 39^\circ\text{C}$  and  $T_H = 30^\circ\text{C}$ .

Dynamic comparison of pressure- and temperature-initiated adsorption at higher temperature is of great interest. For this purpose, additional dynamic experiments were carried out for adsorption transition between the same isosters but at higher methanol pressure and boundary temperatures (Fig. 3). The boundary conditions for isothermal adsorption (5 → 6) were  $T = 60^\circ\text{C}$  and the pressure jump 125 → 204 mbar, and for isobaric adsorption (5\* → 6) -  $P = 204$  mbar, the temperature drop 71 →  $60^\circ\text{C}$ . Such condition can be interesting, for example, for hot water production.

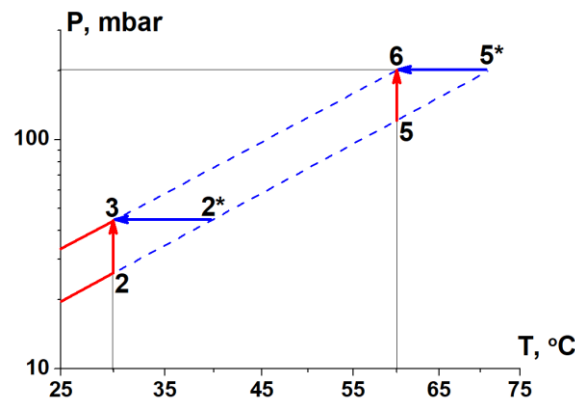


Fig. 3. P-T diagram of the studied adsorption stages for low (2-3 and 2\*-3) and high temperature heating (5-6 and 5\*-6).

The dynamics was studied in a custom-built kinetic set-up presented in [6] (Fig. 4). The experimental kinetic set-up consisted of the three main parts: a measuring cell with the studied adsorbent, a buffering vessel and a condenser/evaporator with liquid methanol. Loose grains of the carbon were placed on a metal support of the measuring cell as a monolayer. Diameter of the grains was 2.2-2.5 mm. The carbon mass was fixed at  $500 \pm 2$  mg.

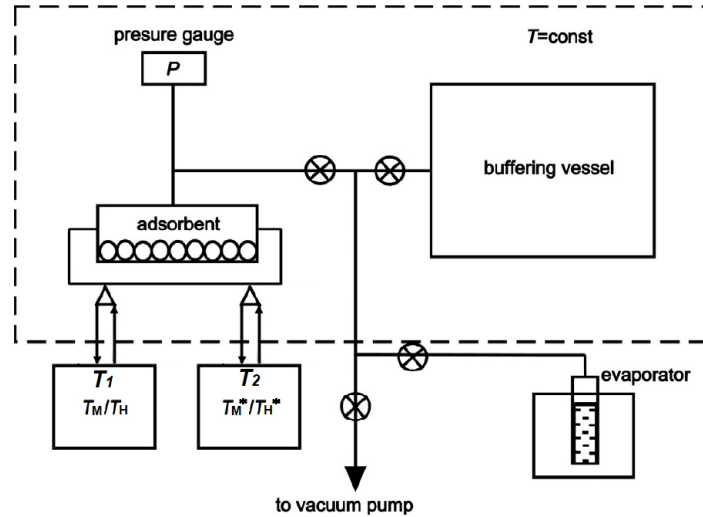


Fig. 4. Schematics of the kinetic set-up.

To measure the dynamics of pressure-initiated desorption the measuring cell was filled with methanol vapour from the evaporator to reach the initial desorption pressure  $P_4 = 4.7$  mbar. The adsorbent was cooled down to the desorption temperature  $T_M$  by thermostat  $T_1$ . After setting the adsorption equilibrium, the measuring cell was disconnected from the evaporator. The buffering vessel was filled with methanol vapour from the evaporator to reach the methanol pressure 3.6 mbar. To start the desorption run, the measuring cell was connected to the buffering vessel which led to a drop of the methanol pressure in the cell to 3.7 mbar. This initiated the methanol desorption from the sample which resulted in the gradual increase in the methanol pressure  $P(t)$  to the final (equilibrium) pressure  $P_1 = 4.7$  mbar. This pressure was recorded each 1 s by an absolute pressure transducer Barocel™ 600 with an accuracy of  $\pm 0.15\%$ . The pressure evolution  $P(t)$  was used for calculating the methanol uptake/release  $q(t)$  as

$$q(t) = \Delta q_{eq} \cdot (P(t) - P(t = 0)) / (P(t \rightarrow \infty) - P(t = 0)). \quad (1)$$

The accumulated error in the absolute methanol loading was  $\pm 10^{-3}$  kg/kg that leads to the accuracy of the differential methanol loading  $q(t)$  equal to  $\pm 3\%$ .

For temperature-initiated desorption the measuring cell was filled with methanol vapour at the pressure  $P_L = 4.7$  mbar and the adsorbent was cooled down to the initial desorption temperature  $T_M^* = -6^\circ\text{C}$  by thermostat  $T_2$ . To initiate methanol desorption, the adsorbent was heated up to the final desorption temperature  $T_M = 2^\circ\text{C}$  by switching from thermostat  $T_2$  to  $T_1$ . Experiments for temperature- and pressure-driven adsorption were carried out in a similar way.

## Results and Discussion

The main finding of this study is that the kinetic curves for both PI and TI desorption stages are identical (Fig. 5a). Hence, the regeneration dynamics does not depend on the regeneration path, either isothermal (4-1) or isobaric (4\*-1). The release curves can be well approximated by the exponential function (Fig. 4a)

$$\Delta q = (0.08 \cdot g/g) \cdot (1 - e^{-t/\tau}) \quad (2)$$

with a single characteristic time  $\tau = 104 \pm 6$  s regardless the way of the desorption initiation (Table 1). This time allows an upper limit of the specific rate of methanol desorption  $R_0 = \Delta q/\tau = 0.8$  g/(kg·s) to be calculated as well as the maximum specific power  $W_{\max}$

supplied to the adsorbent at short desorption time  $W_{\max} = \Delta H \cdot \Delta q / \tau = 0.95 \text{ kW/kg}$ , where  $\Delta H$  is the heat of methanol desorption (1230 kJ/kg [6]).

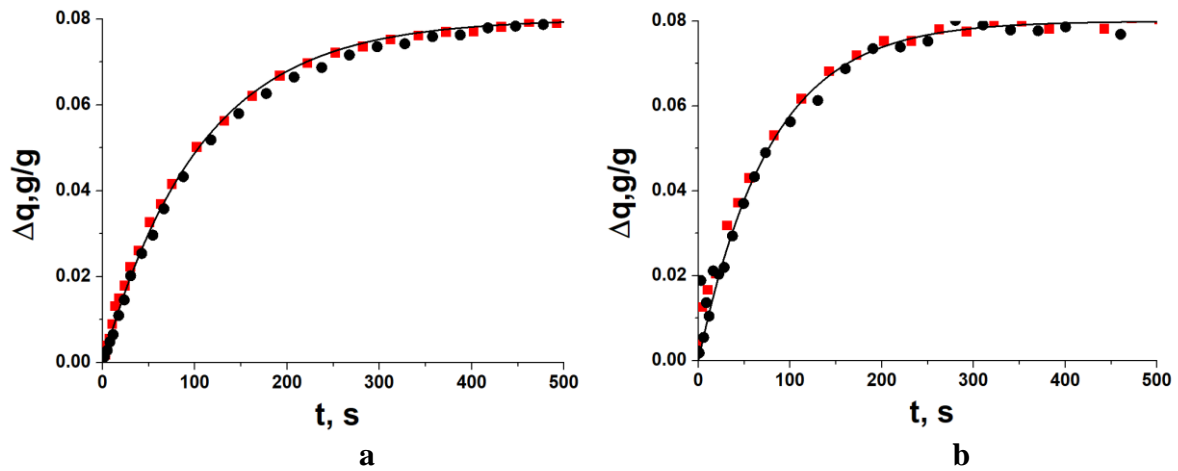


Fig. 5. Methanol release (a) and uptake (b) curves as a function of time for pressure- (4-1) and (2-3) (●) and temperature-initiated (4\*-1) and (2\*-3) (■) stages. Solid lines – exponential approximation.

Table 1. Characteristic time  $\tau$ , specific sorption rate  $R_0$  and maximum specific power  $W_{\max}$  for various experimental runs.

Run	$\tau$ , s	$R_0$ , g/(kg·s)	$W_{\max}$ , kW/kg
1 → 4	115	0.7	0.9
1 → 4*			
4 → 1	104	0.8	0.95
4* → 1			
2 → 3	78	1.0	1.3
2* → 3			
3 → 2	68	1.2	1.4
3 → 2*			
5 → 6	58	1.4	1.7
5* → 6			
6 → 5	49	1.6	2.0
6 → 5*			

The same trend is found for the adsorption dynamics which does not depend on whether the path is isobaric (2\*-3) or isothermal (2-3) (Fig. 5b). Again, both uptake curves are exponential with  $\tau = 78 \pm 4 \text{ s}$  (Table 1) that is shorter than for the desorption run. Accordingly, the initial adsorption rate  $R_0 = 1.0 \text{ g/(kg·s)}$  and the maximum useful power  $W_{\max} = 1.3 \text{ kW/kg}$  are also larger. The specific useful power corresponding to the conversion degree 80%  $W_{0.8} = 0.5 \text{ kW/kg}$ . It means that for generating 5 kW of heating power 10 kg of carbon is necessary that is reasonable and acceptable for practical realization of the HeCol cycle. More compact HeCol units can be expected if utilize smaller grains of the carbon or advanced adsorbents which exchange more methanol in the cycle [8,9].

For the TI desorption, the initial power can be used to evaluate the heat transfer coefficient  $\alpha$  between the carbon grains and the metal support from the heat balance at  $t = 0$ :

$$\alpha \cdot S \cdot \Delta T = W_{\max} \cdot m. \quad (3)$$

Here  $S$  is the heat transfer surface area ( $S = 0.0006 \text{ m}^2$  in our case), and  $\Delta T$  is the initial temperature difference ( $\Delta T = T_M - T_M^* = 8\text{K}$ ). The obtained  $\alpha$ -value is equal to  $97 \pm 10 \text{ W}/(\text{m}^2 \text{ K})$  that is close to the values found in [6]:  $75 \pm 10 \text{ W m}^{-2} \text{ K}^{-1}$  and  $135 \pm 15 \text{ W m}^{-2} \text{ K}^{-1}$  for adsorption and desorption, respectively.

A similar independence of dynamics from the type of ad-/desorption initiation was found for the reverse processes (Fig. 6) and processes at higher pressure/temperature (Fig. 7). For the same  $T$ - or  $P$ -variation, all the desorption runs are faster than the adsorption runs (about 15% in terms of the characteristic time, Table 1). This can be due to a convex shape of the methanol sorption isotherm for ACM-35.4 which is profitable for faster adsorption [10].

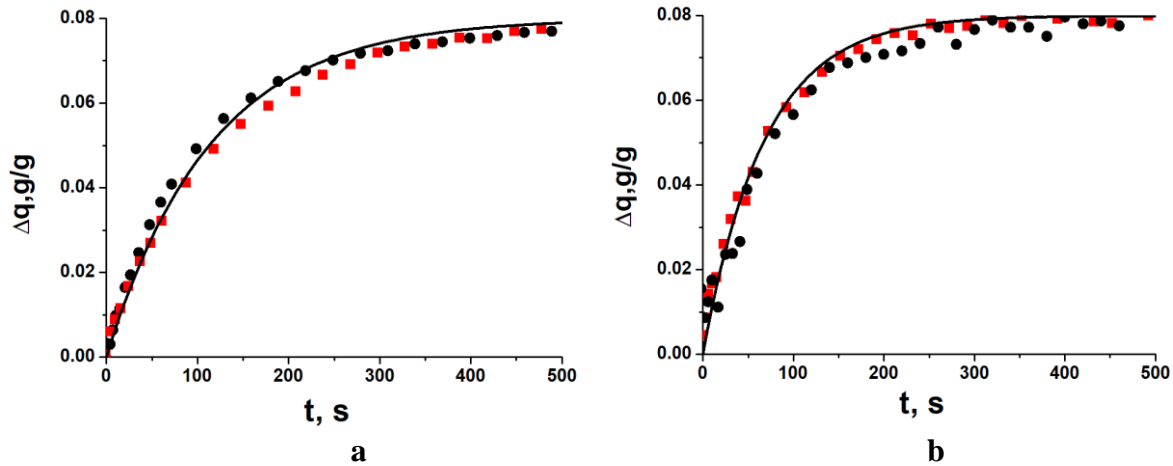


Fig. 6. Methanol uptake (a) and release (b) curves as a function of time for pressure- (1-4) and (3-2) (●) and temperature-initiated (1-4\*) and (3-2\*) (■) runs. Solid lines – exponential approximation.

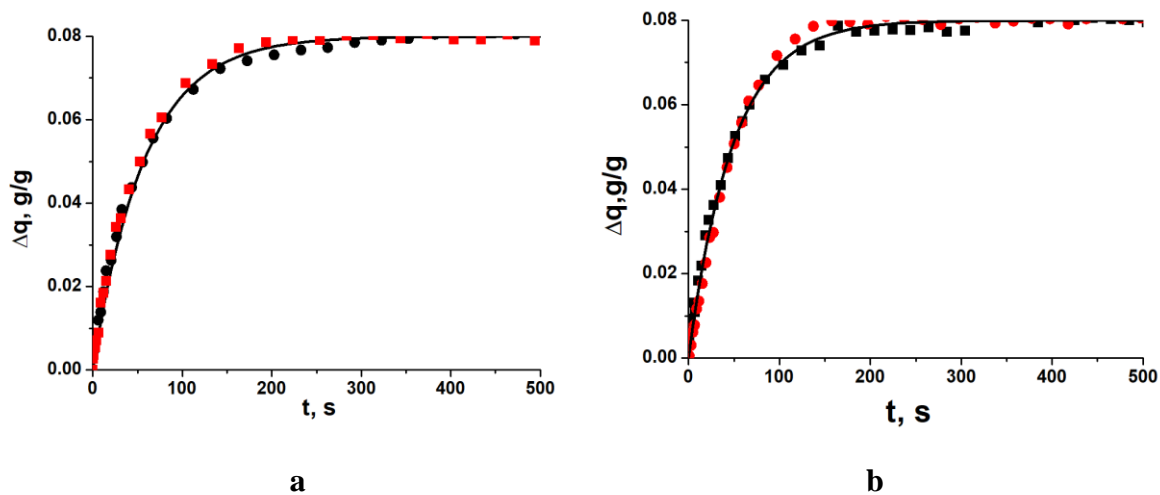


Fig. 7. a - Methanol uptake curves for pressure- (5 → 6) (●) and temperature-initiated (5\* → 6) (■) runs. b - Methanol release curves for pressure- (6 → 5) (●) and temperature-initiated (6 → 5\*) (■) runs. Solid line – exponential approximation.

The revealed invariance of ad-/desorption dynamics is somewhat unexpected because isothermal and isobaric processes are initiated by quite different driving forces, namely, the fast pressure or temperature change, respectively. Indeed, for the PI desorption process, at  $t = 0$ , right after the pressure drop, the driving force for heat transfer *equals zero* because the system is isothermal and there is no temperature gradient. At the same time, the driving force for mass transfer *is maximal*. This is opposite to the TI desorption, for which at  $t = 0$ , right after the temperature

jump, the driving force for heat transfer is *maximal*, whereas the driving force for mass transfer is *zero*. The invariance is likely to indicate that heat and mass transfer processes are strongly coupled so that after a short transient period a steady state regime is established in the adsorbent, which seems to be similar, regardless the initial driving force ( $\Delta P$  or  $\Delta T$ ) applied. The formation of this steady-state regime for TI adsorption cycle was numerically studied in [11], and the time interval for setting the stationary mode was found to be ca. 5 s. At longer time, the heat and mass transfer processes are strongly coupled and can not be separately considered. No similar study has been done yet for PI adsorption cycles.

Mathematical modeling of PI (4 $\rightarrow$ 1) and TI (4\* $\rightarrow$ 1) desorption by utilizing the model presented in [13] confirms that the PI and TI dynamic curves are close to each other at the conditions of HeCol cycle. Analysis of the average grain temperature during the desorption process shows that after 5 s the temperature of the grains during the PI desorption becomes close those during TI desorption. This means that shortly after the start of the process driving force of both PI and TI desorption becomes equal which led to equal kinetic curves.

Since isosters (1-2-5) and (3-4-6) are lines with the constant uptakes  $w_1$  and  $w_2$ , the independence of dynamics of the transitions between them on the transition path may indicate that the process rate can be written as  $A = -k(T) [w(t) - w(t = \infty)]$ , where  $k(T) = k_0 \exp[-E_a/(RT)]$  is the temperature dependent rate constant,  $E_a$  is the apparent activation energy, and  $R$  is the universal gas constant. If so, the temperature dependence of the characteristic time  $\tau(T) = 1/k(T) = \exp[E_a/(RT)]/k_0$  can be used to determine  $E_a$  (Fig. 8). The apparent activation energy is equal to 9 kJ/mol and 10 kJ/mol for adsorption and desorption runs.

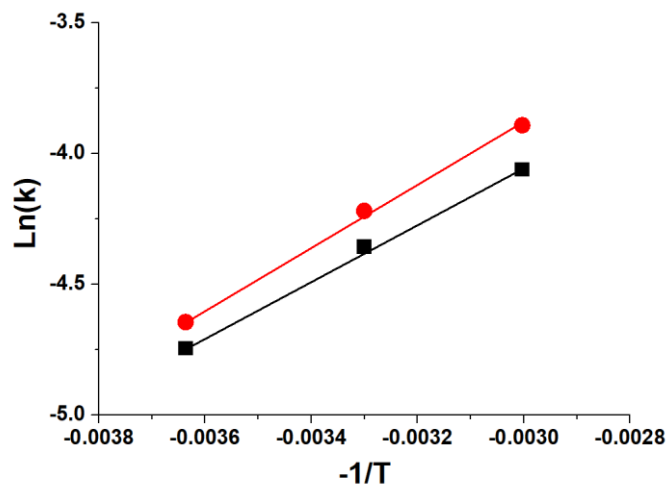


Fig. 8. The Arrhenius plot  $\ln(k)$  vs  $(-1/T)$  for the studied adsorption (■) and desorption (●) runs.

### Summary/Conclusions

Dynamics of the methanol ad-/desorption on/from the loose grains of activated carbon ACM-35.4 was studied for flat configurations of adsorbent bed and two heat amplification cycles – pressure- and temperature-initiated (PI and TI).

The most important findings are: 1) the sorption dynamics does not depend on the way of the process initiation, either PI or TI; 2) all the dynamic curves can be described by exponential function with a single characteristic time equal to 104 and 78 s for the desorption and adsorption, respectively; 3) the maximal specific power reaches 0.9 kW/kg for the desorption

runs and 1.2 kW/kg for the adsorption runs which can be considered acceptable for practical realization of the HeCol cycle.

### Acknowledgements

This work was supported by the Russian Science Foundation (grant 16-19-10259).

### References:

- [1] Aristov, Yu. I., Adsorptive transformation of ambient heat: a new cycle, *Applied Thermal Engineering*, 2017. doi:[10.1016/j.applthermaleng.2017.06.051](https://doi.org/10.1016/j.applthermaleng.2017.06.051)
- [2] Tu, Y.D., Wang, R.Z., Hua, L.J., Ge, T.S., Cao, B.Y. Desiccant-coated water-sorbing heat exchanger: Weakly-coupled heat and mass transfer, *International Journal of Heat and Mass Transfer*, 2017. doi:[10.1016/j.ijheatmasstransfer.2017.05.047](https://doi.org/10.1016/j.ijheatmasstransfer.2017.05.047)
- [3] Freni, A., Maggio, G., Sapienza, A., Frazzica, A., Restuccia, G., Vasta, S. Comparative analysis of promising adsorbent/adsorbate pairs for adsorptive heat pumping, air conditioning and refrigeration, *Applied Thermal Engineering*, 2016. doi:[10.1016/j.applthermaleng.2016.05.036](https://doi.org/10.1016/j.applthermaleng.2016.05.036)
- [4] Deng, J. Wang, R.Z., Han, G.Y. A review of thermally activated cooling technologies for combined cooling, heating and power systems, *Progress in Energy and Combustion Science*, 2011. doi:[10.1016/j.pecs.2010.05.003](https://doi.org/10.1016/j.pecs.2010.05.003)
- [5] Boubakri, A., Arsalane, M., Yous, B., Ali-Moussa, L., Pons, M., Meunier, F., Guillemintot, J. Experimental study of adsorptive solar-powered ice makers in Agadir (Morocco)—2. Influences of meteorological parameters, *Renewable Energy*, 1992. doi:[10.1016/0960-1481\(92\)90055-8](https://doi.org/10.1016/0960-1481(92)90055-8)
- [6] Gordeeva, L., Aristov, Yu., Dynamic study of methanol adsorption on activated carbon ACM-35.4 for enhancing the specific cooling power of adsorptive chillers, *Applied Energy*, 2014. doi:[10.1016/j.apenergy.2013.11.073](https://doi.org/10.1016/j.apenergy.2013.11.073)
- [7] Gordeeva, L.G., Tokarev, M.M., Aristov, Yu.I. New Adsorption Cycle for Upgrading the Ambient Heat, *Theoretical Foundations of Chemical Engineering*, 2018. doi: [10.7868/S0040357118020057](https://doi.org/10.7868/S0040357118020057)
- [8] Gordeeva, L.G., Tokarev, M.M., Shkatulov, A., Aristov, Yu.I. Testing the lab-scale “Heat from Cold” prototype with the “LiCl/silica –methanol” working pair, *Energy Conversion and Management*, 2018. doi:[10.1016/j.enconman.2017.12.099](https://doi.org/10.1016/j.enconman.2017.12.099)
- [9] Tokarev, M.M., Grekova, A.D., Gordeeva, L.G., Aristov, Yu.I. Adsorption cycle "Heat from Cold" for upgrading the ambient heat: the testing a lab-scale prototype with the composite sorbent CaClBr/silica, *Applied Energy*, 2018. doi:[10.1016/j.apenergy.2017.11.015](https://doi.org/10.1016/j.apenergy.2017.11.015)
- [10] Glaznev, I.S., Ovoshchnikov, D.S., Aristov, Yu.I. Kinetics of water adsorption/desorption under isobaric stages of adsorption heat transformers: The effect of isobar shape, *International Journal Heat Mass Transfer*, 2009. doi:[10.1016/j.ijheatmasstransfer.2008.09.031](https://doi.org/10.1016/j.ijheatmasstransfer.2008.09.031)
- [11] Okunev, B.N., Aristov, Yu.I. Modeling of isobaric stages of adsorption cooling cycle: Transient and quasi-stationary mode, *Applied Thermal Engineering*, 2013. doi: [10.1016/j.applthermaleng.2013.01.018](https://doi.org/10.1016/j.applthermaleng.2013.01.018).

# Adsorption heat transformation: applicability for various climatic regions of the Russian Federation

A.D. Grekova<sup>1\*</sup>, L.G. Gordeeva<sup>1</sup>, A. Sapienza<sup>2</sup> and Yu.I Aristov<sup>1</sup>

<sup>1</sup>Boreskov Institute of Catalysis, Ac. Lavrentiev av. 5, Novosibirsk 630090, Russia

<sup>2</sup> Institute for Advanced Energy Technologies "Nicola Giordano", Via Salita S. Lucia sopra Contesse 5, Messina 98126, Italy

\*Corresponding author: grekova@catalysis.ru

## Abstract

Adsorption heat transformation (AHT) is an energy saving and environment friendly emerging technology for conversion of renewable and waste heat of low-temperature potential. For each specific AHT cycle, the adsorbent with particular (optimal) properties is required. They depend on the climatic zone in which the AHT cycle is realized, the specific application (cooling, heating, heat storage, or amplification of the temperature potential), and heat source used for regenerating the adsorbent. Therefore, for effective AHT, a working pair "adsorbent - adsorbate" should be intelligently selected in accordance with the mentioned factors. In this work, the applicability of the ATH technology in the Russian Federation (RF) was analyzed. Proper AHT applications were selected for selected RF zones on the base of their climatic conditions. Adsorption equilibrium data for various "adsorbent – adsorbate" pairs were collected from the literature and analyzed to select the most suitable pairs for the particular application/zone.

**Keywords:** Adsorption heat transformation, water, methanol, adsorption potential, database.

## Introduction/Background

Significant progress has been achieved in AHT over the past decades [1,2]. This emerging technology can be used for various applications, such as heat storage, cooling, heating, amplification of the temperature potential, and their combinations. The choice of application is dictated, first of all, by the particular climatic zone where the AHT unit is used and the heat sources/sinks available. The efficiency of AHT cycles depends mainly on the agreement between the operating conditions of the AHT cycles and the adsorption equilibrium of the employed working pair.

**Table 1.** The types of climate in the RF.

Type of climate
1 arctic
2 subarctic
3 moderate climate
3A moderately continental
3B continental
3C acutely continental
3D monsoon
4 subtropical

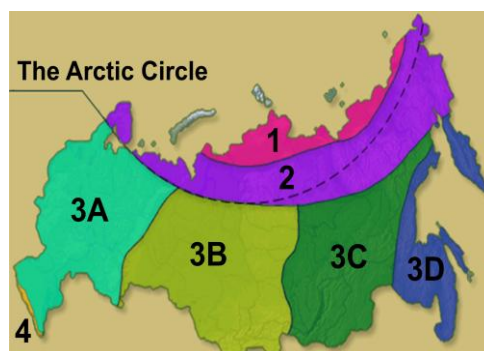


**Figure 1.** Climatic zones of the RF [3].

This work is aimed at the choice of the AHT applications optimal for typical RF climatic regions and selection of the suitable working pairs for them. First, the climatic conditions of various RF regions (Table 1, Fig. 1) are analyzed and the proper AHT applications are selected for each zone. Specific requirements to an adsorbent optimal for the selected zone and application are considered in term of the adsorption potential  $\Delta F = RT \ln[P_0(T)/P]$ ,

corresponding to the adsorption and regeneration stages of the analyzed cycle. Finally, the most suitable working pairs are selected for the specific application/zone by analysis literature data on adsorption equilibrium of numerous common and innovative materials with water and methanol. The latter analysis is based on the use of the adsorption potential as a universal measure of the “adsorptive – adsorbent” affinity that allows the amount of the working fluid exchanged in the cycle to be evaluated.

## Discussion and Results

### *Analysis of the AHT cycles demanded in the RF and appropriate working pairs*

The average day and night temperatures (Fig. 2), the average monthly temperatures are collected for each month of a year using Meteornorm library of climatic data [4] for 7 different locations in the RF. These data are used for further analysis of the relevant AHT applications for each zone.

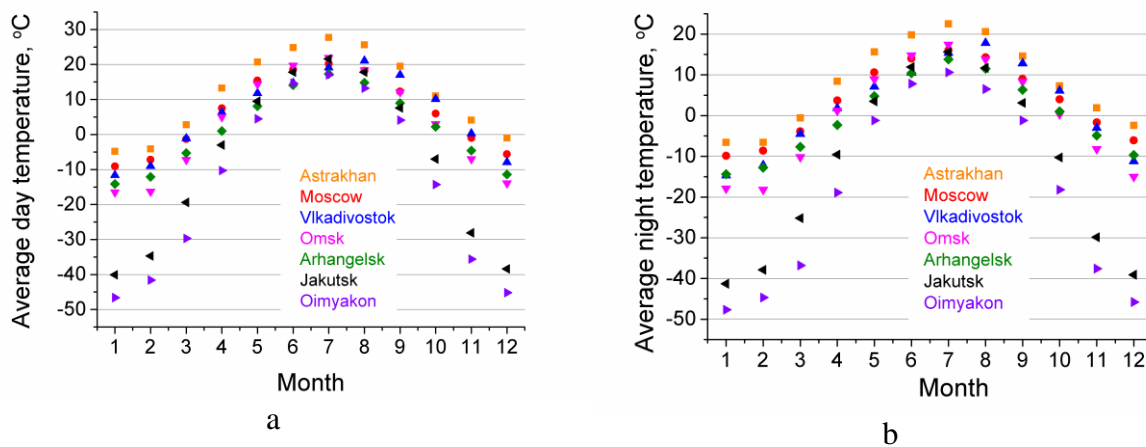


**Figure 2.** Average day (a) and night (b) temperatures for 7 climatic RF regions [4].

The climate in the RF is quite cold, therefore the most demanded AHT applications are heating, seasonal heat storage, and amplification of the heat temperature potential, including the ambient heat [5, 6]. They can be realized during winter time only if a heat source at 2-20°C is available to drive evaporation process, e.g. underground water, heat wastes, etc. Another opportunity is to use highly efficient solar collectors that can provide heat at 10-20°C even at cold climate of zones 1-3 (Fig. 1). The heating/storage modes are more realistic in zone 3A during autumn and spring. For their realization, the adsorbents which ensure a large temperature lift (at least 20-30°C) are required. During summer time there is a certain need for air conditioning in the Southern Russia (zone 4 in Fig.1).

For seasonal heat storage and amplification of temperature potential, methanol and ammonia should be used as working fluids. In this communication, only methanol is considered. Water can be utilised as adsorptive for adsorption applications at above-zero temperature, e.g. air conditioning and warm water production in summer.

Requirements to the adsorbent optimal for specific AHT cycle are formulated in terms of the boundary adsorption potentials  $\Delta F_1$  and  $\Delta F_2$ , corresponding to the regeneration and adsorption stages of the selected cycle, respectively:

$$\Delta F_1 = -RT_{\text{reg}}\{\ln[P(T_{\text{con}})/P(T_{\text{reg}})]\}, \quad (2)$$

$$\Delta F_2 = -RT_{\text{ads}}\{\ln[P(T_{\text{ev}})/P(T_{\text{ads}})]\}, \quad (3)$$



where  $T_{reg}$ ,  $T_{con}$ ,  $T_{ads}$  and  $T_{ev}$  are the regeneration, condenser, adsorption and evaporation temperatures, which are selected in accordance with the climatic data of Fig. 2, the temperature of the driving heat source and the required useful heat.

For the working pairs, whose adsorption equilibrium obeys the Polanyi principle of temperature invariance, the uptake  $w$  is a function of the only parameter – the adsorption potential  $\Delta F$ ,  $w = f(\Delta F)$ . The equilibrium data on water and methanol adsorption on common and innovative adsorbents (silica gels, zeolites, AlPOs, SAPOs, MOFs, Composites “Salt inside Porous Matrix” - CSPMs) are collected from the available literature [7-10]. These data are presented in the coordinates “ $w - \Delta F$ ” (Figs. 3 and 4) and approximated by the function

$$w = (A \cdot \Delta F + B) / \{1 + \exp[-k_1 \cdot (\Delta F - C_1)]\} + L / \{1 + \exp[-k_2 \cdot (\Delta F - C_2)]\}, \quad (1)$$

where  $A$ ,  $B$ ,  $C_1$ ,  $C_2$ ,  $L$ ,  $k_1$ ,  $k_2$  are fitting parameters, estimated using non-linear least squares method. These parameters are presented in Table 2 for selected pairs.

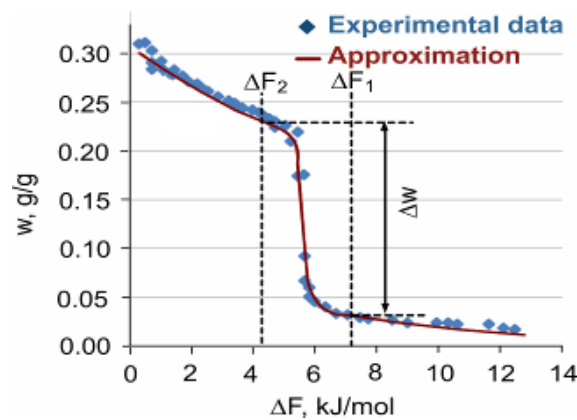


**Figure 3.** Experimental and calculated equilibrium uptakes for the working pair "AlPO-18 – water vapour".

**Table 2.** Approximation parameters for the selected working pairs.

Water							
	A	B	$k_1$	$C_1$	L	$k_2$	$C_2$
Silica Fuji RD	-0.116	0.383	-0.534	2.594	0.190	-0.432	6.563
ALPO -18	0.017	7.930	-0.213	-18.728	0.172	-10	5.607
UiO66	0.048	9.30E-02	-10	3.177	0.414	-0.657	1.373
Ca(NO <sub>3</sub> ) <sub>2</sub> /silica	-0.021	2.18E-01	-10	5.93	2.245	-0.3	-7.257
Methanol							
ACM35	-0.056	0.292	-0.682	8.374	0.149	-6.488	9.038
MIL101Cr	-0.019	0.783	-2.150	2.993	0.65	-0.110	3.313
MaxSorb	-0.216	3.67E-01	-1.236	7.975	0.997	-4.792	10.186
LiCl/silica	-0.196	1.521	-10	4.770	-0.656	-2.623	-1.449

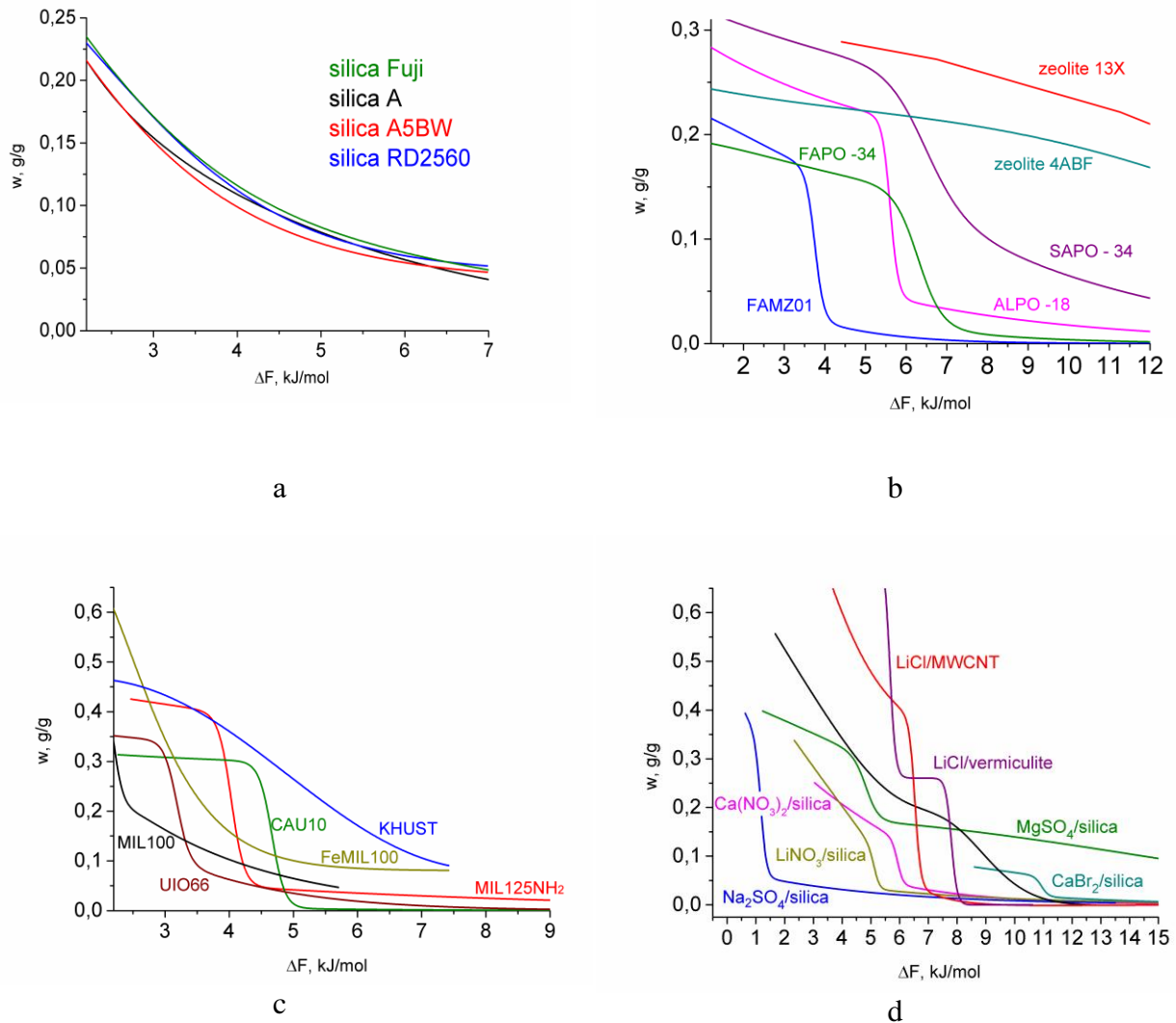


**Figure 4.** The adsorption equilibrium data for tested adsorbents of water vapour [7-10]: a) silica gels, b) zeolites and MeAPOs, c) MOFs, d) CSPMs.

The most suitable working pairs for the AHT cycles demanded for the RF climatic zones were selected taking into account the amount of the working fluid  $\Delta w$  exchanged between the boundary adsorption potential  $\Delta F_1$  and  $\Delta F_2$ ,  $\Delta w = w(\Delta F_2) - w(\Delta F_1)$  (Fig. 3).

### Cooling/Air conditioning

Since the average daily temperature for the analyzed regions does not exceed 25°C, the air conditioning application is considered only for Astrakhan, a city located in the South of Russia. For all other regions, the adsorption cooling of food/drugs is considered. The boundary adsorption potentials  $\Delta F_1$  and  $\Delta F_2$  are calculated (Table 3) according eqs. (2), and (3) taking into account the following operating temperatures:  $T_{con}$  and  $T_{ads}$  are equal to the maximum day time temperature of the hottest month of the year (July) for each location.  $T_{ev}$  equals the required temperature  $T_{req}$  of useful heat (3°C for cooling (Fig. 5) and 10°C for air-conditioning). The regeneration temperature was selected based on the climatic data and the amount of solar days in summer time.

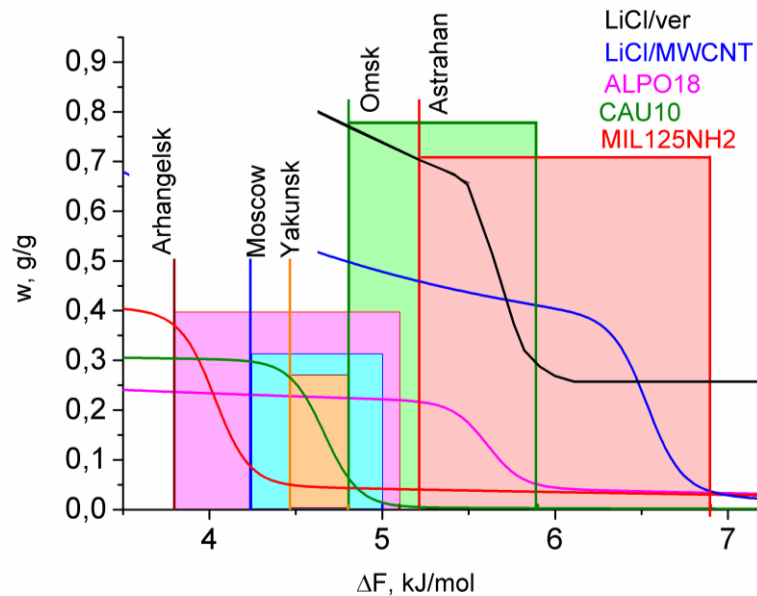


**Figure 5.** Cooling cycles ( $T_{ev} = 3^{\circ}\text{C}$ ) for different climatic regions and the universal curves of water adsorption on the adsorbents, optimal for each region.

The operating conditions of the cooling cycles for different climatic regions for water as refrigerant are presented in Fig. 5 as the frames confined between adsorption potential  $\Delta F_1$  and  $\Delta F_2$ . LiCl/MWCNT, LiCl/vermiculite, CAU10, and MIL125-NH<sub>2</sub> appear to show the best properties for cooling in Omsk, Astrachan, Moscow, and Archangelsk regions, respectively (Table 3).

**Table 3.** The boundary conditions and the water adsorbents promising for cooling.

City	$T_{reg}, ^{\circ}\text{C}$	$\Delta F, \text{kJ/mol}$		Adsorbent	$\Delta w, \text{g/g}$
		$\Delta F_2$	$\Delta F_1$		
Air conditioning					
Astrakhan	85	4.0	6.9	LiCl/MWCNT	0.6
Cooling					
Astrakhan	85	5.2	6.9	LiCl/vermiculite	0.3
				LiCl/MWCNT	0.4
Omsk	75	4.8	5.9	LiCl/vermiculite	0.5
				ALPO - 18	0.2
Yakutsk	65	4.5	4.8	CAU10	0.2
Moscow	65	4.2	5.0	CAU10	0.3
Oimyakon	65	4.2	4.8	CAU10	0.3
Vladivostok	60	3.9	4.7	MIL125NH <sub>2</sub>	0.3
Arkhangelsk	60	3.8	5.1	MIL125 NH <sub>2</sub>	0.3

### Heating

We consider production of the warm water with temperature ( $T_{req} = 45^{\circ}\text{C}$ ) for shower and dishwashing during warm season for countryside summer houses, which are very popular in Russia. At heating mode,  $T_{ev}$  equals the average daily temperature and varies for different months (May – September). The condenser and adsorption temperatures equal the temperature of the useful heat necessary for a consumer ( $T_{con} = T_{ads} = T_{req}$ ). The boundary adsorption potentials  $\Delta F_1$  and  $\Delta F_2$  are calculated for water as the working fluid according to

eqs. (2) and (3) for  $T_{reg}$  varying from 75 to 90 °C (Table 4). Composites LiCl/Ver and LiCl/MWCNT, several MOFs (NH<sub>2</sub>-MIL125, CAU-10) and aluminophosphate FAM-Z01 are the most promising for heating mode with the amount of cycled water  $\Delta w$  varied from 0.1 to 0.9 g/g for different locations and months (Table 4). For some regions, it is possible to obtain water of a given temperature from May to October, for others only in summer months (Table 4). The minimum temperature  $T_{reg}$  required for realization of the heating cycle varies from 75°C for the hottest region (Astrakhan) to 90 °C for the coldest regions (Oimyakon, Arkhangelsk).

**Table 4.** The boundary conditions and promising adsorbents for the heating cycles

City	$T_{reg}$ , °C	$\Delta F_2$ , kJ/mol	$\Delta F_1$ , kJ/mol	$\Delta w$ , g/g	Period
Astrakhan	90	2.5-3.8	6.2	LiCl/Ver 0.6-0.9 LiCl/MWCNT 0.3-0.5	May-Sept
	85		4.8	NH <sub>2</sub> -MIL125 0.3-0.4	
	75	2.5-2.9	4.1	FAMZ01 0.2 LiCl/Ver 0.1-0.3	Jun-Aug
Moscow	90	3.7-5.0	6.2	LiCl/Ver 0.5-0.6	May-Sept
	80	3.7-4.0	4.8	CAU10 0.3 NH <sub>2</sub> -MIL125 0.2-0.4	Jun-Aug
Vladivostok	90	3.5-5.4	6.2	LiCl/Ver 0.4-0.6	May-Oct
Omsk	90	3.4-5.0	6.2	LiCl/Ver 0.4-0.6	May-Sept
	80	3.4-4.0	4.8	NH <sub>2</sub> MIL125 0.2-0.4	Jun-Aug
Arkhangelsk	90	4.1-4.7	6.2	LiCl/Ver 0.4-0.6	Jun-Aug
Yakutsk	90	3.5-4.1	6.2	LiCl/Ver 0.6	Jun-Aug
	80		4.8	CAU10 0.3 NH <sub>2</sub> MIL125 0.2-0.4	
Oimyakon	90	4.2-4.8	6.2	LiCl/Ver 0.5-0.6	Jun-Aug

### *Heat storage*

We consider the seasonal heat storage, when the heat absorbed in summer can be used for heating during cold period. For the RF, the heating during winter months by the stored heat seems to be not realistic due to severe climate and huge demands for the heat. However, the heat storage cycle can be utilized for heating the country houses during moderate cold autumn and spring. Under heat release mode, the evaporator is at ambient temperature during the cold period, when heating is required, and  $T_{ev}$  equals the average night temperature during autumn and spring time. The condenser is at ambient temperature in summer, when the heat is stored and  $T_{con}$  is the average temperature during July. The adsorption temperature equals the temperature  $T_{req}$  required by a consumer. We consider the temperature of useful heat  $T_{req} = 35^\circ\text{C}$ , which can be used for warm flow system. The regeneration temperature was fixed at  $90^\circ\text{C}$ . The adsorption potentials  $\Delta F_1$  and  $\Delta F_2$  are calculated according to eqs. (2) and (3) for methanol and presented in Table 5. For each location, the optimal adsorbent is proposed based on the amount of methanol cycled (Table 5, Fig. 6).

**Table 5.** The boundary conditions and the adsorbents promising for heat storage ( $T_{reg} = 90^{\circ}\text{C}$ ).

City	$\Delta F_2$ , kJ/mol	$\Delta F_1$ , kJ/mol	Adsorbent	$\Delta w$ , g/g	Heating period
Astrakhan	3.8	8.0	LiCl/MWCNT	0.9	Apr, May, Sept, Oct
Moscow	4.3	9.1	LiCl/SiO <sub>2</sub>	0.6	Apr, May, Sept, Oct
Vladivostok	4.6	9.0	UiO67	0.4	Apr, May, Sept, Oct
Omsk	4.9	8.9	MaxSorbIII	0.3	Apr, May, Sept, Oct
Oimyakon	5.1	9.7	LiBr/SiO <sub>2</sub>	0.4	May, Sept
Oimyakon	8.1	9.7	LiBr/SiO <sub>2</sub>	0.1	Apr, Oct
Arkhangelsk	5.3	9.6	LiBr/SiO <sub>2</sub>	0.3	Apr, May, Sept, Oct
Yakutsk	6.6	8.9	LiBr/SiO <sub>2</sub> , MaxSorbIII	0.1	Apr, May, Sept, Oct

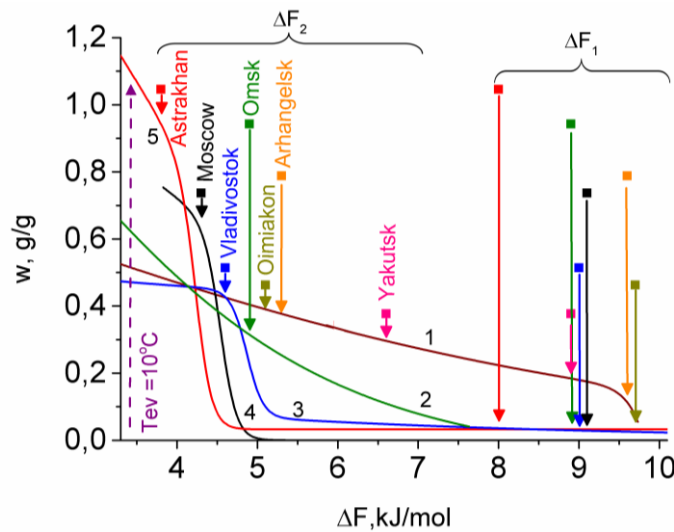


**Figure 6.** Boundary conditions for adsorption heat storage cycles and the universal adsorption curves for: 1- LiBr/SiO<sub>2</sub>, 2 - MaxSorbIII, 3 – UiO67, 4 – LiCl/SiO<sub>2</sub>, 5 – LiCl/MWCNT.

If the groundwater or household waste water at  $10^{\circ}\text{C}$  can be used as the heat source for the evaporation during cold period, the heat can be produced during winter as well, and the best material for all locations is LiCl/MWCNT composite.

**Temperature amplification cycle “Heat from Cold” (HeCol).**

The cycle is based on using two natural heat reservoirs (the ambient air at low  $T_L$  and non-freezing water basins or underground water at medium  $T_M$ ) as the heat sink and heat source to get a useful heat at high temperature  $T_H$  suitable for heating [4]. This process can be realized in regions with a cold climate, where the difference between  $T_L$  and  $T_M$  is  $30\text{-}50^{\circ}\text{C}$ , therefore the calculations are made for Yakutsk and Oimyakon. The boundary adsorption potentials  $\Delta F_1$  and  $\Delta F_2$  are determined as

$$\Delta F_2 = -RT_H \{ \ln [P(T_M)/P(T_H)] \}, \quad (4)$$

$$\Delta F_1 = -RT_M \{ \ln [P(T_L)/P(T_M)] \}. \quad (5)$$

For calculations, we consider  $T_L$  is the average temperature during winter,  $T_M = 3$  and  $10^\circ\text{C}$ , and  $T_H$  varies from  $30$  to  $50^\circ\text{C}$  (Table 6, Fig. 7).

**Table 6.** The boundary conditions and the adsorbents promising for the HeCol process.

$T_M, ^\circ\text{C}$	$T_H, ^\circ\text{C}$	$\Delta F_2,$ kJ/mol	$\Delta F_1,$ kJ/mol	Adsorbent	w, g/g	Period
Yakutsk						
3	30	3.8	5.0-7.2	LiCl/MWCNT	0.97	Nov-Feb
	35	4.5	5.0-7.2	LiCl/SiO <sub>2</sub>	0.38	Nov-Feb
	40	5.1	6.4-7.2	MaxSorbIII	0.14	Dec-Feb
10	30	2.7	4.8-8.4	LiCl/MWCNT	1.37	Nov-March
	40	4.0	4.8-8.4	LiCl/MWCNT, LiCl/SiO <sub>2</sub>	0.67 0.70	Nov-March
	50	5.4	7.4-8.4	MaxSorbIII	0.19	Dec-Feb
Oimyakon						
3	30	3.8	6.7-9.0	LiCl/MWCNT	0.97	Nov- March
	35	4.5	6.7-9.0	LiCl/SiO <sub>2</sub>	0.38	Nov- March
	40	5.1	8.4-9.0	MaxSorbIII	0.14	Dec-Feb
10	30	2.7	7.9-10.2	LiCl/MWCNT	1.37	Nov- March
	40	4.0	7.9-10.2	LiCl/MWCNT, LiCl/SiO <sub>2</sub>	0.67 0.70	Nov- March
	50	5.4	9.6-10.2	LiBr/SiO <sub>2</sub>	0.26	Dec-Feb

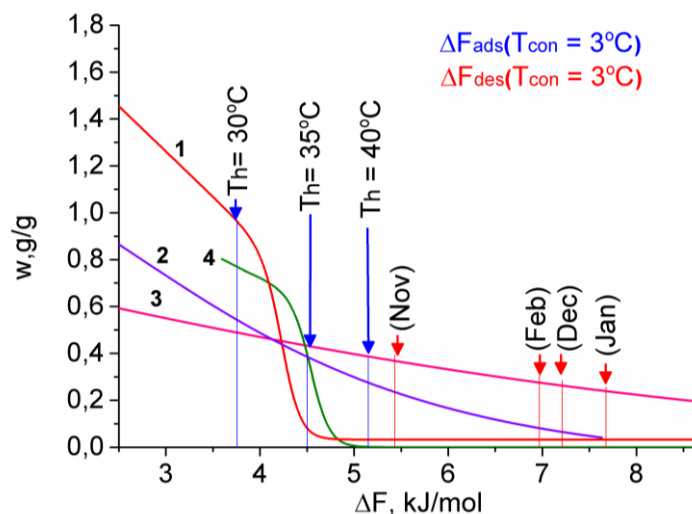


**Figure 7.** The HeCol process for Yakutsk: the boundary conditions and the universal adsorption curves for: 1 - LiCl/MWCNT 2 – MaxSorbIII, 3 - LiBr/SiO<sub>2</sub>, 4 - LiCl/SiO<sub>2</sub>.

The LiCl/MWCNT can be used for cycles with  $T_H = 30^\circ\text{C}$ . The LiCl/ SiO<sub>2</sub> and MaxSorbIII allow the heat at  $T_H = 35^\circ\text{C}$  to be produced. While the LiBr composite with the highest affinity to methanol vapor can be employed for HeCol cycle with  $T_H = 50^\circ\text{C}$  (Table 6).

### Summary/Conclusions

The paper addresses the preliminary feasibility analysis of the AHT technology in the climatic conditions of the Russian Federation. For each of the selected climatic zones, the most demanded applications (cooling, heating, heat storage and amplification) are identified

based on the analysis of the climatic conditions. For a wide range of conventional and innovative adsorbents (activated carbons, silica gels, MeAPOs, MOFs, "salt in porous matrix" composites, etc) the literature data on adsorption equilibrium with water and methanol vapours are analysed. The characteristic sorption curves "uptake vs. adsorption potential" are plotted and approximated by proper analytic equations. That contributes to the equilibrium adsorption database, which can be used for the selection of the suitable working pairs for different AHT applications. Based on these data, the working pairs promising for the demanded cycles for each climatic RF zone are selected. The obtained results will promote the dissemination of the energy and environment saving AHT technology in the RF.

### **Acknowledgment**

The work was supported by the Russian Science Foundation (project № 17-79-10103).

### **References:**

- [1] R. Wang, L. Wang, J. Wu, Adsorption Refrigeration Technology: Theory and Application, 2014, John Wiley & Sons, Singapore Pte. Ltd., <https://doi.org/10.1002/9781118197448>
- [2] Advances in Adsorption Technologies, Eds. B. Saha and K.S. Ng; Nova Science Publishers, 2010, ISBN: 978-1-60876-833-2
- [3] The map <http://meteoinfo.ru/climate>
- [4] <http://www.meteonorm.com/>
- [5] A.D. Grekova, L.G. Gordeeva, Yu.I. Aristov, Composite "LiCl/vermiculite" as advanced water sorbent for thermal energy storage, Appl. Therm. Engn., 2017, v. 124, pp. 1401-1408. <https://doi.org/10.1016/j.applthermaleng.2017.06.122>
- [6] Yu.I. Aristov, Adsorptive transformation of ambient heat: a new cycle, Appl. Therm. Engn., 2017, v. 124, pp. 521-524. <https://doi.org/10.1016/j.applthermaleng.2017.06.051>
- [7] M.F. de Lange, K.J.F.M. Verouden, T.J.H. Vlugt, J.Gascon, , F. Kapteijn, Adsorption-Driven Heat Pumps: The Potential of Metal–Organic Frameworks, Chem. Rev., 2015, v. 115, pp. 12205 – 12250. <https://doi.org/10.1021/acs.chemrev.5b00059>
- [8] L.G. Gordeeva, Y. Aristov, Composites 'salt inside porous matrix' for adsorption heat transformation: a current state-of-the-art and new trends, Int. J. of Low-Carbon Tech., 2012, v. 7, pp. 288–302. <https://doi.org/10.1093/ijlct/cts050>
- [9] K.E. N'Tsoukpoe, H. Liu, N. Le Pierre's, L. Luo, A review on long-term sorption solar energy storage, Ren. Sust. Energy Rev., 2009, v. 13, pp. 2385-2396. <https://doi.org/10.1016/j.rser.2009.05.008>
- [10] K. Johannes, F. Kuznik, J-L. Hubert, F. Durier, C. Obrecht, Design and characterisation of a high powered energy dense zeolites thermal energy storage system for buildings, Appl. Energy, 2015, v. 159, pp. 80–86 <https://doi.org/10.1016/j.apenergy.2015.08.109>.

# Design of a Gas-Fired Carbon-Ammonia Adsorption Heat Pump

A. M. Rivero Pacho\*, S. J. Metcalf, R. E. Critoph, H. Ahmed

The University of Warwick, School of Engineering, Library Road, Coventry, CV4 7AL, UK

\*Corresponding author: A.Rivero-Pacho@warwick.ac.uk

## Abstract

Ammonia – carbon adsorption heat pumps for domestic use have been a focus of research at the University of Warwick for many years. The continuing challenge is to devise a sorption generator which has excellent heat transfer to an inherently poor conducting medium, minimal thermal mass and low manufacturing cost. This paper presents the design and manufacturing of a novel carbon-ammonia adsorption generator heat pump for application to an air source domestic gas fired heat pump and also shows preliminary testing results of the complete heat pump system. This laminated generator has the characteristic of delivering high heating power at a high efficiency but having an inexpensive manufacturing cost. The machine has a predicted power output of 10 kW at an internal COP of 1.38 for low temperature radiators for domestic applications. Testing of the machine shows good repeatability of the results although the refrigerant cycled is lower than expected resulting in poor COP and heating power values delivered.

**Keywords:** Heat Pump, Carbon, Ammonia, Domestic Heating.

## Introduction/Background

The University of Warwick is currently developing a very compact carbon-ammonia adsorption cycle gas fired heat pump so that it can be a box-for-box exchange for a conventional domestic gas boiler, with much reduced size and capital cost compared to alternative machines on the market (<4 times). Also for ease of retrofit, it is an air source machine.

It would have to provide at least 10 kW of heat output, which is the requirement for an average semi-detached UK household of three bedrooms. The working conditions of the machine are heating water to 50°C, for low temperature radiators, and typical ambient temperature range from -5 to 15°C.

The target internal COP should be higher than 1.38 so that the gas utilisation efficiency is higher than 1.25. With this predicted COP, the machine will reduce households' gas consumption by 30% compared to a conventional condensing boiler.

The refrigerant used in the heat pump is ammonia as it has the ability to operate below 0°C evaporating temperature which makes it suitable for air source operation. Also, the high working pressures of the ammonia in the system enables a compact machine and the achievable power density is almost entirely heat transfer, not mass transfer limited. Ammonia is paired with active carbon, as adsorbent, which has been chosen as it is stable to high driving temperatures. It does have lower and more gradual concentration change than adsorbents with S-shaped curves or salts, but does not suffer from a sudden 'switch off'.

Figure 1 shows the schematic of the heat pump. On the left hand side there is the burner that provides heat to the heat transfer fluid. The heat transfer fluid, at a high and at a low temperature, is diverted with two water valves through two sorption generators, one being cooled, adsorbing ammonia, and the other being heated, desorbing ammonia. There are heat and mass recovery systems between the beds.

The ammonia that has been desorbed from Bed 1 first condenses in the condenser, releasing heat to the house heating system, then through the expansion valve, then through the evaporator, where it absorbs heat from the ambient air, and finally it is adsorbed in Bed 2. The cycle is then reversed.



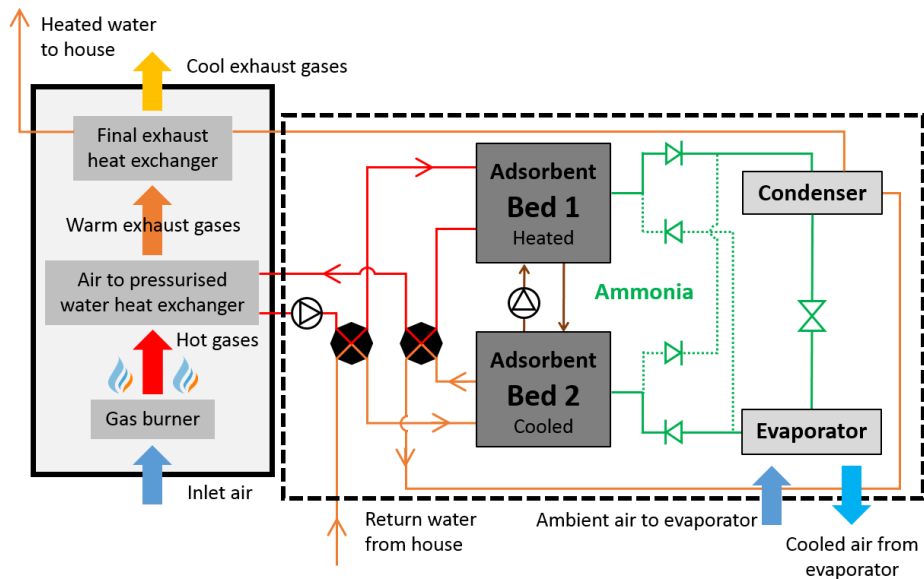


Figure 1. Heat pump machine schematic shown with Bed 1 being heated and Bed 2 being cooled.

The sorption generator is effectively a thermally driven compressor and is the most critical part of the design. The challenge is to design and build a sorption generator that has excellent heat transfer, not just to reduce the size and cost of the machine but to allow effective transfer of heat between the beds in a high COP regenerative cycle. However, it must also have low thermal mass since it is repeatedly cycled in temperature and the sensible heat used, whilst partly recoverable is not multiplied by the heat pump COP. In addition the generator should be capable of reliable mass production at a cost of at most a few tens of pounds. Without this challenge being met it is unlikely that a domestic adsorption heat pump to replace a gas boiler will ever be viable.

Previous research at Warwick focussed on the development of micro-tube adsorption generators (Critoph, 2011). Whilst these achieved high power density and efficiency, they proved difficult and costly to manufacture. The work presented in this paper describes the design and construction of a carbon laminate adsorption generator machine, whose generators have both low thermal mass and high power density whilst being cost effective to manufacture.

### Discussion and Results

Among the number of approaches available to intensify heat transfer in adsorbent beds, the researchers at Warwick have explored the use of conventional metal fins or extended surfaces to transfer heat into the bed material, an approach that has been used in the past by Meunier's group (Zanife, 1988) and Sortech (Schossig, 2011). The disadvantages of this approach are firstly that the introduction of a large thermal mass of metal reduces the efficiency and secondly that the limit on heat transfer rapidly becomes the convective heat transfer between the fin and granular bed, rather than conduction through the fins and bed.

The characteristics of the new generator design, sorption material, simulation of the heat pump machine and machine assembly are presented below:

#### Sorption material:

The sorption material used in the generators is a carbon composite developed by researchers at the University of Warwick and is made with active carbon and a binder in order to obtain enhanced thermal properties compared to loose carbon grains or powder. The active carbon is type 208C, especially good for heat pumping applications, based on coconut shell precursor manufactured by Chemviron Carbon Ltd.

The carbon composites consist of blocks made of a mixture of carbon and a lignin based binder. The composite is made by mixing carbon (grains and/or powder), liginosulfonate and hot water (dissolves the binder and helps to create a homogenous mixture). The mixture needs to rest for at least an hour and then it is compressed to the desired shape and fired in an inert atmosphere in order to carbonise the organic binder.

The mass of refrigerant (ammonia) adsorbed and desorbed in the beds over a heat pump cycle depends on the temperature and pressure of the system. The ammonia concentration is calculated with the modified Dubinin-Astakhov equation presented by Critoph, 1999.

$$x = x_0 e^{-K \left( \frac{T}{T_{sat}} - 1 \right)^n} \quad \text{kg/kg} \quad (1)$$

where T is the refrigerant/adsorbent temperature (K), T<sub>sat</sub> is the saturation temperature (K), x is the adsorbed refrigerant concentration (kg/kg), x<sub>0</sub> is the maximum (limiting) concentration (kg/kg) and K and n are constants.

Since the adsorption characteristics of the carbon composites might vary due to the addition of the binder, adsorption tests were carried out with a Rubotherm magnetic suspension balance. Table 1 shows the Dubinin-Astakhov adsorption coefficients of the different carbons tested.

Table 1. Adsorbent properties.

Adsorbent	Density (kg m <sup>-3</sup> )	Specific heat (J kg <sup>-1</sup> K <sup>-1</sup> )	Conductivity (W m <sup>-1</sup> K <sup>-1</sup> )	x <sub>0</sub>	K	n
Granular carbon (208C)	650	175+2.245*T(K)	0.1	0.2849	4.792	1.448
208C + binder	810	175+2.245*T(K)	0.4	0.2951	4.677	1.359

Apart from the sorption coefficients, Table 1 shows the density of the carbon composite used in the simulations and other thermal characteristics such as specific heat and thermal conductivity and it is compared to the properties of the raw granular carbon.

The thermal conductivity of the samples was obtained with the Quickline-10 Anter machine, using a steady state technique with flat plates. A 2-inch diameter carbon sample is placed in between the flat plates and a heat flux created by a heater and a heat sink travels through the sample. With the recorded heat flux, thickness of the sample and the calibration line of the machine it is possible to obtain the thermal conductivity of the sample.

The thermophysical properties and adsorption characteristics of the lignin-carbon composites were measured in order to model their performance in the simulations.

Figure 2a shows a sample of the carbon laminate used in the construction of the adsorption generators. The carbon is the monolithic type as described above. The laminate is made by compression in a die before pyrolysis in a furnace to bind the carbon composite into a monolithic layer between the fins.

An LTJ (transient technique) rig has been designed, manufactured and constructed at the University of Warwick in order to determine the combined thermal conductivity and wall contact resistance of the carbon composites. A sample laminate heat exchanger is located in the main vessel of the LTJ. This main vessel is connected to a reservoir vessel with ammonia and pressure and temperatures in different parts of the system are recorded throughout the experiment. Once the heat transfer fluid that flows through the tubes of the heat exchanger suddenly increases its temperature, the ammonia adsorbed in the carbon composite desorbs increasing the pressure of the system. This increase in pressure is recorded and matched to a simulation program that predicts the thermal properties of the sample.

The thermal performance of these laminate heat exchangers has been verified by performing a large temperature jump experiment on a test section and comparing it to a transient model developed in MATLAB. Figure 2b shows the comparison and the match between the large temperature jump experiment and the model.

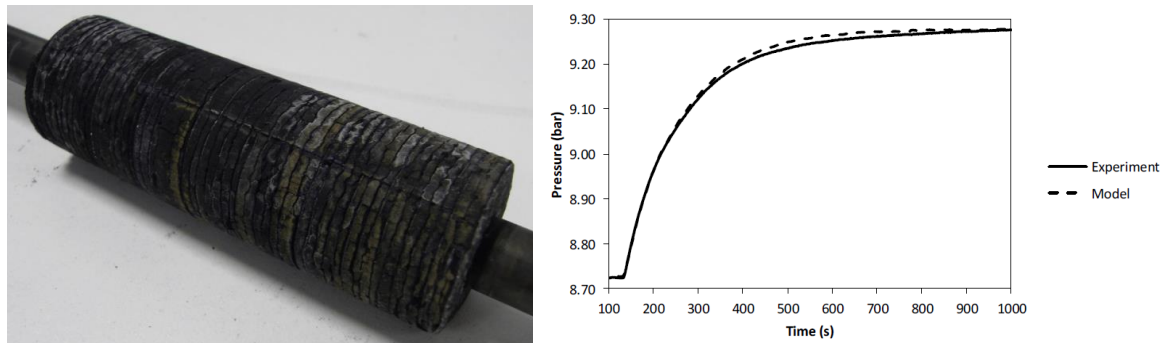


Figure 2. a) Carbon laminate adsorption generator, b) Comparison between large temperature jump experiment and computational model.

Computational modelling:

A two dimensional finite difference simulation model in MATLAB has been written to explore how varying the geometry of the generator, dimensions and control parameters affect the Coefficient of Performance (COP) and power output under specified conditions and sorption materials. The adsorbent thermal properties used in the simulation were the ones previously tested and presented.

The unit cell is a cylindrical section as shown in Figure 3. The lengthwise cell is split into  $n_l$  axial sections allowing the modelling of thermal waves if required and the carbon is split into  $n_r$  equal radial sections. The pressurised water used to heat or cool and steel has only one radial element, but the water can be subdivided into multiple numbers of axial elements if the mass flow rate specified is so high that an element of water could flow past more than one axial element of steel in one time step.

In order to keep the simulation stable whilst the heat transfer in the metallic segments was modelled and whilst keeping the total computation time reasonable, a time step of roughly 0.05 times that of the carbon was used for all the metallic elements.

The geometric variables that can be changed in this model are the inner and outer tube diameter and the tube pitch in addition to the fin thickness and the carbon thickness between fins.

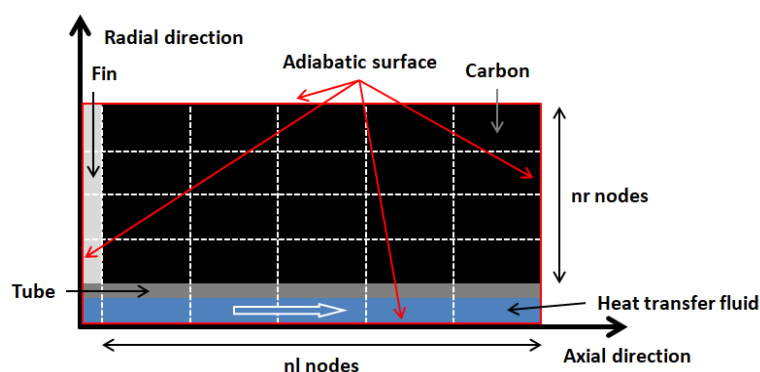


Figure 3. Finned tube unit cell.

Simulation results:

In all the simulations run, in order to compare designs, the cooling phase assumes an inlet water temperature of 50°C, in the heating phase the water inlet is at 200°C, the evaporating

temperature is 5°C and the condensing temperature is 50°C. The heating/cooling cycle times and recovery times used in the simulations vary between 50 and 200s and between 0 and 200s respectively.

The following figures show how the performance of the machine is affected by various geometry variables such as the pitch between tubes (where the heat transfer fluid flows), fin thickness and laminar carbon thickness.

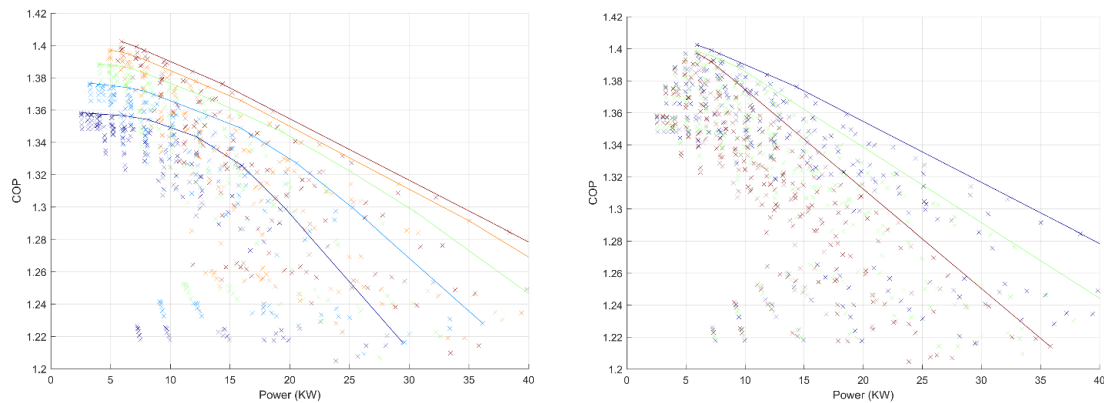


Figure 4. a) Performance envelopes for different tube pitches, b) Performance envelopes for different carbon thicknesses.

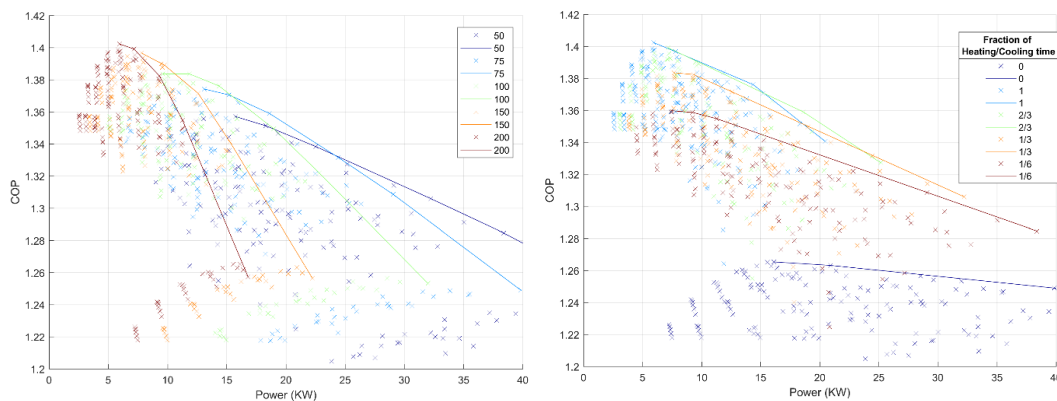


Figure 5. a) Performance envelopes for different heating and cooling times, b) Performance envelopes for different recovery times, being them 0, 1/6, 1/3, 2/3 and 1 times the heating and cooling times.

The performance of the machine also varies depending on the heating, cooling and heat recovery times, giving a trade-off between COP and heating power. This allows the machine to deliver a higher heating power at lower efficiencies if necessary at a certain point.

#### Prototype assembly:

The heat pump prototype is being constructed to test the performance of the generators and to validate the developed computational model of the machine.

The machine has been tested with a system of electrical heating and cooling baths that provide up to 170°C of pressurised water, heat transfer fluid, for high temperature heat input. It also allows 10 kW of heat rejection for the condenser and cooler and provides a glycol flow down to -10°C for the evaporator.

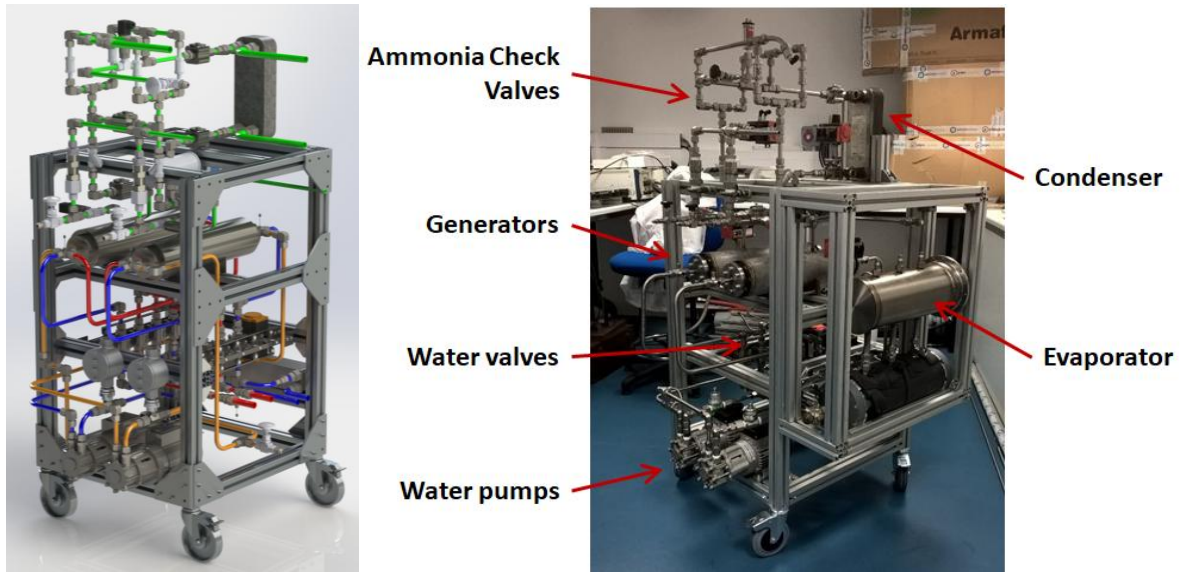


Figure 6. Heat pump machine: a) CAD design, b) Assembly in laboratory.

Flow control:

To control the flow of water (the heat transfer fluid) through system components, the current lab scale test rig contains 10 ball valves. The valves are configured in four pneumatically actuated sub-assemblies, two sub-assemblies contain four connected valves each (Figure 7), while the other two sub-assemblies contain one valve each.

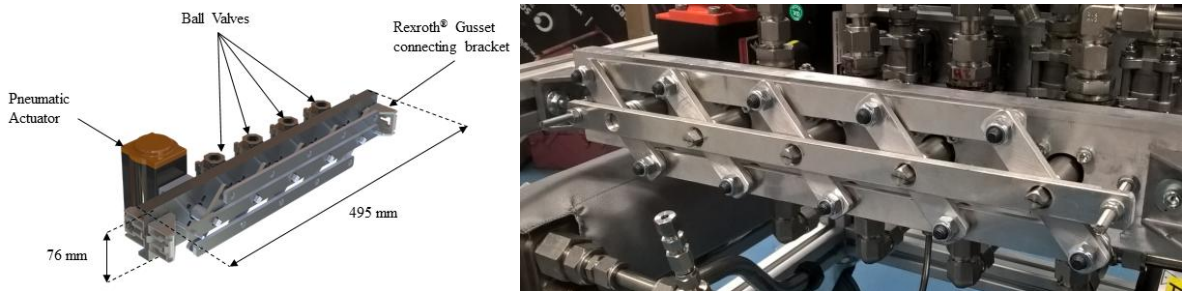


Figure 7. Pneumatically actuated 4-valve sub-assembly a) CAD model representation, b) Constructed sub-assembly fitted into the machine.

The aim of an auxiliary project is to replace the 10 ball valves with 4 custom designed valves, hence reducing final machine cost and package size. The concept being explored is the use of cam operated sealing plungers with the sealing force provided by a single spring per plunger. The cams will be actuated by a linear solenoid through a ratchet mechanism. The spring sealed plunger concept was tested successfully at 3 bar using the single branch assembly in Figure 8.



Figure 8. The single branch assembly.

Conventional solenoid valves are constructed with a spring return that allows them to be normally open or normally closed. A continuous current supply is required to hold the valve at the required position. The concept valve will employ a pull solenoid with a spring return to switch the water flow via a ratcheting mechanism. This will enable the use of a short DC pulse, rather than a continuous supply, reducing electrical power consumption and hence reducing running cost.

Two configurations of the concept valve are being explored, circular and linear. With the linear configuration being close to testing.

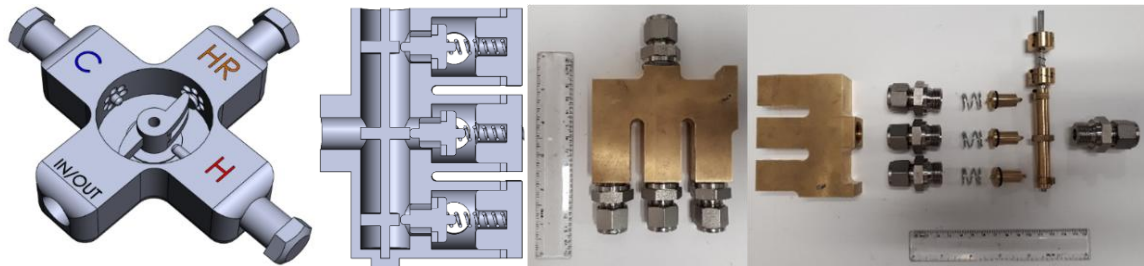


Figure 9. a) CAD representation of the two investigated configurations, b) Assembled and exploded view of the linear configuration.

Testing:

The machine has been tested with a cooling phase inlet water temperature of 40°C, a heating phase the water inlet temperature of 170°C, the evaporating temperature is 10°C and the condensing temperature is 40°C. Figure 10 shows both the temperature profile of the water flowing through the generators and the pressure profile of the ammonia in the generators during testing. The cycle and recovery times during testing were varied in order to obtain different combinations of COP's and heating powers.

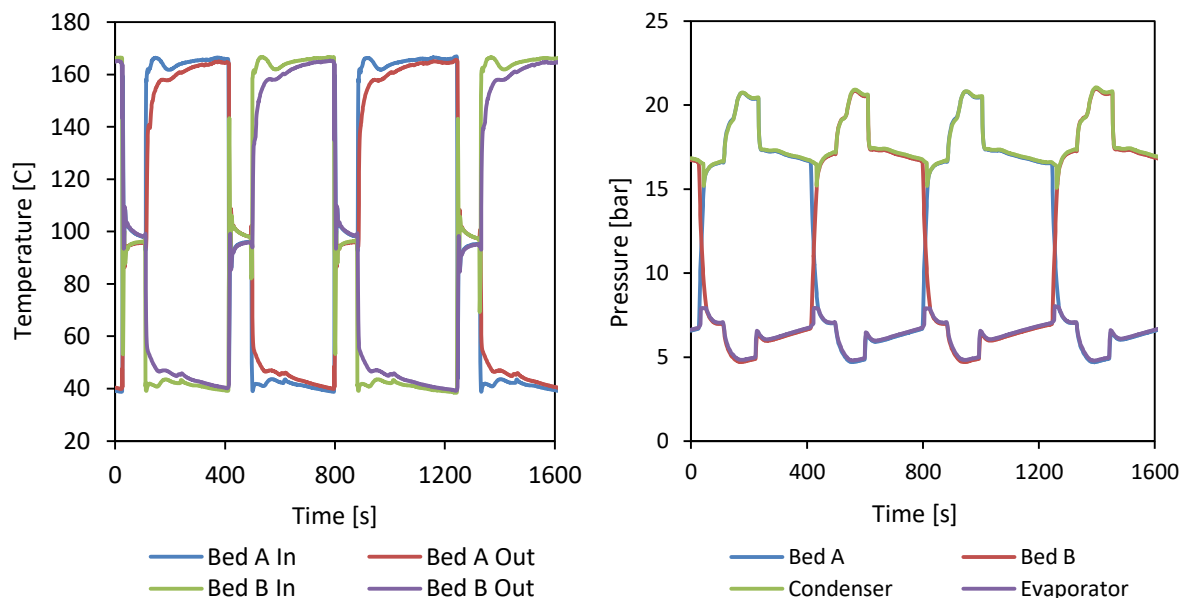


Figure 10. a) Temperature profile of the heat transfer fluid circulating through the generators, b) Pressure profile of the refrigerant in the generators

Although the temperature and pressure profiles of the machine seem correct and very repeatable, the COP and powers delivered were lower than the ones predicted by the simulation model. This was due to an unexpected low amount of refrigerant cycled during the testing, approximately a third lower than the adsorption characteristics of the sorption material predicted.

The adsorption characteristics of the material were tested in the Rubotherm, where after a long set point time equilibrium is reached. But in the machine adsorption and desorption happen in a shorter period of time and it is believed that some of the binder used in the carbon composite is causing blockage of the pores. This pore obstruction is not observed during the desorption phase but during the adsorption phase, affecting the overall refrigerant cycling quantities.

Further work will be done to reevaluate the composite material and the design of the generator in order to avoid the pore blockage.

### **Summary/Conclusions**

The design of a novel carbon composite laminate adsorption generator is presented for application to a 2-bed domestic gas fired heat pump. The chosen cycle uses isothermal beds with heat and mass recovery. The machine is air source and it is intended to be very compact so that it can be used as a drop-in replacement for a conventional gas boiler, perfect for retrofitting. The complete prototype machine, which is currently under construction, has a predicted power output of 10 kW at an internal COP of 1.38, according to simulations.

The machine has been tested and shows good repeatability of the heat transfer fluid temperatures and refrigerant pressure profiles but the amount of refrigerant cycled seems very low which produces low COP's and low heating power outputs.

The sorption material and the generator's geometry will be reassessed in order to solve this problem.

### **Acknowledgements**

This research was supported by the EPSRC grant to the University of Warwick (EP/K011847/1).

### **References:**

- [1] Critoph, R.E., Metcalf, S.J., 2011, Progress in the development of a carbon-ammonia adsorption gas-fired domestic heat pump, Int. Sorption Heat Pump Conf. proc., pp. 849-854.
- [2] Schossig, P., K. T. Witte, et al., 2011, Annex 34 - Thermally Driven Heat Pumps for Heating and Cooling - Aims and State of the Art., Proc. 10th IEA Heat Pump Conference, May 16–19.
- [3] Zanife, T.N., Meunier, F., 1988, Etude de la regulation d'une pompe á chaleur á adsorption a deux adsorbours: cas zeolithe - eau, proc. Pompes á chaleur de hautes performances, Perpignan, pub. Lavoisier.

# High temperature heat and water recovery in steam injected gas turbines using an open absorption heat pump

Annelies Vandersickel\*, Wolf G. Wedel, Hartmut Spliethoff

<sup>1</sup>Institute for Energy Systems, Technical University Munich,  
Boltzmannstr. 15, 85748 Garching b. München, Germany

\*Corresponding author: annelies.vandersickel@tum.de

## Abstract

The advantages of reinjecting steam from the heat recovery steam generator (HRSG) in the preceding gas turbine are increased power and electrical efficiency at low specific cost and a high operating flexibility. The discharge of the injected steam to the ambient has however two major drawbacks: (1) a relevant water consumption and (2) a large thermal loss related to the latent heat of steam. An open absorption heat pump cycle (HT-CBT) downstream of the HRSG can solve both problems, as it allows to recover the steam from the flue gas and use its condensation heat at elevated temperature. This paper presents a concept to efficiently integrate both technologies and assesses the potential of the absorption system for a steam injected gas turbine (STIG). Over a wide range of steam injection rates, the power output of the plant can be varied without the associated energetic penalty achieving improvements in the fuel efficiency of up to 26%.

**Keywords:** open absorption heat pump; steam injected gas turbine; cogeneration; flue gas condensation

## Introduction

In steam injected steam turbines (STIG), steam generated in the HRSG can be either used for district/process heating or injected in the gas turbine to increase its power output. This allows to vary the power-to-heat ratio over a wide range, allowing the plant to respond rapidly to fluctuations in the heat or electricity demand. Economic advantages of the STIG result from (1) the larger number of operating hours, as the plant can run with high steam injection rates when heat demand is low and (2) a reduction of the peak power taken from the grid and the associated cost when electricity demand is high.

The discharge of the injected steam into the ambient has two major drawbacks: (1) a high water consumption and (2) a low fuel efficiency [1, 2]. Heat recovery through flue gas condensation addresses both disadvantages. Condensing the water vapour and using its latent heat increases the fuel efficiency, whereas reinjecting the condensate into the power cycle significantly reduces the cycle's water consumption. Due to the low dew point temperatures of the flue gas, ranging between 45 and 70°C, a flue gas condensing heat exchanger can only be used if a low temperature heat sink is available. This is seldom the case in district heating and industrial applications. Open absorption heat pump cycles, as proposed by Bergmann et al. (e.g. in [3]), allow to exploit the condensation energy contained in the flue gas at significantly higher temperature levels.

This "High temperature Condensation Boiler Technology" (HT-CBT) has been realized in several pilot plants e.g. a diesel engine cogeneration [4] and gas-fired heating plant [3] resulting in a fuel efficiency increase of about 10%. The high humidity of the flue gas in a STIG motivates to integrate the HT-CBT. Up till now, however, no analysis on how to integrate both technologies has been made, nor have the achievable heat and power augmentation and water recovery been assessed. This analysis is performed in the current paper, based on detailed process simulations validated with data from the Cheng cycle



installed at the Technical University in Munich [5] as well design data from the HT-CBT plant in Berlin Buch [6].

### Integration Concept

The Cheng Cycle at the Technical University in Munich (TUM) consists of a single-shaft aeroderivative gas turbine Allison 501-KH 5 and a heat recovery steam generator (HRSG). The HRSG has a single pressure water-steam cycle with a natural convection evaporator. From the evaporator drum, the generated steam (12.5 bar - 190°C) either passes through the superheater and is then injected in the gas turbine (11.5 bar - 530°C) or it is sent to the heating condenser, transferring its heat to the heating network.

The injection steam mass flow rate controls the electricity production and allows to vary the power-to-heat ratio from 0.5 for the minimum steam injection rate ( $\dot{m}_{inj}$ ) to a value of 8.8 for the maximum steam injection. Table 1 shows the performance of the plant for these extreme operating points. The 2 MW higher electricity output comes at the expense of a strong reduction in the thermal output and hence strongly reduced fuel efficiency.

As the Cheng Cycle plant at the TUM is ca. 20 years old, the efficiencies reached are rather moderate and not fully representative of the performance achieved with a state-of-the-art Cheng Cycle. However, because of the excellent availability of time resolved performance data, this plant is very suited to illustrate the potential and limitations of the integration of the HT-CBT.

Table 1 - Performance of the base Cheng Cycle at 15°C and 958 hPa ambient conditions

$\dot{m}_{inj}$ (kg)	thermal power (MW)	Electrical power (MW)	$\dot{m}_{fuel}$ (kg)	$\eta_{el}$	$\eta_{th}$	$\eta_{fuel}$
0,2	7,5	3,9	0,28	28	54	82
2,4	0,67	5,9	0,32	37	4	41

Due to the steam injection, the steam content in the flue gas varies from 10 Vol% to almost 30 Vol%, resulting in a strong variation of the dew point temperature from ca. 45 to 70°C. To recover the energy contained in this humid flue gas, a HT-CBT is integrated downstream of the HRSG, as illustrated in Figure 1. The HT-CBT can process part (using the bypass) or all of the flue gas leaving the HRSG.

A schematic of the HT-CBT unit itself is given in Figure 2. In the adiabatic absorber – the centerpiece of the HT-CBT unit – the flue gas dehumidifies and cools down through direct contact with a hygroscopic water/calcium nitrate ( $\text{Ca}(\text{NO}_3)_2$ ) solution [3]. In this adiabatic absorption process, the solution recovers not only the sensible energy contained in the flue gas but also the latent heat contained in the absorbed water vapor at temperatures well above the dew point temperature – the main advantage of the HT-CBT. The heat absorbed by the solution is transferred to the heating network in the solution cooler.

To regenerate the solution, part of the solution is diverted to a desorber, where the entire humidity absorbed from the flue gas in the absorber is vaporized again. The desorber heat required to drive the desorption process is recuperated completely during condensation of the released vapor and can be used to further increase the temperature of the heating network to the condensation temperature of about 100°C.

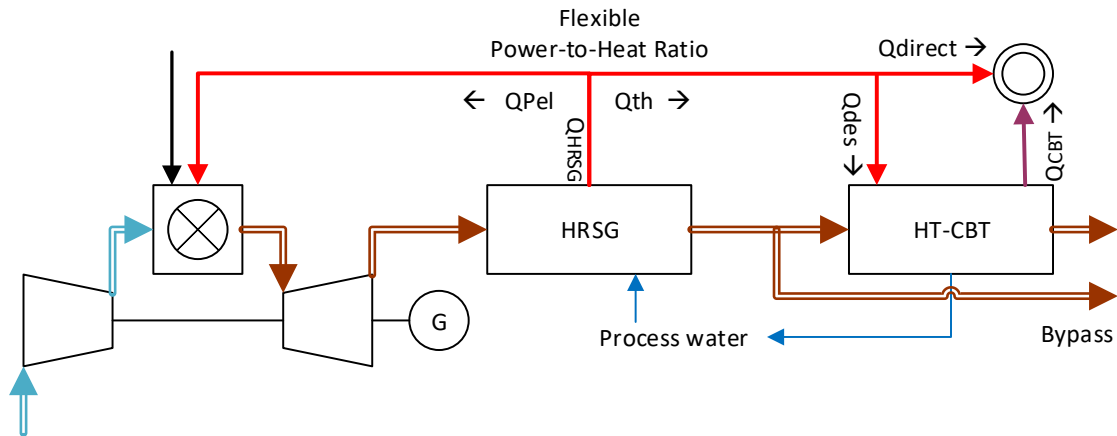


Figure 1: Simplified layout of the Cheng Cycle with integrated HT-CBT Module (Flue gas (brown), Heat streams (red))

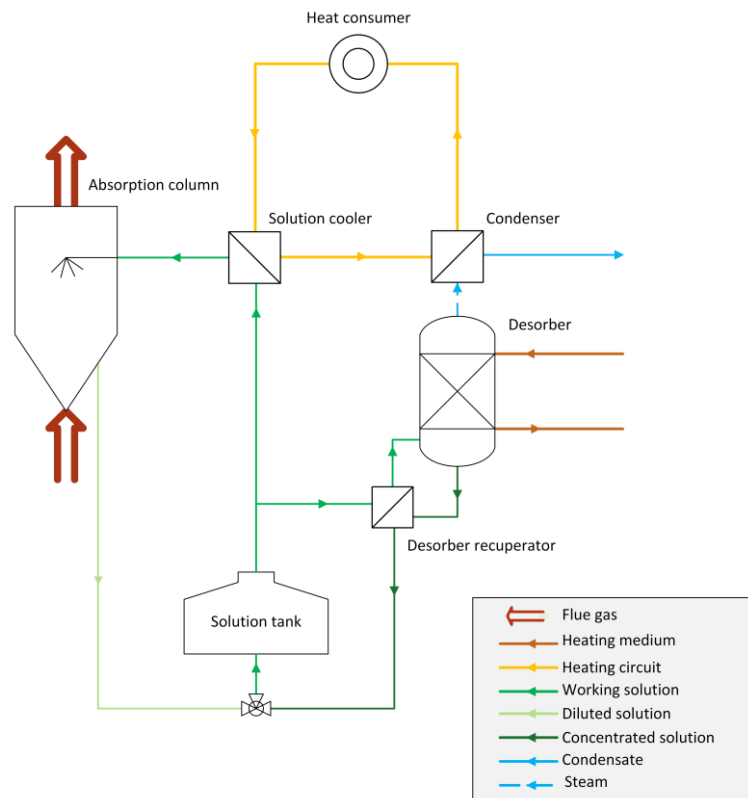


Figure 2: Process flow diagram of the open absorption cycle [3] based on [4]

The HT-CBT rejects its heat to the heating network in the solution cooler and the condenser downstream of the desorber, which are integrated in series with the water preheater and heating condenser of the Cheng Cycle's water-steam cycle.

The desorber is heated with saturated steam at 3.5 bar extracted from the HRSG before the heating condenser. Desorber heating using steam has the advantage that: (1) no modification to the existing HRSG is required, (2) the high heat transfer coefficients during condensation allows for a compact desorber design and (3) most importantly, even if the HT-CBT Module is switched off, the Cheng cycle is able to operate in its current mode, condensing all non-injected steam in the heating condenser.

As illustrated in Figure 1, with the HT-CBT integrated, the flue gas heat recovered in the HRSG ( $Q_{\text{HRSG}}$ ) is hence partly used for the generation of the injection steam controlling the electricity generation ( $Q_{\text{Pel}}$ ), partly for the desorber heating ( $Q_{\text{des}}$ ) and the remaining energy is used for direct heating via the heating condenser ( $Q_{\text{direct}}$ ). The flexible distribution of the recovered heat over these 3 processes defines the operating range extension of the Cheng cycle obtained through the integration of the HT-CBT technology.

## Methodology

Modelling of the Cheng Cycle power plant and the HT-CBT is done using EBSILON Professional, a commercial process simulation software [5]. EBSILON Professional is a stationary simulation tool with a number of pre-implemented power plant components. The Cheng Cycle is modelled using these components and validated based on operational data from the Cheng Cycle Plant at the TUM.

For the HT-CBT, a programmable (Fortran) component was implemented. The HT-CBT model bases on energy and mass balances for each of the components. Apart from the process simulation, the model also includes a preliminary process design for the absorber column and the heat exchangers (using the LMTD method). Details can be found in [3], key assumptions are given in the following.

The core component is the adiabatic absorber column in which the flue gas flows in counter flow with the hygroscopic solution. The achievable dehumidification of the flue gas is determined by the temperature and concentration of the solution entering the absorber at the head ( $w_{\text{work}}$ ). The solution temperature on its turn depends on the lowest temperature in the heating network ( $T_{\text{return}}$ ) – which herein varies from 40°C to 60°C – and the minimal temperature difference in the solution heat exchanger. The lower the temperature and higher the concentration are, the higher is the gain of recovered heat due to the stronger dehumidification of the flue gas.

In practice, perfect equilibrium is never reached. The model therefore assumes quasi-equilibrium at the absorber head, for both thermal and phase equilibrium:

- Thermal, meaning that the flue gas cools down to the solution temperature plus a minimum temperature difference, herein set equal to 2 K.
- Phase quasi-equilibrium, meaning that the water partial pressure of the exiting flue gas stream approaches the equilibrium partial pressure corresponding to the concentration of the hygroscopic solution ( $w_{\text{work}}$ ) and the flue gas temperature at the head with a predefined offset. In this work, this deviation from equilibrium is 10%.

As the absorber operates adiabatically, the maximum use temperature of the absorbed heat is defined by the temperature of the diluted solution at the absorber sump. This maximum temperature on its turn is defined by the equilibrium between the water partial pressure of the inflowing flue gas and the concentration of the diluted solution ( $W_{\text{dil}}$ ). The solution flow should be high enough to absorb both the recovered sensible and latent heat without exceeding this maximum temperature (thermodynamic minimum solution flow). At the same time, the solution flow must be large enough to ensure good gas/liquid contact such that the quasi-equilibrium at the absorber head is effectively achieved (technical minimum flow) [6].

To fulfill both requirements, the model computes the required solution mass flow rate through the absorber as the maximum of the above two solution flows. The thermodynamic limit follows from the energy balance and the assumption that phase quasi-equilibrium is reached in the sump, again with a 10% offset between the vapor pressure of the flue gas and the solution's equilibrium pressure. The technical limit follows from the absorber design based on the gas load factor  $F_{\text{abs}}$  defining the column diameter and the irrigation density  $U_{\text{irr}}$  defining the corresponding design solution mass flow rate (See Table 2).

Table 2 - Input Parameter for the absorber column design

$W_{work}$	70% ( $T_{return}$ 60°C) – 67% ( $T_{return}$ 40°C)
$W_{conc}$	73% ( $T_{return}$ 60°C) – 70% ( $T_{return}$ 40°C)
$F_{abs}$	1 Pa <sup>1/2</sup>
$U_{irr}$	10 m <sup>3</sup> /m <sup>2</sup> h

To reduce the sensible energy required in the desorber to heat the fluid to the desorption temperature: only part of the solution is concentrated to  $W_{conc}$  and then mixed with the absorber outlet solution to yield the working concentration  $w_{work}$ . The design concentrations, chosen to avoid crystallization at high concentration and low solution temperatures are given in Table 2. The solution flow rate to the desorber follows from the constraint that all humidity absorbed in the absorber should be desorbed. The desorber solution outlet temperature follows from the equilibrium of the concentrated solution with the desorbed water vapor at the desorber pressure (atmospheric). As result of the boiling point elevation caused by the nitrate salt, the water vapour released in the desorber enters the condenser superheated. Its temperature is modelled as the average between the temperatures at which desorption starts and ends. After desuperheating, the steam is condensed and the resulting saturated condensate is reintegrated in the water-steam cycle of the Cheng Cycle plant. Similarly, also the condensated desorber heating steam is fed back into the water-steam cycle substituting hot 25°C make-up water. The overall model has been successfully validated with design data of the HT-CBT module in Berlin Buch [7, 8].

### Discussion and Results

Figure 3 shows the maximum achievable extension of the Cheng Cycle's operating range through the integration of the HT-CBT for a heating network return temperature of 60°C. This has been assessed using design computations for each operating point. The grey line corresponds to full load operation of the Cheng Cycle without the HT-CBT. The thick black solid line depicts the maximum achievable operating range through the HT-CBT integration. The fuel efficiency or first law efficiency is defined as the ratio of useful output energy (electric and thermal) to the energy input within the gas feed based on its lower heating value. For a heating network return temperature of 60°C, a maximum increase in fuel efficiency of 26% can be achieved for an intermediate steam injection rate of 1.36 kg/s. For higher steam injection rates, the energy recovered in the HRSG does not suffice to drive both the injection steam generation ( $Q_{Pel}$ ) and the desorber heating ( $Q_{des}$ ). The HT-CBT can therefore process only part of the flue gas, proportional to the energy available for desorption, the rest leaves through the bypass. As a result, the benefit of the HT-CBT and hence the fuel efficiency drop significantly for steam injection rates above 1.36 kg/s.

For lower steam injection rates, the higher humidity of the flue gas and the correspondingly higher heat recovery in the HT-CBT compensates the higher heat demand for steam generation, allowing an increase in power output with nearly constant heat output. The fuel efficiency therefore remains nearly constant at 95%, allowing to vary power output without the associated energetic penalty. Except for steam injection rates above 2.16 kg/s full water recovery further eliminates the high water usage of the Cheng Cycle, making it a suited technology for cogeneration also in dry areas.

In contrast to previous applications, the HT-CBT can in a Cheng Cycle not only be used to increase the heat output for a given power output but also to increase the power output for a given heat demand with a maximum of 33% (from 1no to 3) with only limited impact on fuel efficiency. Increasing electricity prices and higher subsidies due to the higher electricity

rating improve the economic viability of this use case compared to heat recovery only applications.

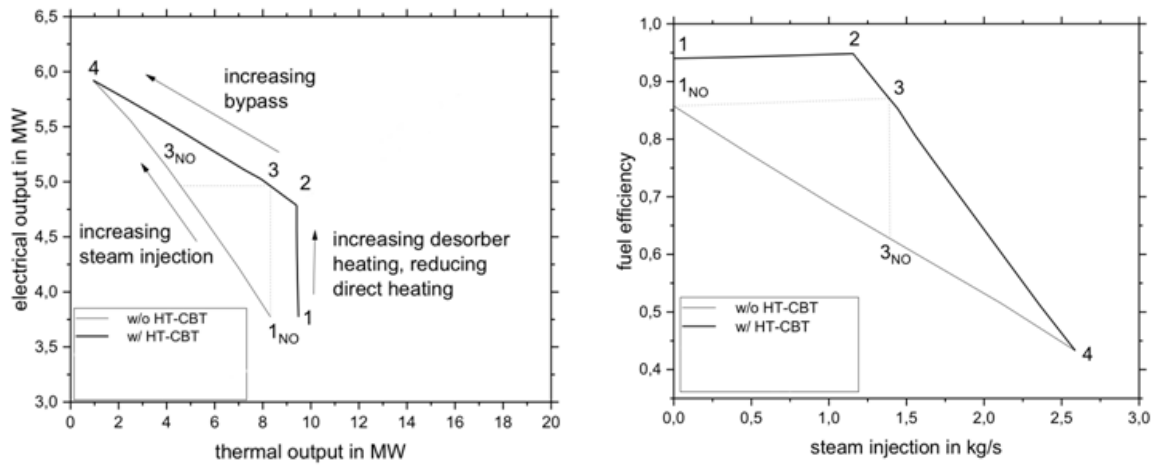


Figure 3: Performance of the Cheng Cycle with and without the HT-CBT for steam injection rates varying from zero (1) till 2.6 kg/s (4) and a network return temperature of 60° C

### Summary/Conclusions

The potential and limitations of the integration of the “high temperature condensation boiling technology” (HT-CBT) in a Cheng Cycle are discussed. In particular, for high steam injection rates, the limited availability of desorber heating in the HRSG was found to restrict the achievable heat recovery. Nevertheless, over a wide range of steam injection rates, the power output of the steam injected gas turbine plant can be varied without the associated energetic penalty achieving improvements in the fuel efficiency of up to 26%. Except for steam injection rates above 2.16 kg/s, full water recovery further eliminates the high water usage of the Cheng Cycle, making it a suited technology for cogeneration also in dry areas.

### Acknowledgements

The authors thank Dr.-Ing. Thomas Bergmann and Dipl.-Ing. Serena Danesi of School of Engineering at the ‘Zürcher Hochschule für Angewandte Wissenschaften’ for the design information of the HT-CBT pilot plant at Berlin Buch and the insights in the functioning of the HT-CBT technology.

### References:

- [1] E. Macchi und A. Poggio, „A cogeneration plant based on a steam injection gas turbine with recovery of the water injected: design criteria and initial operating experience,“ in *ASME 1994 International Gas Turbine and Aeroengine Congress and Exposition*.
- [2] M. De Paepe and E. Dick, "Technological and economical analysis of water recovery in steam injected gas turbines," *Applied thermal engineering* 21, pp. 135-156, 2001.
- [3] R. Gomez Romero, „Modelization and analysis of latent heat recovery systems for the combined heat and power plant Garching,“ Master Thesis Institute for Energy Systems, Technical University Munich, 2016.
- [4] T. Bergmann, „Hochtemperatur (HT)-Brennwerttechnik,“ *Euroheat & Power* 29, 6, pp. 38-44, 2000.
- [5] Steag AG, "EBSILON Professional Dokumentation," 2015.
- [6] P. Bittrich, D. Hebecker und T. Bergmann, „First industrial application of an open

absorption cycle for heat transformation in a district-heating in a district-heating network," *International Journal of Energy Technology and Policy* 3, p. 85, 2005.

[7] M. Pokojski, A. Heuer, T. Bergmann und U. Tamm-Woydt, „Hochtemperatur-Brennwertnutzung in Dampfkesselanlage: Heizkraftwerk Buch," *Euroheat & Power* 36, Nr. 4, pp. 54-55, 2007.

[8] T. Bergmann, Interview, *Personal Communication*. [Interview].

# Methanol and its Sorption Heat Pump and Refrigeration Potential

S. Hinners\*, R.E. Critoph

School of Engineering, University of Warwick, Coventry CV4 7AL, United Kingdom

\*Corresponding author: s.hinners@warwick.ac.uk

## Abstract

Methanol is a relatively under-investigated process fluid within sorption systems. The purpose of this work is to review research utilising methanol and to consider its application within sorption technologies. This covers various previous works as well as new innovations such as the use of metal-organic frameworks (MOFs) as adsorbents. The literature is then discussed considering several possible applications, offering an understanding as to those which best suit adsorption and absorption systems; and coinciding chemical and physical sorbents. The conclusions drawn, suggest the most promising steps in research using methanol to forward the development technologies alternative to ammonia and water based systems.

**Keywords:** Heat Pump, Refrigeration, Energy Transformation, Sorption, Thermal Energy, Absorption, Adsorption, Cycle.

## Introduction

Sorption cycles have maintained their attention in recent years with many recent incisive experiments considering new sorbents. Refrigeration and heating cycles that harness primary energy still hold great appeal, particularly with potential efficiency gains in industrial applications with in-situ generation. The ability to harness low grade thermal energy from solar or waste heat offers renewable potential without the added demand on electricity grids. Refrigerants can be selected with zero global warming potential or ozone depletion potential and can be utilised in noiseless cycles.

The various components and working pairs within sorption systems will be outlined within this research; the aim of which is to highlight the most cost-effective approaches and applications that can be developed. There is much value in comparing the new innovations in sorption against work carried out before the turn of the century. This research focuses on the use of methanol in sorption refrigeration systems, a relatively unexplored but attractive working fluid. This is to highlight it as an alternative to existing refrigerants such as ammonia and water. The main incentives are the inherent safety of methanol compared to ammonia (no more dangerous than a domestic boiler), and methanol's efficacy in ice production, unlike water systems.

## Methanol

In sorption, the energy transformed is equivalent to the latent heat of evaporation of the sorbed fluid and the heat of breaking electrostatic attractions or chemical bonds formed. To maximise this energy, a sorbate must bond *frequently and readily*; by maximising surface area of a solid (and/or porosity) or by increasing polarity within the molecule. It must also have a high latent heat per volume, indicating its energy density per unit volume for heat transformation between its phases. Further considerations for application are the toxicity and harmfulness to the environment of the proposed sorbent [1].

The freezing point of methanol is at 175.59K and it can evaporate at temperatures below 0°C [2]; therefore within cooling systems operating as a vacuum refrigerant, methanol can be used in ice production. The drawback in methanol compared to water is its latent heat. Critoph

reports the latent heats of a number of refrigerants; highlighting water with the greatest latent heat of 2258(kJ/kg), Ammonia at 1368(kJ/kg) and methanol with a latent heat of 1102(kJ/kg). This decrease in energy density seems an issue; but Critoph also highlights how Methanol should achieve coefficients of performance (COPs) that exceed ammonia within refrigeration systems[3]. Methanol is also a highly polar molecule, making it readily reactive with ionic compounds as well as forming physical hydrogen bonds with porous materials. The small size of the molecule also enhances bonding within pores.

Water seems the best process fluid due to its high latent heat and harmlessness, but Boer, Saravanan & Maiya, and Wang & Vineyard allude to the limited working range of water within systems due to the freezing point; and the susceptibility in adsorption systems utilising water as a refrigerant for crystallisation to occur [4-6]. Boer and Saravanan & Maiya, propose methods to enhance methanol systems to utilise its working range. But most interestingly Wang & Vineyard conclude that for systems utilising low grade heat, the optimum working pairs are silica gel-water or activated carbon-methanol. Gordeeva, et al. discuss the use of composite inorganic salt sorbents to enhance the quantity of methanol that can be adsorbed. This produces theoretical COPs that are analogous to those from the best working pairs utilising water[7]. It is clear that methanol has an important role in future sorption systems.

### **Adsorption**

Adsorption cycles utilise the sorption of a vapour in a solid; these can operate with minimal control, low circulation expenditure and minimal noise and vibration when compared to traditional vapour compression cycles [8]. The systems utilise physical or chemical sorption to produce a phase change. Physical adsorption often enables systems to utilise lower grade heat as an energy source enabling solar thermal applications, whereas systems utilising chemisorption increase the heat of sorption and the concentration change enabling greater energy transformations and higher COPs. Adsorption systems which utilise solid sorbents suffer less from corrosion than absorption systems and avoid the volatile absorbents used in liquid-vapour systems [9] such as ammonia. A simple design can utilise one bed with operation in different phases; but for continuous cooling operations, two beds working in semi-batches are required within a system.

### **Physisorption**

The most common pairing of methanol utilising physisorption, physical bonding with the sorbent, is with activated carbon (AC). More recent research into activated carbon-methanol includes work by Ammar et al., highlighting the potential for this working pair to be driven by a solar collector, exploring a number of types of AC, Ammar was able to find an optimal COP of 0.73 for a simple solar collector system [10]. This is a remarkable result and should be followed up, especially as some of the independent variables seem contradictory; the evaporation temperature used is not the same as within the idealised results at  $-3^{\circ}\text{C}$ , but in runs changing other variables is seen to be at  $-1^{\circ}\text{C}$ . Chekirou explores the enhancement of heat recovery on such a system, this work shows a COP can be achieved of 0.682 with the heat recovery and two beds over a single bed system with 0.483 [11]. Dinesh et al., produced a two drum refrigerator which reportedly obtained a COP of 0.34. Some older work, still utilising the pairing with AC by Leite, focuses on a single bed ice maker as well as producing a prototype with an average net solar COP of 0.13 [12].

### **Chemisorption and Composite Adsorption**

Chemisorption utilises chemical bonds forming with the sorbent medium during the adsorption/desorption process. The aim of utilising salts or complex ionic compounds is to enhance the sorption capacities and swing increasing the energy density of the system. The hindrance of using salts are issues with swelling and agglomeration. Agglomeration can affect the heat and mass transfer within the system [1]. Gordeeva et al., explain that during



the adsorption process crystalline solvates form, this leads to an extensive reorganisation within the crystalline structure [7]; this accounts for the swelling of the salt during the reaction. Work by Korhammer illustrates the effect of multiple cycles on the sorption rate, on a system using calcium chloride and methanol [13]. Gordeeva et al., then continue explaining how the swelling can lead to mechanical destruction and dust formation, but can be overcome by embedding the salt within a porous matrix [7].

The nature of the composite sorbents show improved sorption qualities for some applications [14], they behave similarly to both physical and chemical sorbents and can utilise the optimum properties of both [15, 16]. Gordeeva et al., showed that theoretical COPs of cooling in a system utilising lithium chloride within silica gel reach 0.72. In a lab scale experiment a COP of 0.4 was achieved, as well as an Specific Cooling Power (SCP) of 290W/kg [17]. This work is continued in a subsequent paper by Gordeeva & Aristov in which, through dynamic optimisation, it is shown that the maximal SCP for defined metrics of layers of grains within a system can reach 3100W/kg for a single layer, reducing to 1100W/kg with 4 layers, the suggested reason being that a saturated surface layer may likely limit the sorption quantity [18]. The use of salts in adsorption have clear premise in improving systems, particularly in composite sorbents, but there is still a notable gap between theoretical efficiencies and practically achieved ones.

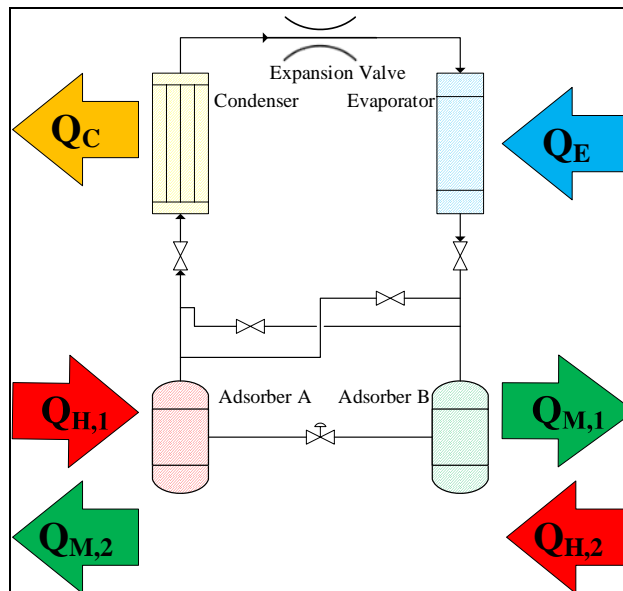


Figure 1 Adsorption Cycle, Mass Recovery

### Improved Cycles and Systems

Much work has been done to enhance the heat and mass transfer and to recover heat and mass in cycles, an example of a system design utilising mass recovery can be seen in Figure 1. This can enable the realisation of systems able to utilise lower grade thermal heat and to enhance the COPs and efficiencies. A prime example of this is the work done by Akahira et al., utilising a silica gel-water adsorption refrigeration system. When utilising a heat source temperature of 50°C, they found mass recovery enhanced their cooling capacity by 40% [19], this obtains a COP of 0.36 and 0.46 without additional heating and cooling to the adsorbing and desorbing beds. Furthermore, an SCP of 134 and 123W/kg without heating and cooling. This works by utilising the pressure difference in a system with two generator beds; when one bed is in desorption phase and the other adsorption, the higher-pressure desorption bed and low-pressure adsorption bed creates a driving force, increasing mass transfer. This was furthered by Alam et al. showing with a four-bed cycle that with a heat source temperature of 70°C the system has a lower COP than a two bed cycle. However, with a generating temperature of 60°C the system out performs with a greater COP and cooling effect [20].

Hu, et al. also considers the process intensification with mass recovery, but in the system based on a composite of Zeolite and foam aluminium with water to enhance thermal conductivity compared to zeolite alone. They note the importance of both temperature and uniform temperature within a system. It was observed an SCP of 500W/kg can be achieved with a generator temperature of 775.15K but with a temperature of 525.15K, this falls to somewhere around 150 W/kg depending on cycle time [21].

In addition it can be useful to utilise heat recovery within a system. One of the methods is to circulate a heat transfer fluid between two adsorbing beds, the flow of the fluid between the beds induces a thermal wave as a temperature profile forms down the bed. A good example is the work by Shelton et al., in which for an ammonia-AC heat pump they observe a COP of 1.87, illustrating that with the fuel ratios the solid-gas heat pump is akin to a heat pump using electricity [22]; utilising zeolite-ammonia. The thermal wave approach, had seen less interest in recent years but may still hold potential within methanol systems. Liu et al. propose a design in which the adsorber, evaporator and condenser are all within a chamber, this utilises mass and heat recovery processes. Much work has occurred since developing this approach. Their approach achieves SCPs of 38-138W/kg, and COPs ranging from 0.2-0.4 [23]. This work has been furthered more recently by Pan & Wang, optimising cycle time for such a system [24]. Lu and Wang pilot a chamber design with lithium chloride in silica gel with methanol, they draw some important observations; such as cycle time having the greatest effect on the COP than SCP and in this system mass recovery had significant effect on COP and cooling.

Work by Hu, et al. considered mass recovery within a system utilising a composite adsorbent. It was seen to shorten the time of pressurisation within the cycle, but one can observe that the enhancement of COP and SCP are moderate apart from at shortest cycle times [21]. Therefore, employing such a system may be unnecessary. Another interesting form of enhancement is a new class of adsorbents called metal-organic frameworks (MOFs). These have been explored by Jeremias et al. and show potential in new sorbents with very high uptake and potential work for bespoke sorbents dependant on the refrigerant [25].

### **Absorption**

Absorptive systems are the alternative to solid vapour systems utilising liquid vapour interactions. In absorption the vapour is distributed throughout the volume of the sorbent rather than upon the surface or within pores. A single effect absorption cycle contains generator, condenser, evaporator, absorber, pump, throttling valve and heat exchanger. Depending on the working pair a rectifier may also be required. A schematic is shown in Figure 2 In a double effect system there is another generator operating at a different pressure plus another heat exchanger dependant on the generation temperatures. Another absorber may be required, or another pump and further equipment. Thermal energy desorbs the refrigerant (working fluid) in the high-pressure generator, which flows to the condenser through the lower pressure generator supplying its latent heat, this is the energy supplied to the lower pressure generator. The refrigerant then condenses in the condenser and is then evaporated and expanded through the evaporator. It is then sorbed by the absorbent within the absorber before being fed via heat exchangers to the generator [26-28].

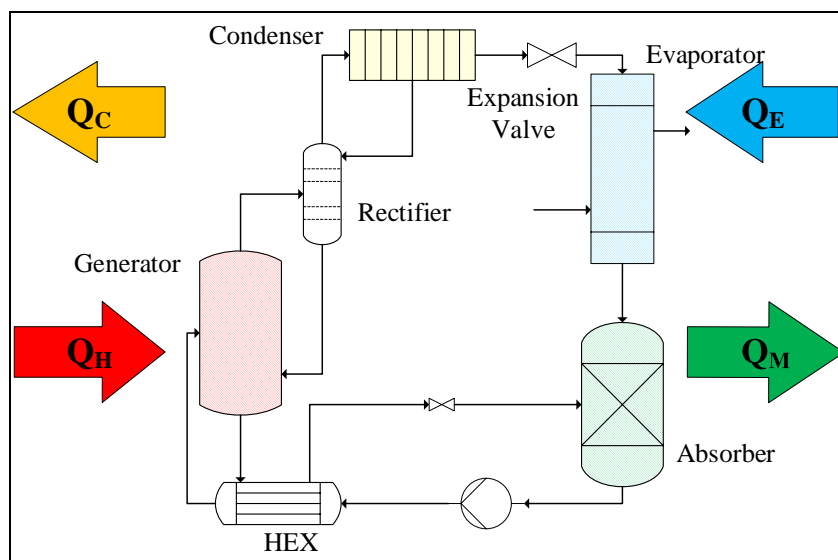


Figure 2 Absorption Single Effect Cycle

Iedema offers judicious observation when considering an absorption heat pump; in that the heat ratio is unaffected in an ideal system by a decrease in the environmental temperature. Whereas in a compression heat pump the generator temperature must be increased; but as they discuss, practically this doesn't occur as within a real absorption heat pump solvent fractions in operation decrease, and the mixture can approach a region of crystallisation. Higher heat production will also be required, and therefore great pump work. This will lead to greater exergy losses in the heat exchanger as more heat is transferred across the same surfaces [28]. From tabulated data within Iedema's work it can be seen that a double effect heat pump will be unlikely to use methanol as a working medium due to such systems often requiring temperatures that would decompose methanol. Based on the findings and discussions of hypothetical working fluids and absorbents, Iedema presents a heat pump using the mixture of lithium bromide/zinc bromide at a ratio of 2:1 which appears the most promising.

#### **Ionic Liquids/ Working fluids and results Complex Organic Solvents**

The most common pairings in absorptive systems are water-ammonia or water-lithium bromide, with products existing in abundance utilising water and ammonia. The downside ammonia-water is the requirement of a well-designed rectifying column [29].

The primary focus of research into methanol based absorption systems has been in the pairing of lithium bromide with methanol. Safarov highlights its benefit in that it has a lower viscosity than water-lithium bromide solutions and therefore in systems it can utilise air cooling condensers operating over a wider temperature range [30]. Kaushik et al. demonstrates theoretically how a methanol- lithium bromide •  $ZnBr_2$  can produce results exceeding that of water-lithium bromide (within refrigeration). With a single effect cycle producing a COP of 0.8, double effect is capable of a COP of 1.6, generally though water-lithium bromide outperforms for the same fixed operating temperatures. The benefit of a methanol based system is the potential for lower evaporation temperatures therefore increasing the number of applications [26]. They further conclude that double effect cycles offer great potential, but at a cost of a reduction in collector efficiency. They notably also discuss that by adding the zinc bromide the problems of crystallisation are reduced. Iyoki et al. highlight the variety of ionic salts applicable, lithium bromide; zinc bromide; lithium bromide/zinc chloride; lithium iodide/zinc bromide; lithium bromide/zinc bromide; and lithium bromide/ethylene glycol. The work models the systems in double effect refrigeration systems and ultimately concluded the superiority of a system using methanol-lithium

bromide. Methanol-lithium bromide producing COPs of 1.15, and second to that being methanol- lithium iodide/zinc bromide also producing COPs exceeding 1 [27]. Unfortunately, they didn't explore methanol-lithium bromide/zinc bromide. When modelling a single stage heat pump, they showed COPs of up to 1.8 with methanol-lithium bromide/zinc bromide performing the best and lithium iodide/zinc bromide producing similar results. Double effect systems also produced COPs of up to 2.4, again lithium bromide/zinc bromide appear the best with lithium iodide/zinc bromide also similar.

Organic solvents offer an alternative to ionic liquids, without disadvantages of corrosion and crystallisation [31]. Absorbents used include tetraethyleneglycol dimethylether (TEGDME), a polar aprotic solvent; but Boer et al. shows this operates well but particularly with compression within the absorption system [4]. 1-methyl-3-methylimidazolium dimethylphosphate ([mmim]DMP) is another alternative which can be paired with methanol, Chen et al. show it has potential but often performs less well than water-ammonia and water lithium bromide with a high circulation ratio [32]. More recent work by Boman et al. illustrates the performance of a number of refrigerants with various absorbents, organic liquids and organic ionic fluids. Over a number of working pairs, methanol performed better than all except water [33]. Boman et al. also illustrate and explain how the maximum COPs for a heat pump are gained at a generating temperature notably higher than that for a cooling system. Boman et al go on to discuss a system that can work in cooling and heating mode and compare the performances in a heat pump; identifying that the best working pair thermodynamically appears to be Methanol- 1,3-diethylimidazolium/diethyl phosphate ([emim]DEP), which produces a cooling COP of 0.79 and a heating COP of 1.63 under their defined conditions. The downside of this pair is the required size of some of the process equipment compared to other systems; particularly ammonia-water, often up to 5 times larger [33]. This paper offers a very useful *modus operandi* when evaluating existing working pairs and new working pairs with empirical thermodynamic data.

## Discussion

Much of the noted research focuses on methanol as a refrigerant in cooling systems, rather than as the process fluid within a heat pump, although there is much evidence for application within both. This may be due to the operating limits of methanol as discussed by Hu et al [34]; in which experiments show that methanol cannot operate at temperatures above 120°C, as it decomposes to dimethyl ether and water. Another reason to support interest in the use of methanol as a refrigerant is its ability to produce ice.

As explained by Boman et al. and discussed earlier, different operating conditions produce the best COP when comparing a system for heat pump and refrigeration applications. But one could draw the conclusion that the most sensible industrial designs would focus on process intensification; utilising heating and cooling within a system. Such a system would likely focus on refrigeration but could utilise simultaneous heating produced. Such a system could be employed within a supermarket, or a food factory. The aim of this is to make a fired refrigeration system more economic. The reason for firing would be for optimal temperature control to ensure the most efficient system, as discussed when talking about the work by Hu et al [21] the importance of system temperature regulation. The system could be powered by renewable sources, including self-generated waste.

There is significance in development of heat for domestic heating applications, particularly when considering the UK government estimates there to be nearly four million homes not on the gas network in 2016. An effective and cheap heating system, which could compete with vapour compression heat pumps powered by renewable fuels would be commercially attractive. These homes often have oil fired boilers; thus they have large oil tanks in the properties, this enables some freedom in the size of system design, which would be valuable when considering methanol systems and trying to gain high efficiencies. Solar thermal systems are losing their appeal due to

the cheapness and efficiencies of vapour compression coolers, but there is potential in some applications for methanol-activated carbon systems, with potential markets not currently existing. Hypothetically the possibilities of harnessing the heat generated in a compost heap to power greenhouse heating in winter could be considered; such an idea would be very specific and require rigorous design but if the concept is proven this could be feasible within certain less industrial applications and may appeal to organisations such as the National Trust.

When considering system specifics, absorption systems appear to perform better than adsorption with heat pump systems getting COPs of 1.56 [28], and 1.8 in single lift and double lift of up to 2.4 [27]. Though an innovative system utilising thermal wave produced COPs of 1.87 [22], which shows opportunity but yet to be implemented with methanol and with system complexity similar to an absorptive system. Refrigeration systems utilising methanol as a refrigerant display the difference even more with absorptive systems producing COPs of 0.79 [33] and 0.8, double effect producing results up to 1.6 [26]. Adsorption systems producing values for COP of 0.5 [35], and 0.4 [23]. The disparity between adsorptive and absorptive cooling is clear but research considering MOFs could make adsorption more appealing. More recent work has been done showing improved uptakes and potential but no developed systems and thus no COPs recorded [36, 37]. It is also worth noting that COP is but one metric that explores thermal efficiency, which shows adsorption as slightly superior, future work should define and compare other metrics of practical results.

Some practical examples of working systems that could be developed also include refrigeration utilising waste heat; this may be something appropriate with haulage, but exhaust temperatures may fluctuate. Therefore, an absorption system, which is slightly more flexible as well as proven to have better COPs may be the best, this could also enable frozen transportation. The most appropriate use would be within ships and fishing vessels, where the exhausts will be at constant temperature outputs. The scale of operation is also much larger. Cruise ships, ferries and similar could also utilise heat pumps for space heating or cycles utilising both heating and cooling.

One thing that should be explored further, is the potential within resorption cycles. This would be limited by operating temperatures but could improve thermal process efficiencies. As well as the consideration of half effect systems utilising lower generation temperatures; which could utilise alternative renewable energy sources and offer other new technologies.

### **Summary/Conclusions**

Sorption cycles have much promise still in the future of heat powered cycles, but as society weans itself from fossil fuel combustion technologies it is important that future sorption cycles consider the source of thermal generation. This is pertinent when considering the applications of methanol as a working fluid for such cycles, due to its promise in cooling systems. This paper aims to present future applications of methanol as a refrigerant and process fluid. A series of potential sorption technologies were discussed as well as some conclusions on the literature. Methanol is second as a refrigerant only to water in sorption cycles, but holds merit due to its ability to produce ice. It has been proven advantageous within heat pumps but with an upper temperature limit that could limit it to domestic use. Absorptive systems appear to produce better COPs when utilising methanol rather than adsorptive systems. The future of methanol absorption appears to be in application with complex organic solvents which offer enhanced performance, whilst the adsorptive work appears to utilise adsorption with MOFs as the adsorbent. Recent research can highlight its application within solar powered chillers, but this requires follow up and would have to pursue future markets. There are a number of commercially attractive applications for the use of methanol within sorption and its merit over other systems is clear.

## Acknowledgements

The authors of this work would like to thank the UK Engineering and Physical Sciences Research Council (EPSRC) for funding the PhD project, as well as the Energy Research Accelerator for funding through Innovate UK.

## References:

- [1] L. W. Wang, R. Z. Wang, and R. G. Oliveira, "A review on adsorption working pairs for refrigeration," *Renewable and Sustainable Energy Reviews*, vol. 13, no. 3, pp. 518-534, 2009.
- [2] H. G. Carlson and E. F. Westrum, "Methanol: Heat Capacity, Enthalpies of Transition and Melting, and Thermodynamic Properties from 5–300°K," *The Journal of Chemical Physics*, vol. 54, no. 4, pp. 1464-1471, 1971.
- [3] R. E. Critoph, "Activated carbon adsorption cycles for refrigeration and heat pumping," *Carbon*, vol. 27, no. 1, pp. 63-70, 1989/01/01/ 1989.
- [4] D. Boer, M. Valles, and A. Coronas, "Performance of double effect absorption compression cycles for air-conditioning using methanol–TEGDME and TFE–TEGDME systems as working pairs: Performances de cycles à compression absorption à double effet pour le conditionnement d'air utilisant les couples méthanol–TEGDME ou TFE–TEGDME," *International Journal of Refrigeration*, vol. 21, no. 7, pp. 542-555, 1998/11/01/ 1998.
- [5] R. Saravanan and M. P. Maiya, *Paris on of methanol-based working fluid combinations for a bubble pump-operated vapour absorption refrigerator*. 1998, pp. 715-731.
- [6] K. Wang and E. Vineyard, *Adsorption Refrigeration System*. 2011, pp. 14-24.
- [7] L. G. Gordeeva, A. Freni, G. Restuccia, and Y. I. Aristov, "Influence of Characteristics of Methanol Sorbents "Salts in Mesoporous Silica" on the Performance of Adsorptive Air Conditioning Cycle," *Industrial & Engineering Chemistry Research*, vol. 46, no. 9, pp. 2747-2752, 2007/04/01 2007.
- [8] L. W. Wang, R. Z. Wang, J. Y. Wu, K. Wang, and S. G. Wang, "Adsorption ice makers for fishing boats driven by the exhaust heat from diesel engine: choice of adsorption pair," *Energy Conversion and Management*, vol. 45, no. 13-14, pp. 2043-2057, 2004.
- [9] R. E. Critoph Dr, "CHAPTER 10 - Adsorption Refrigerators and Heat Pumps A2 - Burchell, Timothy D," in *Carbon Materials for Advanced Technologies*Oxford: Elsevier Science Ltd, 1999, pp. 303-340.
- [10] H. M. A. Ammar, B. Benhaoua, and F. Bouras, "Thermodynamic analysis and performance of an adsorption refrigeration system driven by solar collector," *Applied Thermal Engineering*, vol. 112, pp. 1289-1296, 2017.
- [11] W. Chekirou, N. Boukheit, and A. Karaali, "Heat recovery process in an adsorption refrigeration machine," *International Journal of Hydrogen Energy*, vol. 41, no. 17, pp. 7146-7157, 2016.
- [12] A. P. F. D. Leitea, Michel, "Performance of a new solid adsorption ice maker with solar energy regeneration," *Engineering Conversion and Management*, vol. 41, pp. 1625-1647, 2000.
- [13] K. Korhammer, K. Neumann, O. Opel, and W. K. L. Ruck, "Micro-scale Thermodynamic and Kinetic Analysis of a Calcium Chloride Methanol System for Process Cooling," *Energy Procedia*, vol. 105, pp. 4363-4369, 2017.
- [14] Y. I. Aristov, M. M. Tokarev, L. G. Gordeeva, V. N. Snytnikov, and V. N. Parmon, "NEW COMPOSITE SORBENTS FOR SOLAR-DRIVEN TECHNOLOGY OF FRESH WATER PRODUCTION FROM THE ATMOSPHERE," *Solar Energy*, vol. 66, no. 2, pp. 165-168, 1999/06/01/ 1999.
- [15] L. G. Gordeeva, A. Freni, T. A. Krieger, G. Restuccia, and Y. I. Aristov, "Composites "lithium halides in silica gel pores": Methanol sorption equilibrium," *Microporous and Mesoporous Materials*, vol. 112, no. 1-3, pp. 254-261, 2008.
- [16] R. E. Critoph and Y. Zhong, "Review of trends in solid sorption refrigeration and heat pumping technology," *Proceedings of the Institution of Mechanical Engineers, Part E: Journal of Process Mechanical Engineering*, vol. 219, no. 3, pp. 285-300, 2005.
- [17] L. A. F. Gordeeva, Yuri I. Aristov, Giovanni Restuccia, "Composite Sorbent of Methanol "Lithium Chloride in Mesoporous Silica Gel" for Adsorption Cooling Machines: Performance and Stability Evaluation," *Ind. Eng. Chem. Res.*, vol. 48, pp. 6197-6202, 2009.
- [18] L. G. Gordeeva and Y. I. Aristov, "Composite sorbent of methanol "LiCl in mesoporous silica gel" for adsorption cooling: Dynamic optimization," *Energy*, vol. 36, no. 2, pp. 1273-1279, 2011.
- [19] A. Akahira, K. C. A. Alam, Y. Hamamoto, A. Akisawa, and T. Kashiwagi, "Mass recovery adsorption refrigeration cycle—improving cooling capacity," *International Journal of Refrigeration*, vol. 27, no. 3, pp. 225-234, 2004.
- [20] K. C. A. Alam, A. Akahira, Y. Hamamoto, A. Akisawa, and T. Kashiwagi, "A four-bed mass recovery adsorption refrigeration cycle driven by low temperature waste/renewable heat source," *Renewable Energy*, vol. 29, no. 9, pp. 1461-1475, 2004.

- [21] P. Hu, J.-J. Yao, and Z.-S. Chen, "Analysis for composite zeolite/foam aluminum–water mass recovery adsorption refrigeration system driven by engine exhaust heat," *Energy Conversion and Management*, vol. 50, no. 2, pp. 255-261, 2009.
- [22] S. V. Shelton, W. J. Wepfer, and D. J. Miles, "Square wave analysis of the solid-vapor adsorption heat pump," *Heat Recovery Systems and CHP*, vol. 9, no. 3, pp. 233-247, 1989/01/01/ 1989.
- [23] Y. L. Liu, R. Z. Wang, and Z. Z. Xia, "Experimental study on a continuous adsorption water chiller with novel design," *International Journal of Refrigeration*, vol. 28, no. 2, pp. 218-230, 2005.
- [24] Q. W. Pan and R. Z. Wang, "Experimental study on operating features of heat and mass recovery processes in adsorption refrigeration," *Energy*, vol. 135, pp. 361-369, 2017.
- [25] F. Jeremias, D. Fröhlich, C. Janiak, and S. K. Henninger, "Water and methanol adsorption on MOFs for cycling heat transformation processes," *New J. Chem.*, vol. 38, no. 5, pp. 1846-1852, 2014.
- [26] S. C. Kaushik, S. M. B. Gadhi, R. S. Agarwal, and R. Kumari, "Modeling and simulation studies on single/double-effect absorption cycle using water-multicomponent salt (MCS) mixture," *Solar Energy*, vol. 40, no. 5, pp. 431-441, 1988/01/01/ 1985.
- [27] S. Iyoki, K. Tanaka, and T. Uemura, "Theoretical performance analysis of absorption refrigerating machine, absorption heat pump and absorption heat transformer using alcohol as working medium," *International Journal of Refrigeration*, vol. 17, no. 3, pp. 180-190, 1994/01/01/ 1994.
- [28] P. D. Iedema, "The Absorption Heat Pump," Department of Mechanical Engineering, Delft University of Technology, Laboratory of Refrigeration and Indoor Climate Technology, Mekelweg 2, Delft, 162, 1984.
- [29] K. P. Tyagi and K. S. Rao, "Choice of absorbent-refrigerant mixtures," *International Journal of Energy Research*, vol. 8, no. 4, pp. 361-368, 1984.
- [30] J. T. Safarov, "The investigation of the (p,p,T) and (ps,ps,Ts) properties of  $\{(1-x)\text{CH}_3\text{OH}+x\text{LiBr}\}$  for the application in absorption refrigeration machines and heat pumps," *The Journal of Chemical Thermodynamics*, vol. 35, no. 12, pp. 1929-1937, 2003.
- [31] A. Coronas, M. Vallés, S. K. Chaudhari, and K. R. Patil, "Absorption heat pump with the TFE-TEGDME and TFE-H<sub>2</sub>O-TEGDME systems," *Applied Thermal Engineering*, vol. 16, no. 4, pp. 335-345, 1996/04/01/ 1996.
- [32] W. Chen, S. Liang, Y. Guo, K. Cheng, X. Gui, and D. Tang, "Thermodynamic performances of [mmim]DMP/Methanol absorption refrigeration," *Journal of Thermal Science*, vol. 21, no. 6, pp. 557-563, 2012.
- [33] D. B. Boman, D. C. Hoysall, M. A. Staedter, A. Goyal, M. J. Ponkala, and S. Garimella, "A method for comparison of absorption heat pump working pairs," *International Journal of Refrigeration*, vol. 77, pp. 149-175, 2017/05/01/ 2017.
- [34] E. J. Hu, "A study of thermal decomposition of methanol in solar powered adsorption refrigeration systems," *Solar Energy*, vol. 62, no. 5, pp. 325-329, 1998/05/01/ 1998.
- [35] P. O. D. Offenhardt, R. E. Malsberger, T. V. Rye, and D. Schwartz, "METHANOL-BASED HEAT PUMP FOR SOLAR HEATING. COOLING AND STORAGE. PHASE III," MATERIALS CHEMISTRY AND ENERGY CONVERSION DIVISION DERARTMENT OF ENERGY AND ENVIRONMENT BROOKHAVEN NATIONAL LABORATORY ASSOCIATED UNIVERSITIES. INC., Springfield, VA1981.
- [36] E. Elsayed *et al.*, "Development of MIL-101(Cr)/GrO composites for adsorption heat pump applications," *Microporous and Mesoporous Materials*, vol. 244, pp. 180-191, 2017/05/15/ 2017.
- [37] H. Kummer, M. Baumgartner, P. Hügenell, D. Fröhlich, S. K. Henninger, and R. Gläser, "Thermally driven refrigeration by methanol adsorption on coatings of HKUST-1 and MIL-101(Cr)," *Applied Thermal Engineering*, vol. 117, pp. 689-697, 2017/05/05/ 2017..

# Optimal design and control of a low-temperature geothermally-fed parallel CHP plant

Sarah Van Erdeweghe<sup>1,3\*</sup>, Johan Van Bael<sup>2,3</sup>, Ben Laenen<sup>2</sup> and William D'haeseleer<sup>1,3</sup>

<sup>1</sup> University of Leuven (KU Leuven), Applied Mechanics and Energy Conversion Section, Celestijnenlaan 300 – box 2421, B-3001 Leuven, Belgium

<sup>2</sup> Flemish Institute for Technological Research (VITO), Boeretang 200, B-2400 Mol, Belgium

<sup>3</sup> EnergyVille, Thor Park, Poort Genk 8310, B-3600 Genk, Belgium

\*Corresponding author: sarah.vanerdeweghe@kuleuven.be

## Abstract

In this work, we propose a two-step methodology for the design and off-design optimization of a low-temperature (130°C) geothermally-fed combined heat-and-power (CHP) plant. We investigate electricity production via Organic Rankine Cycle (ORC) and heat delivery to a small high-temperature district heating (DH) system (~90°C/60°C) in Mol (Belgium) in 2016. In the first step, we optimize the design of the heat exchangers and air-cooled condenser, assuming fixed values for the temperature of the environment, heat demand and supply and return temperatures of the DH system – for all of them, the average values are used. When comparing the parallel CHP with a pure electrical power plant for the same conditions, the CHP plant is economically feasible ( $NPV_{CHP} = 1.72\text{MEUR}_{2016}$ ) whereas the pure power plant is not ( $NPV_{\text{power plant}} = -4.60\text{MEUR}_{2016}$ ). However, we found that an off-design analysis is of utmost importance. Therefore, we use hourly data for the heat demand, supply and return temperatures and for the weather data. The off-design optimization results show that the CHP plant cannot satisfy the entire heat demand of the DH system and back-up boilers are needed. This also means that the CHP is not optimally designed – the design for the average DH system heat demand is not justified – and this results in a negative  $NPV_{CHP} = -3.67\text{MEUR}_{2016}$  for actual operation. Taking into account the off-design performance, we might improve the design of the CHP plant. This will be investigated in future work.

**Keywords:** CHP, Design optimization, District heating, Low-grade geothermal energy, Off-design optimization, ORC, Thermoconomics

## Introduction/Background

Many studies have been performed regarding the optimal design and the economic feasibility of a geothermal (power or CHP) plant, e.g., [1]–[7]. Walraven et al. [1] have optimized the design of a binary geothermal power plant towards maximal Net Present Value (NPV). Budisulistyo et al. [2] have proposed a lifetime design strategy for binary geothermal power plants which takes into account heat resource degradation. They have shown that the best design (with highest NPV) is the design for the partly-degraded heat source in year 6. Usman et al. [3] have compared the off-design performance of low-temperature geothermal power plants, located at four different geographical locations. They have used the maximum power output to the grid as the optimization objective and calculated capital investment/kW and the levelized cost of electricity (LCOE) of the system in a post-processing step. All three studies [1]–[3] are based on fixed economic parameter values and monthly-averaged or constant environment conditions. Martelli and Capra et al. [4], [5] have proposed a procedure for simultaneously determining the optimal design and part-load operation of a biomass CHP, where the Organic Rankine Cycle (ORC) condenser heat is fed to a district heating (DH) system. They have shown that a 22% higher annual profit can be obtained, taking into account the part-load operation. Calise et al. [6] have performed a design optimization and part-load performance study of a solar-fueled recuperated ORC and studied varying source



conditions. Marty et al. [7] have investigated a geothermally-fed (185°C, 350m<sup>3</sup>/h) CHP plant with an ORC and a DH system (95°C/65°C) in parallel. Whether the parallel CHP plant or a pure electrical power plant is the most economic depends on the selling price of heat. In this work, we propose a two-step methodology for the design and off-design optimization during operation of a low-temperature (130°C) geothermally-fed combined heat-and-power (CHP) plant. We investigate electricity production via Organic Rankine Cycle (ORC) and heat delivery to a high-temperature district heating (DH) system (~90°C/60°C). From previous thermodynamic comparison of low-T fueled CHP plants [8], we know that the parallel type is the most suitable for heat delivery at higher temperatures. The results are based on hourly data for the heat demand, supply and return temperatures of a small district heating system in Mol (Belgium) and hourly weather data for the year 2016.

## Discussion and Results

### Set-up and parameters in the case study

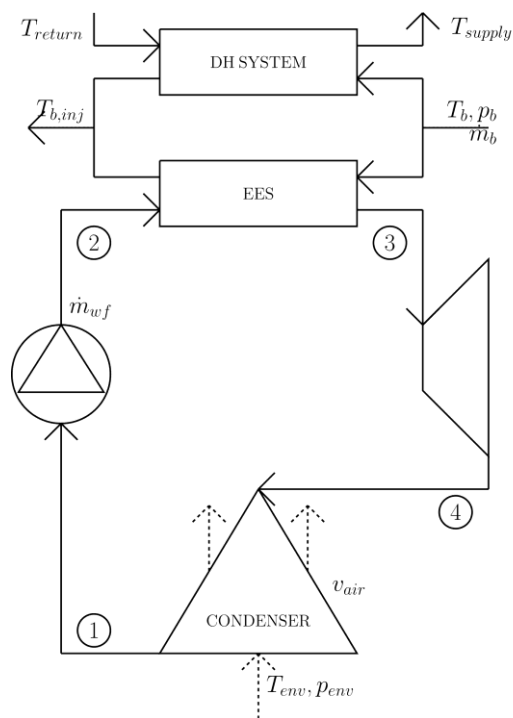


Figure 1: Set-up of the parallel CHP plant. Electricity production via ORC and heat delivery to a DH system. The symbols are explained in the text.

$p_b=40\text{bar}$  and  $\dot{m}_b=150\text{kg/s}$ . There is no constraint on the brine injection temperature  $T_{b,inj}$ . The well pumps power is  $\dot{P}_{wells}=500\text{kWe}$ . The economic parameter values we assume are: well investment costs  $I_{wells}=15\text{MEUR}$ , electricity price  $p_{el}=60\text{EUR/MWh}$ , electricity price increase  $d_{el}=1.25\%/year$ , euro-to-dollar conversion factor of 1.2, discount rate  $dr=5\%$ , heat price  $p_{heat}=25\text{EUR/MWh}$ , plant lifetime  $L=30$  years and availability factor  $N=90\%$ . Whereas we assumed a fixed value of 85% for the turbine isentropic efficiency in our previous work [9], we use the correlation of Macchi and Perdichizzi [11] in this work. Furthermore, the models have been extended for use in off-design: the turbine operating conditions have to satisfy Stodola's law [12] and the turbine efficiency in off-design is calculated via the Keeley correlation [13].

Figure 1 shows the parallel set-up of an ORC and heat delivery to a DH system. All heat exchangers are TEMA E Shell&Tube heat exchangers with the brine flowing through the tubes. The geometry of the heat exchangers will be optimized in the *design optimization step* of the optimization framework (see further). The economizer, evaporator and superheater have the same design and are called "EES" in Figure 1. The condenser is an A-framed air-cooled condenser (ACC) with corrugated fins. The friction and pressure drop correlations are the same as in our previous work [9]. Also, parameter values for the efficiency of the pump, ACC fan, motor and generator and the bare equipment cost functions are the same as in [9]. We use Isobutane as the ORC working fluid because of its low environmental impact and the high electrical power output.

Parameter values which are different our previous work [9] are the brine conditions, the economic parameters and the turbine isentropic efficiency. The brine conditions are based on the Balmatt geothermal project (Mol, Belgium), which is currently under construction [10]. The production temperature, pressure and flow rate are  $T_b=130^\circ\text{C}$ ,

The results are based on hourly data for the heat demand and temperature profiles of a district heating system in Mol. Figure 2 shows the DH system heat demand and the temperature of the environment on the left-hand side. We use a (simplified) control strategy for the supply and return temperatures of the DH system as a function of the environment temperature, which is shown on the right-hand side of Figure 2.

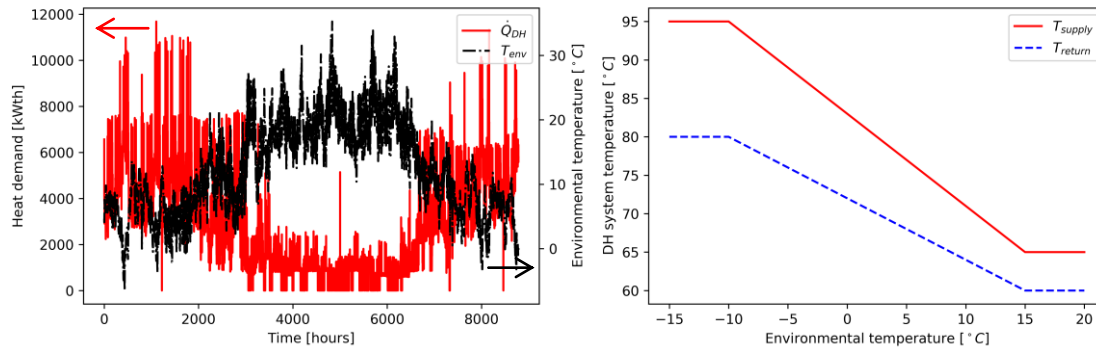


Figure 2: Left: Heat demand (red) and temperature of the environment (black dash-dotted) for the DH system in Mol (Belgium), 2016. Right: control strategy for the DH system supply (red) and return (blue, dashed) temperatures as a function of the environment temperature.

### Optimization methodology

We have implemented our detailed thermodynamic and economic models in Python [14], using the CasADi [15] optimization framework with the IpOpt non-linear solver [16]. Fluid properties are called from the REFPROP database [17].

In the *design* optimization step, we calculate the optimal design of the heat exchangers and of the air-cooled condenser. The design variables are the shell and tube diameters, the tube pitch, baffle cut and the length between baffles for the heat exchangers and the fin height and spacing, and the number of tubes for the air-cooled condenser. Furthermore, the turbine inlet temperature, the evaporator and condenser temperatures, the brine mass flow rates in the DH system branch, the ORC fluid flow rate, DH system water mass flow rates and the air flow rate in the ACC are operating variables which are optimized together with the design variables. Constraints are set for the heat exchangers to satisfy the TEMA standards and for the ACC variables to comply with the validity of the heat transfer and friction factor correlations. In our case, the heat demand must always be satisfied by the geothermal CHP plant, so the DH system heat demand is an additional constraint. The Net Present Value (NPV) is used as the objective function.

In the second step, we optimize the electrical power output of the ORC during CHP plant *operation* – while satisfying the heat demand at every moment in time. We use hourly data for the weather conditions, the heat demand and corresponding supply and return temperatures. Since the design is fixed during operation, only the operating variables are optimized. The objective is maximal net electrical power output.

### Step 1: Design optimization

In the first step, we have designed the parallel CHP plant for the average DH system heat demand of  $\dot{Q}_{DH}^{average} = 2760\text{kWth}$  and for the average environment temperature in Mol in 2016:  $T_{env}^{average} = 12.15^\circ\text{C}$ . If the parallel CHP would always work in the design point, the net present value would be  $\text{NPV} = 1.72\text{MEUR}$ . Other performance indicators are shown in Table . The exergetic plant efficiency is based on the exergy content of the brine at the production state. The energetic cycle efficiency is defined as the ratio of the net electrical power output

and the heat added to the ORC cycle.

Table 1: Performance indicators of the pure electrical power plant and the CHP at design conditions.

	Pure electrical power plant	Parallel CHP
Net present value, NPV	-4.60MEUR <sub>2016</sub>	1.72MEUR <sub>2016</sub>
Net electrical power output, $\dot{P}_{net}$	2974kWe	2455kWe
Energetic ORC cycle efficiency, $\eta_{en,cycle}$	8.53%	8.26%
Exergetic plant efficiency, $\eta_{ex,plant}$	24.57%	27.85%
Brine injection temperature, $T_{b,inj}$	74.87°C	78.61°C

Table 1 also shows the performance indicator if we had used the same geothermal source for producing electrical power only – in a pure electrical power plant. The NPV-value of the pure electrical power plant is negative which means that a power plant is not economically feasible for the considered brine and environment conditions. By selling some (useful) heat, the project becomes realistic. In this case, the NPV value of the designed CHP plant is about 6.3MEUR higher than for the pure power plant and the CHP plant is economically feasible. Furthermore, the ORC cycle efficiency in the CHP is lower, the electrical power output is lower and the brine injection temperature is higher compared to the pure electrical power plant. For the CHP plant, the ORC is smaller since part of the brine energy is used for heat delivery, so a cheaper ORC is installed which is less efficient. The exergetic plant efficiency is 3.28%-pts higher than for the pure electrical power plant. The exergy content of the heat more than compensates the lower electrical power output.

### Step 2: Off-design optimization

The designed CHP plant would however often work in off-design conditions due to the fluctuating heat demand and environment conditions (see Figure 2). In the second step, we optimize the net electrical power output for given heat demand and environment conditions at a certain moment in time (and for a given design of the facility).

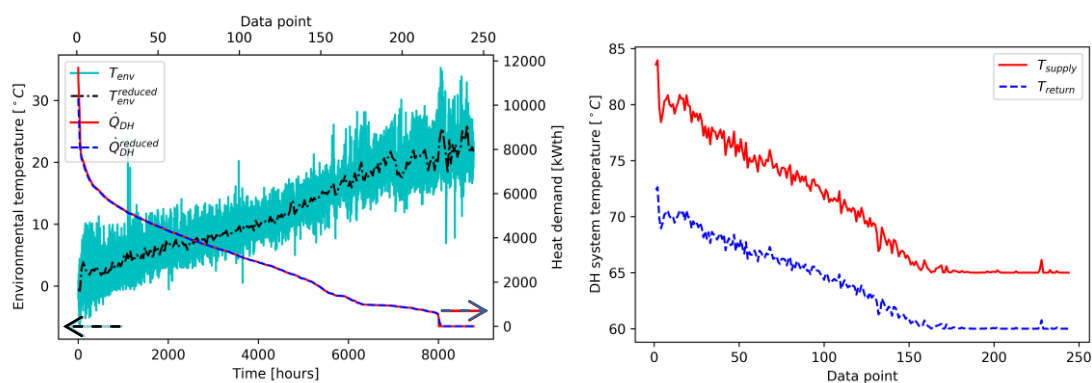


Figure 3: Left: Load duration curve of the heat demand (red: real, blue dotted: reduced) and the environment temperature (cyan: real, black dash-dotted: reduced). Right: Supply (red) and return (blue dashed) temperature corresponding to the data points on the heat load duration curve.

Instead of performing the optimization for 8784 data points (8784 hours in 2016), we reduce the number of actual data points to 244 “reduced” data points ( $244=8784/36$ ), very closely

approximating the real heat load duration curve. On the left-hand side of Figure 3, the full load duration curve for the DH system heat demand is shown in red color (corresponding to the real hourly heat demand of Figure 2) for each actual data point. The blue dotted line is a reduced load duration curve, on which the heat demand for each reduced data point is the average for 36 consecutive points on the load duration curve (so this has no time series relation/information). The cyan line presents the environment temperature corresponding to the heat demand on the load duration curve. The black dashed-dotted line presents the reduced environment temperature. In the right-hand side panel of Figure 3, we present the corresponding reduced supply and return temperatures of the DH system for all reduced data points. From now on, we use the reduced profiles, so we reduce the number of data points to 244 and the calculation time by a factor 36.

Figure 4 presents the off-design optimization results for the reduced profiles. As can be expected, we see that the maximal net electrical power output is delivered at the average heat demand of 2760kWth, for which the CHP plant was designed. For lower or higher heat demands, the ORC operates in off-design which results in a lower electrical power output.

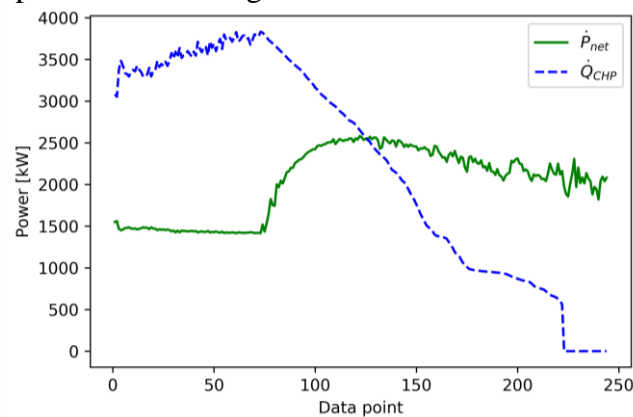


Figure 4: Net electrical power output (green) and thermal power output (blue, dashed) of the designed parallel CHP plant for the reduced number of data points of Figure 3.

For the first ~70 (reduced) data points in Figure 4, the CHP plant is not able to satisfy the entire DH system heat demand. From Figure it follows that the heat demand is high and also the required DH system temperatures are high. The CHP provides as much heat as possible but, in this case, the remaining heat should be delivered by back-up boilers (in combination with a thermal storage tank – this is not further elaborated in this work). The corresponding electrical power output of the ORC is almost constant (~1500kWe, slightly decreasing). This can be explained as follows. The mass flow rate of the brine to the ORC branch is almost constant (slightly increasing due to slightly decreasing DH system temperatures – see Figure 3) and the brine temperature at the ORC outlet is optimized to achieve maximal electrical power output. Additionally, the environment temperature increases with the data points and causes a slightly decreasing electrical power output.

On the other hand, for the last data points there is no heat demand and only electricity is produced via the ORC. The fluctuations in the electrical power production are a direct consequence of the changing environment temperature. If we calculate the real NPV based on the operational results of Figure 4, we find that  $NPV = -3.67$ MEUR. The actual project turns out to be uneconomic, whereas in the design stage we got a positive  $NPV_{design} = 1.72$ MEUR. This can be explained as follows: the design was made for the average yearly heat demand of 2760kWth. However, since the higher thermal power values cannot be satisfied by the CHP and the actual average heat delivered by the CHP is only  $\dot{Q}_{CHP}^{average} = 2267$ kWth. In addition, the net electrical power output of 2455kWe which was

predicted in the design stage is almost never reached. The actual average electrical power output is only 2021kWe. So both incomes from selling heat and electricity are lower than we expected in the design step. Therefore, very likely, it is better to design the CHP plant not for the average heat demand of the district heating system but for a higher heat demand. This is subject for future research. Besides, the real NPV depends strongly on the economic parameter values and a thorough sensitivity study on the economics is a second topic for future research.

#### Note on the accuracy of the data reduction

To get an indication on the error we have made by using the reduced optimization methodology, we take a closer look at the reduced data points 116, 117 and 118 (hours 4177 to 4284) – which are around the design point of the CHP plant. For these three data points we have made the hourly optimization for the corresponding 108 operating hours (being 3 times 36) and have compared the results with the reduced optimization results of using 3 reduced instead of 108 real data points.

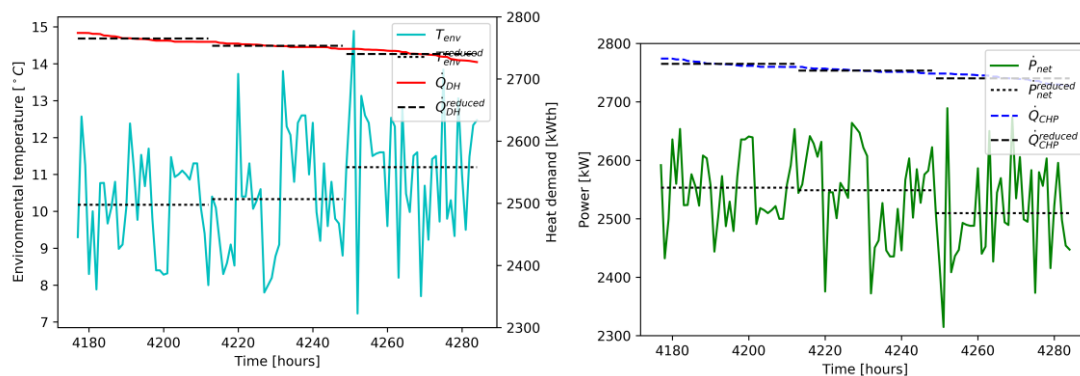


Figure 5: Left: Real hourly data for the heat demand (red) and temperature of the environment (cyan), compared to the reduced profiles (black). Right: The real heat demand (blue) and net electrical power (green) compared to the reduced values (black).

In the reduced methodology, we use the average heat demand in a certain interval of 36 hours (black dashed line in Figure 5) and the average temperature of the environment in the same time interval (black dotted line). The corresponding electrical power output is given by the black dotted lines in the right-hand side panel of Figure 5. If we calculate the hourly electrical power output which corresponds to the real heat demand (red line) and environment temperature (cyan line) at every hour, we get the electrical power output presented by the green line in the right-hand panel of Figure 5. There is a clear (expected) difference with the reduced value of the electrical power output. The maximal deviation is 8.66% (200kWe). In this example the average of the electrical power output for the green line is 2551.54kWe, 2546.62kWe and 2507.42kWe for each interval whereas the values of the black dotted line (power output for the average environment temperature in that interval) are 2553.27kWe, 2549.03kWe and 2509.73kWe. The real average value of the electrical power output is slightly lower than the one used in the reduced calculations. The difference in income from selling the electricity is smaller than 0.1%; so the use of reduced profiles is justified. Remember that the average value of the real hourly heat demand is the same as the reduced value, since that was how the reduced values were defined.

During the last 21 (reduced) data points on the load duration curve (Figure 4), there is no heat demand and only electrical power is produced in the ORC. The electricity only mode mostly happens during summer when environment temperatures are high. Figure 6 shows the actual electrical power output (green) for the last 756 hours (being 21 reduced data points) of the load duration curve. The electrical power output is not constant due to the changing

environment conditions (cyan, dashed) – both are negatively correlated. The black dotted

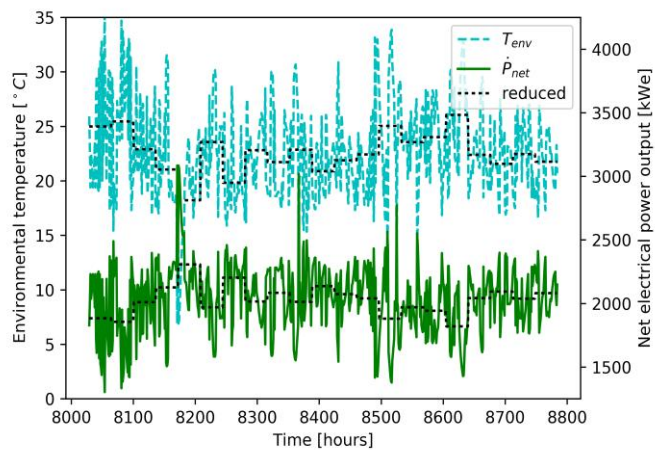


Figure 6: Real temperature of the environment (cyan, dashed) and net electrical power (green) compared to the reduced values (black, dotted).

lines indicate the results for the reduced data points. We observe that the real electrical power output (green) deviates from the reduced one (black, dotted). The minimal, maximal and average difference between the real and the reduced electrical power output are 0.01%, 33.34% and 0.28%. The values are positive, so the average real hourly power output is higher than the reduced one. Converted to cost, the income over the last 21 data points (approximately 1 month) is in reality 262.67EUR (or 0.28%) higher than the predicted income by the reduced profiles. So, also here, the use of the reduced profiles is justified.

### Summary/Conclusions

In this work, we have proposed a two-step optimization framework for the design and off-design performance of a parallel CHP plant. In the first step, we optimized the design of the heat exchangers and the air-cooled condenser of the parallel CHP plant. In the second step, we optimize the electrical power output for each moment in time – and satisfying the varying heat demand of the DH system. Rather than performing the optimization for every hour, we have considered only 244 data points (reducing the calculation time by a factor 36) and we found an acceptable accuracy for the electrical power output and cost calculations.

We have shown the results for a small district heating system in Mol (Belgium) and used hourly weather and DH system data for 2016. For the investigated case, the geothermally-fed CHP is not able to satisfy the DH system heat demand at peak moments, so that additional gas boilers (and thermal storage) are required.

A high-level study on the role of the geothermal CHP, gas boilers and heat storage tanks is considered for future work. Additionally, in future work it would be interesting to investigate the effect of real hourly electricity prices on the results. A final subject for future work is the feedback between the off-design step and the design step (step 2 and 1 of the proposed optimization framework). Based on the off-design results, we might come up with a better CHP plant design.

### Acknowledgements

This project receives the support of the European Union, the European Regional Development Fund ERDF, Flanders Innovation & Entrepreneurship and the Province of Limburg.

### References

- [1] D. Walraven, B. Laenen, and W. D’haeseleer, “Economic system optimization of air-cooled organic Rankine cycles powered by low-temperature geothermal heat sources,” *Energy*, vol. 80, pp. 104–113, 2015.
- [2] D. Budisulistyo, C. S. Wong, and S. Krumdieck, “Lifetime design strategy for binary geothermal plants considering degradation of geothermal resource productivity,” *Energy Convers. Manag.*, vol. 132, pp. 1–13, Jan. 2017.
- [3] M. Usman, M. Imran, Y. Yang, D. H. Lee, and B.-S. Park, “Thermo-economic

- comparison of air-cooled and cooling tower based Organic Rankine Cycle (ORC) with R245fa and R1233zde as candidate working fluids for different geographical climate conditions,” *Energy*, vol. 123, pp. 353–366, Mar. 2017.
- [4] E. Martelli, F. Capra, and S. Consonni, “Numerical optimization of Combined Heat and Power Organic Rankine Cycles – Part A: Design optimization,” *Energy*, vol. 90, pp. 310–328, Oct. 2015.
- [5] F. Capra and E. Martelli, “Numerical optimization of combined heat and power Organic Rankine Cycles – Part B: Simultaneous design & part-load optimization,” *Energy*, vol. 90, pp. 329–343, 2015.
- [6] F. Calise, C. Capuozzo, A. Carotenuto, and L. Vanoli, “Thermoeconomic analysis and off-design performance of an organic Rankine cycle powered by medium-temperature heat sources,” *Sol. Energy*, vol. 103, pp. 595–609, 2014.
- [7] F. Marty, S. Serra, S. Sochard, and J.-M. Reneaume, “Economic optimization of a combined heat and power plant: heat vs electricity,” *Energy Procedia*, vol. 116, pp. 138–151, Jun. 2017.
- [8] S. Van Erdeweghe, J. Van Bael, B. Laenen, and W. D’haeseleer, “Optimal combined heat-and-power plant for a low-temperature geothermal source,” *Energy*, vol. 150, pp. 396–409, May 2018.
- [9] S. Van Erdeweghe, Van Bael, Johan, B. Laenen, and W. D’haeseleer, “Feasibility study of a low-temperature geothermal power plant for multiple economic scenarios,” in *30th International Conference on Efficiency, Cost, Optimization, Simulation and Environmental Impact of Energy Systems (ECOS)*, 2017.
- [10] S. Bos and B. Laenen, “Development of the first deep geothermal doublet in the Campine Basin of Belgium,” *Eur. Geol.*, vol. 43, pp. 16–20, 2017.
- [11] E. Macchi and A. Perdichizzi, “Efficiency predictions for axial-flow turbines operating with nonconventional fluids,” *J. Eng. Power*, vol. 103, no. 4, pp. 718–724, 1981.
- [12] D. H. Cooke, “On Prediction of Off-Design Multistage Turbine Pressures by Stodola’s Ellipse,” *J. Eng. Gas Turbines Power*, 1985.
- [13] K. R. Keeley, “A theoretical investigation of the part-load characteristics of LP steam turbine stages,” *Memo. RD/L/ES0817/M88, Cent. Electr. Gener. Board*, 1988.
- [14] G. van Rossum, “Python Tutorial, Technical Report CS-R9526,” Amsterdam, 2.7.10, 1995.
- [15] J. Andersson, “A General-Purpose Software Framework for Dynamic Optimization,” Arenberg Doctoral School, KU Leuven, 2013.
- [16] A. Wächter and L. T. Biegler, “On the implementation of an interior-point filter line-search algorithm for large-scale nonlinear programming,” *Math. Program.*, vol. 106, no. 1, pp. 25–57, Mar. 2006.
- [17] E. W. Lemmon, M. L. Huber, and M. O. McLinden, “NIST Reference Fluid Thermodynamic and Transport Properties REFPROP.” The National Institute of Standards and Technology (NIST), 2007.

# A Study on Optimum Discharge Pressure of Transcritical CO<sub>2</sub> Heat Pump System under Different Ambient Temperatures and Compressor Frequencies

Xiang Qin, Xinli Wei, Dongwei Zhang\* and Xiangrui Meng

Research Center on the Technology and Equipments for Energy Saving in Thermal Energy System of MOE,  
School of Chemical Engineering and Energy, Zhengzhou University, Henan, 450001, China

\*Corresponding author: zhangdw@zzu.edu.cn

## Abstract

In order to study on how the evaporation temperature, discharge pressure and compressor performance will influence the transcritical CO<sub>2</sub> heat pump cycle, an experimental system for a transcritical CO<sub>2</sub> air source heat pump with internal heat exchanger was established. Under the ambient temperature of 15°C and 30°C, we made the discharge pressure varied from 70bar to 120bar, and changed the compressor frequency from 20Hz to 40Hz. The test results show that under different ambient temperatures and compressor frequencies, the variation trend of the COP of the system, heating capacity and outlet water temperature are almost same. However, as the ambient temperature increases, the COP decreases, the heating capacity does not change, and the outlet water temperature increases. With the increase of compressor frequency, the COP of the system decreases, the heating capacity and outlet water temperatures increase. Finally, two non-generalized correlations are obtained by combining the experimental data. One is the highest outlet temperature under different ambient temperatures and compressor frequencies, the other is the optimum outlet pressure under different ambient temperatures and compressor frequencies. The error range is within  $\pm 5\%$ .

**Keywords:** Transcritical cycle, Carbon dioxide, Compressor frequency.

## Introduction

As a natural refrigerant, CO<sub>2</sub> has been widely used in ships, theaters and other refrigeration systems since the end of the 19th century. However, due to the appearance of artificial refrigerants, CO<sub>2</sub> gradually fades out of the refrigeration system. Nowadays, with the destruction of artificial refrigerants to our environment, the natural refrigerants once again return to the stage. Compared with traditional refrigerants, CO<sub>2</sub> has many advantages, such as non-flammable, non-toxic, and cost-friendly. At the end of the 20th century, Lorentzen proposed the transcritical CO<sub>2</sub> circulation systems for automotive air conditioning and other applications [1]. The critical temperature of CO<sub>2</sub> is only 31.1°C, which is similar to the ambient temperature, so it is beneficial to the direct conversion of CO<sub>2</sub> at both subcritical and supercritical levels [2] And there is no phase change in the exothermic process of CO<sub>2</sub>, the temperature slip of the refrigerant and the increase of the water temperature can better match and produce hot water with higher temperature. Compared to the evaporator in the traditional system, it is called gas cooler [3].

In recent years, many scholars have conducted theoretical and practical studies on the discharge pressure corresponding to the highest system COP in a transcritical CO<sub>2</sub> cycle system under different ambient temperatures. Kauf et al. [4] simulated the change in COP of a transcritical CO<sub>2</sub> refrigeration cycle under ambient temperature of 35°C to 50°C, and summarized the correlation of optimal discharge pressure. Ge et al. [5] conducted a numerical simulation of a medium-temperature food retailing refrigeration system and concluded that the optimal discharge pressure is mainly determined by the ambient temperature. Aprea et al. [6] studied the optimal operating conditions of a two-stage compressed transcritical CO<sub>2</sub> air conditioning system under different ambient temperatures and discharge pressures through simulations and experiments, and made a relevance optimization to the optimal discharge



pressure of Liao et al. In addition, the above have obtained a similar result that by increasing the ambient temperature, the COP of the refrigeration system will decrease, and the optimal discharge pressure will increase.

Wang et al. [7] studied the COP of the transcritical CO<sub>2</sub> heat pump system, the CO<sub>2</sub> outlet temperature of the gas cooler and the evaporation temperature of the air source under different ambient temperatures, and obtained the correlation of the optimal discharge pressure of the heat pump system. Qi et al. [8] studied the transcritical CO<sub>2</sub> heat pump system by changing the ambient temperature and the CO<sub>2</sub> outlet temperature of the gas cooler, and obtained the correlation of the optimal discharge pressure through the CO<sub>2</sub> outlet temperature of the gas cooler. Liu et al. [9] established a transcritical CO<sub>2</sub> heat pump system for water. And they found out that increasing the water source temperature can improve the system's heating capacity, water outlet temperature, and COP.

Most of above studies focused on revealing the evaporation temperature and the gas cooler outlet CO<sub>2</sub> temperature influence the transcritical CO<sub>2</sub> heat pump cycle. Further studies are still needed to the influence of the compressor performance. In this work, we will select the compressor performance as the main research object, and study the transcritical CO<sub>2</sub> heat pump system by changing the compressor frequency.

## Experimental equipment and processes

### Experimental Equipment

The main equipment of this laboratory bench includes transcritical CO<sub>2</sub> compressors, gas coolers, internal heat exchanger, expansion device and evaporators. In order to meet the frequency conversion requirements of the compressor, a high-performance open-loop vector converter from Invt was used. The specific parameters of the equipments are shown in Table 1. The flow chart of the experimental station is shown in Fig. 1.

Table 1 Specific parameters of the equipments

Name	Type
Compressor	GEA, Semi-hermetic transcritical CO <sub>2</sub> compressor
Gas cooler	HZSS, Tube-in-tube heat exchanger, Outside/Inside diameter: Φ33 mm/Φ28 mm
Internal heat exchanger	HZSS, Tube-in-tube heat exchanger, Outside/Inside diameter: Φ33 mm/Φ25 mm
Expansion device	Subel-lok, Manual operating
Evaporator	Fin-and-tube, Tube diameter: Φ9.52 mm, transfer area: 74m <sup>2</sup>

### Introduction of actual operating conditions

There are three variable parameters which influence the actual operating conditions: compressor frequency, discharge pressure, and ambient temperature. The compressor frequency is controlled by frequency converter. The experimental adjustment range of it is 20Hz~40Hz; The discharge pressure is controlled by two parallel expansion devices, each expansion device have 6 kind of openings, and the adjustment range of discharge pressure in the test is 70bar~120bar, 73.1bar meet the CO<sub>2</sub> supercritical demand, and 120bar meet the system safety requirements; The evaporator is an outdoor equipment, which can better simulate the actual working conditions. In other to meet the needs of the ambient temperature, we choose to do the experiment in different time period. The ambient temperature of 15°C

will be completed from October to November, while the ambient temperature of 30°C will be completed in September. In this experiment, the inlet temperature is 15°C and the flow rate is 0.5m<sup>3</sup>/h. When the ambient temperature is 15°C, the range of the outlet water temperature is 45°C~90°C. When the ambient temperature is 30°C, the range of the outlet water temperature is 55°C~105°C.

## Results and discussion

### COP and the Maximum COP

It can be seen From Fig. 2 to Fig. 6 that under the same ambient temperature and different compressor frequencies, the trend of COP is almost same, it first rises rapidly, and then decreases after reaching the peak value. With the increase of the frequency of the compressor, the curve of the later decline of COP gradually flattened. As the ambient temperature increases, the peak value of the COP shifts in the direction of where the discharge pressure increased. It is worth noting that, the peak value of the COP under ambient temperature of 15°C is greater than the ambient temperature of 30°C except for 20Hz and 35Hz.

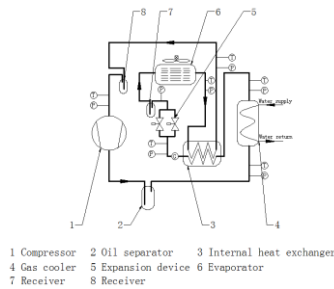


**Fig. 1.** Schematics of a transcritical CO<sub>2</sub> heat pump

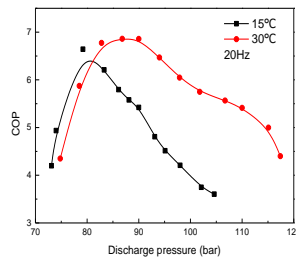


**Fig. 2.** COP at a compressor frequency of 20Hz.

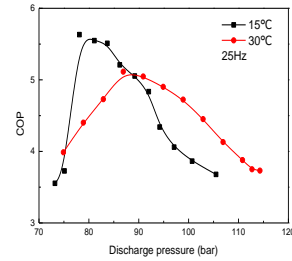


**Fig. 3.** COP at a compressor frequency of 25Hz.

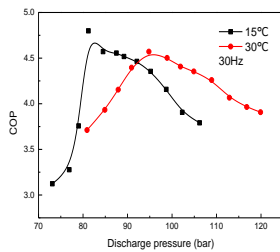


**Fig. 4.** COP at a compressor frequency of 30Hz

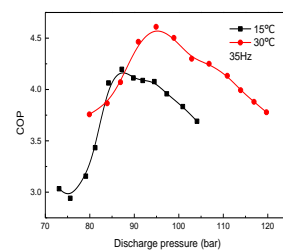


**Fig. 5.** COP at a compressor frequency of 35Hz

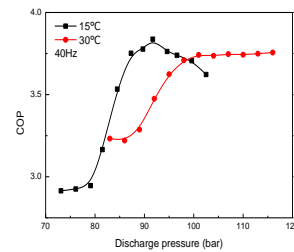


**Fig. 6.** COP at a compressor frequency of 40Hz.

General system COP is defined as, see Eq. (1):

$$\text{COP} = \frac{Q_{gc}}{W_{com}} = \frac{m \cdot \Delta h_{gc}}{m \cdot \Delta h_{com}} \quad (1)$$

It would also be defined as:

$$\text{COP} = \frac{h_2 - h_3}{h_2 - h_1} \quad (2)$$

From above we can study the reasons for the changes of COP through the analysis of gas cooler and compressor enthalpy difference.

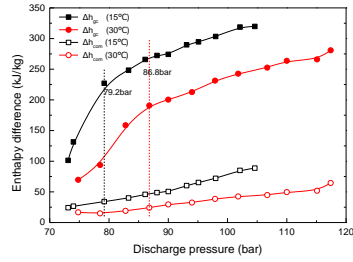


**Fig. 7.** The enthalpy difference of gas cooler and compressor at the compressor frequency of 20 Hz

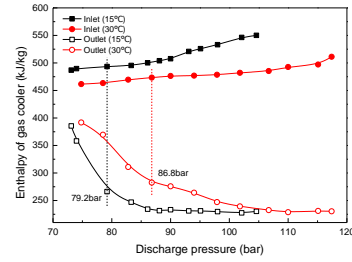


**Fig. 8.** The change of the enthalpy of the gas cooler.

It can be seen from Fig. 7 that there is a small increase of compressor enthalpy difference, and it has a substantial increase at the beginning. When the COP reaches the maximum value, the speed slows down. When the ambient temperature is 15°C, with the cutoff point of 79.2bar, the rising slope of the enthalpy difference in the first half of the gas cooler is 20.6, and the latter half is 3.6. And with the cut-off point of 86.8bar, when the ambient temperature is 30°C, the rising slope of the enthalpy difference in the first half of the gas cooler is 10.1, while the latter half is 2.9. Therefore, the enthalpy difference of the gas cooler is the main cause of the large COP.

Fig. 8 shows the changes of inlet and outlet enthalpy values of the gas cooler. As you can see from the figure, the inlet enthalpy of the gas cooler has not changed much, but the outlet enthalpy has decreased significantly even before the demarcation point. This apparent decline is the reason for the rapid increase in COP of the system. Drag the value of outlet enthalpy into the pressure-enthalpy diagram. We found that the change trend of the outlet enthalpy value of the gas cooler at the second half matches the change trend of the isothermal line of the pressure enthalpy map.

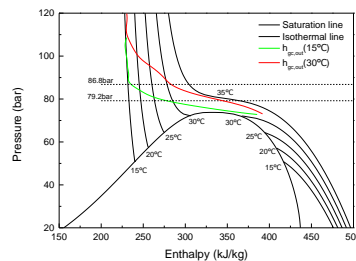


**Fig. 9.** Pressure-enthalpy diagram of the change of the outlet enthalpy of the gas cooler.

As you can see from Fig. 9, as the discharge pressure increases, the outlet temperature of the gas cooler begins to decrease. Due to the influence of convective heat transfer and the inlet water temperature, the outlet temperature of the gas cooler maintained near 15°C (the inlet water temperature), so the change in the second half of the gas cooler's outlet temperature matches the 15°C isothermal. Choose 79.2bar and 86.8bar to be the demarcation point. Since the isotherm above the critical point is almost horizontal and the temperature of the CO<sub>2</sub> outlet of the gas cooler falls slowly, it is almost same as the isotherm trend, which leads to a rapid drop of the CO<sub>2</sub> gas cooler outlet enthalpy. After the demarcation point, the temperature of the gas cooler outlet rapidly decreased, the discharge pressure increased, and the enthalpy value of the gas cooler outlet rapidly increased. The change in enthalpy slows down. This trend is the main reason for the large COP.

### Heating and outlet water temperatures

Another expression of heating is the heat absorbed by the water, see Eq. (3). The change of the volumetric flow rate, density, and specific heat of water is very small, the amount of heat generated directly affects the water temperature difference between the inlet and outlet of the gas cooler. The water inlet temperature of the gas cooler remains 15°C, so the larger the heating capacity, the higher the water outlet temperature of the gas cooler will be. Fig. 10 and Fig. 11 also show the same phenomenon.

$$Q_{gc} = V_w \cdot \rho_w \cdot C_{p,w} \cdot \Delta T_w \quad (3)$$

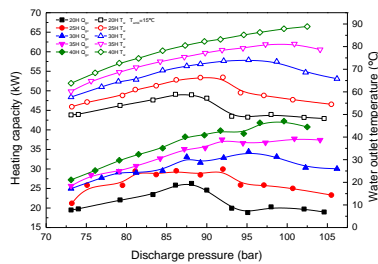


**Fig. 10.** The corresponding heating capacity and water outlet temperature under different discharge pressure when the temperature is 15°C.

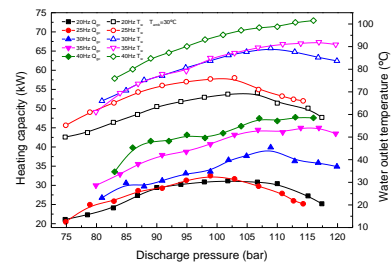


**Fig. 11.** The corresponding heating capacity and water outlet temperature under different discharge pressure when the temperature is 30°C.

As shown in Fig. 10 and Fig. 11, the trend of the water outlet temperature is almost the same as the change trend of the heating capacity. Under different ambient temperatures, both 20Hz and 35Hz show the trend of rising to peak and then downward. Among them, when the ambient temperature is 15°C, the heating capacity rise ratios were 34.9%, 41.2%, 38.0%, and 47.2%, respectively, and the water outlet temperature rise ratios were 15.4%, 19.6%, 28.4%, and 34.9%, respectively. At the ambient temperature of 30°C, the heating capacity ratios were 47.6%, 58.8%, 49.2%, and 50.1%, respectively, and the water outlet temperature rise ratios were 39.2%, 38.0%, 35.3%, and 50.6%, respectively. And under the discharge pressure of 40Hz, no matter how much the ambient temperature is, the heating capacity kept rising. So, we concluded that the water outlet temperature is mainly affected by heating capacity.

We can obtain the maximum water outlet temperature under different compressor frequency. The lower the compressor frequency, the higher the COP will be. Therefore, by studying the temperature demand of hot water and selecting the appropriate compressor frequency, we can save energy. The non-generalized correlation of the highest water outlet temperature corresponding to the compressor frequency at different ambient temperatures was fitted by experimental data. The correlation is shown in Eq. (4). The correlation was further verified and the experimental results were compared with the fitting results in Fig. 12. The correlation error was analyzed by Eq.5. The ambient temperature was 15°C, the error range was  $0.1\% \leq \delta\% \leq 0.7\%$ , the ambient temperature was 30°C, and the error range was  $0 \leq \delta\% \leq 4.7\%$ .

### Optimal discharge pressure

COP changes under different compressor frequencies and ambient temperatures. But under different working conditions, the peak value of COP is different, and the compressor discharge pressure corresponding to the COP peak value is regarded as the optimal discharge pressure. The discharge pressure can be controlled to maintain the optimal operation of the system. Fig. 13 shows the maximum COP and the corresponding discharge pressure under different compressor frequencies and ambient temperatures.

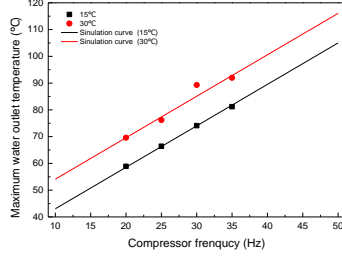


**Fig. 12.** The experimental value and fitting curve for the maximum water outlet temperature

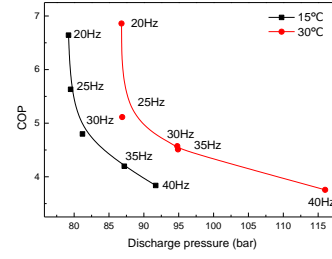


**Fig. 13.** The corresponding COP and Discharge pressure under different compressor frequencies when the temperature is 30°C and 15°C.

$$T_{w,corr} = 16.51 + 0.737T_{amb} + 1.549f_{com} \quad (4)$$

$$\delta\% = \left| \frac{(T_{w,corr} - T_{w,max})}{T_{w,max}} \times 100 \right| \quad (5)$$

From the figure, we can see that under the compressor frequency of 20 Hz, when the ambient temperature is 15°C the maximum COP is 6.6. And when the ambient temperature is 30°C, the maximum COP is 6.8. As the compressor frequency increases, the system COP rapidly decreases. Under the compressor frequency of 40Hz, when the ambient temperature is 15°C the maximum COP is 3.8. And when the ambient temperature is 30°C, the maximum COP is 3.7. Compared with other refrigeration cycles, transcritical CO<sub>2</sub> heat pumps perform better under high ambient temperatures and low compressor frequencies.

We take the changes of compressor frequency and ambient temperature into consideration, and fit it into a non-generalized correlation of optimal discharge pressure, see Eq. (6). its relevance applies of ambient temperatures is from 15°C to 30°C while the compressor frequencies is from 20Hz to 50Hz.

Fig. 14 shows a comparison of test results and fitting correlations. We use Eq. (7) for the error analysis. The analysis shows that when the ambient temperature is 15°C, the error range is 0.1% ≤ δ% ≤ 1.3%. When the ambient temperature is 30°C, the error range is 0.1% ≤ δ% ≤ 4.3%.

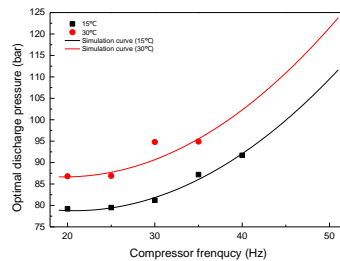


**Fig. 14.** The experimental value and fitting curve for the optimal discharge pressure.

$$P_{opt,corr} = (0.034 + 0.00013T_{amb})f_{com}^2 - 1.493f_{com} + 0.473T_{amb} + 87.18 \quad (6)$$

$$(0^\circ\text{C} < T_{amb} \leq 30^\circ\text{C}, 20\text{Hz} \leq f_{com} \leq 50\text{Hz}) \quad (7)$$

$$\delta\% = \left| \frac{(P_{opt,corr} - P_{opt})}{P_{opt}} \times 100 \right| \quad (8)$$

### Uncertainty analysis

In this paper, one method of estimating uncertainty in experimental results has been presented by Kline and McClintock(1953). The method sums the square of errors:

$$\delta_R = \left[ \sum_{i=1}^j \left( \frac{\partial R}{\partial x_i} \delta_{x_i} \right)^2 \right]^{1/2} \quad (9)$$

Combining Eq. 1 and 9 give:

$$\delta_{COP} = \left[ \left( \frac{\partial COP}{\partial Q_{gc,w}} \delta_{Q_{gc,w}} \right)^2 + \left( \frac{\partial COP}{\partial W_{com}} \delta_{W_{com}} \right)^2 \right]^{1/2} \quad (10)$$

Based on the accuracies of the measurement devices and the experimental data , the uncertainty of COP can be obtained and the maximum value is 5.3487%.

### Conclusion

In this paper, we study on how the evaporation temperature, discharge pressure and compressor performance will influence the transcritical CO<sub>2</sub> heat pump cycle. Based on the experimental results, the conclusion is as follows:

Under different ambient temperatures and compressor frequencies, there will be peaks in the system COP as the discharge pressure rises. Analytical experimental results show that the cause of the peak is the rapid drop in the enthalpy of the outlet gas cooler. The temperature of the CO<sub>2</sub> outlet of the gas cooler decreased slowly at first, then it decreased rapidly, finally it maintained a constant trend. Since the isotherm above the critical point is almost horizontal and the temperature of the CO<sub>2</sub> outlet of the gas cooler falls slowly, it is almost same as the isotherm trend, which leads to a rapid drop of the of the CO<sub>2</sub> gas cooler enthalpy. This rapid decline makes COP reaches its peak. After that, the temperature of the CO<sub>2</sub> outlet of the gas cooler decreased rapidly, and change of the enthalpy of the CO<sub>2</sub> gas cooler outlet slowed down. Finally, because the inlet water temperature is fixed, the CO<sub>2</sub> outlet temperature of the gas cooler will be the same as the water inlet temperature. This result in the stable enthalpy of the CO<sub>2</sub> gas cooler outlet. This is also the main reason for the higher COP in this experiment. According to the change of the compressor frequency and the ambient temperature, we obtained a correlation about the highest outlet temperature, which can provide guidance for the selection of compressor frequency under different water temperature requirements.

We also obtained a correlation about the optimal discharge pressure. We selected the discharge pressure corresponding to the maximum COP as the optimal discharge pressure, and obtained a correlation about the optimal discharge pressure based on the changes of the ambient temperature and the compressor frequency.

### Acknowledgements

The study was supported by National Natural Science Foundation of China (Grants No. 51706208) and Outstanding Young Teachers Development Foundation of Zhengzhou University (Grants No. 1421322060).

### References

- [1] Lorentzen G, Pettersen J., A new efficient and environmentally benign system for car air-conditioning, *International Journal of Refrigeration*, 1993.
- [2] Fartaj A, Ting S K, Yang W W., Second law analysis of the transcritical CO<sub>2</sub>, refrigeration cycle, *Energy Conversion & Management*, 2004.
- [3] Ma Y, Liu Z, Tian H., A review of transcritical carbon dioxide heat pump and refrigeration cycles, *Energy*, 2013.

- [4] Kauf F., Determination of the optimum high pressure for transcritical CO<sub>2</sub> refrigeration cycles, *International Journal of Thermal Sciences*, 1999.
- [5] Ge Y T, Tassou S A., Control optimization of CO<sub>2</sub> cycles for medium temperature retail food refrigeration systems, *International Journal of Refrigeration*, 2009.
- [6] Aprea C, Maiorino A., Heat rejection pressure optimization for a carbon dioxide split system: An experimental study, *Applied Energy*, 2009.
- [7] Wang S, Tuo H, Cao F, et al., Experimental investigation on air-source transcritical CO<sub>2</sub> heat pump water heater system at a fixed water inlet temperature, *International Journal of Refrigeration*, 2013.
- [8] Qi P C, He Y L, Wang X L, et al., Experimental investigation of the optimal heat rejection pressure for a transcritical CO<sub>2</sub> heat pump water heater, *Applied Thermal Engineering*, 2013.
- [9] Liu X, Liu C, Zhang Z, et al., Experimental Study on the Performance of Water Source Trans-Critical CO<sub>2</sub> Heat Pump Water Heater, *Energies*, 2017.

# Numerical analysis for dehydration and hydration of calcium hydroxide and calcium oxide in a packed bed reactor

S. Funayama<sup>1\*</sup>, M. Zamengo<sup>2</sup>, H. Takasu<sup>3</sup>, K. Fujioka<sup>4</sup>, and Y. Kato<sup>5</sup>

<sup>1</sup>Graduate Major in Nuclear Engineering, Tokyo Institute of Technology, 2-12-1-N1-22, Ookayama, Meguro-ku, Tokyo 152-8550, Japan

<sup>2</sup>Department of Materials Science and Engineering, Tokyo Institute of Technology, 2-12-1-S8-29, Ookayama, Meguro-ku, Tokyo 152-8550, Japan

<sup>3</sup>Department of Nuclear Engineering, Tokyo Institute of Technology, 2-12-1-N1-22, Ookayama, Meguro-ku, Tokyo 152-8550, Japan

<sup>4</sup>Functional Fluids Ltd., 5th Fl., Chiyoda Bldg. Annex, 1-4-5, Utsubohonmachi, Nishi-Ku, Osaka 550-0004, Japan

<sup>5</sup>Laboratory for Advanced Nuclear Energy, Institute of Innovative Research, Tokyo Institute of Technology, 2-12-1-N1-22, Ookayama, Meguro-ku, Tokyo 152-8550, Japan

\*Corresponding author: funayama.s.aa@m.titech.ac.jp

## Abstract

Thermochemical energy storage (TCES) using calcium oxide/calcium hydroxide/water (Ca(OH)<sub>2</sub>/CaO/H<sub>2</sub>O) reaction system is a promising technology for thermal energy storage. Practical storage reactor requires high responsivity for heat storage process and heat output process. Enhancement of transport properties of reaction bed can be a solution to improve responsivity as well as optimisation of reactor design. The aim of this study is to investigate effects of thermal conductivity on TCES performances of a reaction bed. Firstly, validation of a numerical model was conducted using experimental data of a packed bed reactor. Secondly, effects of thermal conductivity on hydration conversion, bed temperature, heat output rate and heat output density were examined. It was estimated that heat output rate on the condition that thermal conductivity is 5.0 W m<sup>-1</sup> K<sup>-1</sup> becomes 4.6 times higher than that in case of 0.18 W m<sup>-1</sup> K<sup>-1</sup>. Thus, it was shown numerically that enhancement of thermal conductivity improves heat output rate of the reaction bed.

**Keywords:** Thermochemical energy storage, Calcium hydroxide pellets, Hydration, Numerical analysis.

## Introduction

Thermochemical energy storage (TCES) is a promising technology for thermal energy storage (TES) that can be applied to concentrated solar power and surplus heat recovery system. TES is essential for surplus heat recovery that contributes to improve efficiency of energy utilization where more than 50% of global primary energy is estimated to be released as waste heat [1]. TCES uses reversible gas-solid reactions and converts thermal energy to chemical energy. In general, TCES can store thermal energy with higher energy density and for longer storage period than latent heat storage and sensible heat storage. This study focuses on the TCES using calcium oxide/calcium hydroxide/water (CaO/Ca(OH)<sub>2</sub>/H<sub>2</sub>O) reaction system. The TCES uses the following reaction [2]:



A forward reaction is dehydration of calcium hydroxide and a backward reaction is hydration of calcium oxide. Dehydration is an endothermic reaction and hydration is an exothermic reaction. Thermal storage process and thermal output process use dehydration and hydration, respectively. The storage materials i.e. calcium hydroxide and calcium oxide have advantages of low material cost, high reactivity and less toxicity.



To enhance response speed of a storage reactor, development of storage material of which bed has high transport properties [3,4] is important as well as optimization of reactor design [5]. The aim of this study is to investigate effects of thermal conductivity of storage material on heat output properties of reaction bed numerically. Firstly, this paper evaluates validity of a numerical model of hydration using experimental data of a packed bed reactor. Secondly, present paper reports effects of thermal conductivity on hydration conversion, bed temperature, heat output rate and heat output density.

### Experimental

Packed bed reactor experiment was performed to evaluate a numerical model. Cylindrical pellets of calcium hydroxide (diameter: 1.9 mm, length: 2 -10 mm) was used as  $\text{Ca}(\text{OH})_2$  sample. Total mass of the sample was 59.6 g. **Fig. 1** shows a sectional view of the cylindrical packed bed reactor. To obtain pure atmosphere of water, the reaction chamber that encases the reactor was vacuumed after charging the material.

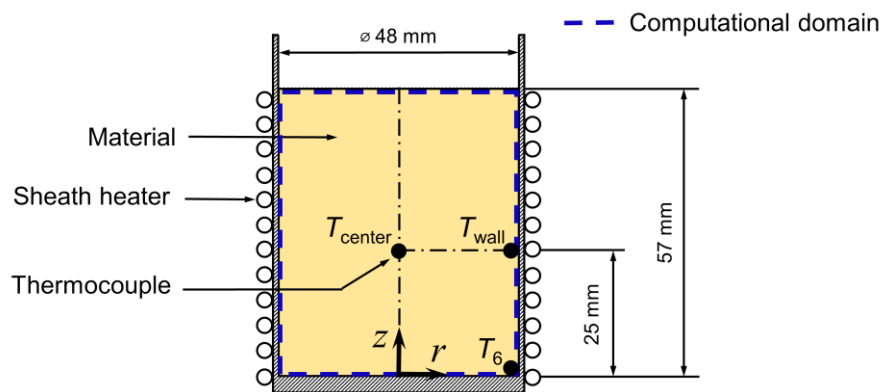


**Fig. 1** The cylindrical packed bed reactor and computational domain.

Initial temperature of the reactor wall ( $T_{\text{wall}}$ ) was set  $350^\circ\text{C}$ . Hydration experiments was performed after dehydration and initiated by introducing water vapour of 57.9 kPa. Bed temperatures and mass change of the reaction chamber were measured and the mass change was used to calculate hydration conversion,  $x_h$  [-] described by the following equation:

$$x_h = \frac{\Delta m / M_{\text{H}_2\text{O}}}{m_{\text{Ca}(\text{OH})_2} / M_{\text{Ca}(\text{OH})_2}} \quad (2)$$

where,  $\Delta m$  [g],  $m_{\text{Ca}(\text{OH})_2}$  [g],  $m_{\text{H}_2\text{O}}$  [ $\text{g mol}^{-1}$ ],  $M_{\text{Ca}(\text{OH})_2}$  [ $\text{g mol}^{-1}$ ] indicate mass change, initial mass of calcium hydroxide pellets, molar mass of water and calcium hydroxide, respectively.

### Numerical analysis method

Computational domain shown in **Fig. 1** was assumed to be continuum and the volume of the domain is constant. Hydration pressure of the domain was assumed to be uniform and constant (57.9 kPa). Heat conduction equation expressed as Eq. (3) and rate equations of hydration derived by Schaube et al. [6] were used as governing equations.

$$\rho c_p \frac{\partial T}{\partial t} = \nabla \cdot (\lambda \nabla T) + \Delta_r H n_{\text{ini}} \frac{\partial x_{\text{h,local}}}{\partial t} \quad (3)$$

where,  $\rho$  [ $\text{kg m}^{-3}$ ],  $c_p$  [ $\text{J K}^{-1} \text{kg}^{-1}$ ],  $T$  [K],  $t$  [s],  $\lambda$  [ $\text{W m}^{-1} \text{K}^{-1}$ ],  $\Delta_r H$  [ $\text{J mol}^{-1}$ ],  $n_{\text{ini}}$  [ $\text{mol m}^{-3}$ ],  $x_{\text{h,local}}$  [-] indicate density, specific heat, temperature, time, thermal conductivity, reaction enthalpy, initial mole per unit volume of the bed, local conversion of hydration, respectively. The density of the bed was obtained by the packed bed reactor experiment and specific heat of the materials were calculated from literature values [7]. Thermal conductivity of the bed of  $\text{Ca(OH)}_2$  pellets was measured by a thermal conductivity meter (QTM-500, Kyoto Electronics, Japan) and the value was  $0.18 \text{ W m}^{-1} \text{K}^{-1}$ .

Initial temperature distribution was predetermined by a heat transfer analysis and boundary conditions described by Eqs. (4)-(7):

$$r < R; z = H_2: \quad -\lambda \frac{\partial T}{\partial z} = h_{\text{top}} (T_s - T_{\infty, \text{top}}) \quad (4)$$

$$r = R; 0 \leq z \leq H_1 / 2: \quad T = \frac{T_{\text{wall,ini}} - T_{6,\text{ini}}}{H_1 / 2} z + T_{6,\text{ini}} \quad (5)$$

$$r = R; H_1 / 2 < z < H_2: \quad T = T_{\text{wall,ini}} \quad (6)$$

$$r < R; z = 0: \quad -\lambda \frac{\partial T}{\partial z} = h_{\text{bottom}} (T_s - T_{\infty, \text{bottom}}) \quad (7)$$

where,  $R$  [m],  $H_1$  [m],  $H_2$  [m] indicate radius of the bed, the height of thermocouples ( $T_{\text{center}}$ ,  $T_{\text{wall}}$ ) and height of the bed, respectively. The Dirichlet boundary condition was applied to the wall using experimental data of temperatures. The Robin boundary condition was applied to the top and bottom surface of the reaction bed. Heat transfer coefficients,  $h$ , and external temperatures,  $T_{\infty}$ , are shown in **Table 1**.

**Table 1** Parameters of boundary conditions

	$h$ [ $\text{W m}^{-2} \text{K}^{-1}$ ]	$T_{\infty}$ [K]
Top	50	615
Bottom	80	572

Simplified boundary conditions expressed by Eqs. (8), (9) were used for the surfaces of the bed in parameter analysis that was performed to examine effects of thermal conductivity on TCES performances of the bed. The temperature of the wall was assumed to be constant during hydration and adiabatic condition was applied to the top and bottom surface of the bed.

$$r = R; 0 < z < H_2: \quad T = 623 \text{ K} \quad (8)$$

$$r < R; z = 0, H_2: \quad \frac{\partial T}{\partial z} = 0 \quad (9)$$

The governing equations imposed the initial conditions and boundary conditions were solved by OpenFOAM (-2.3.x).

## Results and Discussion

### Numerical validation

**Fig. 2** shows numerical results and experimental data of the temperature at the center of the bed and conversion during hydration. Calculated maximum temperature at the center of the bed agreed with experimental data. Conversion curve also was agreement with experimental data.

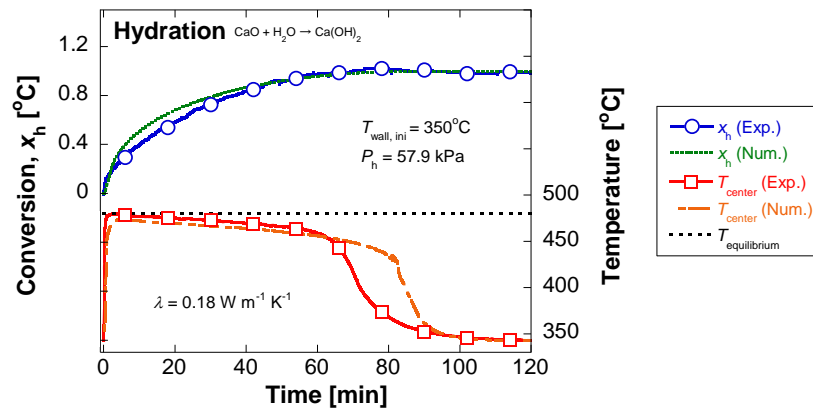


**Fig. 2** Comparison of numerical results and experimental data.

**Fig. 3** shows calculated distribution of temperature during hydration. Temperature around the center was higher than temperature nearby the boundary of the bed and was close to the equilibrium temperature (480°C [6]) corresponding to the pressure of 57.9 kPa. Consequently, reaction rate around the center of the bed is smaller than that of outer region and the reaction front proceeded toward the center of the bed (**Fig. 4**).

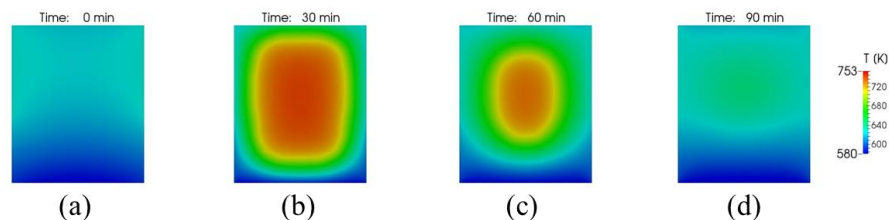


**Fig. 3** Distribution of temperature,  $T$ , on the cross section of the reaction bed during hydration: (a)  $t = 0$  min; (b)  $t = 30$  min; (c)  $t = 60$  min; (d)  $t = 90$  min.

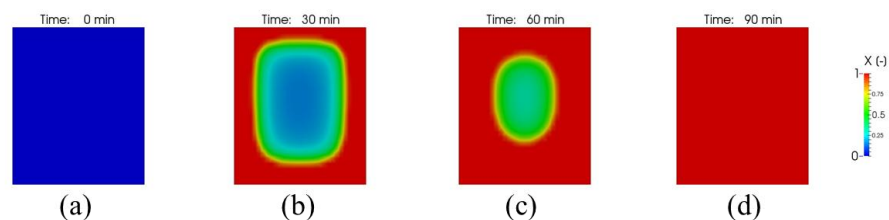


**Fig. 4** Distribution of conversion,  $x_{h,local}$ , on the cross section of the reaction bed during hydration: (a)  $t = 0$  min; (b)  $t = 30$  min; (c)  $t = 60$  min; (d)  $t = 90$  min.

### Effects of thermal conductivity on hydration conversion and bed temperature

**Fig. 5** shows the temperature at the center of the bed and conversion at different thermal conductivities ( $\lambda = 0.18, 1.0, 5.0 \text{ W m}^{-1} \text{ K}^{-1}$ ) during hydration. Conversion rate becomes higher with the larger thermal conductivity. It was demonstrated numerically that the duration

time of temperature plateau was shortened and maximum temperature decreased with higher thermal conductivity of the bed; the maximum temperature was 474, 457, 439°C when thermal conductivity was 0.18, 1.0, 5.0 W m<sup>-1</sup> K<sup>-1</sup>, respectively.

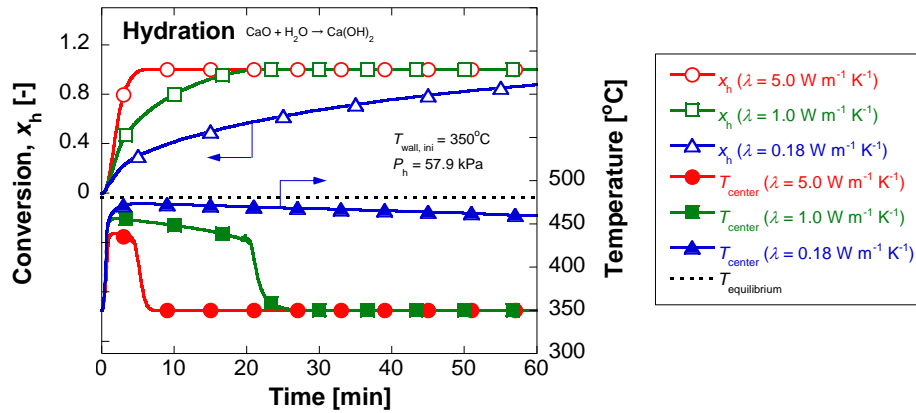


**Fig. 5** Hydration conversion and temperature at the center of the bed at different thermal conductivities.

#### Effects of thermal conductivity on heat output rate and heat output density

Heat output density,  $q_h$ , [J/L-bed] was defined by Eq. (10), where  $V_{bed}$  [L-bed] indicates the volume of the reaction bed. Heat output rate,  $w_h$ , [W/L-bed] was calculated by numerical differentiation of heat output density.

$$q_h = \Delta_r H \frac{m_{ini}}{M_{Ca(OH)_2}} \frac{1}{V_{bed}} x_h \quad (10)$$

**Fig. 6** shows heat storage rate and heat output density at different thermal conductivities. The peak of heat output rate at about 1.8 min with thermal conductivity of 5.0 W m<sup>-1</sup> K<sup>-1</sup> was 4.6 times higher than that with thermal conductivity of 0.18 W m<sup>-1</sup> K<sup>-1</sup>.

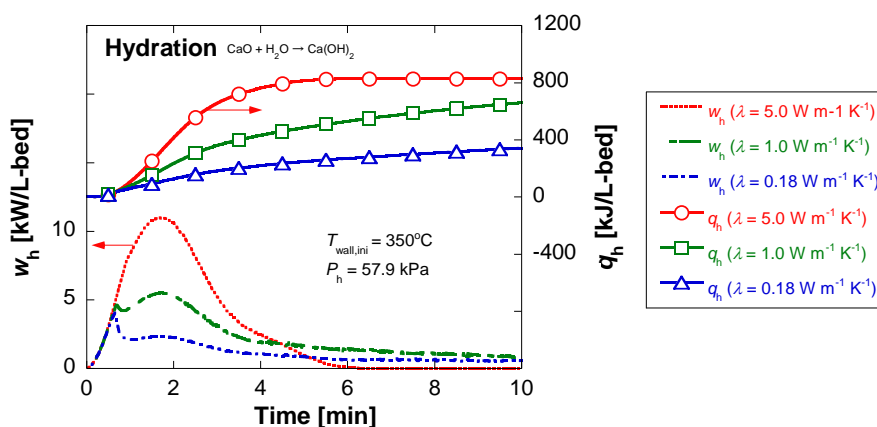


**Fig. 6** Heat storage rate,  $w_h$ , and heat output density,  $q_h$ , at different thermal conductivities.

In this study, to focus on effects of thermal conductivity on thermochemical performances, vapour flow in the bed was neglected. However, a numerical model for practical reactors

requires the effects of the flow of water vapour. Therefore, mass transfer equations will be taken into account in future work.

### Conclusions

This study investigated effects of thermal conductivity on hydration conversion, bed temperature, heat output rate and heat output density numerically. It was estimated that in case thermal conductivity is  $5.0 \text{ W m}^{-1} \text{ K}^{-1}$ , heat output rate becomes 4.6 times higher than that in case thermal conductivity is  $0.18 \text{ W m}^{-1} \text{ K}^{-1}$ . It was shown numerically that enhancement of thermal conductivity of the reaction bed improves heat output rate.

### Acknowledgements

The authors would like to thank Prof. Yasunori Okano and Mr. Keisuke Nishida at Osaka University for their numerical research support.

### References

- [1] Forman, C., Muritala, I. K., Pardemann, R., Meyer, B., “Estimating the global waste heat potential”, *Renewable & Sustainable Energy Reviews*. 2016;57:1568–79. [doi:10.1016/j.rser.2015.12.192](https://doi.org/10.1016/j.rser.2015.12.192)
- [2] Halstead, P. E., Moore, A. E., “769. The thermal dissociation of calcium hydroxide”, *Journal of the Chemical Society*. 1957:3873–5. [doi:10.1039/JR9570003873](https://doi.org/10.1039/JR9570003873)
- [3] Zamengo, M., Ryu, J., Kato, Y., “Thermochemical performance of magnesium hydroxide-expanded graphite pellets for chemical heat pump”, *Applied Thermal Engineering*. 2014;64:339–47. [doi:10.1016/j.applthermaleng.2013.12.036](https://doi.org/10.1016/j.applthermaleng.2013.12.036)
- [4] Kariya, J., Ryu, J., Kato, Y., “Reaction performance of calcium hydroxide and expanded graphite composites for chemical heat storage applications”, *ISIJ International*. 2015;55:457–63. [doi:10.2355/isijinternational.55.457](https://doi.org/10.2355/isijinternational.55.457)
- [5] Mette, B., Kerskes, H., Drück, H., “Experimental and numerical investigations of different reactor concepts for thermochemical energy storage”, *Energy Procedia*. 2014;57:2380–9. [doi:10.1016/j.egypro.2014.10.246](https://doi.org/10.1016/j.egypro.2014.10.246)
- [6] Schaube, F., Koch, L., Wörner, A., Müller-Steinhagen, H., “A thermodynamic and kinetic study of the de- and rehydration of  $\text{Ca}(\text{OH})_2$  at high  $\text{H}_2\text{O}$  partial pressures for thermochemical heat storage”, *Thermochimica Acta*. 2012;538:9–20 [doi:10.1016/j.tca.2012.03.003](https://doi.org/10.1016/j.tca.2012.03.003).
- [7] Barin, I. *Thermochemical data of pure substances*, 3<sup>rd</sup> Ed., VCH Verlagsgesellschaft, 1995.

# Development of a low-cost, electricity-generating Rankine cycle, alcohol-fuelled cooking stove for rural communities

Wigdan Kisha<sup>1\*</sup>, Paul H.Riley<sup>2</sup> and David Hann<sup>3</sup>

<sup>1,3</sup> Faculty of Engineering, University of Nottingham, UK

<sup>2</sup>School of Mathematics, Computer Science & Engineering, City University of London, UK

Corresponding author: \*Email address: wigdan.kisha@nottingham.ac.uk

## Abstract

This article describes a novel design and construction of a helical tube flash boiler that uses a 2kW nominal methylated spirit burner to heat an approximately 2.5m long coil of copper pipe fed by a nominal 8 bar electrically operated solenoid water pump. The final embodiment is for superheated steam to be converted to electricity and the waste exit heat from the generator used either for cooking or for ethanol production for low-income families in developing countries. The performance of the flash boiler has been evaluated experimentally based on the well-known “Direct-Method”; by carefully measuring both the flow of the fuel and the steam. It found that the pressure inside the pipe can reach up to 7.4 bar and the temperature of the steam released by the flashing process can reach 255 °C utilising a low-cost water pump. The research results presented in this paper demonstrate that flash boiler stove has a great potential for generating high-temperature steam for developing a low-cost cooking stove.

**Keywords:** Flash boiler, spirit burner, copper coil, expander, electrical generator

## Background

The development of sustainable and clean energy technologies is of ever-growing worldwide interest due to global warming and environmental disorder resulted from fossil fuel sources [1-3]. In the conventional fossil fuel technologies, only 30% of the fuel energy is converted into useful electricity and the rest is wasted and dumped on earth [4]. Recent forecasts predict that a third of new electricity generation added globally by year 2035 will be generated by renewable energy sources. Despite the dramatic evolution of such technologies, the majority of rural communities in the developing countries face problems in the electricity supply and healthy cooking [5]. The Global Alliance for Clean Cookstoves (GACC), hosted by the UN Foundation aims to reduce the estimated 4 million premature deaths per year by introducing 100 million improved stoves by 2020 [6] to improve health standards for women and children. Other work explores the feasibility of generating electricity whilst cooking [7], how it can be afforded [8] and various technologies to achieve this goal [9]. Besides generating electricity, improved cooking stoves reduced fuel demand as well as greenhouse gases and therefore, increase the sustainability of the natural resources. During the last decades, numerous advanced thermodynamic cycles and variations/ combinations of technologies have been developed for waste heat recovery such as Rankine cycle, Stirling Cycle, Organic Rankine Cycle, Kalina Cycle. Recently, Organic Rankine cycle (ORC) has been developed to recover heat from medium grade combined heat power systems [10-13]. ORC solves the problem of the high fluid flow rate associated with the conventional steam Rankine Cycle. However, this technology is costly and has some operational and maintenance drawbacks. The highest temperature the working fluid can reach is below the source temperature due to the existence of a phase change during heating and superheating of the fluid which implies that inefficient heat transfer between the heat source and the fluid. Also, the lowest temperature of the cycle is normally much lower than the lowest temperature reached by the heat source [14]. Many researchers studied and demonstrated small-scale Steam Rankine Cycles (RCs) and several scientists investigated the feasibility of this technology in relation to the additional costs that such systems can involve [15, 16]. The traditional Rankine cycle is

efficient for waste heat recovery from exhaust streams with temperatures above about 340-370°C. The Rankine cycle becomes less cost-effective at low temperatures where bulkier equipment are required at the low-pressure steam. Furthermore, at low waste temperatures, the energy required to superheat the steam is not sufficient to prevent the steam condensation and to avoid erosion of, or example, turbine blades [17]. The major problems related to using turbines as an expander in small-scale water Rankine cycle are the poor efficiency as well as the high production cost, particularly when having multistage turbines.

A flash boiler is one that is widely used to generate steam from combustion gasses to produce electricity through driving steam turbines. In a flash boiler, the heating surface is a single or a series of tubes into which the feed water pumped against the developed pressure. The heat source is usually a petrol, oil or gas flame directed against the tube. The tube is often coiled and housed in a thin lightweight case of metal, frequently stainless steel and the flame is directed through the center of the coil. The development of high-pressure steam is very rapid, hence the term flash steam [18]. The difference between the flash boiler and the mono-tube steam generator is that the mono-tube is permanently filled with water, while the flash boiler is exposed to heat stream (fire is underneath) to keep it hot so that the water feed is quickly flashed into steam and superheated. Flash boilers have many advantages, the most important one is that they take less time to raise steam from a cold start. Also, they are lighter and less bulky than the other types. Problems are that they are more prone to overheat because there is no large reservoir to cool the tubes if the water flow is inadequate or interrupted. Liquid and gaseous fuel are used to fire the boiler in most of the applications. However, some experiments have been run utilizing solid fuel to fire the boiler. The design method of the flash boiler is similar to the evaluation of the heat exchangers, but since a common practice is to recover heat from exhaust gas typical properties for flue gas are required. The aim of this study is to investigate the potential of a flash boiler stove to boil the water to steam and also to identify general design principles of the boiler.

### Boiler evaluation

As revealed in the heat balance diagram Figure 1, only part of the heat content of the fuel is converted into useful heat, while the rest of the heat is lost through exhaust gases and radiation losses from the boiler. The efficiency of the boiler is usually rated based on combustion efficiency, thermal efficiency, and overall efficiency.

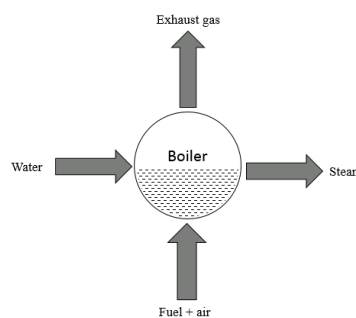


Figure 1. Typical heat flow diagram of a boiler

The typical combustion process in a boiler comprises burning of fuels that contain carbon (oil, gas, and coal) with oxygen to produce heat. Oxygen required for combustion is usually taken from air supplied to the fuel burner of the boiler. Proper heat removal from the flash boiler relies on proper internal distribution and flow of water, proper heat transfer rate in all areas, and proper heat input from the fuel burning.

To evaluate the flash boiler, the well-known “input-output method” is adopted which is based on measuring the mass flow of the burning fuel and the steam generator fluid side conditions

necessary to estimate the output. To obtain reliable results from the boiler, the fuel flow, fuel analysis and the steam output must be determined accurately as they are directly proportional to the uncertainty of the boiler efficiency [19].

$$\dot{Q}_f = m_f^0 \times GCV \quad (5)$$

The available heat from burning of the fuel,  $\dot{Q}_f$  can be expressed as:

Here:  $m_f^0$  is the average mass rate of the fuel used to bring the water to boiling state (kg/sec),

$$m_f^0 = \frac{m_{f,i} - m_{f,e}}{t} \quad (6)$$

$GCV$  is the gross calorific value of the fuel (kJ/kg)

Where  $m_{f,i}$  is the pre-weighed mass of alcohol and  $m_{f,e}$  is the mass of alcohol remaining at the end of the test,  $t$  is the time to reach the boiling condition.

The heat required to raise the boil the water,  $\dot{Q}_w$ :

$$\dot{Q}_w = m_w^0 c_{p,w} (T_b - T_w) \quad (7)$$

Where:  $m_w^0$  is the mass rate of the boiled water (kg/sec),  $c_{p,w}$  is the specific heat of water (kJ/kg.K),  $T_b$  is the boiling temperature of the water (K),  $T_w$  is the ambient temperature of

$$m_w^0 = \frac{m_{w,i} - m_{w,e}}{t} \quad (8)$$

water (K) and  $m_w^0$  is the is the mass rate of the boiled water (kg/sec):

Here  $m_{w,i}$  is the pre-weighed mass of the water inside the pot and  $m_{w,e}$  is the final mass of the water remaining at the end of the test,  $t$  is the time to boil the water in the pot

The energy required to evaporate water,  $\dot{Q}_{evap}$ .

$$\dot{Q}_{evap.} = m_w^0 h_{fg} \quad (9)$$

Where: is the specific evaporation enthalpy for water (kJ/kg).

The heat needed to dry the steam (to be superheated),  $\dot{Q}_s$

$$\dot{Q}_s = m_w^0 c_{p,s} (T_s - T_b) \quad (10)$$

Where:  $c_{p,s}$  is the specific heat of steam (kJ/kg.K) and  $T_s$  is the superheated steam temperature (K)

The boiler efficiency,  $\eta_{boiler}$  is the ratio of the net amount of heat being absorbed by the produced steam to the net amount of heat supplied to the boiler by burning of the fuel [20]. It can be evaluated using the following formula:

$$\eta_{boiler} = \frac{\dot{Q}_w + \dot{Q}_{evap.} + \dot{Q}_s}{\dot{Q}_f} \% \quad (11)$$

### Design Concept & Experimental Apparatus

Our analyses show that a low flow rate steam generating flash boiler is able to extract much more heat from combustion than a pot over the flame stoves, even in case of the stoves with improved efficiency modifications such as pot skirts and increasing the speed of the hot gases that scrape against the pot which increase the cooking efficiency by 20%, by forcing hot gases to heat the bottom and the sides of the pot [21].



In this study, the designed flash boiler uses a 2kW nominal methylated spirit burner, to heat an approximately 2.5m long coil of copper pipe fed by a nominal 8 bar water pump. The intent is for superheated steam to be ejected at sonic steam velocity from a small orifice at the end of the pipe to control mass flow. In its final embodiment, the steam will power an electrical generator and the waste exit heat from the generator used either for efficient cooking by or for ethanol production as displayed in Figure 2 and Figure 3 respectively. Heating in the pipe is achieved in three phases. At the first phase, exit combustion gases heat the water inlet from ambient temperature to the boiling temperature. Then, the water is boiled within the horizontal section of the pipe where two-phase flow occurs. At the last phase of the heating process, steam is superheated in the last section of the pipe by the hot combustion gasses from the ethanol burner. It is predicted that heat is transferred by conduction inside and outside the pipe in phase one, while in phase two heat is transferred by a combination of conduction/convection within the pipe and is by radiation/conduction external to the pipe. Phase three heating is by convection within the pipe and mainly by radiation external to the pipe.

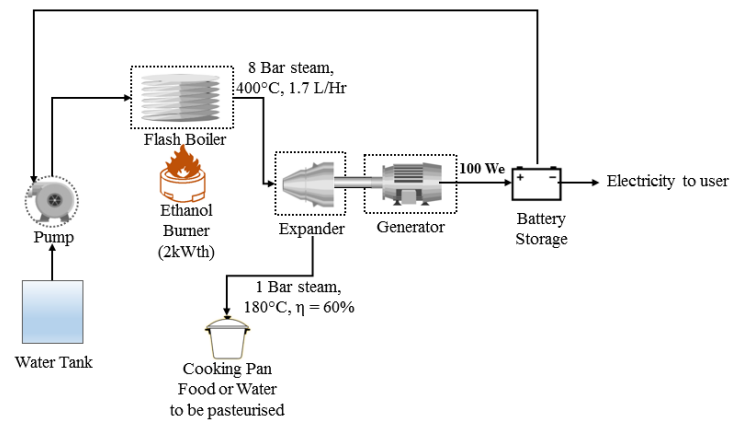


Figure 2. Process of using the flash boiler for cooking purposes

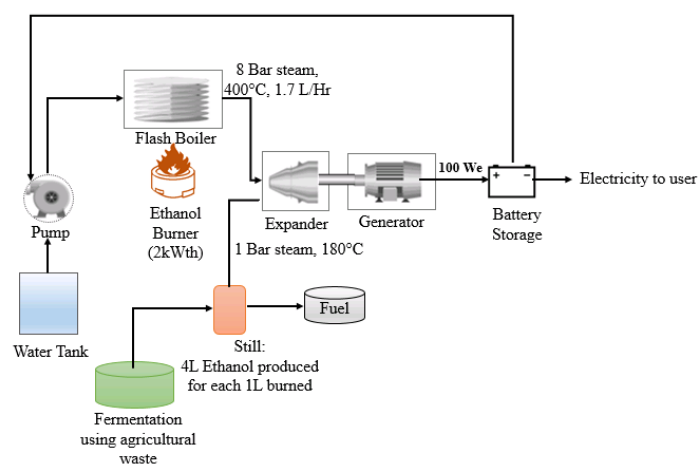


Figure 3. Process of using the flash boiler for fuel production

As shown in Figure 4, the system consists mainly of a 10 mm single copper tube in a multi-layer spiral horizontal configuration with the ethanol burner underneath. The feed water flows inside the tubes after being pumped from a 10L water tank through a 10 mm diameter plastic

pipe utilizing a high-pressure diaphragm pump working intermittently to reduce electrical power consumption. (Model HeroNeo® 12V DC 5L/min 60W) The hot gases from combustion flow around the outside of the pipe. The steam is taken out from the system near the roof via steam take-off pipe of 8.2 cm length before is being directed (in the experimental case) to a cooking pot. For insulation purpose, three aluminium foil layers are introduced between the spiral coil and the wooden cover. In the final embodiment, a generator would convert the superheated steam to electricity and the exhaust heat used for cooking. The fuel used to fire is a clean-burning fuel, contains no sulphur and can be produced from renewable feedstocks. Emissions and nitrogen oxides from burning of alcohol are very low.

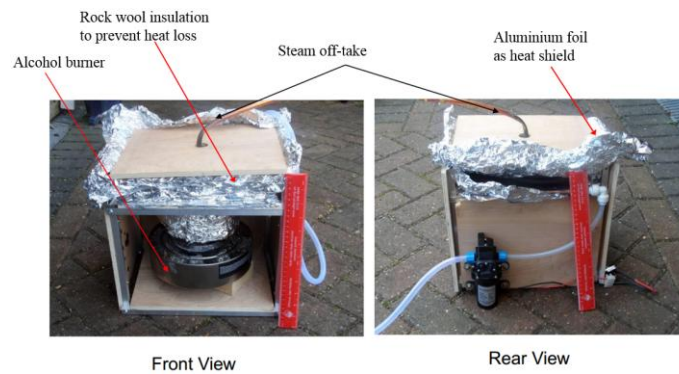


Figure 4. Flash boiler experimental test rig

The copper pipe has a pressure gauge (Model STAUFF 0- 10 bar pressure gauge) at water inlet record pressure, a number of small thermocouples, insulated from gas flow of type-K (RS Components) to capture various temperatures as shown on Figure 5. The LabVIEW platform was used to control the test bench and for Data Acquisition with one thermocouple module (NI 9211) and one bridge module (NI 9237). A scale (OHAUS- Explorer® precision) is used to measure the weight of the fuel and the water before and after the experiment.

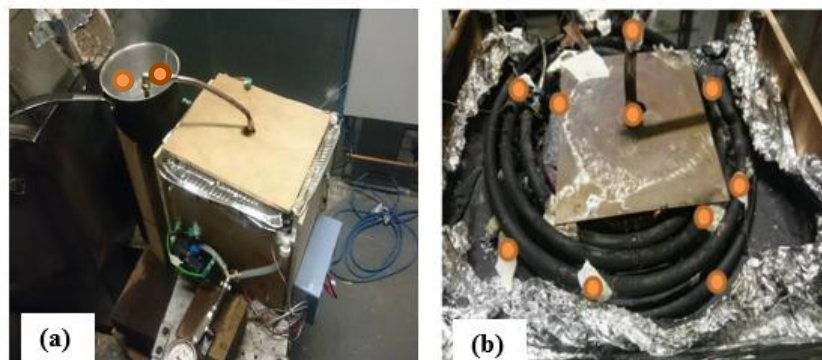


Figure 5. The locations of the thermocouples. (a) At the steam take-off pipe and inside the cooking pot. (b) At the surface of the coil.

### Results and discussion

The thermal performance of a flash boiler stove was investigated and measured in terms of combustion input power, thermal output power, specific fuel consumption, fuel ratio and efficiency. At the beginning of the test, 1.3 kg of alcohol was introduced to fire the boiler and water was pumped through the from the clean water tank. Combustion gasses heat the coil and are directed from the super-heated region towards the cold end to create a contra-flow heat exchanger arrangement. A standard efficiency test named the “water boiling test” [22]

was carried after 16 minutes of operation using 1.3 Kg of ambient water filled inside a cooking pot. The aim was to measure how efficiently the boiler uses steam (from the steam take-off pipe) to heat the cooking water.

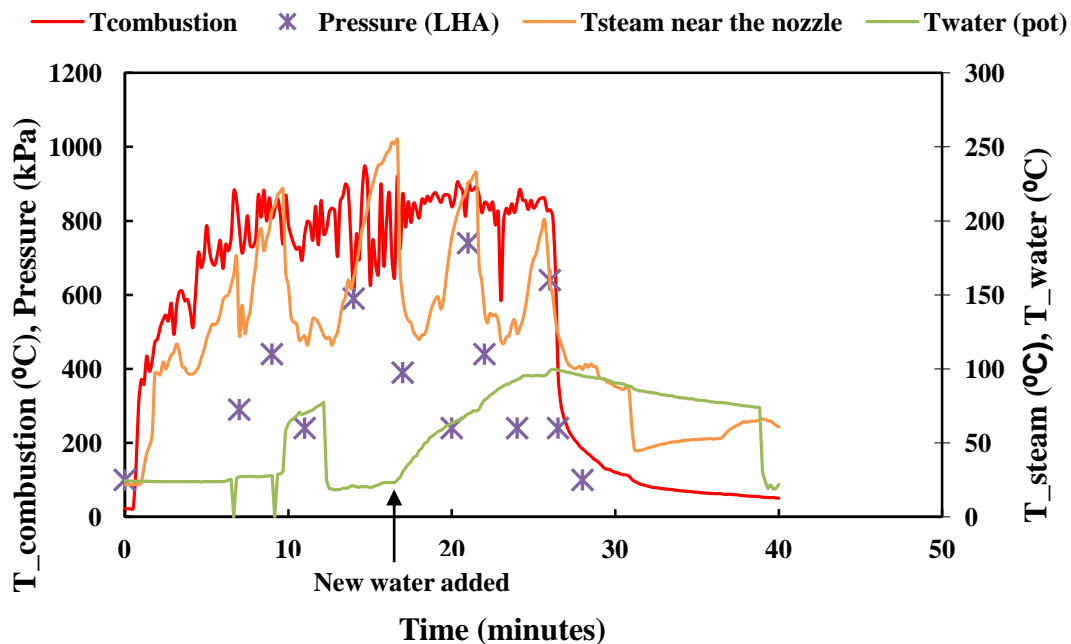


Figure 6. Performance of the flash boiler during the test

The calculated energy output is 0.64kW and the fuel energy input is 1.36kW which gives an efficiency of 47% for the flash boiler stove. Although this is an early non-optimized design, it can bring significant benefits compared to the three stone stove which has a very low thermal efficiency of about 7% and to the other clean-burning stoves of 16 – 42% [7, 23], The measured pressure in the copper pipe was 740 kPa while the maximum temperature of the steam near the nozzle reached 255°C which can be used to drive a Rankine turbine [24]. The important parameters measured during the test are summarized in Table 1.

Table 1. Measured parameters during the experiment

Parameter	Value
Maximum water temperature (°C)	255
Maximum combustion temperature (°C)	949
Mass of alcohol at the beginning (kg)	1.33
Mass of alcohol at the end (kg)	1.23
Mass of the water in the tank at the beginning (kg)	15.5
Mass of the water in the tank at the end (kg)	14
Mass of the water in the pot (kg)	1.32
Maximum pressure in the pipe (bar)	7.4

The thermal efficiency is much higher than conventional cookstoves and may be increased further by better insulation of the top of the wooden cover, which became quite hot, and more gas to pipe surface area. Researchers have noted that the improved insulation can save up to 6–26% [25]. Secondly, there were many leaks from the feed water pipe. Further numerical studies and experiments are required to understand the heat transfer characteristics of the boiler and to quantify the different losses such as: convection and radiation heat loss from the stove, the energy loss from the combustion gases as well as the energy stored in the stove.

### Summary

This paper describes the design and development of a copper-pipe flash boiler stove aiming to generate steam at a high pressure to be expanded through a Rankine cycle turbine, and therefore to deliver electrical power to be utilized by the rural communities of the developing countries all around the world and uses alcohol as the fuel. Boiler performance, was evaluated using the well-known “direct- method. The heat supplied to the boiler from the fuel and the heat absorbed by the water in the boiler at a given period of time were calculated. Interestingly, the experimental results show that the generated steam at the exit of the boiler could reach up to 255°C with 7.4 bar pressure inside the copper pipe and 949°C flame temperature. The efficiency of the boiler was an excellent 47% using 2kW and could be improved with further research. For example, a tesla turbine to expand the steam to generate electrical power.

### References:

- [1] A. M. Omer, "Focus on low carbon technologies: The positive solution," *Renewable and Sustainable Energy Reviews*, vol. 12, pp. 2331-2357, 2008.
- [2] M. Thirugnanasambandam, S. Iniyar, and R. Goic, "A review of solar thermal technologies," *Renewable and sustainable energy reviews*, vol. 14, pp. 312-322, 2010.
- [3] H. Xi, L. Luo, and G. Fraisse, "Development and applications of solar-based thermoelectric technologies," *Renewable and Sustainable Energy Reviews*, vol. 11, pp. 923-936, 2007.
- [4] J. Jadhao and D. Thombare, "Review on exhaust gas heat recovery for IC engine," *International Journal of Engineering and Innovation Technology (IJEIT)*, vol. 2, 2013.
- [5] O. Ellabban, H. Abu-Rub, and F. Blaabjerg, "Renewable energy resources: Current status, future prospects and their enabling technology," *Renewable and Sustainable Energy Reviews*, vol. 39, pp. 748-764, 2014.
- [6] *Global Alliance for Cookstoves*. Available: <http://cleanstoves.org/about/>
- [7] P. H. Riley, C. Saha, and C. Johnson, "Designing a low-cost, electricity-generating cooking stove," *IEEE Technology and Society Magazine*, vol. 29, pp. 47-53, 2010.
- [8] P. H. Riley, "Affordability for sustainable energy development products," *Applied Energy*, vol. 132, pp. 308-316, 2014.
- [9] P. H. Riley, "Designing a low-cost electricity-generating cooking stove for high-volume implementation," PhD, Nottingham, 2014.
- [10] B.-T. Liu, K.-H. Chien, and C.-C. Wang, "Effect of working fluids on organic Rankine cycle for waste heat recovery," *Energy*, vol. 29, pp. 1207-1217, 2004.
- [11] J. Roy, M. Mishra, and A. Misra, "Parametric optimization and performance analysis of a waste heat recovery system using Organic Rankine Cycle," *Energy*, vol. 35, pp. 5049-5062, 2010.
- [12] A. A. Lakew and O. Bolland, "Working fluids for low-temperature heat source," *Applied Thermal Engineering*, vol. 30, pp. 1262-1268, 2010.
- [13] B. F. Tchanche, G. Lambrinos, A. Frangoudakis, and G. Papadakis, "Low-grade heat conversion into power using organic Rankine cycles—A review of various

- applications," *Renewable and Sustainable Energy Reviews*, vol. 15, pp. 3963-3979, 2011.
- [14] T. Nguyen, J. Slawnwhite, and K. G. Boulama, "Power generation from residual industrial heat," *Energy Conversion and Management*, vol. 51, pp. 2220-2229, 2010.
- [15] R. Saidur, M. Rezaei, W. Muzammil, M. Hassan, S. Paria, and M. Hasanuzzaman, "Technologies to recover exhaust heat from internal combustion engines," *Renewable and sustainable energy reviews*, vol. 16, pp. 5649-5659, 2012.
- [16] T. Wang, Y. Zhang, Z. Peng, and G. Shu, "A review of researches on thermal exhaust heat recovery with Rankine cycle," *Renewable and sustainable energy reviews*, vol. 15, pp. 2862-2871, 2011.
- [17] O. Badr, S. Naik, P. O'Callaghan, and S. Probert, "Expansion machine for a low power-output steam Rankine-cycle engine," *Applied Energy*, vol. 39, pp. 93-116, 1991.
- [18] V. Ganapathy, *Industrial boilers and heat recovery steam generators: design, applications, and calculations*: CRC Press, 2002.
- [19] S. Shah and D. Adhyaru, "Boiler efficiency analysis using direct method," in *Engineering (NUICONE), 2011 Nirma University International Conference on*, 2011, pp. 1-5.
- [20] P. Basu, C. Kefa, and L. Jestin, *Boilers and burners: design and theory*: Springer Science & Business Media, 2012.
- [21] M. Bryden, D. Still, P. Scott, G. Hoffa, D. Ogle, R. Bailis, *et al.*, *Design Principals for Wood Burning Cook Stoves*: Aprovecho Research Center, 2005.
- [22] P. R. Bailis, D. Ogle, N. Maccarty, D. S. I. From, K. R. Smith, R. Edwards, *et al.*, "The water boiling test (WBT)," 2007.
- [23] H. Burnham-Slipper, "Breeding a better stove: the use of computational fluid dynamics and genetic algorithms to optimise a wood burning stove for Eritrea," University of Nottingham, 2009.
- [24] R. Stobart and R. Weerasinghe, "Heat recovery and bottoming cycles for SI and CI engines-a perspective," SAE Technical Paper 0148-7191, 2006.
- [25] P. Therkelsen, E. Masanet, and E. Worrell, "Energy efficiency opportunities in the US commercial baking industry," *Journal of Food Engineering*, vol. 130, pp. 14-22, 2014.

# A Micro-Turbine-Generator-Construction-Kit (MTG-c-kit) for Small-Scale Waste Heat Recovery ORC-Plants

A. P. Weiß<sup>1</sup>, T. Popp<sup>1</sup>, G. Zinn<sup>2</sup>, M. Preißinger<sup>3,4</sup> and D. Brüggemann<sup>4</sup>

<sup>1</sup> Competence Center for Combined Heat and Power Systems, University of Applied Sciences Amberg-Weiden, Kaiser-Wilhelm-Ring 23, 92224 Amberg, Germany

<sup>2</sup> DEPRAG GMBH u. CO, Carl-Schulz-Platz 1, 92224 Amberg, Germany

<sup>3</sup> Illwerke vkw Professorship for Energy Efficiency, Energy Research Center, Vorarlberg University of Applied Sciences, 6850 Dornbirn, Austria

<sup>4</sup> Chair of Engineering Thermodynamics and Transport Processes, Center of Energy Technology, University of Bayreuth, Universitätsstraße 30, 95447 Bayreuth, Germany

\*Corresponding author: [a.weiss@oth-aw.de](mailto:a.weiss@oth-aw.de)

## Abstract

Experimentally determined efficiency characteristics of two micro turbines are discussed in this paper. One turbine (15 kW) is working with cyclopentane, the other turbine (12 kW) expands hexamethyldisiloxane (MM). The two turbines are designed and built in accordance to the concept of a micro-turbine-generator-construction-kit (MTG-c-kit) for small scale Organic Rankine Cycle (ORC) waste heat recovery. The motivation for this MTG-c-kit and its architecture will be briefly introduced. Both single stage impulse turbines show a high design point total-to-static isentropic efficiency: the 15 kW cyclopentane turbine achieves 65.0 %, the 12 kW hexamethyldisiloxane turbine achieves even 73.4 %. Furthermore, the discussed off-design characteristics of the turbines prove that their operating behavior is very advantageous for small waste heat recovery plants: the turbine efficiency keeps a high level over a wide range of pressure ratio and rotational speed.

**Keywords:** Organic Rankine Cycle (ORC), turbine, experimental, waste heat recovery.

## Introduction/Background

Organic Rankine Cycle is widely discussed for waste heat recovery. Although the potential for industrial waste heat recovery is high [1,2], only a few solutions in the electric power range of less than 100 kW are on the market [3,4]. The main reason is the huge variety of temperature, pressure and heat transfer medium, which occur in different industrial sectors. Hence, flexible and modular ORC systems are necessary. Manufacturer of such ORC plants must be able to adapt their plant design quickly and cost-efficiently to the requirements of their potential customers to reach economically feasible investment costs of less than 3000 €/kW [5]. Therefore, we focus on affordable, small-scale and customizable turbines, which seems to be the most crucial aspect for efficiency and economics.

Most publications postulate that for small power output and/or small mass flow rate, piston, screw, scroll and rotating vane expanders are advantageous regarding efficiency, rotational speed, size and costs [6,7]. Branchine et al. [8] showed that volumetric expanders dominate the power range below 10 kW electric power and below a volume flow ratio of 10. Latter is due to the built-in volume ratio of volumetric expanders, which is generally  $< 10$  for piston expanders [7] and even  $< 5$  for scroll or screw types. However, to address exhaust heat recovery of internal combustion engines with high temperature differences, volume flow ratios of up to 100 are necessary [9,10]. Compared to volumetric expanders, a turbine can handle this ratio even in one stage. But still, providers for small turbines have been rather seldom [11]. In contrast, small scroll, vane or screw expanders were cheaply available in the

past from refrigeration or compressed air technology where they acted as compressors. In one of our previous works [12], we discussed differences between turbines and volumetric expanders in detail and concluded that small turbines can be superior to volumetric expanders. Turbines allow for high volume flow ratios, small installed size is needed, wear is absent, lubrication may not be necessary and turbines can be customized to a high degree. However, also disadvantages occur, e.g. the demand for a high rotational speed ( $10^4 - 10^5$  rpm), which requires a non-standard high-speed generator. Concerning the turbine type, we already published that an impulse turbine is generally less efficient than a reaction turbine (e.g. a radial-inflow turbine) [12]. The positive effect of the reaction within the impeller on the efficiency, however, limits the volume flow ratio, as we have to avoid a choking rotor flow [13,14]. Furthermore, significant reaction forbids partial admission and, therefore, limits the implementable minimum power size. This is why we decided to rely on a simple stage axial impulse turbine as core component of our “micro-turbine-generator-construction-kit (MTG-c-kit)”.

As already mentioned, waste heat recovery business is characterized by a variety of possible applications in terms of different heat sources, heat flow rates, temperature levels, pressure levels and heat carriers. Hence, it is not appropriate to design and build standard machines to stock. In fact, it is necessary to develop a very flexible “micro-turbine-generator-construction-kit” that allows to quickly design and built a customized turbine generator for any required power output, working fluid and a wide range of boundary conditions.

#### **Micro-turbine-generator-construction-kit (MTG-c-kit)**

The tested micro turbines are built in accordance to the design principles of the addressed “micro-turbine-generator-construction-kit (MTG-c-kit)”.

The simple impulse turbine shows some features which are very valuable for our MGT-c-kit [12]. Compared to a (radial-inflow) reaction turbine, the axial single stage impulse turbine requires lower rotational speed, it does not produce axial thrust and it can be designed with partial admission, thus allowing the implementation of smaller turbines. Furthermore, it is theoretically able to process unlimited pressure ratios (200:1 have already been tested [15]). Figure 1 displays the principal architecture. The characteristic features are:

- Hermetically sealed turbine-generator with an electric power of 3 to 175 kW, implemented with 5 different sizes
- Rotational speed ranges from 10,000 – 70,000 rpm
- Integrally manufactured turbine wheel with a diameter from 50 to 350 mm
- Permanent magnet high-speed generator
- Turbine wheel directly mounted on generator shaft: just one set of bearings required, no gear, no coupling
- Compact design, low material usage

The required mass flow rate or volume flow rate, respectively, determine the size i.e. the wheel diameter of the turbine. The enthalpy drop leads to the necessary circumferential speed and combined with the chosen diameter to an optimal rotational speed. To avoid too high rotational speed or too small blade height, partial admission can be introduced and serves as additional degree of freedom. Volume flow rate and volume flow ratio is taken into account by adjusting overall throat area and area ratio of the supersonic nozzles. An in-house 1D-design tool allows quick design and semi-automatic optimization of the turbine geometry. Thermodynamic properties are taken from the REFPROP database [16].

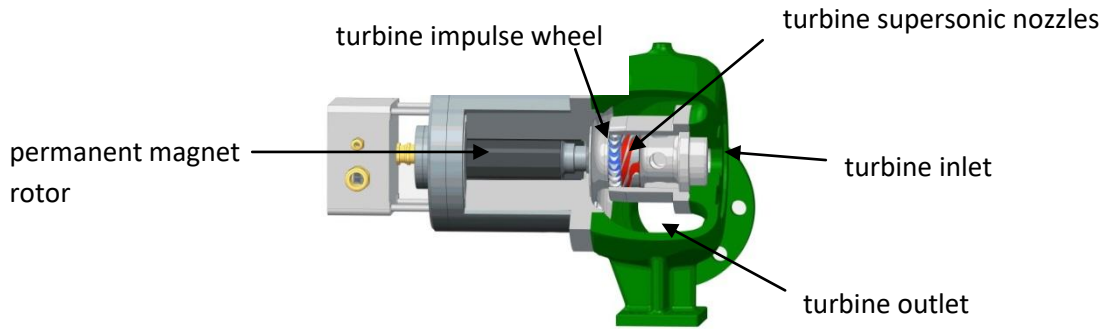


Figure 1: The architecture of the turbo generator (source: DEPRAG)

The main objective of this paper is to prove that efficient and cost effective micro turbo-generators can be reasonably implemented and provided for small scale waste heat recovery. For this purpose, the experimentally determined efficiency characteristics of two representatives of the MTG-c-kit are presented and discussed. The main design data of both turbines are listed in Table 1.

Table 1: Turbine main design data

working fluid		cyclopentane	hexamethydisiloxane (MM)
inlet pressure $p_{in}$	bar	20.0	6.0
outlet pressure $p_{out}$	bar	1.47	0.32
inlet temperature $T_{in}$	°C	182	178
mass flow rate $\dot{m}$	kg/s	0.23	0.32
wheel diameter $D$	mm	120	120
rotational speed $n$	rpm	30,000	24,000
specific speed <sup>a)</sup> $n_s$	-	0.14	0.31
degree of admission $\varepsilon$	%	55	100
pressure ratio $PR$ (ts)	-	13.57	18.75
volume flow ratio $V_r$		16.0	22.3
degree of reaction $r$	%	0	0
nozzle exit Mach number $M_I$	-	1.97	2.11
rotor relative inlet Mach number $M_{rI}$	-	1.14	1.14
expected shaft power	kW	15	12
predicted total-to-static isentropic efficiency (1D loss model) $\eta_{ts}$	%	61.7	68.0

a) the specific speed is defined as: 
$$n_s = \frac{2 \cdot \pi \cdot n}{60} \cdot \frac{V^{0.5}}{\Delta h_{ts, is}^{0.75}}$$

The turbines were tested in two different ORC research plants. The first plant was designed to recover waste heat at 300 °Celsius and worked with cyclopentane. The second plant used hexamethyldisiloxane (MM) as working fluid because it was optimized for 500 °Celsius heat source temperature. A gas burner substituted the piston engine as heat source in both cases. An air-cooler outside the building cooled the ORC plant with an intermediate water/glycol circuit. The ORCs consisted of an evaporator (type plate and shell heat exchanger), an internal recuperator and a condenser (both type plate heat exchanger), a pump and a tank. The



mass flow rate was measured by a Coriolis device. Pressures and temperatures were measured upstream and downstream of each component. The generated electrical power was logged via the 25 kW-feed-in unit. A more detailed description of the ORC plant can be found in one of our previous publications [17].

The total-to-static isentropic turbine efficiency as a function of pressure ratio and rotational speed is our main evaluation criterion. In the following, the total-to-static isentropic turbine efficiencies (Eq. 1) use the actual enthalpy drop determined by ratio of measured turbine power and mass flow rate ( $P_{Tur}/\dot{m}$ ) divided by the ideal total-to-static isentropic enthalpy drop ( $h_{t0} - h_{s2,is}$ ).

$$\eta_{is,ts} = \frac{P_{Tur}/\dot{m}}{h_{t0} - h_{s2,is}} = \frac{P_{el}/(\eta_{el}*\dot{m})}{h_{t0} - h_{s2,is}} \quad (1)$$

The term ( $h_{t0} - h_{s2,is}$ ) is calculated with REFPROP [16] based on the measured inlet temperature and pressure and the outlet pressure. The actual turbine power is calculated using the electric power  $P_{el}$  determined by the feed-in unit and the overall electrical efficiency ( $\eta_{el}$ ) of the entire electrical conversion chain (details can be found elsewhere [17]). The mass flow rate is measured by the Coriolis device. Note that the pressure and temperatures sensors are installed upstream and downstream of the turbine casing flange. Hence, total-to-static turbine efficiencies (Eq. (1)) include flow losses occurring in the inlet and outlet casing.

## Results and Discussion

Figure 2 depicts the total-to-static isentropic efficiency of the cyclopentane turbine depending on rotational speed for different total-to-static pressure ratios ( $PR$ ). Pressure ratio was only changed by inlet pressure (i.e.  $m_{dot}$  = mass flow rate) while outlet pressure was almost constant.

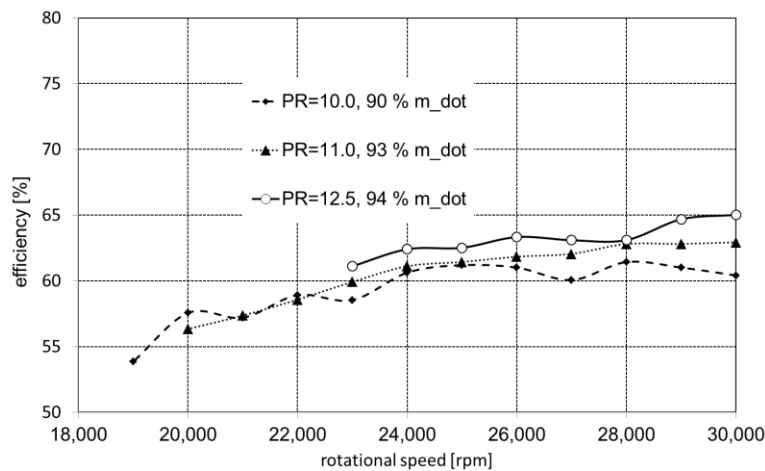


Figure 2: Cyclopentane turbine characteristics, total-to-static isentropic efficiency as function of rotational speed

The maximum measured efficiency is 65.0 % for 94 % mass flow rate and 30,000 rpm. As the gas burner was limited in its thermal power, a mass flow rate of 100 % could not be achieved. Unfortunately, maximum rotational speed was limited to 30,000 rpm with respect to the generator. Most likely, turbine efficiency would be even slightly higher at higher rotational speed. All characteristics are rather flat i.e. they show a weak dependency on rotational speed. Interestingly, measured efficiency is even higher than the predicted one (61.7 %, see Table 1).

Figure 3 depicts the total-to-static isentropic efficiency of the MM turbine depending on rotational speed for different total-to-static pressure ratios ( $PR$ ). Here again, pressure ratio

was only changed by inlet pressure (i.e.  $m_{dot}$  = mass flow rate) while outlet pressure remained almost constant.

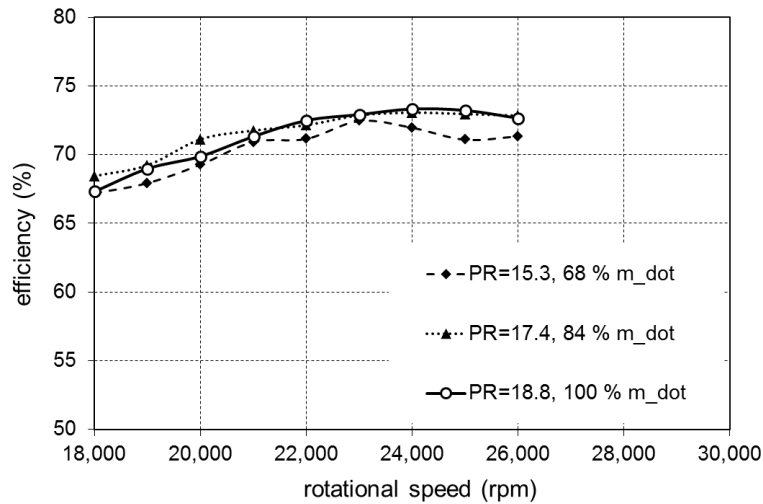


Figure 3: Hexamethyldisiloxane turbine characteristics, total-to-static isentropic efficiency as function of rotational speed

The characteristics at design point (24,000 rpm,  $PR = 18.8$ ) show a flat maximum (73.4 %; solid black line). All curves ( $PR = 15.3$ ,  $PR = 17.4$  and  $PR = 18.8$ ) show similar shapes whereas the rotational speed for maximum efficiency varies slightly between 23,000 rpm and 24,000 rpm. The turbine efficiency reacts rather insensitively on changes of rotational speed or mass flow rate. The MM turbine achieves significantly higher efficiencies compared to the cyclopentane turbine although it has to process higher pressure ratios or volume flow ratios, respectively. Again, measured efficiency (68.0 %, see Table 1) is higher than predicted efficiency. Hence, the 1D loss model in our design tool seems to be too pessimistic.

Figure 4 displays the same data as Fig. 2 und 3 but now the total-to-static isentropic efficiency is plotted as function of total-to-static pressure ratio. The corrected rotational speed  $n_{corr}$  normalized by its design point value serves as parameter. The design pressure ratio of  $PR = 13.6$  could not be achieved for the cyclopentane turbine as mentioned above. The power of the propane gas burner which heated the ORC research plant was not sufficient to evaporate the required mass flow rate. The highest measured efficiency of 65.0 % occurs at design speed and the highest measured pressure ratio ( $PR = 12.8$ ).

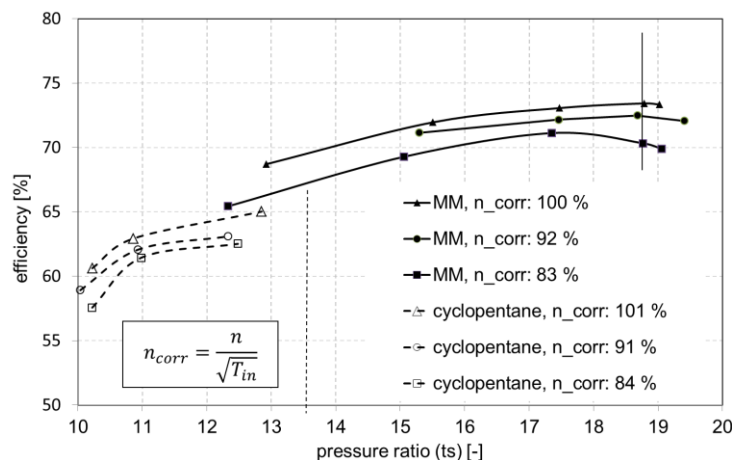


Figure 4: Total-to-static isentropic efficiency as function of pressure ratio; dashed lines: 15kW cyclopentane turbine, solid lines 12 kW MM turbine

Due to the problems with the propane burner in the first ORC plant, the design power output of the MM turbine in the second plant was reduced to 12 kW. Maximum efficiency of 73.4 % occurs at design rotational speed and design pressure ratio ( $PR = 18.8$ ) in the case of the MM turbine. It is significantly higher because the MM turbine works with full admission, the cyclopentane turbine only with about 55 % partial admission. In particular, the characteristics are very flat especially for the MM turbine i.e. the turbines react rather insensitively on deviation from design pressure ratio. This quality is very valuable for micro-turbine-generators applied in small waste heat recovery plants, which are mostly characterized by fluctuating heat fluxes and, therefore, varying mass flow rates.

### Summary/Conclusions

The idea and concept of our micro-turbine-generator-construction-kit (MTG-c-kit) has been introduced and discussed. The presented experimentally determined turbine characteristics of two representatives of the MTG-c-kit confirm the practicality of its approach. Furthermore, the achieved high expansion efficiencies prove that micro turbines are competitive as expander in small ORC plants below 100 kW<sub>el</sub>. Their operating behavior is very advantageous for those small waste heat recovery plants: the turbine efficiency keeps a high level over a wide range of pressure ratio and rotational speed.

Many micro turbine generators out of the MTG-c-kit have been designed and built for various working fluids and different applications within the last five years. They are successfully working in field operation on customer sites. Thus, a micro-turbine-generator is a reasonable solution not only technically but also economically.

### Acknowledgements

From 2011 and 2013 the project called “Entwicklung eines ORC Minikraftwerkes” was funded by the Bavarian Research Foundation. The authors highly appreciated this funding. From 2014 and 2016 the succeeding project was partly funded by the Bavarian State Ministry of Education and Culture, Science and Art within the framework “Competence Center Heat and Power Systems”. The authors highly appreciated this funding.

### References:

- [1] M. Pehnt, J. Bödeker, M. Arens, E. Jochem, F. Idrissova, Die Nutzung industrieller Abwärme - technisch-wirtschaftliche Potenziale und energiepolitische Umsetzung, Institut für Energie- und Umweltforschung Heidelberg, Heidelberg, Karlsruhe, Germany, 2013.
- [2] F. Campana, M. Bianchi, L. Branchini, A. De Pascale, A. Peretto, M. Baresi, A. Fermi, N. Rossetti, R. Vescovo, ORC waste heat recovery in European energy intensive industries: Energy and GHG savings, Energy Conversion and Management. 76 (2013) 244–252. doi:10.1016/j.enconman.2013.07.041.
- [3] C. Gazet, A. Leroux, B. Paillette, A. Pauchet, Operational experience on ORC use for waste heat valorization in biogas power plant, in: Proceedings of the 3rd International Seminar on ORC Power Systems, University of Liège and Ghent University, Brussels, Belgium, 2015.
- [4] D. Gewald, K. Rostek, A. Schuster, R. Amann, From technology development to (pre-series) product - the EPACK HYBRID, in: Proceedings of the 3rd International Seminar on ORC Power Systems, University of Liège and Ghent University, Brussels, Belgium, 2015.
- [5] M. Preißinger, D. Brüggemann, Thermo-economic Evaluation of Modular Organic Rankine Cycles for Waste Heat Recovery over a Broad Range of Heat Source Temperatures and Capacities, Energies. 10 (2017) 269. doi:10.3390/en10030269.

- [6] Y. Glavatskaya, P. Podevin, V. Lemort, O. Shonda, G. Descombes, Reciprocating Expander for an Exhaust Heat Recovery Rankine Cycle for a Passenger Car Application, *Energies*. 5 (2012) 1751–1765. doi:10.3390/en5061751.
- [7] V. Lemort, G. Ludovic, L. Arnaud, S. Declaye, S. Quoilin, A comparison of piston, screw and scroll expander for small Rankine cycle systems, in: *Proceedings of the 3rd International Conference on Microgeneration and Related Technologies*, Naples, Italy, 2013.
- [8] L. Branchini, A. De Pascale, A. Peretto, Systematic comparison of ORC configurations by means of comprehensive performance indexes, *Applied Thermal Engineering*. 61 (2013) 129–140. doi:10.1016/j.applthermaleng.2013.07.039.
- [9] T. Turunen-Saaresti, A. Uusitalo, J. Honkatukia, Design and testing of high temperature micro-ORC test stand using Siloxane as working fluid, *Journal of Physics: Conference Series*. 821 (2017) 012024. doi:10.1088/1742-6596/821/1/012024.
- [10] J.R. Seume, M. Peters, H. Kunte, Design and test of a 10kW ORC supersonic turbine generator, *Journal of Physics: Conference Series*. 821 (2017) 012023. doi:10.1088/1742-6596/821/1/012023.
- [11] G. Qiu, H. Liu, S. Riffat, Expanders for micro-CHP systems with organic Rankine cycle, *Applied Thermal Engineering*. 31 (2011) 3301–3307. doi:10.1016/j.applthermaleng.2011.06.008.
- [12] A.P. Weiß, Volumetric Expander Versus Turbine - Which is the better Choice for Small ORC Plants?, in: *Proceedings of the 3rd International Seminar on ORC Power Systems*, University of Liège and Ghent University, Brussels, Belgium, 2015.
- [13] J. Bao, L. Zhao, A review of working fluid and expander selections for organic Rankine cycle, *Renewable and Sustainable Energy Reviews*. 24 (2013) 325–342. doi:10.1016/j.rser.2013.03.040.
- [14] S. Quoilin, S. Declaye, A. Legros, L. Guillaume, V. Lemort, Working fluid selection and operating maps for Organic Rankine Cycle expansion machines, in: *International Compressor Engineering Conference*, Purdue, 2012: p. Paper 1546. <http://docs.lib.purdue.edu/icec/1925>.
- [15] G. Verdonk, T. Dufornet, Development of a Supersonic Steam Turbine with a Single Stage Pressure Ratio of 200 for Generator and Mechanical Drive, in: *Lecture Series 1987-07*, von Karman Institute for Fluid Mechanics, Brussels, Belgium, 1987.
- [16] E. Lemmon, M. Huber, McLinden, NIST Standard Reference Database 23: Reference Fluid Thermodynamic and Transport Properties-REFPROP, National Institute of Standards and Technology, Gaithersburg, 2010.
- [17] A.P. Weiß, J. Hauer, T. Popp, M. Preißinger, Experimental investigation of a supersonic micro turbine running with hexamethyldisiloxane, in: 2017: p. 020050. doi:10.1063/1.5004384.

# Real-time operational optimization of a complex DHC plant

L. Urbanucci<sup>1\*</sup>, D. Testi<sup>1</sup> and J. C. Bruno<sup>2</sup>

<sup>1</sup>DESTEC (Department of Energy, Systems, Territory and Constructions Engineering), University of Pisa, Largo L. Lazzarino, 56122 Pisa, Italy

<sup>2</sup>Department of Mechanical Engineering, University Rovira i Virgili, Avda. Països Catalans 26, Tarragona 43007, Spain

\*Corresponding author: [luca.urbanucci@ing.unipi.it](mailto:luca.urbanucci@ing.unipi.it)

## Abstract

Performance of polygeneration systems connected to district heating and cooling networks are highly dependent on the operational strategy. The development of advanced control algorithms for real-time operations of CCHP systems must deal with several issues, such as uncertainties in energy demand and weather forecast, non-linear part-load performances, multiple time-varying loads. In this paper, an operational optimization method for a complex DHC plant is proposed. The method is based on the moving average of real-time measurements of energy load demands and ambient conditions, overcoming the need for weather forecasts and a model for the estimation of future load demands. The proposed algorithm is tested with real energy demand data from a DHC close to Barcelona. A complex polygeneration system is considered, including an internal combustion engine, a double-effect absorption chiller, an electric chiller, a boiler and a cooling tower. Part-load behaviour of the components and ambient condition effects are considered to provide a detailed modelling of the system. Results of the real-time optimal control are presented and compared to those of traditional operational strategies.

**Keywords:** Combined Cooling Heat and Power, District Heating and Cooling, Real-time operational optimization, Partial load.

## Introduction/Background

District Heating and Cooling (DHC) networks served by Combined Cooling, Heating and Power (CCHP) plants can be essential to improve efficiency in thermal energy production and are proven to be a reliable and competitive alternative to traditional systems. Nevertheless, the performances of polygeneration systems are very dependent on their synthesis, capacity and operational strategy.

In the last few years, several works have focused on the optimal design of polygeneration systems (to name a few [1-4]), adopting different optimization techniques and trying to strike a balance between accurate modelling and mathematical and computational requirements. Moreover, great effort has been also put on the investigation of management of existing plants, as in the case of [5-9], to identify the optimal operating schedule of CCHP systems with a given design.

Such works are usually based on the hypothesis that the load demand profiles are perfectly known, but this is not the case of practical applications [10,11]. In fact, forecast of weather conditions and energy demands are needed to implement optimal operational strategies in actual CCHP systems. To this end, several Model Predictive Control (MPC) algorithms and methodologies have been proposed, based on forecast information and models of buildings energy demand, such as [11-14].

Nevertheless, several limitations and drawbacks affect these approaches. On the one hand, accurate local weather predictions may be difficult to obtain, and, on the other hand, calibration of building models is an additional obstacle to real implementation of optimal control algorithms [14].

In this paper, we define an operational optimization method based on real-time measurements of energy demands and ambient conditions. The proposed method needs neither weather forecast nor a model for the estimation of future energy load demands, but only a monitoring system of the polygeneration plant. Results of the real-time optimal control are compared to those of traditional operational strategies.

Real energy demand data from a polygeneration plant connected to a DHC close to Barcelona (Spain) [15] are used to test the method. A dense network of sensors that measure temperature, flow and power allows the supervision of the entire plant.

These energy load data consist of hot water demand and chilled water demand and are available on a minute-by-minute basis for the period going from May 1, 2013, to October 13, 2013. Data are described in summary in Table 1 and Fig. 1.

**Table 1**  
Energy demand summary

	Chilled water demand	Hot water demand
Average [kW]	3009	90
Peak [kW]	6401	688

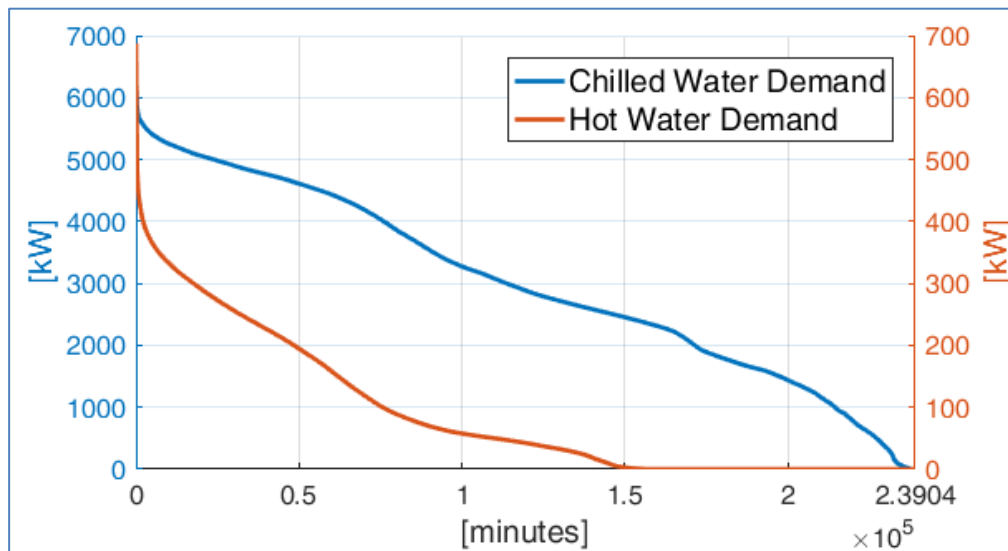


**Fig. 1.** Chilled and hot water demand: load duration curves

The energy system under investigation consists of an internal combustion engine (ICE), a double-effect absorption chiller, an electric chiller, a boiler and a cooling tower. The power plant feeds electricity to the grid, and heating and cooling to the DHC network. The energy system configuration is shown in Fig. 2.

The ICE is fueled by natural gas and its nominal electric power capacity is equal to 2800 kW. The heat recovery system of the ICE is characterized by a low-temperature level (heat from engine jacket and lube oil) and a high-temperature level (exhaust gases). Part-load efficiencies are considered for each energy output.

Both the absorption chiller (nominal cooling capacity: 3300 kW) and the electric chiller (6300 kW) are modelled with the so-called locally constant exergetic efficiency and part-load correction factors. Therefore, the effect of both temperature of heat sources and part-load operations on the chillers COP are considered.

The natural gas boiler has a capacity of 1000 kW and it has been modelled considering part-load efficiency.

The cooling tower must dissipate the heat from the condenser/absorber of the absorption chiller, from the condenser of the compression chiller and from the low-temperature circuit of the ICE. The so-called “fixed approach method” has been considered for its control.

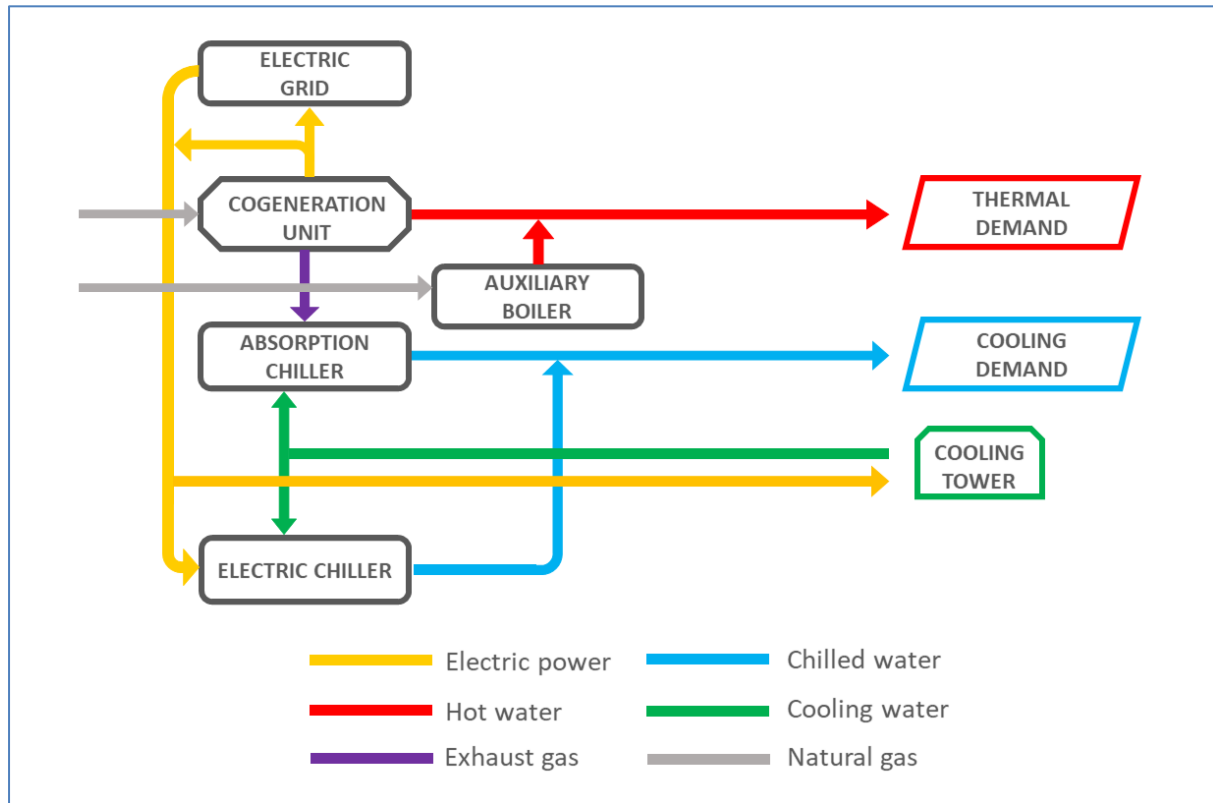


**Fig. 2.** Schematic representation of the Combined Cooling Heat and Power system

The optimization problem consists in the determination of the scheduling that meets the energy demand with the lowest possible cost. The minimization problem of the total energy cost for the considered period ( $n$  timesteps) is defined as follows:

$$\min\{EC\} = \min\left\{\sum_{i=1}^n c_F^i F_{boi}^i + \sum_{i=1}^n c_F^i F_{ICE}^i + \sum_{i=1}^n c_{PEG}^i E_P^i - \sum_{i=1}^n c_{SEG}^i E_S^i\right\} \quad (1)$$

where  $c_F$  is the fuel ( $F$ ) cost for the boiler and the ICE, and  $c_{PEG}$  and  $c_{SEG}$  are the prices for purchasing and selling electricity ( $E$ ), respectively.

Eight decision variables are defined for each  $i$ -th timestep: electric energy ( $E_{ICE}^i$ ), low-temperature heat ( $Q_{LT,ICE}^i$ ) and high-temperature heat ( $Q_{HT,ICE}^i$ ) produced by the ICE, heat produced by the boiler ( $Q_{LT,boi}^i$ ), sold ( $E_S^i$ ) and bought electricity ( $E_P^i$ ), cooling power from the electric ( $C_{EC}^i$ ) and the absorption chillers ( $C_{AC}^i$ ). These eight decision variables are bound to each other and there is only one actual degree of freedom for the minimization of the objective function, as shown in Fig. 3. Therefore, the problem is reduced to find the optimal load factor ( $L_{ICE}$ ) of the ICE, for each timestep. Moreover, as already shown in [16], for the energy system under consideration the overall optimum coincides with the sum of optimums of every single timestep and the overall problem can be split into  $n$  subproblems. Consequently, the optimal load factor for each timestep can be independently calculated and implemented.

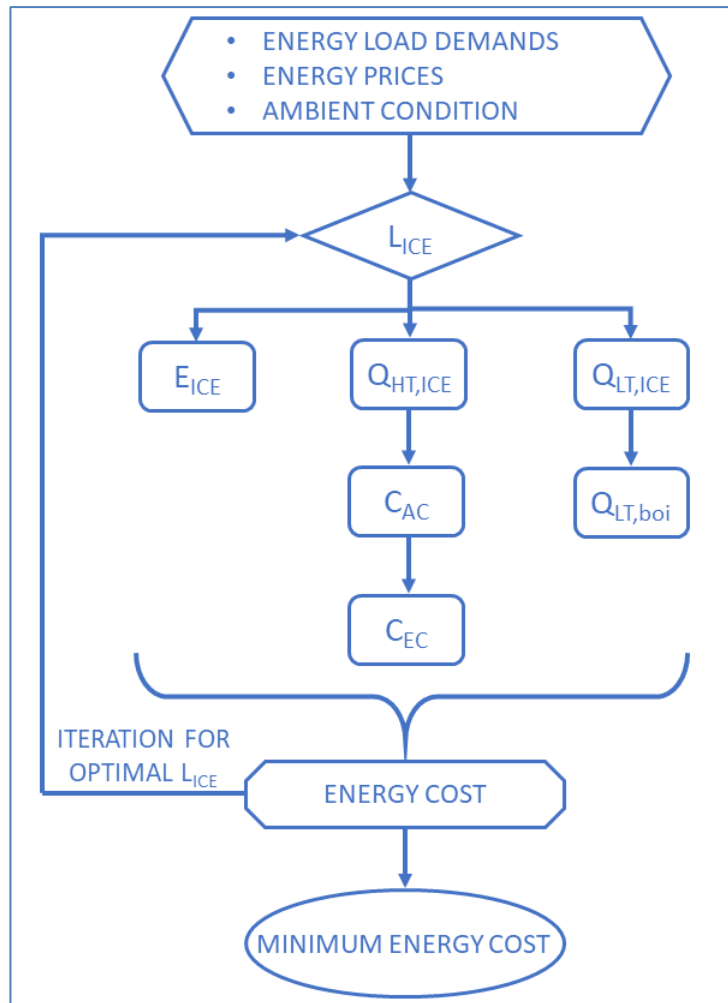


**Fig. 3.** Optimal energy dispatch procedure

As already mentioned, previous measurements of energy demands are used to estimate future loads by means of a sliding window of moving average. The width of the window is also optimized. Moreover, current ambient conditions are considered since they can significantly affect chillers performance.

In summary, energy demands for each timestep are estimated by means of a moving average of recent measures and current ambient conditions, then the optimal load factor for the cogeneration unit is found and the resulting power flows inside the system are determined and implemented in the following timestep (whose length is set to 15 minutes).

### Discussion and Results

The results of all the simulated operational strategies are hereinafter presented and discussed. Table 2 shows the overall energy and economic results for the accounted period. In addition to the proposed *real-time operational optimization* (RTOO), other traditional operational strategies have been simulated. The *electric energy price based operational strategy* considers a value of the ratio between the import and export prices of electricity (which vary considerably) for the on-off switch of the ICE; this strategy is very similar to the one implemented in the real plant. The *following the thermal load* mode means that the ICE is run to have sufficient recovered heat to supply both the cooling and heating requirements. In the *ICE continuous full-load operation* the cogeneration unit is always at its maximum capacity.



The *separate production* simulates the case without ICE, where the hot water demand is met by the boiler and the chilled water load is provided by the electric chiller.

The effectiveness of the proposed algorithm is proven by comparing it with these conventional strategies, which all entail a significant rise in the overall energy cost (from 13% to 58% increase in the cost).

**Table 2.** Summary of the energy and economic results for all the simulated operational strategies

	<b>Real-time operational optimization</b>	<b>Electric energy priced based operational strategy</b>	<b>Following the thermal load</b>	<b>ICE continuous full-load operation</b>	<b>Separate production</b>
<b>Exported electricity [MWh]</b>	4027	6675	8012	10330	0
<b>Imported electricity [MWh]</b>	577.5	616	0	0	0
<b>Natural gas consumption [MWh]</b>	13720	19990	23840	29750	1189
<b>Sold electricity [k€]</b>	242.3	404.6	414.7	509.9	0
<b>Bought electricity [k€]</b>	77.7	83.5	0	0	354.8
<b>Bought natural gas [k€]</b>	411.6	599.6	715.1	892.4	35.7
<b>Total energy cost [k€]</b>	<b>247.0</b>	<b>278.5</b>	<b>300.4</b>	<b>382.5</b>	<b>390.5</b>

A wide range of detailed information is available from the performed simulations. Fig. 4 shows an example of the results under the real-time operational optimization: the cooling load demand and production in each timestep of a typical week are shown. Furthermore, Fig. 5 summarizes how the overall cooling demand is met under the RTOO strategy; the optimal management of the plant under investigation requires an almost even distribution of the cooling load between the absorption and the electric chillers.

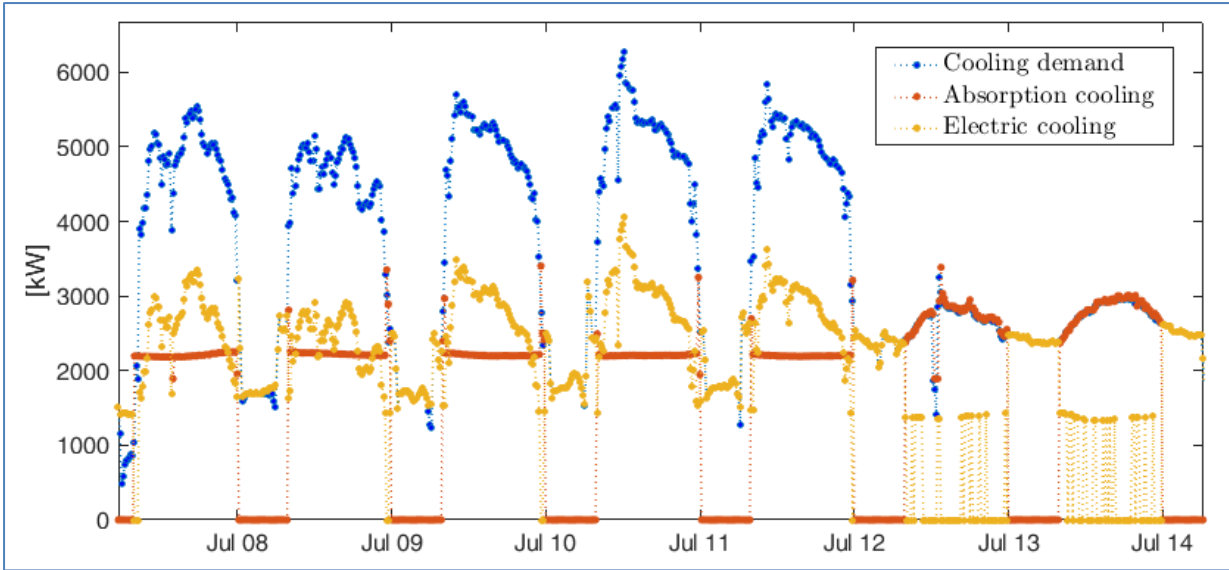


**Fig. 4.** Cooling load demand and production under the RTOO strategy for a typical week

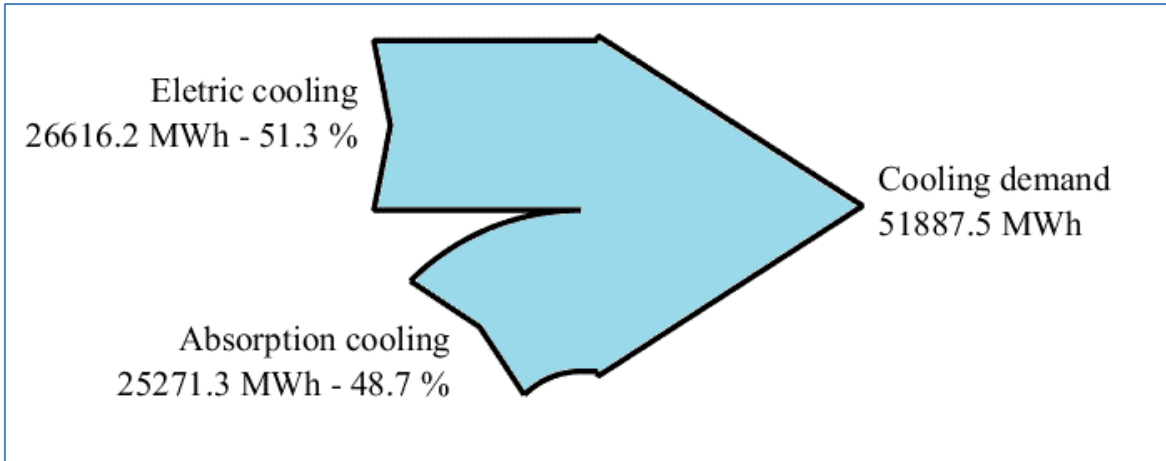


**Fig. 5.** Cooling energy shares under RTOO strategy

Fig. 6 shows, for each simulated operational strategy, the total energy cost saving percentage with respect to the total energy cost for the separate production case. This chart highlights how the operations of a CCHP plant can importantly affect its performances. Moreover, to further analyse the different performance of the RTOO strategy with respect to the separate production mode, Fig. 7 shows how the energy costs vary in each timestep in a typical week. During the nights and the weekend, the difference is slight, while during the working days, when the energy demand is higher, the separate production entails a significant increase in the energy cost.

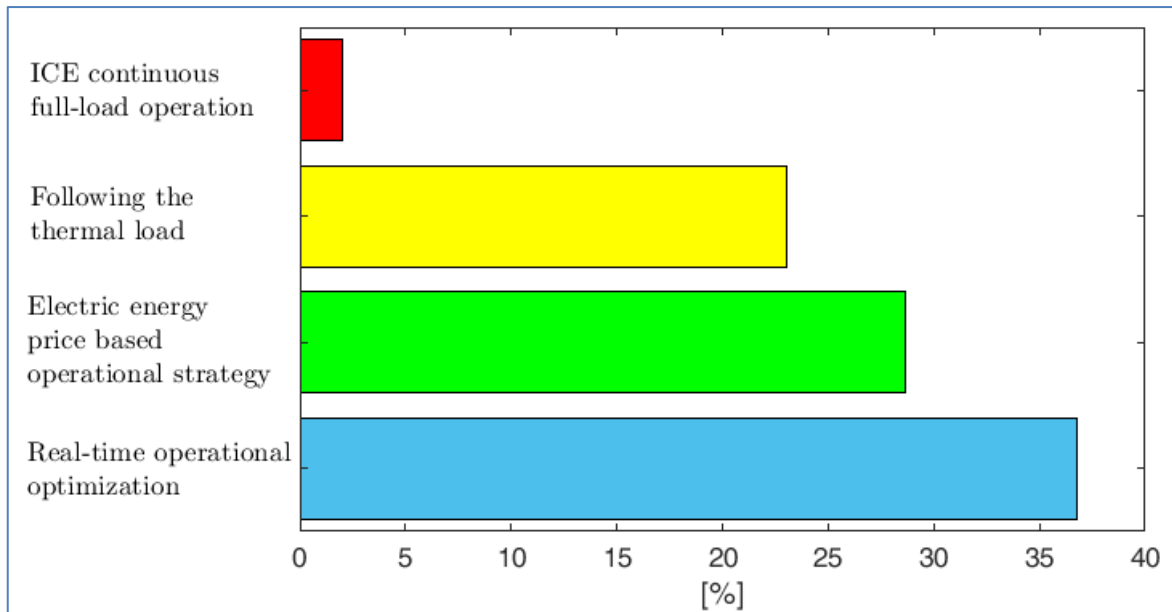


**Fig. 6.** Cost saving with respect to the separate production mode

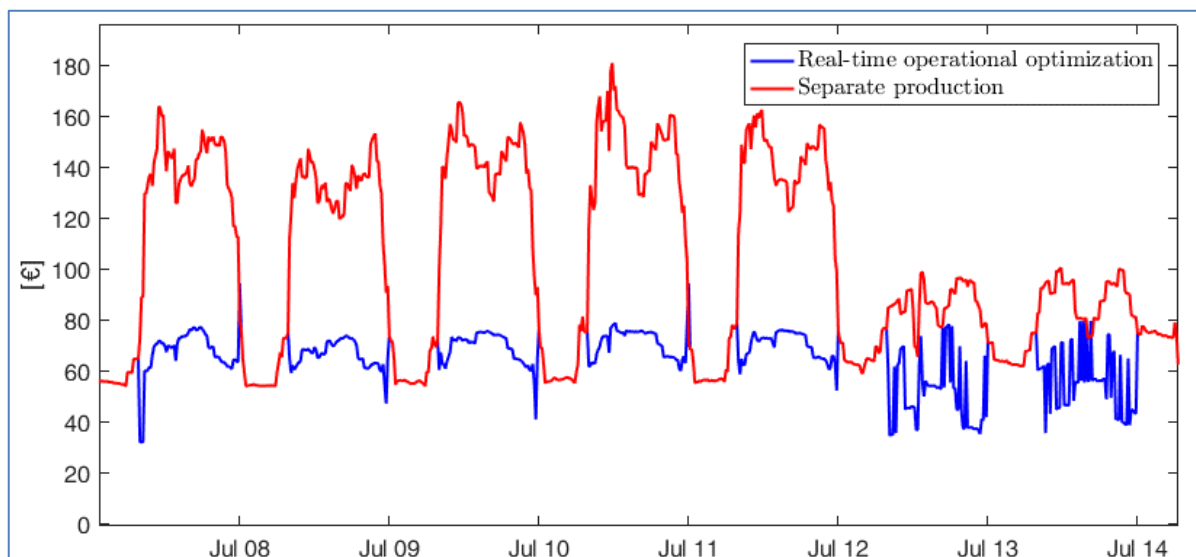


**Fig. 7.** Energy cost comparison between RTOO and separate production: a typical week

### Summary/Conclusions

In this paper, an operational optimization method based on the moving average of real-time measurements of energy demand and ambient conditions has been presented. A complex CCHP system has been considered and each involved energy sub-system has been modelled in detail. Part-load behaviours and ambient condition effects have been considered. The effectiveness of the method has been demonstrated by using real energy demand data from a district heating and cooling network close to Barcelona.

The proposed real-time optimization algorithm has been simulated, as well as other traditional operational strategies. A summary of the results has been presented, which shows how the proposed control strategy performs significantly better than the traditional operational strategies.

Future research may focus on: optimization in case of integration with renewable energy sources and thermal storages; use of combined real-time data and forecast approaches.

## References:

- [1] Arcuri, P., Florio, G., Fragiaco, P., “A Mixed integer programming model for optimal design of trigeneration in a hospital complex”, *Energy*, 2007, [doi:10.1016/j.energy.2006.10.023](https://doi.org/10.1016/j.energy.2006.10.023)
- [2] Guo, L., Liu, W., Cai, J., Hong, B., Wang, C., “A two-stage optimal planning and design method for combined cooling, heat and power microgrid system”, *Energy Conversion and Management*, 2013, [doi:10.1016/j.enconman.2013.06.051](https://doi.org/10.1016/j.enconman.2013.06.051)
- [3] Elsid, C., Bischi, A., Silva, P., Martelli, E., “Two-stage MINLP algorithm for the optimal synthesis and design of networks of CHP units”, *Energy*, 2017, [doi:10.1016/j.energy.2017.01.014](https://doi.org/10.1016/j.energy.2017.01.014)
- [4] Arcuri, P., Beraldi, P., Florio, G., Fragiaco, P., “Optimal design of a small size trigeneration plant in civil users: a MINLP (Mixed Integer Non Linear Programming Model)”, *Energy*, 2015, [doi:10.1016/j.energy.2014.12.018](https://doi.org/10.1016/j.energy.2014.12.018)
- [5] Franco, A., Versace, M., “Multi-objective optimization for the maximization of the operating share of cogeneration system in District Heating Network”, *Energy Conversion and Management*, 2017, [doi:10.1016/j.enconman.2017.02.029](https://doi.org/10.1016/j.enconman.2017.02.029)
- [6] Li, L., Mu, H., Li, N., Li, M., “Analysis of the integrated performance and redundant energy of CCHP systems under different operation strategies”, *Energy and Buildings*, 2015, [doi:10.1016/j.enbuild.2015.04.030](https://doi.org/10.1016/j.enbuild.2015.04.030)
- [7] Ortiga, J., Bruno, J. C., Coronas, A., “Operational optimization of a complex trigeneration system connected to a district heating and cooling network”, *Applied Thermal Engineering*, 2013, [doi:10.1016/j.applthermaleng.2011.10.041](https://doi.org/10.1016/j.applthermaleng.2011.10.041)
- [8] Bischi, A., Taccari, L., Martelli, E., Amaldi, E., Manzoloni, G., Silva, P., Campanari, S., Macchi, E., “A detailed MILP optimization model for combined cooling heat and power system operation planning”, *Energy*, 2014, [doi:10.1016/j.energy.2014.02.042](https://doi.org/10.1016/j.energy.2014.02.042)
- [9] Ünal, A. N., Ersöz, I., Kayakutlu, G., “Operational optimization in simple tri-generation systems”, *Applied Thermal Engineering*, 2016, [doi:10.1016/j.applthermaleng.2016.06.059](https://doi.org/10.1016/j.applthermaleng.2016.06.059)
- [10] Liu, M., Shi, Y., Fang, F., “Optimal power flow and PGU capacity of CCHP systems using a matrix modeling approach”, *Applied Energy*, 2013, [doi:10.1016/j.apenergy.2012.08.041](https://doi.org/10.1016/j.apenergy.2012.08.041)
- [11] Luo, Z., Wu, Z., Li, Z., Cai, H., Li, B., Gu, W., “A two-stage optimization and control for CCHP microgrid energy management”, *Applied Thermal Engineering*, 2017, [doi:10.1016/j.applthermaleng.2017.05.188](https://doi.org/10.1016/j.applthermaleng.2017.05.188)
- [12] Fang, T., Lahdelma, R., “Optimization of combined heat and power production with heat storage based on sliding time window method”, *Applied Energy*, 2016, [doi:10.1016/j.apenergy.2015.10.135](https://doi.org/10.1016/j.apenergy.2015.10.135)
- [13] Cho, H., Luck, R., Eksioğlu, S. D., Chamra, L. M., “Cost-optimized real-time operation of CHP systems”, *Energy and Buildings*, 2009, [doi:10.1016/j.enbuild.2008.11.011](https://doi.org/10.1016/j.enbuild.2008.11.011)
- [14] Yun, K., Cho, H., Luck, R., Mago, P.J., “Real-time combined heat and power operational strategy using a hierarchical optimization algorithm”, *Proceedings of 2011 IMechE Vol. 225 Part A: J Power and Energy*, [doi:10.1177/2041296710394287](https://doi.org/10.1177/2041296710394287)
- [15] Conte, B., Bruno, J. C., Coronas, A., “Optimal cooling load sharing strategies for different types of absorption chillers in trigeneration plants”, *Energies*, 2016, [doi:10.3390/en9080573](https://doi.org/10.3390/en9080573)
- [16] Urbanucci, L., Testi, D., “Optimal integrated sizing and operation of a CHP system with Monte Carlo risk analysis for long-term uncertainty in energy demands”, *Energy Conversion and Management*, 2018, [doi:10.1016/j.enconman.2017.12.008](https://doi.org/10.1016/j.enconman.2017.12.008)

# Thermodynamic analysis of S-CO<sub>2</sub> cycle for coal-fired plant

Yawen Zheng<sup>1</sup>, Jinliang Xu<sup>1\*</sup>, Lei Lei<sup>1</sup>

<sup>1</sup> Beijing Key Laboratory of Multiphase Flow and Heat for Low Grade Energy Utilization, North China Electric Power University, Beijing, 102206, P.R. China

\*Corresponding author: Dr Jinliang Xu, email: xjl@ncepu.edu.cn

## Abstract

A new S-CO<sub>2</sub>(supercritical carbon dioxide) Brayton cycle is analysed in this paper. Coal-fired boiler is used as a heat-source in the cycle. Comparison between S-H<sub>2</sub>O cycle and S-CO<sub>2</sub> cycle was carried out. Optimization of maximum temperature, minimum temperature, intercooling pressure to maximum thermal efficiency is implemented. Comparison of intercooling and non-intercooling is also carried out. Convective heat transfer and radiative heat transfer is distinguished in boiler. Results show that S-CO<sub>2</sub> cycle shows a great advantage than S-H<sub>2</sub>O cycle. For S-CO<sub>2</sub> cycle, there exists a best intercooling pressure, and it's closed to the inlet pressure of LP(low pressure) compressor. The pinch point shifts to inside of the LTR(low temperature recuperator) compares to the non-intercooling case. Invert intercooling can improve thermal efficiency almost 2%, but the exergy efficiency nearly stay the same. However, minimum temperature has a different influence on thermal efficiency and exergy efficiency

**Keywords:** S-CO<sub>2</sub> cycle, thermodynamic , parameter optimization, coal-fired

## Introduction/Background

Steam Rankine cycle is widely used in various types of power plants. The efficiency of existing ultra-supercritical units of coal-fired power plants using steam Rankine cycle has reached 47%. However, vapors and metals react at high temperature, the phenomenon such as high temperature corrosion and stress cracking appear which limits the increase of the inlet temperature of turbine. Thus, to further improve the efficiency encountered the bottlenecks, such as materials. In order to improve the efficiency of the power plant, we can explore a new material to replace the old one, alternatively to find a new working fluid.

Compare to water, carbon dioxide is easy to obtain, inexpensive, and its corrosion rate with metal at high temperature is only one third of that of water. Low corrosion rate can reduce the requirements for material under high parameters. In addition, recycling of CO<sub>2</sub> can also alleviate the greenhouse effect to some extent. Therefore, the CO<sub>2</sub> cycle has received great attention from researchers.

The concept of supercritical CO<sub>2</sub> power generation was first proposed in 1950s. By the 1970s, researchers gradually began to study the S-CO<sub>2</sub> cycle. Feher[1] analysed the performance of a simple regenerative Brayton cycle and pointed out that the system has high cycle efficiency and small turbine volume. Earlier scholars have made a certain degree of research on the S-CO<sub>2</sub> cycle model. Angelino[2] proposed a regenerative and recompression process to further improve the cycle efficiency. For various CO<sub>2</sub> Brayton cycle modes, the recompression cycle is considered as the most promising cycle mode[3]. But due to the lack of suitable heat exchangers and turbo-machinery, the S-CO<sub>2</sub> cycle was not recognized by the general public. Therefore, the research on the S-CO<sub>2</sub> cycle must have been interrupted. However, over the past two decades, the manufacturing process of heat exchangers and turbo-machinery has progressed rapidly. The research on the S-CO<sub>2</sub> cycle has been carried out once again in recent years. Dostal[3] proposed that the S-CO<sub>2</sub> Brayton cycle can be applied to nuclear reactors in 2004, explored the feasibility and economics of S-CO<sub>2</sub> cycle applied to sodium-cooled fast reactors, and analyzed the performance of the system under different cycle modes. It is

considered that the recompression cycle has a high development potential. This study set off a wave of research on the CO<sub>2</sub> cycle.

S-CO<sub>2</sub> cycle has conducted in-depth research in the nuclear and solar energy fields. In the field of nuclear energy, Ahn[4] studied the performance of various Brayton cycles for small reactors, including S-CO<sub>2</sub> Brayton cycle, Helium Brayton cycle and Nitrogen Brayton cycle. As a result, it has been found that the S-CO<sub>2</sub> cycle has relatively high thermal efficiency under various circulation modes, and the heat exchanger has a small volume for S-CO<sub>2</sub> cycle. Fahad[5] studied small nuclear reactors of 20 MWth and compared the performance between S-CO<sub>2</sub> cycle (regeneration, simple intercooling, double intercooling) and Helium Brayton cycle, the results show that S-CO<sub>2</sub> cycle will be a good replacement cycle for nuclear reactors. For solar energy, there are two types of CO<sub>2</sub> cycle: supercritical CO<sub>2</sub> Rankine cycle and supercritical CO<sub>2</sub> Brayton cycle. The research focused on the S-CO<sub>2</sub> Rankine cycle in early stage. However, due to the low critical temperature of CO<sub>2</sub>, which makes big difficulty to condense CO<sub>2</sub> in the cooler. Researchers have gradually shifted their study emphasis to S-CO<sub>2</sub> Brayton cycle. Padilla[6] performed thermodynamic and exergy analysis of a S-CO<sub>2</sub> recompression Brayton cycle. The results show that adding reheat to the S-CO<sub>2</sub> recompression Brayton cycle improves the first law and second law efficiencies.

However, S-CO<sub>2</sub> cycle integrates with coal-fired plant is only a few researches reported[7-9]. Moullec[7] studied the S-CO<sub>2</sub> recompression Brayton cycle for power generation systems using coal-fired power plants and CO<sub>2</sub> capture technology. It is pointed out that the efficiency of the system is 50.3% at 620°C, while the efficiency can reach 54.1% at 700°C. The preliminary conceptual design of the boiler heating surface of the S-CO<sub>2</sub> cycle coal-fired power generation system was further proposed[8]. Based on the S-CO<sub>2</sub> recompression Brayton cycle, Mecheri[9] proposed several ways for the working medium to absorb the heat of the flue gas from the tail of the boiler, in view of the high temperature flue gas at the end of the boiler.

The researches of S-CO<sub>2</sub> cycle applied to the coal-fired power plant is immature and still requires further research. This paper is aimed at combining S-CO<sub>2</sub> cycle with boiler and analysing the performance of the cycle. Using a simplified method to analyse the heat transfer process between boiler and CO<sub>2</sub>. The parameter optimization was also carried out.

## Discussion and Results

### 1. Mathematical model

The S-CO<sub>2</sub> recompression Brayton cycle is most widely adopted in various layout of S-CO<sub>2</sub> cycle. The different characteristics of the heat source have a great influence on the arrangement of the thermal system. For coal-fired thermal power generation system, the temperature of flue gas is relatively high. Firstly, the reheat must be used to fully utilize the temperature of flue gas and heat the working fluid. Due to the high temperature of CO<sub>2</sub> entering the boiler, the temperature of flue gas in the tail of boiler cannot be cooled down to the required value. Excessively high temperature of flue gas will greatly reduce the efficiency of the boiler. Therefore, in order to ensure boiler efficiency, we use the part flow model to absorb the residual heat of flue gas. This paper further considers the introduction of intercooling to optimize the cycle performance.

The layout of S-CO<sub>2</sub> cycle is shown in Figure 1. The boiler model still uses the layout of traditional steam boilers, including economizers, water-cooled walls, superheaters and reheaters. One-stage reheating, one-stage cooling, corresponding to two turbines and three compressors, respectively. The system contains three regenerators, one of which is a low temperature regenerator (LTR) and two high temperature regenerators (HTR). The flow from LTR is split into two streams (point 7); one stream is cooled in cooler 1 (7–8), then compressed by low temperature compressor 1 (LTC1) (8-9), followed by cooling in the cooler 2 (9-10), then

compressed by low temperature compressor 2(LTC2) (10–11) and then absorb the heat in LTR, the others is compressed by high temperature compressor (HTC) and mixed with the flow in the outlet of LTR (point 12), then the total flow exchange heat with turbine outlet flow in HTR (12–13). At the outlet of HTR high-pressure side (point 13), the CO<sub>2</sub> flow into boiler to absorb heat, then flow into the turbine to generate work.

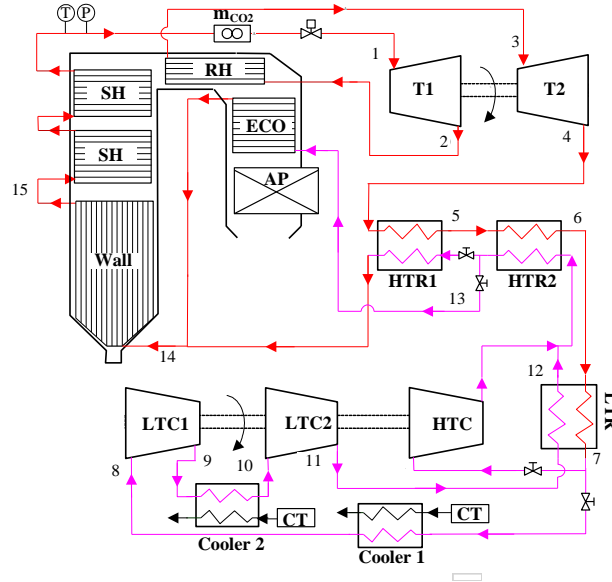


Fig.1 The diagram of S-CO<sub>2</sub> cycle integrates with boiler

## 2. Calculation methods

### 2.1 Calculation assumptions

- 1) The pressure drop in the heat exchanger can be neglected, so the pressure drop in the heat exchanger is not considered here.
- 2) Only one heat exchange mode is considered in each heat exchange process in the boiler. For example, the water wall of the furnace is a radiative heat exchanger, and the reheater, superheater, and economizer are convection heat exchangers, regardless of the mutual influence of the two.

### 2.2 Solution model

The maximum temperature, maximum pressure, minimum temperature, and minimum pressure are given. The cycle introduces reheat, the determination of reheat intermediate pressure is based on the empirical formula in [10], that is

$$P_{i,opt} = \sqrt{P_{min} P_{max}} \left( \frac{T_{max}}{T_{min}} \right)^{0.15} \quad (1)$$

For LTR, energy balance equation is

$$(h_6 - h_7) = (1 - x)(h_{12} - h_{11}) \quad (2)$$

For HTR2, energy balance equation is

$$h_5 - h_6 = h_{13} - h_{12} \quad (3)$$

For HTR1, energy balance equation is

$$h_4 - h_5 = (1 - x_1)(h_{14} - h_{13}) \quad (4)$$

The equation of radiation heat transfer in furnace is

$$Q_f = m_{\text{CO}_2}(h_{15} - h_{14}) \quad (5)$$

The equation of convection heat transfer in superheater is

$$Q_{sh} = m_{\text{CO}_2}(h_1 - h_{15}) \quad (6)$$

The equation of convection heat transfer in reheater is

$$Q_{rh} = m_{\text{CO}_2}(h_3 - h_2) \quad (7)$$

The equation of convection heat transfer in economizer is

$$Q_{ec} = m_{\text{CO}_2} \cdot x_1 \cdot (h_{14} - h_{13}) \quad (8)$$

Table 1. Calculation case of S-CO<sub>2</sub> cycle

Parameters	Values
turbine inlet temperature ( $T_1$ )	650 °C
turbine inlet pressure ( $P_1$ )	20-50 MPa
turbine isentropic efficiency ( $\eta_{st}$ )	93 %
compressor LTC2 inlet temperature ( $T_{10}$ )	35 °C
compressor LTC2 inlet pressure ( $P_{10}$ )	8 MPa
compressors isentropic efficiency ( $\eta_{sc}$ )	89 %
reheater outlet temperature ( $T_3$ )	650 °C
pinch temperature difference of regenerator and cooler ( $\Delta T_p$ )	10 °C
heater inlet temperature of flue gas ( $T_{g1}$ )	1300 °C
mass flow rate of flue gas ( $m_g$ )	1800 kg/s
heat load of radiation heat transfer in furnace ( $Q_f$ )	1000 MW
economizer outlet temperature of flue gas ( $T_{g4}$ )	540 °C
inlet temperature of water ( $T_{c1}$ )	20 °C
outlet temperature of water ( $T_{c2}$ )	27 °C

Table 1 shows the cycle calculation table. It is known that  $P_1=30$  MPa,  $T_1=650$  °C,  $T_3=650$  °C,  $P_4=8$  MPa, and the corresponding state point parameters can be determined. According to equation(1), the pressure and parameters of reheat can be determined. According to  $T_8=T_{10}=35$  °C,  $P_7=8$  MPa,  $P_{11}=30$  MPa, the parameter of point 8 can be determined first. Intermediate pressure of intercooling is a variable, which is calculated in the range of 8-12 MPa. At a fixed intermediate pressure, parameters of point 10 can be determined, and parameters of point 9, 11 can be determined according to isentropic efficiency formulas.

Pinch temperature difference of LTR is 10 °C. By assuming  $T_7$ , an appropriate  $T_7$  is found through iterative calculation so that the pinch temperature difference of LTR meets 10 °C. Parameters of point 12 are then derived from isentropic efficiency formulas. Since the pinch temperature difference of HTR1 is also 10 °C, an appropriate  $T_6$  is found by the same iterative algorithm as LTR, so that the parameter of point 6 is determined. Again according to equation (2) the recompression split ratio  $x$  can be determined.

According to the simplified assumption of boiler and the equation of energy conservation, the parameters of both flue gas and state point of cycle can be determined



### 3. Optimization Analysis

#### 3.1 Comparison with S-H<sub>2</sub>O cycle

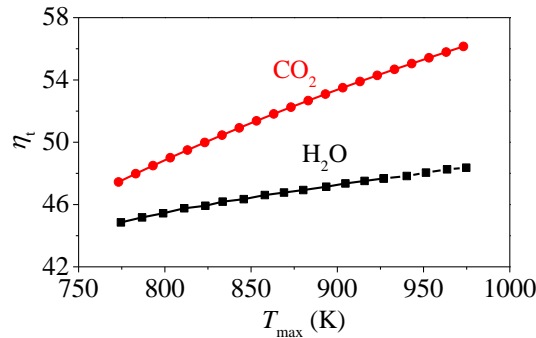


Figure 2. Comparison of S-CO<sub>2</sub> cycle and S-H<sub>2</sub>O cycle

For the selection of materials, ultra-supercritical boilers often use austenitic steels today. Due to the chemical corrosion with water vapor, the main steam temperature of S-H<sub>2</sub>O cycle is limited by 650 °C, and the cycle efficiency of the power plant cannot be further improved. However, the reactivity of CO<sub>2</sub> with metals is weak, so the inlet temperature of turbine can be further increased, thereby improving the cycle efficiency.

Fig. 2 shows the comparison of the new S-CO<sub>2</sub> cycle and S-H<sub>2</sub>O cycle. The results of S-H<sub>2</sub>O cycle can be found in ref.[11]. We can clearly see that the efficiency of S-CO<sub>2</sub> cycle is higher than S-H<sub>2</sub>O cycle, even in relatively low turbine inlet temperature. From the perspective of circulation, thermal efficiency of S-CO<sub>2</sub> cycle is higher. From the perspective of physical property, CO<sub>2</sub> is less corrosive. So we believe that S-CO<sub>2</sub> cycle is expected to replace S-H<sub>2</sub>O cycle for coal-fired power plants.

#### 3.2 Comparison of intercooling and non-intercooling

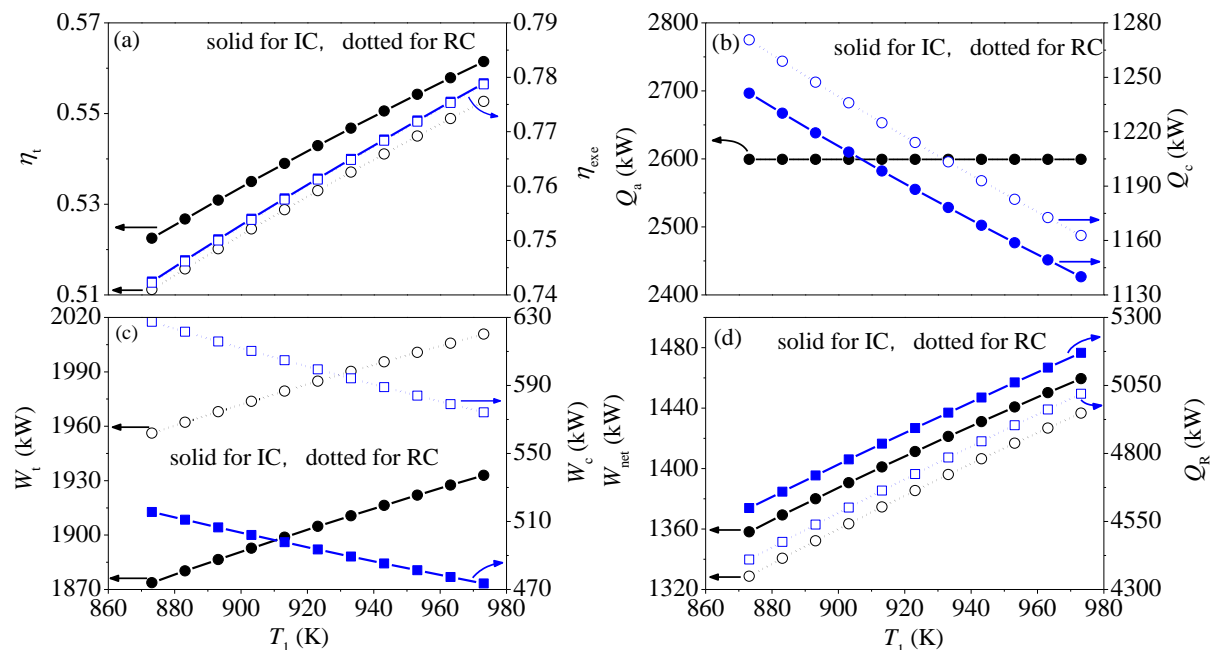


Figure 3. Parameters of S-CO<sub>2</sub> cycle changed with  $T_1$ .

Introduce intercooling can improve the cycle performance[4]. This part compares the cycle in Fig. 1 with intercooling (IC) and without intercooling (recompression cycle, RC) under different maximum temperature( $T_1$ ).

Fig. 3 shows the parameters of IC and RC changed with maximum temperature. As can be seen from Fig. 3(a), the introduction of intercooling can greatly increase the cycle thermal efficiency and increase the efficiency to nearly 2%. And from the research of section 3.3 we can found that when the minimum temperature of cycle is higher, introducing intercooling can increase thermal efficiency more significantly. From Fig. 3, it can be seen that the parameters of maximum temperature and intercooling are relatively independent. The introduction of intercooling increases the thermal efficiency while it has little effect on exergy efficiency which remains almost constant. Increasing maximum temperature can greatly increase the thermal efficiency as well as the exergy efficiency.

The change of thermal efficiency can be explained in Fig. 3(b), (c) and (d). The introduction of intercooling can greatly reduce the power consumption of the compressor, but it also reduces the output power of turbine to a certain extent, finally gets a higher net work ( $W_{net}$ ). And the heat absorbs from the boiler ( $Q_a$ ) is a fixed value. Therefore, the cycle thermal efficiency increases. Introducing intercooling also reduces the heat released to cooler ( $Q_c$ ), thereby increasing the cycle thermal efficiency. Increasing the maximum temperature of the cycle not only increases the output power of the turbine, but also reduces the power consumption of the compressor, which greatly improves the net output work. At the same time, it also increases regenerator power ( $Q_R$ ), thus improves the cycle thermal efficiency. Introduce intercooling have a large influence on LTR. The pinch point of LTR will shift to inside of the LTR compare to the non-intercooling case, thus to influence the performance of LTR dramatically.

### 3.3 Effect of minimum temperature

The minimum temperature of cycle plays an importance role in the analysis of cycle performance. That's because it is close to critical temperature of  $CO_2$ , and the properties near critical point is changed dramatically.

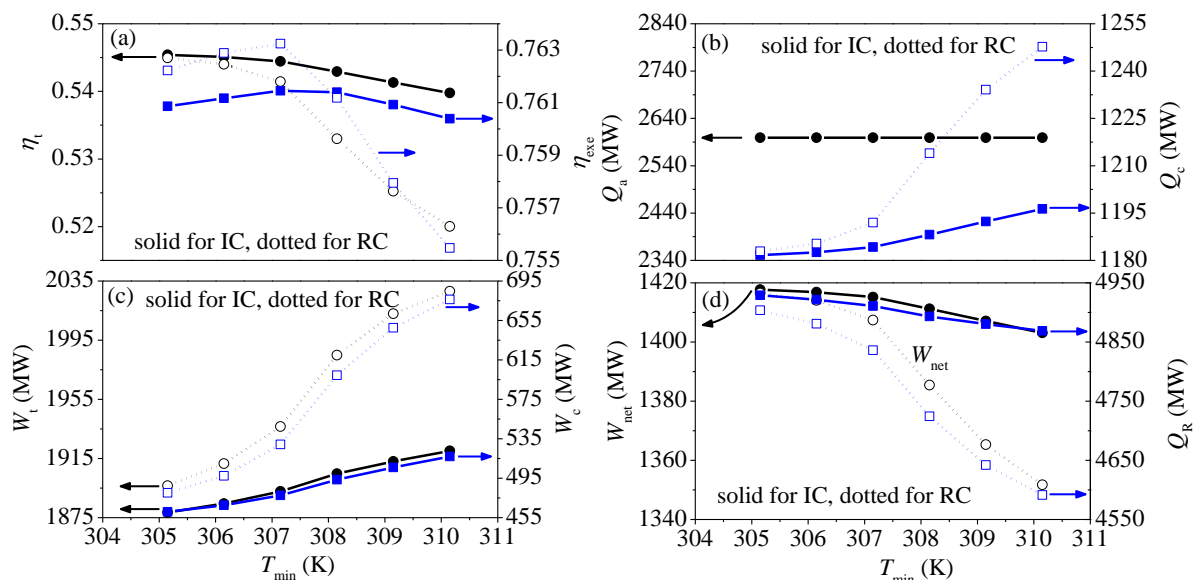


Figure 4. Parameters of S- $CO_2$  cycle changed with  $T_{min}$ .

Fig. 4 shows the effect of  $T_{min}$  on several parameters of cycle. The thermal efficiency sharply decreased with  $T_{min}$  increasing, while the exergy efficiency shows a parabolic trend under the change of  $T_{min}$ , see in Fig. 4(a). With the increase of  $T_{min}$ ,  $Q_c$  increases while  $Q_a$  remains constant. Thus it leads to a decreasing  $W_{net}$ . At the same time, the heat exchanged through regenerator decrease, the cycle performance becomes worse. When  $T_{min}$  close to critical point of  $CO_2$ , that is,

the lower the minimum temperature, the lower power consumption of compressor. However, increasing  $T_{\min}$  will increase the temperature difference inside the cooler, thus to get a higher exergy destruction, while reduce the exergy destruction of the boiler. The trend of exergy efficiency depends on the balance of exergy destruction of each components. From the perspective of thermal efficiency, we'd better chose the lowest  $T_{\min}$  to reach the maximum thermal efficiency. However, while considering exergy efficiency, we might choose the  $T_{\min}$  deviates from critical point slightly. Fig. 4 also compared RC and IC, we can see while the  $T_{\min}$  is high, introducing intercooling is more beneficial to the performance of S-CO<sub>2</sub> cycle.

### 3.4 Effect of intercooling pressure

Introduce intercooling can improve cycle efficiency of S-CO<sub>2</sub> coal-fired power generation system, and how to select intercooling pressure is very important. It has an effect on the performance of each component.

Fig. 5 shows the parameters changed with intercooling pressure. From Fig. 5(a), it can be seen that there is an optimal intercooling pressure of 8.7 MPa, making the thermal efficiency reach a maximum value of 54.29%. The pressure value only slightly deviates from the cycle minimum pressure of 8 MPa, and is far from the maximum pressure of cycle of 30 MPa. It can be seen that the pressure ratio of LTC2 is much lower than that of LTC1.

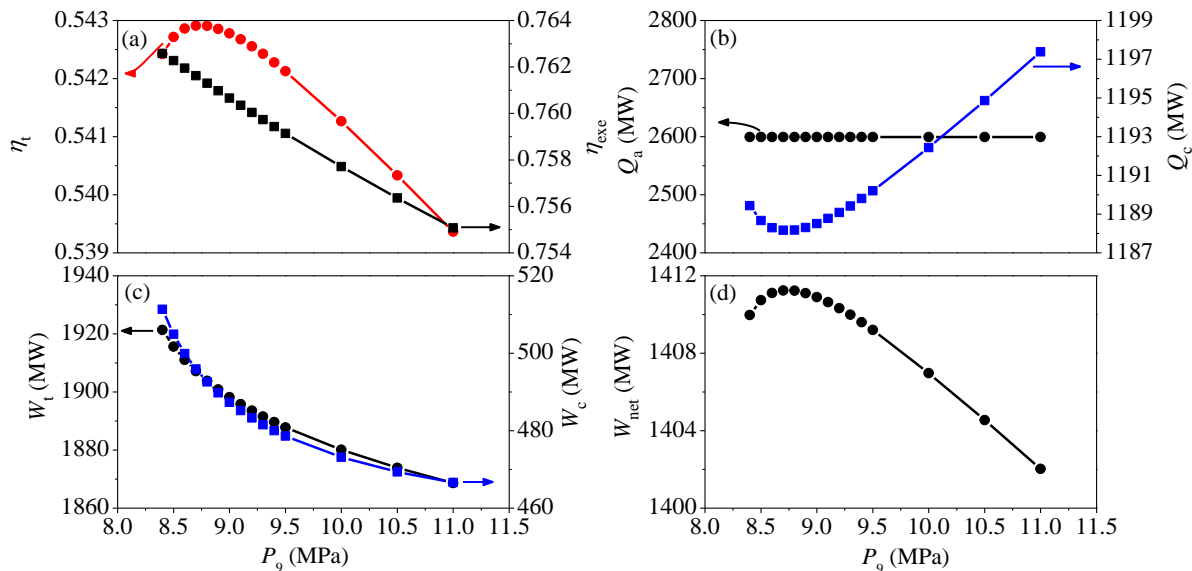


Figure 5. Parameters of S-CO<sub>2</sub> cycle changed with  $P_9$ .

The change of thermal efficiency can be explained from Fig. 5(b), (c) and (d). As can be seen from Fig. 5(b), the introduction of intercooling has a greater impact on cooling side heat transfer. Since  $Q_a$  is a fixed value, the thermal efficiency is negatively correlated with the trend of  $Q_c$ . Under the optimal intercooling pressure,  $Q_c$  is the lowest and the cycle efficiency is the highest. Fig 5(c) and (d) explained the work load in cycle. With intercooling pressure increasing,  $W_t$  and  $W_c$  both decrease. due to the different change rate, the  $W_{net}$  can reach a maximum value.

### Summary/Conclusions

This paper discusses a new S-CO<sub>2</sub> Brayton cycle integrated with boiler and used a simplified method to analyse the performance of the cycle. Comparison between the new S-CO<sub>2</sub> Brayton cycle and S-H<sub>2</sub>O cycle was carried out, the results show a great advantage of S-CO<sub>2</sub> cycle. Parameters analysis of S-CO<sub>2</sub> cycle are carried out. Increase the maximum temperature will enhance the thermal efficiency dramatically, due to the low corrosion rate of CO<sub>2</sub> with metals, using CO<sub>2</sub> as working fluid is beneficial to power generation. Introduce intercooling can

improve the cycle performance, especially at a high  $T_{\min}$ . And introduce intercooling will make the pinch point shifts to inside of the LTR. There exists a optimum intermediate pressure of intercooling, and the pressure value only slightly deviates from the cycle minimum pressure. Minimum temperature has a different influence on thermal efficiency and exergy efficiency. When the minimum temperature approaches to critical temperature of  $\text{CO}_2$ , the thermal efficiency is higher, but exergy efficiency shows a parabolic trend with the change of minimum temperature, thus we should choose the appropriate value according to the purpose.

### Acknowledgements

This paper is supported by the National Key R&D Program of China (2017YFB0601801).

### References:

- [1]Feher, E.G., “The supercritical thermodynamic power cycle”, Energy conversion, 1968, [doi: 10.1016/0013-7480\(68\)90105-8](https://doi.org/10.1016/0013-7480(68)90105-8)
- [2]Angelino, G., “Carbon Dioxide Condensation Cycles For Power Production”, 1968, doi:10.1115/1.3609190
- [3]Dostal, V., Hejzlar, P., “A supercritical carbon dioxide cycle for next generation nuclear reactor”, MIT, 2004.
- [4] Ahn, Y., Lee, J.I., “Study of various Brayton cycle designs for small modular sodium-cooled fast reactor”, Nuclear Engineering and Design, 2014, [doi:10.1016/j.nucengdes.2014.05.032](https://doi.org/10.1016/j.nucengdes.2014.05.032)
- [5] Al-Sulaiman, F.A., Atif, M., “Performance comparison of different supercritical carbon dioxide Brayton cycles integrated with a solar power tower”, Energy, 2015, [doi: 10.1016/j.energy.2014.12.070](https://doi.org/10.1016/j.energy.2014.12.070)
- [6] Padilla, R.V., Soo Too, Y.C., Benito, R., Stein, W., “Exergetic analysis of supercritical  $\text{CO}_2$  Brayton cycles integrated with solar central receivers”, Applied Energy, 2015, [doi: 10.1016/j.apenergy.2015.03.090](https://doi.org/10.1016/j.apenergy.2015.03.090)
- [7] Moullec, Y. L., “Conception of a Pulverized Coal Fired Power Plant with Carbon Capture around a Supercritical Carbon Dioxide Brayton Cycle”, Energy Procedia, 2013, [doi: 10.1016/j.egypro.2013.05.215](https://doi.org/10.1016/j.egypro.2013.05.215)
- [8] Moullec, Y. L., “Conceptual study of a high efficiency coal-fired power plant with  $\text{CO}_2$  capture using a supercritical  $\text{CO}_2$  Brayton cycle”, Energy, 2013, [doi: 10.1016/j.energy.2012.10.022](https://doi.org/10.1016/j.energy.2012.10.022)
- [9] Mecheri, M., Moullec, Y. L., “Supercritical  $\text{CO}_2$  Brayton cycles for coal-fired power plants”, Energy, 2016, [doi: 10.1016/j.energy.2016.02.111](https://doi.org/10.1016/j.energy.2016.02.111)
- [10] Sarkar, J., Bjattacharyya, S., “Optimization of recompression S- $\text{CO}_2$  power cycle with re-heating”, Energy Conversion and Management, 2009, [doi: 10.1016/j.enconman.2009.04.015](https://doi.org/10.1016/j.enconman.2009.04.015)
- [11] Fu, C., Anantharaman, R., Jordal, K., Gundersen, T., “Thermal efficiency of coal-fired power plants: From theoretical to practical assessments”, Energy Conversion and Management, 2015, [doi: 10.1016/j.enconman.2015.08.019](https://doi.org/10.1016/j.enconman.2015.08.019)

# Pumped Thermal Energy Storage (PTES) as Smart Sector-Coupling Technology for Heat and Electricity

W.-D. Steinmann<sup>1</sup>, H. Jockenhöfer<sup>1</sup> and D. Bauer<sup>1\*</sup>

<sup>1</sup>German Aerospace Center (DLR), Institute of Engineering Thermodynamics, Pfaffenwaldring 38, 70569 Stuttgart

\*Corresponding author: dan.bauer@dlr.de

## Abstract

Pumped thermal energy storage is considered as a promising concept for large scale storage of electricity. In contrast to other concepts like pumped hydro or compressed air energy storage, pumped thermal energy storage does not demand specific geological requirements. CHEST (Compressed Heat Energy Storage) is a pumped thermal energy storage variant based on Rankine cycles using either water or organic media as the working fluid in a combination of steam processes. The presentation will give an overview of the different options for the implementation of pumped thermal energy storage systems based on the CHEST concept. For these CHEST variants, characteristic values like operating parameters and power ratio will be given and the required components will be described. The focus will be on the technological possibility of using pumped thermal energy storage as a sector-coupling technology for heat and electricity through low temperature heat integration. In addition, new findings of an in-depth numerical simulation of a fully heat-integrated, subcritical PTES using butene as the working fluid are presented.

**Keywords:** thermo-mechanical energy storage, bulk energy storage, pumped thermal energy storage, CHEST.

## Introduction/Background

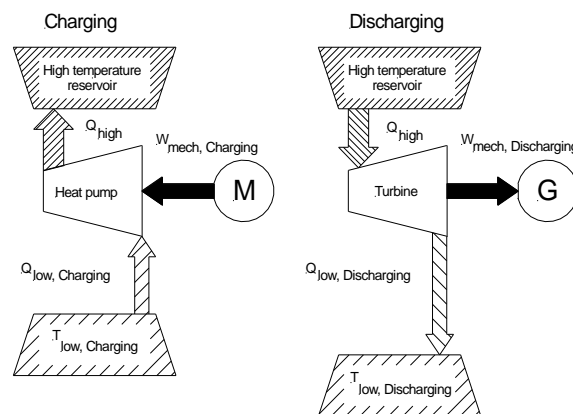


Fig. 1: Schematic of pumped thermal energy storage

Pumped thermal energy storage is a thermo-mechanical storage concept which combines a left running thermal cycle with a thermal storage system and a right running thermal cycle. As shown in Fig.1, the low temperature reservoir used during the charging process needs not to be identical to the low temperature reservoir used during the discharge. This allows additional options for pumped thermal energy storage, both thermal and electric energy can be used during charging, both heat and electricity may be delivered during discharge. If thermal energy is available during the charging process, the electric energy required for operating the heat pump can be reduced accordingly. If the minimal temperature of the

thermal cycle used during discharge is below the temperature of the heat reservoir used during charging, the electric energy delivered during discharge might exceed the electric energy required for charging the system. Alternatively, process heat might be delivered during discharge. This makes pumped thermal energy storage a versatile concept for sector coupling in future scenarios with high penetrations of heat and electricity delivered by renewable energy sources. Key characteristics of pumped thermal energy storage are the absence of geographic restrictions and life expectancies in the range of 20-30 years.

While pumped thermal energy storage has already been suggested in the 1920s the development of this concept has only recently gained momentum. Besides the growing need to integrate an increasing share of energy delivered by renewable sources the progress made in thermal storage technology has fostered the interest in pumped thermal energy storage. For the technical implementation of this concept different variants have been suggested [1]. Concepts based on gas turbine technology use packed bed [2,3] or molten salt thermal storage [4], other authors have suggested CO<sub>2</sub> as working fluid combined with pressurized water storage systems [5].

The CHEST (compressed heat energy storage) foresees the application of subcritical Rankine cycles using either water or organic fluids (Fig.2)[6]. Mandatory for an efficient pumped thermal energy storage system is the minimization of the entropy generation during charging and discharging. Consequently, latent heat storage systems are used to limit the temperature difference in isothermal process sections like the charging with condensing steam or evaporation of water during discharging.

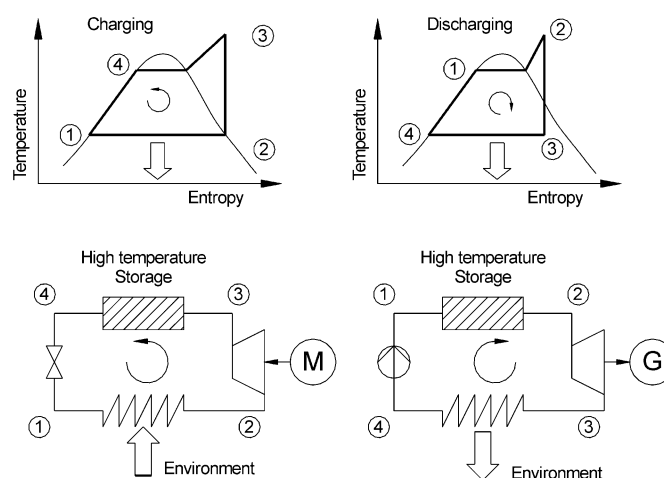


Fig.2 T-s-Diagram and schematic of the CHEST-concept

The choice of the working fluid for the CHEST-concept depends on the type of storage system. For the storage of electric energy water will be the preferred working fluid. The thermal storage unit will be charged with steam at temperatures between 350-400 °C at about 100 bar. The expected roundtrip efficiency is in the range of 70%, the typical nominal power is in the multi-MW range. In order to reach this roundtrip-efficiency with alternative pumped thermal energy storage systems based on gas turbine technology, higher maximum temperatures are required. Alternative pumped thermal energy storage concepts which are operated at lower maximum temperatures are not expected to reach similar roundtrip efficiencies. While many components required for the implementation of a CHEST concept using water as a working fluid are already available or are in an advanced stage of

development other components like the steam compressor require the adaption of existing technology to the specifications of the CHEST-system.

CHEST systems using organic working fluids are intended primarily as energy management tools for balancing heat and electricity sources to meet the demands of heat and power consumers [7]. Compared to CHEST systems operated with water, the maximum temperature of system using organic working fluids is lower, the requirements for the efficiency of turbines and compressors are less stringent, the nominal electric power ranges from several kW to a few MW. CHEST based on organic working fluids is considered as a technology which can be introduced in the medium term and which can also serve as an intermediate step towards the more challenging systems based on water which are mainly intended for the storage of electricity.

Fig.3 shows the exemplary combination of a CHEST system with a geothermal energy source. During charging, geothermal heat is stored after its temperature has been increased by a heat pump operated by electric energy delivered by a wind park. During discharge, the heat stored before is used to drive an orc turbine, additionally thermal energy for district heating is delivered.

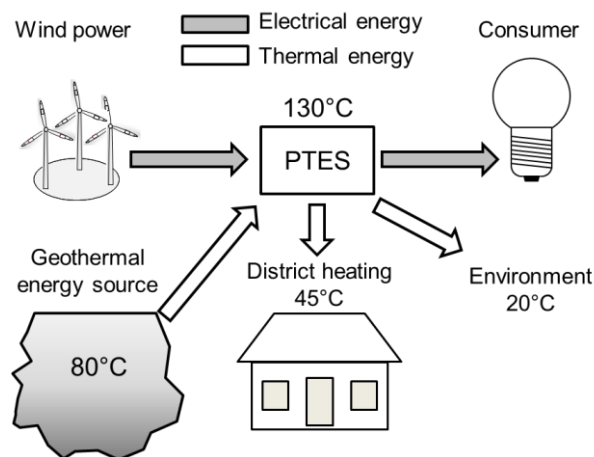


Fig.3: CHEST ins a combined heat and power system using heat from a geothermal energy source and electric power delivered by a wind farm

Another option is the integration of CHEST into a smart district heating system. Smart district heating system use, amongst other energy sources, solar thermal energy to provide heat for domestic applications. The temporal mismatch between availability and demand is balanced by short term water tanks of 1,000 to 10,000 m<sup>3</sup> and by seasonal thermal energy storage in pit thermal energy storage of 10,000 to 200,000 m<sup>3</sup> capacities. Several of these systems are currently in operation, especially in Denmark. Others are in planning, the largest for the district heating of Graz, Austria (with 1.800.000 m<sup>3</sup> of seasonal thermal energy storage). Smart district heating systems were established in Denmark in the past ten years, among other reasons, due to the possibility of taking combined heat and power plants offline during times of high availability of wind power while closing the resulting gap in the heat supply of district heating systems by using other technologies. Because of the high availability of wind power, Power-to-Heat technologies like electrical boilers to support the local district heating are already in use for heat production, and further steps towards 100% renewable energy will be flexible use of electricity for transportation and for hydrogen production (power to gas and liquid fuels). Produced gas and liquid fuels will be needed in the transport sector and maybe for industrial processes, so the dispatchable recovery of used electrical energy in periods without electricity from wind and solar would be another important step on the way to an integrated, sustainable and cross-sectoral energy concept, but

is not yet implemented due to unavailable technologies. Fig.4+5 show the integration of CHEST into a smart district heating system. the CHEST-concept uses the seasonal TES as low-temperature heat source for the heat pump. In addition, the waste heat of the heat engine is fed back to the seasonal TES. In the power range up to about 10 MWe<sub>l</sub> a high technological potential is ascribed to simple ORC engines and corresponding temperature levels between ca. 130°C and 180°C in the high-temperature storage: The integration of an ORC-CHEST concept into an application with two different temperature levels in the low-temperature heat source or sink (here: approx. 90 °C and 40 °C) theoretically compensates for any irreversibility within the energy conversion.

For the evaluation of the concept the gross power ratio  $\epsilon_{gross}$  has been applied:

$$\epsilon_{gross}[\%] = \frac{P_{el,out}}{P_{el,in}} = \frac{P_{el,generator}}{P_{el,compressor}}$$

The value of  $\epsilon_{gross}$  might exceed 100 % if heat from a source which is above the temperature of the heat rejected by the system is available.

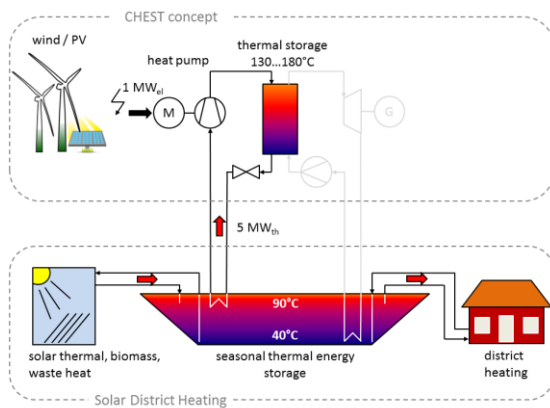


Fig.4: Charging of Chest unit integrated into smart district heating system

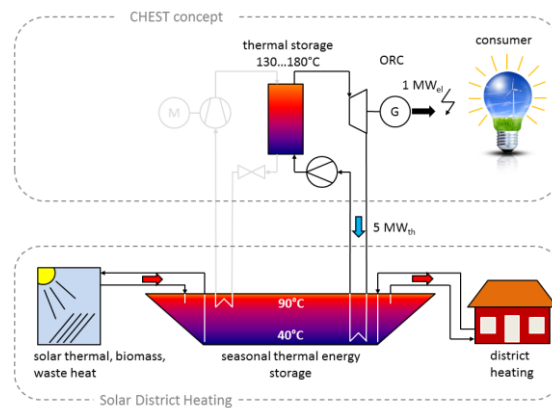


Fig.5: Discharging of Chest unit integrated into smart district heating system

One of the key features of the CHEST concept is the high flexibility that it offers which allows to efficiently respond under different boundary conditions and needs. The CHEST concept integrated into smart district heating system offers a variety of operation modes that can be actively chosen. Depending on the current state of boundary conditions, it offers the possibility to convert more heat into power, or more power into heat (Fig. 6-11).

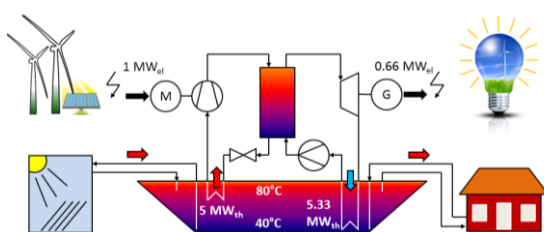


Fig.6: Mode 1: regular mode: the CHEST system consumes 1 MWe<sub>l</sub> during charging; during discharging 0.66 MWe<sub>l</sub> is delivered

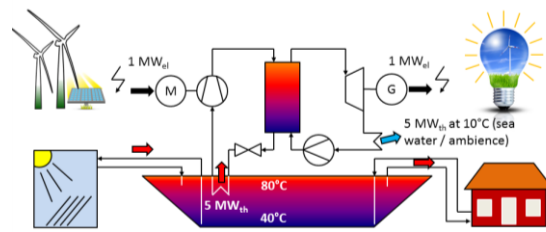


Fig.7: If a  $\epsilon_{gross}$  of 100% is needed, it can be achieved by reducing the temperature of the ORC heat dissipation to 10°C



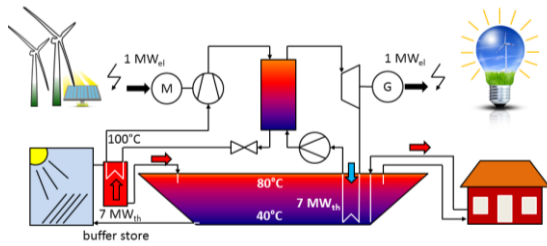


Fig.8: Mode 3:  $\epsilon_{\text{gross}} = 100\%$  can be achieved with other boundary conditions also, for example, using higher temperature RES sources

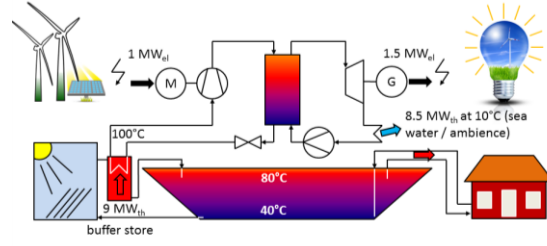


Fig.9: Mode 4: combination of mode 2 and 3;  $\epsilon_{\text{gross}} > 100\%$ . For each  $\text{MWh}_{\text{el}}$  that the system consumes, it is able to deliver 1.5  $\text{MWh}_{\text{el}}$  when needed

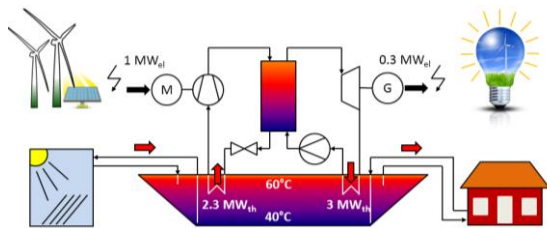


Fig.10: Mode 5: low  $\epsilon_{\text{gross}}$  of 30% but heating of seasonal TES. For each  $\text{MWh}_{\text{el}}$  that the system consumes, 0.7  $\text{MWh}_{\text{th}}$  will be converted into heat

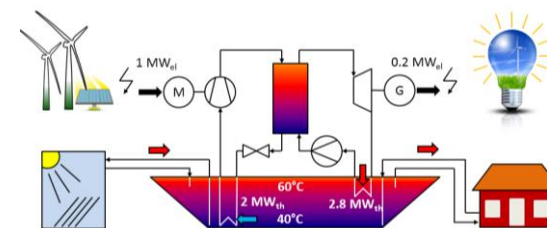


Fig.11: Mode 6: heat pump mode; suitable for weekend / wintertime. Similar to operation mode 5, but stronger heating of upper layer of the seasonal TES at lower  $\epsilon_{\text{gross}}$

If a weekend in winter is assumed as exemplary situation, the demand of the industry for electric energy is low but a lot of wind energy is available and heat demand of the district heating is high, mode 5 or 6 can be chosen. In summer on working days with high demand of electric energy, little demand of district heating and a lot of solar thermal energy, mode 3 or 4 can be chosen. Unlike combined heat and power plants, the use of electricity and heat is independent. The resulting concept will maximize the utilization of renewable energy flows from various sources while ensuring the security of supply. Fig.12 shows how this flexibility can be used along the year to cover the needs depending on energy availability and demand requirements.

Season	Available energy (typical structure)	Demand (typical structure)	Operation strategy
Summer			Storage is mainly used for storage of electric energy
Winter			Storage delivers both heat and electricity Heat pump may be used to provide domestic heat
Transitional period			Storage delivers both heat and electricity, depending on demand Heat pump may be used to (re) charge seasonal storage

Fig.12: Operation strategy of the CHEST concept dependent on seasonal boundary conditions For the CHEST smart district application a detailed numerical analysis has been done using the Epsilon professional software [7]. Fig.13 shows the schematic used in the simulation, the corresponding T-s diagram is shown in Fig.14.

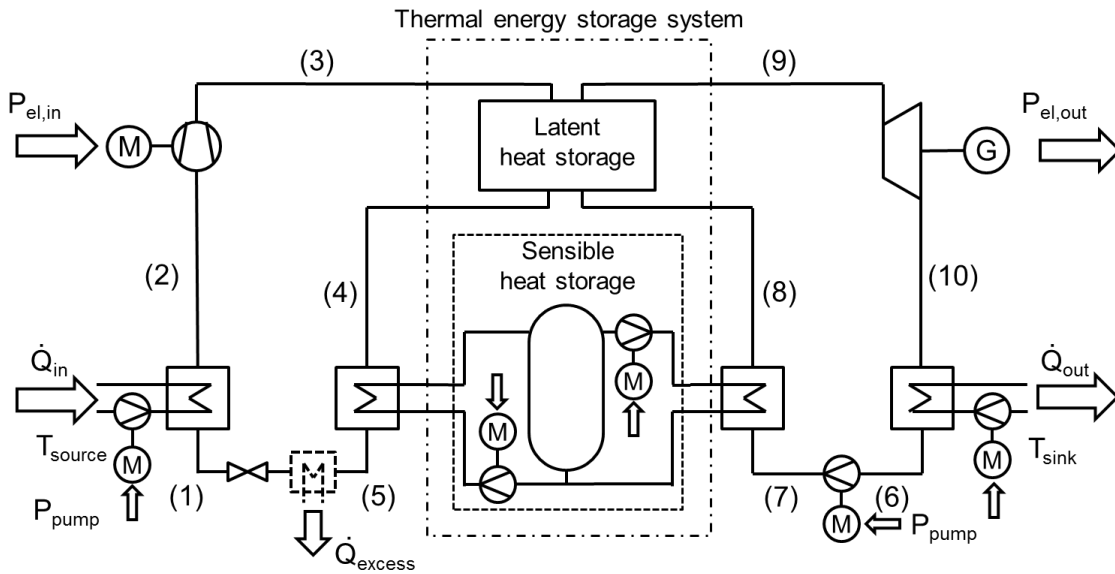


Fig.13: Schematic of CHEST integrated in smart district heating system

During charging the working fluid is evaporated by adding low temperature thermal energy in a heat exchanger (1→2). Excess electrical energy is used to compress the working fluid (2→3). After condensation in a latent heat storage (3→4), the saturated liquid is aftercooled, whereby the sensible heat is transferred to a pressurized water thermocline storage (4→5). Before entering the evaporator, the fluid is throttled to evaporation pressure (5→1). In case the ORC-CHEST system shall be operated with varying source and sink temperatures, an additional heat exchanger between (5) and the throttle is necessary to keep the ratio between energy stored in the latent heat storage and in the sensible heat storage constant.

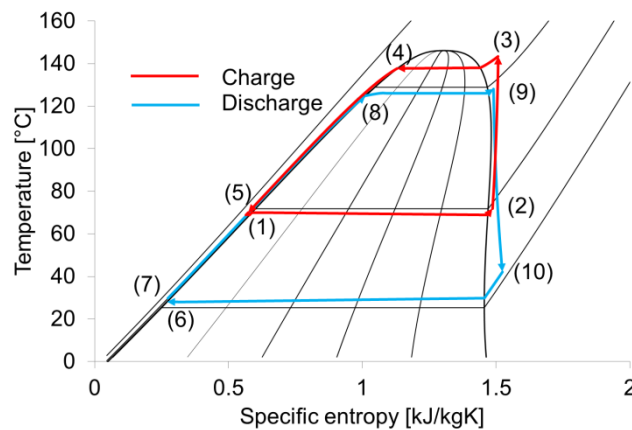


Fig.14: T-s diagram for system according to Fig.13

After compression to evaporation pressure (6→7), the working fluid is preheated to saturation state using the thermal energy from the sensible heat storage (7→8). The evaporation takes place in the latent heat storage (8→9) and the thermal energy is converted back to electrical energy by an expander, driving a generator (9→10). The working fluid is liquefied in a water-cooled condenser (10→6). Due to the temperature difference between working fluid and latent heat storage, the working fluid pressure at (9) is lower than the pressure at (3).

Butene was chosen as the working fluid, a eutectic mixture of  $\text{KNO}_3$  and  $\text{LiNO}_3$  was selected as phase change material.

The dependence of the net power ratio  $\epsilon_{\text{net}}$  on the temperature of the heat source  $T_{\text{source}}$  and on the temperature of the heat sink  $T_{\text{sink}}$  is shown in Figs. 13 and 14. Assuming a temperature difference of 5 K in the storage system the maximum net power ratio is 1.25 for a source temperature of 100 °C and a sink temperature of 15 °C. A heat source temperature of 90 °C is required for a sink temperature of 15 °C if the irreversibilities in the process should be compensated ( $\epsilon_{\text{net}} = 1.0$ ). Fig.14 shows the results for a temperature difference of 10 K in the storage system. The maximum value achieved for the net power ratio is 0.89 at a heat source temperature of 100 °C and a heat sink temperature of 15 °C.

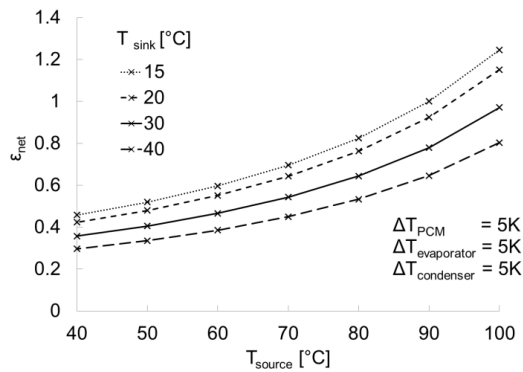


Fig.15: Calculated net power ratio dependent on the temperature of the heat source for various temperatures of the heat sink assuming a temperature difference of 5K in the storage system

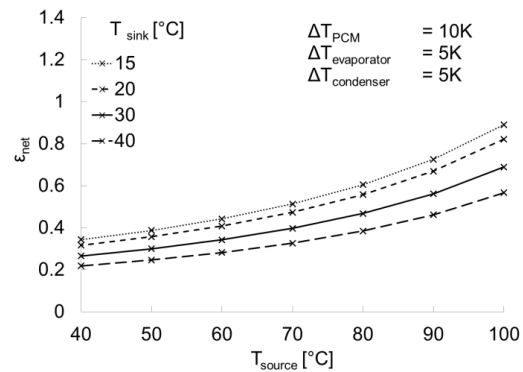


Fig.16: Calculated net power ratio dependent on the temperature of the heat source for various temperatures of the heat sink assuming a temperature difference of 10K in the storage system

The development of CHEST for smart district heating applications is in the focus of the EC Horizon 2020 project CHESTER which has been started in April 2018. In the framework of this project the main components of the CHEST system will be developed for the specific requirements of this application. A complete CHEST system will be demonstrated in pilot scale.

### Discussion and Results


CHEST is considered as a promising option for the implementation of pumped thermal energy storage since many components are already available. Besides using the concept primarily for the delivery of electrical energy, there is also the possibility for providing both electrical energy and heat during discharge. Additionally, low temperature heat from external sources can be integrated during the charging process. These options make CHEST a versatile energy management tool for balancing supply and demand of heat, cold and electricity. Water is the preferred working fluid for systems in the multi-MW range, mainly intended for the delivery of electrical energy. Organic working fluids are intended for systems with a lower capacity, which deliver both heat and electricity during discharging. An in-depth numerical simulation of a fully heat-integrated, subcritical pumped thermal energy storage using butene as the working fluid shows that such systems are additionally able to convert low-temperature heat, e.g. waste heat below 100°C, efficiently into electricity.

### Summary/Conclusions

Pumped thermal energy storage systems could be a key element for a successful implementation of the energy system transformation to renewable energies. Especially systems based on Rankine cycles might play an important future role, as they allow for an

efficient sector coupling of heat and electricity in both directions, leading to a very smart technology for renewable energy management, storage and dispatchable supply.

### **Acknowledgments**

This project has received funding from the European Union's Horizon 2020 research and innovation programme under grant agreement No 764042. This presentation reflects only the author's views and neither Agency nor the Commission are responsible for any use that may be made of the information contained therein. 

### **References:**

- [1] Steinmann, W.-D., *Thermo-mechanical concepts for bulk energy storage*. *Renew Sustain Energy Rev.* 75 (2017), 205-219
- [2] Desrues T, Ruer J, Marty P, Fourmigue JF. *A thermal energy storage process for large scale electric applications*. *Appl. Therm. Eng.* 30 (2010), 425-432
- [3] McTigue JD, White AJ, Markides CN. *Parametric studies and optimisation of pumped thermal electricity storage*. *Appl. Energy* 137 (2015), 800-811
- [4] Morandin M, Marechal F, Mercangöz M, Buchter F. *Conceptual design of a € thermo-electrical energy storage system based on heat integration of thermodynamic cycles - Part A: methodology and base case*. *Energy* 45 (2012), 375-385
- [5] Laughlin, RB. *Pumped thermal grid storage with heat exchange* *J. of Renew. And Sust. Energy* 9 (2017)
- [6] Steinmann, W.-D., *The CHEST (Compressed Heat Energy Storage) concept for facility scale thermo mechanical energy storage*. *Energy* 2014;69:543–52.
- [7] Jockenhöfer, H., Steinmann ,W.-D., Bauer, D., *Detailed numerical investigation of a Pumped Thermal Energy Storage with low temperature heat integration*. Submitted to *Energy*

# A theoretical approach to identify optimal replacement fluids for existing vapour compression refrigeration systems and heat pumps

D. Roskosch<sup>1\*</sup>, V. Venzik<sup>1</sup> and B. Atakan<sup>1</sup>

<sup>1</sup> University of Duisburg-Essen, Thermodynamics, Lotharstr. 1, 47057 Duisburg, Germany

\*Corresponding author: dennis.roskosch@uni-due.de

## Abstract

The nowadays used working fluids for vapour compression refrigeration systems and heat pumps partly have a high global warming potential and will have to be replaced. This holds for systems in operation but also to a large number of existing cycle designs. Therefore, it would be very helpful if alternative working fluids for a given plant could be found which do not require a redesign of the system and which, in best case, also are more efficient. Although it seems possible to achieve this goal with modern process simulation tools, it remains unclear how detailed a concrete plant design must be modelled to obtain a reliable ranking of working fluids, useful for selection. In order to investigate this question a vapour compression heat pump test rig is simulated by thermodynamic models with different levels of complexity. The model results are compared among each other and to measured values for various fluids. It turns out that simple cycle calculations lead to incorrect results regarding the efficiency and thus are not sufficient to find replacement fluids for existing plants. The implementation of a compressor model significantly improves the simulation and leads finally to reliable fluid rankings. However, the information whether the heat exchangers are of sufficient size and whether the fluid is suited at all for a given task can only be obtained, as it turns out, by means of the most complex model which includes extensive models for the heat exchangers.

**Keywords:** refrigerants, retrofit, process simulation, replacement fluids.

## Introduction

As a result of the Montreal Protocol [1], the CFCs such as R12 or R22, which had previously been used in the field of compression refrigeration and heat pumps, were replaced by compounds without an ozone depletion potential. Besides other fluids, from the group of hydrofluorocarbons (HFCs), the fluids R134a, R404A and R410A turned out to be good alternatives. They are still widely used today in a wide range of systems. HFCs do not have an ozone depletion potential but some of them however possess an extremely high GWP (global warming potential) and, thus, contribute significantly to the climate change. Therefore, the United Nations (UN) decided the gradual reduction of the use of these refrigerants. Within the European Union the resolution of the UN is implemented by the F-Gas-Regulation [2], which includes several different instruments. In addition to a direct ban on use, which, however, in a timely manner (2020 or 2022) only concerns refrigerants with a GWP greater than 2500 (e.g. R404A), the regulation also contains a phase-down scenario of the generally available quantities of refrigerants with a global warming potential. Thus, it may already be necessary for manufacturers to retrofit, at least, some of their products to refrigerants with a lower GWP in order to be able to maintain or increase sales volumes. In addition to new plants, it may also be necessary or useful for plant operators to replace the working fluids also of systems, which are already in operation. Addressing this issue, industry and science started to push the research of alternative refrigerants several years ago. Generally, the selection process of alternative refrigerants is subjected to many criteria, such

as environmental aspects or material compatibility, however, thermodynamic criteria are often at the beginning of the selection procedure, as is the focus of the present work. In general, the search for alternative fluids can be divided into two approaches. The industry often focuses on synthesizing pure substances or fluid mixtures that have very similar thermodynamic properties to the fluids to be substituted. In this context, compounds from the group of hydro-fluoro olefins (HFOs) in particular have come into focus. Although this method offers the user the advantage that the selection of a substitute, independent of the concrete plant, is solely based on the refrigerant which was used up to now, but it blocks the possibility of identifying more efficient working fluids with differing thermodynamic properties. In this context, fluid selection methods, which are based on the plants, and not on the fluids that were used up to now, are much more promising. Numerous publications were published in recent years which deal with such an approach and often try to identify potential alternative fluids on a theoretical basis [3–6]. These studies always focus on future plants and are usually based on very simple theoretical models. Heat exchangers often are not modeled, and/or it is assumed that the compressor efficiencies are not fluid dependent. Such studies may be beneficial for new plants, where the fluid selection is part of the design process, but are not very helpful if a replacement fluid for a given existing system is to be found. The same applies to experimental work which investigate individual fluids in a laboratory scale test rig regarding general suitability and efficiency [7–9]. Although these works often lead to interesting heuristics, they are not very helpful to find replacement fluids for concrete plants, since it is not possible to estimate to which COP (coefficient of performance), heat flow rates and compressor power a fluid will have in another concrete system. However, these are important criteria; they determine if a potential replacement fluid is suitable at all or if system components possibly have to be replaced. Due to the large number of individual plants or plant designs, modern process simulation tools seem to be the most promising method to find individual replacement fluids, but it remains unclear how detailed a concrete plant design must be modelled to obtain a reliable ranking of working fluids, useful for selection.

In order to investigate this question a vapour compression heat pump test rig is simulated by thermodynamic models with three different levels of complexity. The simulation results are compared on the one hand along the different model levels and on the other hand with measured values from a heat pump test rig. Here, the fluids R134a, R152a, propane, propene, isobutane and dimethyl ether are investigated under the same operating conditions of the heat pump, while the operating point with R134a is determined to be the reference point. Although the test rig was not specifically designed for this fluid, this referencing, nevertheless, seems reasonable due to the wide use of R134a.

### **Experimental setup and boundary conditions**

The test rig is a simple water / water vapor compression heat pump cycle as shown in Fig 1. The main components are a semi-hermetic reciprocating compressor (GEA Bock: HG12P5.4;  $P_{\max} = 2.2$  kW), an expansion valve, a condenser and an expander. Both heat exchangers are designed as counter flow double pipe heat exchangers. The system is equipped with extensive measuring technology. Pressure and temperature are measured in front of and behind each component, the refrigerant mass flow is determined by a Coriolis flowmeter, and a frequency converter measures the electrical compressor power input. The secondary mass flow rates in the heat exchangers are also adjustable and are measured gravimetrically. The exact specifications of the system components and installed instrumentation can be found in [8]. The recording and processing of the measured values is carried out by the program LabVIEW [10], while enthalpies, entropies and further thermodynamic properties are calculated with REFPROP [11]. The operating conditions of the heat pump are based on the application for the supply of underfloor heating. The secondary fluid water enters the condenser at 25 °C

(index: w, c, i). The water mass flow is adjusted such that its outlet temperature is always 35 °C (index: w, c, o). Water with a constant mass flow rate of 7.5 kg·min<sup>-1</sup> flows through the evaporator; the inlet temperature is constant at 17 °C, while the water outlet temperature depends on the refrigerant and the evaporation temperature. The compressor rotation speed is always fixed at 1500 min<sup>-1</sup>. The water mass flow rate in the condenser and the opening of the expansion valve, which is directly connected to the evaporation temperature, are the two adjusting parameters of the heat pump. Within the experiments, these parameters are always adjusted with the target of maximum COP. The evaporation temperature is subjected to further technical restrictions: The resulting system pressures must be between 1 and 20 bar, the fluid must be superheated by at least 3 K at the compressor inlet and the water temperature at the evaporator outlet must be above 2 °C in order to avoid freezing. The experimental results of the reference fluid R134a are given in Table 1.

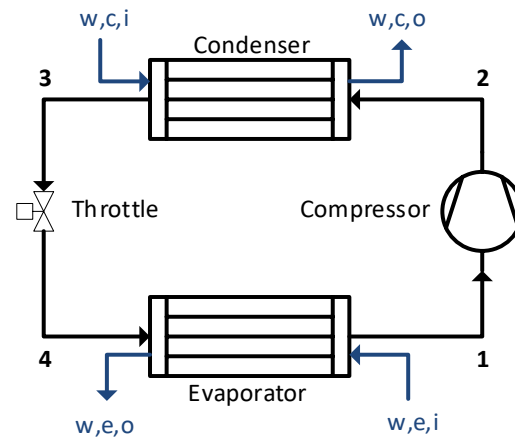


**Fig. 1: Heat pump schema of the simulation models and the experiments**

## Modelling

All simulation programs are written in the programming language Python [12] and the required fluid properties are taken from REFPROP [11]. At simulation level 2, a numerical optimizer NLP (non-linear problem) is used, taken from the OpenOpt network [13]. The simulations are based on the process scheme given in Fig. 1 and the state designations are in the following always referenced to those given in Fig. 1. For all simulation steps isenthalpic expansion in the throttle and adiabatic condition of the heat exchangers against the environment are generally assumed.

### *Simulation level 1*

The simulation level 1 includes only a simple thermodynamic cycle calculation with specific values and largely ideal conditions, such as constant isentropic efficiencies of the compressor or neglecting of pressure losses in the heat exchangers. This type of model is frequently used for fluid selection by other authors [3,14]. Since no physical models are implemented for the different components, numerous cycle states must be specified. These include the evaporation temperature  $T_e$ , the condensation temperature  $T_c$ , the superheating at the compressor inlet  $\Delta T_{\text{superheating}}$ , the sub-cooling  $\Delta T_{\text{subcooling}}$  or the steam quality  $x_3$  at the condenser outlet, and the isentropic compressor efficiency  $\eta_{\text{com}}^s$ . For new plants, where the fluid selection is part of the design process, such parameters may be seen as design variables, but this is not true for existing systems. However, the simulation level 1 does not allow to estimate which operating conditions will follow in the case of a concrete system with another fluid. Here, the simplest and obvious assumption is that all components, such as heat exchangers and compressors,

operate similarly with different fluids. Thus, the required process variables are here set to the measured values with the reference fluid R134a (Table 1).

**Table 1: Measured data of the reference fluid R134a**

$COP$	$\dot{Q}_H$	$\dot{m}_f$	$\eta_{com}^s$	$T_e$	$\Delta T_{supeheating}$	$T_c$	$\Delta T_{subcooling}$
4.76	3.85 kW	0,019 kg·s <sup>-1</sup>	0,47	4,95 °C	9,94 K	34,51 °C	2,11 K

### *Simulation level 2*

Based on the simulation level 1, the second level is significantly expanded by implementing a compressor model. The used compressor model is a semi-physical model, which predicts volumetric and isentropic efficiencies as a function of the inlet state, the outlet pressure and the working fluid; it can be fitted quickly to a concrete reciprocating compressor. It is already described in detail in [15] and will be summarized here only briefly. Apart from the state change of the gas in the cylinder, also, friction of the piston, heat transfer, a clearance volume and the valve flows are modeled. For the fluid dependent characterization of the valve flows, empirical correlations were derived on the basis of extensive measurement data for different fluids, which determine the flow losses as a function of the fluid and the operating conditions. Finally, the model is based on four geometry parameters that commonly are known from the manufacturer, as well as only two further parameters which have to be fitted to compressor dependent measured data. These fitting parameters can be estimated for a concrete compressor only based on the measurement of the volumetric and isentropic efficiencies at one operating point with one fluid. A validation study with different fluids showed mean deviations of 3.0 % for the isentropic and 2.3 % for the volumetric efficiencies, while the maximum errors are still less than 6.0 %. The heat exchangers at this simulation level are modeled by pinch-models, which means for the respective heat exchangers that the lowest temperature difference over the entire length may not fall below a minimum value of  $\Delta T_{p,i}$ . These minimum values are directly related to the transfer capability or the quality of the heat exchangers, but normally depend on the fluid and the flow conditions. However, the implemented models do not allow the exact estimation of the pinch temperatures for different fluids and thus, it is again assumed that the pinch temperatures are equal to the measured values of the reference fluid (evaporator:  $\Delta T_{p, R134a} = 1.43$  K, condenser:  $\Delta T_{p, R134a} = 0.71$  K). Despite the implemented pinch models, there are no closed mathematical solutions for the heat exchangers. In the evaporator, the outlet states of the water and of the refrigerant are unknown and in the condenser the unknown values are the outlet state of the refrigerant and the mass flow rate of the water. In each case, one of these process variables must therefore be fixed, in order to get a mathematical solution. For the sub-cooling at the condenser outlet, it is analogous to level 1, again assumed that the values correspond to the measured values of R134a (Table 1). The values of the superheating of the refrigerant at the evaporator outlet, as well as of the evaporation and condensation temperatures, which are also still degrees of freedom of the simulation, are not taken from the reference fluid, but they are numerically optimized with the goal of a maximal COP, as in the experiment. This optimizations are subjected to the minimum pinch-temperatures as well as to all boundary conditions of the experiment.

### *Simulation level 3*

In addition to the compressor model, at simulation level 3 detailed models of the heat exchangers (counter flow, double pipe) are also included in order to calculate the heat transfer rates and the pressure drops (only for the refrigerant). These models are based on the cell



method [16, S. 34f]. The heat transfer between the refrigerant and the secondary fluid is a series of two convective heat transfers and the heat conduction through the inner pipe wall. According to the different sections, where evaporation, condensation or superheating take place, several different correlations for heat transfer and pressure drop are implemented, as given in Table 2. These correlations were, in a pre-selection study, found to be particularly suitable. The heat exchanger models indeed significantly expand the entire model, but the evaporation and the condensation temperatures are still degrees of freedom of the simulation. The evaporation temperature is, as at the test rig, directly controlled by the orifice opening of the expansion valve, and thus, a degree of freedom, but the resulting condensation temperature depends on the mass flow rate of the secondary fluid and on the interaction between the expansion valve and the compressor. The expansion valve used here is a simple needle valve, which is difficult to model, especially due to the two-phase flow. As a result, at simulation level 3, as well as at level 2, the evaporation and condensation temperatures are again numerically optimized with the aim of achieving maximum COP. These optimizations are subjected to the same boundary conditions as in the second level or in the experiments. In case of a commercial plant equipped with an expansion device with a fixed control characteristic, this can also be implemented in the model and the optimization will no longer be necessary.

**Table 2: Implemented correlations for heat transfer and pressure drop**

Model	Source
pipe flow <sup>1</sup>	Shah / Gnielinski VDI-Heat Atlas [16, S. 693-699]
concentric annular <sup>1</sup>	Martin / Stephan / Gnielinski VDI-Heat Atlas [16, S. 701-705]
pipe flow <sup>2</sup> (evaporation)	Shah [17]
pipe flow <sup>2</sup> (condensation)	Shah [17]
pressure drop <sup>1</sup>	VDI-Heat Atlas [16, S. 1057-1063]
pressure drop <sup>2</sup>	VDI-Heat Atlas [16, S. 1125-1129]

<sup>1</sup>single phase flow, <sup>2</sup>two phase flow

## Discussion and Results

Fig. 2 shows the results of all fluids for the different simulation levels and for the measurements. The results are divided into the coefficient of performance (a), the rejected heat flow rate (b) and the compressor power input (c). In addition to absolute values, the relative comparison to the fluid to be replaced (reference fluid) is of great interest in the search for a direct substitution fluid; thus, the values of the COP (a) are, here, normalized to the corresponding value achieved by the reference fluid R134a in the individual case (simulation levels and measurements). Therefore, R134a is depicted as horizontal line with the value 1.0. It gets clear that the calculations of the simulation level 1 lead to almost identical values of the COP for all fluids, while significant differences are present in the measurements; as an example the COP of propane is 13 % higher than the one of R134a. Of even higher importance is the different order of the fluid dependent COPs. Thus, the results of simple cycle calculations at level 1 will not help to select a good replacement fluid. Another issue of level 1 is that values of the rejected heat flow rate or the compressor power input cannot be calculated, although these are important parameters for the selection of replacement fluids. For example, if a potential replacement fluid would lead to a compressor power above the maximum power input of the used compressor, either the fluid is generally not suitable or the compressor has also to be replaced.

The implementation of a compressor model and a pinch model for the heat exchangers (simulation level 2) also make it possible to estimate the expected heat flow rate and the compressor power. With regard to the COPs (Fig. 2a), the results are now significantly more

meaningful and the comparison with the measured values shows that an adequate statement can already be made whether a fluid will have a higher or lower COP compared to the fluid to be substituted (R134a). However, there are also some deviations. Compared to R134a, it is generally predicted correctly that propane has a higher COP and propene has a lower COP; but the advantage of propane is estimated as too low and the disadvantage of propene is calculated as too large. For isobutane and R152a, the model results in a nearly identical COP, while the measurement for R152a shows a slightly better value. Slightly larger deviations from the measurements can be seen in the rejected heat flow rates (Fig. 2b). This applies especially to the fluids R134a, R152a and dimethyl ether. In all cases, the heat flow rates with respect to the measurements are predicted to be too large, but the relative comparison of the calculated heat flow rates with that of R134a, which is even more important, shows the

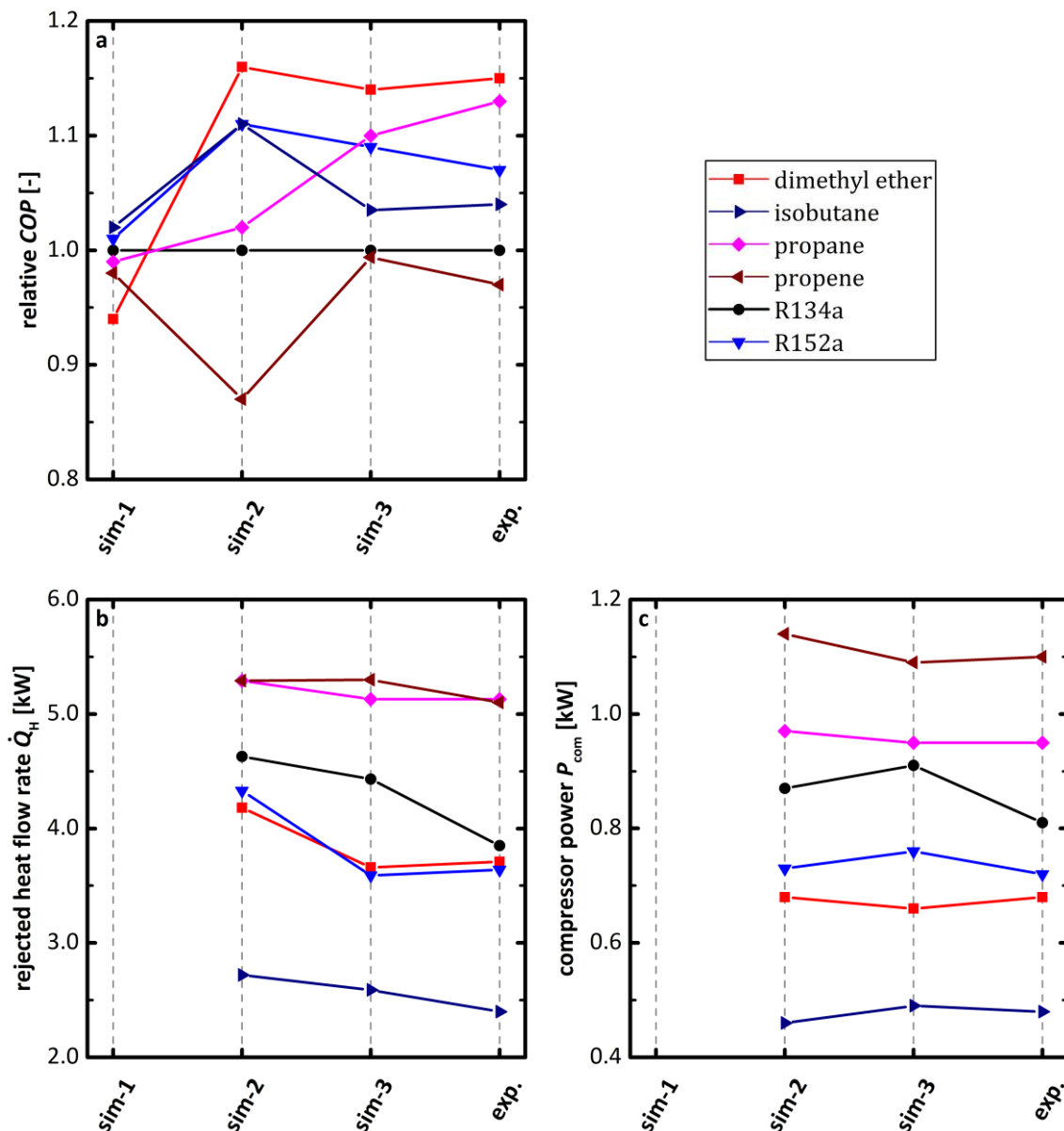


Fig.2: COPs normalized to R134a (a), rejected heat flow rates (b) and compressor power (c) for different fluids and for three simulation levels and the measurements.

correct tendency. It becomes clear that, based on the results, it can be predicted which of the considered fluids achieves at least the same heat flow rate as the fluid to be replaced. This

information can already be used to exclude inappropriate fluids from further investigations. The comparison of the calculated compressor power (Fig. 2c) with the measured values shows first that they are well reproduced by simulations at level 2. For isobutane, propane and R152a, there are only marginal deviations from the measured values, but the calculated values are slightly too high for R134a and propene. In general, based on the calculated values, it is possible to estimate with good accuracy whether the compressor installed in the concrete plant is compatible with the respective fluid in terms of its maximum power. A big advantage of the simulation level 2 is the low computation time. The calculation of one fluid running on a standard computer (CPU: Intel Core i7-4790, RAM: 24 GB) only takes a few minutes, so that even large fluid databases can be searched for suitable fluids in a relatively short time. In addition to the compressor model, the simulation level 3 also includes detailed models for the calculation of heat transfer and pressure drop in the heat exchangers. This leads to further improved results of the estimated relative COPs with respect to level 2 and to the measurements, as obvious from Fig. 2a. Simulations at level 3 reproduce the measured order of fluids with respect to their COPs; thus, level 3 gives a reliable estimation of which fluids will have a higher and which a lower COP than the reference fluid. Propane is now correctly predicted to have a higher relative COP than isobutane and R152a. Also, the advantage of propane relative to R134a is now predicted to be significantly larger and the deviation from the measurement is only marginal. Furthermore, level 3 now predicts a difference between isobutane and R152a, which corresponds almost to the measured values. The results of the rejected heat flow rates (Fig. 2b) are also further improved in level 3; the resulting values only show slight deviations from the measurements. Especially, the estimation for R152a is here significantly improved; also, the result for R134a is improved but still shows a deviation to the measurements. The calculations of simulation level 3 give, for the investigated fluids, a reliable statement whether a fluid will achieve at least the rejected heat flow rate of the fluid to be substituted, being an important criterion for replacement fluid selection.

In general the analysis shows that the results are improved the less values are taken from the fluid to be substituted (reference fluids) and the more physical models are implemented. However, a disadvantage of further implementations of physical models is the increasing computational time. The optimization of the process temperatures in level 3 currently takes up to 6 hours on a standard computer for one fluid. Although it is assumed that the required computational time can be significantly reduced in future, it will always be a multiple of the computational time of level 2.

### **Summary/Conclusions**

In this work, theoretical methods for identifying optimal replacement refrigerants for existing vapour compression refrigeration systems and heat pumps were investigated. The focus was on the so far unclear question of how detailed a concrete plant must be modelled in a simulation to achieve a reliable fluid ranking, useful for fluid selection. In order to investigate this question a vapour compression heat pump test rig was simulated by thermodynamic models with different levels of complexity. The results of the modelling were compared with measurements for different fluids, while R134a was defined as the refrigerant to be substituted. It turned out that simple cycle calculations with the assumption of constant process conditions and constant isentropic compressor efficiencies (level 1) are not suitable for identifying potential substitution fluids for existing concrete plants. The implementation of a compressor model for a fluid-dependent and process-dependent determination of isentropic and volumetric efficiencies in combination with pinch-models for the heat exchangers (level 2) significantly improves the results. The calculated values showed a good agreement with the measured values leading to reliable estimation whether a fluid is more efficient than the fluid to be replaced and whether the rejected heat flow rate and the compressor power will be larger or smaller. The implementation of detailed models for the heat transfer and the pressure drop in the

heat exchangers (level 3) further improved the results. However, due to the high computational effort of level 3 compared to level 2, it currently does not seem useful to scan large refrigerant databases with the model of highest complexity. Rather, it is recommended to carry out a preliminary study with the level 2 and then to consider some of the identified fluids in detail with a detailed model at level 3. Although the simulations do not replace a final experimental test, it is very helpful to reduce the number of potential substitution fluids and the required experiments.

### References:

- [1] United Nations Environment Programme UNEP (ed.), *Montreal Protocol on Substances that Deplete the Ozone Layer*, 1987.
- [2] Europäische Union, *Verordnung über fluorierte Treibhausgase: (EU) Nr. 517/2014*, 2014.
- [3] Dalkilic A.S., Wongwises S., *A performance comparison of vapour-compression refrigeration system using various alternative refrigerants*, International Communications in Heat and Mass Transfer(9), 37, 1340–9, 2010.
- [4] El-Morsi M., *Energy and exergy analysis of LPG (liquefied petroleum gas) as a drop in replacement for R134a in domestic refrigerators*, Energy, 86, 344–53, 2015.
- [5] Roskosch D., Atakan B., *Reverse engineering of fluid selection for thermodynamic cycles with cubic equations of state, using a compression heat pump as example*, Energy, 81, 202–12, 2015.
- [6] Schilling J., Lampe M., Gross J., Bardow A., *1-stage CoMT-CAMD: An approach for integrated design of ORC process and working fluid using PC-SAFT*, Chemical Engineering Science, 159, 217–30, 2017.
- [7] Chang Y., Kim M., Ro S., *Performance and heat transfer characteristics of hydrocarbon refrigerants in a heat pump system*, International Journal of Refrigeration(3), 23, 232–42, 2000.
- [8] Venzik V., Roskosch D., Atakan B., *Propene/isobutane mixtures in heat pumps: An experimental investigation*, International Journal of Refrigeration, 76, 84–96, 2017.
- [9] Sánchez D., Cabello R., Llopis R., Arauzo I., Catalán-Gil J., Torrella E., *Energy performance evaluation of R1234yf, R1234ze(E), R600a, R290 and R152a as low-GWP R134a alternatives*, International Journal of Refrigeration, 74, 269–82, 2017.
- [10] *LabVIEW Professional Development System*, National Instruments, 2013.
- [11] Lemmon, E.W., Huber, M.L., McLinden, M.O., *NIST Standard Reference Database 23: Standard Reference Data Program*, National Institute of Standards and Technology, Gaithersburg, 2013.
- [12] *Python.org*, available from: <https://www.python.org/>, [accessed April 16, 2018].
- [13] *OpenOpt*, available from: <http://openopt.blogspot.de/>, [accessed April 16, 2018].
- [14] Brown J.S., *Predicting performance of refrigerants using the Peng–Robinson Equation of State*, International Journal of Refrigeration(8), 30, 1319–28, 2007.
- [15] Roskosch D., Venzik V., Atakan B., *Thermodynamic model for reciprocating compressors with the focus on fluid dependent efficiencies*, International Journal of Refrigeration, 84, 104–16, 2017.
- [16] Verein Deutscher Ingenieure, *VDI heat atlas, 2nd ed.*, Springer-Verlag Berlin Heidelberg, Berlin, 2010.
- [17] Shah M.M., *A New Correlation for Heat Transfer During Boiling Flow Through Pipes*, ASHRAE Transactions(82), 66–86, 1976..

# Experimental Results of a 1 kW Heat Transformation Demonstrator based on a Gas-Solid Reaction

J. Stengler<sup>1\*</sup>, E. Fischer<sup>1</sup>, J. Weiss<sup>1</sup> and M. Linder<sup>1</sup>

<sup>1</sup>German Aerospace Center (DLR), Institute of Engineering Thermodynamics, Pfaffenwaldring 38-40, 70569 Stuttgart, Germany

\*Corresponding author: jana.stengler@dlr.de

## Abstract

Heat transformation based on reversible chemical reactions has gained significant interest due to the high achievable output temperatures. These chemical heat pumps use a reversible gas-solid reaction in which the back and forward reaction take place at different temperatures: by running the discharge reaction at a higher temperature than the loading reaction, the released heat is thermally upgraded. In this work, we report on the experimental investigation of a salt hydrate with regard to its use for heat transformation in the temperature range from 180 °C to 300 °C on a 1 kW scale. The reaction temperature is set by adjusting the pressure of the gaseous reactant, water vapor, in a range from 1 kPa up to 0.6 MPa. In our prior experimental studies, we found the properties of the solid bulk phase to be subject to considerable changes due to the chemical reaction: amongst others, the particle size distribution shifts, resulting in agglomeration and altered bulk permeability. In order to better understand how this affects the thermal performance of a thermochemical reactor, we combine our experimental work with a modelling approach. Our current work includes the development of a reactor concept that allows handling gas-solid reactions at high specific thermal powers as well as an easy scale-up for industrial applications.

**Keywords:** Heat Transformation, Thermochemical Reaction, Chemical Heat Pump, Thermal Upgrade, Gas-Solid Reaction

## Introduction

Heat transformation processes are discussed in the context of industrial waste heat utilization. The basic concept of heat transformation requires three temperature levels and two pressure stages (see Fig. 1a). In our work, we developed a different approach to achieve thermal upgrade at a higher temperature range. As depicted in Fig. 1b, it requires four temperature stages: the two upper ones are related to the later application process; the two lower ones are used for thermal compression of the gaseous reactant. The lowest temperature level is needed for vapor removal from the reaction chamber (condensation at ambient temperature) in order for the reaction to reach complete turnover. Hence, the endothermic loading process takes place at a low pressure and temperature, respectively. This way, low value process heat is sufficient to charge the thermochemical reactor. During the exothermic discharging process, evaporation is driven by low temperature waste heat. Its temperature defines the vapor pressure and thus the maximum thermal upgrade of the released high value process heat.

With this approach, we are able to re-use low temperature waste heat from industrial processes as driving source for a high temperature heat pump. Depending on the chosen gas-solid working pair, the operating temperature of the heat pump process can be adapted to a specific application.

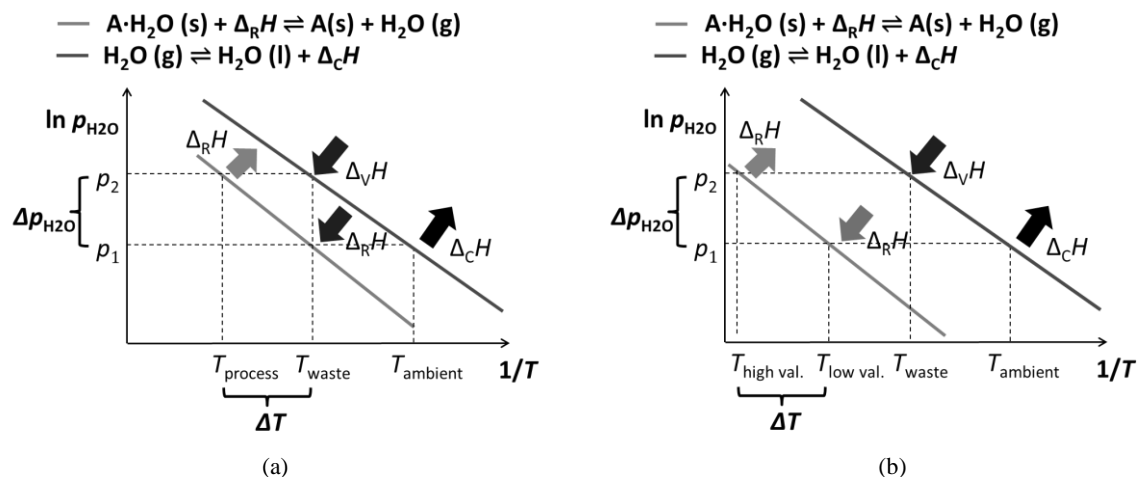
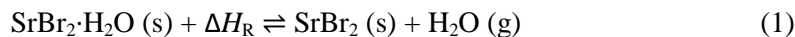


Fig. 1: Van't Hoff diagrams of generic gas-solid reactions combined with the vapor-liquid equilibrium of the gaseous reactant. Depending on the chosen gas-solid working pair, two modes of operation are possible: (a) thermal upgrade of low temperature waste heat, and (b) thermal upgrade of high temperature process heat driven by low temperature waste heat (operation concept of this work).

In a previous study, we identified strontium bromide ( $\text{SrBr}_2$ ) as a suitable candidate for thermochemical heat transformation [1]. This inorganic salt is non-toxic and forms an anhydrous, monohydrate, and hexahydrate phase. Prior to our study, the reaction system  $\text{SrBr}_2/\text{H}_2\text{O}$  has been discussed in literature exclusively in the context of low temperature energy storage for seasonal storage applications [2], [3]. This is achieved by using the reaction from the monohydrate phase to the hexahydrate phase, which happens at a temperature of 50 °C to 80 °C. In contrast, our work is focused on the reaction from the anhydrous salt to its monohydrate, which takes place at temperatures above 150 °C:



Based on standard enthalpy and entropy of formation given in the NBS Tables, reaction enthalpy and entropy is calculated to 71.98 kJ/mol and 143.93 J/(mol·K), respectively [6]. The reaction is reversible, however, a thermal reaction hysteresis was observed in thermogravimetric analysis (TGA) experiments: we found a difference of 22 K between hydration and dehydration temperature at a partial vapor pressure of 5 kPa. Cycling stability was experimentally demonstrated in TGA measurements for 10 dehydration/re-hydration cycles [1]. In a subsequent study, we developed a method to obtain data on the pressure-temperature correlation from experiments under technically relevant operation conditions on a 1 kg scale [4]. In our experimental study we observed that the exothermic reaction from the anhydrous phase to the monohydrate takes place at around 229 °C when water vapor is supplied at a pressure of 70 kPa. During the dehydration process at a vapor pressure of 6.5 kPa, a minimum temperature of 190 °C was measured. When opening the reaction chamber after having conducted 11 dehydration/re-hydration cycles, we found agglomeration effects in the bulk. This was observed consistently during the series of experiments.

Our current work is focused on the investigation of experimental operation conditions that allow for heat transformation in a temperature range of 200 °C to 300 °C at high thermal powers. This includes the development of a reactor concept which is capable of handling a gas-solid reaction at high thermal throughputs and is easily scalable for larger applications.

## Modelling and Experimental Procedure

To charge the storage system, thermal energy is introduced into the solid bulk material via a heat transfer fluid. In the course of the endothermic chemical reaction, the gaseous reactant escapes from the solid bulk and must be separated from the solid phase: the emerging vapor is condensed in a separate heat exchanger in order to keep the pressure at a low value and thus to reach complete reaction turnover. In this work, we focus on the thermal discharge process, which starts when water vapor is introduced into the reaction chamber at a high pressure. The thermal energy released by the subsequent chemical reaction is transferred from the solid bulk to the heat transfer fluid. For vapor generation, we use a tube bundle heat exchanger which is equipped with a level indicator to measure the amount of water being consumed by the chemical reaction.

In simple terms, there are three categories of processes that affect the thermal performance of a thermochemical reactor: vapor mass transfer into the solid bulk phase, heat transfer from the solid bulk phase to the heat transfer fluid, and the reaction rate at the given operation conditions. To qualify how the physical and chemical properties of the reactive material affect the thermal performance of a thermochemical reactor and to quantify these local effects in order to identify possible bottlenecks, we included the relevant physical processes during the chemical reaction in a model based on FEM (finite element method). For numerical calculations, we used solvers from the *Comsol Multiphysics*<sup>®</sup> simulation software. The validity of the simulation studies was verified by comparison with experimental data from distinct measurement points of a packed bed thermochemical reactor.

The packed bed reaction chamber consists of two pillow plates which are mounted back to back and are equally flowed through by heat transfer fluid (HTF). The heat exchanger plates form a 290 mm x 225 mm x 20 mm space filled with 1,050 g of  $\text{SrBr}_2 \cdot \text{H}_2\text{O}$ . Metal filters with a mesh size of 5  $\mu\text{m}$  keep the packed bed in position and minimize undesired release of powder into the vapor supply pipework. A schematic drawing of the setup is depicted in Fig. 2. As model domain, we chose a cross-section of the rectangular reactor geometry.

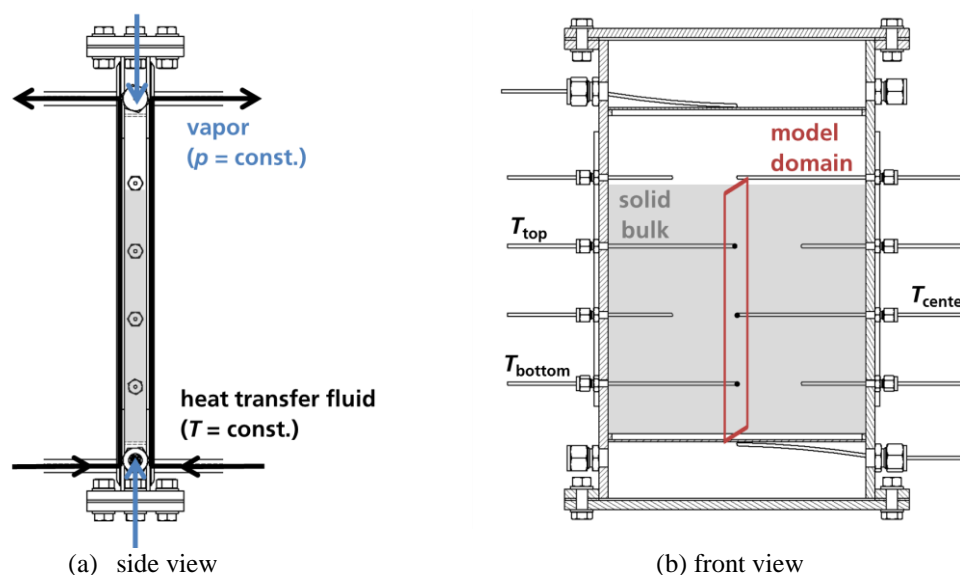


Fig. 2: Schematic reactor geometry used for both modelling as well as experimental studies. The thermochemical reactor is equipped with a pressure sensor and several temperature probes which monitor the solid bulk's temperature at different positions within the fixed bed. During the experiment, the temperature of the heat transfer fluid was kept at a constant value.

A 2D-study was performed for a cross section through the powder bulk. For model implementation, the solid phase is assumed to be a homogenous porous medium. Movement of the solid is neglected, and the porosity remains constant during the reaction. Furthermore, a change in bulk volume or bulk permeability is not yet considered. The gas phase, which consists of pure water vapor with ideal gas properties, penetrates the porous media according to Darcy's law. We assume local thermal equilibrium between the gas and the solid phase. As the temperature differences that occur within the observed volume are very small, heat radiation does not play a significant role and can therefore be neglected. Boundary conditions concerning heat and mass transfer for the relevant model domain are depicted in Fig. 3. Material properties were assessed by the means of literature data or own measurements and calculations. A summary is given in Table 1.

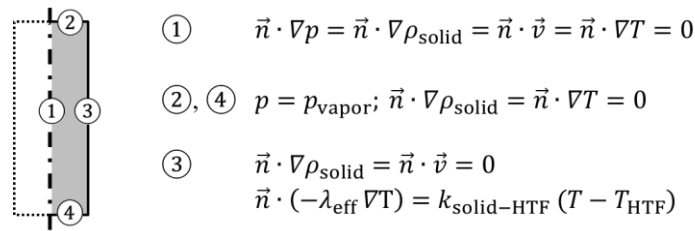


Fig. 3: Model domain boundary conditions for heat and mass transfer with  $\vec{v}$  being the Darcy flux and  $\vec{n}$  the normal vector.

Table 1: Chemical and physical properties of the SrBr<sub>2</sub>/H<sub>2</sub>O reaction system.

Category	Parameter	Value	Reference
solid properties	density SrBr <sub>2</sub>	4216 kg/m <sup>3</sup>	literature data, see [5]
	density SrBr <sub>2</sub> ·H <sub>2</sub> O	3911 kg/m <sup>3</sup>	linear interpolation between SrBr <sub>2</sub> and SrBr <sub>2</sub> ·6H <sub>2</sub> O densities given in [5]
	heat capacity SrBr <sub>2</sub>	75.35 J/(mol·K)	literature data, see [6]
	heat capacity SrBr <sub>2</sub> ·H <sub>2</sub> O	120.9 J/(mol·K)	literature data, see [6]
bulk properties	bulk porosity (SrBr <sub>2</sub> ·H <sub>2</sub> O)	0.72	experimental data
	permeability	1·10 <sup>-10</sup> m <sup>2</sup>	literature data, see [7]
	thermal conductivity $\lambda_{\text{eff}}$	0.15 W/(m·K)	conservative assumption based on data given in [7]
	solid to HTF heat transfer coefficient $k_{\text{solid-HTF}}$	274 W/(m <sup>2</sup> ·K)	own calculation for given reactor geometry and experimental conditions
hydration reaction (SrBr <sub>2</sub> to SrBr <sub>2</sub> ·H <sub>2</sub> O)	reaction enthalpy $\Delta H_{\text{R}}$	71.98 kJ/mol	literature data, see [6]
	reaction entropy $\Delta S_{\text{R}}$	143.93 J/(mol·K)	literature data, see [6]
	pre-exponential factor $A_0$	8.1·10 <sup>4</sup> 1/s	own calculation
	activation energy $E_a$	67.6 kJ/mol	own calculation
	reaction model $f(X)$	2·(1-X)·[-ln(1-X)] <sup>1/2</sup>	own calculation
	pressure term exponent $n$	1.9	own calculation

The chemical reaction is implemented as a heat source with a reaction rate which depends on the vapor pressure  $p$ , Temperature  $T$  and reaction conversion  $X$ :

$$\frac{dX}{dt} = A_0 \exp\left\{-\frac{E_a}{RT}\right\} \cdot f(X) \cdot \left(\frac{p}{p_{\text{eq}}} - 1\right)^n. \quad (2)$$

The equilibrium pressure  $p_{\text{eq}}$  of the hydration reaction is a temperature-dependent function which can be obtained from the thermodynamic data on reaction enthalpy and reaction entropy (Van't Hoff line). The kinetic parameters (pre-exponential factor  $A_0$ , activation energy  $E_a$ , conversion-depending function for reaction model  $f(X)$ , and pressure term exponent  $n$ ) are calculated from our TGA measurements. Please note that the values given in Tab. 1 are preliminary results, and are subject to change as part of our current work.



## Results and Discussion

We conducted several sets of experiments. Within the series, the vapor pressure and, accordingly, the temperature of the heat transfer fluid were varied: as strontium bromide forms a hexahydrate phase ( $\text{SrBr}_2 \cdot 6\text{H}_2\text{O}$ ) at high vapor pressures or low temperatures, respectively, the preheat temperature of the anhydrous solid must be raised for high vapor pressures in order to ensure the exclusive formation of  $\text{SrBr}_2 \cdot \text{H}_2\text{O}$ . Up to 15 dehydration/rehydration cycles were performed in a row with one batch of reactive material. Afterwards, the reactor was refilled with a fresh batch of  $\text{SrBr}_2 \cdot \text{H}_2\text{O}$ . The vapor pressure was varied from roughly 20 kPa up to 150 kPa, and the preheat temperature of the solid bed was set in a range of 150 °C to 210 °C. The maximum temperature measured at the central position in the packed bed during the hydration reaction is plotted against the set vapor pressure in Fig. 4.

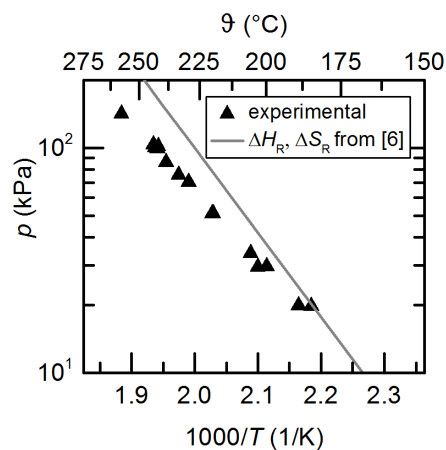


Fig. 4: Van't Hoff plot for the hydration reaction with experimental and thermodynamic data.

The results given in Fig. 4 reveal that the measured values clearly exceed the temperatures derived from thermodynamic data, especially for high pressures. For this reason, a linear regression was calculated for the temperature-dependency of the equilibrium pressure  $p_{\text{eq}}$  in the hydration reaction based on the experimental data points. This correlation was also used for the reaction rate mode described in Eq. (2):

$$\log(p_{\text{eq}}/\text{hPa}) = 8.84 - 3.02 \cdot \frac{10^3}{T/\text{K}} . \quad (3)$$

The results of the simulation study are compared with the results of the prior described experiments, with the measured pressure curve being defined as input variable for the simulation. In Fig. 5a, the temperature progression at different positions within the solid bulk is shown for a preheat temperature of 209 °C and a vapor pressure of 70 kPa. The increase in temperature indicates that the exothermic reaction is in progress. As the reaction approaches complete conversion to the monohydrate, the temperature in the solid bulk begins to decrease. Evidently, temperature progression is not homogenous within the bulk phase: at the lowest temperature measuring point ( $T_{\text{bottom}}$ ), lower maximum temperature is observed. We assume that this effect occurs due to macroscopic inhomogeneities within the porous medium such as cracks that serve as gas channels. In the simulation study, the temperatures trends at the three positions proceeded identically, which is why only the temperature curve  $T_{\text{center}}$  is depicted in Fig. 5a. Maximum temperatures in the experiment were about 4 K higher than in the simulation. In addition, the temperature in the simulation drops steeply to its initial value after just 2.5 hours, whereas in the experiment it was not possible to measure a complete temperature drop even after 4 hours.

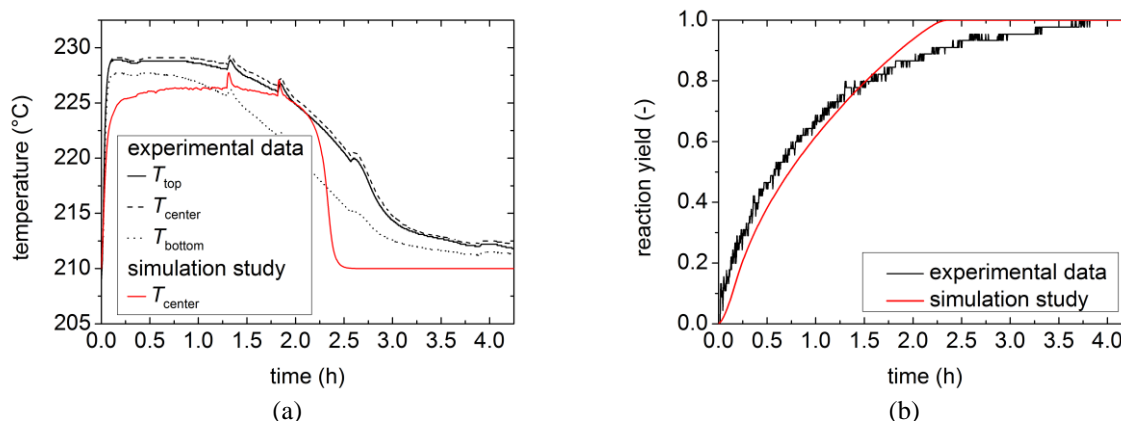


Fig. 5: (a) temperature profile, and (b) reaction conversion during discharge at  $p = 70$  kPa.

In Fig. 5b, the reaction conversion is depicted for both the simulated study as well as the turnover experimentally measured in the evaporator using a fluid level indicator. Up to the time of a turnover of roughly 75 %, the experimental yield is higher than the simulation result. But due to the fact that the progress of the experimental turnover decelerates for high reaction yields, full turnover is achieved significantly faster in the simulation study than in the corresponding experiment.

We assume that the following modifications of the first model can improve the fit between simulation and experiment: Firstly, the mathematical model of the reaction rate overestimates the rate at higher yields. Therefore, the development of an advanced reaction rate model is a subject of our ongoing work. Secondly, the solid bulk is not a homogenous porous medium, therefore slower reaction progress can occur locally, which is not considered in the model. Moreover, in further experimental work, we found that the macroscopic and the microscopic properties of the solid bulk material change considerably due to the chemical reaction: the primary particles agglomerated, which was already observed in the experiments described above, and the overall volume of the porous bulk increased after several dehydration/re-hydration cycles. Consequently, bulk permeability changes, and thus the vapor mass transfer within the bulk is affected. Additionally, the observed structural changes could lead to a reduced bulk thermal conductivity and thus have a negative effect on the thermal performance of a storage reactor. The influence of low bulk thermal conductivities on the reaction turnover curve and, hence, the reactor's overall performance was numerically studied, and it turned out to be a potential bottleneck for high-power applications.

Based on our experimental experience and the results of our simulation studies, we developed a reactor setup which allows for high specific thermal powers, and is easily scalable for industrial applications. Further design considerations include a minimum pressure loss on the vapor side and a reaction chamber design which is robust with respect to changes of the bulk's thermal conductivity. First experimental results of the 1 kW heat transformation demonstrator will be presented at the conference.

## Summary

In a previous study, we identified strontium bromide ( $\text{SrBr}_2$ ) as a suitable candidate for thermochemical heat transformation. Our current work is focused on the investigation of experimental operation conditions that allow for heat transformation in a temperature range of 200 °C to 300 °C at high thermal powers.

In order to quantify how the physical and chemical properties of the reactive material affect the thermal performance of a thermochemical reactor, and to identify possible bottlenecks, we included the relevant physical processes during the chemical reaction into a model based on FEM (finite element method). The validity of the simulation studies was verified by comparison with experimental test data. For this purpose, a reactor geometry and initial and boundary conditions corresponding to those of the experiment were selected for the simulation study.

Based on our experimental experience and the results of our simulation studies, we developed a lab-scale reactor setup which provides high specific thermal powers and is easily scalable to larger applications. In the conference talk, we will present first experimental results from our new test facility that allows for heat transformation with thermal powers of roughly 1 kW per kg of reactive material and output temperatures up to 300 °C, which is far beyond the working range of conventional heat pumps.

## Acknowledgements

We gratefully acknowledge the financial support from the German Federal Ministry for Economic Affairs and Energy (BMW<sub>i</sub>, "Bundesministerium für Wirtschaft und Energie") for the "TheSan" project (03ET1297A).

## References

- [1] Richter, M., Habermann, E.-M., Siebecke, E., Linder, M., "A systematic screening of salt hydrates as materials for a thermochemical heat transformer", *Thermochimica Acta*, 2017, doi:10.1016/j.tca.2017.06.011
- [2] Mauran, S., Lahmidi, H., Goetz, V., "Solar heating and cooling by a thermochemical process. First experiments of a prototype storing 60 kWh by a solid/gas reaction", *Solar Energy*, 2008, doi:10.1016/j.solener.2008.01.002
- [3] Marias, F., Neveu, P., Tanguy, G., Papillon, P., "Thermodynamic analysis and experimental study of solid/gas reactor operating in open mode", *Energy*, 2014, doi:10.1016/j.energy.2014.01.101
- [4] Stengler, J., Ascher, T., Linder, M., "High temperature thermochemical heat transformation based on  $\text{SrBr}_2$ ", 12th IEA Heat Pump Conference 2017, May 14.-18.2017, Rotterdam, Netherlands.
- [5] Perry, D. L., *Handbook of Inorganic Compounds*, Taylor and Francis, 2011.
- [6] Wagman, D. D., Evans, W. H., Parker et al., "The NBS Tables of Chemical Thermodynamic Properties. Selected Values for Inorganic and C1 and C2 Organic Substances in SI Units", *Journal of Physical and Chemical Reference Data*, 1982.
- [7] Michel, B., Neveu, P., Mazet, N., "Comparison of closed and open thermochemical processes, for long-term thermal energy storage applications", *Energy*, 2014, doi:10.1016/j.energy.2014.05.097

# A study on optimizing of pure working fluids in Organic Rankine Cycle (ORC) for different low grade heat recovery

Rong He<sup>1</sup>, Xinling Ma<sup>1,2</sup>, Xinli Wei<sup>1,2\*</sup> and Hui Li<sup>1</sup>

<sup>1</sup> School of Chemical Engineering and Energy, Zhengzhou University, Zhengzhou 450001, Henan, China

<sup>2</sup> Research Centre on the Technology and Equipments for Energy Saving in Thermal Energy System, Ministry of Education, Zhengzhou 450001, Henan, China

\*[herong.0220@foxmail.com](mailto:herong.0220@foxmail.com)

## Abstract

Organic Rankine cycle (ORC) is proved to be reliable technology which is able to efficiently convert low and medium-grade heat sources into useful power [1-3]. But, different working fluids show distinct performances for various low grade heat recovery. This paper conducts research of the optimum working conditions by the 12 different working fluids. Among the group of pure working fluids in this study for different low grade heat recovery, at the temperature of 100 °C, 120 °C, 140 °C, 160 °C, the ORC makes the maximum net power respectively by R-115, R-227ea, R-236fa, R-236ea, R-114, R-245fa and R-601a. The maximum thermal and energetic efficiency are R246ca, R-600, R-236fa, R-114, respectively. The optimum evaporation temperature is about 0.8 to 0.85 times the heat source temperature, and the optimum evaporation temperature is 0.65 times the heat source temperature for the working medium with a critical temperature greater than the heat source.

**Keywords:** organic Rankine cycle, working fluids, performance optimization, net power, thermal/energetic efficiency.

## Introduction

About 50% of the world's energy consumption is wasted as the format of heat due to the limitations of energy conversion processes. Organic Rankine cycle (ORC) is a closed Rankine cycle with low boiling organic fluids instead of water as a circulating medium [4,5]. Due to environmental problems and the consequences of oil crisis, the ORC research has achieved rapid development on all aspects such as alternative organic fluids including zeotropic mixtures, new equipment like cascaded cycle, and innovative applications like the use of ORC in vehicles [6-8]. In the ORC system, the choice of working fluid is a crucial factor. The thermal physical properties of the working fluid exert a great effect for system efficiency, economic feasibility, size of components, system stability, safety and environment problems [9,10]. However, there is no single optimal organic fluid which satisfies all the working conditions.

Saleh et al. [11] studied 31 pure working fluids including dry, isentropic and wet fluids under both simple and recuperated ORC and both subcritical and supercritical configurations. They found that the n-pentane shows the highest thermal efficiency of 13% and the dry fluids always achieve the higher thermal efficiencies in recuperated ORC. He et al. [12] investigated 22 pure working fluids in subcritical region, and point out that the working fluids with the critical temperatures close to the heat source temperature tend to make more net power than those with higher or lower critical temperatures. The optimum critical temperature from Ayachi et al. was 0.7-0.8 times the heat source temperatures, but Andreasen JG et al. thought it was 0.5 times, and Vetter C et al. was about 0.8 times [13-15]. Markus P et al. studied three natural and five synthetic refrigerants within a sub- and supercritical ORC, they found supercritical ORC can make 15% more net power ORC than standard subcritical processes.

There are few studies on the effect of the mass flow on the performance of ORC system in different temperatures. In this paper, 12 pure working fluids (Table 1) are adopted as the refrigerant to study the influence of the change of the mass flow on the net output power, the thermal and energetic efficiency, as well as the heat exchange capacity of the ORC under the waste water with different temperatures. It provides reference for system design, performance optimization and working fluid selection.

**Table 1.** Physical properties of selected pure working fluids

Num.	Ref	Chemical Formula	$P_c$ (Mpa)	$T_c$ (°C)	MW
1	R-227ea	$CF_3CHFCF_3$	2.925	101.75	170.03
2	R-C318	Cyclo- $C_4F_8$	2.778	115.23	200.03
3	R-236fa	$CF_3CH_2CF_3$	3.2	124.92	152.04
4	R-236ea	$CF_3CHFCHF_2$	3.502	139.29	152.04
5	R-114	$CClF_2CClF_2$	3.257	145.68	170.92
6	R-600	$CH_3-2(CH_2)-CH_3$	3.796	151.98	58.12
7	R-245fa	$CF_3CH_2CHF_2$	3.651	154.01	134.05
8	R-245ca	$CHF_2CF_2CH_2F$	3.925	174.42	134.05
9	R-123	$CHCl_2CF_3$	3.662	183.68	152.93
10	R-601a	$(CH_3)_2CHCH_2CH_3$	3.378	187.2	72.15
11	R-601	$CH_3-3(CH_2)-CH_3$	3.37	196.55	72.15
12	R-113	$CCl_2FCClF_2$	3.3922	214.06	187.38

## Methodology

Figure 1 shows a scheme of a standard ORC for waste water applications. The thermodynamic properties of working fluids at any particular point in an ORC were calculated by REFPROP model in Aspen Plus V 9 software.

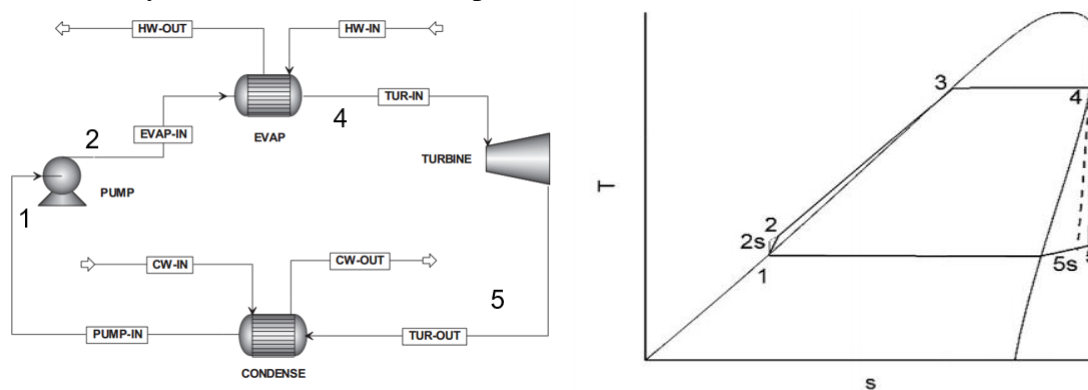


**Figure 1.** A scheme of a standard ORC for heat recovery.

All ORC optimizations are executed following a set of assumptions, specifications and constraints as shown in Table 2. The objective considered function in this work is to maximize the net power output. The variable is the mass flow of the working fluid. With the change of working fluid mass flow, the mass flow of cooling water, condensing pressure and evaporation pressure will change accordingly. Due to the non-linear nature of this optimization problem, we apply the SQP optimization method in ASPEN to solve this problem.

**Table 2.** Assumptions, specifications, and constraints in a conventional ORC model

NO.	Assumptions, specifications, and constraints
1.	The conditions of the heat source are assumed to be at 100°C, 120°C, 140°C, 160°C and 12 bar.
2.	The hot water flow rate is 50,000 kg/h.
3.	The minimum temperature approaches in heat exchangers are specified at 5 K.
4.	Set the vapor fraction of working fluid at the turbine exit to 1.
5.	The cooling water is set 20°C to 30°C.
6.	The isentropic efficiencies of pump and turbine are 85% and 80% respectively.
7.	The heat loss in all heat exchangers and pipelines, pressure drop in the evaporator and condenser are neglected.
8.	There is no chemical loss from the system.
9.	Under subcritical operation.

Thermal efficiency is defined as net power output divided by heat capacity of heater

$$\eta_{th} = \frac{W_T - W_P}{Q_E} = \frac{(h_4 - h_5) - (h_2 - h_1)}{h_4 - h_2} \quad (1)$$

Exergy efficiency is calculated as net power output divided by total exergy flow rate of the fluid [16].

$$\eta_{ex} = \frac{W_{net}}{E_{HS}} = \frac{q_m [(h_4 - h_5) - (h_2 - h_1)]}{E_{Hin} - E_{Hout}} \quad (2)$$

$W_T$  and  $W_P$  are the power of the turbine and the pump, respectively.  $E_{Hin}$ ,  $E_{Hout}$  are the exergy of heat source of evaporator. The  $h_1$ ,  $h_2$ ,  $h_4$ ,  $h_5$  represent enthalpy which corresponded to the points in the figure 1.  $Q_E$  is the heat exchanger capacity of evaporator.

### Results and Discussion.

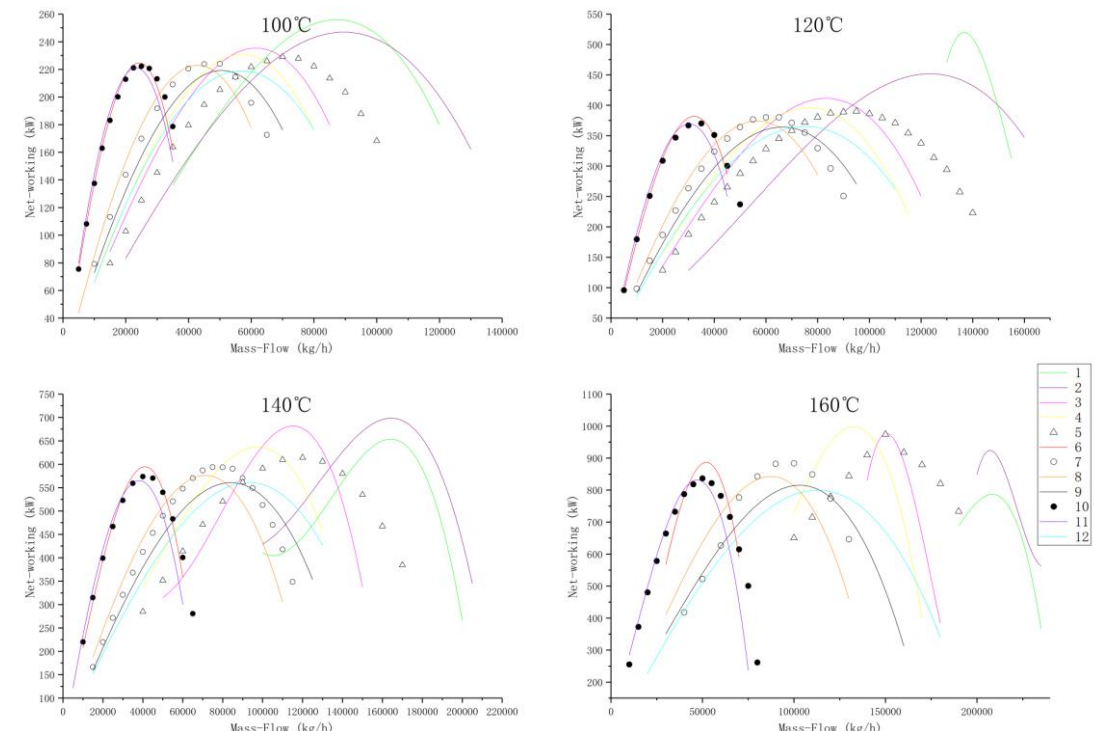


**Figure 2.** The net power variation with flow rate at different temperature.

Figure 2 shows that the variation of the net power with the mass flow changes at different temperature. For all the refrigerants, the net power increases first and decreases with the mass flow rate going up. Two groups can be identified: (1) Group 1 fluids show a perfect cubic equation curve. The  $T_c$  of refrigerant is greater than the heat source temperature, which belongs to the group 1. With the increase of working fluid mass flow, the net power peaks and declines afterwards. (2) Group 2 fluids represent a fault type curve. The  $T_c$  of refrigerant is less than the heat source temperature, which belongs to the group 2. Due to the limitation of the pinch points and the subcritical, with the increase of working fluid mass flow, firstly it increases as the group 1, but when reaching the highest peak, it rapidly declines in fault type, as shown in the blue line in Figure 3.

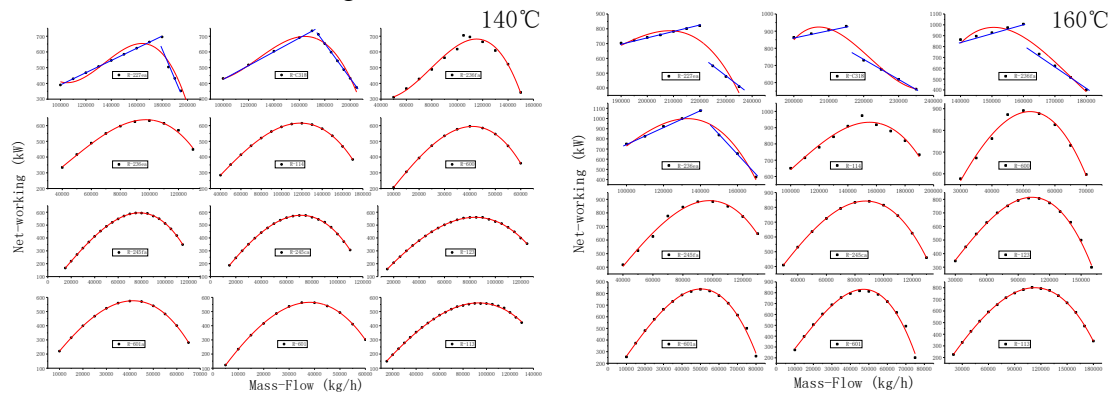


**Figure 3.** The net power variation with flow rate at 140°C to 160°C.

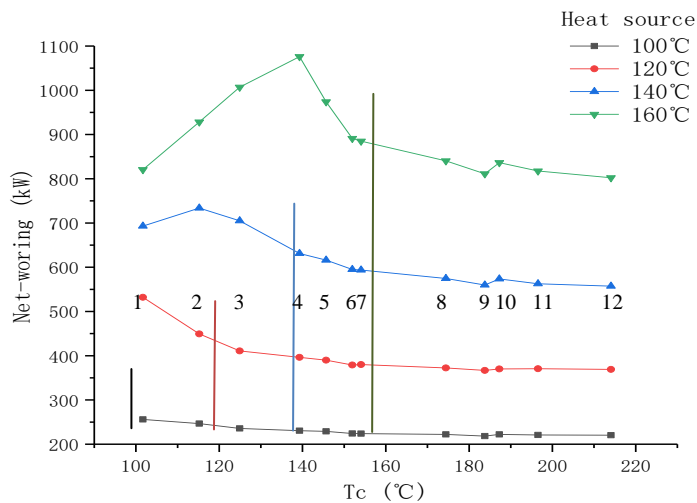


**Figure 4.** The variation of the net power with different working fluids at different temperature.

Figure 4 illustrates the trend of the net power with the critical temperature of the working fluid at different heat source temperature. From figure 3, the refrigerants can be divided into 3 groups: (1) Group 1: The critical temperature of refrigerants is greater than the heat source. With the increase of critical temperature, the net power decreases, but the change is not significant, and the R-601a always does better than the R-123. (2) Group 2: The critical temperature of refrigerants is far less than the heat source temperature. With the increase of critical temperature, the net power increases rapidly until the critical temperature of refrigerants approaches the heat source temperature. (3) Group 3: The critical temperature of refrigerants is close to and less than the heat source temperature. At this section, as the critical temperature of refrigerants goes up, the net power goes down rapidly.

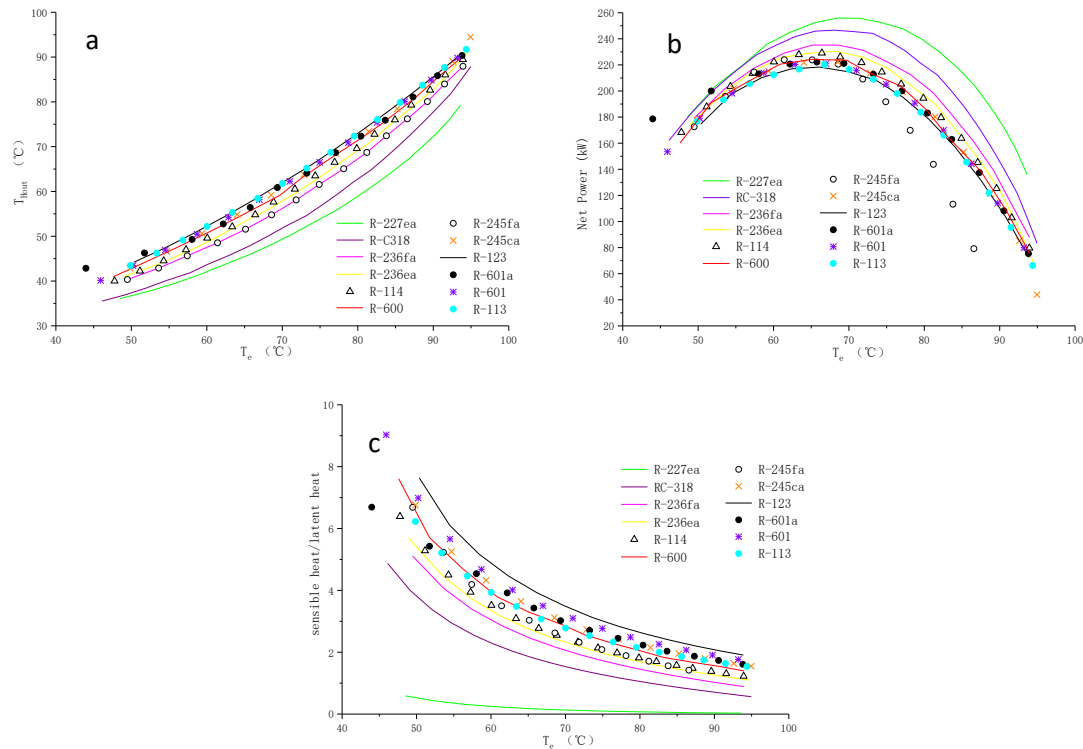


**Figure 5.** The influence of ratio of latent heat and sensible heat for ORC performance at 100°C.

At the same evaporation temperature, the latent heat of evaporation is small and the sensible heat is great, and the circulating flow is large. The heat transfer of working fluids increases because of the increase of circulating flow, and reduce the end temperature of heat source. Therefore, the change regulation of ratio (latent heat/sensible heat) and the end temperature of heat source get out a basic agreement, as shown in the figure 5a. The order of the ratio is: R123>R601>R601a>R245ca>R113≈R600>R114≈R245fa>R236ea>R236fa>RC318>R227ea. The order of net power is: R227ea>RC318>R236fa>R236ea≈R114>R600≈R245ca>R601a>R601>R113≈R123>R245fa. By comparison, the order of net output power is exactly opposite to that of the ratio of latent heat and sensible heat, as shown in the figure 5b.

**Table 3.** Optimization results of ORCs operating with pure working fluids.

HT(°C)	Fluid	W(kW)	$\eta_t$ (%)	$\eta_{ex}$ (%)	$Q_E$ (kW)	$P_E$ (MPa)	$P_C$ (MPa)
100	R-227ea	255.926	7.80	22.09	3281.06	1.44	0.51
120	R-227ea	532.13	10.46	29.62	5087.93	2.86	0.52
140	R-C318	733.73	11.68	33.09	6278.69	2.777	0.349
160	R-236ea	1076.07	14.51	41.09	7415.46	3.41	0.240

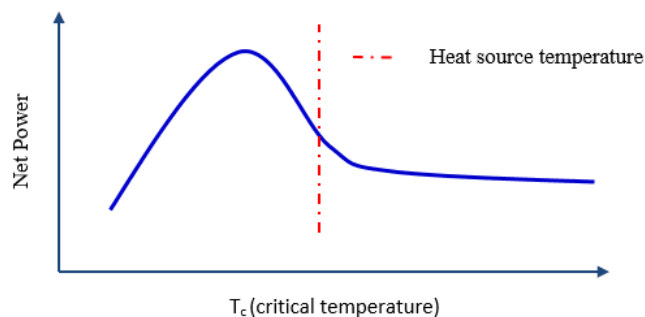


**Figure 6.** The variation trend of net power with critical temperature of working fluids



Table 3 shows the optimization results with the method in this paper. The maximum net power at 100°C, 120 °C, 140 °C, 160 °C is 225.93kW (R-227ea), 532.13 kW (R-227ea), 737.73 kW (R-C318), 1076.07 kW (R-236ea). The maximum thermal and exergy efficiency are always the same fluid, but different from the refrigerants with maximum power. It is R-245ca ( $\eta_t=8.59$   $\eta_{ex}=24.34$ ), R-600( $\eta_t=10.52$   $\eta_{ex}=29.81$ ), R-236fa ( $\eta_t=12.89$   $\eta_{ex}=36.53$ ), R-114 ( $\eta_t=14.72$   $\eta_{ex}=41.71$ ), respectively.

Through the study, we can predict the curves of net power with critical temperature of working fluids, such as the diagram in figure 6. The working fluid which critical temperature is 80%~85% of the heat source temperature always makes the maximum net power. Then we hope to study the thermodynamic properties of the fluid and get the equation between the parameters and the evaporation temperature.

In addition, the optimal evaporation temperature is not very different, when the critical temperature of working fluids are greater than that of the heat source. From table 4, we can get the average evaporation temperature (AET) of maximum net power and the times with the heat source temperature. So the optimum evaporation temperature (working fluids with a critical temperature greater than the heat source) is about 0.65 times the critical temperature. This is not mentioned in the past research.

**Table 4.** The average evaporation temperature (AET) and the optimum evaporation temperature times with critical temperature ( $T_c$  greater than the Heat source)

Ref	100°C	120°C	140°C	160°C
R-227ea	68.547			
R-C318	68.059			
R-236fa	68.589	85.784		
R-236ea	68.353	83.478	92.362	
R-114	66.413	78.898	94.687	
R-600	65.043	76.934	92.889	109.499
R-245fa	67.190	80.642	93.730	110.657
R-245ca	68.522	74.498	89.883	109.438
R-123	66.129	73.629	87.059	102.533
R-601a	65.763	72.949	90.214	101.682
R-601	66.970	77.616	93.630	102.877
R-113	66.744	76.102	89.646	101.253
AET	67.071	78.053	91.567	105.420
AET/HS	67.07%	65.04%	65.41%	65.89%

## Conclusion.

Although the optimizations of ORC using numerous pure fluids have been conducted extensively in the past, the assumptions in previous studies were different from those in this work. We have more variables and different conditions and results in our work. Through our work, we can get the following conclusions.

1. Among the 12 kinds of working fluids we have chosen, the maximum net power at 100°C, 120 °C, 140 °C, 160 °C respectively is 225.93 (R-227ea), 532.13 (R-227ea), 737.73 (R-C318), 1076.07 (R-236ea).
2. The working fluid which critical temperature is 80%~85% of the heat source temperature always makes the maximum net power.
3. The maximum net power first increases and decreases afterwards with the mass-flow increasing. When critical temperature is close and greater than that of the heat source, the curve of maximum net power changed with mass-flow can be perfectly fitted to the cubic equation, the  $R^2$  is greater than 0.99, which is very close to 1. When critical temperature

is much lower than that of the heat source, the maximum net power increases to a peak value as the mass-flow increases under the evaporation of critical temperature, and then sharp decline. It's like two linear equations crossing.

4. When critical temperature of working fluid is greater than that of the heat source, the evaporation temperature of the maximum net power is about 65% of the temperature heat source.
5. The order of net output power is exactly opposite to that of the ratio of latent heat and sensible heat, but the change regulation of ratio and the end temperature of heat source get out a basic agreement.

#### References:

- [1] Preißinger, M., et al. (2013). *Advanced Organic Rankine Cycle for geothermal application*. International Journal of Low-Carbon Technologies 8(suppl 1): i62-i68.
- [2] K. Satanphol, W. Pridasawas, B. Suphanit., *A study on optimal composition of zeotropic working fluid in an Organic Rankine Cycle (ORC) for low grade heat recovery*, Energy, 2017.
- [3] Kiyarash Rahbar, Saad Mahmoud, Raya K., *Review of organic Rankine cycle for small-scale applications*. Energy Conversion and Management, 2017.
- [4] Gu Wei, Weng Yiwu, Wang Yanjie. *Thermal analysis of low-temperature original fluid power generation system*. Acta energiae solaris sinnica, 2008;29(5):608-612.
- [5] Siemens power generation division. *Waste heat recovery with organic Rankine cycle technology*; 2014. [http://www.energy.siemens.com/mx/pool/hq/power-generation/steam-turbines/downloads/brochure-orcorganic-rankine-cycle-technology\\_EN.pdf](http://www.energy.siemens.com/mx/pool/hq/power-generation/steam-turbines/downloads/brochure-orcorganic-rankine-cycle-technology_EN.pdf).
- [6] Bronicki L. *The Ormat Rankine power unit*. In: Proceedings of IECEC, SanDiego, USA.
- [7] Wang XD, Zhao L., *Analysis of zeotropic mixtures used in low-temperature solar Rankine cycles for power generation*. Sol Energy. 2009;83(5):605–13.
- [8] Dolz V, Novella R, García A, Sánchez J. HD., *Diesel engine equipped with a bottoming Rankine cycle as a waste heat recovery system*. Apply Thermal Energy. 2012;36:269–78.
- [9] Stoppato A., *Energetic and economic investigation of the operation management of an Organic Rankine Cycle cogeneration plant*. Energy, 2012;41(1):3–9.
- [10] Bao J, Zhao L. *A review of working fluid and expander selections for organic Rankine cycle*. Renew Sustain Energy Rev, 2013;24:325–42.
- [11] Saleh B, Koglbauer G, Wendland M, Fischer J., *Working fluids for lowtemperature organic Rankine cycles*. Energy, 2007;32(7):1210–21.
- [12] He C, Liu C, Gao H, Xie H, Li Y, Wu S., *The optimal evaporation temperature and working fluids for subcritical organic Rankine cycle*. Energy, 2012;38(1):36-43.
- [13] Ayachi F, Boulawz Ksayer E, Zoughaib A, Neveu P., *ORC optimization for medium grade heat recovery*. Energy, 2014;68:47-56.
- [14] Andreasen JG, Larsen U, Knudsen T, Pierobon L, Haglind F., *Selection and optimization of pure and mixed working fluids for low grade heat utilization using organic Rankine cycles*. Energy, 2014;73:204-13.
- [15] Vetter C, Wiemer H-J, Kuhn D., *Comparison of sub- and supercritical Organic Rankine Cycles for power generation from low-temperature/low-enthalpy geothermal wells, considering specific net power output and efficiency*. Appl Therm Eng, 2013;51(1-2):871-9.
- [16] Preißinger, M. and D. Brüggemann (2017). *Thermoeconomic Evaluation of Modular Organic Rankine Cycles for Waste Heat Recovery over a Broad Range of Heat Source Temperatures and Capacities*. Energies 10(3): 269.

# Numerical analysis of a heat pump based on combined thermodynamic cycles using ASPEN plus software

Mohammed Ridha Jawad Al-Tameemi, Youcai Liang and Zhibin Yu\*

School of Engineering, University of Glasgow, Glasgow, G12 8QQ, Scotland

\*Corresponding author: Zhibin.Yu@glasgow.ac.uk

## Abstract

This paper analyses a gas fuelled heat pump system that integrates an Organic Rankine Cycle (ORC) power generator with an air-sourced heat pump (ASHP). The heat produced by the gas burner is used to drive an ORC power system to produce mechanical power that is then directly used to drive a vapour compression cycle heat pump. The heat rejected by the ORC power system and contained in the flue gases is recovered for heating. Software ASPEN plus is used to model and analyse the proposed heat pump system. Steady state evaluation and the control strategies in response to changes in ambient air temperature have been conducted to analyse the integrated system.

**Keywords:** Heat pump cycle, Organic Rankine cycle, Combined thermodynamic cycles.

## Introduction

In the UK, approximately 50% of its energy consumption is consumed for heating applications, which accounts for nearly one third of the carbon emissions [1]. Gas boilers are the most common appliances for providing domestic hot water and space heating. There are some alternative heating technologies, including heat pumps (HPs), electrical resistive heaters, and micro-CHP (combined heat and power) systems, etc. [2]

Recently, researchers also focused on technologies for heating and/or cooling applications with waste heat recovery, such as gas-powered heat pump cycle (GPHP) which uses a gas fuelled internal combustion engine to drive a conventional vapour compression cycle. The waste heat from the gas engine (exhaust gases and engine cooling jacket) is recovered by the HP cycle to improve the overall system efficiency. An experimental and theoretical study has been carried out by Yang et al [3] to investigate the performance of a GPHP as a water heater. Hu et al. [4] conducted a theoretical and experimental research on a GPHP system for heating applications. In their study, the exhaust gases with ambient fresh air is utilized as a heat source for the HP evaporator, while the rejected heat from the engine cooling jacket is used to superheat the refrigerant of the HP in the suction line. Liu et al. [5] built and tested an experimental prototype to study the stability, and reliability of integrating a gas engine with a HP system for domestic hot water application, Liu et al. [6] also conducted an experimental study on the combined system for providing both hot and cold water.

Collings et al. [2] proposed and studied a gas fuelled water heater that integrates an ORC cycle and HP cycle. Later on, a more detailed investigation by Liang et al. [9] showed that the ambient air temperature has strong effect on the system efficiency.

In this paper, the control strategies have been developed to obtain high thermal efficiency while maintaining the HP's evaporator free of frost. The configuration of the proposed system is shown in Figure 1. It consists of a typical ORC cycle and a vapour compression heat pump cycle, more details can be found elsewhere [2, 9].

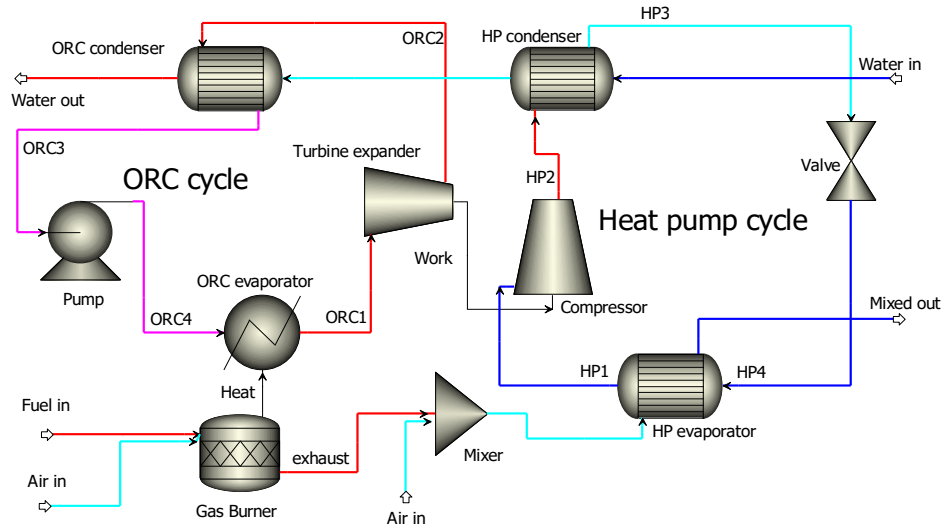


Figure 1 Combined cycle configuration

### Thermodynamic model

The proposed system is simulated and analysed using ASPEN plus software based on REFPROP as a property method. By adapting the same database, an in-house MATLAB code is used to obtain the Temperature – Entropy diagrams for the HP and ORC cycles, as shown in Figures 2(a) and (b), respectively.

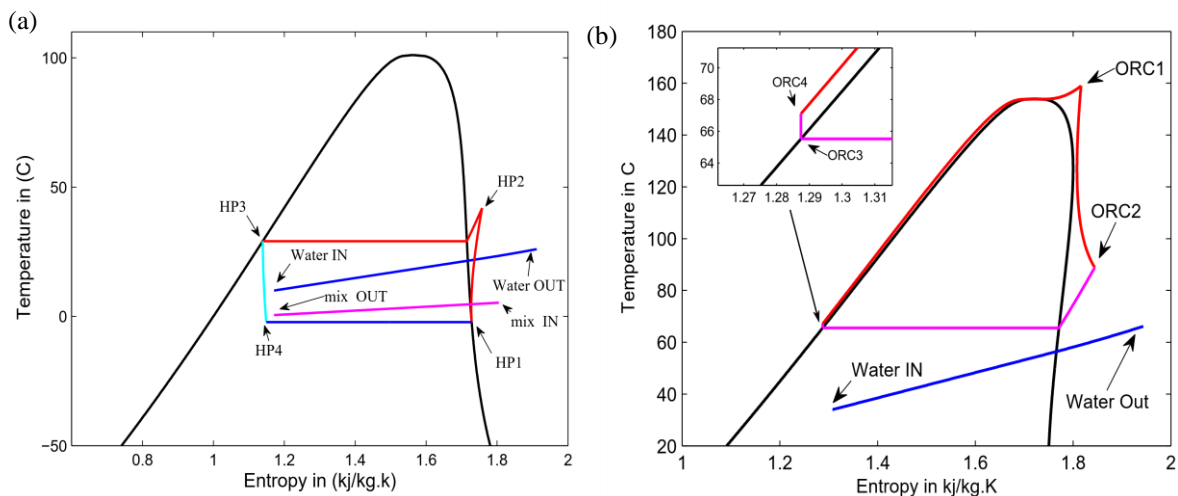


Figure 2 (a) TS diagram for HP cycle (using R134a); (b) TS diagram for ORC cycle (using R245fa).

The operating conditions and assumptions used for modelling are listed below.

- Air has a mixing ratio of 79% nitrogen and 21% oxygen.
- R134a and R245fa are selected as refrigerant for HP and ORC cycles, respectively.
- HP compressor and ORC expander are assumed to have an isentropic efficiency of 70%, while the liquid pump of the ORC system has an efficiency of 90%.
- Power produced by ORC cycle directly drive the HP compressor, and mechanical losses are neglected.

- No heat loss and pressure drop in connecting pipes.
- ORC evaporator temperature is set to a value near the critical temperature of the working fluid to maximize the thermal efficiency.
- Pinch point temperature difference is between 3-5 °C in all heat exchangers.
- The output heating capacity of the system is set as around 20 kW to rise the tap water temperature from 10 to 65 °C.

The energy conservation equation for complete combustion of methane in the burner is:

$$\frac{\dot{Q}_f}{\dot{n}_f} = \sum_P n_e (\bar{h}_f^o - \Delta \bar{h})_e - \sum_R n_i (\bar{h}_f^o - \Delta \bar{h})_i \quad (1)$$

For HP cycle, heat extracted by the evaporator from the mixture of ambient air and the exhaust gases from the burner can be calculated using Equation (2):

$$\dot{m}_A \times C_{PA} \times (T_{A,In} - T_{mix,OUT}) + \dot{m}_{exh} \times C_{P,exh} \times (T_{exh} - T_{mix,OUT}) = \dot{m}_{R134a} \times (h_{HP1} - h_{HP4}) \quad (2)$$

The total heat transferred to water by the HP condenser is calculated as:

$$\dot{m}_w \times C_{Pw} \times (T_{w,OUT,HP} - T_{w,IN,HP}) = \dot{m}_{R134a} \times (h_{HP2} - h_{HP3}) \quad (3)$$

As shown in Figure 2 (b), the ORC evaporator absorbs large proportion of the heat energy produced by the burner to evaporate the working fluid.

$$\dot{Q}_{ORC,ev} = \dot{m}_f \times (h_{exh} - h_{comb}) = \dot{m}_H \times (h_{ORC1} - h_{ORC4}). \quad (4)$$

The net power produced by the ORC is the difference between the expander work output and the pump work. The heat rejected by the power cycle at the condenser is calculated as

$$\dot{Q}_{ORC,co} = \dot{m}_H \times (h_{ORC2} - h_{ORC3}) = \dot{m}_w \times C_{Pw} \times (T_{w,exit} - T_{w,OUT,HP}). \quad (5)$$

The heat pump coefficient of performance (COP<sub>h</sub>) is defined as the ratio of HP condenser heating capacity to HP compressor work. The thermal efficiency of the ORC power generator is defined as ratio of the net power output (i.e., power generated by the expander minus the pump power) over the heat input rate at the evaporator. The overall fuel-to-heat efficiency of the combined system is then defined as

$$\eta_{fuel-to-heat} = \frac{\sum \dot{Q}_w}{\dot{Q}_g} = \frac{\dot{Q}_{HP,co} + \dot{Q}_{ORC,co}}{\dot{Q}_g} \quad (6)$$

The total heat released from the gas burner  $\dot{Q}_g$  is calculated as

$$\dot{Q}_g = \dot{m}_{fuel} \times \dot{Q}_{HV} \times \eta_{com} \quad (7)$$

The heating value of Methane is assumed as 55.5 kJ/kg, with combustion efficiency of 100%.

The required evaporator area

$$Area_{evap} = \frac{Q_{HP-evap}}{U \times F \times \frac{(\Delta T_1 - \Delta T_2)}{\ln \left( \frac{\Delta T_1}{\Delta T_2} \right)}} \quad (8)$$

Assuming a constant average overall heat transfer coefficient  $U = 0.85 \text{ kW/m}^2 \cdot \text{°C}$ , and correction factor  $F=1$ .  $\Delta T_1$  and  $\Delta T_2$  are the temperature difference between the hot and cold streams on the evaporator exit and inlet respectively.

### Steady state simulation results of the optimised model

The steady state simulation results for the proposed system are presented in Table 1. The ambient temperature for this evaluation is assumed to be 7 °C, which is the average temperature for winter months in the UK. The methane mass flow rate can be calculated from the energy conservation equation for Stoichiometric combustion (Eq. (1)) and the result is 0.0002649 kg/s. The results also show that the COP<sub>h</sub> and ORC thermal efficiency are 5.8 and 9.7%, respectively, leading to an overall fuel-to-heat efficiency of around 136%.

Table 1 Heat pump and ORC cycle results

	Heat pump cycle	ORC cycle
Condenser heat duty, kW	8.3	11.7
Water temperature leaving the cycle, °C	32.7	64.9
Evaporator heat duty, kW	6.9	12.9
Condensation temperature, °C	36.3	65.5
Condensation pressure, bar	9.2	5.4
Evaporation temperature, °C	2.5	159
Evaporation pressure, bar	3.2	36.5
Gas mixture temperature exiting the evaporator, °C	5.5	N/A
Power produced by the expander of ORC, kW	N/A	1.438
Power input to the compressor of HP, kW	1.438	N/A
The work of liquid pump, kW	N/A	0.175

### The Gas burner

Methane combusts with oxygen contained in air inside the gas burner to produce the required thermal energy to vaporise the R245fa in the ORC evaporator. To identify the optimum air to fuel ratio to maximise the heat production in the burner, air mass flow rate is increased gradually when the methane mass flow rate is kept constant. Figure 3(a) represents the mass fraction of O<sub>2</sub> and CH<sub>4</sub> in exhaust gases when methane combusts at flow rate of 0.00026406 kg/s and the ambient temperature is 15 °C. With initial rise in air mass flow rate, mass fraction of CH<sub>4</sub> decreases while that of O<sub>2</sub> maintains zero. When air mass flow rate is 0.005 kg/s or higher, O<sub>2</sub> starts to appear in the flue gases with a residual of CH<sub>4</sub>, indicating incomplete combustion. After that, CH<sub>4</sub> mass fraction drops to zero when the air mass flow rate of air is above 0.00503 kg/s, showing an optimal combustion. At this point, the burner heating production reaches the maximum value of 12.9 kW and the air to fuel ratio is approximately 19, indicating that it is a lean combustion (see Figure 3(b)).

### Control strategies when the ambient air temperature varies

The ambient air temperature varies considerably throughout the day as well as over the year. In the UK, the average temperature of the ambient air is between 5 to 15 °C. However, sub-zero temperatures can occur in the winter months. To investigate the effect of ambient temperature variation on the performance of the combined system, two different temperature

ranges were identified. Accordingly, the control strategies in response to the ambient temperatures were studied.

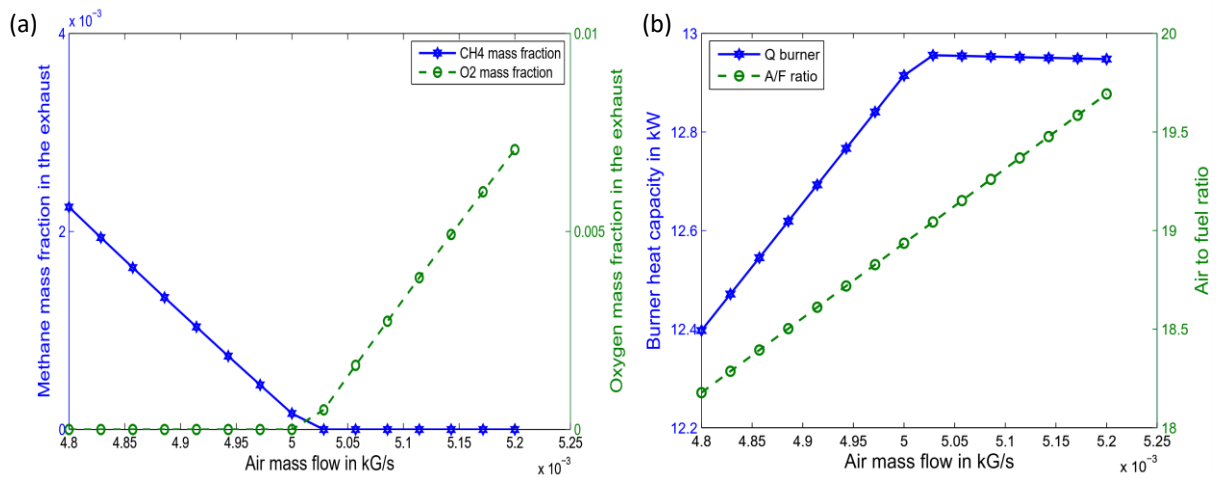


Fig. 3 The optimization of the air mass flow inside the burner.

### Ambient air temperature in the range of 6-15 °C

Generally, with the drop in the ambient air temperature, the extractable thermal energy decreases. However, for the temperature range of 6-15 °C, an increase in the air mass flow rate is the only adjustment required to compensate such a decrease of heat extraction. The increment in the air mass flow rate ensures the required heat supply to the evaporator of HP, which maintains the designed heating capacity and performance as shown in Table 1. For this temperature range, the gas burner exhaust gas temperature is assumed to be 60 °C.

Figure 4(a) shows that the air mass flow rate and the evaporator heat transfer area increase gradually when the ambient temperature decreases from 15 to 7 °C. However, when the temperature further drops to below 7 °C, the mass flow rate of air increases dramatically to 11  $\text{kg/s}$ . In addition, the evaporator area also increases in the same manner, reaching a maximum value of approximately 2.5  $\text{m}^2$ .

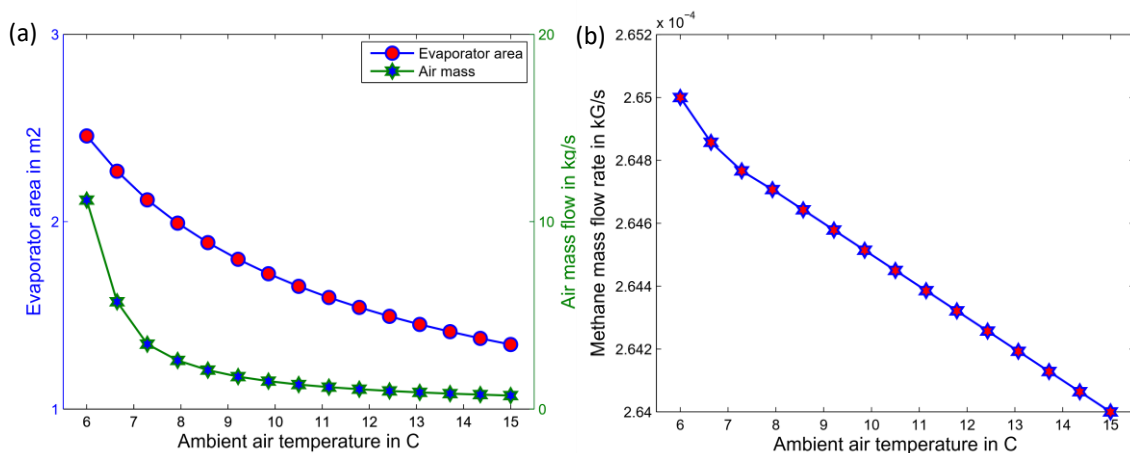


Figure 4 Effects of ambient temperature on evaporator design parameters.

This is due to that the temperature difference ( $\Delta T$ ) across the evaporator, from the hot side, decreases dramatically when the ambient air temperature approaches the assumed evaporator

outlet temperature of 5.5 °C. Hence, the maximum evaporator area of 2.5 m<sup>2</sup> will be required. As the ambient air is also used in the combustion process, the heat of combustion is expected to decrease when the ambient temperature drops. Thus, methane mass flow rate increases slightly to compensate the reduction in the heat production in the burner as shown in Fig. 4 (b).

Figure 5(a) shows that the evaporator thermal duty of the heat pump drops gradually from 7.29 to 6.8 kW when the ambient air mass flow rate increases from 0.7 to 11 kg/s. Such a decrease in the evaporator capacity is acceptable as this procedure aims to maintain the minimum pinch point temperature difference between the hot and cold streams across the evaporator. The reduction in the evaporator capacity led to similar reduction in the HP condenser heating duty. This is due to the constant compressor power consumption of 1.438 kW. In addition, the superheating degree of the working fluid at the exit of the evaporator of the heat pump decreases gradually as shown in Figure 5(b).

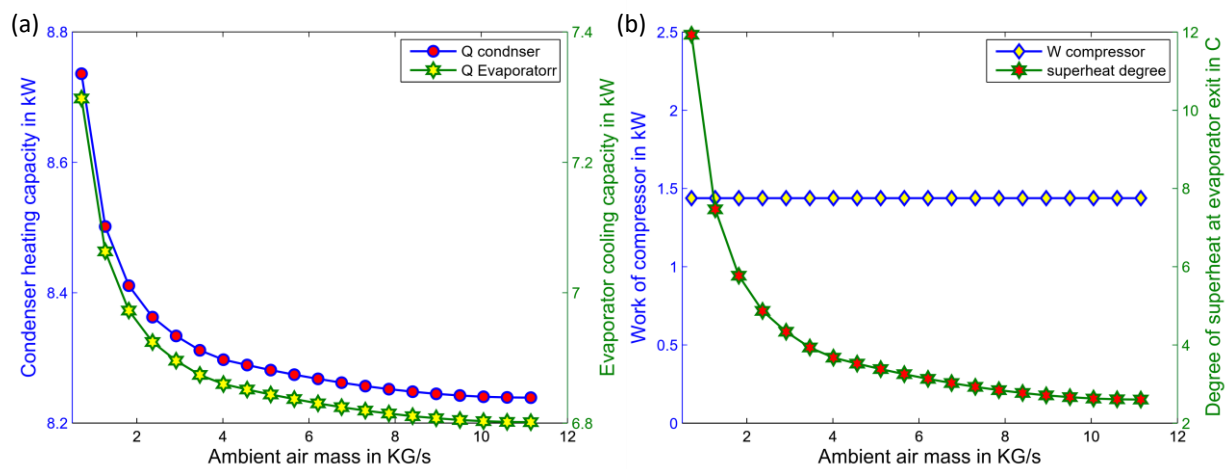


Figure 5 Effects of increasing ambient air mass flow when its temperature drops between (7-15 °C) on the evaporator and condenser thermal duties.

Figure 6 shows that the proposed increment in air mass flow rate have maintained a constant pinch point temperature difference of 3 °C between the heat source stream (a mixture of ambient air and the burner's flue gases) and the refrigerant R134a flow through the evaporator of the HP. In addition, the exit temperature of the mixture is maintained at around 5.5 °C to avoid frost formation on the evaporator [10]. As the compressor power is fixed, the heat pump COP decreases as the heating capacity of the condenser decreases. In addition, as the thermal capacities of both heat exchangers of the heat pump drops, less power is required from the compressor than supplied. This surplus power will lead to a slight increase in the discharged pressure.

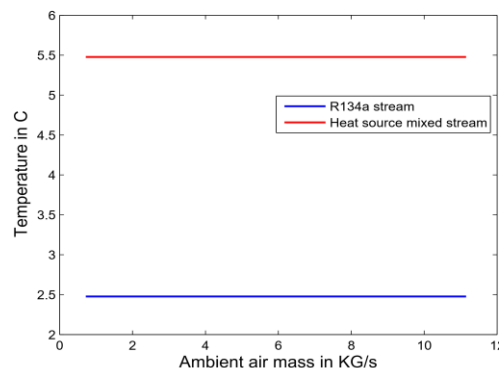


Figure 6. Temperature difference between hot and cold streams across the HP evaporator.



Figure 7(a) shows that, as the ambient air temperature drops, the condenser pressure steadily increases from 8.8 to 9.2 bar while the  $COP_h$  decreases from 6 to 5.7. The decrease of the  $COP_h$  is due to the decrease in the thermal duties of the heat pump heat exchangers when compressor power consumption is kept constant. The fuel-to-heat efficiency decreases from 139.3% to 135.5 % due to the increase in the methane mass flow rate as shown in Figure 4(b). Similarly, the outlet water temperature drops slightly, reaching a minimum value of 64.7 °C when the ambient air temperature is at 6 °C, as shown in Figure 7 (b).

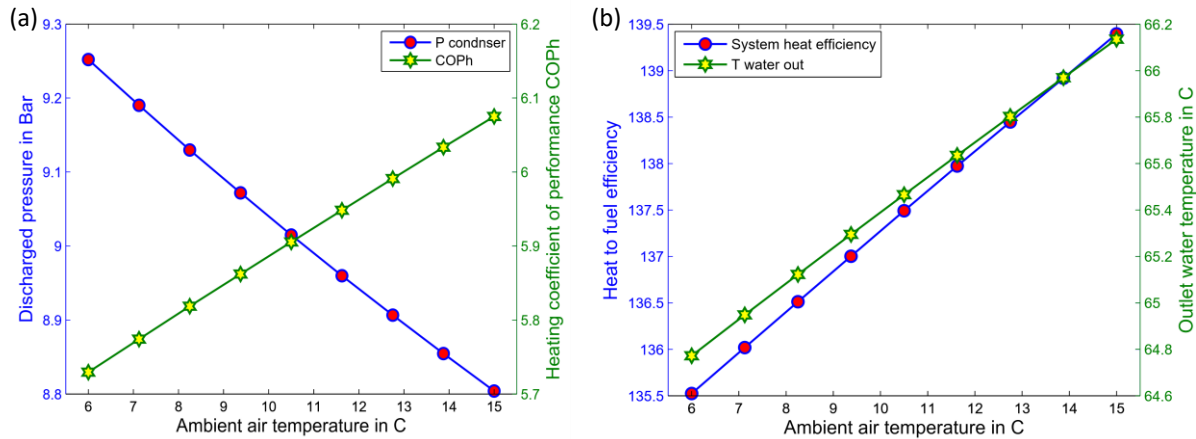


Figure 7 Effects of decreasing ambient air temperature on system design parameters.

### Ambient air temperature below 6 °C

For ambient temperature below 6 °C, another control procedure is adopted, which only utilizes the thermal energy available in the burner's flue gases as heat source for the HP evaporator. Thus, the ambient air stream for the HP evaporator is suspended. However, the ambient air is still used within the burner for combustion process. Further increase in the fuel mass flow rate is then required to supply the evaporator with the required thermal energy. As a result, lower fuel-to-heat efficiency (i.e., slightly below 100%) is expected.

Figure 8 shows the changes in the fuel mass flow rate and the temperature of the flue gas when the ambient air temperature decreases from 6 to -5 °C. The mass flow rate of fuel increases significantly to produce the required heat when the ambient temperature drops from 6 to 5 °C. Thereafter, the fuel mass flow rate is maintained around 0.000355 kg/s.

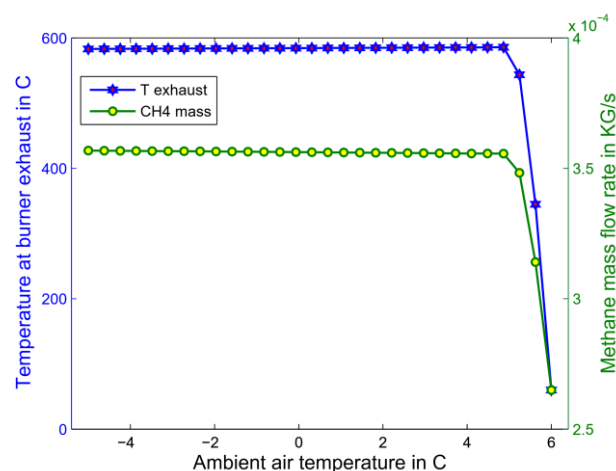


Figure 8 Changes in system design parameters due to air temperature gradient for the temperature below 6 °C.

Similarly, the temperature of the flue gases sharply increased from 60 to 585 °C in order to supply the required thermal energy to the evaporator. There is also a slight decrease in the temperature of the flue gases from 585 to 583 °C, due to the decrease in the air temperature entering the gas burner since the heat production at the burner is fixed at 12.9 kW. As a result, the fuel-to-heat efficiency drops accordingly. However, this approach has the advantage of preventing frost formation in the evaporator of the heat pump at low ambient temperatures.

## Conclusion

This paper presents the control strategies needed to operate the integrated system when the ambient temperature changes. The results show that when ambient air temperature ranges from 6 to 15 °C, the air mass flow rate entering the mixer is the only parameter that needs to be adjusted. Within this range, the system has achieved significantly higher fuel-to-heat efficiency in the range 135.5 % to 139.4%. When ambient air temperature further drops, the ambient air stream in the mixer is suspended and the burner exhaust stream is the only heat source for the HP evaporator. Therefore, the system's thermal efficiency drops accordingly. In addition, the evaporator of the heat pump can be kept frost-free by maintaining the temperature at the evaporator exit at 5.5 °C throughout the entire temperature range under investigation.

## Acknowledgment:

This research is funded by EPSRC (EP/N020472/1, EP/N005228/1, and EP/R003122/1) in the United Kingdom. The author Mohammed Ridha Jawad Al-Tameemi acknowledges the support of his sponsor (University of Diyala / Iraqi Ministry of Higher Education and Scientific Research sponsorship no. 1214).

## References:

- [1] UK Government. The UK Low Carbon Transition Plan.
- [2] Collings, P., Al-Tameemi M., Yu Z., A Combined Organic Rankine Cycle-Heat Pump System for Domestic Hot Water Applications, 12th International Conference on Heat Transfer, Fluid Mechanics and Thermodynamics, Malaga, Spain, 11 - 13 Jul 2016.
- [3] Yang, Z., *et al*, Thermal modeling and operating tests for a gas-engine driven heat pump working as a water heater in winter. *Energy and Buildings* 58 (2013) 219–226.
- [4] Hu, B., *et al*, Thermal modeling and experimental research of a gas engine-driven heat pump in variable condition. *Applied Thermal Engineering* 123 (2017) 1504–1513.
- [5] Liu, F., *et al*, Experimental study on the performance of a gas engine heat pump for heating and domestic hot water. *Energy and Buildings* 152 (2017) 273–278.
- [6] Liu, F., *et al*, Experimental investigation of a gas engine-driven heat pump system for cooling and heating operation. *International Journal of Refrigeration* 86 (2018) 196–202.
- [7] Jiang, W., *et al*, Simulation and validation of a hybrid-power gas engine heat pump. *International journal of refrigeration* 50 (2015) 114-126.
- [8] Wan, X., *et al*, Power management strategy for a parallel hybrid-power gas engine heat pump system. *Applied Thermal Engineering* 110 (2017) 234–243.
- [9] Liang, Y., Al-Tameemi M., Yu Z., Investigation of a gas-fuelled water heater based on combined power and heat pump cycles. *Applied Energy* 212 (2018) 1476–1488.
- [10] Vocale, P., *et al*, Influence of outdoor air conditions on the air source heat pumps performance. 68th Conference of the Italian Thermal Machines Engineering Association, ATI201. *Energy Procedia* 45 (2014) 653 – 662.

# Latent heat storage for direct integration in the refrigerant cycle of an air conditioning system

T. Korth<sup>1\*</sup>, F. Loistl<sup>1</sup>, A. Storch<sup>1</sup>, R. Schex<sup>2</sup>, A. Krönauer<sup>2</sup> and C. Schweigler<sup>1</sup>

<sup>1</sup>Munich University of Applied Sciences, Lothstraße 34, 80335 Munich, Germany

<sup>2</sup>Bavarian Center for Applied Energy Research, Walther-Meißner-Straße 6, 85748 Garching, Germany

\*timo.korth@hm.edu

## Abstract

With increasing use of renewable energy sources storage systems are required for an efficient and consistent use of these energies. The main objective is to provide a time shift, allowing for uncoupling of energy production and consumption. Besides battery storages linked to electrical heat pumps, thermal storages have huge potential to provide energy for heating and cooling purposes. In combination with air/air-based air-conditioning systems in particular latent heat storages (LHS) possess several advantages. In this paper theoretical and experimental investigations on latent heat storages using paraffin as the phase change material with direct heat exchange with an evaporating or condensing refrigerant flow are presented. The focus is laid on the use of the LHS operated as a cold storage serving as a “subcooler” for the refrigerant flow leaving the condenser of a vapour compression cycle. The results of the calculation model underline the feasibility and predict an increase of the cycle’s refrigeration capacity by about 29% during unloading of the LHS, resulting from a sub-cooling of the refrigerant by about 25 K. To prove the concept and to characterize the thermal behavior of the LHS during loading and unloading laboratory experiments are carried out. With the experimental results the theoretical predictions shall be verified, allowing for an improvement of the calculation models.

**Keywords:** Latent heat storage, Phase change material, Air-Conditioning, VRF-System

## Nomenclature

$A$	Area (m <sup>2</sup> )	$\alpha$	Heat transfer coefficient (W/(m <sup>2</sup> K))
$d$	Diameter (m)	$\lambda$	Thermal conductivity (W/(m K))
$h$	Specific enthalpy (kJ/kg)		
$\Delta h$	Enthalpy of the phase change (kJ/kg)	Indices	
$L$	Length (m)	$C$	Condensation
$m$	Mass (kg)	$E$	Evaporation
$\dot{m}$	Mass flow (kg/s)	$i$	Inside
$Q$	Energy (J)	max	Maximum
$\dot{Q}$	Thermal power (W)	$o$	Outside
$R$	Thermal resistance (K/W)	$PCM$	Phase Change Material
SOC	State of charge (-)	$ref$	Refrigerant
$t$	Time (s)	$St$	Storage
$T$	Temperature (°C)		

## Introduction

The increased use of renewable energy sources leads to a growing demand for storage systems facilitating an efficient and consistent use of these energies. In the field of heating and cooling applications huge potential is seen in latent heat storages (LHS). The new approach which is presented in this paper comprises loading and unloading of the LHS by means of direct heat exchange with the refrigerant. The concept shall be applied for a Variable-Refrigerant-Flow heating and cooling system (VRF-System) which is driven by the electricity output of a PV generator. In VRF systems which directly act on the supply air flow

no secondary heat carrier is available for integration of a heat or cold storage. Thus, a thermal storage in direct contact to the refrigerant cycle offers a straightforward solution with minimal technical complexity. In addition, the LHS meets the characteristic of the air-conditioning system as it can serve as heat source or heat sink at an almost constant temperature level. This is seen as the stand out characteristic of the LHS that results from the utilization of the phase change of the material selected.

Phase change materials (PCM) with melting temperatures in a wide temperature range are available. Thus a good match with regard to the targeted application can be found. In addition to that PCMs have a high energy density. As a consequence a very compact design is possible [1], [2]. Several studies deal with investigations on LHS using water as heat transfer medium applying different types of heat exchangers [3], [4], [5]. Furthermore measures are taken in order to increase the heat conductivity of the pure PCM representing the decisive limitation of the performance of the LHS during loading and unloading. To meet this challenge, several approaches are taken into account that can be realized with different storage designs. Mehling et al. [1] and Hauer et al. [2] give an overview of different design concepts. For example, the application of nanostructures, encapsulation of the PCM and the development of a direct contact storage are described. A known approach is the implementation of graphite in form of graphite structures or graphite powder which leads to a PCM-graphite composite. By changing the mixture ratio the storage properties can be adjusted to the specific application [6], [7], [8], [9]. In addition, embedded aluminum structures also provide an increase of the heat conduction across the storage volume [10]. This concept can be implemented by means of conventional finned heat exchanger, commonly used as air-cooled condensers or coolers [11], [12].

To study the storage interacting with a refrigerant cycle under real conditions a pilot plant in form of a VRF-System will be built. As preparation, laboratory experiments shall bring profound knowledge about the thermal performance and dynamic behavior of the thermal storage. Apart from other options, in the current development the heat storage serves as subcooler for the condensed refrigerant leaving the condenser of the refrigerant cycle. Aiming at efficient operation of the heat storage, heat conduction across the phase change material in the storage is increased by addition of graphite powder. Especially, the temporal development of the thermal duty and the underlying heat transfer mechanism in dependence on the propagating solidification of the phase change material are investigated.

## **Methodology**

### The subcooler concept

A latent heat storage is integrated in the refrigerant cycle between condenser and evaporator. By heat extraction from the refrigerant, the enthalpy of the liquid entering the expansion valve is reduced. Thus, the vapor content of the two phase mixture entering the evaporator is reduced, resulting in an increase of refrigeration capacity at unchanged refrigerant flow. Consequently, refrigeration capacity is boosted during constant operation of the compressor. The integration of the latent heat storage acting as subcooler in the refrigerant cycle is shown in Figure 1 (left) together with the resulting enhancement of the evaporator capacity which can be read from the  $\log(p)h$ -diagram for the refrigerant R410a (right). In loading mode the storage is connected in parallel to the evaporator and the cycle (Figure 1, solid line) operates with regular subcooling of the refrigerant at the condenser outlet (state points 1 to 6). During this loading phase the refrigerant evaporates in the LHS and heat is extracted from the storage. It is to be noted that the internal operation parameters of the system do not have to be changed when the storage is activated. In particular, the pressure level of evaporation remains constant during loading of the storage. The dotted line marks the unloading process with

subcooling of the liquid refrigerant by heat transfer to the LHS at the condenser outlet (state point 1' to 6').

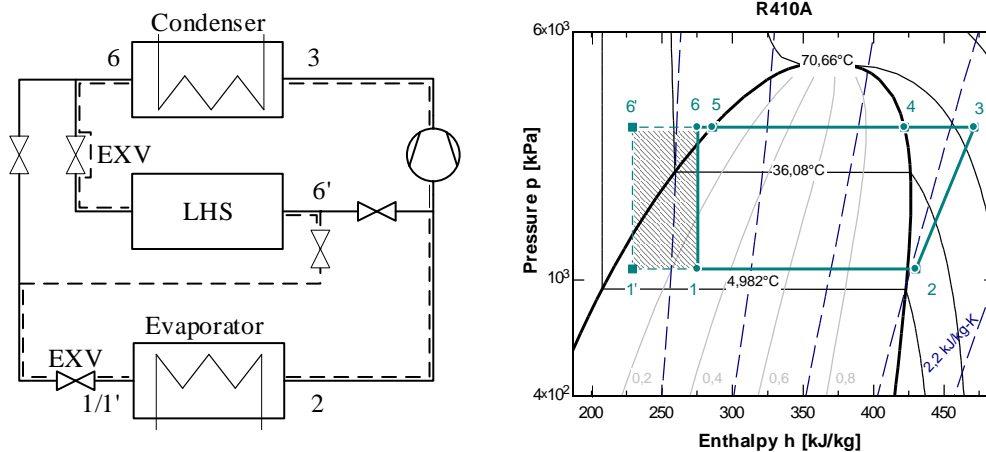


Figure 1: Integration of the latent heat storage in the refrigerant cycle (left) and enhancement of refrigeration capacity during unloading of the storage log(p)-h-diagram (right).

To quantify the effect of subcooling the refrigerant Figure 2 shows the relative increase of the cooling capacity  $\dot{Q}_0$  as the ratio of  $\dot{Q}_{0,subcooling} / \dot{Q}_{0,nominal}$  in dependence on the degree of subcooling  $\Delta T_{subcooling}$  with respect to different condensing temperatures ( $T_C$ ) that are varying from 30 °C to 50 °C. For example with  $\Delta T_{subcooling} = 25$  °C at  $T_C = 45$  °C a capacity gain of 29 % compared to nominal cooling capacity can be reached. For  $T_C = 50$  °C and extreme subcooling the cycle modeling even predicts a capacity gain up to 40 %.

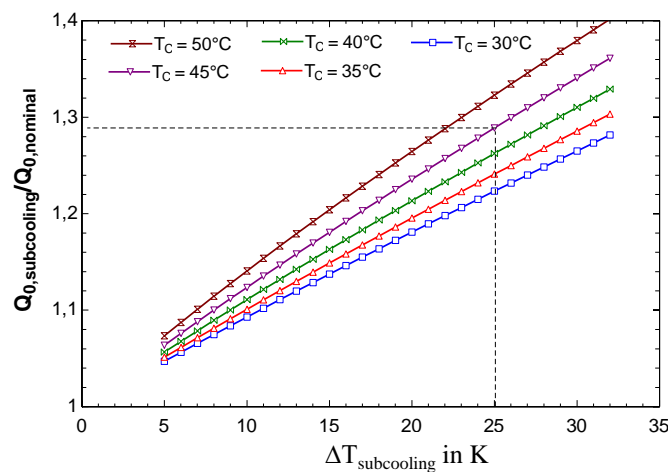


Figure 2: Enhancement of cooling capacity during unloading of the storage, calculated data.

### Thermal model of the latent heat storage

For the description of the dynamic behavior of the storage a simplified one-dimensional model introduced by Loistl (2016) is used [11]. The calculation model incorporates both; growth of the crystallized zone within the PCM volume coupled with direct evaporation of refrigerant inside the heat exchanger tubes passing through the storage.

The heat transfer model for the storage has been implemented, using the Engineering Equation Solver (EES) Software. For the crystallization of the PCM material an ideal radial propagation of the phase front is assumed, starting from the refrigerant tubes passing through the volume of the LHS. As result a time dependent heat resistance  $R_{PCM}(t)$  for thermal conduction across the storage material is obtained.

Finally, the time-dependent overall thermal resistance  $R_{total,St}(t)$  for the heat transfer between the LHS and the refrigerant inside the tubes is calculated by equation 1, taking into account the evaporation of the refrigerant in the tube ( $R_{ref}$ ), and thermal conduction across the tube wall ( $R_{tube}$ ) and in the PCM ( $R_{PCM}(t)$ ). By equation 2, a relation between the time-dependent diameter of crystallized cylindrical PCM zone  $d_{PCM}(t)$  and the current state of charge is given. When the storage volume is completely liquid (SOC=0), the phase front coincides with the outer surface of the tube ( $d_{PCM}(t)=d_{tube,o}$ ); when the storage is fully solidified (SOC=1) the maximum diameter of the crystallized PCM volume is attained ( $d_{PCM}(t)=d_{PCM,max}$ ).

$$R_{total,St}(t) = R_{ref} + R_{tube} + R_{PCM}(t) = \frac{1}{\alpha_{ref} \cdot A_{tube,i}} + \frac{\ln \frac{d_{tube,o}}{d_{tube,i}}}{\pi \cdot L_{tube} \cdot 2 \cdot \lambda_{tube}} + \frac{\ln \frac{d_{PCM}(t)}{d_{tube,o}}}{\pi \cdot L \cdot 2 \cdot \lambda_{PCM,eff}} \quad (1)$$

$$d_{PCM}(t) = ((d_{PCM,max}^2 - d_{tube,o}^2) \cdot SOC(t) + d_{tube,o}^2)^{0,5} \quad (2)$$

Results of the theoretical simulation are presented and discussed in context of the experimental results below. For this purpose, the heat transfer characteristic of the storage will be described by an overall UA-value together with the driving temperature difference between the phase change and the evaporation of the refrigerant.

## Experimental investigations

### Design of the test cycle and the latent heat storage

To verify the theoretical results concerning the capacity gain of the subcooling effect and the dynamic behavior of the LHS a laboratory test rig is used which has been designed to investigate different modes of operation of latent heat storages in a refrigerant cycle with R410a as working fluid. A detailed description of the laboratory test rig is given by Loistl (2016) [11]. For temperature measurements Pt100 resistance thermometers (1/10 DIN, class B) are used, pressure gauges with accuracy class <0,1% are applied. A coriolis mass flow meter measures the refrigerant flow through the storage. All measurement data are gathered digitally and saved for detailed analysis [11].

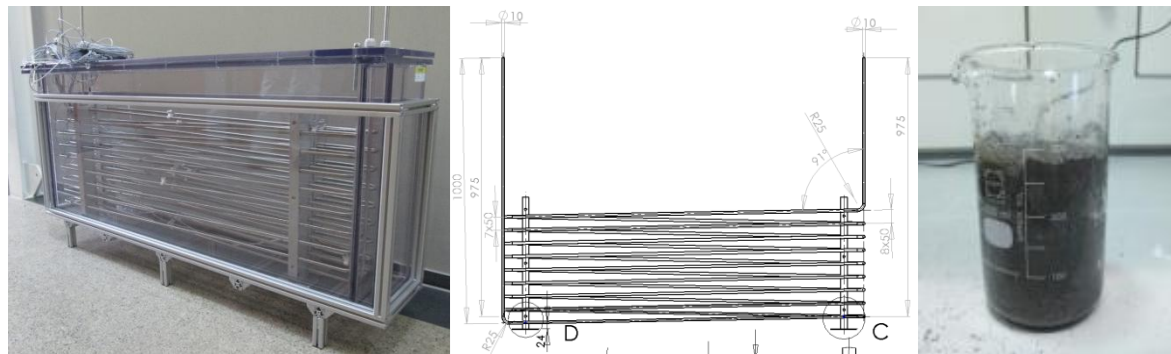


Figure 3: Latent heat storage before filling (left), profile of the serpentine tube duct (middle) and preparation of the paraffin/graphite composite material (right).

The storage itself consists of a two-pass serpentine tube heat exchanger which is inserted in a paraffin-filled cubic tank with transparent walls and a stable framework. The two stainless steel serpentine tubes have a total length of 24 m each with a tube diameter of 0,010 m and a tube spacing of 0,05 m. Following the concept that the integration of the storage should not influence the evaporation and condensing pressure of the system a phase change temperature of 18°C is chosen. Thus, in loading mode the system can be run with the nominal evaporation level which varies between 7°C and 11°C in typical commercial multi-split air conditioning

systems, so called VRF or VRV systems. The chosen paraffin is Parafol 16-97 (Sasol) with a melting temperature of 18°C and a latent heat of 220 kJ/kg. According to the active PCM volume, the storage has a thermal capacity of about 6 kWh. The heat conductivity of the pure material is 0,2 W/(m · K). To reduce the thermal resistance of the PCM graphite powder with a mass ratio of 1:5 has been added. The storage is equipped with 6 temperature sensors in the paraffin and 10 sensors in direct contact to the tubes along the heat exchanger.

#### Experimental investigation: Gain of refrigerant capacity during unloading of the LHS in subcooler mode

The thermodynamic calculation predicts a significant influence of the degree of subcooling on the cooling capacity (Figure 2). Experiments have been carried out in order to verify, whether the designed LHS provides the expected boost of the evaporator capacity in a real system. Figure 4 (left) shows the thermal capacities of the condenser  $\dot{Q}_C$ , the LHS  $\dot{Q}_{St}$  acting as subcooler, and the evaporator  $\dot{Q}_E$ . The storage inlet temperature  $T_{St,in}$  which is equal to the condensing temperature, the storage outlet temperature  $T_{St,out}$  and the evaporation temperature  $T_E$  in dependence on time can be read from Figure 4 (right). Furthermore, the refrigerant mass flow is depicted in Figure 4 (right) referring to the secondary ordinate. It can be seen that the evaporator capacity immediately increases by about 1,2 kW when the storage is activated. This increase of capacity results from the uptake of heat by the LHS which equally amounts to about 1,2 kW at the beginning of the storage cycle. During the course of the experiment the storage capacity yields a decreasing trend with a thermal duty slightly below 1 kW after 5 hours of operation. After 5 ½ to 6 hours the phase change of the entire storage volume is accomplished, thus further cooling of the refrigerant originates from sensible heating of the storage with reduced thermal duty in comparison to the latent heat effect. The capacity gain experienced after activation of the LHS clearly results from the subcooling of the condensed refrigerant approaching the expansion valve of the refrigeration cycle. At the beginning of the test a temperature change of about 19 K is accomplished, resulting in a refrigerant temperature  $T_{St,out}$  of 16 °C at the inlet port of the expansion valve. During the preceding loading phase the LHS had been solidified and cooled by evaporation at about 10 °C. Thus, for a short period of about half an hour the refrigerant is cooled even below the phase change temperature of 18 °C, while the storage takes up sensible heat and approaches the melting point. Over the course of the experiment the subcooling of the refrigerant gradually reduces, reaching a value of about 10 K after 5 ½ hours.

When analyzing the quantitative impact of the subcooling, the interaction of all cycle components has to be taken into account: Assuming a constant pressure level for the evaporation of the refrigerant and constant operation of the compressor, an increase of the evaporator capacity is to be expected upon activation of the subcooler, due to the lower inlet enthalpy of the refrigerant entering the evaporator. This effect is reflected by the theoretical prediction in the section above. Operation of a real system deviates from this scenario due to the following aspects. With constant chilled water inlet temperature at the evaporator and constant UA-value for the heat transfer to the refrigerant, an increase of the evaporator capacity is accompanied by a reduction of the evaporation pressure level. Figure 4 (right) clarifies this aspect as the evaporation temperature  $T_E$  descends from 3,5 °C to 2 °C when the LHS is activated. Consequently, due to the reduced refrigerant density at lower pressure the refrigerant mass flow delivered by the compressor at constant speed is reduced which is confirmed by the recorded data of the refrigerant mass flow plotted in Figure 4 (right) that follows the increasing trend of the evaporation pressure. This finding associates with a decrease of the condenser capacity, as can be found in Figure 4 (left). Thus, finally a reduced refrigerant mass flow is returned to the evaporator, providing a negative feedback to the expected increase of the evaporator capacity.

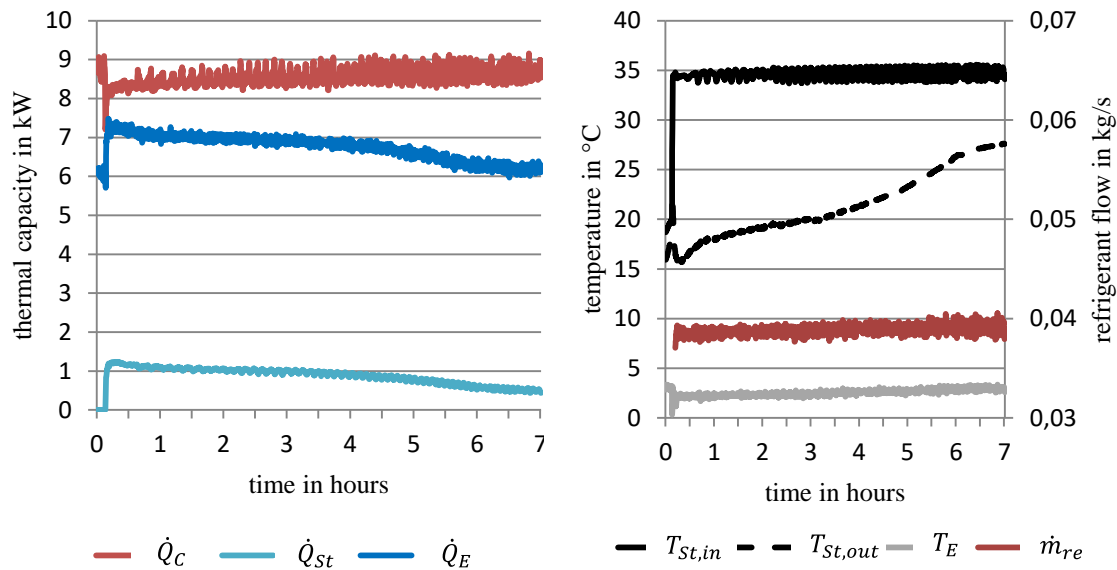


Figure 4: Thermal capacities of condenser, storage and evaporator referring to the duration of the experiment (left) and temperature inlet and outlet of the heat exchanger together with the evaporation temperature (right, primary ordinate) and the refrigerant mass flow (right, secondary ordinate).

Taken as a whole, the increase of evaporator capacity induced by application of the LHS is partly compensated by the decrease of the refrigerant mass flow. Simultaneously, a decrease of the power consumption of the compressor is accomplished, operating with constant volume flow and reduced pressure rise. The positive effect of the LHS could be fully exploited by readjusting the refrigerant mass flow at the expense of a slightly increased compressor power. Results of the experiments showing the effect of refrigerant subcooling by the LHS during operation with condensing temperatures of  $T_C = 35^\circ\text{C}$  and  $37^\circ\text{C}$  are visualized in Figure 5. It shows the increase of the cooling capacity  $\dot{Q}_0$  given by the ratio  $\dot{Q}_{0,subcooling} / \dot{Q}_{0,nominal}$  in dependence on the degree of subcooling  $\Delta T_{subcooling}$ . A capacity increase between 8 % and 15 % is reached with a  $\Delta T_{subcooling}$  from 8 to 18 K.

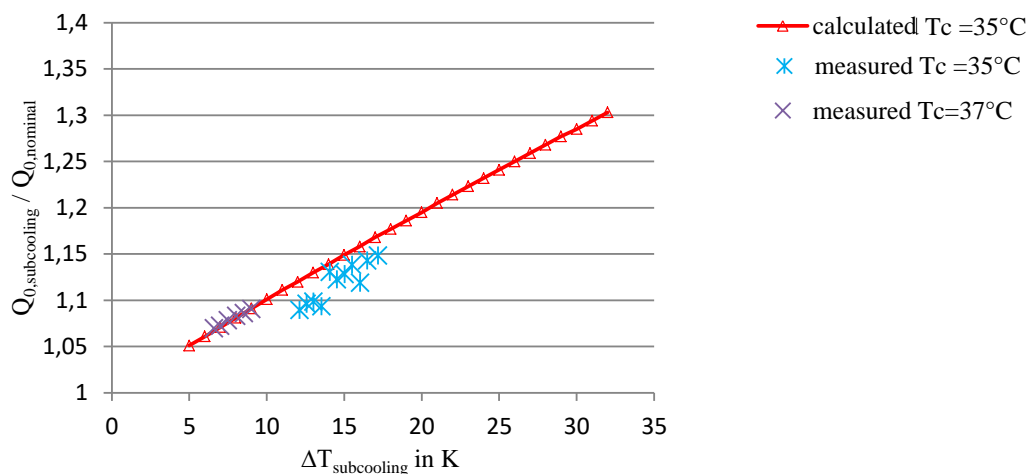


Figure 5: Enhancement of cooling capacity during unloading of the storage, measured vs. calculated data.

#### Experimental investigation: Thermal behavior of the latent heat storage

In order to obtain characteristic data for the thermal behavior of the LHS independently of the absolute size, the UA value is used. As discussed earlier, this quantity varies during the



operational cycle of the heat storage depending on the propagation of the phase front. Apart from the time-dependent variation during operation, its absolute value can be influenced by using a PCM-graphite composite with improved heat conductivity in comparison to the pure PCM. The measured experimental data are used to validate and to calibrate the theoretical model. Figure 6 illustrates the UA characteristic of the LHS during both half-cycles, i.e. loading and unloading. Figure 6 (left) depicts the UA-value during the melting process. The graph shows the latent effect only, excluding the initial heating of the storage until the melting temperature is reached. For the shown operation with uptake of latent heat, the phase change temperature and the inlet and outlet temperature of the liquid refrigerant can be used to define the actual logarithmic temperature difference which is relevant for the characterization of the heat transfer. The UA-value starts with its maximum value of about 490 W/K, following a decreasing trend. After 5 ½ hours a value of 60 W/K is reached. In comparison the UA-value found for the crystallization process starts at about 600 W/K and decreases until a value of 180 W/K is reached after 2,2 hours (Figure 6, right). Due to the more intense heat transfer during loading, i.e. solidification, the duration of this half-cycle is substantially shorter than the unloading phase. In Figure 6 (right) validation and calibration of the theoretical model is shown. The theoretical prediction for three options of the thermal conductivity of the PCM-graphite mixture is shown in order to quantify the impact of the graphite share on the heat transfer characteristic. Best match is found for  $\lambda_{PCM,eff} = 2 \frac{W}{m \cdot K}$ , confirming that a 10-fold increase of the thermal conductivity relative to pure PCM is accomplished by addition of 1/5 graphite per mass. In general higher UA-values are found for the crystallization process compared to melting. This difference is to be attributed to the different states of the refrigerant passing through the heat exchanger tubes and the associated heat transfer mechanisms. During unloading of the storage, i.e. in subcooler mode, convective heat transfer occurs. Whereas loading of the storage depends on evaporation of refrigerant with substantially higher local heat transfer coefficient for the tube-side heat transfer. For improved representation of the melting process in the next step the model will be refined with particular attention to the convective heat transfer within the liquid PCM phase.

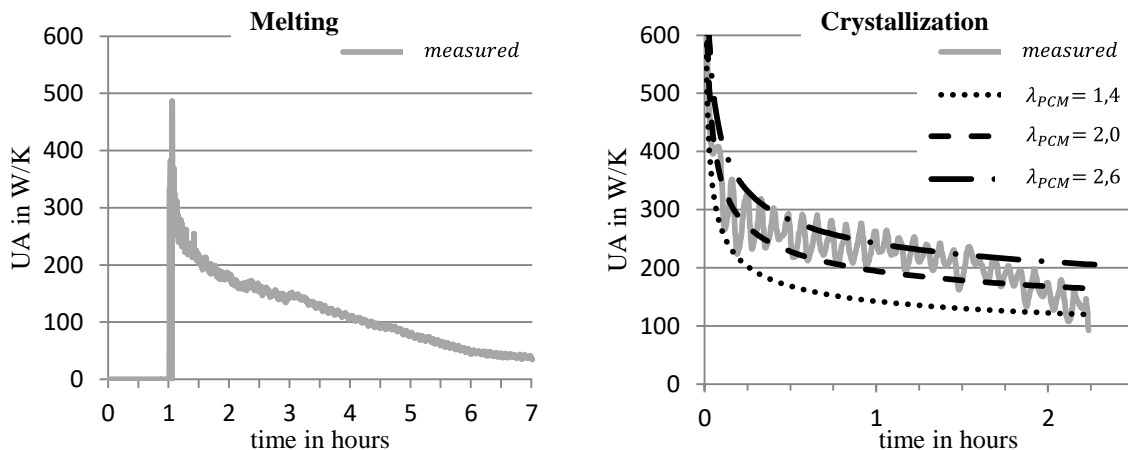


Figure 6: UA characteristic of the LHS during the phase change of the PCM extracted from measured data (left) and comparison of measured data vs. calculated data with different thermal conductivities in W/(m·K) (right).

## Conclusions

A LHS can be implemented in an air-conditioning system in order to subcool the refrigerant at the condenser outlet, allowing for a boost of the refrigeration capacity or a reduction of the power consumption at constant supply of cooling. The characteristic of the latent heat storage allows for a compact design and avoids a negative influence on the performance of the refrigeration cycle due to the constant temperature level of the heat storage. A gain of

refrigeration capacity of about 1% per Kelvin subcooling of the refrigerant R410a is obtained. Thus, maximum gain of capacity of about 40% is predicted by theory for operation with high condensing temperature up to 50 °C. By experiments a gain of 15 % has been proven with condensing temperature up to 37°C. In the next step further investigations with higher condensing temperature will be conducted. Furthermore, the analysis of the UA characteristic of the storage based on a theoretic model and leads to the conclusion that the addition of 1/5 graphite powder per mass to the PCM filling results in an increase of the heat conductivity by factor 10. The gained data is used for further development of the theoretic model.

### References:

- [1] Mehling, Harald; Cabeza, Luisa F., Heat and cold storage with PCM – An up to date introduction into basics and applications, Springer Verlag, Heidelberg, 2008
- [2] Hauer, A., Hiebler, S., Reuß, M., Wärmespeicher, 5., vollständig überarbeitete Auflage, Fraunhofer IRB Verlag, Karlsruhe, 2013
- [3] Frazzica, A., Palomba, V., La Rosa, D., Brancato, V., Experimental comparison of two heat exchanger concepts for latent heat storage applications, IRES, Düsseldorf 2017
- [4] Fan, L., Zhu, Z., Xiao, S., Liu, M., Lu, L., Zeng, Y., Yu, Z., Cen, K., An experimental and numerical investigation of constrained melting heat transfer of a phase change material in a circumferentially finned spherical capsule for thermal energy storage, Applied Thermal Engineering, 2016
- [5] Palomba, V., Frazzica, A., Brancato, V., Experimental investigation of a latent heat storage for solar cooling applications, Applied Energy 2017
- [6] Zhang, Z., Fang, X., Study on paraffin/expanded graphite composite phase change thermal energy storage material. Energy Conversion and Management 47(3), 303-310, 2006
- [7] Satzger, P., Eska, B., (Inventor), ZAE Bayern (Applicant), System zur Speicherung von Wärme oder Kälte in einem Speicherverbund aus gepreßtem Graphitexpandat und einem fest-flüssig Phasenwechselmaterial, Offenlegungsschrift DE 19630073 A1, Deutsches Patentamt, 1998
- [8] Bauer, T., Tamme, R., Christ, M., Öttinger, O., PCM-graphite composites for high temperature thermal energy storage. Proc. of ECOSTOCK, 10th International Conference on Thermal Energy Storage, Stockton, USA, 2006
- [9] AlMaadeed, M. A., Labidi, S., Krupa, I. and Karkri, M., Effect of expanded graphite on the phase change materials of high density polyethylene/wax blends. Thermochemica Acta 600, 35-44, 2015
- [10] Lazzarin, R., Mancin, S., Noro, M., Experiment for the evaluation of aluminium foams for improving heat transfer in PCM thermal storages, 11th IIR Conference on Phase Change Materials and Slurries for Refrigeration and Air Conditioning, Karlsruhe 2016
- [11] Loistl, F., Korth, T., Schweigler, C., Einsatz von Latentwärmespeichern in Klimageräten, DKV-Tagung, Kassel, 2016
- [12] Özcan, T., Gukelberger, E., Kauffeld, M., Latent heat storage with polyethylene enhanced with aluminum stripes, 11th Conference on Phase Change Materials and Slurries for Refrigeration and Air Conditioning, Karlsruhe, 2016
- [13] Korth, T., Loistl, F., Schweigler, C., Experimentelle Untersuchung eines Latentwärmespeichers für den Einsatz in Wärmepumpensystemen, DKV-Tagung, Bremen, 2017

# Detailed exergetic analysis of a packed bed thermal energy storage unit in combination with an Organic Rankine Cycle

A. König-Haagen\* and D. Brüggemann

Chair of Engineering Thermodynamics and Transport Processes (LTTT), Center of Energy Technology (ZET), University of Bayreuth, Universitätsstraße 30, 95447 Bayreuth, Germany

\*Corresponding author: [andreas.koenig-haagen@uni-bayreuth.de](mailto:andreas.koenig-haagen@uni-bayreuth.de), [lttt@uni-bayreuth.de](mailto:lttt@uni-bayreuth.de)

## Abstract

Thermal energy storage systems (TESS) can reduce or overcome the issues that appear when an Organic Rankine Cycle (ORC) is adopted to a fluctuating heat source. However, detailed exergetic studies about the optimisation potential and the influence of the TESS on the overall system are still missing for this application and TESS in systems in general. Therefore, in this work a detailed exergetic evaluation is numerically performed for a packed bed TESS in combination with an ORC. For the chosen boundary conditions, the overall pressure drop and the heat resistance from the heat transfer fluid (HTF) to the particle have the most influence on the overall exergetic efficiency. By optimizing the parameters of the storage unit, the overall exergetic efficiency can be increased from 36 % to 43 %.

**Keywords:** packed bed thermal energy storage, Organic Rankine Cycle, exergetic analysis

## Introduction

In the future energy supply, thermal energy storage systems (TESS) can play a key role. One promising application for TESS is the combination with an Organic Rankine Cycle (ORC) for the utilization of fluctuating waste heat. Here, the TESS allows to downsize the ORC and to run it less in off-design. During the last years, some groups have started to investigate the integration of TESS in fluctuating waste heat flows for electricity production with an ORC [1–3]. For the evaluation and optimization of such systems, exergetic analyses are well suited. However, in most previous exergetic studies of the combination of TESS and ORC, the TESS were strongly simplified like in Manfrida et al. [4] and hence neither a detailed analysis of the TESS nor the overall system was possible. The detailed second law based analysis of TESS in systems is in general rather a new field that has attracted attention recently due to e.g. pumped thermal electricity storage [5]. A so called advanced exergetic analysis of a TESS in combination with an air conditioning system was performed by Mosaffa et al. [6]. The authors [7] applied an exergetic evaluation method that accounts for the influence on the remaining system to sensible and latent TESS in combination with an ORC.

Within this work, a detailed numerical model is adopted for a packed bed thermal storage unit to study the combination of TESS and ORC. The model is set up in MATLAB Simulink and the ORC is implemented based on characteristics deduced from literature [2]. A comprehensive exergetic analysis is performed which takes into account the optimisation limits of the TESS and its influence on the overall system and several components. Later on, a mathematical optimization is applied to optimize the TESS system. Finally, the results of the exergetic analysis and the mathematical optimization are analysed together.

## Method

The exergetic evaluation method applied in this work investigates the influence of physical aspects to strengthen the understanding of the process, shows optimization potentials and helps to check the results of mathematical optimizations for plausibility. For this purpose the

components are once studied as they are – called real – and also idealized – called ideal. The real exergetic efficiency of one component  $\varepsilon_k^{real}$  is given by

$$\varepsilon_k^{real} = \frac{E_{k,P}}{E_{k,F}} \quad (1)$$

and the idealized efficiency of a component  $\varepsilon_k^{ideal}$  is generally defined as

$$\varepsilon_k^{ideal} = \frac{E_{k,P}^{ideal}}{E_{k,F}}. \quad (2)$$

In equation (1) and (2) the fuel exergy of a component is  $E_{k,F}$  and the product exergy of a real component is  $E_{k,P}$  and that of an ideal component  $E_{k,P}^{ideal}$ . The influence of the studied physical aspect in the regarding component  $y_k^{ideal}$  is determined by

$$y_k^{ideal} = \frac{\varepsilon_k^{ideal}}{\varepsilon_k^{real}}. \quad (3)$$

This work shows a special interest in the influence of physical aspects of one component on other components or the overall system. The firstly mentioned is calculated with

$$y_k^{ideal,k} = \frac{\varepsilon_k^{ideal,k}}{\varepsilon_k^{real}} \quad (4)$$

where the efficiency of the influenced component is for the idealized case  $\varepsilon_k^{ideal,k}$ . The influence of a physical aspect of one component on the overall system  $y_{tot}^{ideal}$  is described by

$$y_{tot}^{ideal} = \frac{\varepsilon_{tot}^{ideal}}{\varepsilon_{tot}^{real}} \quad (5)$$

where the efficiency of the total system is in the real case  $\varepsilon_{tot}^{real}$  and in the idealized case it is  $\varepsilon_{tot}^{ideal}$ . If a physical aspect is idealized in several components the influence on one component  $y_k^{ideal,k-k}$  is written as

$$y_k^{ideal,k-k} = \frac{\varepsilon_k^{ideal,k-k}}{\varepsilon_k^{real}} \quad (6)$$

and the influence on the overall system  $y_{tot}^{ideal,k-k}$  is calculated by

$$y_{tot}^{ideal,k-k} = \frac{\varepsilon_{tot}^{ideal,k-k}}{\varepsilon_{tot}^{real}}. \quad (7)$$

Here, the efficiency of the component or the system is in the idealized case  $\varepsilon_k^{ideal,k-k}$  and  $\varepsilon_{tot}^{ideal,k-k}$  respectively. In this work the exergetic efficiency of the storage unit  $\varepsilon_{st}$  is calculated by

$$\varepsilon_{st} = \frac{E_{P,st} - \int P_{fan,st} dt}{E_{F,st}}, \quad (8)$$

that of the storage unit with periphery  $\varepsilon_{st+per}$  by

$$\varepsilon_{st+per} = \frac{E_{P,Sp+Per} - \int P_{fan,st+per} dt}{E_{F,st+per}} \quad (9)$$

and that of the total system  $\varepsilon_{tot}$  by

$$\varepsilon_{tot} = \frac{E_{P,tot} - \int P_{fan,tot} dt}{E_{F,tot}}. \quad (10)$$

Here, the product exergy of the storage unit, the storage unit with periphery and the total system are  $E_{P,st}$ ,  $E_{P,Sp+Per}$  and  $E_{P,tot}$  respectively. The regarding fuel exergies are in the same order  $E_{F,st}$ ,  $E_{F,st+per}$  and  $E_{F,tot}$ . The proportional fan power of the storage unit is  $P_{fan,st}$ , that of the storage unit with periphery is  $P_{fan,st+per}$  and the total fan power is  $P_{fan,tot}$ . Beside the exergetic efficiency also the thermal efficiency is of interest. The thermal efficiency of the storage unit  $\eta_{Sp}$  is defined by

$$\eta_{st} = \frac{H_{P,st}}{H_{F,st}}, \quad (11)$$

that of the storage unit with periphery  $\eta_{Sp+Per}$  is written as

$$\eta_{st+per} = \frac{H_{P,st+per}}{H_{F,st+per}} \quad (12)$$

and that of the overall system  $\eta_{tot}$  is

$$\eta_{tot} = \frac{E_{P,tot} - \int P_{fan,tot} dt}{H_{F,tot}}. \quad (13)$$

The fuel enthalpy of the storage unit, the storage unit with periphery and the overall system are  $H_{F,st}$ ,  $H_{F,st+per}$  and  $H_{F,tot}$ . The product enthalpy of the storage unit and the storage unit with periphery are  $H_{P,st}$  and  $H_{P,st+per}$  respectively. The physical aspects studied in this work are listed in Table 1.

Table 1: Idealized physical aspects

idealized physical aspect	components
heat loss to the surrounding	storage / periphery
heat resistance from the heat transfer fluid (HTF) to the particles and inside the particles	storage
effective thermal conduction in flow direction	storage
pressure drop	storage / periphery

## Numerical Model

The numerical model consists of the TESS, its periphery and the ORC. Except for the ORC, which is implemented by means of results of Preißinger and Brüggemann [8], all components are modelled physically. The energy equation for the storage and the pipes of the periphery generally reads

$$\frac{\partial(\rho h)}{\partial t} + \nabla \cdot (\rho h \mathbf{v}) = \nabla \cdot (\lambda \nabla T) + q \quad (14)$$

with the density  $\rho$ , the enthalpy  $h$ , the time  $t$ , the velocity vector  $\mathbf{v}$ , the heat conductivity  $\lambda$ , the temperature  $T$  and a source term  $q$ . The model of the TESS is primarily based on the Schumann model [9]. The sand and the heat transfer fluid (HTF) are both modelled one dimensionally and are coupled by source terms that account for the heat transfer between both

phases. By substituting  $h$  by the heat capacity  $c_p$  or  $c$  and  $T$ , assuming a constant density for the energy equation and introducing the porosity  $\psi$  equation (14) becomes

$$\psi c_p \rho \frac{\partial T}{\partial t} + \psi u c_p \rho \frac{\partial T}{\partial x} = \psi \frac{\partial}{\partial x} \left( \Lambda \frac{\partial T}{\partial x} \right) + q_{HTF} \quad (15)$$

for the HTF and

$$(1 - \psi) c_p \frac{\partial T}{\partial t} = (1 - \psi) \frac{\partial}{\partial x} \left( \Lambda \frac{\partial T}{\partial x} \right) + q_{Par} \quad (16)$$

for the particles. The assumption of a constant density leads to a constant mass flow in the energy equation over the storage length. For comparison a model with a complete variable density was set up. For the case studied in this work the maximum difference in the HTF temperature inside the storage of the two models is less than 0.25 K, but the model with the complete variable density needs more numerical effort. In equation (15) and (16)  $\Lambda$  is an effective thermal conductivity that is calculated by [10]

$$\Lambda = \lambda_{eff} + \frac{Pe_0}{2} \lambda_{HTF} \quad (17)$$

where the second term on the right hand side with the Peclet number of the superficial velocity  $Pe_0$  and the heat conductivity of the HTF  $\lambda_{HTF}$  accounts for disperse effects. The effective heat conductivity of the packed bed without through flow  $\lambda_{eff}$  is calculated with the detailed model of Bauer/Zehner/Schlünder [11–13]. This model accounts for the heat conduction in the particles and the HTF as well as for radiation. For the HTF the free length of path of the molecules is considered and for the particles factors are included to account for e.g. the contact surfaces. The source term in equation (15) of the HTF is calculated by

$$q_{HTF} = \alpha_{HTF-Par}^{eff} \cdot (T_{Par} - T_{HTF}) + k_{hl} \cdot (T_{amb} - T_{HTF}). \quad (18)$$

Here, the particle temperature is  $T_{Par}$ , the HTF temperature is  $T_{HTF}$ , the ambient temperature is  $T_{amb}$ , the effective heat transfer coefficient between particles and HTF is  $\alpha_{HTF-Par}^{eff}$  and the heat loss coefficient is  $k_{hl}$ . The source term in equation (16) of the particles is defined as

$$q_{Par} = \alpha_{WTF-Par}^{eff} \cdot (T_{WTF} - T_{Par}). \quad (19)$$

The heat resistance in the particle is considered in the definition of  $\alpha_{WTF-Par}^{eff}$ :

$$\alpha_{WTF-Par}^{eff} = \left( \frac{1}{\alpha_{WTF-Par}} + \frac{d_{Par}}{2 \cdot 5 \cdot \lambda_{Par}} \right)^{-1}. \quad (20)$$

In equation (20) the particle diameter is  $d_{Par}$ , the heat conductivity of the particles is  $\lambda_{Par}$  and the heat transfer coefficient between particles and HTF  $\alpha_{WTF-Par}$  is calculated by means of the model of Gnielinski [14,15] based on the flow around a single sphere. For small Pe this model is extended with the correlation found in Kunii and Suzuki [16].

In order to determine the pressure drop in the packed bed, the model of Molerus [17] is used as it shows better agreements with experiments [10] than the Ergun equation [18]. The pressure drop is calculated by

$$\Delta p = \left[ \frac{4}{3} \frac{1}{\rho u^2} \frac{\bar{d}_{Par}}{\Delta l} \frac{\psi^2}{1 - \psi} \frac{1}{Eu(\Phi_D)} \right]^{-1} \quad (21)$$

with the Sauter mean diameter  $\bar{d}_{Par}$ , the length  $\Delta l$  and the Euler number  $Eu(\Phi_D)$  defined in e.g. the VDI Heat Atlas [10].

For the pipes of the periphery equation (14) is

$$c_p \rho \frac{\partial T}{\partial t} + u c_p \rho \frac{\partial T}{\partial x} = \frac{\partial}{\partial x} \left( \lambda \frac{\partial T}{\partial x} \right) + q_{pipe-HTF} \quad (22)$$

for the HTF and

$$c_p \frac{\partial T}{\partial t} = \frac{\partial}{\partial x} \left( \lambda \frac{\partial T}{\partial x} \right) + q_{pipe-wall} \quad (23)$$

for the pipe walls. Where  $q_{pipe-HTF}$  is defined as

$$q_{pipe-HTF} = \alpha_{WTF-W} \cdot (T_W - T_{HTF}) \quad (24)$$

and  $q_{pipe-wall}$  is defined as

$$q_{pipe-wall} = \alpha_{WTF-W} \cdot (T_{HTF} - T_W) + k_{pipe-hl} \cdot (T_{amb} - T_W). \quad (25)$$

Here, the temperature of the pipe wall is  $T_W$ , the heat transfer coefficient between wall and HTF is  $\alpha_{WTF-W}$  and the heat transfer coefficient of the heat loss is  $k_{pipe-hl}$ . A correlation of Gnielinski [19] is used to calculate  $\alpha_{WTF-W}$  and the pressure drops of the pipes, valves, bends and branches are calculated according to the VDI Heat Atlas [10].

The numerical model is implemented in MATLAB Simulink. To discretize equation (15), (16), (22) and (23) the method of lines is applied. Therefore only the spatial discretization is done by hand, resulting in a system of time-dependent ordinary differential equations that can be efficiently treated by solvers provided by MATLAB Simulink. So called C-mex Level 2 s-functions are used to describe the discretization. The query of the temperature dependent material properties is compiled in C-code, too. For the sand the heat capacity and the heat conductivity are implemented temperature dependently, the same is true for the heat conductivity of the insulation of the storage unit and that of the pipes of the periphery. The heat capacity, the heat conductivity, the viscosity and the density – except the density in the energy equation – of the air are implemented temperature dependently with data from REFPROP [20].

## Conditions

A TESS with 4.7 t of sand (this corresponds to one module of the storage system developed by enolcon GmbH and set up at the University of Bayreuth, see Figure 1) with a diameter of about 2 mm is considered in combination with an ORC working with toluene [8]. Air is used as HTF for the vertical flow TESS with six parallel sections. Each section has a size of about 1.1 m x 1.1 m x 0.4 m in depth, height and length, respectively. The inlet and outlet stainless steel pipes length is 5 m each, with an inner diameter of 0.2 m. The insulation of the storage and the pipes is 0.2 m thick and consists of different types of mineral wool and plates. A charging temperature of 600 °C, a discharging temperature of 20 °C and a standard volume flow of 0.667 m<sup>3</sup> are applied for the exergetic analysis. Here, the TESS is studied in the swung-in state, which is already achieved at the fifth charging and discharging cycle. The time for charging and discharging is identical and about 5660 s each. No storage time between the two modes is considered. A mesh of the storage unit consists of 150 nodes for each phase (HTF and storage material) in flow direction. The mathematical optimization including the TESS dimensions and ratios, the sand porosity and diameter as well as the pipe diameter is performed with a downhill simplex method [21] combined with a branch and bound approach.



Figure 1: Storage modules of the combined TESS and ORC facility at the University of Bayreuth

## Results

The numerical model of the storage unit is validated with results of the demonstration plant. Here, the inlet temperature and standard volume flow differ from that for the exergetic analysis. They are not constant over time and are imported from the experiments into the numerical simulation. As depicted in Figure 2, the numerical results agree well with the experimental ones for the charging mode. The minor deviations are caused by e.g. the uncertainties in the measurement of the volume flow, the position of the thermocouples and the material properties as well as slightly untight valves and possibly small by-pass flows in the storage unit.

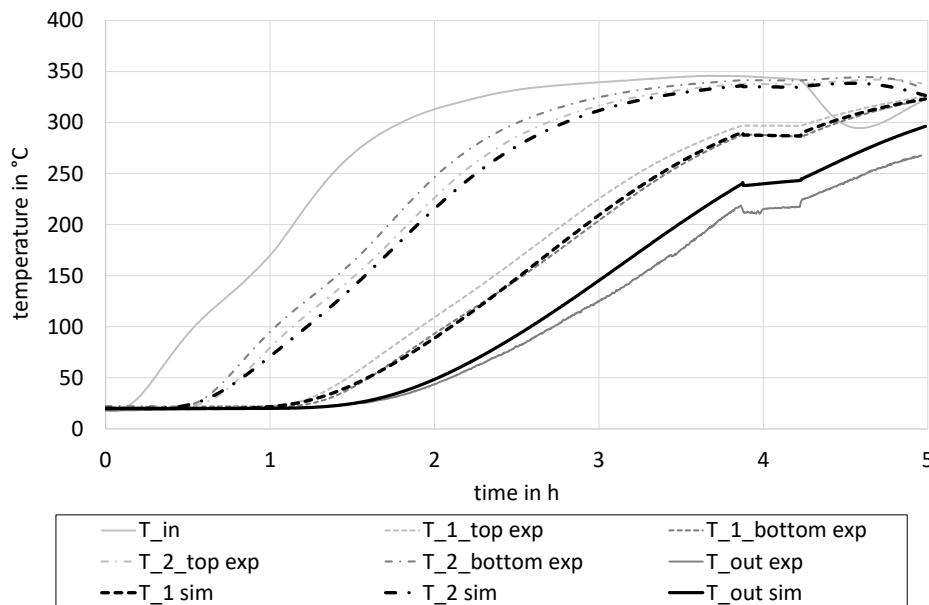


Figure 2: Sand and HTF temperatures for the simulations and the experiments

For the studied case an electrical power of about 78 kW is achieved resulting in an overall thermal efficiency of 16.1 % and a thermal efficiency of the TESS alone of 86.1 %. The exergetic efficiency of the overall system, the TESS with periphery and the TESS alone are 36.1 %, 78.8 % and 81.7 % respectively. Figure 3 depicts the influence of all studied physical aspects on the exergetic efficiency of the overall system and that of components. The heat transfer resistance, the overall pressure drop and the heat conduction in flow direction have the largest influence on the overall exergetic efficiency. For the exergetic efficiency of the storage the physical aspect with the highest influence is the heat transfer resistance followed by the heat conduction in flow direction. After the mathematical optimization, the influences are much more even as seen in Figure 4. Now the overall heat loss and the heat transfer resistance have the highest impact on the overall exergetic efficiency which increased to 43.4 %. The exergetic efficiency of the TESS is 91.3 % after the optimization.



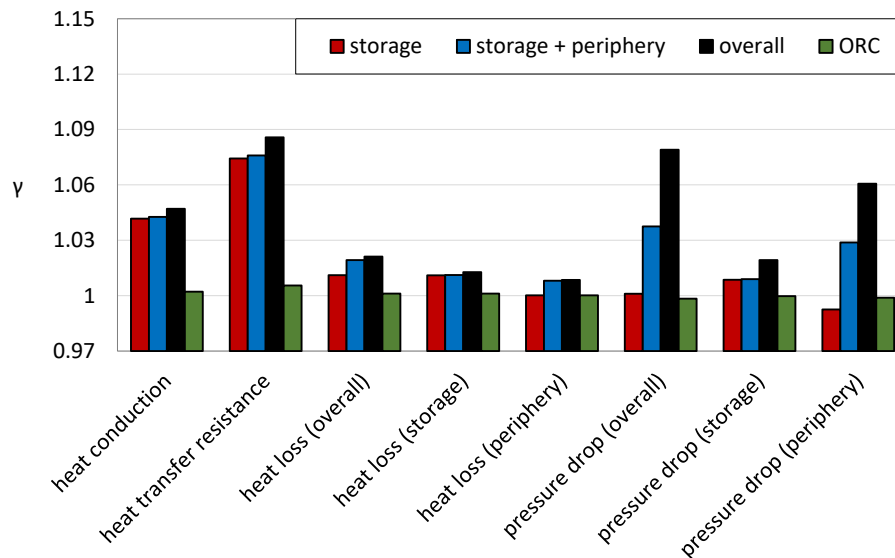


Figure 3: Influence of physical aspects on the exergetic efficiencies of different components and the overall system before optimization

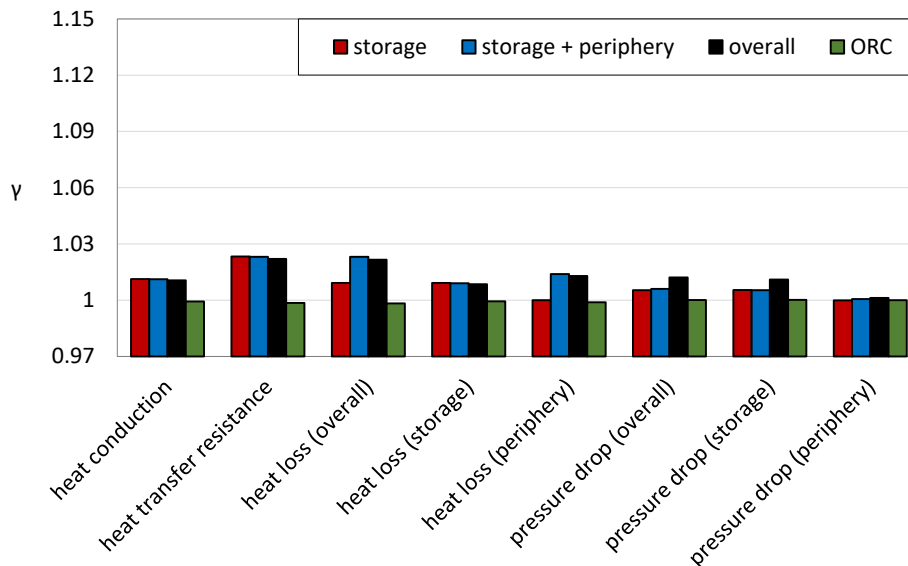


Figure 4: Influence of physical aspects on the exergetic efficiencies of different components and the overall system after optimization

### Summary/Conclusions

A detailed exergetic analysis of a TESS in combination with an ORC is performed. Within this scope validated numerical models are applied and the influence of several physical aspects on the exergetic efficiencies of the TESS and the complete system are analysed. The entire pressure drop and the heat resistance from the HTF to the particles have the highest influence on the overall exergetic efficiency. By means of a mathematical optimization this efficiency increased from 36 % to 43 %.

### Acknowledgements

The authors would like to thank the staff of enolcon GmbH and STORASOL GmbH for the support throughout the project and Prof. Dr.-Ing. Markus Preißinger for editing the results of his PhD thesis.

## References:

- [1] Nardin, G., Meneghetti, A., Dal Magro, F., Benedetti, N., “PCM-based energy recovery from electric arc furnaces”, *Applied Energy*, 2014.
- [2] Dal Magro, F., Meneghetti, A., Nardin, G., Savino, S., “Enhancing energy recovery in the steel industry: Matching continuous charge with off-gas variability smoothing”, *Energy Conversion and Management*, 2015.
- [3] Steinmann, W.-D., Schulte, R., Scherer, P., *EVA-Thermische Energiespeicher zur Verstromung diskontinuierlicher Abwärme*. Forschungsbericht BWPLUS, 2010.
- [4] Manfrida, G., Secchi, R., Stańczyk, K., “Modelling and simulation of phase change material latent heat storages applied to a solar-powered Organic Rankine Cycle”, *Applied Energy*, 2016.
- [5] McTigue, J. D., White, A. J., Markides, C. N., “Parametric studies and optimisation of pumped thermal electricity storage”, *Applied Energy*, 2015.
- [6] Mosaffa, A. H., Garousi Farshi, L., Infante Ferreira, C. A., Rosen, M. A., “Advanced exergy analysis of an air conditioning system incorporating thermal energy storage”, *Energy*, 2014.
- [7] König-Haagen, A., Rösler, F., Brüggemann, D., “Exergetic analysis of thermal energy storages in thermodynamic systems. In: Eurotherm Seminar #99: Advances in Thermal Energy Storage, 2014.
- [8] Preißinger, M., Brüggemann, D., “Thermoeconomic Evaluation of Modular Organic Rankine Cycles for Waste Heat Recovery over a Broad Range of Heat Source Temperatures and Capacities”, *Energies*, 2017.
- [9] Schumann, T., “Heat transfer: A liquid flowing through a porous prism”, *Journal of the Franklin Institute*, 1929.
- [10] *VDI-Wärmeatlas*, 11th ed. Berlin, Heidelberg: Springer-Verlag, 2013.
- [11] Bauer, R., Schlünder, E. U., “Effektive radiale Wärmeleitfähigkeit gasdurchströmter Schüttungen aus Partikeln unterschiedlicher Form”, *Chemie Ingenieur Technik*, 1976.
- [12] Zehner, P., Schlünder, E. U., “Wärmeleitfähigkeit von Schüttungen bei mäßigen Temperaturen”, *Chemie Ingenieur Technik*, 1970.
- [13] Zehner, P., Schlünder, E. U., “Einfluß der Wärmestrahlung und des Druckes auf den Wärmetransport in nicht durchströmten Schüttungen”, *Chemie Ingenieur Technik*, 1972.
- [14] Gnielinski, V., “Gleichungen zur Berechnung des Wärme- und Stoffaustausches in durchströmten ruhenden Kugelschüttungen bei mittleren und großen Pecletzahlen”, *Verfahrenstechnik*, 1978.
- [15] Gnielinski, V., “Berechnung des Wärme- und Stoffaustauschs in durchströmten ruhenden Schüttungen”, *Verfahrenstechnik*, 1982.
- [16] Kunii, D., Suzuki, M., “Particle-to-fluid heat and mass transfer in packed beds of fine particles”, *International Journal of Heat and Mass Transfer*, 1967.
- [17] Molerus, O., *Principles of flow in disperse systems*. London: Chapman & Hall, 1993.
- [18] Ergun, S., “Fluid flow through packed columns”, *Chemical Engineering Progress*, 1952.
- [19] Gnielinski, V., “Neue Gleichungen für den Wärme- und den Stoffübergang in turbulent durchströmten Rohren und Kanälen”, *Forsch Ing-Wes*, 1975.
- [20] Lemmon, E., Huber, M., McLinden, M., *NIST Standard Reference Database 23: Reference Fluid Thermodynamic and Transport Properties-REFPROP*. National Institute of Standards and Technology, 2013.
- [21] Nelder, J. A., Mead, R., “A Simplex Method for Function Minimization”, *Comput J*, 1965.

# Novel High Temperature Steam Transfer Pipes

M. J. Tierney<sup>1</sup>, M. Pavier<sup>1</sup>, P. Flewitt<sup>2</sup>

<sup>1</sup>Department of Mechanical Engineering, University of Bristol, UK, BS8 1TR.

<sup>2</sup>Department of Physics, University of Bristol, UK, BS8 1TR

\*Corresponding author: mike.tierney@bristol.ac.uk

## Abstract

Cycle analysis has been applied to simple versions of supercritical steam plant with novel steam transfer pipes. We have proposed that Advanced Ultra Super Critical (A-USC) power plant might incorporate internally coated and externally cooled sections of transfer pipe. This would keep the temperatures of pipe walls below an acceptable limit enabling more readily available steel alloys to replace some of the 32% nickel comprising the metal content of some very high temperature designs (a throttle temperature of 700°C). As a preliminary modelling step, our throttle temperature has been restricted to 594°C. For co-current cooling, pipe wall resistance and coolant flow rate were adjusted so that pipe wall temperatures were below a limit (mostly 550°C) at all axial locations; ambitious reductions in temperature limits had some small effects on the cycle efficiency. Co-current cooling produced a slightly higher efficiency than counter-current cooling. The reduced cycle efficiencies do not appear justified when current material and electricity prices are considered but there is a strategic argument that the currently envisaged content of nickel in A-USC, if applied globally and to all future power plant, would be unsustainable. In the near future we intend to publish papers showing models of more representative plant.

**Keywords:** A-USC cycles, cycle analysis, thermal coatings

## Introduction

Advanced ultrasupercritical cycles (A-USC) offer cycle efficiencies as high as 55% and hence 15% higher than typical conventional plant [1]. The generation of supercritical steam at 350 bar and 720°C normally necessitates the use of expensive nickel-based alloys (for superheater and reheater tubing and turbine parts), comprising 32% of all metals used. The use of expensive alloys in the superheater is unavoidable, but it might be possible to use cheaper alloys in the transport pipes – possibly ~200-m-long and located between the superheater and the turbines. A proposed modification entails coating with thermal insulation the inner surfaces of pipes transporting steam between plant items. The ensuing reduction in pipe wall temperatures would facilitate the use of cheaper types of steel in these pipes. The aim of the current study is to investigate whether or not the required cooling of such thermally coated zones would result in an unacceptable loss in cycle efficiency.

For the current paper we consider a simple regenerative cycle with no reheat and moderate temperature of operation (<600°C in our current simulations and below the metallurgical limit of interest). (This is a first step in our work. We shall extend later calculations to higher temperatures nearer the region of 700°C, and increase the complexity of plant.) Our aim is to set up a cycle simulation incorporating a thermally cooled zone of pipe, and to probe the impact of pipe cooling on cycle efficiency. Specific objectives are: (1) to model a simple plant in steady-state, exhibiting the cycle efficiencies expected of sub-critical and super-critical operation; (2) to inspect the impact of the coating method on cycle efficiency and pipe

wall temperature; (3) to make a tentative cost/ benefit analysis. Future papers will cover more representative, regenerative cycles with reheat.

Experience of A-USC cycles includes the EPRI project [2] and the Turk project [3]. Marion et al. [1] list industrial, operational plant with reheat temperatures as high as 623 °C where only ferritic and austenitic steels are needed for fabrication, before discussing operation at very high reheat temperatures up to 720 °C and even 760°C. We know of no previous attempts to thermally coat steam pipes, but the use of thermal coatings in turbines and diesel engines is well known [4].

In this document a simple hypothetical plant is postulated. The thermodynamic model allows for thermally coated zones (TCZ) of pipework and the associated heat transfers, and employs steady-state balances of heat and material at all plant items to derive cycle efficiency.

### Thermodynamic modelling of plant

A plant diagram is shown on Figure 1. The coated zone is located between the superheater and turbine set and draws coolant from the feedwater. The cycle is regenerative: some steam is bled from the midpoint of the turbine set (stream #3) and mixed into feedwater at intermediate pressure. The temperature-entropy diagram demonstrates the supercritical operation, regenerative heating, and a (small) reduction in temperature after the TCZ (see circle).

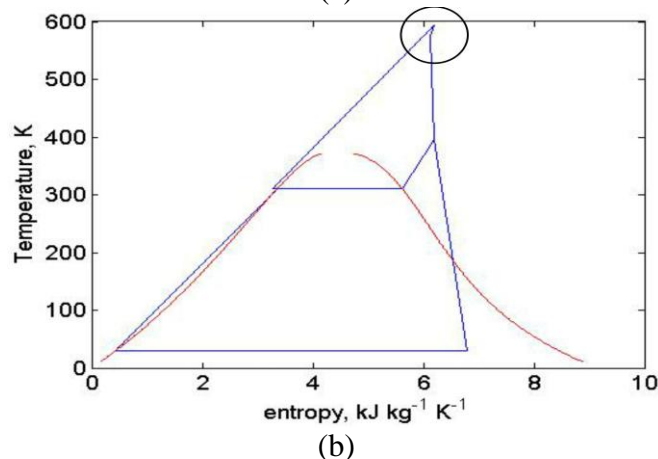
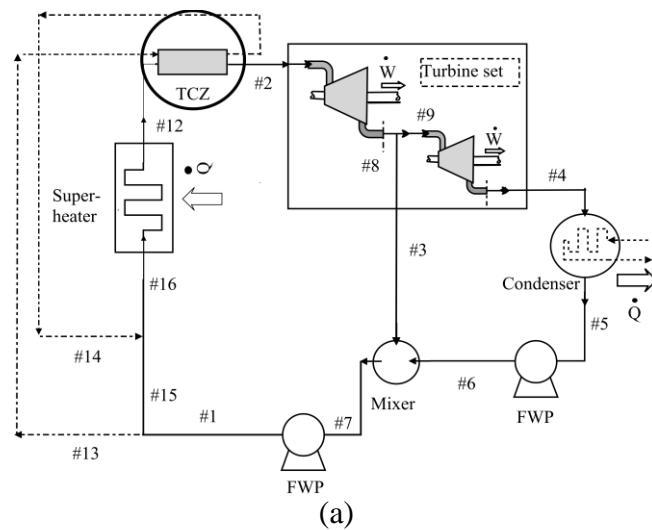


**Figure 1 - Simple regenerative cycle with thermally coated zone - coolant drawn from feedwater (a) plant (b) Ts diagram.**

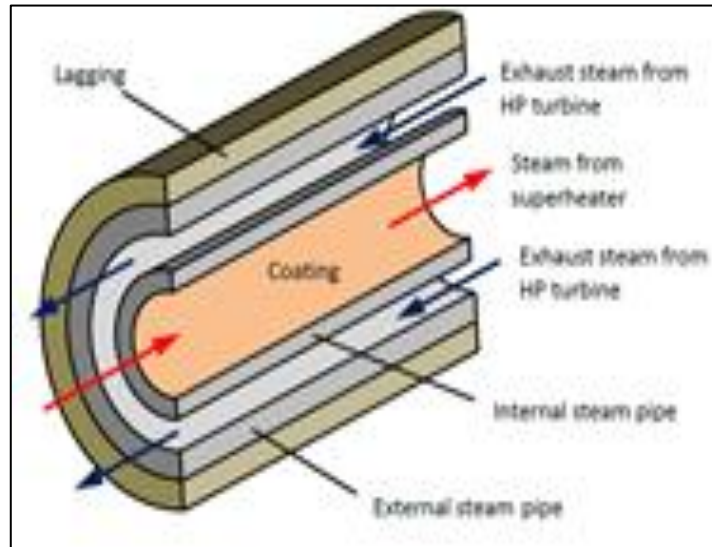


**Figure 2 Proposed arrangement of cooled steam pipe**

For a system boundary around any plant item (heater, boiler, turbine, reheater) the Steady Flow Energy Equation is written thus

$$\sum_{i=1}^I m_{out,i} h_{out,i} - \sum_{j=1}^J m_{in,j} h_{in,j} = \begin{cases} W(\text{if turbine}) \\ Q_{tcz}(\text{if cooling jacket}) \\ 0(\text{if throttle}) \\ Q(\text{if boiler}) \end{cases} \quad 1$$

where  $h$  is specific enthalpy,  $m$  is rate of mass flow  $Q$  is heating power, and  $W$  is mechanical power. The corresponding equation for mass conservation is

$$\sum_{i=1}^I m_{out,i} = \sum_{j=1}^J m_{in,i} \quad 2$$

A tentative estimate of reversible turbine power  $W'$  was found for isentropic expansion ( $h'_{out} = f(p, s_{out})$  and  $s_{out} = s_{in}$ ). To obtain true power  $W$  was corrected with an isentropic efficiency according to  $W = \eta_{isen} W'$ . Regeneration was idealised by a mixer (e.g. streams 3, 6, 7 on Figure 1) - in practice a train of feedwater heaters would be used so as to reduce the number of installed feedwater pumps [2].

The cycle efficiency is the ratio of net power output to heat input.

$$\eta_{cycle} = \frac{\sum W_j}{\sum \max(0, \sum Q_i)} \quad 3$$

The length of the TCZ follows from

$$L = \frac{\sum_{k=1}^4 R_{k,k+1}}{\left( \frac{\theta_{in} - \theta_{out}}{\ln(\theta_{in}) - \ln(\theta_{out})} \right)} Q_{tcz} \quad 4$$

where  $\theta = T_{wf} - T_{co}$  is the temperature difference between the (supercritical) working fluid and the coolant and the subscript (in, out) refers to the inlet and outlet of the TCZ, and the denominator group is the logarithmic mean temperature difference. Also,  $R_{k,k+1}$  is a set of thermal resistances (each between point  $k$  and  $k+1$ ) that will be defined in due course. The temperature  $T_{wf,out}$  was guessed to allow estimation of all four temperatures (Equation 1) and two temperature differences and length  $L$  (Equation 4). Thereafter  $T_{wf,out}$  was adjusted until  $L = 200\text{m}$ .

With regard to  $R_{1,2}$  and in particular the heat transfer coefficient of the (supercritical) working fluid,  $\alpha_{wf}$ , the correlation of Yamagata et al [3a] yielded  $\alpha_{wf}$  within 20% of experimental data.

With regard to  $R_{2,3}$  Stoever and Funke [4] review the composition and stability of thermal barrier coatings. They identify as well-established yttrium stabilized zirconia ( $Y_2O_3$ ) with thermal conductivity  $[1.1, 1.5] \text{ W m}^{-1} \text{ K}^{-1}$  in the range  $[900, 1320]^\circ\text{C}$ . With regard to  $R_{3,4}$  thermal conductivities for 9Cr-1MoVNb steel from reference [5] were taken as appropriate for P91 steels. With regard to  $R_{4,5}$  and heat transfer coefficient of coolant,  $\alpha_{co}$ , the value of  $\alpha_{co}$  was computed with Nunner's correlation [6]. At any axial location  $z$  within the TCZ, the three surfaces/ interfaces were:  $n= 2$  (coating surface facing working fluid);  $n= 3$  (coating-pipe interface);  $n = 4$  (pipe surface facing coolant). The corresponding temperature was:

$$T_n = T_{wf} + (T_{co} - T_{wf}) \frac{\sum_{k=1}^{n-1} R_{k,k+1}}{\sum_{k=1}^4 R_{k,k+1}} \quad 5$$

$T_3$  is the most vulnerable temperature at the interface between coating and pipe,  $R_{2,3}$  being the coating resistance.

Three cases were investigated

- The TCZ was cooled with boiler feedwater in a co-current configuration (Figure 1). The estimates of  $R_{3,4}$  and  $R_{4,5}$  were disregarded,  $(R_{3,4} + R_{4,5})$  was found by rearrangement of Equation 5 so that  $T_3 = T_{limit}$  (normally  $550^\circ\text{C}$ ). The heat capacity ratio (coolant to working fluid), implying the coolant mass flow rate ( $m_{12}$ ), was chosen so that  $T_3 = \text{constant}$  at all positions in the TCZ. Analytical solution of coupled Equations 1 and 4, obviated the need to iterate. Co-current cooling minimised  $Q_{tcz}$  and the concomitant loss of cycle efficiency
- The above was repeated, but with counter-current flow. The flow was set to give  $T_3 = T_{limit}$  at the base of the TCZ but  $T_3$  decreased below the limit above this point.
- Coolant was by means of a steam bleed from the mid-point of the turbine (Figure 3). This meant that the estimated exit temperature ( $T_{12}$ ) had to be iterated to give the required  $L = 200 \text{ m}$ . All four thermal resistances were computed from constitutive data as described above.

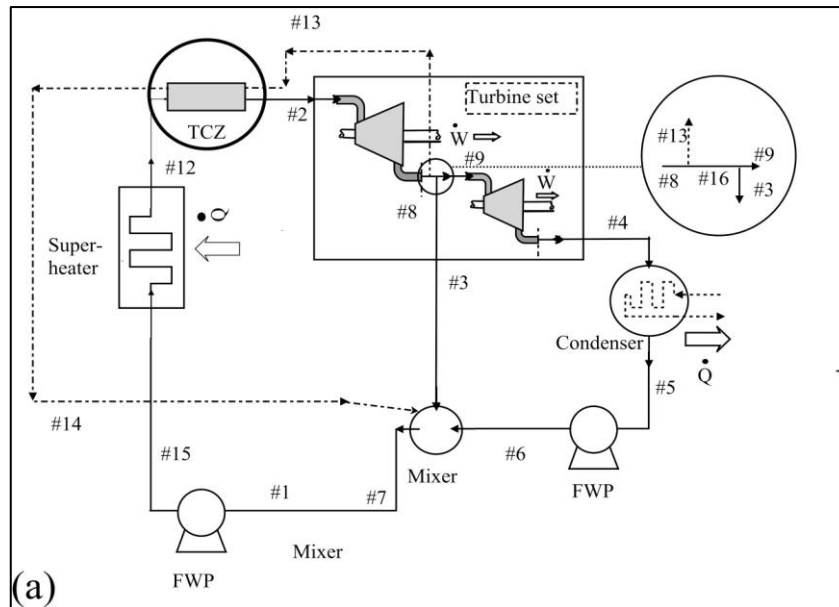


**Fig 3 - Simple regenerative cycle with thermally coated zone - coolant extracted from turbine mid-point**

## Results

Table 1 concerns co-current cooling with feedwater as coolant. In principle, on row #3 the reduction in cycle efficiency was small; from bypass (no cooling used, so the wall temperature achieved  $593.8^{\circ}\text{C}$ ) to  $T_{\text{limit}} = 550^{\circ}\text{C}$  the loss in efficiency was 0.08% only. A corresponding loss of  $5.19^{\circ}\text{C}$  in temperature of working fluid was tolerable only because heat was recovered through the cooling jacket and passed to the feedwater, thereby reducing the load on the boiler. A reduction in the limiting temperature to  $T_{\text{limit}}=450^{\circ}\text{C}$  reduced cycle efficiency by 0.26% only.

On Table 2, switching to counter-current flow and row #2 ( $T_{\text{limit}}= 550^{\circ}\text{C}$  limit and coating thickness  $w = 0.005 \text{ m}$ ) the cycle efficiency was reduced by a further 0.08 % (ie from 44.83% (bypass) to 44.75% (co-current) to 44.67% (counter-current)). Table 2 also probes the effect of coating thickness – clearly thicker coatings are superior: they demand lower rates of coolant flow and minimise efficiency loss. There may well be issues with the mechanical stability of thicker coatings. Also note that the cooling jacket would have to withstand the very high feedwater pressure (100 bar).

The use of turbine steam (Table 3) brings about slightly lower cycle efficiencies (there were problems with our iterative procedure for  $w < 2\text{mm}$ ). However, the practical considerations of plant layout may well militate towards this option - in addition the coolant pressure is more tolerable. At  $w = 2\text{mm}$  the efficiency loss (0.59%) is worthy of economic analysis.

**Table 1 Impact of limiting temperature on cycle efficiency with co-current flow (feedwater as coolant). Throttle pressure = 310 bar. TCZ length = 200 m. Pipe diameters are  $d_i = 0.24$  m and  $d_o = 0.36$  m.**

$T_{limit}, ^\circ\text{C}$	Cycle efficiency, %	Coolant flow as fraction of $m_1$ , %	$T_2, ^\circ\text{C}$	$w_{tcz}$ , m
bypass	44.83	-	593.80	0.005
590	44.82	0.72	593.31	0.005
550	44.75	9.72	588.11	0.005
500	44.66	26.32	581.62	0.005
450	44.57	54.91	575.12	0.005
425	44.52	78.64	571.87	0.005

**Table 2 Impact of coating thickness on cycle efficiency with counter -current flow (feedwater as coolant). Different coating thickness,  $T_{limit} = 550^\circ\text{C}$ .**

Coating thickness, m	Cycle efficiency, %	Coolant flow as fraction of $m_1$ , %	$T_2, ^\circ\text{C}$	$T_{14}, ^\circ\text{C}$
bypass	44.83	-	593.8	-
0.005	44.67	3.088	582.2	509.7
0.003	44.60	5.012	577.6	482.9
0.001	44.39	43.93	562.9	338.6

## Discussion

The key finding is the apparently small reduction in cycle efficiency. Far more work remains to be done, but this first calculation reassures us that the impact of a TCZ is comparatively small and worthy of further investigation.

There are several areas in which the model is to be improved. No allowance was made for pressure losses in pipes. The use of additional channels in the form of cooling jackets will increase such losses and might well impact cycle efficiency.



**Table 3. Impact of coating thickness on cycle efficiency with counter-current flow (mid-turbine steam used as coolant, coolant is exhausted to the feedwater heater (modelled by a mixer).  $T_{\text{limit}} = 550^{\circ}\text{C}$**

Coating thickness, m	Cycle efficiency, %	Coolant flow as fraction $m_1$ , %	$T_2$ , °C	$T_{14}$ , °C
bypass	44.83	-	593.8	-
0.005	44.50	9.197	584.7	509.7
0.003	44.36	16.749	580.7	482.9
0.002	44.24	34.05	567.7	449.3

Practical cycles use a train of nine feedwater heaters (rather than mixers) and use at least single reheat and possibly double reheat. Use of steam properties at higher temperatures (up to  $720^{\circ}\text{C}$ ) is desirable; this requires care in implementation to deal with heat transfer coefficients and steam properties (particularly the supercritical heat transfer coefficients). Real world plant uses single-reheat at least and quite possibly double reheat. This doubles (or triples) the length of pipe requiring cooling while at the same time causing a commensurate efficiency loss. Engineering considerations include joining (nickel-based steels to austenitic steels), mechanical stresses, and stability of coatings.

A further issue is that steam temperatures will overshoot their set-point at start up. A dynamic simulation is desirable, although for economic analysis it is probably sufficient to apply a correction to the applied temperature limit.

The justification for implementing a TCZ is more strategic than economic. High temperature super-alloys (e.g. inconel-600) contain typically 72% by mass nickel and substantially more than steels such as P91 (8% by mass). Thereupon a future global movement towards A-USC risks making newly built power plant the principal user of nickel and unsustainable depletion of natural deposits. An approximate cost analysis hints that changing from P91 to inconel-600 increases costs at today's valuations. Approximately, the net additional cost per unit energy (in \$/GWh) is

$$c_{net} = -\frac{\Delta\eta}{\eta} p_{elec} + (\Delta c_{tp} + c_{jacket} + c_{tcz}) \frac{A M}{G} \quad 6$$

where  $p_{elec} = \$0.12/\text{kW hr}$  was taken as a typical price of electricity in the United States, paid by industrial consumers in the year 2017-2018. We considered a 0.5% change to a cycle efficiency of 50%. Also  $\Delta c_{tp} = 5.65 - 0.77 = \$4.88 \text{ kg}^{-1}$  is change in cost of the transport pipe, estimated from the change in the composition of raw materials and using mid-range prices in the year 2017-2018,  $c_{jacket}$  is the cost of a jacket, estimated as four times the material cost of the transport pipe ( $=4 \times \$0.77 \text{ kg}^{-1}$ ),  $c_{tcz}$  is the cost of ceramic ( $\$54 \text{ kg}^{-1}$ ), allowing for a 5-mm-thick layer of yttrium oxide.  $G$  is the electrical energy produced throughout a 30-year plant lifetime (typically in GW hr),  $M$  is the mass of transport pipe and  $A$  is an amortization factor ( $=1$  if there is no net rate of interest). The net additional cost of \$1202 per GW hr is dominated by the loss of revenue from electricity (\$1200). Further costs are the construction of a cooling jacket (\$8.61) and the cost of the coating (\$6.97) versus a saving of \$13.64 by replacing Inconel-600 with P91. These savings are uncertain because little modelling of the

long-run price of base metals is available [7]. Ahn [7] suggests that long-run prices have declined very slightly since 1900 (with sharp peaks from time to time, e.g. during global conflict) and that depletion of natural resources is compensated for by improvements in the productivity of extraction and processing.

## Conclusions

A simple supercritical plant with regenerative heating has been modelled. This first step in our work applies to supercritical pressures and temperatures although the temperatures are restricted to <600°C. (Future modelling will address very high temperatures > 700 °C.) It is demonstrated that the TCZ can reduce cycle efficiency in the range from 0.08% to 0.6%; the bigger efficiency losses are (not surprisingly) associated with thinner coatings. Two configurations have been tested. The use of boiler feedwater as coolant appears slightly more favourable but there may well be practical difficulties - e.g. manufacturing a cooling jacket to operate at ~100 bar. The loss of revenue from electricity far outweighs any savings in capital cost although future material prices are uncertain.

## Acknowledgements

Funding from the Engineering and Physical Sciences Research Council under grant EP/R000859/1 is gratefully acknowledged.

## References:

- [1] Marion J, Drenik O, Frappart C, Kluger F, Sell M, Skea A, Vanstonee R, Walker P. “Advanced ultra-supercritical steam power plants”. Proc. POWER-GEN Asia KLCC, Kuala Lumpur, Malaysia. 2014.
- [2] Retzlaff KM, Ruegger WA. “Steam turbines for ultrasupercritical power plants”. In POWER-GEN 1996 Aug (Vol. 98, pp. 9-11).
- [3] Weitzel PS. “Steam generator for advanced ultra supercritical power plants 700C to 760C”. In ASME 2011 Power Conference collocated with JSME ICOPE 2011 2011 Jan 1 (pp. 281-291). American Society of Mechanical Engineers.
- [3a] Yamagata K, Nishikawa K, Hasegawa S, Fujii T, Yoshida S. “Forced convective heat transfer to supercritical water flowing in tubes”. International Journal of Heat and Mass Transfer. 1972 Dec 1;15(12):2575-93.
- [4] Stöver D, Funke C. “Directions of the development of thermal barrier coatings in energy applications”. Journal of Materials Processing Technology. 1999 Aug 30;92:195-202.
- [5] Savage DW, Myers JE. “The effect of artificial surface roughness on heat and momentum transfer”. AIChE Journal. 1963 Sep 1;9(5):694-702.
- [6] Kamal S, Grandy C, Farmer M, Brunsvold A. “High strength and heat resistant chromium steels for sodium-cooled fast reactors”. Argonne National Lab., Argonne, IL (US); 2004 Dec 22.
- [7] Anh NB, Semenov A. “Trends of Base Metals Prices”. Theoretical Economics Letters. 2015 Jul 20;5(04):531

# Technical and thermodynamic evaluation of hybrid binary cycles with geothermal energy and biomass

D. Toselli\*, F. Heberle and D. Brüggemann

Chair of Engineering Thermodynamics and Transport Processes (LTTT),  
Center of Energy Technology (ZET), University of Bayreuth  
Universitätsstraße 30, 95447 Bayreuth, Germany

\*Corresponding author: [davide.toselli@uni-bayreuth.de](mailto:davide.toselli@uni-bayreuth.de)

## Abstract

Flexible power generation is an everyday diffused challenge that increasingly affects the German power grid due to rising shares of renewable resources. Enhancing renewable and flexible power generation is one of the most important topics in the so-called Energiewende agenda. The geothermal power plant in Oberhaching is taken as case study since it represents the typical Bavarian geothermal reservoir, with a gross power output equal to  $4.3 \text{ MW}_{\text{el}}$ . The task is to investigate the possibility to design a binary hybrid geothermal power plant and to integrate it into the German energy market, taking as secondary available resource exhaust gases coming from a biogas engine with an available thermal power equal to  $1365 \text{ kW}_{\text{th}}$ . Three main concepts are defined for the hybrid power plant: increasing the geothermal fluid temperature, superheating the working fluid and assuming an additional evaporator where the working fluid is heated only by exhaust gases. Stationary and quasi-stationary simulations have been performed with Aspen Plus 8.8. The results demonstrate how the hybridization allows an increase of electric power of approximately  $250 \text{ kW}_{\text{el}}$ , depending on the followed layout. Off-design conditions are investigated regarding both the unavailability of exhaust gases and the yearly ambient temperature variations. Since the available extra thermal power is not sufficient to comply with the minute reserve market requirements, other possible solutions are investigated. A storage system is firstly applied and, furthermore, the extra thermal power is increased, redefining thus the secondary resource as exhaust gases from a solid biomass power plant. The two proposed solutions allowed separately reaching the two main requirements asked by the minute reserve market: a nominal power equal to  $5 \text{ MW}_{\text{el}}$  and  $1 \text{ MW}_{\text{el}}$  as power granularity.

**Keywords:** Geothermal, Biomass, Flexible power generation, Minute reserve market

## Introduction/Background

Nowadays, ORC geothermal applications allow exploiting even low-enthalpy geothermal fluids (Ennio Macchi, 2015). These applications result interesting since they run on renewable resources and have a very high capacity factor (Ennio Macchi, 2015). In order to increase the nominal power, hybrid geothermal concepts have been proposed, especially considering solar as second available source. The Stillwater triple hybrid power plant, built by Enel Green Power, exploits a geothermal reservoir with additional power provided by a CSP and PV field [2]. Heberle et al. [3] also investigated the possibility to use solar thermal power to superheat the organic working fluid. In addition, also biomass has been considered as possible second available source. Enel Green Power [4] hybridized the existing geothermal power plant Cornia 2 with a biomass combustor, providing an overall power increase of  $5 \text{ MW}_{\text{el}}$ . In this case, the second available source is used to superheat the geothermal steam. The development of geothermal and biomass hybrid systems was also investigated in Japan according to Yoshinobu et al. [5]: the additional resource allows

exploiting a geothermal reservoir even if its fluid temperature is generally too low to be economically interesting. DiPippo et al. [6] investigated three different hybrid layouts at Rotokawa I power plant in New Zealand: the most promising is a biomass power plant which takes advantages of geothermal energy to enhance its performance. Several geothermal and biomass hybrid concepts were also investigated according to economic aspects by Srinivas et al. [7]. The increasing shares of renewables in today's energy market leads to the need of flexibility. The German energy market is divided into: primary reserve, secondary reserve and minute reserve, as shown by Just et al. [8]. Actually, the last one requires the energy producer to provide at least a nominal power of 5 MW<sub>el</sub> and a power granularity of 1 MW<sub>el</sub> [8]. According to this background, hybrid geothermal and biomass systems can represent a key-factor in order to reach both environment-friendly and flexible power generation.

### Boundary Conditions

The evaluated power plant models are created assuming the geothermal reservoir in Oberhaching as primary resource. In fact, it can be considered as a typical Bavarian geothermal reservoir with liquid fluid. The biogas exhaust gases represent the second available resource and a GE Jenbacher JMS 620 GS-B.L is considered as engine model. The main boundary conditions of the two sources are resumed in Table 1:

**Table 1:** Assumed boundary conditions.

Geothermal Fluid		Biogas Exhaust Gases	
Pressure (bar)	10	Inlet Temperature(°C)	467
Mass Flow (kg/s)	150	Outlet Temperature (°C)	180
Temperature (°C)	130	Available Power (kW <sub>th</sub> )	1365

Three different power plant layouts (Concepts A, B and C) are proposed and investigated.

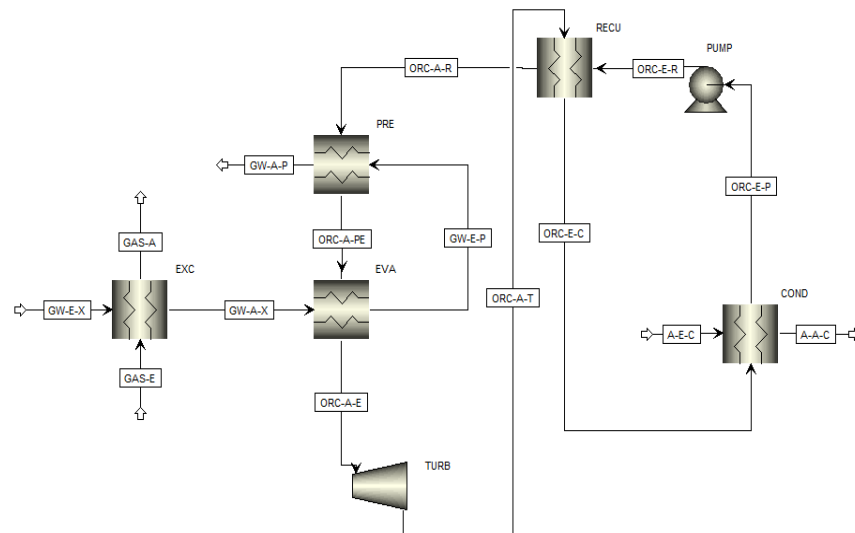


**Figure 1:** Concept A layout: the geothermal fluid is superheated through exhaust gases.

In Figure 1 the layout of concept A is shown. Starting from the typical binary configuration, an additional heat exchanger (EXC) is introduced, in order to increase the geothermal fluid temperature while exploiting the exhaust gases. In Figure 2, concept B relies on exploiting exhaust gases to superheat the organic fluid (SH).

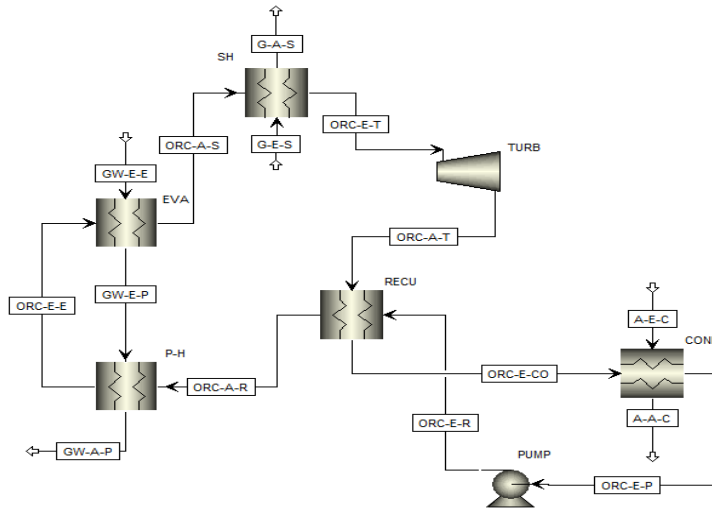


**Figure 2:** Concept B layout: the working fluid is superheated throughout exhaust gases.

The third case, concept C, is presented in Figure 3: two different evaporators (E-GW and E-G) are designed to separately exploit the two available sources.

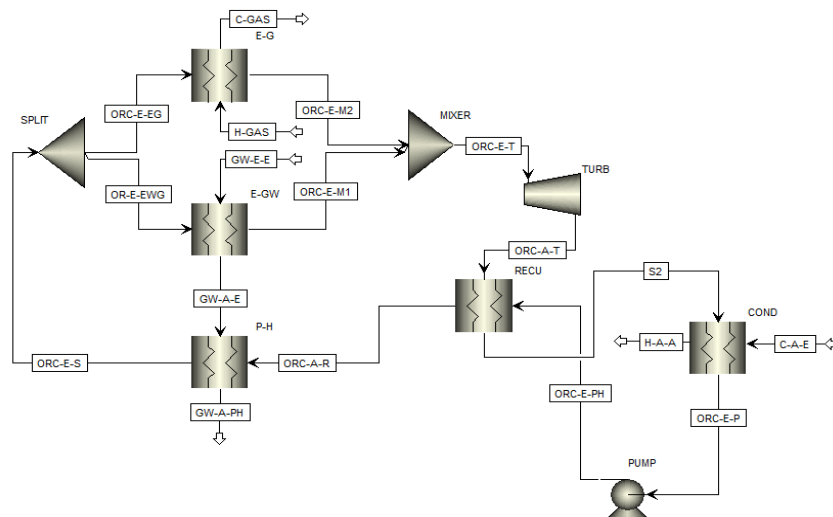


**Figure 3:** Concept C layout: part of the working fluid reaches evaporation throughout exhaust gases exploitation.

### On-Design Model

The on-design model requires several assumptions which are reasonably defined according to Astolfi et al. [9] and resumed in the following table:

**Table 2:** Boundary conditions in assumed layout.

Parameter	Value	Parameter	Value
Evaporator $\Delta T_{pp}$ (K)	5	ACC inlet T ( $^{\circ}$ C)	10
Condenser $\Delta T_{pp}$ (K)	5	ACC outlet T ( $^{\circ}$ C)	25
Recuperator $\Delta T_{pp}$ (K)	5	Turbine efficiency (%)	84
Pump Efficiency (%)	70	Generator efficiency (%)	95

The thermal efficiency of the power plant is calculated according to the following equation:

$$\eta = \frac{\dot{W}_{turb} - \dot{W}_{pump}}{\dot{Q}_{th}} \quad (13)$$

### *Off-Design Model*

The models presented in this work are simulated according to a constant pressure at the pump. In addition, pump efficiency variations are neglected. On the other hand, turbine efficiency variations are considered through the set of equations provided by Ghasemi et al. (Ghasemi, Sheu, Tizzanini, Paci, & Mitsos, 2014). Many cases are calculated considering only the off-design condition of the turbine. Extended off-design evaluations are further considered according to the procedure provided by Toffolo et al. [11]. The following parameters are used to compare on- and off-design:

$$\text{Flexibility Coefficient} = \frac{\dot{W}_{turb-on-des}}{\dot{W}_{turb-off-des}}, \quad (14)$$

$$\Delta\dot{W} = \dot{W}_{turb-on-des} - \dot{W}_{turb-off-des} \quad (15)$$

## **Discussion and Results**

### *Fluid Comparison*

Two potential ORC working fluids are considered for the ORC module. In respect to existing power plants, in the simulations R245fa and R600a are investigated. All the aforementioned power plant layouts are performed with both working fluids, defining the on-design for each example. In concept A, R600a reaches a turbine power of 4594 kW<sub>el</sub> at 14.8 bar with 10.24 % as thermal power plant efficiency. On the other hand, R245fa provides only 4292 kW<sub>el</sub> at 8.3 bar, but with a slightly higher thermal power plant efficiency equal to 10.34 %. Very similar trends are found both in Concept B and C. According to these results, the further cases are performed with R600a as selected working fluid.

### *Defining the On-Design*

In all the three concepts, a sensitivity analysis is performed while varying the pressure at the pump. Therefore, the on-design is chosen as the point with the maximum turbine power output. The reinjection temperature is considered as a variable. According to the assumed boundary conditions and to the chosen layout, concept A and C provide the same results. In Table 3, a comparison between concept A and B shows that increasing the geothermal fluid temperature maximizes the turbine power output. In concept B, a superheating degree of 5.7 °C is assumed.

**Table 3:** Main results regarding Concept A and Concept B in on-design.

Concept	Turbine Power as On-Design (kW <sub>el</sub> )	Evaporating Pressure (bar)	Power Plant Efficiency (%)	Reinjection Temperature(°C)
A	4594	14.8	10.24	66.3
B	4500	14.6	10.41	68.5

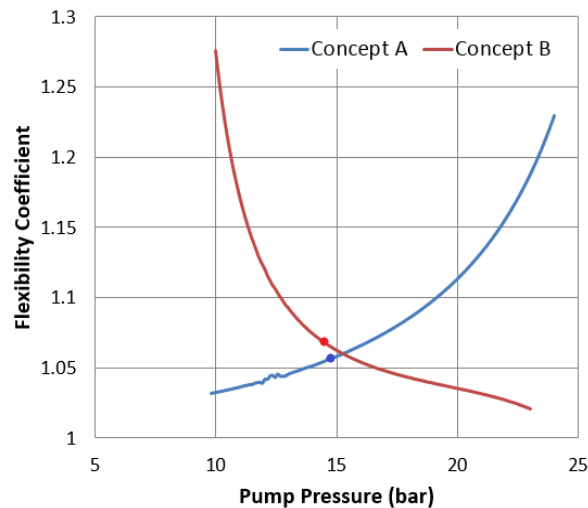
### *Off-Design Behaviour of the Turbine*

Regarding the hybrid concept and its flexibility, it is reasonable to investigate a decoupling of the exhaust gases. This off-design case is performed for the different considered layouts. Since turbine efficiency is variable in off-design, a suitable set of equations is adopted for these examples (Ghasemi, Sheu, Tizzanini, Paci, & Mitsos, 2014). As first step, this procedure is applied maintaining constant pinch point temperatures in the heat exchangers and with the same on-design evaporating pressure. This approach seems valuable, since exhaust gases only represent about 3 % of the total thermal available power. The main results are shown in the following Table 4.

**Table 4:** Turbine off-design main results.

Concept	Turbine Power Off-Design ( $kW_{el}$ )	Turbine Off-Design Efficiency (%)	Flexibility Coefficient	Power Variation ( $kW_{el}$ )
A	4349	83.76	1.056	245
B	4212	81.06	1.068	288

Turbine efficiency in concept A decreases only 0.24 % while 2.94 % is found in concept B. This is a direct consequence of the followed power plant flow sheet. Moreover, concept B provides a higher power flexibility relying on the higher drop in turbine efficiency. In Figure 4, a sensitivity analysis is conducted to show the different flexibility coefficient trends in the two considered cases. As it could be noticed, the two trends are completely different. In Concept B the off-design case provides a higher flexibility at low pressures (generally up to 15 bar). On the other hand, concept A is more flexible than concept B at high pressures. The two curves cross over at approximately 15 bar. Since the on-design points are found before this value, B results more flexible than A. Moreover, it clearly appears how these examples can provide a negative reserve while switching at off-design.

**Figure 4:** Flexibility coefficient in concept A and B as a function of the evaporating pressure. The two points represent the on-designs

### *Complete Off-Design*

A complete off-design is here investigated, according to the procedure proposed by Toffolo et al. [11] and results are summarized in Table 5. Turbine efficiency in concept A becomes slightly higher than in the previous evaluated off-design. Since both pinch point temperatures in evaporator and condenser decrease, the current off-design point of the turbine gets closer to the on-design one. No particular variations affect concept B and its flexibility.

**Table 5:** Off-design results in concept A and B.

Concept	Turbine Power ( $kW_{el}$ )	Turbine Efficiency (%)	Flexibility Coefficient
A Off-Design	4410	83.85	1.041
B Off-Design	4202	81.05	1.071

### *Turbine Off-Design due to seasonality*

During the year, since an air-cooled condenser is assumed, ambient temperature changes affect the power plant outputs. The on-design ambient temperature is set equal to 10 °C, according to the average yearly temperature in Southern Germany. At very low temperatures,

the condensing pressure is limited to prevent further losses in turbine efficiency. While varying the ambient temperature, the off-design is firstly applied only at the turbine. Moreover, both availability and unavailability of exhaust gases are investigated while varying the ambient temperature in both concepts A and B. In Figure 5 and Figure 6 the difference in turbine power output is shown for both concepts: in A the highest flexibility is reached at 10 °C (on-design) with 250 kW power difference while in B major flexibility is available at lower temperatures with almost 500 kW.

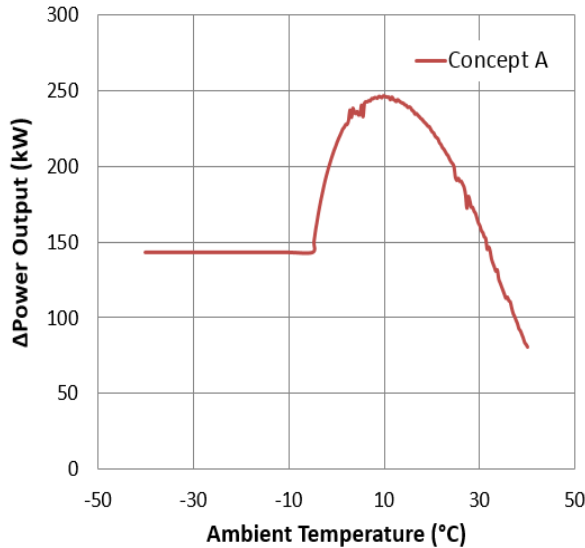


Figure 5: Power variation as a function of the ambient temperature in concept A.

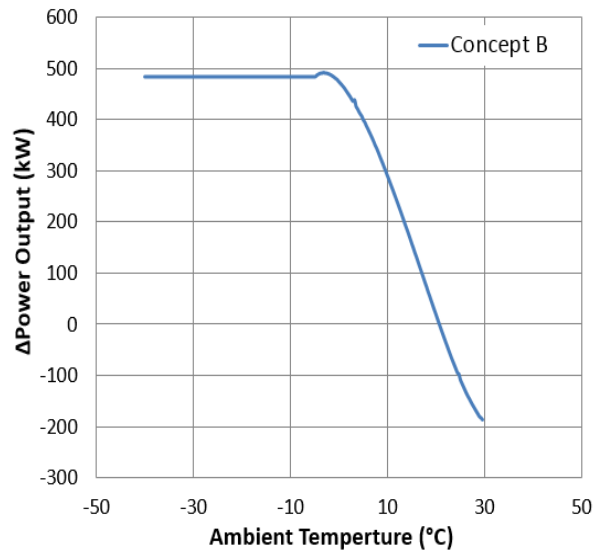


Figure 6: Power variation as a function of the ambient temperature in concept B.

These results allow to consider that a certain model flexibility can vary during the year as a function of the ambient temperature with not negligible consequences over the entire results.

### Integration of a Storage System

Nowadays market flexibility requirements are ruled according to different reserves, such as the secondary reserve and the minute reserve [8]. The minute reserve (MRL), for example, requires a power granularity equal to 1 MW<sub>el</sub> for at least 4 hours. In the previous calculations, due to the assumed thermal power, it is not actually possible to reach a power granularity of 1 MW<sub>el</sub>. Without entering in merit, it is assumed that the considered power plant fits the dynamical requirements of the MRL [12]. Consequently, applying a storage system could appear as an interesting solution to fulfill the requirements of the MRL. The thermal storage system is assumed as virtual, avoiding any thermal losses. It is worthwhile to consider that this different design could be a “key-pathway” to create an even more flexible power plant, entering another market reserve. The daily evaluation is divided into two different parts: the storing phase (20 h) and the extra power phase (which lasts 4 h according to MRL). Since the storing phase is way longer than the extra-power one, the former is assumed as the on-design one. Concept C is chosen as the most promising design to be evaluated according to this application. For a wider evaluation, also an off-design analysis is investigated. The evaporating pressure is assumed constant at 14.8 bar. In Table 6 the main results are summarized. It could be noticed how switching to a complete off-design with the same evaporating pressure, the turbine power decreases. In order to match the required UA at the condenser, the condensing pressure raises lowering the turbine power output. Consequently, an additional case was evaluated optimizing the evaporating pressure: an increase of 1 bar leads to the required power granularity.



**Table 6:** Main results in concept C evaluated with a storage system .

Case	Turbine Power ( $\text{kW}_{\text{el}}$ )	Volume Split (%)	Turbine Efficiency (%)	Exhaust Gases ( $\text{kW}_{\text{th}}$ )	Evaporating Pressure (bar)
On-Design	4360	/	84	/	14.8
Turbine Off-Design	5360	20	82.73	6380	14.8
Off-Design	5237	19.8	83.17	6380	14.8
Off-Design-optimized	5370	21	83.28	6380	15.8

Since MRL requires  $1 \text{ MW}_{\text{el}}$  for at least 4 hours, it means that the total storage capability needs to be about  $25520 \text{ kWh}_{\text{th}}$ , which is approximately 78 % of the entire daily thermal power provided by the exhaust gases.

#### *Solid Biomass Example*

In order to enter the minute reserve market, each power plant is required to provide a minimum nominal power of  $5 \text{ MW}_{\text{el}}$ . Up to now, simulations have always been performed according to  $1365 \text{ kW}_{\text{th}}$  as thermal input in form of biogas exhaust gases, complying with the chosen biogas engine (JMS 620 GS-B.L). Supposing now to increase the thermal input throughout a sensitivity analysis, further simulations are performed: the intent is to reach the required nominal power equal to  $5 \text{ MW}_{\text{el}}$ . A new case is now simulated assuming a thermal available power equal to  $3780 \text{ kW}_{\text{th}}$ : it could be assumed as the usual amount provided by the typical biomass power plant size (Ennio Macchi, 2015). The main results provided by the simulations are resumed in Table 7:

**Table 7:** Main results in concept A considering solid biomass as the second available source.

Case	Turbine Power ( $\text{kW}_{\text{el}}$ )	Turbine Efficiency (%)	Evaporating Pressure (bar)
On-Design	5015	84	15.5
Turbine Off-Design	4280	82.86	15.5
Off-Design	4455	83.35	15.5

The complete off-design provides higher power output since pinch point temperatures both at the condenser and evaporator decrease. The nominal power is now barely higher than  $5 \text{ MW}_{\text{el}}$ . The flexibility coefficient results 1.17 while delta power is equal to  $735 \text{ kW}_{\text{el}}$ . Of course, a higher flexibility is now obtained than in previous examples due to the higher amount of thermal power. Turbine efficiency decrease is now more affected than in concept A.

#### **Summary/Conclusion**

This work aims to provide a valuable and extended overview regarding the possibility to realize a binary hybrid power plant which exploits geothermal energy and exhaust gases coming from a biogas engine. Three different power plant layouts are investigated, showing how not only the major turbine power output is important, but also the capability to provide flexible power appears valuable to get into the minute reserve market. The considered boundary conditions, assumed as typical from the Southern German background, do not allow reaching the main minute market reserve requirements ( $5 \text{ MW}_{\text{el}}$  as nominal power and  $1 \text{ MW}_{\text{el}}$  as power granularity). Consequently, two different ways are followed to at least separately reach these two targets. The former consists into a storage system which is assumed to demonstrate that  $1 \text{ MW}_{\text{el}}$  as power granularity can be reached, exploiting about 78

% of the daily extra thermal power. The latter relies on adopting solid biomass as secondary source, with a thermal power equal to 3780 kW<sub>th</sub>. In conclusion, the proposed hybrid systems can represent valuable solutions to exploit rural renewable sources in Germany, providing also additional flexibility to the national grid.

### Acknowledgments

This work has been partially founded by the Bavarian State Ministry of Education, Science and the Arts in the framework of the project “Geothermie-Allianz Bayern”. The authors gratefully acknowledge this support.

### References

- [1] Macchi, E., Astolfi, M., *Organic Rankine Cycle (ORC) Power Systems - Technologies and Applications*, Woodhead Publishing, 2015, London, UK.
- [2] DiMarzio, G., Angelini, L., Price, W., Chn, C., Harris, S. *The Stillwater Triple Hybrid Power Plant: Integrating Geothermal, Solar Photovoltaic and Solar Thermal Power Generation*, in Proceedings World Geothermal Congress 2015, Melbourne, Australia, April 2015.
- [3] Heberle, F., Hofer, M., Ürlings, N., Schröder, H., Anderlohr, T., Brüggemann, D., *Techno-economic analysis of a solar thermal retrofit for an air-cooled geothermal Organic Rankine Cycle power plant*, Renewable Energy, vol. 113, pp. 494-502, March 2017.
- [4] Font, V., *World's First Integrated Geothermal and Biomass Plant Goes Online*, Renewable Energy World, 3 August 2015, Woodbury, MN, USA.
- [5] Yoshinobu, N., Hideshi, K., Yoshihiro, M., Tetsushiro, I., Masanao, I., Yutaka, W., *Development of Hybrid Geothermal Power Plants Combined with other Thermal Energy Sources*, in Proceedings World Geothermal Congress, Melbourne, Australia, 2015.
- [6] Thain, I., DiPippo, R., *Hybrid Geothermal-Biomass Power Plants: Applications, Designs and Performance Analysis*, in Proceedings World Geothermal Congress, Melbourne, Australia, 2015.
- [7] Srinivas, S., Eisenberg, D., Seifkar, N., Leoni, P., Paci, M., Field, R., *Simulation-Based Study of a Novel Integration: Geothermal-Biomass Power Plant*, Energy&Fuels, vol. 28, pp. 7632-7642, 2014.
- [8] Just, S., *The German Market for System Reserve Capacity*, University of Duisburg-Essen, Duisburg-Essen, 2015.
- [9] Astolfi, M., Romano, M., Bombarda, P., Macchi, E., *Binary ORC (organic Rankine cycles) power plants for the exploitation of medium-low temperature geothermal sources - Part A: Thermodynamic optimization*, Energy, vol. 66, pp. 423-434, 2014.
- [10] Ghasemi, H., Sheu, E., Tizzanini, A., Paci, M., Mitsos, A., *Hybrid solar-geothermal power generation: optimal retrofitting*, in Applied Energy, Elsevier, 2014, pp. 158-170.
- [11] Toffolo, A., Lazzaretto, A., Manente, G., Paci, M., *An Organic Rankine Cycle off-design model for the search of the optimal control strategy*, in Proceedings of ECOS, Perugia, Italy, 2012.
- [12] Baresi, M., *ORC turbogenerators-Turboden experience from R&D to industrial projects*, Brussels, 23rd September, 2015.

# Experimental Analysis of a Regenerative Organic Rankine Cycle using Zeotropic Working Fluid Blends

Peter Collings<sup>1</sup>, Andrew McKeown<sup>1</sup> and Zhibin Yu<sup>1\*</sup>

University of Glasgow, University Avenue, Glasgow G12 8QQ, UK

\*Corresponding author: [zhibin.yu@glasgow.ac.uk](mailto:zhibin.yu@glasgow.ac.uk)

## Abstract

The Organic Rankine Cycle (ORC) has been identified as the most promising technology for exploiting heat sources at temperatures lower than 200°C. There is a lack of published literature on experimental analysis of ORCs, and most of this focuses on pure working fluids and non-regenerative cycles. The motivation for this paper is to address the gap in the literature by constructing a small-scale regenerative ORC test rig capable of being charged with a mixture of the working fluids R245fa and R134a, and comparing the obtained results with numerical predictions. The key findings were that the cycle efficiency increased with the implementation of the regenerative cycle, and that adding a secondary component to the working fluid with a higher vapour pressure increased the temperature glide, however, it only caused an increase in efficiency for the lower heat source temperatures. The maximum net efficiency of the cycle was 8.61% with a heat source temperature of 95°C and a working fluid composed of pure R245fa.

**Keywords:** Organic Rankine Cycle, Zeotropic, Regenerative, Experimental

## Introduction/Background

A large amount of thermal energy is contained in low-temperature sources such as industrial process streams [1] [2], solar thermal [3] [4], geothermal [5] [6] (Astolfi M. , Romano, Bombarda, & Macchi, 2014), bottoming cycles for heat engines [8] [1] and biomass [9] [10] [11]. The majority of these heat sources exist at temperatures lower than 130°C [12]. The Organic Rankine Cycle is currently considered to be the most economic means of extracting useful power from these low temperature heat sources [1], however, it does face certain challenges. Chief among these are low efficiency, generally lower than 10% [13] [14] although this varies with the heat source temperature, high capital cost [15] and a lack of suitable working fluids [16].

Table 1: Representative comparison of experimental Organic Rankine Cycles reported in the literature

Author	Working Fluid	Regen	Heat Source	Expander	Power	Efficiency
Peris et al [17]	R245fa	Yes	165°C	Scroll	7.5 kW	8.8%
Wang et al [18]	R245fa	No	115°C	Piston	1.73kW	4.2%
Pu et al [19]	Pure R245fa/ Pure HFE7100	No	100°C	Turbine	1.98kW	4.01%
Quoilin et al [20]	R123	No	165°C	Scroll	1.8kW	9.9%
Navarro-Esbrí et al [21]	HFO-1336mzz-Z	Yes	160°C	Scroll	1.1kW	8.3%
Jung et al [22]	R245fa/ 365mfc	No	160°C	Scroll	0.47kW	3.1%
Abadi et al [23]	R245fa/R134a	No	120°C	Scroll	1.4kW	7%

Table 1 presents a brief comparison of pre-existing experimental research on the Organic Rankine Cycle. From this information it can be seen that previous research has focused mainly on non-regenerative cycles and pure working fluids. There does not appear to be any

previous experimental research comparing the effects of regenerative and non-regenerative cycles in the same system, zeotropic working fluids have been investigated there were no studies investigating the effect of progressively changing the working fluid composition on a single system. A MATLAB model was developed using REFPROP 9.1 [24], and was used to design a system capable of investigating the effects of these two key parameters. Using the data from this model a 1kW experimental rig, as shown in Figure 1 was built and tested in both regenerative and non-regenerative configurations across a range of working fluid compositions, heat source temperatures and pressure ratios to provide an experimental characterisation of how a real system reacts to variation in these parameters, compared to theoretical predictions.

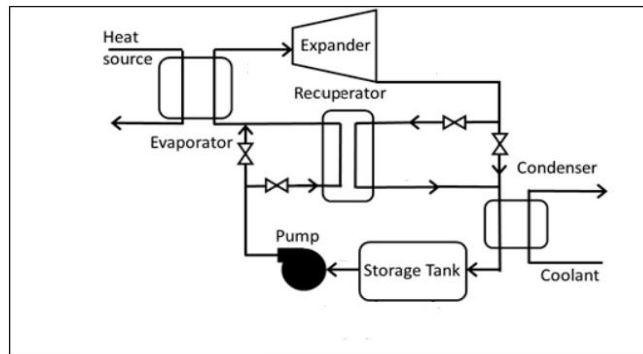


Figure 1: Schematic Diagram of the Organic Rankine Cycle Rig used in this research.

## Discussion and Results

In this section the results of the experimental analysis are presented. Of particular interest are the response of the cycle to being put into a regenerative configuration, and to the introduction of a secondary working fluid component to create a zeotropic mixture.

Figure 2 shows how the efficiency of the cycle varies with changing heat source temperature for both the regenerative and non-regenerative configurations. It can be seen that for lower heat source temperatures the difference in efficiency between the two cycles is slight, with the non-regenerative cycle having an efficiency of 0.4%, and the regenerative cycle having an efficiency of -0.7%, meaning that the pump consumed more power for this case than the generator produced. However, the efficiencies for the two cycles increase and diverge as the heat source temperature increases. The possible reasons for this will be investigated over the following few figures.

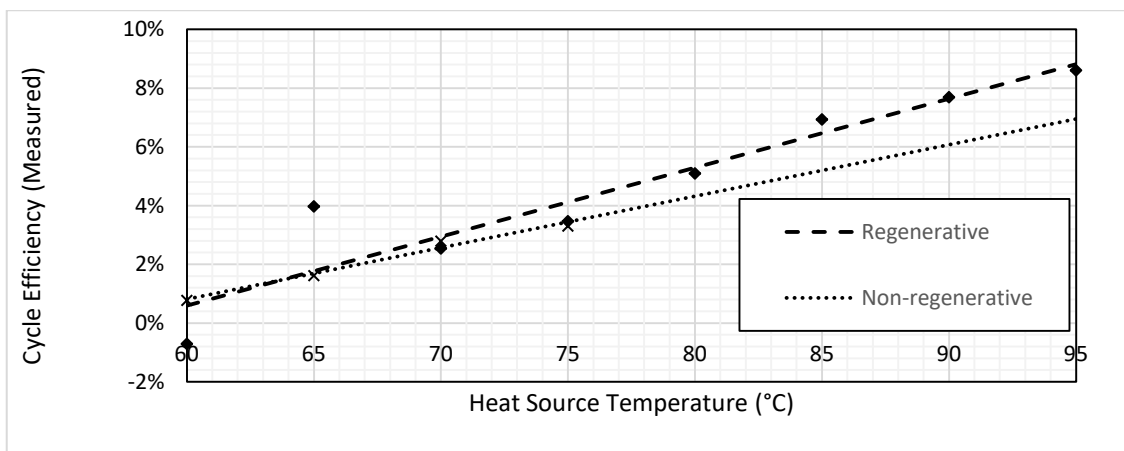


Figure 2: Comparison of maximum cycle efficiency with varying heat source temperature between regenerative and non-regenerative cycles.

As the measured efficiency is obtained by simply dividing the net power output of the cycle by the heat input in the evaporator, the change in the efficiency must be caused by a variation in one of these parameters. Figure 3 shows the variation in power output from the generator for the regenerative and non-regenerative cycles. It can be seen that the output power from both cycles increases with increasing temperature, and that the output power of the regenerative cycle increases more quickly than that of the non-regenerative cycle, resulting in a higher net output power for the regenerative cycle at the highest heat source temperatures. It is clear from this that the increasing net power output could be at least partially responsible for the trend observed in Figure 2. Two potential causes for this were considered. Firstly, a greater drop in specific enthalpy across the expander caused by a higher pressure drop, secondly, a greater mass flow rate in the cycle.

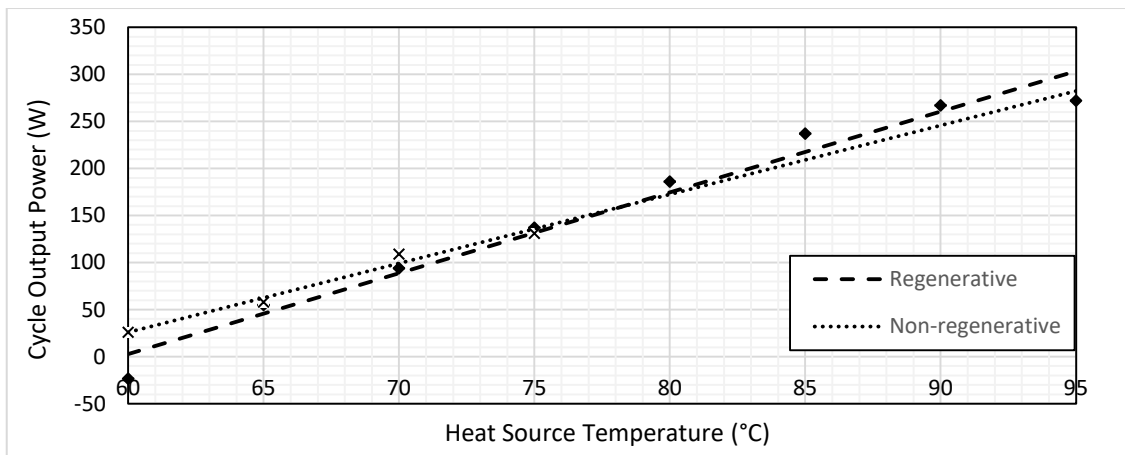


Figure 3: Comparison of cycle output power with varying heat source temperature between regenerative and non-regenerative cycles.

Figure 4(a) shows the variation in the expander inlet pressure for the regenerative and non-regenerative cycles. It can be seen that the pressure is generally higher for the non-regenerative case, which is consistent with there being a loss in pressure as the working fluid passes through the heat exchanger. Figure 4(b) shows the variation in the mass flow rate for the regenerative and non-regenerative cycles with changing heat source temperature. It can be seen that the working fluid mass flow rate increases with increasing heat source temperature in both cases, therefore the working fluid flow rate can be discounted as the cause of the trend observed in Figure 3.

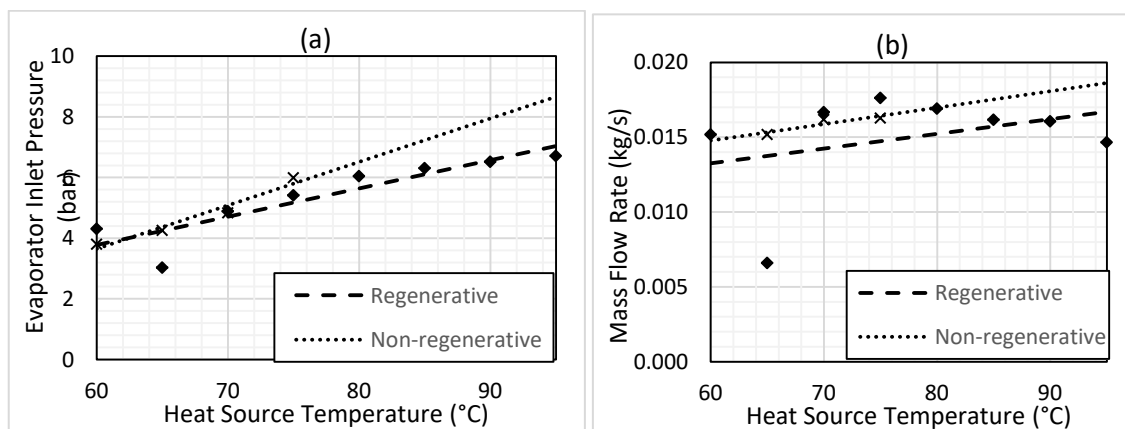


Figure 4: Comparison of evaporator pressure with varying heat source temperature between regenerative and non-regenerative cycles, and Comparison in working fluid mass flow rate with changing heat source temperature between the regenerative and non-regenerative cycles

A further theory was that the heat exchangers were undersized, resulting in the non-regenerative case not being able to reach as high a temperature at the expander inlet. Figure 5 shows the variation in the expander inlet temperature with varying heat source temperature for the regenerative and non-regenerative cases. It can be seen that the trends are very similar for both cases, which means that it is most likely not the cause of the trend seen in Figure 2.

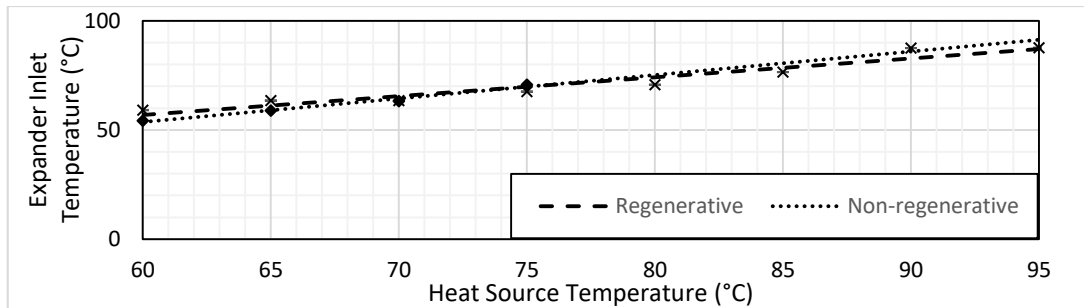


Figure 5: Comparison of expander inlet temperature with changing heat source temperature between the regenerative and on-regenerative cycles

Figure 6 shows the variation in the evaporator heat loading with changing heat source temperature for the regenerative and non-regenerative cycles. The non-regenerative cycle has a higher heat input for all of the heat source temperatures considered, and the two cycles diverge with increasing heat source temperature, with the non-regenerative cycle requiring an even greater heat input relative to that of the regenerative cycle.

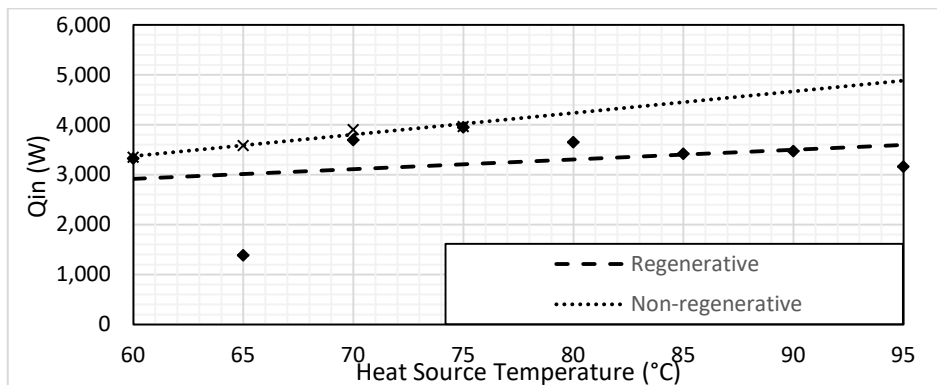


Figure 6: Comparison of Evaporator Heat Transfer ( $Q_{in}$ ) with varying heat source temperature between the regenerative and non-regenerative cycles

Figure 7 shows the variation in the enthalpy transfer in the regenerator with varying heat source temperature. A steady increase in the enthalpy transfer can be seen, as the greater expander inlet temperature results in a higher expander outlet temperature, meaning more heat can be scavenged from the expander exhaust to preheat the working fluid.

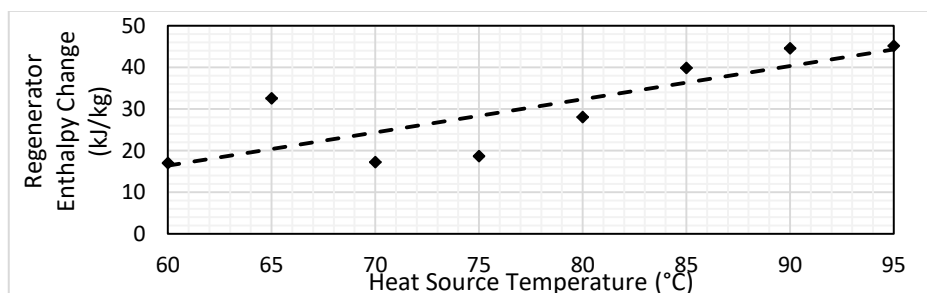


Figure 7: Variation in regenerator enthalpy transfer with changing heat source temperature

One outlying point can be seen in the efficiency plot in Figure 2, with the heat source temperature of 65°C having a higher efficiency than would be expected from observing the trend of the other point. From Figure 4 and Figure 7 it can be seen that the root cause of this is a decrease in the mass flow rate of the cycle, without a corresponding drop in the output power. The reasons for this are unclear from the collected data, and merit further investigation.

The next section examines the effect on the cycle of changing the working fluid composition. R134a was progressively added to the cycle to change its composition up to a mass fraction of 30%, and the data recorded. Figure 8 shows how the cycle efficiency varies with changing working fluid composition. It can be seen that there is a slight increase in efficiency with increasing R134a proportion for the lower heat source temperatures, whereas there is a slight decrease for the highest heat source temperatures. To investigate the causes of these trends, the output power and the evaporator heat demand must be considered, as for the case previously examined for pure R245fa.

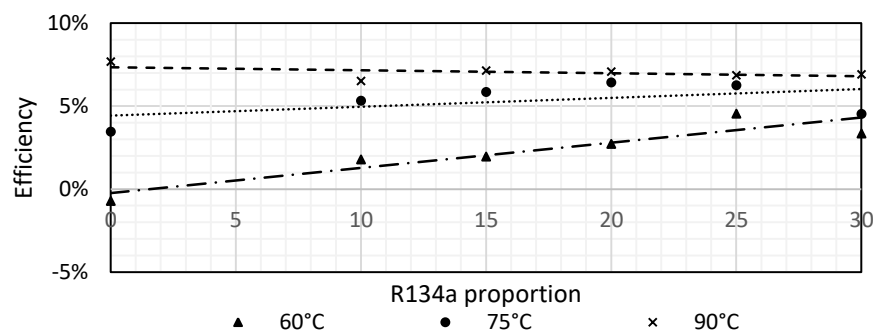


Figure 8: Variation in cycle efficiency for three different heat source temperature with changing working fluid composition

Figure 9 shows how the cycle's output power varies with increasing proportion of R134a in the working fluid. For the heat source temperature of 60°C there is a steady increase in the output power of the cycle with increasing R134a, for the heat source temperature of 75°C there is no overall trend, and for the heat source temperature of 90°C there is an overall downward trend in cycle power with increasing R134a.

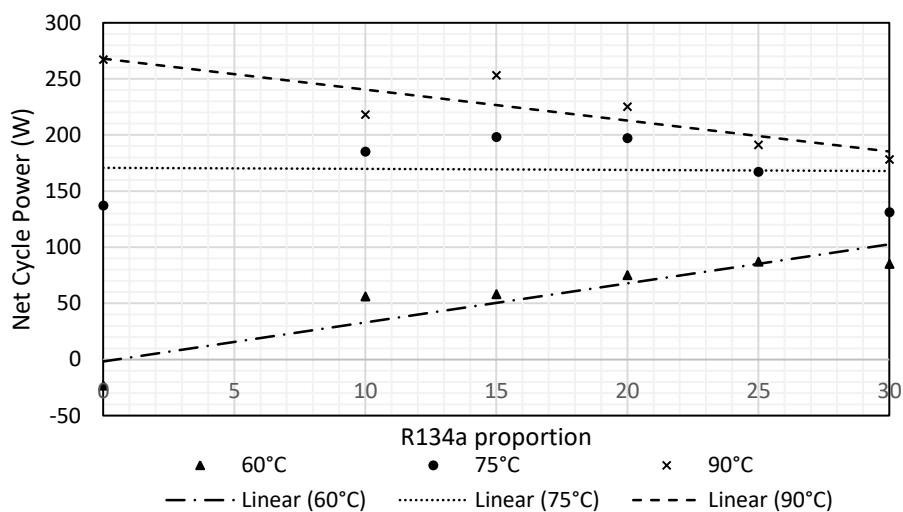


Figure 9: Variation in net cycle power output for three different heat source temperature with changing working fluid composition

Figure 10 shows how the cycle pressure ratio varies with changing working fluid composition. It can be seen that although the pressure ratio decreases with increasing proportion of R134a in the working fluid due to its higher vapour pressure, the effect is more pronounced for the higher heat source temperatures. The plot for a heat source temperature of 75°C begins above 3.5, and finished below 3.5. It is thought that this transition through the built-in volume ratio of the expander is responsible for the power output peaking at 15% R134a, as the cycle changes from under-expansion to over-expansion.

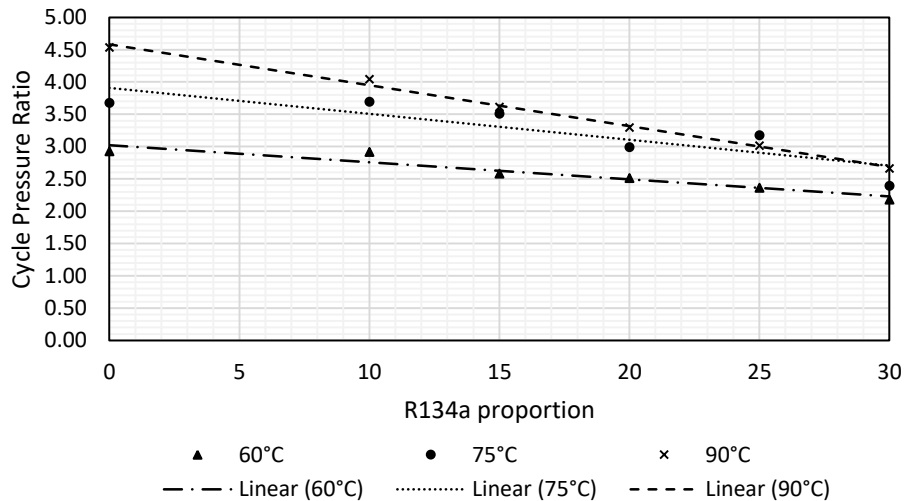


Figure 10: Variation in cycle pressure ratio for three different heat source temperatures with changing working fluid composition.

Figure 11 shows the variation in the evaporator enthalpy change with changing working fluid composition. While there is no obvious trend in the plots for the heat source temperatures of 90°C and 75°C, the plot for 60°C shows an obvious decrease in the specific enthalpy change as the working fluid composition shifts towards R134a.

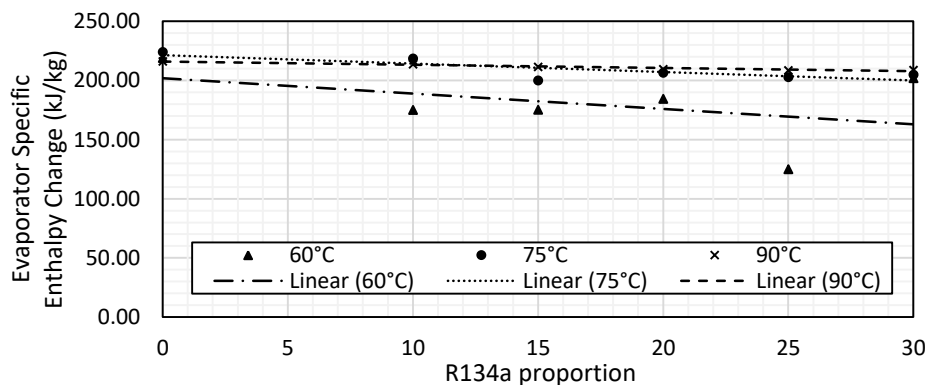


Figure 11: Variation in evaporator enthalpy change for three different heat source temperatures with a changing working fluid composition.

## Summary/Conclusions

This paper used a 1kW experimental rig to investigate the effects on an Organic Rankine Cycle of adding a regenerative heat exchanger and varying the working fluid composition. It was found that the addition of a regenerator caused a significant increase in the efficiency of the cycle, and that this increase was more significant at higher heat source temperatures. It also found that this increase in efficiency was primarily due to a reduction in the heat demand in the evaporator.



Changing the working fluid composition had differing effects depending on the heat source temperature. For all heat source temperatures the power output of the cycle decreased due to decreasing pressure ratio. However, for lower heat source temperatures this was counteracted by a decrease in the evaporator heat demand, resulting in a net increase in efficiency, perhaps due to the working fluid's critical point being shifted closer to the heat source temperature.

Further research highlighted by these results include investigation of the heat transfer processes in the evaporator, regenerator and condenser, and also the expansion process, in order to determine with certainty the reasons for the observed trends.

### **Acknowledgements**

Funding for this project was provided by Innovate UK and the EPSRC

### **References:**

1. Larjola, J., Electricity from Industrial Waste Heat using High-Speed Organic Rankine Cycle (ORC). 1995, *International Journal of Production Economics*, Vol. 41, pp. 227-235.
2. Cayer, E., Galanis, N. and Nesreddine, H., Parametric Study and Optimisation of a Transcritical Power Cycle Using a Low-Temperature Heat Source. 2010, *Applied Energy*, Vol. 87, pp. 1349-1367.
3. Zhang, X. R. et al., Theoretical Analysis of a Thermodynamic Cycle for Power and Heat Production Using Supercritical Carbon Dioxide. 4, April 2007, *Energy*, Vol. 32, pp. 591-599.
4. Wu, Dan, et al., Optimisation and Financial Analysis of an Organic Rankine Cycle Cooling System Driven by Facade Integrated Solar Collectors. 2017, *Applied Energy*, Vol. 185, pp. 172-182.
5. Walraven, Daniël, Laenen, Ben and D'haeseleer, William. Minimising the levelised cost of electricity production from low-temperature geothermal heat sources with ORCs: Water or air cooled? 2015, *Applied Energy*, Vol. 142, pp. 144-153.
6. Liu, Xinghua, Zhang, Yufeng and Shen, Jiang. System Performance Optimisation of ORC-based geo-plant with R245fa under different geothermal water inlet temperatures. 2017, *Geothermics*, Vol. 66, pp. 134-142.
7. Astolfi, Marco, et al., Binary ORC (organic Rankine cycles) power plants for the exploitation of medium-low temperature geothermal sources - Part A: Thermodynamic optimisation. 2014, *Energy*, Vol. 66, pp. 423-434.
8. Hung, T.C., Shai, T.Y. and Wang, S.K., A review of Organic Rankine cycles (ORCs) for the recovery of low-grade waste heat. 7, July 1997, *Energy*, Vol. 22, pp. 661-667.
9. Jradi, M. and Riffat, S, Experimental investigation of a biomass-fuelled micro-scale tri-generation system with an organic Rankine cycle and liquid desiccant cooling unit.. July 2014, *Energy*, Vol. 71, pp. 80-93.
10. Al-Sulaiman, Fahad A., Dincer, Ibrahim and Hamdullahpur, Ferudin, Energy and Exergy Analyses of a Biomass Trigeneration System using an Organic Rankine Cycle.. 1, September 2012, *Energy*, Vol. 45, pp. 975-985.
11. Uris, María, Linares, José Ignacio and Arenas, Eva., Size Optimisation of a Biomass-Fired Cogeneration Plant CHP/CCHP (Combined Heat and Power/Combined Heat, Cooling and Power) based on Organic Rankine Cycle for a District Network in Spain. August 2015, *Energy*, Vol. 88, pp. 935-945.
12. Barbier, Enrico., Geothermal Energy Technology and Current Status: an Overview. 1-2, 2002, *Renewable and Sustainable Energy Reviews*, Vol. 6, pp. 3-65.
13. Dai, Yiping, Wang, Jiangfeng and Gao, Lin., Parametric Optimisation and Comparative Study of Organic Rankine Cycle (ORC) for Low Grade Waste Heat Recovery. 3, March 2009, *Energy Conversion and Management*, Vol. 50, pp. 576-582.
14. Liu, Liuchen, Zhu, Tong and Ma, Jiacheng., Working Fluid Charge Oriented Off-Design Modelling of a Small-Scale Organic Rankine Cycle System. September 2017, *Energy Conversion and Management*, Vol. 148, pp. 944-953.

15. Quoilin, Sylvain, et al., Techno-economic survey of Organic Rankine Cycle (ORC) Systems. 2013, *Renewable and Sustainable energy Reviews*, Vol. 22, pp. 168-186.
16. Collings, Peter, Yu, Zhibin and Wang, Enhua., A Dynamic Organic Rankine Cycle using a Zeotropic Mixture as the Working Fluid with Composition Tuning to Match Changing Ambient Conditions. 2016, *Applied Energy*, Vol. 171, pp. 581-591.
17. Peris, Bernardo, et al., Experimental Characterisation of an Organic Rankine Cycle (ORC) for micro-scale CHP applications. March 2015, *Applied Thermal Engineering*, Vol. 79, pp. 1-8.
18. Wang, X.D., et al., Performance Evaluation of a Low-Temperature Solar Organic Rankine Cycle System utilising R245fa., *Solar Energy* 1, 2009.
19. Pu, Wenhao, et al., Experimental Study on Organic Rankine Cycle for Low Grade Thermal Energy Recovery.. February 2016, *Applied Thermal Engineering*, Vol. 94, pp. 221-227.
20. Quoilin, Sylvain, Lemort, Vincent and Lebrun, Jean., Experimental Study and Modeling of an Organic Rankine Cycle using Scroll Expander. 4, April 2010, *Applied Energy*, Vol. 87, pp. 1260-1268.
21. Navarro-Esbri, Joaquín, et al., Experimental Study of an Organic Rankine Cycle with HFO-1336mzz-Z as a low global-warming potential working fluid for micro-scale low temperature applications. August 2017, *Energy*, Vol. 133, pp. 79-89.
22. Jung, Hyung-Chul, Taylor, Leighton and Krumdieck, Susan., An Experimental and Modelling Study of a 1kW Organic Rankine Cycle Unit with Mixture Working Fluid. March 2015, *Energy*, Vol. 81, pp. 601-614.
23. Abadi, Gholamreza Bamorovat, Yun, Eunkoo and Kim, Kyung Chun., Experimental Study of a 1kW Organic Rankine Cycle with a Zeotropic Mixture of R245fa/R134a. 2, December 2015, *Energy*, Vol. 93, pp. 2363-2373.
24. Lemmon, E.W, Huber, M.L. and McLinden, M.O. NIST Standard Reference Database 23: Reference Fluid Thermodynamic and Transport Properties-REFPROP, Version 9.1. National Institute of Standards and Technology, Standard Reference Data Program. Gaithersburg : s.n., 2013

# Experimental Results from R245fa Ejector Chiller

J. Mahmoudian<sup>1</sup>, A. Milazzo<sup>1\*</sup>, I. Murmanskii<sup>2</sup>, A. Rocchetti<sup>1</sup>

<sup>1</sup>DIEF - Department of Industrial Engineering – University of Florence – via di S.Marta, 3 – 50139 Firenze (ITALY)

<sup>2</sup> Ural Power Engineering Institute, Ural Federal University, Ekaterinburg, Russia

\*Corresponding author: [adriano.milazzo@unifi.it](mailto:adriano.milazzo@unifi.it)

## Abstract

This paper presents new experimental results from the DIEF prototype ejector chiller, which is operating since 2011 and has undergone several refinements, as discussed elsewhere. The prototype features a modified CRMC design of the ejector and a cooling power of a 40 kW<sub>f</sub>. The working fluid, R245fa, has favourable thermodynamic properties (e.g. dry expansion and moderate pressure at generator) and allows sub-zero temperatures at evaporator. Therefore, even if the prototype was designed for 5°C evaporation temperature, a set of low temperature tests has been carried on. The results show that the CRMC ejector chiller is rather flexible with respect to off-design conditions and, once specifically optimized, could be a candidate for sub-zero applications, unfeasible for water-lithium bromide absorption chillers.

**Keywords:** Ejector chiller, CRMC, R245fa, Experimental.

## Introduction

Ejector chillers are often claimed [1,2] as promising competitors for absorption chillers in the heat-powered refrigeration market, but their energy efficiency normally turns out to be lower. Nonetheless, they could be competitive in those applications where the input energy is basically costless (waste heat, solar). In these cases, ejector chillers may offer a low investment cost and a robust operation. From this point of view, steam would be the obvious choice as a working fluid, being costless, safe for operators and environment and available everywhere. In any industrial environment where steam is produced for other purposes, steam ejectors are unrivalled as simple and relatively effective means for refrigeration [3]. However, synthetic fluids may have some peculiar advantages. A first point is undoubtedly the volumetric cooling capacity. Water, notwithstanding its unrivalled latent heat, has a very low vapour density at low temperature (Table 1), while common refrigerants have much higher values. The influence of volumetric cooling capacity on the size of an ejector chiller is not as straightforward as in vapour compression cycles featuring volumetric compressors. However, the values in Table 1 suggest that a steam ejector chiller is likely to be much more bulky for a given cooling capacity.

Table 1 – Fluid properties – comparison

Fluid	Latent heat [kJ/kg]	Vapour density [kg/m <sup>3</sup> ]	Volumetric cooling capacity [kJ/m <sup>3</sup> ]	Saturation pressure [bar]	
				@ 0°C	@ 100°C
Water	2501	0.00485	12.13	0.00612	1.014
R134a	198.6	14.43	2866	2.929	39.72
R245fa	204.5	3.231	660.7	0.5295	12.65
R1233zd(E)	204.9	2.820	577.7	0.4788	10.50

Fluid properties calculated via NIST REFPROP [4]

A second point is the operating pressures within the various parts of the chiller. Water has very low saturation pressure at all temperature levels encountered along an ejector cycle. The generator, if operated e.g. at 100°C, is at ambient pressure, but the evaporator typically works below 1 kPa. This requires very accurate sealing of the circuit. On the other hand, R134a has a rather high pressure at typical generator temperatures (Table 1), which makes the operation and the energy consumption of the generator feed-pump more troublesome. R245fa is a good compromise, as it goes slightly below ambient pressure at evaporator but remains within a moderate 12.6 bar at 100°C.

A third point is the slope of the upper limit curve on the temperature – entropy diagram. R245fa and R1233zd have an inward slope of the limit curve. This means that the primary nozzle and the whole ejector are free from liquid condensation even if the expansion starts on the limit curve with no superheating. R134a and water, on the other hand, have a “wet expansion” and therefore they need a substantial superheating at generator exit.

A last point that favours synthetic fluids is the absence of icing, which may represent a serious problem for steam ejector chillers and limits their operation to above zero.

On the other hand, F-gas regulations limit the use of fluids with GWP>150 in Europe and other countries have similar limitations. Therefore R245fa (GWP = 950) could prove unusable in most applications. HFOs (Hydro-Fluoro-Olefins) are currently proposed as “drop-in” replacement of HFCs [5]. Among them, R1233zd has similar thermodynamic properties (see Table 1) and hence experimental results gathered with R245fa may be an indication for the performance of an equivalent system using the low-GWP alternative fluid.

Everything considered, we decided to continue our experimental activity on the existing prototype and to substitute R245fa with R1233zd in the near future.

R245fa was tested as a working fluid for an ejector chiller in 2006 by Eames et al. [6]. The ejector was a CRMC design, i.e. the flow sections were calculated by imposing a constant rate of deceleration along the mixer/diffuser. The experimental results showed that, for saturation temperatures of 110°C at generator and 10°C at evaporator, the COP could be as high as 0.47, with a critical condenser temperature of 32.5°C. Raising generator temperature to 120°C decreased the COP to 0.31, but the critical condenser temperature increased to 37.5°C. Superior performance of CRMC design has been recently confirmed in [7]. Here we present further experimental results from a modified version of the CRMC ejector, which has been tested on a wide range of operating conditions.

### Experimental set up

Our ejector was designed starting from a scaled-up version of Eames’ design, introducing a bell-shaped end on the suction side and a conical outlet on the discharge side. The manufacturing problems due to the small inner diameter and substantial length forced to build the ejector in three pieces, carefully aligned by flanged connections. In this way, a roughness of the internal surface from 4 to 6 microns was obtained.

The present arrangement is the result of a long refinement work, as described in previous publications [8, 9]. Main geometrical data of the ejector in the present configuration are reported in Table 2.

Table 2 – Main geometrical parameters of the ejector

	Nozzle	Diffuser
Throat diameter [mm]	10.2	31.8
Exit diameter [mm]	20.2	108.3
Length [mm]	66.4	950
Material	Aluminium	Aluminium

Nine ports have been drilled perpendicularly to the ejector inner surface in order to measure the local static pressure. The holes are placed at 100 mm intervals, starting at 50 mm from the inlet flange of the ejector, as shown in Fig. 1.

The primary nozzle can be moved forward and backward from a reference position having the nozzle exit plane coincident with the inlet plane of the bell-shaped inlet of the suction chamber.

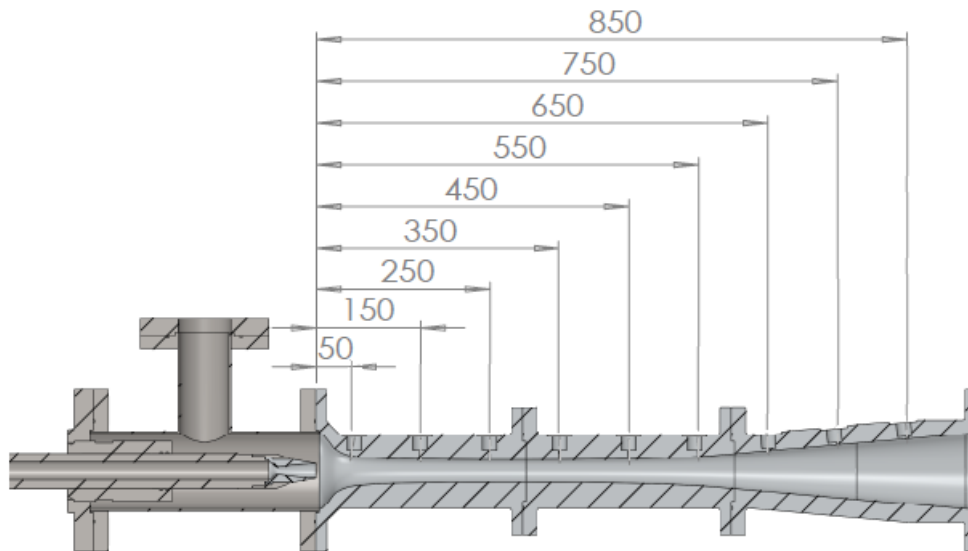


Fig. 1 – CRMC ejector with static pressure ports and movable primary nozzle.

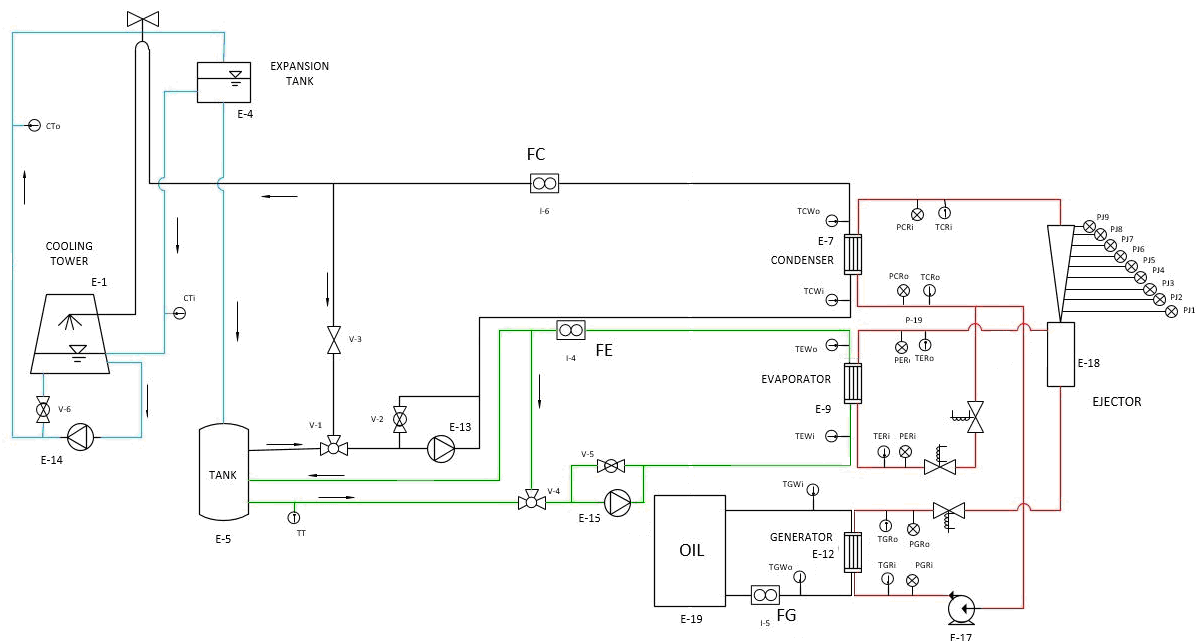


Fig. 2 – Experimental set-up

The ejector is part of a heat-powered refrigeration system (Fig. 2) designed to give 40 kW of refrigeration to a chilled water stream entering at 12 and exiting at 7°C. In the original set-up the heat source was hot water at 90 – 100°C. Now a thermal oil electric heater is used as heat source, in order to explore a wider temperature range. An evaporative cooling tower discharges the system power into the ambient air outside the laboratory. The cooling tower receives the warm water directly from the condenser and feeds a buffer tank, in order to have

a stable water source at near ambient temperature. The tank water is used to give the heat load to the evaporator and to cool the condenser. By-pass branches are used to regulate the temperature at evaporator and condenser inlets. Mass flow meters and temperature sensors are mounted on the condenser and evaporator water circuits, in order to have the instantaneous energy balance of the system. Temperature and pressure sensors are mounted in all the significant points along the refrigerant circuit, while 9 pressure probes are mounted along the ejector as above mentioned. The specifications of the main sensors are reported in Table 3.

Table 3 – Specifications of the sensors and data acquisition

Instrument	Model/type	Position	ADC Module	Total uncertainty
Piezo-resistive pressure transducer	PA25HTT 0-30 bar	Diffuser	NI9208	$\pm(0.1\% + 0.22\% \text{ FS})$
	PR23R 0.5-5 bar	Evaporator	NI9208	$\pm(0.1\% + 0.22\% \text{ FS})$
	PA21Y 0-30 bar	Generator, Condenser	NI9208	$\pm(0.08\% + 1.0\% \text{ FS})$
Resistance temperature detector	Pt100	Whole Plant	NI9216, NI9217	$\pm 0.25^\circ\text{C}$
Thermocouple	T	Cooling Tower, Tank	NI9213	$\pm 1.0^\circ\text{C}$
Electromagnetic water flowmeters	Endress Hauser Promog 50P	Condenser	NI9219	$\pm(0.5\% + 0.04\% \text{ FS})$
Compact Rotamass mass flowmeter	YOKOGAWA RCCT28	Evaporator	NI9219	$\pm(0.05\% + 0.1\% \text{ FS})$
Vortex flowmeter	YOKOGAWA YF105	Generator	NI9219	$\pm(0.8\% + 0.1\% \text{ FS})$

All the experimental points have been measured after at least 15 minutes of stable operation and are averaged over 5 minutes. The generator feed pump has a variable frequency control, but has been always operated at 100% rotation speed.

## Results and discussion

All saturation temperatures reported below are calculated from the pressure measured on top of each plate heat exchanger via NIST REFPROP functions. The experiments presented herein are all referred to a saturation temperature of  $95^\circ\text{C}$  at generator, corresponding to the maximum power of the thermal oil electric heater.

The expansion valve is manually operated in order to fix the saturation temperature at the evaporator.

For each evaporator condition, the water temperature at condenser inlet is raised by  $0.3^\circ\text{C}$  intervals until the cooling power vanishes. The results are reported in terms of COP v/s saturation temperature at condenser.

The higher generator temperature used in these new tests produces lower COP values with respect to those reported in [3]. Furthermore, entrainment ratio and COP have been negatively influenced by the decision to keep chilled water temperature constant ( $12^\circ\text{C}$  at inlet and  $7^\circ\text{C}$  at outlet) throughout the test campaign. This causes a high superheating at evaporator exit, especially at low evaporation temperature, and hence a low vapour density at secondary inlet. On the other hand, the relatively high water temperature avoids any risk of icing.

### a) Effect of evaporator saturation temperature

The system behaviour at reference working condition ( $T_{E-sat} = 5^\circ\text{C}$ ,  $P_E = 0.662$  bar) is shown in Fig. 3. The COP (Fig. 3a) shows a fairly constant value until point 5 and a sudden decrease at a condenser saturation temperature  $T_{C-sat}$  around  $31^\circ\text{C}$ , before point 6. Correspondingly, the static pressure at the wall measured by the 9 pressure transducers shows two easily distinguishable shapes (Fig. 3b). Note that the lines connecting the points are drawn only as a visual aid and do not give any indication about the pressure between the sensors. The curves from 1 to 5 all show a common pressure value at transducers 1 - 3, i.e. until 250 mm from the ejector inlet. The transition between supersonic and subsonic flow is apparently located between 250 and 350 mm, all sensors downstream being sensitive to the condenser pressure. Note that the diffuser throat is located around 300 mm.

The two further points 6 and 7 show a completely different behaviour, featuring a sharp pressure increase before 250 mm and then a slower increase before 550 mm. In any case the pressure recovery after 550 mm is null or even negative, which raises some concern about the design of the final part of the ejector.

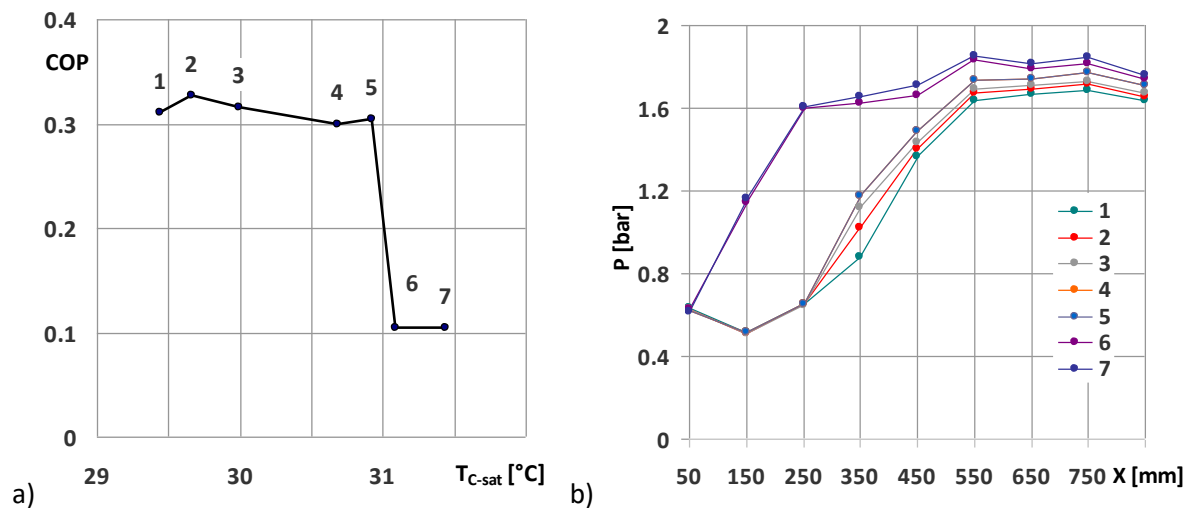


Fig. 3 – COP and static pressure at wall along the ejector @  $T_{E-sat} = 5^\circ\text{C}$  and  $NXP = 0$  mm

Points 6 and 7 show that, once the critical pressure has been surpassed, a small secondary flow can still survive to a further small increase in condenser pressure. This part of the curve is usually truncated and is obviously not significant as a practical working condition. However, it is a quite general feature and represents a safety margin before a dangerous backflow.

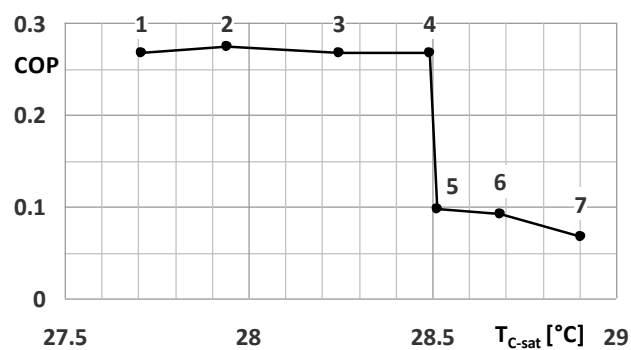


Fig. 4 – COP @  $T_{E-sat} = 0^\circ\text{C}$  and  $NXP = 0$  mm

When the evaporation temperature is lowered to  $0^{\circ}\text{C}$  ( $P_E = 0.529$  bar), the behaviour changes as shown in Fig. 4. Note the lower values of COP and critical pressure. Again, the operation continues beyond the critical condenser temperature even if at very low efficiency.

Further reduction of the evaporation temperature to  $-5^{\circ}\text{C}$  ( $P_E = 0.419$  bar) obviously gives an even lower COP and a very low range in terms of condenser temperature (Fig. 5a). However, the ejector proves to be able to reach such a low value of suction pressure (Fig. 5b), even if designed for a quite different working condition. The transition between on-design and off-design operation is abrupt as in Fig. 3b.

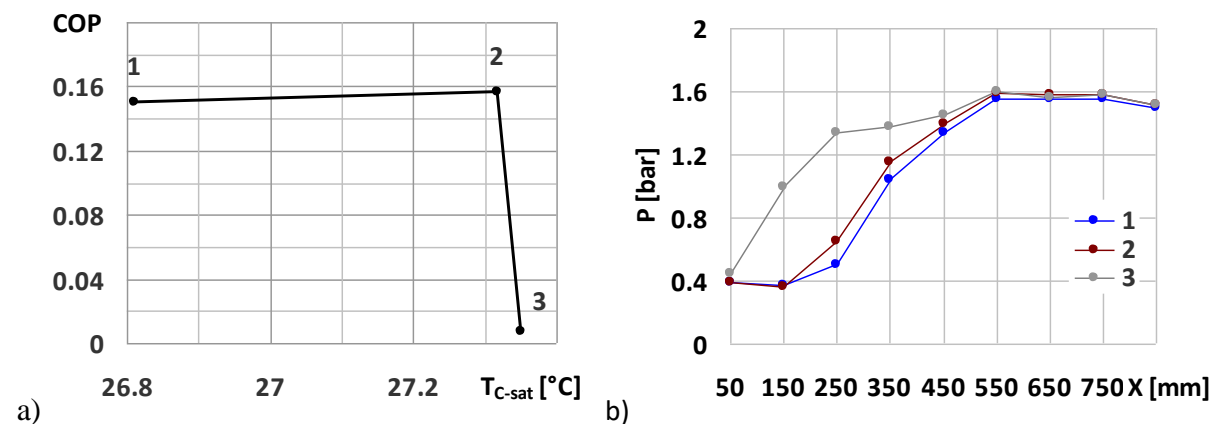


Fig. 5 – COP and static pressure at wall along the ejector @  $T_{E-sat} = -5^{\circ}\text{C}$  and  $NXP = 0$  mm

#### b) Effect of nozzle position

According to the widely accepted model presented by Huang et al. [10] for the supersonic ejector operation, the entrainment ratio should be influenced by the area available for the secondary flow in the section where this latter reaches its sonic velocity. According to this view, an increase in the distance between the nozzle exit and the minimum area of the diffuser should cause an increase in the area occupied by the primary flow and hence a decrease in the secondary flow rate. A more realistic view sees the ejector as a momentum exchanger between the supersonic primary flow and the slow secondary flow [11]. Accordingly, an increased mixing length between the motive and entrained flow should actually increase the entrainment. In the case of present measurements, the situation is complicated by the absence of a cylindrical mixing zone within the diffuser. The available flow section changes continuously from the inlet to the throat of the CRMC diffuser. This makes the effect of the nozzle exit position quite unpredictable.

The experimental results (Fig. 6) show that the COP measured at on-design conditions is actually reduced by a very modest amount, if any. The critical condenser temperature, on the other hand, is significantly decreased. This may be explained considering that a withdrawal of the nozzle causes a corresponding retraction along the diffuser of the section where the flow is fully supersonic. Hence, the working condition that causes this section to overcome the diffuser throat is anticipated.

Another interesting point is the completely different shape of the decreasing part of the COP line. In this case, the transition seems to take place in a rather gradual way, in lieu of a sharp decrease as shown in Figs. 3-5. Correspondingly, the pressure lines in Fig. 6b are equally spaced between the lowest one, surely representing an on-design condition, to the highest. As explained in [11], the primary flow undergoes a sequence of oblique shocks starting from the interface between super and subsonic flow and featuring multiple reflections on the axis and on the interface. The sequence of sharp descents and less inclined parts visible in Fig. 6b could be a trace of the interaction between the oblique shocks and the ejector profile.



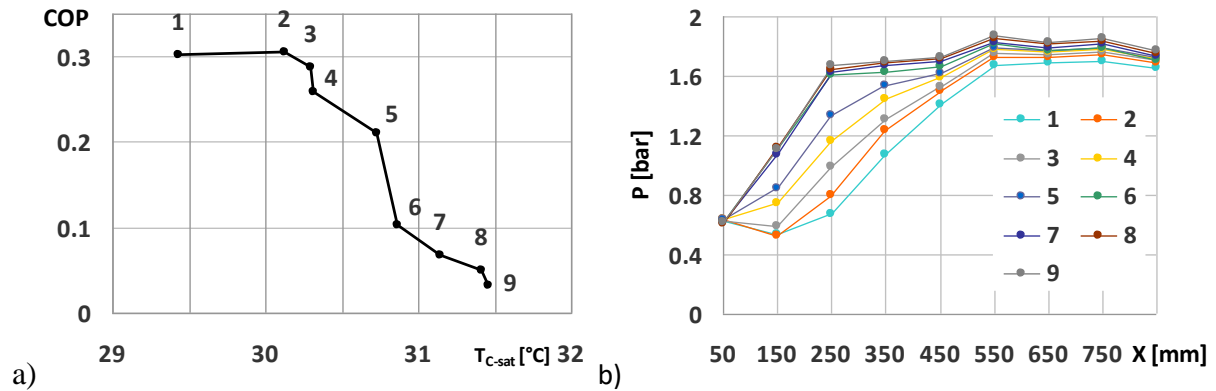


Fig. 6 – COP and static pressure at wall along the ejector @  $T_{E-sat} = 5^{\circ}\text{C}$  and  $\text{NXP} = 5 \text{ mm}$

Obviously a more detailed analysis would be necessary before drawing a conclusive description of this phenomenon.

Quite surprisingly, the behaviour experimented when the nozzle is moved inward by 5 mm is not so different (Fig. 7). Again, we have a basically unchanged COP and a decreased critical condenser temperature. The decrease after point 3 is less steep and operation at point 4 would still be acceptable. Point 6, which still has a  $\text{COP} > 0.1$ , is now above  $31^{\circ}\text{C}$ . As a whole, the off-design behaviour in this condition seems a bit less deteriorated than at  $\text{NXP} = 5 \text{ mm}$ , but the difference is rather subtle when compared to the on-design condition.

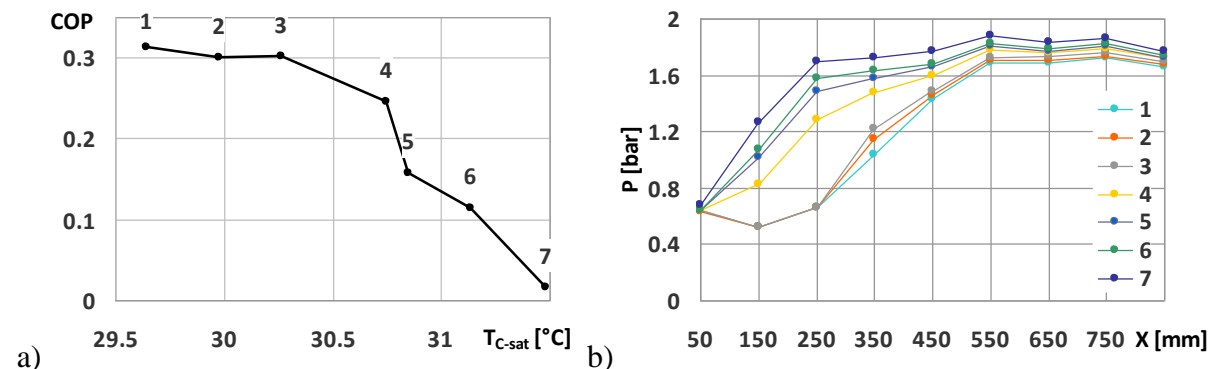


Fig. 7 – COP and static pressure at wall along the ejector @  $T_{E-sat} = 5^{\circ}\text{C}$  and  $\text{NXP} = -5 \text{ mm}$

## Conclusions

The CRMC ejector chiller working with R245fa has proved to be effective even at relatively low evaporation temperatures. The continuous profile offers higher efficiency and increased tolerance with respect to variations in operating conditions. For example, the bell-shaped inlet that smoothly connects the suction inlet to the CRMC profile allows an acceptable operation even when the primary nozzle is moved from the optimal position by significant amounts. On the other hand, an improved design should be sought for the ejector on the discharge side, where the straight cone does not give any contribution in terms of pressure recovery. If specifically designed, an ejector featuring an optimized, continuous profile could give an acceptable performance and superior flexibility when compared to other heat powered cycles. The experimental activity will continue on the same prototype using R1233zd that has a low GWP replacement fluid and requires minor modifications to the chiller. Meanwhile, alternative design options will be explored by CFD analysis. Hopefully this activity will contribute to establish the feasibility of a robust and low-cost refrigeration system, powered by a moderate temperature heat source, using an environmentally safe refrigerant and operating below  $0^{\circ}\text{C}$ .

## Acknowledgements

The research leading to these results has received funding from the MIUR of Italy within the framework of PRIN2015 project «Clean Heating and Cooling Technologies for an Energy Efficient Smart Grid». A special thank goes to Mr. Furio Barbetti, who has given a precious contribution to the design and realization of the experimental set-up.

## References:

- [1] Besagni, G., Mereu, R., Inzoli, F., “Ejector refrigeration: A comprehensive review”, *Renewable and Sustainable Energy Reviews*, 2016, [doi.org/10.1016/j.rser.2015.08.059](https://doi.org/10.1016/j.rser.2015.08.059)
- [2] Chen, X., Omer, S., Worall, M., Riffat, S., “Recent developments in ejector refrigeration technologies”, *Renewable and Sustainable Energy Reviews*, 2013, [doi.org/10.1016/j.rser.2012.11.028](https://doi.org/10.1016/j.rser.2012.11.028)
- [3] Power, R.B., *Steam Jet Ejectors for the Process Industries*, Author-Publisher, 1994, [www.jetwords.com](http://www.jetwords.com)
- [4] NIST REFPROP, Reference Fluid Thermodynamic and Transport Properties Database, version 9.1, 2018. <https://www.nist.gov/srd/refprop>.
- [5] Fang, Y., Croquer, S., Poncet, S., Aidoun, Z., Bartosiewicz, Y., “Drop-in replacement in a R134 ejector refrigeration cycle by HFO refrigerants”, *International Journal of Refrigeration*, 2017, [doi.org/10.1016/j.ijrefrig.2017.02.028](https://doi.org/10.1016/j.ijrefrig.2017.02.028)
- [6] Eames, I.W., Ablwaifa, A.E., Petrenko V., “Results of an experimental study of an advanced jet-pump refrigerator operating with R245fa”, *Applied Thermal Engineering*, 2007, [doi.org/10.1016/j.applthermaleng.2006.12.009](https://doi.org/10.1016/j.applthermaleng.2006.12.009)
- [7] Kittratana, B., Aphornratana, S., Thongtip, T., Ruangtrakoon N., “Comparison of traditional and CRMC ejector performance used in a steam ejector refrigeration”, *Energy Procedia*, 2017, [doi.org/10.1016/j.egypro.2017.10.229](https://doi.org/10.1016/j.egypro.2017.10.229)
- [8] Milazzo, A., Rocchetti, A., Eames, I.W., “Theoretical and experimental activity on ejector refrigeration”, *Energy Procedia*, 2014, [doi.org/10.1016/j.egypro.2014.01.130](https://doi.org/10.1016/j.egypro.2014.01.130)
- [9] Mazzelli F., Milazzo A., “Performance analysis of supersonic ejector cycle working with R245fa”, *International Journal of Refrigeration*, 2015, [doi.org/10.1016/j.ijrefrig.2014.09.020](https://doi.org/10.1016/j.ijrefrig.2014.09.020)
- [10] Huang, B., Chang, J., Wang, C., Petrenko, V. “A 1-D analysis of ejector performance”, *International Journal of Refrigeration*, 1999. [doi.org/10.1016/S0140-7007\(99\)00004-3](https://doi.org/10.1016/S0140-7007(99)00004-3)
- [11] Grazzini, G., Mazzelli, F., Milazzo, A., “Physics of the Ejectors” in *Ejectors for Efficient Refrigeration - Design, Applications and Computational Fluid Dynamics*, Springer, 2018. [doi.org/10.1007/978-3-319-75244-0](https://doi.org/10.1007/978-3-319-75244-0)

# Adapting the MgO-CO<sub>2</sub> working pair for thermochemical energy storage by doping with salts

A. I. Shkatulov<sup>1\*</sup>, S. T. Kim<sup>2</sup>, Y. Kato<sup>2</sup> and Yu. I. Aristov<sup>1,2</sup>

<sup>1</sup>Boreshkov Institute of Catalysis, Ac. Lavrentiev av. 5, Novosibirsk 630090, Russia

<sup>2</sup>Tokyo Institute of Technology, 2-12-1-N1-22, Ōokayama, Meguro-ku, Tokyo 152-8550, Japan

\*Corresponding author: shkatulov@catalysis.ru

## Abstract

In this work, the MgO-CO<sub>2</sub> working pair was adapted for thermochemical energy storage (TCES) at medium temperatures by the MgO modification with various salts. A brief survey of several salts showed that lithium acetate (LiOAc) and mixed lithium-potassium nitrate (Li<sub>0.42</sub>K<sub>0.58</sub>NO<sub>3</sub>) additives considerably promote the MgO carbonation which is unfeasible for pure MgO at P(CO<sub>2</sub>) ≤ 10 bar and T = 300°C. Here, we report de- and re-carbonation kinetics as well as cycling stability of the doped MgO/MgCO<sub>3</sub> to outline its possible TCES operating conditions (T = 280°C-380°C, P(CO<sub>2</sub>) = 0-1 bar). The maximal heat storage capacity evaluated under these conditions reaches 1200 J/g. The MgO-CO<sub>2</sub> working pair promoted with the salts was concluded to be promising for TCES.

**Keywords:** Thermochemical energy storage, Magnesium oxide, Magnesium Carbonate, Salt modification.

## Introduction/Background

Nowadays, around two thirds of the whole energy produced in the USA is wasted in the form of thermal energy [1]. Storage of thermal energy is a powerful tool for thermal management which can be used to increase the efficiency of energy consumption and thus to save primary energy resources. Thermochemical energy storage (TCES) is an emerging, yet underexploited, technology which provides a high storage density and long storage duration due to the use of chemical reactions with large heat effect. New advanced materials for TCES at middle temperatures are desirable to make this promising technology viable and useful for utilization of waste heat from industrial processes and cogeneration systems.

To this day, reactions and processes proposed and studied for TCES at medium temperatures (200-500°C) are not numerous. They include dehydrogenation of ammonia [2], cyclohexane [3], MgH<sub>2</sub> [4], dehydration of Mg(OH)<sub>2</sub> [5] and Ca(OH)<sub>2</sub> [6], and several other reactions [7]. Metal carbonates can be used as a heat storage media due to endothermic decomposition accompanied by release of CO<sub>2</sub>, or de-carbonation:



The metal oxide MO (solid) and CO<sub>2</sub> (gas) are separated from each other and heat is stored in a chemical form for theoretically infinite time. In order to release the stored heat one has to supply CO<sub>2</sub> to the metal oxide and carry out the reverse exothermic reaction of carbonation.

TCES by metal carbonates was proposed in several works, starting with the work of Wentworth in 1976 [8]. In further works, only CaCO<sub>3</sub> and PbCO<sub>3</sub> were considered for TCES [9–12]. Magnesium carbonate, MgCO<sub>3</sub>, is only mentioned in the reviews dedicated to TCES due to lack of the data on its application. This carbonate shows the high reaction enthalpy  $\Delta_r H^\circ_{298} = 101 \text{ kJ/mol}$  [13] and the turning temperature  $T_{\text{turn}} = 398^\circ\text{C}$  at P(CO<sub>2</sub>) = 1 bar which could be interesting for heat storage at medium temperatures (Fig. 1).

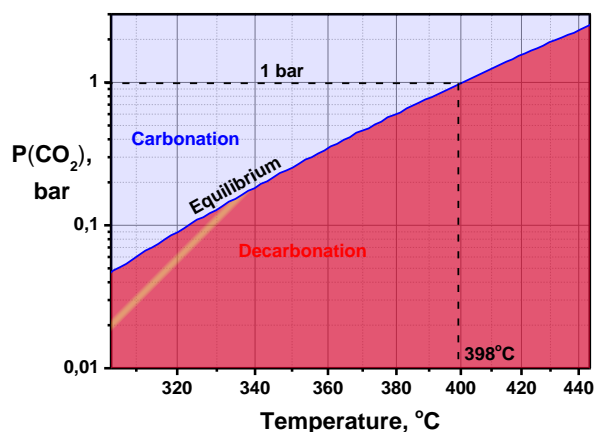


**Figure 1.** The equilibrium  $\text{CO}_2$  pressure over a bulk  $\text{MgCO}_3$  at various temperatures in  $\lg P - 1/T$  coordinates [14].

However, the reaction  $\text{MgCO}_3 = \text{MgO} + \text{CO}_2$  demonstrates poor reversibility, i.e. the interaction of  $\text{MgO}_{(s)}$  with  $\text{CO}_{2(g)}$  is kinetically hindered. This makes release of the stored heat a challenging task.

A promising approach which could enhance the reactivity is its doping with a salt. Previously, this approach was shown to be fruitful for  $\text{Mg}(\text{OH})_2$  and  $\text{Ca}(\text{OH})_2$  as TCES materials [7]. For instance, in the case of the working pair  $\text{CaO}-\text{H}_2\text{O}$ , the dehydration temperature was decreased and the rehydration rate was increased. Doping with salts has already been shown to promote carbonation of  $\text{MgO}$  [15,16]. However, no assessment of the salt-promoted  $\text{MgO}-\text{CO}_2$  system for TCES was reported. In this work, we made a brief survey of salt additives to pure  $\text{MgO}$  aiming at finding salts that increase the oxide reactivity towards carbonation. Cycling stability of these materials, decarbonation and carbonation kinetics in open and closed systems were studied in order to outline the set of conditions ( $T$ ,  $P(\text{CO}_2)$ ) under which the  $\text{MgO}-\text{CO}_2$  working pair can be efficiently used for TCES. The heat storage capacity is evaluated.

## Results and Discussion

The new materials Salt/ $\text{MgO}$  (salt content 10 mol. %) were prepared by dehydration of Salt/ $\text{Mg}(\text{OH})_2$ . They were synthesized by mixing of salt and magnesium hydroxide as described in [7]. In order to distribute salt uniformly some water was added to the mixture. The slurry was subsequently dried under vigorous stirring and decreased pressure. The salts chosen were carbonates, nitrates and acetates of alkali metals. The nitrates and acetates of lithium and potassium were earlier shown to have a considerable effect on dehydration of  $\text{Mg}(\text{OH})_2$  [7].

The carbonation and decarbonation experiments were carried out by using two TG setups, namely, a Rubotherm thermobalance used for studying de-/carbonation in a closed system and an Advance RIKO TGD-9600 thermobalance used for experiments under conditions imitating open TCES system.

The pure  $\text{MgO}$  as a reference material cannot be carbonated in a closed system at  $T = 300^\circ\text{C}$  and  $P(\text{CO}_2) = 10$  bar due to kinetic impediments. Indeed, the conversion  $\alpha_{60}$  after 60 min of carbonation does not exceed 0.01 for pure  $\text{MgO}$  (Fig. 2). Even lowering the temperature does not make the carbonation to proceed despite bringing the reaction conditions further from the equilibrium. The same is true for  $\text{MgO}$  with additives of  $\text{Li}_2\text{CO}_3$  and  $\text{KNO}_3$ . The mixtures with  $\text{Na}_2\text{CO}_3$ ,  $\text{K}_2\text{CO}_3$ , and  $\text{KOAc}$  ( $\text{Ac} = \text{CH}_3\text{CO}$ ) can be carbonated, however, the parameter  $\alpha_{60}$  does not exceed 0.1 and the total heat released during 60 min of carbonation,  $Q_{60}$ , is less than 200

J/g-MgO which is comparable to the latent heat of phase-change materials [17] but quite low for TCES. Additives of LiOAc,  $\text{Li}_{0.42}\text{K}_{0.58}\text{NO}_3$  (further referred to as (LiK)NO<sub>3</sub>), and NaNO<sub>3</sub> considerably increase the conversion  $\alpha_{60}$  and the released heat which may exceed 1400 J/g-MgO in the case of lithium acetate (Fig. 2). For further study, we have chosen (LiK)NO<sub>3</sub> and LiOAc since they exhibit the highest carbonation conversion.

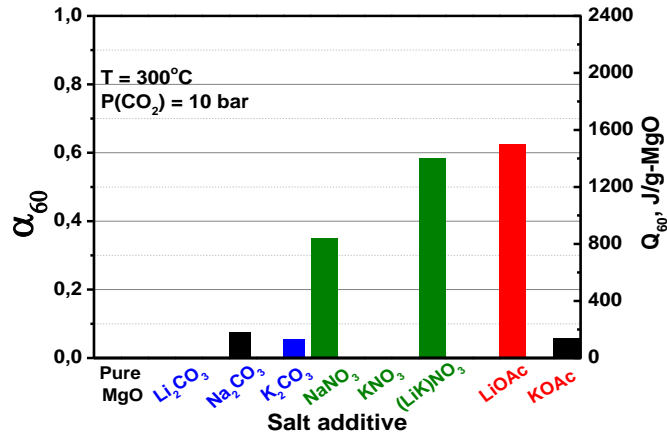


**Figure 2.** Illustration of the effect of salt additives on the MgO carbonation conversion after 60 min ( $\alpha_{60}$ ). Closed system.

Stability of the salt in the cycle operating conditions is of high importance for TCES materials as they must be stable in consecutive heat storage/release cycles. In order to find the stability of the candidate salts – LiOAc·2H<sub>2</sub>O and (LiK)NO<sub>3</sub> – a heating in Ar atmosphere was carried out. Lithium acetate lost hydrate water at 100°C and then, apparently, decomposed upon heating at 310-330°C (most likely, yielding Li<sub>2</sub>CO<sub>3</sub> and acetone [18]) since the weight loss was significant (Fig. 3a). On the contrary, (LiK)NO<sub>3</sub> showed no indication of decomposition and the weight loss was only 3.0% at 500°C (Fig. 3b). Thus, for the further study we selected the material (LiK)NO<sub>3</sub>/MgO.

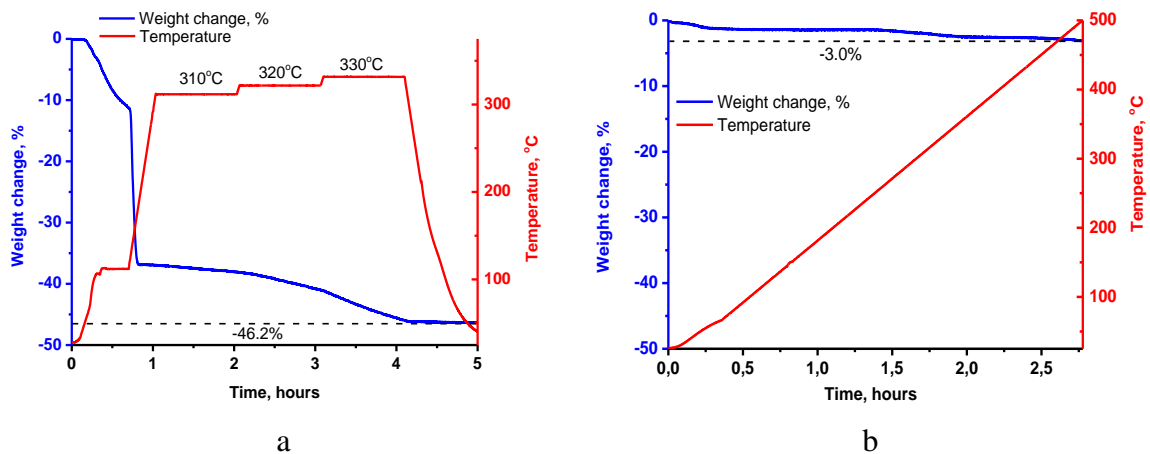


**Figure 3.** Thermogravimetric tests of thermal stability for lithium acetate LiOAc (a) and mixed lithium-potassium nitrate (LiK)NO<sub>3</sub> (b). Open system.

In order to determine suitable conditions of carbonation and decarbonation, the (LiK)NO<sub>3</sub>/MgO composite was heated up to 500°C with a constant rate of 3 K/min at  $P(\text{CO}_2) = 1$  and 2 bar. The material exhibited the onset of weight gaining at  $266 \pm 1$  °C (Fig. 4). The weight gain accelerated upon further heating and ended at 395°C at  $P(\text{CO}_2) = 1$  bar and 420°C at 2 bar in

accordance with the equilibrium displayed in Fig. 1. At higher temperature the decomposition of  $(\text{LiK})\text{NO}_3/\text{MgCO}_3$  is observed.

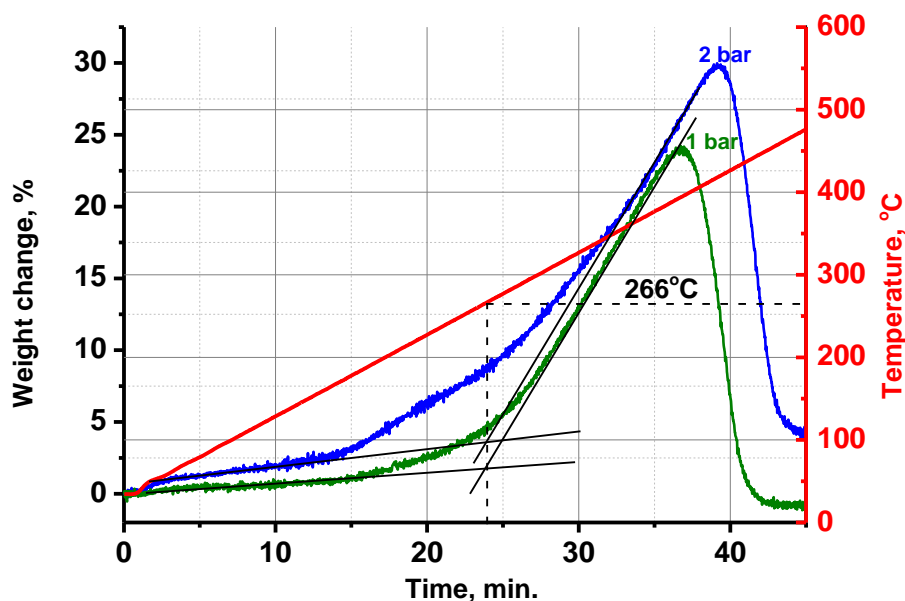


**Figure 4.** Heating of  $(\text{LiK})\text{NO}_3/\text{MgO}$  in the  $\text{CO}_2$  atmosphere.

The stability in consecutive carbonation/decarbonation cycles is the important property of TCES materials. Thirteen consecutive cycles were carried out for  $(\text{LiK})\text{NO}_3/\text{MgO}$  in the open system at  $T = 330^\circ\text{C}$  and  $P = 1$  bar by switching the purge gas from Ar to  $\text{CO}_2$  (Fig. 5). It was found that the decarbonation conversion slightly decreased after two first cycles and remained almost constant while the carbonation conversion increased for 5 cycles and reached 0.43-0.45. The latter increase may be attributed to a more uniform salt distribution throughout the sample after several first cycles.

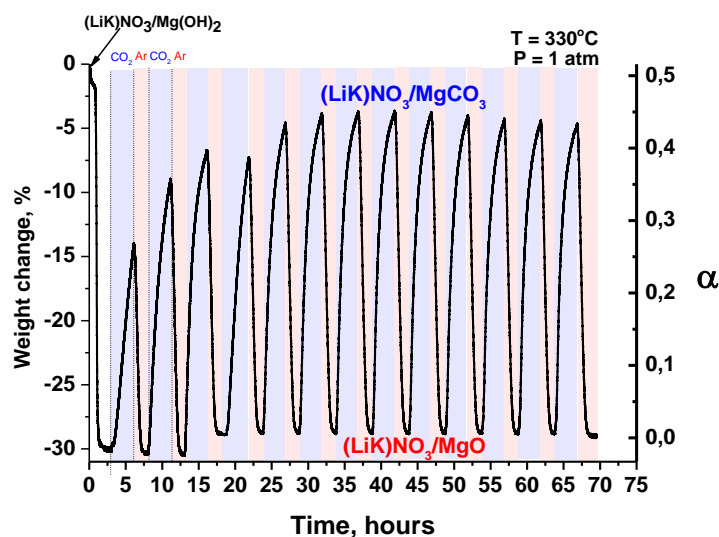


**Figure 5.** Cycling stability of  $(\text{LiK})\text{NO}_3/\text{MgO}$  in 13 carbonation/decarbonation cycles.

Initial, decomposed and cycled materials were characterized by HRTEM (Fig. 6). The initial sample consists of hexagonal platelets of  $\text{Mg}(\text{OH})_2$  covered with salt in accordance with the literature [19]. After decomposition, the form of the crystals is not retained as observed in the case of pure  $\text{Mg}(\text{OH})_2$ - $\text{MgO}$  transition. Instead, the decomposed material consists of intergrown cubic crystallites of  $\text{MgO}$  forming agglomerates of irregular shape (Fig. 6b). After

cycling these agglomerates grown into irregular hexagonal crystals of magnesium carbonate (Fig. 6c).

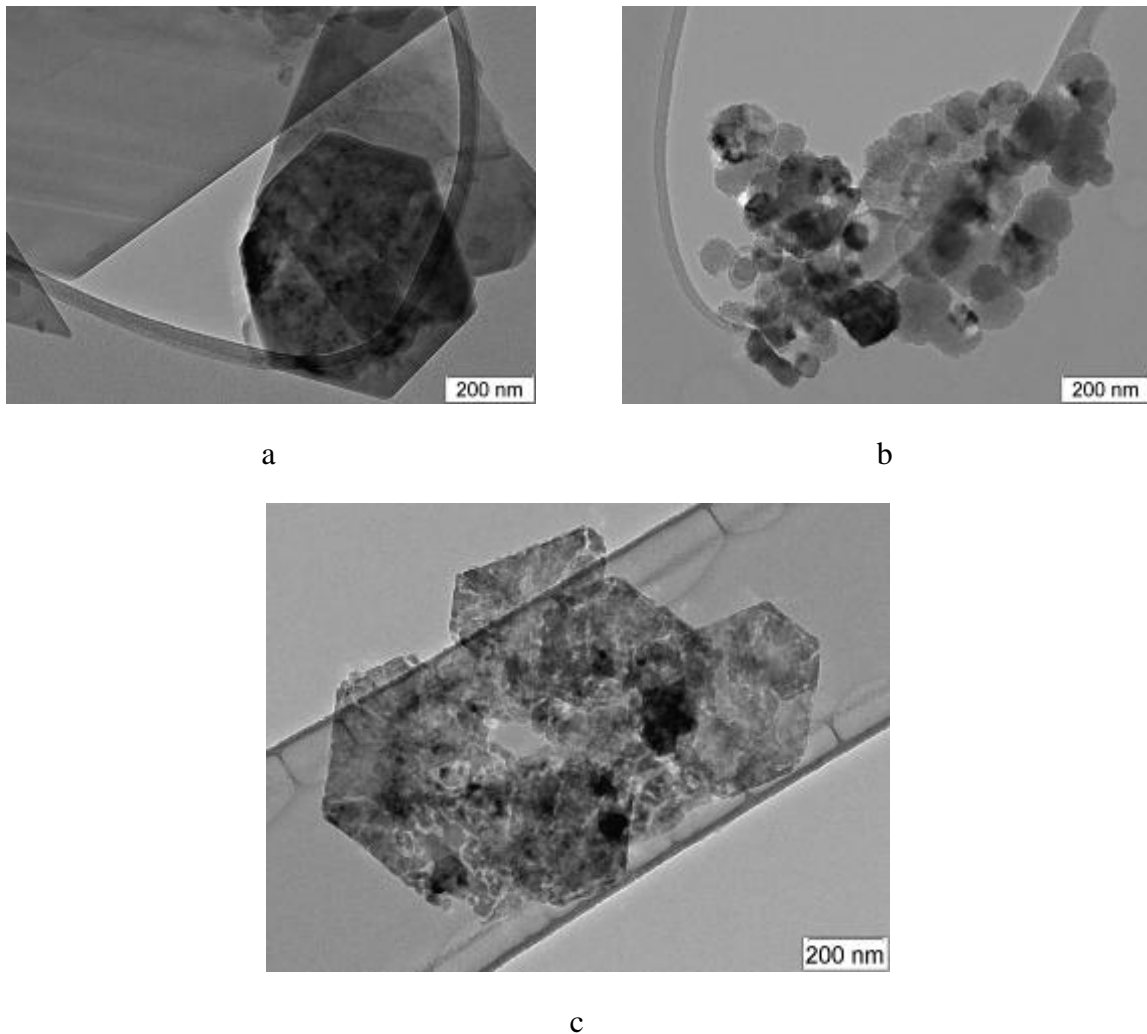


**Figure 6.** HRTEM images of initial (a), dehydrated (b) and cycled (c) (LiK)NO<sub>3</sub>/MgO.

The carbonation kinetics of (LiK)NO<sub>3</sub>/MgO was studied in an open system. The process was initiated by abrupt supply of CO<sub>2</sub> to react with fully decarbonated material ((LiK)NO<sub>3</sub>/MgO) by switching from pure Ar to pure CO<sub>2</sub>.

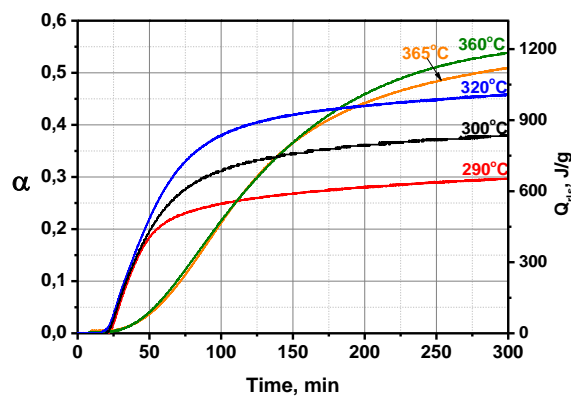


**Figure 7.** Carbonation kinetics of (LiK)NO<sub>3</sub>/MgO in open system at P(CO<sub>2</sub>) = 1 bar.

At 290-320°C, an induction period of 20-25 min was observed, and the initial rates were almost the same, however, the final carbonation conversion gradually increased at higher temperature from 0.30 to 0.45 (Fig. 7). At 360°C, both the induction period and the final carbonation conversion further increased. At 365°C, the final conversion is slightly lower than for 360°C. No carbonation was observed at 370°C. Thus, the final conversion reached a maximum of 0.54 at 360°C. This conversion corresponded to the amount of heat released per 1 g of the (LiK)NO<sub>3</sub>/MgO material  $Q_{rls} = \Delta_r H^0 \cdot \alpha = 1,200 \text{ J/g}$  which is of high interest for TCES (Fig. 7).

The complex dependence of the carbonation kinetics on temperature is a manifestation of the complex carbonation mechanism. The whole process consists of several consecutive stages [15,20,21]:

- Melting of the salt ( $T_{\text{melting}} = 125^\circ\text{C}$ ) forming a thin liquid film on the surface of MgO.
- Dissolution of CO<sub>2</sub> and MgO in the film (MgO dissociates into Mg<sup>2+</sup> and O<sup>2-</sup>).
- Reaction  $\text{O}^{2-} + \text{CO}_2 = \text{CO}_3^{2-}$  in the liquid phase.
- Crystallization of MgCO<sub>3</sub> from the melt due to oversaturation of the solution. This is a complex process that includes stages of nucleation and growth.

In view of this mechanism, the induction period may be attributed to the low solubility of CO<sub>2</sub> in the liquid film [22]. This explains longer induction periods at higher temperature since more time is required to reach the stationary concentration of CO<sub>2</sub> in the film. The final conversion increases with the temperature, perhaps, due to a larger mobility of ions in the liquid at the higher temperature until a threshold is reached. After this, approaching the equilibrium temperature (398°C) decreases the final conversion.

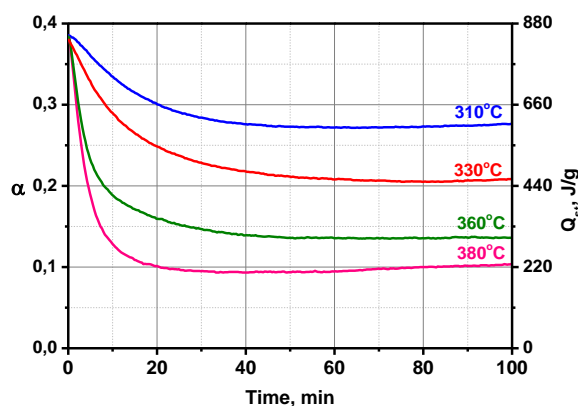


**Figure 8.** Decarbonation kinetics of (LiK)NO<sub>3</sub>/MgCO<sub>3</sub> in vacuum in the closed system.

The decarbonation kinetics was studied in the closed system and initiated by a CO<sub>2</sub> pressure drop from 1 bar to 0.001 bar which lasted less than 1 min. After this, the fully carbonated material (LiK)NO<sub>3</sub>/MgCO<sub>3</sub> started to decompose. The decomposition rate and the final conversion decreased at the lower temperatures (Fig. 8). The amount of heat  $Q_{st} = \Delta_r H^0 \cdot \alpha$  stored at 380°C is 660 J/g which can be promising for TCES.

### Summary

In this work, the MgO-CO<sub>2</sub> working pair was adapted for thermochemical energy storage by using salt modification approach. A brief survey of salt additives (Fig. 2) showed that CH<sub>3</sub>COOLi and Li<sub>0.42</sub>K<sub>0.58</sub>NO<sub>3</sub> considerably promote the MgO carbonation. The additive Li<sub>0.42</sub>K<sub>0.58</sub>NO<sub>3</sub> was chosen for further study as the most thermally stable.



The carbonation kinetics of  $\text{Li}_{0.42}\text{K}_{0.58}\text{NO}_3/\text{MgO}$ , decarbonation kinetics of  $\text{Li}_{0.42}\text{K}_{0.58}\text{NO}_3/\text{MgCO}_3$  and the cycling stability of this composite were studied under tentative conditions of TCES cycles. The material  $\text{Li}_{0.42}\text{K}_{0.58}\text{NO}_3/\text{MgO}$  showed stable decarbonation conversions over 13 cycles with carbonation conversion increasing in the first several cycles and then stabilizing as well. The kinetics of carbonation was studied at 280–360°C in the open system. The heat released reached 1200 J/(g  $\text{Li}_{0.42}\text{K}_{0.58}\text{NO}_3/\text{MgO}$ ) at 360°C and  $P(\text{CO}_2) = 1$  bar. The decarbonation process may be carried out at 380°C to store around 660 J/(g  $\text{Li}_{0.42}\text{K}_{0.58}\text{NO}_3/\text{MgCO}_3$ ) after 20 min. Thus, the results showed that the  $\text{Li}_{0.42}\text{K}_{0.58}\text{NO}_3/\text{MgO}$  composite may be promising for TCES.

### Acknowledgements

The Russian authors are grateful for the WRHI grant of Tokyo Institute of Technology and to the RBFR project mol\_a 16-38-00503. Special thanks are addressed to Dr. E. Gerasimov for the HRTEM images.

### References:

- [1] Rattner, A.S., Garimella, S. “Energy harvesting, reuse and upgrade to reduce primary energy usage in the USA”, *Energy*, 2011, doi:10.1016/j.energy.2011.07.047.
- [2] Lovegrove, K., Luzzi, A., Soldiani, I., Kretz, H. “Developing ammonia based thermochemical energy storage for dish power plants”, *Solar Energy*, 2004, doi:10.1016/j.solener.2003.07.020.
- [3] Aristov, Y.I., Parmon, V.N., Cacciola, G., Giordano, N., “High-temperature chemical heat pump based on reversible catalytic reactions of cyclohexane-dehydrogenation/benzene-hydrogenation: Comparison of the potentialities of different flow diagrams”, *Int J Energy Res*, 1993;17:293–303.
- [4] Bogdanović, B., Ritter, A., Spliethoff, B., “Active  $\text{MgH}_2/\text{Mg}$  Systems for Reversible Chemical Energy Storage” *Angew Chem Int Ed Engl* 1990;29:223–234.
- [5] Kato, Y., Sasaki, Y., Yoshizawa, Y., “Magnesium oxide/water chemical heat pump to enhance energy utilization of a cogeneration system”, *Energy*, 2005, doi:10.1016/j.energy.2004.08.019.
- [6] Azpiazu, M.N., Morquillas, J.M., Vazquez, A., “Heat recovery from a thermal energy storage based on the  $\text{Ca}(\text{OH})_2/\text{CaO}$  cycle”, *Appl Therm Eng*, 2003, doi:10.1016/S1359-4311(03)00015-2.
- [7] Shkatulov, A., Aristov, Y., “Modification of magnesium and calcium hydroxides with salts: An efficient way to advanced materials for storage of middle-temperature heat” *Energy*, 2015, doi:10.1016/j.energy.2015.04.004.
- [8] Wentworth, W.E., Chen, E. “Simple thermal decomposition reactions for storage of solar thermal energy”, *Solar Energy* 1976;18:205–14.
- [9] Kato, Y., Watanabe, Y., Yoshizawa, Y., “Application of inorganic oxide/carbon dioxide reaction system to a chemical heat pump”, *Energy Convers. Eng. Conf. 1996 IECEC 96 Proc. 31st Intersoc.*, vol. 2, IEEE; 1996, p. 763–768.
- [10] Pan, Z.H., Zhao, C.Y., “Gas–solid thermochemical heat storage reactors for high-temperature applications”, *Energy*, 2017, doi:10.1016/j.energy.2017.04.102.
- [11] Pardo, P., Deydier, A., Anxionnaz-Minvielle, Z., Rougé, S., Cabassud, M., Cognet, P. “A review on high temperature thermochemical heat energy storage”, *Renew Sustain Energy Rev* 2014, doi:10.1016/j.rser.2013.12.014.
- [12] André, L., Abanades, S., Flamant, G., “Screening of thermochemical systems based on solid-gas reversible reactions for high temperature solar thermal energy storage”, *Renew Sustain Energy Rev*, 2016, doi:10.1016/j.rser.2016.06.043.
- [13] Barin, I. *Thermochemical Data of Pure Substances*, WCH-Weinheim, 1997.

- [14] Hassanzadeh, A., Abbasian, J., “Regenerable MgO-based sorbents for high-temperature CO<sub>2</sub> removal from syngas: 1. Sorbent development, evaluation, and reaction modelling”, *Fuel*, 2010, doi:10.1016/j.fuel.2009.11.017.
- [15] Harada, T., Simeon, F., Hamad, E. Z., Hatton, T.A. “Alkali Metal Nitrate-Promoted High-Capacity MgO Adsorbents for Regenerable CO<sub>2</sub> Capture at Moderate Temperatures”, *Chem Mater*, 2015, doi:10.1021/cm503295g.
- [16] Vu, A-T., Park, Y., Jeon, P.R., Lee, C-H., “Mesoporous MgO sorbent promoted with KNO<sub>3</sub> for CO<sub>2</sub> capture at intermediate temperatures”, *Chem Eng J*, 2014, doi:10.1016/j.cej.2014.07.088.
- [17] Gil, A., Medrano, M., Martorell, I., Lázaro, A., Dolado, P., Zalba, B., et al. “State of the art on high temperature thermal energy storage for power generation. Part 1— Concepts, materials and modellization”, *Renew Sustain Energy Rev*, 2010, doi:10.1016/j.rser.2009.07.035.
- [18] Roe, A., Finlay, J.B. “The isotope effect. II. Pyrolysis of lithium acetate-1-C<sup>14</sup>”, *J Am Chem Soc*, 1952;74:2442–2443.
- [19] Shkatulov, A., Krieger, T., Zaikovskii, V., Chesalov, Y., Aristov, Y., “Doping Magnesium Hydroxide with Sodium Nitrate: A New Approach to Tune the Dehydration Reactivity of Heat-Storage Materials”, *ACS Appl Mater Interfaces*, 2014, doi:10.1021/am505418z.
- [20] Gao, J., Wang, L.W., Wang, R.Z., Zhou, Z.S., “Solution to the sorption hysteresis by novel compact composite multi-salt sorbents”, *Appl Therm Eng*, 2017, doi:10.1016/j.applthermaleng.2016.09.152.
- [21] Jo, S-I., An, Y-I., Kim, K-Y., Choi, S-Y., Kwak, J-S., Oh, K-R., et al. “Mechanisms of absorption and desorption of CO<sub>2</sub> by molten NaNO<sub>3</sub>-promoted MgO”, *Phys Chem Chem Phys*, 2017, doi:10.1039/C6CP07787K.
- [22] Sada, E., Katoh, S., Yoshii, H., Takemoto, I., Shloml, N., “Solubility of Carbon Dioxide in Molten Alkali Halides and Nitrates and Their Binary Mixtures”, *J Chem Eng Data*, 1981, doi:10.1021/je00025a017.

# Effect of the apex gap size on the performance of a small scale Wankel expander

G. Tozer<sup>1\*</sup>, R. Al-Dadah<sup>1</sup>, S. Mahmoud<sup>1</sup>

<sup>1</sup> The University of Birmingham, Edgbaston, Birmingham, B15 2TT, United Kingdom

\*Corresponding author: gxt357@bham.ac.uk

## Abstract

In this paper, a computational fluid dynamics (CFD) model was developed to investigate the effect of different apex gap sizes on the performance of a small-scale (50-300W) Wankel Expander without apex seals. This expander offers the advantages of ease of manufacturing, lower cost and reduced friction and wear. However, without the seals, leakage increases across the apexes leading to reduction in power output. Therefore, this study investigated the effect of apex gap size on the performance of such a Wankel expander. Results show the expander without apex seals experiences significantly less leakage at high rotational speeds, however suffers from flow throttling at the inlet ports at these speeds. The problem with throttling can be somewhat mitigated with double-sided ports.

**Keywords:** Wankel expander, computational fluid dynamics, Liquid air energy storage

## Introduction/Background

Liquid air energy storage (LAES) is a method of storing energy in which air is liquefied using work and later reheated and expanded to retrieve the work. Two key components in LAES cycles are compressors and expanders. The Wankel engine was first developed in 1951 by Felix Wankel. It's commercial availability and development has primarily been as an internal combustion engine, benefiting from high power to weight ratios, a small number of moving parts and less vibrations during operation. The following equations describe the shape of the Wankel housing (Equations 1 and 2) and the motion of the rotor (Equations 3, 4 and 5).

$$x_h = e \cdot \cos(3\theta) + r \cdot \cos(\theta) \quad \#(1)$$

$$y_h = e \cdot \sin(3\theta) + r \cdot \sin(\theta) \quad \#(2)$$

For the interval  $[0 < \theta < 360]$ , where  $e$  and  $r$  are the generating eccentricity and radius respectively.

The rotor shape was created using the generating radius  $r$  from the housing equation to create the apexes minus the clearance,  $c$  which corresponds to the gap size. The apexes are then joined with arcs of radius  $R$ , as seen in Figure 1.

The motion of the rotor was defined by equations 3, 4 and 5. The rotor rotates at a constant rate ( $\theta$ ) around its own centre of gravity.

$$\varphi = 3\theta \quad \#(3)$$

Where  $\varphi$  is the crankshaft rotational speed, and  $\theta$  is the rotor rotational speed.

Simultaneously the rotor's centre of gravity translates with the following Cartesian velocities:

$$\frac{dx}{dt} = -\varphi \cdot e \cdot \sin(\varphi t) \quad \#(4)$$

$$\frac{dy}{dt} = \varphi \cdot e \cdot \cos(\varphi t) \quad \#(5)$$

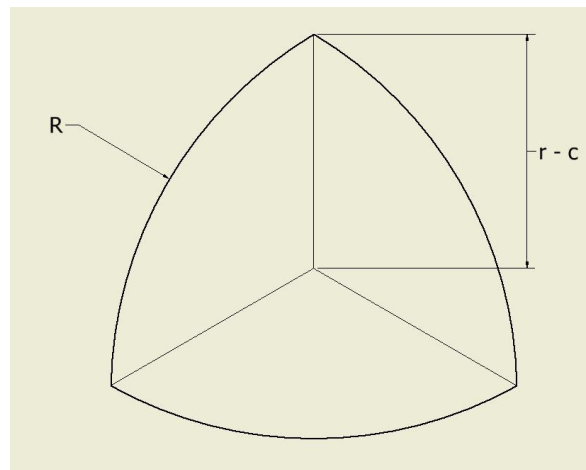


Figure 1 – Rotor shape creation

The Wankel geometry was developed as a compressor by Ogura [1] in 1982. The same advantages over piston compressors were noted here with the added benefit that no oil was burned during operation, unlike the internal combustion variant. In 1991 a series of articles by Badr et al. [2-4] outlined the potential of the Wankel device as an expander, once again pointing out the advantages of high reliability, durability, few moving parts and quietness of operation. They went on to discuss the design considerations including material selection, lubrication, geometry, port location and the use of valves. Antonelli et al. [5-9] have been developing a Wankel expander for use in an organic rankine cycle, having first tested it with air and then moving onto steam. This expander has valves on the inlet and outlet ports to allow specific charge and discharge timings. These are necessary to achieve higher efficiencies with the Wankel expander.

In 2017, a new compressor design was presented by Garside [10] which relied on a tight tolerance (0.05mm gap) with oil saturated air, instead of apex seals. It is further stated that an isentropic efficiency of 75% should be achievable with the described set-up. Zhang and Wang [11] researched into the contributions of friction a Wankel compressor. The conclusion was that the apex seals contribute the 2<sup>nd</sup> largest friction losses (17.75% of total friction) in the Wankel device. In the Wankel compressor design by Heppner et al. [12] a compression ratio of 3.3 could be achieved without the side seals, with a 6µm design tolerance.

This study looked at the concept of removing the Wankel expander's apex seals. The hypothesis being that if a tight fit can be achieved at the apex gaps, the leakage may be reduced to an acceptable amount. If this is the case the expander would additionally benefit from the removal of lubrication system that would use power and add complexity. Furthermore, the removal of the three apex seals and springs reduces the expander's part count by six and removes their associated friction loss contributions. All these would result in less manufacturing, assembly and maintenance costs.

### Methodology

In this study CFD is used utilising the ANSYS Fluent 18.2 software to simulate the operation of different Wankel expander setups. The base simulation model is described in detail within previous work [13], in which two user defined functions (UDFs) were utilised to solve problems with the transient simulation mesh motion. The simulation process is summed up briefly as follows:

1. Create the Wankel housing and rotor geometries in excel as a locus of points using equations 1 and 2.
2. Use CAD software (in this case Autodesk Inventor) to create the 3D geometry using the above locus of points.
3. Import the 3D geometry into Ansys to create a mesh.
4. Import the created mesh to Ansys Fluent and set up relevant boundary conditions and solver settings.
5. 'Hook' the UDFs needed for the transient motion of the mesh, the functions use equations [3-5] and [1,2] to define the motion of the rotor and housing respectively.
6. From the results a Pressure-Volume diagram is created and the enclosed area is the estimated work output. Using the averaged inlet flow rate specific work can be calculated and compared to the specific work of isentropic expansion to find the isentropic efficiency. This is presented in equations 6-8.

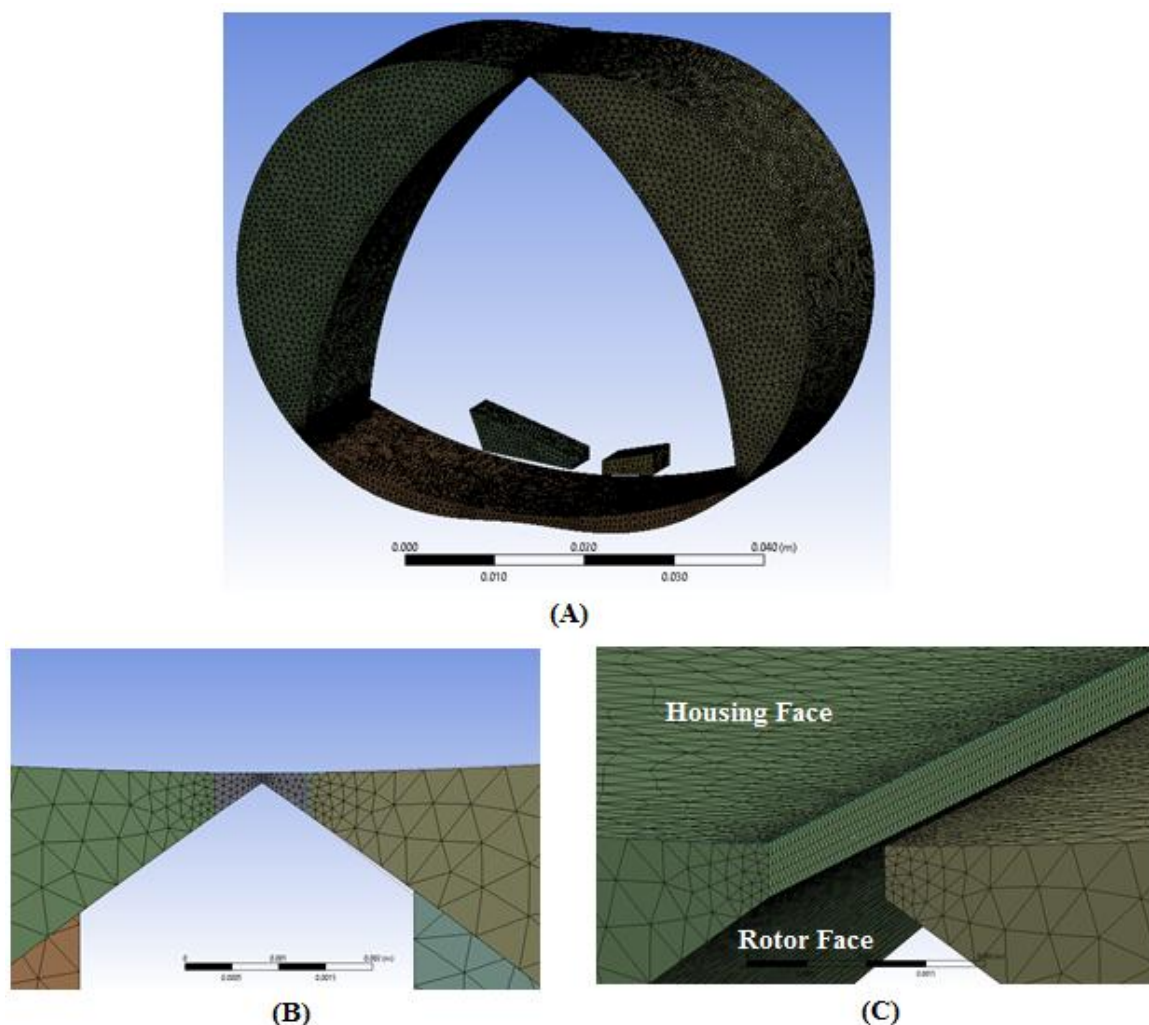


Figure 2 - (A) Mesh from 0.1mm gap case (B) Mesh at the apex gap (C) Face meshing apex gap wall

A third new UDF has been created for this study to allow for more accurate simulation around the apex areas of the Wankel expander. This new UDF allows a fine mesh to be created around the apex areas whilst allowing the three chambers and three apex areas to all be different 'zones' in Fluent. The advantage of separate zones is that pressures, temperatures and flow rates can be specified when collecting results for exactly the zone required. This is

important for the method of calculation that is employed which utilises a Pressure-Volume diagram for each separate ‘chamber’. The mesh used is shown in Figure 2. The different chambers plus the separate gap zones can be seen in different colours.

*Work output for expansion event,  $W = \text{area enclosed by PV diagram}$  # (6)*

*Specific work output,  $w_{actual} = 2 \cdot W \cdot \dot{m}_{inlets}$  # (7)*

*Isentropic efficiency,  $\eta = \frac{W_{actual}}{W_{isentropic}}$  # (8)*

The new Gap UDF works by keeping the lines splitting the zones straight and evenly spaced. This both prevents the overlap of zone interfaces and skewed cells in that area, both of which can lead to errors.

For the Gap UDF to function, the following meshing and Fluent set up are required:

1. The gap faces must be divided into exactly N number of nodes between the housing and the rotor edge.
2. Face meshing must be used to ensure structured layout of the gap face.
3. Housing and rotor UDFs must be executed chronologically before the gap UDF. To achieve this they must be hooked first and then the case must be saved and re-read. This needs to be done as the Gap UDF relies on the fact that the housing and Rotor UDFs move the outer nodes on the Gap face first.

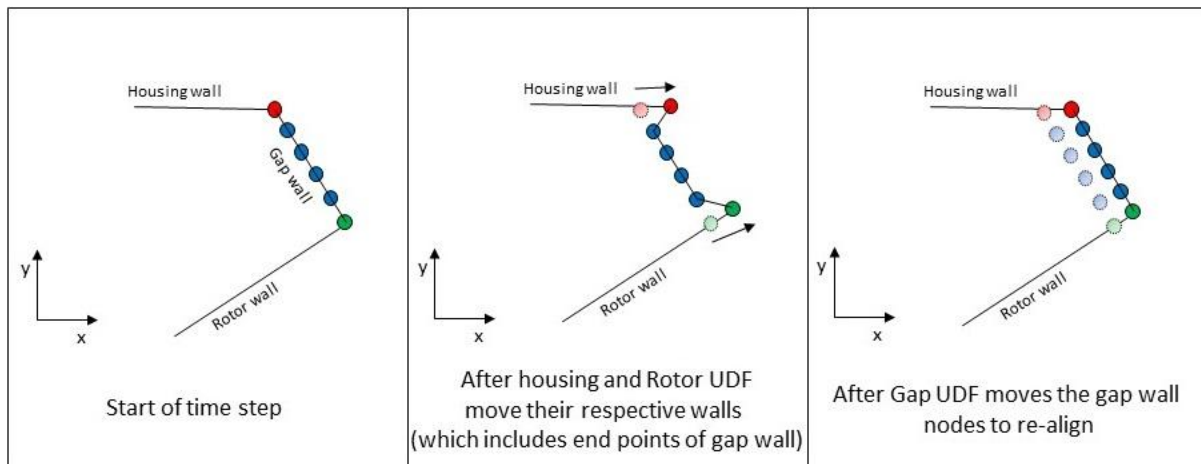


Figure 3 – Movement of nodes on gap face by new UDF

The code for the new gap UDF is described by the pseudocode below in conjunction with Figure 3.

1. First, loop through all the nodes on Gap face, matching all with equal (X,Y) locations and assign each unique (X,Y) location to an array with N locations. (Z location disregarded and calculations simplified to 2D for the time being)
2. Next, find which node in the array is shared by the rotor wall and which is shared by the housing wall (dark green and dark red in Figure 3). This is done by calculating the gradients between all of the nodes in the array. After this the number of equal gradients for each node is compared. As can be seen in Figure , the housing and rotor

shared nodes will have been moved, therefore they will no longer be aligned and have different gradients to all other nodes. Whereas the intermediate nodes (blue in Figure 3) will have multiple of the same gradients as they are still aligned.

3. The rotor and housing node positions from the previous time step are then calculated (light red and light green in diagram). This is done by adding a spacing equal to the spacing between other nodes onto either end of the line created by the unmoved gap nodes (blue).
4. The unmoved gap nodes (blue) are then each given a percentage of distance along the line formed by joining the previous time step housing and rotor nodes (light red and green).
5. This percentage is then used to move each node to the same percentage between the current time step housing and rotor nodes (dark red and green).

At current the simulations of cases with apex gaps takes between 120 to 312 hours using Intel Core i7-4820k 3.7GHz CPU and 48GB RAM, dependent on gap size.

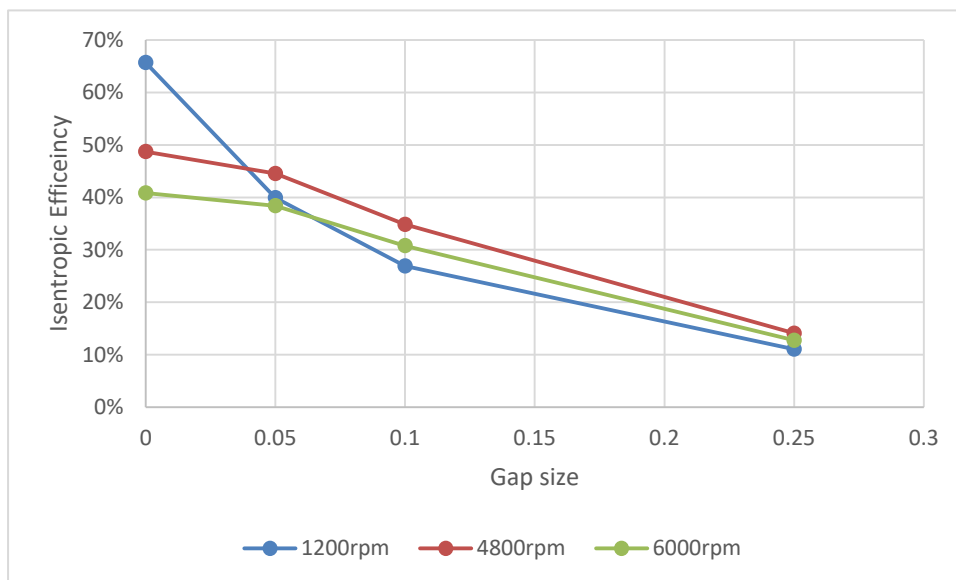


Figure 4 - Isentropic efficiency of expanders with different apex gap sizes and 2 bar inlet pressure

## Discussion and Results

For the results obtained from the CFD simulations in this section the following assumptions were made.

1. The radius and eccentricity used for the housing in the simulations were 30mm and 4.125mm respectively.
2. The rotor sides were considered fully sealed as just the apex gaps were being studied.
3. The inlets and outlets were considered to be constant pressure.

Figure 4 shows how the gap size affects the isentropic efficiency at three different speeds. Although the 1200RPM simulation gives the highest efficiency at the fully sealed case, it suffers most from an increase in apex gap size. The higher RPM cases drop less efficiency when increasing apex gap size. This is because as the expander runs faster, there is less time

in each cycle for the leakage between ‘chambers’ to occur. The 6000rpm 2 bar case gives the lowest efficiency drop from a fully sealed case (only 6% drop compared to 30% drop for 1200RPM) of all the gap cases currently. This being said the 6000RPM simulation has very poor isentropic efficiency at the fully sealed case. This is believed to be due to the heavy throttling of the flow through the inlet port. The higher speed cases could therefore be improved by providing a larger flow area for the inlet. Creating wider ports however, would change the opening and closing times of the inlets which could negatively affect efficiency.

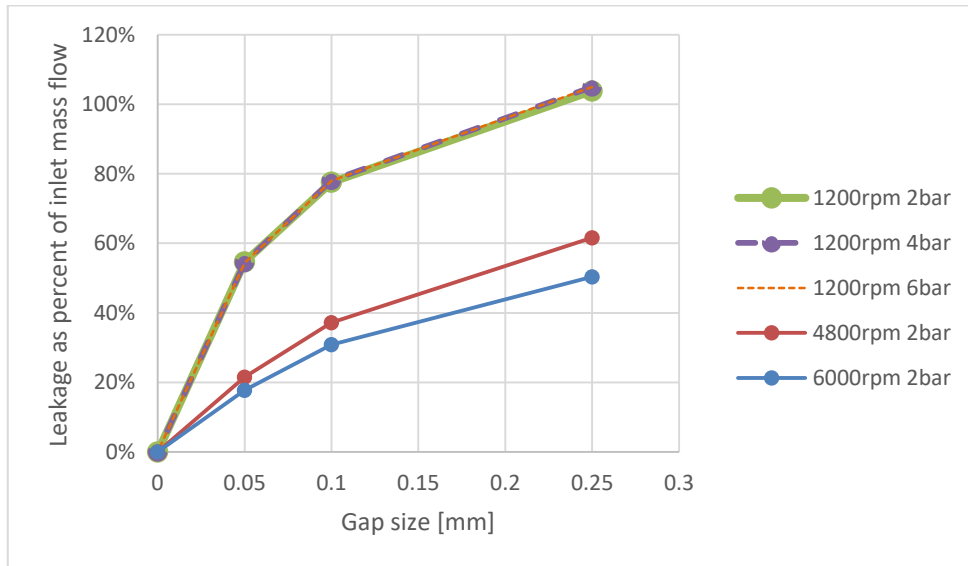


Figure 5 – Leakage of expanders with different apex gap size at different speeds and inlet pressures

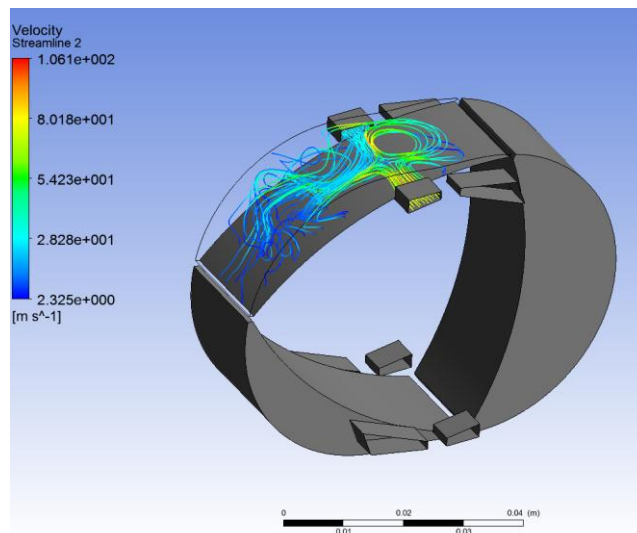


Figure 6 – Double sided ports set-up with streamlines

The results shown in Figure 5 give leakage as a percentage of inlet mass flow rate. This leakage percentage is calculated as:

$$\text{Leakage percentage} = \frac{\text{Averaged mass flow through all apex gaps in one revolution}}{\text{averaged mass flow at inlets in one revolution}} \#(9)$$



Interestingly the results show that the leakage percentage through the apex gaps is independent of inlet pressure. This would suggest that the speed the expander runs at is the most important factor when considering leakage amount. Therefore, if the expander ports can be altered to significantly reduce the throttling of the flow at higher speeds, a higher efficiency should be able to be achieved with the seal less design.

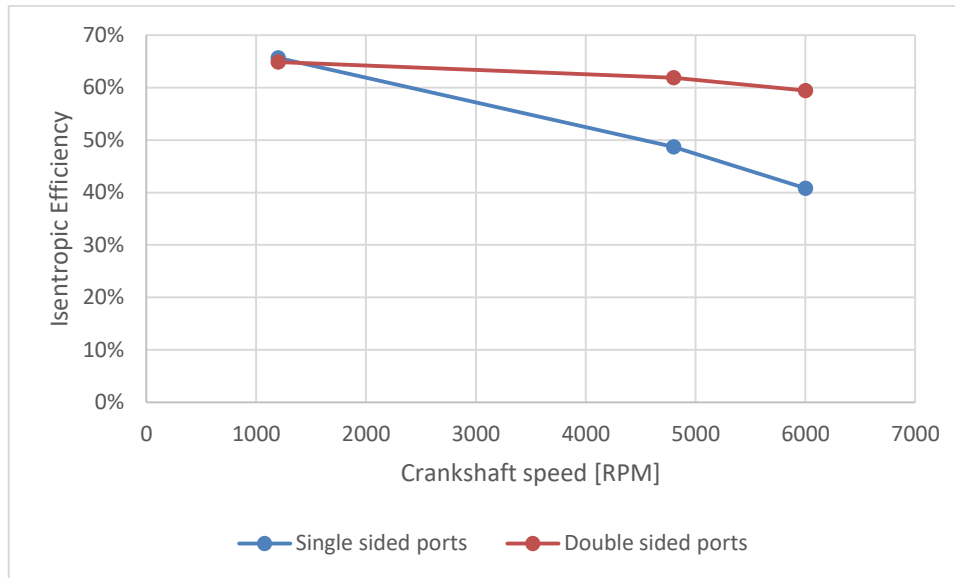


Figure 7 – Comparison of single and double sided ports for sealed apex setups

To attempt to reduce inlet throttling of the high speed cases, a model was setup with inlet and outlet ports on both sides as demonstrated in Figure 6. Figure 7 shows the comparison of double-sided with single sided port setups, results were simulated at 2 bar inlet pressure for a range of speeds. The double-sided setup suffers much less from a speed increase than the single-sided, therefore the double-sided port setup offers potential to improve the cases without seals.

### Conclusions and future work

A CFD model was adapted from previous work to allow for accurate simulations of the apex gaps of a Wankel expander. To achieve this a new user defined function was written for boundaries of the gap zones. Using the new CFD model, different gap sizes were simulated at different operating pressures and speeds. The inlet pressure was found to have no noticeable effect on the leakage through the apex seals. This is very useful information, as the expander can use the optimum inlet pressure for efficiency, without any worry on negative effects on leakage.

It was further noted that the leakage was always reduced at higher operating speeds as a result of reduced time for leakage to occur. However, with the current port configurations the inlet flow is throttled greatly at higher speeds, significantly reducing the efficiency. Therefore to improve this, inlet and outlet ports were placed on both sides of the expander to increase flow area. Results show that with single sided ports the efficiency drops by 25% when speed is increased from 1200RPM to 6000 RPM, whilst with double sided the efficiency only drops 5% for the same speed increase.

Future work will include analysing the different gap sizes for the double sided port configurations, further optimising the inlet ports and analysing the benefit of valves on the inlet ports.

## References

1. Ogura, I., *The Ogura-Wankel Compressor - Application of Wankel Rotary Concept as Automotive Air Conditioning Compressor*. 1982, SAE International.
2. Badr, O., Naik, S., O'Callaghan, P.W., and Probert, S.D., *Rotary Wankel engines as expansion devices in steam Rankine-cycle engines*. Applied Energy, 1991. **39**(1): p. 59-76.
3. Badr, O., Naik, S., O'Callaghan, P.W., and Probert, S.D., *Wankel engines as steam expanders: Design considerations*. Applied Energy, 1991. **40**(3): p. 157-170.
4. Badr, O., Naik, S., O'Callaghan, P.W., and Probert, S.D., *Expansion Machine for a Low Power-Output Steam Rankine-Cycle Engine*. Applied Energy, 1991. **39** p. 93 - 116.
5. Antonelli, M., Baccioli, A., Francesconi, M., Desideri, U., and Martorano, L., *Operating maps of a rotary engine used as an expander for micro-generation with various working fluids*. Applied Energy, 2014. **113**: p. 742-750.
6. Antonelli, M., Baccioli, A., Francesconi, M., and Martorano, L., *Experimental and Numerical Analysis of the Valve Timing Effects on the Performances of a Small Volumetric Rotary Expansion Device*. Energy Procedia, 2014. **45**: p. 1077-1086.
7. Antonelli, M., Baccioli, A., Francesconi, M., and Martorano, L., *Numerical and Experimental Analysis of the Intake and Exhaust Valves of a Rotary Expansion Device for Micro generation*. Energy Procedia, 2015. **81**: p. 461-471.
8. Antonelli, M., Francesconi, M., Baccioli, A., and Caposciutti, G., *Experimental Results of a Wankel-type Expander Fuelled by Compressed Air and Saturated Steam*. Energy Procedia, 2017. **105**: p. 2929-2934.
9. Antonelli, M. and Martorano, L., *A study on the rotary steam engine for distributed generation in small size power plants*. Applied Energy, 2012. **97**: p. 642-647.
10. Garside, D.W., *A new Wankel-type compressor and vacuum pump*. IOP Conference Series: Materials Science and Engineering, 2017. **232**.
11. Zhang, Y. and Wang, W., *Effects of leakage and friction on the miniaturization of a Wankel compressor*. Frontiers in Energy, 2010. **5**(1): p. 83-92.
12. Heppner, J.D., Walther, D.C., and Pisano, A.P., *The design of ARCTIC: A rotary compressor thermally insulated  $\mu$ cooler*. Sensors and Actuators A: Physical, 2007. **134**(1): p. 47-56.
13. Sadiq, G.A., Tozer, G., Al-Dadah, R., and Mahmoud, S., *CFD simulations of compressed air two stage rotary Wankel expander – Parametric analysis*. Energy Conversion and Management, 2017. **142**: p. 42-52.

# Water Mixtures as Working Fluids in Organic Rankine Cycles

P. Bombarda<sup>1\*</sup>, G. Di Marcoberardino<sup>1</sup>, C. Invernizzi<sup>2</sup>, P. Iora<sup>2</sup> and G. Manzolini<sup>1</sup>

<sup>1</sup>Politecnico di Milano, Energy Department, via Raffaele Lambruschini, 4. 20156 Milano

<sup>2</sup>University of Brescia, Department of Mechanical and Industrial Engineering, via Branze, 38. 25123 Brescia

\*Corresponding author: paola.bombarda@polimi.it email address

## Abstract

This work deals with the adoption in ORC plants of a mixture composed by water (acting as solvent) plus an alcohol or a cyclic ether (acting as solute) as working fluid. Initially an evaluation of the thermodynamic properties of the mixture is performed, in order to assess the mixture general properties, and, as it is desired that the mixture behave as a near-azeotropic mixture, to point out the molar fractions which entail a near-azeotropic behaviour. Three different mixtures are considered: two mixtures of water and alcohols (n-butanol and 2,2,2-trifluoroethanol) and a mixture of water plus a cyclic ether (tetrahydrofuran). Simultaneously, the thermal stability of the pure substances considered as possible solute for the mixtures is experimentally investigated in order to estimate the temperature applicability range. The ORC plant performance adopting the selected mixtures as working fluid is finally evaluated, and the analysis includes a discussion on the turbine design; results are compared with respect to the reference case of a hypothetical plant adopting water as working fluid. Results are given for two different case studies: a heat recovery application from a Diesel Engine and a geothermal plant.

**Keywords:** ORC cycles, water mixtures, near-azeotropic mixtures, thermal stability.

## Introduction

It is well known that the choice of the right working fluid in an ORC is a crucial issue. An astonishing number of papers in the open literature deals with this issue: the question is still open because, on one side better performance is desired, and, on the other side, the working fluid must comply with the evolving environmental regulations. Though most of the papers related to this subject deal just with the cycle efficiency, it is essential to investigate also other aspects like the component sizing (mainly the turbine design) and the safety and environmental compliance. Usually pure working fluids are selected as working fluid in ORC plants, mainly refrigerants, hydrocarbons, poly-siloxanes [1]. As it is also well known, water is not a suitable working fluid in Rankine cycles of (relatively) small power size or low temperature, but water is relatively inexpensive and safe. For this last reason, in the present paper, the adoption of a water based mixture is suggested, in order to investigate whether, by the addition of a proper substance, water can become an eligible working fluid in ORC plants.

The adoption of zeotropic mixtures as working fluid has been proposed and discussed, aiming at minimizing the heat introduction irreversibility in the frame of heat recovery applications; however, it should be also considered that, depending on the cold source, the gain at the primary heat exchanger could vanish considering the heat rejection irreversibility at the condenser. Because of this last point, the aim is to investigate a mixture which behaves as a near-azeotropic mixture. Specifically, we will investigate several thermodynamic characteristics of two-component, near-azeotropic mixtures, composed by water plus a substance completely soluble in water. The mixing with water (considered here as the solvent) basically reduces the flammability and the possible toxicity of the solute and substantially modifies the thermodynamic properties of the solvent itself. Mixtures of water

for possible application in ORCs were already investigated in the past [2–4] and recently considered again [5]. There are many fluids totally miscible in water and forming near-azeotropes, for example, alcohols, acids, esters, etc. Here we will discuss mixtures of water and alcohols (n-butanol and 2,2,2-trifluoroethanol) and a mixture of water plus tetrahydrofuran (a cyclic ether).

Two different case studies will be discussed: power production from heat recovery of a Diesel engine and from a geothermal plant. The thermodynamic properties of the different working fluid mixtures and the plant performance were evaluated by means of Aspen Plus v9.0 [6]. Experimental test for the thermal stability of the selected fluids were conducted in order to check the applicability range. The final aim is to find a mixture composition so that it allows a satisfying conversion efficiency together with a convenient turbine sizing and an almost dry expansion (vapour quality at the end of the expansion close to one).

## Discussion and Result

The following issues are relevant for the cycle performance evaluation: the phase diagrams, which are important during the heat introduction and heat rejection process; the shape of the saturation curve in the T-s plane, which has relevance for the turbine expansion process; the flammability of the mixture and the thermal stability of the mixture, which define the applicability range.

### Mixture thermodynamic properties

The influence of the mixture composition on the thermodynamic properties is investigated. The main thermodynamic properties of the pure substances (critical temperature  $T_{cr}$ , critical pressure  $p_{cr}$ , molecular mass MM, parameter of molecular complexity  $\sigma^1$ , normal boiling temperature  $T_b$ ), reported in Table 1, are evaluated from Aspen Properties v9.0 using specific methods for each substance (UNIFAC and PRWS). It can be seen that water is mixed with fluids with a lower critical point (lower critical temperature and pressure) and a higher molecular mass.

Table 1 Thermodynamic properties of the working fluid mixture components.

Fluid	$T_{cr}$ (°C)	$p_{cr}$ (bar)	MM (kg/kmol)	$\sigma$ (-)	$T_b$ (°C)
water	373.95	220.64	18.02	-10.38	100.00
2,2,2-trifluoroethanol	225.42	48.09	100.04	-2.76	73.80
tetrahydrofuran	267	51.90	72.11	1.95	65.97
n-butanol	289.95	44.14	74.12	4.24	118.75

The phase diagrams, obtained by means of theoretical calculations performed with Aspen Plus and presented in Figure 1, show the behaviour of the mixtures at different pressures. It can be seen from the picture that, in case of water/n-butanol mixture, the near-azeotropic behaviour occurs, depending on pressure, in the range 0.7-0.8 of the molar fraction. The other two mixtures, water/2,2,2-trifluoroethanol and water/tetrahydrofuran, show a different behaviour: in the first case, an extended near-azeotropic behaviour is obtained in a wide range of low molar fractions; in the last case, near-azeotropic behaviour is again at low molar fractions, but the effect of pressure is also relevant.

<sup>1</sup>The parameter  $\sigma$  is defined as the dimensionless slope of the vapour saturation curve in the T-s plane  $\sigma = \frac{T_{cr}}{R} \left( \frac{ds}{dT} \right)_{T_r=0.7}$

The amplitude of the saturation curve is relevant for the turbine expansion: the shape of the saturation curve is therefore analysed in the following pictures. This figure shows the saturation curve (or dew and bubble line for a mixture) in T-s plane, which depends on the  $\sigma$  parameter. Pure component curves are also reported in the figure: the curve of water ( $\sigma = -10.38$ ) exhibits a wide “bell” shape, while the curve of 2,2,2-trifluoroethanol ( $\sigma = -2.76$ ) exhibits a narrow shape; the curves corresponding to mixtures of two different compositions show an intermediate behaviour. An unexpected behaviour of the mixture water/tetrahydrofuran in two-phase area in T-s plane at low pressure with  $z_1=0.5$  is found; further investigation could be advisable.

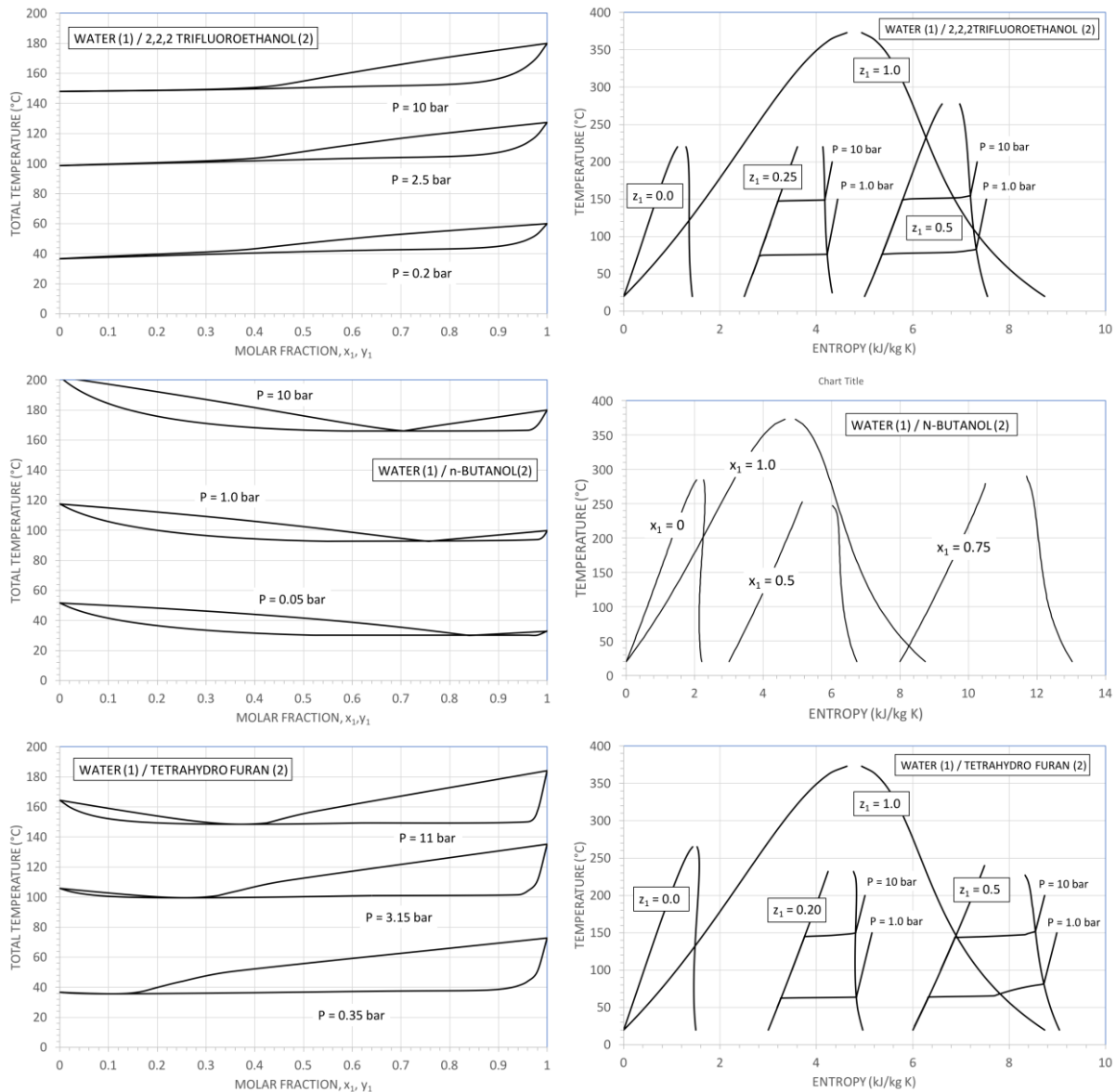


Figure 1 Left: Phase diagram (T-xy) of the investigated mixtures at different pressures where 1 refers to water and 2 refers to 2,2,2-trifluoroethanol (top), n –butanol (center), tetrahydrofuran (bottom). Right: Saturation curves in T-s plane of the three mixtures with different water content.

Regarding the flammability of the mixture, the flash point is the main physical properties used to determine the fire and explosion hazards of liquids. It indicates the lowest temperature at which a volatile fuel ignites or flashes when it contacts a spark or flame. So

the mixing with water, that is an inert, can increase the flash point temperature, decreasing the flammability risk. The most commonly used flash point prediction model for aqueous-organic binary mixtures [7,8] was adopted: the author verified that the model can predict the flash points of binary and ternary aqueous mixtures by considering only the flammable component in the mixtures [9]. The flash point of 2,2,2-trifluoroethanol, for example, is 29°C while considering the mixture with water it increases to 59°C at  $z_1$  equal to 0.25 and 91°C at  $z_1$  0.5.

### Thermal stability

The thermal stability test method, as discussed in [10,11], compares the vapour pressure of the fluid before and after the thermal stress test. Figure 2 shows the test bench and detailed scheme of the test circuit placed in the Fluid Lab Test of University of Brescia. The test circuit, in stainless steel AISI 316, consists of a sample cylinder, one thermocouple (type K), two pressure transmitter to cover a wide range of pressure from 1 to 100 bar and some block valves to charge and isolate the investigated fluid. More details on the experimental apparatus are discussed in [10]. The vapour pressure deviations, or the fluid decomposition, from the virgin fluid behaviour are evaluated both at high temperatures, during the thermal stress tests, and at temperature close to ambient conditions. After the preparation of the fluid sample, the experimental procedure consists of a thermal stress in an electric oven at high temperatures for a time span of 80 h, followed by the measure of the vapour pressure profile of the investigated fluid between 10 °C and 180 °C. Experimental test conditions of the fluids are summarized in Table . As shown in Figure , results are so compared with the values of the p-T curve obtained for the fluid sample before the start of the series/sequence of thermal stresses for the three fluids. The measured values of the vapour pressure  $P_v$  for the virgin fluid were fitted by the equation  $\ln P_v = A + B/T$  whose coefficients A and B are reported in Figure 3.

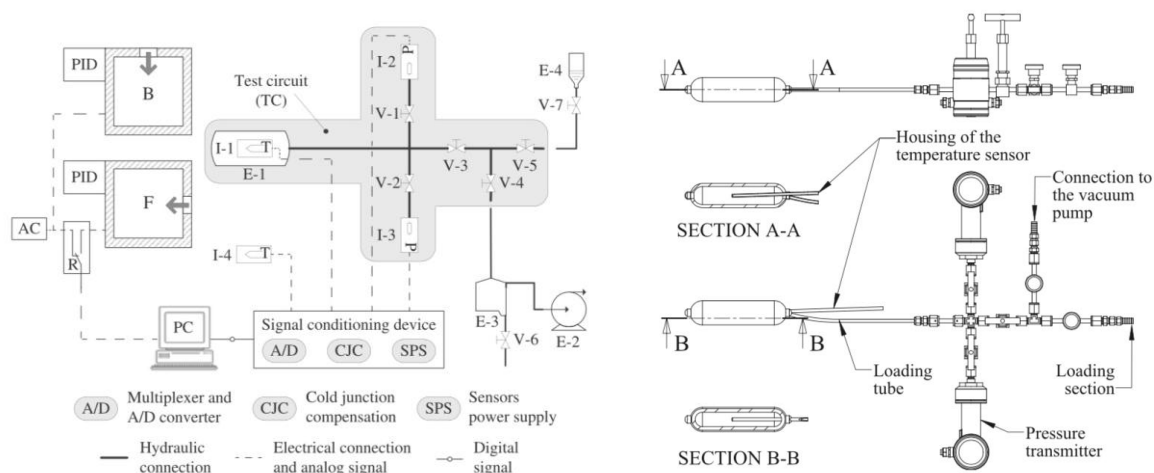


Figure 2 Experimental test bench (left) and details of test circuit (right)

As shown in Figure 3, 2,2,2-trifluoroethanol and tetrahydrofuran are stable up to 250°C while n-butanol profiles reveal first pressure deviations at 220°C. After the thermal stress test at 250°C, pressure deviations of the first two fluids from the reference saturation curve at 20°C are 28 and 58 mbar respectively while n-butanol after stress test at 240°C at 50°C has a pressure increase of 183 mbar. This behaviour can be highlighted by the evaluation of the fluids decomposition rate, as discussed in [11].

Table 2 Thermal stress tests conditions.

Fluid	Fluid charge (g)	T (°C)	$\Delta T_{\text{step}}$ (°C)	Time <sub>step</sub> (h)
2,2,2-trifluoroethanol	35	200÷320	10	80 (60 at 310 °C)
tetrahydrofuran	26	150÷250	20 for T ≤ 190°C 10 for T > 190°C	80
n-butanol	26	150÷300	20 for T ≤ 190°C 10 for T > 190°C	80

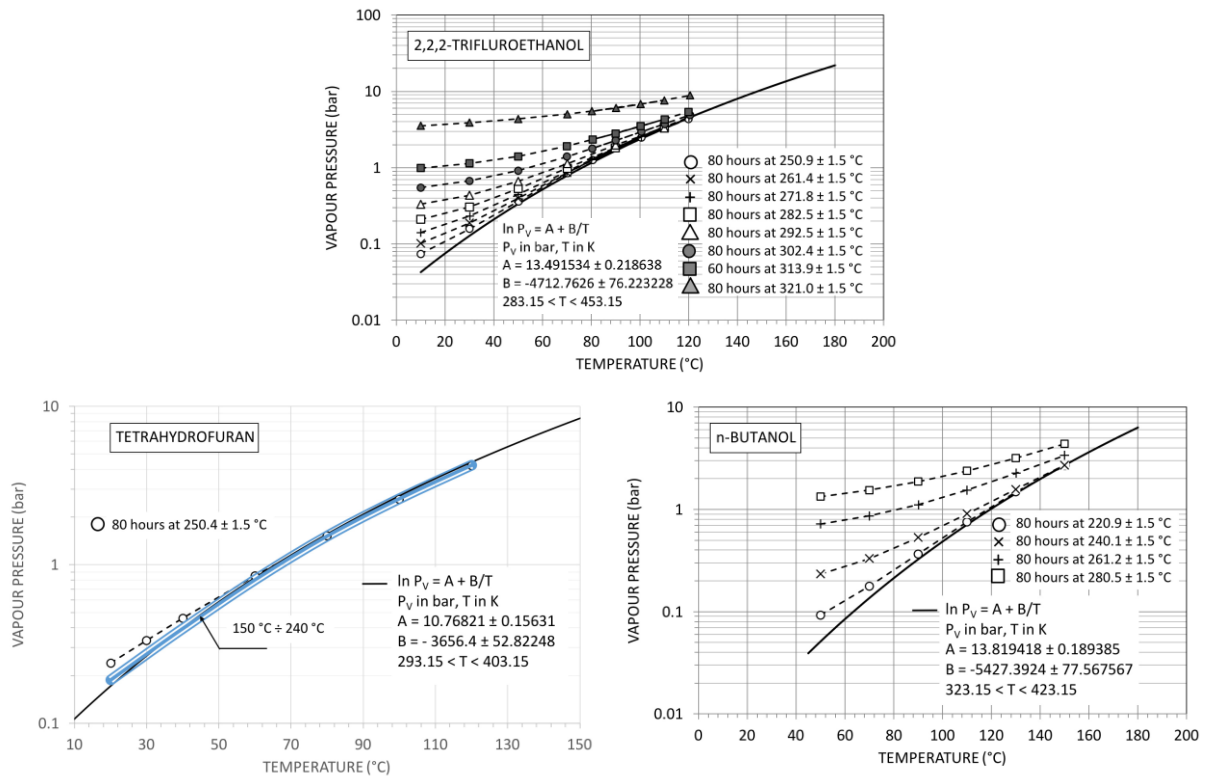


Figure 3 Vapour pressure profile of the three fluids after each thermal stress tests.

Figure 4 reports the quasi-constant of the velocity reaction as a function of the reciprocal of the stress temperature for the fluids 2,2,2-trifluoroethanol, n-butanol. Toluene is added as reference stable fluid for ORC cycle [12].

For a fixed decomposition rate  $k^* = 1 \cdot 10^{-9} s^{-1}$ , the corresponding temperature are about 300 °C and 250 °C for the first and the second fluid respectively. From the temperature point of view, the value of the parameter  $k^*$  at 300 °C for the n-butanol is about ten times respect to the 2,2,2-trifluoroethanol: in fact, the fluorine content makes the latter more stable.

### Cycle performance evaluation with the selected mixtures as working fluid

Afterwards, the performance of different cycles adopting the considered mixtures is evaluated. In all cases the following assumptions are made: non-isothermal hot source, constant condensing temperature, constant minimum temperature difference in the primary heat exchanger and negligible pressure losses; the evaluation is performed for different molar fractions of the mixture. Note that, following the adoption of a non-isothermal hot source, the evaporation pressure becomes the main operating parameter to be selected.

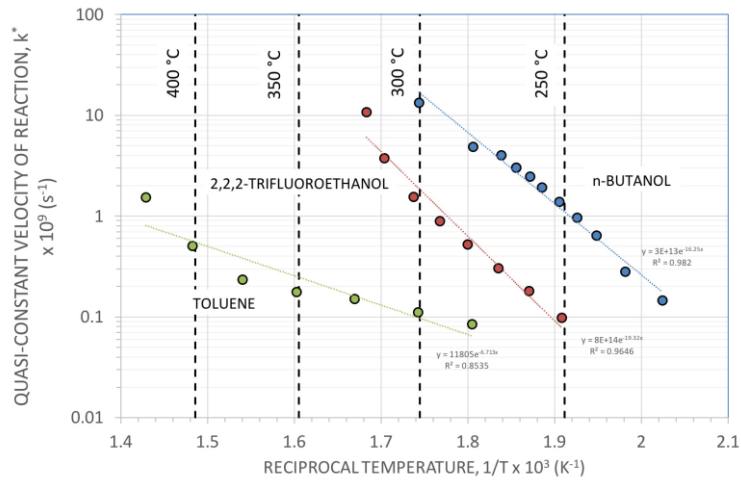


Figure 4 Quasi-constant of the velocity reaction as a function of the reciprocal of the stress temperature for n-butanol, 2,2,2-trifluoroethanol and toluene.

Firstly a high temperature, heat recovery application is evaluated. The heat source is assumed as constituted by exhaust flue gases at 330 °C, from a Diesel engine. After the results of the thermal stability test, a mixture of water plus 2,2,2-trifluoroethanol is selected as working fluid.

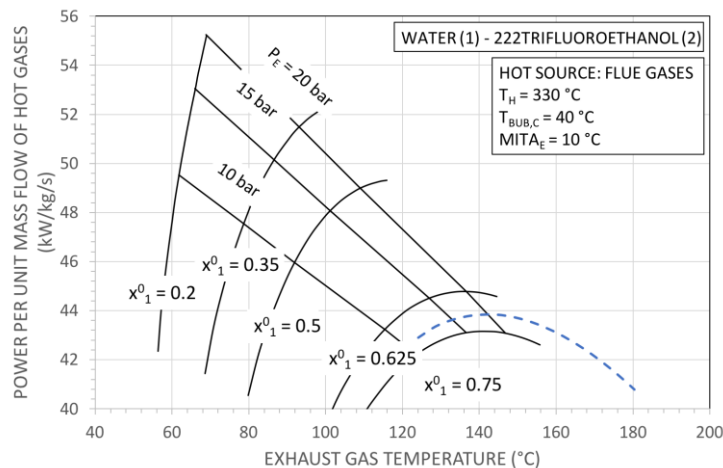


Figure 5 Net power per unit mass flow of hot gases as a function of the exhausts temperature for different molar fractions of the mixture. The curve representing pure water is dashed.

Figure 5 shows the obtainable specific net power: basically, the net power decreases with the increasing of the water molar fraction. For example, for a mixture with  $x_1^0 = 0.5$ , assuming an evaporation pressure of about 13 bar, which is rather close to the optimized value, though allowing a limited isentropic enthalpy drop of about 200 kJ/kg (reasonable for a single stage axial turbine),  $\dot{W}$  results 48 kW per unit mass flow of hot gases, and the isentropic discharge vapour quality turns out to be about 0.9. On the other hand, with  $x_1^0 = 1.0$  (pure water), even at the optimized evaporation pressure  $P_E = 9 \text{ bar}$ , the maximum power results 44 kW, with an isentropic discharge vapour quality of 0.8 and a turbine isentropic enthalpy drop of 716 kJ/kg (which could not be accomplished in a single stage turbine).



As a second case study, the exploitation of heat source at 200°C (possibly a geothermal source) is considered, and three different water based mixtures are considered as working fluid.

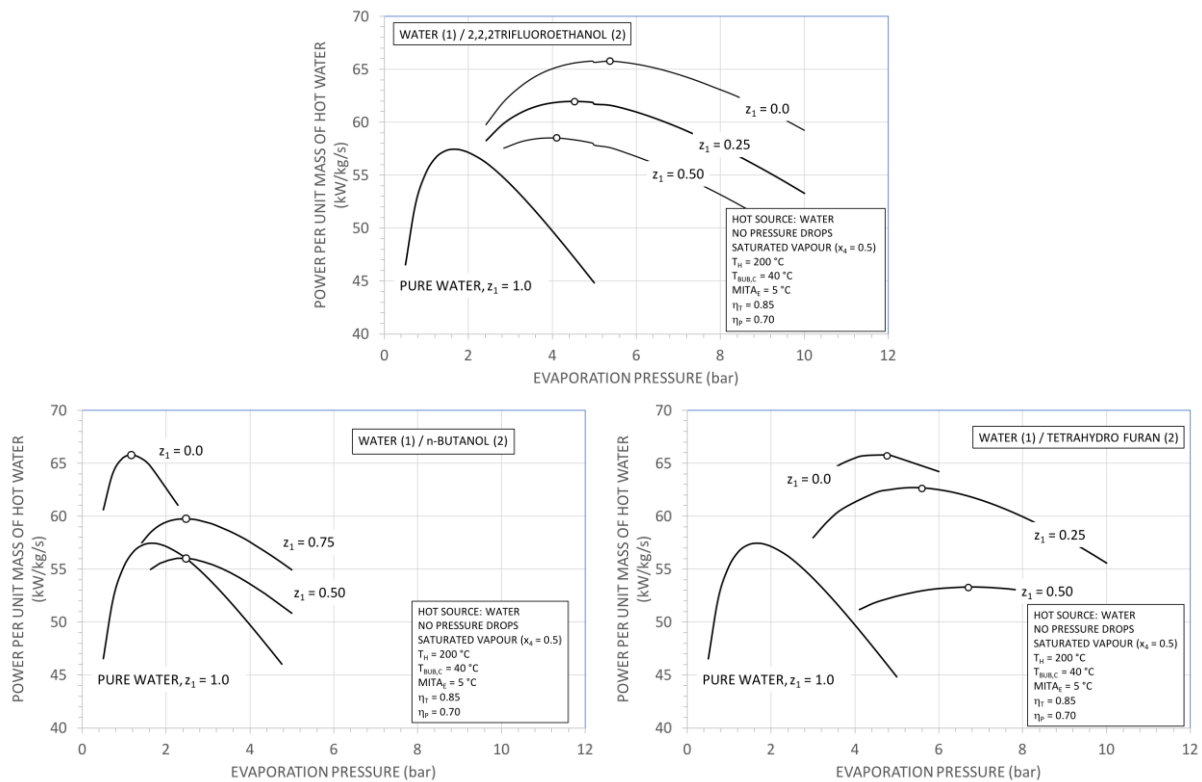


Figure 6 Net power per unit mass flow of hot water as a function of the evaporation pressure.

In all cases it is confirmed that water, if adopted as a pure component, would be a poor working fluid for this application, since the curve corresponding to pure water attains power values lower than those of corresponding curves for the other fluids; moreover, all the three fluids allow roughly the same performance, though with different evaporation pressures. If a mixture is adopted as working fluid, intermediate values are found, and a molar fraction (with respect to water) lower than 0.5 must be selected in order to have an effective gain with respect to water.

The results presented in the previous figures need to be integrated with the results concerning the turbine design, provided in Table 3.

Table 3 Turbine design parameters

Fluid	$z_1$	$p_{ev}$ (bar)	$p_c$ (bar)	$x_{OUT, is}$ (-)	$\dot{V}_{out}$ (m <sup>3</sup> /s/MW)	Turbine <sup>a</sup>		
						$n_{st}$	$M^b$	$U/U_{max}^c$
water	1	1.6	0.078	0.866	35.20	4	0.73	0.97
water/ n-butanol	0.75	2.5	0.096	0.898	27.70	3	0.93	0.87
	0.5	2.45	0.090	0.935	29.38	3	0.97	0.73
	0	1.1	0.026	0.984	88.63	3	1.09	0.63
water/ 2,2,2-trifluoroethanol	0.5	4.15	0.195	0.917	14.62	3	0.94	0.64
	0.25	4.5	0.219	0.942	13.34	3	0.93	0.54
	0	5.4	0.250	0.975	11.78	3	0.91	0.48
water/ tetrahydrofuran	0.5	6.7	0.416	0.919	7.62	2	1.11	0.87
	0.25	5.6	0.433	0.953	8.12	2	1.03	0.70
	0	4.75	0.417	1.0	8.99	2	1.03	0.63

<sup>a</sup> repeating ideal stages: (i) maximum efficiency, (ii) reaction degree 0.5, (iii) nozzle exhaust angle 20° (absolute velocity)

<sup>b</sup> Mach number at nozzle discharge (absolute velocity)

<sup>c</sup> ratio between the mean blade speed and the assumed maximum allowed blade speed  $U_{\max} = 350$  m/s

After the values regarding the turbine sizing, the most promising component for a water-based mixture seems to be the 2,2,2-trifluoroethanol. With a 2,2,2-trifluoroethanol mixture and a water molar fraction comprised in the range 0.5-0.25, a similar or higher power with respect to the base case (100% water) can be obtained, but with a smaller turbine (lower number of turbine stages, 3 instead of 4, and less than the half the volumetric flow rate); moreover the turbine is still subsonic and the quality at the end of the expansion acceptable. A performance gain with an even smaller turbine can be obtained by means of a mixture with a relevant fraction of tetrahydrofuran (in the order of 75%); however in this case the turbine would be supersonic. The adoption of a mixture with n-butanol is questionable, since it would involve performance similar to that of the base water case.

## Conclusions

The analysis shows that the adoption in ORC plants of a mixture composed by water (acting as solvent) plus an alcohol or a cyclic ether (acting as solute) as working fluid may be convenient. Among the mixtures investigated, the 2,2,2-trifluoroethanol mixture appear as the most promising: it allows a satisfying cooling of the heat source, which results in an adequate plant performance, and involves the advantage of a convenient sizing of the turbine; moreover, the presence of water in the mixture reduces the inherent flammability of the alcohol. The analysis may be extended in future work to mixtures with different solutes.

## Acknowledgements

The authors thank Modestino Savoia for his effort and contribution to the laboratory activities.

## References:

- [1] C.M. Invernizzi, P. Iora, M. Preißinger, G. Manzolini, HFOs as substitute for R-134a as working fluids in ORC power plants: A thermodynamic assessment and thermal stability analysis, *Appl. Therm. Eng.* 103 (2016) 790–797. doi:10.1016/J.APPLTHERMALENG.2016.04.101.
- [2] E.D. Rogdakis, Thermodynamic analysis, parametric study and optimum operation of the Kalina cycle, *Int. J. Energy Res.* 20 (1966) 359–370.
- [3] G.S. Somekh, Water-Pyridine Azeotrope is an Excellent Rankine Cycle Fluid, *J. Eng. Power.* 97 (1975) 583–588.
- [4] P. Patel, E.F. Doyle, R.J. Raymond, R. Sakhuia, Automotive Organic Rankine-Cycle Powerplant - Design and Performance Data, in: *Automot. Eng. Congr.*, SAE Paper 740297, Detroit, Michigan, 1974.
- [5] R.A. Victor, J.-K. Kim, R. Smith, Composition optimisation of working fluids for Organic Rankine Cycles and Kalina cycles, *Energy.* 55 (2013) 114–126. doi:10.1016/j.energy.2013.03.069.
- [6] AspenTech, Aspen Plus, (n.d.). <http://www.aspentech.com/products/aspen-plus.aspx>.
- [7] H.J. Liaw, Y.Y. Chiu, The prediction of the flash point for binary aqueous-organic solutions, *J. Hazard. Mater.* 101 (2003) 83–106. doi:10.1016/S0304-3894(03)00168-7.
- [8] R. Jadot, M. Fraiha, Isobaric vapor-liquid equilibrium of 2,2,2-Trifluoroethanol with water and 1-Propanol binary systems, *J. Chem. Eng. Data.* 33 (1988) 237–240. doi:10.1021/je00053a004.

- [9] L.Y. Phoon, A.A. Mustaffa, H. Hashim, R. Mat, A review of flash point prediction models for flammable liquid mixtures, *Ind. Eng. Chem. Res.* 53 (2014) 12553–12565. doi:10.1021/ie501233g.
- [10] M. Pasetti, C.M. Invernizzi, P. Iora, Thermal stability of working fluids for organic Rankine cycles: An improved survey method and experimental results for cyclopentane, isopentane and n-butane, *Appl. Therm. Eng.* 73 (2014) 762–772. doi:10.1016/j.applthermaleng.2014.08.017.
- [11] C.M. Invernizzi, P. Iora, G. Manzolini, S. Lasala, Thermal stability of n-pentane, cyclo-pentane and toluene as working fluids in organic Rankine engines, *Appl. Therm. Eng.* 121 (2017) 172–179. doi:10.1016/j.applthermaleng.2017.04.038.
- [12] V.N. Havens, D.R. Ragaller, L. Sibert, D. Miller, Toluene stability space station Rankine power system, in: 22nd Intersoc. Energy Convers. Eng. Conf., Philadelphia, Pennsylvania, 1987: pp. 121–126.

# Constant power production with an organic Rankine cycle from a fluctuating waste heat source by using thermal storage

K. Couvreur<sup>1</sup>, J. Timmerman<sup>1</sup>, W. Beyne<sup>2</sup>, S. Gusev<sup>1</sup>, M. De Paepe<sup>2</sup>, W.D. Steinmann<sup>3</sup>,  
and B. Vanslambrouck<sup>1\*</sup>

<sup>1</sup>Department of Flow, Heat and Combustion Mechanics, Ghent University – UGent, Graaf Karel de Goedelaan 5, 8500 Kortrijk, Belgium

<sup>2</sup>Department of Flow, Heat and Combustion Mechanics, Ghent University – UGent, Sint-Pietersnieuwstraat 41, 9000 Gent, Belgium

<sup>3</sup>Institute of Technical Thermodynamics, German Aerospace Center (DLR), Pfaffenwaldring 38-40, 70569 Stuttgart, Germany

\*Corresponding author: Bruno.Vanslambrouck@Ugent.be

## Abstract

In energy intensive industries, organic Rankine cycle (ORC) systems can significantly increase energy efficiency and reduce carbon emissions by converting low- and medium-temperature waste heat to electricity. However, fluctuations in waste heat availability can negatively affect the operation of an ORC unit. By integrating intermediate thermal energy storage these fluctuations can be mitigated and part-load operation of the ORC unit can be avoided. This paper describes the design of a test rig to investigate combined LHS ORC systems and the set-up of future experiments. The test rig consists of a 110 kWh latent heat storage (LHS) system, connected to a 250 kW<sub>e</sub> heater and a 11 kW<sub>e</sub> ORC unit. For optimal integration and operation of LHS systems, effective operating strategies and methods to monitor the state of charge (SOC) need to be composed.

**Keywords:** waste heat recovery, organic Rankine cycle, thermal energy storage, latent heat storage.

## Introduction

In 2013, 25% of the total energy consumption of the European Union could be allocated to the industry sector. In 2014, 20% of the greenhouse emissions originated from manufacturing processes [1]. A considerable amount of the industrial primary energy (20 – 50%) is lost in forms of low grade waste heat in large scale thermal systems [2]. However, by exchanging this waste heat between thermal processes or converting it to electricity, fossil fuel consumption and related emissions can be decreased. The recovered energy can be either reused directly in the same industrial site where it is produced, or it can be fed in a distribution network. Waste heat to power (WHP) systems such as ORC create opportunities to increase the energy efficiency in energy intensive industries and reduce emissions [3]. Typically, in WHP applications, two phase power cycles are frequently used to recuperate waste heat. Waste heat is recuperated and transferred to a working fluid of which the properties are adapted to the waste heat source temperature. Subsequently mechanical energy is generated in an expander coupled to an electric generator. Common and well developed power cycles include steam Rankine cycle, ORC and Kalina cycle. The ORC is considered as a viable technology for converting low- and medium-temperature heat to electricity for which it is difficult to apply the normal steam Rankine cycle [4, 5]. The working fluid is an organic fluid with a low boiling temperature, lower latent heat and a small specific volume compared

to water, so the overall power generation system can be designed to be much smaller. Because of this advantage the ORC has been researched extensively since the 1960s.

The availability of the waste heat can significantly fluctuate (Figure 1). While fluctuations are inherent to industrial processes, they negatively affect the operation of ORC systems [6]. However, WHP systems and ORC systems in particular are commonly designed for a single operating point (nominal load) disregarding the waste heat fluctuations. Moreover, system components and working fluids are mostly optimized to increase the cycle efficiency at a certain nominal load [7]. This nominal load is either defined by the upper boundary or by the average values of the operation range. As a result, WHP systems subjected to thermal power fluctuations often operate at part load conditions (off-design) with reduced efficiency [8]. When large thermal power fluctuations occur, a complete bypass of the WHR system might be necessary. Overall, this leads to lower heat recovery which negatively affects the economic feasibility for the implementation of WHP systems. A steady heat load close to the nominal load is thus preferable to operate an ORC.

To keep the WHP system running at constant load under fluctuating waste heat availability, either the mass flows through the system can be manipulated, or thermal storage can be integrated [6, 9]. By integration of a thermal energy storage (TES) system, the fluctuations in heat availability for the WHP system can be flattened. In periods with high waste heat availability, the heat in excess of the nominal load of the WHP is stored in the TES, while in periods with low waste heat availability, the TES complements the heat deficit. As a result, the size of the WHP can be reduced, the duration and depth of part-load operation can be decreased.[9]. Moreover, the mismatch between waste heat availability and electricity demand can be bridged. Also the supply of heat to the WHP system can be extended [10].

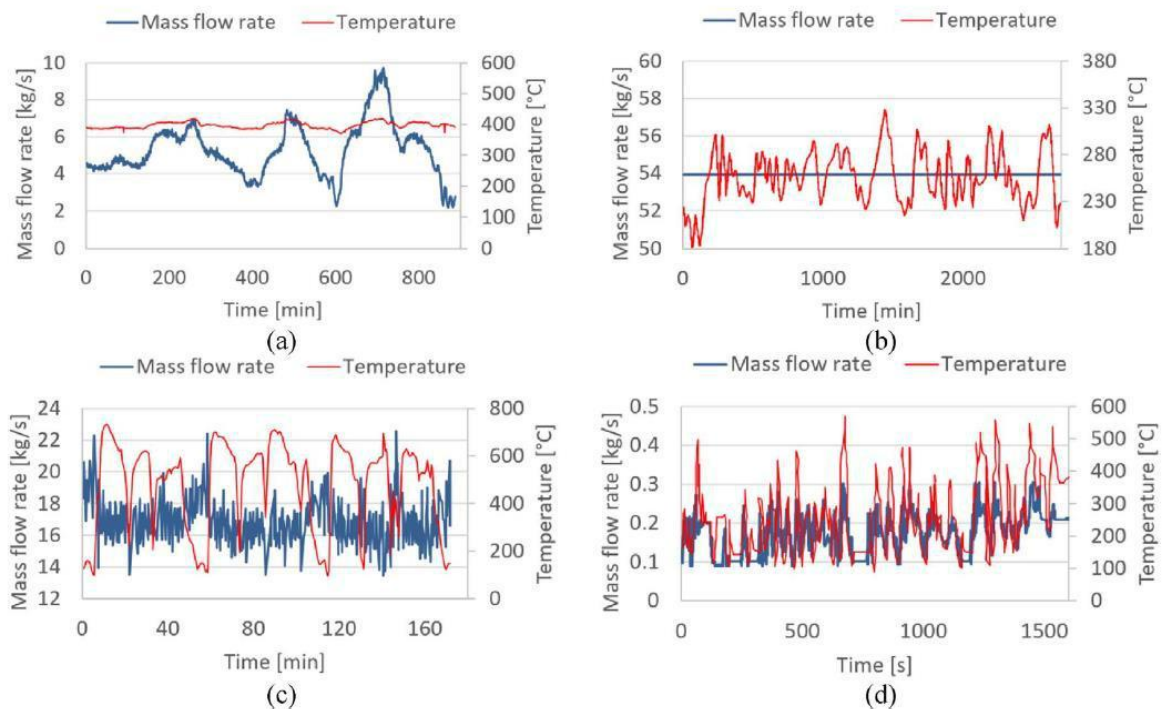


**Figure 1.** Fluctuation in waste heat sources relevant for power production (a) Steel billet reheating furnace: mass flow fluctuations, (b) Clinker cooling: temperature fluctuations, (c) EAF (after water cooling system): fluctuations of both mass flow and temperature, (d) IC engine exhaust: fast fluctuations. Derived from [6].

TES systems can be classified as sensible, latent or thermochemical [11]. Thermochemical storage systems are still in the research phase, but it can potentially store more energy than sensible or LHS systems due to the heat of reaction [12]. In sensible heat systems (water

buffers, concrete blocks, molten salts, etc.) heat is stored by raising the temperature of a storage medium. Consequently, the amount of heat that can be stored depends on the specific heat capacity of the storage medium and is a strong function of the available temperature difference. Latent heat storage (LHS), using phase change materials (PCMs), allows to store more heat than sensible storage due to its higher energy density. Moreover, during charging or discharging the mean temperature of a latent heat storage system stays on a nearly constant level, as long as part of the storage medium is still in the transition phase, which is not the case for sensible heat storage. As a consequence, LHS can act as a heat sink (to cool down a waste heat stream) or heat source (to evaporate the ORC fluid) at nearly constant temperature.

Various studies on TES systems for smoothing fluctuations of waste heat have been conducted. Integration of PCM technology has been investigated by *Nardin et al.* and *Dal Magro et al.* [7, 13, 14]. In [13] PCMs are used to reduce the variability of off-gas temperatures and thermal powers from the electric arc furnace (EAF) process, while in [14] they inserted in the off-gas line of a continuous charge EAF process a temperature smoothing device based on PCMs. The integration of this device enhances the downstream energy recovery system where the reduced fluctuations increased the steam turbine load factor. *Dal Magro et al.* also investigated the impact of retrofitting a PCM based technology in a billet reheating furnace on the existing ORC. Results showed that the introduction of the PCM based technology allows the capacity factor to increase from 38% to 52% with an average thermal efficiency increase from 15.5% to 16.4% [7]. Other TES systems are investigated in *Sung et al.* and *Ramirez et al.* [10, 15]. In [15] a 200 kW ORC is installed in a steel processing plant to recover the energy from flue gases. A water thermal storage tank with 1-ton capacity was installed after a flue gas heat exchanger to suppress variation of the heat source and prevent abrupt temperature increases at the inlet of the ORC evaporator. Results show that the fluctuations are successfully suppressed by the thermal storage. In [10] a 1.8MW ORC is installed along with a waste heat recovery unit in a steel mill to recover waste heat from the fumes of an EAF. A steam accumulator of 150m<sup>3</sup> was implemented between the heat recovery unit and the ORC to reduce fast transients in the waste heat and extend the supply over longer periods. From the accumulator steam is sent to the ORC unit and its flow is controlled to maintain pressure and flow as constant as possible. The relatively steady discharge allows the ORC to provide a power output with only minor oscillations. *Pili et al.* [9] performed a techno-economic analysis of waste heat recovery with ORC from fluctuating industrial sources, with and without thermal storage. Different configurations for three applications are compared in terms of levelized cost of electricity and CO<sub>2</sub>-savings. There is no best solution which serves all applications, but thermal storage seems to be economically and environmentally beneficial when the heat source is affected by large fluctuations in temperature.

## Results and discussion

A fast method to check the economic benefits of a storage system applied for the reduction of the primary energy demand is by means of the payback time which can be estimated by:

$$t_{\text{payback}} = \frac{1}{n_{\text{daily}} \cdot n_{\text{days}}} \cdot \frac{c_{\text{storage}}}{c_{\text{thermal}}} \quad (1)$$

With  $t_{\text{payback}}$  the payback time [years],  $c_{\text{storage}}$  the capacity specific costs of the storage system [€/kWh],  $c_{\text{thermal}}$  the specific costs for thermal energy [€/kWh],  $n_{\text{daily}}$  the number of cycles per day and  $n_{\text{days}}$  the number of days per year with  $n_{\text{daily}}$  cycles.

An example calculation for a LHS based on the parameters in Table 1 results in a payback time of 10.4 years, which is insufficient compared to the currently demanded payback times in industry of 3-5 years. The major cost component is the expensive equipment rather than the storage material. According to literature [16] the costs for LHS systems are ranging between 10 – 50 €/kWh but in practice costs for industrial scale systems can be higher. This leads to LHS systems only being economically viable for applications with a high number of cycles. In order for LHS to enter the market as a viable solution the costs of the equipment should be lowered.

**Table 1.** Parameters and values used in Equation 1.

Parameter – Meaning – [unit]	Value
$c_{storage}$ - the capacity specific costs of the storage system [€/kWh]	100
$c_{thermal}$ - the specific costs for thermal energy [€/kWh]	0.02
$n_{daily}$ - the number of cycles per day [-]	2
$n_{days}$ - the number of days per year with $n_{daily}$ cycles [-]	260

LHS could be a viable solution in situations where the size of WHP system components can be reduced with the integration of LHS. The required nominal load of the WHP system decreases and at this reduced nominal load, the LHS causes the depth and duration of part-load operation to decrease, which results in a more efficient conversion to electricity. The decrease of capital cost is expected to have a greater effect on the economic feasibility than the increase in revenues from electricity production [9]. This saved investment cost can then be used for a LHS.

As an example, the conversion of waste heat from a cement plant is considered. At the Heidelberger Zement AG Plant a 1.5 MW ORC recovers the heat available from the grate cooler and generates heat on a continuous basis without interfering with the clinker production process. Heat is transferred to the ORC by means of a thermal oil flow circulating in a closed loop system (Figure 2).

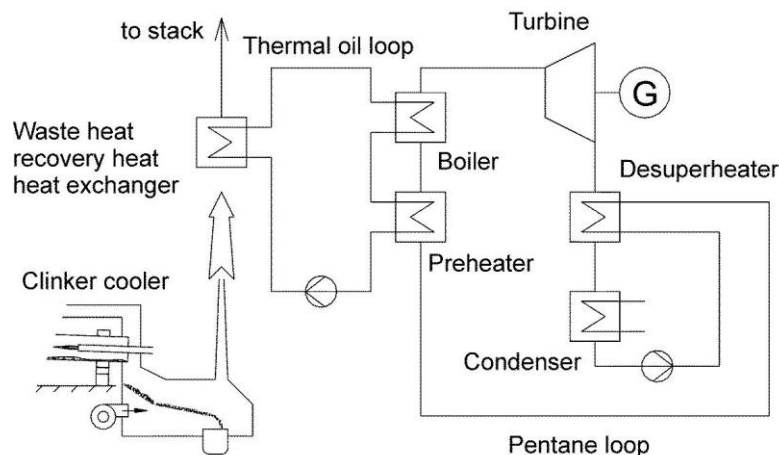


**Figure 2.** Clinker cooler heat recovery system at the Heidelberger Zement factory in Lengfurt. Adapted from [17].

However, this waste heat is continuously varying between temperatures ranging from 180°C to 340°C, causing the thermal oil to fluctuate between 120°C to 230°C (Figure 3). Coping with such fluctuations, the ORC generates between 400 kW and 1500 kW [17]. Instead of installing a 1.5 MW ORC and dealing with part load operation a smaller unit could be

installed and thermal power fluctuations can be reduced with the integration of a PCM storage. As such it could be possible to install a 980 kW ORC at an estimated cost of 3M € while a 1.5 MW ORC is 0.6-1M € more expensive. With the combination of a PCM storage and a smaller ORC the efficiency is improved by avoiding part load operation. With the cost savings by reducing the size of the ORC it is possible to integrate a 1500kWh PCM storage at 100€/kWh which is needed to keep the temperature of the waste gases after the PCM storage constant.

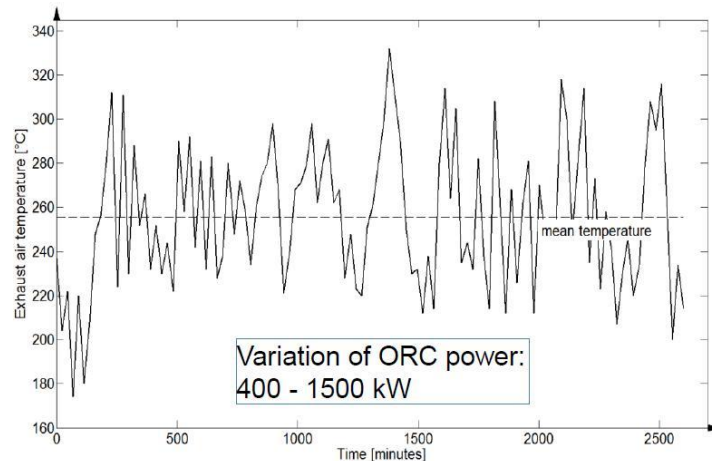


**Figure 3.** Temperature variations of the exhaust gases at the Heidelberger Zement factory in Lengfurt. Due to this variations ORC power varies between 400-1500kW. Adapted from [17].

### Test rig – Simulation and control

To evaluate the behaviour and performance of a combined LHS ORC system a pilot scale system is installed at Ghent University Campus Kortrijk within the frame of the European CORNET ShortStore project. The system consists of: a 110 kWh LHS (Figure 6), a 250 kW electric heater which can simulate a fluctuating waste heat source and a 11 kW<sub>e</sub> ORC, interconnected via a thermal oil circuit (Figure 5). The characteristics of the LHS and ORC are listed in Table 2. A performant control strategy will be developed enabling stable ORC operation under fluctuating waste heat conditions. For optimal operation of these systems effective operating strategies and methods to monitor the state of charge (SOC) are required. However, SOC estimation for LHTS systems during operation is the bottleneck for its application in industry [18]. A heat exchanger with the environment will act as a heat sink to extract heat during LHS discharging and the electric heater as a heat source for charging the LHS. The SOC will be estimated based on continuous monitoring of PCM temperatures orthogonally placed at different axial positions in the LHS based on the method described in Barz *et al.* [18].

Mathematical simulations of the finned shell and tube LHS are performed with a dynamic 2D model in Python based on the apparent heat capacity method. For all tubes of the LHS unit, equal flow of the HTF and equal temperature distribution on both the shell and tube side is assumed. Thus, in the model only one tube is considered and boundary effects near to the limit of the storage device, for example, energy losses to the surrounding, are ignored. The fins are considered only indirectly by an increased heat conduction in the PCM. As a first step, the (dis)charging behaviour of the LHS is analysed at variable mass flow rates and inlet oil temperatures. The results for discharging the LHS are presented in Figure 4. The initial PCM temperature is set at 230°C and is in a completely molten state. Full lines represent the outlet oil temperature and the dotted lines the extracted thermal power. On the upper graph the inlet oil temperature is kept constant while the oil mass flow varies from 1.5 kg/s to 3 kg/s. With increasing mass flow rate the initial extracted thermal power increases but rapidly decreases over time. The outlet oil temperature decreases with increasing mass flow rate. The



sharp decrease of both extracted thermal power and outlet oil temperature after 2000s with a mass flow rate of 3 kg/s is due to the complete PCM solidification and only sensible heat is available after 2000s. On the lower graph the mass flow is constant while the inlet oil temperature varies from 100°C to 210°C. With increasing temperature difference between inlet oil temperature and PCM temperatures the less constant the outlet oil temperature is. Moreover, initial extracted powers increase but rapidly decreases due to faster PCM solidification rates.

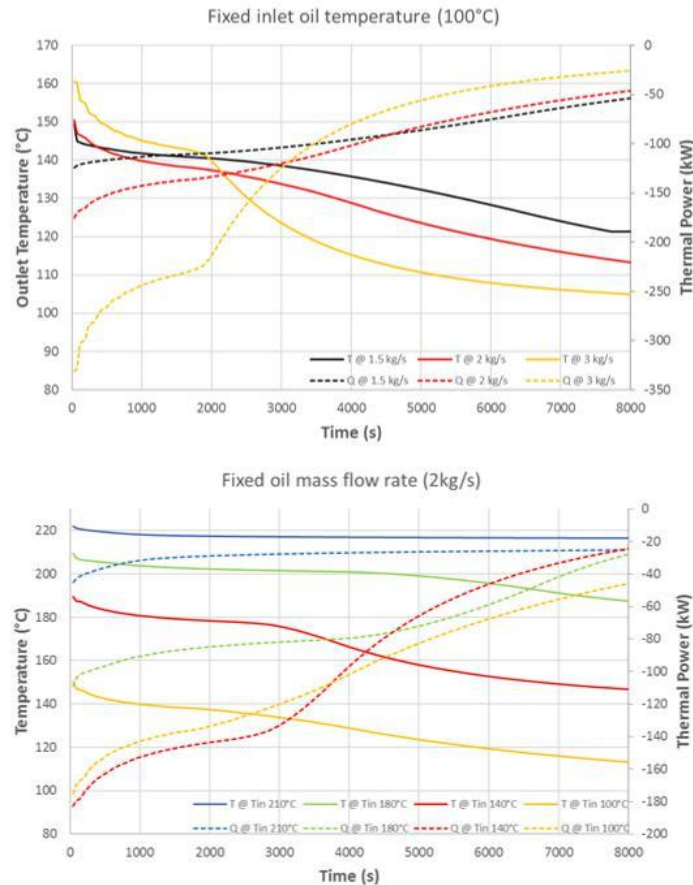


**Figure 4.** Simulation results of the LHS system. The PCM is in an initial completely molten state at 230°C. Upper: Outlet oil temperature and extracted power are plotted for different mass flow rates at constant inlet oil temperature. Lower: Outlet oil temperature and extracted power are plotted for different inlet oil temperatures at constant mass flow rate.

Note, that the oil flow direction in the LHS is different for charging and discharging due to the inherent characteristics of the PCM. During charging the PCM melts and its volume increases. To prevent damage to the storage equipment due to changing PCM volumes, during charging the HTF inlet is at the top of the LHS, while during discharging the HTF inlet is at the bottom.

In a second step the capability of the LHS in reducing fluctuations in waste heat availability due to variations in mass flow rate or temperature are investigated. In a third step, the main aim of this research, a control procedure will be developed to enable stable ORC operation under fluctuating waste heat conditions by charging the LHS when there is an excess of waste heat and discharging the LHS when there is not enough waste heat.

A schematic overview the test set-up is presented in Figure 5. The target operating conditions of the ORC are an incoming oil temperature ( $T_{ORC\_in}$ ) of 130-140°C at a mass flow rate of 2 to 3 kg/s. Because the LHS will be used near the PCM melting temperature (223°C) and  $T_{ORC\_in}$  is limited to 140°C to prevent damage to the evaporator and expander a basic

control mechanism is implemented. The return of the ORC ( $T_{ORC\_out}$ ) is partly mixed at valve ‘TV2’ with the oil coming from the heater and storage to reach a mixing temperature ( $T_{mix}$ ) equal to the target operating temperature. Changing the amount of mixing will result in changing mass flow rates in the LHS and/or heater and accordingly oil temperatures after the heater and LHS will change. Depending on the temperature changes the control system is needed to adjust the position of the three way valves in order to control  $T_{mix}$  as close as possible to the target operation temperature.

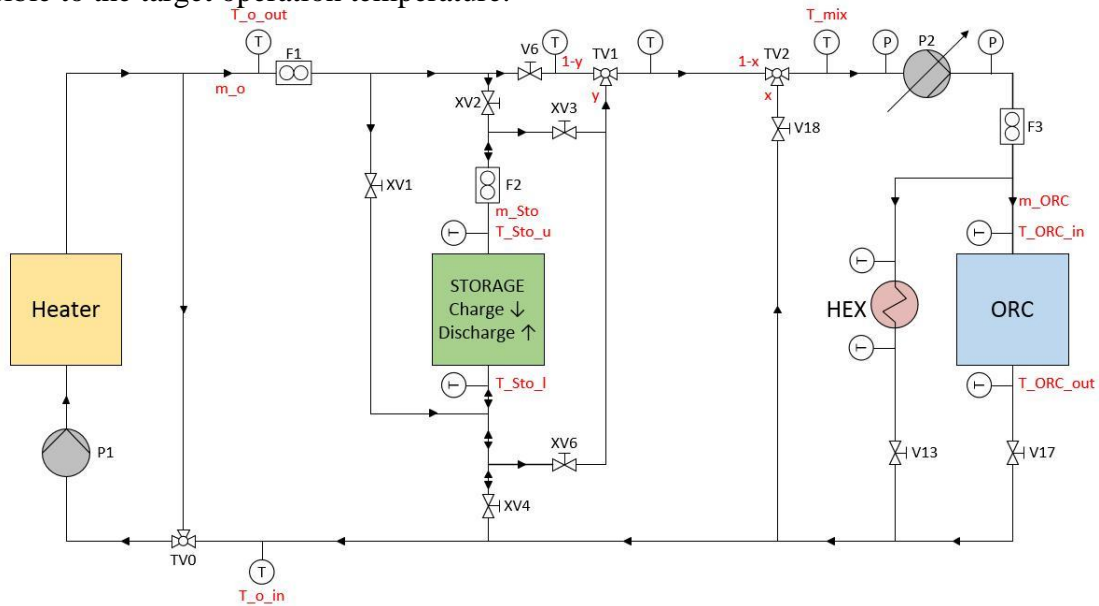


**Figure 5.** Schematic of the test set-up. Flow directions in the system are indicated by arrows. (Motorised) Globe valves are indicated with ‘(X)V’, three way valves with ‘TV’, flowmeters with ‘F’ and temperature measurements with ‘T’.



**Figure 6.** Picture of the LHS installed at UGhent Campus Kortrijk.

### Summary/Conclusions

ORC systems are commonly designed for a single nominal load disregarding the waste heat fluctuations. LHS systems are able to decrease this nominal load and increase the conversion efficiency. The described pilot scale set-up is installed at UGent Campus Kortrijk and serves as a demonstration for the characterization, integration and operation of a combined LHS-ORC system. Heat is generated by an electrical heater and is controlled to simulate a fluctuating waste heat profile. A control strategy will be developed to operate the ORC at constant heat load. The test set-up will be used to characterize the behaviour of a large scale

LHS system with SOC estimations based on the method described in [18]. Therefore, this research contributes to the further development of waste heat recovery technologies.

**Table 2.** ORC and LHS characteristics.

ORC characteristics		LHS characteristics	
<b>Working fluid</b>	R245fa	<b>PCM material</b>	Eutectic mixture KNO <sub>3</sub> /NaNO <sub>3</sub>
<b>Maximum evaporator pressure</b>	14 bar	<b>PCM melting temperature</b>	223°C
<b>Max generator power</b>	11 kW <sub>e</sub>	<b>PCM volume</b>	2 m <sup>3</sup>
		<b>LHS thermal capacity</b>	112 kWh (latent heat) 220 kWh in temperature range 180-250°C

### Acknowledgements

This research is within the frame of the VLAIO-CORNET project HBC.2016.0330 "Short term heat and cold storage in industry - Shortstore" (cornet-shortstore.eu), funded by the Institute for the Promotion and Innovation by Science and Technology in Flanders. This financial support is gratefully acknowledged. The UGhent authors also want to thank DLR for the PCM buffer tank, received as a gift for this common research. Wim Beyne received funding from a Ph.D. fellowship strategic basic research of the Research Foundation - Flanders (FWO) (1S08317N).

### References

- [1] Eurostat, *Statistics Explained. Greenhouse gas emissions by industries and households*. 2016.
- [2] Infiniti Research Limited, *Global waste heat recovery market 2015-2019*. 2015.
- [3] BCS, *Waste Heat Recovery: Technology and Opportunities in U.S. Industry*. 2008.
- [4] Tchanche, B.F., et al., *Low-grade heat conversion into power using organic Rankine cycles - A review of various applications*. *Renewable & Sustainable Energy Reviews*, 2011. **15**(8): p. 3963-3979.
- [5] Lecompte, S., et al., *Review of organic Rankine cycle (ORC) architectures for waste heat recovery*. *Renewable & Sustainable Energy Reviews*, 2015. **47**: p. 448-461.
- [6] Jimenez-Arreola, M., et al., *Thermal power fluctuations in waste heat to power systems: An overview on the challenges and current solutions*. *Applied Thermal Engineering*, 2018. **134**: p. 576-584.
- [7] Dal Magro, F., M. Jimenez-Arreola, and A. Romagnoli, *Improving energy recovery efficiency by retrofitting a PCM-based technology to an ORC system operating under thermal power fluctuations*. *Applied Energy*, 2017. **208**: p. 972-985.
- [8] Kim, I.S., T.S. Kim, and J.J. Lee, *Off-design performance analysis of organic Rankine cycle using real operation data from a heat source plant*. *Energy Conversion and Management*, 2017. **133**: p. 284-291.
- [9] Pili, R., et al., *Techno-Economic Analysis of Waste Heat Recovery with ORC from Fluctuating Industrial Sources*. 4th International Seminar on Orc Power Systems, 2017. **129**: p. 503-510.

- [10] Ramirez, M., et al., *Performance evaluation of an ORC unit integrated to a waste heat recovery system in a steel mill*. 4th International Seminar on Orc Power Systems, 2017. **129**: 535-542.
- [11] Dincer, I. and M. Rosen, *Thermal energy storage : systems and applications*. 2nd ed. 2011, Hoboken, N.J.: Wiley. xviii, 599 p.
- [12] Yu, N., R.Z. Wang, and L.W. Wang, *Sorption thermal storage for solar energy*. Progress in Energy and Combustion Science, 2013. **39**(5): p. 489-514.
- [13] Nardin, G., et al., *PCM-based energy recovery from electric arc furnaces*. Applied Energy, 2014. **136**: p. 947-955.
- [14] Dal Magro, F., et al., *Enhancing energy recovery in the steel industry: Matching continuous charge with off-gas variability smoothing*. Energy Conversion and Management, 2015. **104**: 78-89.
- [15] Sung, T., et al., *Performance characteristics of a 200-kW organic Rankine cycle system in a steel processing plant*. Applied Energy, 2016. **183**: p. 623-635.
- [16] International Energy Agency, *Thermal Energy Storage: Technology Brief*. 2013.
- [17] Legmann, H., *Recovery of industrial heat in the cement industry by means of the ORC process*.
- [18] Barz, T., et al., *State and state of charge estimation for a latent heat storage*. Control Engineering Practice, 2018. **72**: p. 151-166.

# An Investigation of Nozzle Shape on the Performance of an Ejector

Mehdi Falsafiooni<sup>\*</sup>, Zine Aidoun<sup>1</sup>

<sup>1</sup>CanmetENERGY, Natural Resources Canada,  
1615 boul. Lionel-Boulet, Varennes, Québec, Canada J3X 1S6

<sup>\*</sup>Corresponding author: mehdi.falsafioon@canada.ca

## Abstract

A wide range of industrial refrigeration systems are good candidates to benefit from the cooling and refrigeration potential of supersonic ejectors. These are thermally activated and can use waste heat from industrial processes, or low cost heat from biomass or solar. Ejector performance is however typically modest and needs to be maximized in order to take full advantage of the simplicity and low cost of the technology. Several works highlighted the importance of different geometrical parameters of ejectors on the performances; however, few of these studies are related to the ejector primary nozzle exit diameter which have shown contradictory finding regarding the optimal value of this parameter. This question was addressed in current study using CFD simulations on a 2-D model of a typical ejector. The results show that optimum ejector performance for a certain working condition is when the pressure at the nozzle exit is close to the suction pressure. In other words, an over-expansion of the motive flow should be avoided.

**Keywords:** Ejector, Ejector Performance, Nozzle, Numerical Simulation, Refrigeration System.

## Introduction

A gas/gas supersonic ejector system may be heat activated to produce a cooling system. Compared to a conventional mechanical compression cycle, in an ejector cycle, the compressor is replaced by the turbo pump-generator-ejector. Integrating the ejector in a conventional refrigeration system in order to boost its performance or in other cases, simply replacing to a compressor with a circulation pump and a generator offers the opportunity to reduce the overall system electricity consumption. Ejector operation consists of using a high primary energy stream mass flow rate ( $m_1$ ) and expanding it in a supersonic nozzle to entrain and exchange energy with a secondary stream mass flow rate ( $m_2$ ). This procedure acts like a compressor and can be implemented in a cooling system. Numerous experimental and numerical studies have been conducted to provide a better understanding of mixing and compression processes in ejectors. Among these studies, many have tried to improve the performance of ejectors by modifying the dimensions and/or the configuration of the internal components. One of the items that has a significant impact on the efficiency of an ejector is the shape of the primary nozzle. The importance of employing an optimized nozzle inside the ejector is both discussed on the basis of simulations and experimental studies. Matsuo et al. [1] did a study on nozzle shape and reported that the nozzle shape and the mixing area, between the nozzle exit and mixing chamber, has a significant effect on ejector performance. A similar study was also conducted by Fu et al. [2] who with the use of numerical simulations showed that a good design of nozzle geometry can optimize the performance of an ejector. The experiments of Sag and Ersoy [3] also proved that an optimal nozzle can enhance the performance of an ejector by 8-13%. In all these studies the behavior of the motive flow is identified as one of the most important parameters that should be taken into account in an ejector design. Zhu and Jiang [4] studied the Mach wave lengths using Schlieren system and reported that ejector performance can be improved by reducing the first Mach wave length. A study on flow boundaries was also carried out by Addy [5]. Most recently, Chen et al. [6]

investigated the Mach wave profile of the motive flow under off-design working conditions by both numerical and experimental methods. In their report, they have presented an extensive study of the flow regime inside an ejector using the method of characteristics. The primary nozzle exit ratio defined as  $\phi = d_{exit} = d_{throat}$  was reported to affect ejector performance.

Table 1: Working Condition

$P_1$ (kPa)	$T_1$ (°C)	$P_2$ (kPa)	$T_2$ (°C)	$P_{out}$ (kPa)
2748	97.3	450	20.6	710

For fixed operating conditions and overall geometry, a variation of this ratio influences the primary stream expansion. Eames et al. [7] tested two such nozzles having the same throat diameter and divergent angle for which they represented the ejector entrainment ratio ( $\omega$ ) as a function of the nozzle expansion ratio,  $P_1 = P_{exit}$ . The results indicated that for selected  $\phi$ , a corresponding optimal  $\omega$  value exists. On the other hand when  $\phi$  increased,  $\omega$  decreased, which the authors attributed to the increase in the degree of over-expansion occurring in the nozzle flow. A theoretical assessment, using CFD was performed by Ruangtrakoon et al. [8] in which they compared three nozzles differing only by their exit diameter and submitted to the same operating conditions ensuring the same primary mass flow rate. It was found that all nozzles resulted in the same entrainment ratio ( $\omega$ ) and the back pressure ( $P_{out}$ ) increased with outlet Mach number  $M_x$ . Lin et al. [9] numerically performed similar work with a natural gas ejector by varying the nozzle divergent angle  $\gamma$ . They presented the results in terms of nozzle divergent angle for a fixed secondary mass flowrate and for a range of primary throat openings (100% to 50%) by means of a spindle. For full open throat (100%), back-pressure increased monotonically with  $\alpha$ . As the throat was increasingly restricted, an optimal angle value corresponding to maximum back-pressure was identified. This implies that for full throat operation,  $\omega$  remains constant while the back-pressure improves, similarly to Ruangtrakoon et al, [8] findings. With increasing throat restriction, optimal  $\omega$  steadily increased with a lower rate of increase in the back-pressure. The authors attributed the displacement of the optimal angle to the change of the flow inside the nozzle and the critical throat area. This may have as well impacted the importance of the back-pressure. In a recent paper, Thongtip et al. [10] continued this work experimentally. They fixed the primary mass flow rate and varied the Mach number  $M_x$  at the nozzle outlet by changing the nozzle exit area, all the other conditions maintained constant. The result was that  $\omega$  moderately improved but the back-pressure increased with higher  $M_x$ . According to the authors, this may be due to better suction created by higher stream velocity, in such a way that the ejector had a stronger drawing potential of the secondary stream and the expansion wave angle being potentially reduced by the lower nozzle exit pressure, thus resulting in an increase of the effective area for the secondary fluid. These works highlighted the importance of the nozzle exit Mach number, but showed contradictory finding regarding its optimal value. This paper addressed the question by studying the effect of the nozzle exit diameter, and consequently the nozzle exit Mach number, on the ejector performances. To this end, CFD simulations using a 2-D model of an ejector were performed for similar operating conditions and ejector geometry except for different nozzle exit diameters.

## Methodology

In this study, the chosen geometry is based on an in-house ejector design and workbench experimental setup. Figure1 shows the dimensions of the ejector. In this figure, the investigated parameter (the nozzle exit diameter) is shown as  $D_{pnx}$  which is changed from 8.70mm to 13.70mm with an increment of 1.0mm. For the different  $D_{pnx}$ , the length between

the throat and the nozzle exit is fixed and the divergent angle ( $\gamma$ ) is increased from 4 for  $D_{pnx} = 8.70$  mm to 16 for  $D_{pnx} = 13.70$  mm. The change of nozzle exit can be defined based on the diameter  $D_{pnx}$  or the angle of the divergent part ( $\gamma$ ) of the nozzle. However, for the sake of clarity and analysis purposes, the geometry and the results are reported based on  $D_{pnx}$ . The distance between the nozzle exit and the mixing chamber inlet, NXP, was also changed between two different positions (NXP = 32mm and 22mm) in order to investigate whether this change has any effect on the pressure and velocity profiles of the motive flow exiting from the nozzle. CFD simulation is used to determine the effect of the nozzle exit diameter on the performance of a common ejector and consequently to find the optimum value for this parameter.

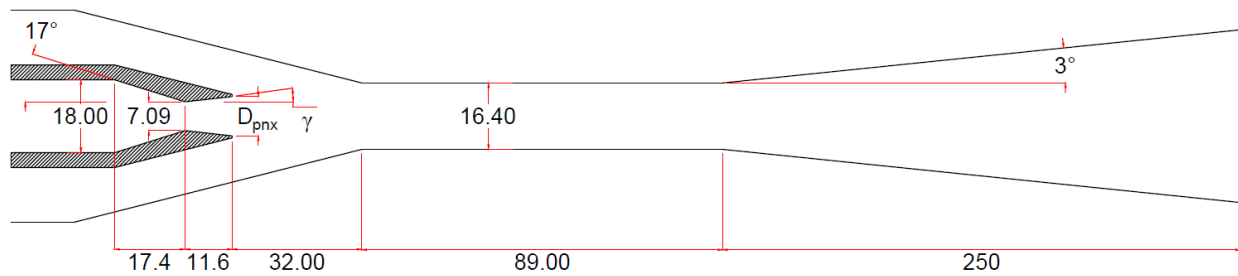


Figure 1: A scheme of the ejector including dimensions (All dimensions are in millimeter. The drawing is not scaled).

The ejector is modeled in 2-D and is assumed to be axi-symmetric along the x-axis. The previous 3D numerical simulations show that there is no significant 3D effect on the performance of an ejector (e.g.[11]). Because of the nature of ejectors, the conservation equations of continuity, momentum and energy are used in their compressible and steady state forms and non-linear sets of discretized equations are solved using the commercial software ANSYS Fluent v.18 for a single-phase supersonic ejector with R134a as the working fluid. NIST standard reference database is coupled with the CFD package to extract R-134a thermophysical properties during the calculations. The  $k-\epsilon$  turbulence model is chosen based on the previous studies reported in the literature, e.g. [12, 13, 14]. A tetra dominant mesh is used with a total number of 77,000 elements. A "pressure inlet" boundary condition is applied for both primary and secondary inlets and a "pressure outlet" boundary condition is imposed at the outlet. All walls are considered to be adiabatic with no-slip boundary condition. It is also assumed that the primary and secondary flows are fully mixed in the mixing chamber and the vapor expansion in the nozzle is isentropic. The CFD model was previously validated using in-house experimental results for the same ejector design [15]. The performance of the ejector is qualified by the entrainment ratio of the secondary to the primary streams ( $\omega = m_2/m_1$ ) and the compression ratio of the outlet pressure to secondary pressure ( $P_r = P_{out}/P_2$ ).

## Result and Discussion

Generally, in an ejector the motive flow leaving the exit nozzle can be in three different states; (1) over-expanded, where the motive pressure at the nozzle exit is lower than the secondary pressure and flow could not expand more in the mixing area and consequently shocks happen; (2) under-expanded where the motive flow pressure at the nozzle exit is higher than the secondary flow pressure, the motive flow could expand more in the mixing area; and (3) finally in a condition where both nozzle exit pressure and secondary flow

pressures are almost equal which is the ideal condition for the motive flow exiting the nozzle [6].

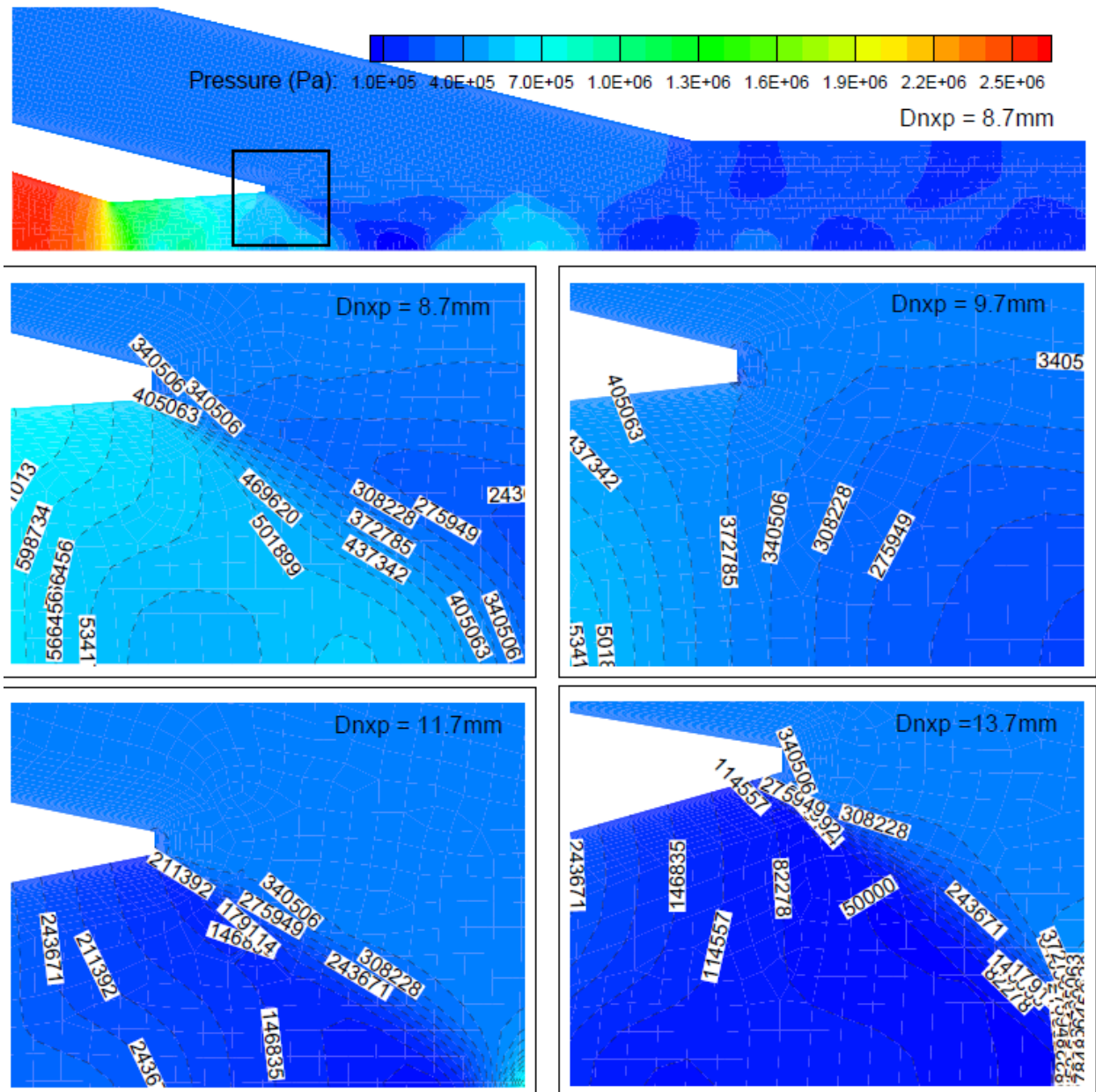
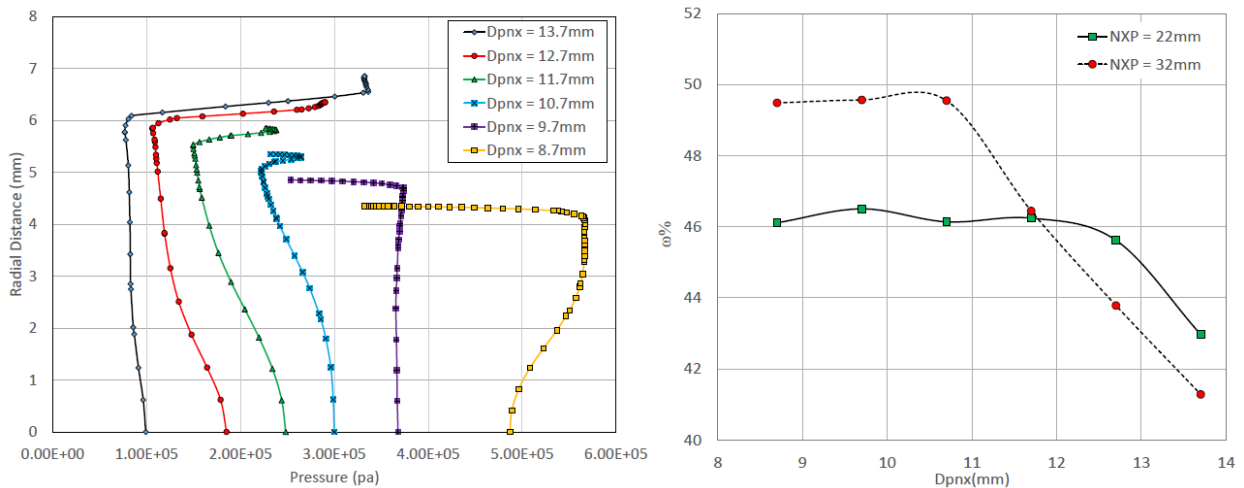


Figure 2: Pressure contours at different nozzle exit diameters (NXP=32mm)

This three states have been demonstrated in Fig. 2 where all three under-expanded, ideally-expanded and over-expanded situations are shown for ejectors with  $D_{pnx} = 8.7\text{mm}$ ,  $D_{pnx}=9.7\text{mm}$  and  $D_{pnx}=11.7\text{mm}$  respectively. This also has been shown in Fig. 3(a) where the pressure profile at the exit of primary nozzle is shown. It can be implied from this figure that with increasing the nozzle exit diameter the exit pressure is decreasing. Figure 3(b) presents the entrainment ratio versus the nozzle exit diameter for two different NXPs. As shown in this figure, there is an optimum range for  $D_{pnx}$  to get the best entrainment ratio. In general, from Fig. 2, Fig. 3(b) and Table 1, it can be concluded that the best diameter for the nozzle exit is where the flow pressure is equal to the secondary pressure. According to Fig.2 for the specified working condition and geometry, the best dimension for  $D_{pnx}$  should be between  $D_{pnx} = 8.7\text{mm}$  and  $D_{pnx} = 9.7\text{mm}$ . This is the state where the flow is ideally expanded at the



nozzle exit. In order to investigate the relation between the nozzle exit diameter and the diameter of mixing chamber ( $D_{mix}$ ), mixing chamber diameter was changed to two different sizes (one smaller and one bigger than the original size) and simulations were repeated for different nozzle exit sizes. The results show that as long as the drawn sonic line is attached to the wall of mixing chamber and the flow is double choked (Fig.4), there is no significant relation between mixing chamber and nozzle exit diameters. Simulations were also carried out for a different NXP (the distance between the nozzle exit and the mixing chamber). Although based on Fig. 3(b) entrainment ratio is changed with NXP, however, this impact is independent of  $D_{pnx}$  [15]. This can also be observed from Fig.5 where the velocity contours are shown for two different NXPs and for different nozzle exits ( $D_{pnx}$ ). According to this figure, although the flow structure is different for two NXPs, there is no significant changes for the flow structure right after the nozzle exit area. Figure 6 shows the pressure profile along the X-axis of the ejector. As shown in this figure, for nozzle exit diameter equal to 9.70mm, the amplitude of the pressure fluctuation are the lowest. This diagram along with Fig.2 imply that high pressure differences between the motive and suction flows at the nozzle exit will amplify the chance of sudden driving flow expansion which is not necessarily useful for the functionality of an ejector as shocks cause a sudden increase of the pressure, temperature and entropy and consequently increase irreversibility.



(a) Pressure profiles at the nozzle exit for different diameters (b) Entrainment ratio versus nozzle exit diameter

Figure 3: Numerical Results

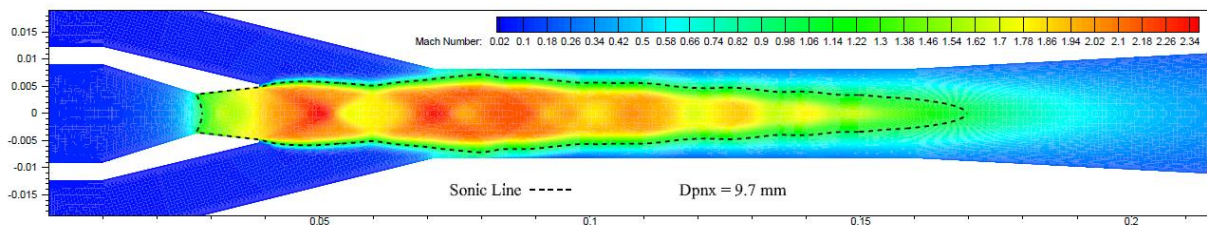


Figure 4: Mach contour from CFD results for the listed working conditions in Table 1

## Conclusion

This study investigated numerical results on driving flow inside an ejector designed for a refrigeration cycle. CFD simulations were conducted in order to study the impact of nozzle shape changes on the performance of the ejector. The results imply that appropriate expansion of the driving flow benefits the ejector functionality from entrainment ratio point

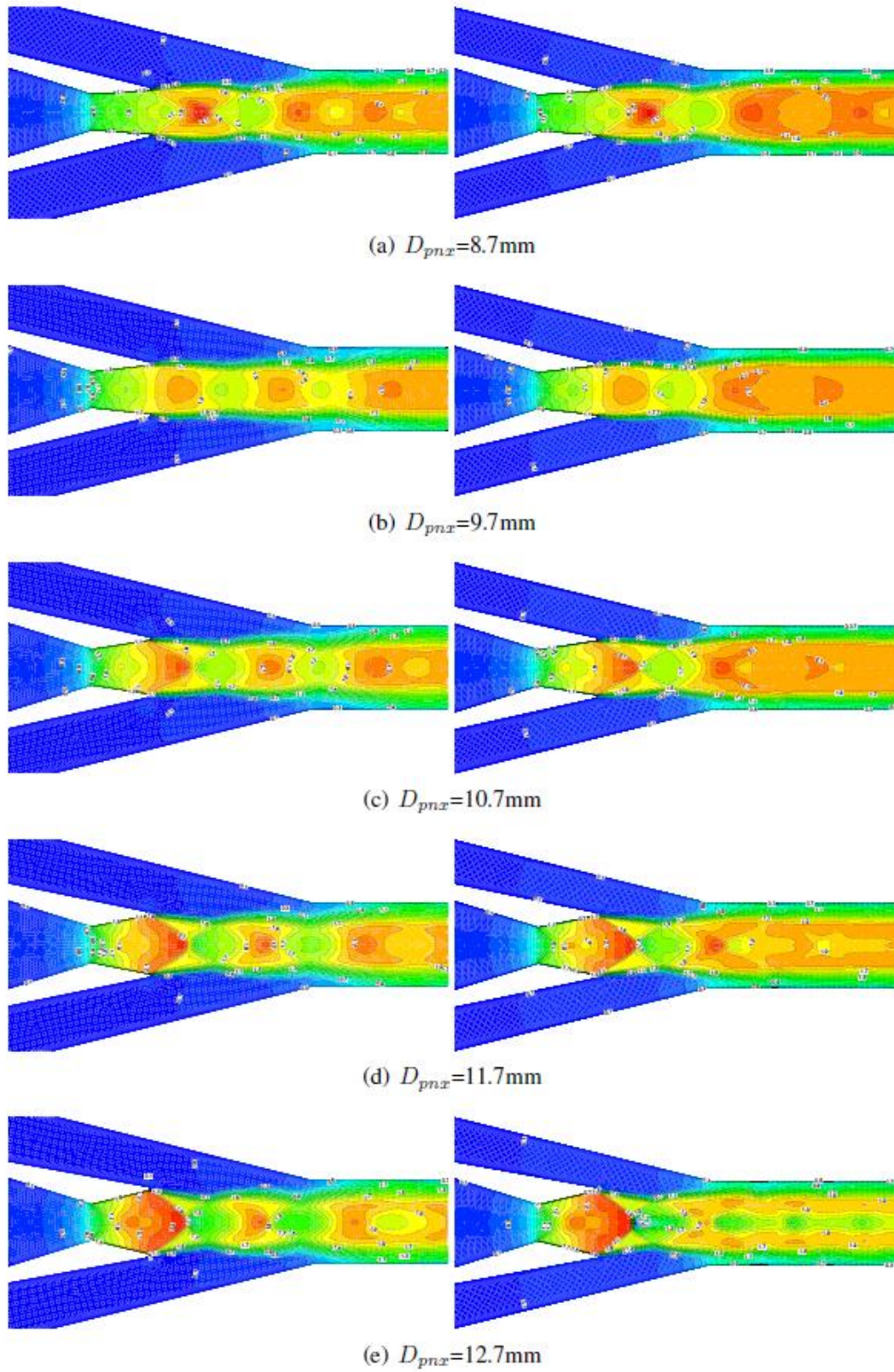
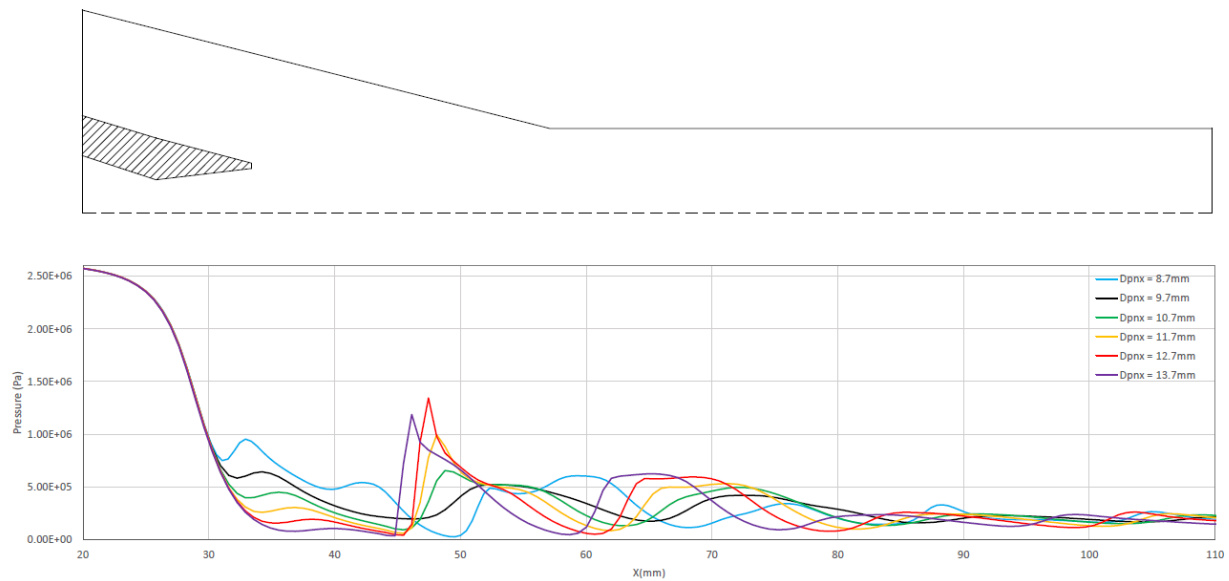


Figure 5: Velocity distribution inside different ejectors for the working conditions listed in Table 1 (Left: NXP=32mm, Right: NXP=22mm)



(b) Entrainment ratio versus nozzle exit diameter

Figure 6: Static pressure profile along the ejector X-axis for different nozzle exit throats (NXP=32mm)

of view. In other words, there is an optimum range of nozzle exit diameter, where ejector is on highest state of its performance. CFD simulation also showed that it is the situation leading to the lowest fluctuation of pressure inside the ejector. These results imply that important over-expansion of the motive flow at the nozzle exit undermines the ejector functionality from the entrainment ratio point of view. In other words, there is an optimum range of nozzle exit diameter for which the ejector performances are the highest. Finally, the simulations also indicated that for ejector having different NXP, the velocity distribution inside the ejector is the same upstream of the nozzle exit, but is different downstream. These finding will allow to design of better ejectors.

### Nomenclature

$P$	[kPa]	pressure	$T$	[ °C]	temperature
$m$	[kg/s]	mass flow rate	$pr$	[-]	compression ratio
$u$	[m/s]	velocity in x direction	$v$	[m/s]	velocity in y direction
$NXP$	[mm]	nozzle exit position	$PNX$	[mm]	nozzle exit diameter
$\gamma$	[degree]	nozzle divergent angle	$\alpha$	[degree]	ejector diffuser angle

### Special characters

$\rho$	[kg=m <sup>3</sup> ]	density (m/s)	$\omega$	[-]	entrainment ratio
--------	----------------------	---------------	----------	-----	-------------------

### Subscripts

1	primary, motive	2	secondary, suction
<i>out</i>	ejector outlet	<i>evap</i>	evaporator
<i>gen</i>	generator	<i>sat</i>	saturation state

### References

- [1] Matsuo K, Sasaguchi K, Kiotogi Y and Mochizuki H 1982 Bulletin of JSME 25 1898–1905
- [2] Fu W, Li Y, Liu Z, Wu H and Wu T 2016 Applied Thermal Engineering 106 1148–1156
- [3] Sag N B and Ersoy H K 2016 Energy Conversion and Management 124 1–12

- [4] Zhu Y and Jiang P 2014 *International Journal of Refrigeration* 40 31–42
- [5] Addy A 1981 *AIAA Journal* 19 121–122
- [6] Chen Z, Dang C and Hihara E 2017 *International Journal of Heat and Mass Transfer* 108 490–500
- [7] Eames I, Aphornratana S and Haider H 1995 *International Journal of Refrigeration* 18 378–386
- [8] Ruangtrakoon N, Thongtip T, Aphornratana S and Sriveerakul T 2013 *International Journal of Thermal Sciences* 63 133–145
- [9] Lin C, Cai W, Li Y, Yan J, Hu Y and Giridharan K 2013 *Applied Thermal Engineering* 61 649–656
- [10] Thongtip T and Aphornratana S 2017 *Applied Thermal Engineering* 110 89–101
- [11] Sriveerakul T, Aphornratana S and Chunnanond K 2007 *International Journal of Thermal Sciences* 46 812–822
- [12] Wang L, Yan J, Wang C and Li X 2017 *International Journal of Refrigeration* 76 219–229
- [13] Watanawanavet S 2008 CFD optimization study of high-efficiency jet ejectors Ph.D. thesis Texas A&M University
- [14] Bartosiewicz Y, Aidoun Z, Desevaux P and Mercadier Y 2005 *International Journal of Heat and Fluid Flow* 26 56–70
- [15] Falsafioon M, Aidoun Z and Poirier M 2017 *IOP Conference Series: Materials Science and Engineering* vol 280 (IOP Publishing) pp 76–83

# Salt hydrate-silicone foam composite for heat storage application

A. Frazzica<sup>1,\*</sup>, V. Palomba<sup>1</sup>, V. Brancato<sup>1</sup>, L. Calabrese<sup>1,2</sup>, A.G. Fernández<sup>3</sup>, M. Fullana-Puig<sup>4,5</sup>, A. Solé<sup>6</sup>, L. F. Cabeza<sup>4</sup>

<sup>1</sup>CNR - Istituto di Tecnologie Avanzate per l'Energia "Nicola Giordano", Via Salita S. Lucia sopra Contesse 5, 98126 Messina, Italy

<sup>2</sup>Department of Engineering, University of Messina, C.da di Dio 98166 Messina, Italy

<sup>3</sup>Energy Development Center, University of Antofagasta, Av. Universidad de Antofagasta 02800 Antofagasta, Chile

<sup>4</sup>GREiA Research Group, INSPIRES Research Centre, University of Lleida, Pere de Cabrera s/n, 25001 Lleida, Spain

<sup>5</sup>CIRIAF – Interuniversity Research Center on Pollution and Environment "Mauro Felli", Via Duranti 67, 06125-Perugia, Italy

<sup>6</sup>Department of Mechanical Engineering and Construction, Universitat Jaume I, Campus del Riu Sec s/n, 12071 Castelló de la Plana, Spain

\*Corresponding author: andrea.frazzica@itae.cnr.it

## Abstract

The present paper deals with the preliminary study carried out on innovative polymeric foams based on silicone and  $\text{MgSO}_4 \cdot 7\text{H}_2\text{O}$ . Composites with variable quantity of embedded salt, from 40 wt.% up to 70 wt.%, were prepared, according to an established foaming procedure. A preliminarily physico-mechanical characterization was carried out to investigate the main properties of the composite foams. Thermo-gravimetric dehydration tests, under real operating conditions, demonstrated that the tested samples are able to efficiently exchange water. Static compression tests evidenced high compression stability indicating high flexibility of the cellular silicone structure. Furthermore, the morphological characterization showed that the foam pores were homogeneously distributed and well interconnected to each other. The high silicone matrix flexibility and interconnected cellular structure of the composite foam were identified as potentially key factor in order to guarantee good durability and water vapour kinetic diffusion of these composite structures for heat storage applications.

**Keywords:** thermal energy storage (TES), polymeric foam, salt hydrate, composite

## Introduction

The use of renewable energy sources (RES), e.g. solar energy, as well as heat losses from engines and industrial waste heat represents an essential opportunity to reduce the impact of the traditional fossil sources. RES are clean, worldwide available and inexhaustible. However, the full exploitation of RES potential requires the presence of a thermal energy storage (TES) system, in order to decouple the availability of the heat source from the user's demands [1]. Different technologies for TES exist, and, among them, thermochemical storage (TCS) represents a promising alternative [2].

Nowadays, thermochemical storage materials (TCMs) are deeply investigated. Several classes of materials are currently being evaluated, such as zeolites [3], zeotypes [4], and salt hydrates [5,6].

Reversible reactions involving salts, such as hy/dehydration reactions, can be used for storing heat using thermochemical technology. Indeed, the salts present outstanding properties, in terms of theoretical storage capacity in the range of temperatures under  $100^\circ\text{C}$ , which can reach  $3 \text{ GJ/m}^3$ . Nonetheless, their practical application still needs research efforts, because different problems arise when these materials are used in a storage system. Among them, agglomeration and swelling phenomena, that limit the vapour diffusion and induce degradation after cycling [7] are the most critical. At the same time, low thermal conductivity of the materials also represents a serious drawback in the use of salt hydrates in a storage system.

In order to prevent such an issue, dispersion of the salt in a matrix has been proposed in literature. Among the available matrices, expanded graphite and porous adsorbent materials (zeolite, silica gels and activated carbons) have been proposed and studied [8]. Whiting et al. [9] and Hongois et al. [10] used the wet impregnation method for the realisation of a  $\text{MgSO}_4$  into different types of zeolites. Posern et al. [11] used wet impregnation technique on a mixture of  $\text{MgSO}_4$  and  $\text{MgCl}_2$  in attapulgite matrices. Jabbari-Hichri et al. [12] studied  $\text{CaCl}_2$  with three different matrices: silica gel, alumina and bentonite showing that the best performance in terms of stored/released heat and water sorption capacity was obtained with the silica gel impregnated composite.

A new approach has been proposed by Calabrese et al. [13] that have realised composites based on zeolites and polymeric foams for adsorption heat pump applications. In these composites, the silicone foam was holding zeolite powders, in order to obtain a sorbent composite with high porosity and adsorption capacity.

In such a context, the present work presents the development of composite materials for thermochemical storage based on magnesium sulphate heptahydrate ( $\text{MgSO}_4 \cdot 7\text{H}_2\text{O}$ ) embedded in a silicone foam, acting as a matrix. The employed matrix is permeable to water vapour, which guarantees a proper hydration/dehydration reaction of the hosted salt. At the same time, the foam structure improves the cycling and mechanical stability of the composite, allowing for an expansion of the salt hydrate volume during the hydration process. The physico-chemical features of the foam composites and the study of water vapour diffusion processes inside the pores under real boundary conditions were measured in order to evaluate its performance for TCS applications.

## Result and discussion

A mixture of poly(methylhydrosiloxane) (code: PDMS) and a silanol terminated polydimethylsiloxane (code: PMHS) with proper catalyst was employed to form the polymeric foam. During the raw components mixing, the  $\text{MgSO}_4 \cdot 7\text{H}_2\text{O}$  was dispersed in different percentages; afterwards the foaming process under controlled temperature was performed.

The flow chart of preparation phases of the salt-silicone foams is represented in Figure 1.

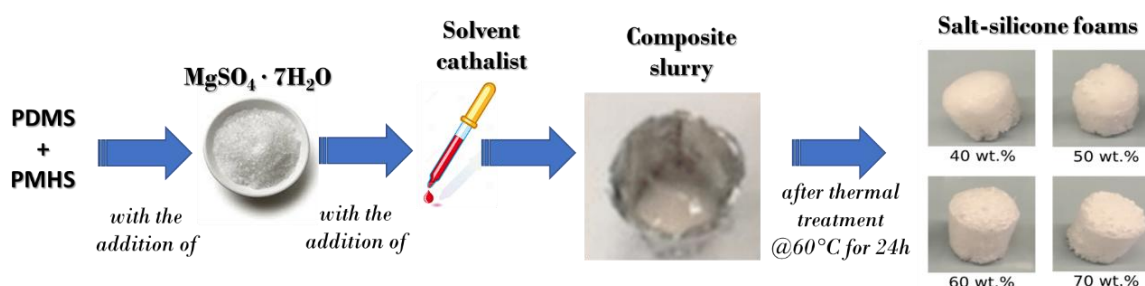


Figure 1: Flow chart of preparation phases of the salt-silicone foams

The composite foams are identified in the paper with the code “Mg\_” followed by a number indicating the salt percentage added to the silicone matrix; e.g. the code “Mg\_40” is referred to a foam constituted by 40 wt.% of salt hydrate.

Foam morphology was evaluated by optical 3D digital microscope (Hirox HK-8700), capturing the images at 50x magnification.

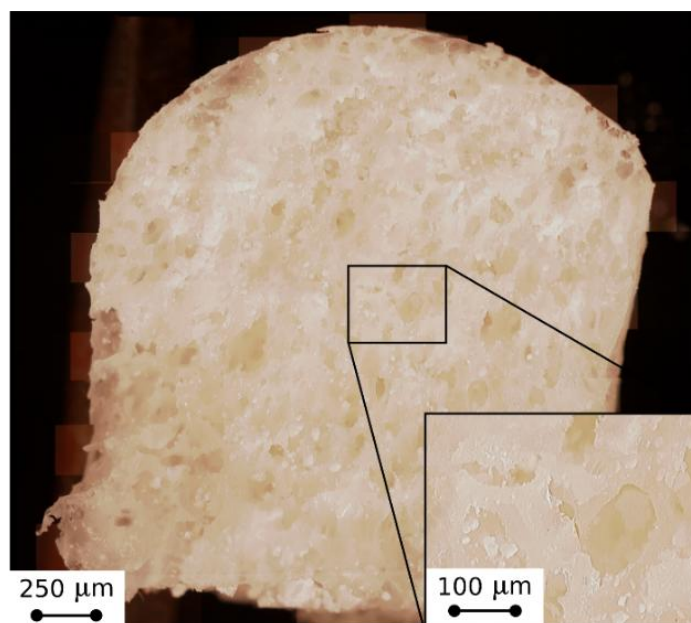


Figure 2: Stereo-microscope image of cross-section along foaming direction of Mg\_50

It was experimentally demonstrated that the porous structure of the foam is quite independent from the amount of the hydrate salt added as filler. As reference, a stereo-microscope image of cross-section along foaming direction of Mg\_50 foam is reported in Figure 2. The sample, characterized by spheroidal shaped cells, presents a mixed open/closed cell structure, as evidenced by the inserted magnification. The bubbles appear homogeneously distributed along the cross section and they are well interconnected each other, so that the water vapour can easily diffuse inside the porous structure.

In order to assess the ability of the synthesized composites foam-salt to properly react with water vapour, under typical working conditions, thermo-gravimetric dehydration tests were performed by means of modified Labsys Evo SETARAM apparatus [14]. The tests were performed as follows: the sample was weighted in an external microbalance and then loaded inside the TG apparatus. Evacuation was performed at room temperature, down to  $10^{-3}$  mbar. Afterwards, water vapour generated by an evaporator at  $20^{\circ}\text{C}$  was admitted in the testing chamber creating a pure water vapour atmosphere at 23.4 mbar. Subsequently, a heating ramp from  $30^{\circ}\text{C}$  up to  $150^{\circ}\text{C}$  was performed to evaluate the amount of water exchanged under these conditions. For each sample, three different specimens were extracted and tested, in order to take into account also possible inhomogeneity of the prepared samples.

The results of the performed thermo-gravimetric dehydration tests are reported in Figure 3.

Particularly, the pure salt  $\text{MgSO}_4 \cdot 7\text{H}_2\text{O}$  was tested as reference, showing a mass loss of about 45% at  $150^{\circ}\text{C}$ , corresponding to about six water molecules released. This reported result is in close agreement with the data reported by van Essen [15].

Calabrese et al. [13], in a previous paper, verified that a negligible weight loss in the range of investigated temperatures occurs in the pure polymeric foam.

Starting from the water mass loss, measured for each tested sample, it was possible to calculate the actual salt content in each foam. None of the tested samples reaches the expected mass loss quantity of the pure salt, demonstrating that the actual salt content for each composite is lower than expected. Table 1 reports the evaluated data.

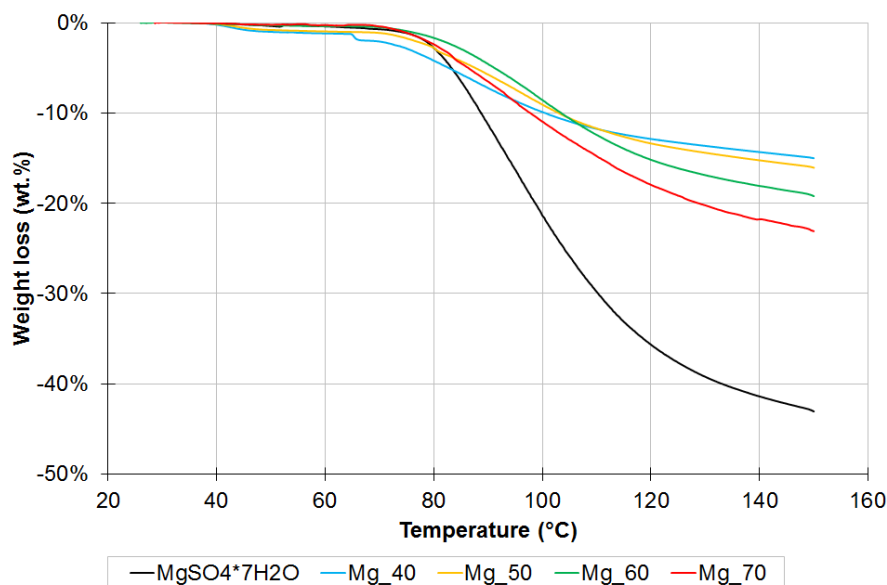


Figure 3: Thermo-gravimetric dehydration measurements in presence of water vapour at 23.4 mbar

Table 1: Water mass loss measured during the TGA measurement and actual salt content calculated for each tested samples

Sample	Nominal salt content [wt.%]	Water mass loss [wt.%]	Actual salt content [wt.%]
Pure MgSO <sub>4</sub> ·7H <sub>2</sub> O	100	43.90	100
FOAM40	40	41.29	37.15
FOAM50	50	36.50	41.08
FOAM60	60	42.02	56.74
FOAM70	70	37.05	58.37

It is reasonable to argue that the spread between the actual salt content and the theoretical one is due to the some experimental issues that involve:

- a partial dissolution of the salt inside the solvent during the foam preparation phase,
- loss of salt during the handling of the samples, and
- an incomplete incorporation of the salt inside the foam during the foaming process, due to the incomplete foaming process induced by the excessive amount of salt employed (Mg\_70).

A scheme of a possible water vapour diffusion mechanism that could take place in the composite foams was proposed according to the experimental characterisation outcomes. Indeed, the knowledge of this aspect is extremely important in order to predict the behaviour of a real thermochemical storage system, considering that the water vapour diffusion inside the matrix affects also its stability.

Figure 4 depicts the vapour diffusion schema inside the foam. The polymers of the matrix (PDMS and PHMS) were chosen for their high permeability to water vapour, in order not to affect the water vapour diffusion during the real operating conditions. In the foam, as evidenced in the schema, the diffusion is ensured by the macro-porous structure of the cell foam. The cellular structure of the foam is mainly characterised by large bubbles interconnection (point A in Figure 4 left) that represents a privileged vapour flow way. Moreover, in consideration of the low thickness of the cell walls, also neighbouring bubbles can effectively contribute to a rapid vapour flow (point B Figure 4, left). In this area, the salt



hydrate embedded in the silicon matrix can easily interact with the vapour phase, undergoing hydration/dehydration phases. Not all of the salt hydrate is able to provide a rapid hydration/dehydration process. The crystals of salt, shielded by thick matrix layer, could be inactive (point C in Figure 4, left). The salt hydration/dehydration can be also allowed by secondary flow lines (point D in Figure 4 left) induced by salt hydrate domains just in proximity of bubble border.

Therefore, based on Figure 4 right, the scheme of possible vapour flow pathways can be summed up in the following manner: the salt hydrated can be considered as a vapour sink and red arrows are the vapour flow paths. The vapour flow takes place mainly by bubbles interconnected paths in the foam and partially by diffusion through PDMS cell walls to obtain hydration/dehydration capabilities of the active salt filler.

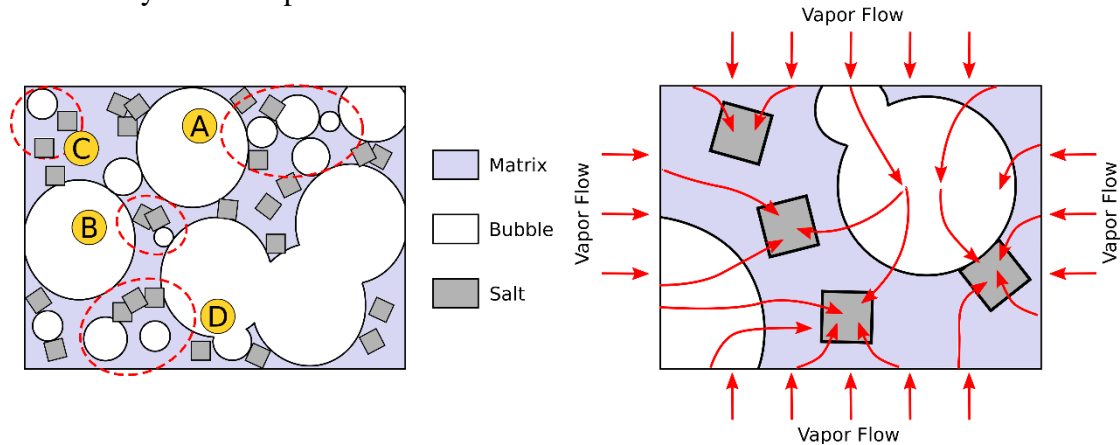


Figure 4: Water vapour diffusion schema inside the foam (left and right)

The choice of the PDMS matrix also plays an important role for assuring the storage energy and mechanical efficiency of the composite foam at high number of hydration/dehydration cycles.

Indeed, when the salt dehydrates, a volume reduction proportional to the number of the lost water molecules occurs. Consequently, as shown in Figure 5, at the matrix/filler interface, tensile or compression radial stresses take place, depending on dehydration or hydration phenomenon, respectively. A flexible matrix, if compared to a brittle one, allows greater local deformation, favoring an easier relaxation of internal forces and thus reducing the risk of damage and the loss of energy storage efficiency of the composite structure. In order to evaluate large deformation capabilities of foamed structure some static compression tests were carried out by using a universal testing machine (UTM – Zwicky 5KN by Swick, Germany).

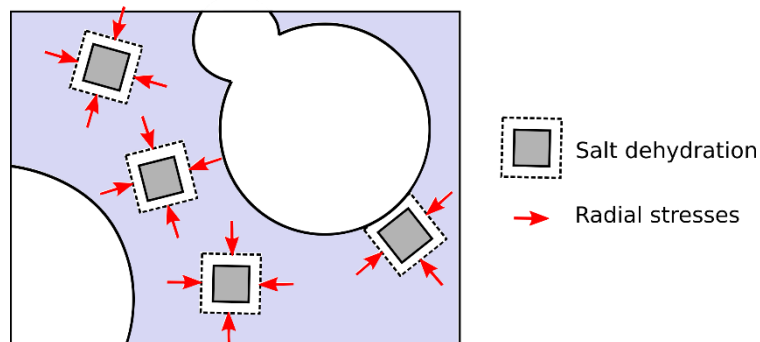


Figure 5: Scheme of internal stresses induced by volume reduction of salt dehydration compression test for unfilled silicone foam b

The results (as reference Figure 6 reports a compression test for an unfilled foam) evidenced very large plateau, bubbles collapse regime, at low stress level (about 20 Pa) indicating a soft mechanical behavior of the foam. Furthermore, a very significant deformation in correspondence of the wall bubbles densification regime is evident (collapse densification regime transition can be identified at about 75% of strain) confirming the high flexibility of the silicone porous structure which supports reversibly high localized deformations. Fifty cyclic compression tests were carried out on same sample without evidence damaging effect of mechanical performance loss.

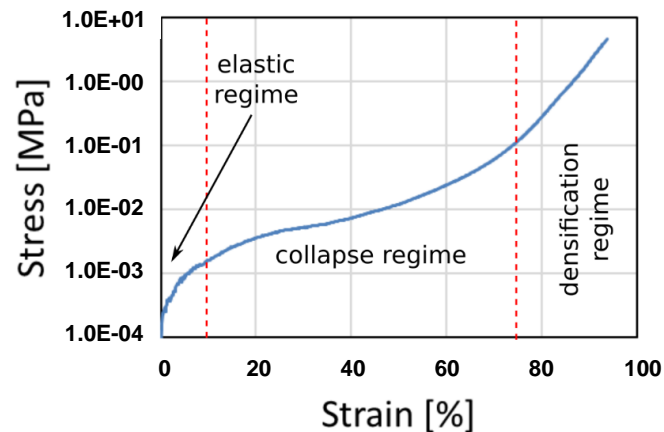


Figure 6: Stress-strain compression curve for unfilled silicone foam

## Conclusions

An innovative composite polymeric foam-salt hydrate (i.e.  $\text{MgSO}_4 \cdot 7\text{H}_2\text{O}$ ) was proposed in order to overcome most of the common material problems related to thermochemical TES applications. The morphological characterization demonstrated that the samples are characterized by a homogenous porosity of the foam. The thermo-gravimetric analysis showed the capacity of the composite samples to efficiently exchange water, under real operating conditions. Mechanical characterization, by static compression test, indicated good stability of the silicone cellular structure also at large deformations. These properties were identified as potentially key factor able to give effective hygro-thermal stability and good water vapour kinetic diffusion of these composite structures for TES applications. Future ageing test of the composite foams will be performed to validate the obtained results.

## Acknowledgements

The work partially funded by the Spanish government (ENE2015-64117-C5-1-R). The authors from UdL would like to thank the Catalan Government for the quality accreditation given to their research group (2014 SGR 123). GREA is certified agent TECNIO in the category of technology developers from the Government of Catalonia.

## References

- [1] D. Aydin, S.P. Casey, S. Riffat, The latest advancements on thermochemical heat storage systems, *Renew. Sustain. Energy Rev.* 41 (2015) 356–367. doi:10.1016/J.RSER.2014.08.054.
- [2] J. Cot-Gores, A. Castell, L.F. Cabeza, Thermochemical energy storage and conversion: A-state-of-the-art review of the experimental research under practical conditions, *Renew. Sustain. Energy Rev.* 16 (2012) 5207–5224. doi:10.1016/J.RSER.2012.04.007.
- [3] J. Jänchen, D. Ackermann, H. Stach, W. Brösicke, Studies of the water adsorption on

- Zeolites and modified mesoporous materials for seasonal storage of solar heat, *Sol. Energy*. 76 (2004) 339–344. doi:10.1016/J.SOLENER.2003.07.036.
- [4] N. Yu, R.Z. Wang, L.W. Wang, Sorption thermal storage for solar energy, *Prog. Energy Combust. Sci.* 39 (2013) 489–514. doi:10.1016/j.peccs.2013.05.004.
- [5] H.U. Rammelberg, T. Osterland, B. Priehs, O. Opel, W.K.L. Ruck, Thermochemical heat storage materials – Performance of mixed salt hydrates, *Sol. Energy*. 136 (2016) 571–589. doi:10.1016/J.SOLENER.2016.07.016.
- [6] P.A.J. Donkers, L.C. Sögütöglü, H.P. Huinink, H.R. Fischer, O.C.G. Adan, A review of salt hydrates for seasonal heat storage in domestic applications, (2017). doi:10.1016/j.apenergy.2017.04.080.
- [7] P.A.J. Donkers, L. Pel, O.C.G. Adan, Experimental studies for the cyclability of salt hydrates for thermochemical heat storage, *J. Energy Storage*. 5 (2016) 25–32. doi:10.1016/j.est.2015.11.005.
- [8] S.K. Henninger, S.-J. Ernst, L. Gordeeva, P. Bendix, D. Fröhlich, A.D. Grekova, L. Bonaccorsi, Y. Aristov, J. Jaenchen, New materials for adsorption heat transformation and storage, *Renew. Energy*. 110 (2017) 59–68. doi:10.1016/j.renene.2016.08.041.
- [9] G.T. Whiting, D. Grondin, D. Stosic, S. Bennici, A. Auroux, Zeolite–MgCl<sub>2</sub> composites as potential long-term heat storage materials: Influence of zeolite properties on heats of water sorption, *Sol. Energy Mater. Sol. Cells*. 128 (2014) 289–295. doi:10.1016/J.SOLMAT.2014.05.016.
- [10] S. Hongois, F. Kuznik, P. Stevens, J.-J. Roux, Development and characterisation of a new MgSO<sub>4</sub>–zeolite composite for long-term thermal energy storage, *Sol. Energy Mater. Sol. Cells*. 95 (2011) 1831–1837. doi:10.1016/J.SOLMAT.2011.01.050.
- [11] K. Posern, C. Kaps, Calorimetric studies of thermochemical heat storage materials based on mixtures of MgSO<sub>4</sub> and MgCl<sub>2</sub>, *Thermochim. Acta*. 502 (2010) 73–76. doi:10.1016/J.TCA.2010.02.009.
- [12] A. Jabbari-Hichri, S. Bennici, A. Auroux, CaCl<sub>2</sub>-containing composites as thermochemical heat storage materials, *Sol. Energy Mater. Sol. Cells*. 172 (2017) 177–185. doi:10.1016/J.SOLMAT.2017.07.037.
- [13] L. Calabrese, L. Bonaccorsi, A. Freni, E. Proverbio, Silicone composite foams for adsorption heat pump applications, *Sustain. Mater. Technol.* 12 (2017) 27–34. doi:10.1016/J.SUSMAT.2017.04.002.
- [14] A. Frazzica, A. Sapienza, A. Freni, Novel experimental methodology for the characterization of thermodynamic performance of advanced working pairs for adsorptive heat transformers, *Appl. Therm. Eng.* 72 (2014). doi:10.1016/j.applthermaleng.2014.07.005.
- [15] V.M. van Essen, H.A. Zondag, J.C. Gores, L.P.J. Bleijendaal, M. Bakker, R. Schuitema, W.G.J. van Helden, Z. He, C.C.M. Rindt, Characterization of MgSO<sub>4</sub>[sub 4] Hydrate for Thermochemical Seasonal Heat Storage, *J. Sol. Energy Eng.* 131 (2009) 41014. doi:10.1115/1.4000275.

# Model based assessment of working pairs for gas driven thermochemical heat pumps

E. Laurenz<sup>1\*</sup>, G. Földner<sup>1</sup>, J. Doell<sup>1</sup>, C. Blackman<sup>2,3</sup>, Lena Schnabel<sup>1</sup>

<sup>1</sup>Fraunhofer Institute for Solar Energy Systems ISE, Heidenhofstr. 2, 79110 Freiburg, Germany

<sup>2</sup>SaltX Technology, Västertorpsvägen 135, 12944 Hägersten, Sweden

<sup>3</sup>Dalarna University, Röda vägen 3, 78170 Borlänge Sweden

\*Corresponding author: [eric.laurenz@ise.fraunhofer.de](mailto:eric.laurenz@ise.fraunhofer.de)

## Abstract

The choice of a working pair for gas driven thermochemical heat pumps requires fast computation of estimates for efficiency (coefficient of performance, COP) and power (specific heating power, SHP) under different boundary conditions. A quasi-stationary cycle description with lumped parameters and linear driving force model with constant effective heat transfer coefficients is used. Further properties of the heating system are included as boundary conditions. This approach intrinsically takes into account the thermodynamic equilibrium data for different working pairs. In this paper two working pairs  $\text{CaBr}_2 \cdot x\text{NH}_3 - \text{NH}_3$  (sorption) and  $\text{MnCl}_2 \cdot x\text{NH}_3 - \text{PbCl}_2 \cdot x\text{NH}_3$  (resorption) are compared. The overall performance is assessed with the seasonal gas utilization efficiency (SGUE) according to EN 12309-6 as weighted averages for different boundary conditions. As a result the  $\text{MnCl}_2 - \text{PbCl}_2$  resorption cycle shows significantly better performance (SGUE = 1.29–1.38) compared to the  $\text{CaBr}_2$  sorption cycle (1.09–1.16). Performance increases with ambient temperature (climate) and decreases with the design temperature level of the heating system.

**Keywords:** thermochemical material, gas heat pump, performance indicators, modelling.

## Introduction/Background

Gas driven thermochemical heat pumps are a promising option to reduce  $\text{CO}_2$  emissions from the heating sector. For this technology a wide range of working pairs are under consideration. Examples of sorption cycles are salt hydrates – water, salt ammoniates – ammonia, and for resorption cycles combinations of two different salt ammoniates (or hydrates). These working pairs have been subject to different screenings and assessments mainly focused on energy storage density [1, 2]. Newer studies include the temperature levels resulting from thermodynamic equilibrium data [3, 4] although neglecting any dynamic effects.

The aim of the present study is to provide sufficiently good estimates for efficiency (coefficient of performance, COP) and power (specific heating power, SHP) at realistic boundary conditions of building heating system. These estimates are required for the choice of working pairs and other basic design considerations and are to our knowledge not available from literature. As an example, results are compared for the two working pairs  $\text{CaBr}_2 \cdot x\text{NH}_3 - \text{NH}_3$  (sorption) and  $\text{MnCl}_2 \cdot x\text{NH}_3 - \text{PbCl}_2 \cdot x\text{NH}_3$  (resorption) which, in contrast to water based systems, are not prone to freezing of the working fluid at sub-zero temperatures. The two working pairs were chosen as they allow for operation of a gas-driven heat pump. Under typical high, middle and low temperature boundaries of a domestic heating application their equilibrium temperatures are suitable to run a sorption and resorption processes respectively.

The method used is based on simulations of a fast and efficient quasi-stationary model of simple thermochemical heat pump cycle. The lumped parameter model is based on the energy and mass balances for each component. The simple thermochemical heat pump consists of a first reactor with a strongly binding salt ( $\text{MnCl}_2$  or  $\text{CaBr}_2$  here) and a combined evaporator/condenser with pure  $\text{NH}_3$  or, for the resorption system, a second reactor with a weakly binding salt ( $\text{PbCl}_2$ ).

The cycle for the case of the working pair  $\text{MnCl}_2 \cdot x\text{NH}_3 - \text{PbCl}_2 \cdot x\text{NH}_3$  is shown in Figure . The simplified cycle consists of several isosteric heating or cooling phases (dashed lines) and reaction phases that are both, isothermal and isobaric, for one salt reaction (solid lines). As  $\text{PbCl}_2$  exhibits three stable ammoniation states in the temperature and pressure region of interest the ammoniation of  $\text{MnCl}_2$  (points 2a, 2b in Figure 1) happens at two different pressures: First determined by the deammoniation of  $\text{PbCl}_2 \cdot 8\text{NH}_3$  to  $\text{PbCl}_2 \cdot 3.25\text{NH}_3$  (1a) and the second by the subsequent deammoniation to  $\text{PbCl}_2 \cdot 2\text{NH}_3$  (1b). For the case of  $\text{CaBr}_2 \cdot x\text{NH}_3 - \text{NH}_3$  the cycle is less complex with

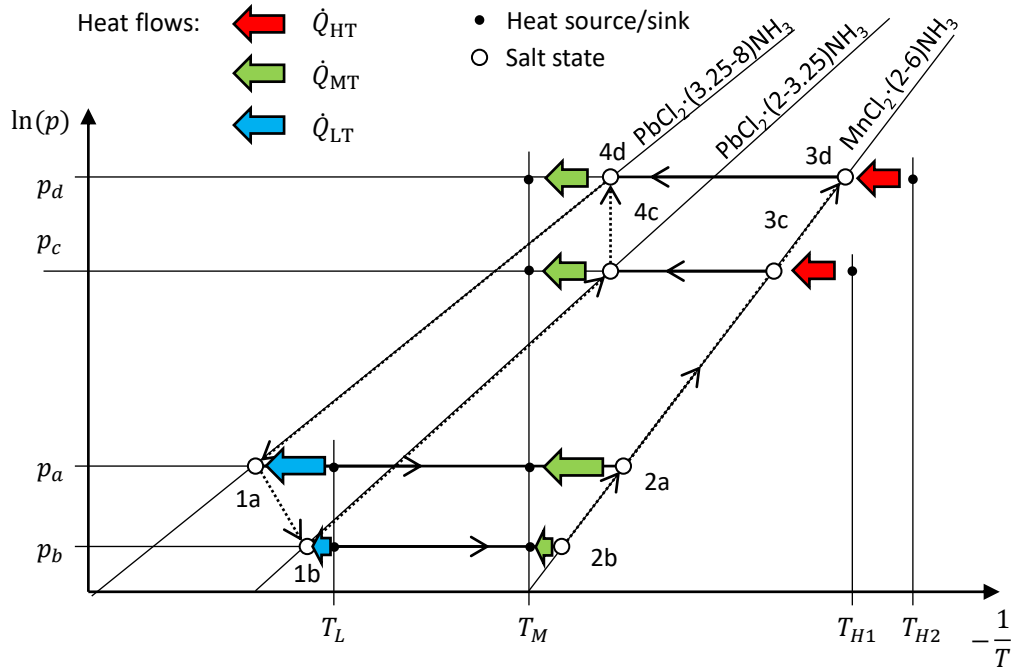


Figure 1: Simplified two-step resorption heat pump cycle for the example  $\text{MnCl}_2 \cdot x\text{NH}_3$  –  $\text{PbCl}_2 \cdot x\text{NH}_3$  with heat transfer limitations, solid lines: isobaric hydration/dehydration reactions, dashed lines: isosteric heating/cooling, arrows indicate heat flows between salt and heat sources/sinks, green: useful heat output to middle temperature, red: driving heat input from high temperature, blue: ambient heat input from low temperature

one pressure level for ammoniation and one for deammoniation, as only the reaction  $\text{CaBr}_2 \cdot (2-6)\text{NH}_3$  is used against the vapor pressure of pure  $\text{NH}_3$ .

Temperature boundary conditions are modelled as infinite heat reservoirs at low (ambient heat source), middle (useful heat delivered to a building heating system) and high (heat input from a gas burner) temperatures  $T_L$ ,  $T_M$  and  $T_H$ . In order to allow for driving differences for heat and mass transfer the salt equilibrium temperature is higher than the corresponding source temperature (or lower than the corresponding sink temperature). A linear driving force (LDF) model with one effective lumped effective transfer coefficient per heat exchanger is used to conveniently approximate both, heat and mass transfer, processes [5]. This effective coefficient is expressed in the form of an overall heat transfer coefficient  $UA_{\text{eff}}$ . It directly relates the heat exchanger heat flow  $\dot{Q}_{\text{HX}}$  (positive direction: to the salt) to the overall temperature difference between the source/sink temperature  $T_{\text{snk,src}}$  (i.e.  $T_L$ ,  $T_M$  or  $T_H$ ) and the saturation temperature at the respective operation pressure  $T_{\text{sat}}(p)$  (white circles in Figure):

$$\dot{Q}_{\text{HX}} = UA_{\text{eff}} (T_{\text{snk,src}} - T_{\text{sat}}(p)). \quad (1)$$

The saturation temperature is taken from pure working fluid properties for the evaporator/condenser [6] and the salt's reaction equilibrium for the reactor. The latter is computed with a modified Van't Hoff equation

$$\ln\left(\frac{p}{p^\circ}\right) = \frac{\Delta S_s^\circ}{R} - \frac{\Delta H_s^\circ}{RT} \quad (2)$$

with data given in Table 1.

For the mass balance void volumes are assumed sufficiently small to be negligible. The energy balance for each component including heat capacities for all parts that undergo temperature changes during isosteric phases (heat exchanger, housing, working fluid and salt). The specific heat capacities of the salt ammoniates are not available from literature and are approximated using Kopp's rule [7] (c.f. Table 1). Dynamic effects of isosteric phases on the power delivered are not taken into account. Heat losses are assumed to be negligible. For model parameters like  $UA$ -values, masses for heat exchangers and active material realistic values were chosen in consultation with an industry partner.

Table 1: Properties of the different salt ammoniation reaction used in the model (sources: [8] for  $\Delta H_s^\circ$  &  $\Delta S_s^\circ$ ; [7] for  $c_p$  estimated with Kopp's rule)

Reaction	$\Delta H_s^\circ$ (J/mol <sub>NH3</sub> )	$\Delta S_s^\circ$ (J/mol <sub>NH3</sub> K)	$c_{p,low,Kopp}^\circ$ (J/mol <sub>salt</sub> K)	$c_{p,hgh,Kopp}^\circ$ (J/mol <sub>salt</sub> K)	$M_{salt}$ (kg/mol <sub>salt</sub> )
PbCl <sub>2</sub> ·(2-3.25)NH <sub>3</sub>	39 339	134.4	126	155	0.278
PbCl <sub>2</sub> ·(3.25-8)NH <sub>3</sub>	34 317	127.9	155	262	0.278
CaBr <sub>2</sub> ·(2-6)NH <sub>3</sub>	48 965	134.7	124	215	0.200
MnCl <sub>2</sub> ·(2-6)NH <sub>3</sub>	47 416	132.2	123	214	0.126

The control algorithm used for the simulation allows modulation of the middle temperature heat flow  $\dot{Q}_{MT}$  delivered to the building heating system as required. During the deammoniation of reactor 1 (high pressure reactions)  $\dot{Q}_{MT}$  is controlled by modulation of the gas burner power. This is modelled by a change of the level of  $T_H$  which represents the coldest temperature to which the hot gas stream is cooled down. The effect of this on the gas utilization and thus overall efficiency is taken into account. During re-ammoniation of reactor 1 (low pressure reactions) the average heat flow  $\bar{Q}_{MT}$  is controlled through a variation of the half cycle time as illustrated in Figure 2. At any time, the current heat flow  $\dot{Q}_{MT}$  is determined by the given  $T_L$  and  $T_M$ , the salt equilibria and the heat exchanger's UA-values. Hence, the middle temperature heat flow is fully determined for each ammoniation step. The required heat flow  $\dot{Q}_{MT,set}$  is achieved on average over the whole re-ammoniation phase by appropriate interruption or extension of the resolution phase. In the model the cycle is stopped on one of the following conditions:

- The average heat flow  $\bar{Q}_{MT}$  would become smaller than set middle temperature heat flow  $\dot{Q}_{MT,set}$  (Figure ).
- Re-ammoniation is complete.

The heat pump cycle is driven by heat from a gas burner. For the gas burner we assume an efficiency of 90% (higher heating value). The heat pump module is designed to a nominal capacity of 60% of the total design heat flow. Based on the application scenarios from EN 12309-6 (see below), it can be expected that with a nominal capacity of 60% over 90% of the energy demand can be covered by the sorption module. Up to this heat flow the module is used to cover the complete heat demand. If a fraction of the application's heat demand is not met by the heat pump cycle or if its COP is below 1 (e.g. because of unfavorable temperature conditions) the heat flow deficit is directly supplied by the burner.

An overall performance indicator is created using the bin method according to EN 12309-6 [9]. For the operation of any real appliance the boundary conditions would not be constant, but changing throughout the year. Furthermore, they depend on the climate and the building/heating system under consideration.

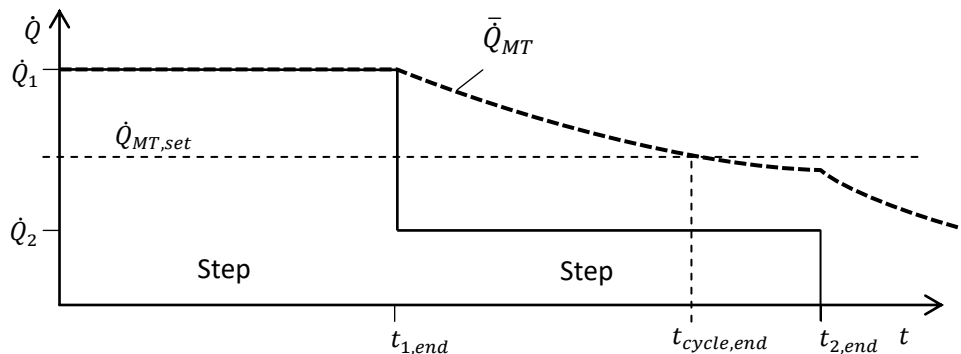


Figure 2: Ideal heat flow over time during re-ammoniation (of reactor 1) to illustrate control approach. Depending on the current step the current heat flow (solid line) changes discontinuously as the driving temperature differences change (thermal masses neglected). The average heat flow (dashed) has a continuous shape. The cycle is stopped when the average heat flow reaches the set point.

Table 2: Design ambient temperatures for different climates and design application temperature levels for different heating systems as defined by EN 12309-6.

Climate	Design ambient temperatures	Heating systems temperature	Design application temperatures (feed/return)
Colder	-22 °C	Low	35/28 °C
Average	-10 °C	Medium	45/35 °C
Warmer	+2 °C	High	55/41 °C
		Very high	65/48 °C

To account for the seasonal variations, the model is simulated at different operating points defined by the actual ambient temperature. For any given climate and heating system temperature level, the actual ambient temperature (i.e. the source temperature  $T_L$ ) determines the demanded heat flow  $\dot{Q}_{dmd}$  (Figure 5) and the demanded feed temperature to the heating system  $T_{MT}$  according to the standard heating curve (Figure 6). From each simulation result, indicators like the gas utilization efficiency (GUE) are calculated and aggregated with a weighted average (Figure 7) to the seasonal gas utilization efficiency (SGUE).

This is done for different climates (design ambient temperature) and heating systems (design application feed and return temperatures) as given in Table 2. As a conservative approximation in the simulations, the feed temperature is chosen as middle temperature  $T_M$ .

### Discussion and Results

The model was implemented in R [10] and verified for overall energy and mass balance throughout a full cycle under different boundary conditions. For the  $\text{CaBr}_2 \cdot x\text{NH}_3 - \text{NH}_3$  (sorption) configuration small errors in the order of 2-6% of the total heat or mass exchanged prevails. This is due to simplifying assumptions on the properties of  $\text{NH}_3$  (constant  $c_p$  in liquid and vapor phase). For the  $\text{MnCl}_2 \cdot x\text{NH}_3 - \text{PbCl}_2 \cdot x\text{NH}_3$  (resorption) configuration the balance errors are only numerical (relative errors  $< 0.01\%$ ).

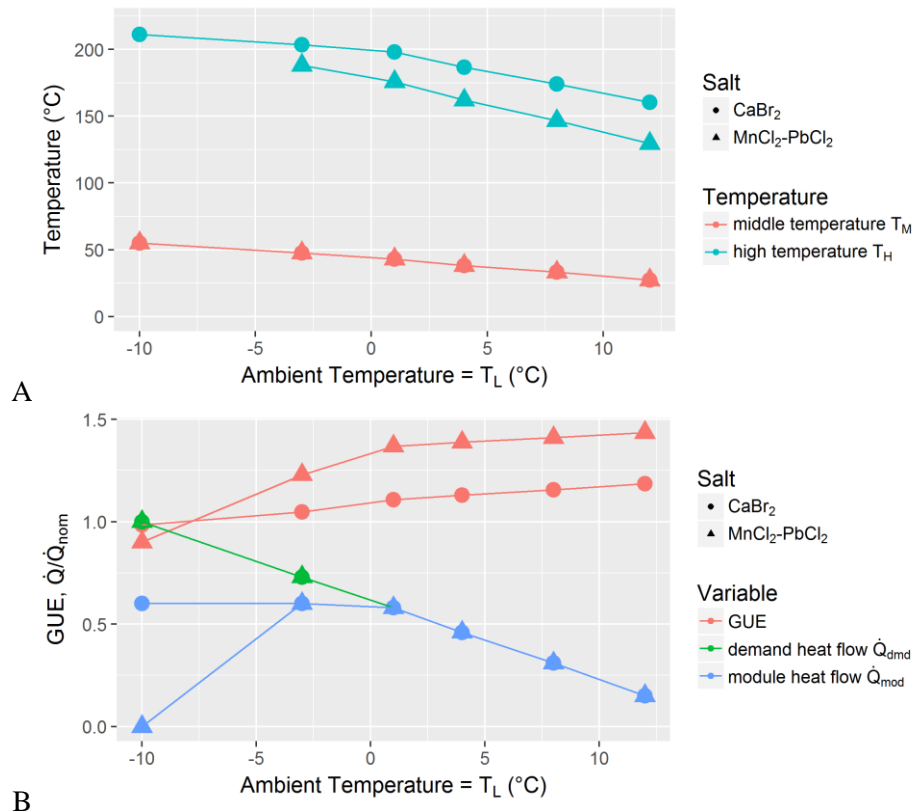


Figure 3: Detailed results for climate "Average" and application temperature "High" as a function of ambient temperature from different operational points according to EN 12309-6. A) Temperature levels  $T_M$  (input to simulations) and  $T_H$  (calculated by controller to ensure module heat flow), missing points: no operation of sorption module (direct gas burner heating only), SGUE for this point is  $\text{CaBr}_2$ : 1.11;  $\text{MnCl}_2\text{-PbCl}_2$ : 1.33

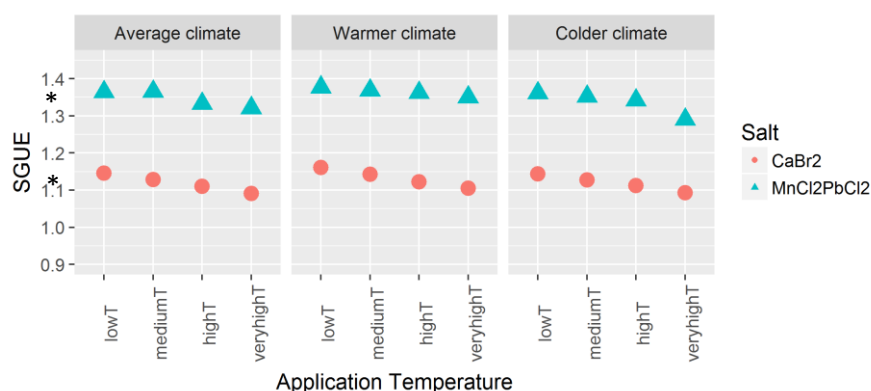


Figure 4: Simulated seasonal gas utilization efficiency of the two materials/material combinations considered for different climate zones and application temperature levels, data points marked with \* are detailed in Figure

Main cycle parameters and performance results vary considerably with ambient temperature as shown exemplarily in Figure for “average” climate and a “high temperature” heating system. For lower ambient temperatures higher driving temperatures are required as higher heat flows have to be provided at higher temperature levels. The GUEs decrease with lower ambient temperature. This is due to the higher driving temperatures and a second effect: a reduced loading spread. The loading spread is reduced, as the controller stops the re-ammoniation in order to ensure the middle temperature heat flow. For the  $\text{MnCl}_2\text{-PbCl}_2$  system this even leads to complete stop of the heat pump cycle at  $-10\text{ }^\circ\text{C}$  where the total heat demand is supplied directly from the gas burner. It should be noted, that the driving temperature level  $T_H$  might be limited (e.g. for stability or safety reasons) which is not represented in this model. This limitation would further reduce the module’s efficiency and/or operability at low ambient temperatures.

However, operation points with low efficiency due to harsh conditions do not happen often throughout the year (c.f. Figure 7). The seasonal gas utilization efficiency ( $\text{CaBr}_2$ : 1.11;  $\text{MnCl}_2\text{-PbCl}_2$ : 1.33) is dominated by operation points with moderate conditions. The results show that with a relative design capacity of 60% the sorption module covers most of the annual heat demand. A higher capacity would increase SGUE only marginally.

The SGUEs mainly depend on application temperature level and – to a lesser extend – on the climate zone (Figure 4). High heating system temperature levels and cold climates lead to lower SGUEs. Throughout all scenarios the simulations predict higher efficiency for the  $\text{MnCl}_2\text{-PbCl}_2$  resorption cycle (1.29–1.38) than for the  $\text{CaBr}_2$  sorption cycle (1.09–1.16). The continuous decline observed for  $\text{CaBr}_2$  can be explained with the rising temperature spreads  $T_H - T_M$  and  $T_M - T_L$  that determine the heat required for the sensible heating and cooling of the reactor and the condenser/evaporator respectively.

The results are comparable to values found by Nienborg et al. [11] for adsorption gas heat pumps. With similar assumptions they reported SGUEs for average climate and medium temperature in the order of 1.08-1.38 depending on working pairs ( $\text{SAPO34-H}_2\text{O}$ ,  $\text{NaY-H}_2\text{O}$ ,  $\text{CuBTC-MeOH}$ ) and heat exchanger mass ratio. The present model gives a SGUE for this point of 1.13 ( $\text{CaBr}_2$ ) and 1.37 ( $\text{MnCl}_2\text{-PbCl}_2$ ). However Nienborg et al. imposed a maximum desorption temperature of  $230\text{ }^\circ\text{C}$  for stability and safety reasons, which was not the case in the present study. However, such a restriction would especially come into play at very low ambient temperature which has little impact on the overall performance.

## Summary/Conclusions

The model presented in this study is a first step assessment of salt based thermochemical processes at realistic boundary conditions. It shows how the working pair’s thermodynamic equilibrium properties match the required temperature level from applications.

The results are reasonable and show comparable performance compared to adsorbent based cycles. For  $\text{MnCl}_2\text{-PbCl}_2$  (SGUE = 1.29–1.38) the results are promising and might be further improved by a heat recovery, which has been out of scope of the present study. The potential of  $\text{CaBr}_2$  (1.09–1.16) for the scenarios evaluated is low.



A more detailed performance analysis requires at least a simple model including heat capacities, evaporator/condenser dynamics and sorption dynamics. This includes a better understanding of the sorption kinetics and underlying heat and mass transfer processes in the salt and possibly reaction dynamics. These questions will be addressed in further studies.

### Acknowledgements

The PhD scholarship from Heinrich-Böll-Stiftung for Eric Laurenz is gratefully acknowledged.

### References

- [1] P. Touzain, “Thermodynamic values of ammonia-salts reactions for chemical sorption heat pumps,” in Proc. Int. Sorption Heat Pump Conf, 1999, pp. 225–238.
- [2] K. E. N’Tsoukpoe, T. Schmidt, H. U. Rammelberg, B. A. Watts, and W. K. L. Ruck, “A systematic multi-step screening of numerous salt hydrates for low temperature thermochemical energy storage,” Applied Energy, vol. 124, pp. 1–16, <http://www.sciencedirect.com/science/article/pii/S0306261914001974>, 2014.
- [3] E. Laurenz, G. Földner, and L. Schnabel, “Assessment of thermodynamic equilibrium properties of salt hydrates for heat transformation applications at different temperature levels,” in Proceedings of the Heat Powered Cycles Conference 2016, Nottingham, 2016.
- [4] P.A.J. Donkers, L. C. Sögütöglü, H. P. Huinink, H. R. Fischer, and O.C.G. Adan, “A review of salt hydrates for seasonal heat storage in domestic applications,” Applied Energy, vol. 199, pp. 45–68, 2017.
- [5] U. Wittstadt et al., “A novel adsorption module with fiber heat exchangers: Performance analysis based on driving temperature differences,” Renewable Energy, vol. 110, pp. 154–161, 2017.
- [6] E.W. Lemmon, M.O. McLinden, and D.G. Friend, “Thermophysical Properties of Fluid Systems,” in NIST Chemistry WebBook, NIST Standard Reference Database 69, P. J. Linstrom and W. G. Mallard, Eds.: National Institute of Standards and Technology, 2016.
- [7] P. E. Liley, G. H. Thomson, D. G. Friend, T. E. Daubert, and E. Buck, “Section 2: Physical and Chemical Data,” in Perry’s chemical engineers’ handbook, 7th ed., New York, NY: McGraw-Hill, 1999.
- [8] J. Berthiaud, “Procédé à sorption solide/gaz pour le transport de chaleur et de froid à longue distance,” Dissertation, Université de Perpignan, Perpignan, 2007.
- [9] Gas-fired sorption appliances for heating and/or cooling with a net heat input not exceeding 70kW - Part 6: Calculation of seasonal performances, EN12309-6, 2014.
- [10] R Core Team, R: A Language and Environment for Statistical Computing. Vienna, Austria: R Foundation for Statistical Computing, 2017.
- [11] B. Nienborg, P. Schossig, M. Aprile, and R. Chritoph, “Seasonal Performance Evaluation of Gas Heat Pumps with Different Working Pairs under Varying Boundary Conditions,” International Sorption Heat Pump Conference 2017, Tokyo, 2017.

### Appendix

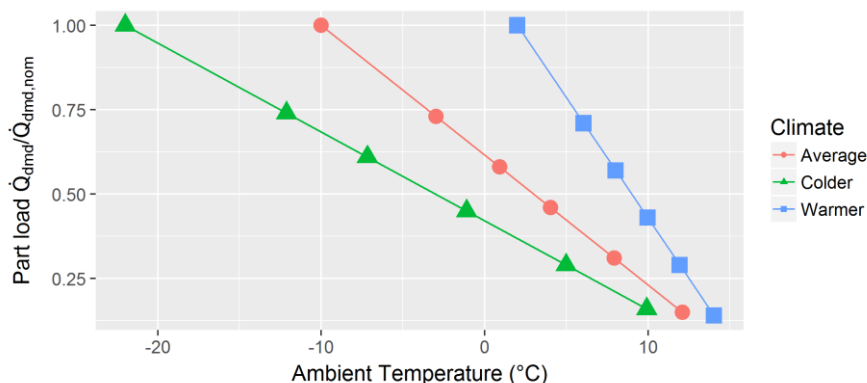


Figure 5: Actual heat demand relative to nominal capacity (design heat demand) over ambient temperature for different climate zones

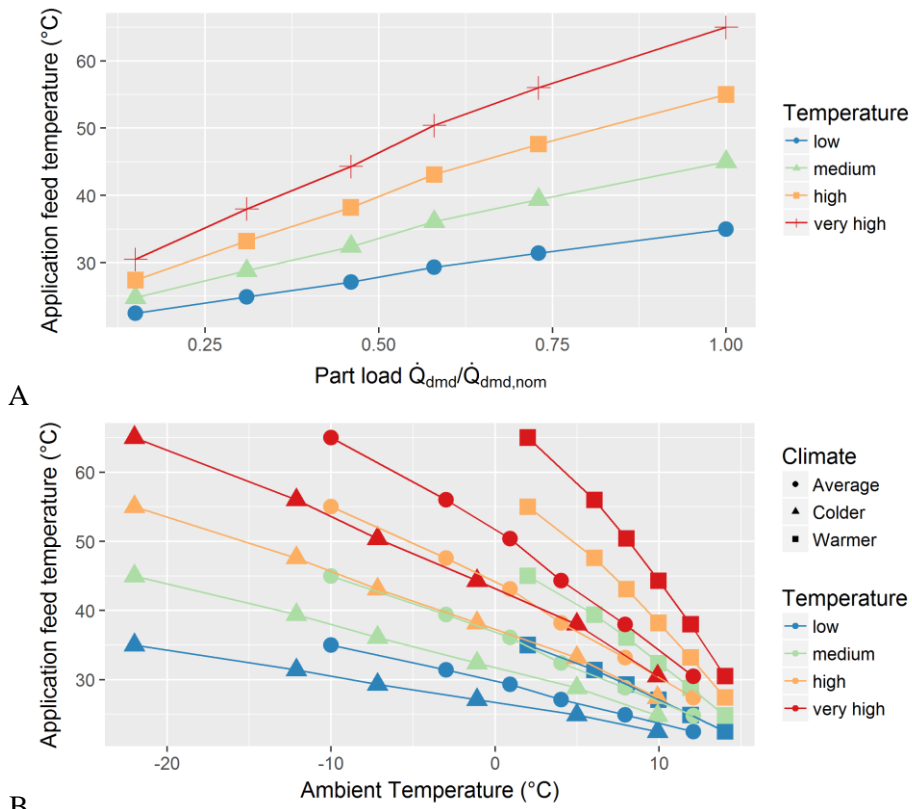


Figure 6: Application feed temperature (middle temperature level  $T_M$  in the simulations) as a function of relative heat demand for different application temperature levels (A) and as a function of ambient temperature for different climates and application temperature levels (B)

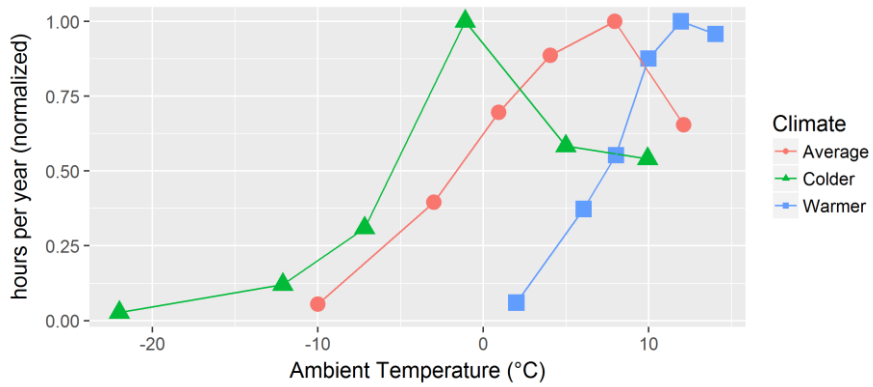


Figure 7: hours per year (normalized) over ambient temperature for different climate zones used as weights for the calculation of seasonal gas utilization efficiencies (GUES) from gas utilization efficiencies (GUE)

# The Obtention of an Ejector Cooling System's Performance Map Through Different Graphical Representations

Jorge I. Hernandez<sup>1\*</sup>, Roberto Best<sup>1</sup>, Ruben Dorantes<sup>2</sup>, Humberto Gonzalez<sup>2</sup>,  
Raul Roman<sup>3</sup>, Jacobo Galindo<sup>1</sup> and Pablo Aragon<sup>1</sup>

<sup>1</sup> Instituto de Energías Renovables, Universidad Nacional Autónoma de México  
Priv. Xochicalco s/n, Col. Centro, CP 62589, Temixco, Morelos, México

<sup>2</sup> Universidad Autónoma Metropolitana Azcapotzalco, Av San Pablo Xalpa 180, Reynosa Tamaulipas,  
CP 02200, Ciudad de México, México

<sup>3</sup> Universidad Autónoma del Estado de Hidalgo, Campus Apan  
Carretera Apan-Calpulalpan Km.8, Col.Chimalpa, C.P. 43920, Apan, Hidalgo, Mexico

\*Corresponding author: jhg@ier.unam.mx

## Abstract

Under the assumption that the performance map of an ejector's cooling system is a basic tool for its optimal operation, a methodology is proposed for its finding. It consists in keeping constant  $P_{GE}$  and  $P_{CO}$  while the secondary mass flow rate is varied. For the resulting  $P_{GE}$ ,  $P_{CO}$  and  $P_{EV}$  values, a series of dimensionless plots are obtained in order to define the ejector's performance map,  $U-T_{CO}$  plot, corresponding to the ejector critical back pressure and should direct the optimal ejector cooling system operation at design and off design conditions.

**Keywords:** ejector cooling system; refrigeration; thermal cooling systems; ejector.

## Introduction

The present development of the ejector cooling system has energy and ecological benefits. It was introduced by Leblanc in 1910 and was a cycle having vapour as its working fluid, a supply of low-grade thermal energy as inlet and producing cooling as outlet. Since then, this system has been studied in order to improve the ejector and system performance, attending to the understanding of ejector's internal processes; optimization of ejector geometry; study of different working fluids; introduction of additional heat exchangers; combination with other refrigeration systems including another ejector system; study of different thermal energy sources considering direct and indirect thermal energy supply to the generator, as Elbel and Hrnjak, as well as, Besagni *et al.* have mentioned [1, 2]. All this research has proved the reliance on the system's experimental operation. Unfortunately, the efforts directed to operate the system at the critical behaviour have been limited and insufficient. Among others, Hernandez *et al.* [3, 4] have presented different graphical representations of the ejector's critical behaviour considering data from the literature. Trying to continue with this contribution, the study of the representation of the optimal ejector behaviour in different plots with own experimental data is presented and analysed.

## The Ejector System

For its compression capacity, the ejector is used in a refrigeration system where phase change takes place at different temperature. So, the ejector cooling system's configuration and thermodynamic cycle are shown in Figs. 1 (a) and (b). The first one shows the system elements arrangement according to a couple of sub-cycles, the upper is a of power represented by the states 1-3-4-5-1 and the lower is of refrigeration given by states 2-3-4-6-2. Fig. 1 (b) shows the 3P system thermodynamic cycle according of being a 3T system.

On the other hand, the ejector is a device without moving parts that is internally crossed by fluids in motion. It can be considered as a mixer, when its discharge port has this resulting effect considering that it's both inlets have different fluid condition; or as a compressor or

pump, considering the effect of boosting fluid from its low pressure inlet to its medium pressure discharge port. For this reason, the ejector has a variety of applications in the chemical, hydraulic, pneumatic and thermal industries. However, its efficiency is low and its sensibility to changes in its operation condition could easily take it to have a low performance. So, keeping its operation efficiently becomes an engineering challenge.

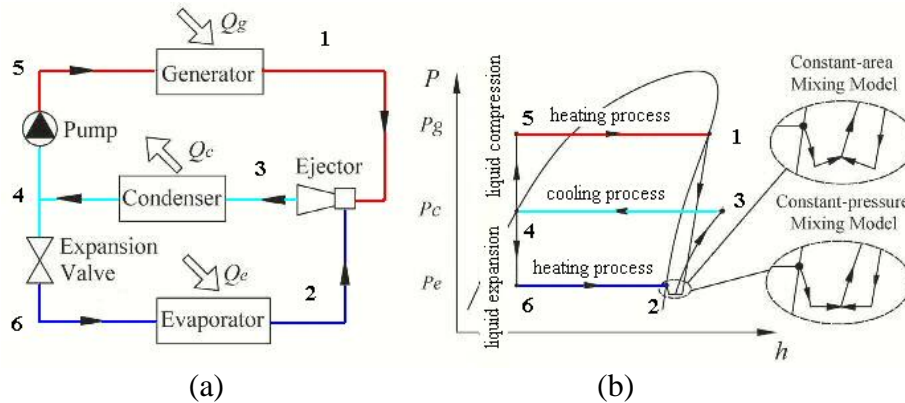


Fig. 1. The ejector's cooling system configuration and its thermodynamic cycle, [5].

In regard to the ejector cooling system's efficiency, the parameter employed for such end is its coefficient of performance, COP, given by

$$\text{COP} = U \frac{(h_2 - h_6)}{(h_1 - h_4)} \quad (1)$$

where  $(h_2 - h_6)$  is the evaporator specific enthalpy difference in kJ/kg producing the system cooling effect;  $(h_1 - h_4)$  is the system specific enthalpy difference required to produce the cooling effect; and  $U$  is the ejector entrainment ratio, defined as

$$U = \frac{\dot{m}_2}{\dot{m}_1} \quad (2)$$

being  $\dot{m}_1$  and  $\dot{m}_2$  the mass flow rates in kg/s for the ejector primary and secondary fluids.

This parameter is also of relevance for the ejector performance.

Thermodynamically, the ejector cooling system is 3T and has the  $T_{GE}$ ,  $T_{CO}$  and  $T_{EV}$  at saturation as its independent variables. Also, these temperatures define the system working pressures, which are also used as independent variables, and are the starting values when superheating and subcooling processes exist.

On the other hand, the expansion and compression processes are commonly defined by pressure ratios. In this regard, the driving pressure ratio  $\Gamma$  is defined as

$$\Gamma = \frac{P_{GE}}{P_{EV}} \quad (3)$$

where  $P_{GE}$  and  $P_{EV}$  in MPa are the generator and evaporator pressures. The compression ratio  $r$  is given as

$$r = \frac{P_{CO}}{P_{EV}} \quad (4)$$

being  $P_{CO}$  the condenser pressure. Finally, the expansion pressure ratio  $\xi$  is defined as

$$\xi = \frac{P_{GE}}{P_{CO}} \quad (5)$$

So, plots of  $U$  and COP should be obtained against the generation, condensation and evaporation pressure as well as against  $r$ ,  $\xi$  and  $\Gamma$ .

### Description of the Experimental Rig

The employed experimental rig is built up by a generator, a condenser, an evaporator, an ejector, a pump, an expansion valve, a preheater, a precooler and a condenser tank, as shown in Fig. 2. The generator, condenser and evaporator are plate heat exchangers; the pump is of the piston type; the expansion valve is manual and the ejector is commercial and made by Schutte and Koerting. The measurement of temperature, pressure and mass flow rates are carried out by PT1000 sensors, membrane pressure sensors and Coriolis mass flow rate sensors, respectively. The working fluid is R134a.

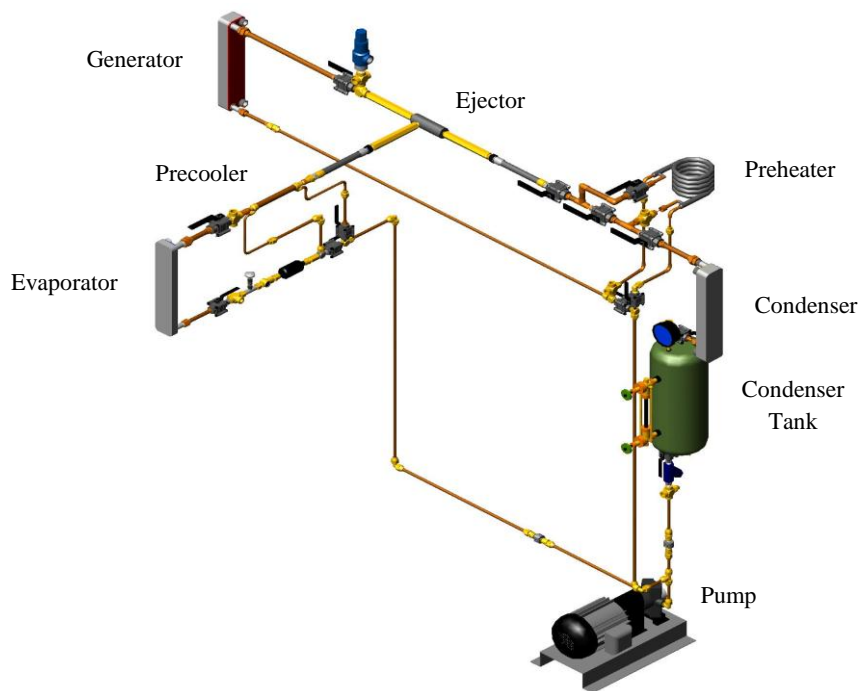


Fig. 2 Experimental rig configuration.

### Obtention of Results

It is well known that the ejector efficiency is low and its highest values are reached at the condenser critical back pressure, for what it is really important to find it in the simplest way. Therefore, some important amount of experimental data will be obtained and transformed in dimensionless parameters to determine a dimensionless and unique condenser critical back pressure curve. With this curve, a critical plot of  $U-T_{CO}$  will be obtained for different generator and evaporator isothermal lines. This plot indicates any triplet of generator, condenser and evaporator temperatures that belong to the ejector critical condition. This procedure will indicate the conditions where the ejector cooling system can operate at its higher efficiency.

Considering that the ejector cooling system is 3T, the ejector performance is defined at the corresponding saturation pressure for each one of these temperatures. So, and during the experimentation,  $P_{GE}$  and  $P_{CO}$  could be controlled and kept constant allowing the main nozzle be choked while the secondary fluid mass flow rate could be varied to achieve different  $U$

and  $P_{EV}$  values. When enough  $U$  values could be obtained, they could belong to the one choking, critical condition and two choking regions.

In order to follow the above mentioned experimental methodology, some couples of  $P_{GE}$  and  $P_{CO}$  values were defined and reached, allowing the generator and condenser work at their higher capacity, in regard to the higher thermal fluid mass flow rates. Once the choked condition is reached for the primary fluid at the main nozzle, without secondary fluid mass flow rate, the initial experimental condition is reached. From this condition, the secondary fluid mass flow rate is continuously increased after its corresponding steady state is reached with superheated vapour at the ejector's inlets and outlet. For the obtained primary and secondary flow mass flow rates, their corresponding  $U$  value is obtained. In Fig. 3(a) there is a plot of  $U$  against  $P_{CO}$  for different starting  $P_{CO}$  and  $P_{GE}$  values. Each experimental series is represented by a colour and it is observed that  $U$  and  $P_{CO}$  have a growing tendency. This results from the increase in the secondary fluid mass flow rate while the heating and cooling in the generator and condenser is kept constant.

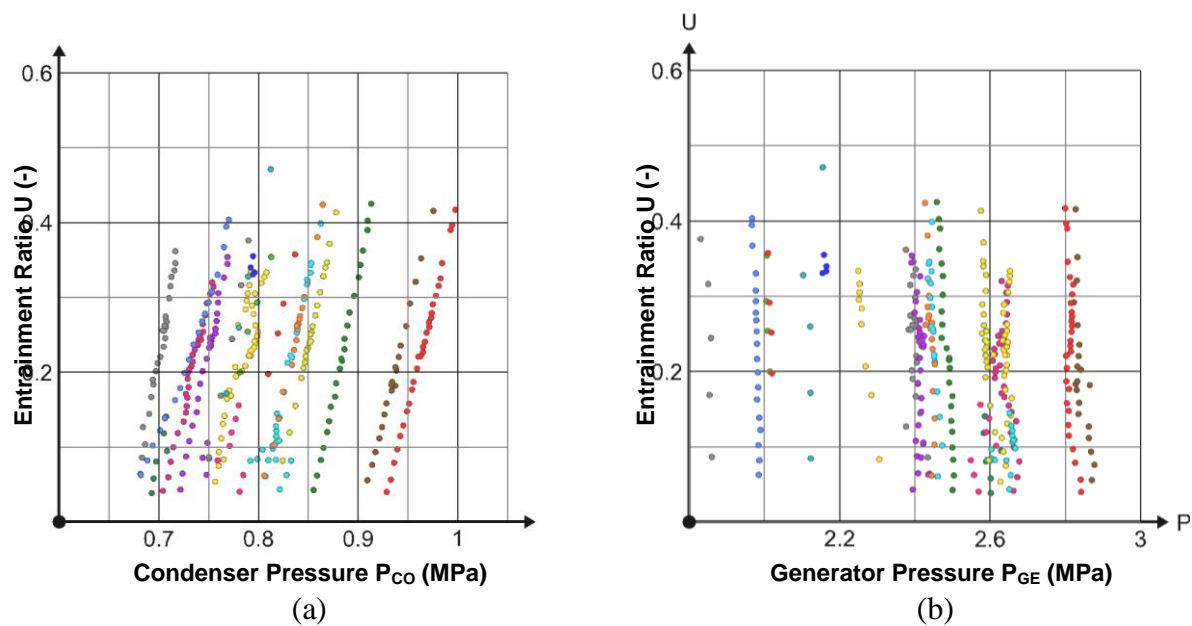


Fig. 3 Plots of the entrainment ratio against the condenser and generator pressure.

The behaviour for  $U$  against  $P_{GE}$  is shown in Fig. 3(b), where this pressure decreases as  $U$  increases as a result of keeping constant the generator and condenser heating and cooling capacity, while the secondary fluid mass flow rate increases and the condenser pressure also increases and the generator pressure decreases.

### Analysis of Results

With the above mentioned data, the dimensionless parameters corresponding to  $\Gamma$ ,  $\xi$  and  $r$  were obtained. In Fig. 4 is shown a 3D view of the dimensionless parameters  $U$ ,  $\Gamma$  and  $r$ , where the critical back pressure line is the limit for the one and two choking zone. Focussing on the  $U$ - $r$  plot shown in Fig. 5, it is observed that the highest  $U$  values fix an upper limit that according to  $Lu$  corresponds to the ejector critical back pressure condition, Hernandez *et al.* [3, 4]. Selecting these highest  $U$  and their corresponding  $\Gamma$  values, its correlation with  $r$  is found and shown in Fig. 6, where  $\Gamma$  goes through the coordinate axis origin. Finally, a plot of  $U$ - $r$  for  $\Gamma$  values is shown in Fig. 7, where the similarity to the  $U$ - $P_{CO}$  plot with  $P_{GE}$  and  $P_{EV}$  constant is a result of being equivalent both representations, as Hernandez *et al.* mentioned [3, 4]. As observed, the constant  $\Gamma$  values are higher for critical higher  $r$  values, and the zones of

one and two chokings correspond to the inclined and horizontal lines respectively which are delimited by the critical back pressure line.

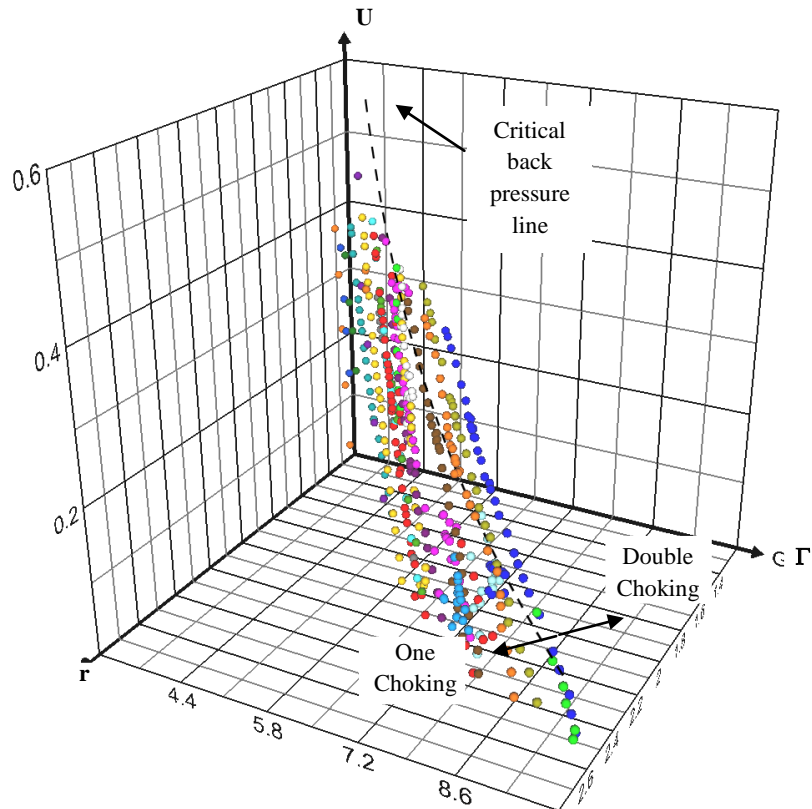


Fig. 4 3D plot of the entrainment ratio against the driving and compression ratios.

Once the critical back pressure line is determined, the performance map given by the  $U$ - $T_{CO}$  plot can be obtained for generator and evaporator isotherm lines, as Fig. 8 shows, in which the temperatures correspond to the saturation. With this plot and in accordance to the required evaporator temperature, for any  $U$  value its generator and condenser temperature are defined. At this point, it is important to mention that this plot corresponds to the ejector critical condition in dimensional parameters. Therefore, in this plot any generator, condenser and evaporator temperature triplet define  $U$  at the ejector critical condition, and any combination of this 4 parameters corresponds to high ejector and system efficiencies.

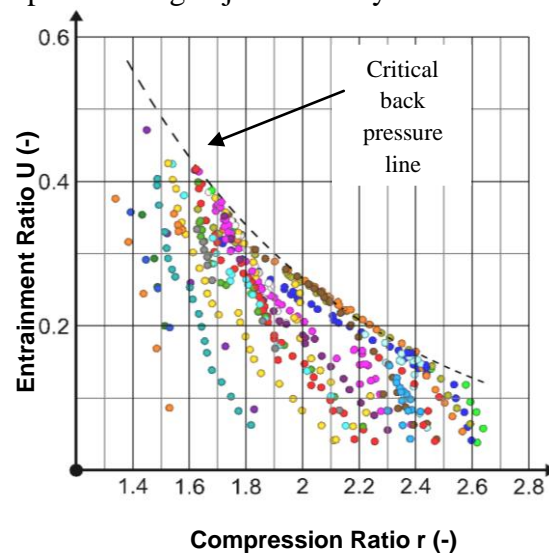


Fig. 5 Plot of the entrainment ratio against the compression ratio.

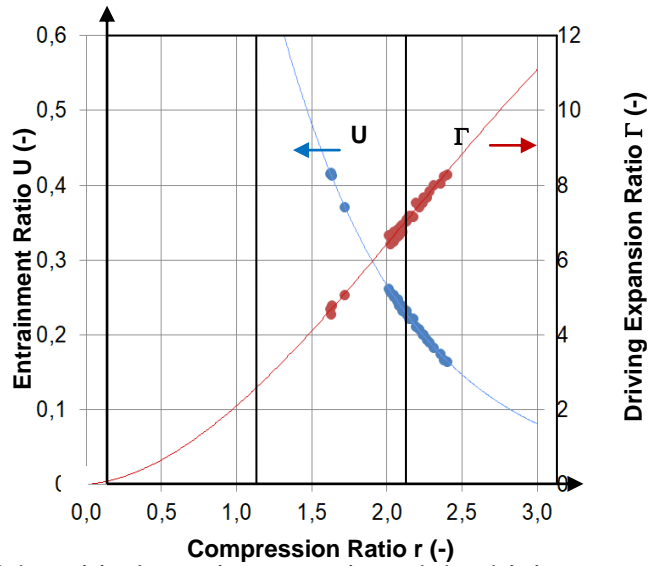


Fig. 6 Plot of the critical entrainment ratio and the driving expansion ratio against the compression ratio.

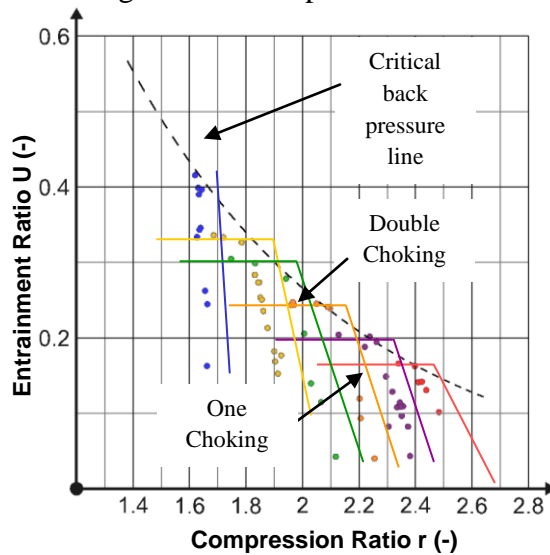


Fig. 7 Plot of the entrainment ratio against the compression ratio.

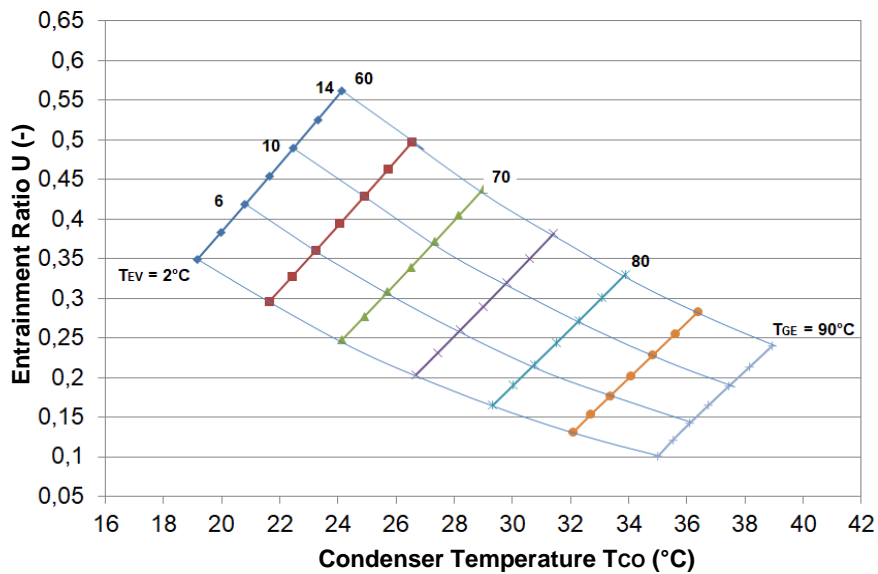


Fig. 8 Plot of the entrainment ratio against the condenser temperature for the ejector critical condition.



The validity of the  $U-T_{CO}$  plot was proved selecting two points and obtained in practice later. They corresponded to the prediction and their differences were very low. These experimental points were also represented in a  $U-r$  plot and fell along the ejector critical condition line.

## Conclusions

As a contribution to find in practice the optimal ejector cooling system operation, a methodology to obtain the performance map of an ejector cooling system was found and consists in:

- Obtain experimental data in which  $P_{GE}$  and  $P_{CO}$  were kept constant and the secondary mass flow rate was varied
- Transform these data in  $U$ ,  $\Gamma$ ,  $\xi$  and  $r$  parameters
- Obtain  $U-r$  plot
- Define critical  $U-\Gamma-r$  data
- Obtain the correlation of  $U$ ,  $\Gamma$  and  $r$  for the critical data
- Obtain  $U-T_{CO}$  critical plot

Such plot should direct the optimal ejector cooling system operation at design and off design conditions.

## Acknowledgements

We appreciate the financial support given by the PAPIIT of the Universidad Nacional Autónoma de México to the Project IT100914 “Operación de un sistema de enfriamiento por efecto-compresión usando R134a como fluido de trabajo”.

## References

- [1] Elbel Stefan and Hrnjak Predrag, *Ejector Refrigeration: An Overview of Historical and Present Developments with an Emphasis on Air-Conditioning Applications*, Proceedings of the International Refrigeration and Air Conditioning Conference at Purdue, Paper 884, 8 Pages, July 14-17, 2008.
- [2] Besagni Giorgio, Mereu Riccardo and Fabio Inzoli, *Ejector refrigeration: A comprehensive review*, Renewable and Sustainable Energy Reviews, 2016, 53 373–407.
- [3] Hernandez Jorge I., Best Roberto, Roman Raul y Galindo Jacobo; *An advantageous representation of the critical behaviour of an ejector cooling system by dimensionless parameters*, Proceedings of the Heat Powered Cycles 2016, Paper No. HPC040, Nottingham, England, June 26-29, 2016.
- [4] Hernandez J., Roman R., Best R. y Galindo J.; *Graphical representations of the behaviour of an ejector cooling system*, Proceedings of the International Conference on Polygeneration 2017, Paper No. ICP51, Cuernavaca, Morelos, Mexico, May 24-26, 2017.
- [5] Chen J., Jarall S., Havtun H., Palm B., *A review on versatile ejector: applications in refrigeration systems*, Renewable and Sustainable Energy Reviews, 49, 2015, 67-90..

# Thermodynamic and Thermo-economic Assessment of a PVT-ORC Combined Heating and Power System for Swimming Pools

Kai Wang<sup>1</sup>, Maria Herrando<sup>1,2</sup>, Antonio Marco Pantaleo<sup>1,3</sup> and Christos N. Markides<sup>1,\*</sup>

<sup>1</sup> Clean Energy Process (CEP) Laboratory, Department of Chemical Engineering, Imperial College London, South Kensington Campus, London SW7 2AZ, United Kingdom

<sup>2</sup> Fluid Mechanics Group, University of Zaragoza, Zaragoza 50007, Spain

<sup>3</sup> Department of Agro-Environmental Sciences, University of Bari, Via Amendola 165/A, 70125 Bari, Italy

\*Corresponding author: [c.markides@imperial.ac.uk](mailto:c.markides@imperial.ac.uk)

## Abstract

The thermodynamic and economic performance of a solar combined heat and power (S-CHP) system based on an array of hybrid photovoltaic-thermal (PVT) collectors and an organic Rankine cycle (ORC) engine is considered for the provision of heating and power to swimming pool facilities. Priority is given to meeting the thermal demand of the swimming pool, in order to ensure a comfortable condition for swimmers in colder weather conditions, while excess thermal output from the collectors at higher temperatures is converted to electricity by the ORC engine in warmer weather conditions. The thermodynamic performance of this system and its dynamic characteristics are analysed on the basis of a transient thermodynamic model. Various heat losses and gains are considered in accordance to environmental and user-related factors for both indoor and outdoor swimming pools. A case study is then performed for the swimming pool at the University Sport Centre (USC) of Bari, Italy. The results show that employing a zeotropic mixture of R245fa/R227ea (30/70%) as the ORC working fluid allows such an ORC system to generate ~50% more power than when using pure R236ea due to the better temperature match of the cycle to the low-temperature hot-water heat source from the output of the PVT collectors. Apart from generating electricity, the ORC engine also alleviates PVT collector overheating, and reduces the required size of the hot-water storage tank. With an installation of 2000 m<sup>2</sup> of PVT collectors, energetic analyses indicate that the proposed S-CHP system can cover 84-96% of the thermal demand of the swimming pool during the warm summer months and 61% of its annually integrated total thermal demand. In addition, the system produces a combined (from the collectors and ORC engine) of 328 MWh of electricity per year, corresponding to 36% of the total electricity demand of the USC, with ~4% coming from the ORC engine. The analysis suggests a minimum payback time of 12.7 years with an optimized tank volume of 125 m<sup>3</sup>.

**Keywords:** organic Rankine cycle, ORC, PV-thermal, PVT, solar energy, swimming pool.

## Introduction

Hybrid PV-thermal (PVT) collectors have attracted interest recently due to their potentially improved electrical efficiency over single PV panels if operated suitably, their ability to provide an additional thermal energy output and the flexibility they allow for further integration with other technologies, including thermal energy storage options. Many different hybrid PVT-based systems have been investigated for various purposes, such as PVT-water systems for domestic heating (hot water, space heating) and power provision [1-3]; here, we extend the capabilities of these systems by including a low-temperature heat-driven thermodynamic cycle [4,5].

Considering the potential of hybrid PVT systems for combined heating and power (CHP), the aim of this work is to assess the energetic and economic feasibility of hybrid PVT technology when applied to swimming pool applications. The majority of previous studies found on solar swimming pool heating focus on solar-thermal collector heating systems [6,7] or solar-assisted heat-pump heating systems with conventional solar-thermal collectors [8,9]; far less effort has been devoted to the employment of hybrid PVT collectors in solar-CHP (S-CHP) systems for

meeting the heating and power demands of swimming pools. To the authors' knowledge, only one study has considered a heating system based on PVT technology for a swimming pool, located in Naples, Italy [10]. Results from transient simulations and sensitivity analyses performed with TRNSYS software showed that the system considered in this study was not profitable without public funding policies and became viable only after introducing thermal feed-in tariffs due to the high collector costs. However, solar irradiation and thermohygro-metric conditions are highly geographically dependent, so the energetic/economic performance of such PVT-based S-CHP systems will differ significantly at different locations, and depends strongly on system configuration and operational strategies, which merits further investigation.

This paper presents a solar-driven PVT-ORC S-CHP system for swimming pool facilities. An ORC engine converts the excess thermal output of the PVT collector array into (secondary) electrical power when the heating demand for the swimming pool is low, which helps to improve the overall system efficiency and prevent overheating of the collectors. The potential of the system for a swimming pool application at the University Sport Centre (USC) of Bari, Italy, is assessed in terms of both thermodynamic and thermoeconomic performance metrics.

### System configuration and modelling methodology

Swimming pool facilities have a heavy thermal demand, and gas boilers are typically used for heating. Figure 1 shows a simplified schematic of the proposed PVT-ORC S-CHP system for the swimming pool application. A hot water storage tank stores thermal energy produced from the PVT-water collectors. The system is designed to prioritise meeting the heat demand of the swimming pool, while the excess thermal output from the collectors is recovered and converted by the ORC engine for generating additional electricity. Due to fluctuations of solar radiation, an auxiliary heating, i.e. gas boiler, is always necessary as the backup heating source.

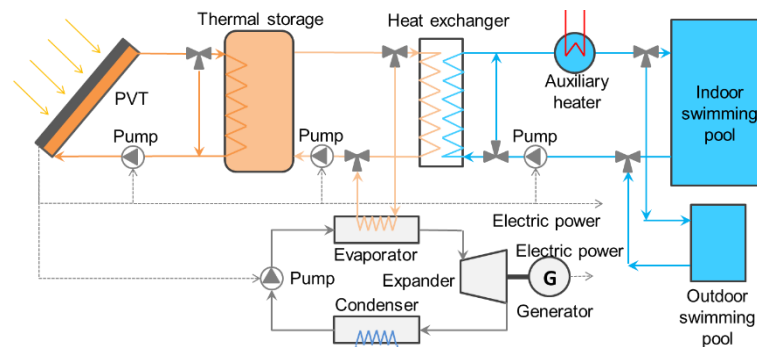


Figure 1. Simplified schematic of PVT-ORC S-CHP system for swimming pool application.

Both indoor and outdoor swimming pools are considered in the present study. A swimming pool model is built by considering various energy transfer mechanisms. Thermal demand ( $\dot{Q}_{sp}$ ) of the swimming pools is calculated from the thermal balance between heat gains and losses, including solar heat absorption ( $\dot{Q}_{sol}$ ), heat generation from swimmers ( $\dot{Q}_{occ}$ ), convection heat loss to air ( $\dot{Q}_{conv}$ ), conduction heat loss to soil ( $\dot{Q}_{cond}$ ), water evaporation heat loss ( $\dot{Q}_{evap}$ ), radiation loss to surroundings ( $\dot{Q}_{rad}$ ), and heat loss from refilling water ( $\dot{Q}_{fill}$ ). The equations for the above energy transfer mechanisms are summarized below:

$$\dot{Q}_{sol} = \alpha G A_{sp} \quad (1)$$

$$\dot{Q}_{occ} = N_{occ} \dot{q}_{occ} \quad (2)$$

$$\dot{Q}_{conv} = h A_{sp} (T_{sp} - T_a) \quad (3)$$

$$\dot{Q}_{cond} = q_{ss}^* k_{soil} h A_{sp} (T_{sp} - T_{soil}) / L_c \quad (4)$$

$$\dot{Q}_{evap} = \dot{m}_{evap} L_w A_{sp} \quad (5)$$

$$\dot{Q}_{\text{rad}} = \varepsilon A_{\text{sp}} \sigma (T_{\text{sp}}^4 - T_{\text{sur}}^4) \quad (6)$$

$$\dot{Q}_{\text{fill}} = \dot{m}_{\text{fill}} c_p (T_{\text{sp}} - T_w) \quad (7)$$

$$\dot{Q}_{\text{sp}} = \dot{Q}_{\text{conv}} + \dot{Q}_{\text{cond}} + \dot{Q}_{\text{evap}} + \dot{Q}_{\text{rad}} + \dot{Q}_{\text{fill}} - \dot{Q}_{\text{occ}} - \dot{Q}_{\text{sol}} \quad (8)$$

Solar radiation ( $\dot{Q}_{\text{sol}}$ ) is only necessary in the outdoor swimming pool, and the absorption coefficient  $\alpha$  is chosen as 0.85 [10]. For the heat generation ( $\dot{Q}_{\text{occ}}$ ) from swimmers, a constant rate ( $\dot{q}_{\text{occ}}$ ) of 200 W per user is assumed. Heat transfer coefficient ( $h$ ) for the convection loss ( $\dot{Q}_{\text{conv}}$ ) of the indoor swimming pool is calculated from the natural convection equation across a horizontal plate [11], while forced convection due to wind effect is considered for the outdoor pool [7]. The thermal conduction to ground ( $\dot{Q}_{\text{cond}}$ ) is evaluated by taking into account the shape effect of swimming pools via a dimensionless conduction rate ( $q_{\text{ss}}^*$ ) and a characteristic length ( $L_c$ ) [11]. A constant soil temperature ( $T_{\text{soil}}$ ) of 12 °C is assumed here. Water evaporation causes the main heat loss in swimming pools. The evaporation rate ( $\dot{m}_{\text{evap}}$ ) is mainly affected by the vapour partial pressure, number of users and wind speed. An empirical model presented by Shah [12,13], which was validated against experimental data, is adopted. Radiation occurs due to the temperature differences between the swimming pools ( $T_{\text{sp}}$ ) and its surroundings ( $T_{\text{sur}}$ ). The surrounding temperature is the sky temperature for outdoor swimming pool, while it is a weighted value between room and outdoor temperatures for indoor swimming pool. In both swimming pools, an emissivity ( $\varepsilon$ ) of 0.9 is assumed [10]. The evaporation and presence of users cause a reduction of the pool water volume. A refilling water flow is necessary to maintain the water level and ensure the water quality. A constant refilling water flow rate ( $\dot{m}_{\text{fill}}$ ), which enables a daily refreshment of 5% of the total pool volume, is assumed in the model.

When the thermal demand of the swimming pool is low and the water temperature exceeds the predefined deadband temperature, excess heat is delivered to the ORC engine to generate electricity. The ORC engine is sized according to the difference between the thermal energy gained at the PVT-water collectors and the swimming pool demand. A subcritical non-regenerative ORC is considered. The temperature difference between the hot water inlet and the ORC working fluid outlet (expander inlet) is taken as 5 °C [14], and a fixed pinch temperature difference of 5 °C is assumed. The evaporation and condensation pressures are then determined to ensure that the pinch temperature condition is met under the constraints of the deadband operating temperature (70 °C) and mains water temperature. The isentropic efficiencies of the pump and the expander are both set to 0.8. The electrical conversion efficiencies of the pump and the expander are assumed as 0.9. Selection of an appropriate working fluid is important for the cycle efficiency. A range of pure working fluids, including R123, R227ea, R236ea, R245ca, R245fa and butane, are screened and R236ea is finally chosen due to its superior performance. As shown in Figure 2, the cycle performance with pure working fluid is limited due to the small temperature difference available from the heat source and sink. Zeotropic mixtures have a temperature slip phenomenon in evaporation and condensation processes, which enables a better matching with the temperature profiles of the heat source and sink, and helps to improve the output performance. Binary zeotropic mixtures including R245fa/R227ea, R245fa/RC318, R245fa/butane, R245fa/R152a and R245fa/R123, which have been studied for low-temperature ORCs [15], are considered for the proposed system. The R245fa/R227ea pair with a mass fraction of 0.3/0.7 is finally selected based on the comparisons of the cycle performance.

The swimming pool and ORC engine models are both implemented in MATLAB, and integrated with the component models of the PVT collector, water tank and other auxiliary facilities to form a dynamic system model in TRNSYS software environment. The PVT collector and water tank are modelled using Type 560 and Type 534 in TRNSYS. If water temperature at the top of the water tank is higher than 45 °C and there is a thermal demand of the swimming pool, the heat transfer fluid is pumped out of the tank to the swimming pool heat exchanger. If the water

temperature exceeds 70 °C and the thermal output of PVT collectors exceeds the thermal demand of the swimming pool (i.e. the auxiliary heating is not required), the ORC engine is utilized. In this way, excess heat at relatively high temperatures is recovered, thus reducing the risk of overheating the collectors and simultaneously generating a useful (secondary) electrical output.

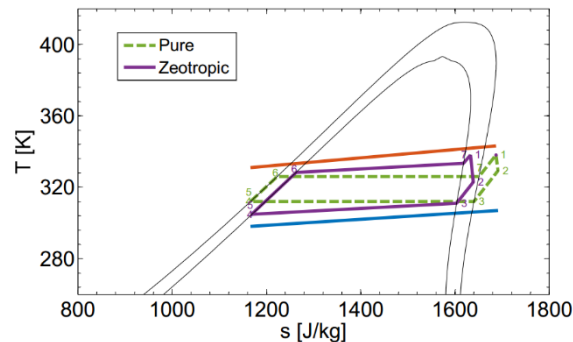


Figure 2.  $T$ - $s$  diagrams of ORC cycle with pure working fluid (R236ea) and zeotropic mixture as working fluid (0.3R245fa/0.7R227ea).

A commercial flat-plate PVT collector [16] with a nominal electric power of 240 W and PV module efficiency of 14.1% is used for the simulation. The temperature coefficient of PV module is assumed to be  $-0.45$  %/K. The collector has the following thermal performance,

$$\eta_{th} = 0.69 - 2.59T_r - 0.012GT_r^2 \quad (9)$$

where  $\eta_{th}$  is the thermal efficiency,  $T_r$  the reduced temperature and  $G$  the incident irradiance.

The investment costs ( $C_0$ ) of the system are mainly associated with the PVT collectors, storage tank, ORC engine, pumps, fluids and installation costs. The storage tank cost is estimated using a correlation based on market prices of existing tanks across a range of storage volumes [17] and the other costs are estimated from the cost models described in Refs. [18,19]. The costs for the auxiliary heater and the water pump at swimming pool side are not considered as they are already installed in an existing swimming pool system. Thermoeconomic analyses are performed in terms of payback time ( $PBT$ ), which is defined as the period of time required to recover the investment of the PVT-ORC S-CHP system. The payback time is calculated by,

$$PBT = \frac{\ln\left[\frac{C_0(t_F-d)}{FS} + 1\right]}{\ln\left(\frac{1+i_F}{1+d}\right)} \quad (10)$$

where  $d$  is the discount rate (taken as 5% [20]), and  $i_F$  refers to the inflation rate considered for the annual fuel savings (taken as 1.23%) [21]. To estimate the annual fuel savings,  $FS$ , the total utility (electricity and natural gas) cost not incurred due to the electricity and thermal energy demand covered by the system is estimated, as follows,

$$FS = E_{cov} \cdot c_e + \frac{Q}{\eta_b} c_{ng} - C_{O\&M} \quad (11)$$

where  $E_{cov}$  and  $Q_{cov}$  are the electrical and thermal demands covered by the system,  $c_e$  is the electricity (0.145 €/kWh) and  $c_{ng}$  the natural gas (0.057 €/kWh) price, and  $\eta_b$  is the efficiency of the boiler. The utility price values correspond to the current tariffs for the USC of Bari.

## Results and discussion

A PVT-ORC combined heating and power system case study is performed for the swimming pool application at the USC of Bari, Italy. The USC has an Olympic indoor swimming pool (50 m) and an outdoor swimming pool (25 m). The outdoor pool is only operated from July to September, and the indoor one is operated in the remaining months during which the thermal demand is met by a natural gas boiler with an efficiency of 85%. The swimming pool has about 95000 users per year. The hourly weather and user data of the university swimming pools over

a whole year are given as the inputs to the model. Based on preliminary estimations of the solar radiation in Bari and the thermal demand for the swimming pools, a total installation area of 2000 m<sup>2</sup> is considered for the PVT collectors in the modelling, which covers about half of the roof area of the nearby buildings at the USC. A large water tank is needed due to the large continuous thermal demand, thus a volume from 50 m<sup>3</sup> to 175 m<sup>3</sup> is considered [10].

The comparisons of the energetic and economic performance of the PVT-ORC S-CHP system with the pure and zeotropic mixture working fluids, when the water tank volume is 100 m<sup>3</sup>, are shown in Table 1. The electricity generated by the ORC engine increases by 50.6%, from 7.9 MWh to 11.9 MWh, when the R245fa/R227ea mixture is used instead of R236ea as the ORC working fluid. The efficiency of the ORC engine increases from 2.79% to 4.21%. This generated electricity corresponds to 3.60% and 2.42% of the total electricity output, respectively. As shown in Table 1, the payback time is smaller when the zeotropic working fluid is used, thus the results analysed below are all based on this fluid.

Table 1. Energetic and economic performance with pure (R236ea) and zeotropic mixture working fluid (0.3R245fa/0.7R227ea).

	R236ea	0.3R245fa/0.7R227ea
$E_{orc}$ [MWh/yr]	7.9	11.9
$E_{pvt}$ [MWh/yr]	318.8	318.8
$E_{orc} / (E_{pvt} + E_{orc})$	2.42%	3.60%
$\eta_{orc}$	2.79%	4.21%
$PBT$ [yr]	13.1	12.8

The water tank is sized based on the energetic and economic performance. As shown in Figure 3, the thermal demand covered by the S-CHP system increases and the auxiliary thermal energy decreases, although progressively less so, at larger tank sizes. The generated electricity is almost independent of the tank volume. The  $PBT$  reaches a minimum at a tank volume of 125 m<sup>3</sup>, with which a payback time of 12.7 years is estimated. It should be noted that incentives available for renewable energy generation have not been included in this analysis, but are expected to reduce significantly the system's payback time. Since the payback times with the tank volumes of 100m<sup>3</sup> and 125 m<sup>3</sup> are almost the same, the size of the water tank is selected as 100 m<sup>3</sup>.

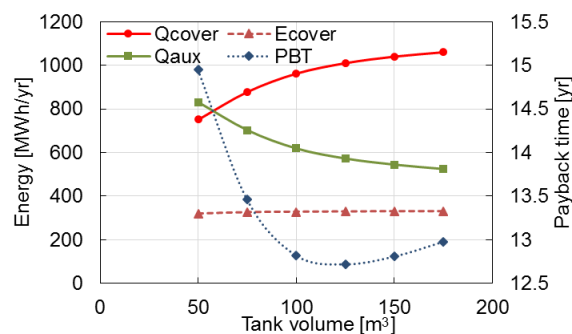


Figure 3. Effect of water tank volume on energetic and economic performance.

Hourly transient simulations are performed over a whole year. The evolutions of the thermal powers of different heat transfer mechanisms for the indoor and outdoor swimming pools are shown in Figure 4. Due to the differences in the surrounded environmental conditions, including wind speed, solar radiation and air temperature, the thermal demand of the indoor swimming pool is much more stable than that of the outdoor pool. The thermal demand of the outdoor pool drops to nearly zero when the solar irradiation is high. In any case, the evaporation loss is always the main contribution of the thermal demand, and it is highly dependent on the number of users.

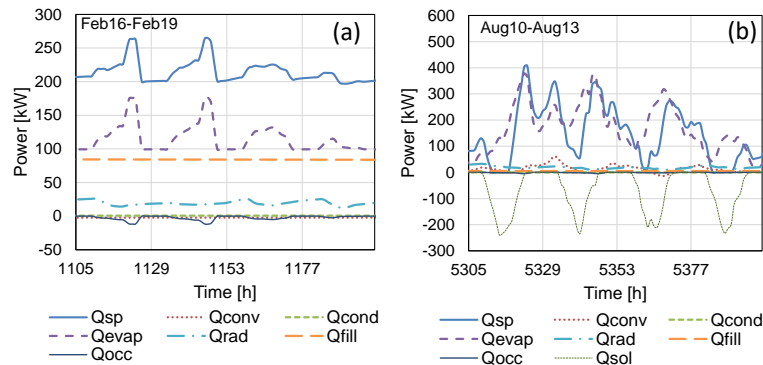


Figure 4. Transient thermal power evolutions for swimming pool: (a) indoor swimming pool, and (b) outdoor swimming pool.

The temperature variations and the pump control signals are shown in Figure 5. When the outlet water temperature of the PVT collectors is higher than the temperature in the water tank, the fluid circulating pump for the PVT collectors starts up to heat the water in the tank. The pump for the swimming pool operates when there is a thermal demand and the water temperature at the top of the tank is higher than the deadband temperature, i.e. 45 °C. Once the top tank water temperature drops below 45 °C, the swimming pool pump stops and the auxiliary heater works to meet the thermal demand. The pump for the ORC engine starts to deliver hot water to the evaporator to generate electricity when the water temperature at the top of the tank exceeds 70 °C. As shown in Figure 5(a), the ORC engine does not work at cold weathers when the water temperature is low. It works occasionally at summer time when water temperature is sufficiently high, as shown in Figure 5(b).

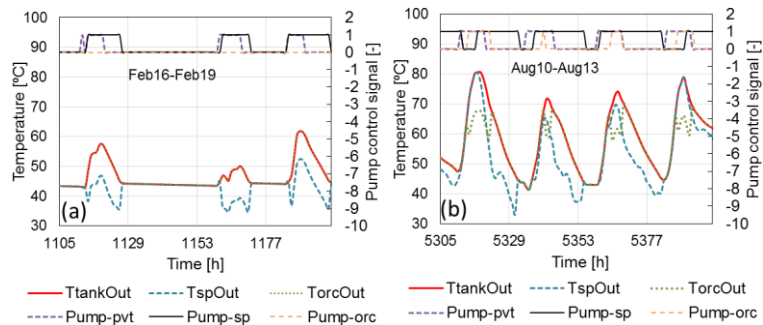


Figure 5. Temperatures and pump on/off control signals: (a) indoor, and (b) outdoor swimming pools.

Figure 6 shows the monthly thermal energy and electricity of the PVT-ORC S-CHP system. The PVT collectors cover most of the thermal demand at warm seasons, while the rest is met by the auxiliary gas boiler. The coverage percentage from the solar heating is at the range of 84%-96% from May to August. The relatively high-temperature thermal energy at summer times is partially delivered to the ORC engine for electricity generation, which reduces the coverage percentage. As shown in Figure 6(b), the PVT collectors produce the majority of the electricity due to the instinct low-efficiency of the ORC engine operated at hot water temperatures. A further comparison study on a PVT-only system without the ORC engine shows that the water temperature easily exceeds 100 °C in summertime, and a significantly larger tank (more than 3 times the current 100 m<sup>3</sup>) is required to prevent the overheating. Therefore, although the presence of the ORC engine reduces the coverage percentage of the thermal demand at summer times, it also acts as an effective measure to prevent PVT collectors from overheating, with the extra benefit of generating electricity. Besides, a considerably smaller tank can be used, which is more feasible for a practical application due to space limitations and commercial products available on the market. With the proposed PVT-ORC S-CHP system, the solar heat covers 61% of the total thermal demand for the swimming pool within the whole year, with an electricity supply of 328 MWh, which covers 36% of the total electricity demand of the entire USC.

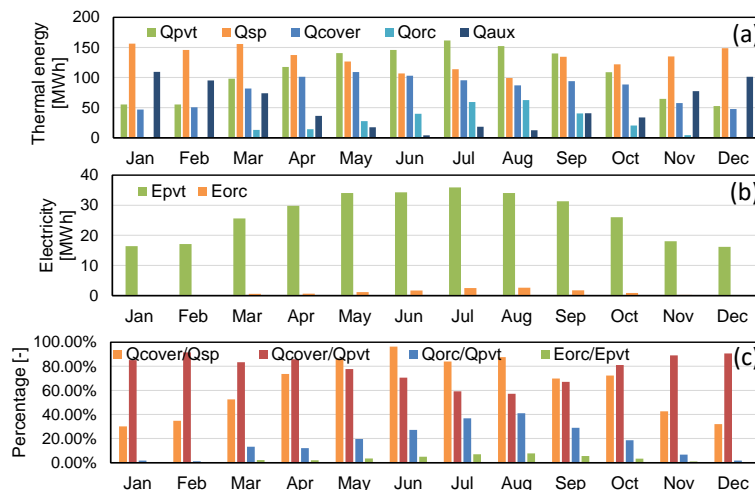


Figure 6. (a) Monthly thermal energy production and consumption, (b) monthly electricity production, and (c) their ratios.

## Conclusions

A S-CHP system for a swimming pool facility based on the integration of a hybrid PVT collector array and an ORC engine has been studied. The thermal energy (i.e. hot water) output of the PVT-water collectors was used primarily to meet the thermal demand of the swimming pool, while excess heat at relatively high temperatures ( $> 70\text{ }^{\circ}\text{C}$ ) was recovered by the ORC engine to generate secondary electricity in addition to the electrical energy output of the PVT collectors. A transient model was defined in the TRNSYS modelling environment. The thermal demands of both indoor and outdoor swimming pools were simulated by considering various heat transfer mechanisms in accordance to relevant environmental and user-related factors. In order to maximize the performance of the ORC engine in this low-temperature application, pure R236ea and the zeotropic mixture R245fa/R227ea (30/70%) were selected for further consideration, following a screening exercise of a range of working fluids. A case study was then performed for the swimming pool at the University Sports Centre (USC) in Bari, Italy. The results show that the ORC system with the zeotropic mixture outperforms the one with the pure fluid in terms of both energetic (by 50%) and economic indicators. With a total installation area of  $2000\text{ m}^2$ , the system covers 61% of the annual thermal demands of the swimming pools, and generates a total of 328 MWh of electricity. The coverage percentage ranges from 84% to 96% in summer months. The electricity generated by the ORC engine corresponds to  $\sim 4\%$  of the total electricity output of the system. An optimized water tank volume of  $125\text{ m}^3$  showed that a minimum payback time of 12.7 years can be expected for the proposed PVT-ORC S-CHP system in this case.

## Acknowledgements

This work was supported by the UK Engineering and Physical Sciences Research Council (EPSRC) [grant numbers EP/M025012/1 and EP/P004709/1]. Data supporting this publication can be obtained on request from [cep-lab@imperial.ac.uk](mailto:cep-lab@imperial.ac.uk).

## References

- [1] Ramos, A., Chatzopoulou, M. A., Guarracino, I., Freeman, J., Markides, C.N., "Hybrid photovoltaic-thermal solar systems for combined heating, cooling and power provision in the urban environment", *Energy Conversion and Management*, 2017;150:838-850. [doi:10.1016/j.enconman.2017.03.024](https://doi.org/10.1016/j.enconman.2017.03.024)
- [2] Herrando, M., Markides, C. N., Hellgardt, K., "A UK-based assessment of hybrid PV and solar-thermal systems for domestic heating and power: System performance", *Applied Energy*, 2014;122:288-309. [doi:10.1016/j.apenergy.2014.01.061](https://doi.org/10.1016/j.apenergy.2014.01.061)



- [3] Guarracino, I., Mellor, A., Ekins-Daukes, N. J., Markides, C. N., “Dynamic coupled thermal-and-electrical modelling of sheet-and-tube hybrid photovoltaic / thermal (PVT) collectors”, *Applied Thermal Engineering*, 2016;101:778-795. doi:10.1016/j.applthermaleng.2016.02.056
- [4] Freeman, J., Hellgardt, K., Markides, C. N., “Working fluid selection and electrical performance optimisation of a domestic solar-ORC combined heat and power system for year-round operation in the UK”, *Applied Energy*, 2017;186(3):291-303. doi:10.1016/j.apenergy.2016.04.041
- [5] Freeman, J., Guarracino, I., Kalogirou, S. A., Markides, C. N., “A small-scale solar organic Rankine cycle combined heat and power system with integrated thermal energy storage”, *Applied Thermal Engineering*, 2017;127:1543-1554. doi:10.1016/j.applthermaleng.2017.07.163
- [6] Singh, M., Tiwari, G. N., Yadav, Y. P., “Solar energy utilization for heating of indoor swimming pool”, *Energy Conversion and Management*, 1989;29(4):239-244. doi:10.1016/0196-8904(89)90027-7
- [7] Ruiz, E., Martínez, P. J., “Analysis of an open-air swimming pool solar heating system by using an experimentally validated TRNSYS model”, *Solar Energy*, 2010;84(1):116-123. doi:10.1016/j.solener.2009.10.015
- [8] Tagliafico, L. A., Scarpa, F., Tagliafico, G., Valsuani, F., “An approach to energy saving assessment of solar assisted heat pumps for swimming pool water heating”, *Energy and Buildings*, 2012;55:833-840. doi:10.1016/j.enbuild.2012.10.009
- [9] Chow, T. T., Bai, Y., Fong, K. F., Lin Z., “Analysis of a solar assisted heat pump system for indoor swimming pool water and space heating”, *Applied Energy*, 2012;100:309-317. doi:10.1016/j.apenergy.2012.05.058
- [10] Buonomano, A., De Luca, G., Figaj, R. D., Vanoli, L., “Dynamic simulation and thermo-economic analysis of a photovoltaic/thermal collector heating system for an indoor–outdoor swimming pool”, *Energy Conversion and Management*, 2015;99:176-192. doi:10.1016/j.enconman.2015.04.022
- [11] Incropera, F. P., Dewitt, D. P., Bergman T. L., Lavine, A. S., *Fundamentals of Heat and Mass Transfer*, 6<sup>th</sup> Ed., John Wiley and Sons, 2006.
- [12] Shah, M. M., “Improved method for calculating evaporation from indoor water pools”, *Energy and Buildings*, 2012;49:306-309. doi:10.1016/j.enbuild.2012.02.026
- [13] Shah, M. M., “Methods for calculation of evaporation from swimming pools and other water surfaces”, *ASHRAE Transactions*, 2014.
- [14] Freeman, J., Hellgardt, K., Markides, C. N., “An assessment of solar-powered organic Rankine cycle systems for combined heating and power in UK domestic applications”, *Applied Energy*, 2015;138:605-620. doi:10.1016/j.apenergy.2014.10.035
- [15] Wu, Y., Zhu, Y., Yu, L., “Thermal and economic performance analysis of zeotropic mixtures for organic Rankine cycles”, *Applied Thermal Engineering*, 2016;96:57-63. doi:10.1016/j.applthermaleng.2015.11.083
- [16] EndeF Engineering. Technical datasheet ECOMESH panel.
- [17] Geiser Inox, Lapesa 2017. <[www.lapesa.es/en/domestic-hot-water/geiser-inox.html](http://www.lapesa.es/en/domestic-hot-water/geiser-inox.html)>.
- [18] Herrando, M., Guarracino, I., del Amo, A., Zabalza, I., Markides, C. N., “Energy characterization and optimization of New Heat Recovery Configurations in Hybrid PVT Systems”, In *Proceedings of ISES Conference, 2016*. doi:10.18086/eurosun.2016.08.22
- [19] Ramos, A., Chatzopoulou, M. A., Freeman, J., Markides, C. N., “Optimisation of a high-efficiency solar-driven organic Rankine cycle for applications in the built environment”, In *Proceedings of ECOS 2017, 2017*.
- [20] Kim, Y., Thu, K., Kaur, H., Singh, C., Choon, K., “Thermal analysis and performance optimization of a solar hot water plant with economic evaluation”, *Solar Energy*, 2012;86(5):1378-1395. doi:10.1016/j.solener.2012.01.030
- [21] Historic inflation – Overview of CPI inflation year, Worldwide inflation data. <[www.inflation.eu/inflation-rates/historic-cpi-inflation.aspx](http://www.inflation.eu/inflation-rates/historic-cpi-inflation.aspx)>

# Application of Liquid-Air and Pumped-Thermal Electricity Storage Systems in Low-Carbon Electricity Systems

S. Georgiou<sup>1</sup>, M. Aunedi<sup>2</sup>, G. Strbac<sup>2</sup> and C. N. Markides<sup>1,\*</sup>

<sup>1</sup>Clean Energy Processes (CEP) Laboratory, Department of Chemical Engineering, Imperial College London, London, UK

<sup>2</sup>Department of Electrical and Electronic Engineering, Imperial College London, London, UK

\*Corresponding author: c.markides@imperial.ac.uk

## Abstract

In this study, we consider two medium- to large-scale electricity storage systems currently under development, namely ‘Liquid-Air Energy Storage’ (LAES) and ‘Pumped-Thermal Electricity Storage’ (PTES). Consistent thermodynamic models and costing methodologies for the two systems are presented, with the objective of integrating the characteristics of these technologies into a whole-electricity system assessment model, and assessing their system-level value in different scenarios for power system decarbonisation. It is found that the value of storage varies greatly depending on the cumulative installed capacity of storage in the electrical system, with the storage technologies providing greater marginal benefits at low penetrations. Two carbon target scenarios showed similar results, with a limited effect of the carbon target on the system value of storage (although it is noted that this may change for even more ambitious carbon targets). On the other hand, the location and installed capacity of storage plants is found to have a significant impact on the system value and acceptable cost of these technologies. The whole-system value of PTES was found to be slightly higher than that of LAES, driven by a higher storage duration and efficiency, however, due to the higher power capital cost of PTES, this becomes less attractive for implementation at lower volumes than LAES.

**Keywords:** liquid-air energy storage, pumped-thermal electricity storage, power system economics, whole-system assessment.

## Introduction

The competitiveness of any energy storage technology is strongly affected by its technical and economic characteristics. A storage system that is both efficient and economically competitive has the potential to support a flexible and efficient low-carbon electricity system. It can support cost-efficient integration of intermittent renewable generation and take advantage of differences between peak and off-peak electricity prices as well as provide local and national services to network and system operators. The application potential of any technology in a power system will depend on its characteristics in combination with the requirements of the whole system.

Electricity storage systems can provide flexibility required for cost-effective integration of variable renewables into future power systems [1]. Energy storage technologies have different characteristics, such as power capacity, energy capacity, charge and discharge durations, and can therefore have different purposes in the electricity grid. Although it is important to determine and analyse both their technical and economic properties, it is also vital to assess their realistic value in an electricity system. This assessment can be challenging for newly proposed technologies with limited data, but on the other hand it can provide a first indication of the attractiveness of such technologies at a system level. This paper focuses on the potential deployment of two newly proposed technologies, namely Liquid-Air Energy Storage (LAES) and Pumped Thermal Electricity Storage (PTES), in low-carbon electricity systems.

## Methodology

A whole-system assessment approach is adopted here in order to determine the whole-system value of contribution of energy storage in low-carbon electricity systems. A full description of the modelling approach is included in Ref. [2]. The whole-system model, WeSIM, determines

optimal decisions for investing into generation, network and/or storage capacity, in order to satisfy the real-time supply-demand balance in a least-cost sense, while at the same time ensuring security of supply. An application of WeSIM was presented in Ref. [3] that quantified the value of energy storage in supporting cost-efficient decarbonisation of the electricity system i.e. delivering the carbon reductions at lower total cost. A similar approach was used in Ref. [4] to assess the role and value of pumped hydro electricity storage in the European power system.

### Electricity storage technologies

LAES is a technology being developed by Highview Power Storage [5]. The LAES system involves four main processes: a) air liquefaction, b) liquid air storage, c) waste cold storage, and d) power generation; see simplified schematic in Figure a. During charging, the system uses inexpensive electricity to liquefy air and gets charged by storing energy in the form of liquid air, and during peak demand periods, when it becomes economically attractive to discharge, the system uses liquid air in the power generation unit where this is pressurised, evaporated, superheated to the temperature of the utilised waste-heat stream (if available) and expanded through a turbine to generate electricity [6]. Although optional, an additional process which was found to be a contributing factor for the enhancement of the system's performance is the storage of waste cold from the power generation unit during the discharging periods and the utilisation of that cold in the air liquefaction process during the charging periods. More details on the workings of a LAES system are given in Refs. [6-10].

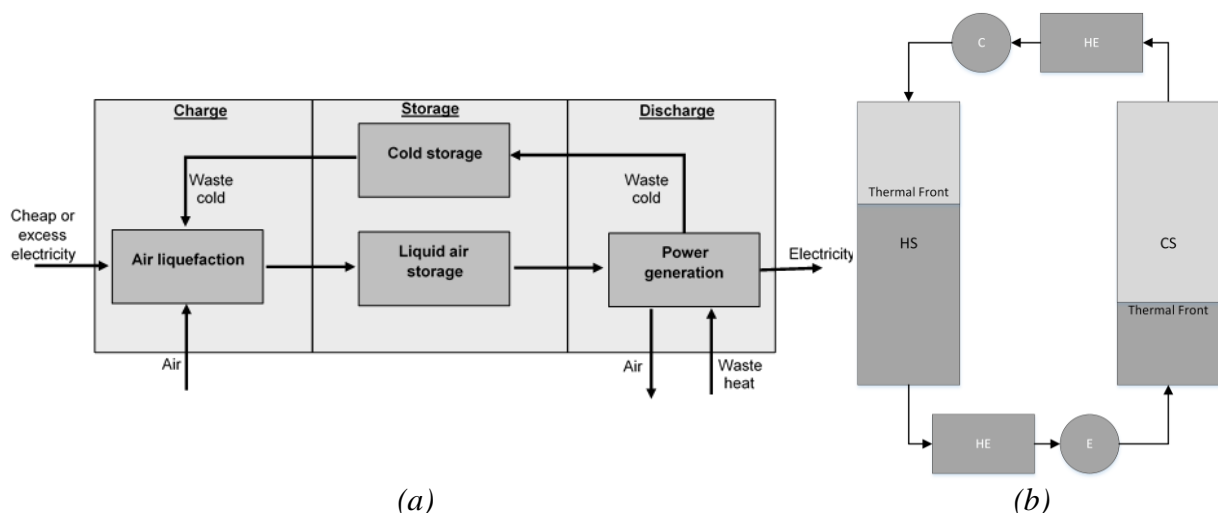


Figure 1. Schematics of: (a) LAES system (adapted from Ref. [9]) and (b) PTES system (adapted from Ref. [11])

PTES is also a newly proposed electricity storage system, but at a lower Technology Readiness Level (TRL) than LAES due to the lack of an operational pilot plant (although one is currently under construction). PTES stores energy in the form of sensible heat in insulated storage tanks containing a storage medium [11]. It operates based on a reverse/forward Joule-Brayton cycle for charging/discharging, respectively [11,12]. The system consists of two thermal reservoirs at different temperatures and pressures when charged, two reversible expansion/compression devices [13,14] and two heat exchangers (see Figure 1b). In the charging mode heat is extracted from the cold reservoir and pumped into the hot reservoir, thus resulting in increased temperature difference. During discharging, the flow of the working fluid is reversed to take advantage of the temperature difference, and a heat engine is used to generate electricity.

The thermodynamic (first law) performance of energy storage systems is typically expressed in terms of a roundtrip efficiency ( $\eta$ ), defined as the net work output ( $W_{out}$ ) during discharge divided by the net work input ( $W_{in}$ ) during charge (Eq. 1):

$$\eta = \frac{W_{\text{out}}}{W_{\text{in}}} \quad (1)$$

Here,  $W_{\text{out}}$  and  $W_{\text{in}}$  for the two systems can be estimated using the charge and discharge thermodynamic cycles associated with each system. For LAES,  $W_{\text{out}}$  is the power generated during the discharge cycle, whereas  $W_{\text{in}}$  is the work input into the liquefaction unit during the charge cycle (see Figure 1a). Several operational and loss parameters can have an impact on the estimation of  $\eta$  of LAES, for example the amount of waste cold and heat utilization as well as the components' efficiencies. For PTES,  $W_{\text{out}}$  and  $W_{\text{in}}$  are estimated by considering forward and reverse Joule-Brayton cycles for discharging and charging, respectively. Similar to LAES, the performance is also significantly affected by a number of operational and component performance variables. The main losses to be considered in such a system include pressure losses, compression and expansion losses, and thermal losses in reservoirs [11-16].

Both LAES and PTES are relatively new technologies and consequently information on their costs is limited in the available literature. Therefore, and in order to obtain consistent estimates of the capital costs of both systems, a costing methodology was developed based on simple thermo-economic models and a costing exercise was performed [7,8]. The overriding aim of this exercise was to perform a preliminary economic feasibility assessment of the two technologies that would allow their assessment from a whole-system perspective.

In the costing model used specifically for the estimation of capital expenditure, the systems were broken down into their fundamental components for costing and then summed to obtain an estimation of the overall system costs. Where possible, installation costs were considered. The model uses various methods for costing the different components. In summary, for expanders/turbines, compressors, pumps and storage vessels the costing correlations based on [17] are used along with their associated factors and parameters to estimate the capital cost. For heat exchangers, the model obtains an approximation of capital costs based on the C-value method [18] which allows for simple costing without the necessity of calculating the heat exchanger area requirement. For the storage material in the storage vessels a specific cost of £100/t is used in the model while assuming magnetite as storage material [15,16]. Finally, for the cost estimation of generators, the model uses a capacity exponent factor approach given that alternative correlations such as the ones presented in Ref. [17] were not found in literature. This approach is based on the following relation in which the exponent factor ( $e$ ) used is 0.94 [19]:

$$C = 1.85 \cdot 10^6 \left( \frac{\dot{W}}{1.18 \cdot 10^4} \right)^e \quad (2)$$

where  $C$  is the capital cost in € and  $\dot{W}$  is the power output capacity of the generator in kW.

#### Whole-systems assessment model

Analysing future electricity systems at sufficient temporal and spatial granularity is essential for adequately assessing the cost-effectiveness of decarbonisation pathways and enabling technologies. In order to accurately quantify system operation and investment cost as well as its carbon performance, quantitative models need to simultaneously consider second-by-second supply-demand balancing issues as well as multi-year investment decisions. Furthermore, it is also critical to adequately consider the synergies and conflicts between local and national (or trans-national) level infrastructure requirements.

To that end, the Whole-electricity System Investment Model (WeSIM) described in Ref. [2] is used in this paper to determine the value energy storage technologies in supporting efficient investment and operation of future electricity systems. The model minimises total system cost, which consists of: a) investment cost of new generation and storage capacity and the reinforcement cost of transmission and distribution networks, and b) operating cost of generators in the system, taking into account the cost of fuel and carbon. A detailed model

formulation is included in Ref. [2]. Key features and constraints include: a) power balance, b) reserve and response, c) generator operating limits, d) demand-side response; e) distribution network investment, f) carbon emissions, and g) security constraints.

#### Assessing the value of energy storage in future electricity systems

A *gross value* approach is adopted in this paper to assess the benefits of energy storage. In the first step, this approach consists of minimising the total system cost for an appropriately constructed *counterfactual* scenario, in which there is no energy storage. In the second step, a series of model runs is carried out with gradually increasing energy storage capacity, and the resulting reduction in total system cost is interpreted as whole-system benefit of energy storage. Scenarios with energy storage do not assume any cost of storage, hence providing gross (rather than net) system benefits. Gross system benefit can be a useful benchmark to compare against the projected cost of a given energy storage technology.

In this paper the gross whole-system value of storage is quantified in two ways:

1. *Average* whole-system value, obtained by establishing the cost reduction between a given energy storage scenario and the corresponding counterfactual scenario, and then dividing cost savings with the total assumed capacity of energy storage (in kW or kWh). For instance, if the scenario with 10 GW of energy storage results in total system cost savings of £1bn per year, the average gross system value or energy storage is £100/kW per year.
2. *Marginal* whole-system value, obtained by establishing the cost reduction between a given energy storage scenario and the previous scenario with lower storage capacity, and then dividing it with the incremental capacity of energy storage. For example, if in the scenario with 10 GW of energy storage the total system cost savings are £1bn per year, and the one with 5 GW of energy storage resulted in £0.6bn of annual cost savings, the marginal gross system value or energy storage is £0.4bn divided by 5 GW, or £80/kW per year.

Marginal value of storage is particularly suitable for comparison with estimated costs of storage technologies. It decreases with the installed capacity of storage, as the benefits of first MWs added will be higher than those of subsequently added storage capacity due to diminishing returns and reduced cost savings opportunities. Marginal value provides an indication of the cost-efficient level of deployment, given the basic economic principle that energy storage should be deployed up to the level where its gross marginal value equals its cost.

#### Description of scenarios used in the analysis

Scenarios used to assess the system value of energy storage technologies in this paper are constructed to capture the key drivers for the value of flexibility provided by energy storage. In all scenarios the power system is designed and operated to meet one of the two levels of *carbon emission intensity*: 100 g/kWh or 50 g/kWh. These carbon targets broadly correspond to the targets for the UK power system in the 2030-2040 horizon.

All scenarios are constructed by optimising the portfolio of generation technologies to meet the carbon target, while meeting electricity demand with adequate level of security of supply. Technologies available for adding to the system included: wind, solar PV, nuclear and CCS, as well as conventional generation technologies such as CCGT and peaking gas generation (OCGT). In order to represent typical variations in renewable output and demand across different geographies, the scenarios were developed to represent either *North* or *South* of Europe, with utilisation factors in the North higher for wind and lower for PV than in the South, and peak demand occurring during winter in the North and during summer in the South.

The electricity system is assumed to be represented by a single node. System demand has been sized to broadly correspond to the GB system demand at 347 TWh annually, of which 8.4% and 7.8% was associated with electrified transport and heat demand, respectively. The central assumption in all scenarios was that the uptake of demand-side response (DSR) was

25% of its theoretical potential, allowing a proportion of demand to be shifted in time. DSR in the model is provided by flexible electric vehicles, heat pumps, residential appliances and industrial and commercial demand. Sensitivity studies were also carried out for DSR uptake levels of 0% and 50% to study the competition between DSR and energy storage.

The counterfactual scenarios were assumed not to contain any energy storage. The capacity of each of the two energy storage technologies studied in this paper, LAES and PTES, was varied between 0 and 25 GW in 5 GW increments. The respective assumed durations (ratios between energy and power) for LAES and PTES were 4 hours and 5.75 hours, while the assumed cycle efficiencies were 55% and 70%. It was assumed that both technologies were connected to the high-voltage electricity distribution grid.

The costs of generation technologies were assumed based on the authors' own projections. The levelised cost of electricity (LCOE) for wind was taken to be £40.85/MWh in the North of Europe and £48.27/MWh in the South, and for solar PV it was taken to be £68.72/MWh in the North and £42.00/MWh in the South. The LCOEs of nuclear and CCS (assuming 90% annual load factor) were £133.67/MWh and £93.38/MWh, respectively. Investment costs for CCGT and OCGT generators were assumed at £687/kW and £568/kW, respectively. The assumed cost of gas was £22.62/kWh, while the carbon price was £29.09/t.

## **Results and Discussion**

### Electricity storage technologies costs

In the case studies considered in this paper, the LAES and PTES systems were analysed within their expected operating parameters: for LAES, a power output capacity of 12 MW and energy capacity of 50 MWh were used, and for PTES a power output capacity of 2 MW and energy capacity of 11.5 MWh were used. Thermodynamic and costing models of LAES and PTES were used to estimate their power capital cost (total capital expenditure divided by the power capacity), and energy capital cost (total capital expenditure divided by the energy capacity).

The estimated power capital cost of PTES and LAES was found to be around £2,700/kW and £1,600/kW, respectively. The equivalent values in terms of the energy capital costs for PTES and LAES were estimated at about £500/kWh and £400/kWh, respectively. It is recognized that at different capacities and power to energy ratios the power and/or capital costs might change and this represents an area for future work. For the cases considered here, these cost estimations indicate a slight competitive advantage of LAES in terms of both power and energy capital cost. However, the capital cost estimates do not reflect the system value of each technology in a given electricity system. Therefore, a combination of both cost and value estimates is adopted to assess the attractiveness of these systems in low-carbon electricity systems.

### System value of energy storage technologies

Generation portfolios in counterfactual scenarios (without any energy storage) are shown in Figure 2 for North and South of Europe scenarios and 100 and 50 g/kWh carbon targets. In the North the carbon target is achieved mostly by installing around 80 GW of wind generation, and CCS capacity (more so at 50 g/kWh). The remainder of the portfolio consists of CCGT and OCGT generation to ensure sufficient capacity margin. South scenarios contain a mix of wind and PV capacity, as well as CCS capacity that is higher than in comparable North scenarios.

System values of LAES and PTES were then quantified as described earlier. Given that the system optimisation provided annual cost savings, these annualised values were converted to capitalised values assuming the same system value would be generated over the lifetime of the storage asset, assuming the lifetime of 20 years and cost of capital of 7%. Figure 3 shows the average and marginal values of the two energy storage technologies expressed in £/kW across a range of scenarios and uptake levels.

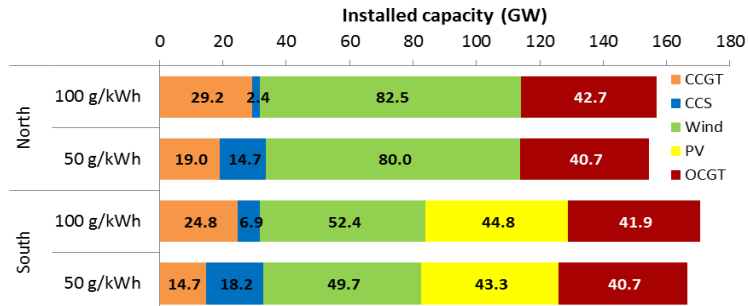


Figure 2. Generation technology mix in counterfactual scenarios (without energy storage)

Several key observations can be made: a) system value of storage decreases with higher uptake levels, as expected, and marginal value decreases faster than the average value; b) the value of PTES is in most cases higher than for LAES due to the positive effect of higher duration and higher efficiency; c) system value is considerably higher in the South than in the North, driven by higher variability of PV generation compared to wind; and d) values in 50 g/kWh scenarios are consistently higher than for 100 g/kWh, although not significantly. The value of storage was found to vary across scenarios between about £800/kW and £2,500/kW. Note that had these values been expressed in £/kWh, i.e. divided by the durations of the two technologies, the value of PTES would reduce relatively to LAES due to the higher assumed duration.

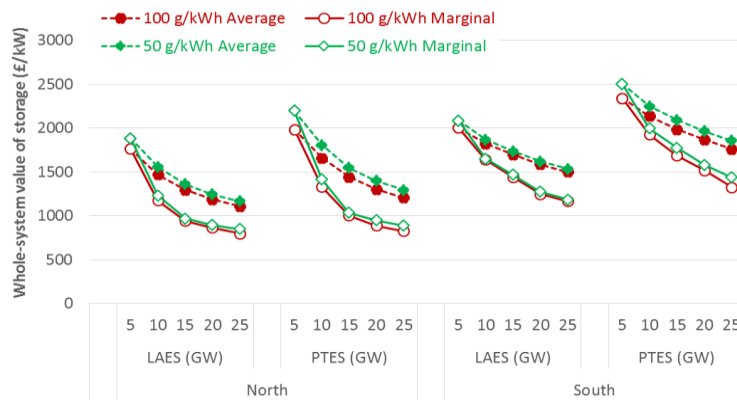


Figure 3. Average and marginal system value of LAES and PTES technologies

The whole-system modelling approach allows for specifying the breakdown of marginal values of LAES and PTES into components: investment cost (CAPEX) and operating cost (OPEX) of low-carbon generation, CAPEX and OPEX of conventional generation and CAPEX of distribution networks. This is illustrated in Figure 4 for 50 g/kWh scenarios.

Key components of system value of energy storage can be identified as: a) avoided CAPEX and OPEX of low-carbon generation (largely CCS), resulting from higher operational efficiency and lower renewable curtailment; b) avoided CAPEX of conventional generation, given that storage can displace conventional generation in contributing to the capacity margin; and c) for lower levels of storage penetration in the North there is avoided distribution CAPEX driven by energy storage reducing peaks in the distribution grid. In most cases deploying energy storage results in a slight increase in the OPEX of conventional generation given that a part of CCS generation is replaced by less expensive but more carbon-intensive CCGT output. It is clear that the value of storage can materialise in different segments of the electricity system. In reality this would mean that to maximise its economic value an energy storage operator would need to simultaneously deliver multiple services to the system [3].

Finally, to quantify the impact of competing flexible providers on the whole-system value of energy storage, two sets of sensitivity studies were run where the uptake level of DSR was set either at a low (0%) or high (50%) level. The effect on the marginal system value of LAES and PTES is shown in Figure 5. As expected, a higher DSR uptake would result in a lower value of storage and vice versa. This occurs because the cost saving opportunities that are accessible to storage are also accessible to DSR, hence there is direct competition between the two flexible options. The effect of higher DSR uptake is moderate, with the average reduction in value across all scenarios around 10%. On the other hand, a low DSR uptake would increase the system value of energy storage by 25% on average.

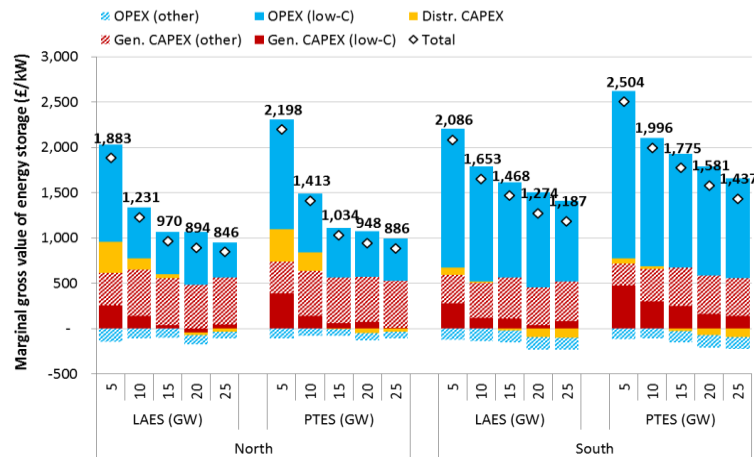


Figure 4. Breakdown of marginal system value of LAES and PTES technologies (50 g/kWh)

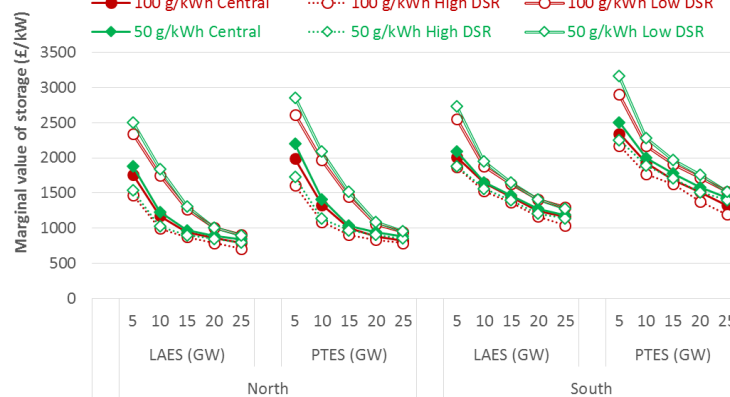


Figure 5. Impact of DSR uptake on marginal system value of LAES and PTES technologies

## Conclusions

Consistent thermodynamic and economic models were developed and applied to determine the characteristics of LAES and PTES systems. Differences in key system characteristics in earlier work [7,8] indicated these should be tested in a network-scale model to identify the conditions in which each technology is more valuable. Therefore, their application in a whole-system model was investigated to determine the system value of storage under different scenarios.

The whole-system value of electricity storage was found to greatly vary depending on the cumulative installed capacity of storage in the system. Considering that the marginal system value of storage can be considered equivalent to the maximum acceptable cost of the storage system at a given penetration, we can use the cost estimates of LAES and PTES to say if the systems are attractive for implementation under different system scenarios, and at what level



of installed capacity. Storage technologies provide greater marginal benefits at low penetrations and can therefore be viable in these conditions at a higher capital cost.

The two carbon target scenarios showed similar results, with limited effect of carbon target on the system value of storage (although this may change for even more ambitious carbon targets). On the other hand, the location and installed capacity were found to have a greater impact on the system value and acceptable cost of the technologies. Whole-system value of PTES was observed to be slightly higher than for LAES, driven by higher duration and efficiency; however, due to the higher power capital cost of PTES, it becomes unattractive for implementation at lower volumes than LAES. The cost of PTES was found to be higher than its whole-system value at the minimum capacity considered, except in cases with low DSR uptake. LAES, on the other hand, is found to be attractive for implementation at installed capacities between 5 and 10 GW in the North of Europe and between 10 and 15 GW in the South. The cost-efficient volume of LAES increases even further in scenarios with low DSR uptake.

Future research in this area will include exploring other costing methods/correlations for these technologies that might result in lower costs. Also, if learning curves are considered as a result of incremental installed capacity which can contribute to the reduction in cost estimates, it is possible that the systems will be economically attractive at even higher installed capacities. Also, investigating LAES and PTES at different capacities and power to energy ratios can be an interesting avenue for future work. Finally, it will be of interest to investigate in more detail the competition between LAES, PTES and other energy storage technologies if they are all simultaneously considered in the system.

### **Acknowledgements**

This work was supported by the UK Engineering and Physical Sciences Research Council (EPSRC) [grant number EP/J006041/1] and UK Natural Environment Research Council (NERC) [grant number NE/L002515/1].

### **References**

- [1] Markides, C.N., “The role of pumped and waste heat technologies in a high-efficiency sustainable energy future for the UK”, *Applied Thermal Engineering*, 2013, doi:10.1016/j.applthermaleng.2012.02.037.
- [2] Pudjianto, D., Aunedi, M., Djapic, P., Strbac, G., “Whole-system assessment of value of energy storage in low-carbon electricity systems”, *IEEE Transactions on Smart Grid*, 2014, doi:10.1109/tsg.2013.2282039.
- [3] Strbac, G., Aunedi, M., Konstantelos, I., Moreira, R., Teng, F., Moreno, R., Pudjianto, D., Laguna, A., Papadopoulos, P., “Opportunities for Energy Storage: Assessing Whole-System Economic Benefits of Energy Storage in Future Electricity Systems”, *IEEE Power and Energy Magazine*, Vol. 15, pp. 32-41, Sep-Oct 2017.
- [4] Teng, F., Pudjianto, D., Aunedi, M., Strbac, G., “Assessment of Future Whole-System Value of Large-Scale Pumped Storage Plants in Europe”, *Energies* 11(1):246, Jan 2018.
- [5] Highview Power Storage, “Liquid air energy storage 2016” – Available at: [www.highview-power.com](http://www.highview-power.com) [accessed 15.2.2016].
- [6] Centre for Low Carbon Futures, “Liquid air in the energy and transport systems: opportunities for industry and innovation in the UK”, York, UK: Centre for Low Carbon Futures; 2013 May, Report No. 021.
- [7] Georgiou, S., Mac Dowell, N., Shah, N., Markides, C.N., “Thermo-economic comparison of liquid-air and pumped-thermal electricity storage”, *Proceedings of ECOS 2017*, San Diego, California, USA.
- [8] Georgiou, S., Shah, N., Markides, C.N., “A thermo-economic analysis and comparison of pumped-thermal and liquid-air electricity storage systems”, *Applied Energy*, 2018, *in press*.

- [9] Morgan, R., Nelmes, S., Gibson, E., Brett, G., “Liquid air energy storage – analysis and first results from a pilot scale demonstration plant”, *Applied Energy*, 2015, doi:10.1016/j.apenergy.2014.07.109.
- [10] Sciacovelli, A., Vecchi, A., Ding, Y., “Liquid air energy storage (LAES) with packed bed cold thermal storage – From component to system level performance through dynamic modelling”, *Applied Energy*, 2017, doi:10.1016/j.apenergy.2016.12.118.
- [11] White, A., Parks, G., Markides, C.N., “Thermodynamic analysis of pumped thermal electricity storage”, *Applied Thermal Engineering*, 2013, doi:10.1016/j.applthermaleng.2012.03.030.
- [12] McTigue, J.D., White, A.J., Markides, C.N., “Parametric studies and optimisation of pumped thermal electricity storage”, *Applied Energy*, 2015, doi:10.1016/j.apenergy.2014.08.039.
- [13] Mathie, R., Markides, C.N., White, A.J., “A framework for the analysis of thermal losses in reciprocating compressors and expanders”, *Heat Transfer Engineering*, 2014, doi:10.1080/01457632.2014.889460.
- [14] Willich, C., Markides, C.N., White, A.J., “An investigation of heat transfer losses in reciprocating devices”, *Applied Thermal Engineering*, 2017, doi:10.1016/j.applthermaleng.2016.09.136.
- [15] White, A.J., McTigue, J.D., Markides, C.N., “Analysis and optimisation of packed-bed thermal reservoirs for electricity storage applications”, *Proceedings of the Institution of Mechanical Engineers, Part A: Journal of Power and Energy*, 2016, doi:10.1177/0957650916668447.
- [16] White, A., McTigue, J., Markides, C., “Wave propagation and thermodynamic losses in packed-bed thermal reservoirs for energy storage”, *Applied Energy*, 2014, doi:10.1016/j.apenergy.2014.02.071.
- [17] Turton, R., Bailie, R.C., Whiting, W.B., Shaeiwitz, J.A., “Analysis, synthesis and design of chemical processes”, London, UK, Pearson Education International, 4th Ed., 2013.
- [18] Hewitt, G.F., Pugh, S.J., “Approximate design and costing methods for heat exchangers”, *Heat Transfer Engineering*, 2007, doi:10.1080/01457630601023229.
- [19] Lemmens, S., “Cost engineering techniques and their applicability for cost estimation of organic Rankine cycle systems”, *Energies*, 2016, doi:10.3390/en9070485

# Pumped Heat Electricity Storage at Intermediate Temperatures: Basics and Limits

B. Atakan<sup>1\*</sup> and D. Roskosch<sup>1</sup>

<sup>1</sup> University of Duisburg-Essen, Thermodynamics, Lotharstr. 1, 47057 Duisburg, Germany

\*Corresponding author: Burak.Atakan@uni-due.de

## Abstract

The rising share of renewable energy sources in power generation leads to the need of energy storage capacities. In this context, also some interest in thermal energy storages, especially in a concept called pumped heat electricity storage (PHES), arises. One possible design of such a PHES system at intermediate temperatures (300-500 K) consists of a compression heat pump, a thermal storage and an Organic Rankine cycle (ORC). The present work analyses the general thermodynamic potential and limits of such a system by means of realistic simple Rankine cycles. The potential analysis starts with the optimal case of combining two reversible Rankine cycles with reversible heat transfer. Afterwards the cycles are transferred to Rankine cycles with irreversible heat transfer and the relation between power output of the discharging cycle and efficiency of the entire process is analysed. The considered working fluid is always a hypothetical one, which is optimized by an inverse engineering approach. It is shown that the total or roundtrip efficiencies are between 55 and 37% for a power output of 80% of the maximal value and decrease with increasing storage temperatures, in contrast to a Carnot cycle analysis. A further expansion of the investigation considers the influence of the isentropic efficiencies of the ORC expander and the HP compressor on the process efficiency. Here, a stronger sensitivity of the isentropic efficiency of the ORC expander on the roundtrip efficiency was found.

**Keywords:** pumped heat electricity storage, thermodynamic limits, inverse engineering, fluid optimization.

## Introduction/Background

Most of the renewable energy sources like wind or solar radiation are not available continuously. This leads to fluctuations of the supplied power to the electricity grid, creating a need of large storage capacities within the grid. Several different technologies are discussed [1] or already applied addressing this issue, which can be divided into two groups, chemical storages like common batteries or power to gas systems and non-chemical storages like pumped hydro storages or compressed air energy storages. A further storage technology recently discussed is the pumped heat electricity storage (PHES). The basic principle of such a PHES system is simple; in case of oversupply of energy to the grid, a thermodynamic cycle transfers heat from a low temperature heat source (e.g. the surrounding) to high temperature thermal energy by using electrical energy  $W_{\text{net,p}}$  and charges the storage. If later, less electrical energy is generated than needed, a further thermodynamic cycle discharges the storage and converts thermal energy back to electrical energy  $W_{\text{net,o}}$  again. There are a few possibilities in the design of a PHES system, one is combining a heat pump with an Organic Rankine Cycle (ORC) [2–4]. The thermodynamic limits with respect to the efficiency, as well as important variables of PHES systems, are nearly unknown so far and is addressed here systematically. The limiting case was in part investigated with reversible Carnot cycles with irreversible heat transfer from or to the environment and a thermal energy storage [5–7], this may be analysed for a maximum of power output or for reduced power output leading to increased roundtrip efficiencies. In the present work, the combination of an ORC and a heat

pump (HP) or a resistive heater (RH) is analysed with respect to the influence of a hypothetical optimal fluid, as obtained from reverse engineering [8][9] and also with respect to further process parameters.

## Discussion and Results

The present work focusses on the PHES designs with vapour compression heat pumps and ORCs and alternatively on combinations of electrical heaters and ORCs. It is analysed, which roundtrip efficiencies are to be expected if real or nearly real cycles are considered and whether the results from Carnot cycles are transferable to real processes, at all. The advantage of analysing reversible comparison cycles is usually, that findings about important process parameters and influencing factors of the real process can be obtained by means of simple equations or correlations. For example, most of the innovations in power plant technology can be traced back to the Carnot cycle. However, it is not clear so far, if it is also true for PHES systems. Addressing this question, the step from reversible Carnot cycles to more realistic Rankine cycles considering typical boundary conditions is taken here. The roundtrip efficiency and the power output are analysed as a function of the storage temperature for different cases. The working fluid is defined by characteristic fluid parameters like e.g. the critical temperature and pressure; these are taken as continuous variables and optimized for every regarded storage temperature by an inverse engineering approach [8]. This procedure ensures the calculation of the highest possible roundtrip efficiencies with respect to the boundary conditions, since the fluid is optimally adapted to the process. Components like pumps, expanders or compressors are initially assumed to be ideal, but subsequently, the influence of the isentropic efficiencies of the ORC expander and the HP compressor on the roundtrip efficiencies is investigated for a constant storage temperature. The Rankine cycle and heat pump parameters were fixed, as it is usually selected in such a way that the condensation in the isobaric heat exchanger always ends at a quality of  $x = 0$  and the evaporation in the evaporator at a quality of  $x = 1$ . The total thermal resistances in each heat exchanger was fixed to  $R = 2.5 \cdot 10^{-4} \text{ K/W}$ , each component is adiabatic towards the surrounding, and the throttle of the heat pump is assumed to be isenthalpic or with a turbine to be isentropic. Further constraints and the parameter regime for the process and the fluid are summarized in Table 1.

Table 1: Variable range for fluid optimization

parameter	variable range
critical temperature, K	$T_c \leq 700$ , but subcritical
critical pressure, MPa	$3 \leq p_c \leq 12$
acentric factor	$0.1 \leq \omega \leq 0.7$
isobaric heat capacity (ideal gas) at 350 K, $\text{J mol}^{-1} \text{K}^{-1}$	$35 \leq c_{p,350} \leq 150$
slope of isobaric heat capacity at 350 K, $\text{J mol}^{-1} \text{K}^{-2}$	$0.09 \leq (dc_p/dT)_{350} \leq 0.45$
system pressures, MPa	$0.1 \leq p \leq 5.0$

The roundtrip efficiency is defined as:

$$\psi = \frac{|W_{\text{net,o}}|}{|W_{\text{net,p}}|} = \frac{|P_{\text{net,o}}|}{|P_{\text{net,p}}|} \quad (1)$$

First, the thermodynamic limit in process temperatures is analysed. Based on the Carnot cycles, the condensation and evaporation temperatures of the Rankine cycles are here always set to the storage temperature or the surrounding temperature, respectively (indicated as reversible Rankine cycle case).

Indeed, this leads, based on the infinitely small temperature differences in the heat exchangers, to heat flow rates and power outputs close to zero, but usually promises the highest efficiencies.

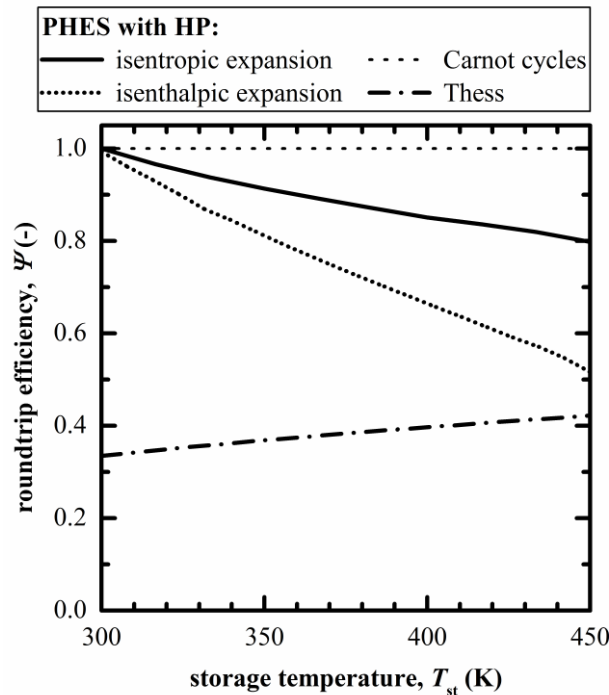


**Fig. 1:** Roundtrip efficiency as a function of storage temperature for the combination of two Carnot cycles and two reversible Rankine cycles.

Figure 1 shows the resulting roundtrip efficiencies for different process configurations as a function of the storage temperature; the solid line represents an isentropic expansion and the dotted line an isenthalpic expansion using a throttle in the heat pump. In addition, the results of combining two full Carnot cycles (dotted line), that always leads to  $\psi = 1$ , and the results of Thess [5] (dotted dashed line) are also included, who combined two reversible Carnot cycles with irreversible heat transfer from/to the surrounding and the thermal storage in such a way that the power output is maximal at each temperature. Regarding the results of [5], for the maximum power cycle, it gets clear that the roundtrip efficiency increases with increasing storage temperature. Thus, the system becomes more efficient if the absolute spreading between the storage temperature and the surrounding temperature rises. However, the achieved roundtrip efficiencies are rather low for ideal cycles, At  $T_{st} = T_{sur}$ , the function is not defined, but a slightly higher storage temperature already leads to a roundtrip efficiency of 33.4 %, but, the power output is expected to be close to zero, then. The roundtrip efficiency for the highest considered storage temperature of  $T_{str} = 450$  K is 42.1 % for the maximum power cycle.

The results of the combination of two Rankine cycles lead to completely different results. For both cases (isentropic and isenthalpic expansion), the reached roundtrip efficiencies are significantly higher, but it is much more crucial that the lines, starting at  $\psi \approx 1$  for  $T_{st} = 300$  K, now decrease with increasing storage temperature. The decrease of the Rankine cycle roundtrip efficiency with increasing storage temperature is strongly related to the implementation of fluid properties. The fluid optimizations for the different storage temperatures, leads to high critical temperatures; this is a typical result from fluid optimizations for processes with isothermal heat sources. If the storage temperature is low, the spreading between the condensation and evaporation temperatures is also very small for both processes, in combination with a high  $T_c$ , this leads to a nearly rectangular form of each

process in a  $T$ - $s$  diagram and thus, to roundtrip efficiencies similar to the ones of Carnot cycles. In contrast, at increased spreading between the two temperature levels, a relatively high amount of heat is needed to reach the saturation temperature in the ORC. This leads to a decreased thermodynamic mean temperature of the ORC compared to a Carnot cycle at the same saturation temperature, mainly due to the part until the fluid is saturated, and thus to lower efficiencies compared to the ideal cycles. Indeed, the thermal efficiency of the ORC is still increasing with the storage temperatures but now, the improvement is not enough to compensate the decrease of the heat pump  $COP$ . Another aspect is the difference between isenthalpic and isentropic expansion step of the HP. An isentropic expansion step leads to a delivery of work, and thus, to a better  $COP$ . However, based on technical and economic aspects the expansion is commonly achieved by a simple nearly isenthalpic expansion valve. An isenthalpic expansion step also leads to a deviation from the shape of a Carnot process and thus, to smaller roundtrip efficiencies. This effect becomes more important for higher storage temperatures, leading to the stronger decrease of  $\Psi$  for increasing  $T_{st}$ .

The process temperatures considered so far lead to high roundtrip efficiencies, but due to the infinitely small temperature differences in the heat exchangers the power output of the ORC is also infinitely small for usual heat exchanger sizes. To achieve a sufficient power output with an adequate plant size, the temperature differences, especially in the storage heat exchanger, has to be increased. Regarding a single power cycle, the decrease of the evaporation temperature at constant heat source temperature leads to an increased heat flow rate to the process. Nevertheless, the spreading between the high and the low thermodynamic mean temperatures is also decreased then, leading to reduced efficiencies. This leads for a single power cycle typically to a Pareto frontier between power output and efficiency and the selection of an optimal operating point is finally based on other, probably economic, aspects. Similar findings are observed for PHES systems.

Analogous to Thess [5], the restriction to maximum power output  $P_{max}$  is one possibility, here. This restriction was also used for the Rankine cycles with an isenthalpic expansion step in the HP. Now, not only the fluid parameters were numerically optimized, but also the evaporation temperature of the ORC  $T_{evap,o}$ . The resulting roundtrip efficiencies are shown in Figure 2 (circles) and the power output is depicted in Figure 3, both as a function of the storage temperature. The slight fluctuations of the points are of numerical origin, induced by the convergence criterion of the optimization routine. The drawn lines are polynomial fits. It is obvious from Fig. 2 that analogues to the pre study (Fig. 1) the roundtrip efficiencies again decrease for increasing storage temperatures, but the absolute values are significantly reduced. Compared to the results of Thess [5] the line starts for a storage temperature of 300 K at a similar value ( $\Psi = 0.31$ ) but then decreases to  $\Psi = 0.22$  for a storage temperature of 430 K. Therefore, small storage temperatures close to the surrounding temperature are superior with respect to the roundtrip efficiency, but Fig. 3, shows that the values of the power output are poor for low storage temperatures and thus, very large heat exchangers would be required in order to get an acceptable power output. Although components like expander, compressor etc. are still assumed to be isentropic, the resulting roundtrip efficiencies are in case of prescribing maximum power output rather poor and thus, lead to a moderate evaluation of this technology. However, Chen et al. [6] have already analysed a single power cycle in terms of endo-reversible thermodynamics and emphasized that prescribing maximum power output is not a reasonable upper bound of the efficiencies of heat engines due to the Pareto frontier which always leads to a compromise between thermal efficiency and power output. Thus, it is worth investigating this topic with respect to PHES systems, too. The fluid parameters and  $T_{evap,o}$  were optimized again, but now with  $\Psi_{max}$  as target value and the additional condition that the power output must be 80 % ( $P_{0.8}$ ) of the maximum power output (as calculated before). The results are shown in Fig. 2 and Fig. 3

(squares). It gets clear, that although the prescribed power output is only reduced by 20 %, the resulting roundtrip efficiencies are on average increased by 66 %, leading to a much better evaluation of PHES system. Both cases were also compared to the simpler process combining an electrical resistive heater (RH) with an ORC. The resulting roundtrip efficiencies are also given in Fig. , the values of the power output are kept constant. Analogues to the Carnot efficiency for a single power cycle, the values start at nearly zero for storage temperatures close to the surrounding temperature and then increase with the storage temperature. If the results for HP and RH charging are compared, it gets clear that at least for the considered storage temperatures the process with HP charging has an advantage. For higher storage temperature, there should be a break-even point, where the lines converge. However, from an economic point of view, the use of a RH instead of a HP will probably be appropriate at even lower storage temperatures, due to the simplicity and low cost of resistive heaters.

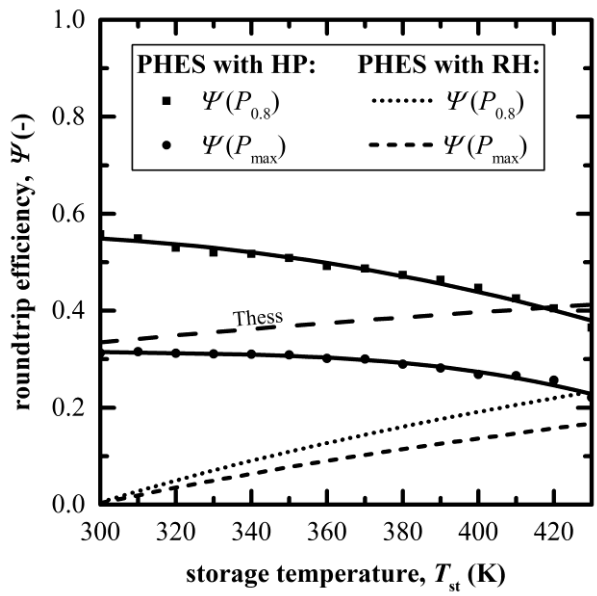


**Fig. 2:** Roundtrip efficiency as a function of storage temperature for the configurations HP / ORC and RH / ORC and for different prescribed values of power output. Line ‘Thess’ according to [5].

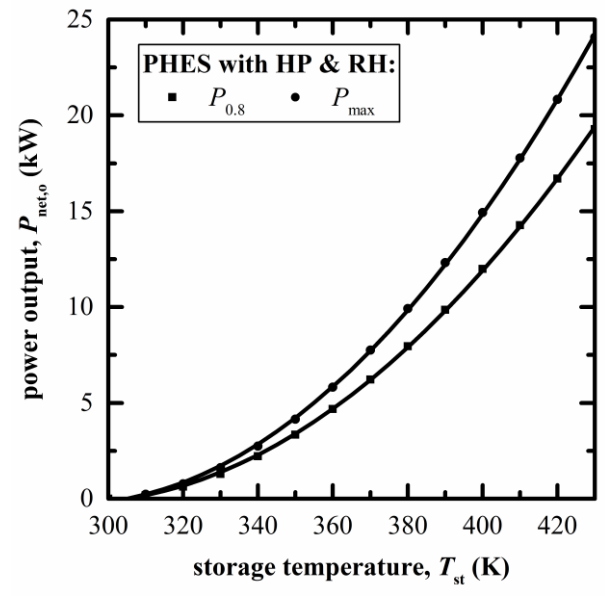


**Fig. 3:** Power output (ORC) as a function of storage temperature for both configurations: HP / ORC and RH / ORC

The optimal fluid parameters found are listed in Table 2. Regarding optimal fluid parameters resulting from the reduced power case it was seen that the optimizations lead always to the highest possible critical temperatures for a given pressure limit, to critical pressures at the higher limit and especially for higher storage temperatures to small values of the acentric factor. The isobaric ideal gas (IG) heat capacity has no impact on saturation pressures but influences the slopes of the saturated-liquid and saturated-vapour lines in a  $T$ - $s$  diagram. The isobaric ideal gas (IG) heat capacity specifies whether a fluid is dry (high  $c_p$ ) or wet, and thus, is the adjusting parameter to prevent wet vapour in the expander and the compressor. Here, the optimizer adjusts the values of  $c_p$  in such a way that no wet vapour is formed, but it also avoids fluid superheating at the expander outlet and the compressor outlet.

**Table 2:** Optimal fluid parameters for different storage temperatures, reversible Rankine cycles with isenthalpic expansion

$T_{st}$ , K	$T_c$ , K	$p_c$ , MPa	$\omega$	$c_1$ , J mol <sup>-1</sup> K <sup>-1</sup>	$c_2$ , J mol <sup>-1</sup> K <sup>-2</sup>	$c_{p,350}$ , J mol <sup>-1</sup> K <sup>-1</sup>
300	446	10.0	0.34	33.9	0.20	93.9
360	505	10.6	0.13	39.2	0.13	78.2
420	516	12.0	0.10	39.6	0.09	66.6

Previously it was assumed that all components such as expander, compressor or pump are isentropic, however the isentropic efficiency of real components usually differ strongly from 1. Crucial for the efficiency of the entire process are especially the efficiencies of the expander of the ORC and of the compressor of the HP [10, 11]. As an example, the influence of these parameters on the roundtrip efficiency was investigated for a storage temperature of 400 K. Here, the case was considered in which the evaporation and condensation temperatures of the Rankine cycles (HP with isenthalpic expansion step) are equal to the storage or the surrounding temperature; this case was previously indicated as reversible Rankine cycles. Fig. 4 shows the resulting contour plot with lines of constant  $\Psi$  as a function of the isentropic compressor efficiency (HP) and the isentropic expander efficiency (ORC). It is obvious, that the roundtrip efficiency strongly depends on the isentropic efficiencies of these components. If usual values for a compressor and an expander, such as  $\eta_{s,c,ex} = 0.6$ , are considered the roundtrip efficiency is approximately halved from 0.66 to 0.32. Furthermore, due to the slope of the lines of constant  $\Psi$ , it is seen from Fig. 4 that the sensitivity of  $\Psi$  on the isentropic efficiency of the ORC expander is slightly higher than on the HP compressor. Therefore, efforts to improve this storage concept should focus on the improvement of the ORC expander.

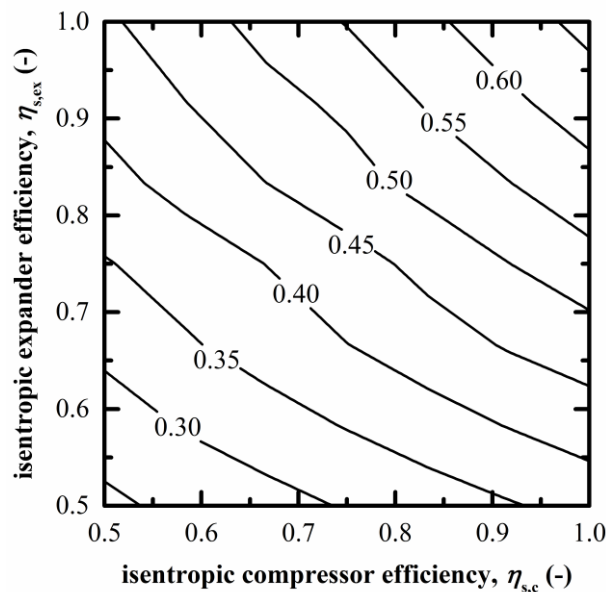


**Fig. 4:** Roundtrip efficiency as a function isentropic expander (ORC) and compressor (HP) efficiencies for the reversible Rankine cycle case.

## Summary/Conclusions

It is concluded that Carnot cycles are of limited use to analyse PHES system. In this context two process steps were identified which lead to the difference. An analysis of the relation between power output and roundtrip efficiency, which was made as an example for a storage temperature of 400 K, emphasized that roundtrip efficiency and power output lead also for PHES systems to a Pareto frontier where values for the power output near to the maximum result in a strong



decrease of the roundtrip efficiency. It was shown that the roundtrip efficiency can be improved by in average 66 % while the power output is only decreased by 20 % based on the maximum power output. The reached roundtrip efficiencies are only between 56 % ( $T_{st} = 300$  K) and 37 % ( $T_{st} = 430$  K), although components like expander, compressor and pump were still assumed to be isentropic in this case. In this context, it was emphasized that the reached roundtrip efficiencies are even further reduced, if typical values for the isentropic efficiencies of HP compressor and ORC expander are assumed.

## References

- [1] Gallo AB, Simões-Moreira JR, Costa HKM, Santos MM, Moutinho dos Santos E. Energy storage in the energy transition context: A technology review. *Renewable and Sustainable Energy Reviews* 2016;65:800–22.
- [2] Wolf B.(EP 1987299 B1).
- [3] Frate GF, Antonelli M, Desideri U. A novel Pumped Thermal Electricity Storage (PTES) system with thermal integration. *Applied Thermal Engineering* 2017;121:1051–8.
- [4] Dietrich A, Dammel F, Stephan P. Exergoeconomic Analysis of a Pumped Heat Electricity Storage System with Concrete Thermal Energy Storage. *Int. J. Thermo* 2016;19(1):43.
- [5] Thess A. Thermodynamic efficiency of pumped heat electricity storage. *Physical review letters* 2013;111(11):110602.
- [6] Chen J, Yan Z, Lin G, Andresen B. On the Curzon–Ahlborn efficiency and its connection with the efficiencies of real heat engines. *Energy Conversion and Management* 2001;42(2):173–81.
- [7] Roskosch D, Atakan B. Pumped heat electricity storage: Potential analysis and orc requirements. *Energy Procedia* 2017;129:1026–33.
- [8] Roskosch D, Atakan B. Reverse engineering of fluid selection for thermodynamic cycles with cubic equations of state, using a compression heat pump as example. *Energy* 2015;81:202–12.
- [9] Roskosch D, Atakan B. Reverse engineering of fluid selection for ORCs using cubic equations of state. *Proceedings of ASME ORC* 2015;3.
- [10] Venzik V, Roskosch D, Atakan B. Propene/isobutane mixtures in heat pumps: An experimental investigation. *International Journal of Refrigeration* 2017;76:84–96.
- [11] Roskosch D, Venzik V, Atakan B. Thermodynamic model for reciprocating compressors with the focus on fluid dependent efficiencies. *International Journal of Refrigeration* 2017;84:104–16.

# Performance analysis of a novel polygeneration plant for LNG cold recovery

Antonio Atienza-Márquez<sup>\*</sup>, Joan Carles Bruno, Alberto Coronas

Universitat Rovira i Virgili, CREVER, Mechanical Engineering Department,  
Av. Països Catalans 26, 47003 Tarragona, Spain

<sup>\*</sup>Corresponding author: antonio.atienza@urv.cat

## Abstract

Because of its low temperature (around  $-162^{\circ}\text{C}$ ) the regasification of Liquefied Natural Gas (LNG) has been proposed extensively for its use as heat sink in many power cycles. However, its application for the simultaneous production of power, refrigeration and cooling has remained relatively unexplored. In this paper it is presented a polygeneration plant to recover cooling from the regasification process of LNG in order to provide mechanical power and cooling at several temperatures using a District Cooling Network. In this way the low temperatures of LNG regasification can be used in the nearby industrial plants demanding refrigeration at low temperatures and also air conditioning. The performance of the plant is analyzed from the thermodynamic and environmental point of view. The polygeneration plant produces an Equivalent Energy Saving of 82.6 kWh/ton-LNG with an exergetic efficiency of 35.5%. Furthermore, the seawater consumption of the typical LNG regasification process is reduced by a 66.8%.

**Keywords:** LNG, cold recovery, polygeneration of energy.

## Introduction/Background

Natural Gas (NG) is one of the cleanest fuels of fossil origin because of its low carbon footprint and clean combustion [1]. Thus, NG will keep play an important role in the next future and it will be an essential primary energy source in the transition from the fossil fuel based energetic model to a decarbonized energetic model based on renewable energy sources [2]. Although, NG is usually transported by pipelines, it is supplied as Liquefied Natural Gas (LNG) by ship when the NG has to be transported over long distances.

LNG is the cryogenic form of NG and it is obtained in liquefaction plants at a temperature of around  $-162^{\circ}\text{C}$  approximately which makes it a valuable exergy source. Its composition is mainly methane (around 90%), ethane and propane and it has a volume that is around six hundred times lower than that of NG, which makes feasible its maritime transport. However, LNG must be regasified before supplying it to the end-users. By now this process is usually done using seawater as heat source, so the cold is rejected to the ambient without any useful application. This not only means a waste of energy, but also it has a negative impact on marine sea life.

The recovery of waste heat and cold is one of the priorities mentioned in the Strategic Energy Technology (SET) Plan published in Nov. 2017 for Energy efficiency in industry [3]. The cold recovery of the LNG regasification process has been reviewed in the literature extensively [4], mainly for power production using the regasification heat as heat sink of a power generation cycle [5, 6]. However, it could be even more interesting to study the combined production of power and refrigeration [7] to replace refrigeration systems with its corresponding benefits in energy costs and environmental impact because it will be no longer necessary the use of GWP refrigerants for the users connected to this system.

Despite that LNG cold has many industrial applications, it is only exploited in a few regasification plants worldwide. Most of these plants with LNG cold recovery are in Japan,

which is the top country in LNG regasification capacity and number of LNG plants. For instance, in the LNG terminal of Semboku II (Osaka, Japan) operated by Osaka Gas Co. [8] exploits LNG cold as heat sink in a power cycle with propane as working fluid and in an LNG direct expansion unit [9]. Other example is the terminal of Negishi (Tokyo, Japan) operated by the Tokyo Gas Co. [10] where LNG cold is used in a refrigerated warehouse where tuna fishes are stored at around  $-50^{\circ}\text{C}$  [11]. Nevertheless, some barriers have blocked so far the development of LNG cold recovery systems. For example, the limited interest of companies that manages LNG plants in providing energy services other than NG to third parties or also the distance between LNG plants and the potential cold consumers [7].

The objective of this paper is to analyze the performance of a polygeneration plant with cold recovery from LNG-regasification to produce mechanical power and cold at different temperature levels using a District Cooling Network. Furthermore, the influence of installing a reheating stage or a recuperator heat exchanger is analyzed by means of some defined performance indicators.

### A polygeneration plant with LNG cold recovery

Figure 1 shows a scheme of a polygeneration plant with cold recovery from LNG-regasification [7]. This plant is engineered to operate in the vicinity of users with refrigeration demand. The selected LNG regasification capacity is  $150,000 \text{ Nm}^3 \text{ h}^{-1}$  which is the equivalent of one open rack vaporizer installed in the LNG plant of Barcelona (Spain). The plant exploits LNG cold in cascade and it is divided into the following operating blocks:

- **Power cycle RC-1:** This power cycle uses seawater as heat source and LNG as heat sink. The working fluid selected is argon, due to its low freezing point and its zero-environmental impact.
- **District Cooling network and power cycle RC-2:** This subsystem of the plant not only provides refrigeration service, but also it uses low-grade waste heat as heat source to produce electrical power. The District Cooling Network supply cold at three different temperature levels, depending on the type of users. The lowest temperature level (LT) is  $-25^{\circ}\text{C}$  (cold chambers); the middle temperature level (MT) is  $-10^{\circ}\text{C}$  (hypermarkets, shopping centers, etc.); and the high temperature level (HT) is  $6^{\circ}\text{C}$  (residential and office buildings, hotels, etc.). The working fluid and heat transfer fluid selected for this subsystem is carbon dioxide.
- **Power cycle RC-3:** This power cycle is driven by the heat from a biomass combustion system. After using LNG cold in the District Cooling network, LNG is still at a temperature low enough to be used again as heat sink of the power cycle RC-3. Carbon dioxide is selected as working fluid for this thermal power cycle.
- **LNG direct expansion unit:** Since the LNG plant operates at a pressure higher than that of the natural gas (city gas) distribution pipeline, an expander is used to take advantage of this pressure drop and produce extra electric power.

The polygeneration plant with LNG cold recovery is modelled with the software Engineering Equation Solver [12] and applying the following assumptions:

- Steady state operation.
- Pressure drop and thermals losses are neglected.
- Natural gas is assumed as pure methane.
- The fluids at the exit of condensers C-1, C-2 and C-3 are at saturated liquid state.
- The carbon dioxide streams leaving the heat exchangers C-4, C-5 and C-6 are at saturated vapor state.

- Isentropic efficiencies of turbines and pumps are 85% and 75%, respectively.
- Effectiveness of recuperators R-1 and R-2 of power cycles RC-1 and RC-3 is 80%.

The main operation parameters are listed in Table 1.

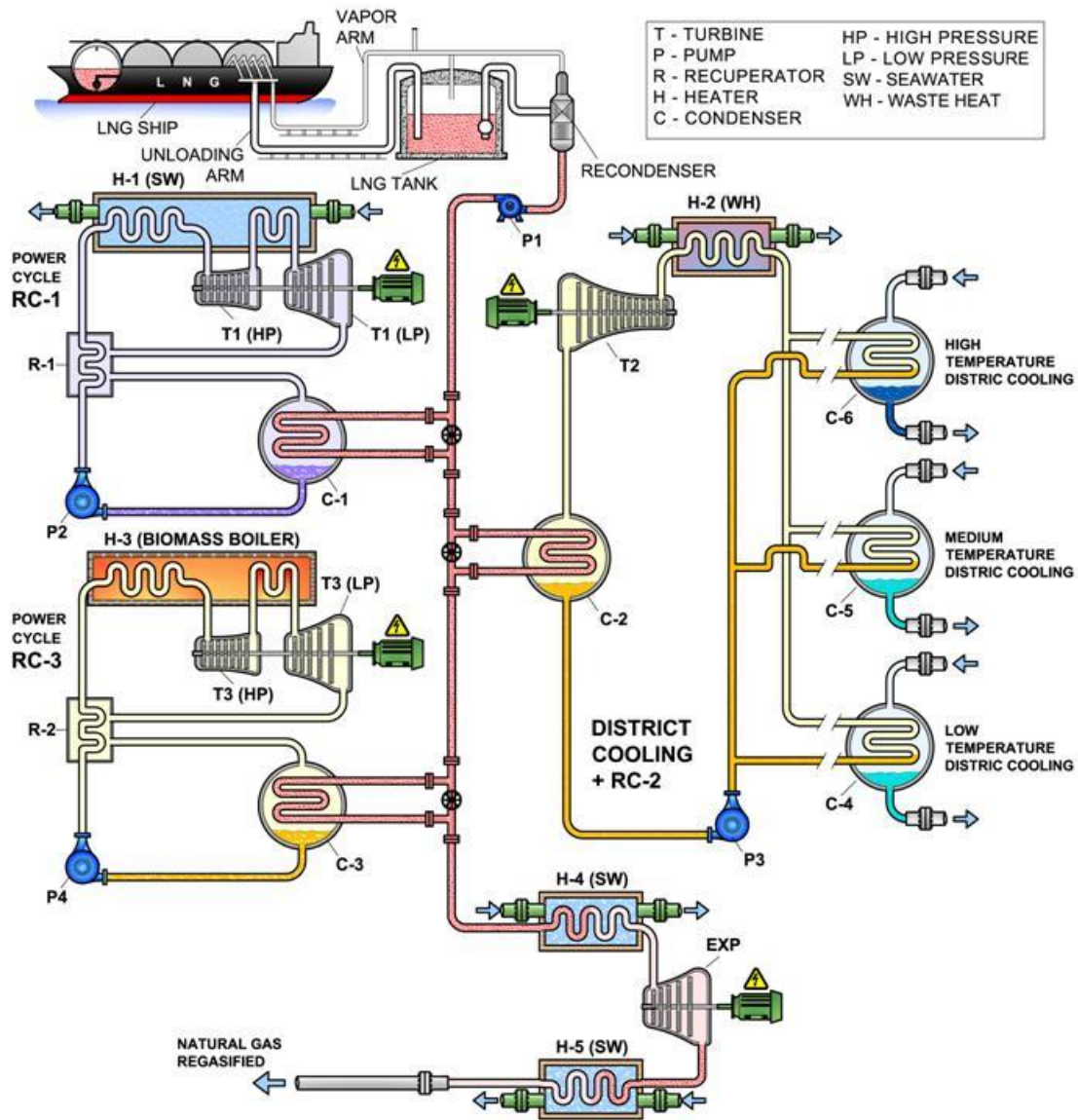


**Figure 1.** Scheme of the proposed polygeneration plant based on LNG cold recovery.

**Table 1.** Simulation parameters.

Parameter	Value	Parameter	Value
LNG mass flow rate	$29.9 \text{ kg s}^{-1}$	DC share of refrigeration demand	50/40/10%
LNG Pressure	8 MPa	LT/MT/HT	
Temperature of regasified NG	$5 \text{ }^\circ\text{C}$	Inlet temperature of turbine T2	$30 \text{ }^\circ\text{C}$
Pressure of city NG	7 MPa	Waste heat (water) stream inlet/outlet temperature	$40/35 \text{ }^\circ\text{C}$
SW inlet/outlet temperature	$20/15 \text{ }^\circ\text{C}$	Heat output of biomass boiler	10 MW
Inlet temperature of turbine T1	$10 \text{ }^\circ\text{C}$	Inlet temperature of turbine T4 (HP and LP)	$400 \text{ }^\circ\text{C}$
DC supply temperature	$-50 \text{ }^\circ\text{C}$	Combustion temperature of biomass boiler ( $T_{bb}$ )	$850 \text{ }^\circ\text{C}$
		Condensing temperature RC-3	$5 \text{ }^\circ\text{C}$

The total net power of the plant is calculated as follows:

$$\dot{W}_{net} = \sum \dot{W}_T - \sum \dot{W}_P \quad (1)$$

The total refrigeration service provided is calculated as:

$$DCS = \dot{Q}_{DC,LT} + \dot{Q}_{DC,MT} + \dot{Q}_{DC,HT} \quad (2)$$

Where the heat transferred in heat exchangers is calculated from energy balance equations:

$$\dot{Q} = \dot{m}_{fluid,hot}(h_{hot,in} - h_{hot,out}) = \dot{m}_{fluid,cold}(h_{cold,out} - h_{cold,in}) \quad (3)$$

On the other hand, the exergy of each point of the plant is calculated as:

$$\dot{E}x_i = \dot{m}_i[(h_i - h_0) - T_0(s_i - s_0)] \quad (4)$$

The dead state temperature ( $T_0$ ) and pressure ( $p_0$ ) are set to 298K (25°C) and 101.3 kPa, respectively.

Besides, to evaluate the performance of the whole plant, we define the following specific performance indicators:

- Equivalent Energy Saving (EES), that considers both the electric energy produced and the refrigeration demand covered by the District Cooling network:

$$EES = \dot{m}_{LNG}^{-1} \left( \dot{W}_{net} + \frac{\dot{Q}_{DC,LT}}{EER_{ref,LT}} + \frac{\dot{Q}_{DC,MT}}{EER_{ref,MT}} + \frac{\dot{Q}_{DC,HT}}{EER_{ref,HT}} \right) \quad (5)$$

To estimate the electric energy saving by the district cooling network we transform the thermal energy to electrical energy by using a reference Energy Efficiency Ratio ( $EER_{ref}$ ) for each temperature level. The  $EER_{ref}$  for the low-, medium- and high-temperature district cooling temperatures are set to 1.3, 2.5 and 4.0, respectively.

- Primary Energy Saving (PES):

$$PES = \eta_{ref}^{-1} \left( \dot{W}_{net} + \frac{\dot{Q}_{DC,LT}}{EER_{ref,LT}} + \frac{\dot{Q}_{DC,MT}}{EER_{ref,MT}} + \frac{\dot{Q}_{DC,HT}}{EER_{ref,HT}} \right) \quad (6)$$

Where the thermal efficiency taken as a reference ( $\eta_{ref}$ ) is the typical thermal efficiency of a combined power plant, i.e., 52%.

- Seawater Saving (SWS):

$$SWS = \left[ 1 - (\sum \dot{m}_{SW}) / \dot{m}_{SW,ref} \right] \times 100\% \quad (7)$$

Where  $\dot{m}_{SW,ref}$  is the seawater mass flow rate required by the typical LNG regasification in which LNG cold is wasted to the ambient.

- Exergetic efficiency:

$$\eta_{ex} = \frac{\sum \dot{W}_T + \dot{W}_{EXP} + \sum \dot{E}x_{us,DC}}{\dot{E}x_{in,LNG} + \dot{E}x_{in,WH} + \dot{Q}_{H-3}(1 - T_0/T_{bb}) + \sum \dot{W}_P} \times 100\% \quad (8)$$

## Discussion and Results

Table 2 shows the performance results obtained by the common LNG regasification plant and the results obtained by the proposed polygeneration plant under possible different configurations for the power cycles RC-1 and RC-3. According to these results, the configuration with the best performance indicators is that where both power cycles RC-1 and RC-3 have a reheating stage and recuperator. In this case, the performance of the plant is slightly better than the case without reheating stage [7]. On the other hand, the effect of the recuperator on the performance of the plant is higher than that of the reheating stages.

The polygeneration plant with LNG cold recovery analyzed in this paper produces an Equivalent Energy Saving of 82.6 kWh/ton-LNG, an annual Primary Energy Saving of 165.1 GWh an exergetic efficiency of 35.5%. Furthermore, it achieves a seawater saving of 66.8% with respect to the conventional LNG regasification process without cold recovery.

**Table 2.** Performance results of the proposed polygeneration plant for different configurations.

Configuration	$\dot{W}_{net}$ , MW	DCS, MW	EES, kWh/ton- LNG	PES, GWh/y	SWS, %	$\eta_{ex}$ , %
0	-0.74	0	-6.2	-12.4	0	0
1	3.39	9.0	71.9	143.6	72.4	29.3
2	3.43	9.0	72.2	144.4	72.2	29.1
3	4.35	9.0	79.9	159.7	68.2	34.2
4	4.50	9.0	81.1	162.0	67.6	34.7
5	4.67	9.0	82.6	165.1	66.8	35.5

0 – Typical LNG regasification process without LNG cold recovery.

1 – RC-1 and RC-3 without reheating and without recuperator.

2 – RC-1 and RC-3 with reheating but without recuperator.

3 – RC-1 and RC-3 without reheating but with recuperator.

4 – RC-1 with recuperator but without reheating; RC-3 with recuperator and reheating [7].

5 – RC-1 and RC-3 with both reheating and recuperator.

## Conclusions

In this paper, we presented a polygeneration plant based on the cold recovery from the LNG-regasification process for the production of power and cold. The results show that the polygeneration plant can recover an important part of the energy that is wasted in the common LNG regasification process. Thus, to use LNG cold in cascade in a polygeneration system is a promising way to save energy and reduce the environmental impact of the LNG supply chain. Furthermore, the exergetic efficiency of the system that operates with reheating and recuperator power plants is 35.5%. However, there is still room for improvement and further modifications could be introduced to increase the efficiency of the plant.

## Acknowledgements

Antonio Atienza-Márquez acknowledges the Spanish Ministry of Education, culture and sports the financial support of the predoctoral contract FPU15/04514, scholarships for the training of university teaching staff.

## Nomenclature

DC	District Cooling	NG	Natural Gas
EER	Energy Efficiency Ratio	P	Pressure (MPa) or pump
$\eta$	Efficiency (%)	$\dot{Q}$	Heat flux (kW)
$\dot{E}_x$	Exergy (kW)	s	Entropy (kJ kg <sup>-1</sup> K <sup>-1</sup> )
h	Enthalpy (kJ kg <sup>-1</sup> )	T	Temperature (K) or turbine

LNG Liquefied Natural Gas  
 $\dot{m}$  Mass flow rate (kg s<sup>-1</sup>)

$\dot{W}$  Net work (kW)  
WH Waste heat

## References:

- [1] International Energy Agency (IEA), CO<sub>2</sub> emissions by fuel combustion 2017, OECD Publishing, Paris, 2017. [http://dx.doi.org/10.1787/co2\\_fuel-2017-en](http://dx.doi.org/10.1787/co2_fuel-2017-en)
- [2] BP Energy Outlook – 2018 Edition. <https://www.bp.com/en/global/corporate/energy-economics/energy-outlook.html> (Accessed 22.04.2018).
- [3] European Commission, *European Strategic Energy Technology Plan (SET-Plan)*, 2017. <[https://setis.ec.europa.eu/system/files/integrated\\_set-plan/issues\\_paper\\_action6\\_ee\\_industry\\_0.pdf](https://setis.ec.europa.eu/system/files/integrated_set-plan/issues_paper_action6_ee_industry_0.pdf)>, (Accessed 15 December 2017)
- [4] B.B. Kanbur, L. Xiang, S. Dubey, F.H. Choo, F. Duan, “Cold utilization systems of LNG: A review”, *Renewable and Sustainable Energy Reviews*. 2017;79:1171-1188. <http://doi.org/10.1016/j.rser.2017.05.161>.
- [5] M. Romero Gómez, R. Ferreiro García, J. Romero Gómez, J. Carbia Carril, “Review of thermal power cycles exploiting the exergy of liquefied natural gas in the regasification process”, *Renewable and Sustainable Energy Reviews*. 2014;38:781-795. <http://doi.org/10.1016/j.rser.2014.07.029>.
- [6] T. Miyazaki, Y. Kang, A. Akisawa, T. Kashiwagi, “A combined power cycle using refuse incineration and LNG cold energy”. *Energy*, 2000;25:639-655. [http://doi.org/10.1016/S0360-5442\(00\)00002-5](http://doi.org/10.1016/S0360-5442(00)00002-5).
- [7] A. Atienza-Márquez, J.C. Bruno, A. Coronas, “Cold recovery from LNG-regasification for polygeneration applications”, *Applied Thermal Engineering*. 2018;132:463-478. <http://doi.org/10.1016/j.applthermaleng.2017.12.073>.
- [8] Osaka Gas Co., Ltd. 2017. <<http://www.osakagas.co.jp/en/index.html>>(Accessed 22.04.2018).
- [9] Y. Akasaka, “Power generation plant using LNG cold in Osaka Gas”, *Journal of Cryogenics and Superconductivity Society of Japan*. 1984;19:12-18. <https://doi.org/10.2221/jcsj.19.12> (In Japanese).
- [10] Tokyo Gas Co., Ltd. 2017. <<http://www.tokyo-gas.co.jp/en/>>(Accessed 22.04.2018).
- [11] S. Hirakawa, K. Kosugi, “Utilization of LNG cold”, *International Journal of Refrigeration*. 1981;4:17-21. [http://doi.org/10.1016/0140-7007\(81\)90076-1](http://doi.org/10.1016/0140-7007(81)90076-1).
- [12] F-Chart Software, Engineering Equation Solver (EES), 2017. <<http://fchart.com/ees/>> (Accessed 22.04.2018)

# Small-scale Pumped Heat Electricity Storage for decentralised combined Heat and Power Generation

Annelies Vandersickel\*, J Loeff, Amir Aboueldahabb, Hartmut Spliethoff

<sup>1</sup>Institute for Energy Systems, Technical University Munich,

Boltzmannstr. 15, 85748 Garching b. München, Germany

\*Corresponding author: annelies.vandersickel@tum.de

## Abstract

Decentralised rural electrification by means of renewable energy poses a challenge to electricity storage devices. Currently used lead-acid batteries have low lifetime and are a threat to human health and environment. Using environmentally friendly and long-lasting materials, Pumped Heat Energy Storage could offer a valuable alternative to these batteries. In this paper, a Pumped Heat Energy Storage is analysed with respect to its potential as a combined heat and power storage for the autarkic cogeneration of heat and power from renewable energy. The charging and discharging operation are modelled in Matlab for a kW-scale configuration using a two-stage heat pump for charging and pressurized water as the thermal energy storage. During discharge, the stored heat can either be reconverted to electricity using a subcritical organic Rankine cycle or immediately be used in various household applications. Finally, the economic feasibility of the Pumped Heat Energy Storage is compared to that of a lead-acid battery system using cost function optimization for different scenarios.

**Keywords:** Pumped heat energy storage, rural electrification, water storage

## Introduction

More than 1.6 billion people worldwide do not have access to electricity and most of these people live in rural areas of the developing world [1]. Renewable energies provide not only the most environmentally friendly but also the most cost-effective means of rural electrification [2]. Besides economical and institutional obstacles, storing inherently intermittent renewable energy sources is a technical challenge, which in practice is solved by the use of cheap and easily available lead-acid accumulators. Their limited cycling capability however leads to replacement every 3-5 years [3] and a lack of infrastructure complicates recycling, thus increasing human exposure to lead and causing severe health problems [4]. In addition, improper disposal causes hydrofluoric acid leakage, which heavily pollutes the environment. Pumped Heat Electricity Storage (PHES) could be a valuable alternative, providing electricity storage while using environmentally harmless materials and having a much longer lifetime.

Several types of PHES<sup>2</sup> have been discussed [5,6,7,8]. The working principle is the same for all proposed schemes: In times of excess electricity generation, a heat pump (HP) is used to extract heat from a low temperature heat reservoir, upgrade it to a higher temperature level and store said heat in a second reservoir till later use. When demand exceeds electricity generation, a heat engine converts the stored thermal energy back to electrical energy.

---

<sup>2</sup> also known as: Pumped Thermal Electricity Storage (PTES), Electrothermal Energy Storage (ETES), Thermo-electrical Energy Storage (TEES), Transformed Heat Energy Storage (THES) or Compressed Heat Energy Storage (CHEST)



All PHES concepts currently found in literature are intended for bulk scale electricity storage and cannot be applied for a decentralised application in the order of only a few kW, as required for rural electrification. There are first attempts to implement reversible heat pumping on a household level [9,10], focussing however on increased utilisation of the already existing heat pump instead of providing a system to store intermittent electrical energy. Objective of this paper is to assess the pumped heat storage concept for use in a rural low cost environment as a small scale combined heat and power system for autarkic cogeneration of power and heat from photovoltaic (PV) and wind.

### PHES concept for decentralised heat and power generation

Besides robust operation and a minimisation of environmental and health hazards, low cost is the main criteria for a design that is applicable for rural areas. To assure cost effective system design, the PHES concept has been reduced to its simplest form, fixing several design criteria beforehand.

- No cold storage is installed, instead the environment is used as the low temperature heat reservoir
- Water is used as the storage medium for the high temperature heat reservoir, a two-tank system with vacuum insulated tanks at 80 and 115 °C.
- Working fluids that would require sub-ambient or supercritical pressure levels to work under given operating conditions are not considered
- Only of the shelf components are considered in the design

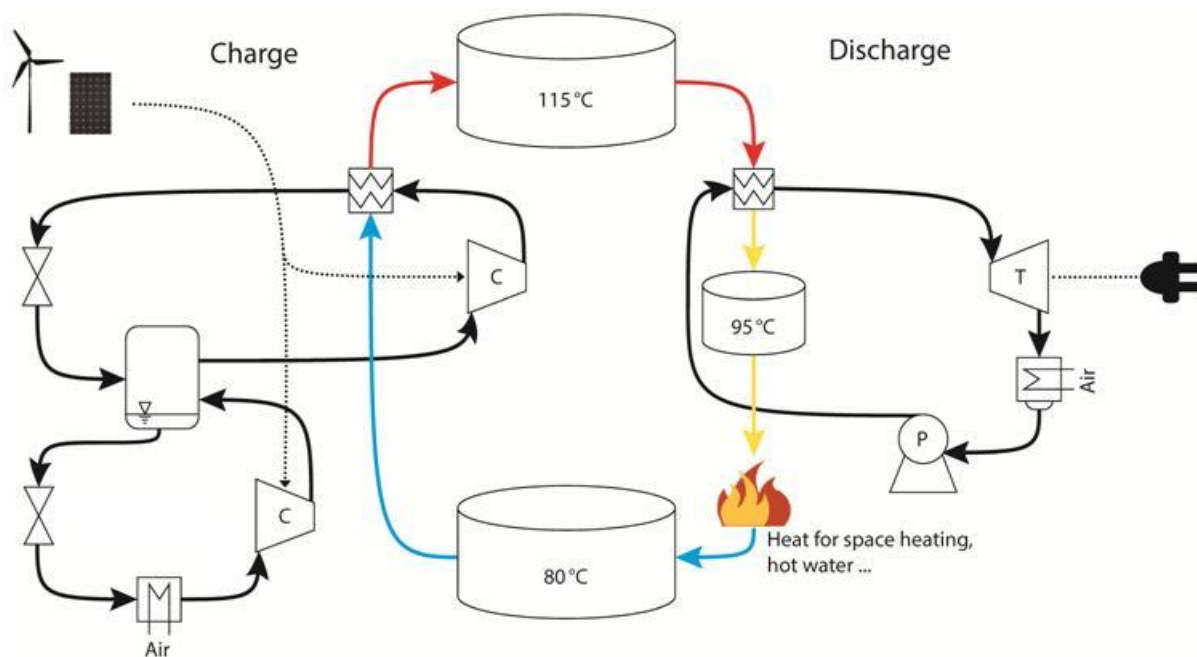


Fig. 1. Set-up of the PHES system: two stage HP, heat storage, single-stage ORC

Direct utilization of power generated by PV and wind is always prioritized and charging/discharging of the PHES storage system only takes place, when there is a mismatch between power generated and electricity demand. During charging, a two stage air heat pump raises the water temperature from 80°C to 115°C (Fig.1). During discharge, the high temperature water is used to drive an ORC and generate electricity. Heat demand is covered from the tank at 95°C or when the latter is not sufficient at 115°C.

As discussed in [11], for the given design constraints a single stage ORC using R245fa and a 2-stage heat pump cycle with a flash intercooled configuration using R142b as working fluid

gave the highest COP. As off-the-shelf scroll compressors are designed for refrigerant condensation temperatures of 85°C at most, the HP herein employs two reciprocating compressors. The resulting HP and ORC efficiencies vary – for the fixed maximum storage temperature of 115°C and for ambient temperatures between 10 and 30°C – between 1.98 and 2.32 for the HP coefficient of performance and 7.28% and 4.71% for the ORC first law efficiency. The HP minimum power uptake is fixed at  $P_{HP,min} = P_{HP,max}/3$  and for the ORC a minimum power output  $P_{ORC,min} = P_{ORC,max}/2$  is assumed.<sup>3</sup>

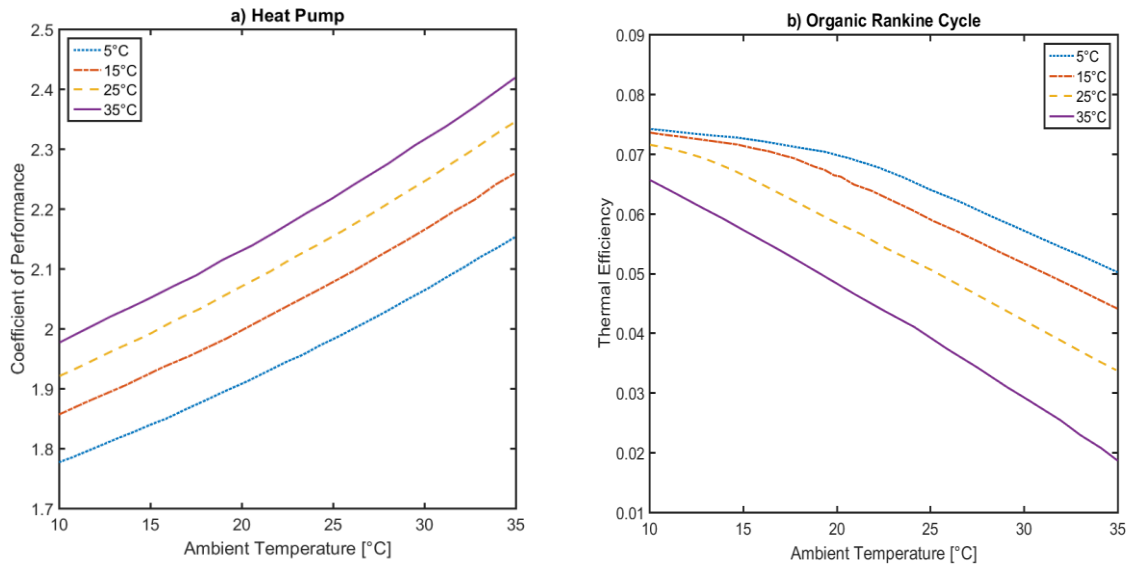


Fig.2: Efficiency of a) HP and b) ORC with respect to ambient temperature and temperature spread between hot tanks of the high temperature storage (upper T fixed at 115°C)

From Figure 2, it is obvious that the heat pump operation benefits from an increasing temperature spread between the two hot tanks whilst it simultaneously downgrades ORC efficiency. To maximize the efficiency of the ORC, while the heat pump is still profiting from the large temperature spread, the heat source (high temperature water) is only partially exploited and the remainder is stored at a temperature of 95°C to be used later to cover heat demand. To absorb excess electricity with insufficient power to drive the heat pump ( $P_{excess} < P_{HP,min}$ ) or to benefit from excessive power generation ( $P_{excess} = P_{in} - P_{HP,min}$ ), the heat pump is assisted by an electrical heater with a maximum capacity that matches  $P_{HP,min}$ .

## Methodology

The economic feasibility of the PHES is compared to that of a lead-acid battery systems using cost function optimization for different scenarios. Different storage technologies may show opposing trends for power and capacity related costs and the efficiency of the storage unit has direct consequences for the amount of electricity needed to cover a given demand. The power generation (in this case from PV and wind) and its associated costs should therefore be included into the comparison to obtain meaningful results [12]. To this end, the Matlab built-in genetic algorithm combined with a process model of the PHES, is used to size the PHES system, PV and wind turbine park, minimizing the invest costs of the entire energy

<sup>3</sup> Reciprocating compressors with at least four pistons have the capability to run any even number of pistons idle, whereas scroll devices can only be controlled by a variable-frequency drive.

supply and storage system for given electricity and heat demand profiles (time series). Details of the model and optimisation strategy can be found in [11].

The same GA-routine is used to size a reference system consisting of PV and wind power generation combined with lead-acid batteries as the only means of electricity storage. Heat demand in this case is supplied by an electrical boiler (max. 10 kW) for simplicity. The GA decision variables are:

- the PV installed nominal power  $P_{PV}$  (kW<sub>p</sub>) and PV inclination angle (°)
- the installed wind turbine power  $P_{Wind}$  (kW) and installation height  $H_{Wind}$  (m).
- the storage capacity, which is either the size of the thermal energy storage  $V_{St}$  (m<sup>3</sup>) for the PHES or the size of batteries  $E_{bat}$  (kWh)
- in selected cases, the installed power of the heat pump (kW) and ORC (kW)

As is typical for rural electrification design, electricity and heat requirements need to be met within certain bounds over the entire considered period (T) only. This is modelled by a maximum allowable loss of power and loss of heat probability of 2% [11]. To account for seasonal variations, optimisation is performed for a yearly simulation with one-hour time steps, matching the resolution of available data sets for solar irradiance, wind speed and ambient temperature.

Finally, to assess the influence of location and consequently weather conditions as well as the composition of the demand side on the profitability of the PHES, the analysis has been repeated for multiple locations and demand scenarios. The chosen locations were San Salvador, the capital of El Salvador, Norderney, one the East Frisian Islands off the North Sea coast of Germany and Munich, a city in Germany. San Salvador represents the global South characterised by a strong solar insolation but rather weak wind velocities. Norderney represents the other extreme, with strong winds but little sun. Munich is a typical central European location with rather low solar and wind potential.

In the absence of reliable data for rural areas, load curves for electricity and thermal energy demand are modelled following [13], as detailed in [11]. This approach yields heat and electricity profiles representative of a typical 4-person western household, slightly shifted towards the evening hours to be more representative of rural demand. Yearly electricity demand is 3602 kWh/a with a maximum electrical power consumption of 4.3 kW. Yearly heat demand is 9554 kWh/a, with a peak of 7.3 kW. Additionally, a sensitivity study with double heat demand and double electricity demand was performed.

## Discussion and Results

Key optimisation results for different system configurations assessed for Munich weather conditions are given in table 1, together with the corresponding specific costs per kWh energy demand. The latter are computed based on the equivalent annual costs divided by the total yearly energy demand, being the sum of the yearly heat and electricity demand.

What stands out when looking at all PHES results is the presence of a small battery of 2.4 kWh, installed in parallel to the PHES. This may seem contrary, given that the aim of the PHES is to replace batteries. It is however not economically viable to run the ORC at its minimum load  $P_{ORC,min}$  of 1.5 kW resp. 0.5kW for every power demand smaller than  $P_{ORC,min}$ . Low power demand is therefore met using the battery as long as it is charged, when the battery is empty, the ORC is operated and the excess electricity generation is used to charge the battery.

In our previous work [11], the power rating of the ORC ( $P_{ORC,max}$ ) was fixed at 3kW based on an assessment of the demand profile. The battery size was fixed at 2.4 kWh, which was found to offer a good balance between minimizing unnecessary electricity production from the ORC while not playing a dominant role as electricity storage (Table 1, row 1). Despite the

battery, ca. 24% of the electrical energy produced by the ORC cannot be used, not even to charge the battery, mainly due to the batteries maximum charge rate. For most of the year (more than 760 hours) the ORC was found running when the residual power demand was actually smaller than the minimum power output of the ORC (1,5 kW) but could not be supplied by the small battery.

Optimisation of the ORC power rating in addition to the other variables results in a smaller ORC size of 1 kW, which corresponds to the smallest available off-the-shelve scroll turbine and hence the lower limit of the ORC rating (Table 1, row 3). Compared to the case with a 3kW ORC, the increased utilization of the ORC and the corresponding reduction of the excess electricity generation allows for a reduction in the overall system size and reduced costs.

The design decision to use only off-the-shelves components significantly affects the system's performance. Despite the 16% cost reduction due to the additional ORC size optimisation, the standard PHES design is not capable of competing with currently used lead-acid batteries. As discussed in [11], significant improvements of all PHES components at little extra cost is required for the PHES to be cost competitive with the battery only system. Although such improvement is technically possible, the development of e.g. scroll compressors for 115°C as required here is currently hindered by a lack of demand. A roundtrip efficiency of 26% would suffice to create a competitive storage system.

Table 1. Key Results from GA optimisation for different configurations in Munich

<i>Configuration</i>	<i>Specific Costs<sup>1</sup></i> [\$/kWh]	<i>Solar</i> [kW <sub>p</sub> ]	<i>Wind</i> [kW]	<i>Storage Tank</i> [m <sup>3</sup> ] [kWh <sub>th</sub> ]		<i>Battery</i> [kWh]	<i>HP</i> [kW]	<i>ORC</i> [kW]
<i>Standard (ORC fixed)</i>	1.40	75.91	2.99	27.6	1006	2.4	43	3
<i>Improved (ORC fixed)</i>	0.97	41.88	2.06	36.5	1333	2.4	25	3
<i>Standard (ORC small)</i>	1.18	70.6	2.7	25.7	939	2.4	43	1
<b><i>Battery</i></b>	0.96	63.30	2.16	-	-	30.6	-	-

<sup>1</sup>specific costs based on total energy demand (heat + power)

The performed variation of the weather (location) and demand profiles (shown in Table 2 and 3), suggests that high wind generation and in particular, high heat-to-power ratios are beneficial for cost competitiveness of the PHES compared to the battery based system. Comparable system cost could for example be achieved for Norderney with a doubled heat demand, even without the above discussed improvement of the system components. In this case, the PHES acts primarily as a high temperature heat pump with decoupling of heat generation and heat demand due to the thermal storage tank. Electricity demand is primarily met through direct usage of the generated electricity and the contribution of the ORC reduces from 20% to 8%.

## Conclusions

For the system model designed based on off-the-shelve system components, the power-to-power roundtrip efficiency reaches an annual averaged value of only 5 to 12% and the system is not capable of competing with currently used lead-acid batteries. Possible improvements of compressor and expander isentropic efficiency as well as larger heat exchange areas could, however, enhance HP and ORC performance. For the Munich case, a roundtrip efficiency of 26% would suffice to create a competitive storage system. Alternatively, more beneficial use

cases can be sought for. The higher the heat-to-power ratio and the more wind based the generation becomes, the more beneficially the PHES becomes compared to the battery alternative.

In addition to low performance of off-the-shelve components in the kW-range, the minimum power output of the ORC was found to restrict the efficient operation of the PHES and impose the use of a small battery. The latter is needed to supply electricity when demand is lower than the minimum power output of the ORC. A further challenge hence is to reduce the minimum load operation of all equipment, allowing eliminating this small battery.

Table 2. Key Results from GA optimisation for different demand scenarios in Norderney

Configuration	Specific Costs <sup>1</sup>	Solar	Wind	Storage Tank		Battery	HP	ORC	
	[\$/kWh]	[kW <sub>p</sub> ]	[kW]	[m <sup>3</sup> ]	[kWh <sub>th</sub> ]	[kWh]	[kW]	[kW]	
<b>PHES</b>	Standard demand	0.68	2.6	12.4	9.6	349	2.4	9.6	1
	Electricity demand x 2	0.79	4.8	15.9	13.8	504	2.4	11.5	1
	Heat demand x 2	0.57	1.1	17.6	19.2	699	2.4	16.8	1
<b>Battery</b>	Standard demand	0.53	2.2	10.9	-	-	16.1	-	-
	Electricity demand x 2	0.62	0.7	13.6	-	-	38.1	-	-
	Heat demand x 2	0.54	2	18.9	-	-	16.2	-	-

<sup>1</sup>specific costs based on total energy demand (heat + power)

Table 3. Key Results from GA optimisation for different demand scenarios in San Salvador

Configuration	Specific Costs <sup>1</sup>	Solar	Wind	Storage Tank		Battery	HP	ORC	
	[\$/kWh]	[kW <sub>p</sub> ]	[kW]	[m <sup>3</sup> ]	[kWh <sub>th</sub> ]	[kWh]	[kW]	[kW]	
<b>PHES</b>	Standard demand	0.28	12.5	0.1	6.3	229	2.4	5	1
	Electricity demand x 2	0.33	25.5	0.1	7.3	265	2.4	10	1
	Heat demand x 2	0.17	15.6	0.1	5.4	197	2.4	5.2	1
<b>Battery</b>	Standard Demand	0.15	9.7	0.1	-	-	10.5	-	-
	Electricity demand x 2	0.17	12.5	0.1	-	-	21.7	-	-
	Heat demand x 2	0.12	17	0.1	-	-	10.2	-	-

<sup>1</sup>specific costs based on total energy demand (heat + power)

## References

- [1] Barnes, Douglas F., The challenge of rural electrification: strategies for developing countries. Washington DC, USA: Earthscan; 2007.
- [2] Urmee T., Harries D., Schlapfer A., Issues related to rural electrification using

- renewable energy in developing countries of Asia and Pacific. *Renewable Energy* 2009; 34:354-357.
- [3] Raman P., Murali J., Sakthivadivel D., Vigneswaran S.S., Opportunities and challenges in setting up solar photo voltaic based micro grids for electrification in rural areas of India. *Renew Sust Energ Rev* 2012; 16:3320-3325.
  - [4] Haeflinger P. et. al., Mass lead intoxication from informal used lead-acid battery recycling in Dakar, Senegal. *Environmental Health Perspectives* 2009; 117:1535-1540.
  - [5] Desrues T., Ruer J., Marty P., Fourmigué J.F., A thermal energy storage process for large scale electric applications. *Applied Thermal Energy* 2010; 30:425-432.
  - [6] Howes J., Concept and Development of a Pumped Heat Electricity Storage Device. *Proceedings of the IEEE* 2012; 100:493-503.
  - [7] Mercangöz M., Hemrle J., Kaufmann L., Z'Graggen A., Ohler C., Electrothermal energy storage with transcritical CO<sub>2</sub> cycles. *Energy* 2012; 45:407-415.
  - [8] Morandin M., Mercangöz M., Hemrle J., Maréchal M., Favrat D., Thermo-economic design optimization of a thermo-electric energy storage system based on transcritical CO<sub>2</sub> cycles. *Energy* 2013; 58:571-587.
  - [9] Dumont O., Quoilin S., Lemort V., Experimental investigation of a reversible heat pump/organic Rankine cycle unit designed to be coupled with a passive house to get a Net Zero Energy Building. *International Journal of Refrigeration* 2015
  - [10] Schimpf S., Span R., Techno-economic evaluation of a solar assisted combined heat pump-Organic Rankine Cycle system. *Energy Conversion and Management* 2015
  - [11] Vandersickel A., Aboueldehab A., Spliethoff H., Small-scale Pumped Heat Electricity Storage for decentralised combined Heat and Power Generation. *Proceedings of ECOS2016, Portoroz, Slovenia*
  - [12] Yang H., Zhou W., Lu L., Fang Z., Optimal sizing method for stand-alone hybrid solar-wind system with LPSP technology by using genetic algorithm. *Solar Energy* 2008; 82:354-367.
  - [13] Paatero J., Lund P.D., A model for generating household electricity load profiles. *International Journal of Energy Research* 2006; 30:273-290.

# Experimental Investigation of the Effect of Magnetic Field on Vapour Absorption Rate of LiBr+H<sub>2</sub>O Nanofluid

Shenyi Wu\* and Camilo Rincon Ortiz

Fluids and Thermal Engineering Research Group  
Faculty of Engineering

University of Nottingham, University Park, Nottingham, NG7 2RD, United Kingdom

\* Shenyi.wu@nottingham.ac.uk

## Abstract

This paper reports an experimental study of using an aqueous lithium bromide solution based nanofluid to enhance the vapour absorption process. The experimental results show that the vapour absorption rate increase with use of the nanofluid. By applying an external magnetic field to influence the movement of the nanofluid, a further increase of the absorption rate was observed. The enhancement seems to associate with the frequency of the nanoparticles movement induced by the magnetic field. Our limited experimental results suggest that the high frequency of the nanoparticles' movement benefits the vapour absorption process.

**Keywords:** Nanofluid, heat and mass transfer, vapour absorption refrigeration, magnetic field

## Introduction

The effectiveness of vapour absorption relies on heat and mass transfer in the process. Due to low mass diffusivity in liquid, an efficient vapour absorption process requires a large ratio of surface area to volume to reduce the resistance of heat/mass transfer in the liquid phase. Creating very thin film on a vertical plate or very fine liquid droplets are the conventional approach to increase heat/mass transfer in the process. Use of surfactant agent to increase instability at the vapour-liquid interface is another way to boost the mass transfer in vapour absorption systems. These technologies have been extensively investigated and widely employed in modern vapour absorption refrigeration/heat pump systems to improve mass transfer. Potential for further improvement with these technologies appears to be limited. New approaches to further improve the process are needed.

Kim *et al* reported their works on bubble absorber with binary nanofluid [1, 2]. With the addition of nanoparticles: Cu, CuO or Al<sub>2</sub>O<sub>3</sub>, to an NH<sub>3</sub>-H<sub>2</sub>O solution, they found that the NH<sub>3</sub>-H<sub>2</sub>O binary nanofluids demonstrated excellent absorption ability. The effective absorption ratio, which is defined as the ratio of the absorption rate by the nanofluid to the base fluid (without addition of nanoparticles), was increased in all cases with the maximum effective absorption ratio of 3.21 when the nanofluid contained 18.7% ammonia and 0.10% of Cu nanoparticles [1]. More encouragingly, their work also found that the absorbers with nanofluids performed better than those without nanofluid as the absorption potential of the solution decreases. Kang *et al* [3] observed that carbon nanotubes at concentrations of 0.01 and 0.1% have a higher rate of mass transfer increase compared with Fe nanoparticles, concluding that CNT is the most optimal nanoparticles to be used in absorption systems. They measured the absorption rate in a H<sub>2</sub>O/LiBr solution for a falling film absorber. The maximum mass transfer for CNT nanoparticles was 2.48 at 0.01 wt% while the maximum enhancement for Fe was 1.90 for 0.1 wt%.

Using magnetic field to enhance the thermal conductivity of nanofluid has been investigated. One of these is the conduction through linear agglomerates of nanoparticles in the working fluid. Philip *et. al* [4] observed a 300% enhancement from the nanofluids with 2–10nm surfactant-coated Fe<sub>3</sub>O<sub>4</sub> magnetic nanoparticles. Angayarkanni & Philip [5] reported an increase in the thermal conductivity in a certain magnetic field range for ferro-oxidizer

nanoparticles. A thermal conductivity increment of 300% was observed with the 6.3vol% particle loading. This intensification in thermal conductivity is accredited to the effective conduction of heat through the chainlike structure formed under a magnetic field when the dipolar interaction energy becomes greater than the thermal energy. Suresh and Bhalerao [6] used a magnetic field of 50Hz to analyse the mass transfer effect using ferromagnetic nanofluids. They found numerically a 40% enhancement in the mass transfer with the oscillating magnetic field on but non-effect with the magnetic field off. However, Komati and Suresh [7] found no further enhancement using a periodic oscillating magnetic field in their experiment using nano ferrofluid/ MDEA for a CO<sub>2</sub> absorption in a wetted wall column. They attributed the difference to the nature of the particles that the 15nm particles lost the single-domain making it difficult to follow the external magnetic field. Komati and Suresh [8] also experimentally investigated the effect of magnetic iron oxide nanoparticles on the gases absorbed where a mixture of carbon dioxide and oxygen is absorbed by liquid nanofluid in a capillary tube and a wetted wall column. They found a considerable increase in mass transfer coefficient at the presence of both the magnetic field and the nanoparticles and the enhancement depends on the size and volume of the particles. They also observed a relation between the increases in Sherwood Number.

The past researches show that nanofluids can enhance vapour absorption process and the enhancement can be further achieved under influence of magnetic field. This work, through experimental tests, investigated the effectiveness of this approach aiming for LiBr-H<sub>2</sub>O vapour absorption refrigeration applications to further explore this technology.

### Experimental setup and testing procedures

The experimental investigation was carried out on a rig as shown in Figures 1. It consists of a generator-condenser assembly at the top and an evaporator-absorber assembly below the generator-condenser assembly. Heating is supplied to the generator and evaporator vessels with a 2.4kW and an 800W, respectively. The generating and evaporating temperatures are separately controlled by two temperature controllers to the set points. Tap water is used to remove the heat from the absorber and the condenser. In the absorber, the solution is sprayed in a hollow cone shape before it contacts the wall and then flows down along the in liquid film.

The absorption test started with releasing a fixed amount of the solution from the generator firstly into the absorber. The solution was then circulated in the absorber during the absorption test. The absorption continued until the water level in the evaporator reached a pre-set point. After the absorption test, the solution was pumped back to the generator where it was concentrated while the water from the concentration process was fed back to the evaporator. All relevant temperature were set and adjusted within the same ranges and so does the solution circulation flow rate in the absorber during the absorption test to maintain a consistent test condition.

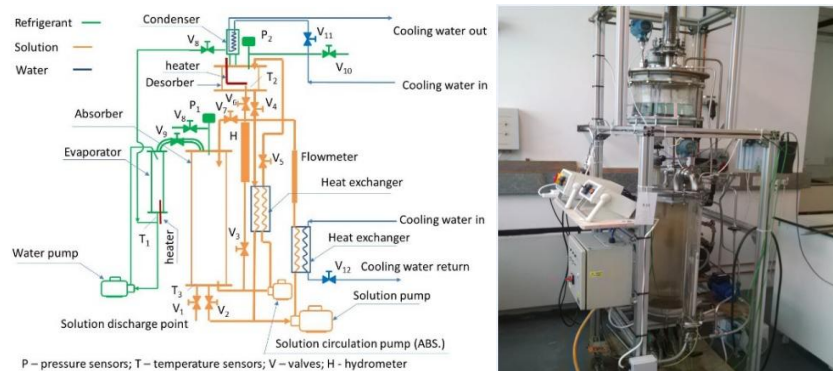


Figure 1 Schematic diagram and Photo of the rig



The absorption rate is calculated from:

$$\dot{m} = \frac{(\text{initial water level} - \text{end water level}) \times \text{mass}}{\text{duration time (sec)}} \quad (1)$$

where the mass in the equation represents the mass for every centimetre water level change in the evaporator vessel. Its value is 0.02kg/mm for this particular setup.

### The experimental conditions and results

The vapour absorption in the absorber vessel is an adiabatic process if neglecting the heat transfer through glass wall of the vessel. The solution in the absorber vessel is circulated at a constant flow rate with a spray nozzle to distribute the solution onto the wall of the absorber vessel. The experiment was carried out with two circulation flow rates either in 3L/min or 3.5L/min. The temperature of the solution was 25°C before spraying, which was achieved by adjusting the cooling water flow rate through the heat exchanger. The amount and mass concentration of the solution released to the absorber vessel for each vapour absorption test were 5.92kg and 54.7%, respectively. The solution concentration decreased to 53.9% and the quantity increased to 6.01kg before recording the data. The test ended when a fixed amount of 0.3kg water at 5°C was absorbed by the solution. Magnetic strip was used to apply the magnetic field to the nanofluid in different configurations for different distribution of magnetic fields in the absorber vessel. Table 1 is a summary of the tests carried out with different combinations of the solutions, the circulating flow rates and the configurations of magnetic strip on the absorption vessel.

Table 1 the tests completed in the investigation

	LiBr+H <sub>2</sub> O (25°C)		LiBr+H <sub>2</sub> O+Fe <sub>2</sub> O <sub>3</sub> (25°C)	
	3.0 L min <sup>-1</sup>	3.5 L min <sup>-1</sup>	3.0 L min <sup>-1</sup>	3.5 L min <sup>-1</sup>
No Magnetic strip	√	√	√	√
Magnetic strip with no gap	N/A	N/A	√	√
Magnetic strip with 2cm gap	N/A	N/A	√	√
Magnetic strip with 3.5cm gap	N/A	N/A	√	√

Base vapour absorption rate

Figure 3 shows the vapour absorption rates of LiBr+H<sub>2</sub>O solution for the solution circulation at 3.0L min<sup>-1</sup> and 3.5L min<sup>-1</sup>. The vapour absorption rate at 3.5L min<sup>-1</sup> is higher than that at 3L min<sup>-1</sup>. This is because the higher circulation flow rate created a larger contacting surface area for the absorption.

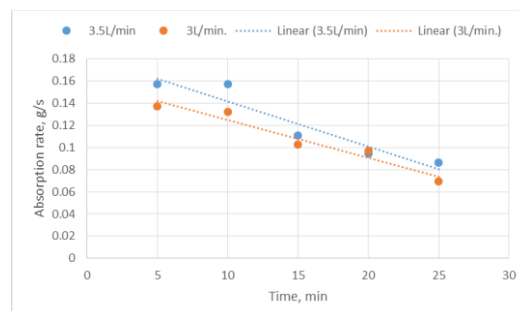


Figure 3 the vapour absorption rate of base absorption solution LiBr+H<sub>2</sub>O

### Vapour absorption rate of the nanofluid

In the nanofluid tests, the absorbent solution is a mixture of LiBr+H<sub>2</sub>O+Fe<sub>2</sub>O<sub>3</sub>. The nanoparticles was Aldrich Iron(III) oxide nanopowder, <50nm. The 25 grams of the nanoparticles was mixed with 15kg LiBr+H<sub>2</sub>O solution of 53% concentration. The nanoparticles were dispersed in the solution with ultrasonic generator for half an hour before being fed into the rig. It was noted the deposition of nanoparticles in the vessel after several

hours; however, the nanoparticles were uniformly suspended in the solution from naked eyes observation after the circulation.

Figure 4 shows the vapour absorption rates from four experimental tests with the circulation flow rates of  $3\text{L min}^{-1}$  and  $3.5\text{L min}^{-1}$ , respectively. It can be found that that the vapour absorption rates continuously decline over the period of the absorption process. One can find in Figure 5 that the vapour absorption rate for the  $3.5\text{L min}^{-1}$  circulation flow rate is always larger than that for  $3.0\text{L min}^{-1}$ . The trend lines indicate that the difference of the vapour absorption rates between the two solution flow rates remains almost constant. The difference between them is due to the solution coverage areas and flow characteristics at the different circulation flow rates.

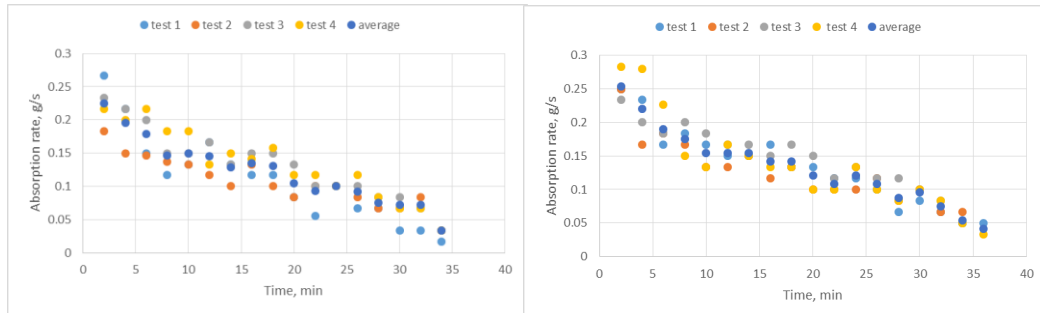


Figure 4 The vapour absorption rates with the solution circulation flow rates  $3\text{L min}^{-1}$ (left) and  $3.5\text{L min}^{-1}$  (right)

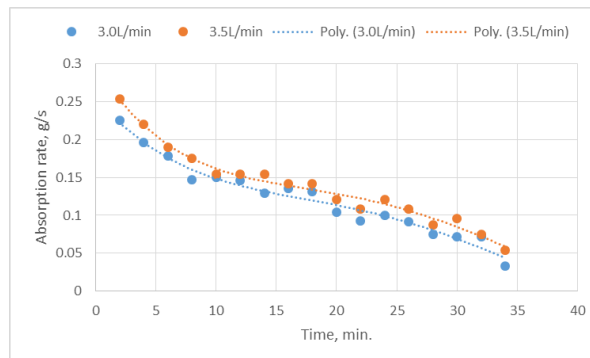


Figure 5 comparison of average absorption rates between the circulating flow rates  $3\text{L min}^{-1}$  and  $3.5\text{L min}^{-1}$

### Vapour absorption rate under influence of the external magnetic field

The external magnetic field was applied to the nanofluid by spirally winding a continue piece of magnetic strip onto the outside of the absorber vessel with different gap “a” and the width of the section covered by magnetic strip (b) as shown in Figure 6 (a). Three configurations were constructed for investigation: a) no gap ( $a = 0\text{cm}$ ,  $b = 15.4\text{cm}$ ), small gap ( $a = 2\text{cm}$ ,  $b = 38.4\text{cm}$ ) and large gap ( $a = 3.5\text{cm}$ ,  $b = 41\text{cm}$ ). Figure 6 (b) is a photo of the vessel wound with magnetic strip.

A handheld Gauss meter GM 08 was used to measure the magnetic flux density. The measured magnetic flux density was  $52.2\text{ mT}$  (milliTesla) without the glass vessel. When measured inside the glass vessel, i.e., a  $14\text{mm}$  thickness of glass wall is in between the probe and the magnetic strip, the magnetic flux density decreased to  $44\text{ mT}$ . The measurement was taken without the solution.

The results from the tests are shown in Figure 7. One can find that the difference of the vapour absorption process responds to the three configurations. In average, the test with  $2\text{cm}$  gap ( $a = 2\text{cm}$ ) gave the highest vapour absorption rate, then  $3.5\text{cm}$  gap ( $a = 3.5\text{cm}$ ) and followed by the no gap ( $a = 0\text{cm}$ ) in the both  $3\text{L min}^{-1}$  and  $3.5\text{L min}^{-1}$  circulation flow rates.

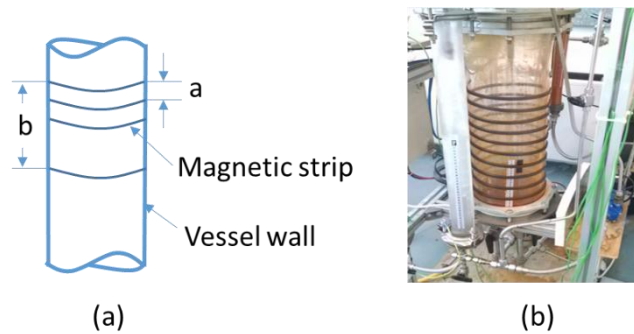


Figure 6 the magnetic strip configuration on the absorber vessel wall

One can find from Figure 8 that the absorption rates increase in the cases of using nanoparticles and the magnetic strip on the absorber vessel on the same operating conditions. Compared with the base fluid at  $3\text{L min}^{-1}$  circulation flow rate, the vapour absorption rates for the nanofluid is 1.32 higher. With the external magnetic field applied, the vapour absorption rate is 1.53 times higher than that of the base fluid. It is also observed that a significant increase of the absorption rate with  $3.5\text{L min}^{-1}$  circulation flow rate and 2cm gap windings. The vapour absorption rate in this case is 1.67 times higher than the base fluid.

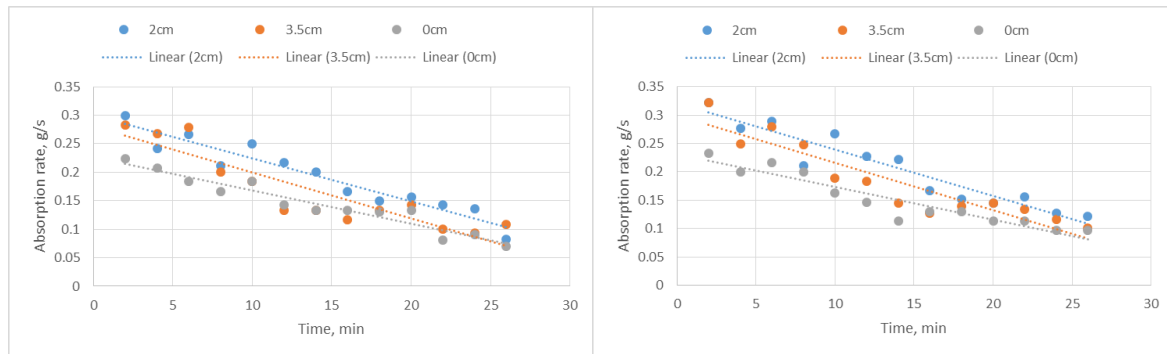


Figure 7 the vapour absorption rates with magnetic strip with  $3\text{L min}^{-1}$  solution circulating flow rate (left) and  $3.5\text{L min}^{-1}$  solution circulating flow rate (right)

### The effectiveness of applying magnetic field to Ferro-nanofluid for vapour absorption process

One can find from Figure 9 that at all sampling points but one the absorption rates in the case with the magnetic field were higher than that without it. The larger difference between the two linear trend lines may suggest that the influence of the magnetic field is more significant at the early stage. This is, perhaps, because the movement of the nanoparticles in the liquid phase accelerates the heat/mass transport there when a large concentration gradient exists in the liquid phase and so enhances the overall vapour absorption process. As the absorption continues, the concentration gradient in the liquid phase becomes smaller at the late stage. So, the movement of nanoparticles becomes less effect on the overall vapour absorption process. A further observation on Figure 8 could find that the influence of the external magnetic field on the vapour absorption rate is stronger in  $3.5\text{L min}^{-1}$  circulation flow rate than  $3.0\text{L min}^{-1}$ . The ratios of the vapour absorption rates delivered by magnetically assisted process to non-magnetically assisted process are 1.46 for  $3.5\text{L min}^{-1}$  and 1.32 for  $3.0\text{L min}^{-1}$ . The high ratio of  $3.5\text{L min}^{-1}$  demonstrates that the magnetically assisted is more effective on the thick film flow according to Table 2.

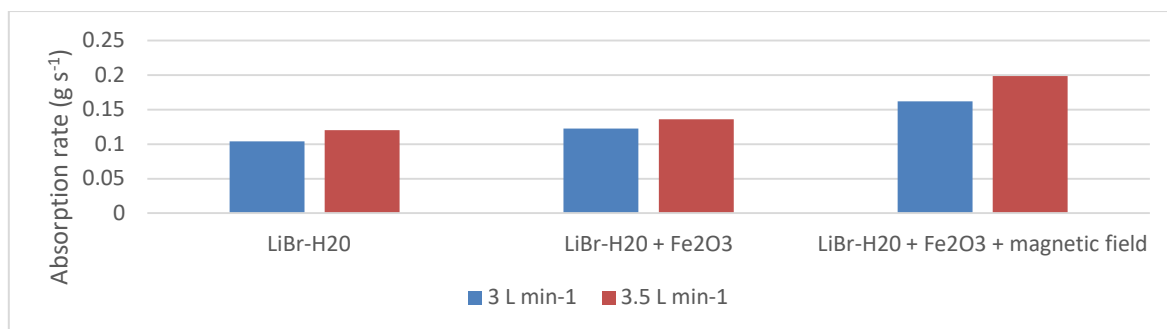


Figure 8 Comparison of the vapour absorption rates from the experimental tests with/without additions of nanoparticles and external magnetic field

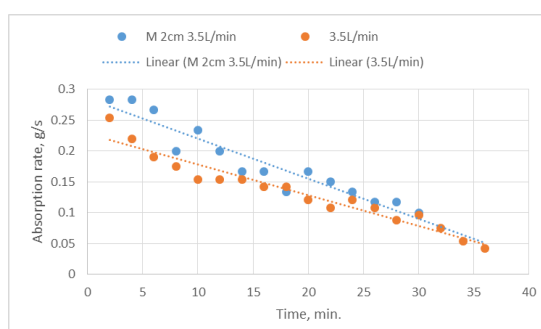


Figure 9 Comparison of the vapour absorption rates of the processes influenced/not influenced by the magnetic field

The thermal images in Figure 10 show the temperature increases on the absorber vessel wall in relation to the influence of magnetic field. The higher temperature increment at  $3.5\text{L min}^{-1}$  than  $3\text{L min}^{-1}$  is consistent with the higher increment of the vapour absorption rate at  $3.5\text{L min}^{-1}$ , which confirms the results shown in Figure 5.

### The frequency of the nanoparticle movement and the vapour absorption rate

The sectional profile of the magnetic strip used for creating the magnetic fields is 10mm by 4mm in width and thickness. The magnetic intensity profile of such a magneto is schematically shown in Figure 11 (a). When the magnetic strip were helically wound on to the absorber vessel as shown in Figure 11 (b), it asserts a variable magnetic field in the absorber vessel, which forces the nanoparticles moving towards the wall of the absorber vessel. However, the force of diffusiophoresis due to concentration gradient in the base fluid does oppositely. Under the influence of these forces, the nanoparticles could slip in the base fluid. Figure 11 (b) graphically illustrates a possible travel route for a single nanoparticle in the film flow under the influence of these forces. The characteristic of the nanoparticles' movement in the film flow may be described by the frequency of the movement. In this case, the number of the magnetos to the time that required for a nanoparticle to pass over these magnetos. Obviously, the frequency is determined by the gap distance "a" and the velocity of the film flow.

The variation of the intensity of the magnetic field makes the nanoparticles to travel between the surface of the film flow and the wall. The movement of nanoparticles can cause local micro flows in the film flow. These micro flows accelerate the heat and mass transfer in the liquid phase; therefore, increase the vapour absorption rate. The experimental results reveal the correlation between the vapour absorption rate and the frequency of the nanoparticles' movement in the film flow.

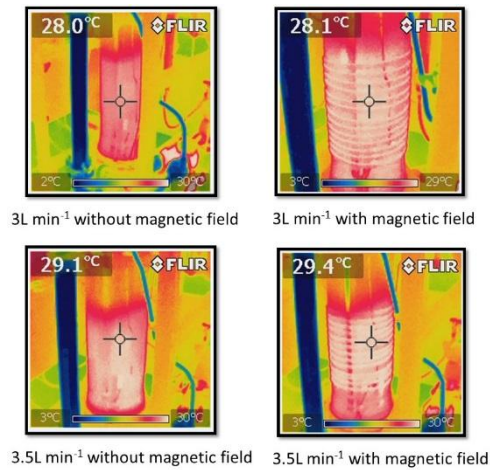


Figure 10 The thermal images of the absorber vessel with different arrangement of flow rate and magnetic field

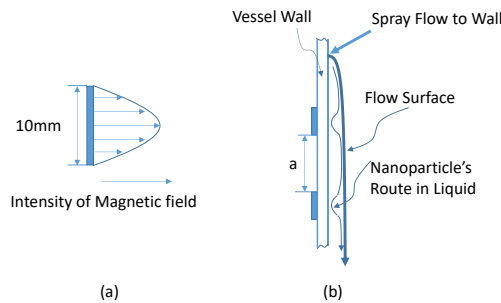


Figure 11 (a) Magnetic field of the magneto (cross-sectional view of the magnetic strip), (b) Nanoparticle's moving route relative to the liquid flow

Of all three cases, the gap distance 2cm gives the highest absorption rate. The vapour absorption rate decreases as the gap distance increases to 3.5cm. The lowest vapour absorption rate takes place in the case of zero gap distance. This phenomenon could be linked to the frequency of nanoparticles movement caused by the magnetic field. Table 2 lists the frequencies of the nanoparticles' movement for three configurations, which are calculated from the film flow's velocities. A zero frequency is given to the zero gap configuration for the understanding that no variation of the magnetic field in this case. With the gap distance increasing from 2.0cm to 3.5cm, the frequency decreases by 43.2% and 42.9% for  $3.0\text{L min}^{-1}$  and  $3.5\text{L min}^{-1}$ , respectively. The less frequent movement of the nanoparticles inevitably reduces the heat and mass transfer in the flow layer and so the vapour absorption rate. The results from this investigation suggest that the vapour absorption process benefits from a high frequency movement of nanoparticles. However, the current data are not sufficient to conclude that the vapour absorption rate increases with the frequency of the nanoparticles movement defined in this paper.

Table 2 The frequencies of nanoparticle movement in different gap distance and flow rate

Gap distance "a" between the magnetos, cm	Nano particle movement frequency, Hz	
	Flow rate $3.0\text{L min}^{-1}$	Flow rate $3.5\text{L min}^{-1}$
0	0	0
2.0	9.5	10.5
3.5	5.4	6.0

Given that the frequency of the nanoparticles' movement is a function of the flow velocity, we can see that the strength and distribution of the magnetic field have to be determined with reference of the flow velocity. Therefore, in order to maximise the vapour absorption rate in a

magnetically assisted vapour absorption process, the film flow velocity, the strength and distribution of the magnetic field have to be arranged to maximise heat and mass transfer in the liquid film flow.

### **Conclusions**

This investigation experimentally tested the vapour absorption rate using the nanofluid of the aqueous lithium bromide solution + ferric oxide nanoparticles as the absorbent and the nanofluid subject to the influence of magnetic fields. The test results show a significant increase in the vapour absorption rate by using this nanofluid and a further increase when applying external magnetic field to the absorption process.

The results show that the nanofluid can enhance the vapour absorption process, particularly, when the heat and mass transfer of the liquid phase dominates the whole process. This is evident by the high absorption rate coming with the high circulation flow rate. While the vapour absorption rate can be further increased by applying external magnetic field, the arrangement of the external magnetic field is appeared to be an influential factor. This investigation reveals the correlation between the vapour absorption rate and the frequency of the nanoparticles' movement in the film flow. It shows that the vapour absorption rate increases with the frequency of the nanoparticles' movement between the wall and the surface of the liquid phase. However, with the limited tests of three cases, the data may not sufficient to confirm the existence of such relationship generally.

This investigation provided some useful information to understand the rolls of nanoparticles' movement in enhancing the vapour absorption process. However, the movement of the nanoparticles in the fluid is influenced by not only the magnetic field but also the flow's characteristics. The combination effect of these factors is complicated to the nanoparticles' movement in the flow. It needs further study in order to understand it.

### **Acknowledgement**

The authors would like to thank our former undergraduate students Yujia Ji and Junjie Li for their contribution of testing the base fluid's vapour absorption rates in their dissertation project.

### **References**

- [1] Kim, J., Jung, J. Y., Kang, Y. T., The effect of nano-particles on the bubble absorption performance in a binary nanofluid, *International Journal of Refrigeration*, 29 (2006) 22-29
- [2] Kim, J. K., Jung, J. Y. & Kang, Y. T., Absorption performance enhancement by nano-particles and chemical surfactants in binary nanofluids. *International Journal of Refrigeration*, 30 (2007) 50-57.
- [3] Kang, H. J. Kim y K. I. Lee, Heat and mass transfer enhancement of binary nanofluids for H<sub>2</sub>O/LiBr falling film absorption process, *International Journal of Refrigeration*, 31 (2008) 850-856.
- [4] Philip, J., Shima PD., Raj, B. Enhancement of thermal conductivity in magnetite based nanofluid due to chainlike structures, *Applied Physics Letter*, 91, 203108 (2007); doi: <http://dx.doi.org/10.1063/1.2812699>.
- [5] Angayarkanni, S. A. & Philip, J. Review on thermal properties of nanofluids: Recent developments. *Colloid and Interface Science*, 225 (2015) 146-176.
- [6] Suresh, A. Bhalerao,. Rate intensification of mass transfer process using ferrofluids, *Indian Physical applied*, 40 (2001) 172-184.
- [7] Komati, S. & Suresh, A. Anomalous Enhancement of Interphase Transport Rates by Nanoparticles: Effect of Magnetic Iron Oxide on Gas-Liquid Mass Transfer. Department of Chemical Engineering, Indian Institute of Technology, 49 (2010) 390-405.
- [8] Komati, S. & Suresh, A. CO<sub>2</sub> absorption into amine solutions: a novel strategy for intensification based on the addition of ferrofluids. *Journal of Chemical Technology and Biotechnology*, 83 (2008) 1094-1100.

# Thermal Performance of Nanofluids Applied to the Temperature Control of Electronic Components

Roger R. Riehl

National Institute for Space Research, INPE – DMC  
Av dos Astronautas 1758, São José dos Campos, 12227-010 SP Brazil, E-mail: roger.riehl@inpe.br

## Abstract

The subject of this article is related to the development of a thermal management solution for a surveillance equipment, which needs to dissipate high levels of heat loads using both active and passive thermal control devices. Therefore, a thermal management system was designed to use both a single-phase forced circulation loop and heat pipes using copper oxide (CuO)-water nanofluid, designed to promote the thermal management of up to 50 kW of heat generated by several arrays of electronic components, being dissipated to the environment by a fan cooling system. The heat pipes collect the heat from electronic components that are far from the main single-phase forced circulation loop, rejecting the heat directly in its cold plates. Results show that with an addition of 20% by mass of CuO nanoparticles to the base fluid in the single-phase system, enhancements of 12% in the heat transfer coefficients were achieved but the increase in the pressure drop was around 32%. The use of nanofluid in the heat pipes resulted in a substantial decrease in the heat source temperature. When applying nanofluids in heat pipes, the maturity of this technology has reached TRL=8 for surveillance systems.

**Keywords:** thermal enhancement, electronics cooling, thermal control, pressure drop, nanofluids.

## Introduction

The need for thermal management has increased over the last decade and the prediction is that a steeper increase is yet to come for the next years. Such an increase is related to more powerful electronics used for data processing in high-tech equipments used for satellites and defense/military purposes. More powerful and compact electronics result in higher heat densities that can significantly contribute to concentrate the heat in certain areas that will result in parasitic heat being transferred to other components, as well as make difficult to promote the heat dissipation using conventional methods. Investigations in this subject have been already reported, bringing the attention to new approaches for current and future applications [1-3], where technologies developed for aerospace thermal control problems have been transferred to ground systems when needed. Hybrid solutions, using single- and two-phase thermal control systems together have presented to be a promising approach to solve the high heat dissipation problem in ground systems. Whilst single-phase systems rely in a pump to drive the working fluid throughout the loop, and a correct hydraulic project ensures the adequate flow velocity in their several branches, two-phase systems apply heat pipe technology as a high performance thermal control device. Both single- and two-phase systems are known to dissipate high levels of heat, but some projects require much higher capacities that lead designers and researchers to seek for new technologies, especially when considering the working fluid responsible for transporting the heat. In this case, nanofluids have been considered and applied with promising results to solve future thermal management limitations [4,5], which has contributed to bring this technology to a level of maturity that enables it to be used commercially.

Several investigations related to nanofluids applications have been conducted with important contributions to many areas [6,7]. Considering current and future thermal management needs, the use of nanofluids is becoming inevitable. Nanofluids present to be an important approach

to enhance the heat transfer capability of heat pipes and loop heat pipes systems, which has already been proven [8,9]. Other applications are related to the use of nanofluids in regular heat exchanger devices already installed in industries [10]. Evaluation of nanofluids have been performed by many researchers in order to better understand the effects of nanoparticles in the transport properties, which are important for the prediction of the pumping requirements [11,12]. Applications related to PCB thermal management using nanofluids have also been reported [13]. However, important issues require attention, especially when considering the verification of a nanofluid regarding its own design, since many authors have reported different results for the same combination of base fluids and nanoparticles [14]. Another issue that requires attention is the operational condition at which the nanofluid will be facing, being at atmospheric or saturation conditions. Differences in the thermal capacity of nanofluids have been reported when a given nanofluid had its thermophysical properties obtained in atmospheric conditions and its behavior was completely different when operating in saturation conditions [14].

Heat pipes and thermosyphons [15-17] have been investigated with different nanofluids as working fluids, and the gains in their overall performances have been reported. Important improvements have been achieved when applying nanofluids in micro channels heat sinks [18], which can potentially be used in more reliable thermal management projects, especially those related to surveillance systems. However, investigations related to the effects of solid nanoparticles added to a given base fluid to form the nanofluid are required, especially to verify the direct impact of nanoparticles sizes and shapes, purity and chemical compatibility with thermophysical properties like thermal conductivity, viscosity, density, surface tension and, most importantly, wettability angle [19-22]. Technological issues still require full attention from researchers and developers, as well as designers, in order to overcome resistances from applying this promising technology and guarantee that systems will operate according to their requirements.

Another aspect that required attention is the technology development of new solutions that result in a maturity for application in the real world, being proved to operate in levels above laboratory conditions and beyond numerical simulations. In this case, systems that present TRL (Technology Readiness Level) equal or above 7 are desirable. Many researches have shown the potentiality in applying nanofluids in laboratory controlled environments, but their operation in the real world are needed to prove their full capability in the long term, which also should consider chemical compatibility and performance variation along time.

Evaluating the technological baseline that are considered for designing a reliable and effective high heat dissipation thermal management systems that need to operate in hostile environments, with potential use of nanofluid, this article presents a solution applied to promote the dissipation of 50 kW of rejected heat. Considerations were given to a hybrid thermal management system, which uses both single- and two-phase thermal control devices operating with nanofluids to enhance the heat dissipation's capabilities, in order to prove the nanofluid application for real systems.

### **Thermal Management System Design**

The design of the thermal management system is a complex task that involves the consideration of several variables related to the conjugate heat transfer process (conduction, convection and radiation), along with materials used, working fluid, operation orientation, temperature, humidity, etc. The approach given for any thermal design should consider both the overall heat dissipation system analysis and the detailed thermal control design. The overall heat dissipation system analysis considers the total amount of heat to be dissipated and the available areas for the heat rejection, along with other overall aspects important for solving the problem. Usually, this is a first approach and it is used to verify the overall capacity of the thermal management system and will point the direction that should be



followed to conceive a reliable and efficient system. The detailed thermal control design considers each and every component of the thermal management system operating separately (as a sub-system) and then together with all other parts (as a system) including all thermal couplings to evaluate, with high degree of details, how the thermal management system will behave during its operation and identify any potential issue.

Both approaches have to deal with well-known thermal solutions in order to verify issues and limitations related to the heat dissipation process, therefore using already known systems like liquid pumped loops with dry coolers and heat pipes, which already present TRL=9. However, upon applying a nanofluid in such systems, the real capabilities of both systems must be extensively verified not only for the thermal management process, but also for reliability over time, chemical stability during long term operation, NCG generation, among other parameters.

### **Thermal Control Design**

The detailed thermal control design was done to evaluate the thermal behavior of each electronic component and its integrated operation in the PCB. Considering that electronic components have their sizes reduced substantially as technology evolves while keeping their heat dissipation, higher heat densities are found and must be carefully considered. Such level of information is extremely important to be shared between those responsible for designing the PCB and those responsible for the thermal control system, as smaller components will present very reduced areas to dissipate the heat, which can result in concentrated heat and high levels of temperature that can damage the electronic component. For example, if an electronic component dissipates 0.5 W and has a surface area of 2.5 mm by 2.5 mm, the total heat flux that needs to be dissipated from it will be  $80 \text{ kW/m}^2$ , which is substantially high.

As a methodology for a detailed thermal control design, the PCB is simulated for conjugated heat transfer (when applied) to verify the heat and temperature concentrations. The parameters involved in this analysis are directly related to the project's requirements and will vary from one to another. Figure 1 presents a mathematical simulation analysis made for this project, considering the PCB architecture based on the electronic components positioning and heat dissipation levels, using as examples the values shown in Table 1. The results from the mathematical simulation presented by Fig. 2 were obtained using a computer code based on a nodal network [26] for the PCB, which considers the conjugated heat transfer with the project's parameters while operating in ambient conditions. It is possible to observe that the PCB presents concentration of temperatures that must be properly addressed in order to avoid any component to shut down due to overheating, which is always referred to the components' manufacturer cold junction temperature levels. Such information is also important for the design of the mechanical interface that will be used to transfer the heat generated to the dedicated heat sink. In many cases, a rugged design of the mechanical interface is not enough to guarantee the adequate heat transfer from the source to the sink, therefore new solutions must be applied.

Once considering each PCB as a sub-system that integrates an entire system composed of several PCBs with their respective thermal control device, interface materials, thermal couplings etc, all interconnected with the main thermal control system (single-phase liquid cooling), the complexity of this design is evident. Therefore, proper consideration of all details must be done which relies in the designer's experience. For this specific project, a surveillance system design dissipating high levels of heat has been conceived to operate in hostile environments where the ambient temperatures can range from +5 to +50 °C and humidity levels up to 95%.

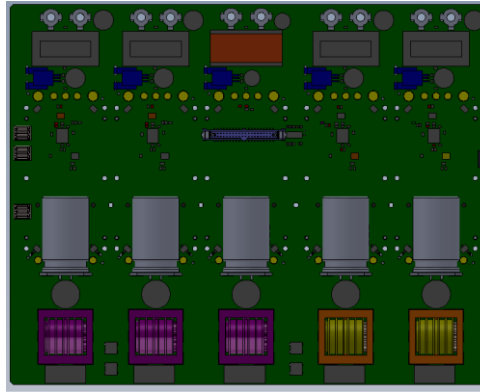


Figure 1. Schematics of a PCB and its electronic components.

Table 1. Example of a list of components and their levels of heat fluxes.

Component	Q (W)	Dimension (mm)		Heat Flux (W/m <sup>2</sup> )
		X	Y	
R15	0.10	1.65	3.25	19,393.94
R16	0.10	1.65	3.25	19,393.94
R17	0.14	1.35	2.20	47,138.05
R32	0.14	1.35	2.20	47,138.05
L1	1.15	1.40	2.20	374,025.97
L5	1.15	1.40	2.20	374,025.97
L12	1.15	1.40	2.20	374,025.97
L9	2.20	1.40	2.20	715,259.74

In this case, a single-phase thermal control loop has been designed to use a nanofluid, presenting a forced circulation using a pump to drive the working fluid throughout the circuit to remove heat from the electronic components through dedicated cold plates, rejecting this heat to the environment by a fan cooling system. For this thermal management system, a hybrid design has been applied where the heat generated by some PCBs (located far from the cold plates) was removed by heat pipes configured as pulsating open loops, delivering the heat to the heat sinks allocated thorough the surveillance equipment (cold plates). The heat sinks were then connected to the single-phase thermal control loop that collected all the heat and dissipated it to the environment. The schematics of such arrangement is presented by Fig. 3a and the surveillance equipment where the system was installed is shown by Fig. 3b, whilst Fig. 3c presents the liquid cooling schematics.

The heat pipe architecture is presented by Fig. 4, where its configuration as an open loop pulsating heat pipe (OLPHP) is shown integrated to the mechanics for a given PCB. It is important to mention that each mechanics is mechanically and thermally connected to their PCB to ensure a fast heat removal and control of the electronic components' temperatures, thus configuring a low thermal inertia thermal control approach. Figures 4b presents the OLPHP used for this analysis.

## 2.2. Nanofluid Selection and Application

As one of the most important component of the thermal management system, the nanofluid selection required careful consideration regarding the selected solid nanoparticles and the base fluid.

For the sake of chemical compatibility for both single- and two-phase thermal control systems (liquid cooling and heat pipes, respectively), the most appropriated selection was the use of copper nanoparticles and water as the base fluid. Purity levels for both substances had to be as high as possible to avoid the interaction of other substances with the nanofluid, which could potentially lead to the generation of non-condensable gases (NCGs) that can negatively impact the thermal operation of the system, especially the heat pipes. The assessment to this issue is based on the chemical reaction analysis for both base fluid, solid nanoparticles and the heat pipe and liquid cooling system's tubing, as the constant heat cycling along with high temperatures will accelerate the reaction and generate NCGs.

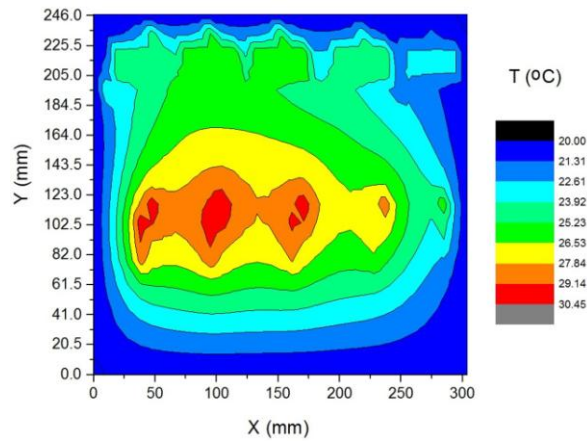


Figure 2. Thermal simulation for the PCB operating in ambient conditions.

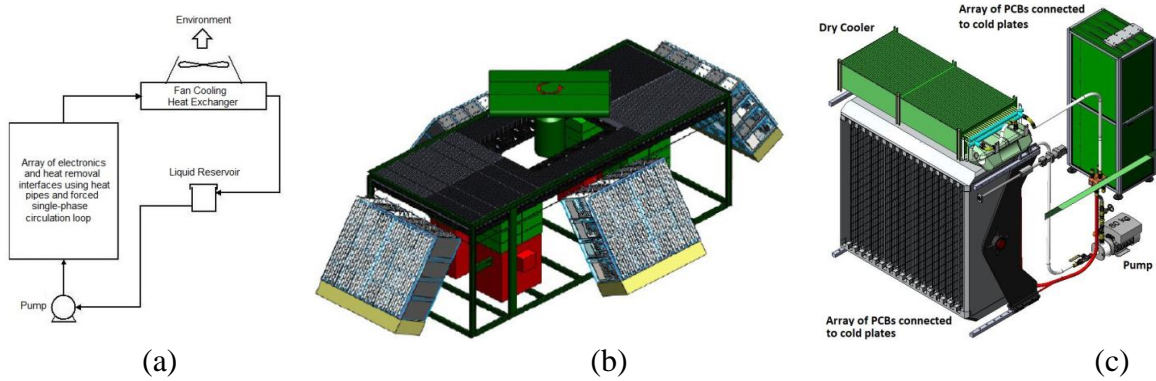


Figure 3: Schematics of the thermal control system arrangement: (a) arrangement schematics; (b) surveillance equipment; (c) liquid cooling schematics.

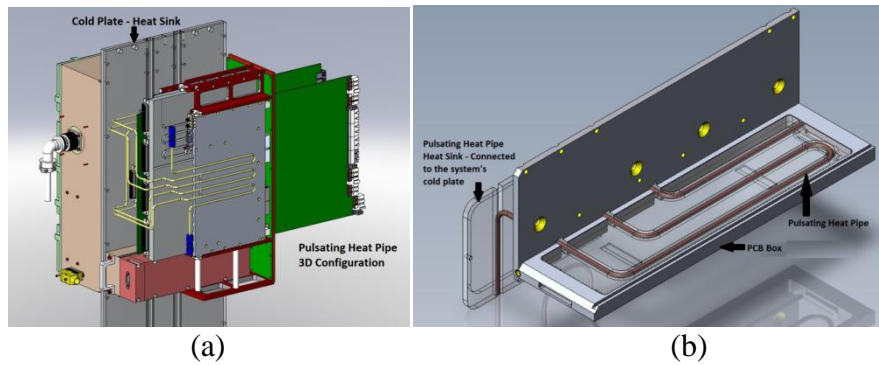


Figure 4. OLPHP schematics: (a) integrated with the PCB's mechanics; (b) setup.

Therefore, an analysis based on the Arrhenius Model can be performed to evaluate the amount of NCG that will be generated based on the interaction between the base fluid and the solid nanoparticles and, upon performing a so-called aging process, the NCG generation can be accelerated and flushed out of the system thus avoiding the negative influence of it during the system's lifetime. Better explanation of this methodology can be found in Ref. [23].

Several solid nanoparticles have been tested during the last years in order to verify their thermal behavior when applied to single- and two-phase systems, like liquid cooling and heat pipes, respectively. The selection range from commercial available and custom made solid nanoparticle, which present high purity and quality in guaranteeing the particles' sizes and distribution and can be used when some preparation methodologies are applied to obtain the nanofluid, which is usually done with a 2-step method [14].

It is important to mention that commercial nanoparticles usually present an acceptable quality related to their purity, geometry and size's distribution. As those parameters increase in

reliability, the costs for those nanoparticles will increase significantly. Such parameters are important to be considered as several publications have shown dispersed results from many authors, related to the nanofluid thermophysical properties, even though the same nanoparticle and base fluid, in the same concentration, have been reported to be used [14]. If discrepancies in results related to the same solid nanoparticle, base fluid and concentration are obtained, one should consider that other parameters are important to guarantee that the same results will be obtained, such as particle shape, its distribution among a sample, etc. Such information is considerably important to be taken into account and should be the object of future investigations in order to obtain a model with a statistical approach to design a nanofluid [14,24].

The augmentation on the thermal conductivity of a given working fluid will directly be dependent on the solid nanoparticle size and geometry, as well as the amount of particles with those characteristics. For better results, the solid nanoparticles must present their size and geometry in at least 95% of the sample to ensure that the nanoparticles have a homogeneous characteristics. This is an important information to be considered, otherwise the nanofluid with the same size of nanoparticles and base fluid will present different results, due to the fact that it is not homogeneous. This can represent a very wide range of results and consequently may impact the thermal management system performance. As seen in Fig. 5, two solid nanoparticles were used for this analysis, which are identified as follows:

1. High purity CuO: purity > 98% and particle sizes (spherical)  $d_p=29$  nm
2. High purity Cu: purity > 99.98% and particle sizes (spherical)  $d_p=2$  nm

Even though both samples clearly present different characteristics, the most important one is that sample 1 presents up to 80% of the particles within those characteristics, while sample 2 has up to 95% of the particles within those characteristics. Guaranteeing that the sample has a high purity and homogeneous size distribution with such certainty will directly impact in the final price.

There is a clear difference between the solubility of sample 1 compared to sample 2. Both nanofluids were prepared without surfactants using the 2-step method, but to reach a homogeneous nanofluid without precipitation of the solid nanoparticles, sample 1 needed 2 hours in an ultrasonic bath whilst sample 2 required only 15 min. This difference was attributed to the fact that sample 2 used the pure Cu with homogeneous particle sizes and distribution, which contributes to a high quality nanofluid.

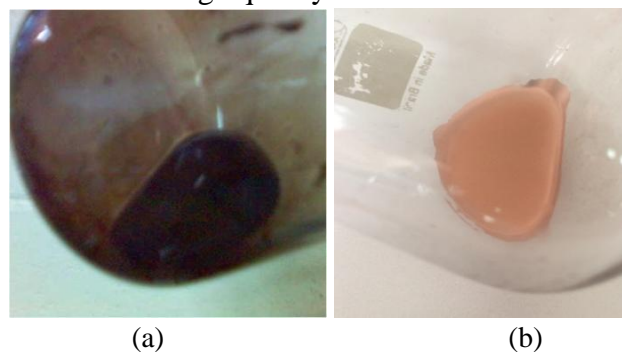


Figure 5. Nanofluids with water as base fluid: (a) sample 1; (b) sample 2.

The homogeneous distribution represents a high impact in the nanofluid's performance while operating in the thermal management system, and will cause an important impact in other transport properties as well, such as the surface tension and wettability angle. This last one is a very important variable for a high efficient heat transfer system, since a high wettability angle will ensure that the nanofluid will be wetting the heat transfer surface more efficiently for values close to  $180^\circ$ . Table 2 presents a laboratory investigation performed for heat pipes application with various wick structures, housing materials and working fluids, where the

observed wettability and chemical compatibility characteristics were compiled. The indication of "Good" wettability means that the working fluid was able to spread on the surface and be absorbed by the wick material (typical of contact angles between 90° and 180° [24]); the indication "Poor" wettability means that the working fluid remained as a bubble without spreading on the surface and without being absorbed by the wick material (typical of contact angles lower than 90° [24]).

Table 2. Wettability characteristics for various working fluids and materials.

		Base Fluid								
		Water			Acetone			Methanol		
Wick Material		Nanoparticle								
		Al <sub>2</sub> O <sub>3</sub>	CuO	NiO	Al <sub>2</sub> O <sub>3</sub>	CuO	NiO	Al <sub>2</sub> O <sub>3</sub> **	CuO	NiO
Copper		*	Good	Poor	Poor	Good	Poor	Poor	Good	Poor
Nickel		*	Poor	Good	Poor	Poor	Good	Poor	Poor	Good
Polyethylene		*	Poor	Poor	Poor	Poor	Poor	Poor	Poor	Poor
* Al <sub>2</sub> O <sub>3</sub> - Water are incompatible substances - NCGs are generated with long term operation during power cycling.										
** Al <sub>2</sub> O <sub>3</sub> - Methanol have presented chemical incompatibilities and unstable solubility with long term operation.										

One of the most investigated nanofluid is composed with water as base fluid and Al<sub>2</sub>O<sub>3</sub> solid nanoparticles. However, when operating in thermal cycles for a long period of time, this combination will generate hydrogen as a NCG that will cause a negative impact in the thermal management system in the long term. Several reports have described the NCG generation when water and Al<sub>2</sub>O<sub>3</sub> were used, especially in heat pipes applications, which resulted in severe recommendations to avoid this combination for thermal control devices used [3,8]. Also, the use of surfactants to improve the solubility of the solid nanoparticles in the base fluid shall not be used as it will also generate NCGs during the thermal management system's operation in the long term.

The most important operational requirements imposed by this application are as follows:

- Liquid cooling system: T<sub>op</sub> = 55 °C maximum
  - Operating with de-ionized water and CuO (sample 1) selected as the nanofluid combination at atmospheric condition
    - Over 400 m of lines with ID=11 mm
    - No use of surfactants due to chemical issues
- Passive system: T<sub>op</sub> = 90 °C maximum – due to cold junction temperature limitation for the electronic components
  - Connects the PCBs that are far from the cold plates
  - Operating with de-ionized water and CuO (sample 1) selected as the nanofluid combination at saturation condition
    - Total of 240 pulsating heat pipes divided in 4 arrays
    - Pulsating heat pipes characteristics:
      - 3.0 mm OD; 1.6 mm ID; L<sub>eff</sub>=225 mm
    - No use of surfactants due to chemical issues

Given the complexity of the presented thermal management system, the use of a nanofluid represents a significant gain in its thermal performance. Considering all important variables for this application based on in-house research and development, evaluating also the project's requirements, de-ionized water has been selected as the base fluid. The performance verification was done using CuO (sample 1) for the liquid cooling system as well as for the heat pipes. The nanoparticles concentration (*f*) shall vary from 3.5% to 20% (by mass of the

base fluid) for the liquid cooling system and up to 3.5% for the heat pipes, in order to verify their effect on the overall thermal performance of the system. Tests were limited to sample 1 due to the high costs involved when using sample 2 in both systems.

## Results and Discussion

The presented results were well correlated to the thermal tests applied to this equipment, and further analysis will be disclosed in future reports. For the sake of presenting the most important results obtained so far, the following data were selected among several hours of operation. However, due to the sensitive technology that used this thermal management systems solution, additional information related to the electronic arrays and their architecture cannot be disclosed.

Figures 6a and 6b present results for the pressure drop and heat transfer coefficients observed during the operation of the liquid cooling system, respectively, on a comparison between the use of pure water and the addition of CuO nanoparticles at different concentrations by mass percentage of the base fluid in the system. The results are related to each individual electronic module (composed of 3 PCBs), which dissipate a maximum of 50 W of heat, thus, based on the module's footprint and heat dissipation, the calculation for the heat transfer coefficient was performed. Regarding solid nanoparticles deposition in the single-phase cooling system's liquid reservoir, this showed to be a minor issue to be consider only for  $f=20\%$ . However, during the long term operation of the single-phase liquid cooling system, the deviation on the results were negligible, showing that the solid nanoparticles were constantly mixed and incorporated with the base fluid.

Upon individually analyzing the heat pipes used to transport the heat from the electronic components to the heat sink connected to the liquid cooling system, the direct impact in their performance caused by the use of a nanofluid is very clear. Figure 8 presents the operational results for the Unit 1 heat pipe while transferring the heat from the electronic components (their respective PCB) and dissipating in the heat sink. The heat loads at which the heat pipes were operating were obtained from the heat dissipation of their PCB upon measuring their electronic operation. For this measurement, the software responsible for controlling the PCB was responsible for reading and acquiring this information, which was a feature promoted by its manufacturer.

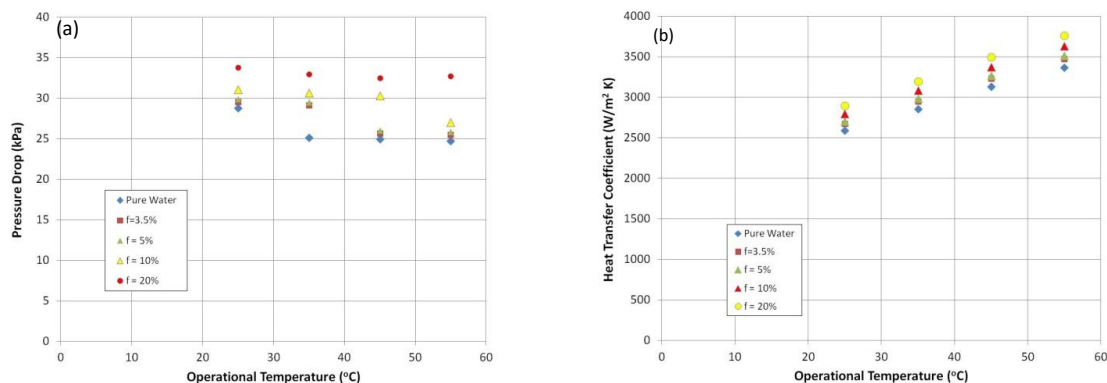


Figure 6: Results for (a) pressure drop and (b) heat transfer coefficient.

Figure 7a presents the results for the OLPHP heat source temperatures according to the heat load given by the PCB. At a higher heat load, the operation with nanofluid presented its reliability as the heat source temperature was lower than the operation with pure water. Since the electronic components used in military applications are very sensitive, it should operate far from their cold junction temperature limitation, which is related to their qualification purpose and set by the manufacturer. For this case, the highest cold junction temperature

allowed was 90 °C, thus while operating at a temperature below 70 °C (for the heat pipe using nanofluid), the electronic components could reach their highest performance. Figure 8b shows the thermal conductances observed during the operation, which are calculated as

$$G = Q / (T_e - T_c), \quad (4)$$

with maximum uncertainties of  $\pm 8.8\%$ . The results show that higher values were obtained for the heat pipe operating with the nanofluid, which is highly dependent on the augmentation of the working fluid's thermal conductivity by adding the solid nanoparticles.

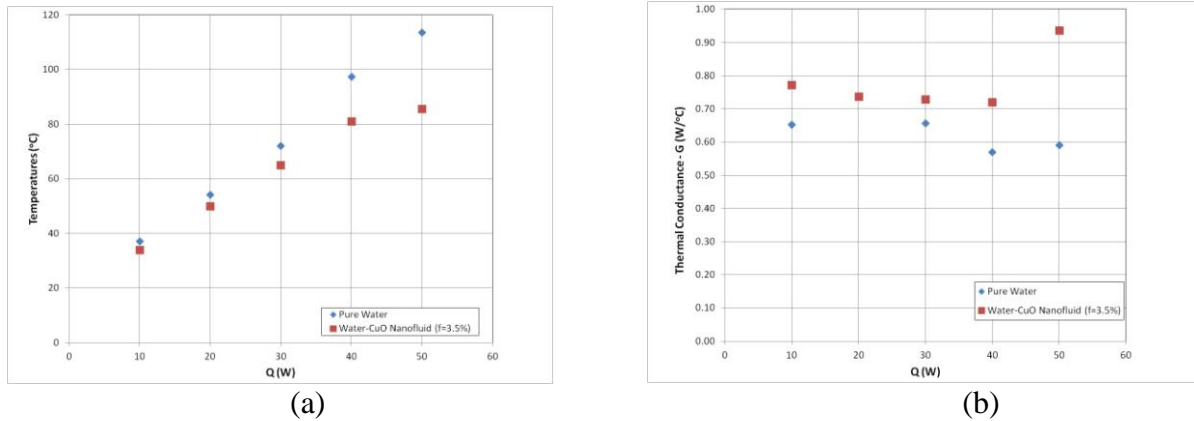


Figure 7. Operational tests with the heat pipe: (a) maximum heat source temperature; (b) thermal conductances.

Better performances were observed for the OLPHP, which impacts in the final heat source temperature as shown in Fig. 7a. Figure 7b shows the results for the thermal conductances during the OLPHP operation. Operating the heat pipe with de-ionized water as working fluid showed to be a real concern as the final equilibrium temperature was higher than the limit (118 °C), which certainly caused the components in the PCB to switch off due to the temperature protection. Operating the OLPHP in this condition is really harmful for the PCBs as well as for the mission requirements imposed by the surveillance equipment. Upon operating with the nanofluid, the final equilibrium temperature of the heat source was substantially decreased (83 °C), which shows the potentially in using the nanofluid in this application. At the highest heat load, the observed temperature of the heat source while the OLPHP was operating with nanofluid was 35 °C lower than the operation with de-ionized water, which is was significant impact in the passive system's operation. The beneficial impact while using the nanofluid in the heat pipe can also be observed in the results related to the thermal conductances (Fig. 7b), with a increase of 55% when compared to the operation with de-ionized water.

## Conclusions

In general, the main conclusions that can be derived from this investigation are:

1. Higher heat transfer coefficients can be reached with the increase of the solid nanoparticles concentration, representing an enhancement of up to 12% for  $f=20\%$  at 55 °C when compared with the operation with water;
2. The pressure drop also increases as the concentration of nanoparticles increases, which could compromise the pump operation;
3. Pulsating heat pipes can keep the heat source temperatures below 90 °C;
4. The overall analysis indicates that the application of the nanofluid with higher concentrations can be used, as the major parameter for this analysis is the heat transfer coefficient, which is reducing the size of the thermal management system applied to control the temperature of the electronics components.

When considering that the thermal management system is operating at higher capacities, while keeping the working fluid's temperature within the project's parameters, the use of a nanofluid presents to be an important innovative approach for this project. This is directly resulting in more gains than losses for the overall thermal system analysis and should remain as the most indicated solution for this application. Another important conclusion that can be taken from this investigation is that while operating the surveillance equipment in real conditions, the thermal management system (single-phase liquid cooling and two-phase heat pipes) has achieved a maturity related to TRL=7. Since other systems have been already equipped with heat pipes operating with nanofluids and have already being used as final products, this technology is mature enough to be related as TRL=8.

### Nomenclature and Acronyms

$d_p$	Particle Diameter [nm]
$f$	Nanoparticle Mass Fraction
ID	Inner Diameter [m]
G	Thermal Conductance [W/°C]
$k_n$	Effective Thermal Conductivity of a Homogeneous Nanofluid [W/m.K]
$k_p$	Particle Thermal Conductivity [W/m.K]
$k_l$	Base Fluid Thermal Conductivity [W/m.K]
$L_{eff}$	Heat Pipe Effective Length [m]
NCG	Non-Condensable Gases
OD	Outer Diameter [m]
OLPHP	Open Loop Pulsating Heat Pipe
PCB	Printed Circuit Board
$Q$	Applied Heat Load to the Evaporator [W]
$T_e$	Average Evaporator Temperature [°C]
$T_c$	Average Condenser Temperature [°C]
$T_{op}$	Operation Temperature [°C]
TRL	Technology Readiness Level
$\rho_n$	Nanofluid Density [kg/m <sup>3</sup> ]
$\rho_p$	Nanoparticle Density [kg/m <sup>3</sup> ]
$\rho_l$	Base Fluid Density [kg/m <sup>3</sup> ]
$\mu_n$	Nanofluid Dynamic Viscosity [Pa.s]
$\mu_l$	Base Fluid Dynamic Viscosity [Pa.s]

### References

1. Riehl, R. R., Cachuté, L. "Thermal Control of Surveillance Systems Using Heat Pipes and Pulsating Heat Pipes", *Proc of 49th AIAA/ASME/SAE/ASEE Joint Propulsion Conference & Exhibit 11th International Energy Conversion Engineering Conference*, San Jose, CA USA, July 14-17 (2013).
2. Riehl, R. R., Cachuté, L. "Thermal Management of Surveillance Equipments Electronic Components Using Pulsating Heat Pipes", *Proc of IEEE-ITherm Conference - Intersociety Conference on Thermal and Thermomechanical Phenomena in Electronics Systems*, Orlando, FL USA, May 27-30, (2014).
3. Riehl, R. R., "Passive Thermal Management Systems Using Pulsating Heat Pipes", *Proc. of IX Minsk International Seminar "Heat Pipes, Heat Pumps, Refrigerators, Power Sources"*, Minsk, Belarus, Sept. 07-10, (2015).
4. Liu, Z. H., Li, Y. L., A new frontier of nanofluid research - application of nanofluids in heat pipes, *Int J Heat and Mass Transfer* 55 (2012) 6786-6797 doi 10.1016/j.ijheatmasstransfer.2012.06.086
5. Murshed, S., de Castro, C. A. N., Nanofluids as advanced coolants, *Green Solvents I: Properties and Applications in Chemistry*, 2012, doi 10.1007/978-94-007-1712-1\_14.



6. E. Ebrahimnia-Bajestan, H. Niazmand, W. Dungthonsuk, S. Wongwises, Numerical investigation of effective parameters in convective heat transfer of nanofluids flowing under a laminar flow regime, *International Journal of Heat and Mass Transfer* 54 (2011) 4376-4388.
7. A. Ghadimi, R. Saidur, H.S.C. Metselaar, A review of nanofluid stability properties and characterization in stationary conditions, *International Journal of Heat and Mass Transfer* 54 (2011) 4051-4068.
8. R.R. Riehl, N. Santos, Water-copper nanofluid application in an open loop pulsating heat pipe, *Applied Thermal Engineering* 42 (2012) 6-10.
9. K. Alizad, K. Vafai, M. Shafahi, Thermal performance and operational attributes of the startup characteristics of flat-shaped heat pipes using nanofluids, *International Journal of Heat and Mass Transfer* 55 (2012) 140-155.
10. K.Y. Leong, R. Saidur, T.M.I. Mahlia, Y.H. Yau Modeling of shell and tube heat recovery exchanger operated with nanofluid based coolants, *International Journal of Heat and Mass Transfer* 55 (2012) 808-816.
11. S.M.S. Murshed, C.A. Nieto de Castro, M.J.V. Lourenço, M.L.M. Lopes and F.J.V. Santos, A review of boiling and convective heat transfer with nanofluids, *Renewable and Sustainable Energy Review* 15 (2011) 2342-2354.
12. S.M.S. Murshed, P. Estellé, A state of the art review on viscosity of nanofluids, *Renewable and Sustainable Energy Reviews* 76 (2017) 1134-1152.
13. L. Colla, L. Fedele, S. Mancin, S. Bobbo, D. Ercole, O. Manca, Nano-PCMs for electronics cooling applications, *Proceedings of the 5th International Conference on Micro/Nanoscale Heat and Mass Transfer*, Biopolis, Singapore, Jan 4-6, 2016.
14. E. Marcelino, R.R. Riehl, A review on thermal performance of CuO-water nanofluids applied to heat pipes and their characteristics, *Proceedings of the 15th IEEE Intersociety Conference on Thermal and Thermomechanical Phenomena in Electronic Systems (ITherm)*, Las Vegas NV, USA, May 31 - June 3, 2016.
15. Alizad, K., Vafai, K., Shafahi, M., Thermal performance and operational attributes of the startup characteristics of flat-shaped heat pipes using nanofluids, *Int J Heat and Mass Transfer* 55 (2012) 140-155, doi 10.1016/j.ijheatmasstransfer.2011.08.050
16. Solomon, A. B., Ramachandran, K., Airvatham, L. G., Pillai, B. C., Numerical analysis of a screen mesh wick heat pipe with Cu/water nanofluid, *Int J Heat and Mass Transfer* 75 (2014) 523-533 doi 10.1016/j.ijheatmasstransfer.2014.04.007
17. Grab, T., Gross, U., Franzke, U., Buschmann, M. H., Operation performance of thermosyphons employing titania and gold nanofluids, *Int J Thermal Sciences* 86 (2014) 352-364, doi 10.1016/j.ijthermalsci.2014.06.019.
18. Snoussi, L., Ouerfelli, N., Sharma, K. V., Vrinceanu, V., Chamkha, A. J., Guizani, A., Numerical simulation of nanofluids for improved cooling efficiency in a 3D copper micro channel heat sink, *Physics and Chemistry of Liquids*, 2017 doi 10.1080/00319104.2017.1336237
19. Khanafer, K., Vafai, K., A critical synthesis of thermophysical characteristics of nanofluids, *Int J Heat and Mass Transfer* 54 (2011) 4410-4428 doi:10.1016/j.ijheatmasstransfer.2011.04.048
20. Mikkola, V., Puupponen, S., Grahbohm, H., Saari, K., Ala-Nissila, T., Seppälä, A., Influence of particle properties on convective heat transfer of nanofluids, *Int J Thermal Sciences* 124 (2018) 187-195, doi: 10.1016/j.ijthermalsci.2017.10.015
21. Cabaleiro, D., Colla, L., Barison, S., Lugo, L., Fedele, L., Bobbo, S., Containing graphene nanoplatelets: design and thermophysical profile, *Nanoscale Research Letters*, 11p, 2017, DOI 10.1186/s11671-016-1806-x.
22. Meyer, J. P., Adio, S. A., Sharifpur, M., Nwosu, P. N., The viscosity of nanofluids: a review of the theoretical, empirical and numerical models, *Heat Transfer Engineering*, 2015, DOI: 10.1080/01457632.2015.1057447.
23. Riehl, R. R., Thermal management using copper-methanol heat pipes for radio transmitter systems, *Heat Pipe Science and Technology, An International Journal*, 2017, doi 10.1615/HeatPipeScieTech.2017021361.
24. Koca, H. D., Doganay, S., Turgut, A., Tavman, I.H., Saidur, R., Mahbulul, I. M., Effect of particle size on the viscosity of nanofluids: A review, *Renewable and Sustainable Energy Reviews* 82 (2018) 1664-1674.

# Two-Phase Pressure Drop Correlation During the Convective Condensation in Microchannel Flows

Roger R. Riehl

National Institute for Space Research, INPE – DMC  
Av dos Astronautas 1758, São José dos Campos, 12227-010 SP Brazil, E-mail: roger.riehl@inpe.br

## Abstract

This paper presents the experimental results on two-phase pressure drop related to microchannel flows during convective condensation. Two pumping systems, one being on a capillary pumped loop (CPL) mode and the other being with a magnetic driven pump with variable flow rate, were used in the experimental apparatus to test microchannel condensers with methanol as the working fluid. Tests were conducted for two different saturation temperatures, for a range of heat dissipation rate from 20 to 350 W, four microchannel condensers and mass flow rates of up to 600 kg/m<sup>2</sup>.s. The results showed that the microchannel condensers presented high pressure drop (up to 63 kPa) for the mass flow rate applied, which is mainly related to the microchannels reduced geometry. The levels of pressure drop observed were also considered high, as only laminar flow was verified during the tests. A correlation for the two-phase multiplier was obtained to correlate the experimental data, which showed to predict 85% of the experimental results within an error range of less than 35% for both saturation temperatures tested. The obtained correlation presented very high sensibility when calculating the pressure drop along the microchannels, considering the geometric factors and heat transfer capabilities of such equipment, which was able to present a good correlation with the experimental data.

**Keywords:** convective condensation, microchannels, thermal control, pressure drop.

## Introduction

The continuing miniaturization of electronic devices and systems has made area restrictions for the heat to be dissipated a significant problem. This issue becomes more important when considering that the device performance and reliability are known to increase when operating temperatures are kept below 80 °C. For applications in space, capillary pumped loops (CPL) and loop heat pipes (LHP) have been used as thermal management devices for electronics and structures, being able to transport high levels of heat from a high temperature source to a low temperature sink with minimal temperature difference. Due to restricted areas on satellites, new designs of condensers have to be conceived.

Considering the challenge of the new design concepts, many investigations were performed during the last two decades towards electronics device cooling. Investigations and applications using forced-air convection and pool boiling for electronics cooling have been performed, proving to be efficient on the thermal management, but limited heat dissipation rates and system integration are still a concern. Tuckermann and Pease [1] first proposed a cooling system for electronic devices using microchannel flows for forced single-phase liquid. This technology demonstrated to be promise for more compact arrangements of electronic devices and cooling systems in future electronic packaging. Based upon initial findings, a compact heat-sink microchannel was found to offer new degrees of freedom for system designs with considerable higher heat dissipation rates, but very significant high-pressure drop penalty.

As microchannel flows are still a field to be explored, few studies in two-phase pressure drop were performed in the past. After Tuckermann and Pease [1], Lazarek and Black [2] performed one of the first investigations on two-phase pressure drop in microchannels on vertical orientation and using R-113 as working fluid. They verified that the pressure drop for saturated vapor was mainly friction dominated, since the contributions as the result of elevation and momentum change of accelerating vapor were small. Lin et al. [3] performed investigations in capillary tubes during evaporation and established a two-phase multiplier correlation, considering the channels roughness. Mishima et al. [4] also investigated the two-phase pressure drop in narrow channels. It was concluded that the two-phase flow characteristics in such narrow channel differ from those in other geometries because of the significant restriction applied to the flow. Bowers and Mudawar [5-7] used the Homogeneous Model

to correlate their experimental data, which showed to accurately predict the pressure drop in miniature heat sinks at low flow rates. Yang and Webb[8] performed an experimental investigation on pressure drop in microchannel geometries, using the Lockhart-Martinelli's equation to correlate their data. Thus Ravigururajan et al. [9] concluded that the flow rate strongly influences the pressure drop in microchannels, when high heat fluxes were achieved for small wall superheat. Han et al. [10] described the development of microchannel heat exchanger used in air conditioning systems, which greatly contributed to the enhancement in their thermal performances. Such enhancements were also verified by other authors [11,12], where it was observed that the two-phase pressure drop in such channels is caused by friction at the wall surface and the acceleration due to the increase of specific volume. Studies presented in the past showed that there is a wide dispersion in information regarding data correlation. Some concluded that the Homogeneous Flow Model could be used to predict the pressure drop in small geometry channels, while others correlated their data using the Separated Flow Model. Such dispersion motivated the presented work to study the two-phase pressure drop in microchannel heat exchangers.

Focusing on such a problem, this paper presents an investigation to contribute to the understanding in two-phase pressure drop in microchannel flows. Four different microchannel heat exchangers were experimentally tested for condensing two-phase flow, in order to determine the mean pressure drop and to further develop a correlation. This procedure has the objective of helping future microchannel heat exchangers designs, to improve electronics and capillary pumping systems cooling.

### **Experimental Apparatus**

To test the microchannel condensers, two pumping methods were used: the first was a capillary evaporator and the second was a magnetic driven pump in conjunction with a flow through evaporator. The capillary evaporator was used for testing at low flow rates along the condensation section, while the mechanic pump promoted higher flow rates. The condensers were designed considering that, as the channel size decreased the number of parallel channels increased. This design was important in tests using the capillary evaporator (CPL mode), since this system presents limitations regarding the maximum allowed pressure drop. Such systems present some limitations regarding its pumping capacity, as capillary forces drive the entire flow. The capillary evaporator presented several other advantages as a pumping device, such as the flowrate is controlled by the heat load applied on the evaporator.

For the tests when higher flow rates had to be reached, a leak-free magnetic driven pump with speed control was used. This pump allowed controlling the flow rate up to a maximum of 3 l/min for a maximum pressure drop of 275 kPa. The details on the design for the loop used for testing the microchannel condensers are presented by Riehl [13].

### **Experimental Apparatus with a Capillary Pumped Loop (CPL) Evaporator**

The use of a CPL presented several advantages for testing the microchannel condensers. Stenger [14] at the NASA Lewis Research Center first proposed the capillary pumped loop (CPL), which is a two-phase thermal management system. Basically, the CPL uses capillary forces to pump a working fluid from a heat source to a heat sink. This system is able to transfer heat efficiently with a small temperature differential and no external power requirements [15]. Heat is acquired in a capillary evaporator and rejected using a condenser. The system is passively pumped by means of surface tension forces developed in a porous structure (called wick) located in the evaporator [16]. Major advantages of a CPL include no moving parts and high heat transport capabilities. Disadvantages include that a CPL requires subcooling and the maximum pressure is limited. In the proposed CPL apparatus, a by-pass condenser was used to better control the vapor volume in the microchannel condenser. Both by-pass condenser and sub-cooler were tube-in-tube heat exchangers. In the test section, heat was removed from the microchannel condenser by a cold plate, placed at the condenser base, which used a mixture 50% ethylene glycol and 50% water as working fluid and a rotameter was used to measure the flowrate. Figure 1a presents the experimental apparatus used for testing the microchannel condensers on the CPL mode and the instrumentation used. This apparatus was built with stainless steel tubes with outer diameter of 6.35 mm for both liquid and vapor lines, the vapor line had a length of 1.0 m and the liquid line 1.8 m.

## Experimental Apparatus with a Magnetic Driven Pump

The objective of using a magnetic driven pump was to reach higher flow rates and, consequently, higher pressure drops along the condensation section to better analyze the heat transfer capability the condensers. Figure 1b shows the experimental apparatus with the magnetic driven pump. The magnetic driven pump was equipped with a DC motor and a variable speed control. A flowmeter was added to the apparatus to measure the liquid flow rate, which was displayed on a LCD and the signal was also taken by the data acquisition system.

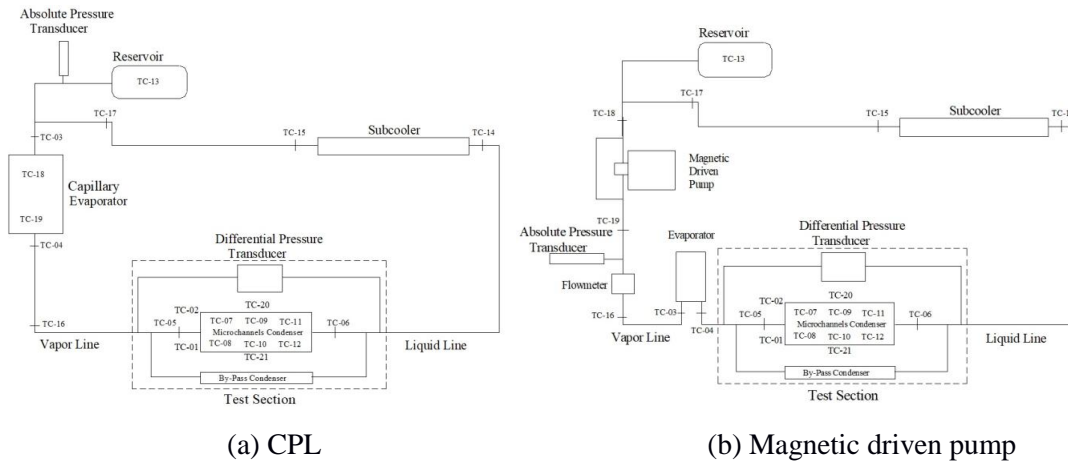


Figure 1. Experimental apparatuses.

## Instrumentation and Data Acquisition

Twenty-one type-T thermocouples were used, along with two pressure transducers (one absolute and one differential). Thermocouples 20 and 21 were placed at each side of the condenser, in order to obtain the wall temperature. Thermocouples 01 and 02 measured the inlet and outlet temperatures of the ethylene glycol, respectively.

An absolute pressure transducer was used to measure the working fluid operation pressure, which was set using a two-phase reservoir. A differential pressure transducer was used to measure the pressure drop along the condensation section. The pressure transducers were manufactured and calibrated by Sensotec Inc. For the absolute and differential pressure transducers, the output signal was 2 mV/V for a maximum excitation of 10 VDC. A description of the instruments used and accuracy is presented on Table 1. All listed instruments were connected to a data acquisition system, composed of a data acquisition card type AT-MIO-16XE-50, a chassis type SCXI-1000, a module type SCXI-1100 and a terminal block type SCXI-1303, being controlled by a computer using LabVIEW. The signals from the instruments were taken under a gain of 100, at a rate of 1 reading per second and filtered at 0.5 Hz.

Table 1. System instrumentation.

Instrument	Type/Model	Manufacturer	Accuracy	Reading Scale
Thermocouple	Type-T	Omega	$\pm 0.3$ °C	-100 to 300 °C
Rotameter	C7646	Omega	$\pm 2.0$ %	0 to 100 ml/min
Absolute Pressure Transducer	THE/0713 – 04TJA	Sensotec	$\pm 0.5$ %	0 to 344.5 kPa
Differential Pressure Transducer	A5/882 – 22A5 – D	Sensotec	$\pm 0.25$ %	0 to 172.25 kPa
Digital Multimeter	34401A	Hewlett Packard	$\pm 0.0045$ %	0 to 100 V
Flowmeter	112	McMillian	$\pm 1$ %	0 to 5 l/min

## Experimental Procedure

Tests were performed over a total condensation length of 150 mm and were conducted with the same procedure for all condensers when either the capillary evaporator or the magnetic pump was

used. The tests for the condensers were performed following the procedure as shown on Table 2. Independent of the pump used to perform the tests, each condenser was tested under two different saturation temperatures and different levels of heat load applied to the evaporator. For the tests with the capillary evaporator, the range of flow rate was dependent on the heat load applied to the evaporator. For the tests where a mechanic pump was used, the range of flow rate varied for each condenser, which was dependent on the presence of two-phase flow in the channels.

After the installation of each microchannel condenser, several steps were followed to ensure reliability of the results. First, the loop had to hold and be under vacuum of  $10^{-3}$  mTorr ( $1.33 \times 10^{-7}$  kPa) for 24 hours. This procedure had to be taken to ensure the absence of non-condensable gases (NCG) in the loop. Then, an amount of methanol was used to charge the loop. The absence of NCG was verified by comparing the absolute pressure (taken from the direct reading of the absolute pressure transducer) with the vapor pressure at the reservoir temperature. After charging, the reservoir temperature was raised to the desired operational temperature, using a silicon heater attached to its wall, where a thermostat was used to control the temperature range. After reaching the operating temperature, the system was ready to start operating.

**Table 2.** Test procedure for the condensers.

Apparatus	Working Fluid	Operation Temperatures	Heat Input to the Evaporator	Acquisition Time During Steady State
Capillary Evaporator	Methanol	45 and 55 °C	20 to 120 W	1000 sec
Magnetic Pump	Methanol	45 and 55 °C	175 to 350 W	1000 sec

Table 3 shows the characteristics of all condensers, which have square shape channels.

**Table 3.** Characteristic of the microchannel condensers.

Condenser	Channel Dimensions (mm)	Aspect Ratio	Number of Channels	Total Heat Transfer Area (m <sup>2</sup> )
1	1.50	1.0	8	0.00180
2	1.00	1.0	10	0.00150
3	0.75	1.0	12	0.00135
4	0.50	1.0	14	0.00105

For the tests where the capillary evaporator was used, heat was applied to the system through the capillary evaporator over a range of 20 to 120 W. For this range, just laminar flow for both liquid and vapor phases was verified. Heat was applied to the capillary evaporator by a silicon heater placed at the evaporator's vapor container wall. The applied heat was controlled by a Variac, connected to a digital multimeter. The tests were performed until steady state was reached for the given heat load applied to the capillary evaporator. The by-pass condenser was designed to be used if more condensation capability was required, when starting the capillary evaporator. However, the by-pass condenser was not needed during the tests. For the tests where the magnetic pump was used, heat was applied to the evaporator through the silicon heater attached to its upper surface while the pump was started at a low flow rate of working fluid. When steady state was reached for a given flow rate and applied power, the flow rate was then increased to the next level. If, for a certain flow rate, no more two-phase flow was verified, higher power was applied to the evaporator and the tests were started again for a low flow rate of working fluid.

The objective of the tests was to acquire temperature and pressure (differential) readings throughout the loop. The temperature readings were used to obtain the heat transfer coefficient, converted later to the Nusselt number. The differential pressure readings were used to verify the pressure drop across the condensation section during the tests.

### Data Reduction

A data reduction program was performed using the software MathCAD. The input data were the temperatures, absolute and differential pressures, the working fluid flow rate (when using the capillary

evaporator, the input was the heat applied to it), the cooling fluid flow rate verified during the experimental tests and the geometric parameters of the transport lines and condenser.

A two-phase pressure drop model was used for this data reduction program, based on the Separated Flow Model [17]. The pressure drop model then calculated the two-phase length in the condenser, and an interactive method was used to perform all the calculations, where the final results were the Nusselt number and pressure drop, with the respective uncertainties.

### Experimental Results

The experimental results obtained with both pumps (CPL and magnetic pump) were separately analyzed. This procedure had to be performed in order to evaluate the pressure drop levels of all microchannel condensers at different working conditions, i.e., according to the vapor quality at the condensation section inlet and saturation temperatures.

Due to the CPL working conditions, only vapor with a slight superheat leaves the capillary evaporator. Thus, at the microchannel condenser inlet, essentially saturated vapor was present. In the case of a magnetic pump driving the fluid throughout the loop, the vapor quality at the microchannel condenser inlet varied for each condition. As the heat load to the evaporator and liquid flow rate varied, the vapor quality at the condenser inlet also varied within a range from 10 to 55%.

### Results for Tests Using the Capillary Evaporator

The total pressure drop per channel that was verified on the microchannel condensers played an important factor. As the condensers presented very small channel or, in other words, capillary channels, high values of pressure drop were expected. The flow was affected by geometric parameters that, in some cases, may result on blocking the flow due to high vapor velocity. As the channel size decreased, the effect of the shear stress on the flow became more important.

Figure 2 presents the average pressure drop observed during the experimental tests versus the mass flow rate per channel for both operation temperatures. It can be observed that the pressure drop increases with the mass flow rate, as expected. The pressure drop for  $T_{sat}=45\text{ }^{\circ}\text{C}$  is greater than for  $T_{sat}=55\text{ }^{\circ}\text{C}$  because for lower temperatures, the working fluid viscosity is greater, which results in a greater flow resistance. A clear influence of the channel size was not verified. In fact, it would be expected that the pressure drop would increase dramatically with decreasing channel size. The highest value of pressure drop observed for  $T_{sat}=45\text{ }^{\circ}\text{C}$  was 221.45 Pa for the microchannel condenser of 0.75 mm and, for  $T_{sat}=55\text{ }^{\circ}\text{C}$  was 169.65 Pa for the same condenser.

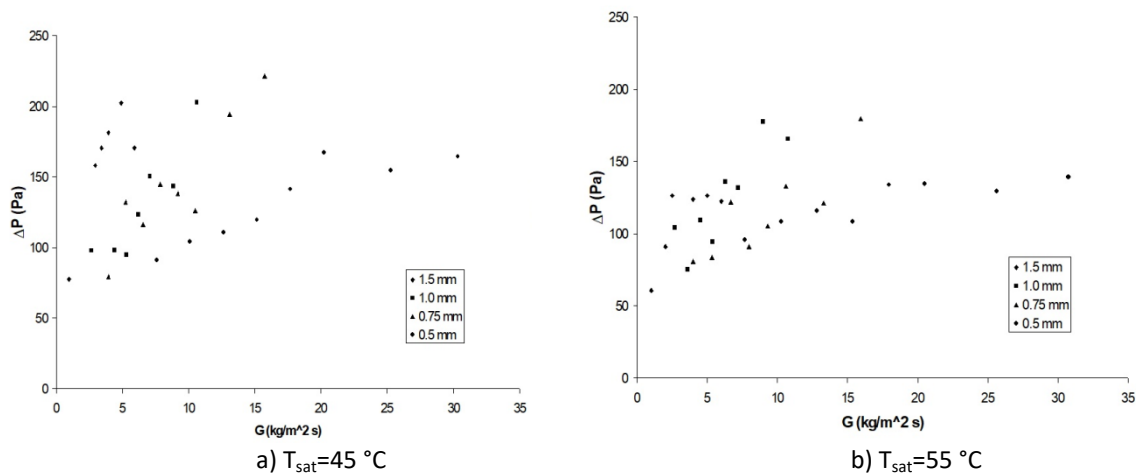


Figure 2 – Pressure drop versus mass flow rate.

In some cases, the pressure drop per channel for the condenser of 1.5 mm (at  $G=4.92\text{ kg/m}^2\text{ s}$  and  $T_{sat}=45\text{ }^{\circ}\text{C}$ :  $\Delta P=202.37\text{ Pa}$ ) was greater than for 0.5 mm (at  $G=25.28\text{ kg/m}^2\text{ s}$  and  $T_{sat}=45\text{ }^{\circ}\text{C}$ :  $\Delta P=154.87\text{ Pa}$ ). This behavior can be explained by the fact that, for smaller channel size, the number of parallel channels increased. With increasing number of parallel channels, the flow rate was divided decreasing the flow rate per channel, which directly affected the pressure drop. Consequently, the

pressure drop per channel was not expected to increase too much. It can be observed from Fig. 2 that, in some cases, the pressure drop for a lower mass flow rate was greater than for a higher mass flow rate.

Upon obtaining higher pressure drops for higher flow rates, the vapor velocity caused higher friction against the channel wall, with greater effect on the interface liquid/vapor. This represented that the shear stress between the phases was the major parameter that causes higher flow resistance, as observed also by Begg et al. [18].

### Results for Tests Using the Magnetic Pump

For tests using the magnetic pump, higher pressure drops were achieved for higher flow rates. Although, the pressure drop results did not present extremely high values due to the flow division in to the various parallel channels present in the condensers tested. Figure 3 presents the pressure drop results for tests performed at 45 and 55 °C.

As presented by Fig. 3, higher pressure drops were reached upon reducing the channels' size, as well as increasing the power applied to the evaporator, which increased the vapor flow rate in the condensers. Higher pressure drops were obtained for  $T_{sat}=45\text{ }^{\circ}\text{C}$  due to its direct effect on the viscosity of the methanol. For the tests performed at high flow rates, the lowest pressure drop was 350 Pa for the condenser with channel size of 1.5 mm at  $T_{sat}=55\text{ }^{\circ}\text{C}$  and the highest pressure drop was 62.8 kPa for the condenser with channel size of 0.5 mm at  $T_{sat}=45\text{ }^{\circ}\text{C}$ . Although higher levels of Nusselt number could be achieved at higher flow rates, the cost is extremely high as well, when considering the obtained results for the pressure drop. The microchannels heat exchangers, in this case represented by condensers, present high heat transfer capability as reported by Tuckermann and Pease [1], but it must be considered if the cost of higher levels of pressure drop is worth for certain applications.

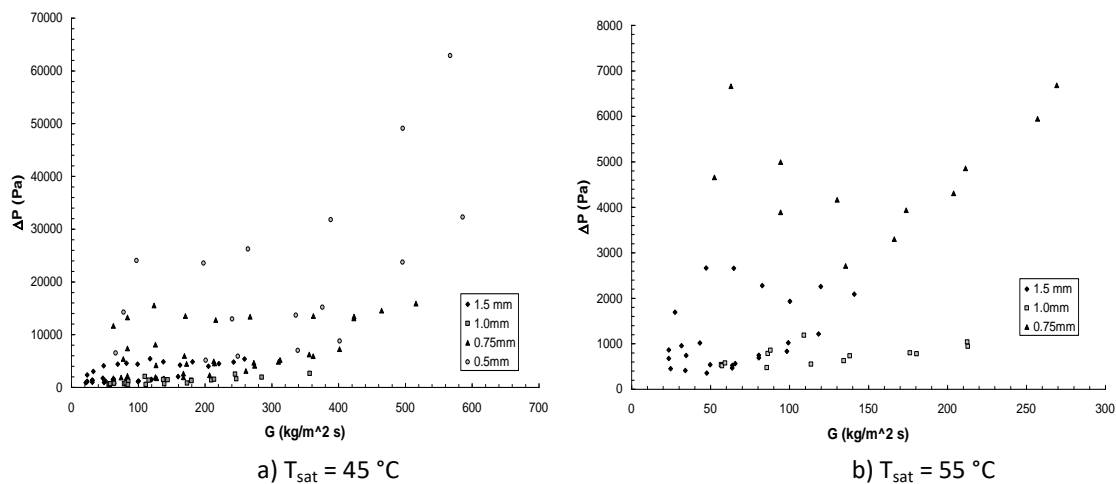


**Figure 3** – Pressure drop for test using a magnetic pump.

As seen on Fig. 3, it was observed different levels of pressure drop for the same flow rate. As explained in the experimental procedure section, the tests with the magnetic pump were performed varying the liquid flow rate for a fixed power applied to the evaporator. When no more two-phase flow was observed, then higher power was applied to the evaporator and the tests were started again for low flow rate, increasing it until no more two-phase flow was observed again. In other words, the vapor flow rate was constant and the liquid flow rate was varying. Then, the vapor flow rate was increased and the tests were started again. As a result, for the same liquid flow rate, the two-phase length presented different, depending on the power applied to the evaporator, resulting in different levels of pressure drop.

### Pressure Drop Correlation

From the obtained results, it became necessary the definition of an equation able to predict the pressure drop in microchannels. As mentioned in item 1, there are many correlations to calculate the

pressure drop available in the literature. However, there is a wide dispersion regarding the calculation presented by the correlations, when applied for microchannels flow conditions.

A first attempt was performed to correlate the experimental data using the correlation presented by Chisholm [19]. The obtained results did not present good correlation and the relative error verified was around 300%. Another attempt to correlate the experimental results was performed, using the Homogeneous Flow Model as suggested by Bowers and Mudawar [5-7]. Such comparison also presented unrealistic results, with relative error around 200%.

As a consequence of unsuccessful attempts in correlating the experimental results with available models, an equation to calculate the pressure drop had to be defined. The equation was defined in terms of the two-phase multiplier, which it is used on the Separated Flow Model [17] to calculate the pressure drop ( $\Delta P$  in Pa) as [20]:

$$\Delta P = \frac{2fLG^2v_l}{D} \left[ 1 + \frac{x}{2} \left( \frac{v_{lv}}{v_l} \right) \right] + G^2v_l \left( \frac{v_{lv}}{v_l} \right) x + \frac{g \sin \theta L}{v_{lv}x} \ln \left[ 1 + x \left( \frac{v_{lv}}{v_l} \right) \right], \quad (1)$$

where  $f$  is the friction factor,  $L$  is the channel length (m),  $G$  is the mass flow rate ( $\text{kg}/\text{m}^2 \text{ s}$ ),  $v_l$  and  $v_{lv}$  are the specific volume ( $\text{m}^3/\text{kg}$ ) of the liquid and liquid-vapor respectively,  $D$  is the hydraulics diameter (m),  $x$  is the vapor quality,  $g$  is the gravity acceleration and  $\theta$  is the channel inclination angle ( $^\circ$ ). Such equation had to be able to predict the pressure drop in microchannels, according to what was observed during the experiments.

Upon obtaining a correlation for the experimental results, the relation that states the two-phase multiplier ( $\phi^2$ ), as defined by Hahne et al. [21],

$$\phi^2 = \frac{(\Delta P / \Delta z)_{tp}}{(\Delta P / \Delta z)_{sp}}, \quad (2)$$

presents that such parameter is a relation between the two phase  $[(\Delta P / \Delta z)_{tp}]$  and single phase  $[(\Delta P / \Delta z)_{sp}]$  pressure drops. In case of evaluating the single-phase pressure drop for the liquid, the two-phase multiplier would be represented as  $\phi_l^2$  and, for the vapor,  $\phi_v^2$ . From the experimental results, an empirical relation for the two-phase multiplier for the liquid that showed better correlation is presented as:

$$\phi_l^2 = \left( 1 + 10X^{0.188} + X^{2.0} \right)^{0.5}, \quad (3)$$

where  $X$  is the Martinelli Parameter defined as:

$$X^2 = \left( \frac{1-x}{x} \right)^{2-n} \left( \frac{\rho_v}{\rho_l} \right) \left( \frac{\mu_l}{\mu_v} \right)^n, \quad (4)$$

where  $\rho_l$  and  $\rho_v$  are the liquid and vapor densities respectively ( $\text{kg}/\text{m}^3$ ),  $\mu_l$  and  $\mu_v$  are the liquid and vapor dynamic viscosities (Pa.s) and  $n$  is related to the flow regime in the channels ( $n=1$  for laminar and  $n=0.25$  for turbulent flow).

Equation (3) was compared against the experimental results for the pressure drop for both saturation temperatures and condensers. Figure 4 presents the comparisons for  $T_{\text{sat}}=45$  and  $55$   $^\circ\text{C}$ .



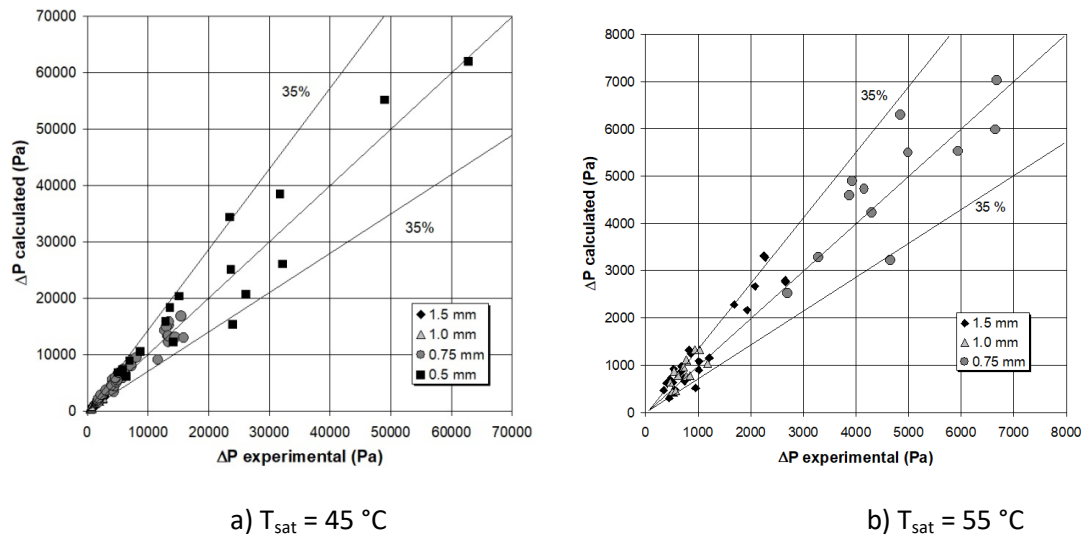


**Figure 4** – Comparison of the experimental results for pressure drop and Eq. (3).

Equation (3) presented, for both saturation temperatures and condensers tested, that 85 % of the overall results were within a relative error of 35 %. Such results showed that Eq. (3) presented a good correlation capability, which also showed to be an important tool in determining the pressure drop for microchannel condenser and that it would be used for new designs. Equation (3) presented a very high sensibility upon calculating the pressure drop along the microchannels, considering the geometric factors and heat transfer capabilities of such equipment, which was able to present a good correlation with the experimental data.

### Conclusions

An experimental investigation regarding the pressure drop during the convective condensation in microchannels flow was presented. The objective of this study was the investigation of the geometric parameters that influence the pressure drop during condensation in microchannels heat exchangers. The identification of such parameters would be used for microchannel heat exchangers design, applied for micro heat exchangers in order to improve their capabilities on heat dissipation. Such experimental investigation was performed to contribute for the knowledge improvement of several variables present in microchannels flow. Tests were performed for low and high flow rates. For low flow rates, a capillary pumped loop (CPL) was designed and used to test the microchannel condensers where the heat load applied to the capillary evaporator controlled the flow rate. This system presented to be easy to operate and control for all range of heat loads applied to the evaporator and saturation temperatures. For high flow rates, the capillary evaporator of the CPL was replaced by a magnetic driven pump with flow control, which allowed reaching flow rates that the CPL could not. Tests were performed for four microchannel condensers with different size and number of parallel channels. From the obtained results, it was possible to conclude that the microchannel condensers present high pressure drop, which presents higher as the hydraulics diameter decreases. The use of parallel channels contributed in managing the pressure drop verified per channel and proved to be important for keeping it on a range that could be handled by the pumping system, i.e., either the capillary evaporator or the magnetic pump. The pressure drop verified was considerable dependent on the geometric factors, but is showed to be influenced by the saturation temperature as well.

A correlation to predict the pressure drop, using the two-phase multiplier from the Separated Flow Model, was derived. The two-phase multiplier correlation, represented by Eq. (3), provided good agreement with all experimental results for both saturation temperatures used, which correlated 85% of the experimental data within an error of +/- 35%.

The information obtained in this investigation can be widely used for new designs of microchannel heat exchangers applied for miniature thermal control equipments such as capillary pumped loops (CPL) and loop heat pipes (LHP). Further investigations on microchannel heat

exchangers are still necessary in order to investigate the influence of different channels cross-sections and working fluids on the Nusselt number and pressure drop behavior.

## References

- [1] Tuckermann, D. B.; Pease, R. F. W., "High-Performance Heat Sinking for VLSI", IEEE Electron Device Letters, Vol. EDL-2, No.5, pp. 126-129, 1981.
- [2] Lazarek, G. M.; Black, S. H., "Evaporative Heat Transfer, Pressure Drop and Critical Heat Flux in a Small Vertical Tube with R-113". Int. J. Heat Mass Transfer, Vol. 25, No. 7, pp. 945-960, 1982.
- [3] Lin, S.; Kwok, C. C. K.; Li, R. -Y.; Chen, Z. -H.; Chen, Z. -Y., "Local frictional pressure drop during vaporizations of R-12 through capillary tubes", Int. J. Multiphase Flow, Vol. 17, No. 1, pp. 95-102, 1991.
- [4] Mishima, K.; Hibiki, T.; Nishihara, H., "Some Characteristics of Gas-Liquid Flow in Narrow Rectangular Ducts". Int. J. Multiphase Flow, Vol. 19, No. 1, pp. 115-123, 1993.
- [5] Bowers, M. B.; Mudawar, I., "Two-Phase Electronic Cooling Using Mini-Channel and Micro-Channel Heat Sinks: Part 1 - Design Criteria and Heat Diffusion Constraints". Transactions of the ASME, Vol. 116, pp. 290-297, 1994.
- [6] Bowers, M. B.; Mudawar, I., "Two-Phase Electronic Cooling Using Mini-Channel and Micro-Channel Heat Sinks: Part 2 - Flow Rate and Pressure Drop Constraints". Transactions of the ASME, Vol. 116, pp. 298-305, 1994.
- [7] Bowers, M. B.; Mudawar, I., "High Flux Boiling in Flow Rate, Low Pressure Drop Mini-Channel and Micro-Channel Heat Sinks". Int. J. Heat Mass Transfer, Vol. 37, No. 2, pp. 321-332, 1994.
- [8] Yang, C. -Y.; Webb, R. L., "Friction pressure drop of R-12 in small hydraulic diameter extruded aluminium tubes with and without microfins", Int. J. Heat Mass Transfer, Vol. 39, No. 4, pp. 801-809, 1996.
- [9] Ravigururajan, T. S.; Cuta, J.; McDonald, C. E.; Drost, M. K., "Effects of Heat Flux on Two-phase Flow Characteristics of Refrigerant Flows in a Micro-Channel Heat Exchanger". ASME - National Heat Transfer Conference, HTD - Vol. 329, pp. 167-178, 1996.
- [10] Han, Y., Liu, Y., Huang, J., "A Review of Development of Micro-Channel Heat Exchanger Applied in Air-Conditioning System", Energy Procedia Vol 14, pp. 148-153, 2012.
- [11] Kandlikar, S., Grande, W., "Evolution of Microchannel Flow Passages - Thermohydraulic Performance and Fabrication Technology", Heat Transfer Engineering, Vol 24, Issue 1, pp 3-17, 2003.
- [12] Jaluria, Y., "Optimization of Microchannel Flow Systems for Application in Practical Thermal Processes", Int Conf on Nanochannels, Microchannels and Minichannels, June 10-13, Dubrovnik, Croatia, 2018.
- [13] Riehl, R. R., "Convective Condensation in Small Diameter Channels With and Without a Porous Boundary", Ph.D. Dissertation, University of São Paulo-EESC/Clemson University-USA, 186p, 2000.
- [14] Stenger, F. J., "Experimental Feasibility Study of Water-Filled Capillary Pumped Heat Transfer Loops", NASA TM-X-1310. NASA Lewis Research Center, Cleveland, OH, 1966.
- [15] Faghri, A., "Heat Pipe Science and Technology", Taylor & Francis, 1995.
- [16] Ku, J., 1997, "Recent Advances in Capillary Pumped Loop Technology", National Heat Transfer Conference, Baltimore, MD, August 10-12, pp.1-21.
- [17] Collier, J. G., *Convective Heat and Mass Transfer*, McGraw-Hill International Book Company, 1981.
- [18] Begg, E.; Khrustalev, D.; Faghri, A., "Complete Condensation of Forced Convection Two-Phase Flow in a Miniature Tube", ASME Journal of Heat Transfer, Vol. 121, pp. 904-915, 1999.
- [19] Chisholm, D., 1973, "Pressure Gradients Due to Friction During the Flow of Evaporating Two-Phase Mixtures in Smooth Tubes and Channels". Int. J. Heat Mass Transfer, Vol. 16, pp. 347-358.
- [20] Carey, V. P., *Liquid-Vapor Phase-Change Phenomena*, Taylor & Francis, 1992.
- [21] Hahne, E.; Spindler, K.; Skok, H., "A New Pressure Drop Correlation for Subcooled Flow Boiling of Refrigerants". Int. J. Heat Mass Transfer, Vol. 36, No. 17, pp. 4267-4274, 1993.

# Numerical Investigation of MOFs Adsorption Cooling System Using Microchannel Heat Exchangers

Majdi M. Saleh<sup>1,2,3\*</sup>, Raya AL-Dadah<sup>1</sup> and Saad Mahmoud<sup>1</sup>

<sup>1</sup>School of Mechanical Engineering, University of Birmingham, Birmingham B15 2TT, UK

<sup>2</sup>University of Benghazi, Mechanical Engineering Department, Libya

<sup>3</sup>University of Ajdabiya, Mechanical Engineering Department, Libya

\*Corresponding author: email address: majdidwas@gmail.com

## Abstract

Adsorption cooling systems have major challenges in terms of the large size and capital cost due to use of conventional heat exchangers for adsorber beds and the poor performance of the currently used adsorbent materials. This work numerically investigates the performance of micro tube heat exchanger packed with Metal-Organic adsorbent material CPO-27(Ni). The investigation involves the effects of micro tube diameter and the layer thickness of the packed MOF on water uptake and the ratio of metal to adsorbent material ratio. Results showed that increasing the adsorbent material thickness reduces the uptake while using a layer thickness of 1mm produces the highest water vapor uptake of  $0.456\text{kg}_{\text{ads.}}/\text{kg}_{\text{ref.}}$  and adsorbent material to the tube metal mass ratio of 1.156. Also, changing the tube diameter results in little change in the uptake for the thicknesses of 1mm while for the thickness of 5mm, an improvement of 25% can be achieved by increasing the diameter from 1mm to 5mm.

**Keywords:** COMSOL Multiphysics, adsorption cooling, CFD model, CPO-27(Ni)/Water, low-temperature refrigeration, micro-channel adsorber bed.

## Introduction/Background

Adsorption refrigeration system has the advantages of being powered by solar and waste heat sources, using working fluids with no ozone depletion and low global warming potential compared to conventional vapor compression refrigeration systems [1]. Metal Organic Frameworks (MOFs) is a new class of adsorbent material with the high surface area, volume and adsorption uptake which were investigated for many applications such as catalysis, gas storage and gas separation [2-4]. The water uptake of many MOFs adsorbent materials is higher than that of silica gel at the same partial pressure [5]. The adsorber bed is the most important part of adsorption cooling system and tends to be the largest and the most expensive component of the system.

Various adsorber bed configurations were investigated for cooling applications. Riffel et al. [6] carried out experimental and simulation work for a finned tube heat exchanger and measured the performance of the system that used silica gel and zeolite as adsorbent materials. Their results showed that the average coefficient of performance of 0.33-0.58 and SCP 125-298, respectively with different operating conditions and the error between simulation model and experimental work was 20%. Sharafian et al. [7] investigated and compared nine adsorber beds such as shell and tube, spiral plate, annulus tube, hairpin, plate fin, finned tube, plate-tube, plate and simple tube to select the best one for use as adsorber bed. Their results indicated that the best bed configuration is the finned tube one for vehicle air conditioning and refrigeration in terms of adsorber bed to adsorbent mass ratio of 3.45, SCP of 80W/kg and COP of 0.25. Zhu et al. [8] compared two configurations of vehicle radiators for use as adsorber beds and the size of bigger one ( $410 \times 365 \times 30\text{mm}$ ) and for smaller one ( $240 \times 170 \times 30\text{mm}$ ) and the distances between the fins of two types was 1.5mm. The results indicated that the smaller size radiator achieved the highest coefficient of performance of 0.30 and specific cooling power of 198.4W/kg. Sharafian et al. [9] carried out

experimental work of two configurations of adsorber bed and measured the vapor water uptake for them. The first design consists of finned tube heat exchanger while the second design used engine oil cooler. The results indicated that the vapor water uptake for the second design is higher than that of the first design. The results indicated that when the time cycle of 10 min, the COP and SCP were 0.34 and 112.9 W/kg, respectively for the second design. A number of researchers have used CFD to simulate the performance of mass and heat transfer for adsorbent materials in various bed designs. Földner et al. [10] developed one dimensional model for the adsorbent layer on metal using COMSOL software and investigated the effect of the adsorbent layer thickness. The results indicated that the adsorbent surface temperature reached during the adsorption process is actually higher than the measured temperature due to the dynamic behavior of the sensor. COMSOL software has been used by Freni et al. [11] to simulate various numbers of loose adsorbent grains of silica gel RD, namely one, two and four grains. Their results indicated that the maximum water uptake for one grain at time 20s faster (0.116 kg/kg) than that of two grains (0.108 kg/kg) and four grains (0.102kg/kg) as well as for adsorbent bed temperature were 303.76, 305.84 and 309.014K, respectively. Shi et al. [12] used the lumped parameter and CFD modeling using COMSOL software to model the mass and heat transfer and simulate the adsorption process in the adsorber bed (finned tube). Their results showed that the water uptake increases by 8% as the fin pitch decreases. Also, results showed that decreasing the fin height from 35mm to 20mm results in increasing the water uptake by up to 19%. Experimental and simulation works have been implemented by Elsayed et al. [13] on the effect of diameter and length of adsorbent pellets of activated carbon on bed design of adsorption refrigeration system performance. Their results indicated that the water uptake increases as the pellet diameter of adsorbent material decreases and as well as when the pellet length increases. Although various configurations of adsorption beds were investigated, these bed configurations have the disadvantages of being large, expensive and their manufacturing is labor intensive. Therefore, this work investigates the performance of micro-tube adsorber bed using CPO-27(Ni) MOF material in terms of the effect of micro-tube diameter and the adsorbent material thickness on the water uptake and the ratio of metal to adsorbent material ratio.

### **Adsorber Bed Description**

The adsorber bed consisting of a micro-channel tube that is covered by a layer of CPO-27(Ni) as adsorbent material that is adsorbed the water vapor refrigerant coming from the evaporator. The cooling water is flowed through the internal tube to be cooled down the adsorber bed until it is adsorbed the water refrigerant. The measurement of adsorber bed is a 30mm x 30mm cross-section area of tube diameter 1mm and the length of tube 100 mm as shown in Figure 1.

### **CFD Model Set up**

Figure 2 illustrates the model set up consisting of a micro-channel tube covered by a layer of CPO-27(Ni) and cooled by water flow. The description equations from 1 to 10 have been solved by COMSOL Multiphysics software for simulating the adsorption process. Equations 1 and 2 [14] describe the conservation of the mass and energy while equations 3, 4 and 5 [14] define the various terms used in equations 1 and 2.

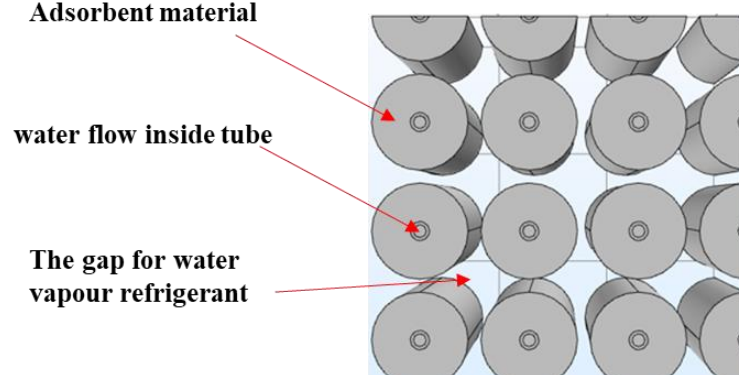


Figure 1. Schematic diagram of the micro-channel tube adsorber bed.

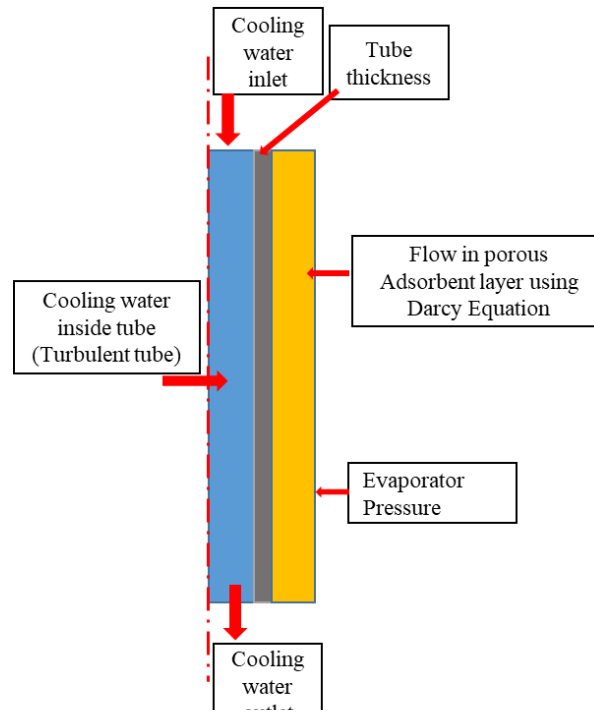


Figure 2. Schematic diagram for the domain of the micro-channel tube.

$$\frac{\partial(\varepsilon_s \rho_w)}{\partial t} + \nabla(\rho_w u_w) = \frac{\partial(\rho_s w)}{\partial t} \quad [1]$$

$$\rho C_p \frac{\partial T_{bed}}{\partial t} + C p_w \nabla(T_{bed} \rho_w u_w) = \nabla(k_s \nabla T_{bed}) + \rho_s \Delta H_s \frac{\partial w}{\partial t} \quad [2]$$

Where  $\varepsilon_s$  is the adsorbent porosity that is taken as 0.868 for CPO-27(Ni).  $\rho_s$  and  $\rho_w$  are the water vapor density and CPO-27(Ni) powder.  $u_w$  is the velocity of water vapor and can be determined by the following equation;

$$u_w = -\frac{\alpha}{\mu} \nabla P_s \quad [3]$$

Where  $\nabla P_s$  is pressure gradient of water vapor.  $\rho C_p$  can be expressed as follows:

$$\rho C_p = (\varepsilon_s \rho_w + \rho_s w) C p_w + \rho_s C p_s \quad [4]$$

$k_s$  is the bed thermal conductivity, that is 0.15575 W/(m.K).  $\alpha$  is permeability which is defined as [15]

$$\alpha = \frac{4\varepsilon_s^3 R_p^2}{150(1-\varepsilon_s)^2} \quad [5]$$

The adsorption kinetics was used to calculate the refrigerant vapor uptake for CPO-27(Ni) using the linear driving force as follows in equations (6-8) [16].

$$\frac{\partial w}{\partial t} = K(w_{max} - w) \quad [6]$$

$$K = \frac{15D_S}{R_p^2} \quad [7]$$

$$D_S = D_{so} \exp\left[-\frac{E_a}{RT_{bed}}\right] \quad [8]$$

Where the values of  $D_{so}$  and  $E_a$  are listed in Table 1.  $w_{max}$  is the maximum water uptake of CPO-27(Ni) powder can be determined using the adsorption isotherm equations (9 and 10).

$$w_{max} = w_0 \exp\left[-\frac{A}{E}\right]^n \quad [9]$$

$$A = -RT_{bed} \ln\left(\frac{P_{ref}}{P_{bed}}\right) \quad [10]$$

Where  $w_0$ ,  $n$  and  $E$  are listed in Table 2.

Table 1 shows the parameters of the adsorption kinetics.

Partial pressure < 0.2	Partial pressure >0.2
$D_{so}=7.8299e10^{-8} \text{ m}^2/\text{s}$	$D_{so}=7.4677e10^{-10} \text{ m}^2/\text{s}$
$E_a=3.2006e10^4 \text{ J/mol}$	$E_a=1.4806e10^4 \text{ J/mol}$

Table 2 shows the parameters of the isotherm equation.

Parameter	CPO-27(Ni)/water
$w_0$	0.46826
$n$	5.6476
$E$	10088.7J/mol

### Model validation

Model validation was carried out using published experimental data for CPO-27(Ni)/water [17]. Figure 3 compares the predicted average bed temperature with the experimental data. The model predictions of the bed temperature during adsorption process are in good agreement with experimental data for CPO-27(Ni)/water with a maximum deviation of 7.49%.

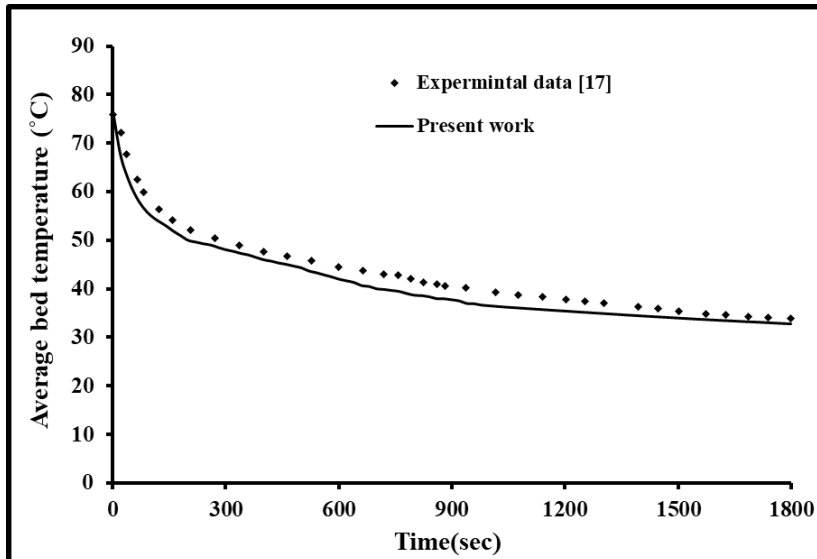


Figure 3. Comparison of the predicted average bed temperature with published experimental results.

### Discussion and Results

The simulation work investigates the effect of different tubes diameters and adsorbent material thickness on the water uptake of CPO-27(Ni). The operating conditions used in this study are evaporator temperature of 15°C, inlet cooling water temperature of 30°C and an initial bed temperature of 90°C with a cycle time of 1800s and the flow rate of cooling water of 0.21 L/min. The CFD model was used to investigate the impact of packing thickness ranging from 1 to 5 mm on the water uptake rate and the average of bed temperature during the adsorption process with microchannel tube diameter ranging from 1mm to 5mm. Figure 4 reveals that the water uptake variation with time using different packing thicknesses ranging from 1mm to 5 mm with a tube diameter of 1mm. It can be seen that when the packing thickness increases, the water uptake decreases. The variation of average bed temperature with the time for various packing thicknesses is presented in Figure 5. It is clear that at the first 100 sec the adsorbent temperature decreases significantly and then decreases at a lower rate. However, as the thickness of the adsorbent decreases, the temperature reached decreases with the lowest value achieved by the 1mm packing thickness.

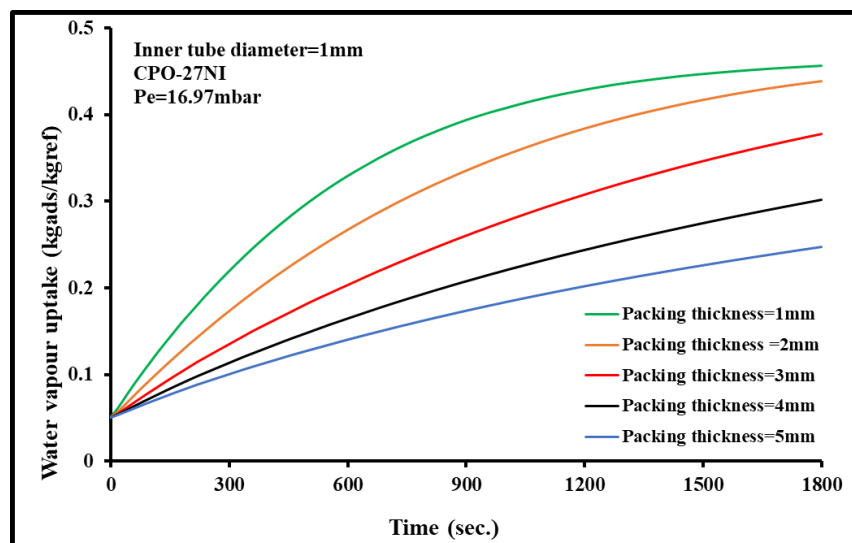


Figure 4. Variation of the water uptake rate with time at different packing thicknesses.

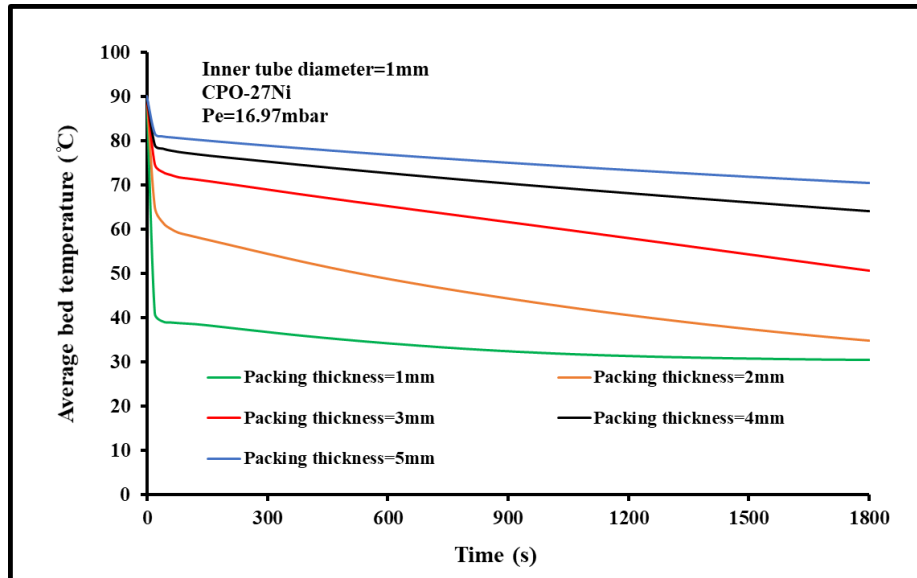


Figure 5. Variation of the adsorbent temperature with time at different packing thicknesses.

Figure 6 illustrates the variation of adsorbent material to tube metal mass ratio with different tube diameter for different adsorbent thickness ranging from 1 to 5mm. It can be seen that as the inner tube diameter increases, the ratio of adsorbent material to tube metal mass decreases. It is clear that for the tube diameter of 1mm and adsorbent packing of 5mm, the ratio of adsorbent material to the tube metal is the highest. Figure 7 shows the variation of maximum water vapor uptake with inner tube diameter for different adsorbent material layer ranging from 1 to 5mm. It can be seen that the maximum water uptake with an adsorbent thickness of 3mm and 5mm increases as the tube diameter increases from 1 to 5mm. However, for the adsorbent thickness of 1mm, the maximum water vapor uptake remains constant as the diameter increases from 1mm to 5mm.

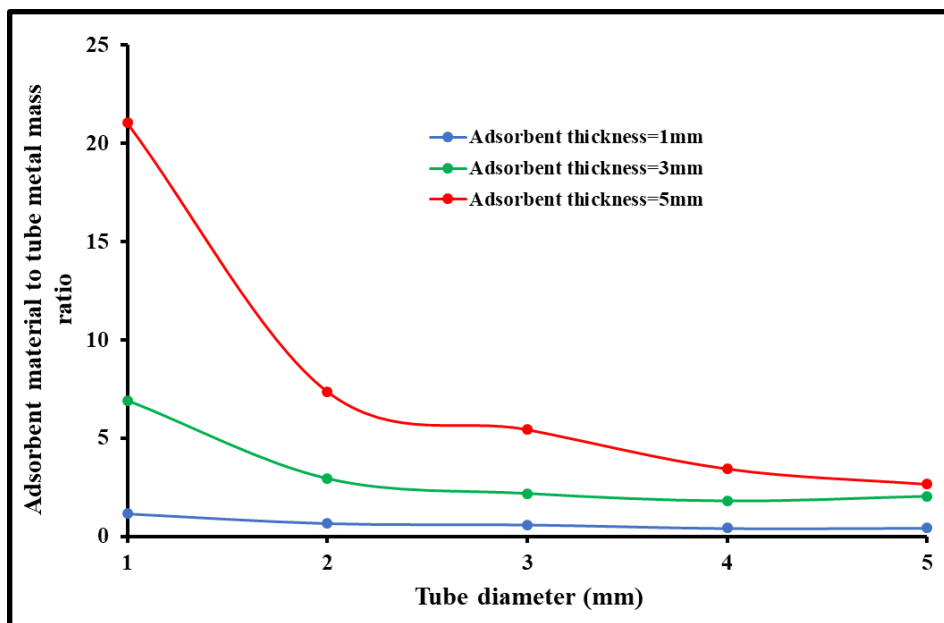


Figure 6. Variation of the adsorbent material to tube metal mass ratio with tube diameter.



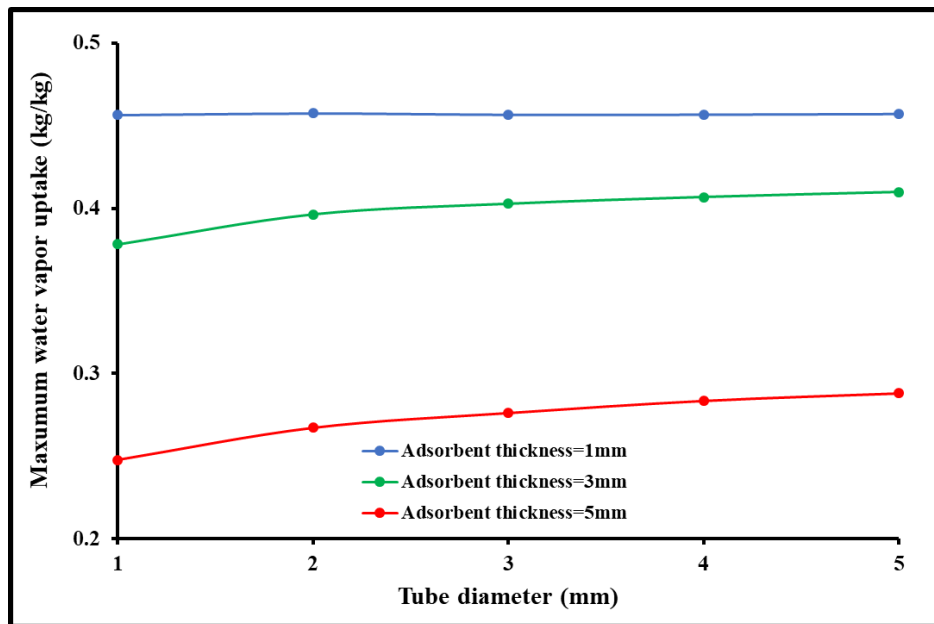


Figure 7. Variation of tube diameter with the maximum water vapor uptake.

## Conclusions

- The developed model predictions are in good agreement with the experimental data for CPO-27(Ni)/water
- Comparison of the adsorbent mass and tube metal mass for various tube diameters showed that the tube diameter of 1mm and adsorbent packing of 5mm, the ratio of adsorbent material to the tube metal is the highest.
- Increasing the adsorbent material thickness results in reducing the water uptake due to the increase in adsorbent material temperature with increasing the thickness.
- The maximum water uptake with an adsorbent thickness of 3mm and 5mm increases as the tube diameter increases from 1 to 5mm.
- The maximum water uptake for the adsorbent thickness of 1mm is not affected by the increase in the tube diameter.

## References

- [1] Rezk, Ahmed RM, and Raya K. Al-Dadah. "Physical and operating conditions effects on silica gel/water adsorption chiller performance." *Applied Energy* 89.1 (2012): 142-149.
- [2] Elsayed, Eman, et al. "Aluminium fumarate and CPO-27 (Ni) MOFs: characterization and thermodynamic analysis for adsorption heat pump applications." *Applied Thermal Engineering* 99 (2016): 802-812.
- [3] Rezk, Ahmed, et al. "Characterisation of metal organic frameworks for adsorption cooling." *International journal of heat and mass transfer* 55.25 (2012): 7366-7374.
- [4] Saha, Dipendu, and Shuguang Deng. "Ammonia adsorption and its effects on framework stability of MOF-5 and MOF-177." *Journal of colloid and interface science* 348.2 (2010): 615-620.
- [5] Henninger, Stefan K., Hesham A. Habib, and Christoph Janiak. "MOFs as adsorbents for low temperature heating and cooling applications." *Journal of the American Chemical Society* 131.8 (2009): 2776-2777.

- [6] Riffel, D.B., Wittstadt, U., Schmidt, F.P., Núñez, T., Belo, F.A., Leite, A.P. and Ziegler, F., 2010. Transient modeling of an adsorber using finned-tube heat exchanger. *International Journal of Heat and Mass Transfer*, 53(7-8), pp.1473-1482.
- [7] Sharafian, A. and Bahrami, M., 2014. Assessment of adsorber bed designs in waste-heat driven adsorption cooling systems for vehicle air conditioning and refrigeration. *Renewable and Sustainable Energy Reviews*, 30, pp.440-451.
- [8] Zhu, L.Q., Gong, Z.W., Ou, B.X. and Wu, C.L., 2015. Performance analysis of four types of adsorbent beds in a double-adsorber adsorption refrigerator. *Procedia Engineering*, 121, pp.129-137.
- [9] Sharafian, A., Mehr, S.M.N., Huttema, W. and Bahrami, M., 2016. Effects of different adsorber bed designs on in-situ water uptake rate measurements of AQSOA FAM-Z02 for vehicle air conditioning applications. *Applied thermal engineering*, 98, pp.568-574.
- [10] Földner, G. and Schnabel, L., 2008, November. Non-isothermal kinetics of water adsorption in compact adsorbent layers on a metal support. In *Proc. COMSOL Conf. 2008 Hann.*
- [11] Freni, A., Maggio, G., Cipiti, F. and Aristov, Y.I., 2012. Simulation of water sorption dynamics in adsorption chillers: One, two and four layers of loose silica grains. *Applied Thermal Engineering*, 44, pp.69-77.
- [12] Shi, B., AL-Dadah, R.K., Mahmoud, S., Elsayed, A. and Rezk, A., 2009. Mathematical and CFD modelling for a rectangular finned tube adsorption bed for automotive cooling system. In *Proc. of the 5th Heat Powered Cycles Conference*.
- [13] Elsayed, A., Mahmoud, S., Al-Dadah, R., Bowen, J. and Kaialy, W., 2014. Experimental and numerical investigation of the effect of pellet size on the adsorption characteristics of activated carbon/ethanol. *Energy Procedia*, 61, pp.2327-2330.
- [14] Jribi, S., Saha, B. B., Koyama, S., Chakraborty, A., Ng, K. C. Study on activated carbon/HFO-1234ze(E) based adsorption cooling cycle. *Applied Thermal Engineering*. 2013;50(2):1570-1575.
- [15] Zhang, L. Z., Wang, L. Effects of coupled heat and mass transfers in adsorbent on the performance of a waste heat adsorption cooling unit. *Applied Thermal Engineering*. 1999;19(2):195-215.
- [16] Chua, H. T., Ng, K. C., Malek, A., Kashiwagi, T., Akisawa, A., Saha, B. B. Modeling the performance of two-bed, silica gel-water adsorption chillers. *International Journal Of Refrigeration-Revue Internationale Du Froid*. 1999;22(3):194-204.
- [17] Shi, B., 2015. *Development of an MOF based adsorption air conditioning system for automotive application* (Doctoral dissertation, University of Birmingham).

# Natural graphite: Potential material for heat exchangers of waste heat recovery systems

N. Mohammadaliha, W. Huttema and M. Bahrami \*

*Laboratory for Alternative Energy Conversion (LAEC), School of Mechatronic Systems Engineering, Simon Fraser University, Surrey, British Columbia, Canada*

\*Corresponding author: mbahrami@sfu.ca

## Abstract

Natural graphite sheets are promising candidates for the material of heat exchangers used in waste heat recovery systems harvesting heat from wet flue gasses, due to their low density, low price, high thermal conductivity, and great corrosion resistance properties. To show the feasibility of using graphite as the material of heat exchangers working in corrosive environments, the performance of graphite as a condensation surface is investigated and compared to similar aluminium surface under different temperature and humidity conditions. It is observed that the condensation rate on a graphite surface is the same as an untreated aluminium surface, although the graphite surface is more hydrophilic than the aluminium one.

**Keywords:** Graphite, Waste heat recovery, Condensation rate, Contact angle, Wet flue gas, Corrosion.

## Introduction

Owing to the low thermal efficiency of industrial processes, a significant portion of the total energy input into the energy conversion systems is released to the environment in form of low-grade thermal energy or waste heat [1]. Waste heat recovery from low-temperature flue gas streams is not only beneficial for compensating the low energy efficiency of industrial units, but also helpful for decreasing fossil fuels consumption, controlling release of harmful chemicals into the ambient, as well as addressing climate change and our environmental footprint. The annual growth rate of the global waste heat recovery market is expected to be 6.8% during 2016 – 2022 [2]. Using phase change heat exchangers, in which recovery of both sensible and latent heat of wet flue gas streams condensation occurs, results in much more efficient heat recovery systems [3,4]. However, since the main source of wet flue gasses is burning fossil fuels such as natural gas and coal, it raises the issue of corrosion in heat exchangers because of water condensation on the heat exchanger surfaces and formation of high-concentration sulfuric acid and some other chemicals [5]. Hwang et al [6] studied the performance of heat exchangers with in-line and staggered arrangements of crushed titanium tubes for latent heat recovery from flue gas. Titanium tubes didn't show any sign of corrosion after one year, which made the titanium a good candidate for the material of heat exchangers working in corrosive environment [6]. Moreover, staggered arrangement of tubes was reported to have a better thermal performance than in-line arrangement for both sensible and latent heat recovery [6]. Xiong et al. [7] investigated the performance of a fluorine plastic heat exchanger for latent heat recovery from flue gas, motivated by the material's corrosion resistance. They showed that 80% and 20% of the recovered heat came from recovering the latent heat and sensible heat, respectively [7].

In addition to corrosion resistance, other factors including cost, fabrication, weight, and thermal properties should be considered to select a material for heat exchangers recovering latent heat from flue gas. Graphite is one of the best potential candidates for such applications due to its great corrosion resistance properties, high thermal conductivity, and light-weight.

Levy et al. [5] performed long-term corrosion tests on some materials, including graphite, under different temperatures and sulfuric acid concentrations. The results of this study showed that graphite had a good corrosion resistance, although it absorbed sulfuric acid at high concentration of the acid. Moreover, no degradation was observed for graphite samples [5].

This study aims to compare condensation on graphite compared to aluminium surfaces. Wettability of a natural graphite sheet surface is compared to a conventional aluminium foil surface. Moreover, the condensation regime on the graphite surface is investigated using some images taken during condensation. Finally, condensation rates on aluminium and graphite surfaces are compared for two different humid air conditions.

## 2. Material and Methods

Sample natural graphite sheets, purchased from Graphtech, were prepared and compared to sample aluminium foil sheets, purchased from McMaster-Carr. Static contact angles of the aluminium and graphite samples were measured using an OCA 15 Contact Angle Goniometer (DataPhysics Instruments, Germany) at least at five different locations on each sample. Further, some images were captured from the samples during condensation, using a digital microscope (AM7915MZTL, Dino-Lite).

Condensation tests on the graphite and aluminium samples were performed inside a standard environmental chamber (ESX-4CA Platinous, ESPEC). All the samples were cut in a rectangular shape with the surface area of  $140 \text{ cm}^2$  ( $14 \text{ cm} \times 10 \text{ cm}$ ). As schematically shown in Fig. 1, the samples were mounted on the cold plate using four screws on the corners. A thermally conductive paste (OMEGATHERM™) was applied at the interface between the cold plate and the samples to enhance the heat transfer between the sample and cold plate by reducing the thermal contact resistance (TCR). A Thermal bath (RK-12122, Cole-Parmer) was used to circulate chilled water as the liquid coolant through the cold plate. Two T-type thermocouples (OMEGA) were attached to the surface of the samples to monitor temperature during the tests. Two different ambient conditions, labelled as: i) A ( $27^\circ \text{C}$  and  $43\% \text{RH}$ ); and ii) B ( $25^\circ \text{C}$  and  $60\% \text{RH}$ ), were arbitrarily selected to perform the condensation tests. As shown in Fig. 2, the average surface temperature of the samples (the average of the two thermocouple readings) remained nearly constant during the tests; considering the uncertainty of the readings, all the tests were conducted at the same average surface temperature. For the condition A, no temperature difference was observed between two thermocouples attached to the surface of aluminium and graphite samples. However, the difference between the readings of two thermocouples for the condition B were  $1.69 \pm 0.10^\circ \text{C}$  and  $2.06 \pm 0.22^\circ \text{C}$  on the graphite and aluminium surfaces, respectively. The reason for the effect of ambient conditions on the surface temperature of samples should be studied in more depth in our future studies.

A relative humidity sensor (HMP110 Humidity and Temperature Probe) was installed near the surfaces to accurately measure the ambient conditions near the condensing surfaces. The temperature and relative humidity of the ambient air near the samples were measured as  $25 \pm$

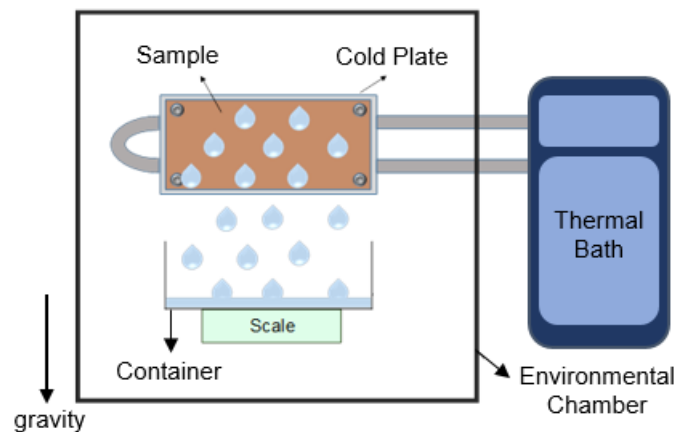
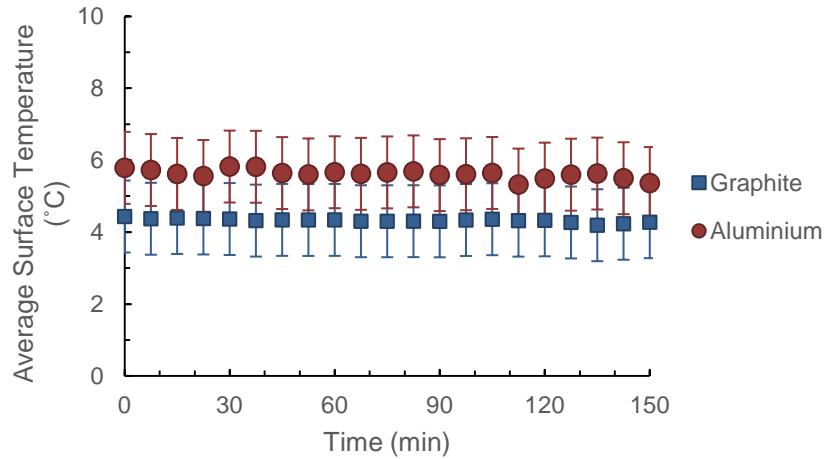


Fig. 1 Schematic of the experimental setup for the condensation tests

0.2 °C and  $47 \pm 0.71$  %RH for condition A and  $23 \pm 0.2$  °C and  $64 \pm 0.96$  %RH for condition B. The corresponding dew points for the conditions A and B were  $13 \pm 1$  °C and  $15 \pm 2$  °C, respectively. As shown in Fig. 1, mass of the condensate was measured using a scale (MXX-612, Denver Instrument) with readability of 0.01 gram, placed inside the environmental chamber. When the condensation surface reached steady-state and constant condensation rate, recording the mass of the condensed water was started.



**Fig. 2** Average surface temperature of the samples during the condensation tests

### 3. Results and Discussion

The surface wettability plays a central role in condensation efficiency, as it determines the condensation regime on the heat exchanger surface [8]. As shown in Fig. 3, The static contact angle of our aluminium and graphite surfaces were measured as  $89.2 \pm 4.0^\circ$  and  $74.8 \pm 2.5^\circ$ , respectively. Therefore, graphite is more hydrophilic than aluminium, although both are categorized as hydrophilic materials. Figure 4 also shows that surface energy of graphite is higher than aluminium, as the shape of the droplets on the graphite surface is less spherical than the ones on the aluminium surface.

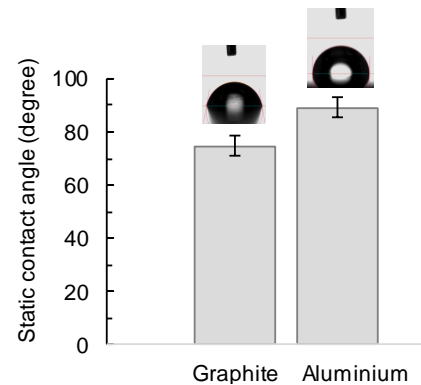


**Fig. 3** Contact angles of graphite and aluminium surfaces

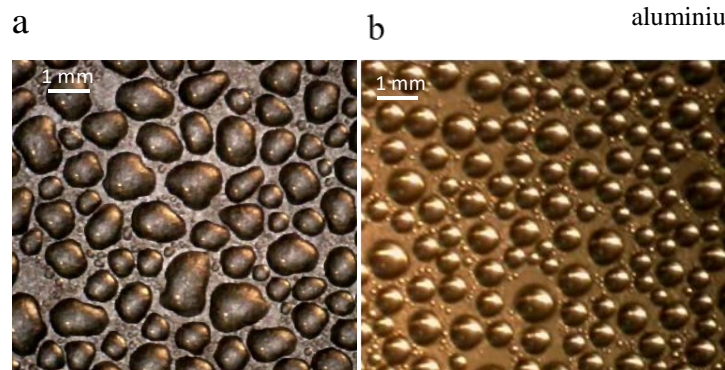


**Fig. 4** Shape of droplets formed on: a) a natural graphite sheet and b) an aluminium surface during condensation

To visualize the condensation regime on the graphite surface, some images were captured from the condensation of humid air (Condition A) on the graphite surface. As shown in Fig.

5, water droplets were nucleated on the graphite surface (Fig. 5 a), and they started to grow by condensation of water vapor on the surface of droplets and coalescence of adjacent droplets (Fig. 5 a-c). As marked by yellow dashed ovals in Fig. 5, smaller droplets (Fig. 5 d) coalesced into new bigger droplets on the surface (Fig. 5 e). The droplets were finally removed from the surface by gravity when they became big enough to overcome the surface tension and slide down the surface (Fig. 5 f). The blue dotted ovals in Fig 5 f-i indicated that after removal of the big droplets from the surface, the surface became available for nucleation of new droplets and the cycle repeated. The green circles in Fig. 5 g and i indicated that small portions of big sliding droplets stuck on the surface due to the high surface energy of the graphite surface, which is not usually observed for hydrophobic surfaces.

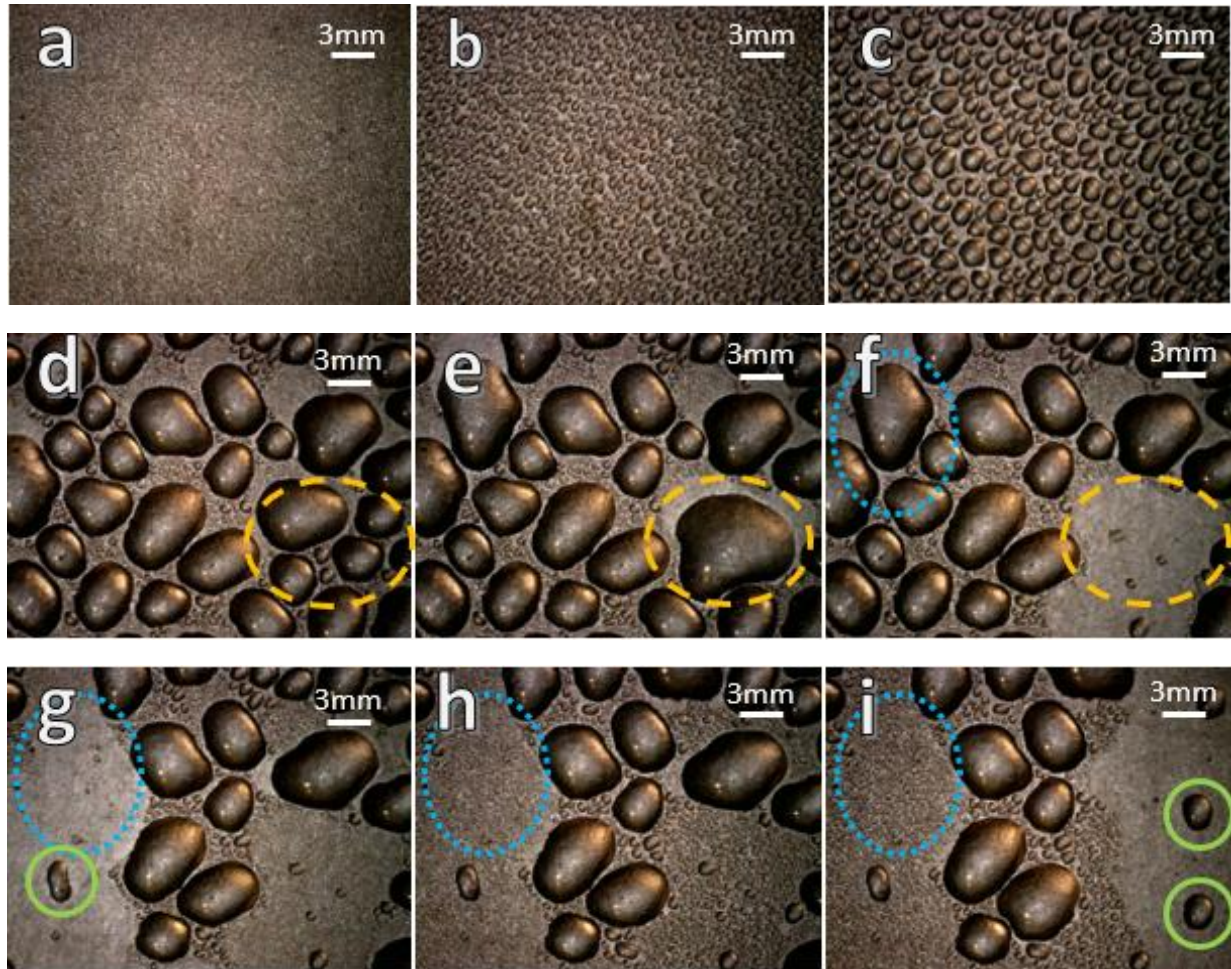


**Fig. 5** (a-c) Images of growth of droplets on a graphite surface in the first 25 minutes of a test; (d-f) Images of coalescence of droplets and droplet removal from the surface (at steady state); (g-i) Growth of new droplets on the surface.

Although film-wise condensation, in which a liquid film is formed on the surface, is the dominant condensation regime for hydrophilic surfaces, non-spherical droplets were observed on a natural graphite surface rather than a liquid film. Moreover, the shape of the droplets on the graphite surface

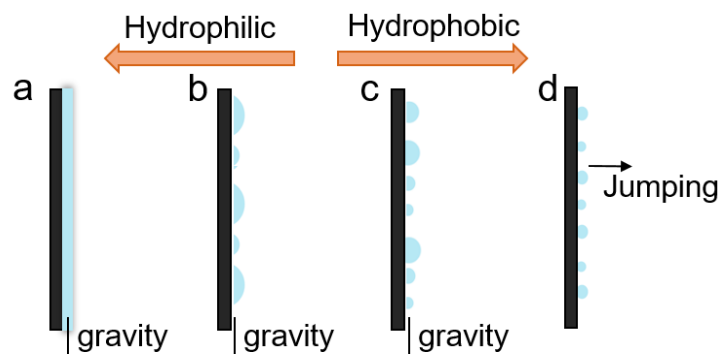


**Fig. 6** Schematic figure demonstrating the shape of condensate formed on surfaces based on the surface wettability. Gravity is the mechanism for condensate removal from the surface for hydrophilic and hydrophobic surfaces. For super hydrophobic surfaces, jumping of micro droplets is the dominant mechanism for condensate removal from the surface.

was not spherical due to high surface free energy and hydrophilicity of the surface (Fig. 5). Based on the well-documented studies in the literature, there are two main mechanisms for condensate removal from the surface [9]. Gravity is the main mechanism for water removal from hydrophilic and hydrophobic surfaces (Fig. 6 a-c). Moreover, droplets leave hydrophobic surfaces (Fig. 6 c) at much smaller sizes than hydrophilic surfaces (Fig. 6 a and b) [10]. Jumping of droplets is the second mechanism which occur on super hydrophobic surfaces whose contact angles higher than 150 degrees (Fig. 6 d). As a result of releasing the excess of surface energy, micro droplets jump from the surface after coalescence, which significantly increases the condensation efficiency [9]. On the other hand, not only the condensate removal from the surface but also the nucleation of droplets plays a crucial role in the condensation efficiency. Using molecular dynamics simulations, Sheng et al. [11] studied the effects of surface wettability and surface energy on nucleation of condensate on a surface. The results of this study revealed that on hydrophilic surfaces with contact angles smaller than  $\sim 40^\circ$ , a liquid film of condensate was formed. However, when the contact angle of the surface was larger than  $\sim 40^\circ$  and smaller than  $\sim 135^\circ$ , droplets formed on the surface instead of a film, and the shape of the droplets depended on the contact angle of the surface. Therefore, as shown in Fig. 6 b, according to literature, the condensation regime on our graphite surface sample can be categorized as dropwise condensation due to the formation of droplets on the surface. However, gravity is the dominant mechanism for droplet removal from the surface, and the condensation rate on the graphite surface is not as efficient as dropwise condensation on hydrophobic surfaces due to the high surface energy of the graphite, resulting in removal of droplets at larger sizes. Moreover, it should be noted that, in this study, the condensation of humid air was investigated, having high concentrations of non-condensable gases, which significantly reduces the condensation rate compared to condensation of water vapor. Therefore, the condensation regime of water vapor on graphite may be a film-wise condensation (see Fig. 6 a), which should be studied in more depth in our future studies.

Figure 7 compares the steady-state condensation rate on the graphite and aluminium surfaces at two different ambient conditions. The results of the condensation tests at the two conditions (A and B) reveals that although the graphite is more hydrophilic than aluminium, the trade-off between nucleation and removal of droplets leads to almost same condensation rate on both graphite and aluminium surfaces.

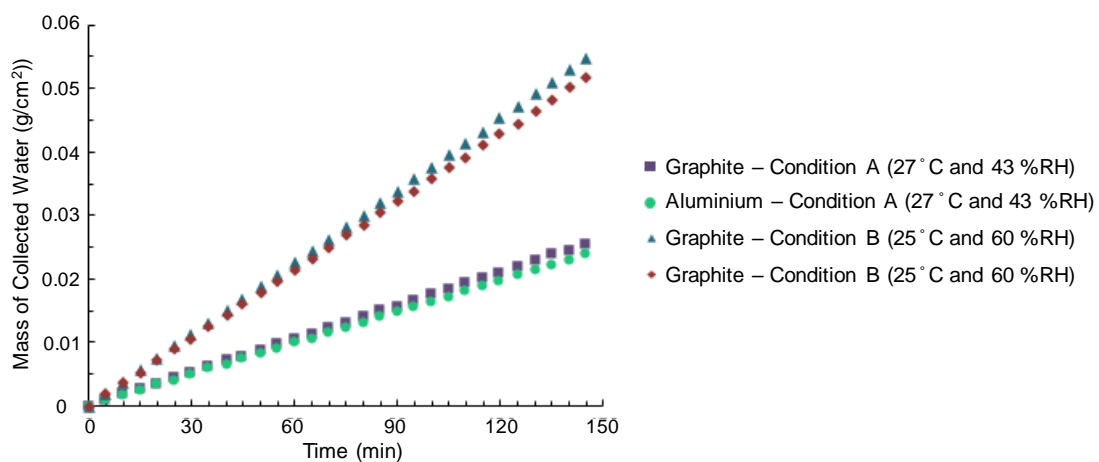


**Fig. 7** Mass of collected water on graphite and aluminium surfaces at two different ambient conditions

It can be concluded that in case of dropwise condensation, as shown in Fig. 6 b and c, increasing the contact angle of the surface does not necessarily increase the condensation performance of the surface. Increasing the contact angle of the surface enhances the water removal from the surface by gravity due to lower surface tension, but it decreases the chance of nucleation and formation of stable droplets on the surface. However, when the contact angle of the surface becomes larger than a threshold, the effect of hydrophobicity of the surface on the condensate removal becomes more significant than the negative effect of hydrophobicity on the nucleation of droplets on the surface.

## Conclusions

Impressive corrosion resistance properties, high thermal conductivity, and low density of natural graphite surfaces make them an excellent candidate for the material of heat exchangers working in corrosive environment like the flue gas latent heat recovery systems. In this work, condensation on a natural graphite surface was compared to a conventional aluminium surface. It was found that the condensation regime of humid air (having non-condensable gasses) on the graphite surface was dropwise, similar to an untreated aluminium surface. Although the graphite surface was more hydrophilic than the aluminium surface, the performance of the graphite as a condensing surface was similar to aluminium.

## References:

- [1] Mawade, P. S., & Watt, K., *Waste Heat Recovery Systems for Refrigeration-A Review*. International Journal of Scientific Research in Science and Technology, 3, 432-442, 2017.
- [2] Sengupta, P., Dutta, S. K., & Choudhury, B. K., *Waste Heat Recovery Policy*. In Sustainable Energy and Transportation (pp. 185-205), Springer, Singapore, 2018.
- [3] Shi, X., Che, D., Agnew, B., & Gao, J., *An investigation of the performance of compact heat exchanger for latent heat recovery from exhaust flue gases*. International Journal of Heat and Mass Transfer, 2011.
- [4] Terhan, M., & Comakli, K., *Design and economic analysis of a flue gas condenser to recover latent heat from exhaust flue gas*. Applied Thermal Engineering, 2016.
- [5] Levy, E., Bilirgen, H., & DuPoint, J., *Recovery of water from boiler flue gas using condensing heat exchangers*. Lehigh University, 2011.
- [6] Hwang, K., ho Song, C., Saito, K., & Kawai, S., *Experimental study on titanium heat exchanger used in a gas fired water heater for latent heat recovery*. Applied Thermal Engineering, 30(17-18), 2730-2737, 2010.
- [7] Xiong, Y., et al., *Pilot-scale study on water and latent heat recovery from flue gas using fluorine plastic heat exchangers*, Journal of Cleaner Production, 2017.
- [8] Zhao, H., & Beysens, D., *From droplet growth to film growth on a heterogeneous surface: condensation associated with a wettability gradient*. Langmuir, 11(2), 627-634, 1995.
- [9] Miljkovic, N., Enright, R., Nam, Y., Lopez, K., Dou, N., Sack, J., & Wang, E. N., *Jumping-droplet-enhanced condensation on scalable superhydrophobic nanostructured surfaces*. Nano letters, 13(1), 179-187, 2012.
- [10] Rose, J. W., *Dropwise condensation theory and experiment: a review*. Proceedings of the Institution of Mechanical Engineers, Part A: Journal of Power and Energy, 216(2), 115-128, 2002.
- [11] Sheng, Q., Sun, J., Wang, Q., Wang, W., & Wang, H. S., *On the onset of surface condensation: formation and transition mechanisms of condensation mode*. Scientific reports, 6, 30764, 2016.



# Ultra-clean Biomass Gasification/Combustion Unit for Micro-CHP based on a Stirling Engine

M. Steiner, S. Beer<sup>1\*</sup>, D. Hummel<sup>1</sup>

<sup>1</sup>Ostbayerische Technische Hochschule Amberg-Weiden, Kaiser-Wilhelm-Ring 23

<sup>2</sup>Ostbayerische Technische Hochschule Amberg-Weiden

\*Corresponding author: s.beer@oth-aw.de

## Abstract

A biomass fired micro-scale CHP unit based on a 1 kW Stirling engine has been developed with a focus on overcoming the well known fouling and corrosion problems that occur at the heat ex-changer of the Stirling engine. The objective is met by combining the principles of an updraft gasi-fier that comprises a fixed biomass fuel bed with a large height to diameter ratio and a low-emission combustion chamber using a swirl burner for the produced combustible gas. A low producer gas temperature of 60 to 80 C at the outlet of the gasifier is the most significant parameter for the stability of the process. The working hypothesis of the project is: The lower the outlet temperature of the producer gas, the more of the chemical compounds produced in the hot oxidizing zone of the gasifier (e.g. oxides and salts of potassium, magnesium, calcium, sodium etc.) remain in the fuel bed and can be removed from the process via the ash. The feasibility of the concept was proven with wood chips made out of beech and spruce. The dust emissions in the flue gas were below the limits set by 1. BImSchV. However, pelletized biomass seemed to be unsuitable for the process due to its tendency to swell in contact with tar and water condensate produced in the upper cold region of the gasifier. To overcome these problems, a new gasifier, accounting for the volume increase of pelletized biomass caused by condensates, was designed.

**Keywords:** Gasification, Biomass, Stirling engine, Micro-CHP

## Introduction/Background

For micro-CHP units using woody biomass and ranging from 1 to 10 kW electrical output, thermo-dynamic processes with external input of heat seem to be more suitable than internal combustion engines. The main advantages are the omission of a gas cleaning system and a continuous com-bustion process resulting in lower emissions. Conventional biomass combustion approaches that utilize flue gas in the heat exchanger of a Stirling engine lead to unsolvable problems with regards to fouling and corrosion on the heat exchanger surfaces. Fouling decreases the heat transfer rate dramatically and on longer terms corrosion caused by chemical compounds containing sulfur and chlorine can severely damage the engines. Therefore, the main goal of the newly developed process is to overcome these problems by using a two stage gasification/combustion unit instead of a conventional combustion unit. Updraft gasifiers for wood chips are well known for producing combustible gases with a high content of tar. If the gas is used in a combustion chamber designed according to the requirements for clean combustion, tar can be combusted completely. If the fuel bed in the gasifier is rather high in comparison to the diameter of the gasifier, the produced gas can be cooled and filtered in the fixed bed. Chemical compounds (e.g. oxides and salts of potassium etc.) will condensate in the fixed bed and will be transferred to the ash. Due to swelling problems of pelletized biomass in contact with the condensates of moisture and tar, a conventional updraft gasifier with cylindrical geometry tends to be clogged. [1]–[5] To

overcome this problem, a new updraft gasifier geometry was designed to allow for a certain increase of the volume of the pellets without clogging.

## Experimental Setup

The main element of the test facility is an updraft gasifier that is supplied with fuel by an overhead pellet storage and a gasification medium (air) from bottom to top. See Fig. 1 for a cross section of the gasification reactor and Fig. 2 for a process flow chart. The producer gas is drawn off from the top end of the reaction chamber and is swirled before entering the burning chamber by tangentially supplying primary air. In order to improve burnout and temperature control, secondary air is supplied to the burning chamber through a spiraled double shell. The residual oxygen content is also controlled by secondary air supply ( $\lambda$  control). A Microgen [6] Stirling generator with 1 kW electrical maximum output is arranged in the flue gas channel of the burning chamber. A carbon heat exchanger, capable of using condensation energy of water vapor in the flue gas (condensing technology), is arranged downstream. The entire system is operated at slight negative pressure by an extraction fan. The Microgen Stirling generator is a 23 bars helium filled Stirling engine with linear generator.

The output was modulated for different operation points and characteristics according to Table 1 and Table 2 were received. Beechwood chips have been used as testing fuel. They are characterized in a highly homogeneous particle distribution, nearly no needle-shaped parts and running properties similar to wood pellets. The amount of potassium was analyzed in the wood chips and at different heights of the gasifier bed, in the dust of the flue gas, in the tar condensate and in the ash. During the test runs, the flue gas emissions (CO, NO<sub>x</sub>, dust, VOC) were measured downstream the combustion chamber. Besides measurements with a Testo 380, thorough parallel measurements with TSI scanning mobility particle sizers and measurements according to VDI 2066 were carried out. Attention should be paid to the fact that only batch experiments with limited duration could be carried out due to a limited fuel storage volume.

Table 1: Gasification Reactor Characteristics

$\dot{V}_{\text{air}}$	7...10	m <sup>3</sup> h <sup>-1</sup>
$u_s$	0.19...0.45	ms <sup>-1</sup>
$Q$	25...50	kW
$\eta_{\text{conversion}}$	65...80	%
$\lambda$	0.2...0.3	-

Table 2: Burning Chamber Characteristics

$Q$	17...40	kW
$T_{\text{adn,t}}$	900...1050	°C
$\lambda$	≈ 2.0	-
$T_{\text{exit}}$	600...750	°C

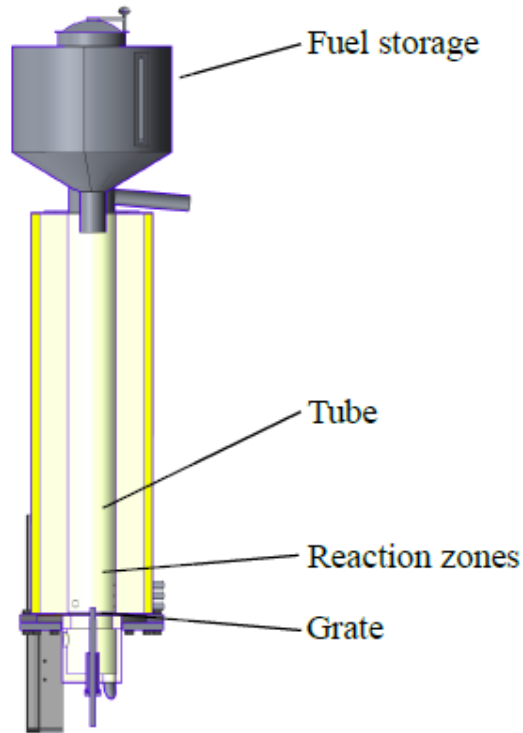


Fig. 1: Cross Section of Cylindrical Reactor Design

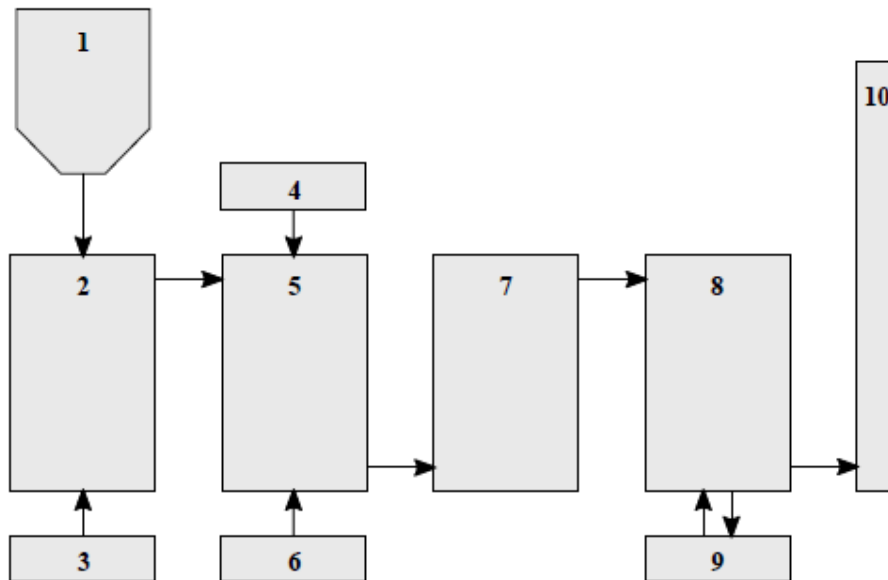


Fig. 2: Test Facility Process Flow Chart: (1) Pellet Storage, (2) Reactor, (3) Gasification Agent, (4) Primary Air, (5) Burning Chamber, (6) Secondary Air, (7) Stirling, (8) Carbon Heat Exchanger, (9) Heating Circuit, (10) Exhaust.

## Discussion and Results

See Fig. 3 for the measured producer gas composition at a typical test run. By means of a long reaction chamber and the counterflow of fuel and gasification medium, the bulk material (wood chips/pellets) acts as a filter, thus the producer gas contains a low amount of particles. Furthermore, the thermo-chemical conversion takes place in the lower part of the reaction chamber, resulting in a low producer gas temperature of about 65 C at the exit.

A result of the low producer gas temperature is that the salts and oxides that form in the oxidation zone already condense in the bulk material and remain in the gasification residues. Tar condensates in the producer gas are burned in the burning chamber. By swirling the producer gas with air, a thorough mixing and thus a high quality of the lean combustion can be achieved, resulting in low carbon monoxide and nitrogen oxide emissions. Upstream the carbon heat exchanger, the VDI 2066 measurements showed dust emissions from 0.26 to 3.95  $\text{mg}/\text{m}^3_{\text{norm,dry}}$  for operation points from 28 to 48 kW. An additional analysis showed that there was no measurable ash content in the tar condensate contained in the producer gas. Considering that condensing tar vapor is strongly attracted by particles by heterogeneous nucleation, this is another indication of the low particle count in the producer gas. Fig. 4 shows the results for the Testo 360 emission measurements for a typical test run. Potassium contents of the original fuel, the ash and filter dust of the measurement according to VDI 2066 were compared and it was verified that potassium salts and oxides nearly completely remained in the bulk material and concentrated in the ash. After about 20 test runs and ca. 100 hours of operation, the Stirling head has not shown measurable signs of corrosion or fouling.

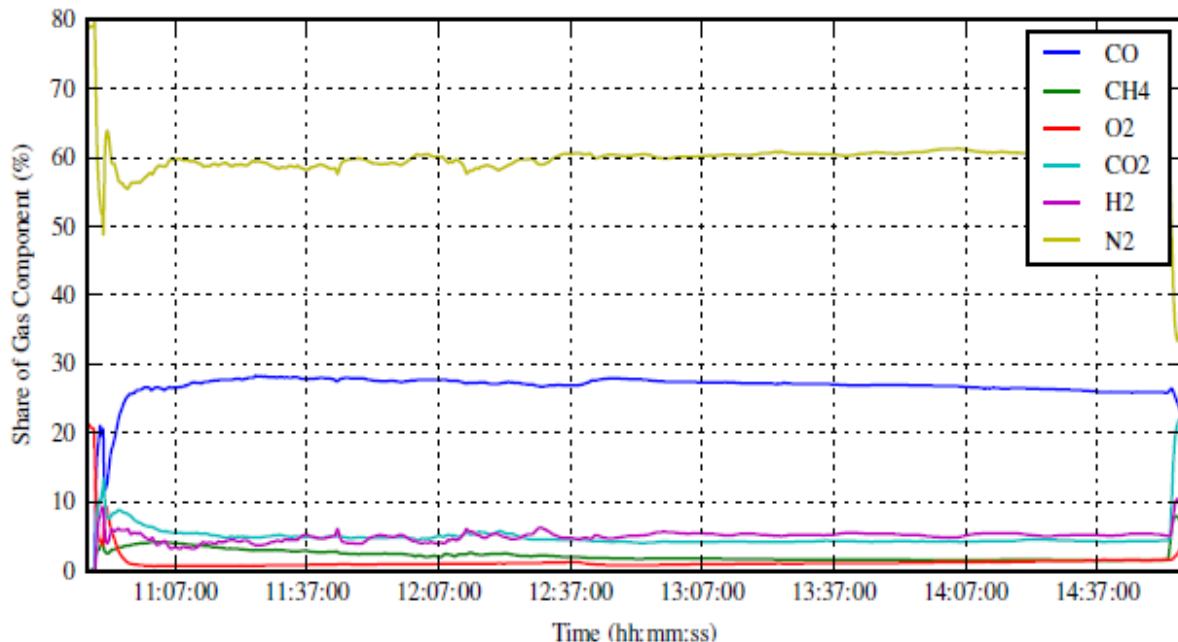


Fig. 3: Producer Gas Composition of Cylindrical Reactor in Volume Fractions

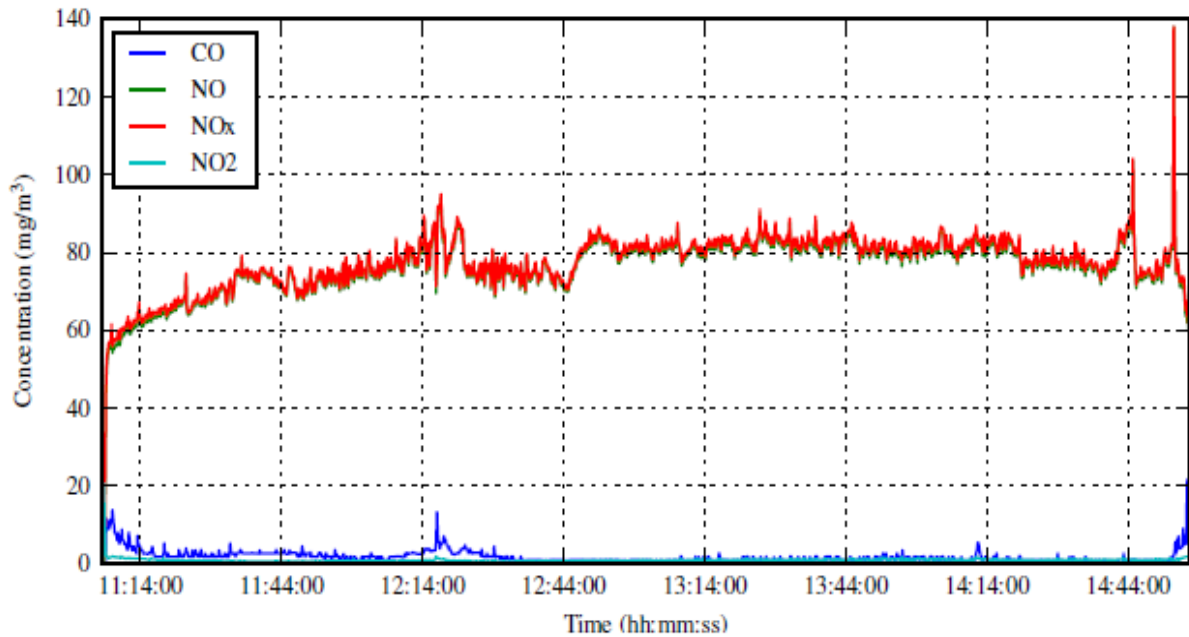


Fig. 4: Emission Measurement of Cylindrical Reactor (norm, dry, 13%  $O_{2,ref}$ )

Already at an early stage of testing pellets proved unsuitable for gasification in a cylindrical reaction chamber. They expand up to 2.5 times of the original volume when being exposed to water, resulting in clogging of the reaction tube and cavitation in the reaction zone. To account for the volume increase of pelletized biomass caused by condensates, a gasifier with variable reaction chamber volume was designed. See Fig. 5 for a cross section of the design. The volume increase was addressed by three measures: 1) A funnel that provides extra volume by moving up when swelling pellets exert a force and a 60 angle and smooth surface to enhance slipping of the pellets. 2) A spring mechanism to push back the funnel to its initial position and to apply a certain force to the pellets to avoid clogging. 3) An inner tube with its length being adjusted to control the height of the bulk pellet volume. The idea was to find a trade-off between the reduction of swelling problems and particle emissions (hypothesis: the lower the height, the lower the probability of clogging, however, the lower the bulk volume, the lower the filter effect and the higher the particle emissions).

Test runs with pellets and different lengths of the inner tube showed that the negative effects of swelling could be prevented with a reaction zone height of 450 mm (see also Fig. 5) and that a steady operation could be achieved. Similar to the test with beechwood chips, low exhaust gas emissions could be observed. Further analyses revealed a carbon fraction of 91% in the ash and that, quite contrary to the beechwood tests, only 3.6% of the potassium contained in the dry pellets (5000 mg/kg) remained in the ash. About 4.1% remained in the bulk volume. Thus, in terms of figures, 92.3% of the potassium is distributed in the producer gas. This is likely caused by the increased producer gas temperature of 140 C, the lowered bulk volume height (1600 mm in the first reactor design) and the significantly higher dust content in the exhaust gas downstream the burning chamber

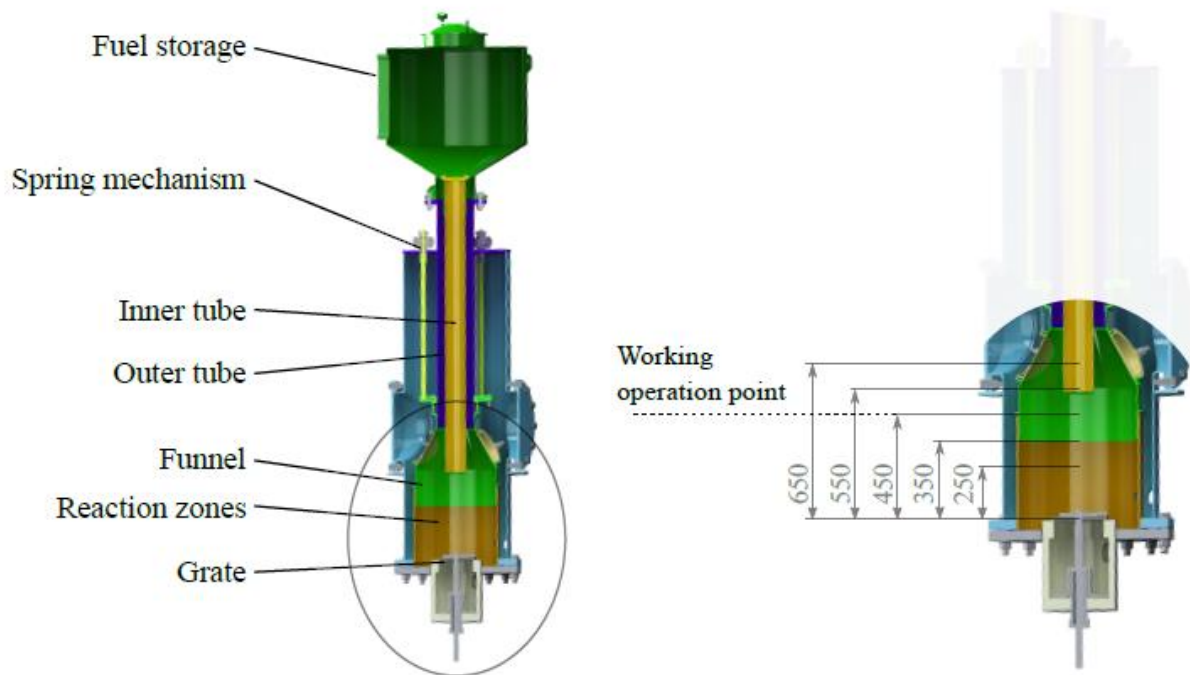


Fig. 5: Pellet Reactor Design. Left: Cross Section, right: Resulting Reaction Zone Heights for Different Lengths of the Inner Tube, Dimensions in mm.

### Conclusion/Summary

A biomass fired micro-scale CHP unit based on a 1 kW Stirling engine has been developed with a focus on overcoming the well known fouling and corrosion problems that occur at the heat ex-changer of the Stirling engine. The objective was met by combining the principles of an up-draft gasifier that comprises a fixed biomass fuel bed with a large height to diameter ratio and a low-emission combustion chamber using a swirl burner for the produced combustible gas. A low producer gas temperature at the outlet of the gasifier was achieved and the chemical compounds produced in the hot oxidizing zone of the gasifier were shown to remain in the fuel bed and ash. The feasibility of the concept was proven with beechwood chips. The resulting emissions clearly satisfied the limit values set by the 1. BImSchV [7]. For the utilization of pellets, a new reactor was designed. The prevention of negative impacts of pellet swelling and a steady operation with pellets could be accomplished. However, the potassium contained in the pellets no longer remained in the fuel and ash. A reliable operation of a Stirling engine, as shown with beechwood chips, cannot be expected.

### Acknowledgements

This research and development project was funded by the Bavarian State Ministry of Education, Science and the Arts within the framework TWO and the German Federal Ministry of Education and Research (BMBF) within the framework SIGNO.

### References

- [1] Reil, S. and Beer, S. and Ultsch, C. and Meiler, M. and Hornung, A., "Thermochemical air-steam gasification of biomass and biomass chars in an updraft gasifier: Effect of air/steam ra-tio," presented at the Integration of Sustainable Energy Conference iSEneC, Nurnberg," 2016.

- [2] Reil, S. and Beer, S. and Ultsch, C. and Meiler, M. and Hornung, A., “Thermochemical gasi-fication of char from biomass with subsequent combustion for heat supply in endothermal biomass conversion processes,” presented at the 24th European Biomass Conference, Ams-terdam, 2016.
- [3] S. Reil and S. Beer, “Betriebserfahrungen bei kleinen Festbettvergasern,” presented at the OTTI Profi-Seminar KWK mit Biomasse, Neumarkt, 2013.
- [4] S. Beer, D. Pocher, D. Hummel, and L. Kinzler, “Entwicklung eines neuartigen Verfahrens zur Mikro-KWK mit biogenen Energietragern,” in Forschungsbericht 2016, Ostbayerische Technische Hochschule (OTH) Amberg-Weiden, 2016.
- [5] S. Reil, S. Beer, and J. Karl, “Experimental study on the impact of gasification conditions on process stability and tar yield in stratified downdraft gasifiers,” presented at the 4th Interna-tional Symposium on Gasification and its Applications, Vienna, 2014.
- [6] Microgen Engine Corporation. (2018), [Online]. Available: <http://www.microgen-engine.com/products/engines/>.
- [7] Bundesministerium der Justiz und für Verbraucherschutz. (2018). 1. BImSchV – Verordnung über kleine und mittlere Feuerungsanlagen vom 26. Januar 2010 (BGBl. I S. 38), die zuletzt durch Artikel 16 Absatz 4 des Gesetzes vom 10. März 2017 (BGBl. I S. 420) geändert worden ist, [Online]. Available: [https://www.gesetze-im-internet.de/bimschv\\_1\\_2010/BJNR003800010.html](https://www.gesetze-im-internet.de/bimschv_1_2010/BJNR003800010.html)

